รายงานวิจัยฉบับสมบูรณ์

วัสดุผสมซีเมนต์และคอนกรีตที่เป็นมิตรต่อสิ่งแวดล้อม ภาคผนวก ก. การตีพิมพ์ในวารสารวิชาการระดับนานาชาติ ภาคผนวก ข. การจดสิทธิบัตร

โดย

ศ.ดร. ปริญญา จินดาประเสริฐ และคณะ

30 สิงหาคม 2560

Mechanical and Thermal Properties of Recycling Lightweight Pervious Concrete

Prinya Chindaprasirt, Peem Nuaklong, Yuwadee Zaetang, Purimpat Sujumnongtokul & Vanchai Sata

Arabian Journal for Science and Engineering

ISSN 1319-8025
Volume 40
Number 2

Arab J Sci Eng (2015) 40:443-450
DOI 10.1007/s13369-014-1563-z

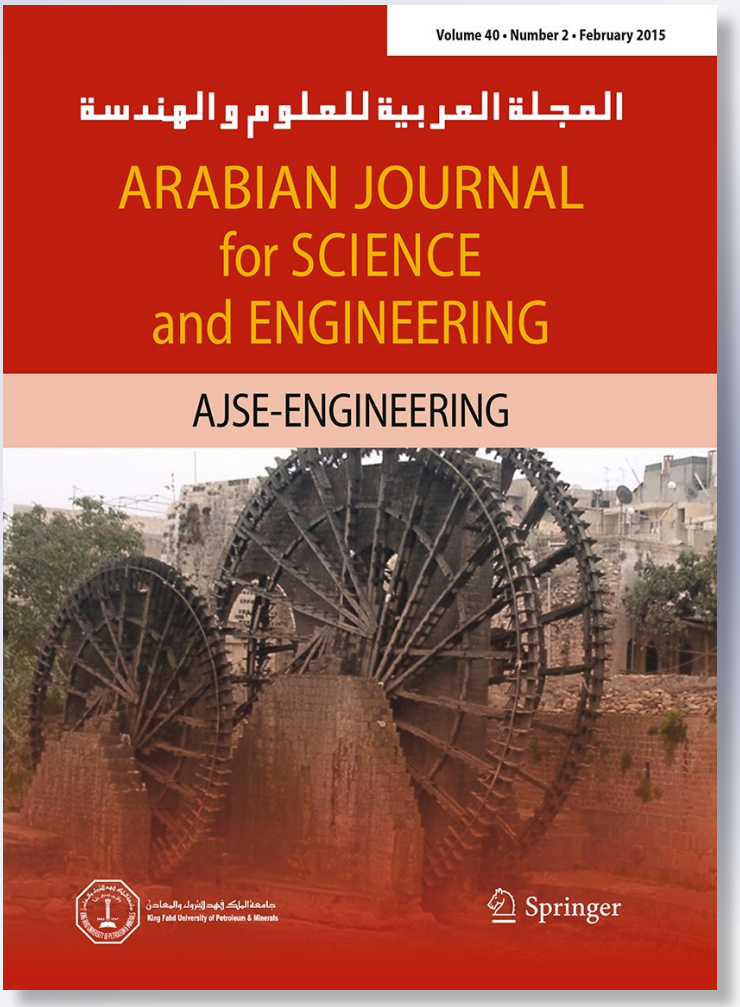

Springer

Your article is protected by copyright and all rights are held exclusively by King Fahd University of Petroleum and Minerals. This e-offprint is for personal use only and shall not be self-archived in electronic repositories. If you wish to self-archive your article, please use the accepted manuscript version for posting on your own website. You may further deposit the accepted manuscript version in any repository, provided it is only made publicly available 12 months after official publication or later and provided acknowledgement is given to the original source of publication and a link is inserted to the published article on Springer's website. The link must be accompanied by the following text: "The final publication is available at link.springer.com".

Author's personal copy

Arab J Sci Eng (2015) 40:443–450
DOI 10.1007/s13369-014-1563-z

RESEARCH ARTICLE - CIVIL ENGINEERING

Mechanical and Thermal Properties of Recycling Lightweight Pervious Concrete

Prinya Chindaprasirt · Peem Nuaklong · Yuwadee Zaetang · Purimpat Sujumnongtokul · Vanchai Sata

Received: 23 May 2014 / Accepted: 30 November 2014 / Published online: 27 December 2014
© King Fahd University of Petroleum and Minerals 2014

Abstract This paper presents an investigation of the use of recycled lightweight aggregate from waste autoclaved aerated concrete block to make lightweight pervious concrete (LWPC). The effects of fine sand (SA) and fly ash (FA) as additive materials on LWPC properties were also studied. The density, total void ratio, water permeability, compressive strength, splitting tensile strength, flexural strength, thermal conductivity, and surface abrasion of LWPC were tested. The results showed that all LWPCs had low density of 775–900 kg/m^3 and low thermal conductivity coefficient of 0.15–0.27 W/m K. The use of SA and FA improved the compressive strength, splitting tensile strength, flexural strength, and abrasion resistance of LWPC, while the total void ratio and water permeability seemed to reduce. The low thermal conductivity and low density of LWPC with reasonable 28-day compressive strength of 1.9–4.1 MPa suggested that it is suitable for use as thermal insulating concrete.

Keywords Lightweight recycled aggregate · Autoclaved aerated concrete · Porous concrete · Thermal conductivity · Additive material · Insulating concrete

P. Chindaprasirt · P. Nuaklong · V. Sata (✉)
Sustainable Infrastructure Research and Development Center, Department of Civil Engineering, Faculty of Engineering, Khon Kaen University, Khon Kaen 40002, Thailand
e-mail: vancsa@kku.ac.th

Y. Zaetang
Department of Civil and Environmental Engineering, Faculty of Science and Engineering, Kasetsart University, Chalermphrakiat Sakon Nakhon Province Campus, Sakon Nakhon 47000, Thailand

P. Sujumnongtokul
Department of Mechanical Engineering, Faculty of Engineering, Khon Kaen University, Khon Kaen 40002, Thailand

1 Introduction

The use of lightweight aggregate concrete (LWC) is beneficial in terms of reducing structural dead load, improving sound and thermal insulations, and ease of handling and transportation. According to ACI 213 [1], LWC can be classified into different types based on density and compressive strength. The low-density LWC with compressive strengths of 0.7–6.9 MPa is used as insulating concrete. Structural LWC with minimum compressive strength of 17.2 MPa is used to reduce structural dead load. Moderate strength LWC with compressive strengths of 6.9–17.2 MPa is sometimes designated as "fill" concrete, and its thermal characteristics are intermediate.

Generally, the density of concrete can be reduced by using lightweight aggregate (LWA) or replacing solid part with air void [2]. LWA used for producing LWC is generally a porous material, which can be classified into two groups, viz. natural LWA (such as pumice and diatomite) and artificial LWA (such as perlite and expanded clay) [3]. Many researchers [4–7] found that recycled materials can be used as LWA in LWC. Kralj [4] presented an experimental study of LWC with recycled aggregate containing expanded glass and showed that the thermal conductivity was low at 0.19–0.22 W/m K compared with other masonry materials, which were necessary for the production of a low-cost and environmentally friendly LWC. Fraj et al. [5] found that the use of low-density coarse aggregate from valorization of polyurethane foam waste enabled the reduction of concrete dry density by 29–36 % compared with that of normal weight concrete. Recycled lightweight block was used as aggregates in making lightweight geopolymer concrete with satisfactory compressive strengths (1.0–16.0 MPa) and densities (860–1,400 kg/m^3), which was suitable for use as LWC for wall and partition [6]. The long-term behaviors of LWC produced by both crushed structural

Author's personal copy

and non-structural lightweight concretes were also studied [7].

Pervious concrete is a special type of LWC consisting of Portland cement, coarse aggregate, little or no fine aggregate, admixture, and water [8]. It contains high porosity to allow air or water to move through the concrete and gives its low density. It has been developed as an environmentally friendly material and used in a number of civil engineering applications. In addition, the high porosity gives useful characteristics in thermally insulating and sound absorption [8]. The use of LWAs gave lightweight pervious concrete (LWPC) with very low density and excellent thermal insulating property [9], while their compressive strengths were also lowered. However, many researchers [10–12] found that the reduction of porosity in cement matrix by incorporating fine materials such as fly ash, metakaolin, rice husk ash, and biomass ash in concrete mixture contributes to the strength development as a result of both chemical and physical effects.

In this study, recycled lightweight aggregate (RLWA) from waste autoclaved aerated concrete was used to make LWPC. To improve its strengths, fine natural sand (SA) and high-calcium fly ash (FA) were used as fine additive materials. The parameters of study were the types of fine materials (SA and FA) and the amount of addition (10, 20, and 30 % by weight of cement). The density, total void ratio, water permeability, compressive strength, splitting tensile strength, flexural strength, thermal conductivity, and surface abrasion resistance tests were carried out. The obtained data are valuable for the use of new alternative lightweight concrete with acceptable properties and also to recycled waste materials.

2 Materials and Methods

2.1 Materials

In this study, Portland cement type I (OPC) with specific gravity of 3.15 and Blaine fineness of 3,120 cm^2/g, standard type F superplasticizer (SP), and tap water were used. The RLWA was obtained from broken autoclaved aerated concrete block from manufacturing and construction site. The original autoclaved aerated concrete block in accordance with TIS 1505 [13] with compressive strengths of 5.0–7.5 MPa was selected. They were crushed and sieved into particle sizes of 4.8–9.5 mm with fineness modulus (FM) of 7.0. The specific gravity of RLWA was 1.16. Its dry-rodded density was 335 kg/m^3, and its dry-loosed density was 300 kg/m^3, which were lower than 800 kg/m^3 as specified for LWA according to ACI 213 [1]. The Los Angeles abrasion loss was 90.0 % with water absorption of 68.4 %. The high water absorption is due to the high porosity and rough surface of RLWA particle, which is in line with other published results [6,9]. Figure 1 shows the particle shapes and surface textures of RLWA. High-calcium fly ash (FA) by-product from Mae Moh Electricity Power Station in northern Thailand and fine natural sand (SA) were used as fine additive materials. The chemical compositions of OPC, RLWA, SA, and FA are presented in Table 1, while Table 2 shows particle size distribution of these materials. The FM of SA was 1.84. The values of specific gravity of SA and FA were 2.58 and 2.47, respectively.

Fig. 1 Recycled lightweight aggregate (RLWA)

Table 1 Chemical composition of materials

Chemical composition (%)	OPC	RLWA	Fine sand (SA)	Fly ash (FA)
SiO_2	14.44	38.48	94.66	27.94
Al_2O_3	2.71	2.45	2.10	10.97
Fe_2O_3	3.43	1.83	0.95	12.66
CaO	70.44	36.33	0.21	33.37
MgO	0.86	0.71	0.23	2.39
Na_2O	0.18	0.26	0.25	1.99
K_2O	0.57	1.48	0.39	2.36
SO_3	4.29	5.71	0.14	6.29
TiO_2	0.25	0.11	0.24	0.44
LOI	2.4	12.40	0.6	0.9

2.2 Mix Proportions and Preparation of Samples

The typical mixture consist of 388 kg/m^3 of OPC and 630 kg/m^3 of RLWA. The water to binder ratio was kept constant at 0.24. In order to control concrete workability, the SP in the range of 1–3 % by weight of binder was used to maintain the flow of cement paste at 170–180 mm [14]. The SA and FA were used as additives at the levels of 10, 20, and 30 % by weight of binder. To control the water absorption of aggregates, RLWA with saturated surface dry condition were used

Author's personal copy

Table 2 Particle size distribution of additive materials

Materials	% Passed on #100 Sieve (150 μm)	% Passed on #200 Sieve (75 μm)	% Passed on #325 Sieve (45 μm)
SA	17.0	5.8	2.4
FA	100.0	78.4	61.0

Table 3 Mix proportions of pervious concretes (kg/m^3)

Mixes	OPC	Additive materials		Water	SP	RLWA
		SA	FA			
CP	388	–	–	94	4.85	630
SA10	388	39	–	102	5.82	630
SA20	388	78	–	112	6.79	630
SA30	388	117	–	122	7.76	630
FA10	388	–	39	102	5.82	630
FA20	388	–	78	112	6.79	630
FA30	388	–	117	122	7.76	630

in the mixture. The total of 7 mix proportions of LWPC is summarized in Table 3.

After being mixed, the fresh concretes were cast in three types of molds. The 100 × 200 mm cylindrical samples were for compressive strength, splitting tensile strength, density, total void ratio, and water permeability tests. The 100 × 100 × 400 mm samples were for the flexural strength testing. The 300 × 300 × 35 mm samples were for thermal conductivity and surface abrasion resistance tests. Generally, pervious concrete was placed with minimal or no compaction at all. However, for a low water content and very low slump mix, some compaction could be applied [15]. To obtain uniform pervious concrete samples, they were compacted using vibrating table for 10 s. After that, the cast samples were covered with plastic sheet, demolded after 24 h, and stored in a moist room. The samples were then taken out from the moist room and dried in air before testing.

2.3 Testing Procedures

The density, total void ratio, and water permeability coefficient of LWPC were tested using 100 × 200 mm cylindrical samples. Density and total void ratio of LWPC were tested in accordance with ASTM C 1754 [16]. The water permeability coefficient was measured using the constant head method [8]. To prevent flow between sample and surface of measuring cylinder, the side of cylindrical sample was wrapped by rubber tube and tightened by circular clamps. The coefficient of water permeability was calculated as steady-state flow following Darcy's Law as shown in Eq. (1).

$$k = QL/HAt \quad (1)$$

where k is the water permeability coefficient (cm/s), Q is the quantity of water (cm^3) over time t (s), L is the length of sample (cm), H is the water head (cm), and A is the cross-sectional area of sample (cm^2).

LWPC samples were tested for compressive, splitting, and flexural strengths in accordance with ASTM C 39 [17], ASTM C 496 [18], and ASTM C 293 [19], respectively. The thermal conductivity coefficients were determined using commercially available instrument (ISOMET2114, Applied Precision Ltd.). It was performed with surface probe method. The water content of the specimens strongly affects their thermal conductivity. A variation of as much as 5–6 % on the conductivity can be expected for each % of water content [1]. Therefore, all samples were air-dried to a constant weight (water content of 2.8–3.0 %) to reduce the effects of humidity before the thermal conductivity tests.

In addition, surface abrasion resistance was tested by the rotating-cutting method in accordance with ASTM C 944 [20]. The samples were left to air-dry for 1 day before the test. The sample was abraded for 30 s after contact between the cutter and the surface with 98 N loads on the surface. All the tests were carried out at the age of 28 days, and the results were the average of three samples.

3 Results and Discussions

3.1 Density

The density, total void ratio, water permeability, and their relative values (the value in percentage as compared to those of CP concrete) of LWPC are shown in Table 4. It can be seen that the density of all pervious concretes varied between 755 and 900 kg/m^3, which were about 3 times lower than that of conventional concrete (2400 kg/m^3). This was due to the very low density of recycled coarse aggregate (300–335 kg/m^3) and the high void content of pervious concrete. According to ACI 213 [1], LWPC in this report may be classified as low-density LWC. The densities of concretes are reduced substantially by replacing normal aggregate with LWA [2,5,21–23]. The adding of fine materials in pervious concrete mixtures increased the paste content, resulting in increased density. For example, the densities of LWPCs containing 10, 20, and 30 % SA were 820, 850, and 900 kg/m^3, respectively, while the density of the control pervious concrete (CP) was 775 kg/m^3. The density values increased with the adding for both FA and SA in a narrow range between 820 and 900 kg/m^3 due to the small difference in the specific gravity of FA and SA.

3.2 Total Void Ratio and Water Permeability Coefficient

Table 4 gives the results of the total void ratios, water permeability coefficient, and theirs relative values compared with

Author's personal copy

Table 4 Density, total void, water permeability coefficient, and relative values of LWPC

Mixes	Density (kg/m^3)-(Relative values) (%)	Total void ratio (%)-(Relative values) (%)	Water permeability coefficient (cm/s)-(Relative values) (%)
CP	775-(100)	23.7-(100)	1.16-(100)
SA10	820-(106)	22.0-(93)	0.75-(65)
SA20	850-(110)	19.5-(82)	0.17-(15)
SA30	900-(116)	18.7-(79)	0.17-(15)
FA10	820-(106)	22.4-(95)	0.81-(70)
FA20	865-(112)	19.1-(81)	0.40-(34)
FA30	865-(112)	14.8-(62)	0.24-(21)

control concrete (CP). The total void ratios ranged from 14.8 to 23.7 %, and water permeability coefficients from 0.17 to 1.16 cm/s, which were similar to the values reported by ACI 522 [8]. The control concrete had the highest total void ratio of 23.7 % and water permeability coefficient of 1.16 cm/s. With added fine materials, the paste covering the coarse aggregates of LWPCs was thicker than that without fine materials. The increase in paste content and the reduction in total void ratio of LWPCs were observed as a result of the addition of fine materials. For example, SA10, SA20, and SA30 concretes had the total void ratios of 22.0, 19.5, and 18.7 %, which were 93, 82, and 79 % of the control concrete, respectively. For the incorporation of FA, the same trend of results was found.

The results of water permeability test showed a similar trend to that of total void ratios. The CP concrete had water permeability coefficient of 1.16 cm/s. As the amount of fine materials increased, the water permeability coefficient decreased to 0.17–0.75 and 0.24-0.81 cm/s for SA and FA concretes, respectively. With added fine materials, the high cement paste content reduced the connected pore and water permeability coefficients of LWPCs. The relationship between water permeability coefficient and total void ratio of LWPCs was described by Eq. (2).

$$k = 0.0063e^{0.2082(V)} \quad (2)$$

where k is coefficient of water permeability coefficient (cm/s) and V is total void ratio (%).

This relationship was similar to that of pervious concrete containing various LWAs [9] as shown in Fig. 2. In addition, many researchers [24–26] reported that the water permeability of normal weight pervious concrete also increased exponentially with the void ratio.

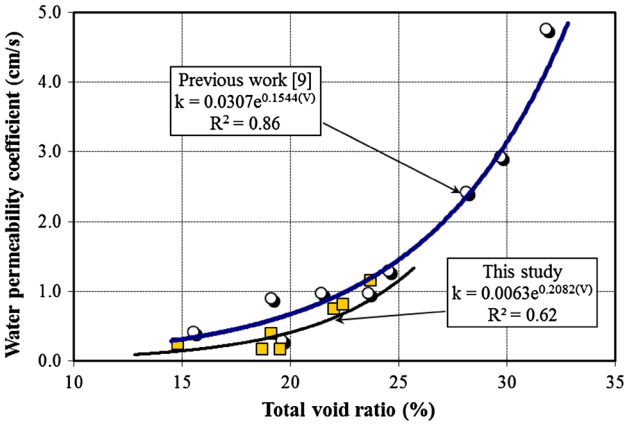

Fig. 2 Relationship between water permeability coefficient and total void ratio of LWPC

3.3 Compressive, Splitting Tensile, and Flexural Strengths

The compressive strength, splitting tensile strength, flexural strength, and relative strength of LWPC at the age of 28 days are shown in Table 5. The strengths of LWPC in this study were low as expected with compressive strengths of 1.9–4.1 MPa, splitting tensile strength of 0.46–0.79 MPa, and flexural strengths of 0.73–1.14 MPa. This was due the very low density and high porosity of LWPC. Unal et al. [27] studied LWC with diatomite and reported that its low strength was justified by the weak interconnection of its microstructure. The CP concrete had lowest compressive strength of 1.9 MPa. However, the adding of fine materials gave high paste content and resulted in a decrease in total void ratio. Therefore, the strengths increased with increasing amount of fine materials. For example, the 28-day compressive strength of SA10, SA20, and SA30 concretes were 2.5, 2.5, and 2.7 MPa, respectively. Compared with CP concrete, the compressive, splitting tensile, and flexural strengths of LWPCs containing fine materials increased 21–116, 11–72, and 4–56 %, respectively.

It should be noted that the strengths of LWPCs containing FA increased more than those of SA. It is likely that these results were due to the role of FA in the pozzolanic reaction and packing effect, while the non-reactive SA gave only the packing effect [12,28]. In addition, the volume of FA was higher than that of SA for the same weight of addition. This resulted in reduced total void ratio of mix with FA compared with that with SA. Adding 30 % FA by weight of cement (FA30) gave the highest strength of 4.1 MPa (216 %

Author's personal copy

Table 5 Strength and relative strength at 28 days of LWPC

Mixes	Compressive strength (MPa)-(Relative values) (%)	Splitting tensile strength (MPa)-(Relative values) (%)	Flexural strength (MPa) -(Relative values) (%)
CP	1.9-(100)	0.46-(100)	0.73-(100)
SA10	2.5-(132)	0.50-(109)	0.74-(104)
SA20	2.5-(132)	0.66-(143)	0.94-(129)
SA30	2.7-(142)	0.63-(137)	1.14-(156)
FA10	2.4-(126)	0.63-(137)	0.84-(115)
FA20	3.0-(158)	0.71-(154)	0.90-(123)
FA30	4.1-(216)	0.79-(172)	1.14-(156)

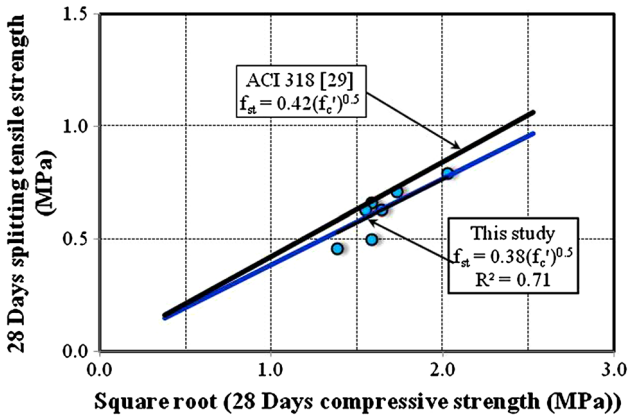

Fig. 3 Relationship between compressive strength and splitting tensile strength of LWPC

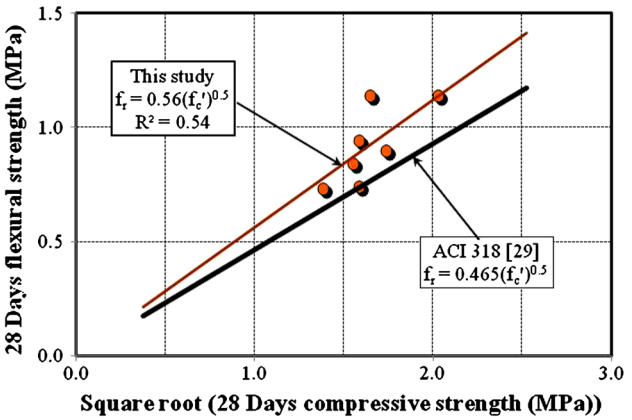

Fig. 4 Relationship between compressive strength and flexural strength of LWPC

of CP), splitting tensile strength of 0.79 MPa (172 % of CP), and flexural strength of 1.14 MPa (156 % of CP).

The results showed that as compressive strength increased, the splitting tensile and flexural strengths also increased. The square root of compressive strengths was plotted against the splitting tensile strengths and flexural strengths and compared with those of structural LWC (multiplied the square root of normal concrete compressive strength by a λ coefficient of 0.75) as suggested by ACI 318 [29] and shown in Figs. 3 and 4. Equation (3) was derived for the splitting tensile strength, while Eq. (4) was for the flexural strength of LWPC in this study.

$$f_{st} = 0.38(f_c')^{0.50} \quad (3)$$

$$f_r = 0.56(f_c')^{0.50} \quad (4)$$

where f_{st} is the splitting tensile strength (MPa), f_r is the flexural strength (MPa), and f_c' is the compressive strength of LWPC (MPa).

The results also showed that as the total void ratio reduced, the compressive strength and density of LWPC increased. Crouch et al. [30] indicated that the compressive strength of pervious concrete reduced linearly with the increasing effective void content. In addition, Kevern et al. [25] demonstrated that the unit weight of pervious concrete also decreased linearly with the decreasing void ratio. The compressive strength and density of LWPC in this study were plotted as a function of total void ratio as shown in Fig. 5. By linear regression, the empirical relationships were derived as shown in Eqs. (5) and (6).

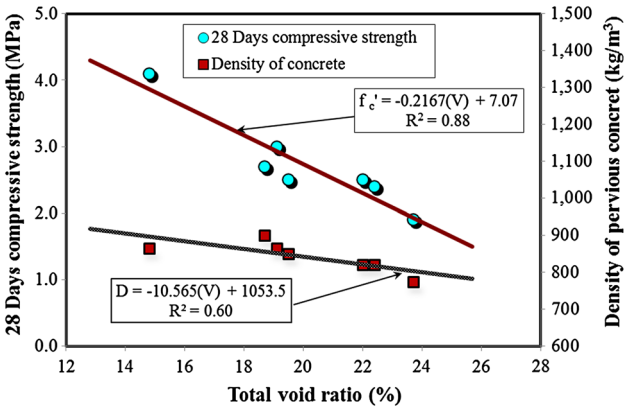

Fig. 5 Relationship between total void ratio, 28 days compressive strength, and density of LWPC

Author's personal copy

Table 6 Thermal conductivity and weight losses from abrasion resistant test of LWPC

Mixes	Thermal conductivity (W/m K)	Weight losses from abrasion test (g)
CP	0.15	11.2
SA10	0.17	11.3
SA20	0.21	11.2
SA30	0.27	9.9
FA10	0.20	10.1
FA20	0.21	10.0
FA30	0.22	9.5

Fig. 6 External and internal surface of LPWC

$$f_c' = -0.2167(V) - 7.07 \quad (5)$$

$$D = -10.565(V) - 1053.5 \quad (6)$$

where f_c' is the compressive strength (MPa), D is the density of aggregate (kg/m^3), and V is total void ratio (%) of LWPC.

3.4 Thermal Conductivity

The results of thermal conductivity coefficient and weight losses from abrasion test of LWPCs are shown in Table 6. All LWPCs had low thermal conductivity ranging from 0.15 to 0.27 W/m K depending on the type and content of addition. This was due to the high porosity with low density of LWA [31,32] and high void content of LWPC [33,34]. The high void content from pervious concrete and the porosity of aggregate is shown in Fig. 6. The thermal conductivity values of LWPC in this study were nearly the same as those in the previous research [9], which reported that the thermal conductivity of pervious concrete with different types of LWAs ranged from 0.16 to 0.25 W/m K. The control pervious concrete (CP) presented the lowest thermal conductivity coefficient of 0.15 W/m K. The use of all fine additive materials significantly increased the thermal conductivity coefficient of LWPCs. The adding of fine materials increased the paste content, reduced the total void ratio, and increased overall density of LWPC, resulting in the rise of their thermal conductivity coefficient [35]. For example, in SA series, the total void ratio decreased from 22.0 to 18.7 %, the density increased from 820 to 900 kg/m^3, and thermal conductivity increased from 0.17 to 0.27 W/m K. In contrast, the use of FA also increased the thermal conductivity coefficient but in the narrow range of 0.20–0.22 W/m K.

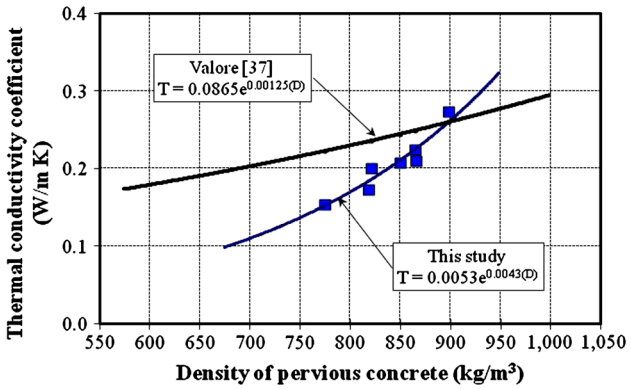

Fig. 7 Relationship between density and thermal conductivity coefficient of LWPC

Topcu and Uygunoglu [31] investigated the properties of LWC made with diatomite and pumice after autoclaved curing. By increasing dry density of LWC from 900 to 1,500 kg/m^3, the thermal conductivity coefficient increased from 0.13 to 0.52 W/m K. Demirboga and Gul [36] studied the use of silica fume and fly ash as cement replacement in concrete containing expanded perlite aggregate. The thermal conductivity decreased with the increases in silica fume and fly ash between 14 and 18 %, and the densities of concrete decreased from 522 to 483 kg/m^3.

The relationship between density and thermal conductivity coefficient of LWPC in this study was plotted and compared with equation of Valore [37] as given in Fig. 7. From this relationship of LWPC in this study, the following Eq. (7) is proposed. The large difference between the suggested curve and that of Valore [37] may be due to the narrow range of LWPC density in this study. Moreover, the Valore equation [37] was built for masonry and structural concrete with density range from 400 to 2,200 kg/m^3. The type of fine material had little influence on thermal conductivity (0.15–0.27 W/m K) due to the small difference in the density values of all LWPCs (775–900 kg/m^3).

$$T = 0.0053e^{0.0043(D)} \quad (7)$$

where T is the coefficient of thermal conductivity (W/m K) and D is the density of f LWPC (kg/m^3).

Author's personal copy

The low thermal conductivity (0.15–0.27 W/m K) and low density (755–900 kg/m^3) indicated better insulating properties of LWPC compared with the values of 0.25–1.00 W/m K and 720 to 2,000 kg/m^3, respectively, of the other construction materials, viz. fire brick, aerated brick, fly ash brick, and hollow lightweight concrete block [34]. LWPC in this study could thus be used for thermal insulation concrete.

3.5 Surface Abrasion Resistance

The surface abrasion in terms of average weight losses in abrading of LWPC are presented in Table 6. The better surface abrasion resistance is presented by a lower average weight loss value. Although the differences in the weight loss of the samples due to abrasion were not large (9.5–11.3 g), there was a tendency that the low weight loss was associated with the large addition of FA and SA, which corresponded to the increases in strengths of concrete. The incorporation of 10 and 20 % SA resulted in almost no change in the resistance to abrasion resistance as the weight losses of concrete with 0, 10 and 20 % SA were approximately the same at 11.2–11.3 g, while the use of 30 % SA showed higher abrasion resistance with weight loss of 9.9 g. The abrasion resistance of LWC increased with the increase in the FA content due to the increase in compressive strength [38]. The weight losses of concretes with 0, 10, 20 and 30 % FA were 11.2, 10.1, 10.0, and 9.5 g, respectively, which were lower than those of SA concretes. The increase in abrasion resistance of LWAC with fine materials was due to the increase in paste content, reduced void ratio, and increase in the strength of concrete. Many researchers [38–40] mentioned that abrasion resistance was related to compressive strength of concrete. The adding of SA as inert material produced the filler effect and thus reduced the void of concrete, but the adding of FA as pozzolanic material results in both the pozzolanic and filler effect and hence produced better compressive strength and abrasion resistance. Atis [38] reported that the abrasion resistance of concretes containing a large amount of fly ash increased with the increase in compressive strength. In addition, Yuksel et al. [40] studied on the use of granulated blast-furnace slag (GBFS) as fine aggregate in production of plain concrete element and found that the aggregate–GBFS–cement interface characteristics of GBFS concrete were better than normal concrete and thus results in improved surface abrasion resistance.

4 Conclusions

The RLWA from broken autoclaved aerated concrete blocks could be used as coarse aggregate to make LWPC with low density of 775–900 kg/m^3 and low thermal conductivity coefficient of 0.15–0.27 W/m K.

The additions of both fine sand (SA) and fly ash (FA) at 10–30 % by weight of cement in LWPC were effective for increasing the compressive, splitting tensile, and flexural strengths by 32–116, 9–72, and 4–56 %, respectively, while their water permeability coefficients and total void ratios were reduced from 1.16 to 0.17 cm/s and 23.7 to 14.8 %, respectively. However, the increasing of strength was faced with the slight increases both density and thermal conductivity coefficient from 775 to 900 kg/m^3 and 0.15 to 0.27 W/m K, respectively. The adding of FA was more effective than SA for the increasing of LWPC strength and abrasion resistance due to the additional pozzolanic property of FA. In addition, the use of FA offers a greater potential to provide economic benefits, preserves virgin resources, and avoids negative environmental impacts.

The LWPC with low thermal conductivity and low density in this study could be used for thermal insulation concrete. In addition, LWPC is a new environmental friendly lightweight concrete, which is suitable for various applications in construction industry.

Acknowledgments This work was supported by the Higher Education Research Promotion and National Research University Project of Thailand, Office of the Higher Education Commission, through the Advanced Functional Materials Cluster of Khon Kaen University. The authors also would like to acknowledge the support of the Thailand Research Fund (TRF) and Khon Kaen University under the TRF Senior Research Scholar, Grant No. RTA5780004.

References

1. ACI Committee 213.: Guide for structural lightweight aggregate concrete (ACI 213R-03), American Concrete Institute, Detroit (2003)
2. Aguilar, A.A.; Diaz, O.B.; Garcia, J.I.E.: Lightweight concretes of activated metakaolin-fly ash binders, with blast furnace slag aggregates. Constr. Build. Mater. **24**, 1166–1175 (2010)
3. Sales, A.; Souza, F.R.de ; dos Santos, W.N.; Zimer, A.M.; doCoutoRosa Almeida, F.: Lightweight composites concrete product with water treatment sludge and sawdust: Thermal properties and potential application. Constr. Build. Mater. **24**, 1069–1077 (2010)
4. Kralj, D.: Experimental study of recycling lightweight concrete with aggregate containing expanded glass. Process Saf. Environ. Prot. **87**, 267–273 (2009)
5. Fraj, A.B.; Kismi, M.; Mounanga, P.: Valorization of coarse rigid polyurethane foam waste in lightweight aggregate concrete. Constr. Build. Mater. **24**, 1069–1077 (2010)
6. Posi, P.; Teerachanwit, C.; Tanutong, C.; Limkamoltip, S.; Lertnimoolchai, S.; Sata, V.; Chindaprasirt, P.: Lightweight geopolymer concrete containing aggregate from recycle lightweight block. Mater. Des. **52**, 580–586 (2013)
7. Alexander Bogas, J.; Brito, J.de ; Cabaco, J.: Long-term behavior of concrete produced with recycled lightweight expanded clay aggregate concrete. Constr. Build. Mater. **65**, 470–479 (2014)
8. ACI Committee 522.: Pervious Concrete (ACI 522R-10), American Concrete Institute, Detroit (2010)

Author's personal copy

9. Zaetang, Y.; Wongsa, A.; Sata, V.; Chindaprasirt, P.: Use of lightweight aggregates in pervious concrete. Constr. Build. Mater. **48**, 585–591 (2013)
10. Kathirvel, P.; Saraswathy, V.; Karthik, S.P. Sekar A.S.S.: Strength and durability of quaternary cement concrete made with fly ash, rice husk ash and limestone powder. Arab. J. Sci. Eng. **38**, 589–598 (2013)
11. Guneyisi, E.; Gesoglu, M.; Mermerdas, K.: Improving strength, drying shrinkage, and pore structure of concrete using metakaolin. Mater. Struct. **41**, 937–949 (2008)
12. Sata, V.; Tangpagasit, J.; Jaturapitukkul, C.; Chindaprasirt, P.: Effect of W/B ratios on pozzolanic reaction of biomass ashes in Portland cement matrix. Cem. Concr. Compos. **34**(1), 94–100 (2012)
13. TIS 1505: Autoclaved aerated lightweight concrete elements, Thailand Industrial Standard (1998)
14. Japanese Industrial Standard (JIS) R5201. Physical testing methods for cement (1997)
15. Hatanaka, S.; Mishima, N.; Nakagawa, T.; Morihana, H.; Chindaprasirt, P.: Finishing methods and compressive strength-void ratio relationships of in-situ porous concrete pavement. Comput. Concr. **10**(3), 231–240 (2012)
16. ASTM, C 1754: Standard test method for density and void content of hardened pervious concrete. Annual book of ASTM standards, American Society for Testing and Materials (2012)
17. ASTM, C 39/C 39M-01: Standard test method for compressive strength of cylindrical concrete specimens. Annual book of ASTM standards, American Society for Testing and Materials (2003)
18. ASTM, C 496-96: Standard test method for splitting tensile strength of cylindrical concrete specimens. Annual book of ASTM standards, American Society for Testing and Materials (2003)
19. ASTM, C 293-02: Standard test method for flexural strength of concrete (Using sample beam with center-point loading). Annual book of ASTM standards, American Society for Testing and Materials (2003)
20. ASTM, C 944: Standard test method for abrasion resistance of concrete or mortar surfaces by the rotating-cutter method. Annual book of ASTM standards, American Society for Testing and Materials (1999)
21. Uysal, H.; Demirboga, R.; Sahin, R.; Gul, R.: The effect of different cement dosage, slumps, and pumice aggregate ratios on the thermal conductivity and density of concrete. Cem. Concr. Res. **34**, 845–848 (2004)
22. Sengul, O.; Azizi, S.; Karaosmanoglu, F.; Tasdemir, M.A.: Effect of expanded perlite on the mechanical properties and thermal conductivity of lightweight concrete. Energy Build. **43**, 671–676 (2011)
23. Kim, H.K.; Jeon, J.H.; Lee, H.K.: Workability, and mechanical, acoustic and thermal properties of lightweight aggregate concrete with a high volume of entrained air. Constr. Build. Mater. **29**, 193–200 (2012)
24. Neithalath, N.; Sumanasooriya, M.S.; Deo, O.: Characterizing pore volume, sizes, and connectivity in pervious concretes for permeability prediction. Mater. Character **61**, 802–813 (2010)
25. Kevern, J.T.; Schaefer, V.R.; Wang, K.: Portland cement pervious concrete: A field experience from Sioux City. Open Constr. Build. Technol. J. **2**, 82–88 (2008)
26. Sata, V.; Wongsa, A.; Chindaprasirt, P.: Properties of pervious geopolymer concrete using recycled aggregates. Constr. Build. Mater. **42**, 33–39 (2013)
27. Unal, O.; Uygunoglu, T.; Yildiz, A.: Investigation of properties of low-strength lightweight concrete for thermal insulation. Build. Environ. **42**, 584–590 (2007)
28. Tanyildizi, H.; Coskun, A.; Somunkiran, I.: An experimental investigation of bond and compressive strength of concrete with mineral admixtures at high temperatures. Arab. J. Sci. Eng. **33**(2B), 443–449 (2008)
29. ACI Committee 318.: Building code requirements for structural concrete and commentary (ACI 318R-11). American Concrete Institute, Detroit (2011)
30. Crouch, L.K.; Pitt, J.; Hewitt, R.: Aggregate effects on pervious portland cement concrete static modulus of elastic. J. Mater. Civ. Eng. **19**(7), 561–568 (2007)
31. Topcu, I.B.; Uygunoglu, T.: Properties of autoclaved lightweight aggregate concrete. Build. Environ. **42**, 4108–4116 (2007)
32. Jerman, M.; Keppert, M.; Vyborny, J.; Cerny, R.: Hygric, thermal and durability properties of autoclaved aerated concrete. Constr. Build. Mater. **41**, 352–359 (2013)
33. Losiewicz, M.; Halsey, D.P.; Dews, S.J.; Olomaiye, P.; Harris, F.C.: An investigation into the properties of micro-sphere insulating concrete. Constr. Build. Mater. **10**(8), 583–588 (1996)
34. Saygili, A.; Baykal, G.: A new method for improving the thermal insulation properties of fly ash. Energy Build. **43**, 3236–3242 (2011)
35. Wongkeo, W.; Thongsanitgarn, P.; Pimraksa, K.; Chaipanich, A.: Compressive strength, flexural strength and thermal conductivity of autoclave concrete block made using bottom ash as cement replacement materials. Mater. Des. **35**, 434–439 (2012)
36. Demirboga, R.; Gul, R.: The effects of expanded perlite aggregate, silica fume and fly ash on the thermal conductivity of lightweight concrete. Cem. Concr. Res. **33**(5), 723–727 (2003)
37. Valore, R.C.: Insulating concretes. ACI J. Proc. **53**(11), 509–532 (1956)
38. Atis, A.D.: High volume fly ash abrasion resistant concrete. J. Mater. Civ. Eng. **14**(3), 274–277 (2002)
39. Yuksel, I.; Bilir, T.: Usage of industrial by-products to produce plain concrete elements. Constr. Build. Mater. **21**(3), 686–694 (2007)
40. Yuksel, I.; Bilir, T.; Ozkan, O.: Durability of concrete incorporating non-ground blast furnace slag and bottom ash as fine aggregate. Build. Environ. **42**(7), 2651–2659 (2007)

Materials and Structures (2015) 48:531–540
DOI 10.1617/s11527-014-0413-5

ORIGINAL ARTICLE

Properties of alkali activated silica fume–$Al(OH)_3$–fluidized bed combustion fly ash composites

Ubolluk Rattanasak · Prinya Chindaprasirt

Received: 22 April 2014 / Accepted: 27 August 2014 / Published online: 25 September 2014
© RILEM 2014

Abstract This study aims to improve the compressive strength of alkali-activated fluidized bed combustion (FBC) fly ash by incorporating silica fume and $Al(OH)_3$. Interground silica fume–$Al(OH)_3$–FBC fly ash powder was activated with sodium silicate and 15 M sodium hydroxide solutions curing at 65 °C for 24 h. Morphology and mineralogy of composites were studied using scanning electron microscope, X-ray diffraction and Fourier transform infrared spectroscopic analyses. Thermal stability of composites was also evaluated using thermogravimetry analysis. The results showed that homogeneous, dense and strong matrix could be obtained with addition of $Al(OH)_3$ and silica fume to FBC fly ash. Additional aluminosilicate, calcium-silicate compounds and some zeolite were formed as a result of geopolymerization and hydration reaction of the composites. Si–O vibration mode of composites shifted to lower wavenumber suggesting the chemical bonding change to form a new molecule in composite.

U. Rattanasak
Department of Chemistry and Center of Excellence for Innovation in Chemistry, Faculty of Science, Burapha University, Chonburi 20131, Thailand

P. Chindaprasirt (✉)
Sustainable Infrastructure Research and Development Center, Department of Civil Engineering, Faculty of Engineering, Khon Kaen University, Khon Kaen 40002, Thailand
e-mail: prinya@kku.ac.th

Keywords Alkali-activated composite · Morphology · Silica fume · Aluminium hydroxide · FBC fly ash

1 Introduction

Alkali-activated composites or geopolymers are receiving a lot of attention due to the beneficial use of wastes as starting materials and its associated low carbon footprint. These composites possess excellent mechanical properties and resistance to aggressive environments [1]. Pulverized coal combustion (PCC) fly ash is one of the effective source materials for geopolymer synthesis because of its high glassy phase, availability and ability to produce high strength composites. This PCC fly ash possesses pozzolanic property and is generally used to replace Portland cement in concrete production. Alternative source materials for geopolymer synthesis are now being studied extensively. Researchers have reported the properties of various source materials for geopolymer such as metakaolin [2, 3], rice husk ash [4], fluidized bed combustion (FBC) fly ash [5–8], blast-furnace slag [8, 9], Al-rich waste [8, 10], Si-rich material [11] and red mud [12]. Alternative source materials usually produce geopolymer with low strength and the blending with additives such as PCC fly ash results in improved mechanical properties of geopolymers [6, 7, 10]. Several successful works on non-PCC fly ash

based geopolymers have been reported [3, 4, 9, 11, 12].

FBC fly ash has recently been used as an alternative ash for geopolymer synthesis since the FBC process is environmentally-friendly [6, 13] and its ash is becoming abundant. Low burning temperatures at 800–900 °C result in low glassy phase and low pozzolanic property of FBC fly ash. High contents of sulfur and calcium compounds are obtained in the ashes due to lime feeding to capture sulfur gas from coal burning [14, 15]. Therefore, FBC fly ash is less preferable for use in concrete mixture. The quality of FBC fly ash is low and thus its use is limited and is normally disposed of at landfill site. Alkali-activated FBC fly ash has been studied for uses as alternative low strength cementitious binders and products [6, 7].

This research aims to improve the mechanical property of alkali activated FBC fly ash by adding $Al(OH)_3$ and silica fume since the calcium compounds in FBC fly ash can react with aluminium and silicon compounds in the presence of alkaline solution to form additional alumino-silicate and calcium-silicate compounds in the composite. Sodium silicate and NaOH solution were used as alkali activators. High concentration NaOH solution of 15 molar was selected in order to control the ettringite formation in the composites in the presence of $Al(OH)_3$ [16, 17].

2 Experimental procedure

2.1 Materials

FBC fly ash was obtained from a paper mill in Thailand and used for preparing the composites. Mixed pulverized lignite and sub-bituminous coals with 10 wt% of biomass (eucalyptus bark and bio-sludge) were used as feedstock of FBC unit with combustion temperature of 850 °C. Commercial grade silica fume and $Al(OH)_3$ from local supplier were used as the additional sources of alumina and silica. Chemical compositions of raw materials were determined by X-ray fluorescence (XRF, Philips PW-2404) and are shown in Table 1. The standard procedure for LOI as per ASTM C-114 was used with a heating temperature of 950 ± 50 °C. FBC fly ash consisted of quartz (SiO_2), aluminium oxide (Al_2O_3) and lime (CaO) as major oxide components. High CaO content was obtained as a result of adding lime to absorb sulfur. The median particle size (D50) of FBC fly ash as measured by particle size analyzer (Malvern Mastersizer S) was 28 μm, while those of silica fume and $Al(OH)_3$ were 55 and 65 μm, respectively. Mineralogy of source materials was analyzed by X-ray diffraction (XRD, PANalytical/Expert, Cu Kα radiation) and is shown in Fig. 1. From the quantitative XRD analyses, the amorphous phase contents of fly ash and silica fume were 37 and 97 %, respectively. Silica fume consisted of amorphous SiO_2 and a small

Table 1 Chemical compositions of FBC fly ash, silica fume and $Al(OH)_3$

Chemical composition	FBC fly ash (wt%)	Silica fume (wt%)	$Al(OH)_3$ (wt%)
SiO_2	21.2	96.4	–
Al_2O_3	10.7	–	74.4
CaO	38.7	–	–
Fe_2O_3	7.0	–	–
SO_3	14.9	–	–
Na_2O	2.5	0.5	0.3
K_2O	0.9	0.6	0.4
TiO_2	1.1	–	0.5
MgO	1.9	0.7	0.3
P_2O_5	0.1	–	–
Loss on ignition (LOI)	1.0	1.9	24.1

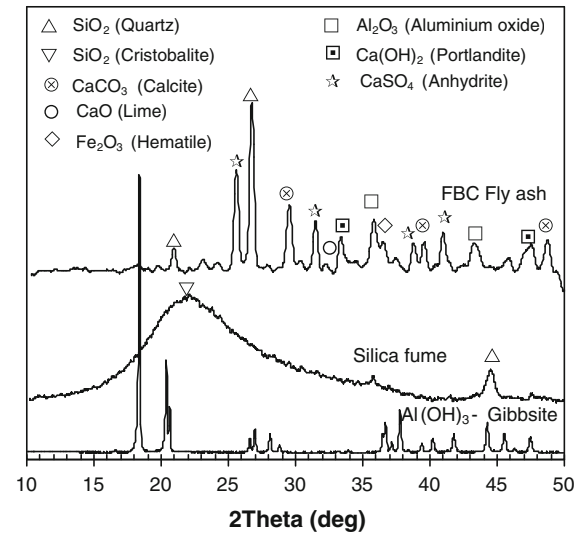

Fig. 1 XRD patterns of source materials

Table 2 Mix proportions of composites (g)

Samples	Ground blends			15 M NaOH solution	Water glass	SiO_2/Al_2O_3 Mol ratio
	FBC fly ash	Silica fume	$Al(OH)_3$			
Control	100	0	0	33	67	6.5
A	97.5	0	2.5	33	67	5.4
0AS	96.25	3.75	0	33	67	7.3
2.5AS	93.75	3.75	2.5	33	67	5.9
5AS	91.25	3.75	5	33	67	4.9

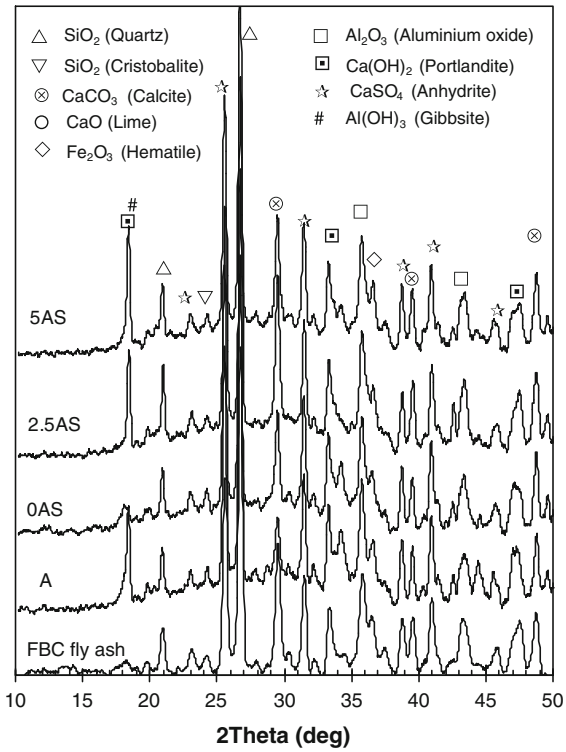

Fig. 2 XRD patterns of blended powders

amount of crystalline quartz; and $Al(OH)_3$ consisted mainly of gibbsite. The LOI of $Al(OH)_3$ was 24.1 % as shown in Table 1, however, theoretically the LOI of $Al(OH)_3$ should be 35 %. This indicated that $Al(OH)_3$ was partly dehydrated, However, XRD of $Al(OH)_3$ showed only the existence of gibbsite.

In order to control the ettringite formation in the composite, high concentration NaOH solution of 15 M was used by dissolving NaOH pellet in distilled water [17]. Sodium silicate solution (water glass, 30 wt% SiO_2 and 9 wt% Na_2O) was also used as another alkali activator.

2.2 Composite preparation and testing

Silica fume and $Al(OH)_3$ were used to replace FBC fly ash in the mixtures as shown in Table 2. The blended powder was interground to obtain homogeneous source material. From previous research [17, 18], the replacement levels of 2.5–5.0 wt% $Al(OH)_3$ and 3.75 wt% silica fume were selected to produce the geopolymer composites of adequate compressive strengths in the range of 20–30 MPa. All powder materials were interground with ceramic ball mills at 500 rpm for 2 h to obtain homogeneous blends with median particle sizes of 5–7 μm and percentage retained on sieve No. 325 (45 μm opening) of 3.5–4.0 wt%. XRD patterns of ground blends are shown in Fig. 2. The addition of silica fume and $Al(OH)_3$ into FBC fly ash, and the intergrinding process increased the availability of glassy phase and reactivity of the blends. The amorphous SiO_2 from silica fume was visible in the blends by the increased background of XRD diffractogram. Anhydrite was detected at 25.5° 2θ in all blended powders. For $Al(OH)_3$ addition, gibbsite was found at 18° 2θ overlapping with portlandite.

It has been reported that no ettringite formation in FBC geopolymer was founded with the use of 15 M NaOH [17]. The high NaOH solution concentration converted the sulfate compound in the FBC fly ash system to calcium hydroxide and soluble sodium salt as shown in Eq. (1) [19]. $CASO_4{\cdot}H_2O$ (gypsum) was formed when $CaSO_4$ (anhydrite) came into contact with water. In situ $Ca(OH)_2$ was then available for a pozzolanic reaction with silica fume and $Al(OH)_3$.

$$CaSO_4 \cdot 2H_2O\ (s) + 2\ NaOH\ (aq) \rightarrow Ca(OH)_2\ (s) + Na_2SO_4\ (aq) \quad (1)$$

In this experiment, water glass-to-NaOH solution mass ratio of 2 was used. Mix proportions of

composites are tabulated in Table 2. The blended powders were thoroughly mixed with 15 M NaOH and water glass for 3 min by hand mixer (Philip mixer HR 1456) at 120 rpm and cast in plastic mold. Specimens were vibrated for 10 s to remove air bubbles using vibrating machine; then wrapped and cured at 65 °C for 24 h. Hardened specimens were continuously cured in 25 °C-chamber and tested at the age of 28 days.

Composites were ground and used for the X-ray diffraction (XRD, PANalytical/Expert, Cu Kα radiation), Fourier transform infrared spectroscopic (FT-IR, Perkin Elmer system 2000, KBr pellet, 1 cm^{-1} resolution) and thermogravimetry (TGA, Mettler Teledo TGA/SDTA 851, heating ramp rate of 20 °C/min, pursed with N_2 gas) analyses. The amount of $Ca(OH)_2$ was calculated directly from TGA curves at its decomposition temperature of 400–450 °C using Eq. (2).

$$\%\ \ Ca(OH)_2 = \%\ \text{weight loss}_{Ca(OH)_2} \cdot \frac{MW_{Ca(OH)_2}}{MW_{water}} \quad (2)$$

where $MW_{Ca(OH)_2}$ and MW_{water} are molecular weight of $Ca(OH)_2$ (74 g/mol) and water (18 g/mol), respectively. For the scanning electron microscopy (SEM, JEOL JSM 5600LV, gold coating) analysis, small pieces of pastes were employed.

Graded river sand with specific gravity of 2.65 and fineness modulus of 2.8 was used. Sand-to-blended powder mass ratio of 2 was applied. After the paste was mixed in Hobart mixer, sand was added and the mixing was continued for another 1 min. The sample was cast in 5-cm cubic acrylic molds and cured in the same way as those of the paste preparation. The compressive strengths of mortars were tested at the age of 28 days in accordance with ASTM C109. Compressive strength was tested by compression testing machine (CB-10 M). The results were reported as the average of three samples.

3 Results and discussions

3.1 Compressive strength

Strength results of composites at 28-day curing time are shown in Fig. 3. The addition of $Al(OH)_3$ and silica fume improved the strengths of composites. The mixes with 2.5 wt% $Al(OH)_3$ (sample A) and 3.75 wt% silica fume (sample 0AS) gave high 28-day compressive strengths of 22.1 and 21.2 MPa, respectively compared with 10.2 MPa of the control mix. Both $Al(OH)_3$ and silica fume increased the hydration reaction and geopolymerization of mixes. Sample 2.5AS (2.5 wt% $Al(OH)_3$ and 3.75 wt% SiO_2) gave a higher 28-day strength of 26.5 MPa compared with 21.2 MPa of sample 0AS and 20.8 MPa of sample 5AS. With the combined addition of $Al(OH)_3$ and silica fume, dense matrix with aluminosilicate, calcium silicate and calcium aluminate were formed which was confirmed by XRD patterns and SEM micrographs resulting in high strength composites.

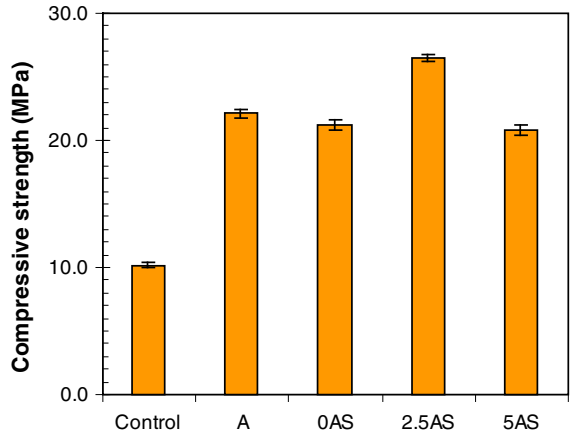

Fig. 3 28-day compressive strengths of composites

3.2 Morphology of composites

3.2.1 Scanning electron microscope (SEM)

Morphological analysis of composites at 28-day curing time was conducted by SEM and the results are shown in Fig. 4. Figure 4a shows that a non-homogeneous matrix with numerous pores was detected in the control mix due to the high porosity of low glassy phase and high calcium content (low silica and alumina) of FBC fly ash particles. Since the fly ash composed of crystalline phase, i.e. quartz in the interior and glassy phase at the surface layer, the products of alkali-activated reaction occurred at the surface of fly ash particles [20, 21]. The glassy phase

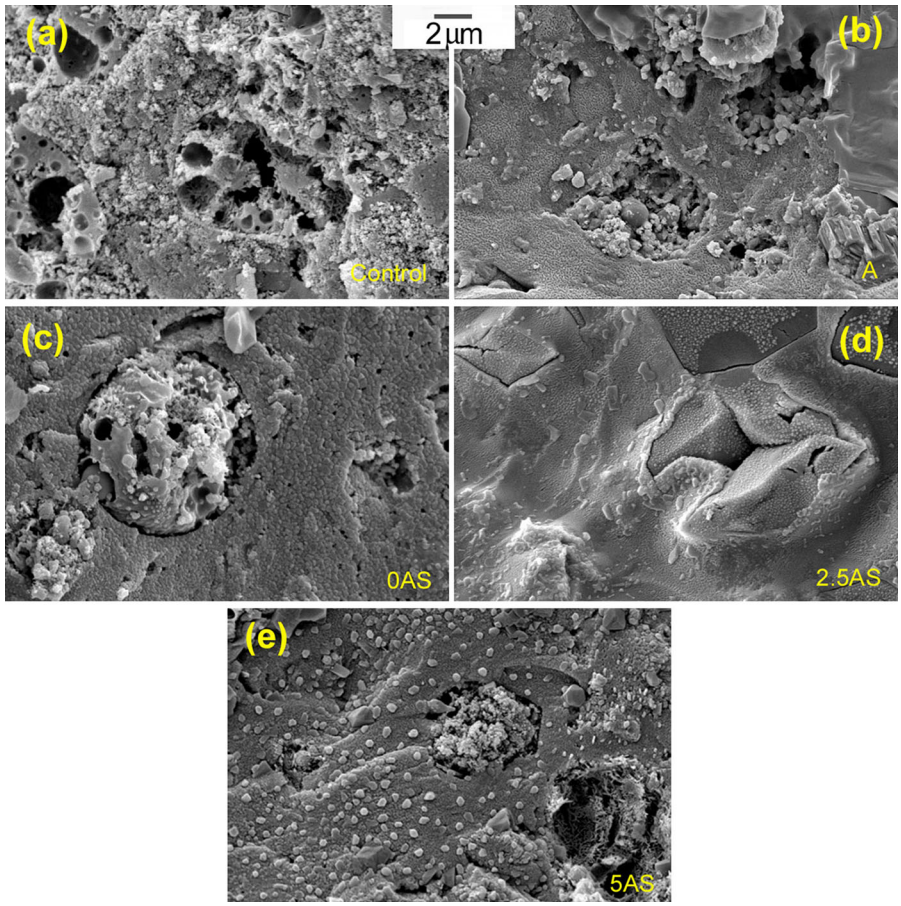

Fig. 4 SEM micrographs of composites after curing for 28 days

played an important role in geopolymer formation owing to the high solubility in the alkaline solution. Unreacted and sponge-like surface was also observed. This resulted in low mechanical properties of the composites. Addition of $Al(OH)_3$ (Fig. 4b) and silica fume (Fig. 4c) provided a denser and more homogeneous composites than the control. The addition of $Al(OH)_3$ led to an increase in aluminate ($Al(OH)_4^-$) species in alkali solution resulting in a faster rate of condensation [22]. In the presence of excess calcium in FBC fly ash, calcium alumino–silicate hydrate (C–A–S–H) can be formed [17, 23, 24]. Aluminate ion also reacted with reactive silica compound in FBC fly ash and formed alumino-silicate composite. In addition to $Al(OH)_3$, silica fume also helped to refine the pores. Silica fume which contained reactive silica reacted with 15 M NaOH and calcium oxide, and this resulted in additional calcium silicate hydrate. Due to high reactivity of silica fume, sodium silicate could also be formed in the presence of high NaOH concentration. Denser matrix was detected compared with the control.

The incorporation of both $Al(OH)_3$ and silica fume into FBC fly ash mixtures resulted in composites with significant amount of sodium aluminate, sodium silicate, crystallized zeolite and cementitious binder as shown in Fig. 4d and e. For mix 2.5AS with addition of 2.5 wt% $Al(OH)_3$ and 3.75 wt% silica fume, its surface and pores were coated with geopolymeric gel as shown in Fig. 4d. In the NaOH solution, the Si^{4+} and Al^{3+} ions leached from fly ash surface; and reactive $Al(OH)_3$ and silica reacted and formed hydration product and geopolymerization gel [24, 25]. The addition of 2.5 wt% $Al(OH)_3$ produced some zeolite as indicated by the crystal structure embedded in the continuous matrix. The presence of a small

content of zeolite in the composites resulted in an increase in strength. Similar observation was also reported by other researchers [26, 27]. The increase in $Al(OH)_3$ content to 5 % (Fig. 4e) provided the formation of sodium aluminate and zeolites as indicated by the crystal shape structures and also as detected on XRD patterns. This was due to the reaction between NaOH solution and excess $Al(OH)_3$. Zeolite formation in substantial quantity adversely affected the mechanical properties, e.g. low compressive strength [4]. The zeolite formation firstly increased the strength in mix 2.5AS, then decreased the strength in mix 5AS. For formation of high amount of zeolite, the strength of geopolymer decreased. This is probably due to the increased heterogeneity and increased interfaces between zeolite crystal and matrix. It was also reported that in the presence of a large amount of zeolite, the porosity of cement matrix increased which resulted in low strength mix [28].

3.2.2 X-ray diffraction (XRD)

XRD patterns of semi-crystalline composites after curing for 28 days are shown in Fig. 5. Sharp peaks were assigned to crystal structure, and broad hump represented the glassy phase of reaction products. Alkali solutions, i.e. sodium silicate and NaOH solutions, activated the reaction of the FBC fly ash particles and other source materials ($Al(OH)_3$ and silica fume). The reaction was further enhanced with heat curing which resulted in phase conversion with formation of crystalline and glassy phase products. These products consisted of calcium silicate (tobermorite, $Ca_3HO_9Si_3$, 29.80° and 29.77° 2θ), calcium aluminate (hydrogarnet, $Al_{2.849}Ca_3H_{9.6}O_{12}$, 32.13° 2$\theta$), aluminosilicate (kyanite, Al_2O_5Si, 26.66° and 35.72° 2θ), and natrolite zeolite ($Al_2H_4Na_2O_{12}Si_3$, 27.94° and 30.39° 2θ). Usually, hydrogarnet peak should also be detected at 17° 2θ, however in this case, this reflection of hydrogarnet peak disappeared in the presence of inorganic salt with a sodium cation and an anion consisting of sulfate, carbonate, and silicate [29]. In addition to kyanite and hydrogarnet, a complex structural tobermorite was detected. This complex molecule differed from a normal tobermorite which had lost some of its interlayer water molecules due to the heat curing. The –Si–O– linkages in tobermorite caused the rearrangement of single chains

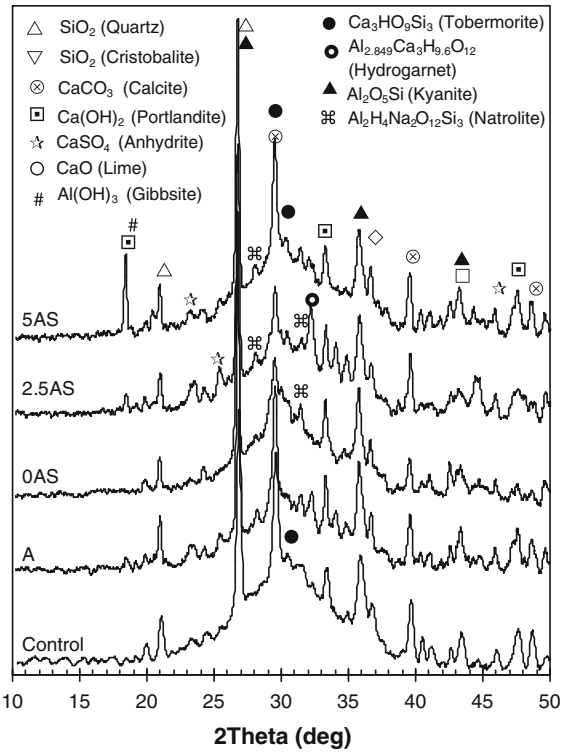

Fig. 5 XRD patterns of composites after curing for 28 days

to double chains in order to fulfill the coordination requirement of interlayer calcium ion [30, 31].

Two peaks between about 22–25° 2θ represented quartz and anhydrite deriving from raw materials. The height of sharp peaks at 29° 2θ decreased with the additions of $Al(OH)_3$ and silica fume due to the reaction of $Ca(OH)_2$ to form calcium silicate and calcium aluminate compounds. Composites had broad hump from 24° to 38° 2θ with sharp peaks in contrast to that of the original FBC fly ash. This confirmed the conversion to semi-crystalline material during the alkali-activated reaction. The addition of silica fume resulted in the formation of calcium silicate hydrate.

For sample 2.5AS, additional peaks of alumino-silicate were noticeable at 27°, 36° and 43° 2θ and those of calcium silicate could be observed at 31° 2θ. These alumino-silicate and calcium silicate played important roles in the mechanical properties of composites. Zeolite was also identified and conformed to the highly crystalline structure on SEM micrograph. The formation of large quantity of zeolites weakened the composites.

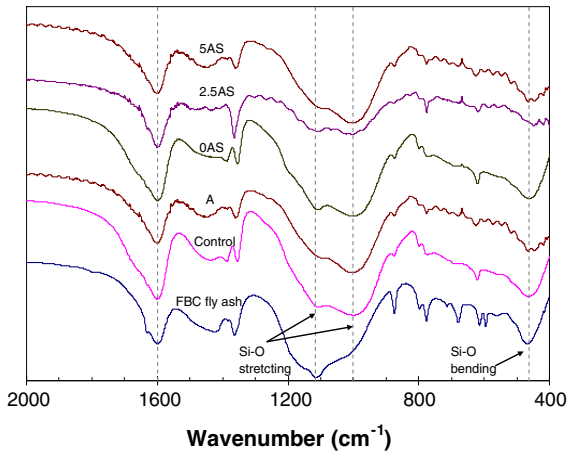

Fig. 6 FT-IR spectra of composites after curing for 28 days

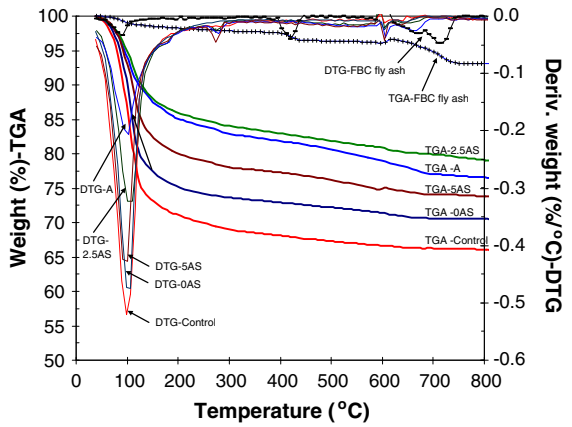

Fig. 7 TGA/DTG curves of composites after curing for 28 days

3.2.3 *Fourier transform infrared spectroscopy (FT-IR)*

FT-IR spectra of FBC fly ash and composites after curing for 28 days were recorded in wavenumber range of 3,000–400 cm^{-1}. However, significant peaks were noticeable in range of 2,000–400 cm^{-1} as shown in Fig. 6. Absorption band was related to the vibration at a specific configuration of chemical bonding. Oxide compounds of Si and Al are the main product of the reaction and the peak shifts were focused. Broad bands were observed at 3,450 cm^{-1} and 1,650–1,600 cm^{-1} for O–H stretching and O–H bending of water molecule, respectively. Si–O–Si and Si–O–Al stretching vibrations were detected at the wave number at approximately 1,000 cm^{-1}. Si–O–Al stretching vibration was more prominent than that of Si–O–Si bending mode; therefore Si–O–Al stretching vibration was logically used to indicate the degree of geopolymerization [25] as broad peak was presented at 980–1,050 cm^{-1}. The stretching modes were sensitive to the framework of alumino-silicate composite. These modes shifted to lower wavenumbers with increasing number of tetrahedral aluminum atoms [32]. From FT-IR spectra of FBC fly ash, Si–O stretching mode was found at 1,090 cm^{-1}. This peak shifted to lower wavenumber of 1,000 cm^{-1} as a result of the chemical bond change in composites. In addition, IR doublet was also found near 1,100 cm^{-1} particularly for sample 2.5AS owing to Si(Al)–O–Si. This doublet probably resulted from asymmetry in the tetrahedral sites due to Al substitution [33]. This doublet indicated the OH-deformation in Al–OH leading to the possible assignment of a new arrangement of Al–O bonds in the composite. Doublet of CO_3^{2-} was observed around 1,400 cm^{-1}. Two different types of CO_3^{2-} due to carbonation could be present in the interlayer of composite, possibly associated with the location near octahedron either containing Si or Al [34].

Wavenumber is directly proportional to energy and frequency (i.e. number of vibrations per second) of molecules. A decrease in wavenumber of composite is related to the formation of new molecule with low bonding strength in the composite when exposed to infrared radiation. Hence, Si–O bond of SiO_2 in raw materials was converted to new Si–O bond in composites.

3.3 Thermal analysis

Thermal property of composites after curing for 28 days was presented by thermogravimetric analysis (TGA) and differential thermogravimetry (DTG) as shown in Fig. 7. TGA/DTG monitored fraction of volatile components of composites by measuring the weight change during heating of specimens. FBC fly ash showed the weight change at approximately 100, 400 and 700 °C due to water evaporation, and decompositions of calcium hydroxide ($Ca(OH)_2$) and calcium carbonate ($CaCO_3$) into CaO and CO_2, respectively.

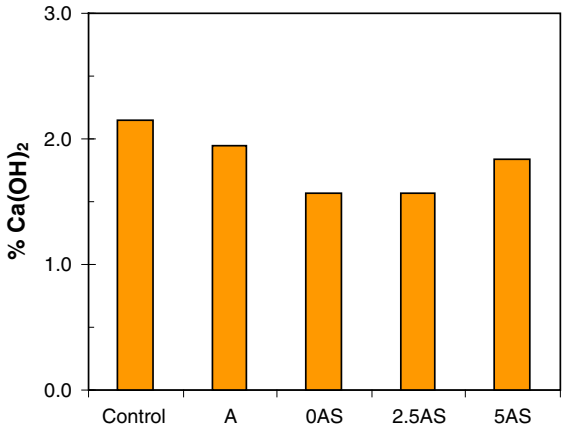

Fig. 8 $Ca(OH)_2$ contents of composites after curing for 28 days

The weight changes of composites were higher than that of FBC fly ash owing to the incorporation of alkali solutions in the mixtures and the presence of bound water of composites. The control sample had higher weight change than those of the blended composites due to less formation of thermal resistant product or strong binding materials. However, the remained weights of the control of 65.5 % was similar to those of OPC pastes with W/C ratios of 0.30–0.33 [35, 36].

The addition of both $Al(OH)_3$ and silica fume into composites gave lower weight change than that of $Al(OH)_3$/FBC fly ash composite (sample A). Composites showed thermal stability due to additional reaction among free lime (in FBC fly ash), $Al(OH)_3$, silica fume and alkali solutions which resulted in aluminosilicate and calcium silicate and calcium aluminate compounds. Weight change at 100 °C was due to the evaporation of bound water, and small peaks at 300 °C represented the start of dehydroxylation of $Al(OH)_3$ [17]. Less decomposition of $Ca(OH)_2$ at 400 °C implied that calcium compound reacted with aluminate and silicate ions which resulted in more complex and thermal resistant compounds. Although the differences in $Ca(OH)_2$ decomposition is not really visible in the TGA curves, small differences could be obtained from the calculations from TGA curves. This result conformed with the amount of $Ca(OH)_2$ content of composites shown in Fig. 8. It could be implied that $Ca(OH)_2$ contents of composites reduced with the addition of $Al(OH)_3$ and silica fume indicating its conversion to calcium aluminate and calcium silicate hydrates. Silica fume/FBC fly ash composites with 0 and 2.5 wt% $Al(OH)_3$ gave low $Ca(OH)_2$ contents.

At 600 °C, a comparable high weight loss was found in sample A (2.5 wt% $Al(OH)_3$). It was due to the dehydroxylation of AlO(OH) derived from calcination of excess $Al(OH)_3$. For high 5 wt% $Al(OH)_3$ (sample 5AS), the consumption of calcium was reduced. In the presence of high $Al(OH)_3$ content in alkali condition, Al^{3+} hindered the calcium absorption leading to an increased quantity of calcium remaining in the composite [37]. In addition, an increase in weight was found at 600 °C on the TGA/DTG curve of sample 5AS. This was likely the results of gamma to alpha transformation of Al_2O_3 [10, 38]. This led to an upward swing of the TGA/DTG curve prior to the bulk of the weight loss.

A low weight change in samples 2.5AS and A corresponded to the obtained high compressive strengths. This was possibly due to the low amount of free bound water and, hence, more water was bound in structure of hydration products.

4 Conclusion

Mechanical properties of alkali-activated FBC fly ash composites could be improved by adding $Al(OH)_3$ and silica fume. They provided denser and more homogeneous composites than the control. The addition of $Al(OH)_3$ led to an increase in aluminate ($Al(OH)_4^-$) species in alkali solution resulting in high strength gain. For silica fume, it reacted with alkali solutions and calcium oxide resulting in additional calcium silicate hydrate. The differences in $Ca(OH)_2$ of the samples are only minor which implies that they do not cause significant differences in thermal resistance. A broad hump of XRD pattern was detected implying the conversion of crystalline FBC fly ash to semi-crystalline material during the alkali-activated reaction. A shift of Si–O vibration to lower wavenumber confirmed the chemical bonding change and formation of complex molecule with strong bonding in the composite. The addition of 2.5 %wt $Al(OH)_3$ and 3.75 %wt silica fume into FBC fly ash provided the homogeneous geopolymer composite with the strength of 28 MPa at 28-day curing age.

Acknowledgments This work was supported by Khon Kaen University and the Thailand Research Fund (TRF) under TRF

Senior Research Scholar contract no. RTA5780004. Appreciation is also extended to the Center of Excellence for Innovation in Chemistry (PERCH-CIC), Office of the Higher Education Commission, Ministry of Education, Thailand.

References

1. Hussain M, Varley RJ, Cheng YB, Mathys Z, Simon GP (2005) Synthesis and thermal behavior of inorganic-organic hybrid geopolymer composites. J Appl Polym Sci 96(1):112–121
2. Palomo A, Glasser FP (1992) Chemically-bonded cementitious materials based on metakaolin. Br Ceram Trans 91(4):107–112
3. Rowles M, O'Conner B (2003) Chemical optimisation of the compressive strength of aluminosiliacte geopolymers synthesised by sodium silicate activation of metakaolinite. J Mater Chem 13(5):1161–1165
4. Rattanasak U, Chindaprasirt P, Suwanvitaya P (2010) Development of high volume rice husk ash alumino-silicate composite. Int J Miner Metall Mater 17(5):654–659
5. Xu H, Li H, Shen L, Zhang M, Zhai J (2010) Low-reactive circulating fluidized bed combustion (CFBC) fly ashes as source material for geopolymer synthesis. Waste Manag 30(1):57–62
6. Chindaprasirt P, Rattanasak U (2010) Utilization of blended fluidized bed combustion (FBC) ash and pulverized coal combustion (PCC) fly ash in geopolymer. Waste Manag 30(4):667–672
7. Chindaprasirt P, Rattanasak U, Jaturapitakkul C (2011) Utilization of fly ash blends from pulverized coal and fluidized bed combustions in geopolymeric materials. Cem Concr Compos 33(1):55–60
8. Kani EN, Allahverdi A, Provis JL (2012) Efflorescence control in geopolymer binders based on natural pozzolan. Cem Concr Compos 34(1):25–33
9. Cheng TW, Chiu JP (2003) Fire-resistant geopolymer produced by granulated blast furnace slag. Miner Eng 16(3):205–210
10. Chindaprasirt P, Rattanasak U, Vongvoradit P, Jenjirapanya S (2012) Thermal treatment and utilization of Al-rich waste in high calcium fly ash geopolymeric materials. Int J Min Met Mater 19(9):872–878
11. Jiao X, Zhang Y, Chen T (2013) Thermal stability of a silica-rich vanadium tailing based geopolymer. Constr Build Mater 38(1):43–47
12. He J, Jie Y, Zhang J, Yu Y, Zhang G (2013) Synthesis and characterization of red mud and rice husk ash-based geopolymer composites. Cem Concr Compos 37:108–118
13. Havlica J, Brandstetr J, Odler I (1998) Possibilities of utilizing solid residues from pressured fluidized bed coal combustion (PSBC) for the production of blended cements. Cem Concr Res 28(2):299–307
14. Basu P (1999) Combustion of coal in circulating fluidized-bed boilers: a review. Chem Eng Sci 54(22):5547–5557
15. Botha FD (2004) Overview of the fluidized bed combustion process and material. In: Proceedings of the state regulation of coal combustion by-product placement at mine sites: a technical interactive forum, Harrisburg, pp 1–4
16. Sheetz BE, Kwan SPI (2003) Control of ettringite swelling. Ashlines 4(1):1–10
17. Chindaprasirt P, Thaiwitcharoen S, Kaewpirom S, Rattanasak U (2013) Controlling ettringite formation in FBC fly ash geopolymer concrete. Cem Concr Compos 41(1):24–28
18. Chindaprasirt P, Paisitsrisawat P, Rattanasak U (2014) Strength and resistance to sulfate and sulfuric acid of ground fluidized bed combustion fly ash–silica fume alkali-activated composite. Adv Powder Technol 25(3):1087–1093
19. Clark BA, Brown PW (1999) Formation of ettringite from monosubstituted calcium sulfoaluminate hydrate and gypsum. J Am Ceram Soc 82(10):2900–2905
20. Inada M, Tsujimoto H, Eguchi Y, Enomoto N, Hojo J (2005) Microwave-assisted zeolite synthesis from coal fly ash in hydrothermal process. Fuel 84(12–13):1482–1486
21. Chindaprasirt P, Rattanasak U, Taebuanhuad S (2013) Resistance to acid and sulfate solutions of microwave-assisted high calcium fly ash geopolymer. Mater Struct 46(3):375–381
22. Steveson M, Sagoe-Crentsil K (2005) Relationships between composition, structure and strength of inorganic polymers. J Mater Sci 40(8):2023–2036
23. Garcia-Lodeiro I, Palomo A, Fernández-Jiménez A, MacPhee DE (2011) Compatibility studies between N–A–S–H and C–A–S–H gels: study in the ternary diagram Na_2O–CaO–Al_2O3–SiO_2–H_2O. Cem Concr Res 41(9): 923–931
24. Hong SY, Glasser FB (2002) Alkali sorption by C–S–H and C–A–S–H gels: part II. Role of alumina. Cem Concr Res 32(7):1101–1111
25. Rattanasak U, Chindaprasirt P (2009) Influence of NaOH solution on the synthesis of fly ash geopolymer. Miner Eng 22(12):1073–1078
26. Somna K, Jaturapitakkul C, Kajitvichyanukul P, Chindaprasirt P (2011) NaOH-activated ground fly ash geopolymer cured at ambient temperature. Fuel 90(6):2118–2124
27. Alvarez-Ayuso E, Querol X, Plana F, Alastuey A, Moreno N, Izquierdo M, Font O, Moreno T, Diez S, Vazquez E, Barra M (2008) Environmental, physical and structural characterisation of geopolymer matrixes synthesised from coal (co-combustion) fly ashes. J Hazard Mater 154(1): 75–83
28. Poon CS, Lam K, Kou SC, Lin ZS (1999) A study on the hydration rate of natural zeolite blended cement paste. Constr Build Mater 13(8):427–432
29. Fu Y, Ding J, Beaudoin JJ (1997) Conversion-preventing additive for high alumina cement products. US patent US5624489
30. Taylor HFW (1997) Cement chemistry, 2nd edn. Thomas Telford Publishing, London
31. Merlino S, Bonaccors E, Armbruster T (2011) The real structure of tobermorite 11 Å: normal and anomalous forms, OD character and polytypic modifications. Eur J Miner 13(3):577–590
32. Lee WKW, Van Deventer JSJ (2002) Structural reorganization of class F fly ash in alkaline silicate solutions. Colloids Surf A 211(1):49–66
33. Bishop JL, Murad E (2004) Characterization of minerals and biogeochemicalmarkers on Mars: a Raman and IR spectroscopic study of montmorillonite. J Raman Spectrosc 35(6):480–486

34. Theo KJ, Ray FL, Leisel H (2004) FT-Raman and FT-IR-spectroscopic study of the local structure of synthetic Mg/Zn/Al-hydrotalcites. J Raman Spectrosc 35(11):967–974
35. Villain G, Thiery M, Platret G (2007) Measurement methods of carbonation profiles in concrete: thermogravimetry, chemical analysis and gammadensimetry. Cem Concr Res 37(8):1182–1192
36. Alarcon-Ruiz L, Platret G, Massieu E, Ehrlacher A (2005) The use of thermal analysis in assessing the effect of temperature on a cement paste. Cem Concr Res 35(3):609–613
37. Zafar TA, Weaver CM (1999) Effect of aluminium on calcium absorption, growth and bone calcium content. Int J Agric Biol 1(3):138–141
38. Youn HJ, Jang JW, Kim IT, Hong KS (1999) Low-temperature formation of α-alumina by doping of alumina-sol. J Colloid Interface Sci 221(1):110–113

Setting Time, Strength, and Bond of High-Calcium Fly Ash Geopolymer Concrete

Pattanapong Topark-Ngarm[1]; Prinya Chindaprasirt[2]; and Vanchai Sata[3]

Downloaded from ascelibrary.org by Suranaree University Of Technology on 07/10/15. Copyright ASCE. For personal use only; all rights reserved.

Abstract: In this paper, setting time, strength and bond of high-calcium fly ash geopolymer concrete were investigated. The high-calcium fly ash was from Mae Moh power plant in northern Thailand. Both sodium silicate solution and sodium hydroxide solution were used as alkali activators in every mix. Sodium hydroxide solution with 10 M, 15 M, and 20 M concentrations, sodium silicate to sodium hydroxide ratios of 1.0 and 2.0, alkaline liquid to fly ash ratio of 0.5 and two curing regimes viz., heat curing at 60 ± 2°C for 24 h and room temperature curing at 23 ± 2°C were used. The results indicated that fresh geopolymer concrete had short setting time of 28–58 min due to the presence of high calcium content of fly ash. In general, strengths and modulus of elasticity increased with the increase in NaOH concentration. For compressive strength, the optimum Na_2O content was around 12% of fly ash. The high-strength geopolymer concrete with 28-day compressive strength of 54.4 MPa was obtained for mix with 15M NaOH. The modulii of elasticity of geopolymer concrete were related to the compressive strengths and comparable to those of portland cement concrete. The tensile splitting strength and bond strength were also related to the compressive strength and the values were higher than those of portland cement concrete. In particular, the bond strengths were significantly higher than those given by the current design code. **DOI: 10.1061/(ASCE)MT.1943-5533.0001157.** © *2014 American Society of Civil Engineers.*

Author keywords: High-calcium fly ash; Geopolymer concrete; Mechanical properties; Bond strength.

Introduction

The global production of portland cement (PC) increases every year and has shown no sign of slowing down (USGS 2013). Large amount of natural resources such as limestone, fossil fuels, electricity, and natural gas are required in PC production. High temperatures are required in the production of PC, and this has resulted in a larger amount of carbon dioxide (CO_2) emission into the atmosphere. In Thailand, approximately 33 million tons of portland cement were produced in 2012 (USGS 2013).

In an effort to reduce the growth of PC consumption, alternative pozzolanic materials such as fly ash, slag, palm oil fuel ash, bagasse ash, and rice husk ash are used as alternative cementitious materials to replace part of portland cement (Chindaprasirt et al. 2007c; Sata et al. 2007; Tangchirapat et al. 2009). These materials are by-products from industrial processes and thus require less energy to produce compared to PC production. These pozzolanic materials contain rich silica (SiO_2) and alumina (Al_2O_3) and can also be used to produce geo-binder when mixed with alkaline solutions. Geopolymers or "chains or networks of mineral molecules linked with covalent bonds" can be produced from aluminosilicate, an inorganic material rich in SiO_2 and Al_2O_3, activated by alkaline solution such as sodium hydroxide (NaOH) or potassium hydroxide (KOH) and sodium silicate (Na_2SiO_3) solution with the help of elevated temperature (Davidovits 2008). Geopolymers, in general, exhibit good mechanical properties, high durability, and strength maintenance in extreme conditions such as elevated temperatures, high corrosion, and high radiation (Binici 2013; Kong and Sanjayan 2008; Sata et al. 2012; Sufian Badar et al. 2014).

Fly ash is commonly used to produce geopolymers due to its availability around the world. Fly ash is classified as either class C or class F according to its chemical composition. It has been shown that low-calcium fly ash-based geopolymer concretes (LCGC) have similar mechanical properties to concretes produced with PC (Hardjito and Rangan 2005). In Thailand, approximately three million tons of fly ash is produced from lignite coal-fired Mae Moh power station in Lampang province. This fly ash contains relatively high calcium oxide content, typically around 12–25% by weight. According to previous researches, geopolymer paste and mortar produced from high-calcium fly ash exhibited good strength and durability (Chindaprasirt et al. 2010; Chindaprasirt et al. 2007c; Wongpa et al. 2010). Rattanasak and Chindaprasirt (2009) reported that leaching of silica and alumina was enhanced at high concentration of NaOH and thus a high strength geopolymer was normally obtained with a high concentration NaOH solution.

One of the problems with high-calcium fly ash is the fast setting due to the presence of calcium and the formation of calcium silicate hydrate and/or calcium aluminate silicate hydrate (Chindaprasirt et al. 2012). The use of high NaOH concentration in the high-calcium fly ash geopolymer can prolong the setting by limiting the leaching of calcium and allows normal geopolymerization process to control the setting of paste (Hanjitsuwan et al. 2014).

In the utilization of geopolymer concrete, the reinforcement is an important aspect (Esfahani and Rangan 1998). Since concrete is weak in tension, bond strength between rebar and concrete is thus a critical strength to transfer externally applied load from concrete to rebar. Sarker (2011) and Sofi et al. (2007a) indicated that bond

[1]Ph.D. Candidate, Dept. of Civil Engineering, Faculty of Engineering, Khon Kaen Univ., Khon Kaen 40002, Thailand. E-mail: p.toparkngarm@gmail.com

[2]Professor, Sustainable Infrastructure Research and Development Center, Dept. of Civil Engineering, Faculty of Engineering, Khon Kaen Univ., Khon Kaen 40002, Thailand (corresponding author). E-mail: prinya@kku.ac.th

[3]Assisstant Professor, Sustainable Infrastructure Research and Development Center, Dept. of Civil Engineering, Faculty of Engineering, Khon Kaen Univ., Khon Kaen 40002, Thailand. E-mail: vancsa@kku.ac.th

Note. This manuscript was submitted on March 6, 2014; approved on July 1, 2014; published online on August 19, 2014. Discussion period open until January 19, 2015; separate discussions must be submitted for individual papers. This paper is part of the ***Journal of Materials in Civil Engineering***, © ASCE, ISSN 0899-1561/04014198(7)/$25.00.

strengths between low-calcium fly ash geopolymer concrete and reinforcement were higher than those with the PC system. This is supported by the work of Songpiriyakij et al. (2011), which reported that high-calcium geopolymer paste had higher bond strength at 3 days than that of traditional epoxy agent.

Fresh and hardened properties of geopolymer concrete are affected by several factors such as alkaline liquid to fly ash ratio, NaOH concentration, ratio of alkaline solutions, curing conditions, and admixtures (Sathonsaowaphak et al. 2009). A number of reports (Hardjito and Rangan 2005; Rangan et al. 2006b) on the properties of geopolymer concrete and the effects the factors previously mentioned were based on low-calcium fly ash. In this research, fresh properties, and strengths including bond strength of high-calcium fly ash geopolymer concrete (HCGC) were investigated.

Experimental Details

Materials

Fly Ash

High-calcium fly ash (FA) from Mae Moh power station in Lampang province, Thailand was used in this study. The fly ash was greyish-brown color and consisted of 45.23% SiO_2, 19.95% Al_2O_3, 13.15% Fe_2O_3, and 15.51% CaO, which was analyzed using X-ray fluorescence (XRF). The particles were mainly spherical with median particle size of 57 microns as determined by Particle Size Analyzer Laser model Mastersizer S (Malvern Instruments and 38% was retained on 45 μm sieve. The fly ash was a high-calcium fly ash according to the chemical composition requirement per ASTM C618 (ASTM 2008a).

Aggregate

Commercially available limestone with maximum size of 20 mm and specific gravity of 2.65 in saturated surface dry (SSD) conditions was used as coarse aggregate. For fine aggregate, river sand with specific gravity of 2.58 and fineness modulus of 2.9 in SSD conditions was used.

Alkaline Solutions

For alkali activated solutions, sodium hydroxide (NaOH) and sodium silicate (Na_2SiO_3) with 15.32% Na_2O, 32.87% SiO_2, and 51.81% H_2O were used. For the NaOH solution, NaOH pellets were mixed with distilled water and stirred until all the pellets were completely dissolved. The solution was then left for 24 h before use.

Rebar

The steel bar used in this experiment was DB16 SD 40 with cross-sectional area of 201 mm^2 and perimeter of 50.3 mm. The rebar conformed to ASTM A615 grade 60 [A615/A615M-09b (ASTM 2009a)]. The average yield strength and ultimate strength were 520 MPa and 650 MPa, respectively.

Mix Proportions, Mixing Procedure, Casting and Curing Details

Mix Design

The combined aggregate was 73% of total weight of the mix. The ratio of coarse aggregate to fine aggregate was 65:35 and the alkali liquid to fly ash (L:A) ratio by weight was fixed at 0.5 for all mixes. The concentrations of NaOH were 10 M, 15 M, and 20 M and two sodium silicate to NaOH ratios (S:H) by weight of 1.0 and 2.0 were used. Table 1 shows the mix proportions of geopolymer concrete and initial molar ratios of starting materials. Total moles of Na_2O were calculated from Na_2O in fly ash, sodium hydroxide, and sodium silicate solutions.

Table 1. Mixing Proportion of Geopolymer Concrete by Weight (kg/m^3)

Mixes	Aggregate		Fly ash	NaOH (Molar)	Sodium silicate	Na_2O ($moles/m^3$)
	Coarse	Fine				
S/H 1-10M	1091	588	414	104 (10M)	104	682.9
S/H 1-15M	1091	588	414	104 (15M)	104	831.7
S/H 1-20M	1091	588	414	104 (20M)	104	965.5
S/H 2-10M	1091	588	414	69 (10M)	138	637.7
S/H 2-15M	1091	588	414	69 (15M)	138	736.4
S/H 2-20M	1091	588	414	69 (20M)	138	825.2

Mixing Procedure

The mixing procedure was adopted from previous researches on high-calcium geopolymer mortar (Chindaprasirt et al. 2010; Rattanasak and Chindaprasirt 2009). The geopolymer concretes were mixed in a $23 \pm 2^{\circ}C$ controlled room. The procedure started by mixing fly ash with NaOH solution for 5 min. Coarse and fine aggregates were then added to the mixer and mixed for another 5 min. Sodium silicate solution was then added to the mixture and mixing was continued for additional 5 min.

Casting of Specimens

For compressive strength and splitting tensile strength tests, geopolymer concrete was cast into 100×200 mm cylindrical steel molds in accordance with ASTM C192 (ASTM 2007). For the modulus of elasticity test, geopolymer concrete was cast into 150×300 mm cylindrical steel molds. For the pullout bond test, geopolymer concrete was cast into 100×150 mm cylindrical steel molds with rebar placed vertically at the center. A 10-mm-thick acrylic circular plate with a hole cut at the center was placed inside the steel mold to help align the rebar. The specimen was cast upside-down to ensure smooth contact surface between concrete and bearing plate.

Curing of Specimens

Two types of curing conditions were used in this study. The first was oven curing at $60 \pm 2^{\circ}C$ for 24 h after a 2 h delay time. The delay time was the time after the casting of concrete. The delay time allows concrete to be finished and reach initial setting before transportation to the curing oven or curing rack. The second curing condition was in a $23 \pm 2^{\circ}C$ controlled room. All concrete cylinders were removed from the molds after 24 h curing and wrapped with a vinyl sheet and cured in a $23 \pm 2^{\circ}C$ controlled room until testing.

Testing of Specimens

Slump Flow and Setting Time

A slump flow test was performed on a plastic sheet placed on flat wooden board according to ASTM C1611 (ASTM 2009b) within 5 min after mixing. The reported slump flow values were the average of four diagonal measurements. The setting time of geopolymer concrete was measured according to ASTM C807 (ASTM 2008b) using mortar collected from fresh concrete by passing fresh concrete through a #4 sieve to remove coarse aggregate. The setting time was measured from the time the fly ash made a contact with NaOH solution until the penetration of a 2 mm diameter needle was less than 10 mm. The reported setting time results were the average of two specimens.

Downloaded from ascelibrary.org by Suranaree University Of Technology on 07/10/15. Copyright ASCE. For personal use only; all rights reserved.

Compressive Strength and Splitting Tensile Strength

The concrete cylinders for compressive strength test were capped at both ends to ensure smooth surfaces. Concrete cylinders were tested for compressive strength according to ASTM C39 (ASTM 2001) at the ages of 7 and 28 days. The reported results were the average of three concrete samples. The splitting tensile strengths of concrete at 7 and 28 days were tested according to ASTM C496 (ASTM 2010).

Modulus of Elasticity

The modulus of elasticity was determined at the age of 28 days using 150 × 300 mm concrete cylinders in accordance with ASTM C469 (ASTM 2002). The reported results were the average of three concrete samples.

Bond Strength

The bond strength between geopolymer concrete and reinforcement was tested at the age of 7 days in accordance with ASTM C234 (ASTM 2000). The reported results were the average of three concrete samples.

Results and Discussions

Slump Flow and Setting Time

Fresh characteristics, slump flow, and setting time of concrete with different mix designs are shown in Table 2. Flows of fresh concrete were 470–620 mm. For the mixes with high NaOH content (S:H = 1), the flow values decreased with the increase in NaOH concentrations. The flow values of mixes with 10, 15, and 20 M NaOH were 580, 560, and 470 mm, respectively. The increase in NaOH concentration increased the viscosity and leaching of silica and alumina from fly ash particles and thus reduced the workability (Rattanasak et al. 2011). For the mixes with low NaOH content (S:H = 2), the flow values (500–530 mm) remained relatively unaffected with the change in NaOH concentration. In this system, the amount of NaOH was low and thus the effect of NaOH on flow was less than that of the former system.

The setting times of concrete were 28–68 min and were also influenced by S:H ratio. The setting times of geopolymer mortar in this research were relatively short compared to those of geopolymer concrete produced from low-calcium fly ash (Hardjito and Rangan 2005). The short setting time of HCGC was associated with the high calcium content of the system (Rattanasak et al. 2011). For mixes with high NaOH content (S:H = 1), the setting times decreased with the increase in the NaOH concentrations. The setting times of mixes with 10, 15, and 20 M NaOH were 50, 36, and 28 min, respectively. At high NaOH concentrations, setting was controlled by normal geopolymerization (Chindaprasirt et al. 2012). At high NaOH concentrations, the dissolution of Si^{4+} and Al^{3+} ions from fly ash increased (Rattanasak and Chindaprasirt 2009), which improved the geopolymerization and thus shortened the setting time. For the mixes with low NaOH (S:H = 2), the setting times were slightly increased with the increase in NaOH concentrations. At low NaOH content, setting was controlled by the presence of calcium, and the high NaOH concentrations hindered the dissolution of calcium to the system and thus setting was slightly delayed (Chindaprasirt et al. 2012).

Table 2. Flow and Setting Time of Geopolymer Concrete

Mixes	Flow (mm)	Setting time (min)
S:H 1-10M	580	50
S:H 1-15M	560	36
S:H 1-20M	470	28
S:H 2-10M	500	52
S:H 2-15M	550	68
S:H 2-20M	530	58

Compressive Strength

The results of compressive strength of HCGC are shown in Table 3. The compressive strengths of HCGC at 7 and 28 days were 19.9–42.9 MPa and 32.6–54.4 MPa, respectively. It was clear that high curing temperature influenced the early strength of HCGCs. For HCGCs cured at high temperature, the compressive strength increased rapidly until 7 days and continued at slower rate to 28 days. This characteristic of HCGC is similar to the strength gain of high strength concrete reported by the American Concrete Institute (ACI) in ACI 363R-92 (ACI 1997).

The compressive strengths increased with the increase in NaOH concentration. At high NaOH concentrations, the leaching of alumina and silica was enhanced and this resulted in increased geopolymerization, and thus the strength increased (Rattanasak and Chindaprasirt 2009). For the mix series with S:H ratio of 1.0, the high NaOH concentration of 20 M resulted in a reduction of strength, which were in line with other researches (Chindaprasirt et al. 2007b; Hardjito and Rangan 2005; Temuujin et al. 2009; Wongpa et al. 2010). The reduction of strength at high NaOH concentration was due to the high concentration of hydroxide ions (OH^-), which caused aluminosilicate gel precipitation at the early stage of development (Somna et al. 2011).

HCGC continued to gain strength after temperature curing. On the other hand, for low-calcium fly ash cured at high temperature, the strength gain after curing is not large (Rangan et al. 2006a). The presence of calcium also contributed to the strength gain after some temperature curing (Chindaprasirt et al. 2012; Dombrowski et al. 2007; García-Lodeiro et al. 2010; Guo et al. 2010; Temuujin et al. 2009). For high temperature curing at 60°C, the hydration was accelerated and the moisture was consumed. The strength gain at later age was therefore not large. For curing at 25°C, HCGC continued to gain strength from 7 to 28 days due to continued hydration and the availability of H_2O.

Fig. 1 shows the plot of 7 and 28 days compressive strengths against mass ratio of Na_2O to fly ash in the matrix. The optimum compressive strengths were obtained with total mass proportion of Na_2O to fly ash of approximately 12% for both curing regimes. The result in this study was in line with that reported by Guo et al. (2010) on geopolymer produced with class C fly ash. The 28 days compressive strength of HCGC could be expressed as function of total moles of Na_2O as shown in Eqs. (1) and (2) with R^2 equal to 0.82 and 0.84.

For 25°C curing

$$f'_{c28} = -1.13(M_{Na_2O})^2 + 28.1(M_{Na_2O}) - 130 \quad (1)$$

For 60°C for 24 h curing

$$f'_{c28} = -1.27(M_{Na_2O})^2 + 31.2(M_{Na_2O}) - 140 \quad (2)$$

where f'_{c28} = the 28-day compressive strength; and M_{Na_2O} = mass proportion of Na_2O to fly ash (%) of starting material.

Downloaded from ascelibrary.org by Suranaree University Of Technology on 07/10/15. Copyright ASCE. For personal use only; all rights reserved.

Table 3. Properties of Geopolymer Concrete

Mixes	Curing	γ (kg/m^3)	Compressive strength 7d MPa	(Std.)	Compressive strength 28d MPa	(Std.)	Tensile strength 7d MPa	(Std.)	Tensile strength 28d MPa	(Std.)	E_c MPa	(Std.)	u_c MPa	(Std.)
S:H 1-10M	Room	2,409	19.89	(0.81)	39.67	(1.12)	2.11	(0.23)	3.87	(0.29)	30,400	(1200)	9.04	(0.31)
	Oven	2,432	40.73	(3.01)	46.67	(5.56)	2.80	(0.09)	4.15	(0.05)	31,000	(2000)	13.41	(0.66)
S:H 1-15M	Room	2,417	22.30	(1.74)	45.34	(2.13)	2.77	(0.18)	4.36	(0.24)	34,800	(600)	8.73	(0.36)
	Oven	2,447	42.91	(4.94)	54.40	(2.79)	3.59	(0.25)	4.91	(0.48)	37,800	(1800)	13.57	(0.53)
S:H 1-20M	Room	2,439	20.50	(0.89)	37.64	(2.57)	2.48	(0.22)	3.96	(0.46)	38,400	(2800)	10.05	(0.59)
	Oven	2,450	41.20	(10.15)	43.42	(3.77)	3.73	(0.39)	4.43	(0.46)	38,000	(4200)	14.59	(0.86)
S:H 2-10M	Room	2,384	21.27	(2.29)	33.80	(2.10)	2.55	(0.19)	3.07	(0.43)	23,400	(2600)	7.85	(0.59)
	Oven	2,393	37.69	(3.70)	40.09	(3.15)	3.52	(0.42)	3.62	(0.18)	24,200	(1200)	13.83	(0.20)
S:H 2-15M	Room	2,403	22.99	(4.24)	39.02	(0.29)	3.02	(0.19)	3.47	(0.12)	26,800	(800)	10.39	(0.06)
	Oven	2,412	38.85	(4.78)	48.18	(3.58)	3.59	(0.50)	4.03	(0.73)	31,000	(2200)	14.47	(0.44)
S:H 2-20M	Room	2,421	23.06	(0.63)	46.69	(1.17)	3.15	(0.04)	3.84	(0.24)	35,400	(2600)	8.80	(0.58)
	Oven	2,409	39.27	(4.74)	49.50	(1.43)	3.92	(0.08)	3.99	(0.27)	31,800	(1200)	14.13	(1.16)

Note: Std. = standard deviation.

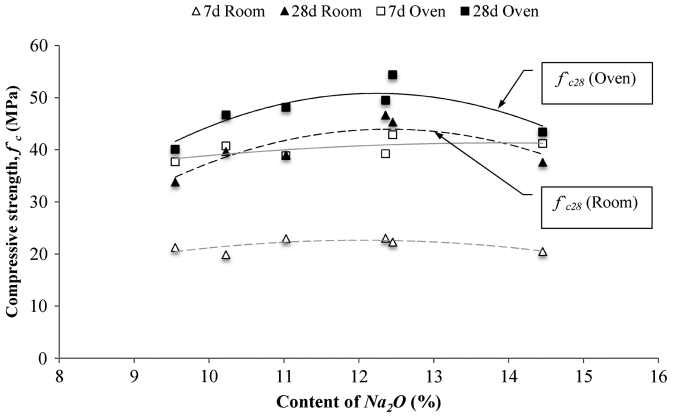

Fig. 1. Compressive strength of geopolymer concrete versus total content of Na_2O (%)

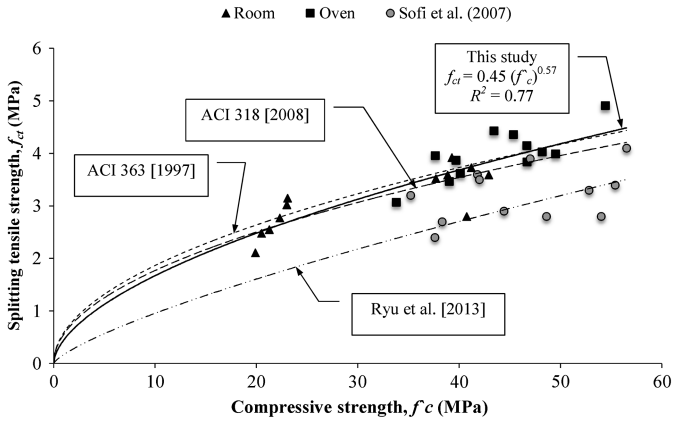

Fig. 2. Splitting tensile strength of geopolymer concrete versus compressive strength

Splitting Tensile Strength

The results of splitting tensile strength are shown in Table 3. The splitting tensile strength of HCGC at 7 and 28 days were 2.11–3.92 and 3.07–4.91 MPa. In general, the average splitting tensile strengths of concrete were affected by the concrete's mix proportions, a finding similar to that for compressive strength. It appears that the splitting tensile strength at 7 days for the series with S:H ratio of 1 was generally lower than that of the series with S:H ratio of 2. The strength continued to gain at the higher rate up to 28 days. This was true for both curing regimes.

Fig. 2 shows the plot of splitting tensile strength against the square root of compressive strength. The splitting tensile strength of concrete increased with increasing compressive strength. The mean splitting tensile strengths in this experiment were between 6.9 and 13.7% of its mean compressive strength, which was similar to those of PC of 8–14% (Sagoe-Crenstil et al. 2001). A number of researchers described the relationship between the splitting tensile strength and compressive strength of concrete using Eq. (3)

$$f_{ct} = k(f'_c)^n \tag{3}$$

where k and n are constants obtained from a regression analysis of experimental data. Ryu et al. (2013) suggested Eq. (4) for the calculation of splitting tensile strength of low-calcium fly ash-based geopolymer concrete. ACI 318-08 (ACI 2008) and ACI 363R-92 (ACI 1997) suggest Eqs. (5) and (6) for the calculation of splitting tensile strengths of normal and high-strength concretes, respectively

$$f_{ct} = 0.17(f'_c)^{0.75} \tag{4}$$

$$f_{ct} = 0.56(f'_c)^{0.5} \tag{5}$$

$$f_{ct} = 0.59(f'_c)^{0.5} \tag{6}$$

where f_{ct} = splitting tensile strength (MPa); and f'_c = compressive strength (MPa).

These equations are plotted along with experimental data as shown in Fig. 2. It can be seen that splitting tensile strengths of HCGC in this study were generally higher than those reported by Sofi et al. (2007b) and those obtained from Eq. (5) for low-calcium fly ash geopolymer concrete. This was due to strong interfacial transition zone (ITZ) between geopolymer paste and aggregate reported by several authors (Chen et al. 2013; Lee and van Deventer 2004; Ryu et al. 2013; Temuujin et al. 2010). Lee and van Deventer (2004) reported that geopolymer produced with high hydroxide content and higher silicate solution tended to have higher ITZ strength due to lower porosity in geopolymer paste. In the geopolymer system with the presence of high calcium compound, it was suggested that voids in aluminosilicate matrix were filled with

Downloaded from ascelibrary.org by Suranaree University Of Technology on 07/10/15. Copyright ASCE. For personal use only; all rights reserved.

calcium silicate hydrate (CSH) products, resulting in a low porosity geopolymer paste with increased strength (Hanjitsuwan et al. 2014). The splitting tensile strength results in this study were generally higher than the strengths calculated using standard design codes. However, it was reported that the equation given in ACI 318-08 (ACI 2008) generally overestimated the splitting tensile strength of high compressive strength concrete (Arioglu et al. 2006). The splitting tensile strengths of HCGC in this study were related to the compressive strengths as shown in Eq. (7) with R^2 equal to 0.77

$$f_{ct} = 0.45(f'_c)^{0.57} \tag{7}$$

Modulus of Elasticity

The results for the modulus of elasticity are shown in Table 3. The values were 23,400–41,000 MPa. The concrete with S:H ratio of 1 showed higher modulus of elasticity values than those with S:H ratio of 2. Fig. 3 shows the plot of modulus of elasticity against Na_2O content. It can be concluded that modulus of elasticity increased with increasing amounts of Na_2O. Similar to compressive strength development, with S:H ratio of 1, high content of the sodium hydroxide solution enhanced the leaching of silica and alumina ions, hence a higher degree of geopolymerization was obtained. The relationship between modulus of elasticity and Na_2O is shown in Eq. (8) with $R^2 = 0.79$

$$E_c = 2{,}700(M_{Na_2O}) + 400 \tag{8}$$

The results of modulus of elasticity were plotted against the square root of compressive strength as shown in Fig. 4. It can be seen that the modulus of elasticity of concrete generally increased as compressive strength increased, which was similar to the current design code, ACI 318-08 (ACI 2008) and alternative equation for high strength concrete ACI 363R-92 (ACI 1997) as shown in Eqs. (9) and (10), respectively. In fact, the results of this investigation were between those given by the two codes. It is widely known that the modulus of elasticity of concrete depends on mix proportion, properties of the aggregates, and the curing conditions of the concrete. Several researchers (Hardjito and Rangan 2005; Sofi et al. 2007b; Yost et al. 2013) reported on geopolymer concrete with a lower modulus of elasticity when compared to those calculations using a normal concrete equation, with the exception of Joseph and Mathew (2012) who reported a higher modulus of elasticity. It can be seen that the results in this study were close to the values calculated with the ACI 363R-92 (ACI 1997) equation as

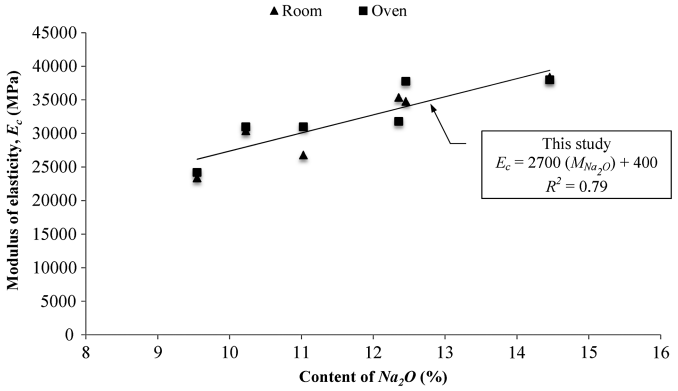

Fig. 3. Modulus of elasticity of geopolymer concrete total content of Na_2O (%)

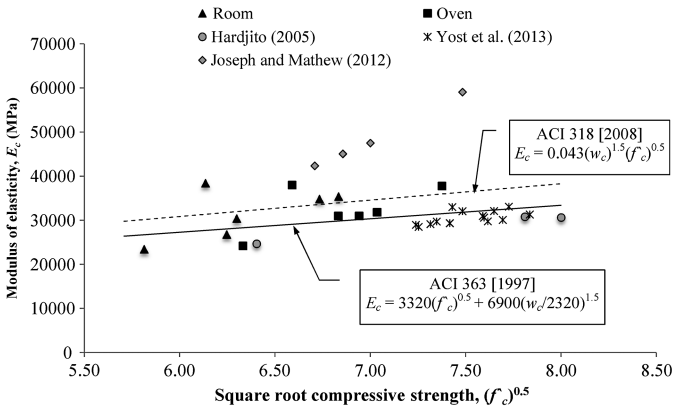

Fig. 4. Modulus of elasticity of geopolymer concrete versus square root of compressive strength

follows and in line with other reports on low-calcium geopolymer concretes

$$E_c = 0.043(w_c)^{1.5}(f'_c)^{0.5} \tag{9}$$

$$E_c = 3{,}320(f'_c)^{0.5} + 6{,}900(w_c/2{,}320)^{1.5} \tag{10}$$

Bond Strength

The results for bond strength between HCGC and rebar are shown in Table 3. The bond strengths were 8.73–14.59 MPa. All specimens in this experiment failed by concrete rupture and thus the ultimate bond strength was reached. In general, the bond strength of the HCGC was related to the compressive strength of the concrete. Many equations have been proposed to estimate bond strength between deformed bar and concrete as shown below.

Orangun et al. (1977) proposed Eq. (11) for normal concrete without transverse reinforcement, which is the basis for current development length calculation in ACI 318 [ACI 408R-03 (ACI 2003)] as follows:

$$u_c = (0.101 + 0.268c_{\min}/d_b + 4.4d_b/l_d)(f'_c)^{0.5} \tag{11}$$

where u_c = ultimate bond strength (MPa); $c_{\min}$ = minimum concrete cover (mm); d_b = nominal bar diameter (mm); l_d = development length (mm); and f'_c = compressive strength (MPa). Esfahani and Rangan (1998) suggested that bond strength between reinforcing steel and concrete was related to splitting tensile strength of concrete and proposed Eq. (12) as follows:

$$u_c = 4.9[(c_{\min}/d_b + 0.5)/(c_{\min}/d_b + 3.6)](f_{ct}) \tag{12}$$

where f_{ct} = tensile strength of concrete taken as $0.55(f'_c)^{0.5}$ (MPa); and f'_c = compressive strength (MPa) less than 50 MPa. Hadi (2008) proposed Eq. (13) for bond strength between high strength steel and high strength concrete based on the pullout test as follows:

$$u_c = 0.083045(22.8 + 0.208c_{\min}/d_b - 38.212d_b/l_d)(f'_c)^{0.5} \tag{13}$$

The bond strengths in this study can be written as shown in Eq. (14) with $R^2 = 0.85$ to obtain

$$u_c = 2.12(f'_c)^{0.5} \tag{14}$$

Fig. 5 shows a plot of bond strength of geopolymer concrete against the square root of compressive strength along with the results of LCGC (Chang et al. 2009; Sofi et al. 2007a). The bond

Downloaded from ascelibrary.org by Suranaree University Of Technology on 07/10/15. Copyright ASCE. For personal use only; all rights reserved.

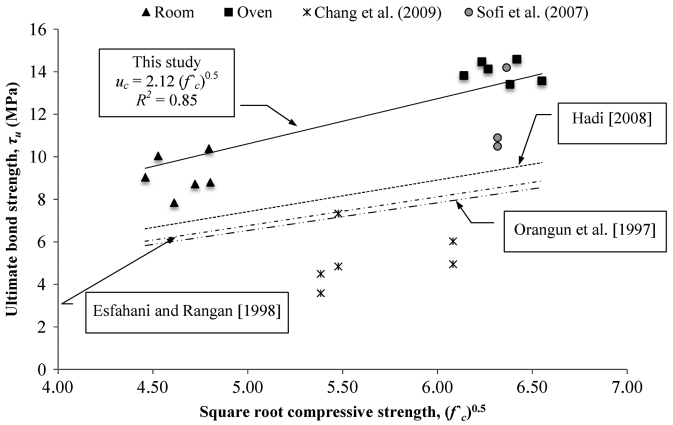

Fig. 5. Ultimate bond strength between rebar and geopolymer concrete versus square root of compressive strength

strengths of the HCGC and reinforcing bar were significantly higher than those found in Orangun et al. (1977), Esfahani and Rangan (1998), and Hadi (2008). In fact, Eq. (14) from this investigation gave the bond strengths nearly double the values of those obtained using Eq. (11) from Orangun et al. (1977). The high bond strength was due to the relatively high splitting tensile strength as reported by several authors on bond strength between deformed bar and LCGC (Sarker 2011; Sofi et al. 2007a). The high splitting tensile strength was related to ITZ strength and was also influenced by the amount Na_2O and Na_2SiO_3. The NaOH concentration played an important role in bond strength. Songpiriyakij et al. (2011) reported the bond strength of 4.41 and 6.38 MPa of fly ash geopolymer paste activated with NaOH concentrations of 10 and 18 molar. This was due to the leaching ability of silica and alumina in high alkaline solution, as stated in previous sections.

For the bond strength of low-calcium fly ash concrete, the results of Sofi et al. (2007a) were from pullout test and results of Chang et al. (2009) were from a splice-beam test. In general, splice-beam tests give more realistic bond behavior between rebar and concrete while the pullout test is simple to set up and can be used for comparison purposes [ACI 408R-03 (ACI 2003)]. The bond strengths from the pullout test reported by Sofi et al. (2007a) were also high but slightly lower than the bond strengths obtained in this study. The superior bond strength characteristics of the HCGC was due to the good ITZ characteristics of geopolymer matrix and may be due in part to the presence of calcium and additional calcium silicate hydrate. This aspect needs further investigation.

Conclusion

Based on the obtained data in this experiment, the following conclusions can be made. The results in this study indicated that high-calcium fly ash was suitable to use in producing high strength geopolymer concrete with high bond strength between concrete and rebar. The fresh concrete had short setting time of 28–58 min due to the presence of high calcium content in the system. For compressive strength, curing at 60°C for 24 h accelerated the strength development as indicated by the high 7-day compressive strengths. The strength of HCGC continued to develop with time similar to portland cement concrete, which was due to the presence of calcium and the formation of additional calcium silicate hydrate. The compressive strength of HCGC was related to the NaOH concentration and the Na_2O content. The optimum Na_2O content was approximately 12% by weight of fly ash. Optimum compressive strength of 54.4 MPa was obtained for the mix with 15 M NaOH. The splitting tensile strength and modulus of elasticity of HCGC were related to the compressive strength. The splitting tensile strengths of HCGC were relatively high in terms of percentage of compressive strength, which was probably due to the strong interfacial zone of the aggregate and the high calcium geopolymer matrix. The bond strengths between HCGC and rebar were significantly higher than those of normal portland cement concrete given by the current ACI 318 design code. There was also an indication that the bond strength of HCGC was slightly higher than that of the low-calcium fly ash geopolymer concrete.

Acknowledgments

This work was financially supported by the Thailand Research Fund (TRF) under the TRF Senior Research Scholar, Grant No. RTA5480004. It was also supported by the Higher Education Research Promotion and National Research University Project of Thailand, Office of the Higher Education Commission, through the Advanced Functional Materials Cluster of Khon Kaen University AFM-2554-Ph.D. 54402.

References

American Concrete Institute (ACI). (1997). "State-of-the-art report on high-strength concrete." *363R-92*, Farmington Hills, MI.

American Concrete Institute (ACI). (2003). "Bond and development of straight reinforcing bars in tension." *408R-03*, Farmington Hills, MI, 56.

American Concrete Institute (ACI). (2008). "Building code requirements for structural concrete (ACI 318-08) and commentary." *318-08*, Farmington Hills, MI.

Arioglu, N., Girgin, Z. C., and Arioglu, E. (2006). "Evaluation of ratio between splitting tensile strength and compressive strength for concretes up to 120 MPa and its application in strength criteria." *ACI Mater. J.*, 103(1), 18–24.

ASTM. (2000). "Standard specification for comparing concrete on basis of the bond developed with reinforcing steel." *C234*, West Conshohocken, PA.

ASTM. (2001). "Standard test method for compressive strength of cylindrical concrete specimens." *C39*, West Conshohocken, PA.

ASTM. (2002). "Standard test method for static modulus of elasticity and poisson's ratio of concrete in compression." *C469*, West Conshohocken, PA.

ASTM. (2007). "Standard test method for making and curing concrete test specimens in the laboratory." *C192*, West Conshohocken, PA.

ASTM. (2008a). "Standard specification for coal fly ash and raw or calcined natural pozzolan for use in cement." *C618*, West Conshohocken, PA.

ASTM. (2008b). "Standard test methods for time of setting of hydraulic cement mortar by modified vicat needle." *C807*, West Conshohocken, PA.

ASTM. (2009a). "Standard specification for deformed and plain carbon-steel bars for concrete reinforcement." *A615/A615M-09b*, West Conshohocken, PA.

ASTM. (2009b). "Standard test methods for slump flow of self-consolidating concrete." *C1611*, West Conshohocken, PA.

ASTM. (2010). "Standard test method for splitting tensile strength of cylindrical concrete specimens." *C496*, West Conshohocken, PA.

Binici, H. (2013). "Engineering properties of geopolymer incorporating slag, fly ash, silica sand and pumice." *Adv. Civ. Environ. Eng.*, 1(3), 108–123.

Chang, E. H., Sarker, P., Lloyd, N., and Rangan, B. V. (2009). "Bond behaviour of reinforced fly ash-based geopolymer concrete beams." *24th Biennial Conf. of the Concrete Institute of Australia*, R. I. Gilbert, ed., Concrete Institute of Australia, Luna Park, Sydney, 10.

Downloaded from ascelibrary.org by Suranaree University Of Technology on 07/10/15. Copyright ASCE. For personal use only; all rights reserved.

Chen, X., Wu, S., and Zhou, J. (2013). "Influence of porosity on compressive and tensile strength of cement mortar." *Constr. Build. Mater.*, 40, 869–874.

Chindaprasirt, P., Chareerat, T., Hatanaka, S., and Cao, T. (2010). "High-strength geopolymer using fine high-calcium fly ash." *J. Mater. Civ. Eng.*, 10.1061/(ASCE)MT.1943-5533.0000161, 264–270.

Chindaprasirt, P., Chareerat, T., and Sirivivatnanon, V. (2007a). "Workability and strength of coarse high calcium fly ash geopolymer." *Cem. Concr. Compos.*, 29(3), 224–229.

Chindaprasirt, P., Chotithanorm, C., Cao, H. T., and Sirivivatnanon, V. (2007b). "Influence of fly ash fineness on the chloride penetration of concrete." *Constr. Build. Mater.*, 21(2), 356–361.

Chindaprasirt, P., Homwuttiwong, S., and Jaturapitakkul, C. (2007c). "Strength and water permeability of concrete containing palm oil fuel ash and rice husk-bark ash." *Constr. Build. Mater.*, 21(7), 1492–1499.

Chindaprasirt, P., De Silva, P., Sagoe-Crentsil, K., and Hanjitsuwan, S. (2012). "Effect of SiO_2 and Al_2O_3 on the setting and hardening of high calcium fly ash-based geopolymer systems." *J. Mater. Sci.*, 47(12), 4876–4883.

Davidovits, J. (2008). *Geopolymer chemistry and application*, 2nd Ed., Institute Geopolymer, Saint-Quentin, France.

Dombrowski, K., Buchwald, A., and Weil, M. (2007). "The influence of calcium content on the structure and thermal performance of fly ash based geopolymers." *J. Mater. Sci.*, 42(9), 3033–3043.

Esfahani, M. R., and Rangan, B. V. (1998). "Bond between normal strength and high-strength concrete (HSC) and reinforcing bars in splices in beams." *ACI Struct. J.*, 9.

García-Lodeiro, I., Fernández-Jiménez, A., Palomo, A., and MacPhee, D. E. (2010). "Effect of calcium additions on N-A-S-H cementitious gels." *J. Am. Ceram. Soc.*, 93(7), 1934–1940.

Guo, X., Shi, H., and Dick, W. A. (2010). "Compressive strength and microstructural characteristics of class C fly ash geopolymer." *Cem. Concr. Compos.*, 32(2), 142–147.

Hadi, M. N. S. (2008). "Bond of high strength concrete with high strength reinforcing steel." *Open Civ. Eng. J.*, 2, 5.

Hanjitsuwan, S., Hunpratub, S., Thongbai, P., Maensiri, S., Sata, V., and Chindaprasirt, P. (2014). "Effects of NaOH concentrations on physical and electrical properties of high calcium fly ash geopolymer paste." *Cem. Concr. Compos.*, 45, 9–14.

Hardjito, D., and Rangan, B. V. (2005). *Development and properties of low-calcium fly ash-based geopolymer concrete*, Curtin Univ. of Technology, Perth, Australia.

Joseph, B., and Mathew, G. (2012). "Influence of aggregate content on the behavior of fly ash based geopolymer concrete." *Sci. Iran.*, 19(5), 1188–1194.

Kong, D. L. Y., and Sanjayan, J. G. (2008). "Damage behavior of geopolymer composites exposed to elevated temperatures." *Cem. Concr. Compos.*, 30(10), 986–991.

Lee, W. K. W., and van Deventer, J. S. J. (2004). "The interface between natural siliceous aggregates and geopolymers." *Cem. Concr. Res.*, 34(2), 195–206.

Orangun, C. O., Jirsa, J. O., and Breen, J. E. (1977). "A reevaluation of test data on development length and splices." *ACI J.*, 74(3), 114–122.

Rangan, B. V., Hardjito, D., Wallah, S. E., and Sumajouw, D. M. J. (2006a). "Properties and applications of fly ash-based concrete." *Mater. Forum*, 30, 170–175.

Rangan, B. V., Wallah, S., Sumajouw, D., and Hardjito, D. (2006b). "Heat-cured, low-calcium, fly ash-based geopolymer concrete." *Indian Concr. J.*, 80(6), 47–52.

Rattanasak, U., and Chindaprasirt, P. (2009). "Influence of NaOH solution on the synthesis of fly ash geopolymer." *Miner. Eng.*, 22(12), 1073–1078.

Rattanasak, U., Pankhet, K., and Chindaprasirt, P. (2011). "Effect of chemical admixtures on properties of high-calcium fly ash geopolymer." *Int. J. Miner. Metall. Mater.*, 18(3), 364–369.

Ryu, G. S., Lee, Y. B., Koh, K. T., and Chung, Y. S. (2013). "The mechanical properties of fly ash-based geopolymer concrete with alkaline activators." *Constr. Build. Mater.*, 47, 409–418.

Sagoe-Crenstil, K. K., Brown, T., and Taylor, A. H. (2001). "Performance of concrete made with commercially produced coarse recycled concrete aggregate." *Cem. Concr. Res.*, 31(5), 707–712.

Sarker, P. K. (2011). "Bond strength of reinforcing steel embedded in fly ash-based geopolymer concrete." *Mater. Struct./Mater. Constr.*, 44(5), 1021–1030.

Sata, V., Jaturapitakkul, C., and Kiattikomol, K. (2007). "Influence of pozzolan from various by-product materials on mechanical properties of high-strength concrete." *Constr. Build. Mater.*, 21(7), 1589–1598.

Sata, V., Sathonsaowaphak, A., and Chindaprasirt, P. (2012). "Resistance of lignite bottom ash geopolymer mortar to sulfate and sulfuric acid attack." *Cem. Concr. Compos.*, 34(5), 700–708.

Sathonsaowaphak, A., Chindaprasirt, P., and Pimraksa, K. (2009). "Workability and strength of lignite bottom ash geopolymer mortar." *J. Hazard. Mater.*, 168(1), 44–50.

Sofi, M., Deventer, J. S. J., Mendis, P. A., and Lukey, G. C. (2007a). "Bond performance of reinforcing bars in inorganic polymer concrete (IPC)." *J. Mater. Sci.*, 42(9), 3107–3116.

Sofi, M., van Deventer, J. S. J., Mendis, P. A., and Lukey, G. C. (2007b). "Engineering properties of inorganic polymer concretes (IPCs)." *Cem. Concr. Res.*, 37(2), 251–257.

Somna, K., Jaturapitakkul, C., Kajitvichyanukul, P., and Chindaprasirt, P. (2011). "NaOH-activated ground fly ash geopolymer cured at ambient temperature." *Fuel*, 90(6), 2118–2124.

Songpiriyakij, S., Pulngern, T., Pungpremtrakul, P., and Jaturapitakkul, C. (2011). "Anchorage of steel bars in concrete by geopolymer paste." *Mater. Des.*, 32(5), 3021–3028.

Sufian Badar, M., Kupwade-Patil, K., Bernal, S. A., Provis, J. L., and Allouche, E. N. (2014). "Corrosion of steel bars induced by accelerated carbonation in low and high calcium fly ash geopolymer concretes." *Constr. Build. Mater.*, 61, 79–89.

Tangchirapat, W., Jaturapitakkul, C., and Chindaprasirt, P. (2009). "Use of palm oil fuel ash as a supplementary cementitious material for producing high-strength concrete." *Constr. Build. Mater.*, 23(7), 2641–2646.

Temuujin, J., van Riessen, A., and MacKenzie, K. J. D. (2010). "Preparation and characterisation of fly ash based geopolymer mortars." *Constr. Build. Mater.*, 24(10), 1906–1910.

Temuujin, J., van Riessen, A., and Williams, R. (2009). "Influence of calcium compounds on the mechanical properties of fly ash geopolymer pastes." *J. Hazard. Mater.*, 167(1–3), 82–88.

U.S. Geological Survey (USGS). (2013). "U.S. geological survey, mineral commodity summaries." Reston, VA, 38.

Wongpa, J., Kiattikomol, K., Jaturapitakkul, C., and Chindaprasirt, P. (2010). "Compressive strength, modulus of elasticity, and water permeability of inorganic polymer concrete." *Mater. Des.*, 31(10), 4748–4754.

Yost, J. R., RadliÑska, A., Ernst, S., and Salera, M. (2013). "Structural behavior of alkali activated fly ash concrete. Part 1: Mixture design, material properties and sample fabrication." *Mater. Struct.*, 46(3), 435–447.

Downloaded from ascelibrary.org by Suranaree University Of Technology on 07/10/15. Copyright ASCE. For personal use only; all rights reserved.

Construction and Building Materials 91 (2015) 1–8

Contents lists available at ScienceDirect

Construction and Building Materials

journal homepage: www.elsevier.com/locate/conbuildmat

Effects of sodium hydroxide and sodium silicate solutions on compressive and shear bond strengths of FA–GBFS geopolymer

Tanakorn Phoo-ngernkham [a], Akihiro Maegawa [b], Naoki Mishima [c], Shigemitsu Hatanaka [c], Prinya Chindaprasirt [d,*]

[a] Program in Civil Engineering, Faculty of Engineering and Architecture, Rajamangala University of Technology Isan, Nakhon Ratchasima 30000, Thailand
[b] Mie Prefecture Industrial Research Institute, Mie 514-0819, Japan
[c] Dept. of Architecture, Faculty of Engineering, Mie University, Mie 514-8504, Japan
[d] Sustainable Infrastructure Research and Development Center, Dept. of Civil Engineering, Faculty of Engineering, Khon Kaen University, Khon Kaen 40002, Thailand

HIGHLIGHTS

- FA–GBFS geopolymer activated with sodium silicate (cured at 23 °C) resulted mainly in amorphous gel.
- Activated with sodium hydroxide resulted in significant crystalline CSH.
- Incorporation of GBFS enhanced compressive strength and microstructure of FA geopolymer pastes.
- Shear bond strength depended on strength and amount of NASH gel of FA–GBFS geopolymer.

ARTICLE INFO

Article history:
Received 27 December 2014
Received in revised form 16 March 2015
Accepted 1 May 2015

Keywords:
Geopolymer
Granulated blast furnace slag
Fly ash
Compressive strength
Shear bond strength
Repair material

ABSTRACT

This article investigated the effects of sodium hydroxide and sodium silicate solutions on the properties of fly ash (FA)–granulated blast furnace slag (GBFS) geopolymer. Three types of geopolymer pastes viz., FA paste, FA + GGBS paste and GGBS paste were tested. They were activated with three types of alkaline solutions viz., sodium hydroxide solution (NH), sodium silicate solution (NS), and sodium hydroxide plus sodium silicate solution (NHNS). NH with 10 molar concentration, alkaline liquid/binder ratio of 0.60 and curing at ambient temperature of 23 °C were used for all mixes. The results indicated that the reaction products and strengths of geopolymer depended on the types of source materials and alkali activators. The use of NH and NHNS solutions resulted in the formation of crystalline calcium silicate hydrate (CSH) which co-existed with amorphous gel. Whereas the use of NS solution resulted in mainly the amorphous products with only a small amount of crystalline CSH in GBFS paste. The increase in GBFS content enhanced the compressive strength and microstructure of geopolymer pastes due to the formation of additional CSH. The shear bond strength between Portland cement concrete substrate and geopolymer paste was found to relate to both compressive strength and amount of NASH gel of geopolymer paste.

© 2015 Published by Elsevier Ltd.

1. Introduction

The manufacturing of Portland cement (OPC) results in high emission of carbon dioxide (CO_2) to atmosphere causing greenhouse effect [1]. To solve this problem, the use of geopolymer as an alternative binder for application in concrete industry is recommended [2–5]. Geopolymeric material is formed using source materials containing silica (SiO_2) and alumina (Al_2O_3) such as fly ash (FA), calcined kaolin or metakaolin and granulated blast furnace slag (GBFS) activated with alkali solutions [6–10]. Specifically, sodium hydroxide based geopolymer is more attractive as it gives lower carbon footprint than sodium silicate based geopolymer. For normal strength concrete, Turner and Collins [11] showed that the CO_2 footprint of a sodium silicate based geopolymer concrete was approximately 9% less than comparable OPC concrete.

Fly ash is a by-product from coal burning in thermal power plants. Both low calcium fly ash [6,12] and high calcium fly ash [8,13] are suitable source materials due to their high SiO_2 and Al_2O_3 contents. One obstacle with the use of fly ash is the low

* Corresponding author. Tel./fax: +66 4320 2355.
E-mail address: prinya@kku.ac.th (P. Chindaprasirt).

http://dx.doi.org/10.1016/j.conbuildmat.2015.05.001
0950-0618/© 2015 Published by Elsevier Ltd.

strength development with ambient temperature curing [6]. A number of researchers [14–16] have incorporated additives containing calcium to enhance the strength development of fly ash geopolymer. The presence of calcium has a positive effect on the mechanical properties of geopolymeric material [9] by forming additional calcium silicate hydrate (CSH) which coexists with the geopolymer products [17,18]. However, a certain amount of calcium can lead to a decrease on compressive strength of geopolymers [19,20]. Pacheco-Torgal et al. [21] reported that when calcium hydroxide percentages above 10% are used, strength decrease after curing for 14 days is noticed.

GBFS is usually utilized as a binder in concrete industry due to its high content of CaO; and SiO_2 and Al_2O_3 in an amorphous state [22,23]. Therefore GBFS shows pozzolanic and binding properties in an alkaline medium [24]. A number of researchers [6,24,25] found that the incorporation of GBFS to FA geopolymer resulted in additional calcium in the system and the mechanical properties and microstructure of geopolymer were improved.

Several researchers indicate that sodium silicate and sodium hydroxide based activators are suitable considering the mechanical properties of GBFS and FA geopolymers [6,25,26]. The main reaction products formed as a result of alkali activation of GBFS are CSH and/or CASH gels similar to those of PC [27], whereas the main product of alkali activation of FA is NASH gel [28]. As GBFS is a glassy phase material, it is, therefore, easier to activate than fly ash. Fly ash contains a larger portion of crystalline phase and usually requires temperature between 40 and 85 °C to accelerate the reaction [24]. Previous studies suggested that the incorporation of GBFS results in the enhancement of strength development of fly ash geopolymers [29,30]. Bond strength is one of the most important properties of high performance binder for application as a repair material. Several tests i.e. pull-out, splitting, flexural, and slant shear are used to evaluate the bond strength of repair materials [3]. The slant shear test was successfully used to study the shear bond strength of concrete repair [31] and bond between concrete substrate and geopolymer [3,4].

Therefore, the use of GBFS to improve the strength of FA geopolymer is very attractive. The objective of this study is to investigate the mechanical properties viz., compressive strength and shear bond strength, and microstructure of FA–GBFS geopolymer with types of alkaline solutions. The obtained results should be beneficial to the understanding and to the future applications of FA–GBFS geopolymer.

2. Experimental details and testing analysis

2.1. Materials

The materials used in this research were fly ash (FA) from Hekinan power plant and ground granulated blast furnace slag (GBFS) from Nippon Steel & Sumitomo Metal Corporation. 10 M sodium hydroxide (NH) and sodium silicate (NS) with 11.67% Na_2O, 28.66% SiO_2, and 59.67% H_2O were used as activators.

The chemical compositions and physical properties of FA and GBFS are shown in Tables 1 and 2. The specific gravity of FA and GBFS were 2.20 and 2.91. The median particle sizes of FA and GBFS were 12.3 and 12.4 μm with the corresponding Blaine finenesses of 3100 and 4950 cm^2/g, respectively. Fig. 1 shows the scanning electron micrographs (SEM) of FA and GBFS. The FA consisted of spherical particles with smooth surface, while the GBFS consisted of irregular and angular particles similar to the previously published results [32]. The XRDs of FA and GBFS as shown in Fig. 2 showed that as-received FA mainly consisted of amorphous phase as shown by a hump around 18–28 °2theta with some crystalline phases of mullite ($Al_6Si_2O_{13}$), quartz (SiO_2), magnesioferrite (Fe_3O_4) and calcium oxide (CaO), while as-received GBFS mainly consisted of amorphous phase as shown by a hump around 25–35 °2-theta [27] with a small amount of magnetite.

Table 2
Physical properties of FA and GBFS.

Materials	Specific gravity	Median particle size (μm)	Blaine fineness (cm^2/g)
FA	2.20	12.3	3100
GBFS	2.91	12.4	4950

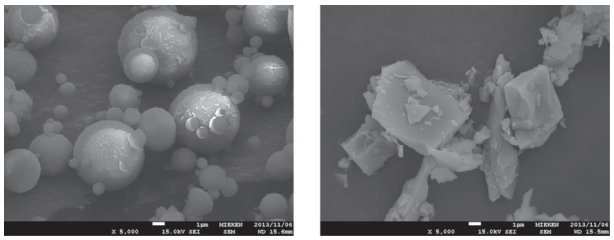

(a) FA (b) GBFS

Fig. 1. SEM of FA and GBFS.

2.2. Mix proportion and curing

The mix proportions of geopolymer pastes are shown in Table 3. Constant liquid alkaline to binder ratio of 0.60 was used for all mixes. Three types of geopolymer pastes viz., FA paste, FA + GGBS paste and GGBS paste and three types of alkaline solutions viz., sodium hydroxide solution (NH), sodium silicate solution (NS), and sodium hydroxide plus sodium silicate solution (NHNS) were used. The NHNS solution was prepared with NS/NH ratio of 2.0. For the other series the NH and NS solutions were used directly. For the mixing of pastes, FA and GBFS were dry mixed until the mixture was homogenous. Right after, the liquid solution was added and the mixing of paste was done for another 3 min.

2.3. Testing and analysis

2.3.1. Compressive strength of geopolymer pastes

After being mixed, the fresh geopolymer pastes were placed into cylindrical moulds of 50 mm in diameter and 100 mm in height. They were covered with vinyl sheet and placed in ambient temperature curing (23 °C). The samples were demoulded at the age of 1 day and immediately wrapped with vinyl sheet to protect moisture loss and kept in the 23 °C controlled room until the testing age. The compressive strengths were tested at the ages of 7, 28, and 60 days. The reported results were the average of three samples.

2.3.2. X-ray diffraction (XRD) and scanning electron microscopy (SEM) of geopolymer pastes

At the age of 28 days, the geopolymer paste samples were broken and the middle portion was collected and ground to fine powder. The XRD scans were performed at 5–60 °2theta with an increment of 0.02°/step and a scan speed of 0.5 s/step. The amorphous phases of geopolymer pastes were determined by quantitative XRD analysis using Bruker's TOPAS software. The specimen was placed on a brass stub sample holder with double stick carbon tape. The specimen was dried using infrared light for 5 min and then coated with a layer of gold using a blazer sputtering coater. The micrographs were recorded at 20 kV and 1000× magnification.

2.3.3. Shear bond strength between concrete substrate and geopolymer paste

The shear bond strength was evaluated using the slant shear test of concrete substrate and geopolymer paste. The slant angle of 30° to the vertical is recommended by ASTM C882 [33] because the failure stress is close to the minimum stress [31]. However, stiffer angle of 45° is also officially used for the standard

Table 1
Chemical compositions of FA and GBFS (by weight).

Materials	SiO_2	Al_2O_3	Fe_2O_3	CaO	MgO	K_2O	Na_2O	SO_3	LOI
FA	52.31	27.04	6.85	3.32	1.23	1.29	1.15	0.99	1.60
GBFS	30.53	13.67	0.33	46.00	5.09	0.36	0.24	–	0.22

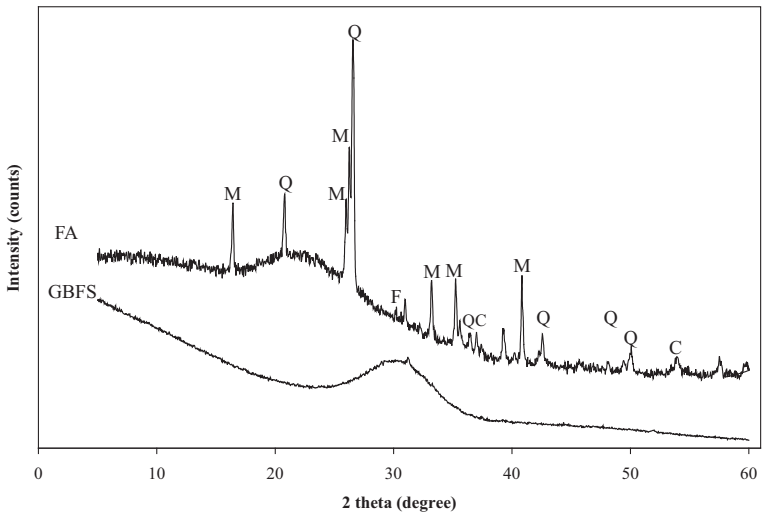

Fig. 2. XRD of FA and GBFS.

Table 3
Mix proportions of geopolymer pastes.

Mix No.	Source material	Activator	FA (g)	GBFS (g)	NaOH (g)	Na_2SiO_3 (g)	SiO_2/Al_2O_3 ratio	CaO/SiO_2 ratio
1	FA	NH	100	–	60	–	1.94	0.06
2	FA + GBFS	NH	50	50	60	–	2.04	0.60
3	GBFS	NH	–	100	60	–	2.23	1.51
4	FA	NHNS	100	–	20	40	2.36	0.05
5	FA + GBFS	NHNS	50	50	20	40	2.56	0.47
6	GBFS	NHNS	–	100	20	40	3.07	1.10
7	FA	NS	100	–	–	60	2.57	0.05
8	FA + GBFS	NS	50	50	–	60	2.88	0.42
9	GBFS	NS	–	100	–	60	3.49	0.96

evaluation of epoxy bond with concrete [34]. Preliminary test showed that the 45° concrete substrate was easier to cut with less chipping and cracking than the 30° concrete substrate. The slant angle of 45° was, therefore, used in this study. The results could be compared within the context of this work and the results should thus be interpreted with care.

The preparations of concrete specimens and the casting of slant shear specimens were based on the previous study [3,4]. The concrete substrates were prepared using the aged slant shear concrete prisms by cutting in half at 45° line to the vertical. The saw cut surface was used as it was shown to be suitable substrate concrete surface for shear bond strength assessment [35]. The compressive strength of concrete substrate was 35.0 MPa. The paste was then cast into the mold with the other half filled with concrete substrate. After the casting of samples, they were covered with vinyl sheet to protect moisture loss and kept in the 23 °C controlled room until the testing ages. The shear bond strength was calculated as the ratio of maximum load at failure and the bond area. The shear bond strength was measured at the age of 28 days with a constant loading rate of 0.30 MPa/s. The reported results were the average of three samples.

In addition, two available commercial repair material products (Epoxy A and Epoxy B) were tested for shear bond strengths with concrete substrate and compared with those of geopolymer pastes. Epoxy A was a general purpose non-shrink grout mortar and Epoxy B was a multi-purpose non-shrink grout. The recommended water to binder ratio of 0.15 was used for Epoxy-A and the 28-day compressive strength was 62.0 MPa. For Epoxy-B, the recommended water to binder ratio of 0.14 was used and the 28-day compressive strength was 70.0 MPa. The preparation of the slant shear prism was the same as those of the geopolymer slant shear test.

3. Results and discussions

3.1. Compressive strength

The results of compressive strengths of geopolymer pastes are shown in Table 4. The compressive strength of pastes obviously increased with increasing GBFS content for all NH, NHNS and NS series. For example, the 28-days compressive strengths of FA, FA + GBFS and GBFS pastes with NHNS were 42.8, 114.5, and 171.7 MPa, respectively. The readily available free calcium ions reacted with silica and alumina and formed C(A)SH gel which coexisted with the geopolymer gels [27,36]. In addition, the reaction of GBFS and alkali solutions was an exothermal process and generated heat which promoted the geopolymerization process. The increase in GBFS content, therefore, led to high compressive strength geopolymer pastes.

Table 4
Compressive strength of geopolymer pastes.

Mix No.	Source material	Activator	Compressive strength (MPa)		
			7 days	28 days	60 days
1	FA	NH	0*	1.5	4.4
2	FA + GBFS	NH	6.5	18.3	26.2
3	GBFS	NH	15.5	27.1	34.4
4	FA	NHNS	0*	42.8	52.9
5	FA + GBFS	NHNS	84.9	114.5	127.2
6	GBFS	NHNS	144.4	171.7	176.4
7	FA	NS	0*	0*	1.1
8	FA + GBFS	NS	38.7	54.9	62.4
9	GBFS	NS	119.6	173.0	197.1

0* = very low strength.

According to Table 4, the mixes with 100% FA gave low early strengths for all NH, NHNS and NS series. The NH solution is important for dissolving of Si^{4+} and Al^{3+} ions from raw materials and subsequent geopolymerization process [17]. However, the strength development of FA paste activated by either NH or NS at ambient

temperature was very low [17,37]. The use of NHNS showed significant improvement in the strength development at later ages. For the FA paste with NHNS, although the 7-day compressive strength was very low, the 28-day and 60-day compressive strengths were relatively high at 45.0 and 52.9 MPa, respectively. The low strength at early stage of FA paste was due to low reaction process at ambient temperature, however, the strength development of FA paste over time is similar to that of Portland cement concrete [15].

For the mix with increased GBFS content (FA + GBFS paste), the paste with NH gave lower strength than those with NHNS and NS. As mentioned, NaOH is needed for the leaching of silica and alumina. However, the leaching and subsequent reaction is low at ambient temperature around 23 °C [38]. The use of NS alone or in conjunction with NH resulted in additional silicate in the system and this helped speed up the geopolymerization leading to increased compressive strength [26]. In addition, the FA + GBFS paste with NHNS showed higher strength than those of NH and NS for all of curing age. The FA + GBFS blend with NHNS was the most effective alkali activated binder and high strength mixes were obtained. Similarly, high strength mixes were also reported with the GBFS geopolymer with sodium sulfate [39].

For the GBFS paste, the paste with NS showed the highest compressive strength at the ages of 28 and 60 days due to the reaction between CaO from GBFS and SiO_2 with subsequent formation of CSH [27]. Ismail et al. [27] reported that the alkali activation of GBFS involved the dissolution of Ca and participation of Si and Al to form CSH and CASH gel and thus led to high mechanical strength. Furthermore, the compressive strength of geopolymer depends primarily on SiO_2/Al_2O_3 mole ratio [40]. Previous research reported that SiO_2/Al_2O_3 around 3.50 gave a high strength high calcium geopolymer [41]. It should be noted here that the SiO_2/Al_2O_3 ratio of GBFS paste with NS was 3.49 (see Table 3). The 28-day compressive strength of this paste cured at ambient temperature was very high at 171.7 MPa.

3.2. XRD analysis

The results of XRD patterns of geopolymer pastes are shown in Figs. 3–5. As shown in Fig. 3 for the NH series, the FA paste consisted of glassy phase as indicated by the hump at 28–35 °2theta [41] and crystalline phases of quartz, mullite, magnetite and hydrosodalite ($Na_4Al_3Si_3O_{12}(OH)$). These crystalline phases were mainly from the remain of non-reacted elements from FA. The presence of sodium alumino-silicate zeolite in the form of hydrosodalite indicated some geopolymerization, but the strength of geopolymer paste was still low [17]. For the mix with increased GBFS content (FA + GBFS paste), the XRD pattern of paste with NH showed both amorphous and crystalline phases. The peak of the crystalline phases viz., quartz, mullite, magnetite and hydrosodalite were reduced and additional peak of calcium silicate hydrate (CSH) was present. This indicated the reaction of calcium to form CSH and also the presence of NASH gel with reduced hydrosodalite resulting in an increase in the strength of paste. For the GBFS paste with NH, the major phase of paste was amorphous with additional CSH and calcite with no appearances of quartz, mullite, magnetite and hydrosodalite. The high CaO content contributed to the development of CSH and the excess CaO reacted with CO_2 and formed calcite [9]. The CSH gel and calcite coexisted with the NASH gel [27] and reasonable 28-days compressive strength of 27.1 MPa was obtained.

For the NHNS mixes as shown in Fig. 4, the FA paste consisted of glassy phase as indicated by the hump at 28–35 °2theta and the crystalline phases of quartz, mullite and magnetite with no hydrosodalite. The strength came mainly from the NASH gel and relatively high 28-days strength of 42.8 MPa was obtained. For the FA + GBFS paste with NHNS, additional CSH was formed with reduced amount of quartz and mullite. Additional CSH was responsible for the increase in strength and the high 28-days compressive strength of 114.5 MPa was obtained. For the GBFS paste with NHNS, the XRD pattern showed a large amount of amorphous phase with additional CSH and only a small amount of magnetite (from GBFS). With only GBFS, the amorphous phases were easily detected as broad hump around 28–35 °2theta due to the formation of amorphous components in geopolymer gel. Calcium element also reacted to form CSH which coexisted with geopolymer gel [27] and high 28-days compressive strength of 171.7 MPa was obtained. The presence of CSH and relatively high compressive strength is in line with the previous research [6]. For mixes with NSNH, the incorporation of GBFS provided calcium to react and form CSH in the geopolymer system. Without GBFS, there was insufficient calcium and no CSH was, therefore, detected similar to the mixes with NH solution only.

For the NS mix as shown in Fig. 5, the XRD of FA paste showed the amorphous phase of NASH gel with hump around

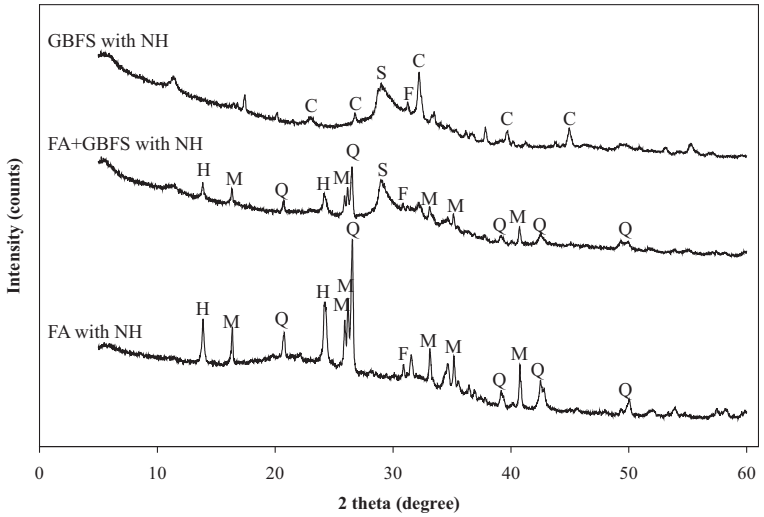

Q = Quartz (SiO_2), M = Mullite ($Al_6Si_2O_{13}$), H = Hydrosodalite ($Na_4Al_3Si_3O_{12}(OH)$), F=Magnetite (Fe_3O_4), C= Calcite, S= Calcium Silicate Hydrate

Fig. 3. XRD of geopolymer pastes with NH.

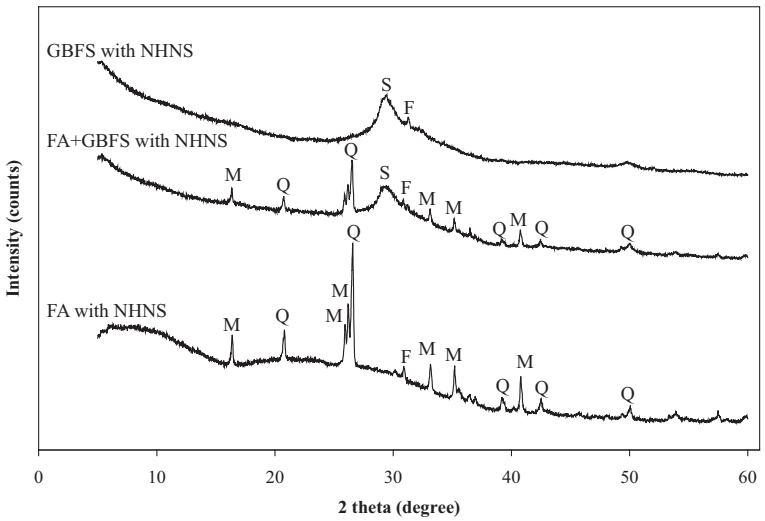

Q = Quartz (SiO_2), M = Mullite ($Al_6Si_2O_{13}$), F=Magnetite (Fe_3O_4), S= Calcium Silicate Hydrate

Fig. 4. XRD of geopolymer pastes with NHNS.

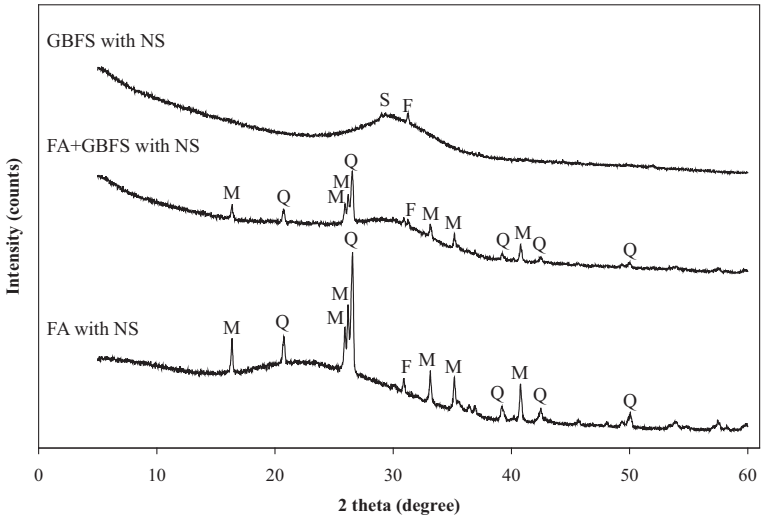

Q = Quartz (SiO_2), M = Mullite ($Al_6Si_2O_{13}$), F=Magnetite (Fe_3O_4), S= Calcium Silicate Hydrate

Fig. 5. XRD of geopolymer pastes with NS.

18–32 °2theta with crystal of quartz, mullite and magnetite. With the incorporation of 50% GBFS (FA + GBFS paste), the paste with NS showed also amorphous phases, however, with a shift in the location of the hump to a broad hump around 28–35 °2theta with associated decreases in quartz and mullite peaks. The reductions of crystalline phase were similar to the behaviors of NHNS paste. The shift in the broad hump was significant indicating the increased disorder of the glass phase and the presence of some CASH compound [42]. While, the XRD of GBFS paste with NS indicated the existence of amorphous gel and a small amount of crystalline CSH with only the crystalline phases of magnetite. Mixes with NS only should also have a high pH condition initially, therefore a small amount of crystalline CSH could thus be formed [43]. The lowering of pH condition in the mix favored the formation of the NASH gel [41] while the crystalline phase of magnetite from GBFS remained. This resulted in high 28-day compressive strength of GBFS paste with NS of 173.0 MPa.

3.3. SEM analysis

The results of SEM analyses of fracture surfaces of geopolymer pastes are shown in Fig. 6. In general, the FA pastes had rather loose matrix as shown in Fig. 6a, d and g. The FA pastes with NH and NS showed less dense and loose matrix while the SEM of FA paste with NHNS showed a larger number of non-reacted and/or partially reacted fly ash particles embedded in a continuous matrix. The FA paste with NHNS appeared to be slightly denser than those NH and NS. This is in line with the previous research which indicated that the use of NH in conjunction with NS could accelerate the geopolymerization process [38].

Noticeable difference was found with the FA + GBFS mix compared to that of FA paste. The micrograph showed less number of unreacted fly ash particles and the matrices appeared denser than those of FA pastes. FA is relatively slow to react at ambient temperature and temperature curing is needed to accelerate the strength

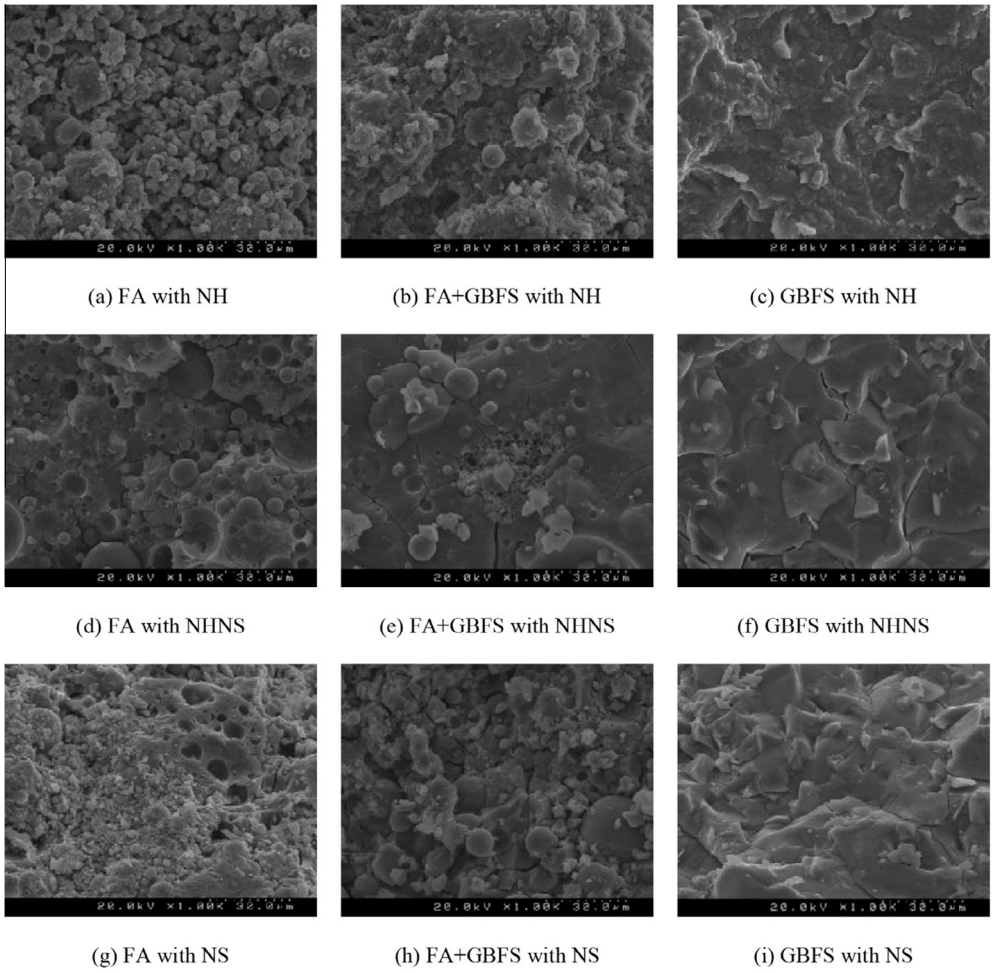

Fig. 6. SEM of geopolymer pastes.

development [44,45]. The increasing in GBFS content enhanced the reaction. Also, the reaction of GBFS with alkali solution is an exothermal process and liberated heat and thus formation of additional CSH and CASH led to the overall strength development [7,27]. According to Fig. 6, the FA + GBFS paste with NHNS appeared denser than those of with NH and NS. It appeared that the activation with NHNS solution enhanced the geopolymerization of the FA–GBFS geopolymer paste compared with the activation with single activator as reported by previous research [46]. The relatively high 28-day strength of 114.5 MPa was obtained with the FA + GBFS mix with NHNS.

For the GBFS mix, the matrix appeared denser and more homogenous than the pastes with 50% and 0% GBFS. As mentioned, additional CSH from the reaction of GBFS and alkali solution was formed [27]. This additional CSH modify the microstructure of paste. In addition, mixes with sodium silicate i.e. pastes with NHNS (see Fig. 6f) and NS (see Fig. 6i) appeared denser than the mix with NH (see Fig. 6c). The silicate in the system promoted the reaction between calcium and silicate and formed calcium silicate products.

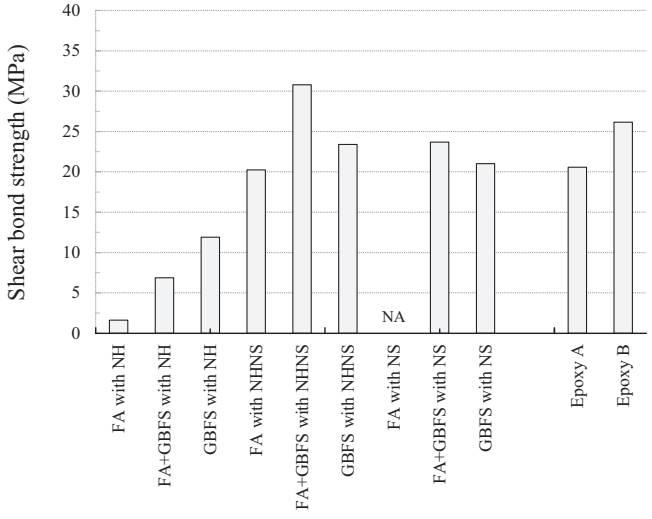

Fig. 7. Shear bond strength between concrete substrate and geopolymer paste or epoxy with interface line at 45° to the vertical.

3.4. Shear bond strength between concrete substrate and geopolymer pastes

The results of slant shear capacity of Portland cement concrete substrate (compressive strength of 35 MPa) and geopolymer paste at 45° of interface line to the vertical are shown in Fig. 7. The shear bond strengths tended to increase with the increasing GBFS content for all three series.

For the NH series, the strengths increased with increasing GBFS content. The shear bond strengths of FA, FA + GBFS and GBFS pastes

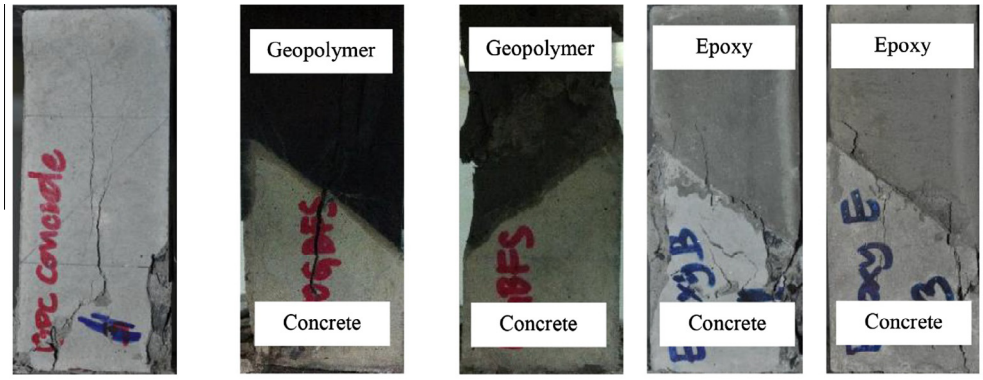

Fig. 8. Specimen failure modes.

were 3.0, 7.0 and 12.0 MPa, respectively. The increase in shear bond strength was directly related to the increase in compressive strength of geopolymer paste. It had been reported that the tensile strength and bonding of geopolymer were higher than those of conventional Portland cement system [47]. In addition, the high CaO content from GBFS promoted the formation of additional CSH and/or CASH gel, therefore, the bonding at the interface transition zone between old concrete and geopolymer was enhanced [3,4].

For the NS series, the compressive strength tended to increase with the increase in GBFS content. However, the shear bond strength at high 100% GBFS content (GBFS paste with NS) started to drop compared with that of 50% GBFS mix (FA + GBFS paste with NS). For the FA + GBFS mix, the paste contained predominantly NASH gel with some CSH/CASH products. At high 100% GBFS content, with the presence of a large amount of calcium, CSH and/or CASH gel formed in a substantial quantity in addition to NASH gel. This is considered somehow offsetting the excellent bonding behavior resulting in a slight drop in the shear bond strength at this high level of GBFS content. It is worth mentioning that the shear bond strength does not only depend on the strength of geopolymer, the strength of a weaker portion i.e. concrete substrate also has a large influence.

For the NHNS series, the trend of the result was similar to those of NS series. The optimum shear bond strength was obtained with the 50% GBFS content mix, and at high 100% GBFS content, the bond strengths were slightly lowered. However, the shear bond strengths of this series were higher than those of the other series. The high shear bond strengths generally corresponded to the high compressive strengths of geopolymer pastes.

The shear bond strengths of two available commercial repair material products (Epoxy A and Epoxy B) and concrete substrate are also shown in Fig. 7. The shear bond strength between concrete substrate and Epoxy A and Epoxy B were 20.6 and 26.2 MPa, respectively. The shear bond strengths of 5 mixes i.e. all three NHNS mixes viz., FA, FA + GBFS and GBFS pastes with NHNS; and the other two NS mixes viz., FA + GBFS and GBFS with NS were comparable to those of the epoxy mixes. This indicated that the FA–GBFS geopolymer pastes should be look into more extensively for the application as repair materials.

The failure patterns of the concrete sample and samples from the shear bond tests (slant angle of 45°) are given in Fig. 8. The failure pattern of concrete sample was in a monolithic failure mode (Fig. 8a). For the high shear bond strength of FA + GBFS paste with NHNS (Fig. 8b), the monolithic failure mode was also observed. Namely, the geopolymer and concrete substrate acted as one unit and the crack formed and run in the vertical direction passed through the slant bond area similar to the failure mode of normal concrete specimen (Fig. 8a). This confirmed the excellent bonding between geopolymer and concrete substrate. The failure patterns of FA paste with NS, Epoxy A and Epoxy B are shown in Figs. 8c – e. The failure modes were similar and were between the combined failure with monolithic failure and bond failure. Crack path covered the concrete substrate, bonding surface and geopolymer paste. This was considered due to the similar shear bond strengths of the FA paste with NS and the two epoxy samples (Fig. 7). The results in Figs. 7 and 8 thus indicated the suitability of the FA + GBFS mix with NHNS for high shear bond strength requirement.

The 28-day shear bond strengths of usable geopolymer pastes obtained from this work were approximately 21–31 MPa which were higher than the previously published results [3]. This was due to the use of slant angle of 45° to the vertical in this study compared to 30° in the previous work. Similar trend of result was reported in the previously published work [31].

4. Conclusions

The effect of using sodium hydroxide and sodium silicate solutions as liquid portions in the mixture on properties of FA–GBFS geopolymer was investigated in this study. The FA paste contains amorphous NASH gel and some crystalline phases of the remain of fly ash. The increase in GBFS content enhanced the compressive strength and microstructure of geopolymer pastes due to the formation of additional CSH. The use of NH and NHNS solutions resulted in crystalline CSH and amorphous gel, whereas the use of NS solution resulted in mainly the amorphous products.

For the FA and FA + GBFS pastes, the use of NH solution or NS solution alone gave low strengths when cured at ambient temperature. Better strength development was obtained with the use of NHNS solution. For the GBFS paste, the presence of silicate enhanced the strength development and thus pastes containing NS solution performed better. Relatively high 28-day compressive strengths of 171.7 and 173.0 MPa were obtained for GBFS pastes with NHNS and NS solutions, respectively.

The shear bond strength (slant angle of 45°) between concrete substrate and geopolymer paste was increased with the increase in compressive strength and amount of NASH gel of geopolymer paste. The highest 28-day shear bond strength of 31.0 MPa was obtained with FA + GBFS paste with NHNS solution. This indicates that it may be possible to use FA–GBFS geopolymer pastes as a repair material. However, additional tests are required to confirm this.

Acknowledgements

The authors gratefully acknowledge the financial supported from Higher Education Research Promotion and National Research University Project of Thailand, Office of the Higher Education Commission, through the Advanced Functional Materials Cluster of Khon Kaen University; Khon Kaen University and the Thailand Research Fund (TRF) under the TRF Senior Research Scholar, Grant No. RTA5780004. The authors also would like to acknowledge the support of the Mie Prefecture Industrial Research Institute and Department of Architecture, Faculty of Engineering, Mie University, Japan.

References

[1] Kroehong W, Sinsiri T, Jaturapitakkul C, Chindaprasirt P. Effect of palm oil fuel ash fineness on the microstructure of blended cement paste. Constr Build Mater 2011;25(11):4095–104.
[2] Hu S, Wang H, Zhang G, Ding Q. Bonding and abrasion resistance of geopolymeric repair material made with steel slag. Cement Concr Compos 2008;30(3):239–44.
[3] Pacheco-Torgal F, Castro-Gomes JP, Jalali S. Adhesion characterization of tungsten mine waste geopolymeric binder. Influence of OPC concrete substrate surface treatment. Constr Build Mater 2008;22(3):154–61.
[4] Phoo-ngernkham T, Chindaprasirt P, Sata V, Hanjitsuwan S, Hatanaka S. The effect of adding nano-SiO_2 and nano-Al_2O_3 on properties of high calcium fly ash geopolymer cured at ambient temperature. Mater Des 2014;55:58–65.
[5] Suksiripattanapong C, Horpibulsuk S, Chanprasert P, Sukmak P, Arulrajah A. Compressive strength development in geopolymer masonry units manufactured from water treatment sludge. Constr Build Mater 2015;82:20–30.
[6] Kumar S, Kumar R, Mehrotra SP. Influence of granulated blast furnace slag on the reaction, structure and properties of fly ash based geopolymer. J Mater Sci 2010;45(3):607–15.
[7] Li C, Sun H, Li L. A review: The comparison between alkali-activated slag (Si+Ca) and metakaolin (Si+Al) cements. Cem Concr Res 2010;40(9):1341–9.
[8] Phoo-ngernkham T, Chindaprasirt P, Sata V, Pangdaeng S, Sinsiri T. Properties of high calcium fly ash geopolymer pastes containing Portland cement as additive. Int J Miner Metall Mater 2013;20(2):214–20.
[9] Ravikumar D, Peethamparan S, Neithalath N. Structure and strength of NaOH activated concretes containing fly ash or GGBFS as the sole binder. Cement Concr Compos 2010;32(6):399–410.
[10] Bagheri A, Nazari A. Compressive strength of high strength class C fly ash-based geopolymers with reactive granulated blast furnace slag aggregates designed by Taguchi method. Mater Des 2014;54:483–90.
[11] Turner LK, Collins FG. Carbon dioxide equivalent (CO_2-e) emissions: a comparison between geopolymer and OPC cement concrete. Constr Build Mater 2013;43:125–30.
[12] Diaz EI, Allouche EN, Eklund S. Factors affecting the suitability of fly ash as source material for geopolymers. Fuel 2010;89(5):992–6.
[13] Phoo-ngernkham T, Chindaprasirt P, Sata V, Sinsiri T. High calcium fly ash geopolymer containing diatomite as additive. Indian J Eng Mater Sci 2013;20(4):310–8.
[14] Palomo A, Fernández-Jiménez A, Kovalchuk G, Ordoñez LM, Naranjo MC. Opc-fly ash cementitious systems: study of gel binders produced during alkaline hydration. J Mater Sci 2007;42(9):2958–66.
[15] Temuujin J, van Riessen A, Williams R. Influence of calcium compounds on the mechanical properties of fly ash geopolymer pastes. J Hazard Mater 2009;167(1–3):82–8.
[16] Williams PJ, Biernacki JJ, Walker LR, Meyer HM, Rawn CJ, Bai J. Microanalysis of alkali-activated fly ash–CH pastes. Cem Concr Res 2002;32(6):963–72.
[17] Somna K, Jaturapitakkul C, Kajitvichyanukul P, Chindaprasirt P. NaOH-activated ground fly ash geopolymer cured at ambient temperature. Fuel 2011;90(6):2118–24.
[18] Guo X, Shi H, Chen L, Dick WA. Alkali-activated complex binders from class C fly ash and Ca-containing admixtures. J Hazard Mater 2010;173(1–3):480–6.
[19] Yip CK, Lukey GC, Van Deventer JSJ. The coexistence of geopolymeric gel and calcium silicate hydrate at the early stage of alkaline activation. Cem Concr Res 2005;35(9):1688–97.
[20] Lee WKW, Van Deventer JSJ. The effects of inorganic salt contamination on the strength and durability of geopolymers. Colloids Surf, A 2002;211(2–3):115–26.
[21] Pacheco-Torgal F, Castro-Gomes JP, Jalali S. Investigations on mix design of tungsten mine waste geopolymeric binder. Constr Build Mater 2008;22(9):1939–49.
[22] Aydın S, Baradan B. Effect of activator type and content on properties of alkali-activated slag mortars. Compos B Eng 2014;57:166–72.
[23] Imbabi MS, Carrigan C, McKenna S. Trends and developments in green cement and concrete technology. Int J Sustainable Built Environ 2012;1(2):194–216.
[24] Puertas F, Marfınez-Ramírez S, Alonso S, Vázquez T. Alkali-activated fly ash/slag cements: strength behaviour and hydration products. Cem Concr Res 2000;30(10):1625–32.
[25] Rashad AM. Properties of alkali-activated fly ash concrete blended with slag. Iran J Mater Sci Eng 2013;10(1):57–64.
[26] Ravikumar D, Neithalath N. Effects of activator characteristics on the reaction product formation in slag binders activated using alkali silicate powder and NaOH. Cement Concr Compos 2012;34(7):809–18.
[27] Ismail I, Bernal SA, Provis JL, San Nicolas R, Hamdan S, van Deventer JSJ. Modification of phase evolution in alkali-activated blast furnace slag by the incorporation of fly ash. Cement Concr Compos 2014;45:125–35.
[28] Garcia-Lodeiro I, Fernandez-Jimenez A, Palomo A. Hydration kinetics in hybrid binders: early reaction stages. Cement Concr Compos 2013;39:82–92.
[29] Ismail I, Bernal SA, Provis JL, San Nicolas R, Brice DG, Kilcullen AR, et al. Influence of fly ash on the water and chloride permeability of alkali-activated slag mortars and concretes. Constr Build Mater 2013;48:1187–201.
[30] Parthiban K, Saravanarajamohan K, Shobana S, Bhaskar AA. Effect of replacement of slag on the mechanical properties of fly ash based geopolymer concrete. Int J Eng Technol 2013;5(3):2555–9.
[31] Austin S, Robins P, Pan Y. Shear bond testing of concrete repairs. Cem Concr Res 1999;29(7):1067–76.
[32] Memon SA, Lo TY, Barbhuiya SA, Xu W. Development of form-stable composite phase change material by incorporation of dodecyl alcohol into ground granulated blast furnace slag. Energy Build 2013;62:360–7.
[33] ASTM C882. Standard test method for bond strength of epoxy-resin systems used with concrete by slant shear. Annual book of ASTM standard, vol. 04.02; 2005.
[34] FM 3-C 882. Florida Test Method for Performance of epoxy-resin systems with concrete by slant shear and compressive strength. In: Florida department of transportation standard specifications for road and bridge construction; 2015.
[35] Naderi M. Effects of cyclic loading, freeze-thaw and temperature changes on shear bond strengths of different concrete repair systems. J Adhes 2008;84(9):743–63.
[36] Puertas F, Palacios M, Manzano H, Dolado JS, Rico A, Rodríguez J. A model for the C-A-S-H gel formed in alkali-activated slag cements. J Eur Ceram Soc 2011;31(12):2043–56.
[37] Temuujin J, Williams RP, van Riessen A. Effect of mechanical activation of fly ash on the properties of geopolymer cured at ambient temperature. J Mater Process Technol 2009;209(12–13):5276–80.
[38] Rattanasak U, Chindaprasirt P. Influence of NaOH solution on the synthesis of fly ash geopolymer. Miner Eng 2009;22(12):1073–8.
[39] Rashad AM, Bai Y, Basheer PAM, Milestone NB, Collier NC. Hydration and properties of sodium sulfate activated slag. Cement Concr Compos 2013;37:20–9.
[40] Duxson P, Provis JL, Lukey GC, van Deventer JSJ. The role of inorganic polymer technology in the development of 'green concrete'. Cem Concr Res 2007;37(12):1590–7.
[41] Chindaprasirt P, De Silva P, Sagoe-Crenstil K, Hanjitsuwan S. Effect of SiO_2 and Al_2O_3 on the setting and hardening of high calcium fly ash-based geopolymer systems. J Mater Sci 2012;47(12):4876–83.
[42] Hunnicutt WA. Characterization of calcium-silicate-hydrate and calciumalumino-silicate-hydrate: University of Illinois at Urbana-Champaign; 2013.
[43] Khale D, Chaudhary R. Mechanism of geopolymerization and factors influencing its development: a review. J Mater Sci 2007;47(3):729–46.
[44] Pangdaeng S, Phoo-ngernkham T, Sata V, Chindaprasirt P. Influence of curing conditions on properties of high calcium fly ash geopolymer containing Portland cement as additive. Mater Des 2014;53:269–74.
[45] Wongpa J, Kiattikomol K, Jaturapitakkul C, Chindaprasirt P. Compressive strength, modulus of elasticity, and water permeability of inorganic polymer concrete. Mater Des 2010;31(10):4748–54.
[46] Oh JE, Monteiro PJM, Jun SS, Choi S, Clark SM. The evolution of strength and crystalline phases for alkali-activated ground blast furnace slag and fly ash-based geopolymers. Cem Concr Res 2010;40(2):189–96.
[47] Sofi M, van Deventer JSJ, Mendis PA, Lukey GC. Engineering properties of inorganic polymer concretes (IPCs). Cem Concr Res 2007;37(2):251–7.

Thermochimica Acta 600 (2015) 20–27

Contents lists available at ScienceDirect

Thermochimica Acta

journal homepage: www.elsevier.com/locate/tca

Curing kinetic, thermal and adhesive properties of epoxy resin cured with cashew nut shell liquid

Pornnpa Kasemsiri [a], Arthit Neramittagapong [a,**], Prinya Chindaprasirt [b,*]

[a] Sustainable Infrastructure Research and Development Center and Department of Chemical Engineering, Faculty of Engineering, Khon Kaen University, Khon Kaen 40002, Thailand

[b] Sustainable Infrastructure Research and Development Center and Department of Civil Engineering, Faculty of Engineering, Khon Kaen University, Khon Kaen 40002, Thailand

ARTICLE INFO

Article history:
Received 13 September 2014
Received in revised form 28 November 2014
Accepted 29 November 2014
Available online 2 December 2014

Keywords:
Cashew nut shell liquid
Epoxy resin
Curing agent
Adhesive

ABSTRACT

The curing kinetic, thermal and adhesive properties of epoxy resin cured with cashew nut shell liquid (CNSL) were investigated. The CNSL was used as a curing agent for epoxy resin. The epoxy resin cured with 10, 20 30, 40 and 50 wt% of CNSL showed two-stages curing process between 165–170 °C and 230–235 °C. The solvent extraction experiment indicated that the CNSL content should not exceed 40 wt% to avoid the presence of unreacted CNSL. The apparent activation energy (E_a) of 60/40 epoxy resin/CNSL copolymer was obtained from Friedman's model-free method for both stages of curing process. The kinetic model and kinetic parameters were determined by Málek's method and the reaction processes was simulated favorably by Sestak–Berggren (SB (m, n)) model. In addition, silica powder was used to improve the adhesion and thermal properties of copolymer. The epoxy resin/CNSL copolymer with 0.5 wt % silica showed a substantial increase in the lap shear strength and thermal stability tended to increase with increasing silica content. The epoxy resin/CNSL composite showed a great potential for use as a high performance adhesive with good thermal stability.

© 2014 Elsevier B.V. All rights reserved.

1. Introduction

Epoxy resins are the most important thermosetting polymers which have been extensively used as adhesives in various applications such as aerospace and surface coating industries [1]. This is due to their outstanding properties viz., good adhesion to various substrates, high modulus, high temperature performance, low shrinkage and good corrosion resistance [2,3]. However, the application of this polymer is limited to certain areas due to its rather high rigidity and brittleness. In principle, toughness of epoxy resin can be enhanced by incorporating a rubber or a thermoplastic polymer [4–6].

Recently, the development of epoxy resin-based renewable organic material has attracted a lot of attention [7,8]. Cardanol-based novolac resins have been also studied as modifiers and curing agent for commercial epoxy resins to improve the toughness and other mechanical properties [8]. Cardanol is the main component of cashew nut shell liquid (CNSL) obtained as a by-product during the process of removing cashew kernel from its nut [9]. The major components of CNSL are anacardic acid, cardanol, and traces of cardol and 1-methylcardol.

From previous work, Mathew et al. [10] investigated the curing behavior of epoxy resin with a conventional amide-type hardener and CNSL and showed that the presence of multifunctionalities such as OH, COOH and aliphatic unsaturations in CNSL's molecule provides the chemical reaction with epoxy resin. Generally, CNSL has various applications in different industries such as friction linings, paints and varnishes, laminating resins, rubber compounding resin, urethane based polymer, surfactant, modifier agent of benzoxazine resin for wood composite production and intermediate for chemical industries [11–18]. Consequently, CNSL is an excellent candidate material to modify the properties of epoxy resin and to reduce the adhesive cost.

In order to optimize the final product of epoxy resin modified with CNSL, it is important to understand its curing process and kinetic parameters [19]. The curing of a resin system is a major controlling step for fabrication and thermosetting of matrix composites. The curing process of epoxy resin is the crosslinking of linear macromolecules with complicated mechanism [20]. To monitor the curing process, kinetic models obtained from reliable

* Corresponding author. Tel.: +66 4 336 2240; fax: +66 4 4336 2142.
** Corresponding author.
E-mail addresses: artyner@kku.ac.th (A. Neramittagapong), prinya@kku.ac.th (P. Chindaprasirt).

http://dx.doi.org/10.1016/j.tca.2014.11.031
0040-6031/© 2014 Elsevier B.V. All rights reserved.

methods are crucial for the process control, optimization of the polymer network processing and analysis of kinetic parameters. Kinetic analysis of non-isothermal resin cured system can be performed by multiple heating rates [21]. A multiple heating-rate method provides good reliable kinetic parameters and is suitable for evaluating both simple and complex chemical reactions [22,23]. Currently, there is a lack of information about the properties of adhesive based epoxy resin cured by hardener based on renewable organic material, without conventional or synthesized hardener. Therefore, the objective of this work is to investigate the effects of epoxy resin cured with CNSL on the curing process by isoconventional method. Furthermore, the thermal properties and adhesion performance of epoxy resin/CNSL copolymer reinforced with silica are also examined.

2. Experimental details

2.1. Materials

Epoxy resin based on Bisphenol A diglycidyl ether (DGEBA) was supplied by Dow Chemical (Thailand) Co., Ltd. Cashew nut shell liquid (CNSL) from Maboonkrong Sirichai 25 Ltd., was used as the curing agent. Amorphous silica powder HDK T40 from Wacker Chemie AG was used as filler. The specific gravity of silica powder is 2.20 and its particle size is less than 10 nm.

2.2. Chemical characterization of CNSL compositions

The CNSL's fractions were analyzed by gas chromatography–mass spectrometry (GC–MS) 2010: DB capillary column (30m × 0.25 mm, 0.25 μm film thickness). The initial oven temperature of GC was 40 °C for 2 min and then programmed to increase at a rate of 5 °C/min to 270 °C. Helium was used as the carrier gas with a rate of 0:7 ml/min. The percent of area was obtained electronically from GC–MS response without the use of internal standard.

2.3. Preparation of epoxy resin–cashew nut oil matrix

Mixtures were prepared with epoxy resin/CNSL mass ratios of 10/90, 20/80, 30/70, 40/60 and 50/50 by blending with magnetic stirrer at 80 °C for 30 min. They were for the curing behaviors and kinetic tests.

2.4. Preparation of epoxy resin–CSNL reinforced with silica adhesives

The quality of preparation of the epoxy resin–CSNL reinforced with silica was important factor affecting the adhesives properties. Therefore, the epoxy resin/CSNL reinforced with silica adhesives were prepared following the preparation process used successfully by a number of researchers [24,25]. The adhesive samples were prepared by compounding epoxy resin–CSNL matrix with 0–1.5 wt % silica. Silica was added into epoxy resin and it was dispersed using ultrasonic instruments for 30 min at 80 °C. After that, CNSL was mixed with the epoxy resin and silica mixture using ultrasonication for another 30 min at 80 °C. The mixture was continuously stirred until homogeneous compound was obtained. The compound was placed in a vacuum chamber at 80 °C to remove bubbles trapped in the mixture during the stirring and sonicating steps. The obtained compound was applied uniformly onto both sides of the overlapped area of aluminum substrates and then cured at 200 °C under a constant pressure of 0.05 MPa for 1 h. The thickness of the adhesive layers after curing was 0.3 mm.

2.5. Measurements and characterizations

The curing behavior and kinetic parameters of epoxy resin/CNSL copolymers were evaluated using a differential scanning calorimeter (DSC) pyris diamond model from PerkinElmer. The heating rates were 3, 5, 10 and 20 °C min^{-1} from 30 to 300 °C under nitrogen gas purging. The overlapping exothermic peaks were separated and analyzed by PeakFit v4.11 software.

Attenuated total reflection infrared (FTIR-ATR) spectra of all epoxy resin/CNSL samples after curing were acquired by Bruker Tensor 27 spectrometer. All spectra were taken as a function of time with 64 scans at a resolution of 4 cm^{-1} and a spectral range of 4000–650 cm^{-1}. The selected intensity data was normalized using the C=C of benzene ring at 1507 cm^{-1} and was used as internal standard to compensate for the variation in mass and thickness of sample after curing at 170 °C for 1 h and 200 °C for 1 h.

The gel content or insoluble fraction produced by crosslinking was determined by measuring the weight loss after extracting at room temperature for 24 h in accordance with ASTM D 2765-95 standard using test method C. The percent extraction was calculated as follows:

$$\%\text{Extraction} = \frac{W_o - W_d}{W_o} \times 100 \quad (1)$$

where W_o is the original polymer weight and W_d is the weight of dried gel.

The experiment was done strictly in accordance with ASTM D 2765-95 standard using test method C to evaluate gel content or insoluble fraction produced by crosslinking after placing the samples in chloroform. After removal of sample from chloroform solution, some part of the solution still penetrated in the gel sample and needed to be evaporated before the percent extraction could be calculated. Therefore, the total amount of chloroform solution could not be collected to evaluate exactly the composition of extractive substances.

The adhesive behavior was evaluated for mechanical tests using single-lap shear joint. The adhesion test was carried out according to ASTM D 1002-01 employing a Universal Testing Machine, Instron, Model 5567 equipped with a 10 kN load cell. Aluminum (alloy 2024) was used as metal for adhesive test.

The thermal degradation of adhesives was studied using a TGA-50, Shimadzu. The testing temperature program was ramped at a heating rate of 20 °C min^{-1} from room temperature to 700 °C under nitrogen atmosphere. The purge nitrogen gas flow rate was maintained at 20 ml min^{-1}. The sample mass used was 10–20 mg. Degradation temperature of each specimen was evaluated from the temperature at 5% weight loss.

3. Results and discussion

3.1. Characterization of CNSL's compositions

CNSL is a by-product of the cashew nut industry waste. CNSL contains several phenolic compounds such as cardol, anacardic acid, cardanol, and methyl cardol. The CNSL's compositions were analyzed by gas chromatography–mass spectrometer as shown in Fig. 1. CNSL contained mainly cardol (36.16%), cardanol (31.53%), anacardic acid (24.59%), and traces of methyl cardol.

3.2. Curing reaction and thermal properties of epoxy resin/CNSL

The results of dynamic DSC measurements of the epoxy resin/CNSL mixtures are shown in Fig. 2. Two overlapped exothermic peaks were observed and the peaks became more distinct when the CNSL content was higher than 20 wt%. The two overlapped exothermic peaks were between 165–170 °C and 230–235 °C.

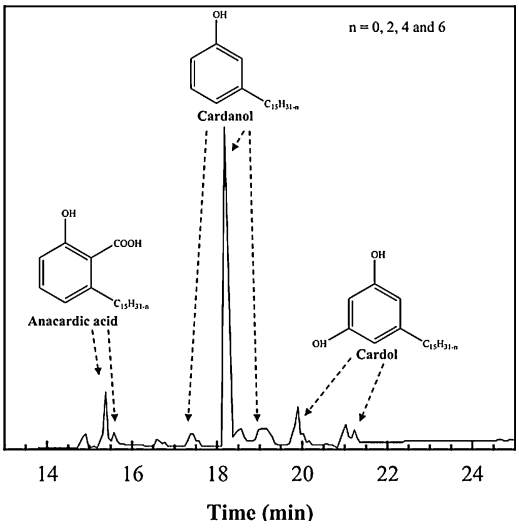

Fig. 1. GC–MS chromatogram of CNSL.

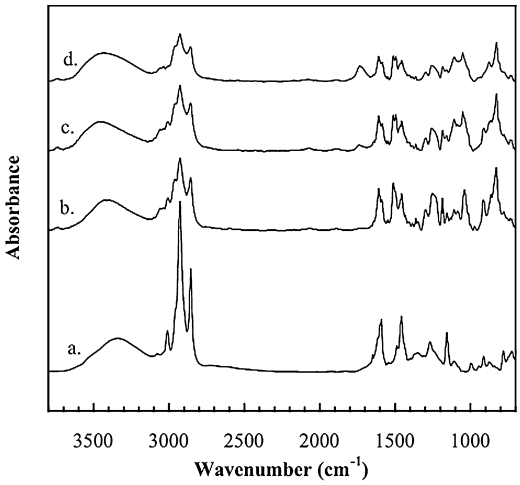

Fig. 3. IR spectra of (a) uncured CNSL (b) uncured epoxy resin/CNSL 60/40, (c) cured epoxy resin/CNSL 60/40 at 170 °C/1 h and (d) cured epoxy resin/CNSL 60/40 at 200 °C/1 h.

The two peaks strongly indicated that the curing of epoxy resin/CNSL underwent a two-stages curing process. Furthermore, areas of the exothermic peaks implied the total heat of reaction (ΔH) between epoxy resin and CNSL. The ΔH values of two-stages curing process tended to increase with increasing CNSL content up to 40 wt%. This phenomenon indicated the greater extent of conversion in crosslink formation of epoxy resin [26]. The first exothermic peak was attributed to the reaction between epoxy groups and hydroxyl groups of cardanol and cardol as well as carboxylic groups of anacardic acid. The second peak was due to the esterification reaction of epoxy group with carboxylic groups which were generated from the epoxy resin-acid reaction in first step. Similar reactions were also observed in the epoxy resin cured with dicarboxylic acid [2], bisphenol-A [27], and novolac based cardanol [8]. Sinh et al. [2], observed that the epoxy resin cured with dicarboxylic acid also provided two exothermic peaks at 180 °C and 218 °C corresponding to the reaction of epoxy resin and carboxylic acid and the esterification reaction, respectively. However, from the reaction between epoxy group and hydroxyl of phenolic, Campaner et al. [8] found that the epoxy resin cured with novolac based cardanol showed only one exothermic peak at 150 °C.

To evaluate the cross-linking mechanism, FTIR spectroscopy was employed to follow the changes of chemical bonds during curing reaction. The obtained rotation and vibration information was very specific to the chemical bonds, and the peaks in the spectrum corresponded to certain chemical bonds allowing simple identifications. The relative intensity of peaks was also directly proportional to the relative concentration of components in the sample [20,28,29]. Fig. 2 shows FTIR spectra for epoxy resin/CNSL at a fixed mass ratio of 60/40. In Fig. 3(a), the characteristic adsorption bands of CNSL were observed at 990 and 912 cm^{-1} which corresponded to phenol containing the pendant chain at meta position. The bands at 1264 and 1156 cm^{-1} were assigned to the symmetric and asymmetric stretching of the bound C=C, respectively and the peak at 1588 cm^{-1} was also related to the stretching of carbon double (C=C). The characteristic bands at 1650 cm^{-1} corresponded to C=O of anacardic. The peaks at 2852 and 2922 cm^{-1} corresponded to asymmetric and symmetric stretching of CH_3 and the peak around 3320 cm^{-1} was the characteristic of stretching of OH [30–32]. For epoxy resin/CNSL as shown in Fig. 3(b), the characteristic adsorption peak of epoxy resin was 915 cm^{-1} which was assigned to the epoxide group. The intensity of peak at 915 cm^{-1} tended to decrease with increasing temperature during curing. After curing for 1 h at 170 °C, the peak of epoxide group disappeared. This implied the opening of epoxide group in the crosslinking process [33] as shown in Fig. 3(c). In addition, two other peaks were also observed at 3470 cm^{-1} and 1114 cm^{-1}. The broad peak around 3470 cm^{-1} was assigned to the hydroxyl group formed due to ring opening reaction of epoxy group [20], whereas the peak at 1114 cm^{-1} corresponded to the stretching of C—O—C group generated from interaction between epoxy resin and hydroxyl group of cardanol and cardol. For curing at 200 °C for 1 h, the adsorption bands of carbonyl group appeared in the region of 1750–1550 cm^{-1} which was assigned to the strong interaction between epoxy resin and carboxylic acid [18]. This result is in good agreement with the DSC results. The probable reaction between the epoxy resin and CNSL component is as shown in Scheme 1. The results from DSC and FTIR suggested that CNSL is a good candidate for use as a low cost curing agent for epoxy resin.

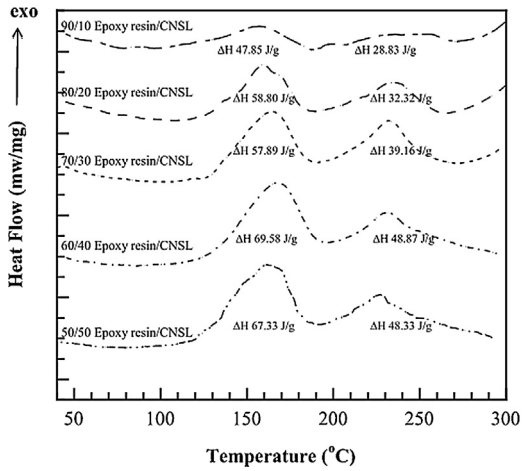

Fig. 2. DSC thermograms of epoxy resin/CNSL at various compositions.

3.3. Network formation ability of epoxy resin/CNSL alloys

The network formation ability of epoxy resin/CNSL matrices at various composition of CNSL was evaluated by solvent extraction method. In this test, the alloy specimens were immersed in chloroform for 24 h in accordance with ASTM D 2765. After the immersion, it was observed that epoxy resin blended with CNSL at 10 wt%, 20 wt% and 50 wt% showed a deep color change of solvent

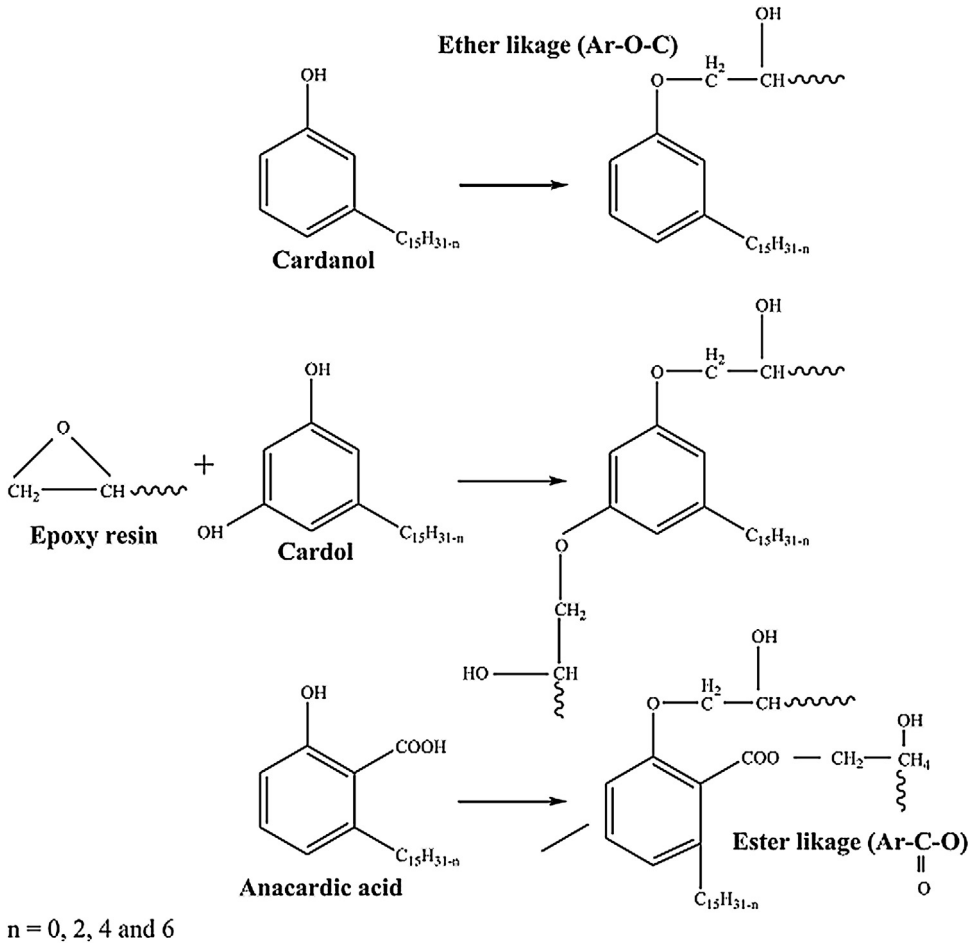

Scheme 1. A possible reaction between epoxy resin and CNSL.

due to the release of significant amount of extractives from each specimen. Furthermore, when the amount of CNSL in the polymer alloys was 50 wt%, the specimen disintegrated. It was possible that excessive amount of CNSL caused the formation of discontinuous network or network clusters. On the other hand, the 70/30 epoxy resin/CNSL specimen exhibited only slight color change and the 60/40 epoxy resin/CNSL specimen showed almost no color change. The results of percentages of solvent extraction are depicted in Fig. 4. The percentage of extraction tended to decrease with increasing CNSL content up to 40 wt%. It was due to an increase in network formation of epoxy resin with increasing CNSL content. The 40 wt% content of CNSL was optimum to achieve a good network formation.

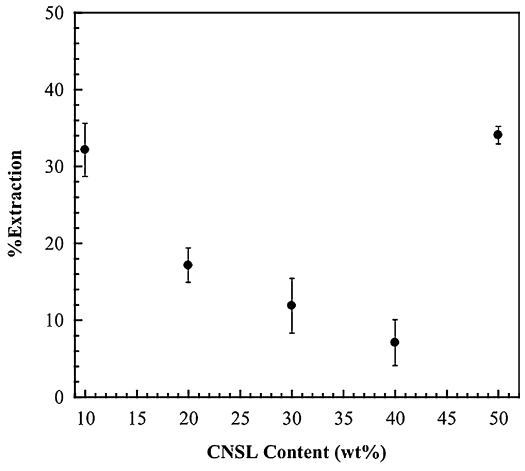

Fig. 4. Percent extraction as a function of CNSL content.

3.4. Curing kinetic model of epoxy resin/CNSL matrix

For curing of thermosetting polymer, activation energy (E_a) can be calculated by model-fitting kinetics methods and model-free kinetics methods (MFK). The MFK model can avoid the effect of kinetic compensation, which is the main drawback of the model-fitting kinetics method. The MFK methods based on curing rate at a given curing degree depends only on temperature. Among the conventional MFK methods, Friedman method is the most appropriate method for gaining insight into the curing mechanism of polymers. The Friedman method is a widely used differential method, and provides accurate value of activation energy even if the activation energy is a function of the reacted fraction [22,23].

3.4.1. Friedman model

The Friedman method is used to determine a kinetic model of curing process. The method is based on the rate equation as follows:

$$\frac{d\alpha}{dt} = k(T)f(\alpha) \quad (2)$$

where t is the time, $k(T)$ is the rate constant which depends on temperature and $f(\alpha)$ is a function of the fraction extent of

conversion rate and is associated with the reaction mechanism. $k(T)$ is usually evaluated by Arrhenius equation as shown in Eq. (3).

$$k(T) = A\exp\left(-\frac{E_a}{RT}\right) \tag{3}$$

where A is the pre-exponential factor, E_a is the curing activation energy, R is the universal gas constant and T is the absolute temperature.

From Eqs. (2–3), Eq. (4) can be derived as:

$$\ln\left(\frac{d\alpha}{dt}\right) = \ln[Af(\alpha)] - \frac{E_a}{RT} \tag{4}$$

where E_a is calculated by linear regression after plotting $\ln(d\alpha/dt)$ versus $1/T$. The rate, $d\alpha/dt$, at each temperature can be determined from

$$\frac{d\alpha}{dt} = \frac{dH/dt}{\Delta H} \tag{5}$$

where $d\alpha/dt$ is reaction rate, and dH/dt is partial heat of reaction at time.

The values of ΔH were used to calculate E_a as shown in Table 1. The ΔH values decreased with increasing of heating rate. The values of E_a of 60/40 (epoxy resin/CNSL) obtained at different degrees of curing are depicted in Fig. 5. The obtained E_a values from two stage curing showed a similar trend. The E_a values increased with increasing α from 0.1 up to 0.5 and then remained constant for $\alpha > 0.5$. This observation indicated that the values of E_a were influenced by the propagation of polymer chain and temperature. At initial curing, the propagation of polymer chain played more influential role to the overall energetic barrier, which led to an increase in E_a value with increasing α. When the curing progressed further, the elevated temperature could efficiently compensate the effect of propagation of polymer chain. Therefore, the apparent activation energy was practically constant [22]. The average values of E_a in the curing process were 45 kJ/mol and 60 kJ/mol for the first and second curing stages, respectively. These E_a values represented the apparent activation energy in the conversion range of 0.1–0.9. For both reactions, the activation energy values are in excellent agreement with the activation energy of 60/40 epoxy resin/CNSL and amine hardener. The activation energy values of the first and second curing stages were approximately 47 kJ mol and 68 kJ/mol, respectively [10].

3.4.2. Model fitting kinetics

Málek method is the most reliable method for the determination of probable mechanism function in the kinetic model. Málek suggested two special functions, $y(\alpha)$ and $z(\alpha)$. The shape and maximum value of these functions provides valuable for determining the most suitable kinetic model [23]. The characteristic functions of $y(\alpha)$ and $z(\alpha)$ can be obtained as follows:

$$y(\alpha) = \left(\frac{d\alpha}{dt}\right)\exp(x) \tag{6}$$

Table 1
Characteristic peak conversion values, α_M and $\alpha^{\alpha}{}_p$ for first and second curing stages.

β (°C/min)	First curing stage			Second curing stage		
	H_T (J/g)	α_M	$\alpha^{\alpha}{}_p$	H_T (J/g)	α_M	$\alpha^{\alpha}{}_p$
3	74.49	0.407	0.486	54.47	0.321	0.563
5	72.40	0.398	0.589	50.60	0.290	0.501
10	69.58	0.295	0.508	48.87	0.302	0.515
20	62.41	0.407	0.486	46.90	0.312	0.535

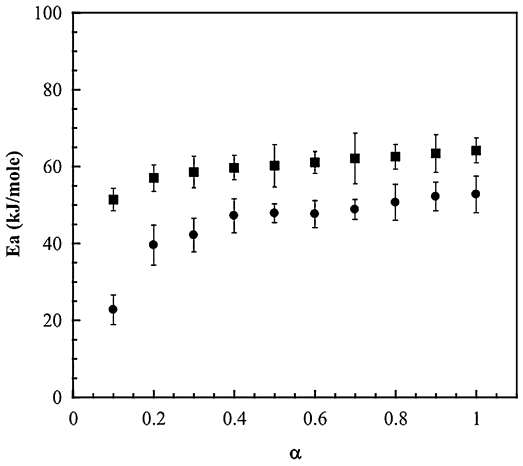

Fig. 5. Values of E_a as function of conversion for (●) first curing stage and (■) second curing stage.

$$z(\alpha) = \pi(x)\left(\frac{d\alpha}{dt}\right)\frac{T}{\beta} \tag{7}$$

where x is the reduced activation energy (E_a/RT), β is the heating rate, T is the absolute temperature and $\pi(x)$ function can be approximated using the 4th order rational expression of Senum and Yang [34–36] as shown in Eq. (8).

$$\pi(x) = \frac{x^3 + 18x^2 + 88x + 96}{x^4 + 20x^3 + 120x^2 + 240x + 120} \tag{8}$$

The plots of $y(\alpha)$ and $z(\alpha)$ values versus fraction of conversion are depicted in Fig. 5. The plots obtained from 10 °C/min heating rate were used as an example (Fig. 6). The maximum values of $y(\alpha)$ and $z(\alpha)$ corresponded to α_M and $\alpha^{\alpha}{}_p$, respectively. All α_M and $\alpha^{\alpha}{}_p$ values obtained from various heating rate are summarized in Table 1. The values of α_M and $\alpha^{\alpha}{}_p$ for first curing process were between 0.295 and 0.407 and 0.486–0.589, respectively. For the second curing stage, α_M values were 0.290–0.321 and $\alpha^{\alpha}{}_p$ values were 0.501–0.563. Both curing stages showed similar results i.e., α_M values were lower than $\alpha^{\alpha}{}_p$ values, and $\alpha^{\alpha}{}_p$ values were not equal 0.632. According to Málek' standard, the two parameter Sestak–Berggren model (SB(m, n)) was shown to be suitable for the investigating of crosslinking process of epoxy resin/CNSL. The SB (m, n) model can be expressed by Eq. (9) [23,37].

$$\frac{d\alpha}{dt} = k(T)f(\alpha) = A\exp\left(-\frac{E_a}{RT}\right)(1-\alpha)^n\alpha^m \tag{9}$$

By taking logarithm of Eq. (9), a linear expression for logarithm of curing rate is obtained as follows:

$$\ln\left(\frac{d\alpha}{dt}\exp\left(\frac{E_a}{RT}\right)\right) = \ln A + n\ln[\alpha^p(1-\alpha)] \tag{10}$$

where n and m are the reaction orders. In order to obtain kinetic parameters such as m, n and A, it is necessary to appeal to special parameter p (ratio m/n) which can be calculated from the maximum of $y(\alpha)$ function as

$$p = \frac{m}{n} = \frac{a_m}{1-a_m} \tag{11}$$

From Eq. (10), the values of n and $\ln A$ can be obtained by the slope and intercept, respectively, of the $\ln[(d\alpha/dt)\exp(E_a/RT)]$ versus $\ln[\alpha^p(1-\alpha)]$ plot. Then the second kinetic parameter (m) is $m = p \times n$. The kinetics parameters n, m and $\ln A$ were determined from each heating rate, and their average values were used to determine the kinetics model. The obtained results are given in Table 2.

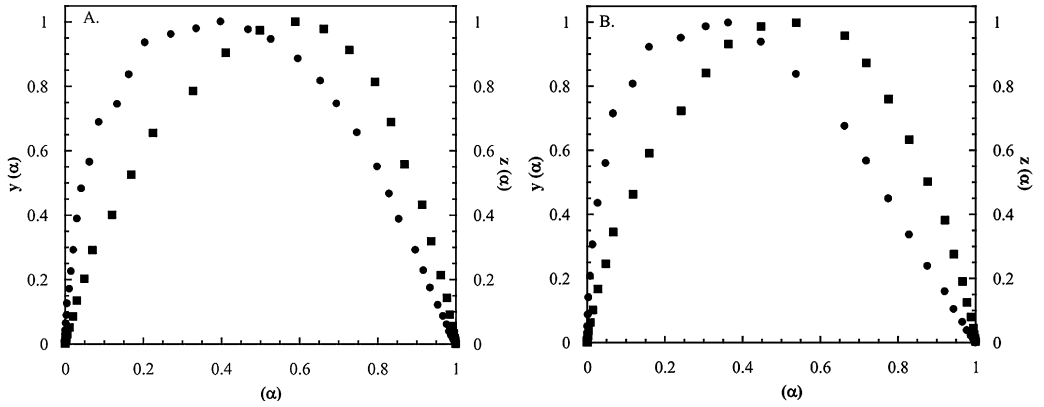

Fig. 6. Normalized (●) $y(\alpha)$ and (■) $z(\beta)$ versus conversion for first curing stage (a) and second curing stage (b) of epoxy resin/CNSL at 10 °C/min heating rate.

The explicit rate equations of the curing reaction can be obtained by substituting the calculated kinetic parameters such as E_a, n, m, and $\ln A$ into Eq. (9). The mathematic models for the first and second curing processes of epoxy resin/CNSL are present in Eqs. (12) and (13).

$$\frac{d\alpha}{dt} = k(T)f(\alpha) = (1.75 \times 10^4)\exp\left(-\frac{4.515 \times 10^4}{RT}\right)(1-\alpha)^{1.19}\alpha^{0.74} \quad (12)$$

$$\frac{d\alpha}{dt} = k(T)f(\alpha) = (2.26 \times 10^5)\exp\left(-\frac{6.002 \times 10^4}{RT}\right)(1-\alpha)^{1.14}\alpha^{0.5} \quad (13)$$

The predicted values from the model are comparable with the experimental results as illustrated in Figs. 7 and 8. It is clearly seen that the calculated data from model are in good agreement with the experimental data.

3.5. Curing behavior of epoxy resin–CNSL reinforced with silica

The curing behavior of epoxy resin–CNSL copolymer reinforced with 0–1.5 wt% silica powder was investigated by DSC as depicted in Fig. 9. After thermal curing at 200 °C for 1 h, the exothermic heat of reaction for all samples disappeared corresponding to the fully cured stage of samples [18]. In theory, the fully cured stage has been reported to provide a polymer with desirable properties including sufficiently high thermal and mechanical integrity.

3.6. Adhesive properties of epoxy resin–CNSL reinforced with silica

To enhance the properties of epoxy resin adhesives, various types of inorganic particles have been utilized to increase lap shear strength of adhesives. In this research, 0–1.5 wt% silica powder were incorporated with epoxy resin–CNSL. The lap shear strengths of epoxy resin–CNSL copolymer with silica powder are shown in Fig. 10. The lap shear strength of epoxy resin cured with CNSL was

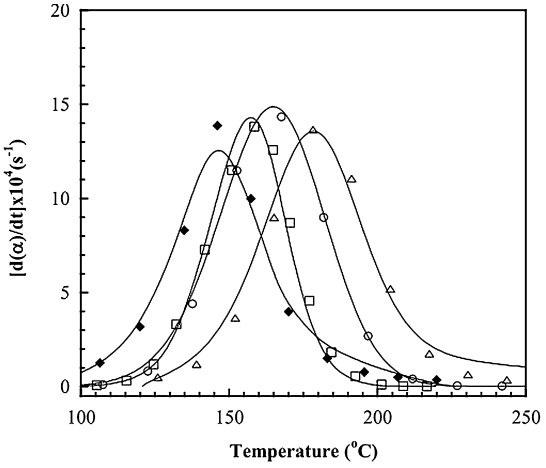

Fig. 7. Experimental (solid lines) and calculated (symbols) DSC peak corresponding to the first curing stage of epoxy resin/CNSL: (◆) 3 °C/min, (□) 5 °C/min, (O) 10 °C/min and (Δ) 20 °C/min.

Table 2
The calculated kinetic parameters E_a, $\ln A$,m and n of Sestak–Berggren model for first and second curing stages.

Curing stage	β (K/min)	E_a (kJ/mol)	m	Mean	n	Mean	$\ln A$ (s^{-1})	Mean
First curing stage	3	45	1.09	0.74	1.59	1.19	10.04	9.77
	5		0.69		1.03		9.57	
	10		0.44		1.06		9.34	
	20		0.73		1.06		10.13	
	SD	±0.879		±0.02		±0.014		±0.614
Second curing stage	3	60	0.51	0.50	1.08	1.14	12.63	12.33
	5		0.51		1.24		12.34	
	10		0.51		1.18		11.34	
	20		0.49		1.08		13.01	
	SD	±0.739		±0.027		±0.017		±0.415

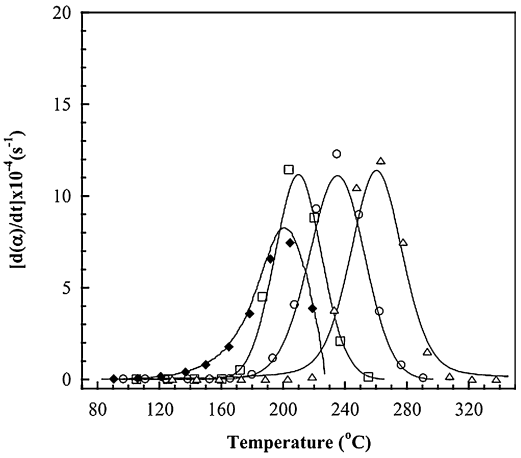

Fig. 8. Experimental (solid lines) and calculated (symbols) DSC peak corresponding to the second curing stage of epoxy/CNSL: (◆) 3 °C/min, (□) 5 °C/min, (O) 10 °C/min and (Δ) 20 °C/min.

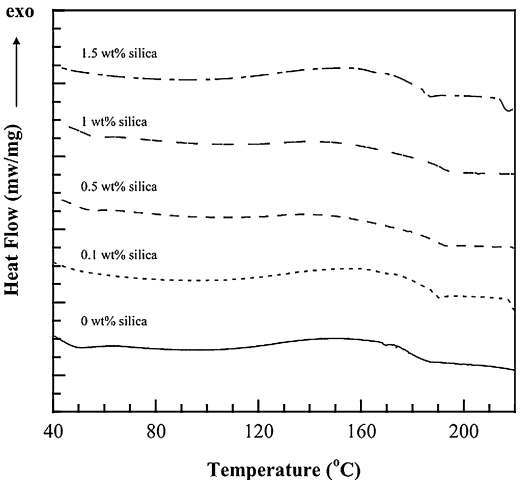

Fig. 9. DSC thermograms of epoxy resin/CNSL adhesives at various silica contents after curing at 200 °C for 1 h.

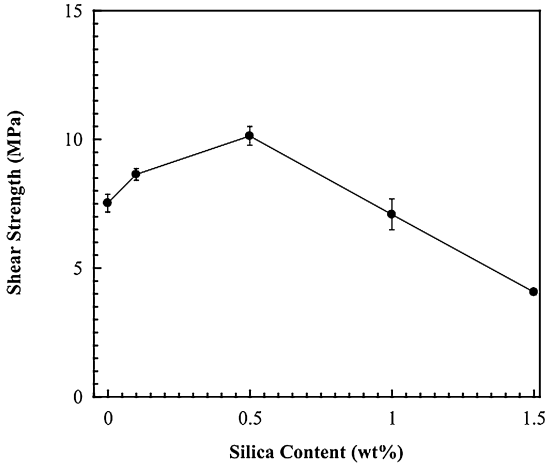

Fig. 10. Lap shear strength for epoxy resin/CNSL adhesives at various silica contents.

7.5 MPa which is comparable to the lap shear strength obtained from epoxy resin cured with commercial hardener such a triethylenetetramine [38]. For epoxy resin–CNSL reinforced with silica, the lap shear strength values of samples increased with

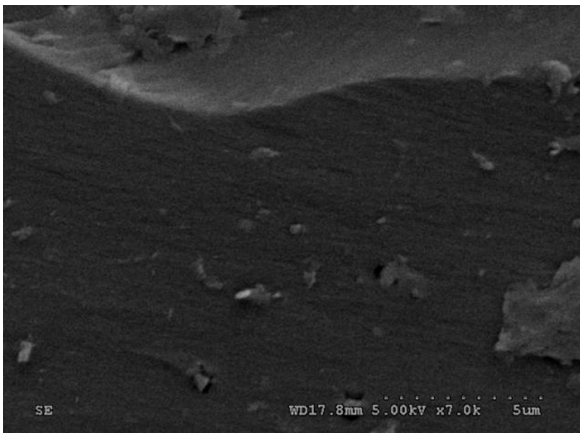

Fig. 11. Scanning electron micrograph of epoxy resin/CNSL adhesive reinforced with 0.5 wt% of silica.

increasing silica powder content up to 0.5 wt%. It is clearly observed that the epoxy resin–CNSL containing 0.5 wt% silica powder presents about 34% improvement in the lap shear strength as compared to the neat adhesive. The good distribution of filler in polymer matrix improves the roughness surface and interface by increasing the interaction area and the lap shear strength [38,39]. As shown in Fig. 11, a typical scanning electron photomicrographs of epoxy resin–CNSL adhesive sample loaded with 0.5 wt% silica particles indicated well dispersion of silica powder in the epoxy resin–CNSL adhesive. The decreasing of lap shear strength with increasing silica powder in range of 1–1.5 wt% was due to the excess addition which led to the agglomeration of nanoparticles.

3.7. Thermal stability of epoxy resin–CNSL reinforced with silica

Thermal degradation of epoxy resin–CNSL reinforced with silica powder is shown in Fig. 12. The degradation temperature (T_d) of epoxy resin–CNSL was 346 °C whereas epoxy resin/CNSL reinforced with 0.1 to 1.5 wt% silica powder showed the T_d values of 351 to 367 °C. As shown in Fig. 10, thermal stability of the epoxy resin–CNSL adhesive increased with increasing silica content. Generally, inorganic filler such a silica dispersed in polymeric matrix can serve as a good thermal cover layer, avoiding the direct thermal decomposition of the polymer by heat [40,41]. The reinforcing effect of silica on epoxy resin/CNSL adhesive is rather

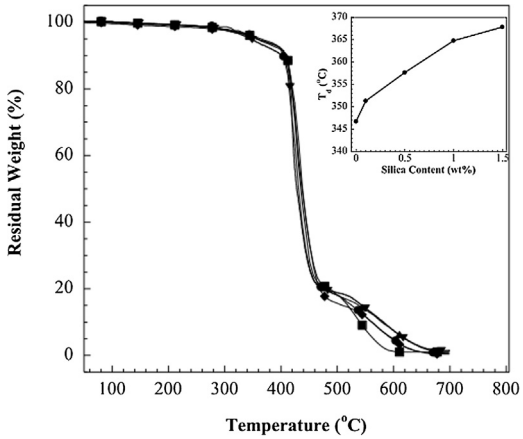

Fig. 12. TGA thermograms of epoxy resin/CNSL adhesives at various silica contents: (▼) 0 wt% silica, (▲) 0.1 wt% silica, (■) 0.5 wt%, (◆) 1 wt% silica and (●) 1.5 wt% silica.

complex, other thermomechanical properties such as storage modulus and glass transition temperature should be further investigated to compare and consolidate the findings.

4. Conclusion

Epoxy resin cured with CNSL showed two-stages curing process. The first stage was the reaction between epoxy groups and hydroxyl and carboxylic groups of CNSL's components. The second stage was the esterification reaction of epoxy group with hydroxyl groups generated from the epoxy resin-acid reaction in first step. The apparent activation energy values of 60/40 epoxy resin/CNSL were determined using Friedman method and were 45 kJ/mol and 60 kJ/mol for the first and second curing stages, respectively. Further kinetic parameters analysis with Málek's method confirms that the SB (m, n) model is suitable for these kinetic reaction systems. The kinetic parameters for this model are calculated and the kinetic equations were established. The kinetic models of the curing reactions are in good agreement with non-isothermal DSC. Silica powder reinforced epoxy resin/CNSL adhesive showed a substantial increase in lap shear strength with increasing silica powder content up to 0.5 wt%. Furthermore, thermal stability of adhesives increased with increasing silica power content. Epoxy resin-CNSL reinforced with silica powder showed a great potential as low cost high performance adhesive.

Acknowledgements

This work was financially supported by Khon Kaen University Fund. The authors also would like to acknowledge the support of Thailand Research Fund (TRF) and Khon Kaen University under the TRF Senior Research Scholar, Grant No. RTA5780004 and the Higher Education Research Promotion and National Research University Project of Thailand, Office of the Higher Education Commission, through the Advanced Functional Materials Cluster of Khon Kaen University.

References

[1] D. Rosu, C.N. Cascaval, F. Musta, C. Ciobanu, Cure kinetics of epoxy resins studied by non-isothermal DSC data, Thermochim. Acta 383 (2002) 119–127.
[2] L.H. Sinh, N.N. Trung, B.T. Son, S. Shin, D.T. Thanh, J.Y. Bae, Curing behavior, thermal, and mechanical properties of epoxy resins cured with a novel liquid crystalline dicarboxylic acid curing agent, Polym. Eng. Sci. 54 (2014) 695–703.
[3] H. Wang, Y. Zhang, L. Zhu, Z. Du, B. Zhang, Curing behaviors and kinetics of epoxy resins with a series of biphenyl curing agents having different methylene units, Thermochim. Acta 521 (2011) 18–25.
[4] R.J. Varley, J.H. Hodgkin, G.P. Simon, Toughening of a trifunctional epoxy system part VI. Structure property relationships of the thermoplastic toughened system, Polymer 42 (2001) 3847–3858.
[5] S.M. George, D. Puglia, J.M. Kenny, P. Jyotishkumar, S. Thomas, Cure kinetics and thermal stability of micro and nanostructured thermosetting blends of epoxy resin and epoxidized styrene-block-butadiene-block-styrene triblock copolymer systems, Polym. Eng. Sci. 52 (2012) 2336–2347.
[6] G. Wang, G. Jiang, J. Zhang, Preparation, curing kinetic and properties of a novel amine with flexible polyoxypropylene side chain curing agent for epoxy resin, Thermochim. Acta 589 (2014) 197–206.
[7] R. Yadav, P. Srivastava, D. Srivastava, Studies on synthesis of modified epoxidized novolac resin from renewable resource material for application in surface coating, J. Appl. Polym. Sci. 114 (2009) 1471–1484.
[8] P. Campaner, D. D'Amico, L. Longo, C. Stifani, A. Tarzia, Cardanol-based novolac resins as curing agents of epoxy resins, J. Appl. Polym. Sci. 114 (2009) 3585–3591.
[9] B. Lochab, I.K. Varma, J. Bijwe, Thermal behaviour of cardanol-based benzoxazines monomers and polymers, J. Therm. Anal. Calorim. 102 (2011) 769–774.
[10] G. Mathew, J.M. Rhee, B.S. Hwang, C. Nah, Cure behavior of epoxy resin containing castor oil and cashew nut shell liquid and its derivative, J. Appl. Polym. Sci. 106 (2007) 178–184.
[11] A.C.H. Barreto, D.S. Rosa, P.B.A. Fechine, S.E. Mazzetto, Properties of sisal fibers treated by alkali solution and their application into cardanol-based biocomposites, Composites A 42 (2011) 492–500.
[12] E.T.N. Bisanda, M.P. Ansell, Properties of sisal–CNSL composites, J. Mater. Sci. 27 (1992) 1690–1700.
[13] P. Peungjitton, P. Sangvanich, S. Pornpakakul, A. Petsom, S. Roengsumran, Sodium cardanol sulfonate surfactant from cashew nut shell liquid, J. Surfact. Deterg. 12 (2009) 85–89.
[14] E. Papadopoulos, K. Chrissafis, Thermal study of phenol–formaldehyde resin modified with cashew nut shell liquid, Thermochim. Acta 512 (2011) 105–109 Sestak.
[15] L.Y. Mwaikambo, M.P. Ansell, Hemp fibre reinforced cashew nut shell liquid composites, Compos. Sci. Technol. 63 (2003) 1297–1305.
[16] P. Campaner, D. D'Amico, P. Ferri, L. Longo, A. Maffezzoli, C. Stifani, A. Tarzia, Cardanol based matrix for jute reinforced pipes, Macromol. Symp. 296 (2010) 526–530.
[17] P. Kasemsiri, S. Hiziroglu, S. Rimdusit, Properties of wood polymer composites from eastern redcedar particles reinforced with benzoxazine resin/cashew nut shell liquid copolymer, Composites A 42 (2011) 1454–1462.
[18] P. Kasemsiri, S. Hiziroglu, S. Rimdusit, Effect of cashew nut shell liquid on gelation cure kinetics, and thermomechanical properties of benzoxazine resin, Thermochim. Acta 520 (2011) 84–92.
[19] C. Jubsilp, S. Damrongsakkul, T. Takeichi, S. Rimdusit, Curing kinetics of arylamine-based polyfunctional benzoxazine resins by dynamic differential scanning calorimetry, Thermochim. Acta 447 (2006) 131–140.
[20] S.F. Zhao, G.P. Zhang, R. Sun, C.P. Wong, Curing kinetics, mechanism and chemorheological behavior of methanol etherified amino/novolac epoxy systems, Express Polym. Lett. 8 (2014) 95–106.
[21] C. Jubsilp, K. Punson, T. Takeichi, S. Rimdusit, Curing kinetics of benzoxazine–epoxy copolymer investigated by non-isothermal differential scanning calorimetry, Polym. Degrad. Stabil. 95 (2010) 918–924.
[22] S.P. Huo, G.M. Wu, J. Chen, G.F. Liu, Z.W. Kong, Curing kinetics of lignin and cardanol based novolac epoxy resin with methyl tetrahydrophthalic anhydride, Thermochim. Acta 587 (2014) 18–23.
[23] S. Vyazovkin, A.K. Burnham, J.M. Criado, L.A. Perez-Maquedac, C. Popescud, N. Sbirrazzuolie, ICTAC kinetics committee recommendations for performing kinetic computations on thermal analysis data, Thermochim. Acta 520 (2011) 1–19.
[24] U. Pongsa, C. Samthong, A. Somwangthanaroj, Direct functionalization with 3,5-substituted benzoic acids of multiwalled carbon nanotube/epoxy composites, Polym. Eng. Sci. 53 (2013) 2194–2204.
[25] S. Kang, S.I. Hong, C.R. Choe, P. Min, R. Soonho, K. Junkyung, Preparation and characterization of epoxy composites filled with functionalized nanosilica particles obtained via sol–gel process, Polymer 42 (2001) 879–887.
[26] S.G. Tan, W.S. Chow, Thermal properties, curing characteristics and water absorption of soybean oil-based thermoset, Express Polym. Lett. 5 (2011) 480–492.
[27] F. Liu, Z. Wang, D. Liu, J. Li, Curing of diglycidyl ether of bisphenol-A epoxy resin using a poly(aryl ether ketone) bearing pendant carboxyl groups as macromolecular curing agent, Polym. Int. 58 (2009) 912–918.
[28] G. Lia, Z. Huang, P. Lib, C. Xina, X. Jiab, B. Wangb, Y. Hea, S. Ryuc, X. Yang, Curing kinetics and mechanisms of polysulfone nanofibrous membranes toughened epoxy/amine systems using isothermal DSC and NIR, Thermochim. Acta 497 (2010) 27–34.
[29] I.B. Recalde, D. Recalde, R. Garcia-Lopera, C.M. Gomez, FTIR isothermal cure kinetics and morphology of dicyanate ester resin/polysulfone blends, Eur. Polym. J. 41 (2005) 2635–2643.
[30] F.G. Souza, J.C. Pinto, G.E. de Oliveira, B.G. Soares, Evaluation of electrical properties with DOP and CNSL using ai of SBS/Pani blends plasticized empirical statistical model, Polym. Test. 26 (2007) 720–728.
[31] L.Y. Mwaikambo, M.P. Ansell, Cure characteristics of alkali catalysed cashew nut shell liquid-formaldehyde resin, J. Mater. Sci. 36 (2001) 3693–3698.
[32] R. Chelikani, Y.H. Kim, D.Y. Yoon, D.S. Kim, Enzymatic polymerization of natural anacardic acid and antibiofouling effects of polyanacardic acid coatings, Appl. Biochem. Biotechnol. 157 (2009) 263–277.
[33] X. Xiong, P. Chen, R. Ren, F. Lu, Q. Yu, Cure mechanism and thermal properties of the phthalide-containing bismaleimide/epoxy system, Thermochim. Acta 559 (2013) 52–58.
[34] N. Sbirrazzuoli, S. Vyazovkin, A. Mititelu, C. Sladic, L. Vincent, A study of epoxy-amine cure kinetics by combining isoconversional analysis with temperature modulated DSC and dynamic rheometry, Macromol. Chem. Phys. 204 (2003) 1815–1821.
[35] H. Sun, Y. Liu, Y. Wang, H. Tan, Curing behavior of epoxy resins in two-stage curing process by non-isothermal differential scanning calorimetry kinetics method, J. Appl. Polym. Sci. 131 (2014) 8761–8768.
[36] G. Zhang, J. Cheng, L. Shi, X. Lin, J. Zhang, Study on curing kinetics of diallyl-bearing epoxy resin using sulfur as curing agent, Thermochim. Acta 538 (2012) 36–42.
[37] J. Sestak, G. Berggren, Study of the kinetics of the mechanism of solid-state reactions at increasing temperatures, Thermochim. Acta 3 (1971) 1–12.
[38] M. Mansourian-Tabaei, S.H. Jafari, H.A. Khonakdar, Lap shear strength and thermal stability of diglycidyl ether of bisphenol a/epoxy novolac adhesives with nanoreinforcing fillers, J. Appl. Polym. Sci. 131 (2014) .
[39] L.L. Zhai, G.P. Ling, Y.W. Wang, Effect of nano-Al_2O_3 on adhesion strength of epoxy adhesive and steel, Int. J. Adhes. Adhes. 28 (2008) 23–28.
[40] T. Periadurai, C.T. Vijayakumar, M. Balasubramanian, Thermal decomposition and flame retardant behaviour of SiO_2-phenolic nanocomposite, J. Anal. Appl. Pyrol. 89 (2010) 244–249.
[41] I. Dueramae, C. Jubsilp, T. Takeichi, S. Rimdusit, High thermal and mechanical properties enhancement obtained in highly filled polybenzoxazine nanocomposites with fumed silica, Composites B 56 (2014) 197–206.

Materials Science and Engineering C 51 (2015) 1–6

Contents lists available at ScienceDirect

Materials Science and Engineering C

journal homepage: www.elsevier.com/locate/msec

Apatite formation on calcined kaolin–white Portland cement geopolymer

S. Pangdaeng [a], V. Sata [a], J.B. Aguiar [b], F. Pacheco-Torgal [b], P. Chindaprasirt [a,*]

[a] Sustainable Infrastructure Research and Development Center, Department of Civil Engineering, Faculty of Engineering, Khon Kaen University, Khon Kaen 40002, Thailand
[b] C-TAC Research Centre, Department of Civil Engineering, University of Minho, Campus of Azurém, 4800-058 Guimarães, Portugal

ARTICLE INFO

Article history:
Received 20 October 2014
Received in revised form 16 January 2015
Accepted 24 February 2015
Available online 25 February 2015

Keywords:
Geopolymer
Apatite
Simulated body fluid
Kaolin
White Portland cement

ABSTRACT

In this study, calcined kaolin–white Portland cement geopolymer was investigated for use as biomaterial. Sodium hydroxide and sodium silicate were used as activators. In vitro test was performed with simulated body fluid (SBF) for bioactivity characterization. The formation of hydroxyapatite bio-layer on the 28-day soaked samples surface was tested using SEM, EDS and XRD analyses. The results showed that the morphology of hydroxyapatite was affected by the source material composition, alkali concentration and curing temperature. The calcined kaolin–white Portland cement geopolymer with relatively high compressive strength could be fabricated for use as biomaterial. The mix with 50% white Portland cement and 50% calcined kaolin had 28-day compressive strength of 59.0 MPa and the hydroxyapatite bio-layer on the 28-day soaked sample surface was clearly evident.
© 2015 Elsevier B.V. All rights reserved.

1. Introduction

A geopolymer is a three-dimensional aluminosilicate network formed by polycondensation of monomers $-OSi(OH)_3$ and $Al(OH)_4$ [1]. In the presence of high alkaline solution, SiO_2 and Al_2O_3 from source materials leach out and react to form a geopolymer. Several source materials such as calcined kaolin, fly ash, bottom ash, and slag are used as starting materials to obtain high strength geopolymers [2–4]. Portland cement is also successfully used as a source material to produce geopolymer as it contains high silica and alumina [5]. To use geopolymer material as biomaterial, clean source material with minimum contamination is needed. Calcined kaolin (CK) with white color seems to be the best source material for this purpose. For the blend of source material, white Portland cement (WPC) with low iron and magnesium oxide obtained from specific process and fuel used in clinker manufacture [6] is a preferred choice.

Investigations of bioactivity on the surface of cementitious material such as WPC [7,8] and aluminosilicate/inorganic polymer [9–12] have been studied. Apatite-like layer forming on calcium silicate based material from WPC has been reported [7,8,13]. These bio-reactive apatite-like layers such as hydroxyapatite (HA) and hydroxyl carbonate apatite (HCA) are responsible for bone bonding [14]. In the system, the leached calcium hydroxide gives a high pH condition and enhances the apatite precipitations with the presence of calcium ions [8]. A high Si–OH group in calcium silicate materials promotes the HA precipitation through the increased nucleation sites [15]. For aluminosilicate/inorganic polymer, the studies on bioactive functional group on its surface were presented for both in vivo and in vitro studies [9–12,16]. However in this system, the high alkalinity condition was not conducive for the existence of HA and the cell [17]. For CK geopolymer, a study has indicated that the condition is not favorable for the formation of bioactive HA [16]. Therefore, co-existence of both calcium compound and Si–OH group is probably the favorable condition for precipitation of bioactive hydroxyapatite layer on the surface of materials. In addition, it has been reported that the curing temperature at 250–625 °C of aluminosilicate materials lowers the pH from 10 to 7 and renders the condition more biocompatible [18].

A number of researches on aluminosilicate material application for bone repair cement have been carried out, but poor strength and low bioactivity are still problems [9–12,19]. Previous works reported the enhancement of mechanical properties of geopolymer matrixes with the incorporation of Portland cement [20]. High compressive strength is preferable for material used for bone substitution. Moreover, both Portland cement and CK geopolymer contain calcium and Si–OH functional compounds. These compounds promote the precipitation of bioactive layer-like HA on the material surface [21].

In this paper, the CK–WPC geopolymer was fabricated and tested for use as a bone-like material with suitable strength and bioactivity function. Simulated body fluid (SBF) was used to investigate the bioactivity of materials. The formation of bioactive layer-like HA was characterized with the aids of scanning electron microscopy (SEM), energy dispersive spectrometry (EDS) and X-ray diffraction (XRD) techniques.

* Corresponding author.
E-mail address: prinya@kku.ac.th (P. Chindaprasirt).

http://dx.doi.org/10.1016/j.msec.2015.02.039
0928-4931/© 2015 Elsevier B.V. All rights reserved.

Table 1
Chemical composition of CK and WPC.

Materials	Chemical composition (%)								Blaine fineness (cm^2/g)	Specific gravity
	SiO_2	Al_2O_3	CaO	Fe_2O_3	MgO	Na_2O	SO_3	LOI[a]		
CK	59.7	34.1	0.1	0.9	0.2	0.2	0.1	1.2	13,800	2.59
WPC	15.9	1.9	73.5	0.2	0.9	0.0	4.9	2.3	3430	3.10

[a] LOI = loss on ignition.

2. Materials and methods

2.1. Sample preparation

CK and WPC were used as source materials in this experiment. Their main chemical compositions are shown in Table 1. WPC contains a high amount of CaO (73.5%) and CK contained a high amount of SiO_2 (59.7%) and Al_2O_3 (34.1%). Geopolymer samples were prepared with liquid/binder ratio of 1.0. Sodium hydroxide (NH, 10 M) and sodium silicate (NS, 15.32% Na_2O, 32.87% SiO_2 and 51.81% H_2O) with NH/NS ratio of 1.0 were used. The geopolymer pastes with CK:WPC by weight of 100:0, 75:25, 50:50, 25:75 and 0:100 (PC0, PC25, PC50, PC75 and PC100) were prepared. Paste samples were cast in 25 mm^3 acyclic molds for compressive strength test and in 10 mm diameter and 2 mm disc molds for bioactivity test. Samples were wrapped with plastic film to protect moisture loss and were left for 1 h in a 23 °C room and then cured at 23 °C and 60 °C for 24 h. The samples were then demolded, wrapped with plastic film and stored in a 23 °C controlled room.

2.2. Test method

Immediately after the mixing of the geopolymer pastes, the initial and final setting times of pastes were measured using Vicat apparatus in accordance with ASTM C191 [24]. Compressive strengths of geopolymer pastes at the age of 7 days were tested in accordance with ASTM C109 [25]. Three 25 mm cube samples were used for the compressive strength test and the reported results were the average values. The relative pH values of hardened geopolymer pastes were also tested using 15 mg of paste ground and mixed with 150 cm^3 distilled water [26]. For apatite formation characterization, the soaked samples were dried in a desiccator and the surface structures were studied using JEOL JEM-5910LV scanning electron microscopy (SEM). The chemical compositions of the products were analyzed using energy dispersive spectrometry (EDS). The formed apatite layer was confirmed by crystallography technique using X-ray diffraction (XRD) method between 15.0–59.9916°2θ with 0.0229° step and step time of 240.5 s.

2.3. In vitro test

Simulated body fluid (SBF) with ion concentration similar to human blood plasma was prepared in accordance with the method given by Kokubo [22]. At the age of 7 days, the geopolymer paste discs were submerged in SBF solution in sealed plastic containers and controlled soaking environment of 37 °C. The contact disc surface area to solution volume ratio was 0.1 cm^{-1} [23]. Soaking duration was 28 days to allow the formation of apatite layer on the sample surface. The pH levels of solutions were also monitored at 1, 3, 6, 12, 24 h and 7, 14, and 28 days. After removal from SBF, samples were gently washed with distilled water and kept dry in the desiccator. The SBF was not refreshed during the 28 day soaking period in order to lessen the chance of disturbing the samples.

3. Results and discussions

3.1. Properties of geopolymer

The results of setting times of CK-WC geopolymer pastes are shown in Table 2 and illustrated in Fig. 1a. The initial and final setting times of CK geopolymer were reasonable at 47 and 72 min. The incorporation of 25% WPC did not reduce both initial and final setting times of the geopolymer pastes. For increased incorporation of 50% and beyond, the initial and final setting times of pastes were reduced. For example, the initial setting times of geopolymer pastes with 0, 25, 50, 75 and 100% WPC were 47, 47, 35, 26 and 20 min, respectively. The reduction was due to the increase in calcium content as WPC contained a high CaO content (73.4%). The increase in calcium in the system, through the provision of extra nucleation sites for precipitation of dissolved species [27], significantly accelerated the setting and hardening of the geopolymer [20,28]. The calcium hydration products were formed and co-existed with the geopolymer products [29]. The fast setting of cement binders is desirable for bone repair material and dental cement [30].

The results of the strength of geopolymer pastes as shown in Table 2 and Fig. 1b showed that the strength was affected by the incorporation of WPC and curing temperature. The compressive strengths of geopolymer pastes cured at 23 and 60 °C were 45.4 and 49.9 MPa, respectively. High curing temperature of the geopolymer accelerates the strength development at the early age [31]. In this case, the difference in strength was not large as the alkali activation of CK was an endothermic process [32] and the geopolymerization of CK could thus proceed with the ambient 23 °C curing temperature. In addition, the incorporation of a proper amount of WPC increased the strength of the geopolymer. The strength of the CK geopolymer cured at 23 °C was 45.4 MPa and improved to 63.8 MPa with the incorporation of 50% WPC. Optimum calcium in geopolymerization caused the precipitation of calcium components viz., calcium silicate hydrate and calcium hydroxide and led to high compressive strengths [27,33]. However, a high amount of WPC resulted in the reduction of compressive strength as the development of C–S–H was retarded due to the rapid removal of available Si from geopolymer formation [5]. For curing at 60 °C, the optimum WPC of 50% was also observed with optimum strength of 55.0 MPa. In this case, the increase in strength was not as large as the case of 23 °C curing. For high WPC content of 50%, the compressive strength gain was significant at the early age and noticeably slowed down at the later age [34]. High curing temperature adversely affected the strength development at the later age due to the modifications of microstructure of hydration products [35].

The results of the test of relative pH of geopolymer pastes are shown in Table 2. The relative pH values of geopolymer pastes increased with the increase in WPC content. The mixes with 0, 25, 50, 75 and 100% WPC cured at 23 °C resulted in the relative pH values of 10.2, 10.6, 11.1, 11.2 and 11.6, respectively. Similar increases were also observed for the samples cured at 60 °C. An increase in pH was caused

Table 2
Properties of geopolymer pastes.

Mix	CK	WPC	Setting time (minutes)		Compressive strength (MPa)		pH of pastes	
	(wt.%)	(wt.%)	Initial	Final	23 °C	60 °C	23 °C	60 °C
PC0	100	0	47	72	45.4	49.9	10.2	9.8
PC25	75	25	47	91	51.3	48.9	10.6	10.6
PC50	50	50	35	67	63.8	55.0	11.1	11.0
PC75	25	75	26	48	35.9	30.5	11.2	11.2
PC100	0	100	20	35	14.6	10.6	11.6	11.7

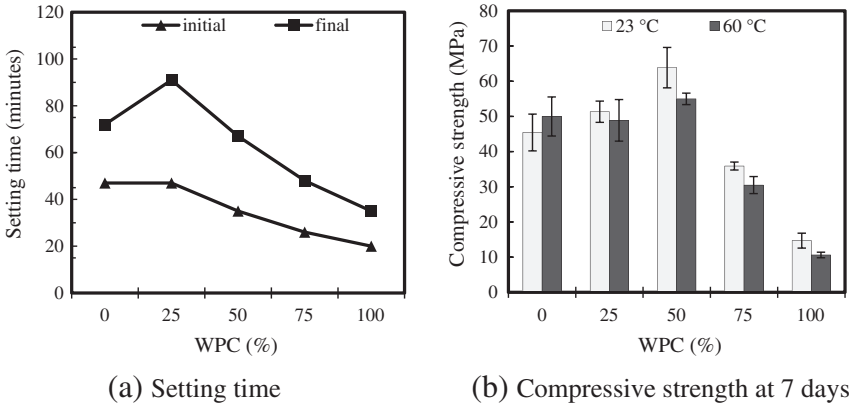

Fig. 1. Setting time and compressive strength of geopolymer pastes.

by the increased amount of calcium since it reacted and formed calcium hydration products that created greater alkalinity than those obtained from geopolymerization [17].

3.2. Bioactivity

Bioactivity property of the geopolymer was indicated by the pH change of SBF solution after immersion. The measured pH of SBF increased with soaking time. High pH level was observed for mixes with high WPC content as shown in Fig. 2. The initial increases in pH of SBF solutions were noticeably different. The mix with 100% PC showed a high initial rate of increase of pH and a small tendency to increase after 24 h of soaking. On the other hand, the mix with 0% PC displayed a low initial rate of increase and also a small tendency to increase after 24 h of soaking. With regard to different curing methods, higher curing temperature at 60 °C obviously showed lower pH increment than those with 23 °C curing. The increase in pH of SBF was caused by the dissolution of $Ca(OH)_2$ from the geopolymer paste and contributed to the high alkalinity environment [8]. The high curing temperature increased the degree of geopolymerization and strength of paste [31]. For curing at low temperature, the geopolymerization was less advanced resulting in pastes with lower strengths with the remains of some alkali liquid in the gel and matrix pores [36]. This resulted in the high relative pH values for mixes with low temperature curing.

The surface morphology by SEM of samples soaked for 28 days is displayed in Fig. 3. For 23 °C curing, the mix with 0% PC showed no bio-layer formed on the surface as presented in Fig. 3a. However, for the PC25 mix, only a small amount of particles (both spherical and non-spherical shapes) was found deposited at the surface of the sample. For higher WPC content mix (PC50), the deposition of spherical particles of approximately 1 μm in diameter was clearly observed. The formed spherical particles were identified as the HA apatite bio-layer as indicated by the EDS spectrum of calcium and phosphate [7,37,38] on high magnification SEM as shown in Fig. 4b and c. For the PC100 mix, a small amount of spherical particles was also found at the surface of the sample as shown in Fig. 3a.

For 60 °C curing, the formation of apatite was observed for mixes PC25, PC50 and PC100 as shown in Fig. 3b. The morphology of apatite on PC50 and PC100 surfaces was significantly different from that of the low temperature curing. The apatite layer of the PC50 sample was dense as displayed in Fig. 4c. It should be noted that, when the sample contacted SBF solution, the alkali ions leached out and resulted in high concentration of ions near the contact surface and supersaturation of SBF. This limited the ability of calcium and negative phosphate ion dissolutions and finally affected the growth of HA formation. Furthermore, it has been shown that the pore volume as measured by mercury intrusion porosimetry slightly increases with increasing temperature of curing [31]. With the increase of pore volume, the release of OH^- usually will be promoted. However, for the curing at high temperature, the increase in pore volume occurred in conjunction with the increase in strength and micro-structural development of paste and thus the release of OH^- was reduced. The enlarged pore size and pore volume of paste led to a higher contact area to SBF solution and increased the leaching of calcium ions from calcium hydroxide and produced biocompatible calcium carbonate. Large amounts of calcium carbonate (calcite) on PC50 and PC100 samples with 60 °C heat curing were evident as observed by the XRD analysis (Fig. 5). Similar HA induction on heat-treated surface was demonstrated for CaO containing titanium [37,39]. For the PC100 mix, SEM results indicated the presence of apatite particles of approximately 1 μm in diameter as shown in Fig. 4d.

Fig. 5 shows the XRD pattern of PC100 and PC50 samples with 23 and 60 °C curing. The graphs showed HA observation on samples. Calcium phosphate was located by the prominent peaks at 25.1, 31.6 and 49.4°2θ. Calcite ($CaCO_3$) was also detected by high peak in the PC50 mix cured at 60 °C and the amount was lower in the same mix cured at 23 °C. A high amount of calcite was also presented in the PC100 mix cured at 60 °C. In addition, calcium silicate (Ca_3SiO_5) was detected at 32.5°2θ in both PC50 and PC100 mixes with 60 °C curing. As this peak

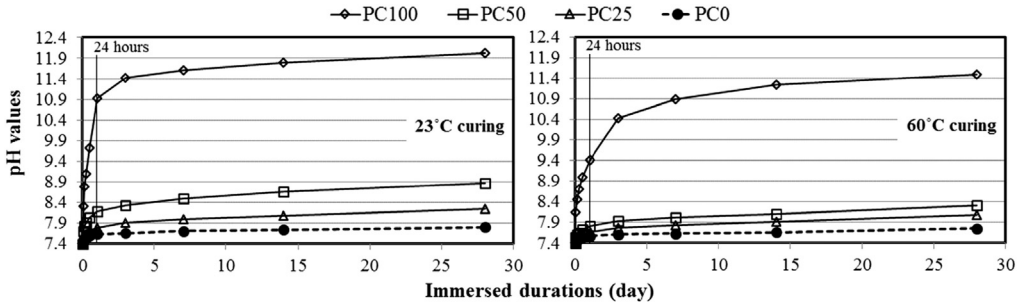

Fig. 2. pH values of SBF at different intervals of soaking of geopolymer disc.

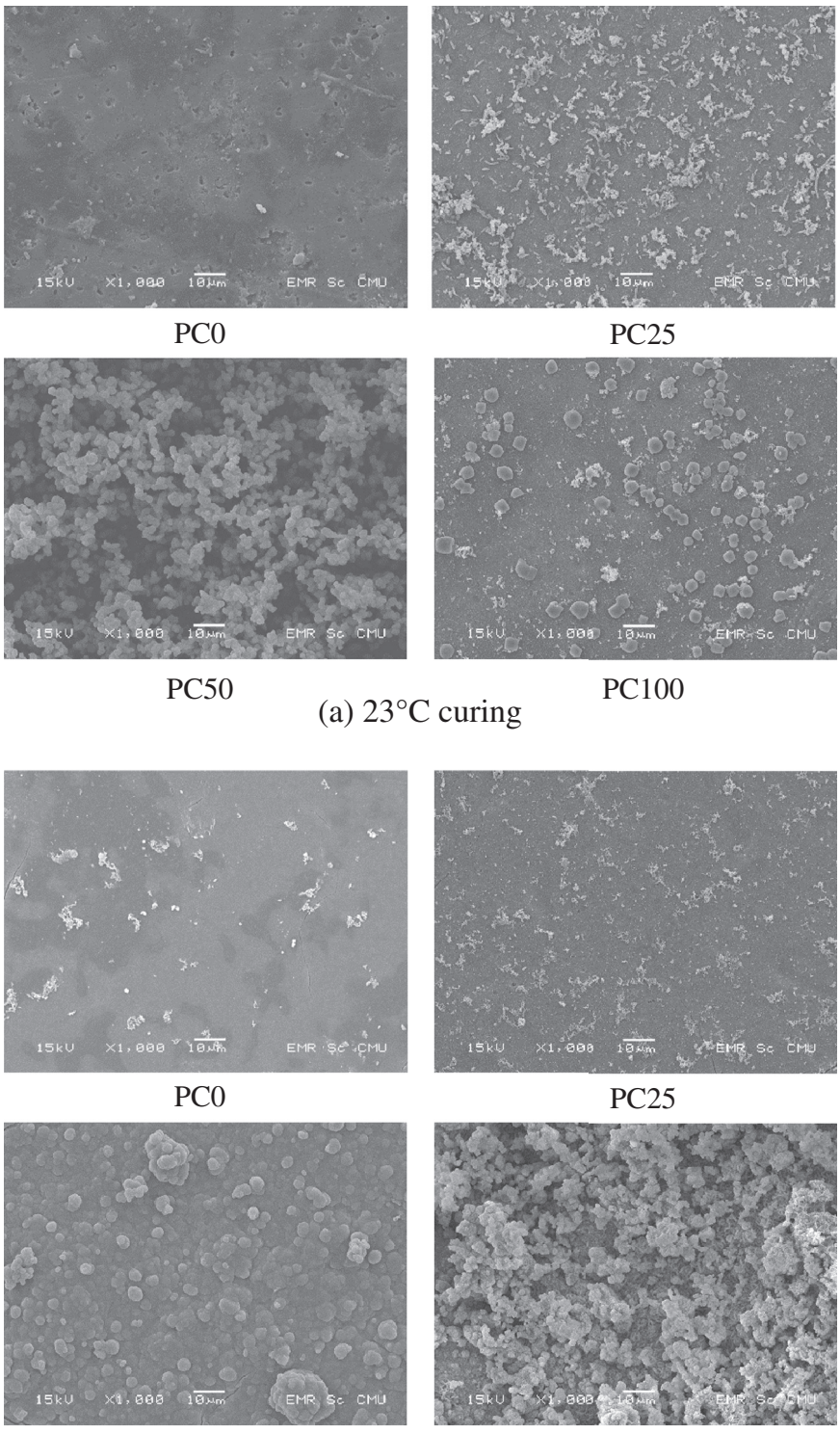

Fig. 3. SEM images of geopolymer pastes after 28 days in SBF.

was near the 31.6° peak of calcium phosphate, the clarity of the two peaks was thus hindered. Another observed peak was quartz (SiO_2) in the PC50 mix which was from the unreacted CK in the system. The addition of WPC increased calcium ions into the geopolymer system and contributed to the precipitation of HA on the sample surfaces. The HA crystal formed on geopolymer surface showed main characteristic peaks similar to that reported by previous work [40].

The in vitro test of the CK–WPC geopolymer soaked in SBF solution indicated good bioactivity. Calcium hydroxide ($Ca(OH)_2$) reacted with SBF and released calcium ions into SBF solution [41] and further transformed to calcium carbonate ($CaCO_3$) with good bioactivity [8]. Moreover, the Si–OH in geopolymer products promoted the forming ability of HA layer on its surface since the formation of HA layer depended on the content of Ca^{2+} ions and silicate groups at the sample surface [42,

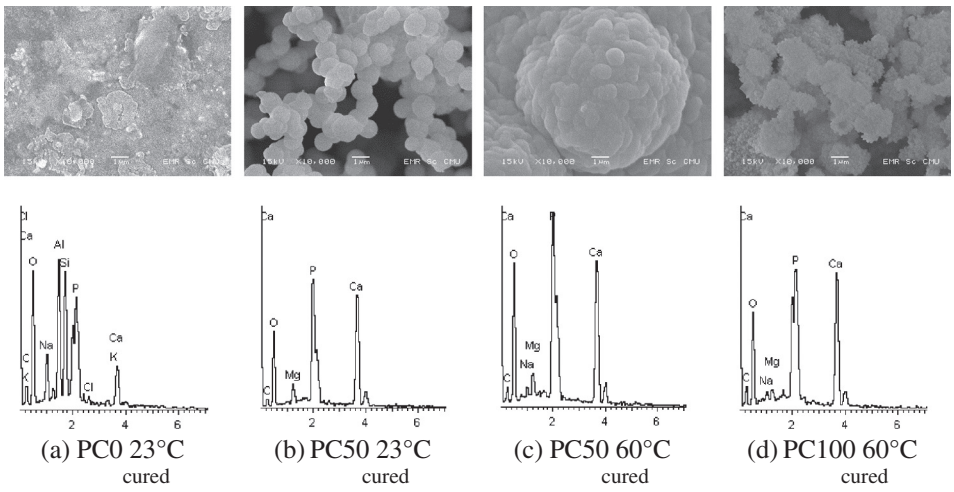

Fig. 4. SEM and EDS analyses of apatite formed on geopolymer surfaces after soaking in SBF.

43]. Possible explanation of behavior was given in the literatures [10,44, 45] that when sodium aluminosilicate materials contacted SBF, Na^+ ions leached out and reacted with H_3O^+ in SBF and formed Si–OH and Al–OH groups on its surface and dissociated to Si–O— negative functional group. This reaction caused a slight increase in pH value. Consequently, the presence of positive charges of Ca^{2+} in the fluid combined with those groups and imposed an increase of positive charge on the surface and promoted the Ca^{2+} to combine with negative charges of phosphate ions to spontaneously form hydroxyapatite. Moreover, leached Ca^{2+} ions also enhanced the super-saturation of SBF and enhanced the HA layer formation [8]. The bioactivity of geopolymer cement system was shown to be improved by the addition of WPC.

The results from this study indicated that the CK–WPC geopolymer paste showed promising properties for use as biomaterial. However, it should also be pointed out that the release of OH^- from the material can cause severe cytotoxic effects to cells. Therefore, further cytotoxic study is suggested for this CK–WPC geopolymer for application as biomaterial.

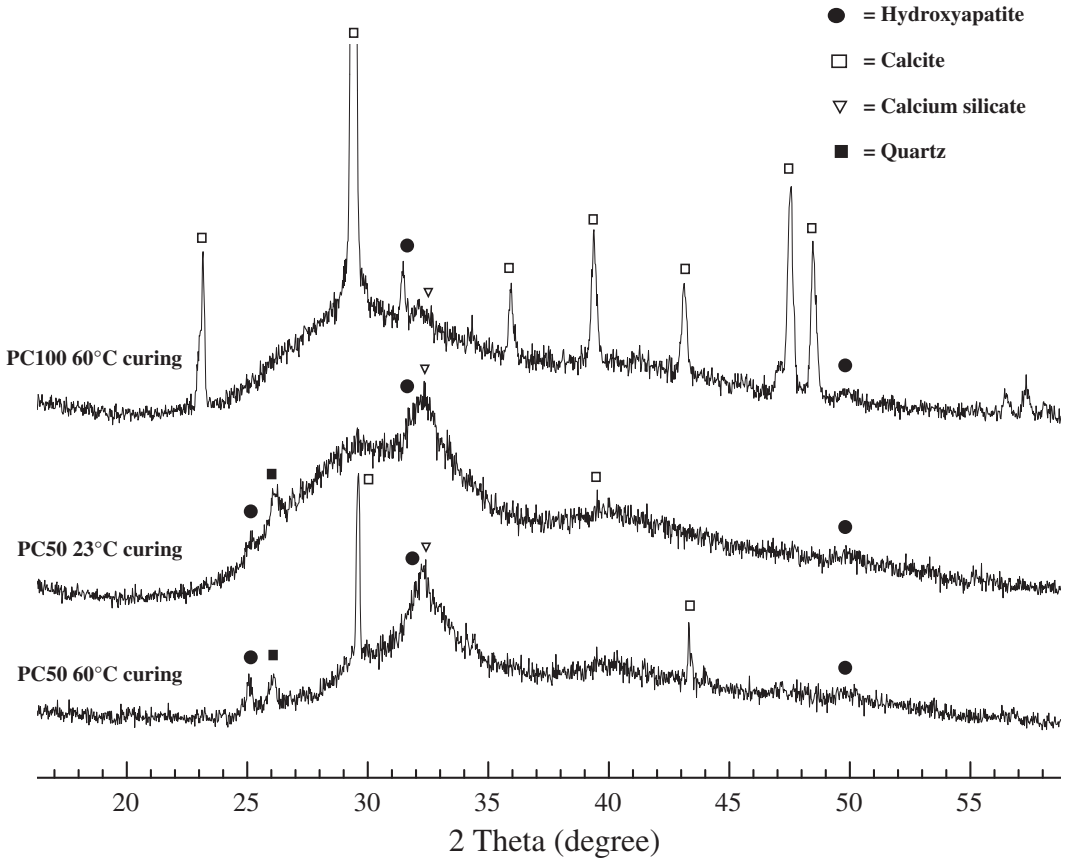

Fig. 5. XRD of hydroxyapatite formed on geopolymer surfaces after soaking in SBF.

4. Conclusions

The addition of appropriate portion of white Portland cement into the calcined kaolin geopolymer system enhanced the mechanical properties of the geopolymer and provided a suitable bone repair and implant material in terms of rapid setting and high compressive strength. The addition of 50% WPC into the system increased the calcium compounds in the geopolymer matrices and enhanced the performance of geopolymer pastes. When exposed to SBF, the geopolymer exhibited good bioactivity. A large amount of hydroxyapatite bio-layer obviously formed on the matrix surfaces. The curing at 60 °C resulted in the reduction of pH of SBF solution and promoted the precipitation of hydroxyapatite on blended geopolymer surface compared to the samples cured at 23 °C.

Acknowledgments

This work was financially supported by the Thailand Research Fund (TRF) and Khon Kaen University under the TRF-Royal Golden Jubilee Ph.D. program (Grant No. PHD/0143/2554) and TRF-Senior Research Scholar (Grant No. RTA5780004).

References

[1] A. Buchwald, H.D. Zellmann, C. Kaps, Condensation of aluminosilicate gels—model system for geopolymer binders, J. Non-Cryst. Solids 357 (5) (2011) 1376–1382.
[2] Y.M. Liew, et al., Processing and characterization of calcined kaolin cement powder, Constr. Build. Mater. 30 (2012) 794–802.
[3] V. Sata, A. Sathonsaowaphak, P. Chindaprasirt, Resistance of lignite bottom ash geopolymer mortar to sulfate and sulfuric acid attack, Cem. Concr. Compos. 34 (5) (2012) 700–708.
[4] P. Duxson, et al., Geopolymer technology: the current state of the art, J. Mater. Sci. 42 (9) (2007) 2917–2933.
[5] J. Tailby, K.J.D. MacKenzie, Structure and mechanical properties of aluminosilicate geopolymer composites with Portland cement and its constituent minerals, Cem. Concr. Res. 40 (5) (2010) 787–794.
[6] K.K. Veiga, A.L.G. Gastaldini, Sulfate attack on a white Portland cement with activated slag, Constr. Build. Mater. 34 (2012) 494–503.
[7] A. Chaipanich, P. Torkittikul, Microstructure: surface and cross-sectional studies of hydroxyapatite formation on the surface of white Portland cement paste in vitro, Appl. Surf. Sci. 257 (20) (2011) 8385–8390.
[8] N.J. Coleman, J.W. Nicholson, K. Awosanya, A preliminary investigation of the in vitro bioactivity of white Portland cement, Cem. Concr. Res. 37 (11) (2007) 1518–1523.
[9] S. Martin, et al., Implantation of aluminosilicate/calcium phosphate materials: influence on bone formation in rabbit tibias, Eur. Cells Mater. 9 (1) (2005) 71–72.
[10] M. Catauro, et al., Mechanical and Biological Characterization of Geopolymers for Potential Application as Biomaterials, AZojomo, 2012.
[11] H. Oudadesse, et al., Surface and interface investigation of aluminosilicate biomaterial by the "in vivo" experiments, Appl. Surf. Sci. 255 (2) (2008) 593–596.
[12] M. Todea, et al., Surface structure changes on aluminosilicate microspheres at the interface with simulated body fluid, Corros. Sci. 54 (2012) 299–306.
[13] P. Torkittikul, A. Chaipanich, Investigation of the mechanical and in vitro biological properties of ordinary and white Portland cements, ScienceAsia 35 (2009) 358–364.
[14] M. Mami, et al., Investigation of the surface reactivity of a sol–gel derived glass in the ternary system SiO_2–CaO–P_2O_5, Appl. Surf. Sci. 254 (22) (2008) 7386–7393.
[15] L.L. Hench, Biomaterials: a forecast for the future, Biomaterials 19 (16) (1998) 1419–1423.
[16] K.D. MacKenzie, et al., Calcium-containing inorganic polymers as potential bioactive materials, J. Mater. Sci. 45 (4) (2010) 999–1007.
[17] D. Gallego, et al., Bioactive coatings on Portland cement substrates: surface precipitation of apatite-like crystals, Mater. Sci. Eng. C 28 (3) (2008) 347–352.
[18] H. Oudadesse, et al., MAS-NMR studies of geopolymers heat-treated for applications in biomaterials field, J. Mater. Sci. 42 (9) (2007) 3092–3098.
[19] J. Leivo, et al., Sol–gel derived aluminosilicate coatings on alumina as substrate for osteoblasts, Acta Biomater. 2 (6) (2006) 659–668.
[20] S. Pangdaeng, et al., Influence of curing conditions on properties of high calcium fly ash geopolymer containing Portland cement as additive, Mater. Des. 53 (2014) 269–274.
[21] M. Nilsson, et al., Characterization of a novel calcium phosphate/sulphate bone cement, J. Biomed. Mater. Res. 61 (4) (2002) 600–607.
[22] T. Kokubo, H. Takadama, How useful is SBF in predicting in vivo bone bioactivity? Biomaterials 27 (15) (2006) 2907–2915.
[23] D.C. Greenspan, J.P. Zhong, G.P. LaTorre, in: O.H. Andresson, A. Yli-Urpo (Eds.), Effect of Surface Area to Volume Ratio In Vitro Surface Reactions of Bioactive Glass Particulates, Butterworth-Heinemann Ltd., Turku, Finland, 1994.
[24] ASTM C191, Standard Test Method for Time of Setting of Hydraulic Cement by Vicat Needle, American Society for Testing and Materials, Annual Book of ASTM Standard, 2005, pp. 179–185.
[25] ASTM C109, Standard test method of compressive strength of hydraulic cement mortars (using 2-in. or [50 mm] cube specimens), American Society for Testing and Materials, Annual Book of ASTM Standard, 2005, pp. 76–81.
[26] A.C. Derrien, et al., Thermal behaviour of composites aluminosilicate–calcium phosphates, J. Therm. Anal. Calorim. 75 (3) (2004) 937–946.
[27] W.K.W. Lee, J.S.J. van Deventer, The effects of inorganic salt contamination on the strength and durability of geopolymers, Colloids Surf. A Physicochem. Eng. Asp. 211 (2–3) (2002) 115–126.
[28] P. Chindaprasirt, et al., Effect of SiO_2 and Al_2O_3 on the setting and hardening of high calcium fly ash-based geopolymer systems, J. Mater. Sci. 47 (12) (2012) 4876–4883.
[29] K. Somna, et al., NaOH-activated ground fly ash geopolymer cured at ambient temperature, Fuel 90 (6) (2011) 2118–2124.
[30] M.P. Ginebra, T. Traykova, J.A. Planell, Calcium phosphate cements as bone drug delivery systems: a review, J. Control. Release 113 (2) (2006) 102–110.
[31] P. Rovnaník, Effect of curing temperature on the development of hard structure of metakaolin-based geopolymer, Constr. Build. Mater. 24 (7) (2010) 1176–1183.
[32] Sotya Astutiningsih, H.W. A, Hendra Widhatra, Kresnadya Desha Rousstia, Maria Elizabeth Suryatriyastuti, Utilization of concrete waste aggregates using geopolymer cement, J. Civ. Eng. Archit. 4 (6) (2010) 11–15.
[33] J. Temuujin, A. van Riessen, R. Williams, Influence of calcium compounds on the mechanical properties of fly ash geopolymer pastes, J. Hazard. Mater. 167 (1–3) (2009) 82–88.
[34] F. Pacheco-Torgal, J.P. Castro-Gomes, S. Jalali, Investigations on mix design of tungsten mine waste geopolymeric binder, Constr. Build. Mater. 22 (9) (2008) 1939–1949.
[35] Y. Maltais, J. Marchand, Influence of curing temperature on cement hydration and mechanical strength development of fly ash mortars, Cem. Concr. Res. 27 (7) (1997) 1009–1020.
[36] X. Yao, et al., Geopolymerization process of alkali-metakaolinite characterized by isothermal calorimetry, Thermochim. Acta 493 (1–2) (2009) 49–54.
[37] X.J. Wang, et al., In vitro bioactivity evaluation of titanium and niobium metals with different surface morphologies, Acta Biomater. 4 (5) (2008) 1530–1535.
[38] P. Li, et al., Apatite formation induced on silica gel in a simulated body fluid, J. Am. Ceram. Soc. 75 (1992) 2094–2097.
[39] M. Wei, et al., Apatite-forming ability of CaO-containing titania, Biomaterials 23 (1) (2002) 167–172.
[40] J. Zhang, et al., Calcium phosphate/chitosan composite coating: Effect of different concentrations of Mg^{2+} in the m-SBF on its bioactivity, Appl. Surf. Sci. 280 (2013) 256–262.
[41] M. Kawashita, et al., Apatite-forming ability of carboxyl group-containing polymer gels in a simulated body fluid, Biomaterials 24 (14) (2003) 2477–2484.
[42] Z. Huan, J. Chang, Self-setting properties and in vitro bioactivity of calcium sulfate hemihydrate–tricalcium silicate composite bone cements, Acta Biomater. 3 (6) (2007) 952–960.
[43] M.V. Cabañas, L.M. Rodríguez-Lorenzo, M. Vallet-Regí, Setting behavior and in vitro bioactivity of hydroxyapatite/calcium sulfate cements, Chem. Mater. 14 (8) (2002) 3550–3555.
[44] L.L. Hench, Bioceramics: from concept to clinic, J. Am. Ceram. Soc. 74 (7) (1991) 1487–1510.
[45] H. Takadama, et al., X-ray photoelectron spectroscopy study on the process of apatite formation on a sodium silicate glass in simulated body fluid, J. Am. Ceram. Soc. 85 (8) (2002) 1933–1936.

Advanced Powder Technology 26 (2015) 1053–1057

Contents lists available at ScienceDirect

Advanced Powder Technology

journal homepage: www.elsevier.com/locate/apt

Original Research Paper

Comparative study on morphology of ground sub-bituminus FBC fly ash geopolymeric material

Manisara Eiamwijit [a], Katavut Pachana [a,b], Supranee Kaewpirom [a,b], Ubolluk Rattanasak [a,b,*], Prinya Chindaprasirt [c]

[a] Environmental Science Program and Center of Excellence on Environmental Health and Toxicology (EHT), Faculty of Science, Burapha University, Chonburi 20131, Thailand
[b] Department of Chemistry, Faculty of Science, Burapha University, Chonburi 20131, Thailand
[c] Sustainable Infrastructure Research and Development Center, Department of Civil Engineering, Faculty of Engineering, Khon Kaen University, Khon Kaen 40002, Thailand

ARTICLE INFO

Article history:
Received 2 January 2015
Received in revised form 13 March 2015
Accepted 20 April 2015
Available online 28 April 2015

Keywords:
Geopolymer
Fluidized bed coal combustion fly ash
Compressive strength
Morphology

ABSTRACT

Fluidized bed coal combustion (FBC) is a clean coal combustion and environmentally friendly process with low emission of SO_2 and NO_x to atmosphere. However, fly ash from FBC process is not suitable for further utilization due to the high sulfate and low glassy phase contents. FBC fly ash was ground to reduce pore and increase specific surface area for use as a source material in geopolymer. FBC fly ash geopolymers with different sodium silicate to sodium hydroxide (G/N) mass ratios were studied and characterized using X-ray diffraction (XRD), scanning electron microscopy with energy dispersive X-ray spectroscopy (SEM–EDX), and Fourier transform infrared spectroscopic (FTIR) techniques. Compressive strength of materials was also tested. Test results indicated that G/N ratio had a significant effect on morphology and strength of geopolymer. Low G/N ratio gave low strength geopolymer with a large amount of calcium hydroxide. The high G/N ratio mixes with increased water glass content gave dense and homogeneous composites. The presence of a high amount of calcium resulted in the formation of calcium silicate products which coexisted with the sodium aluminosilicate products.

© 2015 The Society of Powder Technology Japan. Published by Elsevier B.V. and The Society of Powder Technology Japan. All rights reserved.

1. Introduction

Fluidized bed coal combustion (FBC) is a clean coal combustion process which is widely used to reduce the pollutant emissions to atmosphere. This environmentally friendly process gives low emission of SO_2 and NO_x due to the feeding of limestone as a sorbent material in order to capture the flue gas [1]. In addition, the combustion temperature of 800–900 °C results in low NO_x formation compared to the conventional pulverized coal combustion (PCC), which the combustion temperature is over 1200 °C. However, the use of fly ash from FBC process as cement replacement material in concrete is limited since sulfate content (as SO_3) falls outside the range set forth in ASTM C618 with the maximum SO_3 requirement of 5.0%. Low glassy phase of fly ash is also produced by FBC process [2].

Presently, researchers are focusing on the use of FBC fly ashes because of its large annually output due to the growing installation of this process in small factories [3–6]. Most of these ashes are disposed of at landfill and only a small amount is used as aggregate in concrete. FBC fly ash contains silica and alumina and thus can be used as a source material for making alkali-activate composite or geopolymer. Reactive alumina and silica react with alkaline solutions, i.e. sodium hydroxide and sodium silicate solutions, and form the geopolymeric material. Heat curing is normally required in order to accelerate the reaction [7–9]. Geopolymer gains strength after a short heat curing period and also possesses good acid resistance property [2]. However, the use of FBC fly ash results in a low strength geopolymer. FBC fly ash with low glassy phase, high porosity thus requires improvement in its properties before it can be used as a source material for making geopolymer [2,6,10].

In this paper, the effects of alkaline activator on the properties of ground FBC fly ash geopolymer were studied. Ground FBC fly ash geopolymers with various contents of alkaline activators were studied using X-ray diffraction (XRD), scanning electron microscopy with energy dispersive X-ray spectroscopy (SEM–EDX), and Fourier transform infrared spectroscopic (FTIR) techniques. Compressive strength of geopolymers was also tested. The obtained knowledge would serve as an important guideline for

* Corresponding author at: Department of Chemistry and Center of Excellence on Environmental Health and Toxicology (EHT), Faculty of Science, Burapha University, Chonburi 20131, Thailand.
E-mail address: ubolluk@buu.ac.th (U. Rattanasak).

http://dx.doi.org/10.1016/j.apt.2015.04.013
0921-8831/© 2015 The Society of Powder Technology Japan. Published by Elsevier B.V. and The Society of Powder Technology Japan. All rights reserved.

the potential of FBC fly ash for use as an alternative source in geopolymer production.

2. Materials and experimental procedure

2.1. Materials

FBC fly ash, the solid waste from the power plants of paper mill in Thailand, was used as an aluminosilicate source material. Sub-bituminous coal was a feedstock of the combustion process with burning temperature of 800 °C. As-received FBC fly ash had a median particle size (D50) of 28.16 μm (Malvern Mastersizer S, Fraunhofer diffraction method). FBC fly ash was ground for 2 h using the laboratory ball mill (1-liter ceramic pot, 500 rpm, 1000 g of 16-mm∅ ceramic balls and 500 g FBC fly ash). The median particle size of ground fly ash was 2.03 μm. Chemical compositions of fly ash determined by X-ray fluorescence (XRF, Philips PW-2404) are shown in Table 1. Loss on ignition (LOI) was measured in accordance with ASTM C-114 (950 ± 50 °C, 30 min). Fly ash contained mainly quartz (SiO_2), aluminium oxide (Al_2O_3), iron oxide (Fe_2O_3), lime (CaO) and sulfur trioxide (SO_3). This fly ash had high Fe_2O_3 content of 17.5%. Reasonable CaO content of 12.8% and SO_3 content of 6.4% were detected owing to the feeding of lime to capture SO_2 flue gas. These amounts were not very high since the use of sub-bituminous coal reduced the retention time in FBC bed and resulted in dilute CaO and SO_3 [4]. Mineralogy of fly ash was analyzed by X-ray diffraction (XRD, PANalytical/Expert, Cu Kα radiation).

Water glass (sodium silicate solution, 30 wt% SiO_2 and 9 wt% Na_2O) and 15 M NaOH were used as alkali activators [6]. 15 M NaOH was for the leaching of minerals from fly ash and water glass was added to increase dissolved silica in the mixture. In order to prepare geopolymer mortar for strength test, graded river sand with specific gravity of 2.65 was used.

2.2. Geopolymer preparation and testing

Ground fly ash was thoroughly mixed with NaOH solution and water glass with the mix proportions shown in Table 2. Geopolymers consisted of 60% fly ash and 40% solution by weight. Water glass-to-NaOH solution (G/N) mass ratios were varied in the range of 1.0–2.5. Geopolymer paste was mixed for 2 min by hand mixer (Philip mixer HR 1456) to obtain homogeneous geopolymer paste. Geopolymer paste was cast in 25-mm∅ and 25-mm height plastic cylinder mold with 10 s vibration in order to remove air bubble. Heat curing at 65 °C was applied for 24 h to accelerate the reaction. Hardened specimens were then demolded and cured in 25 °C cabinet until the testing age. Characterization of paste specimens was performed using XRD, SEM–EDX (JEOL JSM 5600LV, gold coating) and FTIR (Perkin Elmer system 2000, KBr pellet, 1 cm^{-1} resolution) techniques.

In the case of geopolymer mortar for strength test, graded river sand was added to the geopolymer paste at the final step of mixing with sand-to-fly ash mass ratio of 2. For mortar, 50-mm acrylic cube mold was used. Casting and heat curing were done the same way as those of paste specimens. After demolding, specimens were cured at 25 °C cabinet until the testing ages. Strength tests were performed at the ages of 7, 30 and 90 days.

Table 2
Mix proportion of geopolymer pastes.

Samples	Fly ash (g)	Water glass (g)	NaOH (g)	G/N mass ratio	SiO_2/Al_2O_3 mole ratio	Na_2O/SiO_2 mole ratio
10FA	60	20	20	1.0	4.52	0.75
15FA	60	24	16	1.5	4.72	0.60
20FA	60	26.5	13.5	2.0	4.85	0.51
25FA	60	28.5	11.5	2.5	4.95	0.44

3. Results and discussions

The results of compressive strength test of geopolymer mortars are shown in Fig. 1. Results showed that the strength development was dependent on G/N ratio. At low G/N ratios of 1.0 and 1.5, the 90-day strengths decreased compared to the 30-day strengths. It could result from the excess NaOH solution in the mixture. In addition, formation of zeolite in the geopolymer matrix could also hinder the strength development of materials [11,12]. The SiO_2/Al_2O_3 ratios of 10FA and 15FA mixes were 4.52 and 4.72 and, the Na_2O/SiO_2 mole ratios were 0.75 and 0.60, respectively. The SiO_2/Al_2O_3 ratios were just a little higher than the recommended range of 3.3–0.48. However, the Na_2O/SiO_2 ratios were outside the recommended range of 0.2–0.48 [7,13]. Both SiO_2/Al_2O_3 and Na_2O/SiO_2 mole ratios played important roles on compressive strength development of geopolymers. At high G/N ratios of 2.0 and 2.5, the normal increase in strength with time of curing was observed. High G/N ratio resulted in high SiO_2/Al_2O_3 and low Na_2O/SiO_2 ratios in the system. For the 20FA and 25FA mixes, the SiO_2/Al_2O_3 ratios were 4.85 and 4.95 and the Na_2O/SiO_2 ratios were 0.51 and 0.44, respectively. Although, the SiO_2/Al_2O_3 ratios were a little high, the Na_2O/SiO_2 ratios were within the recommended range for high compressive strength development. The compressive strength between 20 and 30 MPa was obtained for mortars with G/N ratios of 2.0 and 2.5. It should be noted here that the concrete for structural use should have a characteristic strength in excess of 25 MPa [14].

In addition, this FBC fly ash contained a high amount of calcium. It was very likely that additional pozzolanic reaction occurred in

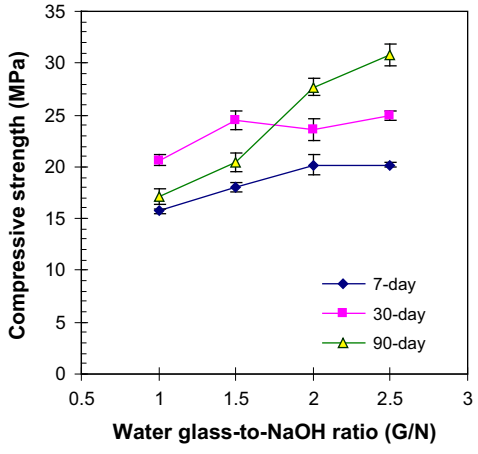

Fig. 1. Compressive strengths of geopolymer mortars with various G/N ratios.

Table 1
Chemical compositions of ground FBC fly ash and LOI.

Compositions (%)	SiO_2	Al_2O_3	Fe_2O_3	CaO	SO_3	MgO	K_2O	Na_2O	LOI
Fly ash	34.1	16.6	17.5	12.8	6.4	3.6	1.1	1.1	6.7

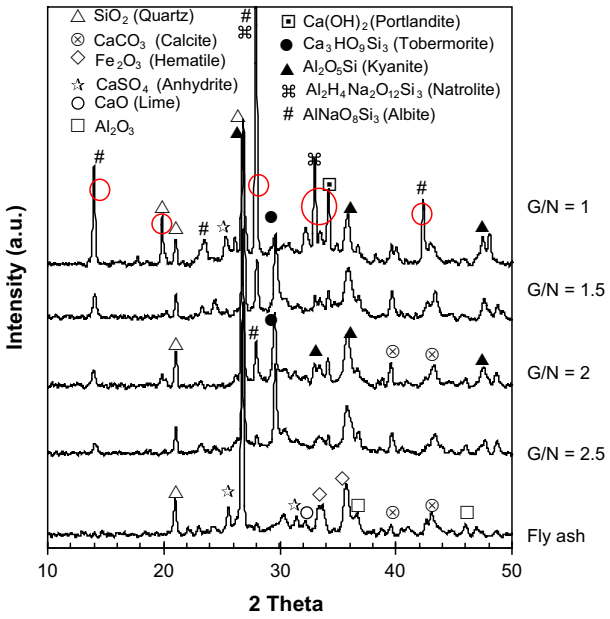

Fig. 2. XRD patterns of fly ash and 90-day geopolymer pastes.

the presence of strong base condition [2]. It should be noted here that this fly ash also contained a high Fe_2O_3 content which inhibited a high degree of geopolymerization and could result in a low compressive strength geopolymer [7].

The strength reductions at 90-day curing with G/N ratios of 1.0 and 1.5 warranted further investigation and thus geopolymer pastes at this age were subjected to the XRD analysis. The results of XRD analyses of these pastes are shown in Fig. 2.

XRD patterns showed the sharp peaks for crystalline structure, and broad hump for amorphous structure of geopolymer products. Sharp peak of quartz was strongly detected at 27° 2θ in both fly ash and geopolymers. Height of this quartz peak was reduced after the geopolymeric synthesis. The raw minerals from fly ash and new products were also found in geopolymers. Products included calciumsilicate (tobermorite, 29.80° 2θ), aluminosilicate (kyanite, 26.66° and 35.72° 2θ), zeolites (natrolite, 27.94°, 32.99° 2θ; and albite, 13.86°, 23.47°, 42.33° 2θ) and calcium hydroxide (portlandite, 34° 2θ). Due to the high content of calcium compound in fly ash, pozzolanic reaction occurred in the presence of base and silica. Complex tobermorite phase of calciumsilicate compound were also detected.

As mentioned, the strength reductions at 90-day curing led to the XRD analyses of geopolymer pastes at this age. According to the literatures, the strength reduction at later age is normally associated with the mix with low water glass content [15]. Two explanations viz., excessive formation of crystal phases in the geopolymer matrix [11,12] and shrinkage and cracking of the matrix [16] have been proposed. For the paste with G/N ratio of 1.0 (high content of NaOH solution), sharp peaks were found extensively due to the formation of zeolites and the remain of raw material. Peaks of natrolite and albite were identified, particularly at 13.86°, 27.94°, 32.99° and 42.33° 2θ. The polymorph of SiO_2 with different crystal structure could be detected at 19.79° 2θ. It occurred as a metastable phase, and with sufficient time and temperature change, it transformed to quartz (crystalline phase). With the decrease in NaOH content (increase in G/N ratio to 1.5), the zeolite peaks were reduced. The 90-day strengths of geopolymer with G/N ratio of 1.5, however, showed the same trend of result as that with G/N ratio of 1. It was, therefore, likely that the strength reduction was due to the formation of excessive crystalline compounds.

For the paste with G/N ratio of 2.5, the peaks of zeolites were dramatically reduced. In this case, the peaks of tobermorite and kyanite became dominant. Water glass helped to increase the amount of soluble silica in the mixture and the formation of geopolymer matrix. High content of water glass, however, reduced the workability of the mixture and also resulted in rapid setting.

For the geopolymer pastes, SEM micrographs at 90-day curing were taken and shown in Fig. 3. For paste with G/N ratio of 1, cracks, pores and unreacted fly ash particle were detected. The reaction occurred at the surface of fly ash particles due to the presence of glassy phase [17]. This glassy phase could be easily leached and reacted with base solutions. The high content of NaOH solution increased the liquid portion in the mixture resulting in cracks and pores during heat curing and geopolymerization reaction.

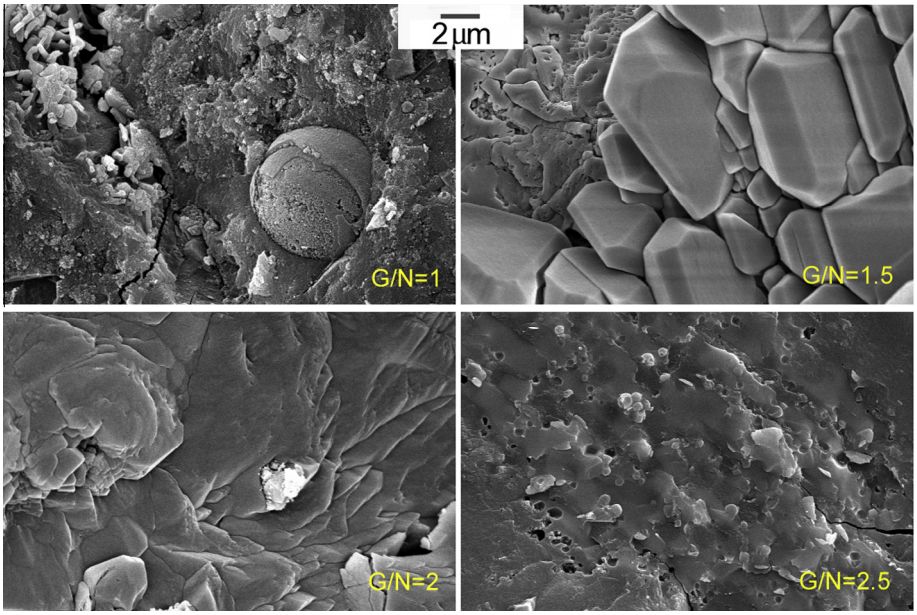

Fig. 3. SEM micrographs of 90-day geopolymer pastes.

Crystalline phase was observed in a small quantity probably due to their small sizes and the formation in cracks and pores. For pastes with G/N ratio of 1.5, crystalline phases were present in a large quantity. This resulted in the low binding capacity of heterogonous geopolymeric matrix and thus led to low strength composite. More homogeneous matrices were obtained with pastes with G/N ratios of 2.0 and 2.5. Increases in water glass enhanced the binding of materials throughout the matrix. Soluble silica in water glass helped the formation of aluminosilicate matrix. SiO_2 and Al_2O_3 were leached out by NaOH solution from fly ash particles, and consequently formed the aluminosilicate bridge [15]. This resulted in high strength pastes. However, a high amount of water glass gave excess silica in the mixture which remained in the form of solid silica gel or sodium silicate and could hinder the strength development.

The 90-day geopolymer paste with G/N ratio of 1.5 was selected to study the element content using SEM–EDX. Crystalline phase was subjected to EDX investigation. SEM–EDX spectra are presented in Fig. 4. The main elements in crystalline phase consisted of oxygen, sodium and calcium as shown in Fig. 4(a). These elements were from the raw materials i.e. fly ash, water glass and sodium hydroxide. Calcium hydroxide crystal with excess sodium hydroxide could be identified. Generally, calcium hydroxide has hexagonal shape, however, other shape can be observed depending on the concentration of solution and crystal age. Fig. 4(b) shows numerous high-intensity peaks of element

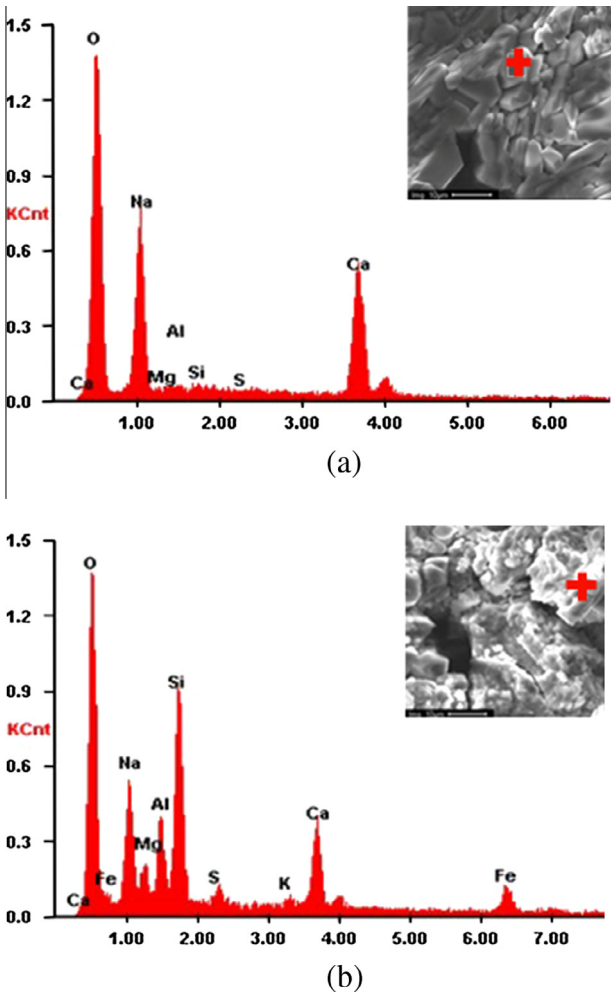

Fig. 4. SEM–EXD spectrum of 90-day geopolymer pastes with G/N of 1.5. (a) Crystalline phase at Position 1. (b) Crystalline phase at Position 2.

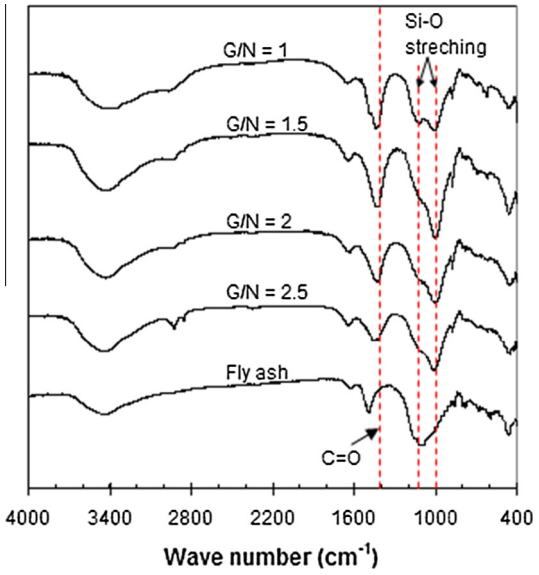

Fig. 5. FT-IR spectra of 90-day geopolymer pastes.

including oxygen, sodium, magnesium, aluminium, silicon and calcium. This spectrum indicated the present of calciumsilicate and aluminosilicate compounds.

In addition, FT-IR spectra of fly ash and 90-day geopolymer pastes were recorded at wavenumber range of 4000–400 cm^{-1} as shown in Fig. 5. Broad bands were located at 3450 cm^{-1} and 1600 cm^{-1} which were assigned to O–H stretching and O–H bending of water molecule, respectively. CO_3^{2-} bond was also observed around 1400 cm^{-1} resulting from carbonation.

Absorption band is related to the vibration at a specific configuration of chemical bonding. Oxide compounds of Si and Al are the focused product of geopolymeric reaction and the peak shifts are concerned. In addition, wavenumber is directly proportional to energy and frequency of molecules [18]. Si–O–Al stretching vibration is more prominent than Si–O–Si bending mode in geopolymer, therefore it is logically used to indicate the degree of geopolymerization. The stretching modes were sensitive to the framework of aluminosilicate composite. In fly ash, Si–O was detected at the wavenumber of approximately 1150 cm^{-1}. Formation of geopolymer resulted in the shift of Si–O peak to lower wavenumber of 1000 cm^{-1} owing to the change in chemical bonding of composites. Si–O bond of SiO_2 (at 1150 cm^{-1}) in raw materials converted to new Si–O bond in geopolymer at 1000 cm^{-1} [4,10]. This peak was strong with the increase in water glass (increase in G/N ratio). In addition, IR doublet was found near 1100 cm^{-1} (particularly for sample with G/N ratio of 1.0) probably due to asymmetry of Al substitution in the tetrahedral sites [19]. Shift of peak to lower wavenumber is related to the formation of new molecule resulting in low bonding strength with exposure to infrared radiation.

4. Conclusion

Alkali activator ratio (G/N) affected the morphology of FBC fly ash geopolymer. Low G/N ratio adversely affected the strength development of geopolymer with a large amount of crystalline compounds. From SEM–EDX spectrum, calcium hydroxide and excess sodium hydroxide could possibly be identified. Increase in water glass resulted in dense and homogeneous composites. Products of reaction consisted of aluminosilicate and zeolites. Due to the high content of calcium compound in fly ash, pozzolanic reaction occurred in the presence of base and silica resulting in formation of calciumsilicate. This compound contributed the strength

development of composite with curing time. In addition, geopolymer formation resulted in the shift of Si–O peak to lower wavenumber of 1000 cm^{-1} indicating the change in chemical bonding of composites.

Acknowledgements

This work was supported by the Thailand Research Fund (TRF) and Khon Kaen University under TRF Senior Research Scholar Contract No. RTA5780004. Appreciation is also extended to Center of Excellence on Environmental Health and Toxicology (EHT), Faculty of Science, Burapha University.

References

[1] P. Basu, Combustion of coal in circulating fluidized-bed boilers: a review, Chem. Eng. Sci. 54 (1999) 5547–5557.
[2] P. Chindaprasirt, P. Paisitsrisawat, U. Rattanasak, Strength and resistance to sulfate and sulfuric acid of ground fluidized bed combustion fly ash–silica fume alkali-activated composite, Adv. Powder. Technol. 25 (2014) 1087–1093.
[3] H. Xu, H. Li, L. Shen, M. Zhang, J. Zhai, Low-reactive circulating fluidized bed combustion (CFBC) fly ashes as source material for geopolymer synthesis, Waste Manage. 30 (2010) 57–62.
[4] P. Chindaprasirt, S. Jenjirapanya, U. Rattanasak, Characterizations of FBC/PCC fly ash geopolymeric composites, Constr. Build Mater. 66 (2014) 72–78.
[5] P. Chindaprasirt, U. Rattanasak, C. Jaturapitakkul, Utilization of fly ash blends from pulverized coal and fluidized bed combustions in geopolymeric materials, Cem. Concr. Compos. 33 (2011) 55–60.
[6] P. Chindaprasirt, S. Thaiwitcharoen, S. Kaewpirom, U. Rattanasak, Controlling ettringite formation in FBC fly ash geopolymer concrete, Cem. Concr. Compos. 41 (2013) 24–28.
[7] J. Davidovits, Geopolymer: Chemistry and Applications, Lulu Enterprises, USA, 2008.
[8] A. Palomo, F.P. Glasser, Chemically-bonded cementitious materials based on metakaolin, Br. Ceram. Trans. 91 (1992) 107–112.
[9] W.K.W. Lee, J.S.J. Van Deventer, Structural reorganization of class F fly ash in alkaline silicate solutions, Colloids Surf. A 211 (2002) 49–66.
[10] U. Rattanasak, P. Chindaprasirt, Properties of alkali activated silica fume–$Al(OH)_3$–fluidized bed combustion fly ash, Mater. Struct. 48 (2015) 31–540.
[11] E. Alvarez-Ayuso, X. Querol, F. Plana, A. Alastuey, N. Moreno, M. Izquierdo, et al., Environmental, physical and structural characterisation of geopolymer matrixes synthesized from coal (co-)combustion fly ashes, J. Hazard. Mater. 154 (2008) 75–83.
[12] J.G.S. Van Jaarsveld, J.S.J. van Deventer, L. Lorenzen, Factors affecting the immobilization of metals in geopolymerized fly ash, Metall. Mater. Trans. B 29 (1998) 283–291.
[13] V. Barbosa, K. MacKenzie, C. Thaumaturgo, Synthesis and characterisation of materials based on inorganic polymers of alumina and silica: sodium polysialate polymer, Int. J. Inorg. Mater. 2 (2000) 309–317.
[14] British Standards Institution, BS 8110: Structural Use of Concrete — Part 1: Code of Practice for Design and Construction, London, 1997.
[15] U. Rattanasak, P. Chindaprasirt, Influence of NaOH solution on the synthesis of fly ash geopolymer, Miner. Eng. 22 (2009) 1073–1078.
[16] J. Wongpa, K. Kiattikomol, C. Jaturapitakkul, P. Chindaprasirt, Compressive strength, modulus of elasticity, and water permeability of inorganic polymer concrete, Mater. Des. 31 (2010) 4748–4754.
[17] M. Inada, H. Tsujimoto, Y. Eguchi, N. Enomoto, J. Hojo, Microwave-assisted zeolite synthesis from coal fly ash in hydrothermal process, Fuel 84 (2005) 1482–1486.
[18] H. Günzler, H. Gremlich, IR Spectroscopy: An Introduction, Wiley-VCH Verlag GmbH, Germany, 2002.
[19] J.L. Bishop, E. Murad, Characterization of minerals and biogeochemicalmarkers on Mars: a Raman and IR spectroscopic study of montmorillonite, J. Raman Spectrosc. 35 (2004) 480–486.

Construction and Building Materials 94 (2015) 408–413

Contents lists available at ScienceDirect

Construction and Building Materials

journal homepage: www.elsevier.com/locate/conbuildmat

Properties of lightweight high calcium fly ash geopolymer concretes containing recycled packaging foam

Patcharapol Posi [a], Charoenchai Ridtirud [a], Chatchavan Ekvong [a], Duangchai Chammanee [a], Khuanchai Janthowong [a], Prinya Chindaprasirt [b,*]

[a] Dept. of Civil Engineering, Faculty of Engineering, Rajamangala University of Technology Isan Khon Kaen Campus, Khon Kaen 40000, Thailand
[b] Sustainable Infrastructure Research and Development Center, Dept. of Civil Engineering, Faculty of Engineering, Khon Kaen University, Khon Kaen 40002, Thailand

HIGHLIGHTS

- Lightweight geopolymer (LG) block was fabricated from high calcium fly ash and recycled foam aggregate.
- LG with NH = 5–15 molars, NS/NH = 0.33–3, liquid/ash = 0.5–1, curing at 25–60 °C, aggregate content = 0.85–1.05 %wt. were tested.
- Low densities of 1000–1300 kg/m^3 and 28-day compressive strengths of 4.0–11.2 MPa were obtained.

ARTICLE INFO

Article history:
Received 5 February 2015
Received in revised form 23 May 2015
Accepted 12 July 2015

Keywords:
Geopolymer
Recycled foam
Lightweight geopolymer concrete
Thermal conductivity

ABSTRACT

In this research, the properties of lightweight geopolymer concretes containing recycled packaging foam were studied. The recycled foam was crushed to sizes of 2.35–4.75 mm and used as lightweight aggregate. Compressive strengths and densities with liquid alkaline/ash ratios of 0.5–1.0, sodium silicate/NaOH ratios of 0.33–3.0, NaOH concentrations of 5–15 molars, curing temperatures at 25 and 60 °C, and foam contents of 0.85–1.05 %wt. were tested. In addition, the thermal conductivities of geopolymer blocks were determined. Results showed that the lightweight geopolymer blocks of densities of 1000–1300 kg/m^3, with satisfactory strength and low thermal conductivity can be made. This gave a twofold advantageous viz. the use of low carbon footprint fly ash geopolymer and the reuse of packaging foam.

© 2015 Elsevier Ltd. All rights reserved.

1. Introduction

The production of Portland cement is an energy intensive operation and releases a large amount of green house gas to the atmosphere, which accounts for about 5% of green house gas produced annually [1]. Therefore, new cementitious material using silica and alumina activated in a high alkali solution was developed to supplement Portland cement [2]. This new material is geopolymer or alkali-activated binder [3].

In Thailand, the lignite important coal mine and large power plant are located in Mae Moh district, Lampang province. The annual output of fly ash from this source is 3 million tons. A substantial amount is not utilized and is deposited at the landfill site. This fly ash contains high calcium content. It also contains high amount of silica and alumina and is used successfully in making geopolymer binder with adequate strength and excellent durability characteristics [4–6].

The construction of building and structures in Thailand and other countries relies heavily on Portland cement products. The structural members, walls and panels are made of Portland cement [7] and the problems of the weight of structural members and wall panels are of great concern [8]. In order to reduce the weight of structure, lightweight construction materials in the form of lightweight concrete block or wall using cast-in-place lightweight concrete have been developed. The purpose of this work is to reduce the dead load of structure resulting in lighter structures and also with reduced cement content.

Lightweight concretes (LC) is usually defined as concretes with unit weight less than 1840 kg/m^3 [9]. The low unit weights LC of 400–1200 kg/m^3 are for block production and the high unit weights of 1300–1840 kg/m^3 are for structural concrete [10]. The LC are classified into three types viz., LC with lightweight aggregate, LC with large voids, and LC with no fine aggregate [11]. LC with lightweight aggregate are mostly used for masonry due to high strength and good sound and thermal insulation properties from the air void in lightweight aggregate [12]. Both natural and synthesized lightweight aggregates are used in the manufacturing

* Corresponding author.
E-mail address: prinya@kku.ac.th (P. Chindaprasirt).

http://dx.doi.org/10.1016/j.conbuildmat.2015.07.080
0950-0618/© 2015 Elsevier Ltd. All rights reserved.

of LC. The common natural lightweight aggregates are pumice, perlite, and diatomite; and the synthesized ones are expanded clay and sintered fly ash [13].

Polystyrene foam (PSF) is a thermoplastic polymer with a closed cellular structure [14]. A large amount of PSF materials is now being used as food container and industrial product packaging. As a result, this foam in huge amount is now a waste and need special attention or proper disposal [15]. If burnt, they pollute the atmosphere or if discarded at landfill sites, it took a very long time to decompose.

PSF has interesting properties such as low unit weight (less than 300 kg/m^3), good thermal insulation, hydrophobicity, and chemical resistance [14,16]. There have been a number of studies on the use of PSF for making lightweight concretes [14–18]. The PSF dosage and water to cement ratio are important parameters affecting the density and strength of the lightweight concrete. The low density lightweight of 1050 kg/m^3 was successfully fabricated with the emphasis on strengthening the cement paste matrix with the aids of silica fume and plasticizer [16,17].

Thus, in this research, high calcium fly ash geopolymer paste was used as a new binder for making lightweight concrete containing used packaging foam as lightweight aggregate. This would give a twofold advantageous viz. the use of low carbon footprint fly ash geopolymer instead of Portland cement and the reuse of packaging foam to reduce the burden of waste disposal.

2. Experimental program

2.1. Materials

Materials used in this research consisted of lignite fly ash from Mae Moh power station in the north of Thailand, sodium silicate with 15.32% Na_2O, 32.87% SiO_2, and 51.8% water, and 5, 10, and 15 molars (M) NaOH and recycle packaging foam (RF). The RF was the discarded packaging foam from the household electricity appliances. The foam was broken into 3.0–4.0 cm pieces by hand and then crushed using a food blender. The crushed foam was sieved to obtain the size of 2.36–4.75 mm as shown in Fig. 1 and used as fine aggregate. Chemical compositions of fly ash determined using X-ray fluorescence (XRF) technique are shown in Table 1 and its X-ray diffraction (XRD) is shown in Fig. 2. The sum of SiO_2, Al_2O_3 and Fe_2O_3 was over 75% which was in accordance which ASTM C618 [18], however, the CaO content was high indicating a high calcium fly ash. The XRD analysis showed mainly amorphous phase with some peaks of crystalline phases of magnetite, magnesioferrite, dachiardite, and calcium aluminum oxide. The fly ash was 30% retained on sieve No. 325 (45 μm) with median particle size of 18.6 μm and Blaine fineness of 2800 cm^2/g. It consists mainly of spherical particles with smooth surface as shown in Fig. 3. The physical properties of materials are shown in Table 2. The RF has particle sizes between 2.36 and 4.75 mm with unit weight of 215 kg/m^3 and water absorption of 225%. River sand with specific gravity of 2.61 and fineness modulus of 2.65 was used as normal fine aggregate.

2.2. Mix proportion

2.2.1. Mix compositions

Five series of mixes were used to test the effects of liquid alkaline/ash ratios (series A), sodium silicate/NaOH ratios (series B), concentration of NaOH (series C), temperature of curing (series D), and volume of foam (Series E). The details of mixes are shown in Table 3.

Fig. 1. Lightweight aggregates from recycled foam.

Table 1
Chemical composition of materials (by weight).

Chemical compositions (%)	Fly ash
SiO_2	45.23
Al_2O_3	19.95
Fe_2O_3	13.15
CaO	15.50
K_2O	2.15
TiO_2	0.39
Na_2O	0.52
P_2O_5	0.81
MgO	2.02
LOI	0.88

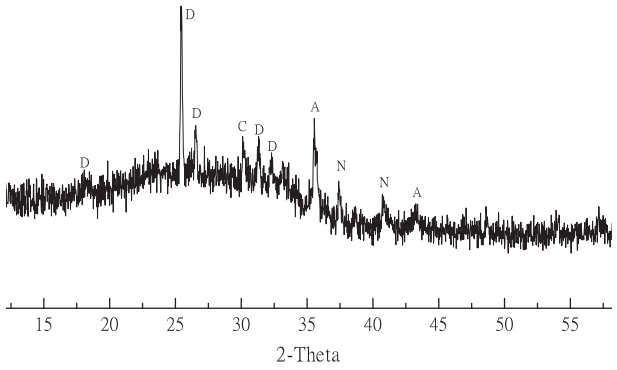

Fig. 2. XRD patterns of fly ash. A-Magnetite: Fe_3O_4; C-Magnesioferrite: Fe_2MgO_4; D-Dachiardite: $Na_{1.1}K_7Ca_{1.7}Al_{5.2}Si_{18.8}O_{48}$ $(H_2O)_{12.7}$; N-Calcium Aluminum Oxide: $CaAl_2O_4$.

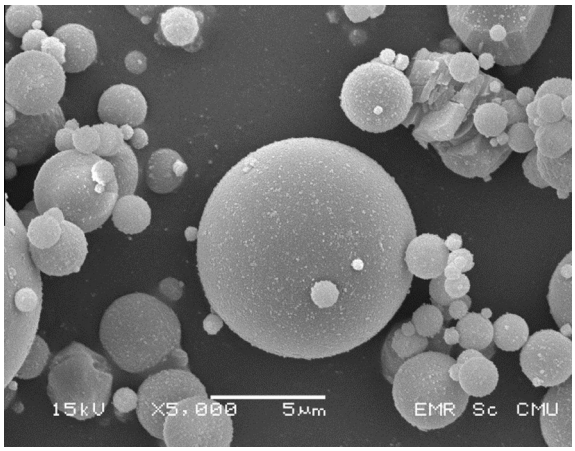

Fig. 3. SEM of fly ash.

Table 2
Physical properties of materials.

Materials	Fly ash	Sand	Recycled foam
Specific gravity	2.52	2.61	–
Median particle size (μm)	18.6	–	–
Particle size (mm)	–	–	2.36–4.75
Fineness modulus	–	2.65	–
Density (kg/m^3)	–	1360	215
Water absorption (%)	–	1.17	225

2.2.2. Details of mixing

Constant sand to fly ash ratio of 1.00 was used for all mixes. The mixing was done in a pan mixer with the following steps:

- NaOH solution and fly ash were mixed for 5 min.
- Sand was added and mixed for 5 min.

Table 3
Weight ratios of lightweight geopolymer concrete mixes.

Series	L/A ratio	NS/NaOH ratio	NaOH (M)	Curing temp. (°C)	Aggregate % by weight
A	0.5, 0.6, 0.7, 0.8, 0.9, 1.0	1.00	10	40	1.05
B	0.7	0.33, 0.67, 1.00, 1.50, 3.00	10	40	1.05
C	0.7	1.00	5, 10, 15	40	1.05
D	0.7	1.00	10	25, 40, 60	1.05
E	0.7	1.00	10	40	0.85, 0.90, 0.95, 1.00, 1.05

– Sodium silicate solution (NS) was added and mixed for 5 min.
– Aggregate was added and mixed for 1.5 min.

The fresh lightweight geopolymer concretes were placed into 50 mm and 100 mm cube molds in accordance with ASTM C109/C109M-13 [19]. This standard is for cement mortars and was used since samples could be considered as mortars as the maximum aggregate size of the lightweight concrete was 4.75 mm which was similar to that of fine aggregate as specified by ASTM C33/C33M-13 [20]. The specimens were covered with damp cloth and plastic sheet to prevent moisture loss and placed in a 25 °C controlled room for 1 h [5]. The specimens were then transferred to oven curing at 25, 40, and 60 °C for 48 h. Finally, the specimens were demolded and wrapped with plastic sheet and stored in a 25 °C controlled room.

2.3. Details of test

2.3.1. Compressive strength and density

The density of concrete was determined at the ages of 28 days using the compressive strength specimens as described in ASTM C138/C138M-14 [21]. The compressive strength was tested after the density determination. The cube specimens were tested to determine the compressive strength in accordance with ASTM C109/C109M-13 [19]. The report results were the average of three samples.

2.3.2. Thermal conductivity

The thermal conductivity of concrete was measured using portable heat transfer analyzer ISOMET2114. This analyzer is based on ASTM D5930-09 [22] method for finding thermal conductivity of plastics by means of a transient line-source technique. Similar device was successfully used for testing of cementitious materials [23–25]. The 100 × 100 × 100 mm cube specimens were used for this test. The tests were performed on the oven-dried samples at the age of 28 days and the report results were the average of three samples.

3. Results and discussions

3.1. Compressive strength and density

3.1.1. Liquid alkaline/ash ratio

The results of compressive strength of geopolymer lightweight concrete with various liquid alkaline/ash ratios are shown in Fig. 4. The compressive strength decreased with the increasing liquid alkaline/ash ratios. The 28-day compressive strength of samples with liquid alkaline/ash ratios of 0.5, 0.6, 0.7, 0.8, 0.9, and 1.0 were 11.2, 8.3, 6.4, 5.3, 4.0, and 4.3 MPa, respectively. The increase in liquid to ash ratio increased the inter-particle distance of the solid particle and thus increased the workability and reduced the strength of the geopolymer [4]. High liquid content also produced mixture which was very workable and prone to segregation and bleeding with substantial shrinkage. The increase in liquid content reduced the concentration of silica and alumina in the solution and hence the rate of geopolymerization was also reduced [6]. The compressive strength thus decreased due to the excess liquid similar to Portland cement concretes [7,26–28].

3.1.2. Sodium silicate/NaOH ratio

The results of compressive strength of lightweight geopolymer concrete with various NS/NaOH ratios are shown in Fig. 5. The 28-day compressive strengths of concretes with NS/NaOH ratios of 0.33, 0.67, 1.00, 1.50, and 3.00 were 5.1, 5.9, 6.4, 6.0, and 5.5 MPa, respectively. The optimum compressive strength of 6.4 MPa was obtained with NS/NaOH ratio of 1.00. An increase in NS/NaOH ratio from 0.33 to 1.00 increased the strength of concrete. The increase in strength in this range of NS/NaOH ratio was due to the increased silica content of mixture. However, when the NS/NaOH ratio was increased to 1.5, the strength started to drop due to the difficulty in compaction [4]. The density of geopolymer concrete increased with increasing NS/NaOH from 0.33 to 1.00 due to the increase in NS content as the density of NS was higher than that of NaOH. Similar trend of result was reported for the normal weight high calcium fly ash (HCFA) geopolymer mortars. The compressive strengths of mortars with high NS/NaOH ratios of 1.5 and 3.0 were reduced compared to that with NS/NaOH ratio of 1.0 [5,29].

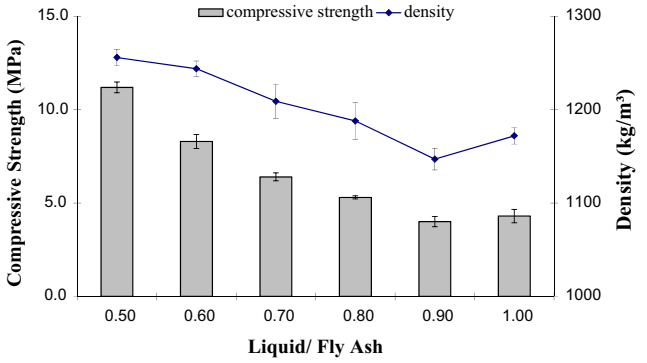

Fig. 4. Compressive strength and density at 28 days of lightweight geopolymer concretes at various L/A ratios (series A).

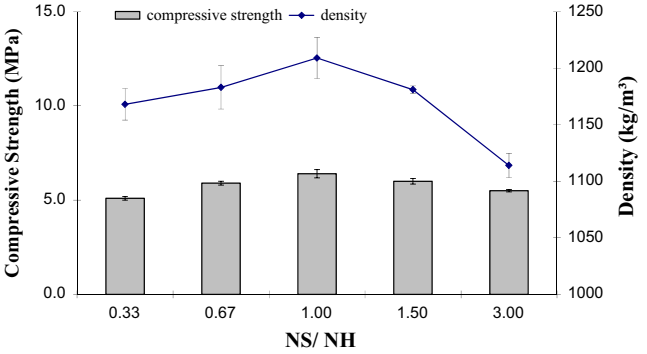

Fig. 5. Compressive strength and density at 28 days of lightweight geopolymer concrete at various NS/NaOH ratios (series B).

3.1.3. Concentration of NaOH solution

The results of the effects of NaOH solution concentrations on compressive strength are shown in Fig. 6. The concentration of NaOH solution had an influence on the strength of geopolymer but the influence was rather small. The compressive strength of mortar with 10 M NaOH solution was slightly higher than those of 5 and 15 M NaOH concretes. An increase in the concentration of NaOH solution from 5 M to 10 M resulted in the increase in compressive strengths from 5.3 MPa to 6.4 MPa. The increase in

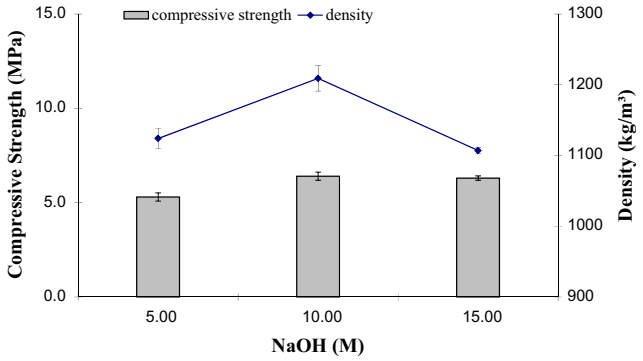

Fig. 6. Compressive strength and density at 28 days of lightweight geopolymer concrete at various concentrations of NaOH solution (series C).

concentration of NaOH in this range helped the leaching of silica and alumina from the source material and thus increased the geopolymerization reaction [4,30]. In addition, calcium oxide from high calcium fly ash reacted with silicate compounds and formed CSH similar to the hydration of Portland cement [30–32]. The CSH products co-existed with the geopolymer gel and contributed to the strength development [32]. However, an increase in the concentration of NaOH solution from 10 M to 15 M resulted in no further increase in compressive strength. The 28-day compressive strength with concentration of NaOH solutions of 15 M was 6.3 MPa. Approximately the same or even a slight drop in strength at high NaOH concentration was due to the excessive hydroxide ions causing aluminosilicate gel precipitation at the very early stages [7,32–34]. In this case, no increase in strength could also be in part due to the lower density of concrete compared with that of concrete with 10 M NaOH. The slight drop in density of geopolymer concrete was from the reduced compactability of the mix with increased concentration of NaOH.

3.1.4. Temperature of curing

The results of compressive strengths of lightweight geopolymer concretes with various temperatures of curing are shown in Fig. 7. The optimum temperature of curing was 40 °C and the maximum strength of 6.4 MPa was obtained. An increase in temperature of curing from 25 °C to 40 °C resulted in the increase in compressive strength. The increase in temperature of curing to 40 °C enhanced the geopolymerization and increased the compressive strength [5,7,35,36]. However, temperature curing at 60 °C lowered the strength of lightweight concrete. The 28-day compressive strength with temperature of curing of 25, 40, and 60 °C were 4.5, 6.4, and 5.1 MPa, respectively.

Temperature curing at 60 °C should increase the intrinsic strength of the matrix. However, the density of lightweight concrete cured at 40 °C was 1210 kg/m^3 and reduced to 1130 kg/m^3 when cured at 60 °C. Previous researches also indicated that the density of foam lightweight concrete reduced with the increase in curing temperature due to the expansion of matrix under heat curing [37,38]. The reduction in strength with curing at temperature of 60 °C was due to the reduced density resulted from the increase in porosity of lightweight geopolymer concrete under heat curing. The strength of normal weight geopolymers cured at high temperature could also be reduced due to the loss of moisture from samples [5,39]. The porous microstructure of lightweight geopolymer allowed heat to penetrate into the sample more easily and facilitated the evaporation or migration of moisture from the interior of the sample.

3.1.5. Foam content

The results of compressive strengths of lightweight geopolymer concretes with various foam contents are shown in Fig. 8. The compressive strength decreased with the increasing foam content. The 28-day compressive strength with RF contents of 0.85, 0.90, 0.95, 1.00, and 1.05 %wt. were 9.5, 7.4, 6.5, 6.5, and 6.4 MPa, respectively. This was accompanied by the weight of the samples of 1340, 1250, 1285, 1220 and 1200 kg/m^3, respectively as also shown in Fig. 8. The recycled foam is normally weaker than the geopolymer matrix and the increased amount thus reduced the strength of geopolymer lightweight concrete [7,40–42]. The density decreased with the increase in RF content as the density of RF was only 215 kg/m^3 compared with that of geopolymer concrete of 2030 kg/m^3. The porosity of RF is high and thus it is not strong [14]. The incorporation of foam at the dosage of 1.05% by weight was able to reduce the density of concrete to approximately 1200 kg/m^3. Similar finding of reduction in strength with increasing foam content was reported for lightweight geopolymer concrete [43].

3.2. Thermal conductivity

The results of thermal conductivity of oven-dried lightweight geopolymer concrete with various foam contents are shown in Fig. 9. The thermal conductivity decreased with the increasing foam contents as expected. For example, the values of thermal conductivity at the age of 28-day with volumes of foam of 0, 0.85, 0.90, 0.95, 1.00, and 1.05 were 0.77, 0.35, 0.33, 0.30, 0.29 and 0.27 W/mK, respectively. The thermal conductivity values of lightweight aggregate foamed geopolymer concrete were reported to be 0.47–0.58 W/mK [43] and those of metakaolin geopolymers were 0.55–0.65 W/mK and increased to 0.91 W/mK with the addition

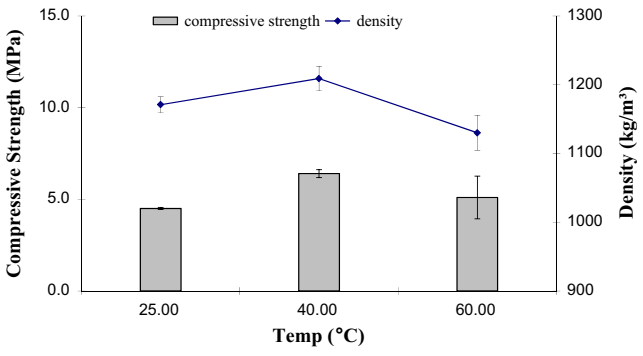

Fig. 7. Compressive strength and density at 28 days of lightweight geopolymer concrete at various curing temperatures (series D).

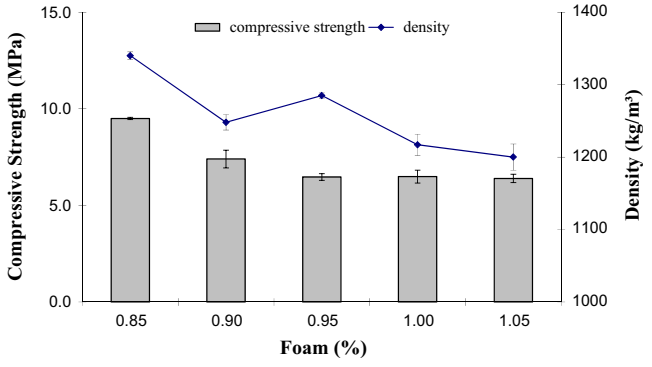

Fig. 8. Compressive strength and density at 28 days of lightweight geopolymer concrete at various foam contents (series E).

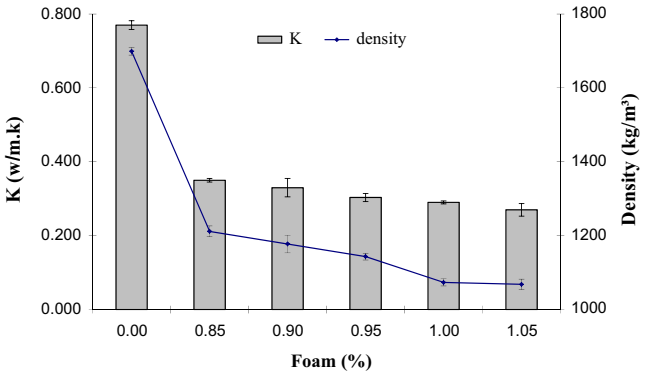

Fig. 9. Thermal conductivity at 28 days of lightweight geopolymer concrete at various foam contents (series E).

of quartz sand [44]. These values were comparable to the obtained results of 0.27–0.35 W/mK for lightweight geopolymer concretes and 0.77 W/mK for normal weight geopolymer concrete. It should be noted here that the samples in this test were oven-dried at 110 °C for 24 h. The thermal conductivity reduced by more than half with the incorporation of recycled foam. The thermal conductivity decreased with the decreasing density as the thermal conductivity depended on the density of geopolymer lightweight concrete [13]. The increase in porosity of the system resulted in the lowering of thermal conductivity [45,46].

4. Conclusion

Based on the obtained data, the following conclusions can be drawn:

(1) The compressive strength decreased with the increasing liquid alkaline/ash ratios and volume of foam due to the excess liquid and porosity effect to low compressive strength.
(2) There were optimum level of NS/NaOH ratio, NaOH concentration and curing temperature. The optimum NS/NaOH ratio was 1.00 as compressive strength of 6.4 MPa. The optimum concentration of NaOH solution was 10 M and temperature of curing was 40 °C for maximum compressive strength.
(3) The volume of foam had significant effects on strength, density and thermal properties of lightweight geopolymer concrete. The increase in the volume of foam decreased the strength, density and thermal conductivity of the lightweight concrete.
(4) The results showed that the lightweight geopolymer concrete with 28-day compressive strength of 4.0–11.2 MPa, densities of 1000–1300 kg/m^3, and thermal conductivities of 0.52–0.69 W/mK could be made.

Acknowledgments

This work was financially supported by the Higher Education Research Promotion and National Research University Project of Thailand, Office of the Higher Education Commission, through the Advanced Functional Materials Cluster of Khon Kaen University, and Khon Kaen University and the Thailand Research Fund (TRF) under the TRF Senior Research Scholar Contract No. RTA5780004. The support of the Siam Research and Innovation Co., Ltd. and the Dept. of Civil Engineering, Faculty of Engineering, Rajamangala University of Technology Isan Khon Kaen Campus is also acknowledged here.

References

[1] F. Fouchal, F. Gouny, P. Maillard, L. Ulmet, S. Rossignol, Experimental evaluation of hydric performances of masonry walls made of earth bricks, geopolymer and wooden frame, Build. Environ. 87 (2015) 234–243.
[2] J. Davidovits, Geopolymers – inorganic polymeric new materials, J. Therm. Anal. 37 (8) (1991) 1633–1656.
[3] A. Palomo, M.W. Grutzeck, M.T. Blanco, Alkali-activated fly ashes: a cement for the future, Cem. Concr. Res. 29 (8) (1999) 1323–1329.
[4] A. Sathonsaowaphak, P. Chindaprasirt, K. Pimraksa, Workability and strength of lignite bottom ash geopolymer mortar, J. Hazard. Mater. 168 (1) (2009) 44–50.
[5] P. Chindaprasirt, T. Chareerat, V. Sirivivatnanon, Workability and strength of coarse high calcium fly ash geopolymer, Cement Concr. Compos. 29 (3) (2007) 224–229.
[6] U. Rattanasak, P. Chindaprasirt, Influence of NaOH solution on the synthesis of fly ash geopolymer, Miner. Eng. 22 (12) (2009) 1073–1078.
[7] P. Posi, C. Teerachanwit, C. Tanutong, S. Limkamoltip, S. Lertnimoolchai, V. Sata, et al., Lightweight geopolymer concrete containing aggregate from recycle lightweight block, Mater. Des. 52 (2013) 580–586.
[8] M. Nadim Hassoum, Structural Concrete; Theory and Design, Prentice-Hall Inc., Upper Sandle River, New Jersey, 2002.
[9] ASTM C330-89, Specification for lightweight aggregates for structural concrete, Annual Book of ASTM Standard, 1989, vol. 04.02.
[10] S.B.L. Chandra, Lightweight Aggregate Concrete: Science, Technology and Application, William Andrew Publishing, Norwich, New York, USA, 2002.
[11] A.M. Neville, Concrete Technology, Longman Scientific & Technical, New York, USA, 1987.
[12] S. Demirdag, I. Ugur, S. Sarac, The effects of cement/fly ash ratios on the volcanic slag aggregate lightweight concrete masonry units, Constr. Build. Mater. 22 (8) (2008) 1730–1735.
[13] P. Posi, S. Lertnimoolchai, V. Sata, P. Chindaprasirt, Pressed lightweight concrete containing calcined diatomite aggregate, Constr. Build. Mater. 47 (2013) 896–901.
[14] V. Ferrándiz-Mas, E. García-Alcocel, Durability of expanded polystyrene mortars, Constr. Build. Mater. 46 (2013) 175–182.
[15] P. Mounanga, W. Gbongbon, P. Poullain, P. Turcry, Proportioning and characterization of lightweight concrete mixtures made with rigid polyurethane foam wastes, Cement Concr. Compos. 30 (9) (2008) 806–814.
[16] K.G. Babu, D.S. Babu, Behaviour of lightweight expanded polystyrene concrete containing silica fume, Cem. Concr. Res. 33 (5) (2003) 755–762.
[17] N. Liu, B. Chen, Experimental study of the influence of EPS particle size on the mechanical properties of EPS lightweight concrete, Constr. Build. Mater. 68 (2014) 227–232.
[18] ASTM C 618. Standard specification for coal fly ash and raw or calcined natural pozzolan for use in concrete, Annual Book of ASTM Standard, 2012, vol. 04.01.
[19] ASTM C109/C109M-13, Standard test method of compressive strength of hydraulic cement mortars (using 2-in. or [50 mm] cube specimens), Annual Book of ASTM Standard, 2013, vol. 04.01.
[20] ASTM C 33/C33M-13, Standard specification for concrete aggregate, Annual Book of ASTM Standard, 2013, vol. 04.02.
[21] ASTM C138/C138M-14, Standard test of method for unit weight of mortar, Annual Book of ASTM Standard, 2014, vol. 04.01.
[22] ASTM D5930, Standard test method for thermal conductivity of plastics by means of a transient line-source technique, Annual Book of ASTM Standard, 2009, vol. 04.01.
[23] A.H.-C. Shin, U. Kodide, Thermal conductivity of ternary mixtures for concrete pavements, Cement Concr. Compos. 34 (4) (2012) 575–582.
[24] W. Wongkeo, P. Thongsanitgarn, K. Pimraksa, A. Chaipanich, Compressive strength, flexural strength and thermal conductivity of autoclaved concrete block made using bottom ash as cement replacement materials, Mater. Des. 35 (2012) 434–439.
[25] Y. Zaetang, A. Wongsa, V. Sata, P. Chindaprasirt, Use of lightweight aggregates in pervious concrete, Constr. Build. Mater. 48 (2013) 585–591.
[26] S. Rols, J. Ambroise, J. Péra, Effects of different viscosity agents on the properties of self-leveling concrete, Cem. Concr. Res. 29 (2) (1999) 261–266.
[27] J. Wongpa, K. Kiattikomol, C. Jaturapitakkul, P. Chindaprasirt, Compressive strength, modulus of elasticity, and water permeability of inorganic polymer concrete, Mater. Des. 31 (10) (2010) 4748–4754.
[28] M.H. Kharita, S. Yousef, M. AlNassar, The effect of the initial water to cement ratio on shielding properties of ordinary concrete, Prog. Nucl. Energy 52 (5) (2010) 491–493.
[29] D. Hardjito, S.E. Wallah, D.M.J. Sumajouw, B.V. Rangan, On the development of fly ash-based geopolymer concrete, ACI Mater. J. 101 (6) (2004) 467–472.
[30] P. Chindaprasirt, C. Jaturapitakkul, W. Chalee, U. Rattanasak, Comparative study on the characteristics of fly ash and bottom ash geopolymers, Waste Manage. 29 (2) (2009) 539–543.
[31] X. Guo, H. Shi, W.A. Dick, Compressive strength and microstructural characteristics of class C fly ash geopolymer, Cement Concr. Compos. 32 (2) (2010) 142–147.
[32] K. Somna, C. Jaturapitakkul, P. Kajitvichyanukul, P. Chindaprasirt, NaOH-activated ground fly ash geopolymer cured at ambient temperature, Fuel 90 (6) (2011) 2118–2124.
[33] W.K.W. Lee, J.S.J. Van Deventer, The effects of inorganic salt contamination on the strength and durability of geopolymers, Colloids Surf., A 211 (2–3) (2002) 115–126.

[34] K. Pimraksa, P. Chindaprasirt, A. Rungchet, K. Sagoe-Crentsil, T. Sato, Lightweight geopolymer made of highly porous siliceous materials with various Na_2O/Al_2O_3 and $SiO_2/Al2O_3$ ratios, Mater. Sci. Eng., A 528 (21) (2011) 6616–6623.
[35] S. Lee, M.-D. Seo, Y.-J. Kim, H.-H. Park, T.-N. Kim, Y. Hwang, et al., Unburned carbon removal effect on compressive strength development in a honeycomb briquette ash-based geopolymer, Int. J. Miner. Process. 97 (1–4) (2010) 20–25.
[36] B. Joseph, G. Mathew, Influence of aggregate content on the behavior of fly ash based geopolymer concrete, Sci. Iran. 19 (5) (2012) 1188–1194.
[37] J. Henon, A. Alzina, J. Absi, D.S. Smith, S. Rossignol, Porosity control of cold consolidated geomaterial foam: temperature effect, Ceram. Int. 38 (1) (2012) 77–84.
[38] S. Delair, É. Prud'homme, C. Peyratout, A. Smith, P. Michaud, L. Eloy, et al., Durability of inorganic foam in solution: the role of alkali elements in the geopolymer network, Corros. Sci. 59 (2012) 213–221.
[39] G. Görhan, G. Kürklü, The influence of the NaOH solution on the properties of the fly ash-based geopolymer mortar cured at different temperatures, Compos. B Eng. 58 (2014) 371–377.
[40] Y. Xu, L. Jiang, J. Xu, Y. Li, Mechanical properties of expanded polystyrene lightweight aggregate concrete and brick, Constr. Build. Mater. 27 (1) (2012) 32–38.
[41] C.-C. Yang, R. Huang, Approximate strength of lightweight aggregate using micromechanics method, Adv. Cem. Based Mater. 7 (3–4) (1998) 133–138.
[42] N.U. Kockal, T. Ozturan, Strength and elastic properties of structural lightweight concretes, Mater. Des. 32 (4) (2011) 2396–2403.
[43] M.Y.J. Liu, U.J. Alengaram, M.Z. Jumaat, K.H. Mo, Evaluation of thermal conductivity, mechanical and transport properties of lightweight aggregate foamed geopolymer concrete, Energy Build. 72 (2014) 238–245.
[44] Subaer, A. van Riessen, Thermo-mechanical and microstructural characterisation of sodium-poly(sialate–siloxo) (Na-PSS) geopolymers, J. Mater. Sci. 42 (9) (2007) 3117–3123.
[45] Z. Zhang, J.L. Provis, A. Reid, H. Wang, Geopolymer foam concrete: an emerging material for sustainable construction, Constr. Build. Mater. 56 (2014) 113–127.
[46] K. Ramamurthy, E.K. Kunhanandan Nambiar, G. Indu Siva Ranjani, A classification of studies on properties of foam concrete, Cement Concr. Compos. 31 (6) (2009) 388–396.

Construction and Building Materials 96 (2015) 289–295

Contents lists available at ScienceDirect

Construction and Building Materials

journal homepage: www.elsevier.com/locate/conbuildmat

Use of coal ash as geopolymer binder and coarse aggregate in pervious concrete

Yuwadee Zaetang [a], Ampol Wongsa [b], Vanchai Sata [b,*], Prinya Chindaprasirt [b]

[a] Dept. of Civil and Environmental Engineering, Kasetsart University, Chalermphrakiat Sakon Nakhon Province Campus, Sakon Nakhon 47000, Thailand
[b] Sustainable Infrastructure Research and Development Center, Dept. of Civil Engineering, Faculty of Engineering, Khon Kaen University, Khon Kaen 40002, Thailand

HIGHLIGHTS

- Waste from coal ash was used to produce pervious geopolymer concrete (PGC).
- Fly ash was used as geopolymer binder and bottom ash as coarse aggregate.
- NaOH concentration, level OPC replacement, and curing temperature were varied.
- The obtained PGCs are suited for use as an environment friendly concrete.

ARTICLE INFO

Article history:
Received 19 March 2015
Received in revised form 28 July 2015
Accepted 9 August 2015

Keywords:
Pervious concrete
Geopolymer
Fly ash
Bottom ash
Environment friendly material

ABSTRACT

Fly ash (FA) and bottom ash (BA) are wastes from coal combustion power plant. Due to its coarse and porous particle, BA is usually disposed of at landfill sites. While, as-received FA can be used as pozzolanic material and source material to produce geopolymer binder. This study focused on the use of FA as geopolymer binder and BA as coarse aggregate to produce pervious concrete. The effect of NaOH concentration, partial replacement of FA with ordinary Portland cement (OPC), and curing temperature on the properties of pervious geopolymer concrete (PGC) were investigated. The results showed that the strengths of PGC increased with both NaOH concentration and level of OPC replacement. The curing at elevated temperature (90 °C) was a significant factor for the strength development. The PGCs containing BA had the thermal conductivity of 0.30–0.33 W/m K, density of 1466–1502 kg/m^3, and compressive strength of 5.7–8.6 MPa and are suited for use as an environment friendly concrete.

© 2015 Published by Elsevier Ltd.

1. Introduction

The coal fired thermal power plant produces a large amount of ash. Fly ash (FA) is the major waste ash and is used as a pozzolan for partial replacement of Portland cement in concrete work. Due to its aluminosilicate composition and fine particle size, FA is also used as a source material to produce geopolymer binder with excellent early age compressive strength, sulfate resistance, and chloride resistance [1–3]. Apart from FA, a significant quantity of bottom ash (BA) is also produced. As-received BA is low in pozzolanic property as a result of its coarse particle size and is generally dumped in a disused mine. With similar chemical compositions to FA and ground to a proper fineness, BA can be used as a pozzolan [4] and can also be utilized as a source material for making geopolymer [5]. In addition, BA can be used as a lightweight aggregate for making lightweight concrete due to its high porosity and low density [6–8].

Pervious or permeable concrete has interconnected voids as a result of lacking in fine aggregate. It can be used for green pavement design [9–11] because of various environmental benefits such as reducing storm water runoff rates, protecting water supplies, and adjusting temperature and humidity of earth's surface. In a framework of pervious concrete, coarse aggregates are bound together with a binder. Using Portland cement as a binder can make pervious concrete with sufficient strength for porous pavement applications [10,12]. However, cement production uses significant amounts of natural resources and has a large environmental footprint. The previous studies [13,14] showed that fly ash-based pervious geopolymer concrete gave the compressive strength within the ACI 522 [11] recommended range. Therefore, the utilization of geopolymer binder in the production of pervious concrete offers an alternative environment friendly material.

This research aimed to study the properties of pervious geopolymer concrete (PGC) made from FA geopolymer binder

* Corresponding author.
E-mail address: vancsa@kku.ac.th (V. Sata).

http://dx.doi.org/10.1016/j.conbuildmat.2015.08.076
0950-0618/© 2015 Published by Elsevier Ltd.

Table 1
Chemical composition of OPC, FA, and BA.

Chemical compositions (%)	OPC	FA	BA
SiO_2	14.4	35.9	31.8
Al_2O_3	2.7	15.1	12.1
Fe_2O_3	3.4	17.3	18.0
CaO	70.4	17.2	25.3
MgO	0.9	2.3	2.4
Na_2O	0.2	0.9	0.9
K_2O	0.6	3.2	2.5
SO_3	4.3	5.9	3.7
TiO_2	0.3	0.9	0.5
LOI	2.4	1.1	2.6

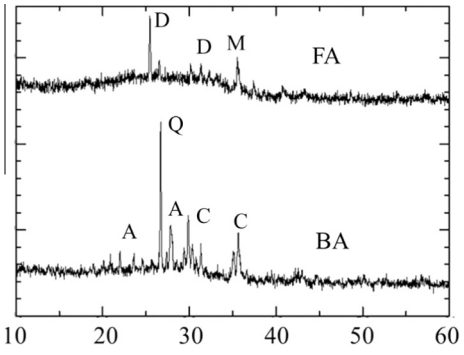

Fig. 1. XRD patterns of FA, and BA. D = Dachiardite, M = Magnetite, Q = Quartz, A = Anorthite, C = Diopside.

and BA as coarse aggregate. The effects of NH concentration, partial replacement of FA with OPC, and curing temperature were investigated. The obtained knowledge and data should help to promote the use of waste from coal fired thermal power plant for producing an environment friendly concrete.

2. Experimental details

2.1. Materials

The fly ash (FA) and bottom ash (BA) were from Mae Moh power station in the north of Thailand. FA was used as a source material for making geopolymeric binder and BA was used as a coarse aggregate. The results of the XRF analysis of the coal ashes are shown in Table 1. FA can be classified as high calcium fly ash according to ASTM C618 [15]. The XRD patterns of FA showed higher amorphous phase than BA as indicated by the hump between 20° and 30° 2-theta as shown in Fig. 1. BA with specific gravity of 2.40, unit weight of 1230 kg/m^3 (in saturated surface dry condition), water absorption of 3.83%, and Los Angeles abrasion resistance of 39.4% was crushed and sieved to obtain particle size range of 4.75–9.50 mm. BA was angular in shape with high porosity and rough surface as shown in Fig. 2. Sodium hydroxide (NH) (10 and 15 M), and sodium silicate (NS) with 13.8% Na_2O, 31.8% SiO_2 and 54.4% H_2O by weight were used as alkaline activators. In addition, Portland cement type I (OPC) was used as an additive to replace of FA at the levels of 5%, 10%, and 15% by weight of binder. The use of OPC to partially replace FA results in the reduction of setting time and increase in the strength of fly ash geopolymer paste [16].

2.2. Mix proportions

The designed void ratio of 32% and the paste volume of 22% were used for all PGC mixes to avoid the variation. This condition provided appropriate thickness of paste covering of aggregate without dripping of paste. NS/NH ratio of 0.6 and liquid/binder ratio of 0.3 were selected to control a suitable flow value of paste between 150 and 230 mm [17,18]. The first series was designed to study the effect of concentration of NH and replacement of FA with OPC on the properties of PGC. Two NH concentrations of 10 and 15 M were used. FA was replaced with OPC at 0%, 5%, 10%, and 15% by weight of binder. The second series was designed to study the effect of curing temperature on the properties of PGC. Three curing temperatures of 60, 90 and 120 °C were selected.

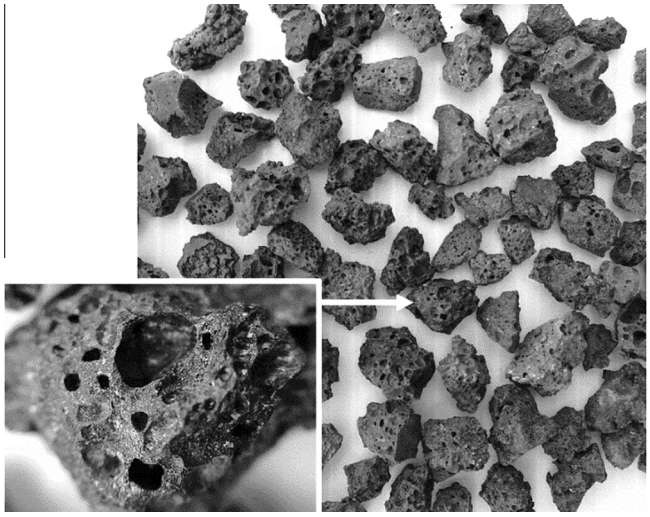

Fig. 2. BA particles.

Table 2
Mix proportions per m^3 and curing temperature of PGCs.

Mix	BA (kg)	Geopolymer paste					Curing temperature (°C)
		FA (kg)	OPC (kg)	NH (kg)		NS (kg)	
				10 M	15 M		
Effect of the concentration of NH and the replacement of FA with OPC							
10M0C90T	1175	320	–	60	–	36	90
10M5C90T	1175	304	16	60	–	36	90
10M10C90T	1175	288	32	60	–	36	90
10M15C90T	1175	272	48	60	–	36	90
15M0C90T	1175	327	–	–	61	37	90
15M5C90T	1175	311	16	–	61	37	90
15M10C90T	1175	294	33	–	61	37	90
15M15C90T	1175	278	49	–	61	37	90
Effect of the curing temperature							
10M10C60T	1175	288	32	60	–	36	60
10M10C90T	1175	288	32	60	–	36	90
10M10C120T	1175	288	32	60	–	36	120

Note: In all mixes, the designed void ratio = 32% and paste volume = 22%.

The names of PGCs were given by NH concentration (M), level of the replacement (C), and curing temperature (T). For example, 10M5C90T is PGC with 10 M NH, 5% OPC replacement and 90 °C curing temperature. The mix proportions of PGC are shown in Table 2.

2.3. Mixing and preparation of samples

For mixing, FA and OPC were mixed in the mixer to obtain a homogenous blend. NH was added and mixed for 5 min, and NS was then added and mixed for another 2 min. In the last step, BA in saturated surface dry condition was added and mixing was continued for 1 min.

The mixture was molded using the standard tamping rod and vibrating table. The cast samples were covered with plastic sheet, cured at temperature of 60, 90, and 120 °C for 48 h, demolded and stored in a 25 °C moist room until the testing ages. The 100 × 200 mm cylindrical samples were used for density, total void ratio, water permeability, compressive strength, splitting tensile strength, and ultrasonic pulse velocity tests and the 150 × 150 × 60 mm prism samples for the thermal conductivity and surface abrasion resistance tests.

3. Testing

The properties of PGCs were tested at the age of 7 days. The samples for compressive strength tests were capped at both ends with sulfur capping compound in accordance with ASTM C39 [19] to fill the voids and level both ends of concrete cylinder. The splitting tensile strengths were tested in accordance with ASTM

C496 [20]. The reported results were the average of 3 samples. Surface abrasion resistance samples were tested by the rotating-cutting method in accordance with ASTM C944 [21]. The samples were left to dry for 1 day before testing (air-dry condition). The surfaces of the samples were abraded with 98 N load for 120 s after contact between the cutter and the surface. The abrasion resistances of PGC were done on the two opposite faces of the samples.

The test of ultrasonic pulse velocity (UPV) was done in accordance with ASTM C597 [22]. The ultrasonic wave time elapsed to pass through a sample was measured. The transducers were 50 mm in diameter with a frequency of 50 kHz. The pulse velocity was calculated following Eq. (1).

$$V = L/T \quad (1)$$

where V is the pulse velocity (km/s), L is the length of a sample (mm), and T is the time measured (μs).

The density and total void content of samples were tested in accordance with ASTM C1754 [23]. The water permeability coefficient of pervious concrete with the recommendation of ACI 522 [11] was determined by using the constant head method and calculated following Darcy's law as shown in Eq. (2).

$$k = QL/HAt \quad (2)$$

where k is the water permeability coefficient (cm/s), Q is the quantity of water collected (cm^3) over time t (s), L is the length of sample (cm), H is the water head (cm), and A is the cross sectional area of the sample (cm^2).

The thermal conductivity coefficients were tested using a direct measuring instrument with a surface probe ISOMET2114. This method was successfully used for testing of thermal conductivity of pervious concrete [24]. The measurement ranges of the device were 0.04–6.0 W/m K. Samples were oven dried for 24 h to reduce the effect of humidity before testing.

4. Results and discussions

4.1. The compressive strength, splitting tensile strength, and surface abrasion resistance

4.1.1. Effect of NH concentration and replacement of FA with OPC

The results of compressive strength, splitting tensile strength and surface abrasion resistance of previous geopolymer concrete are shown in Table 3. An increase in concentration of NH from 10 to 15 M resulted in the improvement in strengths of PGCs. For instance, the compressive strength of mix 15M0C90T increased to 7.6 MPa (128% of 10M0C90T), the splitting tensile strength of 15M0C90T increased to 0.88 MPa (120% of 10M0C90T), and the weight loss of 15M0C90T decreased to 6.8 g (69% of 10M0C90T). With regards to the replacement with OPC, an increase in the level of replacement resulted in increase of PGCS strengths for both 10 and 15 M NH mixes. For instance, for PGCs with 10 M NH, the compressive strength of 10M15C90T increased to 7.7 MPa (132% of 10M0C90T), the splitting tensile strength of 10M15C90T increased to 1.01 MPa (137% of 10M0C90T), and the weight loss of 10M15C90T decreased to 6.2 g (63% of 10M0C90T). In addition, the incorporation of 15 M NH and 15% level of OPC replacement (15M15C90T) showed the best performance with the compressive strength at 8.6 MPa (147% of 10M0C90T), the splitting tensile strength at 1.28 MPa (173% of 10M0C90T), and the weight loss at 5.5 g (56% of 10M0C90T). The graph of strengths versus the levels of OPC replacement are plotted in Figs. 3–5 and the equations with good relationship were also reported.

Table 3
Compressive strength, splitting tensile strength, and weight loss by surface abrasion.

Mix	Compressive strength (MPa)-(relative values, %)	Splitting tensile strength (MPa)-(relative values, %)	Weight loss by surface abrasion (g)-(relative values, %)
Effect of NH concentration and replacement of FA with OPC			
10M0C90T[a]	5.9-(100)	0.74-(100)	9.9-(100)
10M5C90T	6.6-(112)	0.92-(125)	7.1-(72)
10M10C90T	7.2-(122)	0.94-(128)	6.6-(67)
10M15C90T	7.7-(132)	1.01-(137)	6.2-(63)
15M0C90T	7.6-(128)	0.88-(120)	6.8-(69)
15M5C90T	7.9-(135)	1.05-(143)	6.2-(63)
15M10C90T	7.9-(135)	1.08-(147)	5.3-(54)
15M15C90T	8.6-(147)	1.28-(173)	5.5-(56)
Effect of curing temperature			
10M10C60T[b]	5.7-(100)	0.69-(100)	11.2-(100)
10M10C90T	7.2-(126)	0.94-(137)	6.6-(59)
10M10C120T	7.5-(131)	1.08-(157)	6.1-(54)

Note:
[a] A control mix for effect of NH concentration and replacement of FA with OPC.
[b] A control mix for effect of curing temperature.

The increase in compressive strength of PGC with the increase in NH concentration from 10 to 15 M was consistent with the previous published work. Tho-in et al. [13] found that as NH concentration increased from 10 to 15 M, the strengths of PGCs increased. Rattanasak and Chindaprasirt [25] reported that fly ash geopolymer mortars using 15 M NH and NS/NH between 0.5 and 1.0 had the highest compressive strength. Furthermore, a study on chloride penetration of fly ash-based geopolymer concrete by Chindaprasirt and Chalee [2] indicated that increasing NH concentration in geopolymer concrete resulted in a low porosity paste and an increase in the compressive strength. The high concentration of NH increased the amount of leaching of silica and alumina ions and resulted in a high degree of geopolymerization [26,27]. In addition, the silica and alumina in BA aggregate could also leach out and assisted the geopolymerization at high NH concentration.

Fly ash-based geopolymer paste and mortar incorporating OPC reduced the porosity and water absorption and improved compressive strength [16,28]. The addition of OPC produced the hydration products (C–S–H and C–A–S–H) [29] and the liberated heat from hydration also assisted the geopolymerization reaction. Moreover, the pozzolanic reaction in fly ash-alkaline system took place fast [30] and form additional C–S–H and C–A–S–H.

4.1.2. Effect of curing temperature

With curing temperatures of 60, 90, and 120 °C, the results of compressive strengths of PGCs with 10 M NH and 10% OPC are

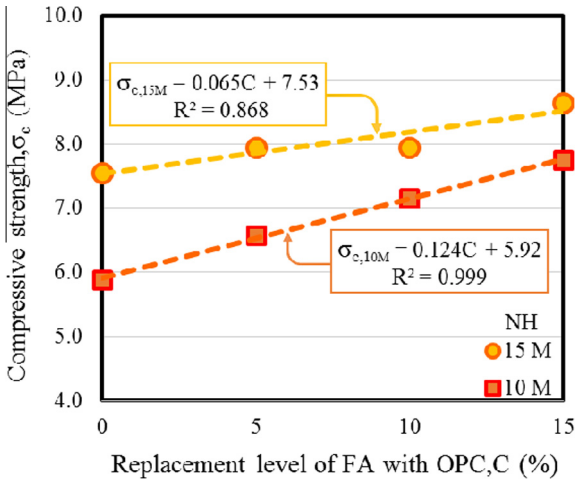

Fig. 3. Compressive strength and replacement level of FA with OPC.

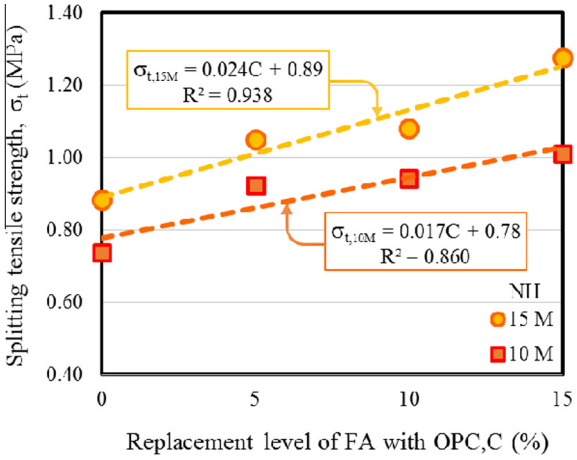

Fig. 4. Splitting tensile strength and replacement level of FA with OPC.

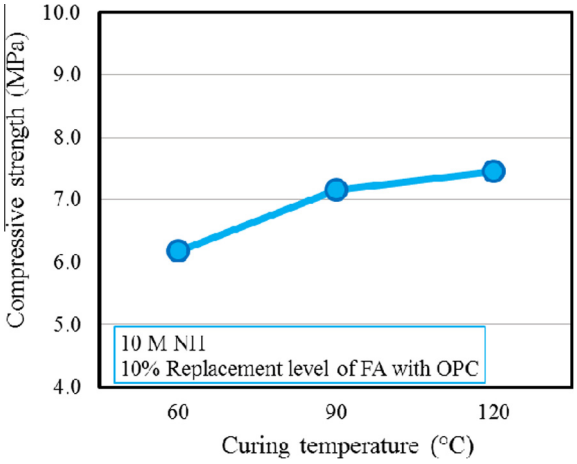

Fig. 6. Compressive strength and curing temperature.

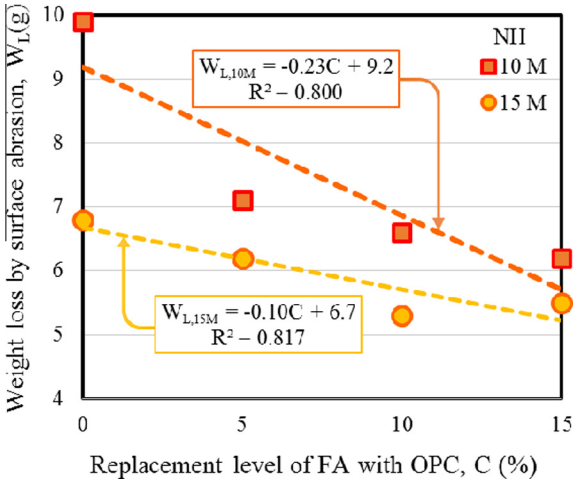

Fig. 5. Weight loss by surface abrasion and replacement level of FA with OPC.

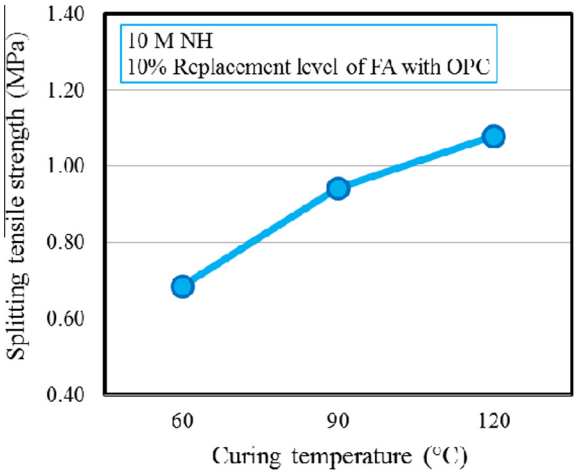

Fig. 7. Splitting tensile strength and curing temperature.

reported in Table 3. When curing temperature increased, strengths of geopolymer pastes improved significantly. For instance, the compressive strength of 10M10C90T mix increased to 7.2 MPa (126% of 10M10C60T), the splitting tensile strength of 10M10C90T increased to 0.94 MPa (137% of 10M10C60T), and the weight loss of 10M10C90T decreased to 6.6 g (59% of 10M10C60T). The findings were similar to the previously published results [31–33].

The relationship between PGCs mechanical properties and curing temperature are shown in Figs. 6–8. A review by Khale and Chaudhary [34] concluded that the curing at elevated temperature was effective and had significant contribution to geopolymeric reactions. It was observed that the increases in strengths from curing temperatures of 60 to 90 °C were larger than those from 90 to 120 °C. For instance, the compressive strength increased from 5.7 to 7.2 MPa for the increase in curing temperature from 60 to 90 °C while the compressive strength increased from 7.2 to only 7.7 MPa for the increase in curing temperature from 90 to 120 °C. The results thus suggested that for the optimization of strength and energy used in processing this pervious concrete, the curing temperature of 90 °C was attractive.

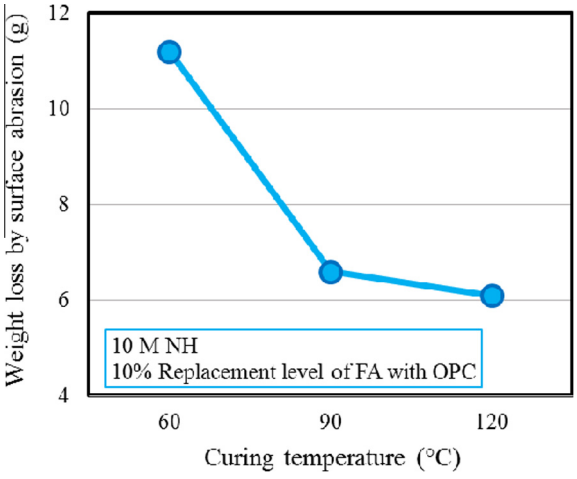

Fig. 8. Weight loss by surface abrasion and curing temperature.

4.1.3. Relationship between compressive strength and splitting tensile strength

The splitting tensile strengths and compressive strengths of PGCs in this study, the previous studies [13,14], and OPC pervious concrete [35] were plotted in Fig. 9. The relationship was explained by the exponential equation with high R^2 value of 0.913 as shown in Eq. (3).

$$\sigma_t = 0.179\sigma_c^{0.85} \quad (3)$$

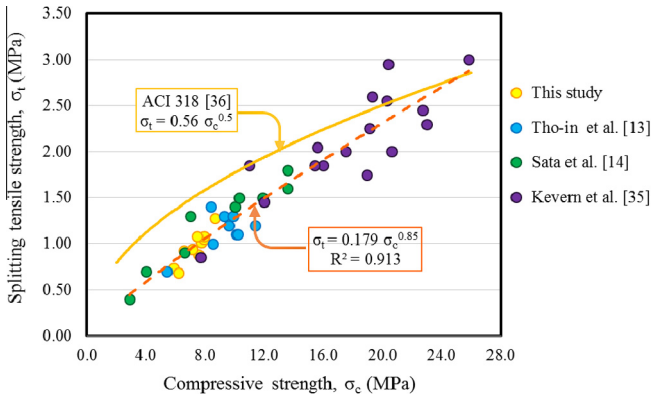

Fig. 9. Splitting tensile strength and compressive strength.

Table 4
The results of UPV test.

Mix	Pulse velocity (km/s)
10M0H90T	1.726
10M5H90T	1.880
10M10H60T	1.853
10M10H90T	2.333
10M10H120T	2.257
10M15H90T	2.433
15M0H90T	2.058
15M5H90T	2.259
15M10H90T	2.437
15M15H90T	2.566

where σ_t is the splitting tensile strength (MPa), and σ_c is the compressive strength (MPa).

The relationship between compressive strength and splitting tensile strength of PGC was also compared with the value of conventional concrete suggested by ACI 318 [36]. It was observed that the splitting tensile strength of PGC was lower than that of conventional concrete. This was due to the high void content of PGC compared to that of normal concrete. Under load, cracks could develop from the existing voids more easily and thus resulted in lower splitting tensile strength than that of normal concrete.

4.1.4. The relationships between the compressive strength and pulse velocity

The results of UPV tests are shown in Table 4. The pulse velocity of PGCs ranged between 1.726 and 2.566 km/s and was related to the compressive strength as shown in Fig. 10. The pulse velocity values increased with the increase in compressive strengths. This

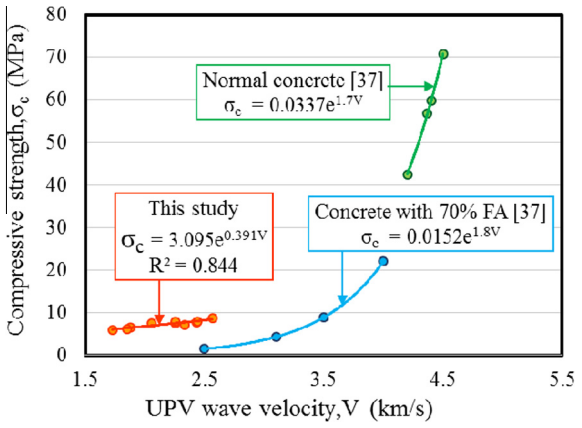

Fig. 10. Compressive strength and pulse velocity.

Table 5
Density, total void content, water permeability coefficient, and thermal conductivity of PGCs.

Mix	Density (kg/m^3)	Total void content (%)	Coefficient of water permeability (cm/s)	Coefficient of thermal conductivity (W/m K)
Effect of NH concentration and replacement of FA with OPC				
10M0C90T	1496	31.6	1.1	0.33
10M5C90T	1468	32.5	0.9	0.33
10M10C90T	1488	33.0	0.9	0.33
10M15C90T	1466	33.4	1.3	0.33
15M0C90T	1487	33.7	0.6	0.32
15M5C90T	1497	33.5	0.8	0.33
15M10C90T	1487	33.5	0.7	0.33
15M15C90T	1502	33.5	0.8	0.31
Effect of curing temperature				
10M10C60T	1495	32.1	0.8	0.33
10M10C90T	1488	33.0	0.9	0.33
10M10C120T	1492	30.5	1.1	0.30

is in line with the other findings [37]. Previous research [37–39] suggested that the relationship between pulse velocity and compressive strength of concrete was in the form of exponential equation. For this set of result, the relation between pulse velocity and compressive strength of PCG could be expressed with exponential function as shown in Eq. (4) with the R^2 value of 0.844.

$$\sigma_c = 3.095e^{0.391V} \quad (4)$$

where σ_c is compressive strength (MPa), and V is pulse velocity (km/s). The pulse velocities of PGCs were lower than those of normal concrete due to the large void content and also the large porosity of BA particle. It should be noted here that the ranges of pulse velocity and compressive strength in this research were small and thus the generalization of this finding should be done with care.

4.2. The density, total void content, and coefficient of water permeability

The results of physical property of PGC with BA are shown in Table 5. The density, total void content, and coefficient of water permeability varied in a narrow range between 1466–1502 kg/m^3, 30.5–33.7%, and 0.6–1.3 cm/s, respectively. The physical properties of PGC depend on the liquid/binder ratio, paste volume, and size of aggregate while in this study they were kept constant. Previous studies [13,14] suggested the appropriate volume of geopolymer paste between 15% and 17% for PGCs containing limestone and recycled aggregate. The geopolymer paste volume in this study was higher at 22% due to the porous and rough surface of BA particle. However, the total void ratios and coefficient of water permeability of PGCs containing BA were in the range recommending by ACI 522 [11]. Generally, the density of pervious concrete depends on the mass of aggregate per cubic meter [11]. The relationship between density and the mass of aggregate per cubic meter of pervious concretes in the previous studies [13,14,40,41] and this study are plotted in Fig. 11. The linear relationship is shown in Eq. (5) with a high R^2 value of 0.801.

$$D = 0.6931A + 607.7 \quad (5)$$

where D is the density (kg/m^3), and A is the mass of aggregate per cubic meter of pervious concrete (kg).

4.3. Thermal conductivity

The coefficients of thermal conductivity of all PGCs were nearly the same at 0.30–0.33 W/m K (Table 5). Wong et al. [42] reported that the thermal conductivity coefficients of pervious concrete

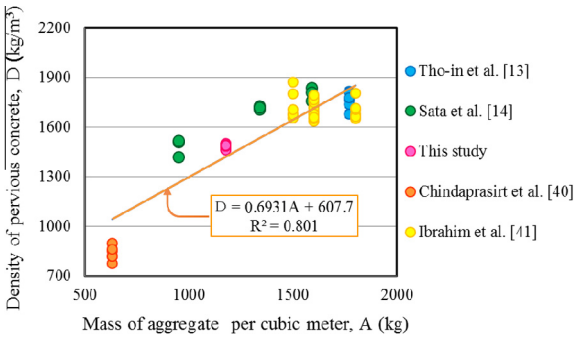

Fig. 11. Density and mass of aggregate per cubic meter.

with normal aggregate ranged from 0.19 to 1.49 W/m K depending on the degree of filling and water to cement ratio of cement paste. Zaetang et al. [24] and Chindaprasirt et al. [40] reported the thermal conductivities of 0.15–0.27 W/m K for pervious concrete with porous lightweight aggregate. The porosity of BA aggregate played a significant role in lowering the coefficients of thermal conductivity of PGCs in this study. Pervious concrete gave a lower thermal conductivity when porous aggregate was used instead of solid aggregate.

5. Conclusions

This study investigated the effects of NH concentration, partial replacement of FA with OPC, and curing temperature on the properties of fly ash-based pervious geopolymer concrete containing bottom ash as coarse aggregate. The results indicated that the increase from 10 to 15 M in NH concentration and from 0% to 15% in OPC replacement, increased the strengths of PGCs. The incorporation of 15 M NH and 15% OPC replacement gave the highest strength PGC. In addition, the pulse velocity of UPV test was found to relate to the compressive strength.

The thermal conductivity of fly ash-based PGCs ranged between 0.30 and 0.33 W/m K, the density between 1466 and 1502 kg/m^3, and the compressive strength between 5.7 and 8.6 MPa. The results also suggested that for the optimization of strength and energy used in processing this pervious concrete, the curing temperature of 90 °C was recommended.

Acknowledgements

The authors would like to acknowledge the research fund of the Faculty of Engineering, Khon Kaen University; the Higher Education Research Promotion and National Research University Project of Thailand, Office of the Higher Education Commission, through the Advanced Functional Materials Cluster of Khon Kaen University; the Thailand Research Fund (TRF) and Khon Kaen University under the Royal Golden Jubilee Ph.D. Program (Grant No. PHD 0083/2556), TRF Research Career Development (Grant No. RSA5780013), and TRF Senior Research Scholar (Grant No. RTA5780004).

References

[1] X. Guo, H. Shi, W.A. Dick, Compressive strength and microstructural characteristics of class C fly ash geopolymer, Cement Concr. Compos. 32 (2) (2010) 142–147.
[2] P. Chindaprasirt, W. Chalee, Effect of sodium hydroxide concentration on chloride penetration and steel corrosion of fly ash-based geopolymer concrete under marine site, Constr. Build. Mater. 63 (2014) 303–310.
[3] D. Reddy, J. Edouard, K. Sobhan, Durability of fly ash-based geopolymer structural concrete in the marine environment, J. Mater. Civ. Eng. 25 (6) (2013) 781–787.
[4] C. Jaturapitakkul, R. Cheerarot, Development of bottom ash as pozzolanic material, J. Mater. Civ. Eng. 15 (1) (2003) 48–53.
[5] P. Chindaprasirt, C. Jaturapitakkul, W. Chalee, U. Rattanasak, Comparative study on the characteristics of fly ash and bottom ash geopolymers, Waste Manage. 29 (2) (2009) 539–543.
[6] W. Wongkeo, A. Chaipanich, Compressive strength, microstructure and thermal analysis of autoclaved and air cured structural lightweight concrete made with coal bottom ash and silica fume, Mater. Sci. Eng. A 527 (16–17) (2010) 3676–3684.
[7] H. Kurama, İ.B. Topçu, C. Karakurt, Properties of the autoclaved aerated concrete produced from coal bottom ash, J. Mater. Process. Technol. 209 (2) (2009) 767–773.
[8] H.K. Kim, H.K. Lee, Use of power plant bottom ash as fine and coarse aggregates in high-strength concrete, Constr. Build. Mater. 25 (2) (2011) 1115–1122.
[9] B. Rushton, Low-impact parking lot design reduces runoff and pollutant loads, J. Water Resour. Plan. Manage. 127 (3) (2001) 172–179.
[10] J. Yang, G. Jiang, Experimental study on properties of pervious concrete pavement materials, Cem. Concr. Res. 33 (3) (2003) 381–386.
[11] ACI 522R-10, Report on Pervious Concrete, ACI 522R-102010.
[12] M.-G. Lee, Y.-S. Huang, T.-K. Chang, C.-H. Pao, Experimental study of pervious concrete pavement, in: D.-H. Chen, J.-R. Chang, M. Zaman, C. Zhao, Z. Yao, R.E. Beighley Ii, et al. (Eds.), GeoHunan International Conference 2011, ASCE, Hunan, China, 2011, pp. 93–99. 47629 1 41173 ed..
[13] T. Tho-in, V. Sata, P. Chindaprasirt, C. Jaturapitakkul, Pervious high-calcium fly ash geopolymer concrete, Constr. Build. Mater. 30 (2012) 366–371.
[14] V. Sata, A. Wongsa, P. Chindaprasirt, Properties of pervious geopolymer concrete using recycled aggregates, Constr. Build. Mater. 42 (2013) 33–39.
[15] American Society for Testing and Materials, Standard Specification for Coal Fly Ash and Raw or Calcined Natural Pozzolan for Use in Concrete, ASTM C618: Annual Book of ASTM Standard, 2012.
[16] T. Phoo-ngernkham, P. Chindaprasirt, V. Sata, S. Pangdaeng, T. Sinsiri, Properties of high calcium fly ash geopolymer pastes with Portland cement as an additive, In. J. Miner., Metall., Mater. 20 (2) (2013) 214–220.
[17] Japan Cement Association, Physical Testing Methods for Cement, JIS R5201: Japanese Industrial Standards, 1997.
[18] P. Chindaprasirt, S. Hatanaka, T. Chareerat, N. Mishima, Y. Yuasa, Cement paste characteristics and porous concrete properties, Constr. Build. Mater. 22 (5) (2008) 894–901.
[19] American Society for Testing and Materials, Standard Test Method for Compressive Strength of Cylindrical Concrete Specimens, ASTM C39/C39M: Annual Book of ASTM Standard, 2003.
[20] American Society for Testing and Materials, Standard Test Method for Splitting Tensile Strength of Cylindrical Concrete Specimens, ASTM C496/C496M: Annual Book of ASTM Standard, 2011.
[21] American Society for Testing and Materials, Standard Test Method for Abrasion Resistance of Concrete or Mortar Surfaces by the Rotating-Cutter Method, ASTM C944/C944M: Annual Book of ASTM Standard, 2012.
[22] American Society for Testing and Materials, Standard Test Method for Pulse Velocity Through Concrete, ASTM C597: Annual Book of ASTM Standard, 2002.
[23] American Society for Testing and Materials, Standard Test Method for Density and Void Content of Hardened Pervious Concrete, ASTM C1754: Annual Book of ASTM Standard, 2012.
[24] Y. Zaetang, A. Wongsa, V. Sata, P. Chindaprasirt, Use of lightweight aggregates in pervious concrete, Constr. Build. Mater. 48 (2013) 585–591.
[25] U. Rattanasak, P. Chindaprasirt, Influence of NaOH solution on the synthesis of fly ash geopolymer, Miner. Eng. 22 (12) (2009) 1073–1078.
[26] E. Álvarez-Ayuso, X. Querol, F. Plana, A. Alastuey, N. Moreno, M. Izquierdo, et al., Environmental, physical and structural characterisation of geopolymer matrixes synthesised from coal (co-)combustion fly ashes, J. Hazard. Mater. 154 (1–3) (2008) 175–183.
[27] S. Hanjitsuwan, S. Hunpratub, P. Thongbai, S. Maensiri, V. Sata, P. Chindaprasirt, Effects of NaOH concentrations on physical and electrical properties of high calcium fly ash geopolymer paste, Cement Concr. Compos. 45 (2014) 9–14.
[28] S. Pangdaeng, T. Phoo-ngernkham, V. Sata, P. Chindaprasirt, Influence of curing conditions on properties of high calcium fly ash geopolymer containing Portland cement as additive, Mater. Des. 53 (2014) 269–274.
[29] P. Nath, P.K. Sarker, Use of OPC to improve setting and early strength properties of low calcium fly ash geopolymer concrete cured at room temperature, Cement Concr. Compos. 55 (2015) 205–214.
[30] J. Temuujin, A. van Riessen, R. Williams, Influence of calcium compounds on the mechanical properties of fly ash geopolymer pastes, J. Hazard. Mater. 167 (1–3) (2009) 82–88.
[31] J. Feng, R. Zhang, L. Gong, Y. Li, W. Cao, X. Cheng, Development of porous fly ash-based geopolymer with low thermal conductivity, Mater. Des. 65 (2015) 529–533.
[32] A. Nazari, J.G. Sanjayan, Johnson–Mehl–Avrami–Kolmogorov equation for prediction of compressive strength evolution of geopolymer, Ceram. Int. 41 (2, Part B) (2015) 3301–3304.
[33] G. Görhan, G. Kürklü, The influence of the NaOH solution on the properties of the fly ash-based geopolymer mortar cured at different temperatures, Compos. B Eng. 58 (2014) 371–377.
[34] D. Khale, R. Chaudhary, Mechanism of geopolymerization and factors influencing its development: a review, J. Mater. Sci. 42 (3) (2007) 729–746.
[35] J. Kevern, K. Wang, V. Schaefer, Effect of coarse aggregate on the freeze-thaw durability of pervious concrete, J. Mater. Civ. Eng. 22 (5) (2010) 469–475.

[36] ACI committee 318, Building Code Requirements for Structural Concrete (ACI 318-99) and Commentary (ACI 318R-99), American Concrete Institute, Detroit, 1999. p. 391.
[37] R. Demirboğa, İ. Türkmen, M.B. Karakoç, Relationship between ultrasonic velocity and compressive strength for high-volume mineral-admixtured concrete, Cem. Concr. Res. 34 (12) (2004) 2329–2336.
[38] M.T. Liang, J. Wu, Theoretical elucidation on the empirical formulae for the ultrasonic testing method for concrete structures, Cem. Concr. Res. 32 (11) (2002) 1763–1769.
[39] G. Trtnik, F. Kavčič, G. Turk, Prediction of concrete strength using ultrasonic pulse velocity and artificial neural networks, Ultrasonics 49 (1) (2009) 53–60.
[40] P. Chindaprasirt, P. Nuaklong, Y. Zaetang, P. Sujumnongtokul, V. Sata, Mechanical and thermal properties of recycling lightweight pervious concrete, Arab. J. Sci. Eng. (2014) 1–8.
[41] A. Ibrahim, E. Mahmoud, M. Yamin, V.C. Patibandla, Experimental study on Portland cement pervious concrete mechanical and hydrological properties, Constr. Build. Mater. 50 (2014) 524–529.
[42] J.M. Wong, F.P. Glasser, M.S. Imbabi, Evaluation of thermal conductivity in air permeable concrete for dynamic breathing wall construction, Cement Concr. Compos. 29 (9) (2007) 647–655.

Strength and chloride resistance of the blended Portland cement mortar containing rice husk ash and ground river sand

Prinya Chindaprasirt & Sumrerng Rukzon

Materials and Structures

ISSN 1359-5997

Mater Struct
DOI 10.1617/s11527-014-0438-9

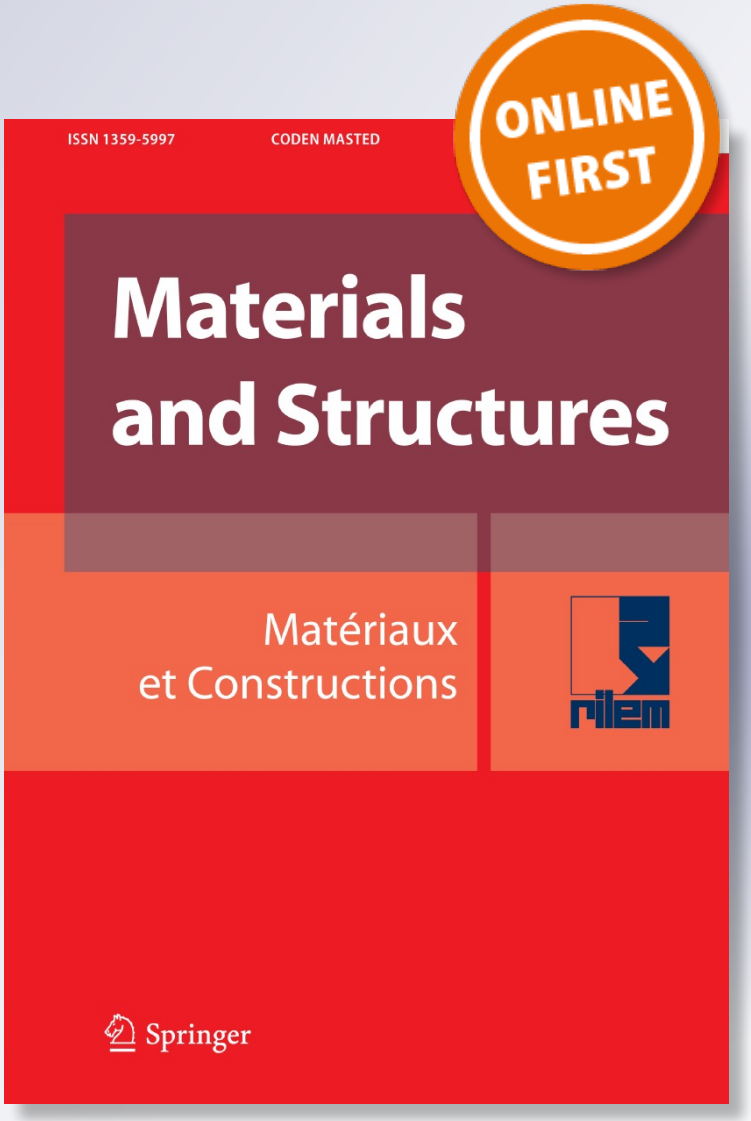

Springer

Your article is protected by copyright and all rights are held exclusively by RILEM. This e-offprint is for personal use only and shall not be self-archived in electronic repositories. If you wish to self-archive your article, please use the accepted manuscript version for posting on your own website. You may further deposit the accepted manuscript version in any repository, provided it is only made publicly available 12 months after official publication or later and provided acknowledgement is given to the original source of publication and a link is inserted to the published article on Springer's website. The link must be accompanied by the following text: "The final publication is available at link.springer.com".

Author's personal copy

Materials and Structures
DOI 10.1617/s11527-014-0438-9

ORIGINAL ARTICLE

Strength and chloride resistance of the blended Portland cement mortar containing rice husk ash and ground river sand

Prinya Chindaprasirt · Sumrerng Rukzon

Received: 15 December 2013 / Accepted: 3 October 2014
© RILEM 2014

Abstract In this paper, the strength and chloride penetration resistance of the blended Portland cement mortar containing rice husk ash (RHA) and ground river sand (GS) were studied. Portland cement type I (OPC) was partially replaced with RHA and GS and a blended of RHA and GS. The mortar mixtures were made with OPC containing 0–40 % of RHA and GS. RHA and GS with 3 % by weight retained on sieve No. 325 (opening 45 μm of sieve No. 325) were obtained using ball mill. The study includes compressive strength, rapid chloride penetration test, chloride ion diffusion coefficient and chloride penetration depth of mortars. Test results indicated that the use of RHA produced mortars with relatively high strength and excellent resistance to chloride penetration. However, the incorporation of GS reduced the strength and resistance to chloride penetration of mortars indicating that it asserted only the packing effect. The blend of equal portions of RHA and GS produced relatively high strength mortars with good resistance to chloride penetration which is probably due to the synergy of the pozzolanic effect of RHA and packing effect of GS.

Keywords Cement · Chloride · Ground river sand · Rice husk ash · Strength

1 Introduction

Pozzolanic materials such as fly ash, silica fume and calcined kaolin are normally used to replace part of Portland cement to improve the properties of paste and concrete. The addition of a fine pozzolan whose particles are finer than those of Portland cement causes segmentation of large pores and increases nucleation sites for the precipitation of hydration products in cement paste [11]. The increase in pozzolanic reaction leads to a reduction of calcium hydroxide and refinements of the pore structure of paste. With regards to permeability, the incorporation of pozzolan such as fly ash reduces the average pore size and results in a less permeable paste [7, 13]. Rice husk ash (RHA) when properly prepared contains high silica content in non-crystalline or amorphous form. Therefore, it is a pozzolanic material and can be used as supplementary cementitious material [9, 14, 17, 18].

It is generally accepted that hydration reaction is a chemical reaction between the reactive constituents of Portland cement and water, while the pozzolanic reaction is the reaction between silica and/or alumina

P. Chindaprasirt
Sustainable Infrastructure Research and Development Center,Dept. of Civil Engineering, Faculty of Engineering, Khon Kaen University, Khon Kaen 40002, Thailand

S. Rukzon (✉)
Department of Civil Engineering, Faculty of Engineering, Rajamangala University of Technology Phra Nakhon, Bangkok 10800, Thailand
e-mail: rerng197@rmutp.ac.th; sumrerng.r@rmutp.ac.th

Published online: 11 October 2014

Author's personal copy

and calcium hydroxide produced by cement hydration reaction. In addition, Rukzon and Chindaprasirt [16] reported that the physical effects of the finer particles allow denser packing of cement and pozzolan and reduce the wall effect in the transition zone between paste and aggregates. Finely ground inert material has also been incorporated to Portland cement to make silica cement or mixed cement with slightly lower strength than the conventional Portland cement but with better cohesion, longer setting/working time, and lower cost [8].

Two of the most important properties of mortar and/or concrete are strength and durability. Compressive strength is one of the most important mechanical properties and the test is easy to perform. For durability, resistance to chloride penetration is one of the most important parameter especially when the concrete structure is in the vicinity or exposes to chloride environment. In addition, there are several other tests such as rapid chloride penetration test (RCPT), chloride ion diffusion coefficient (CIDC), and chloride immersion test (CIT). This enables the test results to be compared.

The objective of this research is to investigate the strength and resistance to chloride penetration of the blended Portland cement mortar containing RHA and ground river sand (GS). The effects of pozzolanic reaction of RHA and the effects of the blend of RHA and GS were studied. The information should be valuable for the future use of RHA and GS to replace part of Portland cement to improve the quality of mortar and concrete.

2 Experimental details

2.1 Materials

Portland cement type I (ordinary Portland cement, OPC), local rice husk, river sand and type-F superplasticizer (SP) were used. Rice husk ash was obtained from open burning of rice husk in a small heap of approximately 18–20 kilogram of rice husk with maximum burning temperature of 650 °C. Rice husk ash and river sand were ground using ball mill until the percentage retained on sieve No. 325 (opening 45 μm of sieve No. 325) was 3 %. Their particle size distributions are given in Fig. 1. The typical chemical compositions of RHA and GS determined by X-ray fluorescence (XRF) are shown in Table 1. RHA consisted of 93.0 % SiO_2 and GS consisted of 93.5 % SiO_2. Silica in RHA is in an amorphous phase and, therefore, quite reactive as indicated by the XRD

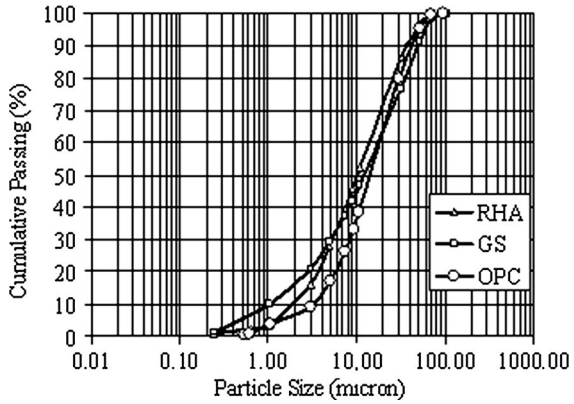

Fig. 1 Particle size distribution of RHA, GS and OPC

Table 1 Chemical composition of OPC, RHA and GS

Oxides	OPC	RHA	GS
SiO_2	20.9	93.2	93.5
Al_2O_3	4.8	0.4	5.0
Fe_2O_3	3.4	0.1	NA
CaO	65.4	1.1	NA
MgO	1.3	0.1	NA
Na_2O	0.2	0.1	NA
K_2O	0.4	1.3	NA
SO_3	2.7	0.9	NA
LOI	0.9	3.7	NA
$SiO_2 + Al_2O_3 + Fe_2O_3$	–	93.7	98.5

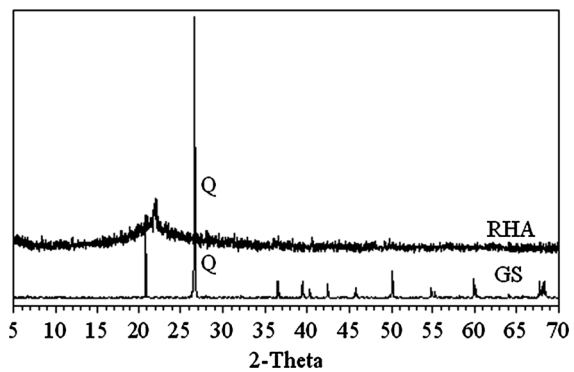

Fig. 2 XRD analysis of RHA and GS (Q = Quartz)

Author's personal copy

Table 2 The physical properties of OPC, RHA and GS

Sample	Median particle size (μm)	Retained on sieve No. 325 (%)	Specific gravity	Blaine fineness (cm^2/g)
OPC	15	–	3.14	3,600
RHA	10	3	2.23	12,100
GA	11	3	2.63	3,200

Table 3 Mortar mix proportions

Mix. ID	Cement (OPC)	RHA	GS	SP (%)*
OPC	100	–	–	1.9
20RHA	80	20	–	2.2
40RHA	60	40	–	3.7
20GS	80	–	20	1.3
40GS	60	–	40	1.9
20BRGS	80	10	10	1.5
40BRGS	60	20	20	1.9

* Percentage of cement + RHA + GS

result shown in Fig. 2. The silica in GS was, however, in a stable form. The river sand with specific gravity of 2.63 and fineness modulus of 2.82 was used to make mortars. The physical properties of OPC, RHA and GS are given in Table 2.

2.2 Mix proportion and curing

The OPC was partially replaced with 0–40 % of RHA and GS. In addition to normal replacement, a blend of equal weight portion of RHA and GS (BRGS) was also used to study the effects of blending of RHA and GS. Water to binder plus fine material (OPC + RHA + GS) ratio of 0.5 and sand-to-binder plus fine material ratio of 2.75 by weight were used. Table 3 gives the mortar mix proportions. The mortar mixes with constant flow of 110 ± 5 % were obtained with the aid of superplasticizer (SP). The mortar samples were cured by covering with damped cloth and polyurethane sheet and placed in a 23 ± 2 °C room. The demoulding was done at the age of 1 day and the samples were then cured in water at 23 ± 2 °C until the test age.

2.3 Compressive strength

Cubes of 50 × 50 × 50 mm were used for the compressive strength test. The tests were done at the ages of 7, 28 and 90 days in accordance with ASTM C109 [2]. Three samples were used for each test.

2.4 Tests on chloride penetration

For testing of chloride penetration, 100 mm in diameter and 200 mm in height cylindrical specimens were prepared in accordance with ASTM C39 [1]. The demoulding was done at the age of 24 h. They were cured in water until the age of 27 and 89 days (for testing at the ages of 28 and 90 day, respectively). They were then cut into 50 mm thick slices and the 50 mm end pieces were discarded. The 50 mm center slices were epoxy coated around the cylinder. The prepared samples were used for the determination of RCPT, CIDC, and CIT. All three tests were selected so that the results could be compared and solid conclusion could be made.

2.5 Rapid chloride penetration test (RCPT)

For this test, the epoxy-coated cylindrical specimens of 100 mm in diameter and 50 mm in height were conditioned and tested at the ages of 28 and 90 days in accordance with the method described in ASTM C1202 [5]. Two samples were tested for each set of results.

2.6 Chloride ion diffusion coefficient (CIDC)

For CIDC test, the samples were prepared in the same manner as the RCPT samples. The epoxy-coated sample slices of 100 mm in diameter and 50 mm in height were conditioned and tested for the chloride ion diffusion coefficient at the ages of 28 and 90 days using the modified rapid migration test. The solution employed was 3 % NaCl (in limewater) in the cathode side and limewater in the anode side. Applied voltage of 30 V DC for 8 h was employed. The depths of the chloride penetration into the specimens were then measured by splitting the samples and spraying with 0.1 M $AgNO_3$ solution [12]. This depth of penetration was used to determine a chloride ion diffusion coefficient following equation derived from the Nernst–Plank equation [19]. The chloride ion diffusion coefficient was calculated using Eq. (1).

$$D_c = \frac{RTL}{zFE} \times \frac{x_f}{t} \quad (1)$$

Author's personal copy

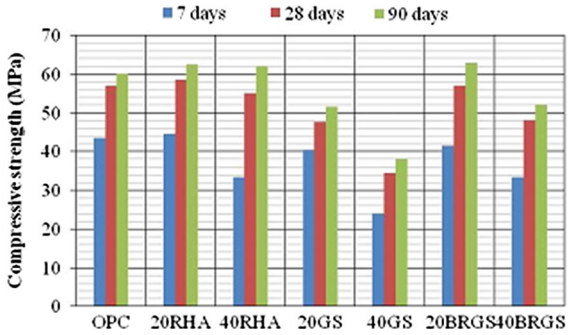

Fig. 3 Compressive strength of mortar

where, D_C is chloride ion diffusion coefficient (cm^2/s), R is gas content (J/K mol, 8.314),T is temperature (K),L is the thickness of specimens (cm),z is the ion valence,F is Faraday content (C/mol, 9.65×10^4),E is values of potential (V), x_f is the inflection point of the chloride ion profiles that needs to be related to the depth given by the colorimetric technique, and$t$ is the time of test duration (s).

2.7 Chloride immersion test (CIT)

The CIT of mortar was performed using 3 % NaCl solution. The test set-up was taken from RTA T263 [20]. The procedures for mixing and curing were the same as those for the preparation of RCPT samples. The cylindrical specimens of 100 mm in diameter and 50 mm in height were used. The specimens were epoxy coated around the cylindrical surface and the top surface. At the ages of 28 and 90 days, the specimens were immersed in NaCl solution for 30 days. The depths of the chloride penetration into specimens were then measured by splitting the samples and spraying with 0.1 M $AgNO_3$ solution [12].

3 Results and discussion

3.1 Compressive strength

The results of compressive strength of mortars are given in Fig. 3. Test results indicated that the compressive strengths of GS mortars were reduced with the increase in the replacement of OPC by GS. The 7, 28 and 90-day compressive strengths of GS mortars were lower than those of OPC mortars at the same ages. At the replacement dosages of 20 and 40 %, the strengths of GS mortars were between 83–93 and 55–63 % of those of OPC mortars. The strength reduction was due to the reduction in the OPC content since GS acted as inert filler and only contributed to the packing effect [16].

For RHA mortars, the 7, 28 and 90 day strengths of 20RHA mortars were between 102 and 104 % of those of OPC mortars. At the replacement dosages of 40 %, the strengths of RHA mortars were between 77 and 103 % of those of OPC mortars. ASTM C618 [4] specifies that pozzolan mortar should have a strength activity index of at least 75 % of the control mortar (OPC mortar) at the ages of 7 or 28 days when the pozzolan is used to replace Portland cement at the dosage of 20 % by weight of binder in accordance with ASTM C311 [3]. This, therefore, indicated that RHA is a good pozzolan. Furthermore, the higher strengths of RHA mortars compared to those of GS mortars confirmed that RHA exerted the pozzolanic effect and contributed to the strength development of mortars [16]. For the higher replacement level of 40 %, the strengths of RHA mortar were 77, 96 and 103 % of those of OPC mortars at the ages of 7, 28 and 90 days, respectively. Again, the strengths of RHA mortars were significantly higher than those of GS mortars.

For the blend of RHA and GS, the compressive strengths of 20BRS (10 %RHA + 10 %GS) mortars were excellent at 95–105 % of those of OPC mortars. For the replacement level of 40 %, the strengths of 40BRGS mortars (20 %RHA + 20 %GS) were between 77 and 87 % of those of OPC mortars at the same age. At the 40 % replacement (20 % RHA + 20 %GS), the strength of 40BRS mortar was 77 % of that of OPC mortar as compared to 55–77 % at 7 days when single replacement material was used. At the ages of 28 and 90 days, the strengths of the 40BRGS mortars were still reasonably high at 84 and 87 % of those of OPC mortars. These compressive strength values were significantly higher than the average strength values of 40RHA and 40GS mortars. The relatively high strength obtained with the use of blend of RHA and GS was probably due to the synergic effect between a fine pozzolanic material and a fine inert material. It has been shown that the use of two pozzolans of equal portions (50/50) produced concrete with higher strength than the use of single pozzolan (100/0) [16]. The improvement in the use of

Author's personal copy

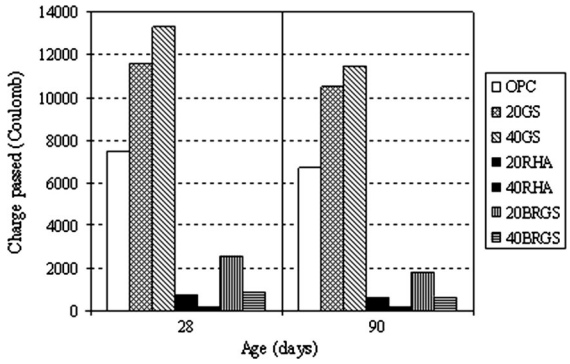

Fig. 4 Total charge passed in coulombs of rapid chloride penetration test (RCPT)

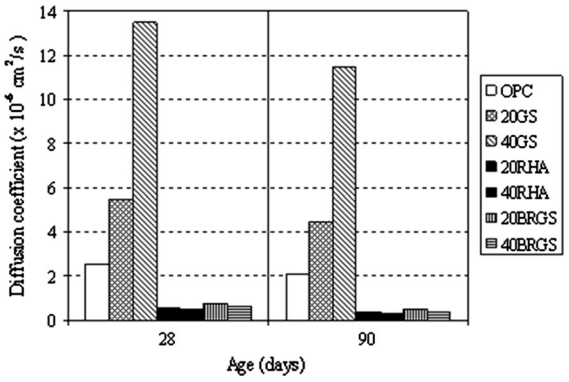

Fig. 5 Chloride ion diffusion coefficients of mortars at 28 and 90 day

blend of fine pozzolanic materials was attributed to the synergic effect of the two pozzolans in the cementitious system [10]. The synergic effect could be due to the use of two fine materials and more work is needed to confirm this.

3.2 Chloride penetration

3.2.1 Results of RCPT

The results of the RCPT are given in Fig. 4. The resistances to chloride penetration of OPC mortars were intermediate at the charges passed of 7,500 and 6,700 Coulombs at the ages of 28 and 90 days, respectively. The replacements of OPC by GS greatly reduced the resistance to chloride penetration and the reductions were more with the increase in GS replacement level. At the age of 28 days, incorporations of 20 and 40 % of GS increased the charges passed to 11,500 and 13,500 Coulombs and to 10,500 and 11,500 Coulombs at the age of 90 days. The reduced chloride penetration resistance was from the reduction in OPC content and the reduced hydration products [16]. The GS acted as a filler and contributed only to the packing effect and its incorporation reduced both strength and resistance to chloride penetration of mortars.

At the age of 28 days, incorporations of 20 and 40 % of RHA improved the resistance to chloride penetration by reducing the charges passed to 800 and 200 Coulombs. At the age of 90 days, the charges passed of RHA mortars were very low. This improvement in chloride penetration resistance was associated with the pozzolanic effect and filling effect of fine RHA. It was reported that the incorporation of fine pozzolan increased the nucleation sites and hydration of fine RHA particles with the much reduced $Ca(OH)_2$ of mortar [16]. In particular, the incorporation of RHA produced good quality concrete with reduced porosity and reduced $Ca(OH)_2$ [21].

For the use of blend of equal part of RHA and GS, the charges passed of BRGS mortars were also low compared to those of OPC and GS mortars as shown in Fig. 5. The charges passed at the age of 28 days of 20BRGS and 40BRGS mortars were 2,500 and 800 Coulombs. For the replacement of 20 % RHA alone, the charges passed was also around 800 Coulombs which was the same order as those of 40BRGS mortars. The incorporation of 20 % RHA and 20 % GS reduced the amount of OPC by 40 % whereas the incorporation of 20 %RHA reduced the amount of OPC by 20 %. Similar improvement in chloride penetrations of 40BRGS mortar (60 %OPC) and 20RHA mortar (80 %OPC) suggested the existence of synergic effect on resistance to chloride penetration of mortar containing blend of RHA and GS. As expected, the resistances to chloride penetration at the age of 90 days were slightly better than those at the age of 28 days owing to the hydration and pozzolanic reactions with time.

The RCPT value for the OPC control mortar at 28 days of 7,400 coulombs was high but consistent with the previous research [15]. The use of GS resulted in extremely high RCPT values and should be for comparison only.

Author's personal copy

3.2.2 Results of CIDC

The results of CIDC using 30 V DC as shown in Fig. 5 were similar to those of RCPT. The diffusion coefficients of GS mortars were higher than those of OPC mortars at the same age. At the age of 28 days, the diffusion coefficients of 20GS and 40GS mortars were 5.5×10^{-6} and 13.5×10^{-6} cm^2/s compared to 2.5×10^{-6} cm^2/s of OPC mortar. For mortar with RHA, the diffusion coefficients of mortars were significantly lower than those of OPC and GS mortars. The diffusion coefficients of 20RHA and 40RHA mortars were 0.4×10^{-6} and 0.5×10^{-6} cm^2/s. This is consistent with the results of RCPT which also gave low charges passed of 200–800 Coulombs for these mortars. Again, the diffusion coefficients of the mortars reduced with an increase in age as expected. This was due to the increase in hydration of cementitious materials. At the age of 90 days, the diffusion coefficients of 20GS and 40GS mortars were 4.5×10^{-6} and 11.5×10^{-6} cm^2/s compared to 2.1×10^{-6} cm^2/s of OPC mortar at the same age. The diffusion coefficients of 20RHA and 40RHA mortars at 90 days were only 0.3×10^{-6} and 0.2×10^{-6} cm^2/s confirming the excellent resistance to chloride penetration with the incorporation of RHA. Previous research also showed that RHA was the most effective pozzolan compared with the palm oil fuel ash and fly ash in improving the resistance to chloride [6]. For the use of blend of RHA and GS, the diffusion coefficients of mortars were also very low in comparison with those of OPC mortar at the same age. The diffusion coefficients of 20BRS and 40BRS mortars at the age of 28 days were 0.7×10^{-6} and 0.6×10^{-6} cm^2/s which were only slightly higher than those of RHA mortar at the same replacement levels. The results confirmed the synergic effect of the blend of RHA and GS in reducing the chloride diffusion coefficients of mortars.

3.2.3 Results of CIT

Figure 6 shows the results of chloride penetration test of mortar immersed in 3 % NaCl solution for 30 days. In general, the results were similar to those of RCPT and CIDC. The immersion tests gave the direct measure of chloride penetration depth of samples immersed in NaCl solution. The results thus confirmed that the incorporation of RHA or blend of RHA and GS gave mortars with excellent resistance to chloride penetration.

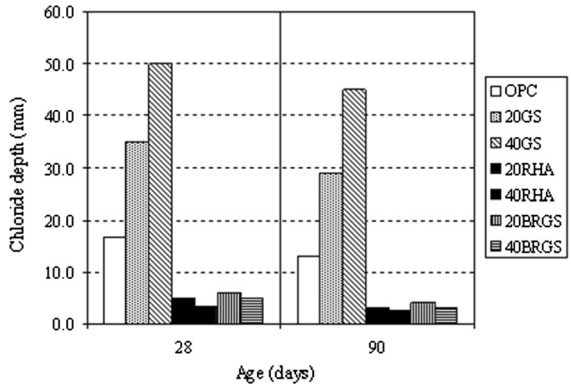

Fig. 6 Chloride depths of mortars after 30 days immersion in 3 % NaCl solution

4 Conclusion

From the tests, it can be concluded that the resistance to chloride penetration of mortars increased with the incorporation of RHA and blend of RHA and GS. The use of GS to replace part of OPC in mortar, however, resulted in only a filler effect and the strengths and resistances to chloride penetration were thus greatly reduced. For the incorporation RHA, the relatively high compressive strengths were obtained owing to its pozzolanic reaction while the resistances to chloride penetration as measured by RCPT, CIDC and CIT tests were significantly improved. The improvements were associated with the filling effect, the increased nucleation sites and hydration of fine RHA particles, and the much reduced $Ca(OH)_2$ of mortars. The blend of GS and RHA also produced mortars with relatively good strength and good resistance to chloride penetration as a result of the synergic effect of RHA and fine GS. The results encourage the use of blend of RHA and GS as a base material for cement replacement as it can reduce the cost of cement and the negative environmental effects of disposing waste ash.

Acknowledgments This work was supported by the Thailand Research Fund (TRF) under the TRF Research Grant for New Scholar No. MRG5580120; Rajamangala University of Technology Phra Nakhon (RMUTP); and Khon Kaen University and the TRF under the TRF-Senior Research Scholar grant No. RTA5780004.

Author's personal copy

References

1. ASTM C39 (2005) Standard test method for compressive strength of cylindrical concrete specimens. ASTM Standard 04.02, pp 21–27
2. ASTM C109 (2005) Standard test method for compressive strength of hydraulic cement mortars (Using 2–in or [50 mm] Cube Specimens). ASTM Standard 04.01, pp 76–81
3. ASTM C311 (2005) Standard test methods for sampling and testing fly ash or natural pozzolans for use in Portland-cement concrete. ASTM Standard 04.02, pp 204–212
4. ASTM C618 (2005) Standard specification for coal fly ash and raw or calcined natural pozzolan for use as a mineral admixture in concrete. ASTM Standard 04.02, pp 323–325
5. ASTM C1202 (2005) Standard test method for electrical indication of concrete's ability to resist chloride ion penetration. ASTM Standard 04.02, pp 651–656
6. Chindaprasirt P, Rukzon S, Sirivivatnanon V (2008) Resistance to chloride penetration of blended Portland cement mortar containing palm oil fuel ash, rice husk ash and fly ash. Constr Build Mater 22(5):932–938
7. Chindaprasirt P, Jaturapitakkul C, Sinsiri T (2005) Effect of fly ash fineness on compressive strength and pore size of blended cement paste. Cem Concr Compos 27(4):425–428
8. Chindaprasirt P, Buapa N, Cao HT (2005) Mixed cement containing fly ash for masonry and plastering work. Constr Build Mater 19:612–618
9. Chindaprasirt P, Kanchanda P, Sathonsaowaphak A, Cao HT (2007) Sulfate resistance of blended cements containing fly ash and rice husk ash. Constr Build Mater 21:1356–1361
10. Isaia GC, Gastaldini ALG, Moraes R (2003) Physical and pozzolanic action of mineral additions on the mechanical strength of high-performance concrete. Cem Concr Compos 25(1):69–76
11. Mehta PK (1987) Studies on the mechanisms by which condensed silica fume improves the properties of concrete: durability aspects. Proceeding International workshop on condensed silica fume in concrete Ottawa, 1–17
12. Otsuki N, Nagataki S, Nakashita K (1993) Evaluation of $AgNO_3$ solution spray method for measurement of chloride penetration into hardened cementitious matrix materials. Constr Build Mater 7(4):195–201
13. Poon CS, Wong YL, Lam L (1997) The influence of different curing conditions on the pore structure and related properties of fly ash cement pastes and mortars. Constr Build Mater 11(7–8):383–893
14. Rudzionis Z, Ivanauskas E (2004) Investigations into effective fly ash used in concrete. J Civ Eng Manag 10(4):303–309
15. Rukzon S, Chindaprasirt P (2008) Use of waste ash from various by-product materials in increasing the durability of mortar. Songklanakarin J Sci Technol 30(4):485–489
16. Rukzon S, Chindaprasirt P (2009) Strength and chloride penetration of Portland cement mortar containing palm oil fuel as and ground river sand. Comput Concr 6(5):391–401
17. Rukzon S, Chindaprasirt P, Mahachai R (2009) Effect of grinding on chemical and physical properties of rice husk ash. Int J Miner Metall Mater 16(2):245–247
18. Rukzon S, Chindaprasirt P (2010) Strength and carbonation model of rice husk ash cement mortar with different fineness. J Mater Civ Eng 22(3):253–259
19. Tang L, Nilsson LO (1995) Calculation of chloride diffusivity in concrete from migration experiments in non-steady-state. Cem Concr Res 25(5):1133–1137
20. The Road & Traffic Authority (2001) Test method RTA T362-Interim test for verification of curing regime-Sorptivity. NSW Australia February 1, pp 1–3
21. Zhang MH, Malhotra VM (1996) High performance concrete incorporating rice husk ash as a supplementary cementing materials. ACI Mater J 93(6):629–636

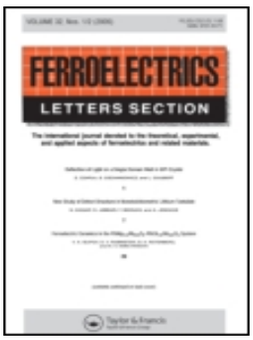

Ferroelectrics Letters Section

ISSN: 0731-5171 (Print) 1563-5228 (Online) Journal homepage: http://www.tandfonline.com/loi/gfel20

Dielectric Properties of 0–3BCTZO/High Calcium Fly Ash Geopolymer Composites

Sitchai Hunpratub, Sumalin Phokha, Santi Maensiri & Prinya Chindaprasirt

To cite this article: Sitchai Hunpratub, Sumalin Phokha, Santi Maensiri & Prinya Chindaprasirt (2015) Dielectric Properties of 0–3BCTZO/High Calcium Fly Ash Geopolymer Composites, Ferroelectrics Letters Section, 42:4-6, 115-121, DOI: 10.1080/07315171.2015.1068967

To link to this article: http://dx.doi.org/10.1080/07315171.2015.1068967

Published online: 04 Dec 2015.

Submit your article to this journal

View related articles

View Crossmark data

Full Terms & Conditions of access and use can be found at
http://www.tandfonline.com/action/journalInformation?journalCode=gfel20

Download by: [223.206.17.43] **Date:** 04 December 2015, At: 18:36

Ferroelectrics Letters Section, 42:115–121, 2015
Copyright © Taylor & Francis Group, LLC
ISSN: 0731-5171 print / 1563-5228 online
DOI: 10.1080/07315171.2015.1068967

Downloaded by [223.206.17.43] at 18:36 04 December 2015

Dielectric Properties of 0–3BCTZO/High Calcium Fly Ash Geopolymer Composites

SITCHAI HUNPRATUB,[1] SUMALIN PHOKHA,[2] SANTI MAENSIRI,[3] AND PRINYA CHINDAPRASIRT[4,*]

[1]Material Science and Nanotechnology Programs, Faculty of Science, Khon Kaen University, Khon Kaen 40002, Thailand
[2]Department of Physics, Faculty of Science, Udon Thani Rajabhat University, Udon Thani 41000, Thailand
[3]School of Physics, Institute of Science, Suranaree University of Technology, Nakhon Ratchasima 30000, Thailand
[4]Sustainable Infrastructure Research and Development Center, Department of Civil Engineering, Faculty of Engineer, Khon Kaen University, Khon Kaen 40002, Thailand

Communicated by Dr. Deborah J. Taylor
(*Received in final form February 9, 2015*)

0–3 $Ba_{0.85}Ca_{0.15}Ti_{0.9}Zr_{0.1}O_3$ (BCTZO)/geopolymer composites were fabricated by normal mixing of geopolymer paste and BCTZO ceramic particles. Four composites were prepared with BCTZO concentrations of 0, 30, 50 and 70% wt. of total solid (BCTZO+FA). Phase and morphology of composite samples were characterized. The effect of addition of BCTZO ceramic particles on the dielectric properties of composite samples was also investigated. The results showed that high dielectric constant values in the order of $\sim 10^5$ at frequency of 10^3 Hz for all composites were obtained. This was due to space charge polarization mechanism.

Keyword $Ba_{0.85}Ca_{0.15}Ti_{0.9}Zr_{0.1}O_3$; geopolymer; composites; dielectric properties

1. Introduction

The most used construction materials suitable to a wide variety of civil engineering and structural designs are cement and concrete. Ordinary Portland Cement (OPC) is the common binder and is widely used in the construction industry. However, the production of OPC requires a large amount of energy and the process emits significant amount of carbon dioxide (CO_2). In producing a ton of OPC, approximately 0.8 ton of CO_2 is released. It is estimated that 7% of green house gas is produced annually from this worldwide [1, 2].

In order to reduce the use of OPC, researches on alternative cementitious material have been initiated. Geopolymer is a new binding material with similar strength development to OPC but with higher durability and fire resistance. Geopolymer or alkali-activated binder is made from source materials rich in silica and alumina and activated with high alkali solution

*Corresponding author; E-mail: prinya@kku.ac.th

[3, 4]. The Al or Si source can be obtained as based material from various pozzolans such as fly ash (FA), silica fume, ground bottom ash and ground agricultural waste ashes.. FA is the most common pozzolan and extensively used in the concrete industry and also in making geopolymer due to its availability and low cost. In particular, the high calcium fly ash is shown to be suitable as source material for making geopolymer for its strength development with ambient temperature curing []. To fully utilize this new binder, researches on fly ash geopolymer with various additives for functional use such as the incorporations of nano-materials viz., SiO_2, and Al_2O_3 [5,6] and OPC as additive [7] is now being undertaken.

Recently, the improvements of optical and electrical properties of cement and cementitious materials (geopolymer, epoxy, etc.) for use as smart materials in construction have been researched quite extensively [8–23]. There has also been increasing interest on the applications of TiO_2 and Ti-Zn-Al as photocatalytic in concrete and other binders for air pollution remediation, self-cleaning and self-disinfection purposes [8, 9]. It is believed that the concrete structure with photocatalytic surface can maintain their aesthetic appearance and help improve the air quality at the same time. Furthermore, researches have shown that the addition of carbon (nanotubes, fibers) into cement composites remarkably increases the sensitivity of the electrical resistance of composites to compressive stress and reversible piezoresistive response [10]. These findings indicate that the cement composite has great potential for monitoring the concrete structure response to loading, and for traffic-monitoring applications such as vehicle detection, weighing and speed measurement [10]. In addition, piezoelectric materials (lead zirconate titanate (PZT), lead magnesium niobate titanate (PMNT), $BaTiO_3$, Ca and Zr modified $BaTiO_3$) have been added in cements or cementitious materials for application as sensors and actuators in civil work [11–23].

In this paper, the dielectric properties of $Ba_{0.85}Ca_{0.15}Ti_{0.9}Zr_{0.1}O_3$ (BCTZO)/high calcium fly ash geopolymer composites were studied. The high dielectric constants, produced by the normal mixing of BCTZO ceramic particles and geopolymer were reported.

2. Experimental

$Ba_{0.85}Ca_{0.15}Ti_{0.9}Zr_{0.1}O_3$ (BCTZO) ceramic particles were prepared using a solid state reaction method. $BaCO_3$ (99%), $CaCO_3$ (96%), TiO_2 (99%) and ZrO_2 (99%) were used as the starting materials. Initially, all starting materials were thoroughly mixed with 2-propanol and then the mixture was ball milled for 24 h. After drying, the mixture precursor powders were calcined at 1300 °C for 3 h. The calcined BCTZO powders were compacted into disk-shaped pellets with a diameter of 13 mm and thickness of 2 mm using 221 MPa pressure. The green pellets were sintered at 1450°C for 3 h. The sintered BCTZO ceramics were grounded and sieved to obtain the BCTZO particles less than 106 μm. High calcium fly ash was obtained from Mae Moh power plant in northern Thailand and its chemical composition is given in Table 1. To fabricate BCTZO /geopolymer composites, 10M NaOH solution was added to fly ash and the mixture was stirred for 5 min. The Na_2SiO_3 solution was added and stirring was continued for another 2 min. The BCTZO ceramic was then added and stirring was maintained for 2 more min. Finally, the paste was cast into a 20 mm-diameter and 4 mm-thick plastic mould. The samples were covered with plastic sheet and left at 25°C controlled room for 1 h and at 60°C in an oven for 2 days. The mix proportions of composites are given in Table 2.

The phase and morphology of these samples were characterized by XRD (PW3040 Philips X-ray diffractometer with Cu K_α radiation ($\lambda = 0.15406$ nm), the Netherlands) and Scanning electron microscopy (SEM, LEO VP1450, UK). Silver paint was used as the

Downloaded by [223.206.17.43] at 18:36 04 December 2015

Table 1
Typical chemical compositions of fly ash

Chemical compositions	wt.%
SiO_2	29.32
Al_2O_3	12.96
CaO	25.79
Fe_2O_3	15.64
MgO	2.94
K_2O	2.93
Na_2O	2.83
SO_3	7.29
LOI	0.3

Downloaded by [223.206.17.43] at 18:36 04 December 2015

electrode and the dielectric properties of composite discs were measured at room temperature (25°C) after 7 days of curing using Agilent 4294A Precision impedance analyzer. The dielectric constant (ε') was calculated from the following equation:

$$\varepsilon' = \frac{C_p t}{\varepsilon_0 A}$$

where C_p is the sample capacitance, t is the thickness, ε_0 is the permittivity of free space (8.854×10^{-12} F/m) and A is the electrode area.

3. Results and Discussion

XRD patterns of BCTZO/geopolymer composites with various BCTZO concentrations (0, 30, 50 and 70 wt.%) are shown in Fig. 1. The geopolymer paste (0 wt.% BCTZO) consisted of an amorphous phase as indicated by the broad hump around 20–38 $^{o}2\Theta$ and crystalline phase as indicated by the sharp peaks of quartz (SiO_2), hematite (Fe_2O_3), and mullite [23,24]. When the BCTZO concentrations were increased, the peak intensity of BCTZO phase was also increased. As expected, the phases of geopolymer decreased with increasing BCTZO concentration.

The morphologies of geopolymer and BCTZO/geopolymer composites with various BCTZO concentrations (0, 30, 50 and 70 wt.%) are shown in Fig. 2. The geopolymer

Table 2
Mixed proportion of BCTZO/geopolymer composites

	Mix proportion (g)			
Sample	FA	BCTZO	NaOH (g)	Na_2SiO_3 (g)
Geopolymer	100	0	30	30
30 wt.% BCTZO	70	30	21	21
50% wt.% BCTZO	50	50	15	15
70% wt.% BCTZO	30	70	9	9

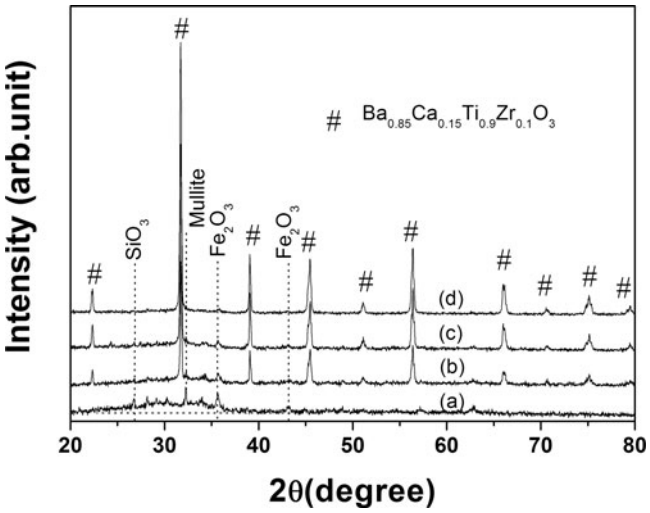

Figure 1. XRD patterns of BCTZO/geopolymer composites with various BCTZO concentrations (a) geopolymer, (b) 30, (c) 50 and (e) 70 wt.%.

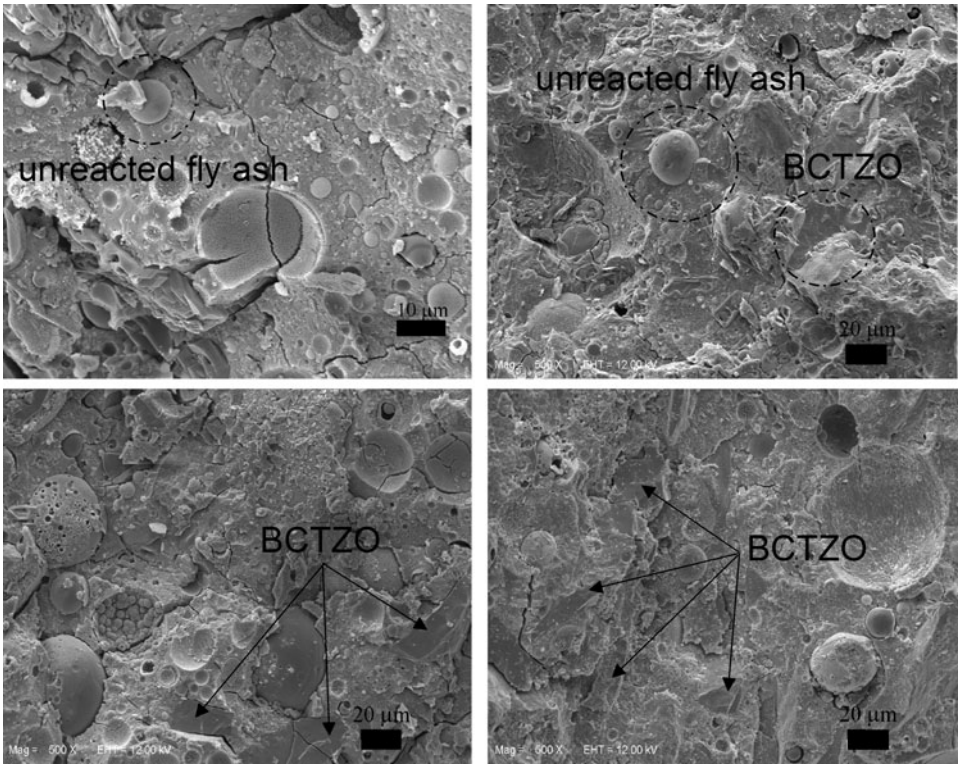

Figure 2. SEM images of BCTZO/geopolymer composites with various BCTZO concentrations (a) geopolymer, (b) 30, (c) 50 and (e) 70 wt.%.

Downloaded by [223.206.17.43] at 18:36 04 December 2015

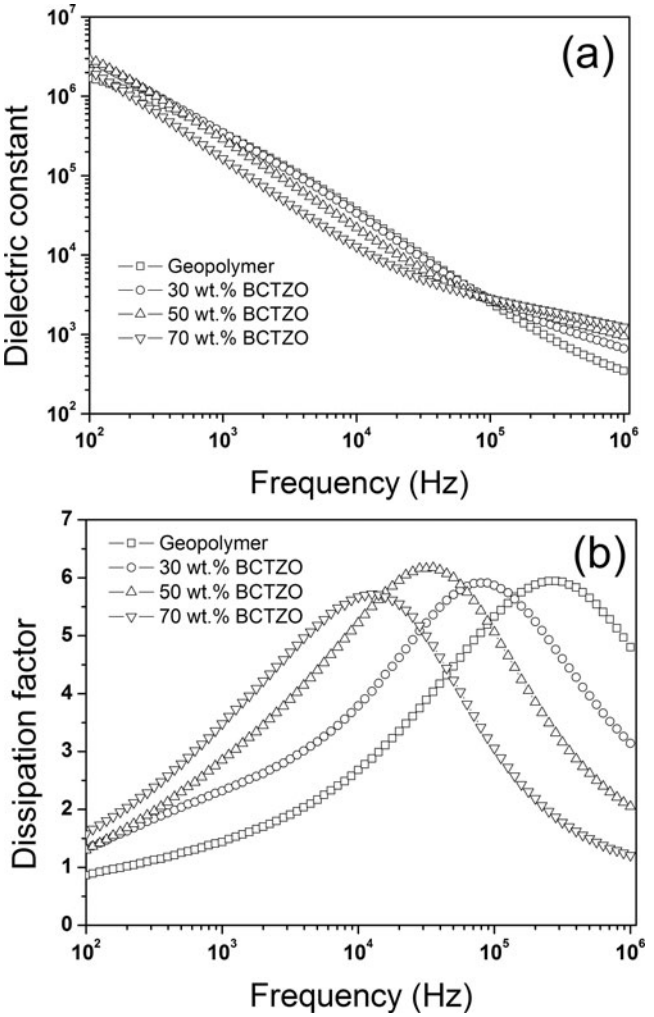

Figure 3. Dielectric constant (a) and dissipation factor (b) of BCTZO/geopolymer composites with various BCTZO concentrations.

Downloaded by [223.206.17.43] at 18:36 04 December 2015

matrix consisted of a number of unreacted fly ash particles, cracks and pores. The findings were similar to the previously reported results [23, 24]. For the morphologies of BCTZO/geopolymer composites, all the composite samples displayed the even distribution of BCTZO particles which were surrounded by the geopolymer matrix. This suggested the composites were arranged with 0–3 connectivity. The uniformity of the distribution increased with an increase in BCTZO concentration in the BCTZO/geopolymer composites. However, a number of unreacted fly ash particles, cracks and pores were found in the composite samples.

Frequency dependence of dielectric constant for the BCTZO/geopolymer composites with various BCTZO concentrations is shown in Fig. 3(a). The dielectric constant (ε') values of all the BCTZ/geopolymer composites decreased with increasing frequency. The decrease in dielectric constant may be explained on the basis of a decrease in polarization with increasing frequency. It is known that the polarization is the sum of dipolar, electronic,

ionic and interfacial polarizations. At low frequencies, all polarizations respond easily to the time varying electric field and as the frequency increases, different polarization contributions filter out. As a result, the net polarization of composite decreases which leads to a decrease in the dielectric constant. The results are similar to those reported by Hanjitsuwan et al. [24, 25].

The dielectric values of the composites were also related to the BCTZO concentration. At low frequency (10^2–10^5 Hz), the ε' values of BCTZO/geopolymer composites reduced with the increase in BCTZO concentration. The geopolymer paste consisted of a number of free ions such as Ca^{2+}, Na^{+}, HO^{-} and $SO_4{}^{2-}$ in the geopolymer matrix arising from the geopolymerization process. Therefore, the high ε' value could be attributed to these ions leading to high space charge polarization in this frequency range. However at high frequency (10^5–10^6 Hz), the ε' values increased with the increase in BCTZO concentration as expected. However, the ε' values were low at this range of frequency due to the structure phase. The phase of geopolymer was non-polar and the constrained polymer chain hindered the contribution of electrical polarization. Therefore, the ε' values were lower than those of the BCTZO ceramics.

The results of frequency dependence of dissipation factor (tanδ) of BCTZO/geopolymer composite with various BCTZO concentrations are shown in Fig. 3(b). The maximum value of tanδ shifted to the low frequency due to the decrease of geopolymer paste.

4. Conclusion

0–3 $Ba_{0.85}Ca_{0.15}Ti_{0.9}Zr_{0.1}O_3$ (BCTZO)/high calcium fly ash geopolymer composites were successfully fabricated by normal mixing of geopolymer paste and BCTZO ceramic particles. Four different composites were prepared with BCTZO concentrations of 0, 30, 50, and 70% by weight of solid. The addition of 0-70% wt. of BCTZO ceramic particles to high calcium fly ash geopolymer resulted in composites with high dielectric constant values in order of $\sim 10^5$ at high frequency of 10^3 Hz. This was due to space charge polarization mechanism.

Downloaded by [223.206.17.43] at 18:36 04 December 2015

Funding

This work was supported by the Higher Education Research Promotion and National Research University Project of Thailand, Office of the Higher Education Commission, through the Advanced Functional Materials Cluster of Khon Kaen University; Khon Kaen University and the Thailand Research Fund (TRF) under the TRF Senior Research Scholar, Grant No. RTA5780004 and the Royal Golden Jubilee PHD program, Grant No. PHD/0358/2551.

References

1. F. Ridi, E. Fratini, P. Baglioni, Cement: A two thousand year old nano-colloid. *J. Colloid Interface Sci.* **357**, 255–264 (2011).
2. J. Deja, A. Uliasz-Bochenczyk, E. Mokrzycki, CO_2 emissions from polish cement industry. *Int. J. Greenh. Gas Con.* **4**, 583–588 (2010).
3. J. Davidovits, Geololymers. Inorganic polymeric new materials, *J. Therm. Anal.* **37**, 1633 (1991).
4. C. Shi, A. Fernández Jiménez, A. Palomo, New cements for the 21st century: The pursuit of an alternative to Portland cement. *Cement Concrete Res.* **41**, 750–763 (2011).
5. T. Phoo-ngernkham, P. Chindaprasirt, V. Sata, S. Hanjitsuwan, S. Hatanaka, The effect of adding nano-SiO_2 and nano-Al_2O_3 on properties of high calcium fly ash geopolymer cured at ambient temperature. *Mater. Design* **55**, 58–65 (2014).

6. Y. Huang, M. Han, The influence of alpha-Al_2O_3 addition on microstructure, mechanical and formaldehyde adsorption properties of fly ash-based geopolymer products. *J. Hazard.Mater.* **193**, 90–94 (2011).
7. S. Pangdaeng, T. Phoo-ngernkham, V. Sata, P. Chindaprasirt, Influence of curing conditions on properties of high calcium fly ash geopolymer containing Portland cement as additive. *Mater. Design* **53**, 269–274 (2014).
8. A. Folli, C. Pade, T. B. Hansen, T. De Marco, D. E. Macphee, TiO_2 photocatalysis in cementitious systems: Insights into self-cleaning and depollution chemistry. *Cement Concrete Res.* **42**, 539–548 (2014).
9. T. Vulic, M. Hadnadjev-Kostic, O. Rudic, M. Radeka, R. Marinkovic-Neducin, J. Ranogajec, Improvement of cement-based mortars by application of photocatalytic active Ti–Zn–Al nanocomposites. *Cement Concrete Comp*. **36**, 121–127 (2013).
10. B. Han, K. Zhang, X. Yu, E. Kwon, J. Ou, Electrical characteristics and pressure-sensitive response measurements of carboxyl MWNT/cement composites. *Cement Concrete Comp.* **34**, 794–800 (2012).
11. Z. J. Li, D. Zhang, K. Wu, Cement-Based 0–3 Piezoelectric Composites. *J. Am. Ceram. Soc. Adv. Mater.* **85**(2), 305–313 (2002).
12. S. F. Huang, J. Chang, F. T. Liu, L. C. Lu, Z. M. Ye, X. Cheng, Poling process and piezoelectric properties of lead zirconate titanate/sulphoaluminate cement composites. *J. Mater. Sci.* **39**, 6975–6979 (2004).
13. C. Xin, H. Shifeng, C. Jun, X. Ronghua, L. Futian, L. Lingchao, Piezoelectric and dielectric properties of piezoelectric ceramic–sulphoaluminate cement composites. *J. Eur. Ceram. Soc.* **25**, 3223–3228 (2005).
14. A. Chaipanich, Dielectric and piezoelectric properties of PZT-cement composites. *Curr. Appl. Phys.* **7**, 537–539 (2007).
15. N. Jaitanong, A. Chaipanich, T. Tunkasiri, Properties 0–3 PZT-Portland cement composites. *Ceram. Inter.* **34**, 793–794 (2008).
16. A. Chaipanich, G. Rujiganagul, T. Tunkasiri, Properties 0–3 PZT-Portland cement composites, Properties of Sr- and Sb-doped PZT-Portland cement composites, *Appl. Phys. A.* **94**, 329–337 (2009).
17. R. Rianyoi, R. Potong, N. Jaitanong, R. Yimnirun, Dielectric, ferroelectric and piezoelectric properties of 0–3 barium titanate-Portland cement composites. *Appl. Phys. A.* **104**, 661–666 (2011).
18. R. Potong, R. Rianyoi, A. Ngamjarurojana, A. Chaipanich, Dielectric and piezoelectric properties of 1–3 non-lead barium zirconate titanate-Portland cement composites. *Ceram. Inter.* **39**, S53–S57 (2013).
19. R. Potong, R. Rianyoi, A. Chaipanich. Dielectric Properties of Lead-Free Composites from 0–3 Barium Zirconate Titanate-Portland Cement Composites. *Ferr. Lett.* **38**, 18–23 (2011).
20. H. Shifeng, L. Lingchao, C. Jun, X. Dongyu, F. Futian, C. Xin, Influence of Ceramic Particle Size on Piezoelectric Properties of Cement-Based Piezoelectric Composites. *Ferr. Lett.* **332**, 187–194 (2006).
21. Z. J. Li. H. Y. Yu, Y. J. Zhang, Fabrication and piezoelectricity of 0–3 cement based composite with nano-PZT powder, *Curr. Appl. Phys.* **33** (2009) 588–591.
22. S. Hunpratub, T. Tamwong, S. Srilomsak, S. Maensiri, P. Chindaprasirt. Effects of NaOH concentrations on physical and electrical properties of high calcium fly ash geopolymer paste. *Cement Concrete Comp.* **45**, 9–14 (2014).
23. K. Somna, C. Jaturapitakkul, P. Kajitvichyanukul, P. Chindaprasirt, NaOH-activated ground fly ash geopolymer cured at ambient temperature. *Fuel* **90**, 2118–2124 (2011).
24. S. Hanjitsuwan, P. Chindaprasirt, K. Pimraksa, Electrical conductivity and dielectric property of fly ash geopolymer pastes. *International Journal of Minerals, Metallurgy and Materials* **18**, 94–99 (2011).
25. S. Hanjitsuwan, S. Hunpratub, P. Thongbai, S. Maensiri, V. Sata, P. Chindaprasirt. Effects of NaOH concentrations on physical and electrical properties of high calcium fly ash geopolymer paste. *Cement Concrete Comp.* **45**, 9–14 (2014).

Downloaded by [223.206.17.43] at 18:36 04 December 2015

Construction and Building Materials 98 (2015) 482–488

Contents lists available at ScienceDirect

Construction and Building Materials

journal homepage: www.elsevier.com/locate/conbuildmat

High calcium fly ash geopolymer mortar containing Portland cement for use as repair material

Tanakorn Phoo-ngernkham [a], Vanchai Sata [b], Sakonwan Hanjitsuwan [c], Charoenchai Ridtirud [d], Shigemitsu Hatanaka [e], Prinya Chindaprasirt [b,*]

[a] Research Center for Advances in Civil Engineering and Construction Materials, Program in Civil Engineering, Faculty of Engineering and Architecture, Rajamangala University of Technology Isan, Nakhon Ratchasima 30000, Thailand
[b] Sustainable Infrastructure Research and Development Center, Dept. of Civil Engineering, Faculty of Engineering, Khon Kaen University, Khon Kaen 40002, Thailand
[c] Program of Civil Technology, Faculty of Industrial Technology, Lampang Rajabhat University, Lampang 52100, Thailand
[d] Dept. of Civil Engineering, Faculty of Engineering, Rajamangala University of Technology Isan, Khon Kaen Campus, Khon Kaen 40000, Thailand
[e] Dept. of Architecture, Faculty of Engineering, Mie University, Mie 514-8504, Japan

HIGHLIGHTS

- FA geopolymer mortars (GPM) containing PC could be used as alternative repair material (RM).
- GPM gave sufficiently high slant bond and bending strengths compared with RM.
- The interface zone of concrete and GPM was more homogeneous and denser than that of concrete and RM.

ARTICLE INFO

Article history:
Received 6 June 2015
Received in revised form 23 August 2015
Accepted 27 August 2015

Keywords:
Geopolymer
High calcium fly ash
Portland cement
Shear bond strength
Bending stress
Repair material

ABSTRACT

This article investigated the utilization of high calcium fly ash geopolymer mortars (GPM) containing ordinary Portland cement (PC) for use as Portland cement concrete (PCC) repair material. The shear bond strength of PCC substrate and repair binder and bending strength of notched concrete beam filled with repair binder were used to evaluate the performances of GPM and commercial repair binders (RM). Test results indicated that the use of GPM gave sufficiently high shear bond and bending strengths compared with the use of RM suggesting that it could be used as an alternative product for concrete repair works. In addition, the results from scanning electron microscopy of fracture surfaces indicated that the interface zone of concrete and GPM was more homogeneous and denser than that of concrete and RM. The GPM with 14 M NaOH solution and 10% PC was the optimum mixture for improving the shear bond and bending strengths.

© 2015 Elsevier Ltd. All rights reserved.

1. Introduction

Geopolymer is made from silica and alumina source materials activated with high alkali solutions such as sodium hydroxide (NaOH), potassium hydroxide (KOH), sodium silicate and potassium silicate [1]. A number of supplementary cementitious materials such as ground granulated blast furnace slag, metakaolin and fly ash are commonly used source materials in geopolymer for their availability and favorable mechanical properties [2–6].

Several researchers [7–10] reported that high calcium fly ash is also a suitable source material for making good geopolymer. The high calcium fly ash geopolymer mixture can be cured at room temperature as a result of the reaction of calcium in the system. However, the geopolymerization of high calcium fly ash without additives is still slow at ambient condition [10,11], therefore, low strength is normally obtained. The use of Portland cement to enhance the strength of high calcium fly ash geopolymer is very attractive [8,12–14]. In addition to the formation of calcium silicate hydrate, the heat from the reaction of Portland cement and water can assist the geopolymerization process and enhances the strength development [15]. High calcium geopolymer mortar with compressive strength of 65 MPa has been fabricated with the addition of Portland cement cured at 25 °C ambient temperature [8].

The commercial repair materials with good mechanical property and bonding strength are widely used for repair work in concrete. However, the costs of these products are rather expensive. Alternative repair material with comparable properties but less

* Corresponding author.
E-mail address: prinya@kku.ac.th (P. Chindaprasirt).

http://dx.doi.org/10.1016/j.conbuildmat.2015.08.139
0950-0618/© 2015 Elsevier Ltd. All rights reserved.

expensive is, therefore, a subject of interest. A number of researchers [9,16–19] have tried to utilize geopolymer as a repair material by testing slant shear, pull-out and direct shear. Hu et al. [16] studied the bond strength between mortar substrate and geopolymer in sandwich specimens and reported that geopolymer exhibited higher bonding strength than that of comparable Portland cement mixture. Pacheco-Torgal et al. [17] determined the bond strength between concrete substrate and geopolymer mortar produced from tungsten mine waste containing calcium hydroxide and found that the geopolymeric binders had very high bond strength even at early ages compared with that of commercial repair products. In addition, Songpiriyakij et al. [18] also tested the bond strength between rebar and concrete substrate by using geopolymer paste as the bonding agent, and reported that the bond strengths of rice husk ash and silica fume geopolymer pastes were approximately 1.5 times higher than those of comparable repair epoxies. Therefore, the bond strengths of geopolymer materials are sufficiently high and should be used as an alternative bonding material for repair works.

The objective of this research is, therefore, to investigate the utilization of high calcium fly ash geopolymer mortars containing ordinary Portland cement as additive for use as a repair binder. The obtained knowledge would be very beneficial to the understanding and to the future application of geopolymer products as an alternative repair material.

2. Experimental details and testing analysis

2.1. Materials

2.1.1. Geopolymer mortars

The geopolymer mortar (GPM) was made from high calcium fly ash (HFA) from Mae Moh power plant in northern Thailand and local river sand with specific gravity of 2.63 and fineness modulus of 1.80. Sodium hydroxide solution (NaOH) and sodium silicate solution (13.89% Na_2O, 32.15% SiO_2, and 46.04% H_2O) were used as liquid activators. Four levels of HFA replacement by ordinary Portland cement (PC) of 0%, 5%, 10%, and 15% by weight and three NaOH concentrations of 6, 10, and 14 M (molar) were investigated. The chemical composition and physical properties of HFA and PC are shown in Tables 1 and 2, respectively. The mix proportions and strengths of GPM are shown in Table 3. For the mixing of mortars, NaOH and Na_2SiO_3 solutions were mixed together prior to the start of mixing. The HFA, PC and sand were dry mixed until a homogenous mass was obtained. The prepared liquid solution was then added and the mixing was done for 5 min. The setting time of mortar was also tested in accordance with ASTM C807 [20]. As shown in Table 4, the setting time of GPM was dependent on NaOH concentration and PC content. The final setting times ranged between 12 and 130 min and this could be used advantageously in adjusting the setting of repair material.

2.1.2. Ordinary Portland cement concrete

The mix proportions and strengths of ordinary Portland cement concrete (PCC) are shown in Table 5. The local river sand with specific gravity of 2.61 and fineness modulus of 2.40 was used as fine aggregate. While, crushed limestone with specific gravity of 2.71 and fineness modulus of 6.05 was used as coarse aggregate. The PCC was used for preparing two types of specimen viz., slant shear test specimens and bending test specimens. For the slant shear specimens, the fresh PCC was cast in $50 \times 50 \times 125$ mm prism molds. They were cured in water for 28 days and then wrapped with vinyl sheet to protect moisture loss and cured for another 60 days. This long curing period was chosen to provide advanced hydration as in the old concretes in the construction field based on the previous research [21]. The PCC prisms were cut in the middle section with the interface line at 45° to the vertical (see Fig. 1) to provide the PCC substrate for the slant shear specimens. For the preparation of specimens for bending stress, the PCC was cast in $75 \times 75 \times 300$ mm long beams. They were cured similarly to the slant shear specimens. A notch with height to beam depth (a_0/d) ratio of 0.4 and notch width to notch height (w_0/a_0) ratio of 0.4 was cut in the middle of beam (see Fig. 2).

Table 2
Physical properties of materials.

Materials	Specific gravity	Median particle size, d_{50} (μm)	Blaine fineness (cm^2/g)
HFA	2.61	8.5	4300
PC	3.16	14.6	3600

2.1.3. Commercial repair material products

Five available commercial repair material products (RM) were also tested. This was done so that the performance of GPM could be compared with those of commercial products. RM1 is general purpose non-shrink grout mortar; RM2 is high performance repair and finishing mortar; RM3 is fiber-reinforced non-shrink mortar; RM4 is multi-purpose non-shrink grout; and RM5 is polymer modified repair mortar. The amount of water in these products directly influences the compressive and flexural strengths including the bond adhesion; therefore, the recommended water/binder (W/B) ratios were strictly used. The obtained strengths of these repair materials are summarized in Table 6.

2.2. Testing and analysis

2.2.1. Shear bond strength between PCC substrate and GPM or RM

The shear bond strength was evaluated using the slant shear test of PCC substrate and GPM or RM as described in ASTM C882 [22] with stiffer slant shear angle of 45°. The slant shear angle of 45° is officially used for standard evaluation of epoxy bond with concrete [23] and was also used successfully in testing shear bond of concrete and geopolymer [6]. For casting of the specimens, the GPM was placed in two equal layers into a $50 \times 50 \times 125$ mm prism mold, half-filled with slant PCC substrate. Each layer was tamped 25 times and vibrated for 45 s. The samples were covered with vinyl sheet and kept in the 25 °C controlled room. The specimens (as shown in Fig. 1) were tested in a constant loading rate of 0.30 MPa/s. The shear bond strength was the ratio of maximum load at failure and the bond area. The reported results of shear bond strength were the average of five samples.

2.2.2. Bending stress of PCC notched beam with filled GPM or RM

This test used the same type of specimens as in the test of fracture characteristics as shown in Fig. 2. For casting of specimens, the GPM or RM was mixed and filled in the notch to act as repair materials. The samples were covered with vinyl sheet to protect moisture loss and kept in the 25 °C controlled room until the testing age of 28 days. The specimens were tested by three point bending with deflection control using loading rate of 0.05 mm/min [24]. The reported results were the average of five samples.

2.2.3. Interface zone between PCC substrate and GPM or RM

The samples between PCC substrate and repair materials were broken and analysed by the scanning electron microscopy (SEM). The samples were cut, then coated with a layer of gold approximately 20–25 Å thick using a blazer sputtering coater. After that, they were placed on a brass stub sample holder with double stick carbon tape. A JEOL JSM-700IF scanning electron microscopy was used to study interface zone between PCC substrate and GPM or RM.

3. Results and discussion

3.1. Shear bond strength between PCC substrate and GPM or RM

The results of 45° slant shear load carrying capacity of PCC substrate and GPM or RM are shown in Fig. 3. The shear bond strengths increased with the increased PC content and NaOH concentration. The noticeable increase in shear bond strength was due to the increase in the reaction products. This is in line with the previous report [25]on the improved strength of fly ash based geopolymers with increased calcium content which the additional C–S–H and C–A–S–H gel co-existed with N–A–S–H gel of GPM. The increase in reaction products at the interface transition zone between PCC substrate and GPM enhanced the strength at contact

Table 1
Chemical composition of HFA and PC (by weight).

Materials	SiO_2	Al_2O_3	Fe_2O_3	CaO	MgO	K_2O	Na_2O	SO_3	LOI
HFA	29.32	12.96	15.64	25.79	2.94	2.93	2.83	7.29	0.30
PC	20.80	4.70	3.40	65.30	1.50	0.40	0.10	2.70	0.90

Table 3
Mix proportions and strengths of GPM.

Mix symbol	HFA (g)	PC (g)	Sand (g)	NaOH (g)			Na_2SiO_3 (g)	Properties of GPM	
				6 M	10 M	14 M		f_c (MPa)	f_t (MPa)
6M0PC	100	–	100	20	–	–	40	38.5	2.91
6M5PC	95	5	100	20	–	–	40	40.2	3.79
6M10PC	90	10	100	20	–	–	40	45.3	4.77
6M15PC	85	15	100	20	–	–	40	48.2	4.93
10M0PC	100	–	100	–	20	–	40	50.5	6.22
10M5PC	95	5	100	–	20	–	40	56.7	6.85
10M10PC	90	10	100	–	20	–	40	60.4	7.17
10M15PC	85	15	100	–	20	–	40	64.1	7.32
14M0PC	100	–	100	–	–	20	40	56.0	7.07
14M5PC	95	5	100	–	–	20	40	58.5	8.51
14M10PC	90	10	100	–	–	20	40	63.3	8.96
14M15PC	85	15	100	–	–	20	40	62.0	7.49

f_c = compressive strength at the age of 28 days (50 × 50 × 50 mm^3 cube specimen).
f_t = flexural strength at the age of 28 days (75 × 75 × 300 mm^3 rectangular specimen).

Table 4
Setting time of GPM.

Symbols	6 M NaOH		10 M NaOH		14 M NaOH	
	Initial (min)	Final (min)	Initial (min)	Final (min)	Initial (min)	Final (min)
0PC	21	50	47	88	80	130
5PC	14	25	30	45	65	105
10PC	12	19	15	30	23	40
15PC	7	12	10	20	18	25

zone [17]. However, the GPM with high 15% PC content and high 14 M NaOH exhibited a slight decrease in the shear bond strength. The drop in strength at high NaOH concentration was also reported by Somna et al. [10]. At high NaOH concentration, the dissolution silica and alumina was accelerated but polycondensation was hindered [26]. An excess hydroxide ion caused aluminosilicate gel precipitation at the early stage and resulted in lower strength geopolymers [27]. In addition, the dissolution of calcium was suppressed at high NaOH concentration resulting in less hydration products.

According to Fig. 3, the results of 45° slant shear load carrying capacity of PCC substrate and RM were between 11.8 and 26.2 MPa with the average of 17.9 MPa comparing with those of 14.2–24.2 MPa for GPM with the average of 20.0 MPa. The mixes with 10 M and 14 M NaOH exhibited significantly higher shear bond strengths than the average of RM. This indicated that the GPM containing PC as additive can be used as an alternative repair material.

3.2. Bending stress of PCC notched beam with filled GPM or RM

The bending stresses of PCC notched beams filled with GPM or RM are shown in Fig. 4. The bending stress of PCC notched beam

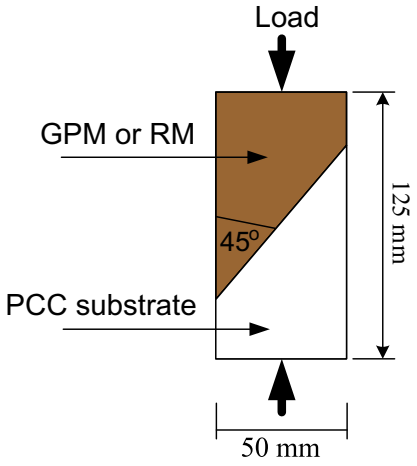

Fig. 1. Test set up of slant shear specimens.

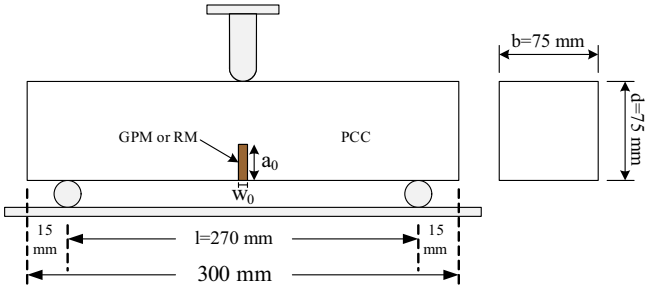

Fig. 2. Test set up of bending stress of PCC notched beam with filled GPM or RM specimens.

Table 5
Mix proportions and strengths of PCC.

Components	PC (kg/m^3)	Aggregates (kg/m^3)		Water (kg/m^3)	Properties of PCC	
		Fine	Coarse		f_c (MPa)	f_t (MPa)
Proportions	495	510	938	238	35.9	8.5

f_c = compressive strength at the age of 28 days (100 mm in diameter and 200 mm in length specimen).
f_t = flexural strength at the age of 28 days (40 × 40 × 160 mm^3 rectangular specimen).

Table 6
Properties of RM.

Repair materials	Water/binder ratios	f_c at 28 days (MPa)	f_t at 28 days (MPa)
RM1	0.15	62.0	8.2
RM2	0.25	48.3	11.0
RM3	0.15	60.0	5.5
RM4	0.14	70.0	7.8
RM5	0.17	42.6	8.5

Remark: Water/binder ratios of RMs were based on the recommendation of manufacturer.

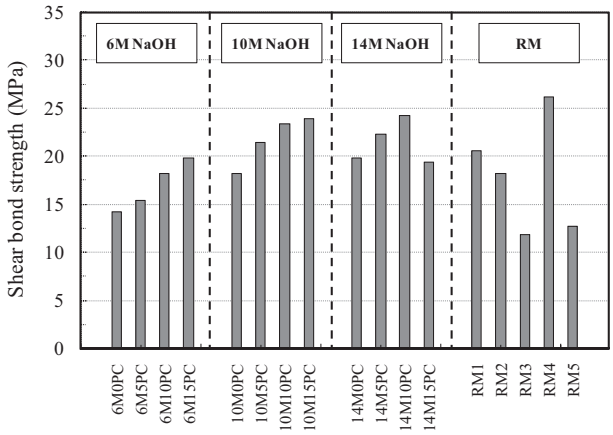

Fig. 3. Shear bond strength of GPM or RM with interface line at 45° to the vertical.

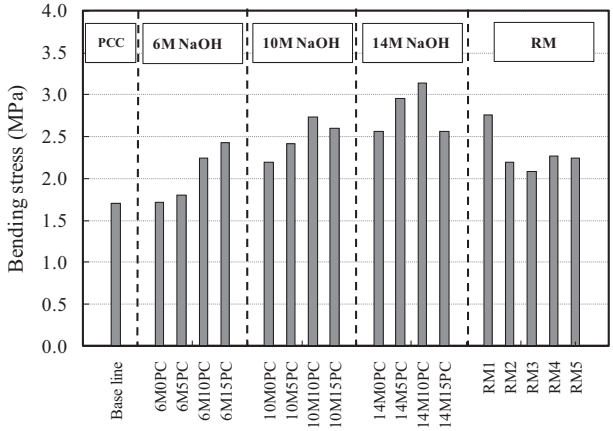

Fig. 4. Bending stress of PCC notched beam with filled GPM or RM as repair materials.

without filled materials (base line) was 1.7 MPa, while those with filled materials were increased as expected. For the use of RM materials, the bending stresses were 2.1–2.8 MPa with the average of 2.3 MPa representing an average improvement of 36% from the base line. For the GPM, the bending stresses were 1.7–3.1 MPa. With the exception of mixes with low NaOH concentration (6 M) and PC content of 0% and 5%, all other mixes produced sufficiently high bending stresses especially mixes with high NaOH concentrations and high PC contents. This was due to the increase in reaction products with associated improvements of strength and bonding capacity of GPM which led to overall improvement in the bending stresses of PCC notched beams. According to Fig. 4, the notched beam filled with GPM at 10% PC and 14 M NaOH gave excellent bending stress of 3.1 MPa representing 85% improvement from the base line. The good performance with high NaOH concentration mixes could be attributed to the interaction between the NaOH and PCC substrate at the transition zone. The results of bending stress test confirmed the suitability of GPM containing PC as additive as an alternative repair material.

3.3. Failure mode and interface zone between PCC substrate and GPM or RM

The failure patterns of the slant shear prisms are shown in Figs. 5 and 6. Two failure patterns could be identified. The first was the failure in the GPM from which the cracks were formed in the GPM and the interface while the PCC substrate remained relatively intact. This occurred with the low NaOH concentration and without PC and low PC content (6M0PC and 6M5PC mixes) geopolymer mortars. For other mixes with relatively high strengths, high NaOH and high PC such as 10M10PC and 14M10PC mixes, the slant shear bond prisms failed in the monolithic mode where cracks were formed in both sections of GPM and PCC substrate. This indicated the relatively high resistance to cracking of GPM and the high bonding between the two surfaces. Thus cracks went through the slant plane resulted in monolithic type of failure. For the RM, two types of failure modes were observed. The first type, cracks were formed in the RM and the interface while the PCC substrate remained relatively intact. These were observed with the prisms with RM2, RM3 and RM5 as shown in Fig. 6. The results were in line with the low shear bond strengths of the prisms with RM2, RM3 and RM5 (Fig. 3). For the prisms with RM1 and RM4, the failures occurred in the monolithic mode as shown in Fig. 6a and d. This again indicated the relatively high resistance to cracking of RM1 and RM4 and the high bonding between the two surfaces. The results were in line with the high shear bond strengths of the prisms with RM1 and RM4 (Fig. 3).

The SEM results of some of the fracture interfaces between PCC substrate and GPM or RM are shown in Fig. 7. The fracture surface of mortar with low NaOH concentration and without PC (6M0PC) as shown in Fig. 7a showed the relatively plane fracture surface between the PCC substrate and GPM indicating the clean separation of the two surfaces and the low bonding. This result corresponded to a low bending stress and low shear bond strength of

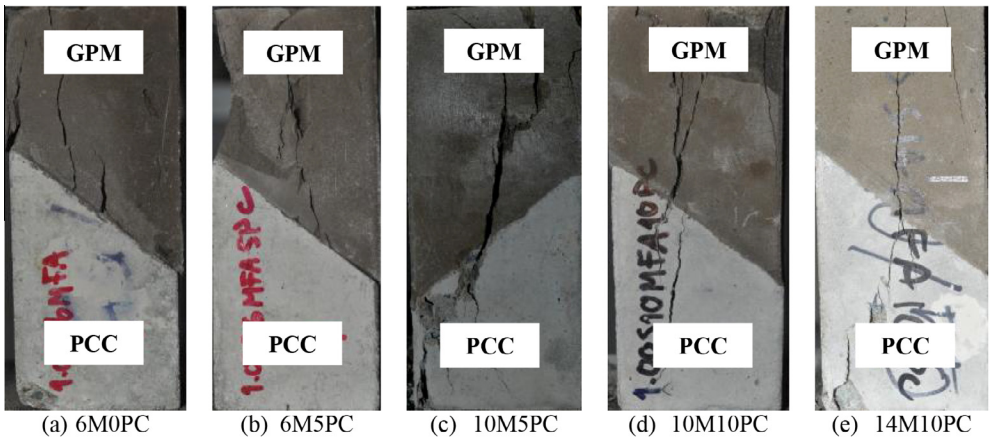

Fig. 5. Fracture surface between PCC substrate and GPM.

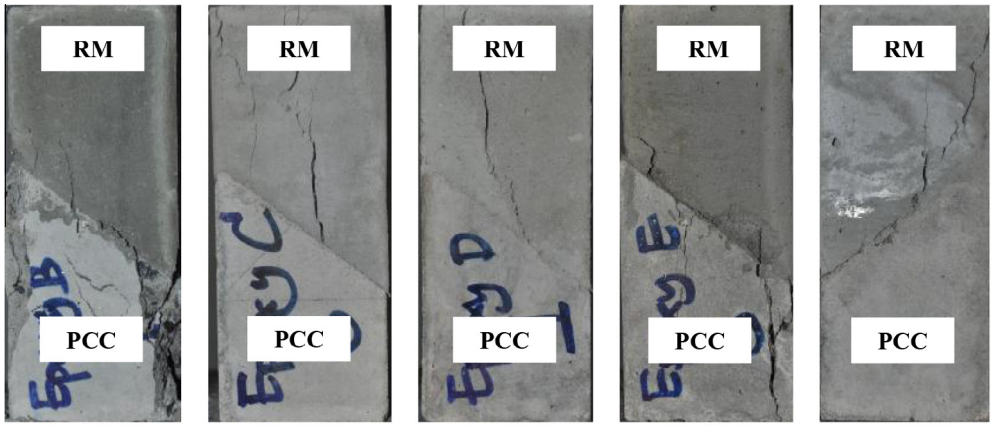

Fig. 6. Fracture surface between PCC substrate and RM.

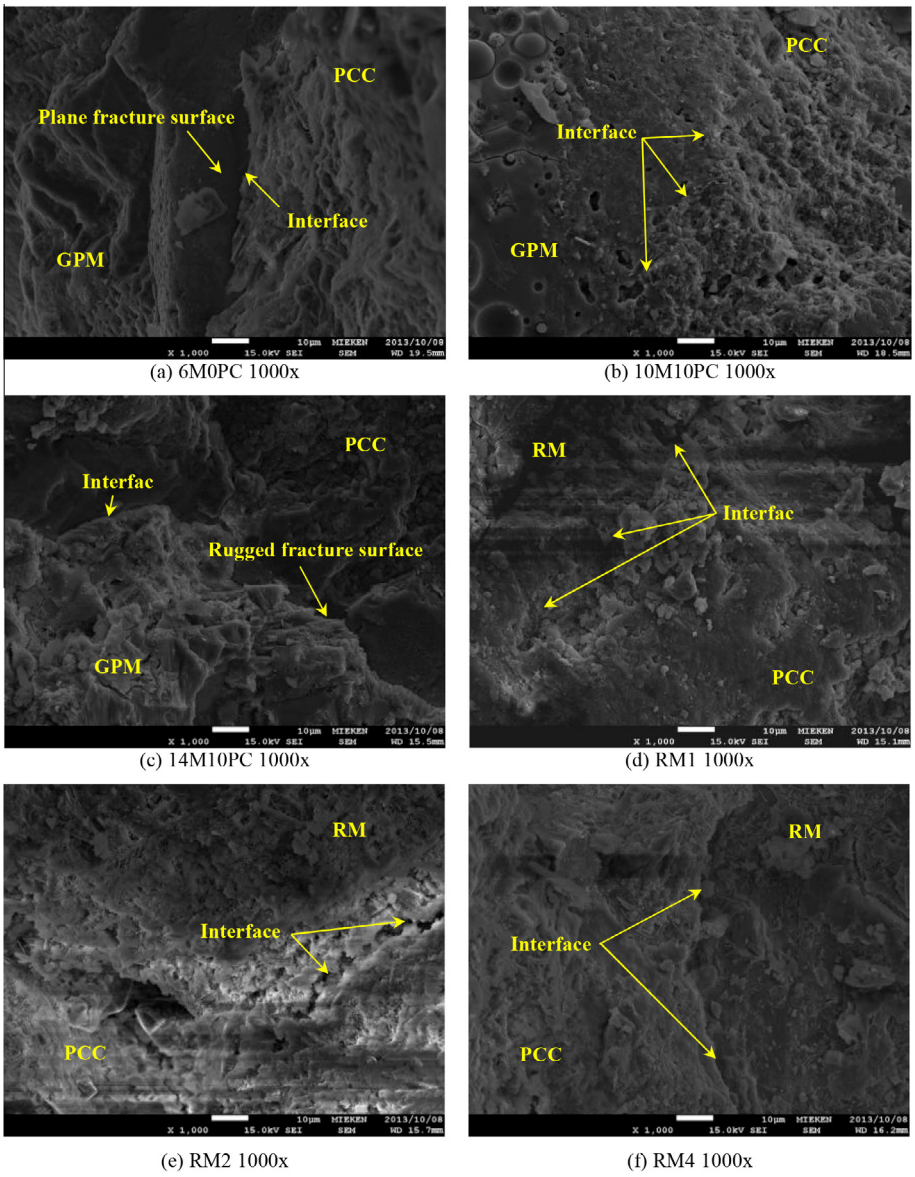

Fig. 7. SEM of interface zone between PCC substrate and GPM or RM.

the mix with low NaOH and without PC mortar (6M0PC). The fracture interfacial zone of the mix with high NaOH and high PC mortar (10M10PC) as shown in Fig. 7b indicated that the bonding surface was still intact. The cracks passed through the PCC substrate and GPM interface, and there was no significant gap between the two bonding surfaces. For the 14M10PC mix as shown in Fig. 7c, the SEM showed a highly irregular or rugged fracture surface with no visible plane fracture surface indicating the good bonding between the two surfaces. The results confirmed the increase in shear bond strength and bending stress with high NaOH and high PC mortar and the associated monolithic failure mode as shown in Fig. 5d and e. The increase in bonding has been reported by Pacheco-Torgal et al. [17]. Also, Shi et al. [28] reported the high tensile strength ratio indicating the better bonding of alkali activated binder than that of conventional Portland cement. Furthermore, it has been reported that when recycled concrete is used, the cementing property is activated both by the alkali activation and by the calcium hydroxide presented in the residual paste [29]. Generally, geopolymer is rich in Si^{4+} and Al^{3+} ions, therefore, it can react with $Ca(OH)_2$ at the surface of PCC substrate leading to increased strength development at the contact zone. Moreover, the increase in Ca^{2+} ion balanced the negative charge of Al^{3+} ions, which resulted in the increase in reaction products at the interface transition zone between PCC substrate and geopolymer matrix leading to a dense interface zone and high strength geopolymer.

For the prism with RM1 (high shear bond and high bending strengths), the SEM result as shown in Fig. 7d indicated that the bonding surface was relatively dense with only a small gap. For the prism with RM2 (high shear bond and high bending strengths) as shown in Fig. 7e, a noticeable gap existed at the interface indicating a relatively low bonding. This corresponded well with the failure mode which cracks were formed in the RM and the interface while the PCC substrate remained relatively intact. For the prism with RM4 (high shear bond and high bending strengths), the SEM result as shown in Fig. 7f indicated that only a small gap was observed at the interface. The SEM results of RM1 and RM4 indicated the good bonding and strength of repair material and corresponded well with the monolithic failure mode.

The results indicated that the performances of GPM containing PC with high NaOH concentrations as a repair material was at least equal to those of commercially available ones according to the slant shear bond test and beam notch filled bending test.

4. Conclusion

The GPM with high NaOH concentration containing PC as additive material gave good performances in the shear bond strength prism test and bending stress of PCC notched beam test. The highest shear bond strength of 24.2 MPa was obtained with 14 M NaOH geopolymer with 10% Portland cement (14M10PC mix). The bending stresses of PCC notched beams with filled GPM were enhanced as expected. The GPM mix with 14 M NaOH and 10% PC gave excellent bending stress of 3.1 MPa. However, with high NaOH concentration (14 M) and high PC (15%), slight decreases in shear bond strength and bending stress were observed. The performance of GPM was found to be comparable to those of the commercial repair materials. The average shear bond strength of RM was 17.9 MPa, while that of GPM was slightly higher at 20.0 MPa. The average improvement of bending stresses of PCC notched beam with filled GPM or RM were 44% and 36%, respectively. In addition, the interface zones between PCC substrate and GPM containing PC as additive were dense and homogenous at contact zone due to the increase in reaction products. The results confirmed the finding of high bending stress and high shear bond strength of mixes with high NaOH and high PC. This indicates the suitability of GPM containing PC as additive for use as an alternative repair material.

Acknowledgements

This work was financially supported by the Higher Education Research Promotion and National Research University Project of Thailand, Office of the Higher Education Commission, through the Advanced Functional Materials Cluster of Khon Kaen University; and KhonKaen University and the Thailand Research Fund (TRF) under the TRF-Senior Research Scholar Contract No. RTA5780004. The authors also would like to acknowledge Dr. Akihiro Maegawa (Mie Prefecture Industrial Research Institute, Japan) for the help with SEM analysis.

References

[1] J. Davidovits, Geopolymers – inorganic polymeric new materials, J. Therm. Anal. 37 (8) (1991) 1633–1656.
[2] F. Pacheco-Torgal, J.A. Labrincha, C. Leonelli, A. Palomo, P. Chindaprasirt, Handbook of Alkali-Activated Cements Mortars and Concretes, Wood Head Publishing Limited – Elsevier Science and Technology, 2014.
[3] P.D. Silva, K. Sagoe-Crenstil, V. Sirivivatnanon, Kinetics of geopolymerization: role of Al_2O_3 and SiO_2, Cem. Concr. Res. 37 (4) (2007) 512–518.
[4] S. Kumar, R. Kumar, S.P. Mehrotra, Influence of granulated blast furnace slag on the reaction, structure and properties of fly ash based geopolymer, J. Mater. Sci. 45 (3) (2010) 607–615.
[5] P. Sukmak, S. Horpibulsuk, S.L. Shen, Strength development in clay–fly ash geopolymer, Constr. Build. Mater. 40 (2013) 566–574.
[6] T. Phoo-ngernkham, A. Maegawa, N. Mishima, S. Hatanaka, P. Chindaprasirt, Effects of sodium hydroxide and sodium silicate solutions on compressive and shear bond strengths of FA–GBFS geopolymer, Constr. Build. Mater. 91 (2015) 1–8.
[7] P. Chindaprasirt, T. Chareerat, S. Hatanaka, T. Cao, High strength geopolymer using fine high calcium fly ash, J. Mater. Civ. Eng. 23 (3) (2011) 264–270.
[8] S. Pangdaeng, T. Phoo-ngernkham, V. Sata, P. Chindaprasirt, Influence of curing conditions on properties of high calcium fly ash geopolymer containing Portland cement as additive, Mater. Des. 53 (2014) 269–274.
[9] T. Phoo-ngernkham, P. Chindaprasirt, V. Sata, S. Hanjitsuwan, S. Hatanaka, The effect of adding nano-SiO_2 and nano-Al_2O_3 on properties of high calcium fly ash geopolymer cured at ambient temperature, Mater. Des. 55 (2014) 58–65.
[10] K. Somna, C. Jaturapitakkul, P. Kajitvichyanukul, P. Chindaprasirt, NaOH-activated ground fly ash geopolymer cured at ambient temperature, Fuel 90 (6) (2011) 2118–2124.
[11] D. Panias, I.P. Giannopoulou, T. Perraki, Effect of synthesis parameters on the mechanical properties of fly ash-based geopolymers, Colloids Surf., A 301 (1–3) (2007) 246–254.
[12] H.M. Abdalla, B.L. Karihaloo, Determination of size-independent specific fracture energy of concrete from three-point bend and wedge splitting tests, Mag. Conc. Res. 55 (2) (2003) 133–141.
[13] P. Nath, P.K. Sarker, Use of OPC to improve setting and early strength properties of low calcium fly ash geopolymer concrete cured at room temperature, Cement Concr. Compos. 55 (2015) 205–214.
[14] T. Phoo-ngernkham, P. Chindaprasirt, V. Sata, S. Pangdaeng, T. Sinsiri, Properties of high calcium fly ash geopolymer pastes containing Portland cement as additive, Int. J. Miner. Metall. Mater. 20 (2) (2013) 214–220.
[15] T. Suwan, M. Fan, Influence of OPC replacement and manufacturing procedures on the properties of self-cured geopolymer, Constr. Build. Mater. 73 (2014) 551–561.
[16] S. Hu, H. Wang, G. Zhang, Q. Ding, Bonding and abrasion resistance of geopolymeric repair material made with steel slag, Cement Concr. Compos. 30 (3) (2008) 239–244.
[17] F. Pacheco-Torgal, J.P. Castro-Gomes, S. Jalali, Adhesion characterization of tungsten mine waste geopolymeric binder. Influence of OPC concrete substrate surface treatment, Constr. Build. Mater. 22 (3) (2008) 154–161.
[18] S. Songpiriyakij, T. Pulngern, P. Pungpremtrakul, C. Jaturapitakkul, Anchorage of steel bars in concrete by geopolymer paste, Mater. Des. 32 (5) (2011) 3021–3028.
[19] C. Suksiripattanapong, S. Horpibulsuk, P. Chanprasert, P. Sukmak, A. Arulrajah, Compressive strength development in geopolymer masonsy units manufactured from water treatment sludge, Constr. Build. Mater. 82 (2015) 20–30.
[20] ASTM C807, Standard Test Method for Time of Setting of Hydraulic Cement Mortar by Modified Vicat Needle, vol. 04.01, Annual Book of ASTM Standard, 2003.
[21] K.E. Hassan, J.J. Brooks, L. Al-Alawi, Compatibility of repair mortars with concrete in a hot–dry environment, Cement Concr. Compos. 23 (1) (2001) 93–101.
[22] ASTM C882, Standard Test Method for Bond Strength of Epoxy-Resin Systems used With Concrete by Slant Shear, vol. 04.02, Annual Book of ASTM Standard, 2005.

[23] FM 3-C 882, Florida Test Method for Performance of epoxy-resin systems with concrete by slant shear and compressive strength, In Florida Department of Transportation Standard Specifications for Road and Bridge Construction, 2015, July.
[24] B. Bharatkumar, B. Raghuprasad, D. Ramachandramurthy, R. Narayanan, S. Gopalakrishnan, Effect of fly ash and slag on the fracture characteristics of high performance concrete, Mater. Struct. 38 (1) (2005) 63–72.
[25] K. Dombrowski, A. Buchwald, M. Weil, The influence of calcium content on the structure and thermal performance of fly ash based geopolymers, J. Mater. Sci. 42 (9) (2007) 3033–3043.
[26] Z. Zuhua, Y. Xiao, Z. Huajun, C. Yue, Role of water in the synthesis of calcined kaolin-based geopolymer, Appl. Clay Sci. 43 (2) (2009) 218–223.
[27] W.K.W. Lee, J.S.J. Van Deventer, The effects of inorganic salt contamination on the strength and durability of geopolymers, Colloids Surf., A 211 (2–3) (2002) 115–126.
[28] X.S. Shi, F.G. Collins, X.L. Zhao, Q.Y. Wang, Mechanical properties and microstructure analysis of fly ash geopolymeric recycled concrete, J. Hazard. Mater. 237–238 (2012) 20–29.
[29] S. Achtemichuk, J. Hubbard, R. Sluce, M.H. Shehata, The utilization of recycled concrete aggregate to produce controlled low-strength materials without using Portland cement, Cement Concr. Compos. 31 (8) (2009) 564–569.

Chiang Mai J. Sci. 2016; 43(2) : 402-408
http://epg.science.cmu.ac.th/ejournal/
Contributed Paper

Interfacial Transition Zone of Pervious Cement and Geopolymer Concrete Containing Crushed Clay Brick

Vanchai Sata [a], Ampol Wongsa [a], Kiatsuda Somna*[b] and Prinya Chindaprasirt [a]

[a] Sustainable Infrastructure Research and Development Center, Department of Civil Engineering, Faculty of Engineering, Khon Kaen University, Khon Kaen 40002, Thailand.

[b] Department of Civil Engineering, Faculty of Engineering and Architecture, Rajamangala University of Technology Isan, Nakhon Ratchasima, 30000, Thailand.

*Author for correspondence; e-mail: kiatsuda.somna@gmail.com

Received: 15 September 2015
Accepted: 24 January 2016

ABSTRACT

This research studies the interfacial transition zones (ITZ) of pervious geopolymer concrete and pervious cement concrete containing recycled coarse aggregate from crushed broken clay brick (RCB). Geopolymer and cement pastes were used as binder. Geopolymer was synthesized using fly ash, sodium hydroxide solution and sodium silicate. Physical observation, optical microscope (OM) and SEM, EDS techniques were used to characterize ITZ of both pervious concretes. XRD technique also used to characterize the crystalline phases of geopolymer pastes and cement paste. In addition, the compressive strength of geopolymer pastes, cement paste, pervious geopolymer concrete, and cement pervious concrete were also determined at the age of 7 days. The results showed that the ITZ of pervious geopolymer concrete and pervious cement concrete were totally different in shape. The ITZ of pervious cement concrete was wider than those of geopolymer system. It was also found that geopolymerization reaction occurred rapidly when fly ash was mixed with alkali activated solutions and it might not contribute to the network in ITZ while hydration reaction from cement paste and water had $Ca(OH)_2$ which had an opportunity to coat around the aggregates. Although cement paste presented the highest compressive strength as a binder, the compressive strength of cement pervious concrete was lower than those of geopolymer pervious concrete.

Keywords: pervious concrete, geopolymer, recycled aggregate, crushed clay brick

1. INTRODUCTION

Pervious concrete is special type of concrete with a high porosity compared to normal concrete. It made by coarse aggregates and used cement paste to coat the aggregates. This type of concrete allows water to pass through the concrete [1-3]. Basically, pervious concrete consists of binder, coarse aggregates, water and admixture. The binder volume can be composed of cement and water. Then, the binder consistency coats each aggregate particle and provides a good workability performance. Not only cement paste but also cementitious material such as geopolymer can be used as binder for

pervious geopolymer. Geopolymer is an innovative material which was synthesized by mixing between aluminosilicate material such as fly ash and alkali activated solution such as sodium hydroxide (NaOH). Generally, there are three types of geopolymer products which are polysialate (Si-O-Al), polysialate siloxo (Si-O-Si-O-Al) and polysialate disiloxo (Si-O-Si-O-Si-O-Al). Geopolymer presented excellent mechanical properties such as high compressive strength, low shrinkage and acid resistance [4]. In addition, Sata et al. [5] crushed recycle structural concrete member and RCB can be used as an aggregate for pervious concrete instead of natural coarse aggregate. Pervious concrete have been applied to civil engineering field such as permeable pavement and thermal insulation.

There are at least three phase composite in concrete which are (1) bulk cement paste, (2) ITZ cement paste, and (3) rock and sand, collectively called aggregates [6]. Since pervious concrete had only binder coats around aggregate, the interfacial transition zone (ITZ) between binder and aggregates is very essential and should be discussed. It was found that ITZ is a weakness zone in the microstructure of concrete, but it is one of the most important factors influencing the performance of concrete. The ITZ is not a definite "zone", but a region of "transition" [7]. The characterizations of ITZ in concrete have been reported. Nevertheless, the ITZ of pervious concrete is complex and has not been fully understood yet.

Thus, this research aims to study ITZ microstructure of pervious geopolymer and pervious cement concrete containing recycled coarse aggregate from crushed broken clay brick (RCB). ITZ was described by using optical microscope (OM) and scanning electron microscope (SEM) in order to clearly observe fracture surface at ITZ. X-ray diffraction also used to characterize binder both cement paste and geopolymer pastes. Compressive strength of binder pastes and pervious concretes were investigated at the age of 7 days. The understanding of ITZ in pervious concrete was obtained.

2. MATERIALS AND MOTHOD

2.1 Materials

Fly ash was obtained from Mae Moh Electricity Power Plant Station, Lumpang province, Thailand. It had a median particle size of 50 μm, a Blaine fineness of 2250 cm^2/g, and 45% (by weight) retained on 45 μm sieve. Fly ash had sum of SiO_2, Al_2O_3 and Fe_2O_3 of 71.7% and high calcium content of 19.4% indicated Class C pozzolan according to ASTM C618 [8].

Two concentrations of sodium hydroxide (NaOH) at 15 and 20 molar, and a commercial grade sodium silicate solution (Na_2SiO_3) were used to be an alkaline activator for geopolymer pastes.

Recycled aggregate from crushed broken clay brick (RCB) with 4.5-9.5 mm diameter obtained from construction site. RCB was from local clay bricks with compressive strengths of 5.0-9.0 MPa. The specific gravity of RCB was 2.02 with dry-rodded density of 950 kg/m^3. RCB had high water absorption at 16.2% and high Los Angeles abrasion loss at 42.4%.

2.2 Synthesis Pervious Geopolymer Concrete and Pervious Cement Concrete

The mixing of geopolymer pervious concrete, fly ash was used to be starting material of geopolymer. A ratio of fly ash to RCB of 1 to 8 by weight was applied. The Na_2SiO_3/NaOH was kept at 0.5 and NaOH concentration at 15 and 20 M were prepared for geopolymer pastes. The liquid to binder ratio was kept constant at 0.45.

The mixing of pervious geopolymer concrete, fly ash and NaOH were mixed in a

pan-type mixer for 5 min. Then, RCB was added and mixed for 4 min. The last step mixing, Na_2SiO_3 was added and mixed for another min.

The mixing of pervious cement concrete, cement was mixed with water at liquid to binder ratio of 0.45 for 5 min, then, RCB was added and mixed for 4 min.

After mixing both two types of pervious concrete, they were cast in cylinder mold with 100 mm diameter and 200 mm height.

2.3 Study Property of Pervious Concrete

The cement specimens were cured in water until the testing age. For geopolymer specimens were cured at 60 °C for 48 hr. After that, they were wrapped with a thin plastic sheet and stored in the 25°C controlled. The compressive strength of both geopolymer and cement pervious concrete were determined at the age of 7 days in accordance with ASTM C39. The results were presented as the average value of three specimens.

2.4 Study Microstructure of ITZ

After the compressive strength test, a piece of geopolymer pervious concrete and cement pervious concrete were collected to study microstructure of ITZ as followed:

Optical microscope (OM) was used to observe surface of pervious geopolymer and pervious cement concrete containing RCB by visible light.

Scanning electron microscope (SEM) and Energy Dispersive Spectroscopy (EDS) technique were used to characterize ITZ zone of pervious geopolymer and pervious cement concrete containing RCB.

2.5 Characterization Binder by XRD Technique

X-Ray Diffractometer (XRD) was used to study the crystalline phase of cement paste, geopolymer pastes and RCB. X-ray diffractometer using D8000 with CuKα (k =1.54056 Å) radiation generated at 40 mA and 40 kV. Data collection was carried out in the 2q range 10° - 80°, with a step time of 0.1 sec.

3. RESULTS AND DISCUSSION

3.1 Physical Observation of Pervious Cement and Pervious Geopolymer Concretes Containing RCB

Figure 1 show physical observation of pervious cement and pervious geopolymer concretes containing RCB, respectively. Both pervious cement concrete and pervious geopolymer concrete had a surface that looks similar. It was clearly seen the color of materials by physical observation. RCB was red and binders (cement paste and geopolymer paste) were gray. It can be noticed that pervious cement concrete had ITZ wider than pervious geopolymer concrete and surrounded RCB. In order to clearly observe ITZ of pervious geopolymer and pervious cement concrete, OM technique have been used and discussed in the next session.

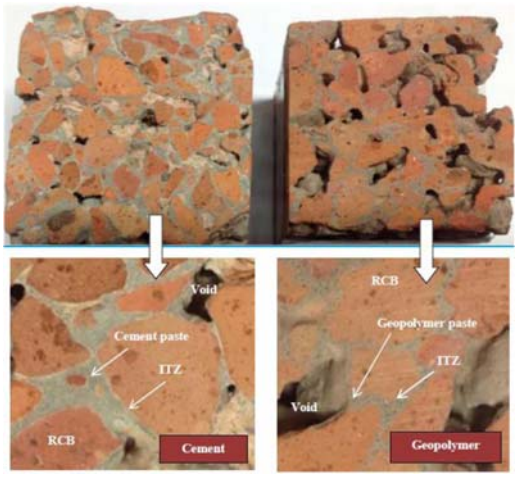

Figure 1. Physical observation of pervious concrete containing RCB.

3.2 Characterized the Interfacial Transition Zone (ITZ) by OM Technique

Figure 2 shows ITZ between geopolymer pastes and RCB (Figure 2 (a) and Figure 2 (b)) and Figure 2(c) shows ITZ between cement paste and RCB. ITZ was characterized by optical microscope (OM) technique.

Geopolymer pervious concrete both 15 molar (15M GEO) and 20 molar (20M GEO) showed the same texture which were connected by without shape of ITZ. On the other hand, ITZ between cement paste and RCB had a large thickness. In addition, different color of geopolymer pastes, cement paste and RCB were clearly observed. It can be obvious that RCB were red, cement pastes were gray, geopolymer pastes were brown and the white-yellow color which was possible be reaction between cement paste and RCB was occurred at ITZ. After using high magnification in OM technique, it was clearly seen white-yellow color at ITZ.

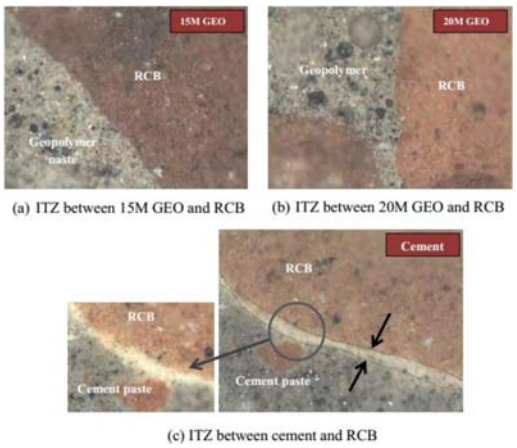

(a) ITZ between 15M GEO and RCB (b) ITZ between 20M GEO and RCB

(c) ITZ between cement and RCB

Figure 2. ITZ of pervious concrete.

It can be mentioned that fly ash react with alkali solution quickly, ITZ zone between geopolymer and RCB hardly seen in the surface. On the other hand, hydration reaction from cement paste has product of calcium hydroxide (CH) which can form CSH gel when it had silica source to react with CH. It is possible that calcium hydroxide from hydration product react with silica from RCB and present ITZ zone as can be seen by OM technique. In order to deeply understand ITZ of geopolymer pervious concrete and cement pervious concrete, SEM and EDX techniques were investigated to characterize fracture surface and element composition on surface of pervious concrete as described in the next session.

3.3 Characterized the Interfacial Transition Zone (ITZ) by SEM and EDS Techniques

After study the ITZ zone of pervious concrete by OM technique, the results show the different shape of ITZ between pervious geopolymer concrete and pervious cement concrete containing RCB. Thus, SEM observations aim to characterize ITZ zone in high magnification. EDS analysis also investigated at binder, aggregate and ITZ zone in order to discuss the influence of the element with respect to aggregate.

ITZ between 15M GEO and RCB; 20M GEO and RCB are shown in Figure 3 and Figure 4, respectively. The reaction products in the ITZ grew and clearly observed in all samples. 15M GEO and 20M GEO had the similar ITZ morphology. The high percentages of silicon were found. Interestingly, the percentage of silica at ITZ (position 2) was slightly higher than that of geopolymer paste (position 1) which might be the results of leaching from RCB (position 3). The morphology of 20M GEO can be noticed that it hardly seen ITZ between geopolymer paste and RCB. Both of geopolymer and RCB had a tendency homogeneous.

ITZ between cement and RCB is shown in Figure 5. It is noticed that cement paste presented thickness of ITZ at most. It can be seen the different texture of each materials.

RCB had rough texture while cement paste had smooth texture. At ITZ zone, the long rough shape can be observed. It was found high percentage calcium element in position 2 as can be detected by EDS technique. A few researchers suggested that calcium hydroxide had rich in ITZ area and presented weakness point of concrete [9].

From EDS technique at 1000X magnification, it was found that ITZ morphology had high percentage of calcium and silicon. The product at ITZ might be from pozzolanic reaction between calcium hydroxide from cement hydration and silica in RCB. Scrivener et al. [7] suggested that ITZ depended on the microstructural feature being considered and the degree of reaction. At the early state of hydration, calcium silicate hydrate (CSH gel) and calcium hydroxide (CH) are formed through the solution.

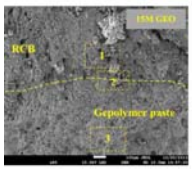

Element	Atomic %		
	Position 1	Position 2	Position 3
	RCB	ITZ	Geopolymer paste
Al	6.05	5.38	5.04
Si	21.37	18.24	12.56
Ca	0.30	0.61	2.25
Na	1.09	1.14	3.67

Figure 3. ITZ between 15M GEO and RCB.

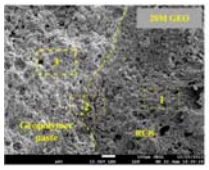

Element	Atomic %		
	Position 1	Position 2	Position 3
	RCB	ITZ	Geopolymer paste
Al	5.22	5.13	4.14
Si	14.16	14.39	12.34
Ca	0.61	0.82	2.15
Na	1.10	6.44	4.75

Figure 4. ITZ between 20M GEO and RCB.

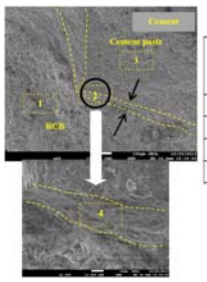

Element	Atomic %			
	Position 1	Position 2	Position 3	Position 4
	RCB	ITZ	Cement paste	ITZ (1000X)
Al	1.51	13.88	25.21	1.47
Si	68.06	32.78	119.33	17.01
Ca	11.51	46.48	18.07	53.06
Na	-	-	-	-

Figure 5. ITZ between cement and RCB.

3.4 X-ray Diffraction Analysis

Figure 6 shows XRD patterns of geopolymer pastes and cement paste. It was found that XRD patterns of both 15M GEO and 20M GEO had both amorphous phase and crystalline phases. The XRD pattern was changed slightly after the specimen had 20M NaOH concentrations. Nevertheless, both 15M GEO and 20M GEO found that amorphous hump of SiO_2 were observed at 2q between 20° - 40°. New crystalline phases of sodium aluminum silicate hydrate, calcium silicate hydrate and chabazite-Na were found which came from geopolymerization reaction of geopolymer. In addition, the remaining of unreacted fly ash which was crystalline of quartz (SiO_2) was also found.

In cement paste, The major products of phase hydration would be calcium silicate hydrate gel (CSH) and calcium hydroxide ($Ca(OH)_2$) [10]. XRD pattern of cement pastes had crystalline phases of katoite silicatian, cebollite and portlandite which occurred from hydration reaction.

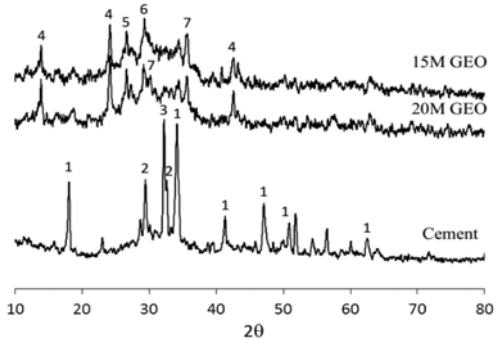

Figure 6. XRD pattern of geopolymer pastes (15M GEO and 20M GEO) and cement paste.

Figure 7 showed XRD pattern of RCB. It was found that RCB mainly composed of crystalline phases of quartz. Actually, RCB made from clay, lime, sand and concrete. Clay has high in silica content.

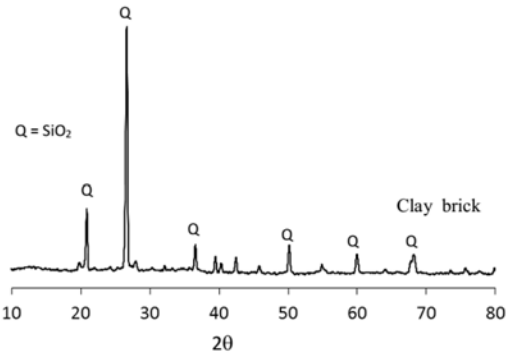

Figure 7. XRD pattern of RCB.

3.5 Mechanical Properties of Binder Pastes and Pervious Concretes

3.5.1 Compressive strength of pastes

Figure 8 shows compressive strength of cement paste and geopolymer pastes at the age of 7 days. Cement paste and geopolymer pastes were used to be binder which coated RCB in this research. The compressive strength of pastes was investigated in order to study effect of strength of pastes on ITZ of pervious concrete. The results showed that cement paste provided the highest compressive strength of 78.1 MPa. For geopolymer paste, compressive strength of 15M GEO was higher than that of 20M GEO. It can be described that the use of exceed concentration of sodium hydroxide leads to inhibit dissolution of the initial solid materials and decreased geopolymerization reaction and hence lower compressive strength was occurred [11-13].

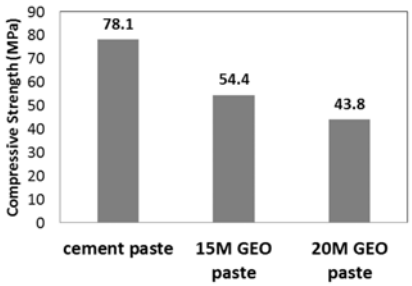

Figure 8. Compressive strength of cement paste and geopolymer pastes (15M GEO and 20M GEO) at the age of 7 days.

3.5.2 Compressive strength of pervious concrete

The compressive strength of pervious cement and pervious geopolymer concretes at the age of 7 days is shown in Figure 9. The results showed that 20M GEO was the highest compressive strength of 6.6 MPa while compressive strength of cement and 15M GEO were 4.5 and 4.0 MPa, respectively. Although pervious cement concrete had high compressive strength in term of binder paste, ITZ of pervious cement concrete was weak point and high porosity as shown in compressive strength of pervious concrete results. It was mentioned that the interfacial transition zone (ITZ) in cementitious composite is often considered as a weak phase, compared to aggregate and bulk paste [14-15]. On the other hand, 20M GEO paste presented the lowest compressive strength, but, 20M GEO concrete provided the slightly higher compressive strength than that of 15M GEO concrete. It might be described that the 20M GEO with high concentration NaOH solution increased the amount of silica and alumina ions and resulted in a high degree of geopolymerization. In addition, the silica and alumina in RCB aggregate could also leach out and assisted the geopolymerization which led to a strong bonding between geopolymer paste and aggregate causing the improvement of compressive strength [16].

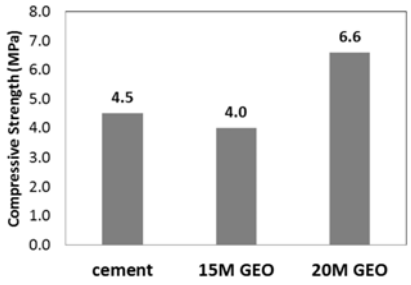

Figure 9. Compressive strength of pervious cement concrete and pervious geopolymer concretes at the age of 7 days.

4. CONCLUSIONS

The study of interfacial transition zone microstructure of pervious cement concrete and pervious geopolymer concrete containing RCB can conclude as follows:

1. ITZ of pervious cement concrete was totally different from ITZ of pervious geopolymer concrete due to difference on starting material and reaction mechanism.

2. ITZ of cement concrete had larger than ITZ of geopolymer concrete as can be seen by both OM and SEM techniques.

3. Although cement paste presented the highest compressive strength, pervious cement concrete provided the lowest compressive strength due to the different in ITZ.

ACKNOWLEDGMENT

The authors would like to acknowledge the financial supports from the Higher Education Research Promotion and National Research University Project of Thailand, Office of the Higher Education Commission, through the Advanced Functional Materials Cluster of Khon Kaen University; the Thailand Research Fund (TRF) and Khon Kaen University under TRF Research Career Development (Grant No. RSA5780013) and TRF Senior Research Scholar (Grant No. RTA5780004).

REFERENCES

[1] Park S.B. and Tia M., *Cement and Concrete Research*, 2004; **34(2)**: 177-184.

[2] Park S.B., Seo D.S. and Lee J., *Cement and Concrete Research*, 2005; **35(9)**: 1846-1854.

[3] Wong J.M., Glasser F.P. and Imbabi M.S., *Cement and Concrete Composites*, 2007; **29(9)**: 647-655.

[4] Davidovits J., *Geopolymer Chemistry and Application. Institute Geopolymer*. 16 rue Galilee F-02100 Saint-Quentin, France; 2008. p. 585.

[5] Sata V., Wongsa A. and Chindaprasirt P., *Construction and Building Materials,* 2013; **42**: 33-39.

[6] Garboczi E.J., and Bentz D.P., American Society of Civil Engineers, Proceedings of the Fourth Materials Conference, November, 1996, Washington, DC.

[7] Scrivener K.L., Crumbie A.K. and Laugesen P., *Interface Science*, 2004; **12**: 411-421.

[8] ASTM C618-08a. Standard Specification for Coal Fly Ash and Raw or Calcined Natural Pozzolan for Use in Concrete. *Annual Book of ASTM Standards*, American Society for Testing and Materials, Philadelphia, USA, 2008; 04.02.

[9] Gao J.M., Qian C.X., Liu H.F., Wang B. and Li L., *Cement and Concrete Research*, 2005; **35(7)**: 1299-1304.

[10] Taylor H.F.W, *Cement Chemistry*, Academic Press, London, 1990.

[11] Lee W.K.W. and Van Deventer J.S.J., *Colloids and Surfaces A*, 2002; **211**: 49-66.

[12] Zuhua Z., Xiao Y., Huajun Z. and Yue C., *Applied Clay Science*, 2009; **43(2)**: 218-223.

[13] Somna K., Jaturapitakkul C., Kajitvichyanukul P. and Chindaprasirt P., *Fuel*, 2011; **90**: 2118-2124.

[14] Gao Y., De Schutter G., Ye G., Tan Z. and Wua K., *Engineering*, 2014; **60**: 1-13.

[15] Rangaraju P.R., Olek J. and Diamond S., *Cement and Concrete Research*, 2010; 40**(11)**: 1601-1608.

[16] Zaetang Y., Wongsa A., Sata V. and Chindaprasirt P., *Construction and Building Materials,* 2015; **96**: 289-295.

Applied Surface Science 369 (2016) 334–340

Contents lists available at ScienceDirect

Applied Surface Science

journal homepage: www.elsevier.com/locate/apsusc

Dielectric and piezoelectric properties of lead-free $Ba_{0.85}Ca_{0.15}Ti_{0.9-x}Zr_{0.1}Cu_xO_3$ ceramics synthesized by a hydrothermal method

Sitchai Hunpratub[a], Sumalin Phokha[b], Santi Maensiri[c], Prinya Chindaprasirt[d,*]

[a] Material Science and Nanotechnology Programs, Faculty of Science, Khon Kaen University, Khon Kaen 40002, Thailand
[b] Department of Physics, Faculty of Science, Udon Thani Rajabhat University, Udon Thani 41000, Thailand
[c] School of Physics, Institute of Science, Suranaree University of Technology, Nakhon Ratchasima 30000, Thailand
[d] Sustainable Infrastructure Research and Development Center, Department of Civil Engineering, Faculty of Engineering, Khon Kaen University, Khon Kaen 40002, Thailand

ARTICLE INFO

Article history:
Received 14 October 2015
Received in revised form 29 January 2016
Accepted 30 January 2016
Available online 11 February 2016

Keywords:
$Ba_{0.85}Ca_{0.15}Ti_{0.9}Zr_{0.1-x}Cu_xO_3$
Lead-free ceramics
Hydrothermal method
Dielectric constant
Ferroelectric hysteresis loop
Piezoelectric charge coefficient

ABSTRACT

$Ba_{0.85}Ca_{0.15}Ti_{0.9}Zr_{0.1-x}Cu_xO_3$ (BCTZC) nanopowders were synthesized using a hydrothermal method after which they were pressed into discs and sintered in air at 1300 °C for 3 h to form ceramic samples. The phase and microstructure of the powder and ceramic samples were characterized by X-ray diffraction (XRD) and scanning electron microscopy (SEM). The XRD results indicated that the ceramic samples exhibited a tetragonal structure and that CuO, $BaZrO_3$ or $CaTiO_3$ impurity phases, which had been present in the powder samples, were not observed. The average grain sizes in the ceramic samples were found to be 17.0, 16.1, 20.0, 18.1 and 19.6 μm for Cu mole fractions x of 0.002, 0.004, 0.006, 0.008 and 0.01, respectively. The dielectric constants, ferroelectric hysteresis loops and piezoelectric charge coefficients of the BCZTC ceramic samples were also investigated. Optimum values for the relative dielectric constant (ε'), $\tan\delta$ and piezoelectric charge coefficient (d_{33}) of the samples were 3830, 0.03 and 306 pC/N, respectively, in the Cu mole fraction samples with $x = 0.002$.

© 2016 Elsevier B.V. All rights reserved.

1. Introduction

To achieve satisfactory piezoelectric properties in materials from which electronic devices are to be fabricated most attention has been given to the materials lead zirconate ($PbZrO_3$) and lead titanate ($PbTiO_3$) or mixtures of these compounds (PZT) which are strongly piezoelectric, a property which is thought to be due to the coexistence of two phases with a composition dependent phase transition between them (morphotropic phase boundary or MPB) [1]. In such a material the polarization can be easily rotated between the $<111>_R$ and $<001>_T$ states by the application of an external stress or an electric field [2]. There are many lead-free materials with the perovskite structure such as $BaTiO_3$ (BT) [3,4], $(Bi,Na)TiO_3$ (BNT) [5], and $(Na,K)NbO_3$ (NKN) [6] which could replace lead compounds in electronic devices however the piezoelectric coefficients of these compounds are low compared with the lead-containing compounds. Recently, Liu and Ren [7] found enhanced piezoelectric properties in $0.5BaZr_{0.2}Ti_{0.8}O_3$–$0.5(Ba_{0.7}Ca_{0.3}TiO_3)$ or BZT–BCT ceramics with a piezoelectric coefficient d_{33} of ~600 pC/N which is higher than that obtained with the PZT material system. It is also thought that this enhanced property in BZT–BCT has been achieved due to the existence of an MPB near room temperature and this has stimulated considerable interest in this compound [8–14].

Previously, BZT–BCT compounds have been formed by high temperature synthesizing (~1300 °C) and sintering (~1450 °C) although some efforts have been focused on reducing the processing temperature of by the addition of oxides such as MnO_2, CuO, CeO_2, Ga_2O_3 and Y_2O_3 to aid the sintering process [15–19]. For example, an optimum piezoelectric values of d_{33} ~306 pC/N was obtained from $Ba_{0.85}Ca_{0.15}Ti_{0.9}Zr_{0.1}O_3$–$MnO_2$ ceramics synthesized at the low calcining temperature of 1100 °C for 4 h followed by sintering at 1300 °C for 2 h [15]. Cui et al. [16] also reported d_{33} values of 510 pC/N obtained from CuO–$Ba_{0.85}Ca_{0.15}Ti_{0.9}Zr_{0.1}O_3$ ceramics which had been sintered at a temperature of 1350 °C for 4 h. d_{33} values in the range of 440–600 pC/N were also obtained when CeO_2, Ga_2O_3 and Y_2O_3 were incorporated into $(Ba,Ca)(Ti,Zr)O_3$ ceramics that were sintered at a temperature of 1350 °C [17–19]. Even though the sol–gel and hydrothermal sample preparation methods are associated with lower sintering temperatures compared to conventional solid state methods [20,21] the d_{33} values obtained have

* Corresponding author.
E-mail address: prinya@kku.ac.th (P. Chindaprasirt).

http://dx.doi.org/10.1016/j.apsusc.2016.01.273
0169-4332/© 2016 Elsevier B.V. All rights reserved.

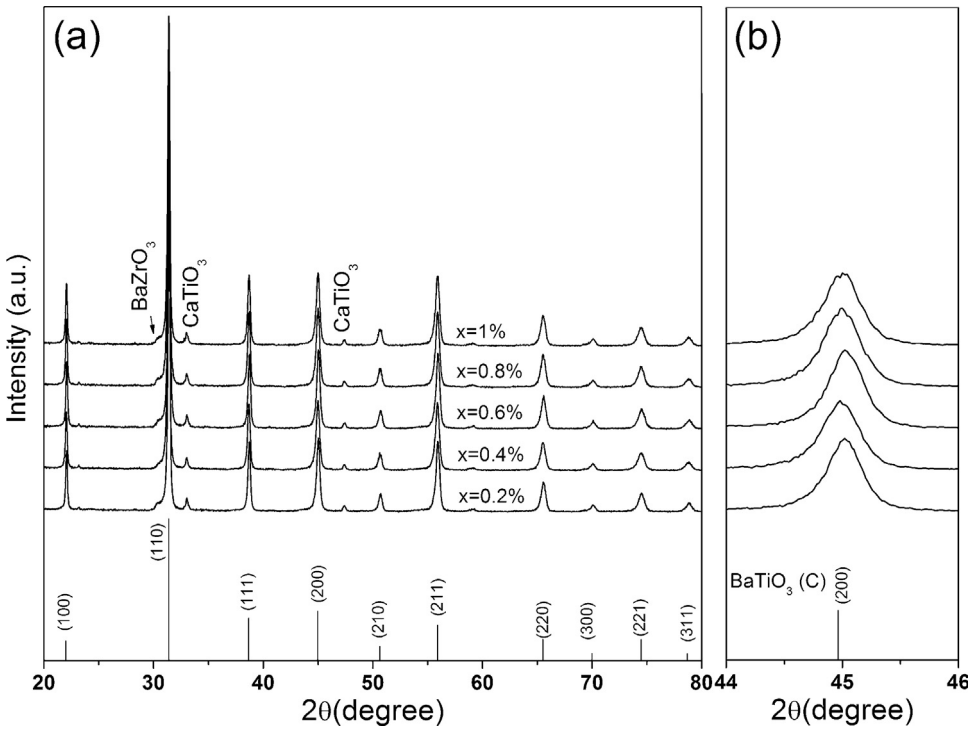

Fig. 1. XRD patterns of BCTZC powders with different Cu mole fractions which were hydrothermally treated for 16 h at 240 °C.

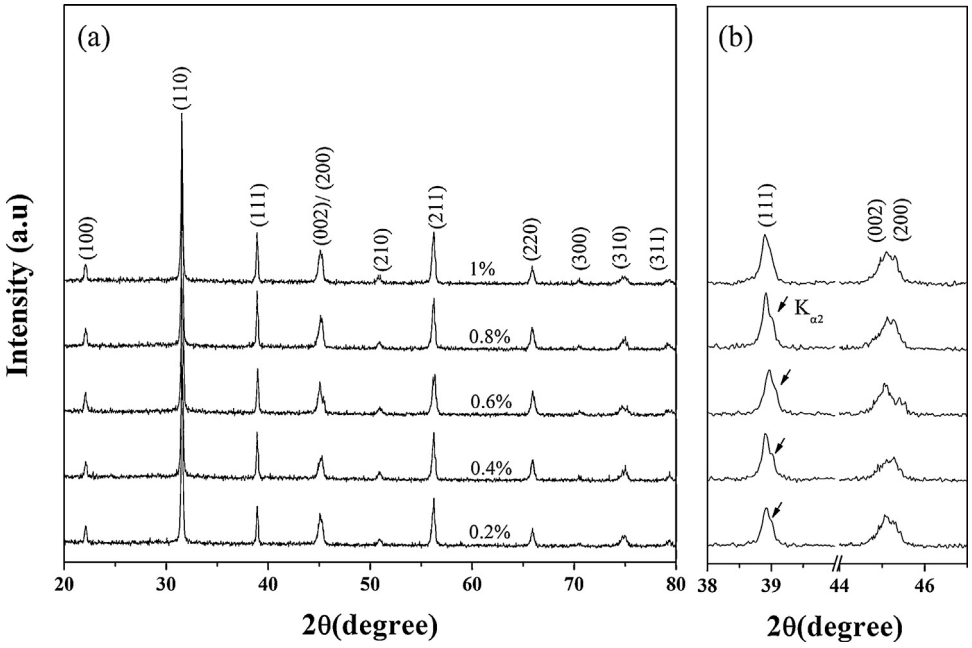

Fig. 2. XRD patterns obtained from BCTZC ceramics with different Cu contents which were sintered at 1300 °C for 3 h. (a) $20^\circ < 2\theta < 80^\circ$ and (b) $38^\circ < 2\theta < 47^\circ$.

generally been lower than for materials prepared by the conventional solid state method. Thus to obtain higher d_{33} values, most studies have added other oxides or employed a higher sintering temperature to create materials that are suitable for application in actuator devices.

In this study, we report on the synthesis of $Ba_{0.85}Ca_{0.15}Ti_{0.9-x}Zr_{0.1}Cu_xO_3$ ($x = 0.002, 0.004, 0.006, 0.008$ and 0.01) nanopowders using a hydrothermal method, from which ceramic samples were prepared by sintering for 3 h at the low temperature of 1300 °C. The crystal structure and morphology of the samples were investigated by X-ray diffraction (XRD) and scanning electron microscopy (SEM) after which the dielectric constants, ferroelectric hysteresis loops and piezoelectric charge coefficients of the BCZTC ceramics were also measured.

2. Experimental

The $Ba_{0.85}Ca_{0.15}Ti_{0.9-x}Zr_{0.1}Cu_xO_3$ powders were prepared by a hydrothermal method using $Ba(OH)_4$ (95%, Aldrich), $Ca(NO_3)_2{\cdot}4H_2O$ (99.9%, Kanto Chemical), $ZrCl_2O{\cdot}8H_2O$ (99%, Kanto Chemical), $Cu(NO_3)_2{\cdot}3H_2O$ (99.5%, Carlo Erba) and TiO_2 (99%, Aldrich) as the starting materials. Initially, all materials were added

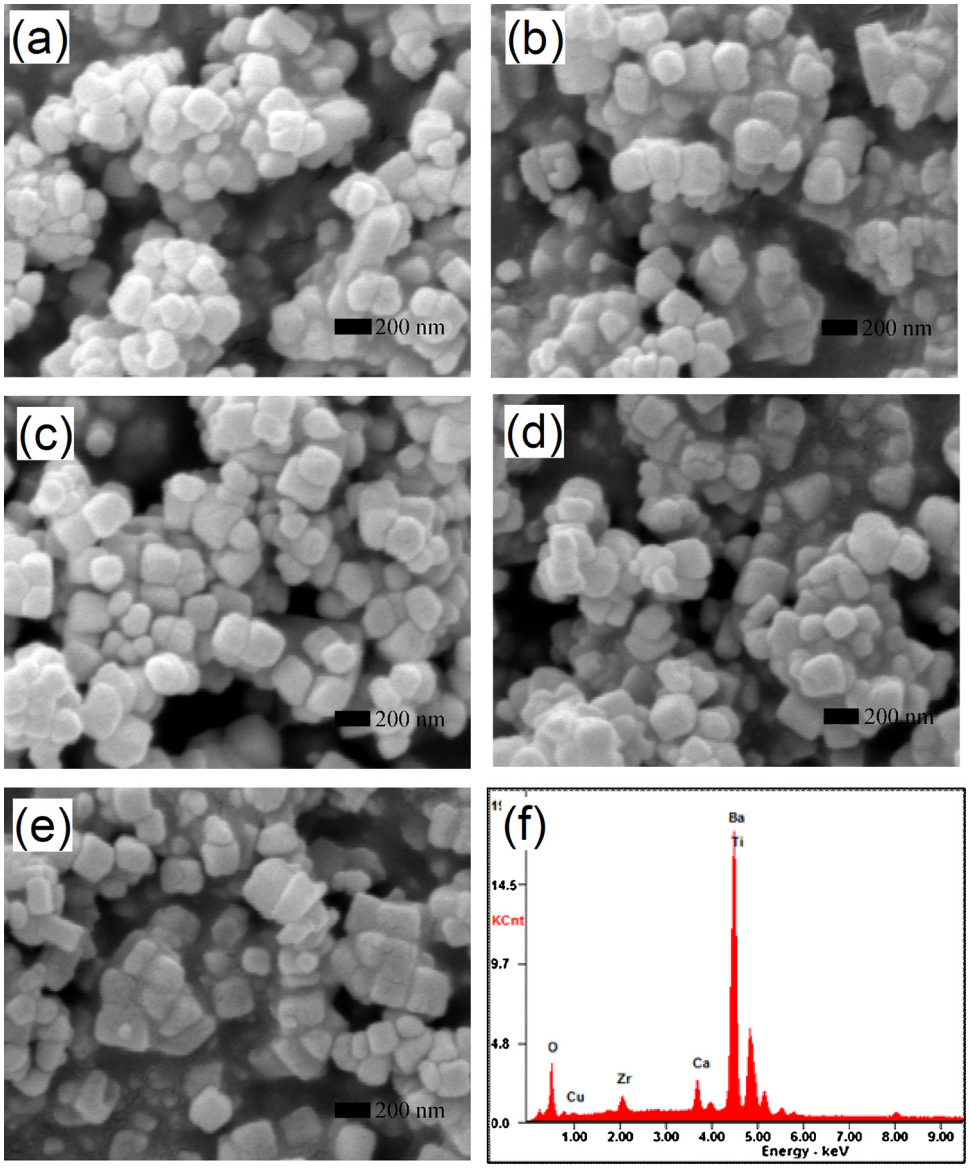

Fig. 3. SEM images obtained from BCTZC powders hydrothermally treated at 240 °C for 16 h and containing Cu mole fractions of: (a) 0.002; (b) 0.004; (c) 0.006; (d) 0.008; and (e) 0.01 and (f) typical EDX spectrum obtained from the sample containing a Cu mole fraction of 0.01.

to de-ionized water at room temperature and dissolved using vigorous magnetic stirring for 10 h after which 10 M NaOH was added to promote the formation of nanopowders at the relatively low temperatures employed in the hydrothermal treatment. This solution was then stirred at room temperature for a further 10 h to ensure complete dissolution before being transferred to a teflon-lined stainless steel autoclave for hydrothermal treatment at 240 °C for 16 h after which it was cooled to room temperature. The product was washed with de-ionized water to remove sodium ions and dried in an oven at 80 °C before characterization by XRD and SEM. The powders obtained by the process described above were ground and mixed with 3% wt. polyvinyl alcohol (PVA) binder before being pressed into 13 mm diameter discs of 1.5 mm thickness. The discs were pre-sintered at 500 °C for 1 h to burn off the PVA and then sintered in air at 1300 °C for 3 h to form a set of ceramic samples.

Both the nanopowder and ceramic samples were characterized by XRD (PW3040 Philips X-ray diffractometer, the Netherlands) using CuK_α radiation ($\lambda = 0.15406$ nm) and the morphology and composition of the samples were characterized using an SEM (JEOL VP1450, UK). The ceramic samples were polished to a thickness of about 1 mm and were silver painted on both sides to form electrodes. The dielectric properties of the polished ceramics were measured at different frequencies in the temperature range from −50 °C to 200 °C using an Agilent 4294A precision impedance analyzer. The ferroelectric hysteresis loops obtained at room temperature from the ceramic samples were measured by a Sawyer–Tower circuit at a frequency of 50 Hz. The ceramic samples were polarized at room temperature in silicon oil for 20 min with the use of an electric field of 1.5 kV/mm and after being held at room temperature for 24 h their piezoelectric charge coefficients (d_{33}) were measured using a d_{33} meter.

3. Results and discussion

The XRD patterns obtained from the BCTZC powders hydrothermally treated at 240 °C for 16 h are shown in Fig. 1 from which it can be seen that the main peaks in all powder samples suggest a cubic phase similar to cubic $BaTiO_3$ (PDF file No. 31-0174). In addition to the main set of peaks there are also peaks associated with

Table 1
Comparing EDX results obtained from BCTZC powder and ceramic samples with different Cu mole fractions.

Element (AT%)	Doping Cu contents														
	0.2%			0.4%			0.6%			0.8%			1%		
	Cal.	Powder	Ceramic	Cal.	Powder	Ceramic	Cal.	Powder	Ceramic	Cal.	Powder	Ceramic	Cal.	Powder	Ceramic
Ba	17.0	18.57	20.15	17.0	18.79	17.81	17.0	19.89	19.3	17.0	20.28	17.1	17.0	20.56	18.88
Ca	3.0	3.51	3.19	3.0	3.93	3.04	3.0	3.77	3.53	3.0	3.66	2.82	3.0	3.06	3.07
Ti	17.96	17.72	19.32	17.92	17.22	18.07	17.88	16.46	19.49	17.84	16.39	18.22	17.8	16.33	18.21
Zr	2.0	2.00	2.56	2.0	2.00	2.54	2.0	2.2	2.76	2.0	2.04	2.46	2.0	2.25	2.54
Cu	0.04	0.33	0.22	0.08	0.67	0.21	0.12	0.87	0.36	0.16	1.24	0.41	0.2	1.36	0.3
O	60.0	57.87	54.56	60.0	57.39	58.33	60.0	56.81	54.56	60.0	56.39	58.98	60.0	56.44	56.97

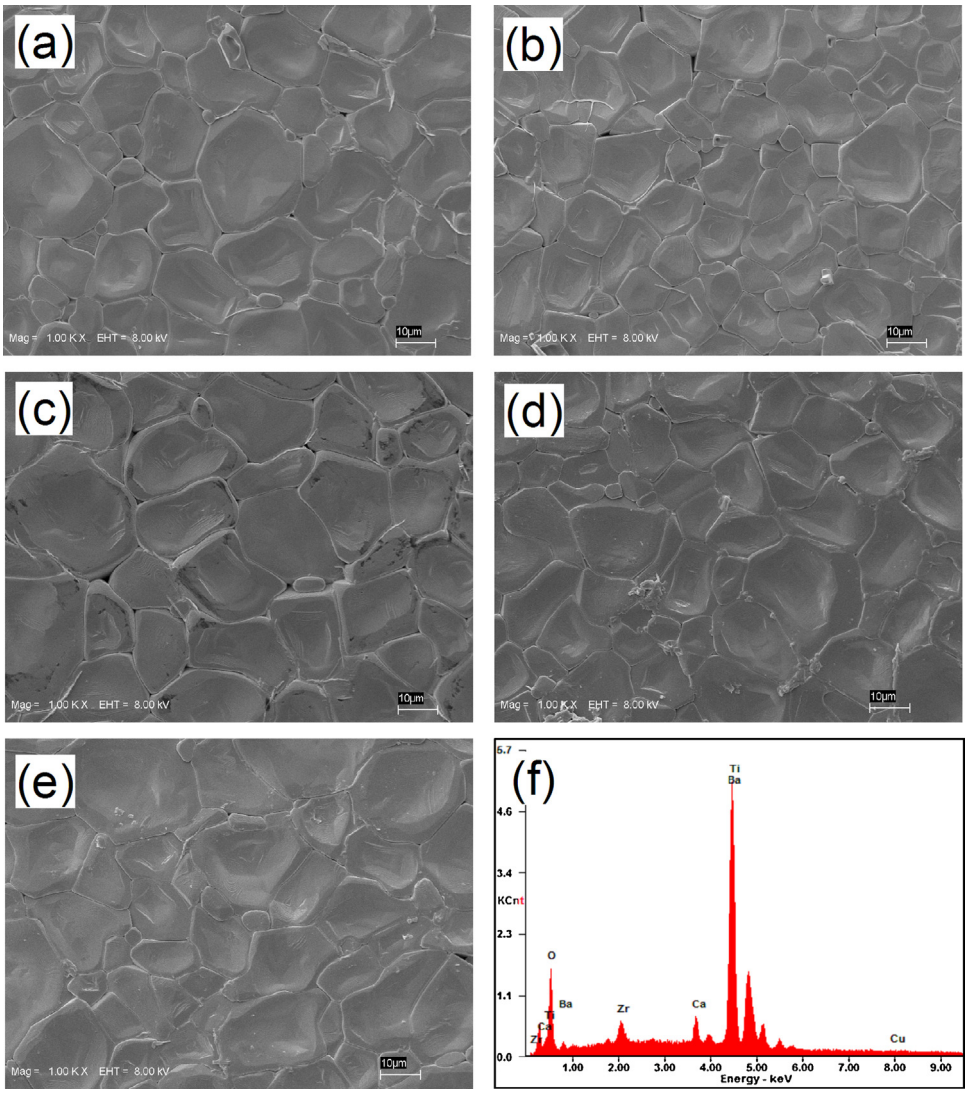

Fig. 4. SEM images obtained from BCTZC ceramic samples sintered at 1300 °C for 3 h and containing Cu mole fractions of: (a) 0.002; (b) 0.004; (c) 0.006; (d) 0.008; and (e) 0.01 and (f) typical EDX spectrum obtained from the Cu mole fraction 0.01 sample.

the starting materials used to synthesize the powders ($CaTiO_3$ and $BaZrO_3$). The XRD patterns obtained from the BCTZC ceramics sintered at 1300 °C for 3 h are shown in Fig. 2(a) and the splitting of the {200} peaks at around 45° shown enlarged in Fig. 2(b) [16] indicates a tetragonal phase in line with other reported results [7]. In addition, the impurity phases associated with $CaTiO_3$ and $BaZrO_3$ were not observed following sintering, suggesting that all Ca^{2+} (ionic radius = 1.34 Å), Zr^{4+} (0.72 Å) and Cu^{2+} (0.73 Å) ions have substituted on Ba^{2+} (1.61 Å) and Ti^{4+} (0.605 Å) sites within a $BaTiO_3$ structure to form a homogeneous solid solution.

SEM micrographs obtained from the BCTZC powder samples are shown in Fig. 3 from which it can be seen that all samples contained homogeneous particles with sizes in the range of 158–357 nm. A typical EDX spectrum obtained from one of the powder samples is also shown in Fig. 3, from which it can be seen that all samples contain Ba, Ca, Ti, Zr and Cu as expected and their atomic percentages are given in Table 1. The SEM micrographs obtained from BCTZC ceramic samples are shown in Fig. 4 and reveal considerable agglomeration and re-crystalisation resulting in a dense microstructure in comparison to the powder samples.

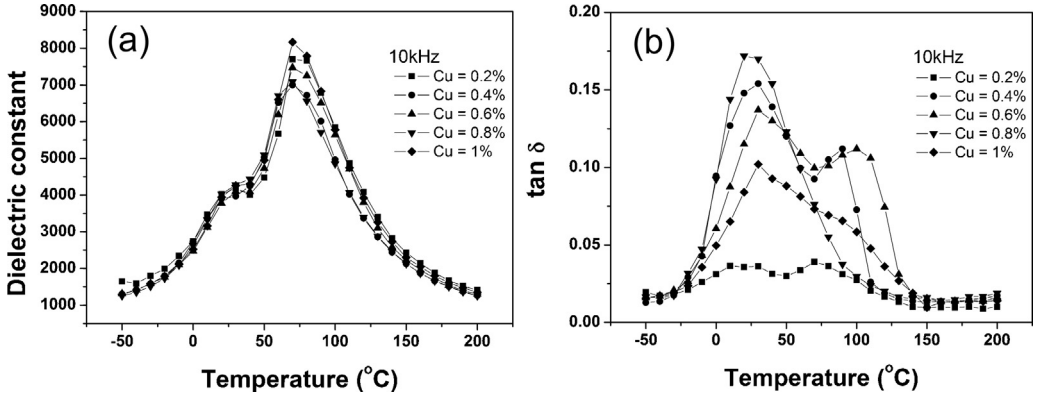

Fig. 5. The temperature dependence of the dielectric constant (a) and tan δ (b) obtained from BCTZC ceramic samples measured at a frequency of 10 kHz.

The average grain sizes in the case of the BCTZC ceramic samples were 17.0, 16.1, 20.0, 18.1 and 19.6 μm for nominal Cu mole fractions of 0.002, 0.004, 0.006, 0.008 and 0.01, respectively, showing little change with increasing Cu content across the samples. However, the grain sizes are larger than have been found for pure BCTZO ceramic samples (12.0 μm) prepared by a similar method [21]. The increase in grain sizes could be attributed to the addition of Cu ions into BCTZO, which might have an effect similar to other oxides such as MnO_2, Ga_2O_3 and CeO_2 in aiding the sintering process. These oxides can create oxygen vacancies which promote diffusion and leads to the enlargement of grains and a concomitant reduction in the sintering temperature [15–17].

From Table 1 it can be seen that apart from Ba, the calculated and measured atomic percentages for all other elements in both the powder and ceramic samples show significant discrepancies. Ca levels are higher than expected in the powder samples but were reduced somewhat in the ceramic samples. Measured Ti and Zr mole fractions were close to the expected values in the powder samples but were significantly higher than expected in all the ceramic samples. The O levels were slightly lower than expected but there was no significant difference between the O atomic percentages measured in the powder and ceramic samples. The EDX measurements of Cu atomic percentages in the powder samples are higher than expected but follow an approximately linear trend, suggesting the possibility of either a calibration error at the synthesis stage or a systematic error introduced by the EDX analysis software. The latter is more likely since Cu atomic percentages were between one and two orders of magnitude lower than the other species in the samples and therefore likely to be subject to larger percentage errors. However following sintering to produce the ceramic samples the measured Cu atomic percentages have reduced by between 30% and 80% from the values measured in the powder samples. Because the EDX measurements of Ba, Ti, Zr and O atomic percentages are in reasonable agreement with their expected values in the powder samples it is unlikely that the discrepancies observed for Cu in the powder samples and Ca, Ti, Zr and Cu in the ceramic samples are due to the effects of surface contamination of the samples. Indeed, the most likely surface contaminants are C-based originating from atmospheric exposure, however appreciable levels of C were not observed in the EDX spectra. A more likely explanation is that as the ceramic samples were being sintered at 1300 °C there was appreciable diffusion of some species to the surface of the samples, enriching the surface at the expense of the near surface layer. Species which diffuse to the surface may or may not evaporate. If they enrich the surface the EDX measurement, which has a typical sampling depth of 1–2 μm, will detect an enhanced signal unrepresentative of the bulk material and if they evaporate the EDX measurement will underestimate the concentration of that species because it is both absent from the surface and has been depleted from the near surface layer. By this argument we might speculate that Ti and Zr, both of which have melting temperatures well in excess of 1300 °C, are enriching the surface and that Cu, with a melting temperature of 1083 °C, is depleted from the near surface layer and the surface by diffusion and subsequent evaporation, however the complexity of the EDX process demands further analysis before a definite conclusion can be drawn. Nevertheless, it is likely that the EDX measurements reflect compositional changes in the near surface layer as a result of the sintering process and that the bulk of the ceramic samples contained the same levels of Cu as were measured in the powder samples before sintering.

The temperature dependences of the dielectric constant (ε') and dissipation factor (tan δ) for BCTZC ceramic samples at 10 kHz are shown in Fig. 5(a) and (b). From Fig. 5(a) it is observed that there are two phase transition temperatures in all ceramic samples at the rhombohedral–tetragonal (~30 °C) and tetragonal–cubic ($T_c \sim 70$ °C) phase transition temperatures [21]. It can be seen that the T_c values do not change with increasing Cu content, in contrast to other material systems for which it is found that the T_c value can change as a result of distortion of the lattice due to doping or strain [22,23]. In particular, Moura et al. [22] reported that substituting Zr ions for Ti in $BaTi_{1-x}Zr_xO_3$ (Zr mole fractions x between 0 and 0.15) reduced T_c values from 120 °C to 30 °C as the Zr mole fraction was increased from 0.05 to 0.15. It was found that the lattice constants increased with increasing Zr content, leading to the shift in T_c to lower temperatures. Transition ion doped (Ba,Ca)(Ti,Zr)O_3 has also been widely investigated, for example Jiang et al. [24] reported that for $Ba_{0.95}Ca_{0.05}Ti_{0.95}Zr_{0.05}O_3$–$Mn_x$ (Mn mole fractions x between 0 and 0.022) the changes in T_c were also found to be small, 109 °C for an undoped sample and 102 °C for a doped sample. Li et al. [20] also reported that the addition of Cu ions to form $Ba_{0.85}Ca_{0.15}Ti_{0.9}Zr_{0.1}O_3$–$(CuO)_x$ (CuO mole fractions x between 0 and 0.015) reduced T_c from 93 °C to 73 °C. In contrast, Cui et al. [16] reported that the addition of CuO to the $Ba_{0.85}Ca_{0.15}Ti_{0.9}Zr_{0.1}O_3$ system (to form $Ba_{0.85}Ca_{0.15}Ti_{0.9}Zr_{0.1}O_3$–$(CuO)_x$ (CuO mole fraction x between 0.0002 and 0.001) did not affect the T_c value of the system, supporting the conclusion of the present work. From Fig. 5(b), it is observed that the tan δ values measured in the sample with Cu mole fraction 0.002 are lower than those of other samples which is an indication of improved piezoelectric properties.

Fig. 6 shows the ferroelectric hysteresis loops measured at room temperature and 50 Hz obtained from BCTZO ceramics with different Cu mole fractions and the remnant polarization ($2P_r$) and coercive electric field ($2E_C$) values obtained from all samples are summarized in Table 1. The ceramic samples exhibit ferroelectric hysteresis loops from which it can be seen that the $2P_r$ and $2E_C$ values fluctuate with Cu doping content with no systematic trend, a result similar to that reported by Sun et al. [25] who studied $Ba_{0.98}Ca_{0.02}Zr_{0.02}Ti_{0.98}O_3$–$(CuO)_x$ (CuO mole fractions x between 0

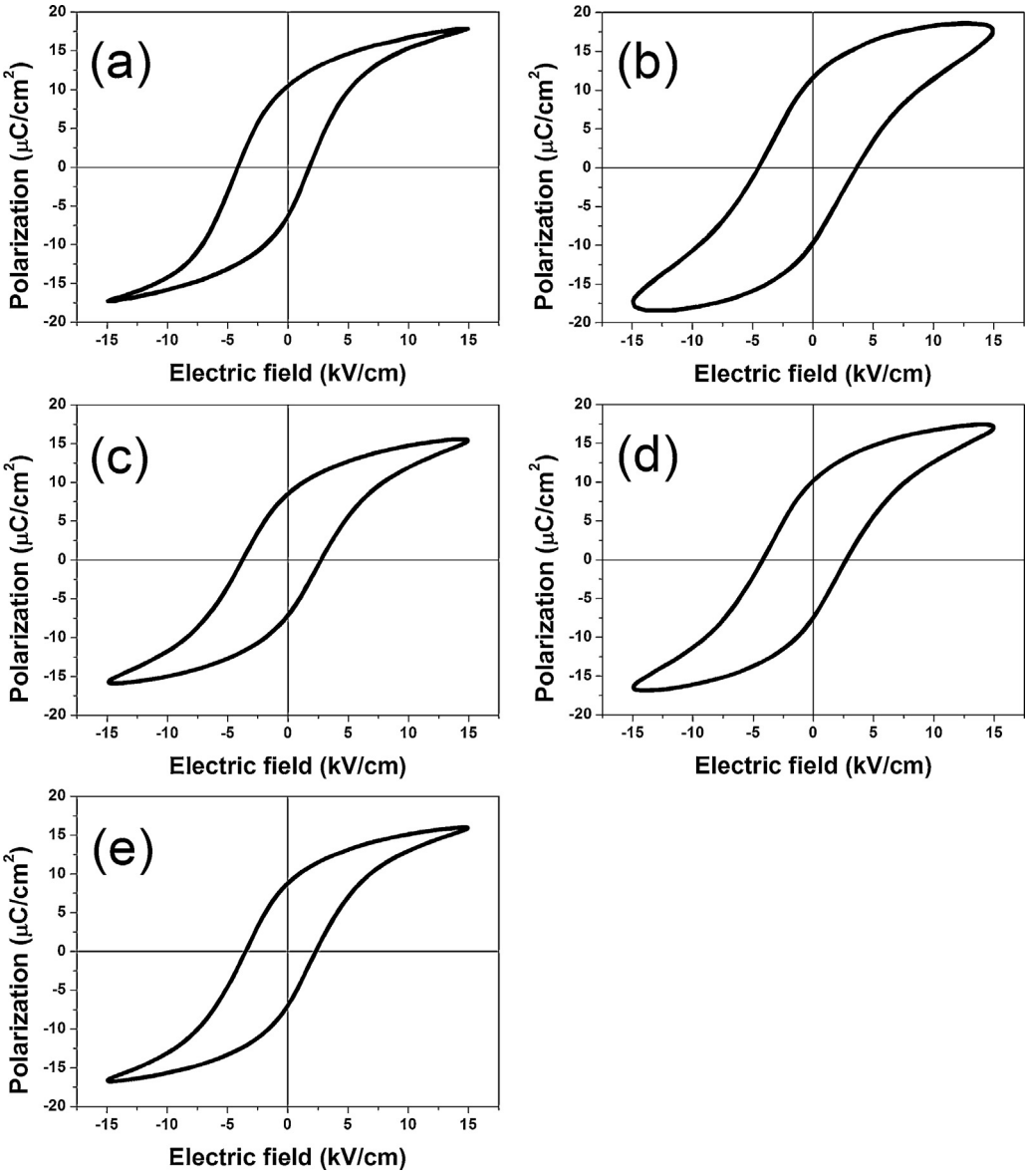

Fig. 6. Ferroelectric hysteresis loops obtained from BCTZC ceramic samples with different Cu mole fractions measured at a frequency of 50 Hz.

Table 2
Various parameters measured from BCTZC ceramic samples with different Cu mole fractions.

Parameter	Doping Cu contents				
	0.002	0.004	0.006	0.008	0.01
Average grain size (μm)	17.0	16.1	20.0	18.1	19.6
ε' (T_{RT}, 10 kHz)	3830	3560	3560	3770	3730
tan δ (T_{RT}, 10 kHz)	0.03	0.08	0.08	0.1	0.05
T_m (°C) (10 kHz)	70	70	70	70	70
$2P_r$ (μC/cm^2)	16.78	21.14	15.81	17.58	15.72
$2E_c$ (kV/cm)	5.91	8.10	6.62	6.81	5.82
d_{33} (pC/N)	306	254	209	285	210

and 0.02). The maximum $2P_r$ and $2E_C$ were found for the Cu mole fraction 0.004 sample, with values of 21.14 μC/cm^2 and 8.10 kV/cm, respectively.

The piezoelectric charge coefficient measurements (d_{33}) made on the BCZTC ceramic samples are shown in Table 2. The observed d_{33} values are fluctuating with the Cu mole fractions with no clear trend apparent. According to the thermodynamic theory of ferroelectricity proposed by Haun et al. [26] d_{33} values are proportional to the remnant polarization (P_r) and the dielectric constant and can be expressed as $d_{33} = 2Q_{11}P_r\varepsilon'$ where Q_{11} is the electrostrictive coefficient and ε' is the dielectric constant. The data follow this relationship if Q_{11} is allowed to vary, however the span of values for Q_{11} is covered by the first two Cu compositions and it is for this reason that the $2P_r$ value for the $x = 0.002$ Cu sample is lower than for the $x = 0.004$ sample. The observed d_{33} values are higher than the 169 pC/N obtained for pure $Ba_{0.85}Ca_{0.15}Ti_{0.9}Zr_{0.1}O_3$ ceramic samples [21] and the maximum value of 306 pC/N was found for the sample with Cu mole fraction 0.002. This suggests that Cu doping can improve the piezoelectric properties of $Ba_{0.85}Ca_{0.15}Ti_{0.9}Zr_{0.1}O_3$ ceramics and this finding is in line with other reported results [16,20]. The doping with Cu ions can induce the enhancement of grain size and results in the high d_{33} values.

4. Conclusions

$Ba_{0.85}Ca_{0.15}Ti_{0.9-x}Zr_{0.1}Cu_xO_3$ ceramic nanopowders were synthesized using a hydrothermal method after which they were pressed into discs and sintered in air at 1300 °C for 3 h to form

ceramic samples. XRD results indicated that the ceramic samples exhibited a tetragonal structure and that the average grain sizes were 17.0, 16.1, 20.0, 18.1 and 19.6 μm for Cu mole fractions of 0.002, 0.004, 0.006, 0.008 and 0.01, respectively. The optimum values of the relative dielectric constant, tan δ and the piezoelectric charge coefficient were found in the BCZTC ceramic sample with a Cu mole fraction of 0.002 and the values were 3830, 0.03 and 306 pC/N, respectively. The optimum values for the remnant polarization and coercive electric field were obtained for the Cu mole fraction 0.004 sample with values of 21.14 μC/cm^2 and 8.1 kV/cm, respectively.

Acknowledgements

This work was supported by the Higher Education Research Promotion and the National Research University Project of Thailand, Office of the Higher Education Commission, through the Advanced Functional Materials Cluster at Khon Kaen University. It was also supported by the Thailand Research Fund (TRF) and Khon Kaen University under the TRF Senior Research Scholar program, grant No. RTA5780004 and the Royal Golden Jubilee PhD program, grant No. PHD/0352/2551.

References

[1] T.R. Shrout, S.J. Zhang, J. Electroceram. 19 (2007) 113–126.
[2] D. Damjanovic, Rep. Prog. Phys. 61 (1998) 1267–1324.
[3] H. Takahashi, Y. Numamoto, J. Tani, S. Tsurekawa, Jpn. J. Appl. Phys. 45 (2006) 7405.
[4] K. Tomoaki, Y. Kang, A. Masatoshi, Jpn. J. Appl. Phys. 46 (2007) 7035.
[5] G. Shirane, R. Newnham, R. Penisky, Phys. Rev. Lett. 96 (1954) 581–588.
[6] E. Aksel, J.L. Jones, Sensers 10 (2010) 1935–1954.
[7] W. Liu, X. Ren, Phys. Rev. Lett. 103 (2009) 257602.
[8] P. Mishra Sonia, P. Kumar, J. Alloy. Compd. 545 (2012) 210–215.
[9] J. Wu, D. Xiao, B. Wu, W. Wu, J. Zhu, Z. Yang, J. Wang, Mater. Res. Bull. 47 (2012) 1281–1284.
[10] P. Wang, Y.X. Li, Y.Q. Lu, J. Eur. Ceram. Soc. 31 (2011) 2005–2012.
[11] S. Su, R.Z. Zuo, S.B. Lu, Z.K. Xu, X.H. Wang, L.T. Li, Curr. Appl. Phys. 11 (2011) S120–S123.
[12] S.W. Zhang, H. Zhang, B.P. Zhang, S. Yang, J. Alloy. Compd. 506 (2010) 131–135.
[13] W. Li, Z.J. Xu, R.Q. Chu, P. Fu, G.Z. Zang, J. Am. Ceram. Soc. 4 (2010) 93.
[14] Q.R. Lin, D.Y. Wang, B.C. Luo, R. Ding, D.L. Lorenzen, S. Li, Appl. Surf. Sci. 331 (2015) 477–481.
[15] M. Jiang, Q. Lin, D. Lin, Q. Zheng, X. Fan, X. Wu, H. Sun, Y. Wan, L. Wu, J. Mater. Sci. 48 (2013) 1035–1041.
[16] Y. Cui, X. Liu, M. Jiang, Y. Hu, Q. Su, H. Wang, J. Mater. Sci. Mater. Electron. 23 (2012) 1342–1345.
[17] Y. Cui, X. Liu, M. Jaing, X. Zhao, X. Shan, W. Li, C. Yuan, C. Zhou, Ceram. Int. 38 (2012) 4761–4764.
[18] J. Ma, X. Liu, W. Li, J. Alloy. Compd. 581 (2013) 642–645.
[19] Y. Cui, C. Yuan, X. Liu, X. Zhao, X. Shan, J. Mater. Sci. Mater. Electron. 24 (2013) 654–657.
[20] J. Li, D. Xiao, W. Wu, Q. Chen, J. Zhu, Z. Yang, J. Wang, Phys. Status Solidi A 210 (2013) 533–537.
[21] S. Hunpratub, S. Maensiri, P. Chindaprasirt, Ceram. Int. 40 (2014) 13025–13031.
[22] F. Moura, A.Z. Simoes, B.D. Stojanovic, M.A. Zaghete, E. Longo, J.A. Valela, J. Alloy. Compd. 462 (2008) 129–134.
[23] X.G. Tang, H.L.W. Chan, J. Appl. Phys. 97 (2005) 034109.
[24] X.P. Jiang, L. Li, C. Chen, X.J. Wang, X.H. Li, J. Alloy. Compd. 574 (2013) 88–91.
[25] H. Sun, Y. Zhang, X. Liu, Y. Liu, W. Chen, Ceram. Int. 41 (2015) 555–565.
[26] M.J. Han, E. Furman, S.J. Jang, L.E. Cross, Ferroelectrics 99 (1989) 13–25.

Journal of Cleaner Production 112 (2016) 2300–2307

Contents lists available at ScienceDirect

Journal of Cleaner Production

journal homepage: www.elsevier.com/locate/jclepro

Influence of recycled aggregate on fly ash geopolymer concrete properties

Peem Nuaklong, Vanchai Sata*, Prinya Chindaprasirt

Sustainable Infrastructure Research and Development Center, Department of Civil Engineering, Faculty of Engineering, Khon Kaen University, Khon Kaen 40002, Thailand

ARTICLE INFO

Article history:
Received 12 December 2014
Received in revised form
7 October 2015
Accepted 24 October 2015
Available online 31 October 2015

Keywords:
Recycled aggregate
High calcium fly ash
Geopolymer concrete
Mechanical properties
Durability

ABSTRACT

Geopolymer binder and recycled aggregate are environment friendly products and is thus considered as part of sustainable development. This paper presents a study of the effect of recycled aggregate on strength and durability of fly ash based geopolymer concrete. Geopolymer concrete samples were prepared from high calcium fly ash, sodium silicate solution, sodium hydroxide solution, fine aggregate from river sand, and two types of coarse aggregate viz., recycled concrete aggregate and crushed limestone coarse aggregate. Test results indicated that recycled concrete aggregate can be used as a coarse aggregate in high calcium fly ash geopolymer concretes with the 7-day compressive strengths of 30.6–38.4 MPa which were slightly lower than those of high calcium fly ash geopolymer concretes containing crushed limestone. The use of high sodium hydroxide concentrations of 12 and 16 M resulted in better performances both in strength and durability than that of 8 M.

© 2015 Elsevier Ltd. All rights reserved.

1. Introduction

Portland cement is the most common cement for concrete and is used extensively in the construction industry. However, Portland cement production is an energy intensive process, depletes a large amount of natural resource, and releases a large amount of greenhouse gas. The cement industry contributes about 7% by weight of the total worldwide carbon dioxide emissions (Ali et al., 2011). The use of supplementary materials to partially replace Portland cement and other form of cementing materials should be emphasized to reduce Portland cement consumption. Fly ash (Bagheri et al., 2013), bottom ash (Carrasco et al., 2014), and biomass ash (Sata, 2010) are some supplementary materials commonly used to replace Portland cement in concrete. However, these materials can only partially replace Portland cement.

Geopolymer binder is another form of cementing materials compared with the common technology based on Portland cement. It is synthesized by mixing aluminosilicate material and alkali solutions (Davidovits, 1999). Several researchers found that geopolymer has excellent bond strength (Sarker, 2011; Songpiriyakij et al., 2011), good performance in acid (Temuujin et al., 2011), and good fire resistant (Zhao and Sanjayan, 2011). Most waste materials, such as fly ash, bottom ash, and blast furnace slag contain sufficient amounts of reactive alumina and silica and thus can be used as source materials for geopolymer binder. As fly ash contains both alumina and silica and is available in many parts of the world, therefore, it is commonly used as a source material in making geopolymer binder (Duxson et al., 2007). The fly ash-based geopolymer mortar with compressive strength of 60–70 MPa was obtained when 10–15 M NaOH, Na_2SiO_3 to NaOH ratio of 1.0, and separate mixing were used (Rattanasak and Chindaprasirt, 2009). In addition, Turner and Collins (2013) found that the CO_2 footprint of a sodium silicate based geopolymer for normal strength concrete was approximately 9% less than Portland cement concrete.

Huge amount of construction and demolition wastes are produced every year. In Thailand, these wastes are usually sent to landfills or dumped illegally. The disposal of these wastes is a severe social and environmental problem. The recycling of these wastes as aggregate to produce new concrete can reduce the problem of waste and help the preservation of natural aggregate resources. Many researchers found that recycled aggregate offers a good alternative aggregate for making concrete in terms of both environment friendly and economically. Marinkovic et al. (2010) studied the environment impact of recycled aggregate using life cycle assessment (LCA) methodology (ISO, 2006) and reported that the impact of aggregate production for recycled aggregate concrete

* Corresponding author. Tel.: +66 4320 2846x127; fax: +66 4320 2846x102.
E-mail address: vancsa@kku.ac.th (V. Sata).

http://dx.doi.org/10.1016/j.jclepro.2015.10.109
0959-6526/© 2015 Elsevier Ltd. All rights reserved.

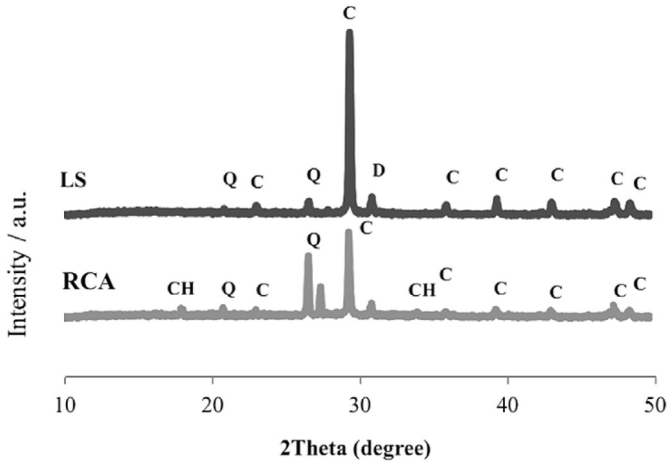

Fig. 1. X-Ray Diffraction (XRD) pattern of LS and RCA [C: Calcium carbonate, Q: Quartz, D: Dolomite, CH: Calcium hydroxide].

was slightly larger than that of natural aggregate concrete depending on transport distances and types. In addition, Marie and Quiasrawi (2012) reported that the use of up to 20% replacement of natural aggregate with recycled concrete aggregate allowed the production of acceptable quality concretes while maintaining the sustainability of natural resources and environment. Ping and Yidong (2011) thus suggest that the recycled aggregate concrete is a good eco-material.

This study aims to study the properties of fly ash based geopolymer concrete containing recycled concrete aggregate. Geopolymer concrete samples were prepared from high calcium fly ash, sodium silicate and sodium hydroxide solutions, natural sand, and recycled coarse aggregate. The mechanical properties and durability were investigated. The results were compared to those containing normal coarse aggregate (crushed limestone). The obtained data should lay a foundation for t the use of both fly ash geopolymer as an alternative binder to Portland cement and recycled aggregate which is a novel way to reduce waste materials and conserve natural aggregate resources.

2. Materials and methods

2.1. Materials

High calcium fly ash (FA) from Mae Moh power plant, Lampang, Thailand with specific gravity of 2.41, chemical compositions of 35.9% SiO_2, 15.1% Al_2O_3, 17.3% Fe_2O_3, and 17.2% CaO was used as source material. Sodium silicate (NS) with 12.5% Na_2O, 30.2% SiO_2, and 57.2% H_2O and sodium hydroxide (NH) with concentrations of 8, 12, and 16 M (M) were used alkali activator solutions.

River sand with a fineness modulus of 2.6 and two types of coarse aggregates viz., natural crushed limestone (LS) and recycled concrete aggregates (RCA) were used in this study. RCA was obtained from old concrete test samples with compressive strengths of 30–40 MPa and attached mortar content about 38%. The concrete samples were crushed and sieved into 4.5–9.5 mm particle size with fineness modulus of 6.0 similar to those of LS. The XRD pattern of aggregates (as shown Fig. 1) showed that LS consisted mainly of calcium carbonate (C) with some quartz (Q) and dolomite (D). RCA consisted of calcium carbonate (C), quartz (Q), and calcium hydroxide (CH, from attached mortar). The properties of aggregates are shown in Table 1.

Table 2
Mix proportions of geopolymer concretes (kg/m3).

Mixes	FA	NaOH			Na_2SiO_3	Sand	Coarse aggregate	
		8 M	12 M	16 M			LS	RCA
GL8	450	108		–	162	500	1150	–
GL12	450	–	108	–	162	500	1150	–
GL16	450	–	–	108	162	500	1150	–
GR8	450	108	–	–	162	500	–	1036
GR12	450	–	108	–	162	500	–	1036
GR16	450	–	–	108	162	500	–	1036

2.2. Mix proportions and preparing of samples

Table 2 shows the mix proportions of geopolymer concrete (GC) in this study. Liquid to ash ratio (L/A) of 0.6 and NS to NH ratio of 1.5 by weight were used for all mixes. Fly ash and NH solution were mixed for 5 min and then coarse aggregate and fine aggregate in saturated surface dry condition were added and mixed for another 5 min, and finally NS solution was added and again mixed for 5 min.

After mixing, cylindrical samples with 100 mm diameter and 200 mm height were cast for compression and splitting tensile strengths, and for chloride penetration test. The 75 × 75 × 300 mm^3 prism was used to measure the flexural strength and 300 × 300 × 35 mm^3 slab for surface abrasion resistance. In addition, 100 × 100 × 100 mm^3 cube samples were used for sulfuric acid resistance test. After casting, they were covered with plastic sheet and left standing for 1 h, and then cured at 60 °C for 2 days. Then, they were demoulded and kept in 23 °C and 50% R.H. controlled room until the age of 7 days. Fig. 2 shows the internal surface pattern of GC containing LS (GL) and GC containing RCA (GR).

2.3. Testing procedures

2.3.1. Strength and abrasion resistance

GC samples were investigated for compressive (ASTM C39, 2003), splitting tensile (ASTM C496, 2003), and flexural strengths (ASTM C78, 2003). Surface abrasion resistance was tested using the rotating-cutting method in accordance with ASTM C944 (1999). The GC samples were abraded with normal load (98 N) on the surface for 2 min. The abrasion resistance was presented in term of average weight loss in grams after 3 abrasion periods.

2.3.2. Water absorption and sorptivity

The water absorption and volume of permeable voids (VPV) of GC discs with 100 mm diameter and 50 mm in thickness were tested at the age of 7 days of curing according to ASTM C642 (2003). GC discs with 100 mm diameter and 50 mm in thickness were used

Table 1
Properties of aggregates.

Aggregates	Specific gravity	Dry-rodded density (kg/m^3)	Absorption (%)	Los Angeles abrasion loss (%)	Fineness modulus
LS	2.63	1580	0.54	31.0	6.0
RCA	2.32	1240	5.77	38.0	6.0
Sand	2.63	–	1.07	–	2.6

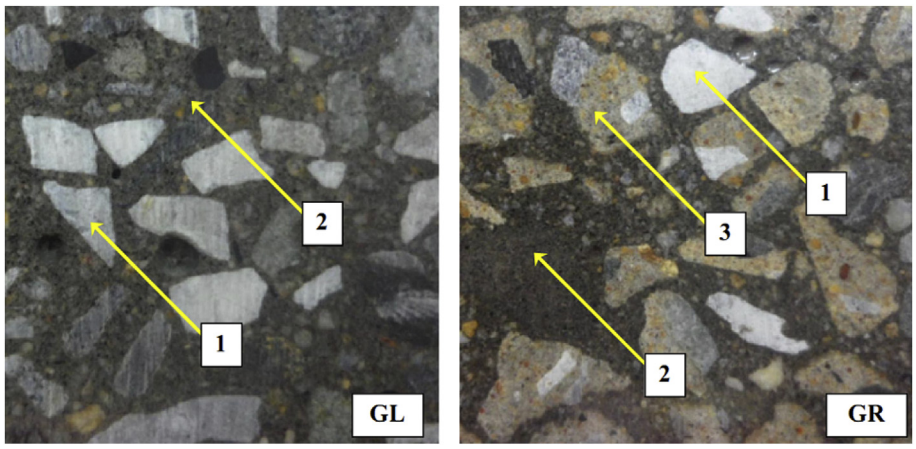

Fig. 2. Internal surface pattern of GL and GR; (1) limestone; (2) geopolymer mortar; and (3) attached mortar.

for the determination of rate of sorptivity (ASTM C1585, 2011). The side of GC sample was sealed with epoxy to allow the water to penetrate from the bottom end of sample only. A 5 mm head of water above the bottom of sample was chosen for this test. At selected time, the samples were removed from the water and weighted. The gain in weight per absorbed area over the water density was plotted versus the square root of elapsed time. The slope of the best fit line was reported as the rate of sorptivity.

2.3.3. Chloride penetration depth

After 7 days curing, two cylindrical samples with 100 mm in diameter and 100 mm in height were coated with epoxy resin around the cylindrical surface to allow chloride ion to diffuse into sample in one direction. After that, they were immersed in 3% NaCl solution. The GC samples ware then splitted and spayed with 0.1 N $AgNO_3$ solution. The white color of AgCl indicated the chloride penetration depth (Otsuki et al., 1993). These depths were measured and the reported results were the average of 10 measurements of two samples.

2.3.4. Sulfuric acid resistance

The sulfuric acid resistances of GC were tested by modified test according to ASTM C267 (2003). At the age of 7 days, the 100 × 100 × 100 mm cube GC samples were immersed in 3% sulfuric acid solution. After immersed time of 7, 14, 28, 56, 84 and 120 days, the samples were brushed softly under water to remove loose surface debris before drying and weighting. The resistance was assessed by an evaluation on the weight loss of specimens. The sulfuric acid solution was replaced with fresh solution after the measurement of weight loss.

3. Results and discussions

3.1. Workability of fresh geopolymer concrete

Due to the high viscosity of geopolymer concrete, the workability of fresh geopolymer concrete was tested in term of slump flow according to ASTM C1611 (2010). The results as shown in Fig. 3 indicated that fresh geopolymer concrete had the slump flow between 550 and 660 mm. These slump flow values suggested that the geopolymer concretes in this study was class SF1 self-compacting concrete in accordance with EFNARC (2005). The use of saturated surface dry RCA tended to give a higher workability than that with LS. Because of the RCA particles contain a larger volume of pore and water at saturated surface dry condition than

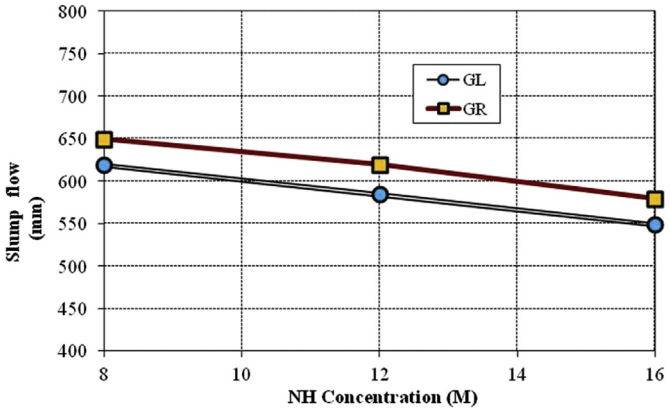

Fig. 3. Slump flow of geopolymer concrete.

that of LS particles. The water inside RCA particles was available and improved the workability of the mixes (Poon et al., 2004). The report of Mefteh et al. (2013) showed that the use of RCA in pre-wetting and saturated surface dry conditions improved the concrete workability. In addition, at the same liquid to ash ratio, the use of high NH concentration gave geopolymer concrete with low slump flow. This was due to the increase in NH concentration resulted in leaching of more silica and alumina and thus increase the geopolymerization and the stiffness of the system (Chindaprasirt et al., 2009).

3.2. Density and strength

The density and compressive strength of GC at the age of 7 days and their normalized values are shown in Table 3. The density of GL ranged between 2350 and 2390 kg/m^3 which were approximately the same as conventional concrete (about 2400 kg/m^3). The use of RCA in GC (GR) decreased GC density by 6–10% (2160–2210 kg/m^3)

Table 3
Density, compressive strength, and normalized values.

NaOH concentration (M)	Density (kg/m^3)–normalized (%)		Compressive stren. (MPa)–normalized (%)	
	GL	GR	GL	GR
8	2390–100	2160–90	40.0–100	30.6–76
12	2350–100	2190–93	41.4–100	38.4–93
16	2360–100	2210–94	38.4–100	34.8–91

due to the low density of RCA. In addition, the NH concentrations also had a slight effect on the density of GC.

The compressive strengths of GL with 8, 12, and 16 M NH were 40.0, 41.4, and 38.4 MPa, while those of GR at the same NH concentrations were slightly lower at 30.6, 38.4, and 34.8 MPa, representing a reduction between 76 and 93% with the average of 87% of those of GL. This result is in line with a number of published reports on Portland cement concretes (Rahal, 2007) indicating that RCA concretes had lower compressive strengths compared to conventional concretes. The lower in GR strength was due to the low abrasion resistance from the weakness of attached mortar in RCA (Tu et al., 2006). In addition, Etxeberria et al. (2007) presented that the attached mortar in RCA was lower in strength than conventional aggregate and new paste. However, the GR with compressive strengths of 30.6–38.4 MPa can be used for structural concrete member.

The results also showed that the optimum NH concentration to produce good strength GC was 12 M. Because of the formation of gel depended on the concentration of alkali OH ion, low NH concentration resulted in a weak chemical reaction and low compressive strength. An increase in alkali concentration enhanced strength development of geopolymer, but excess hydroxide ion concentration caused aluminosilicate product precipitation at early stage, resulting in a decrease in strength of geopolymer (Lee and van Deventer, 2002). A maximum compressive strength of 41.4 MPa were obtained with GL and 12 M NH concrete.

The results of splitting tensile and flexural strengths of all GCs as shown in Table 4 showed similar trend to those of compressive strength. The use 12 M NH gave the highest splitting tensile and flexural strengths. GL12 and GR12 concretes gave the maximum splitting tensile concrete of 4.0 MPa, while GR12 concrete gave the maximum flexural strength of 5.3 MPa. The average splitting tensile strength was about 10% of their respective compressive strengths and about 78% of their respective flexural strengths. The results were similar to those of conventional concrete. With regards to the use of LS and RCA, GR concretes with 12 and 16 M NH gave slightly higher splitting tensile and flexural strengths than those of GL concretes. This was due to the increased calcium hydroxide (CH) and other calcium products in the system (from RCA as shown in Fig. 1). The high calcium content, the additional CSH and CASH gels were formed, which modified the microstructure of the paste and acted as micro-aggregate (Phoo-ngernkham et al., 2013). The increase in reaction products at the interface transition zone between normal concrete and geopolymer material enhanced the strength at contact zone. In addition, Shi et al. (2012) reported that the physical and chemical characteristics of geopolymer concrete with recycled aggregate was changed and caused a decrease in the volume of void and led to overall improvement the density and homogeneity of matrix.

3.3. Surface abrasion resistance

The results of surface abrasion resistance are shown in Fig. 4. The better surface abrasion resistance of GC is presented by a lower average weight loss value. The weight losses of GL concretes with 8, 12, and 16 M NH were 1.24, 0.92, and 1.16 g, while GR concretes gave slightly higher values at 1.45, 0.92, and 1.53 g. This suggested that the use of recycled aggregate in geopolymer concrete gave lower abrasion resistance than that of natural aggregate. With regards to the effect of NH concentration, the GL and GR with 12 M NH had the highest surface abrasion resistance with the weight loss of 0.92 g. The trend of result was similar to the results of compressive strength.

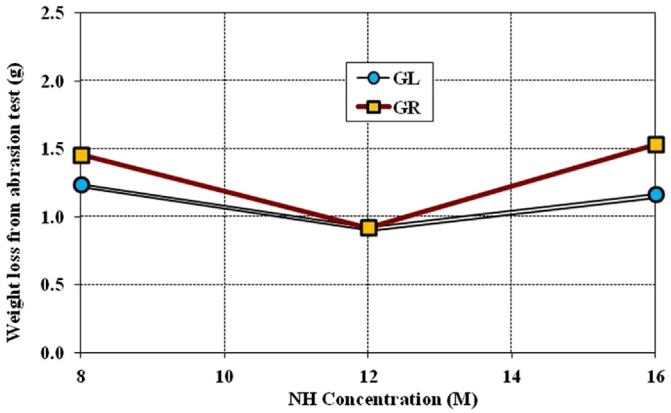

Fig. 4. Weight loss of GCs from surface abrasion resistance test.

Table 4
Splitting tensile strength, flexural strength, and normalized values.

NaOH concentration (M)	Splitting tensile strength (MPa)–normalized (%)		Flexural strength (MPa)–normalized (%)	
	GL	GR	GL	GR
8	3.5–100	2.9–83	4.2–100	4.0–95
12	4.0–100	4.0–100	5.1–100	5.3–104
16	3.4–100	3.9–114	4.3–100	4.6–107

3.4. Water absorption, volume of permeable void, and sorptivity

The relationship between water absorption, volume of permeable voids and NH concentration of GCs are presented in Fig. 5. The water absorption of GL and GR varied in a narrow range of 5.3–6.5% and 9.6–11.2%, while the volume of permeable voids were 14.5–17.5% and 22.1–25.3%. The water absorptions of geopolymer concrete in this study were nearly the same as 5.8–7.1% of self-compacting concrete (Siddique, 2013). The use of 12 M NH seemed to give low water absorption and volume of permeable void as shown in Fig. 5(a) and 5 (b). The low water absorption and volume of permeable void are mainly influenced by the denseness and limited open porosity of the matrix. The high compressive strength of GC was related to the low water absorption and volume of permeable void. The use of RCA in fly ash based geopolymer concrete gave higher water absorption and volume of permeable void than those with LS. This was due to the high porosity from attached mortar of RCA particle which served as a potential conduit for water transport in the matrices.

As shown in Fig. 6, the relationship between volume of permeable void and water absorption of GC in this study gave a good correlation. As the water absorption increased, the volume of permeable void also increased correspondingly. This result is in the same direction of that of Portland cement concrete reported by Dinakar et al. (2008).

Fig. 7 shows the effect of NH concentration on the sorptivity of geopolymer concrete containing RCA compared with natural aggregate. The geopolymer concrete containing RCA exhibited higher sorptivity than that with LS. The lowest sorptivity was 6×10^{-3} and 15×10^{-3} mm/s$^{1/2}$ for GL12 and GR12 concretes. These results were in the line with water absorption and volume of permeable void results. In addition, the correlation between compressive strength and sorptivity were very good with a correlation coefficient (R^2) of 0.92 as shown in Fig. 8. The high compressive strength concretes showed low sorptivity.

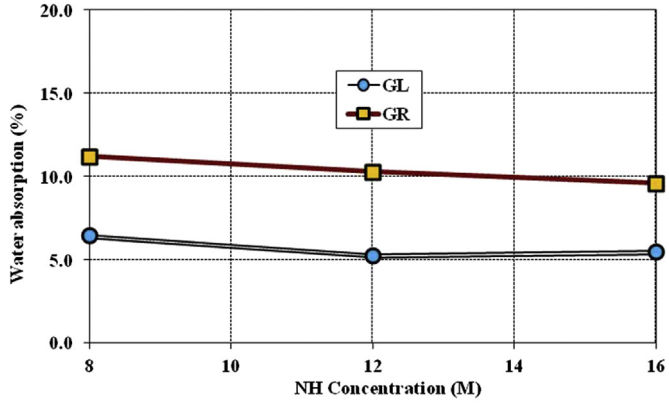

(a) Water absorption of all GCs.

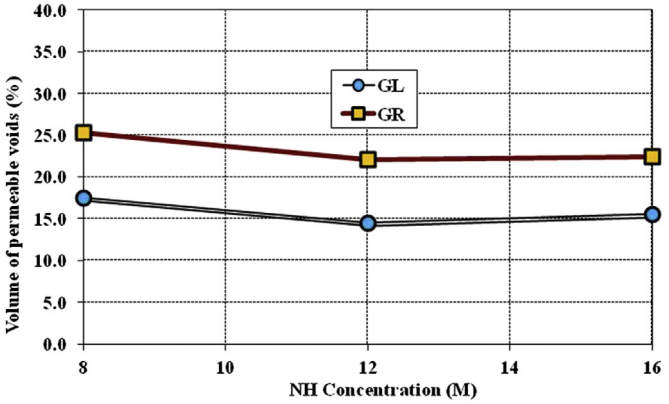

(b) Volume of permeable void of all GCs.

Fig. 5. Water absorption and volume of permeable void of geopolymer concrete.

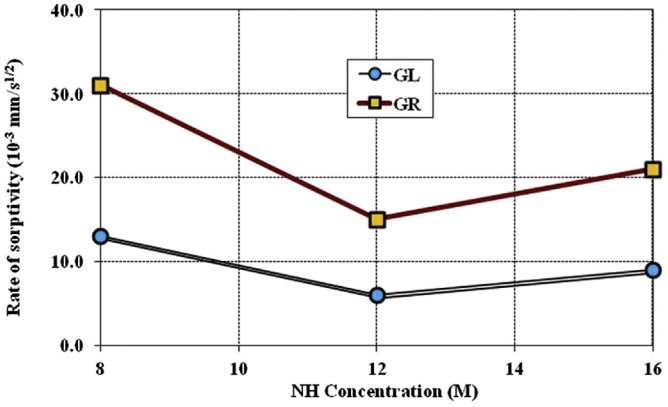

Fig. 7. Rate of sorptivity of all GCs.

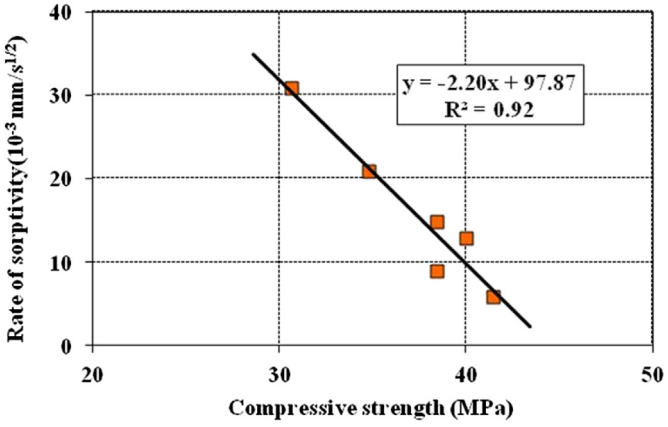

Fig. 8. Relationship between sorptivity and compressive strength of GC.

3.5. Chloride penetration depth

The results of chloride penetration depth of GCs immersed in 3% NaCl solution at 30, 60, 90, and 120 days are shown in Fig. 9. At the same NH concentration, GR showed lower chloride penetration resistance (higher chloride penetration depth) than that of GL. The 3% NaCl solution penetration depth of GR16 concrete at the immersed time of 30, 60, 90, and 120 days were 10.3, 21.4, 20.9, and 20.9 mm, while those GL16 concrete were 10.4, 16.9, 18.9, and 21.5 mm. Because of the high porosity at the new interfacial transition zone (ITZ) between RCA and new mortar of GR provided an easier path to aggressive chloride ion (Shi et al., 2012). The chloride ion could penetrate through the pores and looser structure in the attached mortar on the surface of RCA (Somna et al., 2012). Hwang et al. (2013) found that RCA concrete always revealed the lower strength and resistance to chloride, frost, and sulfate attack compared to control concrete.

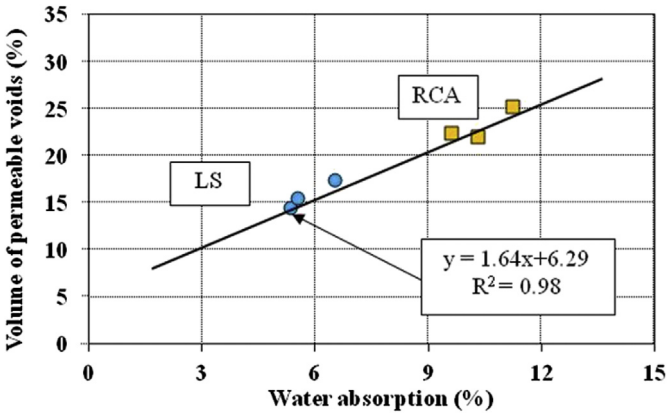

Fig. 6. Relationship between volume of permeable void and water absorption of GC.

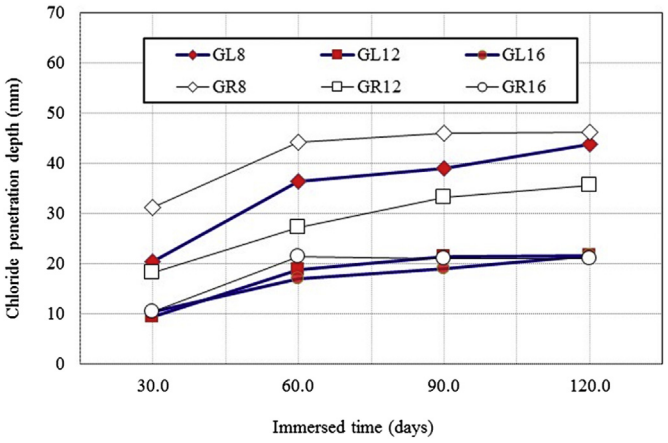

Fig. 9. The chloride penetration depths of GCs immersed in 3% NaCl solution for 30, 60, 90, and 120 days.

With regards to the effect of NH concentration on chloride penetration depth, the results showed that the chloride penetration depth decreased with the increasing NH concentration for both GL and GR concretes. The reduction in chloride penetration depth from 8 to 12 M NH was higher than that from 12 to 16 M. For example, the chloride penetration depth at 90 days immersion of GL with 8 and 12 M NH were 39.0 and 21.0 mm; while the 16 M NH concrete was 18.9 mm. The result was consistent with Chindaprasirt and Chalee (2014) who reported that the increase NH concentration resulted in decreasing chloride diffusion and steel corrosion in geopolymer concrete. A number of researchers (Mikuni et al., 2007; Li et al., 2011) indicated that the dissolution of Si and Al in fly ash increased with increased NH solution concentration. The higher amount of dissolved Si and Al produced a better polycondensation reaction in geopolymer matrix and reduced porosity and chloride ingression. Fig. 10 shows the boundaries of chloride penetration depths of GC for 30 and 120 days of immersion.

3.6. Sulfuric acid resistance

Fig. 11 shows the weight losses of GL and GR concretes exposed to 3% sulfuric acid solution up to 120 days of immersion. At 14 days of exposure, the weight losses of GC were very low at less than 1.4%. All GC samples were slightly damaged at the surface and around the edges of specimen as shown in Fig. 12(a). Generally, the deleteriation under acid attack in cement binder is due primarily on the reaction between calcium (Ca) compound and acid, which induces tensile stress and results in cracking and scaling in cement binder system. The high sulfuric acid resistance of geopolymer matrix may be due to the low water absorption and low calcium (Ca) content which generated less soluble compounds (Pacheco-Torgal and Jalali, 2011). Ariffin et al. (2013) found that geopolymer concretes performance better than Portland cement concrete when exposed to sulfuric acid due to the differences in chemical and phase composition. The deterioration of bottom ash geopolymer mortar

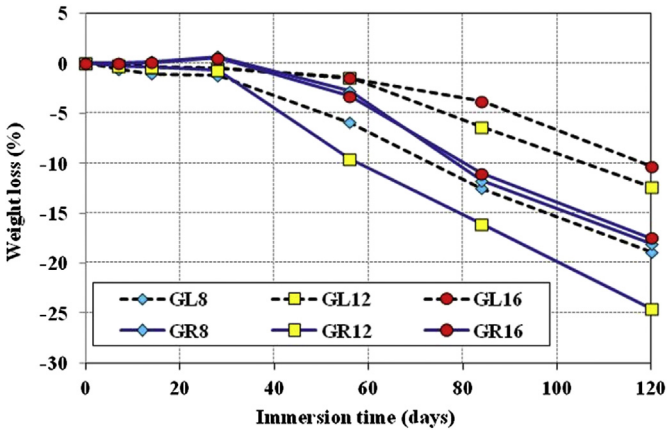

Fig. 11. Weight loss of GCs after 120 days immersed in 3% H_2SO_4 solution.

in sulfuric acid solution showed better performance than those of OPC mortar was found by Sata et al. (2011).

The major components of geopolymer concrete were O, Si, Na, and Al which had better resistance than cement based binder. After 14 days of immersion, the weight loss of GC started to be significant and increased with immersion time. As shown in Fig. 12(b), the damage of aggregate particles was also significant. This was due to sulfuric acid reacted with calcium compounds in limestone leading to destruction of aggregate in GC sample (Pacheco-Torgal and Jalali, 2011). For GL, there was a clear indication that the weight loss after 28 days of exposure was related to the NH concentration. The resistance to acid attack increased with the increase in NH concentration. The weight losses of GL concretes with 8, 12 and 16 M NH after 120 days of immersion were 18.9, 12.4 and 10.3%. At the same NH concentrations, the GR concretes showed lower acid resistance than that of GL concrete. This was due to the high water absorption, volume of permeable void, and sorptivity of GR compared to those of GL. In addition, the calcium compound in RCA

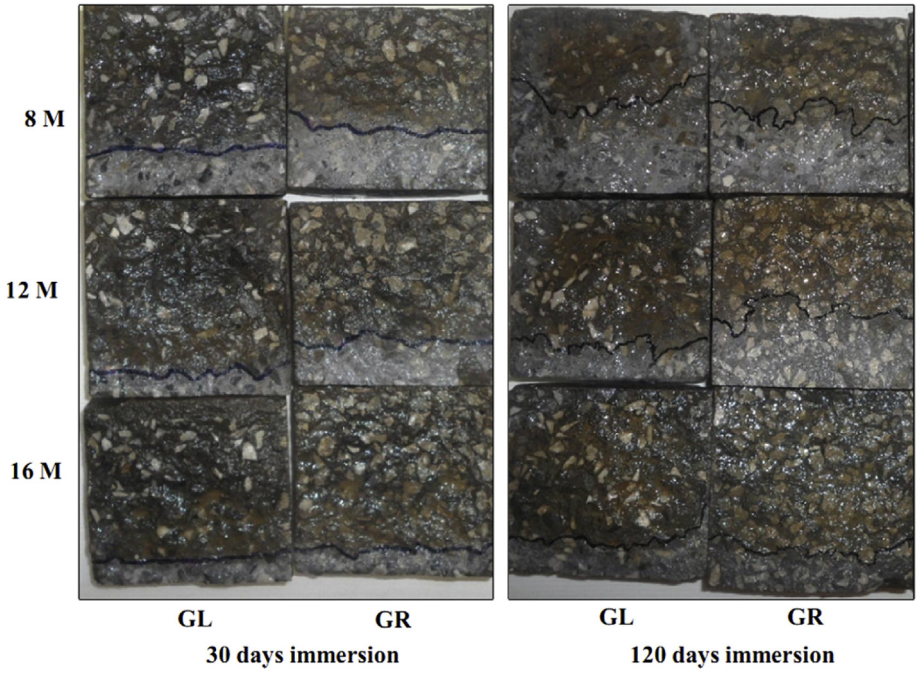

Fig. 10. The boundary of chloride penetration depth of GCs at 30 and 120 days of immersion.

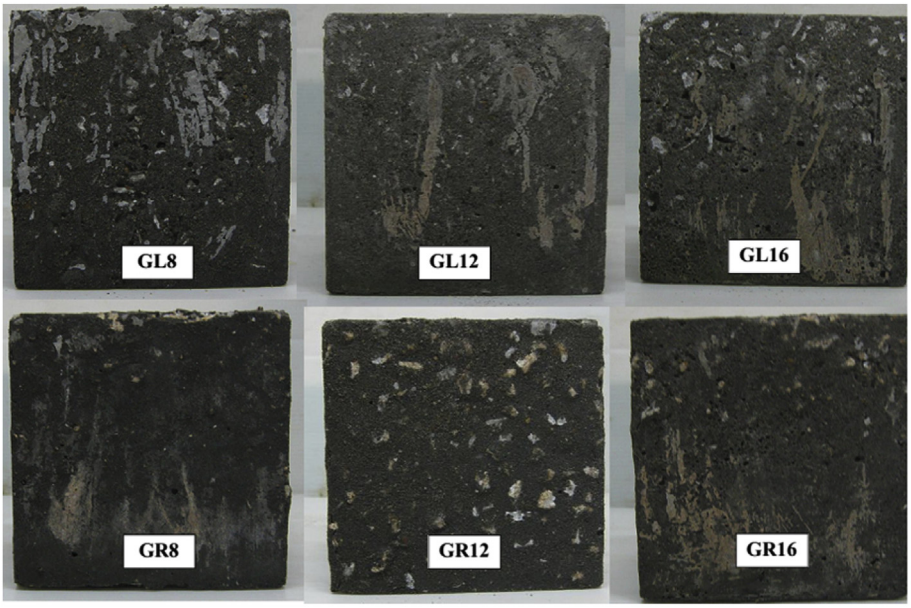

(a) 14 days immersed

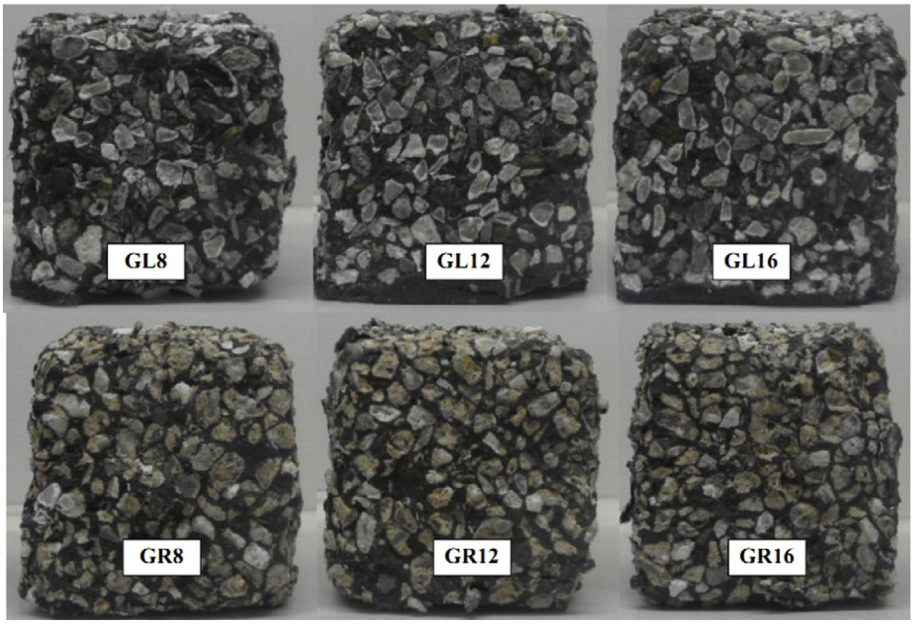

(b) 120 days immersed

Fig. 12. Physical appearance of GCs after 14 and 120 days immersed in 3% H_2SO_4 solution.

and attached mortar reacted with acid solution and resulted in more deterioration.

These results indicated that RCA could be used as a coarse aggregate in fly ash geopolymer concrete with acceptable compressive strength of 30.6–38.4 MPa (76–93% of LS geopolymer concretes) and the concretes are thus suitable for various construction works and some structural applications. In addition, the use of RCA as a coarse aggregate in high calcium fly ash geopolymer concrete can help reduce the problem of waste disposal at landfill sites and promote the use of geopolymer as an alternative binder.

4. Conclusions

The results indicate that recycled concrete aggregate can be used as a coarse aggregate in high calcium fly ash geopolymer concrete. The obtained strengths and durability were slightly lower than those containing crushed limestone. However, geopolymer concrete containing recycled concrete aggregate still possessed sufficiently high compressive strength of 30.6–38.4 MPa or approximately 76–93% of the same geopolymer concretes containing crushed limestone.

Sodium hydroxide solution of 12 M was an optimum concentration for the fabrication of high calcium fly ash geopolymer concrete in terms of compressive strength, splitting tensile strength, flexural strength, and surface abrasion resistance. While, both 12 and 16 M gave geopolymer concretes with good water absorption, volume of permeable void, rate of sorptivity, chloride penetration depth, and weight loss from sulfuric acid solution.

Acknowledgements

This work was supported by research fund of the Faculty of Engineering, Khon Kaen University; the Higher Education Research Promotion and National Research University Project of Thailand, Office of the Higher Education Commission, through the Advanced Functional Materials Cluster of Khon Kaen University. The authors also would like to acknowledge the support of the Thailand Research Fund (TRF) and Khon Kaen University under the Royal Golden Jubilee Ph.D. Program (Grant No. PHD/0195/2557), TRF Research Career Development (Grant No. RSA5780013), and TRF Senior Research Scholar (Grant No. RTA5780004).

References

Ali, M.B., Saidur, R., Hossain, M.S., 2011. A review on emission analysis in cement industries. Renew. Sust. Energy Rev. 15 (5), 2252–2261.
Ariffin, M.A.M., Bhutta, M.A.R., Hussin, M.W., Modh Tahir, M., Aziah, N., 2013. Sulfuric acid resistance of blended ash geopolymer concrete. Constr. Build. Mater. 43, 80–86.
ASTM C39/C39M-01, 2003. Standard Test Method for Compressive Strength of Cylindrical Concrete Specimens. American Society for Testing and Materials, West Conshohocken, USA.
ASTM C78-02, 2003. Standard Test Method for Flexural Strength of Concrete (Using Sample Beam with Third-point Loading). American Society for Testing and Materials, West Conshohocken, USA.
ASTM C267, 2003. Standard Test Methods for Chemical Resistance of Mortars, Grouts, and Monolithic Surfacings and Polymer Concretes. American Society for Testing and Materials, West Conshohocken, USA.
ASTM C496-96, 2003. Standard Test Method for Splitting Tensile Strength of Cylindrical Concrete Specimens. American Society for Testing and Materials, West Conshohocken, USA.
ASTM C642, 2003. Standard Test Method for Density, Absorption, and Voids in Hardened Concrete. American Society for Testing and Materials, West Conshohocken, USA.
ASTM C944, 1999. Standard Test Method for Abrasion Resistance of Concrete or Mortar Surfaces by the Rotating-cutter Method. American Society for Testing and Materials, West Conshohocken, USA.
ASTM C1585, 2011. Standard Test Method for Measurement of Rate of Absorption of Water by Hydraulic-cement Concretes. American Society for Testing and Materials, West Conshohocken, USA.
ASTM C1611/C1611M-09b, 2010. Standard Test Method for Slump Flow of Self-consolidating Concrete. American Society for Testing and Materials, West Conshohocken, USA.
Bagheri, A., Zanganeh, H., Alizadeh, H., Shakerinia, M., Marian, M.A.S., 2013. Comparing the performance of fine fly ash and silica fume in enhancing the properties of concretes containing fly ash. Constr. Build. Mater. 47 (6), 1402–1408.
Carrasco, B., Cruz, N., Terrados, J., Corpas, F.A., Pérez, L., 2014. An evaluation of bottom ash from plant biomass as a replacement for cement in building blocks. Fuel 118, 272–280.
Chindaprasirt, P., Chalee, W., 2014. Effect of sodium hydroxide concentration on chloride penetration and steel corrosion of fly ash-based geopolymer concrete under marine site. Constr. Build. Mater. 63, 303–310.
Chindaprasirt, P., Jaturapitakkul, C., Chalee, W., Rattanasak, U., 2009. Comparative study on the characteristics of fly ash and bottom ash geopolymers. Waste. Manage 29, 539–543.
Davidovits, J., 1999. Geopolymer: inorganic polymeric new materials. J. Therm. Anal. 37, 1633–1656.
Dinakar, P., Babu, K.G., Santhanam, M., 2008. Durability properties of high volume fly ash self compacting concretes. Cem. Concr. Compos. 30, 880–886.
Duxson, P., Fernández-Jiménez, A., Provis, J.L., Lukey, G.C., Palomo, A., Van Deventer, J.S.J., 2007. Geopolymer technology: the current state of the art. J. Mater. Sci. 42, 2917–2933.
EFNARC, 2005. Specification and Guidelines for Self-compacting Concrete. English ed. European Federation for Spec Constr Chem & Concr Syst.
Etxeberria, M., Vázquez, E., Marí, A., Barra, M., 2007. Influence of amount of recycled coarse aggregates and production process on properties of recycled aggregate concrete. Cem. Concr. Res. 37 (5), 735–742.
Hwang, J.P., Shim, H.B., Lim, S., Ann, K.Y., 2013. Enhancing the durability properties of concrete containing recycled aggregate by use of pozzolanic materials. KSCE J. Civ. Eng. 17 (1), 155–163.
ISO, 2006. Environmental Management-Life Cycle Assessment. Set of International Standards: ISO 14040–14043. International Organization for Standardization, Ganeva, Switzerland.
Lee, W.K., van Deventer, J.S.J., 2002. The effects of inorganic salt contamination on the strength and durability of geopolymer. Colloids Surf. A 211 (2–3), 115–126.
Li, C., Li, Y., Sun, H., Li, L., 2011. The composition of fly ash glass phase and its dissolution properties applying to geopolymeric materials. J. Am. Ceram. Soc. 94 (6), 1733–1778.
Marie, I., Quiasrawi, H., 2012. Closed-loop recycling of recycled concrete aggregates. J. Clean. Prod. 37, 243–248.
Marinkovic, S., Radonjanin, V., Malesev, M., Ignjatovic, I., 2010. Comparative environmental assessment of natural and recycled aggregate concrete. Waste Manag. 30, 2255–2264.
Mefteh, H., Kebaili, O., Oucief, H., Berredjem, L., Arabi, N., 2013. Influence of moisture condition of recycled aggregates on the properties of fresh and hardened concrete. J. Clean. Prod. 54, 282–288.
Mikuni, A., Komatsu, R., Ikeda, K., 2007. Dissolution properties of some fly ash fillers applying to geopolymeric materials in alkali solution. J. Mater. Sci. 42, 2953–2957.
Otsuki, N., Nagataki, S., Nakashita, K., 1993. Evaluation of $AgNO_3$ solution spray method for measurement of chloride penetration into hardened cementitious matrix materials. Constr. Build. Mater. 7 (4), 195–201.
Pacheco-Torgal, F., Jalali, S., 2011. Resistance to acid attack, abrasion and leaching behavior of alkali-activated mine waste binders. Mater. Struct. 44, 487–498.
Phoo-ngernkham, T., Chindaprasirt, P., Sata, V., Pangdaeng, S., Sinsiri, T., 2013. Properties of high calcium fly ash geopolymer paste with Portland cement as an additive. Int. J. Min. Metall. Mater. 20 (2), 214–220.
Ping, W., Yidong, X., 2011. Life cycle assessment of recycled aggregate concrete containing fly ash. In: Second International Conference on Mechanic Automation and Control Engineering (MACE), 15–17 July, Inner Mongolia, China, pp. 2287–2290.
Poon, C.S., Shui, Z.H., Lam, L., Fok, H., Kou, S.C., 2004. Influence of moisture of natural and recycled aggregates on the slump and compressive of concrete. Cem. Concr. Res. 34, 31–36.
Rahal, K., 2007. Mechanical properties of concrete with recycled coarse aggregate. Build. Environ. 42, 407–415.
Rattanasak, U., Chindaprasirt, P., 2009. Influence of NaOH solution on the synthesis of fly ash geopolymer. Miner. Eng. 22, 1073–1078.
Sarker, P.K., 2011. Bond strength of reinforcing steel embedded in fly ash-based geopolymer concrete. Mater. Struct. 44, 1021–1030.
Sata, V., 2010. The use of local pozzolanic materials in fiber reinforced concrete. KKU Eng. J. 37 (1), 29–37.
Sata, V., Sathonsaowapak, A., Chindaprasirt, P., 2011. Resistance of lignite bottom ash geopolymer mortar to sulfate and sulfuric acid attack. Cem. Concr. Compos. 34 (5), 700–708.
Shi, X.S., Collins, F.G., Zhao, X.L., Wang, Q.Y., 2012. Mechanical properties and microstructure analysis of fly ash geopolymeric recycled concrete. J. Hazard. Mater. 237–238, 20–29.
Siddique, R., 2013. Compressive strength, water absorption, sorptivity, abrasion resistance and permeability of self-compacting concrete containing coal bottom ash. Constr. Build. Mater. 47, 1444–1450.
Somna, R., Jaturapitakkul, C., Rattanachu, P., Chalee, W., 2012. Effect of ground bagasse ash on mechanical and durability properties of recycled aggregate concrete. Mater. Des. 36, 597–603.
Songpiriyakij, S., Pulngern, T., Pungpremtrakul, P., Jaturapitakkul, C., 2011. Anchorage of steel bars in concrete by geopolymer paste. Mater. Des. 32 (5), 3021–3028.
Temuujin, J., Minjigmaa, A., Lee, M., Chen-Tan, N., van Riessen, A., 2011. Characteristic of class F fly ash geopolymer pastes immersed in acid and alkalie solutions. Cem. Concr. Compos. 33 (10), 1086–1091.
Tu, T.Y., Chen, Y.Y., Hwang, C.L., 2006. Properties of HPC with recycled aggregates. Cem. Concr. Res. 36 (5), 943–950.
Turner, L.K., Collins, F.G., 2013. Carbon dioxide equivalent (CO_2-e) emissions: a comparison between geopolymer and OPC cement concrete. Constr. Build. Mater. 43, 125–130.
Zhao, R., Sanjayan, J.G., 2011. Geopolymer and Portland cement concretes in simulated fire. Mag. Concr. Res. 63 (3), 163–173.

Journal of Cleaner Production 112 (2016) 3057–3062

Contents lists available at ScienceDirect

Journal of Cleaner Production

journal homepage: www.elsevier.com/locate/jclepro

Utilization of waste glass to enhance physical–mechanical properties of fired clay brick

Nonthaphong Phonphuak [a, b], Siwadol Kanyakam [a, b], Prinya Chindaprasirt [c, *]

[a] Department of Engineering Management, Faculty of Engineering, Rajabhat Maha Sarakham University, Maha Sarakham 44000, Thailand
[b] Engineering Management Research Unit, Rajabhat Maha Sarakham University, Maha Sarakham 44000, Thailand
[c] Sustainable Infrastructure Research and Development Center (SIRDC), Department of Civil Engineering, Faculty of Engineering, Khon Kaen University 40002, Thailand

ARTICLE INFO

Article history:
Received 10 April 2015
Received in revised form
6 October 2015
Accepted 19 October 2015
Available online 27 October 2015

Keywords:
Clay brick
Waste glass
Firing temperature
Physical–mechanical properties
Brick manufacture

ABSTRACT

The aim of this study was to investigate the enhancement of physical–mechanical properties of fired clay brick by incorporating waste glass in order to reduce the firing temperature. The ground waste glass was incorporated to the clay body at the dosages of 0, 5 and 10% by weight. Three temperatures viz., 900, 950 and 1000 °C were used for firing. Compressive strength, water absorption, density, and porosity of the fired clay bricks were tested. The study showed that the incorporation of up to 10 wt.% of waste glass to clay bricks and fired at the temperatures of 900–1000 °C enhanced the properties of fired clay bricks. The SEM micrographs showed the increased glass phase and reduced porosity with waste glass addition. The use of 10 wt.% waste glass and firing at 900 °C yielded bricks with similar strength compared to that of normal clay brick fired at 1000 °C. This allowed the use of low firing temperature of 900 °C instead of the normally used 1000 °C. The study also revealed that in addition to the glass phase fused-bond with the clay brick bodies, the fusion of crystalline quartz in clay also played an important role in enhancing the properties of clay bricks. As a conclusion, waste glass can be utilized in making brick to enhance the physical–mechanical properties of the fired clay brick or to lower the firing temperature.

© 2015 Elsevier Ltd. All rights reserved.

1. Introduction

Fired clay bricks are construction materials which have been used since ancient times and currently display different states of deterioration in numerous historic buildings (Cultrone et al., 2005). Nowadays, bricks are still being used for the same purpose (Karaman et al., 2006). However, the higher quality fired brick is essential for modern construction. Bricks have been designed to become more homogenous and porous, harder and stronger due to the ceramic bond from the fusion phase of silica and alumina constituents in clay (Adeola, 1977). The firing process sinters the particles of clay together to form a bond which gives the bricks its characteristic strength and durability (Phonphuak and Chindaprasirt, 2014). The sintering process is achieved by heating silicon dioxide or quartz (SiO_2) which occurs naturally in clay and shale to high temperatures, causing it to melt. Upon cooling, the quartz forms a bond between adjacent clay or shale particles at the points of contact.

The brick production is an energy intensive process. The average specific energy consumption for fired clay brick in the United Kingdom was reported at 706 kWh/ton of brick (Industrial Energy Efficiency Accelerator, 2015). Owing to the high energy demands of the sintering process, additives called fluxes are often used to lower the temperature required to form the glassy phase bond. The brick industry can easily accommodate by-product materials because the making of brick is relatively uncomplicated (Turgut, 2012). Common additive is a soda-lime-silica glass (SiO_2–Na_2O–CaO) (Grimshaw, 1971). In fact, soda-lime-glass is a vitreous silicate generated during the maturation of clay bodies. The reducing clay body maturation temperature is a strong indication that the addition of soda-lime-glass to clay body could increase the efficiency of firing and is thus a value-added application for recycled glass fines (Mustafi et al., 2011).

One waste material which has potential as a brick additive is waste glass (soda-lime glass). In European Union, approximately 9 million ton of waste glass was collected in 2010 (Eurostat Statistics Explained, 2010). As a brick additive, glass acts as a flux owing to its

* Corresponding author.
E-mail address: prinya@kku.ac.th (P. Chindaprasirt).

http://dx.doi.org/10.1016/j.jclepro.2015.10.084
0959-6526/© 2015 Elsevier Ltd. All rights reserved.

sodium oxide (Na_2O) content and its noncrystalline composition, thus lowering the temperature required for sintering bricks. In addition, the increased glassy phase in the finished brick has the potential for improvement in both structural and durability properties, while reducing manufacturing costs (Chidiac and Federico, 2007). A number of researchers have investigated the use of waste glass particularly in ceramic industry. Example includes waste glass incorporated as an alternative ceramic raw material or as a fluxing agent in cement and/or concrete, stoneware tile and brick (Shao et al., 2000; Shayan and Xu., 2004; Hwang et al., 2006). As an additive, waste glass, when incorporated into a mixture, could induce the vitrification in clay bricks, resulting in higher density, less water absorption, and lower drying shrinkage (Loryuenyong et al., 2009). However, there is still a need to relate the effect of waste glass on strength, porosity and firing shrinkage characteristics of fired clay brick. In this research, the effects due to the use of waste glass were investigated in laboratory and the firing behavior, physical–mechanical properties and microstructure were discussed.

2. Materials and methods

2.1. Preparation of the test specimens

The clay used in this study was typical clay from a well known local area for making bricks. Chemical analyses of clay and waste glass (soda-lime glass) were carried out using X-ray fluorescence technical (Horiba Mesa-500 w). The chemical composition of raw materials is given in Table 1. The waste glass was first crushed for 1 h using a ball mill. The particle-size distribution test was carried out for waste glass using sieve size analysis. The results of the particle size analysis are shown in Fig. 1. The mineralogical composition of clay and waste glass were achieved using an X-ray diffractometer technique (XRD: X'Pert PRO MPD, Philips, Netherlands). The major crystalline phases found in clay were quartz, muscovite and rutile (Fig. 2) and waste glass contained only glassy phase (Fig. 3).

2.2. Specimen preparation

In order to compare the clay brick (0% waste glass) and bricks made of clay and glass (5% and 10% waste glass), each batch of specimens was mixed in a porcelain ball mill to ensure homogenous mixing. In normal brick production, however, normal mixing would be sufficient to save time and cost. Then, 20–25% of water was added and mixed to obtain plastic condition of mixture. Soft-mud rectangular clay bricks with dimension of 140 mm × 65 mm × 40 mm were formed using brick hand molding. The clay brick specimens were air-dried at room temperature (25–30 °C) for 24 h, and then over dried at 110 ± 5 °C for another 24 h to remove water content. The green specimens were fired at three temperatures viz., 900, 950 and 1000 °C. The time taken to reach the required temperature was 8 h and the specimens were kept at this temperature for 1 h.

Table 1
Chemical compositions of raw materials.

Composition	Clay (wt.%)	Waste glass (wt.%)
SiO_2	58.76	68.70
Al_2O_3	21.34	21.34
MgO	–	2.45
CaO	0.21	9.86
Fe_2O_3	5.10	0.65
MnO	1.18	–
TiO_2	0.93	0.12
Na_2O	–	13.67
K_2O	3.10	1.00
LOI	8.74	–

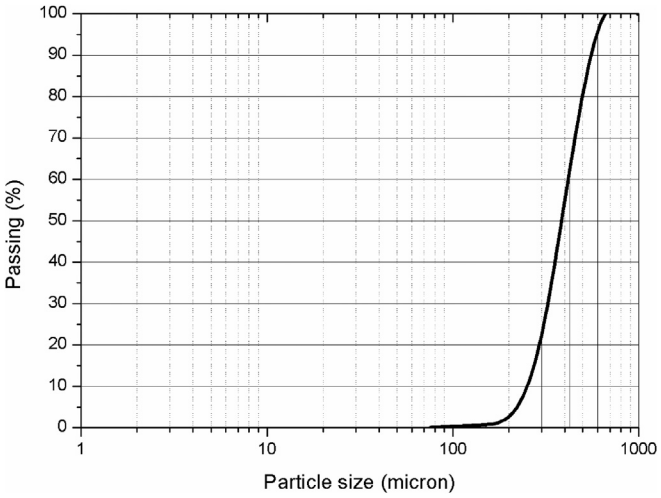

Fig. 1. Particle size analysis of waste glass.

2.3. Testing method for the physical and mechanical properties of specimens

Shrinkage was determined by direct measurement of specimen length before and after firing. The linear drying shrinkage and total linear shrinkage were measured and compared to the length before shrinkage in accordance with the standard of ASTM C326-09 (2014). Archimedes method based on ASTM C373-14a (2014) was used to determine the water absorption, bulk density, apparent density and apparent porosity. The compressive strengths of specimens were measured in accordance with ASTM C773-88 (2011). The reported results of all tests were the average of 10 samples.

3. Results and discussion

The bricks in this research were manufactured from clay and waste glass by controlling the optimum sintering temperatures and ratio. The properties of fired clay bricks are shown in Fig. 4(a)–(d).

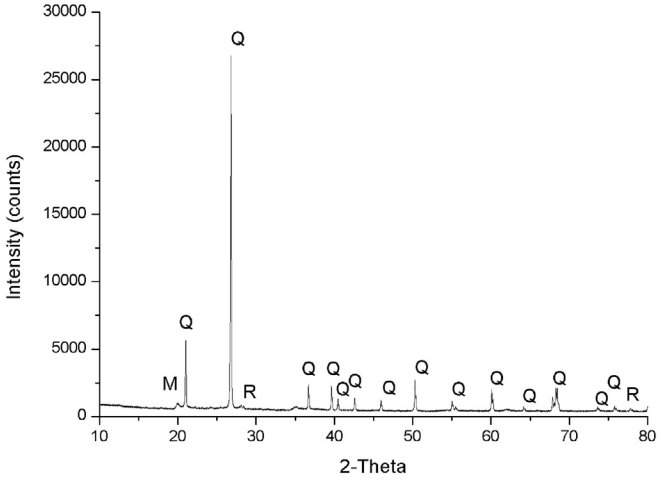

Fig. 2. XRD pattern of clay material (Q = quartz, M = muscovite, R = rutile).

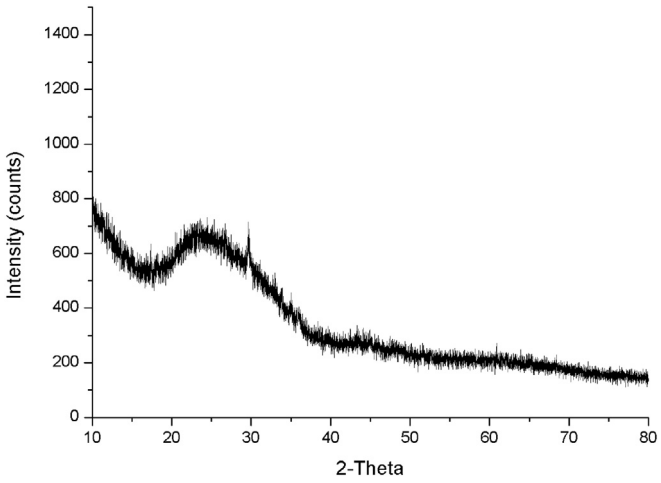

Fig. 3. XRD pattern of waste glass.

The investigated and reported physical and mechanical properties are firing shrinkage, water absorption, bulk density, apparent porosity compressive strength and microstructure analysis of vitrification.

3.1. Effects of waste glass addition on the physic-mechanical properties of the fired clay bricks

3.1.1. Firing shrinkage

Firing shrinkage is related to the loss of water between clay particles resulting in the closer packing of clay particles and resulted shrinkage. To minimize shrinkage, firing temperature which is an important parameter affecting the degree of shrinkage must be controlled during the firing process (Karaman et al., 2008). Normally, a good quality of brick exhibits a shrinkage below 8% (Okunade, 2008). In this study, fired clay bricks were fired at temperatures of 900, 950 and 1000 °C. The firing shrinkage increased with increasing firing temperature and decreased with increasing amounts of waste glass. There was a linear decrease in the total shrinkage as the amount of waste glass in the mixture increased (Fig. 4a). The results showed that shrinkage occurred in the fired clay brick was in the range of 3.41–4.34%. Whereas, the control fired clay bricks without any waste glass addition had comparable firing shrinkage between 3.43% and 4.83%.

3.1.2. Density

Density of clay brick depends on specific gravity of the raw material, method of manufacturing and degree of burning (Karaman et al., 2008). As the density of a clay brick increases, its strength also increases, while its water absorption decreases. The bulk density of clay bricks was proportional to the quantity of waste glass added in the mixture. The bulk density of clay bricks increased with an increase in the amount of waste glass. Bulk density of clay bricks also increased with an increase in firing temperature. As a result, the bulk densities of bricks containing waste glass were in the range of 1.70–1.76 g/cm^3 (Fig. 4b). The bulk density is related to durability and water absorption of clay bricks.

3.1.3. Water absorption and apparent porosity

Water absorption is an important factor for the durability of clay bricks. When water infiltrates brick, it decreases the durability of brick (Demir, 2009). Thus, the internal structure of brick must be sufficiently dense to void the intrusion of water. To increase density and decrease water absorption of clay bricks, the firing temperature must be raised. According to Fig. 4c, the water absorptions of clay bricks fired at the temperatures between 900 and 1000 °C were in the range of 14.78–18.66%.

Water absorption is indirectly proportional to apparent porosity. Therefore, similar trends were observed in water absorption and apparent porosity (Eliche-Quesada et al., 2011). The study showed that the apparent porosity of fired clay bricks depended on the amount of waste glass addition. The highest porosity was 35.17% with no waste glass addition fired at 900 °C, and the lowest was 29.71% with 10% of waste glass addition fired at 1000 °C. This result revealed that the lowest porosity in fired clay brick occurred when the highest percentage of waste glass was added (Fig. 4d). Thus the pores of fired clay brick were affected due to the increased formation of glassy phase during firing process.

The reduction in water absorption after firing at 1000 °C suggested the increase in the local liquid-phase at high firing temperature and thus contributed to a decrease in the pore volume and water absorption rate. However, the addition of waste glass contributed to the vitrification and enhanced the compressive strength development by closing the internal pores with glassy phase especially at the high firing temperatures. The waste glass particles fused with the clay bodies and this contributed to the densification of the clay brick.

According to ASTM C62-13a (2013), the Grade MW and SW bricks must have an average maximum absorption of 22.0 and 17.0%, respectively. The firing temperature of 900 °C produced bricks with the required average maximum absorption for Grade MW and firing temperatures of 950 and 1000 °C met the requirement for Grade SW.

3.1.4. Compressive strength

The compressive strength is a mechanical property used in clay brick specification. It has assumed great importance for two reasons. Firstly, with a higher compressive strength, other properties like flexure, resistance to abrasion are also improved. Secondly, while other properties are relatively difficult to evaluate, the compressive strength is easy to determine (Okunade, 2008). The compressive strength of clay brick is the most important engineering-quality index for building materials. In this study the result indicated that the strength of fired clay bricks greatly depended on the amount of waste glass addition and firing temperature. The result of the compressive strength (Fig. 5) indicated that compressive strength of fired clay bricks increased with increasing firing temperature. An increase in compressive strength was due to a decrease in porosity and increase in bulk density with increasing temperature (Fig. 6). The results revealed that the compressive strengths were in the ranges of 19.30–24.65 MPa when waste glass addition increased from 5 to 10% and firing temperatures from 900 to 1000 °C (Fig. 5). However, the addition of waste glass considerably contributed to vitrification and enhanced the strength development by closing the internal pores with glassy phase, especially during firing.

The incorporation of 10% waste glass significantly increased the compressive strength of bricks. In fact, the compressive strength of brick with no waste glass and fired at 1000 °C was 20.18 MPa which was the same as that of brick with 10% waste glass but fired at lower temperature of 900 °C. According to ASTM C62-13a (2013), the Grade MW bricks must have an average minimum compressive strength of 17.2 MPa. The incorporation of 5 and 10% waste glass with firing temperature of 900 °C produced fired bricks with adequate strength. Furthermore, the porosity of the brick with 10% waste glass but fired at 900 °C was 35.11% which was significantly higher that the value of 32.11% of brick with no waste glass and fired at 1000 °C. The optimum firing temperature was the lowest temperature used to produce bricks with required properties. In

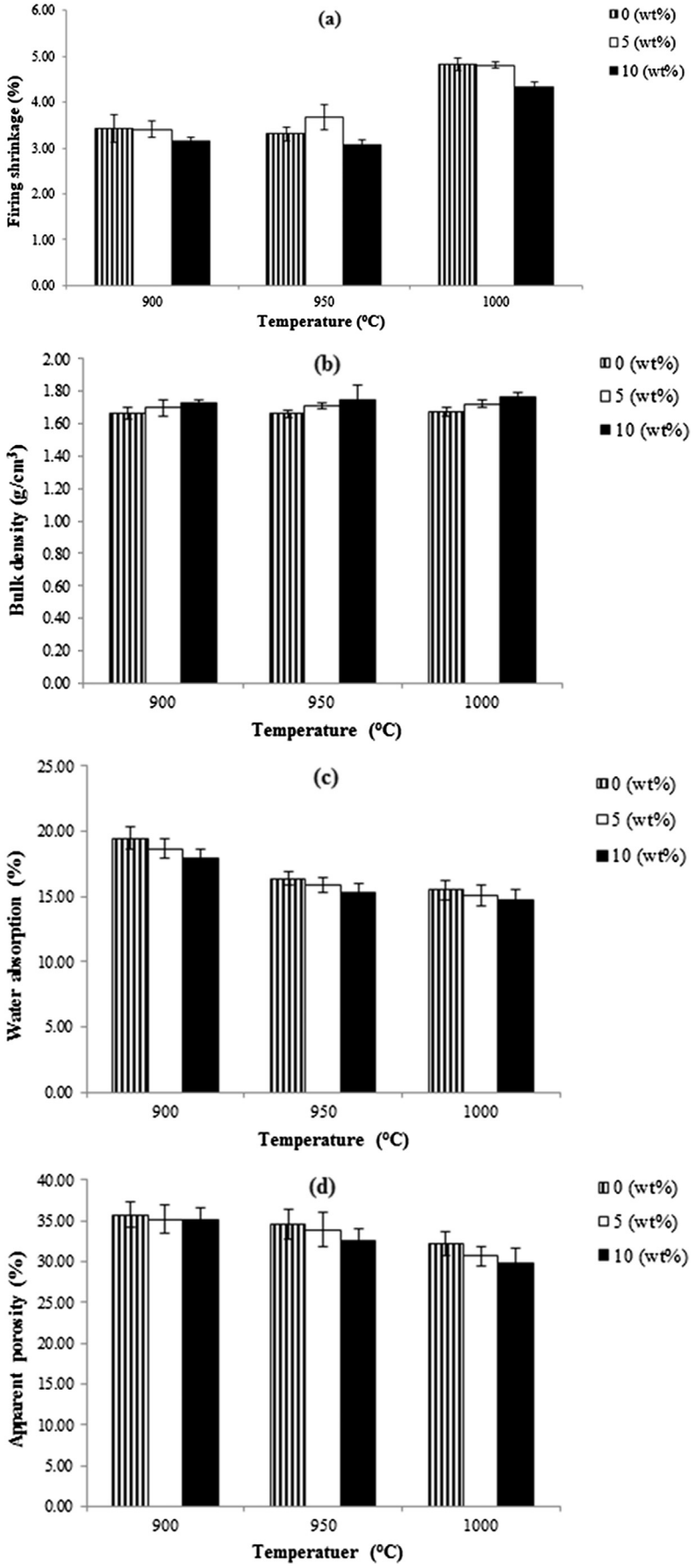

Fig. 4. Physical properties of fired clay bricks fired at 900–1000 °C: (a) firing shrinkage, (b) bulk density, (c) water absorption and (d) apparent porosity.

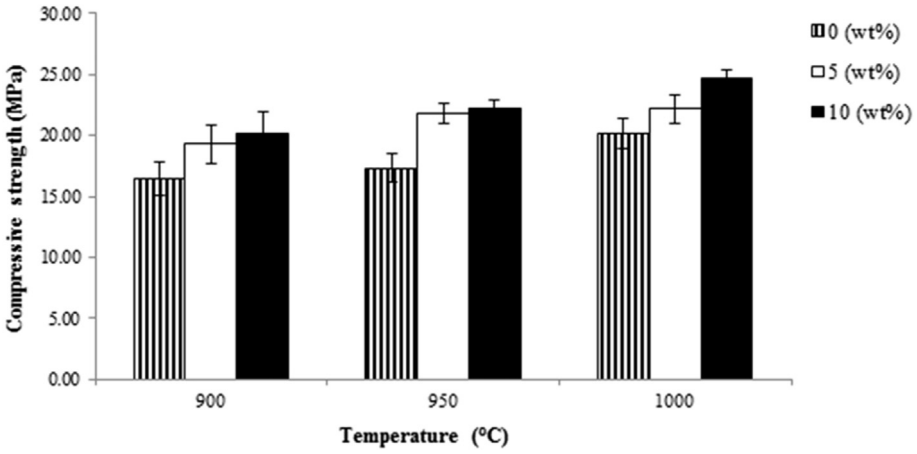

Fig. 5. Compressive strengths of fired clay bricks.

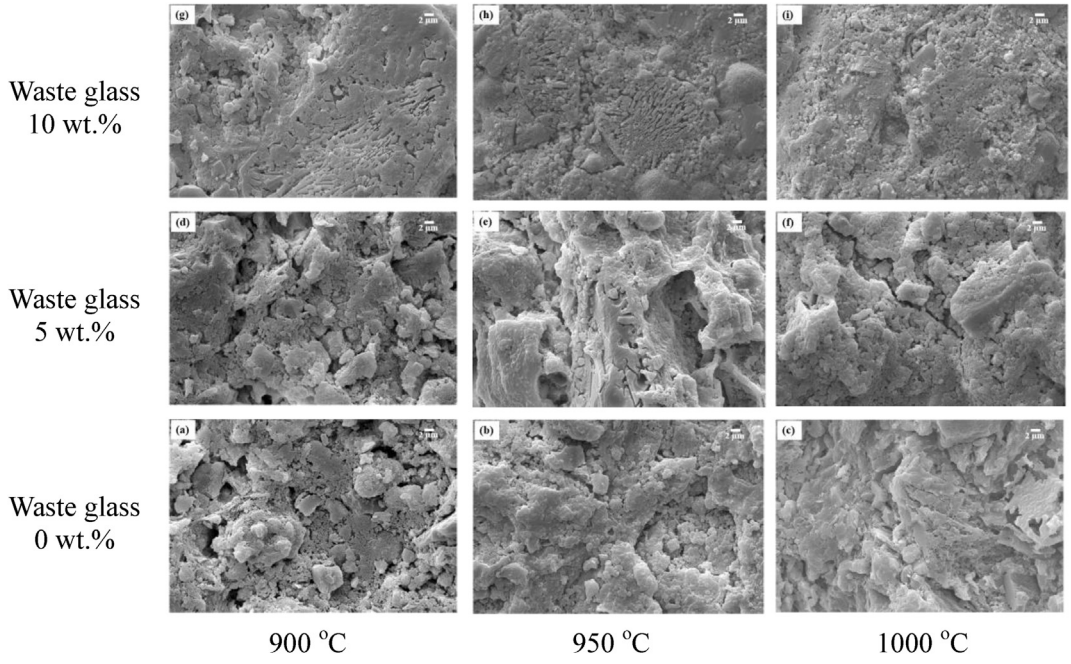

Fig. 6. SEM images of specimens fired at 900, 950 and 1000 °C.

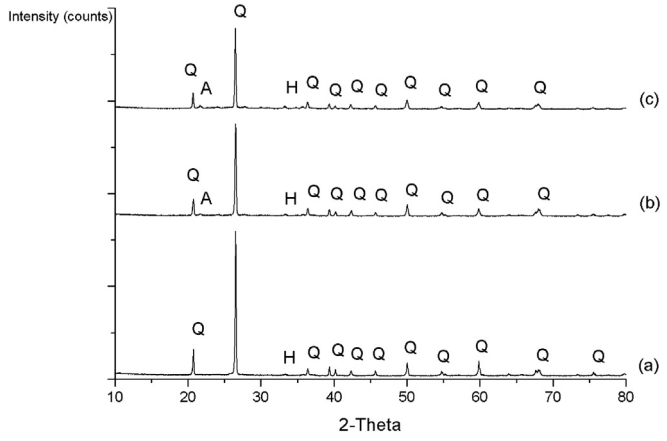

Fig. 7. XRD pattern of clay brick fired at 1000 °C (a) 0 wt.% waste glass, (b) 5 wt.% waste glass and (c) 10 wt.% waste glass (Q = Quartz, A = Anorthite, H = Hematite).

other words, a lower firing temperature of 900 °C could be used in conjunction with the incorporation of 10% waste glass to produced bricks with similar or better physical properties to normal brick fired at 1000 °C.

3.2. Microstructure analysis of fired clay bricks vitrification

The SEM results of bricks specimen fired at 900–1000 °C with different amount of waste glass are shown in Fig. 6. The images showed that as waste glass contents increased, the matrix became denser with increased glass phase fused-bond with the clay brick bodies. Moreover, the waste glass addition facilitated the glassy phase transformation in the clay bodies. Therefore the addition of waste glass made a positive contribution to the compressive strength of the fired clay brick. The crystalline phases of fired clay bricks containing waste glass fired at 1000 °C are shown in Fig. 7. At low waste glass level (0 wt.%), the major phase was dominated by

the existence of quartz (α-SiO_2) with a dominant peak at 27° 2Θ. As the waste glass level was increased to 5 and 10 wt.%, a small peak of anorthite ($Ca(Al_2SiO_8)$) was detected around 22° 2Θ with the reduction in overall crystalline quartz. With the presence of waste glass, a small amount of amorphous silica converted to anorthite upon firing at high temperatures of 950 and 1000 °C. The reduction of the crystalline quartz with the incorporation of waste glass confirmed that some of crystalline quartz in clay fused and formed the dense fired clay body and resulted in the reduction of peaks of quarts. This is in line with the results of Lin et al. (2013) who reported the reduction of crystalline quartz with incorporation of 10% solar panel waste glass. The results also conformed with the porosity values of the fired brick which indicated that the increased in the waste glass content and firing temperature resulted in the formation of increased glassy phase content of the brick with reduced porosity. This result indicated that α-SiO_2 plays an important role as a back-bone in the structure of ceramic brick with the modification of the increased glassy phase content on waste glass addition.

4. Conclusions

The physical and mechanical properties of fired clay brick with waste glass addition were studied. The results showed that the compressive strength of bricks increased with increases in waste glass addition from 0 to 10 wt.% and firing temperatures from 900 to 1000 °C. The values of apparent porosity and water absorption of bricks also decreased with increases in waste glass addition and firing temperatures. The optimum waste glass content of 10 wt.% enabled the clay brick to be fired at lower temperature of 900 °C and resulted in bricks with similar strength and a slight increase in porosity compared to those of normal clay bricks fired at 1000 °C. The study also revealed that the glass phase fused-bond with the clay brick bodies as well as the fusion of the crystalline quartz in clay resulting in the acceleration of densification process with some positive effects viz., increased strength; and lowering of open porosity and water absorption. The waste glass could thus be used as a potential fluxing agent to help lowering firing temperature or improving the physical and mechanical properties of fired clay bricks.

Acknowledgment

This work was financially supported by Khon Kaen University and the Thailand Research Fund (TRF) under the TRF Senior Research Scholar Contract No. RTA5780004. The authors also would like to acknowledge the support of Rajabhat Maha Sarakham University.

References

Adeola, J.O., 1977. A Review of Masonry Block/Brick Types Used for Building in Nigeria (M. Eng. thesis). University of Benin, Benin-City.
ASTM C62-13a, 2013. Standard Specification for Building Brick (Solid Masonry Units Made from Clay or Shale). In: ASTM Book of Standards, vol. 04.05.
ASTM C326-09, 2014. Standard Test Method for Drying and Firing Shrinkages of Ceramic Whiteware Clays. In: ASTM Book of Standards, vol. 15.02.
ASTM C373-14a, 2014. Standard Test Method for Water Absorption, Bulk Density, Apparent Porosity, and Apparent Specific Gravity of Fired Whiteware Products, Ceramic Tiles, and Glass Tiles. In: ASTM Book of Standards, vol. 15.02.
ASTM C773-88, 2011. Standard Test Method for Compressive (Crushing) Strength of Fired Whiteware Materials. In: ASTM Book of Standards, vol. 15.02.
Chidiac, S.E., Federico, L.M., 2007. Effects of waste glass additions on the properties and durability of fired clay brick. Can. J. Civ. Eng. 34, 1458–1466.
Cultrone, G., Sebastián, E., Torre de la, M.J., 2005. Mineralogical and physical behavior of solid bricks with additives. Constr. Build. Mater 19, 39–48.
Demir, I., 2009. Reuse of waste glass in building brick production. Waste Manag. Res. 27, 572–577.
Eliche-Quesada, D., Martínez-García, C., Martínez-Cartas, M.L., Cotes-Palomino, M.T., Pérez-Villarejo, L., Cruz-Pérez, N., Corpas-Iglesias, F.A., 2011. The use of different forms of waste in the manufacture of ceramic bricks. Appl. Clay Sci. 52, 270–276.
Eurostat Statistics Explained, 2010. Recycling – Secondary Material Price Indicator – Statistics. Referenced 05.10.15. Available from: http://ec.europa.eu/eurostat/statistics-explained/index.php/Recycling_%E2%80%93_secondary_material_price_indicator.
Grimshaw, R.W., 1971. The Chemistry and Physics of Clays and Allied Ceramic Materials. Ernest Benn Limited, London.
Hwang, J.Y., Huang, X., Garkida, A., Hein, A., 2006. Waste colored glasses as sintering aid in ceramic tile production. J. Miner Mater Character Eng. 5, 119–129.
Industrial Energy Efficiency Accelerator, 2015. Guide to the Brick Sector. Referenced 29.09.15. Available from: https://www.carbontrust.com/media/206484/ctg043-brick-industrial-energy-efficiency.pdf.
Karaman, S., Ersahin, S., Gunal, H., 2006. Firing temperature and firing time influence on mechanical and physical properties of clay bricks. J. Sci. Ind. Res. 65, 153–159.
Karaman, S., Gunal, H., Ersahin, S., 2008. Quantitative analysis of pumice effect on some physical and mechanical properties of clay bricks. Appl. Clay Sci. 8 (7), 1340–1345.
Lin, K.L., Huang, L.S., Shie, J.L., Cheng, C.J., Lee, C.H., Chang, T.C., 2013. Elucidating the effects of solar panel waste glass substitution on the physical and mechanical characteristics of clay brick. Environ. Technol. 34 (1), 15–24.
Loryuenyong, V., Panyachai, T., Kaewsimork, K., Siritai, C., 2009. Effects of recycled glass substitution on the physical and mechanical properties of clay bricks. Waste Manag. 29, 2717–2721.
Mustafi, S., Ahsan, M., Dewan, A.H., Ahmed, S., Khatun, N., Absar, N., 2011. Effect of waste glass powder on physic-mechanical properties of ceramic tile. J. Sci. Res. 24 (2), 169–180.
Okunade, E.A., 2008. The effect of wood ash and sawdust admixtures on the engineering properties of a burnt laterite-clay brick. J. Appl. Sci. 8 (6), 1042–1048.
Phonphuak, N., Chindaprasirt, P., 2014. Types of waste, properties and durability of pore forming waste-based fired masonry bricks. In: Pacheco-Torgal, F., Lourenço, P.B., Labrincha, J.A., Kumar, S., Chindaprasirt, P. (Eds.), Eco-efficient Masonry Bricks and Blocks: Design, Properties and Durability, first ed. Woodhead Publishing, pp. 103–127.
Shao, Y., Lefort, T., Moras, S., Rodriguez, D., 2000. Studies on concrete containing ground waste glass. Cem. Concr. Res. 30, 91–100.
Shayan, A., Xu, A., 2004. Value-added utilization of waste glass in concrete. Cem. Concr. Res. 34, 81–89.
Turgut, P., 2012. Manufacturing of building bricks without Portland cement. J. Clean. Prod. 37, 361–367.

Computers and Concrete, *Vol. 17, No. 3 (2016) 337-351*
DOI: http://dx.doi.org/10.12989/cac.2016.17.3.337

Properties of pervious concrete containing high-calcium fly ash

V. Sata[a], C. Ngohpok[b] and P. Chindaprasirt[*]

Sustainable Infrastructure Research and Development Center, Department of Civil Engineering, Faculty of Engineering, Khon Kaen University, Khon Kaen 40002, Thailand

(Received January 20, 2014, Revised December 13, 2015, Accepted January 22, 2016)

Abstract. This paper presents the properties of pervious concrete containing high-calcium fly ash. The water to binder ratios of 0.19, 0.22, and 0.25, designed void ratios of 15, 20, and 25%, and fly ash replacements of 10, 20, and 30% were used. The results showed that the use of fly ash as partial replacement of Portland cement enhanced the mixing of paste resulting in a uniform mix and reduced amount of superplasticizer used in the mixture. The compressive strength and flexural strength of pervious concrete were slightly reduced with an increase in fly ash replacement level, while the abrasion resistance increased due mainly to the pozzolanic and filler effects. The compressive strength and flexural strengths at 28 days were still higher than 85% of the control concrete. The aggregate size also had a significant effect on the strength of pervious concrete. The compressive strength and flexural strength of pervious concrete with large aggregate were higher than that with small aggregate.

Keywords: cement paste; pervious concrete; void ratio; fly ash; compressive strength; flexural strength

1. Introduction

Pervious concrete is a concrete with high porosity and continuous void (ACI 522R, 2010). The difference between pervious concrete and normal concrete is pervious concrete mixture contains little or no-fine aggregate (Sumanasooriya and Neithalath 2011, Tennis *et al*. 2004, Zaetang *et al*. 2013). In addition, pervious concrete has very low workability similar to a roller-compacted concrete with required compaction energy (Aamer Rafique Bhutta *et al*. 2012). Generally, the compressive strength of pervious concrete is between 2.8-28.0 MPa depending on the void ratio (ACI 522R 2010, Chindaprasirt *et al*. 2011, Lian *et al*. 2011). To obtain good quality and high strength pervious concrete, the flow of cement paste, void ratio, and the energy of compaction need to be controlled. In England and the US, pervious concrete has been used for over 30 years (Golroo and Tighe 2011, Shu *et al*. 2011). It has been studied and researched extensively in the US, Japan, and other countries (Aamer Rafique Bhutta *et al*. 2012, Yang and Jiang 2003). Pervious

*Corresponding author, Professor, E-mail: prinya@kku.ac.th
[a]Associate Professor, E-mail: vancsa@kku.ac.th
[b]Ph.D. Student, E-mail: chanchai.ng@gmail.com

Copyright © 2016 Techno-Press, Ltd.
http://www.techno-press.org/?journal=cac&subpage=8 ISSN: 1598-8198 (Print), 1598-818X (Online)

Table 1 Characteristics of ordinary Portland cement and fly ash

Properties	Cement	Fly ash
SiO_2 (%)	20.81	37.62
Al_2O_3 (%)	4.97	20.45
Fe_2O_3 (%)	3.51	12.37
CaO (%)	66.80	19.48
MgO (%)	0.78	2.79
SO_3 (%)	2.34	2.11
K_2O (%)	0.40	2.48
Na_2O (%)	0.01	1.97
Loss on ignition (%)	0.13	1.40
Specific gravity	3.14	2.27
Specific surface area (cm^2/g)	3300	2700

concrete has been used in the paving of roads and parking lots in order to efficiently solve the problem of storm water runoff and ground water (Golroo and Tighe 2011, Putman and Neptune 2011, Haselbach *et al*. 2006, Leming *et al*. 2007), and the drainage of retaining walls which help reduce the pressure of water. It can be used for paving the river, sewage and water treatment filters to reduce the pollution in water. In addition, it can be used for foundation of grass planting in the lawn or deck in order to reduce heat reflection, and also used for sound absorption. For these reasons, it can be said that pervious concrete is an environmentally friendly material.

Fly ash is a by-product obtained from coal burning process to produce electricity in a power generating plant. Generally, fly ash enhances concrete workability, segregation resistance, later age strength, and durability (Rukzon and Chindaprasirt 2008, Siddique and Khatib 2010, Ramanathan *et al*. 2013, Vimonsatit *et al*. 2015, Sunil *et al*. 2015). Furthermore, the electrical resistivity and capillarity of self-compacting concrete at the later age is improved with incorporation of fly ash (Silva and De Brito 2013). The high calcium fly ash contains high CaO and thus possesses the self cementing property. Moreover, the use of fly ash as a replacement of cement is another way to reduce the amount of cement, energy use and CO_2 emission (Siddique 2004, Limbachiya *et al*. 2012).

The purpose of this study is to investigate the use of high-calcium fly ash in pervious concrete. The first part dealt with property and workability of paste containing high-calcium fly ash and the second part dealt with void, compressive strength, flexural strength, water permeability, and abrasion of concrete. In addition, an expression predicting their properties was proposed.

2. Materials

Ordinary Portland cement type I with specific gravity of 3.14 and Blaine fineness of 3300 cm^2/g was used in this study. Fly ash was obtained from Mae Moh power station from Lampang Province in Thailand with specific gravity of 2.27 and Blaine fineness of 2700 cm^2/g. The chemical composition and physical properties of ordinary Portland cement and fly ash are shown in Table 1. The sum of SiO_2, Al_2O_3, and Fe_2O_3 of fly ash was around 70.0% with a high CaO

Table 2 Mix proportions of pervious concrete

Mixes	Cement	Fly ash	Aggregate	Water	SP	W/B
	(kg/m^3)	(kg/m^3)	(kg/m^3)	(kg/m^3)	(% of binder)	
0FA0.19-20I	438	0	1604	83	1.78	0.19
10FA0.19-20I	385	43	1604	81	1.68	0.19
20FA0.19-15I	410	102	1604	97	1.19	0.19
20FA0.19-20I	335	84	1604	79	1.55	0.19
20FA0.19-25I	260	65	1604	62	1.85	0.19
30FA0.19-20I	286	123	1604	78	1.44	0.19
20FA0.19-15II	435	109	1529	103	1.19	0.19
20FA0.19-20II	360	90	1529	85	1.56	0.19
20FA0.19-25II	285	71	1529	68	1.83	0.19
20FA0.22-20I	317	79	1604	87	0.71	0.22
20FA0.25-20I	301	75	1604	94	0.16	0.25

content of 19.5% which indicated a high-calcium fly ash according to ASTM C618 (2008). Two coarse limestone aggregates were used in this study. The first had diameter of 4.75-9.0 mm with specific gravity of 2.79, dry unit weight of 1604 kg/m^3, and void content of 44.0%. The second had diameter of 9-19 mm with specific gravity of 2.75, dry unit weight of 1529 kg/m^3 and void content of 43.2%. Water to binder ratios (W/B) of 0.19, 0.22, and 0.25 were used. Water reducing agent type F superplasticizer (SP) used in this investigation was selected based on previous work (Chindaprasirt *et al.* 2008).

3. Experimental study

3.1 Cement paste

To study the properties of paste, the water to binder ratios of 0.19, 0.22, and 0.25, the fly ash replacements of 10, 20, and 30% by weigh of binder were used. The mixing method of paste was set at 50 rpm for 30 s after the addition of binder, water, and admixture. This was followed by mixing at speed of 200 rpm for 240 s. After the mixing of paste, flow value was measured in accordance with JIS R 5201 (1997).

3.2 Concrete

3.2.1 Mixing of concrete

In this study, the designed void ratio of 15, 20, and 25% with flow values of paste of 150, 190, and 230 were selected. The mix proportions of concrete are given in Table 2. The symbol of mix proportion is given as xxFAyy-zzI., where xxFA is the amount of cement replaced by fly ash (%); yy is the water to binder ratio; zz is the designed void ratio (%); I and II stand for aggregate sizes of 9 mm and 19 mm, respectively. After the mixing of paste, the coarse aggregate was added to the mixture and mixed at 200 rpm for 120 s. The mixture was placed in two layers into 100×200 mm

cylindrical mould and 150×150×500 mm beam mould on a vibrating table. The vibration time was 10 s for each layer.

3.2.2 Testing of concrete

The void of concrete was measured using test method for pervious concrete in accordance with ASTM C 1754-12 (2012) as shown in the following Eq. (1)

$$A_T(\%) = \left(1 - \frac{W_2 - W_1}{\rho_W V}\right) \times 100 \quad (1)$$

where A_T is the total void of the concrete (%); W_1 is the weight of the specimen in water (g); W_2 is the weight of air dried of the specimen after being placed in room temperature conditions for 24 hr (g); ρ_W is the density of water at temperature of water bath (g/cm^3); and V is the volume of the specimen (cm^3).

The compressive strengths of concrete were determined in accordance with ASTM C 39/C 39M-01 (2003). Compression test cylinders were capped at both ends with a sulfur capping compound. The reported strengths were the average of three specimens.

The flexural strength were determined by simple beam with the third-point loading method and determined in accordance with ASTM C 78-02 (2003). The span length of 450 mm and the load rate was about 0.15±0.05 MPa/s. The flexural strength values were acquired from three samples from each group.

Water permeability was determined using a constant head permeability test apparatus which was successfully used by Zaetang et al. (2013). The coefficient of permeability (k) was calculated in accordance with Darcy's Law, as following Eq. (2).

$$k = \frac{H}{h} \times \left(\frac{Q}{A(T_2 - T_1)}\right) \times 100 \quad (2)$$

where k is the permeability coefficient (cm/s); H is the length of sample (cm); h is the difference in level (cm); Q is the flow quantity during the period from T_1 to T_2 (cm^3); A is the cross sectional area of test piece (cm^2); and T_2-T_1 is the measurement period of time (s).

The abrasion resistant of concrete was evaluated according to ASTM C 944-99 (2003), test method for abrasion resistance of concrete or mortar surfaces by the rotating-cutter method. The abrading cutter rotated at a speed of 200 rpm and exerted a force of a normal load of 98 ± 1 N. Each specimen was abraded for 2 min. In this test, the 150 mm cubic concrete samples were used and the surface abrasion test was performed at the age of 28 days. The extent of abrasion was determined from the difference in weight before and after the abrasion test.

4. Experimental results and discussion

4.1 Effect of fly ash and SP on flow of cement paste

The results showed that for W/B ratio of 0.19 and cement paste with fly ash replacement of 0, 10, 20, and 30% by weight, the dosages of SP were between 1.55-2.06, 1.38-2.02, 1.20-1.96, and 1.04-1.93%, respectively. The use of fly ash to replace part of cement increased the workability of

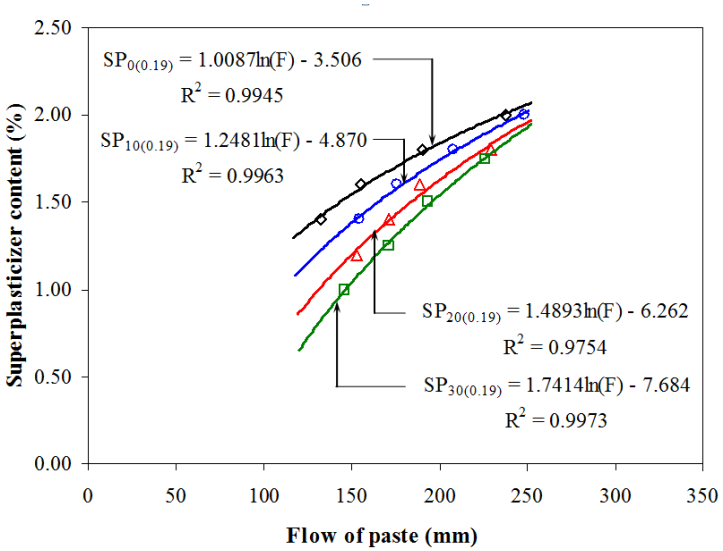

Fig. 1 Relationship between flow of paste and SP content with various fly ash replacements at W/B ratio of 0.19

paste. This was due to the spherical and the smoothness of surface texture of fly ash particles, thus allowing a better flow of cement paste (Sata *et al*. 2011, Siddique 2004). For OPC and replacements with fly ash of 10, 20, and 30% by weigh of cement and W/B ratio of 0.19, the dosage of SP can be calculated by Eqs. (3)-(6) as shown in Fig. 1. At the same fly ash replacement, the increase of water to binder ratio reduced the demand of SP as shown in Fig. 2. For the fly ash replacement of 20%, the SP dosage for W/B ratios of 0.22 and 0.25 can be calculated by Eqs. (7) and (8), respectively.

$$SP_{0(0.19)} = 1.0087\,ln(F) - 3.506,\ R^2 = 0.9945 \quad (3)$$

$$SP_{10(0.19)} = 1.2481\,ln(F) - 4.870,\ R^2 = 0.9963 \quad (4)$$

$$SP_{20(0.19)} = 1.4893\,ln(F) - 6.262,\ R^2 = 0.9754 \quad (5)$$

$$SP_{30(0.19)} = 1.7414\,ln(F) - 7.684,\ R^2 = 0.9973 \quad (6)$$

$$SP_{20(0.22)} = 1.4970\,ln(F) - 6.930,\ R^2 = 0.9743 \quad (7)$$

$$SP_{20(0.25)} = 1.5026\,ln(F) - 7.678,\ R^2 = 0.9690 \quad (8)$$

where $SP_{0(0.19)}$ is the dosage of SP with 100% OPC, W/B ratio of 0.19; $SP_{10(0.19)}$, $SP_{20(0.19)}$, and $SP_{30(0.19)}$ are the dosage of SP with 10, 20, and 30% fly ash (%), respectively, W/B ratio of 0.19; $SP_{20(0.22)}$, and $SP_{20(0.25)}$ are the dosage of SP with 20% fly ash (%), W/B ratio of 0.22 and 0.25, respectively; and F is flow of paste (mm).

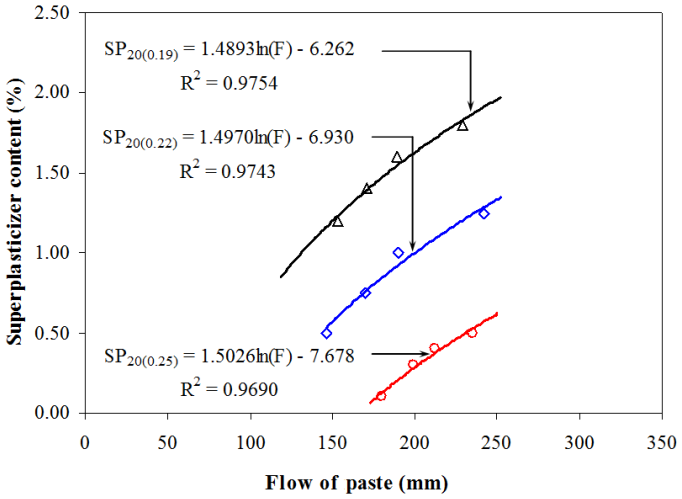

Fig. 2 Relationship between flow of paste and SP content at W/B ratios of 0.19, 0.22, 0.25 and 20% fly ash replacement

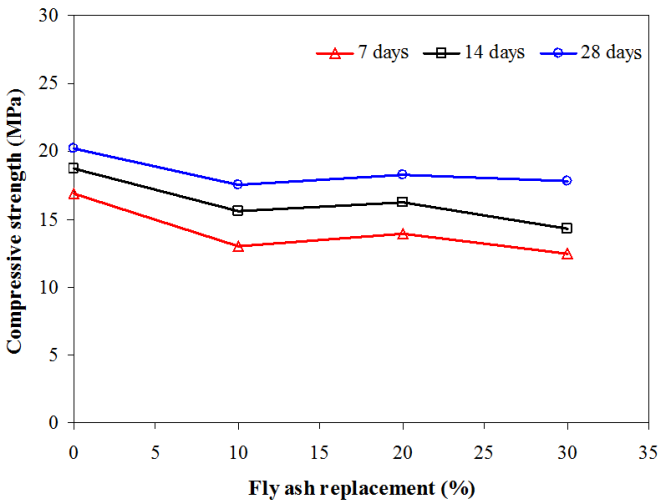

Fig. 3 Fly ash replacement and compressive strength of 9 mm aggregate pervious concrete with designed void ratio of 20% and W/B ratio of 0.19

4.2 Compressive strength

The results of compressive strength of pervious concrete with designed void ratio of 20%, W/B ratio of 0.19, fly ash replacements of 10, 20, and 30% by weigh of binder are shown in Fig. 3. The compressive strengths of pervious concrete at early ages of 7 and 14 days decreased as the amount of replacement by fly ash increased. This is because of the pozzolanic reaction of fly ash at early age is lower than the reaction of cement hydration (Siddique 2004, Tangpagasit *et al.* 2005). Thus, pervious concrete with fly ash gave compressive strength less than the pervious concrete without fly ash. At 28 days, the pervious concrete with fly ash replacements of 0, 10, 20, and 30% by

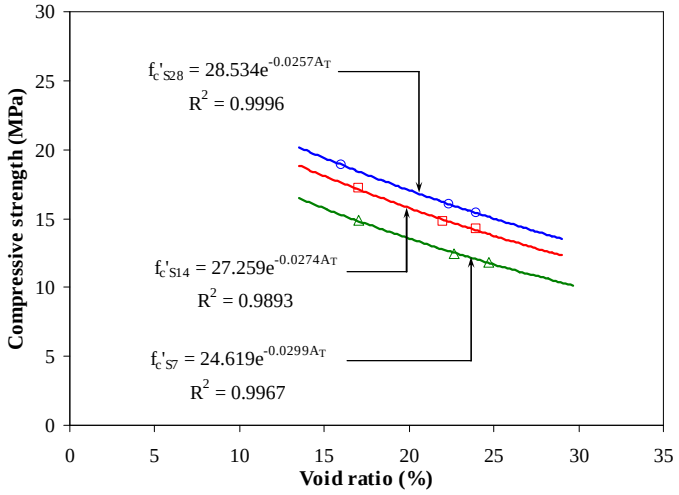

Fig. 4 Void ratio and compressive strength of 9 mm aggregate pervious concrete

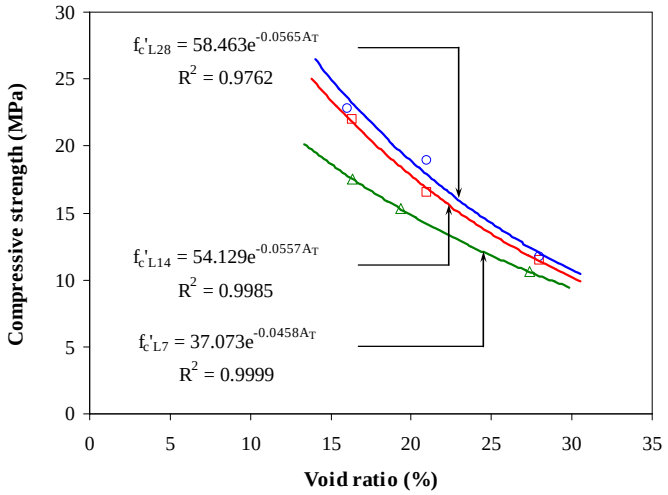

Fig. 5 Void Ratio and compressive strength of 19 mm aggregate pervious concrete

weight had the compressive strengths of 20.2, 17.5, 18.3, and 17.8 MPa with the corresponding normalized values of 100, 86.6, 90.6, and 88.1%, respectively. These values were higher than the minimum strength activity index requirement of 75% according to ASTM C 618 (2010). In addition, the compressive strength of pervious concrete was related to the void ratio as shown in Figs. 4 and 5. The compressive strength of concrete increased with a decrease of void ratio. This finding was similar to the studies of Lian *et al*. (2011), Shu *et al*. (2011), and Kim *et al*. (2010). With regard to the effect of aggregate size, the effect is significant for the small void ratio of 0.15. The strength of 9 mm aggregate concrete was significantly less than that with 19 mm aggregate concrete. As the overall surface area of large aggregate was less than that of small aggregate, the large aggregates required less paste to cover the surface and the paste covering large aggregate was thicker resulting in the better bonding between aggregates (Chindaprasirt *et al*. 2009). The

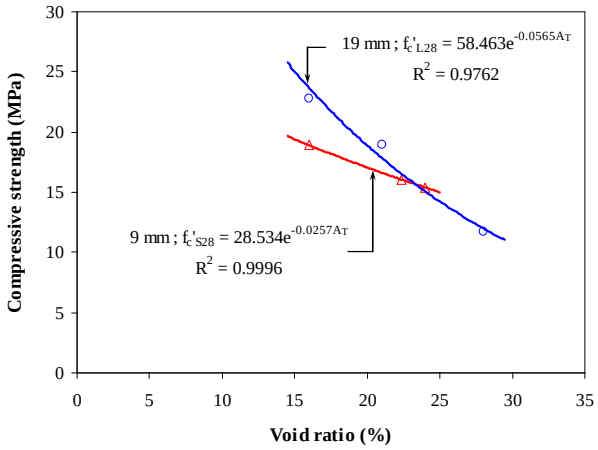

Fig. 6 Relationship between void ratio and compressive strength of pervious concrete with various aggregate sizes at 20% fly ash replacement and W/B ratio of 0.19

concrete with void ratio higher than about 23%, the 9 mm aggregate concretes had a similar strength to those of 19 mm aggregate concretes. At low paste content, the amount of surplus paste would also be low. In addition, the contact areas between the smaller aggregates were higher than those of the large aggregates and thus offset the influence of aggregate size on strength.

The relationship between void ratio and compressive strength of pervious concrete using 9 mm aggregate at 7, 14, and 28 days could be fitted using exponential curve as shown in Eqs. (9)-(11), and Eqs. (12)-(14) for 19 mm aggregate.

$$f_c'_{S7} = 24.619e^{-0.0299A_T},\ R^2 = 0.9967 \quad (9)$$

$$f_c'_{S14} = 27.259e^{-0.0274A_T},\ R^2 = 0.9893 \quad (10)$$

$$f_c'_{S28} = 28.534e^{-0.0257A_T},\ R^2 = 0.9996 \quad (11)$$

$$f_c'_{L7} = 37.073e^{-0.0458A_T},\ R^2 = 0.9999 \quad (12)$$

$$f_c'_{L28} = 54.129e^{-0.0557A_T},\ R^2 = 0.9985 \quad (13)$$

$$f_c'_{L28} = 58.463e^{-0.0565A_T},\ R^2 = 0.9762 \quad (14)$$

where $f_c'_{S7}$, $f_c'_{S14}$, and $f_c'_{S28}$ are the compressive strengths of pervious concretes using 9 mm aggregate at 7, 14, and 28 days, respectively (MPa); $f_c'_{L7}$, $f_c'_{L14}$, and $f_c'_{L28}$ are those of 19 mm aggregate; and A_T is the total void ratio (%).

It is generally accepted that compressive strength of pervious concrete is related to the strength of paste (Chindaprasirt *et al*. 2008). Thus, the increasing of W/B ratio in pervious concrete decreased the compressive strength. At 28 days, the pervious concretes with water to binder ratios of 0.19, 0.22, and 0.25 had compressive strengths of 18.25, 15.14, and 12.74 MPa, respectively, as shown in Fig. 7.

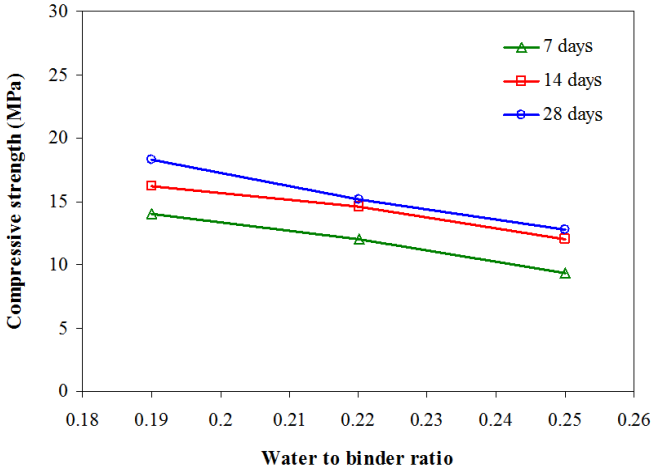

Fig. 7 W/B ratio and compressive strength of pervious concrete with 20% fly ash replacement and designed void ratio of 20%

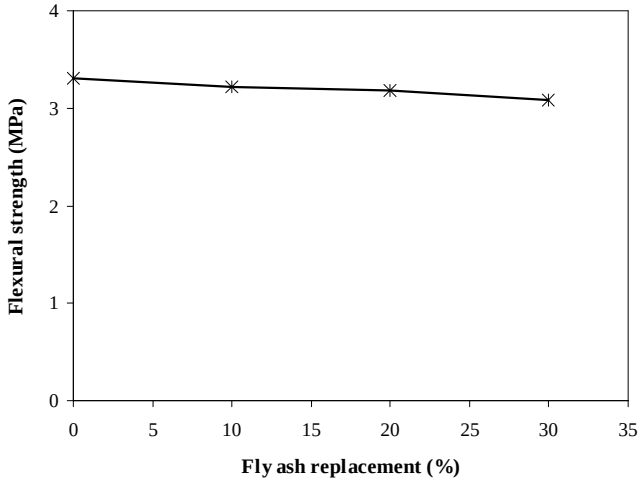

Fig. 8 Fly ash replacement and flexural strength of 9 mm aggregate pervious concrete with designed void ratio of 20% and W/B ratio of 0.19

4.3 Flexural strength

The flexural strength of pervious concretes with 20% designed void ratio with fly ash replacement levels of 0, 10, 20, and 30% were 3.31, 3.22, 3.18, and 3.09 MPa, respectively as shown in Fig. 8. At 28 days, the use of fly ash replacement in the pervious concrete had little effect on flexural strength due to the low pozzolanic reaction at early age (Park *et al.* 2009). Fig. 9 presents the flexural strength of pervious concrete with the two aggregate sizes. The flexural strength of pervious concrete with 19 mm aggregate was higher than that with 9 mm aggregate. The trend of results of flexural strength was consistent with the compressive strength of pervious concrete. At low total void ratio, the use of smaller aggregate seemed to give higher strength than that with the larger aggregate. The relationship between void ratio and flexural strength of

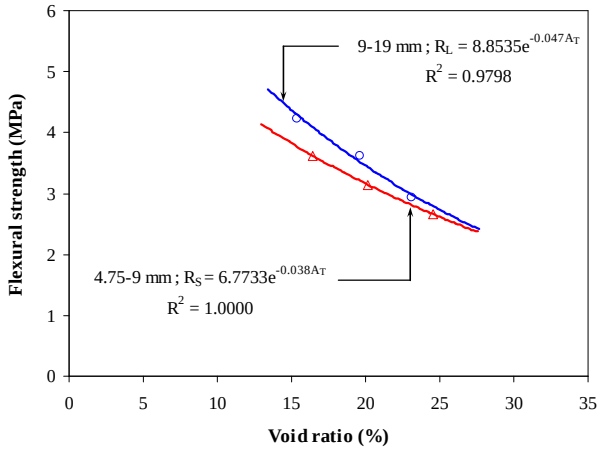

Fig. 9 Relationship between void ratio and flexural strength of pervious concrete with various aggregate sizes at 20% fly ash replacement and W/B ratio of 0.19

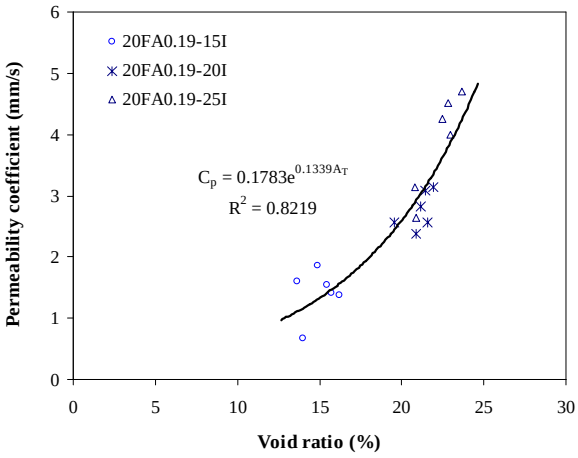

Fig. 10 Relationship between void ratio and water permeability coefficient of 9 mm aggregate pervious concrete with 20% fly ash replacement and W/B ratio of 0.19

pervious concrete using 9 mm aggregate could be fitted using exponential curve as shown in Eq. (15) and in Eq. (16) for 19 mm aggregate.

$$R_S = 6.7733e^{-0.038A_T}, \; R^2 = 1.0000 \tag{15}$$

$$R_L = 8.8535e^{-0.047A_T}, \; R^2 = 0.9798 \tag{16}$$

where R_S and R_L are flexural strengths of pervious concretes using aggregate sizes of 9 and 19 mm (MPa), respectively; and A_T is total void ratio (%).

4.4 Water permeability coefficient

Generally, the water permeability of pervious concrete is related to the continuous void, pore

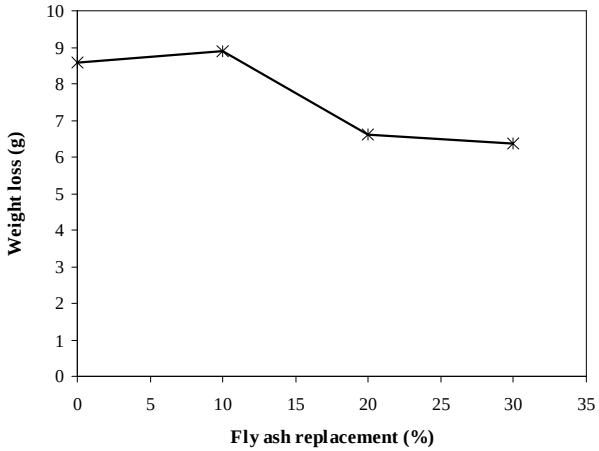

Fig. 11 Fly ash replacement and weight loss on abrasion tests of 9 mm aggregate pervious concrete with designed void ratio of 20%, W/B ratio of 0.19

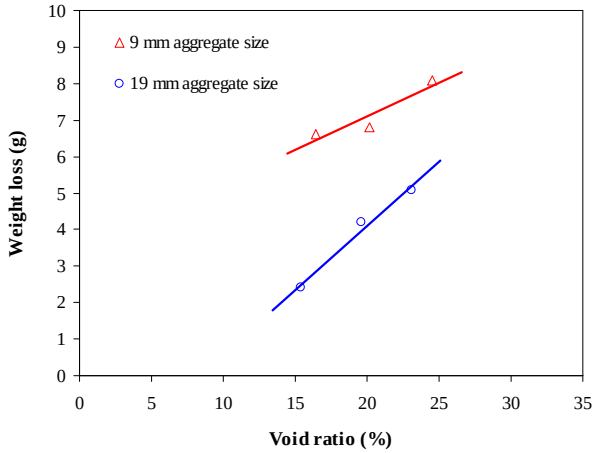

Fig. 12 Void ratio and weight loss on abrasion test of pervious concrete with fly ash replacement of 20% and W/B ratio of 0.19

size distribution, and pore roughness. Many researchers (Neithalath *et al*. 2010, Aamer Rafique Bhutta *et al*. 2012, Tho-in *et al.* 2012, Haselbach *et al.* 2006, Zaetang *et al*. 2013) found that the permeability increased exponentially with the continuous void. The result revealed that the water permeability coefficients of pervious concretes for the mixes 20FA0.19-15I, 20FA0.19-20I, and 20FA0.19-25I were in the ranges of 0.67-1.86, 2.38-3.14, and 2.64-4.70 mm/s with corresponding ranges of void ratios of 13.64-16.20, 19.57-21.96, and 20.83-23.65%, respectively. The relationship between water permeability coefficient and void ratio could also be fitted using exponential curve as shown in Fig. 10 with the equation as follows.

$$C_P = 0.1783e^{0.1339A_T},\ R^2 = 0.8219 \tag{17}$$

where C_P is water permeability coefficient of pervious concrete (mm/s) and A_T is void ratio (%).

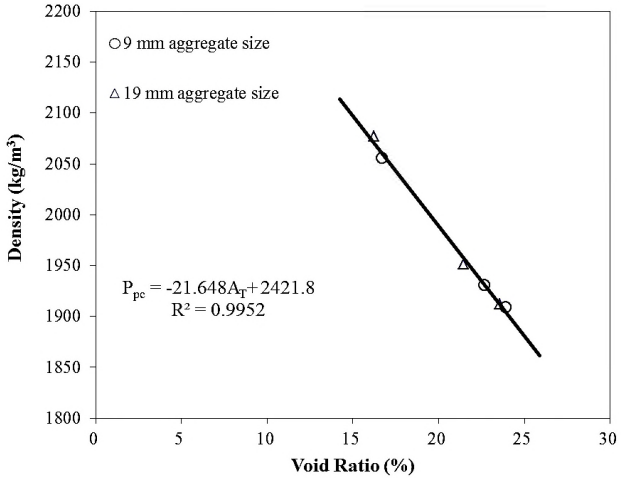

Fig. 13 Void ratio and density of pervious concrete with 20% fly ash replacement and W/B ratio of 0.19

4.5 Abrasion resistance

The abrasion resistance of pervious concrete in term of weight loss was determined at the age of 28 days. Pervious concrete using fly ash dosages of 0, 10, 20, and 30% had the weight loss of 8.6, 8.9, 6.6, and 6.4 g, respectively, as shown in Fig. 11. The weight loss of 10% fly ash concrete was similar to no fly ash concrete. As the amount of fly ash replacement increased, the abrasion resistance increased similar to the results reported by Woo *et al*. (2011) and Yen *et al*. (2007). The decreasing in weight loss with the increase in percentage of fly ash replacement was attributed to the densification of the paste structure from the pozzolanic reaction between fly ash and calcium hydroxide and the filler effect, which increased abrasion resistance (Siddique and Khatib 2010). It was also likely that the self cementing of high calcium fly ash also contribute to this dense structure. It was also found that weight loss increased with the increasing void ratio. The weight loss of pervious concrete using small aggregate was higher than that of large aggregate. This was related to the strength of concrete. Large-sized aggregates produced stronger concrete and with lower surface area required lower content of paste hence their surface areas were completely coated. On the other hand, small-sized aggregate produced lower strength concrete and with higher surface area required higher content of paste thus thinner coating of paste resulted. The relationship between void ratio and weight loss on abrasion test is given in Fig. 12.

4.6 Density

The density of pervious concrete depends on the void ratio. The pervious concrete with 20% fly ash using aggregate of 9 mm with void ratio of 16.67, 22.67, and 23.89% had the density of 2056, 1931, and 1909 kg/m^3, respectively, while the 19 mm aggregate with void ratio of 16.22, 21.44, and 23.56% had the density of 2077, 1951, and 1912 kg/m^3, respectively, as show in Fig. 13. According to the report by Tennis *et al*. (2004), pervious concrete had density of around 1600-2000 kg/m^3. The relationship between void ratio and density of pervious concrete could be fitted in linear as shown in the Eq. 18. It should be noted that this equation has a limitation and is for pervious concretes with the voids in the range of 15-25%.

$$\rho_{pc} = -21.648A_T + 2421.8,\ R^2 = 0.9952 \quad (18)$$

where ρ_{pc} is the density of pervious concrete (kg/m^3) and A_T is the total void ratio (%).

5. Conclusions

The increase in the high calcium fly ash replacement levels helped increase the workability of cement paste and also reduced the amount of superplasticizer in the mixture. The compressive strength and flexural strength of pervious concrete slightly decreased as the high calcium fly ash replacement level increased. However, up to 30% replacement level, the strengths of concrete were still higher than 85% of those of the control concretes. The slight reduction in strength at the early age is due to the lower reaction of fly ash compared to that of Portland cement. In addition, the abrasion resistance of pervious concrete increased with the increase in fly ash replacement. This was attributed to the densification of the paste structure from the pozzolanic reaction between fly ash and calcium hydroxide and the filler effect which increased abrasion resistance. The effect of aggregate size was significant at the low total void ratio (< 23%). The compressive strengths of 19 mm aggregate concretes were significantly higher than those of the 9 mm aggregate concretes due to the difference in the thickness of paste covering the aggregates. The abrasion resistance of small aggregate pervious concrete was also lower than that of large aggregate concrete which was related to the strengths of concrete.

Acknowledgements

The authors sincerely acknowledge the financial support by Rajamangala University of Technology Isan (RMUTI), the Higher Education Research Promotion and National Research University Project of Thailand, Office of the Higher Education Commission, through the Advanced Functional Materials Cluster of Khon Kaen University, and the Thailand Research Fund (TRF) and Khon Kaen University under TRF Senior Research Scholar Contract No. RTA5780004.

References

Aamer Rafique Bhutta, M., Tsuruta, K. and Mirza, J. (2012), "Evaluation of high-performance pervious concrete properties", *Constr. Build. Mater.*, **31**, 67-73.

ACI Committee 522 (2010), *ACI 522R-10 Report on pervious concrete*, American Concrete Institute, Farmington Hills, MI, USA.

ASTM C 39/C 39M-10 (2010), *Standard Test Method for Compressive Strength of Cylindrical Concrete Specimens*, Annual Book of ASTM Standards, 04.02, USA.

ASTM C 78-10 (2010), *Standard Test Method for Flexural Strength of Concrete (Using Simple Beam with Third-Point Loading)*, Annual Book of ASTM Standards, 04.02, USA.

ASTM C 618-08a (2008), *Standard Test Method for Coal Fly Ash and Raw or Calcined Natural Pozzolan for Use in Concrete*, Annual Book of ASTM Standards, 04.02, USA.

ASTM C 944/C 944M-12 (2012), *Standard Test Method for Abrasion Resistance of Concrete or Mortar Surfaces by the Rotating-Cutter Method*, Annual Book of ASTM Standards, 04.02, USA.

ASTM C 1754/C 1754-12 (2012), *Standard Test Method for Density and Void Content of Hardened Pervious Concrete*, Annual Book of ASTM Standards, 04.02, USA.
Chindaprasirt, P., Hatanaka, S., Chareerat, T., Mishima, N. and Yuasa, Y. (2008), "Cement paste characteristics and pervious concrete properties", *Constr. Build. Mater.*, **22**(5), 894-901.
Chindaprasirt, P., Hatanaka, T., Mishima, N., Yuasa, Y. and Chareerat, S. (2009), "Effects of binder strength and aggregate size on the compressive strength and void ratio of porous concrete", *Int. J. Minerals Metall. Mater.*, **16**(6), 714-9.
Delatte, N., Miller, D. and Mrkajic, A. (2007), *Portland cement pervious concrete pavement: Field performance investigation on parking lot and roadway pavements*, RMC Research & Education Foundation, Cleveland, Ohio, USA.
Deo, O. and Neithalath, N. (2010), "Compressive behavior of pervious concretes and a quantification of the influence of random pore structure features", *Mater. Sci. Eng.*, **528**(1), 402-412.
Deo, O. and Neithalath, N. (2011), "Compressive response of pervious concrete proportioned for desired porosities", *Constr. Build. Mater.*, **25**(11), 4181-4189.
Golroo, A. and Tighe, S.L. (2011), "Alternative modeling framework for pervious concrete pavement condition analysis", *Cement Concrete Res.*, **25**(10), 4043-4051.
Hatanaka, S., Mishima, N., Yuasa, Y., Maegawa, A., Nakagawa, T. and Kuroda, M. (2006), "Fundamentals and a few recent applications of environmentally friendly pervious concrete", *International Conference on Pozzolan, Concrete and Geopolymer*.
Haselbach, L.M., Valavala, S. and Montes, F. (2006), "Permeability predictions for sand-clogged Portland cement pervious concrete pavement systems", *J. Environ. Manage.*, **81**(1), 42-49.
JIS Committee (1997), *Physical Testing Methods for Cement (JIS R 5201)*, Japanese Industrial Standards, Japan.
Kim, H.K. and Lee, H.K. (2010), "Influence of cement flow and aggregate type on the mechanical and acoustic characteristics of pervious concrete", *Appl. Acoust.*, **71**(7), 607-615.
Leming, M.L., Malcom, H.R. and Tennis, P.D. (2007), *Hydrologic design of pervious concrete*, Portland Cement Association (PCA), Skokie, Illinois, USA.
Lian, C., Zhuge, Y. and Beecham, S. (2011), "The relationship between porosity and strength for pervious concrete", *Constr. Build. Mater.*, **25**(11), 4294-4298.
Limbachiya, M., Meddah, M.S. and Ouchagour, Y. (2012), "Use of recycled concrete aggregate in fly-ash concrete", *Constr. Build. Mater.*, **27**(1), 439-449.
Neithalath, N., Sumanasooriya, M.S. and Deo, O. (2010), "Characterizing pore volume, sizes, and connectivity in pervious concretes for permeability prediction", *Mater. Charact.*, **61**(8), 802-813.
Park, S.B., Jang, Y.I., Lee, J. and Lee, B.J. (2009), "An experimental study on the hazard assessment and mechanical properties of pervious concrete utilizing coal bottom ash coarse aggregate in Korea", *J. Hazard. Mater.*, **166**(1), 348-355.
Park, S.B. and Tia, M. (2004), "An experimental study on the water-purification properties of pervious concrete", *Cement Concrete Res.*, **34**(2), 177-184.
Putman, B.J. and Neptune, A.I. (2011), "Comparison of test specimen preparation techniques for pervious concrete pavements", *Constr. Build. Mater.*, **25**(8), 3480-3485.
Ramanathan, P., Baskar, I., Muthupriya, P. and Venkatasubramani, R. (2013), "Performance of self-compacting concrete containing different mineral admixtures", *KSCE J. Civil Eng.*, **17**(2), 465-472.
Rukzon, S. and Chindaprasirt, P. (2008), "Mathematical model of strength and porosity of ternary blend Portland rice husk ash and fly ash cement mortar", *Comput. Concrete*, **5**(1), 1-6.
Sata, V., Khammathit, P. and Chindaprasirt, P. (2008), "Efficiency factor of high-calcium Class F fly ash in concrete", *Comput. Concrete*, **8**(5), 583-595.
Shu, X., Huang, B., Wu, H., Dong, Q. and Burdette, E.G. (2011), "Performance comparison of laboratory and field produced pervious concrete mixtures", *Constr. Build. Mater.*, **25**(8), 3187-3192.
Siddique, R. (2003), "Effect of fine aggregate replacement with Class F fly ash on the abrasion resistance of concrete", *Cement Concrete Res.*, **33**(11), 1877-1881.
Siddique, R. (2004), "Performance characteristics of high-volume Class F fly ash concrete", *Cement*

Concrete Res., **34**(3), 487-493.
Siddique, R. and Khatib, J.M. (2010), "Abrasion resistance and mechanical properties of high-volume fly ash concrete", *Mater. Struct.*, **43**, 709-718.
Silva, P. and De Brito, J. (2013), "Electrical resistivity and capillarity of self-compacting concrete with incorporation of fly ash and limestone filler", *Adv. Concrete Constr.*, **1**(1), 65-84.
Sumanasooriya, M.S. and Neithalath, N. (2011), "Pore structure features of pervious concretes proportioned for desired porosities and their performance prediction", *Cement Concrete Compos.*, **33**(8), 778-787.
Sunil, B.M., Manjunatha, L.S., Ravi, L. and Yaragal, S.C. (2015), "Potential use of mine tailings and fly ash in concrete", *Adv. Concrete Constr.*, **3**(1), 55-69.
Tamai, M., Mizuguchi, H., Hatanaka, S., Nakazawa, T., Yanagibashi, K. and Kunieda, M. (2004), "Design, construction and recent applications of pervious concrete in japan", *Proceedings of the JCI Symposium on Design, Construction and Recent Applications of Pervious concrete*, JCI., Tokyo, April.
Tangpagasit, J., Cheerarot, R., Jaturapitakkul, C. and Kiattikomol, K. (2005), "Packing effect and pozzolanic reaction of fly ash in mortar", *Cement Concrete Res.*, **35**(6), 1145-1151.
Tennis, P.D., Leming, M.L. and Akers, D.J. (2004), *Pervious Concrete Pavements*, Portland Cement Association (PCA), Skokie, Illinois, USA.
Tho-in, T., Sata, V., Chindaprasirt, P. and Jaturapitakkul, C. (2012), "Pervious high-calcium fly ash geopolymer concrete", *Constr. Build. Mater.*, **30**, 366-371.
Uchida, T., Ooyabu, K., Nakano, N. and Matsumoto, H. (2004), "A method of pervious concrete work for construction of high permeability steep revetment with permeable blocks", *Proceedings of the JCI Symposium on Design, Construction and Recent Applications of Pervious concrete*, Tokyo, April.
Vimonsatit, V., Chindaprasirt, P., Ruangsiriyakul, S. and Sata, V. (2015), "Influence of fly ash fineness on water requirement and shrinkage of blended cement mortars", *KKU Eng. J.*, **42**(4), 311-316.
Woo, S.K., Song, Y.C. and Won, J. (2011), "Enhanced durability performance of face slab concrete in concrete-faced rock-filled dam using fly ash and PVA fiber", *KSCE J. Civil Eng.*, **15**(5), 875-882.
Yang, J. and Jiang, G. (2003), "Experimental study on properties of pervious concrete pavement materials", *Cement Concrete Res.*, **33**(3), 381-386.
Yen, T., Hsu, T.H., Liu, Y.W. and Chen, S.H. (2007), "Influence of class F fly ash on the abrasion-erosion resistance of high-strength concrete", *Constr. Build. Mater.*, **21**(2), 458-463.
Zaetang, Y., Wongsa, A., Sata, V. and Chindaprasirt, P. (2013), "Use of lightweight aggregates in pervious concrete", *Constr. Build. Mater.*, **48**, 585-591.

CC

Journal of Cleaner Production 115 (2016) 273–283

Contents lists available at ScienceDirect

Journal of Cleaner Production

journal homepage: www.elsevier.com/locate/jclepro

Hydrothermal synthesis of calcium sulfoaluminate–belite cement from industrial waste materials

A. Rungchet [a], P. Chindaprasirt [b], S. Wansom [c], K. Pimraksa [d, e, *]

[a] Department of Physics and Materials Science, Faculty of Science, Chiang Mai University, Chiang Mai 50200, Thailand
[b] Sustainable Infrastructure Research and Development Center, Faculty of Engineer, Khon Kaen University, Khon Kaen 40002, Thailand
[c] National Metal and Materials Technology Center, National Science & Technology Development Agency, Pathumthani 12120, Thailand
[d] Materials Science Research Center, Faculty of Science, Chiang Mai University, 50200, Thailand
[e] Department of Industrial Chemistry, Faculty of Science, Chiang Mai University, Chiang Mai 50200, Thailand

ARTICLE INFO

Article history:
Received 18 February 2015
Received in revised form
4 November 2015
Accepted 18 December 2015
Available online 29 December 2015

Keywords:
Calcium-sulfoaluminate–belite cement
Hydrothermal–calcination method
Lignite fly ash
FGD-gypsum
Aluminum rich sludge

ABSTRACT

This study investigated the use of industrial waste materials viz., fly ash, Al-rich sludge and flue gas desulfurization gypsum in the production of calcium sulfoaluminate–belite cement using hydrothermal –calcination method. The lime deficit in the waste starting materials was recompensed by the addition of hydrated lime. Various factors viz., type of hydrothermal solvent, time of hydrothermal process and calcinations temperature of the hydrothermal products were studied. Phase developments during various synthesized conditions were studied using X-Ray Diffraction. The cement products were mixed with 20 wt% flue gas desulfurization to allow ettringite formation for solidification. The hydration development was investigated in terms of mineralogical composition, microstructures and compressive strength of the hydration products. The largest numbers of calcium sulfoaluminate–belite cement could be obtained by calcination at temperature of 1050 °C. The synthesized cement developed an acceptable 28-day compressive strength of 30.0 MPa. The main hydration products were ettringite, portlandite, calcium silicate hydrate and calcium aluminosilicate hydrate resulting from the hydration of calcium sulfoaluminate and belite phases.

© 2015 Elsevier Ltd. All rights reserved.

1. Introduction

Nowadays, Portland cement industry is under pressure to reduce energy consumption and CO_2 emission due to the issues of energy scarcity and global warming, respectively (Benhelal et al., 2013; Ishak and Hashim, 2015). The industry is, therefore, compulsorily seeking alternative cement to replace traditional cement binder i.e. ordinary Portland cement (OPC). In recent years, much attention has been given to the development of modified special cement clinkers because of low energy consumption and low CO_2 emission resulting from lower temperature synthesis and lower lime content, respectively, when compared with OPC production. . Belite or dicalcium silicate, one of special cements is not only used for strength development, but also for zinc encapsulation (Romano et al., 2011). However, belite alone undergoes hydration very slowly that results in very low early strength of the set cement and concrete. Mixed phases become one of the promising methods for the good strength development. Calcium sulfoaluminate–belite ($C\hat{S}AB$) cement, a type of special cements containing dicalcium silicate ($2CaO\cdot SiO_2$; C_2S), calcium sulfoaluminate ($4CaO\cdot 3Al_2O_3\cdot SO_3$; $C_4A_3\hat{S}$), tetracalcium aluminoferrite ($4CaO\cdot Al_2O_3\cdot Fe_2O_3$; C_4AF) and calcium sulfate ($CaO\cdot SO_3$; $C\hat{S}$) were, therefore, developed (Arjunan et al., 1999; Collepardi et al., 1972; Singh et al., 1996). All of the phases in $C\hat{S}AB$ cement are stable at a temperature of approximately 1250 °C, which is about 200 °C lower than the temperature used for OPC production. $C\hat{S}AB$-based concrete has shown good dimensional stability, low alkalinity, low permeability, comparable compressive strength to Portland cement concrete and high resistance to chemical attack (seawater, sulfates, chloride) due to the dense structures of $C\hat{S}AB$ hydration products (Glasser and Zhang, 2001). Previous publication has shown successful production of $C\hat{S}AB$ cement from reagent-grade chemical, and natural and waste materials using clinkerization method, which is controlled by solid-state reaction at temperature over 1200 °C (Chen and Juenger, 2012; El-Didamony et al.,

* Corresponding author. Department of Industrial Chemistry, Faculty of Science, Chiang Mai University, Chiang Mai 50200, Thailand. Tel.: +66 5394 3401; fax: +66 5389 2262.
E-mail address: kedsarin.p@cmu.ac.th (K. Pimraksa).

http://dx.doi.org/10.1016/j.jclepro.2015.12.068
0959-6526/© 2015 Elsevier Ltd. All rights reserved.

2013; Martin-Sedeno et al., 2010). This conventional synthesis is not attractive nowadays because of high temperature requirement.

Hydrothermal synthesis was therefore developed several years ago by Jiang and Roy (1992). It has several advantages over clinkerization method; low temperature requirement and better morphology control (Pimraksa et al., 2009). Only a few research works was carried out using hydrothermal synthesis for CŜAB synthesis. Previous works using hydrothermal method focused only on belite synthesis. Literature data (Kacimi et al., 2010; Mazouzi et al., 2014; Pimraksa et al., 2009) suggests the possibility of synthesis of belite cement at temperature less than 1000 °C by hydrothermal–calcination method. During the hydrothermal treatment, the pozzolanic reaction of fly ash (reaction between reactive SiO_2 and Al_2O_3 and $Ca(OH)_2$) is strongly activated, leading to the formation of calcium silicate hydrate (C–S–H) or/and calcium aluminosilicate hydrate (C–A–S–H) with very high surface area. The hydration products are then dehydrated by calcinations at temperatures between 500 and 1000 °C resulting in a mixture of β-C_2S, $\acute{\alpha}_L$-C_2S and mayenite ($12CaO{\cdot}7Al_2O_3$; $C_{12}A_7$) (Byrappa and Adschiri, 2007). Ishida et al. (1992, 1993) and Sasaki et al. (1993) showed that the intermediate phases after hydrothermal process are very crucial to obtain various types and characteristics of products after calcinations. From these previous works, the α-dicalcium silicate hydrate ($Ca_2(HSiO_4)(OH)$), hillebrandite ($Ca_2(SiO_3)(OH)_2$) and dellaite ($Ca_6(SiO_4)(Si_2O_7)(SiO_4)(OH)_2$) phases as intermediate phases were obtained by hydrothermal treatment at temperatures between 100 and 250 °C. Hillebrandite phase is recommended to produce more reactive C_2S than α-dicalcium silicate hydrate and dellaite phases. The intermediate phases are therefore concerned in this study as one of the main factors to obtain the cement products.

Hydration degree of CŜAB cement depends on the type of final binding phases. The mechanisms of $C_4A_3\hat{S}$ hydration and its product development are dependent on calcium sulfate addition. The hydration reaction of $C_4A_3\hat{S}$ with gypsum ($CaSO_4{\cdot}2H_2O$; $C\hat{S}H_2$) is very fast, leading to the formation of ettringite ($C_3A.3C\hat{S}{\cdot}32H$; $C_6A\hat{S}_3H_{32}$) (Hanic et al., 1989; Winnefeld and Barlag, 2009; Winnefeld and Lothenbach, 2010). In the absence of calcium sulfate, $C_4A_3\hat{S}$ reacts with water forming monosulfoaluminate ($C_3A{\cdot}C\hat{S}{\cdot}12H$; $C_4A\hat{S}H_{12}$) (Winnefeld and Lothenbach, 2010). The formations of these two hydrates contribute different strength development with larger contribution from ettringite than from monosulfoaluminate (Kaprálik and Hanic, 1989; Mehta and Klein, 1965).

For the hydration of C_2S (Brouwers, 2003), the reaction undergoes much slower than that of $C_4A_3\hat{S}$. The hydration products are C–S–H and calcium hydroxide ($Ca(OH)_2$; CH), at which C–S–H phase contributes to long-term strength of CŜAB cement.

This research aimed to synthesis of CŜAB cement from a mixture of industrial waste materials viz., fly ash, Al-rich sludge and FGD-gypsum, and commercial grade hydrated lime ($Ca(OH)_2$) using hydrothermal-calcination method. The designed cement phase was based on a calculation of Bogue equation which was commonly applied for cement synthesis using solid state reaction (Taylor, 1997). The effects of various parameters viz., type of hydrothermal solvent, time of hydrothermal process and calcination temperature of the hydrothermal products or intermediate phases on cement phase formation were investigated in term of mineralogical compositions Moreover, the CŜAB cement quality was evaluated in terms of their characteristics (morphology, particle size, specific surface area), physical and mechanical properties. In addition, products resulting from hydration between CŜAB and gypsum were observed. The knowledge of the use of hydrothermal-calcination method to produce CŜAB cement, therefore, would be beneficial to the understanding for the future improvement of CŜAB cement synthesis. Furthermore, the environmental issues viz., CO_2 emission and limitation of waste landfill would be mitigated.

2. Experimental procedure

2.1. Raw materials

The raw materials used to prepare the mixture were industrial waste materials: Class F fly ash (FA) and FGD-gypsum (FGDG) from Mae Moh power plant in the north of Thailand, and Al-rich sludge (AS) from aluminum anodizing or powder coating industrial process of Zodiac Aircatering Equipment (Thailand) Ltd. The particle sizes ($d_{4,3}$) of FA, FGDG and AS used for the synthesis were 75, 50 and 110 μm, respectively. Mineralogical compositions using X-ray diffraction (XRD) of FA consisted of anhydrite ($CaSO_4$; CŜ), calcite ($CaCO_3$), hematite (Fe_2O_3), magnesioferrite ($MgFe_2O_3$) and traces of quartz (SiO_2) with some of amorphous phases as given in Fig. 1(a). The glassy phases were approximately 41 wt% detected by dissolving FA powders in 1% HF solution. The procedure was carried out as follow. 1 g of FA was added to 100 ml of 1% HF in a HDPE beaker and the suspension was stirred for 6 h and then filtered. The filter paper containing the insoluble residue was then washed and oven-dried for 2 h at 110 °C. The percentage of glassy phase was determined by subtraction of the final and initial masses (Fernández-Jimenez et al., 2006). The FGDG mainly composed of gypsum ($CaSO_4{\cdot}2H_2O$). XRD pattern of AS as shown in Fig. 1(b) revealed that gibbsite ($Al(OH)_3$) was the major phase with weak degree of crystallinity with the major peak at 49.2° (2Θ). The commercial-grade hydrated lime was used as CaO source for stoichiometrically corrective material. The hydrated lime (CH) mainly composed of portlandite ($Ca(OH)_2$) and some calcite ($CaCO_3$), resulted from carbonation. The chemical compositions of these materials from X-ray fluorescence (XRF) analysis are shown in Table 1.

2.2. Materials proportioning

All industrial wastes were dried in an oven at 60 °C for 24 h and then ground to obtain particles passed sieve No. 100. Lime deficiency in mix design was recompensed by the addition of CH. Theoretical phase compositions were predicted from each batch using a modified Bogue's equation for CŜAB cement (Majling et al., 1993; Mehta, 1980; Sharp et al., 1999). The phase expected to synthesis were C_4AF, $C_4A_3\hat{S}$, C_2S, CŜ and free CaO (C), as shown in Eqs. (1)–(5). The theoretical phase compositions of mixture are given in Table 2. The proportion of mix was stoichiometrically weighed by combining the raw materials (45% CH, 20% FA, 25% AS and 10% FGDG by weight).

$$\%C_4AF = 3.043(\%Fe_2O_3) \quad (1)$$

$$\%C_4A_3\hat{S} = 1.995(\%A1_2O_3) - 1.273(\%Fe_2O_3) \quad (2)$$

$$\%C_2S = 2.867(\%SiO_2) \quad (3)$$

$$\%C\hat{S} = 1.700(\%SO_3) - 0.445(\%A1_2O_3) + 0.284(\%Fe_2O_3) \quad (4)$$

$$\%C = 1.000(\%CaO) - 1.867(\%SiO_2) - 1.054(\%Fe_2O_3) - 0.550(\%Al_2O_3) - 0.700(\%SO_3) \quad (5)$$

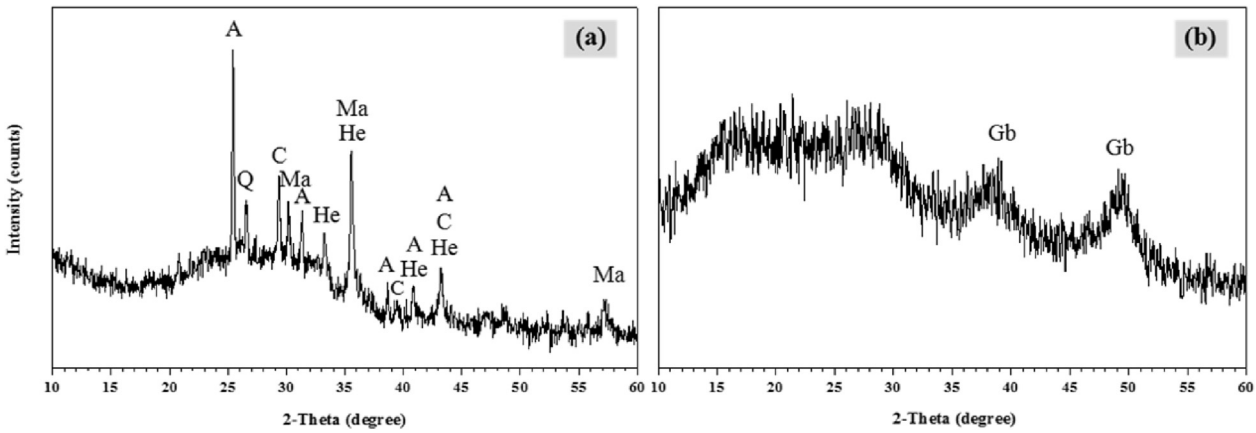

Fig. 1. XRD patterns of (a) FA and (b) AS. A: Anhydrite ($C\hat{S}$); Q: Quartz (SiO_2); C: Calcite ($CaCO_3$); Ma: Magnesioferrite ($MgFe_2O_3$); He: Hematite (Fe_2O_3); Gb: Gibbsite ($Al(OH)_3$).

Table 1
Chemical composition of raw materials.

Raw materials	Chemical composition (wt%)										
	SiO_2	Al_2O_3	Fe_2O_3	CaO	Na_2O	K_2O	MgO	MnO	TiO_2	SO_3	LOI
FA	42.05	22.95	12.52	15.57	1.24	2.54	2.47	0.09	0.34	–	0.23
FGDG	1.26	0.12	0.39	47.81	–	–	–	–	–	50.42	–
AS	1.00	70.72	0.32	0.77	–	–	–	0.20	–	21.99	5.00
CH	0.67	0.79	0.29	73.25	0.15	0.02	1.10	0.01	0.02	–	23.70

LOI: loss on ignition at 950 °C.

2.3. Synthesis procedure

The proportioned raw mixes were dispersed in deionized water with a liquid to solid ratio of 7 by stirring at 250 rpm for 1 h to allow the homogenous mixing and pre-dissolving of starting materials. In order to accelerate the dissolubility, 1 M NaOH was added to the mixture. The synthesis process was divided into two stages; hydrothermal treatment and calcination. The first stage was a hydrothermal treatment to produce hydration products or intermediate phases and used as the precursors of next stage. The mixed slurry was subjected to hydrothermal condition with rotation for various reacting times of 1, 3, 6 and 9 h under atmospheric pressure (1 bar) at 130 °C. After hydrothermal treatment, the suspension was filtered and dried at 60 °C for 24 h. The second stage of the synthesis was calcination of the dried samples in an electric furnace at various temperatures between 750 and 1150 °C, with a heating rate of 5 °C/min and soaking at the maximum temperature for 1 h. This was followed by rapid cooling. The resulting products were friable and easy to grind, leading to energy saving. The calcination product or synthesized cement was co-ground with 20 wt% FGDG in order to produce $C\hat{S}AB$ cement powders.

Table 2
Phase compositions of non-alkaline activated cement and alkaline activated cement obtained from modified Bogue calculation and Rietveld method measurement.

Phase	Phase composition (wt%)		
	Calculated by modified Bogue equation	Rietveld method	
		Non-alkaline activated-$C\hat{S}AB$	Alkaline activated-$C\hat{S}AB$
$C_4A_3\hat{S}$	48.43	76.2	45.1
C_2S	30.27	9.7	20.5
$C_{12}A_7$	0.00	6.9	17.1
C_4AF	9.71	2.6	9.2
$C\hat{S}$	10.02	3.6	0.0
C	1.57	0.8	5.0
$N\hat{S}$	0.00	0.0	2.5
MgO	0.00	0.2	0.6

2.4. Sample characterization and testing

2.4.1. Thermal analysis

Simultaneous thermogravimetric and differential scanning calorimetric (TG/DSC) analysis (Netzsch STA 409C) was used to follow the physical and chemical changes with temperature of the hydrothermal products in order to design the calcination temperature. The instrument was operated from ambient to 1200 °C at a heating rate of 5 °C/min in atmospheric air.

2.4.2. Mineralogy and microstructure analysis

The mineralogical compositions of hydrothermal products and calcination products were identified by XRD (Rigaku Miniflex II). Data were collected from 5 to 60° (2Θ) for the hydrothermal products and 10–60° (2Θ) for the calcination products. Quantitative information for each cement phase was obtained using Rietveld method with X'Pert Highscore Plus software from PANalytical B.V., version 2.2d. The calcination products were observed for morphology by scanning electron microscopy and energy dispersive spectroscopy (SEM&EDS; JEOL JSM-5910 LV). Particle size distribution by laser diffractometer (Malvern Mastersizer 2000) and specific surface area by Blaine air permeability test according to ASTM C204. The Blaine fineness and particle size distribution results were compared to Portland cement Type I (OPC).

2.4.3. Physico-mechanical property

Particle size distribution and specific surface area of the synthesized cements were detected by laser diffractometer (Malvern Mastersizer 2000) and Blaine air permeability test according to ASTM C204, respectively. The Blaine fineness and particle size distribution results were compared to Portland cement Type I

(OPC). For hydration study, cement pastes were prepared with constant water to cement ratio (w/c) of 0.8. The fresh and paste were cast into 25 mm acrylic cube molds. The higher water content used to prepare the cement paste than that of OPC paste was because of the very high surface area of the hydrothermally synthesized products. The setting time tests were performed on the cement paste using procedure described in ASTM C191. The specimens were demoulded at the age of 1 day and cured in moist chamber (at 20 °C ± 5 and 95% relative humidity). The compressive strength tests were carried out at the ages of 1, 7, 28 and 90 days in accordance with ASTM C109. Three specimens were used for each test. The hydration products were studied using the broken pieces from the compressive strength samples. The hydration of samples was stopped by immersing the samples in ethanol solution for 2 days followed by drying at 60 °C for 24 h. Phase developments of hydration products were analyzed using XRD with the scan range of 5–60° (2Θ) and SEM&EDS (gold coated samples).

3. Results and discussion

3.1. Synthesis of CŜAB cement

3.1.1. Phase development and product quality

The effects of non-alkaline activated and alkaline activated hydrothermal treatments (H_2O and 1 M of NaOH), and hydrothermal time (1, 3, 6 and 9 h) on phase development and hydrothermal product quality were studied. In addition, effect of calcination temperatures (750–1150 °C) on phase development was investigated.

3.1.1.1. Alkali activation condition. Hydrothermal conditions were fixed at 130 °C and atmospheric pressure. The continuous rotating time of 6 h was used. The starting materials consisted of 45% CH, 20% FA, 25% AS and 10% FGDG. The mineralogical compositions of the hydrothermal products in different solvents (H_2O and 1 M NaOH), are shown in Fig. 2. This figure also presented raw mixes homogenized in water at 25 °C for 1 h without hydrothermal treatment (taken as the reference here). Non-alkaline activation hydrothermal treatment (H_2O) led to a complete dissolution of anhydrite and a precipitation of ettringite from the reaction between the dissolved anhydrite and aluminum species containing in AS and FA as shown Fig. 2(a). The formation of cebolite, a calcium aluminum silicate hydroxide ($Ca_5Al_2Si_3O_{12}(OH)_4$; $C_5AS_3H_2$) could also be observed. The presence of C–S–H ($Ca_{1.5}SiO_{3.5}\cdot xH_2O$; $C_{1.5}SH_x$) was confirmed with DSC thermogram as shown in Fig. 3 with an endothermic peak at 160–180 °C (Alarcon-Ruiz et al., 2005; Yen et al., 2011). The sources of silicon and aluminum for both cebolite and C–S–H formations came from the dissolution of amorphous phases of FA and AS.

The alkaline activated hydrothermal treatment (1 M NaOH) resulted in the formation of new hydration phases called katoite ($Ca_3Al_2SiO_4(OH)_8$; C_3ASH_4) as shown in Fig. 2(b). The reflection of portlandite indicated that the pozzolanic reaction of FA under steam pressure and alkaline activation were limited. While the reaction with water under the same hydrothermal temperature showed no portlandite leftover. In alkaline activated system, sulfate available from the dissolution of anhydrite was found as thenardite (Na_2SO_4; NŜ) according to the following reaction: $CaSO_4 + NaOH \rightarrow Ca(OH)_2 + Na_2SO_4$ (Kacimi et al., 2010). However, no trace of either ettringite or monosulfoaluminate was found, even though sulfates was available in the system. This was probably due to the formation of calcium aluminum silicate sulfate gel as confirmed by the presence of broad hump around 10–30° (2Θ) region. Moreover, with the use of water without hydrothermal treatment, phase development as shown in Fig. 2(c) was very similar to those with hydrothermal treatment as shown in Fig. 2(a). The only difference was the higher contents of ettringite and monosulfoaluminate phases with hydrothermal treatment. Hydrothermal treatment assisted more rapid precipitation and growth of the products.

The TG/DSC analysis of raw mix after hydrothermal treatment in H_2O (selected as an example) is shown in Fig. 3. Two small endothermic peaks between 50 °C and 120 °C corresponded to the dehydration of ettringite (Hargis et al., 2014; Song et al., 2015). At 160–180 °C an endothermic effect due to the decomposition of high crystallization degree of formed C–S–H was observed. The weight loss between 190 and 250 °C was mainly due to the dehydration of monosulfoaluminate (Hargis et al., 2014). Pimraksa et al. (2009) reported that the dehydroxylation of $Ca(OH)_2$ at

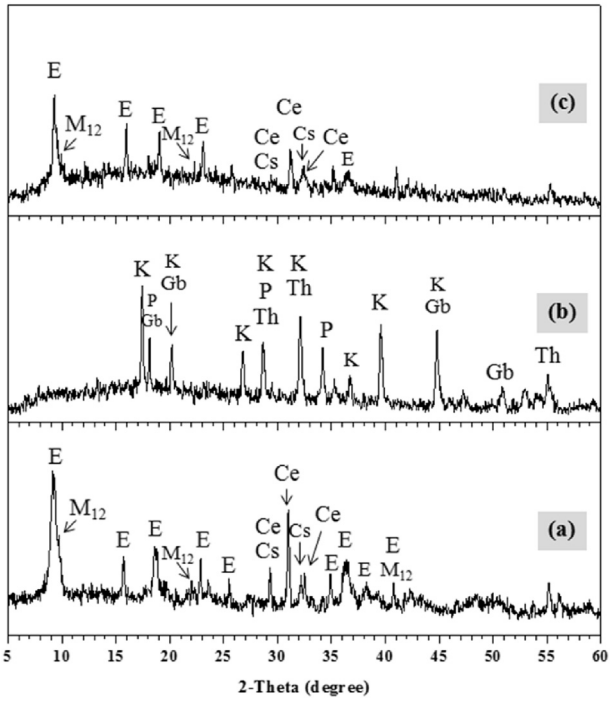

Fig. 2. XRD pattern of hydrothermal products (a) under water and hydrothermal treatment, (b) under 1 M NaOH and hydrothermal treatment and (c) under water and no hydrothermal treatment. E: Ettringite ($C_6A\hat{S}_3H_{32}$); Ce: Cebolite ($C_5AS_3H_2$); Cs: Calcium silicate hydrate ($C_{1.5}SH_x$); M_{12}: Monosulfate ($C_4A\hat{S}H_{12}$); K: Katoite (C_3ASH_4); P: Portlandite ($Ca(OH)_2$); Gb: Gibbsite ($Al(OH)_3$); Th: Thenardite ($N\hat{S}$).

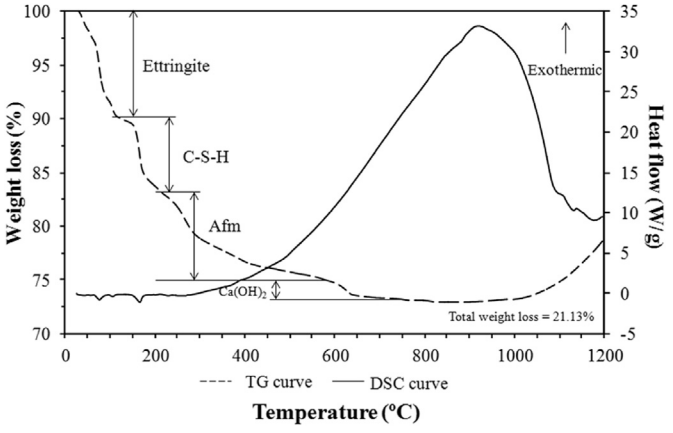

Fig. 3. TG and DSC curves of raw mix after hydrothermal treatment in water.

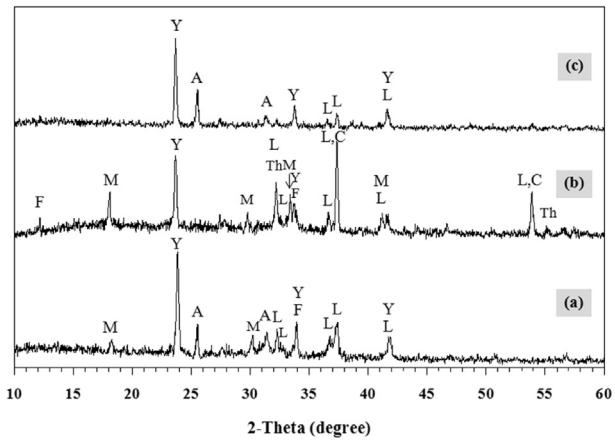

Fig. 4. XRD pattern of calcination products after calcining at 1050 °C obtained from hydrothermal products (a) under water and hydrothermal treatment, (b) under 1 M NaOH and hydrothermal treatment and (c) under water with no hydrothermal treatment. Y: Yeelimite ($C_4A_3\hat{S}$); L: Larnite (β-C_2S); A: Anhydrite ($C\hat{S}$); M: Mayenite ($C_{12}A_7$); Th: Thenardite ($N\hat{S}$); F: Brownmillerite (C_4AF); C: Lime (C).

440–600 °C for belite synthesis using the same method. A small endothermic peak at this temperature range indicated the effective consumption of hydrated lime in the reaction. The board exothermic peak at ~920 °C corresponded to the formation of new phases. At the final stage, a large downward trend corresponded to the partial melting of the aluminate and silicate phases. Therefore, calcination between 750 and 1150 °C was used to transform hydrate phases to cement phases in this research.

The XRD patterns of compounds obtained after calcination (1050 °C) of the reference and hydrothermal products are shown in Fig. 4. $C_4A_3\hat{S}$ and β-C_2S phases were obtained in all cements, but the intensities or the quantities of phases differed depending on the treatment used.

Mixtures with non-alkaline activation under hydrothermal treatment gave the highest content of $C_4A_3\hat{S}$ but only small amount of β-C_2S as shown in Fig. 4(a). In addition, the calcination products contained anhydrite indicating an incomplete combination of calcium, aluminum and sulfate to form $C_4A_3\hat{S}$ phase. However, $C_{12}A_7$, an intermediate phase taken place during calcinations reacted further with anhydrite and formed $C_4A_3\hat{S}$, one of hydraulic phase as shown in Eq. (6).

$$3(C_{12}A_7) + 7C\hat{S} \rightarrow 7C_4A_3\hat{S} + 15C \quad (6)$$

Here, intermediate phase such an ettringite played an important role in the conversion reaction to form $C_4A_3\hat{S}$ as shown in Eq. (7).

$$C_6A\hat{S}_3H_{32} + 2AH_3 \rightarrow C_4A_3\hat{S} + 2C\hat{S} + 38H \quad (7)$$

Alkaline activation with 1 M NaOH condition led to the complete

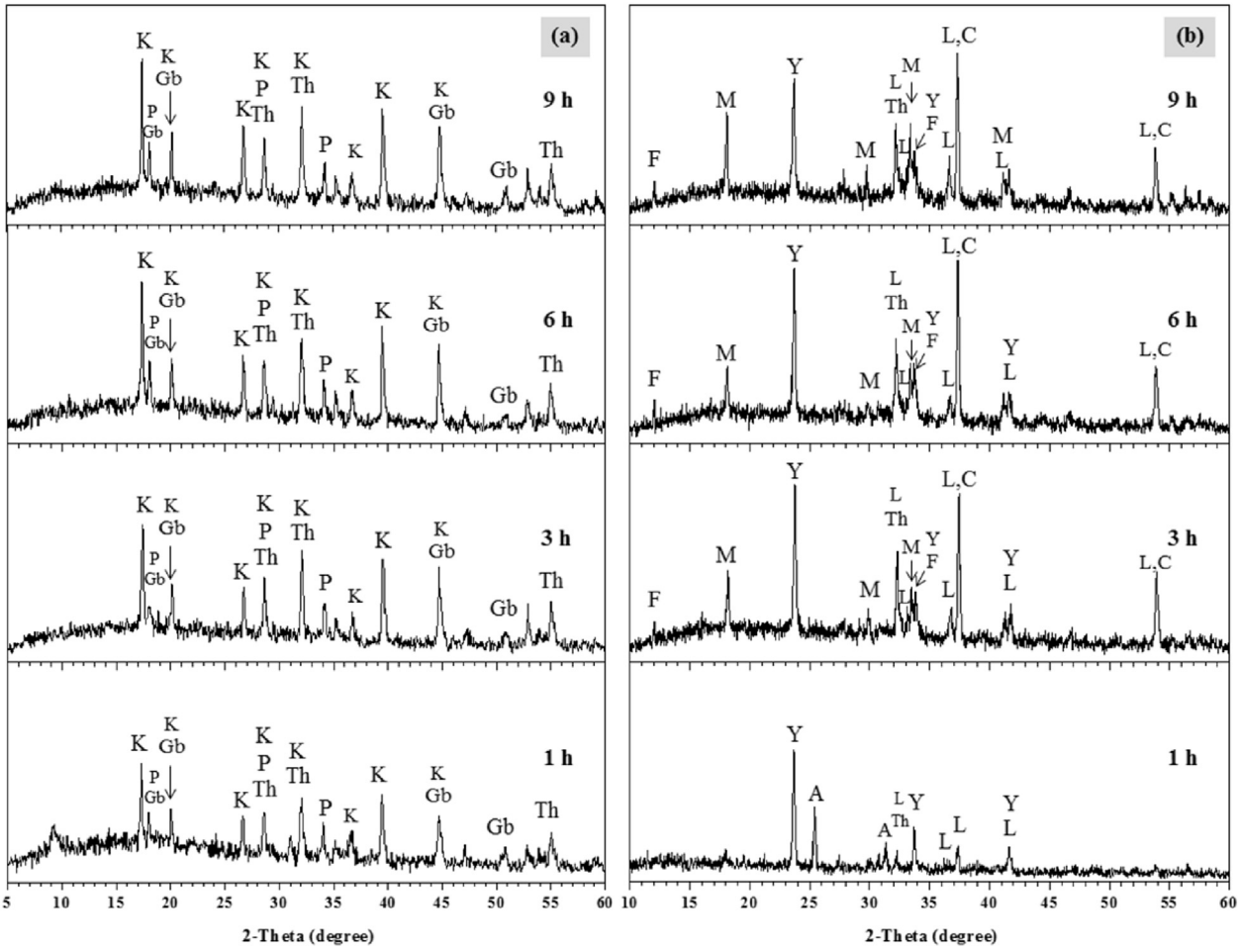

Fig. 5. XRD pattern of (a) hydrothermal products and (b) calcinations products at different hydrothermal times (1, 3, 6 and 9 h) using 1 M NaOH activation. K: Katoite (C_3ASH_4); P: Portlandite ($Ca(OH)_2$); Gb: Gibbsite ($Al(OH)_3$); Th: Thenardite ($N\hat{S}$); Y: Yeelimite ($C_4A_3\hat{S}$); L: Larnite (β-C_2S); A: Anhydrite ($C\hat{S}$); M: Mayenite ($C_{12}A_7$); Th: Thenardite ($N\hat{S}$); F: Brownmillerite (C_4AF); C: Lime (C).

formation of both $C_4A_3\hat{S}$ and β-C_2S phases. Although no ettringite phase was developed, $C_4A_3\hat{S}$ could be formulated via the reaction between katoite, gibbsite, portlandite and thenardite. In addition, katoite also played an important part on the formation of β-C_2S as shown in Eq. (8), where N = Na_2O.

$$3C_3ASH_4 + 13AH_3 + 21CH + 3N\hat{S} \rightarrow 3C_4A_3\hat{S} + C_{12}A_7 + 3(C_{2-x}N_x)S + 72H \quad (8)$$

The alkaline activation also enhanced the formation of $C_{12}A_7$ after calcinations. This product is known to be highly reactive phase which can give mechanical strengths at early-age hydration (Martín-Sedeño et al., 2010; Mazouzi et al., 2014). Intensities of the characteristic peak of β-C_2S were much stronger than non-alkaline activation. The pH of mixture with non-alkaline activation and alkaline activation were 11.9 and 13.2, respectively. The 1 M NaOH activation assisted the dissolving of SiO_2 contained in FA as pH of a system was over 13 (Guerrero et al., 2004). The Si ions species therefore precipitated as katoite which served as the reactive hydrate phase to form both $C_4A_3\hat{S}$ and β-C_2S as mentioned before. Moreover, several authors suggested that the incorporation of impurities such as heavy metal, alkaline and sulfur in the C_2S lattice can increase its hydraulic reactivity because Ca and Si which were substituted by these elements could create disorders in the crystal lattice (Chen et al., 2013; Gies and Knofel, 1987, 1986; Ichikawa and Kanaya, 1997; Quillin, 2001). C–S–H and cebolite obtained from both hydrothermal treatment and room temperature with non-alkaline activation did not help promoting the formation of β-C_2S. Therefore, alkaline activated system with hydrothermal treatment was selected as a suitable method for $C\hat{S}AB$ cement synthesis in the next following experiments.

3.1.1.2. Time of hydrothermal process. The effect of hydrothermal time on the formation of $C\hat{S}AB$ phases was studied. The hydrothermal treatments were carried out in 1 M NaOH solution at 130 °C for 1, 3, 6 and 9 h.

Fig. 5(a) reports the effect of hydrothermal times on hydrothermal product development. The formation of katoite was promoted with increasing time of treatment from 1 to 6 h. With the increase in reaction time from 6 to 9 h, there was no significant improvement of katoite formation. Gibbsite slightly increased with an increase in hydrothermal time from 6 to 9 h.

The calcination products obtained at 1050 °C for various hydrothermal times were $C_4A_3\hat{S}$, β-C_2S and $C_{12}A_7$ as shown in Fig. 5(b). Anhydrite was present in the 1 h hydrothermally treated mixture and decreased with the increase in hydrothermal times. For the increase in hydrothermal time to 3–6 h, the $C_4A_3\hat{S}$ and β-C_2S phases were completely formed. Prolongation of hydrothermal time to 9 h decreased the $C_4A_3\hat{S}$ content and increased the formation of $C_{12}A_7$ phase after calcinations due to the additional reaction between gibbsite and lime compound, in addition to the conversion of katoite.

3.1.2. Calcination temperature

To decrease the temperature of cement synthesis and make the $C\hat{S}AB$ cement manufacturing more economical, the optimum synthesis condition obtained from the Section 3.1.1 was chosen in order to study the effect of calcination temperatures between 750 and 1150 °C. The hydrothermal treatment for 3 h was selected. XRD patterns of calcination products are shown in Fig. 6.

At 750 and 850 °C, hydrothermal products disappeared with formations of β-C_2S and $C_{12}A_7$ as main phases. However, no trace of $C_4A_3\hat{S}$ was found at these temperatures. With increasing calcination temperature from 750 to 850 °C, the intensities of β-C_2S and $C_{12}A_7$ were slightly increased.

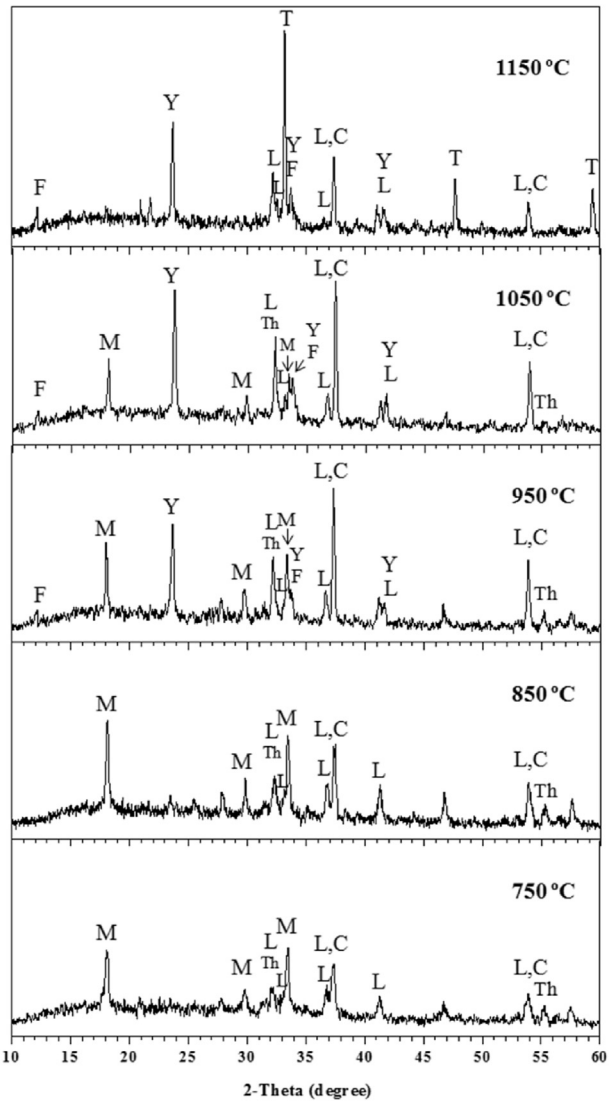

Fig. 6. XRD pattern of calcination products at different. Calcination temperatures using alkaline activated condition (750–1150 °C). Y: Yeelimite ($C_4A_3\hat{S}$); L: Larnite (β-C_2S); A: Anhydrite ($C\hat{S}$); M: Mayenite ($C_{12}A_7$); Th: Thenardite ($N\hat{S}$); T: Tricalcium aluminate (C_3A); F: Brownmillerite (C_4AF); C: Lime (C).

At 950 °C, $C_4A_3\hat{S}$ and C_4AF phases started to form with an increase in β-C_2S and reduction of $C_{12}A_7$ content.

At 1050 °C, there were significant changes of $C_4A_3\hat{S}$, β-C_2S and C_4AF contents with a gradual reduction of $C_{12}A_7$. $C_{12}A_7$ decomposed at this high temperature and reacted with sulfate and ferric compounds to form $C_4A_3\hat{S}$ and C_4AF, respectively.

At 1150 °C, $C_{12}A_7$ lost its stability and converted to tricalcium aluminate (C_3A), a new-formed product. At this temperature, the partial melting of aluminate and silicate phases led to the decomposition of $C_4A_3\hat{S}$ and β-C_2S as also indicated by TG/DSC results (Fig. 3). With this method of synthesis, C_3A, a high temperature product (normally about 1300 °C for clinkerization method) could be obtained at only 1150 °C.

To summarize, $C\hat{S}AB$ phase could be synthesized at temperatures between 950 and 1050 °C, which was about 300 °C lower than the temperature used in traditional $C\hat{S}AB$ production. Not only $C_4A_3\hat{S}$ and β-C_2S phases were formed but also cement phase in a form of $C_{12}A_7$ was formed.

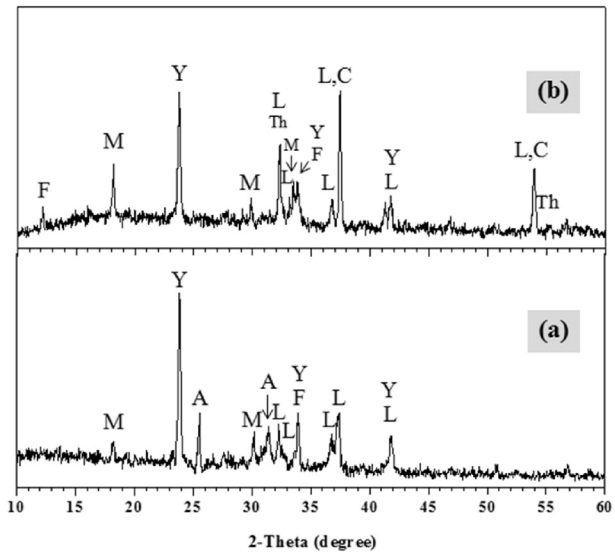

Fig. 7. XRD pattern of CŜAB cements obtained using calcinations temperature of 1050 °C. (a) Non-alkaline activation and (b) alkaline activation. Y: Yeelimite ($C_4A_3\hat{S}$); L: Larnite (β-C_2S); A: Anhydrite ($C\hat{S}$); M: Mayenite ($C_{12}A_7$); Th: Thenardite ($N\hat{S}$); F: Brownmillerite (C_4AF); C: Lime (C).

3.2. Characterizations of CŜAB cements

3.2.1. Phase quality and quantity of CŜAB cement

From the above results, CŜAB cements were synthesized using either non-alkaline or alkaline treatments. Both conditions were used to prepare CŜAB cements using hydrothermal time for 3 h and 1050 °C calcinations for 1 h. These conditions were used for the study in terms of physical, mechanical and morphological properties of products in following experiments. The XRD patterns of CŜAB cements qualitatively obtained from both conditions are shown in Fig. 7. Their quantitative phase compositions determined by Boque equations and Rietveld method are shown in Table 2 as comparison. For non-alkaline treatment, $C_4A_3\hat{S}$ was the main phases (up to 76.2 wt%) with some β-C_2S, $C_{12}A_7$ and C_4AF. $C\hat{S}$ was also found in this treatment about 3.6 wt% indicating that incomplete reaction of calcium aluminate and sulfate to form $C_4A_3\hat{S}$. While with alkaline activated treatment $C_4A_3\hat{S}$, β-C_2S, $C_{12}A_7$ and C_4AF compounds were obtained as 45.1, 20.5, 17.1 and 9.2 wt%, respectively with a small amount of $N\hat{S}$ (2.5 wt%). The impurity such periclase (MgO) contained in waste materials was also found in both synthesized cements. It was worth to note here that alkaline activated treatment promoted the formation of β-C_2S while non-alkaline activated treatment promoted the formation of $C_4A_3\hat{S}$.

The quantitative results obtained by Bogue estimation and Rietveld method were significantly different. In case of non-alkaline activated cement (NA-CŜAB) cement, $C_4A_3\hat{S}$ content overestimated to Bogue calculation. For alkaline activated cement (A-CŜAB), $C_4A_3\hat{S}$, β-C_2S and C_4AF contents were relatively close to the calculated values. The difference between the calculation and the measurement was attributed to the fact that Bogue method was based on an ideal stoichiometry for solid state reaction without taking into consideration of solid solutions and other pathways such as conversion of hydrate phases into final products such in this research.

3.2.2. Fineness and particle size distribution

The ground CŜAB cements, both NA-CŜAB and A-CŜAB cements had similar Blaine finenesses as shown in Table 3. The specific surface areas for NA-CŜAB and A-CŜAB cements were 1331 and 1355 m^2/kg, respectively. These values were higher than 400–450 m^2/kg of the rapid hardening Portland cement synthesized using clinkerization method (Barnes and Bensted, 2002; Pimraksa et al., 2009). It should be noted here that dissolution-precipitation of hydrothermal synthesis produced very large surface area of the final products. In addition, Blaine fineness measured the rate of air passing through a pressed powder and thus the results were affected by particle surface, morphology and porosity. The difference in these parameters between CŜAB cement and Portland cement resulted in the different measured Blaine values (Chen and Juenger, 2012; Iyer and Stanmore, 1995).

Particle size distribution of OPC and synthesized CŜAB cements obtained from hydrothermal treatment with and without alkaline treatment are given in Fig. 8. It was found that OPC and CŜAB cements had similar particle size distributions and the difference in their median particle sizes (d_{50}) were not large (17–23 μm) as shown in Table 3. However, A-CŜAB cement contained finer particles than NA-CŜAB cement. The similarity of particle size distribution of OPC and both CŜAB cements but difference in specific surface area as mentioned above, was due to the agglomeration of CŜAB cements.

3.2.3. Setting time, compressive strength and hydration products

Table 3 presents the initial and final setting time results of synthesized CŜAB cements. The setting times of the cements were relatively short as a result of high finenesses and the associated increased rate of hydration reaction. Both NA-CŜAB and A-CŜAB cements contained $C_{12}A_7$, which was a highly reactive phase. Without the presence of gypsum and anhydrite phases, $C_{12}A_7$ underwent hydration very quickly to form calcium aluminate hydrate ($Ca_2Al_2(OH)_{10}\cdot 3H_2O$; C_2AH_8) as shown in Eq. (9). $C_4A_3\hat{S}$ and β-C_2S reacted with water to form monosulfoaluminate phase and calcium silicate hydrate according to Eqs. (10) and (11), respectively. In addition, monosulfoaluminate phase was not as attractive as trisulfoaluminate phase (ettringite) in term of mechanical properties. Therefore, 20% gypsum in a form of FGD-gypsum was added in this research in order to slow down the hydration of $C_{12}A_7$ and to promote the ettringite formation instead of monosulfoaluminate phase. $C_{12}A_7$ phase reacted very quickly (faster than the $C_4A_3\hat{S}$ phase) with gypsum, leading to the formation of ettringite, according to Eq. (12) (Martín-Sedeño et al., 2010).

$$C_{12}A_7 + 51H \rightarrow 6C_2AH_8 + AH_3 \quad (9)$$

$$C_4A_3\hat{S} + 18H \rightarrow C_4A\hat{S}H_{12} + 2AH_3 \quad (10)$$

$$C_2S + 2H \rightarrow C-S-H + CH \quad (11)$$

$$C_{12}A_7 + 12C\hat{S}H_2 + 113H \rightarrow 4C_6A\hat{S}_3H_{32} + 3AH_3 \quad (12)$$

Table 3
Characteristics and properties of CŜAB cements.

Sample	Main phases	d_{50} (μm)	Fineness (m^2/kg)	Initial setting time (min)	Final setting time (min)
NA-CŜAB	Yeelimite	23.23	1331	15	31
A-CŜAB	Yeelimite, belite, mayenite	17.37	1355	7	13

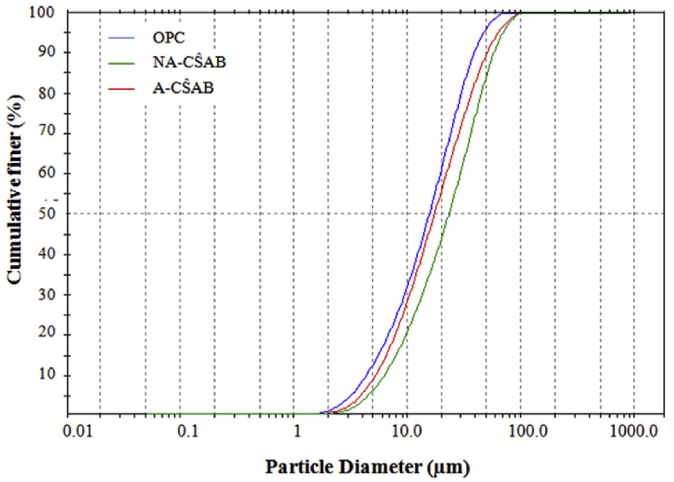

Fig. 8. Particle size distributions of OPC, NA-CŜAB and A-CŜAB cements.

$C_4A_3\hat{S}$ also reacted with gypsum and formed additional ettringite according to Eq. (13). From the result of setting times, the initial set of A-CŜAB cement was only 7 min while the initial set of NA-CŜAB cement was much longer at 15 min. NA-CŜAB and A-CŜAB cements had similar phase compositions except CŜ and NŜ. To this respect, NA-CŜAB contained a surplus of calcium sulfate compound compared to A-CŜAB. However, only A-CŜAB contained sodium sulfate compound. Chen and Juenger (2012) showed that alkali can significantly accelerate hydration kinetics of CŜAB cement system. Therefore, sodium sulfate compound contained in A-CŜAB cement facilitated the dissolution of $C_4A_3\hat{S}$ and formed ettringite and AH_3 according to Eq. (13). The surplus calcium sulfate compound in NA-CŜAB cement was could also slow down the hydration reaction.

$$C_4A_3\hat{S} + 2C\hat{S}H_2 + 34H \rightarrow C_6A\hat{S}_3H_{32} + 2AH_3 \quad (13)$$

The compressive strength results of CŜAB cements with 20 wt% FGD-gypsum addition and OPC are shown in Fig. 9. In general, strengths of CŜAB cements were lower than Portland cement at all stages of hydration. It should be noted that the w/c ratio of Portland cement was relatively low compared with 0.8 for CŜAB cement. The higher water requirement was from higher surface areas of CŜAB cements and the chemical reaction to transform CŜAB to ettringite phase needed large amount of water. However, the compressive strength development of CŜAB cement from industrial waste

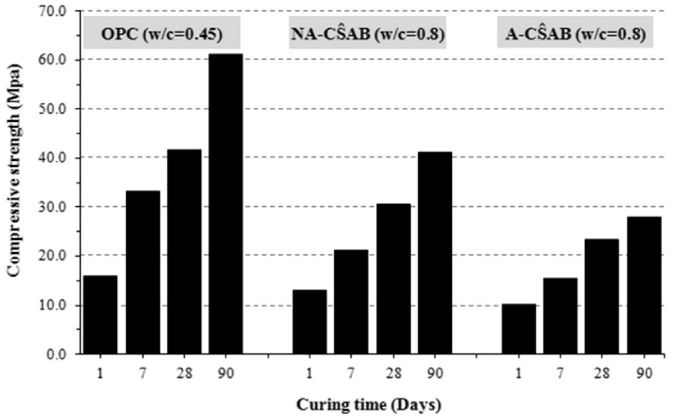

Fig. 9. Compressive strength of the NA-CŜAB and A-CŜAB cement pastes with different curing times.

materials was very good. Relatively high compressive strength of paste specimens was obtained after one day of hardening. The compressive strength of NA-CŜAB cement was slightly higher than those of A-CŜAB cement. The 28-day compressive strength of OPC, NA-CŜAB and A-CŜAB cements were 41.6, 30.5 and 23.3 MPa, respectively. The compressive strength of the synthesized cements developed with curing time in a similar manner to OPC. For example, the compressive strength of NA-CŜAB cement at the ages of 1, 7, 28 and 90 days were 12.9, 21.1, 30.5 and 41.1 MPa, respectively. The reasonably high strength development of NA-CŜAB cement could be attributed to the formation of a significant amount of ettringite from the high $C_4A_3\hat{S}$ content in the system. Moreover, the NA-CŜAB cement showed better strength development with curing time than the A-CŜAB cement, even though β-C_2S content in NA-CŜAB was less than A-CŜAB as shown in Fig. 7. The rather poor strength development with time of A-CŜAB cement was due to its very rapid setting which resulted in a poor initial matrix framework and hindered the compressive strength development at the later stage.

The XRD patterns of the hydration products of NA-CŜAB and A-CŜAB cements with different curing times are shown in Fig. 10. For NA-CŜAB cement (Fig. 10(a)) with additionally 20 wt% gypsum ($CaSO_4.2H_2O$) plus anhydrite ($CaSO_4$) originated from the synthesis (about 3.6 wt% as shown in Table 2), almost all calcium sulfate compounds were consumed after 1 day hydration to form ettringite due to high content of $C_4A_3\hat{S}$. At 1 day, unhydrated $C_4A_3\hat{S}$ and β-C_2S phases were observed implying to no balance between calcium sulfate compounds and $C_4A_3\hat{S}$ and additional gypsum can be possible in order to form more ettringite. Therefore, the reaction of NA-CŜAB cement with insufficient gypsum would generate ettringite and crystalline gibbsite ($Al(OH)_3$; AH_3) in the first stage according to Eq. (13). As reported in several researches (Chen and Juenger, 2010, 2012), the hydration reactions of $C_4A_3\hat{S}$ and C_4AF with calcium sulfate compounds could be concurrent as a result of no trace of unhydrated C_4AF found at 1 day of hydration. Thus, C_4AF with sufficient gypsum contributed to form ettringite according to Eq. (14) rather than to form monosulfoaluminate according to Eq. (15) (Meller et al., 2004).

$$C_4AF + 3C\hat{S}H_2 + 30H \rightarrow C_6A\hat{S}_3H_{32} + FH_3 + CH \quad (14)$$

$$C_4AF + C\hat{S}H_2 + 14H \rightarrow C_4A\hat{S}H_{12} + FH_3 + CH \quad (15)$$

In addition, in this research β-C_2S simply underwent hydration only with water to form calcium silicate hydrate (C–S–H) and calcium hydroxide according to Eq. (11) which could be observed after 7 days of curing.

The leftover $C_4A_3\hat{S}$ reacted further with β-C_2S and formed monosulfoaluminate phase ($C_4A\hat{S}H_{12}$) and stratlingite ($Ca_2Al_2SiO_2(OH)_{10}\cdot 3H_2O$; C_2ASH_8) confirmed by the XRD results at 28 days of curing according to Eq. (16) (Yang et al., 2013).

The XRD pattern at 90 days was almost the same as that at 28 days indicating that there was no other chemical reaction or new products formed. In similar synthesis conditions, it was reported that C_2ASH_8 could also be formed as a result of the chemical reaction between the leftover β-C_2S and gibbsite ($Al(OH)_3$) according to Eq. (17) (Martin-Sedeno et al., 2010; Winnefeld and Lothenbach, 2010).

$$C_4A_3\hat{S} + 2C_2S + 23H \rightarrow C_4A\hat{S}H_{12} + C_2ASH_8 + AH_3 \quad (16)$$

$$C_2S + AH_3 + 5H \rightarrow C_2ASH_8 \quad (17)$$

Fig. 10(b) confirmed the faster hydration reaction of A-CŜAB than NA-CŜAB cement. The greater quantity of ettringite after 1 day

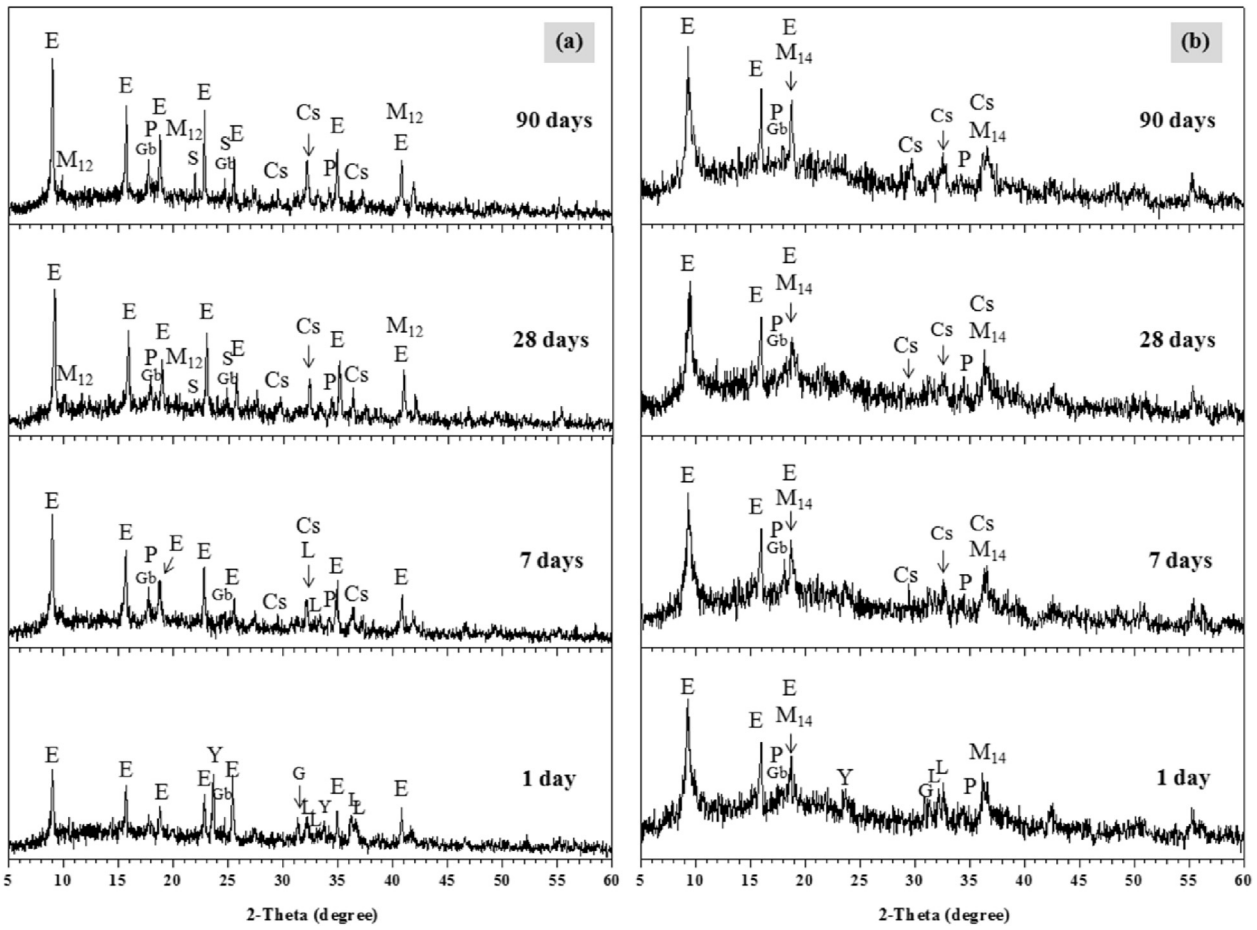

Fig. 10. XRD patterns of (a) NA-CŜAB and (b) A-CŜAB cement pastes after 1, 7, 28 and 90 days of curing. Y: Yeelimite ($C_4A_3\hat{S}$); L: Larnite (β-C_2S); Cs: Calcium silicate hydrate ($C_{1.5}SH_x$); E: Ettringite ($C_6A\hat{S}_3H_{32}$); G: Gypsum ($C\hat{S}H_2$); P: Portlandite ($Ca(OH)_2$); Gb: Gibbsite ($Al(OH)_3$); M_{12}: Monosulfoaluminate ($C_4A\hat{S}H_{12}$); S: stratlingite (C_2ASH_8); M_{14}: Monosulfoaluminate ($C_4A\hat{S}H_{14}$).

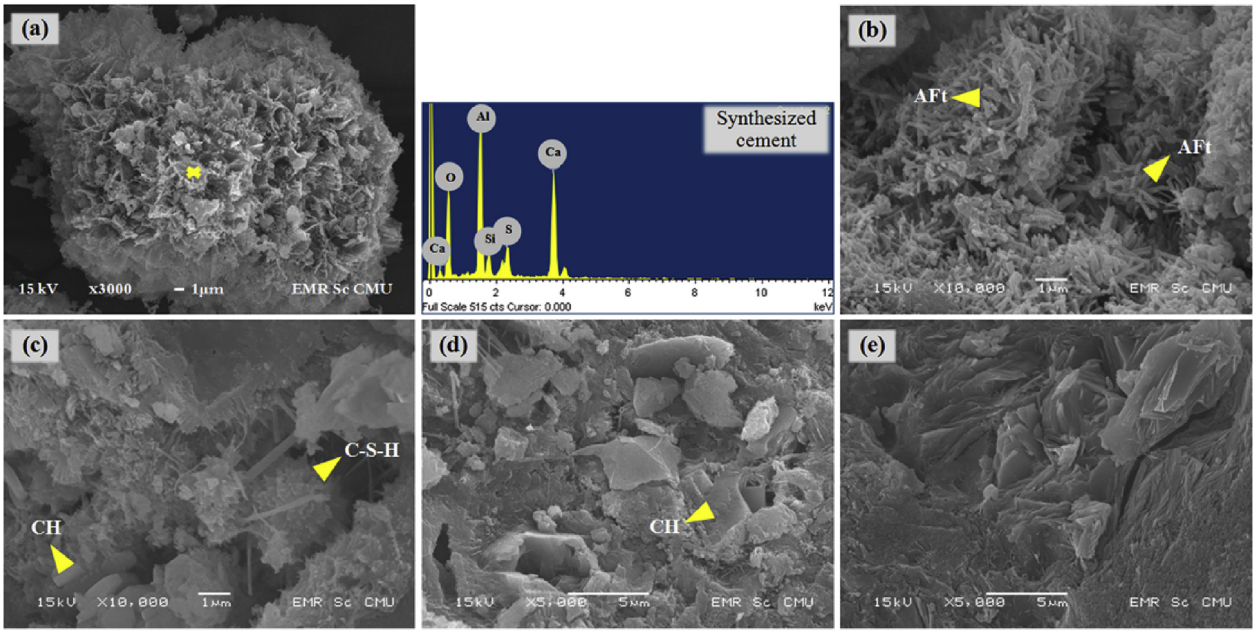

Fig. 11. SEM images of (a) synthesized NA-CŜAB cement and its hydration products after (b) 1 day, (c) 7 days, (d) 28 days and (e) 90 days of curing.

curing could be observed in spite of the fact that calcium sulfate compound in A-CŜAB was less than that of NA-CŜAB system. $C_{12}A_7$ in A-CŜAB cement reacted with gypsum to form ettringite faster than $C_4A_3\hat{S}$ according to Eq. (12) with the leftover $C_4A_3\hat{S}$ at 1 day curing. At the age of 1 day, almost all gypsum was consumed by the reaction of $C_{12}A_7$, leading to the formation of monosulfoaluminate ($C_3A{\cdot}C\hat{S}{\cdot}14H$; $C_4A\hat{S}H_{14}$) from hydration of the leftover $C_4A_3\hat{S}$ as shown in Eq. (18) (Yang et al., 2013). C_4AF also underwent hydration without gypsum to form meta-stable hydrogarnet such CAH_{10} or C_2AH_8 which were poorly crystallized and could not be detected by XRD method (Taylor, 1997).

$$C_4A_3\hat{S} + 20H \rightarrow C_4A\hat{S}H_{14} + 2AH_3 \quad (18)$$

At the age of 28 days, the hydration products obtained were ettringite, calcium silicate hydrate and monosulfoaluminate phases with no stratlingite which could be found in NA-CŜAB hydration products. In addition, broad peaks of products observed from A-CŜAB hydration suggested a poorly crystallized formation resulting from a very fast chemical reaction. The development of compressive strength of the A-CŜAB cement was thus not as good as NA-CŜAB cement.

3.2.4. Microstructures of NA-CŜAB hydration products

The NA-CŜAB cement particles obtained from hydrothermal-calcination synthesis were irregular in shape and highly porous as shown in Fig. 11(a). EDS analysis of NA-CŜAB cement indicated elementary compositions consisting of Ca, Al, Si and S with approximate $CaO:Al_2O_3:SiO_2:SO_4$ molar ratio of 7:4:1:1 which corresponded well with the theoretical chemical formula of mixtures between $C_4A_3\hat{S}$, C_2S and some of calcium aluminate phase ($C_{12}A_7$). After hydration as shown in Fig. 11(b), column-shaped ettringite particles were observed in pore structures at the age of 1 day. Pore of cement paste was between 0.02 and 1 μm in radius and provided sufficient space for crystallization. After 7 days of hydration, small amount of C–S–H particles and calcium hydroxide flakes were observed as shown in Fig. 11(c). Fig. 11(d) and (e) shows considerably dense microstructures of pastes cured for 28 and 90 days.

4. Conclusions

Based on the study, the following conclusions could be drown.

- Lignite fly ash, Al-rich sludge, FGD-gypsum and hydrated lime were promising starting materials to produce calcium sulfoaluminate–belite cement via hydrothermal-calcination method with calcination temperature of only 1050 °C. The obtained cement underwent setting very quickly with acceptable compressive strength, 30.0 MPa and 23.0 MPa at 28 days of curing for non-alkaline activated cement and alkaline activated cement, respectively.
- The synthesis using 1 M NaOH activation provided measurable ye'elimite ($4CaO{\cdot}3Al_2O_3{\cdot}SO_3$), larnite ($2CaO{\cdot}SiO_2$), mayenite ($12CaO{\cdot}7Al_2O_3$) and tetracalcium aluminoferrite ($4CaO{\cdot}Al_2O_3{\cdot}Fe_2O_3$) with some sodium sulfate ($NaSO_4$). Thus, products obtained after hydration were poorly crystallized ettringite and calcium silicate hydrate phases as major phases with monosulfoaluminate ($C_3A{\cdot}C\hat{S}{\cdot}14H$), portlandite ($Ca(OH)_2$) and gibbsite ($Al(OH)_3$) as minor phases.
- The Non-alkaline activated synthesis provided ye'elimite ($4CaO{\cdot}3Al_2O_3{\cdot}SO_3$) as major phase with some larnite ($2CaO{\cdot}SiO_2$), mayenite ($12CaO{\cdot}7Al_2O_3$), tetracalcium aluminoferrite ($4CaO{\cdot}Al_2O_3{\cdot}Fe_2O_3$) and anhydrite ($CaSO_4$). Thus, products obtained after hydration were ettringite, calcium silicate hydrate, stratlingite ($4CaO{\cdot}Al_2O_3{\cdot}SiO_2{\cdot}8H_2O$) and monosulfoaluminate ($C_3A{\cdot}C\hat{S}{\cdot}12H$) phases with more well-crystallized precipitates. The strength development was thus better than the alkaline activated cement.
- For non-alkaline activated cement, the formation of stratlingite ($4CaO{\cdot}Al_2O_3{\cdot}SiO_2{\cdot}8H_2O$) phase, one of the binding phases took place via the chemical reaction between ye'elimite ($4CaO{\cdot}3Al_2O_3{\cdot}SO_3$) and larnite ($2CaO{\cdot}SiO_2$) rather than via the reaction between larnite and gibbsite ($Al(OH)_3$).
- The recycles of high alumina and silica containing waste materials such as Al-rich sludge and fly ash could reduce the use of expensive alumina-silica bearing materials such as bauxite and clay mineral. Utilization of Al-rich sludge, fly ash and FGD-gypsum could also mitigate the problem of landfill limitation thereby reducing cost and the environmental impact of cement manufacturing.

Acknowledgments

The authors gratefully acknowledge the financial supports from the Royal Golden Jubilee (RGJ) Ph.D. program, Grant No. PHD/0070/2556; Khon Kaen University and the Thailand Research Fund (TRF) under the TRF Senior Research Scholar, Grant No. RTA 5780004 and the National Research University Project under Thailand's Office of Higher Education Commission.

References

Alarcon-Ruiz, L., Platret, G., Massieu, E., Ehrlacher, A., 2005. The use of thermal analysis in assessing the effect of temperature on a cement paste. Cem. Concr. Res. 35, 609–613.
Arjunan, P., Silsbee, M.R., Della, M.R., 1999. Sulfoaluminate–belite cement from low-calcium fly ash and sulfur-rich and other industrial by-products. Cem. Concr. Res. 29, 1305–1311.
Barnes, P., Bensted, J., 2002. Structure and Performance of Cements. CRC Press.
Benhelal, E., Zahedi, G., Shamsaei, E., Bahadori, A., 2013. Global strategies and potentials to curb CO_2 emission in cement industry. J. Clean. Prod. 51, 142–161.
Brouwers, H.J.H., 2003. Chemical reactions in hydrated ordinary Portland cement based on the work by Powers and Brownyard. In: Fisher, H.B. (Ed.), Proceedings of the 15th Ibausil, International Conference on Building Materials (Internationale Baustofftagung). F.A. Finger-Institut fur Baustoffkunde, Weimar, Germany, p. 1-0553.
Byrappa, K., Adschiri, T., 2007. Hydrothermal technology for nanotechnology. Prog. Cryst. Growth Charact. Mater. 53, 117–166.
Chen, I.A., Juenger, M.C.G., 2010. Synthesis and hydration of calcium sulfoaluminate–belite cements with varied phase compositions. J. Mater. Sci. 46, 2568–2577.
Chen, I.A., Juenger, M.C.G., 2012. Incorporation of coal combustion residuals into calcium sulfoaluminate–belite cement clinkers. Cem. Concr. Compos. 34, 893–902.
Chen, Y.-L., Lai, Y.-C., Lin, C.-J., Chang, Y.-K., Ko, M.-S., 2013. Controlling sintering atmosphere to reduce the hazardous characteristics of low-energy cement produced with chromium compounds. J. Clean. Prod. 43, 45–51.
Collepardi, M., Turriziani, R., Marcialis, A., 1972. The paste hydration of $4CaO{\cdot}3Al_2O_3{\cdot}SO_3$ in presence of calcium sulphate, tricalcium silicate and dicalcium silicate. Cem. Concr. Res. 2, 213–223.
El-Didamony, H., Heikal, M., Khalil, K.A., 2013. Characteristics of cement pastes containing sulphoaluminate and belite prepared from nano-materials. Constr. Build. Mater. 38, 14–21.
Fernández-Jimenez, A., de la Torre, A.G., Palomo, A., López-Olmo, G., Alonso, M.M., Aranda, M.A.G., 2006. Quantitative determination of phases in the alkali activation of fly ash. Part I. Potential ash reactivity. Fuel 85, 625–634.
Gies, A., Knöfel, D., 1986. Influence of alkalies on the composition of belite-rich cement clinkers and the technological properties of the resulting cements. Cem. Concr. Res. 16, 411–422.
Gies, A., Knöfel, D., 1987. Influence of sulfur on the composition of belite-rich clinkers and the technological properties of the resulting cements. Cem. Concr. Res. 17, 317–328.
Glasser, F.P., Zhang, L., 2001. High-performance cement matrices based on calcium sulfoaluminate–belite compositions. Cem. Concr. Res. 31, 1881–1886.
Guerrero, A., Goñi, S., Campillo, I., Moragues, A., 2004. Belite cement clinker from coal fly ash of high Ca content. Optimization of synthesis parameters. Environ. Sci. Technol. 38, 3209–3213.
Hanic, F., Kaprálik, I., Gabrisová, A., 1989. Mechanism of hydration reactions in the system C_4A_3S–CS–CaO–H_2O referred to hydration of sulphoaluminate cements. Cem. Concr. Res. 19, 671–682.

Hargis, C.W., Telesca, A., Monteiro, P.J.M., 2014. Calcium sulfoaluminate (ye'elimite) hydration in the presence of gypsum, calcite, and vaterite. Cem. Concr. Res. 65, 15–20.
Ichikawa, M., Kanaya, M., 1997. Effect of minor components and heating rates on the fine textures of alite in Portland cement clinker. Cem. Concr. Res. 27, 1123–1129.
Ishak, S.A., Hashim, H., 2015. Low carbon measures for cement plant – a review. J. Clean. Prod. 103, 260–274. Carbon emission reduction: policies, technologies, monitoring, assessment and modeling.
Ishida, H., Mabuchi, K., Sasaki, K., Mitsuda, T., 1992. Low-temperature synthesis of β-Ca_2SiO_4 from hillebrandite. J. Am. Ceram. Soc. 75, 2427–2432.
Ishida, H., Yamazaki, S., Sasaki, K., Okada, Y., Mitsuda, T., 1993. α-Dicalcium silicate hydrate: preparation, decomposed phase, and its hydration. J. Am. Ceram. Soc. 76, 1707–1712.
Iyer, R., Stanmore, B., 1995. Surface area of fly ashes. Cem. Concr. Res. 25, 1403–1405.
Jiang, W., Roy, D.M., 1992. Hydrothermal processing of new fly ash cement. Ceram. Bull. 71, 642–647.
Kacimi, L., Cyr, M., Clastres, P., 2010. Synthesis of α'_L-C_2S cement from fly-ash using the hydrothermal method at low temperature and atmospheric pressure. J. Hazard. Mater. 181, 593–601.
Kaprálik, I., Hanic, F., 1989. Phase relations in the subsystem C_4A_3S–CSH_2–CH–H_2O of the system CaO–Al_2O_3–CS–H_2O referred to hydration of sulphoaluminate cement. Cem. Concr. Res. 19, 89–102.
Majling, J., Sahu, S., Vlna, M., Roy, D.M., 1993. Relationship between raw mixture and mineralogical composition of sulphoaluminate belite clinkers in the system CaO–SiO_2–Al_2O_3–Fe_2O_3–SO_3. Cem. Concr. Res. 23, 1351–1356.
Martín-Sedeño, M.C., Cuberos, A.J.M., De la Torre, Á.G., Álvarez-Pinazo, G., Ordónez, L.M., Gateshki, M., Aranda, M.A.G., 2010. Aluminum-rich belite sulfoaluminate cements: clinkering and early age hydration. Cem. Concr. Res. 40, 359–369.
Mazouri, W., Kacimi, L., Cyr, M., Clastres, P., 2014. Properties of low temperature belite cements made from aluminosilicate wastes by hydrothermal method. Cem. Concr. Compos 53, 170–177.
Mehta, P., 1980. Investigations on energy-saving cements. World Cem. Technol. 11, 166–177.
Mehta, P.K., Klein, A., 1965. Formation of ettringite by hydration of a system containing an anhydrous calcium sulfoaluminate. J. Am. Ceram. Soc. 48, 435–436.
Meller, N., Hall, C., Jupe, A.C., Colston, S.L., Jacques, S.D.M., Barnes, P., Phipps, J., 2004. The paste hydration of brownmillerite with and without gypsum: a time resolved synchrotron diffraction study at 30, 70, 100 and 150 °C. J. Mater. Chem. 14, 428–435.
Pimraksa, K., Hanjitsuwan, S., Chindaprasirt, P., 2009. Synthesis of belite cement from lignite fly ash. Ceram. Int. 35, 2415–2425.
Quillin, K., 2001. Performance of belite–sulfoaluminate cement. Cem. Concr. Res. 31, 1341–1349.
Romano, J.S., Miranda, M.S., Oliveira, M.B.R., Rodrigues, F.A., 2011. Biogenic cements and encapsulation of zinc. J. Clean. Prod. 19, 1224–1228.
Sasaki, K., Ishida, H., Okada, Y., Mitsuda, T., 1993. Highly reactive β-dicalcium silicate: V, influence of specific surface area on hydration. J. Am. Ceram. Soc. 76, 870–874.
Sharp, J.H., Lawrence, C.D., Yang, R., 1999. Calcium sulfoaluminate cements – low-energy cements, special cements or what? Adv. Cem. Res. 11, 3–13.
Singh, M., Upadhayay, S.N., Prasad, P.M., 1996. Preparation of special cements from red mud. Waste Manag. 16, 665–670.
Song, F., Yu, Z., Yang, F., Lu, Y., Liu, Y., 2015. Microstructure of amorphous aluminum hydroxide in belite–calcium sulfoaluminate cement. Cem. Concr. Res. 71, 1–6.
Taylor, H.F.W., 1997. Cement Chemistry. Thomas Telford.
Winnefeld, F., Barlag, S., 2009. Calorimetric and thermogravimetric study on the influence of calcium sulfate on the hydration of ye'elimite. J. Therm. Anal. Calorim. 101, 949–957.
Winnefeld, F., Lothenbach, B., 2010. Hydration of calcium sulfoaluminate cements – experimental findings and thermodynamic modelling. Cem. Concr. Res. 40, 1239–1247.
Yang, L., Yan, Y., Hu, Z., Xie, X., 2013. Utilization of phosphate fertilizer industry waste for belite–ferroaluminate cement production. Constr. Build. Mater. 38, 8–13.
Yen, C.-L., Tseng, D.-H., Lin, T.-T., 2011. Characterization of eco-cement paste produced from waste sludges. Chemosphere 84, 220–226.

Construction and Building Materials 107 (2016) 95–102

Contents lists available at ScienceDirect

Construction and Building Materials

journal homepage: www.elsevier.com/locate/conbuildmat

Mechanical and micromechanical properties of alkali activated fly-ash cement based on nano-indentation

Hyuk Lee [a,*], Vanissorn Vimonsatit [a], Prinya Chindaprasirt [b]

[a] Department of Civil Engineering, Curtin University, WA, Australia
[b] Sustainability Infrastructure Development and Research Centre, Department of Civil Engineering, Faculty of Engineering, Khon Kaen University, Thailand

HIGHLIGHTS

- Mix design using Taguchi's method was presented to determine critical factors.
- Silica fume has the most adverse impact on the compressive strength.
- Using deconvolution technique confirms four phases of reaction products.
- High strength is achieved N-A-S-H phase greater than 40% of total volume fraction.
- Activation degree is recommended to be 60% to achieve high strength mixture.

ARTICLE INFO

Article history:
Received 26 March 2015
Received in revised form 19 October 2015
Accepted 5 December 2015

Keywords:
Alkali activated cement
Fly-ash based cement
Micromechanics
Mechanical properties
Nanoindentation

ABSTRACT

This paper presents mechanical and micromechanical properties of alkali activated fly-ash cement (AAFA) based on statistical analysis with nano-indentation test. Mix proportions of AAFA are designed using Taguchi's approach. Four variables viz, silica fume (SF), sand to cementitious material ratio (s/c), liquid to solid ratio (l/s) and superplasticiser (SP) content were the parameters tested. Indentation elastic modulus, hardness and packing density are studied. The results show that the increase in sand has the greatest contribution to the increase in density. For compressive strength, normal paste without SF, sand and SP with l/s of 0.6 gives the highest strength and the increase in SF significantly contributes to the adverse effect on compressive strength. For the indentation data, the analysis using deconvolution technique confirms the four phases of reaction products of AAFA. The main phase is sodium aluminosilicate hydrate (N-A-S-H), which is over 40% of the volume fraction. The microporomechanics of AAFA paste and mortar also demonstrate the relationships between the N-A-S-H volume fraction and strength; and activation degree and strength.

© 2015 Elsevier Ltd. All rights reserved.

1. Introduction

Alkali activated cement (AAC) is a potential cementitious system for sustainable development [1]. Its main constituent is pozzolan, which can react with alkali activator to form binder [2]. A number of researches [2–4] reported the difference between the composition of traditional Portland cement and fundamental rock forming minerals of the earth crust. The common chemical compositions of Portland cement and fundamental rock are silica and alumina which can also be found in a number of industrial wastes. Ground industrial wastes or by-products containing aluminosilicate when mixed with rich alkalis could form a hydraulic binder which is a type of inorganic polymer called 'geopolymer' or alkali activated cement (AAC). Davidovits [5] classified different types of geopolymer according to Si to Al ratio in the mixtures for various industry applications. Lloyd et al. [6] reported that calcium contents in geoploymer is important for alkali mobility that may be significant to limit the durability of embedded steel reinforcement. A precaution should be taken as some of ground industrial wastes or by-products such as those containing calcium aluminate and metakaolin geopolymer have loss of strength during long-term ageing [7]. Despite extensive research in this area, the entire polymerization process of AAC is not totally understood. It is classified as a polymer because of its huge molecule formed by a number of smaller groups of molecules. AAC has superior mechanical, chemical and thermal properties compared to ordinary Portland cement (OPC) [8]. The main benefit of AAC is that the source material is not a carbonate bearing material; therefore, it does not release vast

* Corresponding author.
E-mail addresses: leehyuk1982@gmail.com (H. Lee), V.Vimonsatit@curtin.edu.au (V. Vimonsatit), prinya@kku.ac.th (P. Chindaprasirt).

http://dx.doi.org/10.1016/j.conbuildmat.2015.12.013
0950-0618/© 2015 Elsevier Ltd. All rights reserved.

quantities of CO_2 as in the case of Portland cement. Turner et al. [9] reported that the carbon emission of AAC concrete is around 9% less than comparable OPC concrete as alkali activators are high carbon footprint materials. Also, high early age strength, high chemical durability and resistance to high temperature are beneficial properties of AAC.

Normally, cementitious materials have several phases that contribute to the mechanical properties. A number of researchers [10–13] studied the characterization of alkali-activated materials by a variety of experimental methods including XRD, SEM, DTA and TGA. Jennings et al. [14] and Tennis et al. [15] proposed a model for the determination of two types of calcium silicate hydrate (C-S-H) viz., high density (HD) and low density (LD) C-S-H, at different points of the specimens geometry. The content of C-S-H is determined in term of its volume fraction of the indentation grid. Constantinides et al. [16] determined the two C-S-H types, Portlandite (CH), and clinker using this nano-indentation method. The result shows that decalcification of C-S-H phases is the primary source of nanometer-scale elastic modulus degradation.

Recently, Němeček et al. [17] studied the reaction products of AAFA paste using NaOH solution with the liquid to solid ratio of 0.531 cured at 80 °C for 12 h. Nano-indentation and environmental scanning electron microscope (ESEM) were used, and four phases of reaction products were found. The four phases were identified as N-A-S-H (sodium aluminosilicate hydrate), partly-activated slag (N-A-S-H gel intermixed with slag-like particles), non-activated slag (porous non-activated slag-like particles), and non-activated compact glass (solid non-activated glass spheres or their relicts). N-A-S-H is the main reaction product which is linked to the atomic scale and nano-structure and is independent of precursor material or the temperature curing regime. N-A-S-H phase is pure and is related to the mechanical strength of AAFA matrix. The contents of Si ions in N-A-S-H can be increased by the presence of Si ions in the raw materials. It has been found that the increasing condensation degree of Si ions in N-A-S-H relates directly to the mechanical strength gain [11,18]. The partly-activated slag phase is intermixed with the slag-like particles. The non-activated slag phase is porous and contains non-activated slag-like particles. The non-activated compact glass phase is solid, non-activated glass sphere.

The aim of this research is to investigate the mechanical and micromechanical properties of AAFA paste and mortar. The experimental program is designed according to Taguchi's method [19], which is efficient for investigating optimum design parameters for the required performances. The investigated parameters are density and compressive strength of AAFA. Nano-indentation and statistical analysis of the test data are used for the evaluation of microporomechanics of AAFA samples. A background on nano-indentation and how to determine the indentation modulus, hardness, Poissons ratio, cohesion, friction coefficient and packing density of materials are presented in brief.

2. Nano-indentation

2.1. Principal nano-indentation

Nano-indentation test method is now well established that the response of material upon the reversal of touch loading provides access to the elastic properties of indentation materials [20]. The measurement of the hardness and elastic modulus of material can be obtained from the relationship between indentation loads (P) and depth (h) during loading and unloading [21–27]. Fig. 1 shows a typical indentation load-depth ($P-h$) curve. The important quantities that must be measured from the $P-h$ curve are the maximum indentation load (P_{max}), the maximum indentation

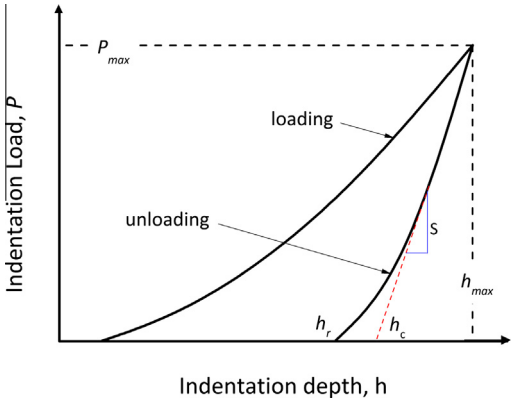

Fig. 1. Typical indentation load-depth ($P-h$) curve.

depth (h_{max}), and the elastic unloading stiffness ($S = dP/dh$), which is defined as the slope of the upper portion of unloading curve. The modulus of material can be estimated from the elastic unloading stiffness (S), and is generally called 'indentation modulus (M)', which is affected by the testing method. Nevertheless, an indentation test provides the rate of piling-up and sinking-in of the test surface around the indentation points, thus, ideally the indentation modulus (M) has the same meaning as the elastic modulus, or Youngs modulus, measured by other conventional test methods.

The contact mechanics between a rigid indenter and a non-rigid flat surface of a specimen can be written as [26]:

$$\frac{1}{M} = \frac{1-\nu^2}{E} + \frac{(1-\nu'^2)}{E'} \tag{1}$$

where E is the elastic modulus of the specimens, ν is the Poissons ratio, E' is the indenter elastic modulus and ν' is the indenter Poissons ratio. The analysis of indentation hardness and modulus of any axis-symmetric indenter can be estimated from Eq. (2).

$$H = \frac{P_{max}}{A_c} \quad M = \frac{\sqrt{\pi}}{2}\frac{S}{\sqrt{A_c}} \tag{2}$$

The indentation depth h_r and h_c correspond to the applied load; h_r is the depth of the residual impression and h_c is the contact depth. The contact depth h_c can be determined as:

$$h_c = h_{max} - \xi \cdot \frac{P_{max}}{S} \tag{3}$$

According to Oliver and Pharrs methodology [26], h_c can be determined by setting $\xi = 0.75$ for Berkovich indenter. The project contact area A_c in Eq. (2) can be expressed by the indentation depth h_c in the form of the following relationship:

$$A_c = 3\sqrt{3} \cdot h_c^2 \cdot tan^2\theta \tag{4}$$

where θ is the face angle, which is 65.35° for Berkovich indenter, which is used in the present case. It should be noted that composite materials exhibit several types of heterogeneity which can be observed from the perspective of different lengths scale. One of the most important elements of continuum approach is the use of Representative Volume Element (RVE) to describe heterogeneous material statistically [28–31]. A proper indentation grid [28] is necessary to ensure that the statistical analysis of each material phase will present the surface fraction of the total phases.

2.2. Microporomechanics

Based on the nano-indentation tests, the indentation modulus and hardness can be used to determine the particle properties such as particle stiffness (λ), Poisson's ratio (ν_s), cohesion (κ), friction

Table 1
Chemical composition of fly-ash (wt.%).

SiO_2	Al_2O_3	CaO	Fe_2O_3	K_2O
65.9	24.0	1.59	2.87	1.44

coefficient (ζ) and packing density (η) [20,28,32–34]. The equations can be written as:

$$M = \lambda \times \Pi_M(v_s, \eta, \eta_o) \tag{5}$$

$$H = \kappa \times \Pi_H(\zeta, \eta, \eta_o) \tag{6}$$

where Π_M and Π_H are dimensionless scaling relating to stiffness and hardness. This scaling relationship can be determined by linear and non-linear microporomechanics theory. A hypothesis is required to apply microporomechanics to indentation analysis. In this case, the tested material is assumed to be porous. It is also assumed that the characteristic size of the porosity is much smaller than the maximum indentation depth (h) for scaling separability reason.

The self-consistent or polycrystal micromechanical model is similar to micro-elasticity of a porous material whose solid is a granular material [20]. The self-consistent scheme assumes that each particle of a given phase (pore or solid) reacts as if it is embedded in an equivalent homogeneous medium [35]. The solid percolation threshold η_o is the limit that the solid fraction requires for providing a continuous force path through the system. Clear matrix-porosity morphology has continuous packing density in the solid phase,i.e. $0 < \eta \leqslant 1$. However, a perfectly disordered porous material has a solid percolation thread of $\eta = 0.5$ and below, i.e.,if $\eta < 0.5$,then the values of the composite bulk and shear modulus become negative, which will be considered unstable. The modulus function is provided by the following relationship [34,35]:

$$\Pi_M(r_s, \eta, \eta_o = 0.5) = G \cdot \frac{(9\eta r_s + 4G + 3r_s)(3r_s + 1)}{4(4G + 3r_s)(3r_s + 1)} \tag{7}$$

where $r_s = 2(1 + v_s)/3(1 - 2v_s) > 0$ and G is the composite bulk and shear modulus defined as:

$$G = \frac{1}{2} - \frac{5}{4}(1 - \eta) - \frac{3}{16}(2 + \eta) + \frac{1}{16} \times \left[144(1 - r_s) - 480\eta + 400\eta^2 + 408 r_s \eta^2 + 9 r_s^2 (2 + \eta)^2\right]^{0.5} \tag{8}$$

For solid Poissons ratio of $v_s = 0.5$, Eq. (8) becomes a linear scaling of modulus with packing density (η):

$$\Pi_M = 2\eta - 1 \geqslant 0 \tag{9}$$

The hardness with packing density (η) for the scaling relation is introduced by non-linear micromechanics:

$$\Pi_H(\zeta) = \Pi_0 \times [1 + (1 - \eta)\zeta - (d - e \cdot \eta)\zeta^2 - (f - g \cdot \eta)\zeta^5] \tag{10}$$

where Π_o is a function of frictionless portions as:

$$\Pi_0 = \frac{12\eta(a - b \cdot \eta)[(2\eta - 1)(2 + \eta)]^{0.5}}{(1 - c \cdot \eta)(2 + \eta)} \tag{11}$$

Based on microporomechanics, the coefficients suitable for Berkovich indenter are: $a = 0.19567, b = 0.03739, c = 0.77999, d = 20.3138, e = 31.5352, f = 52.1817$ and $g = 99.3465$ with $\eta = 0.5$ [34].

An inverse application to determine the solid properties and packing density is introduced by Ulm et al. [34] and Bobko et al. [36]. In an inverse application, the solid properties ($\lambda, v_s, \kappa, \zeta$) and local packing density (η) are unknowns. An algorithm implemented as a quadratic minimization problem between the experimental values and the theoretical scaling relationship can be written as:

$$\min \sum_{i=1}^{N} [(M_i - \lambda \times \Pi_M(v_s, \eta_i)) - (H_i - \kappa \times \Pi_H(\zeta, \eta_i))]^{0.5} \tag{12}$$

where N is the total number of the indentation tested points; M_i and H_i are obtained from Eq. (2). Solving Eq. (12) will provide the analytical results of the scaling relationship between the indentation modulus and hardness versus the packing density of the tested material.

2.3. Deconvolution technique

Heterogeneous materials or composite materials are generally complex, thus, a statistical technique is used for analysis of indentation results. It is computationally more convenient to deconvolute the cumulative distribution function (CDF) rather than the probability density function (PDF) [34]. The reason for using CDF rather than PDF is that the generation of the experimental PDF usually requires a choice of bin-size for histogram construction. Thus, the deconvolution technique starts with the generation of the experimental CDF. In the following equations, let X be a type of the mechanical properties and, as before, N is the number of indentation tests conducted on the specimen. The experimental CDF ($\Phi^e(X)$) can be written as:

$$\Phi^e(X) = \frac{i}{N} - \frac{1}{2N} \quad \text{for } i \in [1, N] \tag{13}$$

in which, the theoretical CDF ($\Phi_j^t(X)$) for each phase is given by the following Gaussian distribution:

$$\Phi_j^t(X) = \frac{1}{\sigma_j \sqrt{2\pi}} \int_{\infty}^{X_i} \exp\left(\frac{-(s - \mu_j)^2}{2\sigma_j^2}\right) dt \quad \text{for} \quad i \in [1, N] \tag{14}$$

where μ_j is the mean, σ_j is the variance of the distribution and j is a phase present in the sample. The function ($\Phi_j^t(X)$) can be found by minimising the following error function:

$$min \sum_{i=1}^{N} \sum (f_j \cdot \Phi_j^t(X) - \Phi^e(X))^2 \tag{15}$$

and the total volume fraction can be expressed by a summation of all single phases f_j as:

$$\sum_{j=1}^{n} f_j = 1 \tag{16}$$

where n is the total number of phases identifiable from the analysis. To avoid the overlapping of each phase, the constraint of the minimisation problems is required as:

$$\mu_j(X) + \sigma_j(X) \leqslant \mu_{j+1}(X) + \sigma_{j+1}(X) \tag{17}$$

The mean and standard deviation of the results from the deconvolution technique can then be used to determine the mechanical properties and surface volume fraction of each phase.

3. Experimental program

In this experimental work, class F (low calcium) fly-ash from Australia was used to prepare AAFA paste and mortar samples. The chemical composition of fly-ash is presented in Table 1. The Loss on Ignition (LOI) of fly-ash was 1.53% and the median particle size was 45 μm. The sand with specific gravity of 2.6 was used as fine aggregate. The alkali activator was prepared by dissolving NaOH pellet in water and left for 24 h and Na_2SiO_3 (water glass) was then added and again left for 24 h before mixing. The chemical composition of the Na_2SiO_3 was $Na_2 = 14.7\%$ $SiO_2 = 29.4\%$ and water 55.9% by mass. The effect of Na_2SiO_3 to NaOH solution by mass on compressive strength reported that higher Na_2SiO_3 to NaOH ratio

Table 2
Parameters and levels.

	Parameter	Level 1	Level 2	Level 3
SF (%)	Silica fume	0	2	4
s/c	Sand to cementitious material ratio	0	0.25	0.5
l/s	Liquid to solid ratio	0.6	0.65	0.7
SP (%)	Superplasticiser	0	2	4

Table 3
Mix proportion with density and compressive strength test result.

Mix No.	Fly-ash	SF	s/c	l/s	SP	ρ_{28} (kg/m^3)	f_{c28} (MPa)
1	1	0	0	0.6	0	1570	20.30
2	1	0	0.25	0.65	0.02	1598	15.84
3	1	0	0.5	0.70	0.04	1615	12.45
4	1	0.02	0	0.65	0.04	1509	6.79
5	1	0.02	0.25	0.70	0	1586	10.40
6	1	0.02	0.5	0.60	0.02	1685	9.92
7	1	0.04	0	0.70	0.02	1521	8.82
8	1	0.04	0.25	0.60	0.04	1602	9.92
9	1	0.04	0.5	0.65	0	1717	13.25

Table 4
ANOVA on density and compressive strength at 28 days.

	Source	DF[a]	SS[b]	MS[c]	Contribution (%)
Density (kg/m^3)	SF	2	790.1	395.0	2.14
	s/c	2	29155.0	1457.5	79.14
	l/s	2	3270.0	1635.0	8.88
	SP	2	3624.5	1812.2	9.84
Compressive strength (MPa)	SF	2	133.4	66.7	55.48
	s/c	2	5.7	2.9	2.38
	l/s	2	31.2	15.6	12.99
	SP	2	70.1	35.1	29.15

[a] Degree of freedom.
[b] Sum of square.
[c] Mean Square.

increases the compressive strength [37]. The NaOH to Na_2SiO_3 ratio of 2 was used for all mixtures. Specimens were cast in 50 mm cubic moulds and cured in a chamber at 60 °C and 70% R.H. for 24 h. This temperature is commoly used for curing alkali activated binders [37,38]. After that, the specimens were placed in a 23 °C controlled room until the testing age. The compressive strength and density of AAFA samples were tested at the age of 28 days in accordance with ASTM C109 [39]. The reported results are the average of 5 samples.

Four variable viz., silica fume (SF), sand to cementitious material ratio (s/c), liquid to solid ratio (l/s) and superplasticiser (SP) content were that parameters tested. Taguchi's design experimental approach, 4 parameters and 3 level of test variable were selected as shown in Table 2. The standard L_9 (3^4) orthogonal array was then used to define the contents of the nine mixtures. Detail of different mix proportions and their test results are presented in Table 3. The influence of the factors are in line with previously reported results [40–42] and thus reinforced the methodology used.

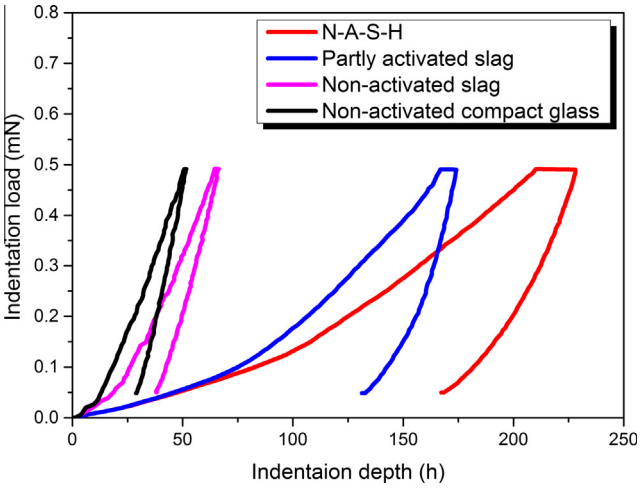

Fig. 2. Typical indentation load-depth $(P-h)$ curve on AAFA.

Table 5
Properties of the reaction products.

Mix No.	Stiffness (GPa)	Poisson's ratio	Cohesion (GPa)	Friction coefficient	Friction angle (degree)
1	144.57	0.50	1.46	0.62	31.85
2	87.06	0.50	0.48	0.62	31.78
3	84.30	0.50	0.39	0.67	33.93
4	84.40	0.50	0.32	0.63	32.31
5	103.80	0.50	0.48	0.62	31.81
6	87.93	0.50	0.38	0.64	32.64
7	84.87	0.50	0.43	0.56	29.13
8	84.81	0.50	0.40	0.62	31.93
9	94.95	0.50	0.25	0.78	37.93

For nano-indentation tests, after 28 days curing, each specimen was cut using a diamond saw to obtain 10 mm cube core part. The reaction of specimens were stopped using solvent exchange and oven dry method [43,44]. Miller et al. [45] pointed out that it was important to reduce the surface roughness of specimen to get an accurate nano-indentation results because the specimen's surface has a significant influence on the test results [46]. Therefore, fine emery paper was used to grind all specimens to reduce the surface roughness. After that, the surface was polished using a suspension solution ranging from 6.0 μm to 0.1 μm for 45 min and with 0.05 μm for another 15 min. Nano-indentation test was then carried out on the four sets of 10 mm cube specimens with XP (all-purpose) testing mode (applied load: 0.5 mN); each set was specified 10 ×10 grid (100 indentations) with 20 μm grid spacing. Berkovich indenter was used for the entire test.

4. Density and compressive strength

Nine mixtures of AAFA samples were prepared according to Taguchi's design of experiment. Details of the mixtures and the

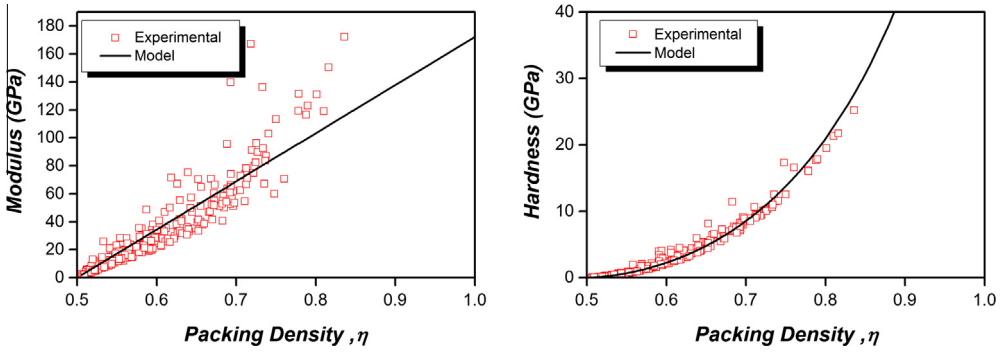

Fig. 3. Packing density relationship distribution of AAFA on MIX NO.1.

Table 6
ANOVA on deconvolution results of N-A-S-H phases at 28 days.

	Source	DF[a]	SS[b]	MS[c]	Contribution (%)
Modulus (GPa)	SF	2	74.06	37.1	47
	s/c	2	11.54	5.8	7
	l/s	2	34.66	17.4	22
	SP	2	37.50	18.8	24
Hardness (GPa)	SF	2	0.09	0.044	29
	s/c	2	0.014	0.007	4
	l/s	2	0.014	0.007	4
	SP	2	0.20	0.10	63
Volume fraction (%)	SF	2	0.19	0.10	76
	s/c	2	0.003	0.002	1
	l/s	2	0.036	0.002	14
	SP	2	0.022	0.01	9

[a] Degree of freedom.
[b] Sum of square.
[c] Mean Square.

Table 7
Statistical analysis of volume fraction of AAFA (%).

Mix No.	N-A-S-H	Partly-activated slag	Non-activated slag	Non-activated compact slag
1	53	8	14	24
2	48	27	18	7
3	24	26	29	21
4	29	16	25	31
5	28	9	30	32
6	42	23	25	10
7	6	31	33	31
8	9	35	31	25
9	8	27	26	39

Table 8
ANOVA on activation degree and porosity.

	Source	DF[a]	SS[b]	MS[c]	Contribution (%)
Activation degree	SF	2	0.06697	0.033486	49
	s/c	2	0.02721	0.013603	20
	l/s	2	0.02831	0.014156	21
	SP	2	0.01384	0.006921	10
Porosity	SF	2	0.004125	0.002063	60
	s/c	2	0.000055	0.000028	1
	l/s	2	0.001927	0.000964	28
	SP	2	0.000723	0.000361	11

[a] Degree of freedom.
[b] Sum of square.
[c] Mean Square.

experimental results of density (ρ_{28}) and compressive strength at 28 days (f_{c28}) are presented in Table 3. The analysis of variance (ANOVA) is performed to observe the relative influence of parameters and their interaction to the variation of results. Results of ANOVA analysis are presented in Table 4.

The density of AAFA at 28 days is between 1521 and 1717 kg/m^3. The ANOVA results show that s/c is the most influencing parameter on the density of AAFA with 79% contribution. The other influencing parameters are SP and l/s with approximately 10% and 9% contributions, respectively. It is observed that SF has the least influence on the density. The optimal mix proportion for minimisation of density is when there is no sand with 2% of SF, 0.7 of l/s and 4% of SP.

It is observed that the 28 days compressive strength of AAFA is in a range of 6.8 to 25.3 MPa. From ANOVA results, SF has a significant effect on the compressive strength with 55% contribution. It

Table 9
Activation degree and porosity.

MIX No.	Activation degree (%)	Porosity (%)
1	61	40
2	59	35
3	34	33
4	43	30
5	29	31
6	43	32
7	35	30
8	34	33
9	23	32

can be seen that there is a minimal effect of s/c on the compressive strength with about 2% contribution. The second most important parameter is the SP content with 29% contribution. The optimum mix proportion for 28 days compressive strength is a normal paste, i.e., no SF, no sand, no SP with l/s of 0.6.

5. Nano-indentation results

5.1. Deconvolution and particle properties

The results of nano-indentation test using deconvolution technique in terms of the CDF and PDF of the tested AAFA specimens confirm the presence of the four phases in AAFA. This is similar to the previously reported results [17]. The typical indentation load depth ($P-h$) curves are illustrated in Fig. 2. The mean indentation depth is 240 ± 7 nm in the N-A-S-H phase, 143 ± 3 nm in the partly-activated slag, 82 ± 1 nm in the non-activated slag and 54 ± 4 nm in the non-activated compact glass phases.

With the hypothesis that AAFA is porous, the quadratic minimisation problem, Eq. (12), can be solved using a commercial software package [47]. The results of the quadratic minimisation procedure of scaling indentation modulus and hardness exhibit the properties of reaction products. A typical packing density relationship distribution of AAFA is shown in Fig. 3. The results of the solid properties of reaction products of AAFA from the quadratic minimisation are presented in Table 5. The ranges of stiffness, cohesion and friction angle are 84.30–144.57 GPa, 0.25–1.46 GPa and 29.13–37.93°, respectively.

Eq. (16) is used to calculate the volume fraction of N-A-S-H, partly-activated slag, non-activated slag, and non-activated compact glass phases of AAFA mixtures. The summary of nano-indentation deconvolution results of indentation modulus (M), hardness (H), packing density (η) and volume fraction are

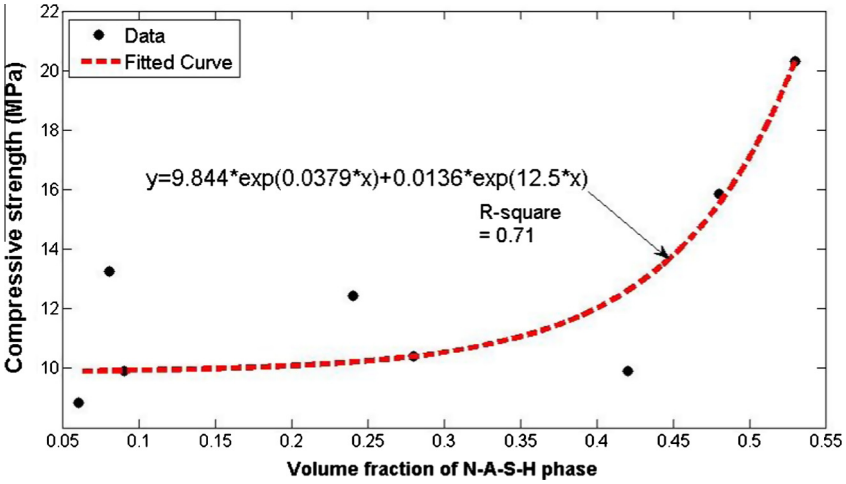

Fig. 4. Relationship between compressive strength and volume fraction of N-A-S-H phase.

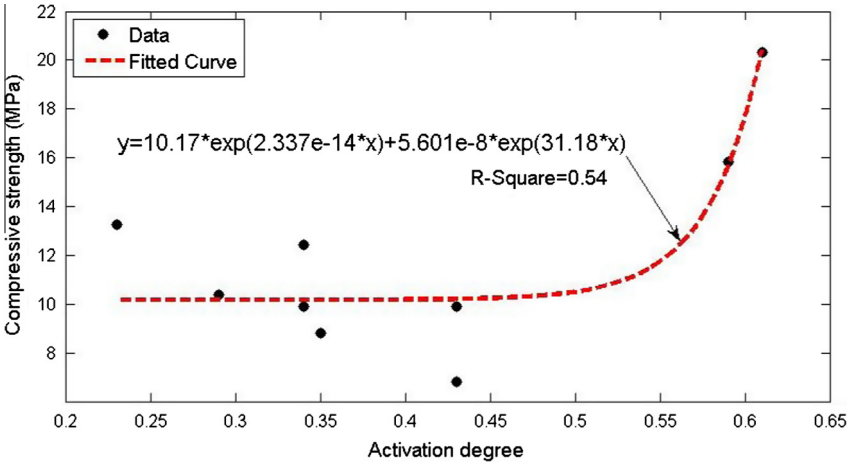

Fig. 5. Relationship between 28 days compressive strength and activation.

obtained. N-A-S-H phase is the major hydration product which relates directly to the mechanical strength gain [11,18]. The lowest indentation modulus, hardness and packing density are with reference to pure N-A-S-H phase, the deconvolution results of N-A-S-H phases vary from 4.44 to 16.78 GPa for indentation modulus, 0.11–0.75 GPa for indentation hardness, and 6–53% of volume fraction. The summary of deconvolution results are shown in Tables A1–A3. The ANOVA results as shown in Table 6 indicate that SF is the most significant effect on indentation modulus of N-A-S-H phase with 47% contribution, and s/c has the minimal effect on indentation modulus of N-A-S-H phase. The best mix proportion for the indentation modulus of N-A-S-H phase is 2% SF, s/c of 0.5, l/s of 0.65, and 0% SP content.

For the indentation hardness of N-A-S-H, SP has the most effect with almost 63% contribution, while the l/s has minor effect with just over 4% contribution. The optimum mix design of indentation hardness of N-A-S-H phase is 4% SF, s/c of 0.25, l/s of 0.6 and 4% SP content. It is also found that the relationship between indentation modulus and hardness of N-A-S-H phase of AAFA is an inverse relationship. SF is found to have the most adverse effect on the volume fraction of N-A-S-H phase with almost 76% contribution. This outcome correlates well with the compressive strength results, i.e. the best mix for maximum volume fraction of N-A-S-H phase is a normal paste mixture. The summary of the volume fraction of each phase is presented in Table 7.

Of particular interest is the relationship between compressive strength and volume fraction of N-A-S-H phase of the AAFA mixtures, as shown in Fig. 4. The compressive strength increases only slightly with the increase in volume fraction of N-A-S-H phase from 0.05 to 0.42. When the volume fraction of N-A-S-H is over 0.42, the strength increases significantly. This finding is similar to those reported by other researchers [11,18]. The N-A-S-H phase relates directly to the mechanical strength. From Fig. 4, the result of the relationship indicates that in order to obtain high strength AAFA, the volume fraction of N-A-S-H phase should be larger than 0.50.

5.2. Activation degree and porosity

The total activated reaction phases can also provide an estimation of the activation degree in the form of:

$$\xi = \sum_{j=1}^{\varphi} f_j \times \frac{\gamma}{\varepsilon} \tag{18}$$

where φ is the number of activated reaction phases, γ is the fly-ash mass in the mixture and ε is the total mass of mixture. Thus, the total activation degree in the present case is the sum of the volume fraction of the reaction phases which are N-A-S-H and partly-activated slag phase.

Mercury intrusion porosimetry (MIP) is a common measurement for a valid estimation of the pore size distribution of porous solid [48]. However, the measurement of porosity with MIP appears to be valid with limited application and difficulty in estimating the porosity of a cementitious based material. A way to determine porosity with statistical indentation technique is by a new nonintrusive way [34]. Therefore, it is possible to calculate the total porosity of the cementitious materials from:

$$\phi = \sum_{j=1}^{N} f_j(1-\eta_j) \tag{19}$$

In the present case, the activation degree and the porosity are found ranging from 23 to 61% and 30 to 40%, respectively. From ANOVA results as shown in Table 8, SF has the most significant effect on the activation degree and the porosity with 49% and 60% contributions, respectively. SP has a minor effect on the activation degree with 10% contribution, and s/c has a minor effect on the porosity with less than 1% contribution. The optimum mix proportion in terms of the activation degree of AAFA is 4% SF, s/c of 0.25, l/s of 0.6 and 0% SP content. For the porosity, the optimum mix is 2% SF, s/c of 0.25, l/s of 0.7 and 4% SP content. Table 9 shows summary of activation degree and porosity of AAFA mixtures.

The relationship between the compressive strength and the activation degree at the age of 28 days is also plotted as shown in Fig. 5. The compressive strength increases with the activation degree. When the activation degree is greater than 0.5, the compressive strength increases exponentially. Thus, to optimize the compressive strength of AAFA mixtures, the aim should be to ensure the activation degree of around 0.6.

6. Conclusion

The results obtained from this investigation are based on Taguchi's experimental design approach and statistical analysis of nano-indentation results of AAFA. The results are then used to determine the effect of test factors on the compressive strength, density, and nano-indentation deconvolution results of AAFA. Based on the results of this study, the following conclusions can be drawn:

(1) In terms of compressive strength, the normal AAFA paste, i.e., no SF, no sand, no SP with l/s of 0.6 is the optimum mix. For the four parameters investigated, SF has the most adverse impact on the compressive strength. Increases of SP and l/s also contribute to the decrease in compressive strength. There is no significant effect of s/c on compressive strength. In terms of density, the increase in the sand content significantly increases the density of mixture. The increasing of l/s and SP dosage further decreases the density of AAFA mixture.

(2) An application of nano-indentation technology is applied for the microporomechanics of AAFA mixtures. Statistical analysis based on deconvolution technique is carried out to determine the mechanical properties. AAFA is considered as porous material, thus the packing density (η) of each phase can be estimated by solving a quadratic minimisation. Four main phases of the reaction products viz., N-A-S-H, partly activated slag, non-activated slag and non-activated compact glass phases are identified. Other properties of the reaction products such as stiffness, Poissons ratio, and cohesion and friction coefficient are also determined.

(3) The analysis confirms that N-A-S-H phase is major reaction product of AAFA. The compressive strength is shown to relate to the volume fraction of N-A-S-H phase. To obtain high strength AAFA, the volume fraction of N-A-S-H phase should be larger than 0.42. The volume fraction of N-A-S-H phase of 0.50 or over is recommended.

(4) The compressive strength is also shown to relate to the activated degree of AAFA. When the activation degree is greater than 0.5, the compressive strength increases exponentially. Thus, it is recommended that the activation degree should be around 0.6 to obtain high strength mixture.

The test results confirm that mechanical and micromechanical properties of AAFA can be studied using statistical analysis of nano-indentation technology.

Acknowledgements

The authors would like to acknowledge the assistance by Dr. Kornkanok Boonserm, Department of Applied Chemistry, Rajamangala University of Technology in Thailand. The third author would like to acknowledge the support of Khon Kaen University and Thailand Research Fund (TRF) under the TRD Senior Research Scholar Contract No.RTA5780004.

Appendix A

In this appendix, deconvolution results of indentation modulus, hardness and packing density are presented:

Table A1
Deconvolution results of indentation modulus (GPa).

MIX No.	A		B		C		D	
	μ	σ	μ	σ	μ	σ	μ	σ
1	10.2	4.54	22.25	3.42	36.33	8.69	69.58	22.11
2	11.76	2.84	19.45	5.83	46.21	11.44	70.47	7.27
3	7.9	3.3	16.11	4.76	33.4	9.33	53.07	20.69
4	16.32	4.72	18.72	8	28.93	6.9	55.05	18.21
5	16.41	5.67	22.02	1.4	29.32	7.91	66.25	20.59
6	16.25	4.22	23.56	6.9	40.51	18.89	66.43	19.2
7	10.5	1.69	16.56	1.98	25.28	6.47	56.62	18.15
8	4.44	2.47	14.29	3.02	23.48	6.99	56.51	16.92
9	16.78	0.98	19.23	2.75	24.43	7.6	47.61	25.39

Table A2
Deconvolution results of indentation hardness (GPa).

MIX No.	A		B		C		D	
	μ	σ	μ	σ	μ	σ	μ	σ
1	0.61	0.33	2.09	0.52	4.2	3.1	10.04	4.88
2	0.52	0.19	1.21	0.55	4.75	1.75	7.47	0.39
3	0.25	0.13	0.82	0.45	3.01	1.33	6.6	1.6
4	0.53	0.24	1.42	0.35	1.56	0.74	5.45	2.76
5	0.75	0.28	0.91	0.43	1.71	0.96	7.18	2.23
6	0.62	0.27	1.25	0.51	4.05	1.95	8.15	0.49
7	0.52	0.1	0.77	0.11	1.11	0.57	6.24	2.84
8	0.11	0.08	0.69	0.17	1.22	0.74	6.46	2.09
9	0.57	0.12	0.92	0.1	1.22	0.59	5.08	3.16

Table A3
Deconvolution results of packing density.

MIX No.	A		B		C		D	
	μ	σ	μ	σ	μ	σ	μ	σ
1	0.55	0.02	0.61	0.01	0.61	0.12	0.72	0.05
2	0.58	0.02	0.63	0.03	0.77	0.05	0.83	0.01
3	0.56	0.02	0.61	0.03	0.71	0.05	0.8	0.04
4	0.6	0.03	0.64	0.02	0.69	0.02	0.82	0.07
5	0.6	0.03	0.62	0.01	0.66	0.04	0.82	0.05
6	0.61	0.03	0.63	0.04	0.75	0.07	0.86	0.01
7	0.58	0.01	0.62	0.01	0.65	0.04	0.84	0.07
8	0.53	0.02	0.61	0.02	0.64	0.05	0.83	0.05
9	0.6	0.03	0.62	0.01	0.63	0.04	0.76	0.08

A: N-A-S-H
B: Partly-activated slag
C: Non-activated slag
D: Non-activated compact glass

References

[1] C. Shi, D. Roy, P. Krivenko, Alkali-activated Cements and Concretes, CRC Press, 2006.
[2] C. Shi, A.F. Jiménez, A. Palomo, New cements for the 21st century: The pursuit of an alternative to portland cement, Cem. Concr. Res. 41 (7) (2011) 750–763, http://dx.doi.org/10.1016/j.cemconres.2011.03.016. URL http://www.sciencedirect.com/science/article/pii/S0008884611000925.
[3] F. Pacheco-Torgal, J.A. Castro-Gomes, S. Jalali, Alkali-activated binders: a review. Part 2. About materials and binders manufacture, Constr. Build. Mater. 22 (7) (2008) 1315–1322, http://dx.doi.org/10.1016/j.conbuildmat.2007.03.019. http://www.sciencedirect.com/science/article/pii/S0950061807000918.
[4] D.M. Roy, Alkali-activated cements opportunities and challenges, Cem. Concr. Res. 29 (2) (1999) 249–254, http://dx.doi.org/10.1016/S0008-8846(98)00093-3. URL http://www.sciencedirect.com/science/article/pii/S0008884698000933.
[5] J. Davidovits, High-alkali cements for 21st century concretes, ACI Special Publication 144.
[6] R.R. Lloyd, J.L. Provis, J.S. Van Deventer, Pore solution composition and alkali diffusion in inorganic polymer cement, Cem. Concr. Res. 40 (9) (2010) 1386–1392.
[7] R. Lloyd, Accelerated ageing of geopolymers, geopolymers: structure, processing, properties and industrial applications, 2009, pp. 139–166.
[8] P. Duxson, J.L. Provis, G.C. Lukey, J.S.J. van Deventer, The role of inorganic polymer technology in the development of green concrete, Cem. Concr. Res. 37 (12) (2007) 1590–1597, http://dx.doi.org/10.1016/j.cemconres.2007.08.018. URL http://www.sciencedirect.com/science/article/pii/S0008884607002001.
[9] L.K. Turner, F.G. Collins, Carbon dioxide equivalent (co 2-e) emissions: a comparison between geopolymer and opc cement concrete, Constr. Build. Mater. 43 (2013) 125–130.
[10] M. Criado, A. Fernández-Jiménez, A. Palomo, I. Sobrados, J. Sanz, Effect of the sio2/na2o ratio on the alkali activation of fly ash. part ii: 29si mas-nmr survey, Microporous Mesoporous Mater. 109 (13) (2008) 525–534, http://dx.doi.org/10.1016/j.micromeso.2007.05.062. URL http://www.sciencedirect.com/science/article/pii/S1387181107003514.
[11] A. Fernández-Jiménez, A. Palomo, Composition and microstructure of alkali activated fly ash binder: effect of the activator, Cem. Concr. Res. 35 (10) (2005) 1984–1992, http://dx.doi.org/10.1016/j.cemconres.2005.03.003. URL http://www.sciencedirect.com/science/article/pii/S0008884605000864.
[12] I. Garcia-Lodeiro, A. Palomo, A. Fernández-Jiménez, D. Macphee, Compatibility studies between nash and cash gels. study in the ternary diagram na2ocaoal2o3sio2h2o, Cem. Concr. Res. 41 (9) (2011) 923–931.
[13] H. Xu, J.S.J. Van Deventer, The geopolymerisation of alumino-silicate minerals, Int. J. Miner. Process. 59 (3) (2000) 247–266, http://dx.doi.org/10.1016/S0301-7516(99)00074-5. URL http://www.sciencedirect.com/science/article/pii/S0301751699000745.
[14] H.M. Jennings, A model for the microstructure of calcium silicate hydrate in cement paste, Cem. Concr. Res. 30 (1) (2000) 101–116, http://dx.doi.org/10.1016/S0008-8846(99)00209-4. URL http://www.sciencedirect.com/science/article/pii/S0008884699002094.
[15] P.D. Tennis, H.M. Jennings, A model for two types of calcium silicate hydrate in the microstructure of portland cement pastes, Cem. Concr. Res. 30 (6) (2000) 855–863, http://dx.doi.org/10.1016/S0008-8846(00)00257-X. URL http://www.sciencedirect.com/science/article/pii/S000888460000257X.
[16] G. Constantinides, F.-J. Ulm, The effect of two types of c-s-h on the elasticity of cement-based materials: results from nanoindentation and micromechanical modeling, Cem. Concr. Res. 34 (1) (2004) 67–80, http://dx.doi.org/10.1016/S0008-8846(03)00230-8. URL http://www.sciencedirect.com/science/article/pii/S0008884603002308.
[17] J. Němeček, V. Šmilauer, L. Kopecký, Nanoindentation characteristics of alkali-activated aluminosilicate materials, Cem. Concr. Compos. 33 (2) (2011) 163–170, http://dx.doi.org/10.1016/j.cemconcomp.2010.10.005. URL http://www.sciencedirect.com/science/article/pii/S0958946510001642.
[18] A. Fernández-Jiménez, A. Palomo, Characterisation of fly ashes. Potential reactivity as alkaline cements, Fuel 82 (18) (2003) 2259–2265, http://dx.doi.org/10.1016/s0016-2361(03)00194-7. URL http://www.sciencedirect.com/science/article/pii/S0016236103001947.
[19] R.K. Roy, A primer on the Taguchi method/Ranjit K. Roy, Van Nostrand Reinhold, New York, 1990.
[20] G. Constantinides, F.-J. Ulm, The nanogranular nature of csh, J. Mech. Phys. Solids 55 (1) (2007) 64–90.
[21] Y.-T. Cheng, C.-M. Cheng, Scaling, dimensional analysis, and indentation measurements, Mater. Sci. Eng. R: Reports 44 (45) (2004) 91–149, http://dx.doi.org/10.1016/j.mser.2004.05.001. URL http://www.sciencedirect.com/science/article/pii/S0927796X04000415.
[22] A.C. Fischer-Cripps, A simple phenomenological approach to nanoindentation creep, Mater. Sci. Eng. A 385 (12) (2004) 74–82, http://dx.doi.org/10.1016/j.msea.2004.04.070. URL http://www.sciencedirect.com/science/article/pii/S0921509304005362.
[23] F.F. Ling, Nanoindentation, third edition., Springer, New York, 2011.
[24] P. Lura, P. Trtik, B. Münch, Validity of recent approaches for statistical nanoindentation of cement pastes, Cem. Concr. Compos. 33 (4) (2011) 457–465, http://dx.doi.org/10.1016/j.cemconcomp.2011.01.006. URL http://www.sciencedirect.com/science/article/pii/S0958946511000126.
[25] J. Mencik, M. Swain, Micro-indentation tests with pointed indenters, Materials Forum, vol. 18, Institute of Metals and Materials Australasia, 1994, pp. 277–288.
[26] W. Oliver, G. Pharr, An improved technique for determining hardness and elastic modulus using load and displacement sensing indentation experiments, J. Mater. Res. 7 (06) (1992) 1564–1583, http://dx.doi.org/10.1557/JMR.1992.1564. URL http://dx.doi.org/10.1557/JMR.1992.1564http://journals.cambridge.org/download.php?file= 470%2FJMR%2FJMR7_06%2FS0884291400017039a.pdf&code=e86e617df13647f5589a28152cc6112a.
[27] W.C. Oliver, G.M. Pharr, Measurement of hardness and elastic modulus by instrumented indentation: advances in understanding and refinements to methodology, J. Mater. Res. 19 (01) (2004) 3–20.
[28] G. Constantinides, K. Ravi Chandran, F.-J. Ulm, K. Van Vliet, Grid indentation analysis of composite microstructure and mechanics: principles and validation, Mater. Sci. Eng. A 430 (1) (2006) 189–202.
[29] T. Kanit, S. Forest, I. Galliet, V. Mounoury, D. Jeulin, Determination of the size of the representative volume element for random composites: statistical and numerical approach, Int. J. Solids Struct. 40 (1314) (2003) 3647–3679, http://dx.doi.org/10.1016/S0020-7683(03)00143-4. URL http://www.sciencedirect.com/science/article/pii/S0020768303001434.
[30] C. Pichler, R. Lackner, A multiscale creep model as basis for simulation of early-age concrete behavior, Comput. Concr. 5 (4) (2008) 295–328.
[31] A. Zaoui, Continuum micromechanics: survey, J. Eng. Mech. 128 (8) (2002) 808–816. doi: 10.1061/(ASCE)0733-9399(2002) 128:8(808). URL http://ascelibrary.org/doi/abs/10.1061/%28ASCE%290733-9399%282002%29128%3A8%28808%29.
[32] R.D. Dukino, M.V. Swain, Comparative measurement of indentation fracture toughness with berkovich and vickers indenters, J. Am. Ceram. Soc. 75 (12) (1992) 3299–3304.
[33] H.M. Jennings, J.J. Thomas, J.S. Gevrenov, G. Constantinides, F.-J. Ulm, A multi-technique investigation of the nanoporosity of cement paste, Cem. Concr. Res. 37 (3) (2007) 329–336, http://dx.doi.org/10.1016/j.cemconres.2006.03.021. URL http://www.sciencedirect.com/science/article/pii/S0008884606000846.
[34] F. Ulm, M. Vandamme, C. Bobko, J. Alberto Ortega, K. Tai, C. Ortiz, Statistical indentation techniques for hydrated nanocomposites: concrete, bone, and shale, J. Am. Ceram. Soc. 90 (9) (2007) 2677–2692.
[35] L. Dormieux, D. Kondo, F.-J. Ulm, Microporomechanics, John Wiley and Sons, 2006.
[36] C. Bobko, F.-J. Ulm, The nano-mechanical morphology of shale, Mech. Mater. 40 (45) (2008) 318–337, http://dx.doi.org/10.1016/j.mechmat.2007.09.006. URL http://www.sciencedirect.com/science/article/pii/S016766360700138X.
[37] S. Wallah, B.V. Rangan, Low-calcium fly ash-based geopolymer concrete: long-term properties, Res. Report-GC2, Curtin University, Australia, 2006, pp. 76–80.
[38] P. Duxson, A. Fernández-Jiménez, J.L. Provis, G.C. Lukey, A. Palomo, J. Van Deventer, Geopolymer technology: the current state of the art, J. Mater. Sci. 42 (9) (2007) 2917–2933.
[39] A. International, Test method for compressive strenght of hydraulic cement mortars using 50 mm cube specimens, 2011.
[40] D. Brew, K. MacKenzie, Geopolymer synthesis using silica fume and sodium aluminate, J. Mater. Sci. 42 (11) (2007) 3990–3993.
[41] J. Davidovits, Properties of geopolymer cements, in: First International Conference on Alkaline Cements and Concretes, vol. 1, 1994, pp. 131–149.
[42] N. Lloyd, V. Rangan, Geopolymer Concrete-sustainable Cementless Concrete, ACI Special Publication 261 (2009) 33–54.
[43] J. Zhang, G.W. Scherer, Comparison of methods for arresting hydration of cement, Cem. Concr. Res. 41 (10) (2011) 1024–1036, http://dx.doi.org/10.1016/j.cemconres.2011.06.003. URL http://www.sciencedirect.com/science/article/pii/S0008884611001645.
[44] X. Chen, A. Meawad, L.J. Struble, Method to stop geopolymer reaction, J. Am. Ceram. Soc. 97 (10) (2014) 3270–3275.
[45] M. Miller, C. Bobko, M. Vandamme, F.-J. Ulm, Surface roughness criteria for cement paste nanoindentation, Cem. Concr. Res. 38 (4) (2008) 467–476, http://dx.doi.org/10.1016/j.cemconres.2007.11.014. URL http://www.sciencedirect.com/science/article/pii/S0008884607002955.
[46] ISO-14577-1, Metallic materials – instrumented indentation test for hardness and materials parameters, 2002.
[47] Matlab and statistics toolbox release 2014a.
[48] S. Diamond, Mercury porosimetry: an inappropriate method for the measurement of pore size distributions in cement-based materials, Cem. Concr. Res. 30 (10) (2000) 1517–1525, http://dx.doi.org/10.1016/S0008-8846(00)00370-7. URL http://www.sciencedirect.com/science/article/pii/S0008884600003707.

Arab J Sci Eng (2016) 41:1263–1271
DOI 10.1007/s13369-015-1906-4

RESEARCH ARTICLE - CIVIL ENGINEERING

Compressive strength, Bending and Fracture Characteristics of High Calcium Fly Ash Geopolymer Mortar Containing Portland Cement Cured at Ambient Temperature

Tanakorn Phoo-ngernkham[1] · Vanchai Sata[2] · Sakonwan Hanjitsuwan[3] · Charoenchai Ridtirud[4] · Shigemitsu Hatanaka[5] · Prinya Chindaprasirt[2]

Received: 24 April 2015 / Accepted: 6 October 2015 / Published online: 23 October 2015
© King Fahd University of Petroleum & Minerals 2015

Abstract This article presented the compressive strength, modulus of rupture and fracture characteristics of high calcium fly ash (FA) geopolymer mortars containing Portland cement type I (PC) with different sodium hydroxide (NaOH) concentrations (6, 10 and 14 molars). PC was added at the dosages of 0, 5, 10 and 15 % by weight of solid powder binder. Sodium silicate (Na_2SiO_3) and NaOH solutions were used as the alkali activators. Na_2SiO_3 to NaOH ratio of 2.0, alkaline liquid to binder ratio of 0.60, sand to binder ratio of 1.00 and curing at ambient temperature were used for all mixtures. Test results indicated that the use of PC as additive enhanced compressive strength, modulus of rupture and fracture characteristics of high calcium fly ash geopolymer mortar and NaOH concentrations also had significant affect on these properties. The use of 10 % PC with 14M NaOH resulted in high calcium FA geopolymer mortar with improved modulus of rupture and fracture characteristics.

Keywords Geopolymer · High calcium fly ash · Portland cement · NaOH concentration · Fracture characteristics · Ambient temperature

✉ Prinya Chindaprasirt
prinya@kku.ac.th

1 Research Center for Advances in Civil Engineering and Construction Materials, Program in Civil Engineering, Faculty of Engineering and Architecture, Rajamangala University of Technology Isan, Nakhon Ratchasima, 30000, Thailand

2 Sustainable Infrastructure Research and Development Center (SIRDC), Department of Civil Engineering, Faculty of Engineering, Khon Kaen University, Khon Kaen, 40002, Thailand

3 Program of Civil Technology, Faculty of Industrial Technology, Lampang Rajabhat University, Lampang, 52100, Thailand

4 Department of Civil Engineering, Faculty of Engineering, Rajamangala University of Technology Isan, Khon Kaen campus, Khon Kaen, 40000, Thailand

5 Department of Architecture, Faculty of Engineering, Mie University, Mie, 514-8504, Japan

1 Introduction

Manufacturing of Portland cement is an energy intensive process and releases a large amount of greenhouse gas [1]. The use of pozzolan to replace part of Portland cement is, therefore, quite attractive. One of the novel methods to reduce the use of Portland cement in concrete industry is the use of alternative binder such as geopolymer [2,3]. Geopolymer is normally made from silica and alumina-rich source materials such as fly ash, bottom ash, granulated blast furnace slag and calcined kaolin activated with high alkali solutions [3–5].

In Thailand, the annual output of lignite fly ash from Mae Moh power station is around 3.0 million tons [6]. Chindaprasirt et al. [7] reported that around 1.8 million tons of this fly ash is used as pozzolanic material in the cement and concrete industry; however, a large portion of this fly ash is still left over and discarded at landfill site which poses a serious environmental problem. This fly ash has been shown to be a suitable source material for making geopolymer [8–10]. In addition, the mechanical properties, fire resistance, acid resistance of geopolymer binder are superior to those of Portland cement [11–13].

Normally, the alkali solution is used for the activation by dissolving of Si^{4+} and Al^{3+} ions from the source material and from geopolymeric material. The most commonly used alkaline activators are sodium hydroxide and sodium silicate solutions [3]. Somna et al. [8] reported that sodium hydrox-

Table 1 Chemical compositions of FA and PC (by weight)

Materials	SiO_2	Al_2O_3	Fe_2O_3	CaO	MgO	K_2O	Na_2O	SO_3	LOI
FA	29.32	12.96	15.64	25.79	2.94	2.93	2.83	7.29	0.30
PC	20.80	4.70	3.40	65.30	1.50	0.40	0.10	2.70	0.90

ide concentration significantly affects both the compressive strength and structure of geopolymers. Sodium hydroxide concentration in the aqueous phase of geopolymeric system affects the dissolution process as well as the bonding of solid particles in the final structure [12,14]. Rattanasak and Chindaprasirt [15] reported that the leaching of Si^{4+} and Al^{3+} ions depends on sodium hydroxide concentration and leaching time which affects the geopolymerization and mechanical properties of hardened geopolymer.

At ambient temperature of 25 °C, the strength development of high calcium fly ash geopolymer is quite low [16] even though this FA consists of a substantial CaO content. In order to improve the strength development of high calcium fly ash geopolymer, improvements in strength development of fly ash geopolymers have thus been studied by several researchers [17–19]. The incorporation of Portland cement in the high calcium fly ash geopolymer is beneficial as the heat generated from the exothermic reaction of Portland cement hydration can assist the geopolymerization process [16,20–22]. Furthermore, the existence of calcium produces calcium silicate hydrate (C–S–H) gel which co-exists with geopolymer gel and results in higher compressive strength geopolymer [19].

One of the important properties of cementitious materials is its fracture characteristics which are related to the formation and propagation of cracks in the materials [23]. It depends on the mechanical interaction between aggregate and binder matrix [24]. Therefore, it is desirable to evaluate the fracture properties of cement and concrete materials for the proper design and safety of structure [25]. This property is related to the mechanical behaviors of materials under the loading and failure conditions.

Therefore, this research aims to study on the compressive strength, modulus of rupture and fracture characteristics of high calcium fly ash geopolymer mortars containing Portland cement with various sodium hydroxide solutions. The obtained results should be very beneficial to the understanding and to the future applications of geopolymer mortars as alternative repair material.

2 Experimental Details and Testing Analysis

2.1 Materials

The binder materials used in this study were high calcium fly ash (FA) from Mae Moh power plant in northern Thailand and Portland cement Type I (PC). The liquid portions in the mixture were sodium hydroxide (NaOH) of 6, 10 and 14 M concentrations and sodium silicate (Na_2SiO_3) with 13.89 % Na_2O, 32.15 % SiO_2 and 46.04 % H_2O by weight. Local river sand with specific gravity of 2.63 and fineness modulus of 1.80 were used.

The chemical composition of FA and PC is shown in Table 1. The specific gravities of FA and PC were 2.61 and 3.16, respectively. The median particle sizes of FA and PC were 8.5 and 14.6 μm with the corresponding Blaine finenesses of 4300 and 3600 cm^2/g, respectively.

2.2 Mix Proportion of Geopolymer Mortars

The mix proportions of geopolymer mortars (GPM) are shown in Table 2. Constant liquid alkaline to binder ratio of 0.60, Na_2SiO_3 to NaOH ratio of 2.0 and sand to binder ratio of 1.0 were used. The effects of NaOH concentrations (6, 10 and 14 M) were also studied. Four levels of PC replacement by FA of 0, 5, 10 and 15 % by weight were used. For the mixing of mortars, NaOH and Na_2SiO_3 solutions were firstly mixed together and used as the liquid solution. The FA, PC and sand were dry mixed until the mixture was homogenous. Right after, the liquid solution was added and the mixing of mortars was done for 5 min. In this paper, the geopolymer mortars are specified by the NaOH molar and Portland cement content. For example, 6M10PC stands for geopolymer mixture with 6 M NaOH and 10 % PC replacement.

3 Testing and Analysis

3.1 Compressive Strength of Geopolymer Mortars

Fresh mortar was cast in $50 \times 50 \times 50\ mm^3$ cube molds for the compressive strength test in accordance with ASTM C109 [26]. The samples were demolded at the age of 1 day and immediately wrapped with vinyl sheet to protect moisture loss and kept in the 25 °C controlled room. The compressive strengths were tested at the ages of 28 days and the reported results were the average of three samples.

3.2 Modulus of Rupture of Geopolymer Mortars

The fresh mortar was cast in $75 \times 75 \times 75\ mm^3$ prisms molds for the modulus of rupture (MOR) tests in accordance with

Table 2 Mix proportions of geopolymer mortars

Mix no.	Mix symbol	FA (g)	PC (g)	Sand (g)	NaOH (g)			Na_2SiO_3 (g)
					6 M	10 M	14 M	
1	6M0PC	100	–	100	20	–	–	40
2	6M5PC	95	5	100	20	–	–	40
3	6M10PC	90	10	100	20	–	–	40
4	6M15PC	85	15	100	20	–	–	40
5	10M0PC	100	–	100	–	20	–	40
6	10M5PC	95	5	100	–	20	–	40
7	10M10PC	90	10	100	–	20	–	40
8	10M15PC	85	15	100	–	20	–	40
9	14M0PC	100	–	100	–	–	20	40
10	14M5PC	95	5	100	–	–	20	40
11	14M10PC	90	10	100	–	–	20	40
12	14M15PC	85	15	100	–	–	20	40

the ASTM C293-02 [27]. The samples were demolded and cured the same way as the compressive strength samples. At the age of 28 days, the samples were tested in deflection control with loading rate of 0.05 mm/min [25]. The reported results were the average of three samples.

3.3 Fracture Characteristics of Geopolymer Mortars

The fresh mortar samples were cast in $75\times75\times300$ mm^3 long beams for fracture characteristics test. They were demolded at the age of 1 day and immediately wrapped with vinyl sheet to protect moisture loss and kept in the 25 °C controlled room. After curing, the samples were cut with a notch height to beam depth (a_0/d) ratio of 0.4 and notch width to notch height (w_0/a_0) ratio of 0.2 in the middle of the beam as shown in Fig. 1. The fracture characteristics were tested at the age of 28 days using three-point bending. The tests were performed in deflection control mode with constant loading rate of 0.05 mm/min [25], and the deflection data at middle span were recorded by LVDT. The reported results were the average of three samples.

The fracture energy (G_F) is the energy needed to create a crack of unit area and can be calculated by measuring the area under load-defection curve of geopolymer mortar notched beam and deformation at the mid-span of concrete beam. The fracture energy or specific fracture energy (G_F) was calculated from the work of fracture using Eq. (1) [28].

$$G_F = \frac{W_0 + mg\delta_{\max}}{A_{lig}} \tag{1}$$

where G_F is fracture energy (N/m), W_0 is the area under the load deflection curve (N-m), m is the mass of the beam between supports (kg), g is the acceleration due to gravity (m/s^2), $\delta_{\max}$ is the deflection at final failure of beam (m), and A_{lig} is the area of the ligament that was intact before the test (m^2).

For the determination of fracture toughness, the term fracture toughness or critical stress intensity factor (K_{IC}) was used to indicate the magnitude of stress concentration that exists in front of the crack tip when the crack starts to propagate [24]. The most common method of calculation of the critical stress intensity factor is to use the peak load from three-point bending test of notched beam [24,25,29]. The fracture toughness or critical stress intensity factor (K_{IC}) was calculated using Eqs. (2)–(4) [28].

$$K_{IC} = \frac{3Pl}{2bd^2}\sqrt{(\pi a_0)}F(a) \tag{2}$$

where $F(a)$ is

$$\frac{(1/\sqrt{\pi})\left(\left(1.99-\frac{a_0}{d}\left(1-\frac{a_0}{d}\right)\left(2.15-3.93\frac{a_0}{d}+2.7\left(\frac{a_0}{d}\right)^2\right)\right)\right.}{\left.\left(\left(1+2\frac{a_0}{d}\right)\left(1-\frac{a_0}{d}\right)^{1.5}\right)\right.} \tag{3}$$

Therefore, this could be re-written as

$$K_{IC} = \frac{3Pl}{2bd^2}\sqrt{a_0}\left[\left(1.93-3.07\left(\frac{a_0}{d}\right)+14.53\left(\frac{a_0}{d}\right)^2 -25.11\left(\frac{a_0}{d}\right)^3+25.80\left(\frac{a_0}{d}\right)^4\right)\right] \tag{4}$$

where K_{IC} is fracture toughness or critical stress intensity factor (MPa-mm$^{0.5}$), P is the maximum load (N), l is the span length of beam (mm), b is the width of beam (mm), d is the depth of beam (mm), and a_0 is the depth of notch (mm).

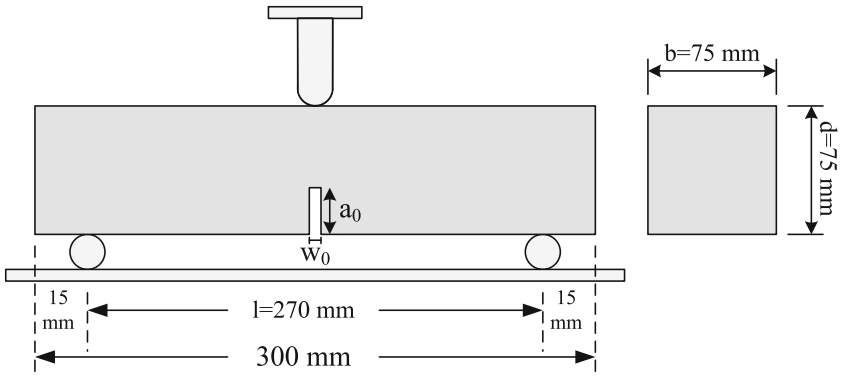

Fig. 1 Samples for fracture test

4 Results and Discussions

4.1 Compressive Strength of Geopolymer Mortars

The results of compressive strength of geopolymer mortar are shown in Fig. 2. The increase in both PC replacement level and NaOH concentration resulted in the increase in compressive strengths of mortars. For example, the compressive strengths of 6M0PC, 6M10PC, 14M0PC and 14M10PC mortars were 38.5, 45.3, 56.0 and 63.3 MPa, respectively. Also, the increase in PC replacement resulted in a reduction in setting time of geopolymer mortars as shown in Fig. 3. The increase in calcium content significantly accelerated the setting and hardening of geopolymer system [16]. Lee and van Deventer [30] reported that additional calcium content increased its solidification rate and cause rapid hardening; therefore, the improvement in strength of mortar was due to the increase in the reaction products with additional C–S–H and C–A–S–H gel co-existed with N-A-S-H gel [18]. With regard to the effect of NaOH concentration, the strength and setting time of geopolymer mortar increased with the increase in NaOH concentration. As shown in Fig. 3, the high NaOH concentrations resulted in the delay of setting

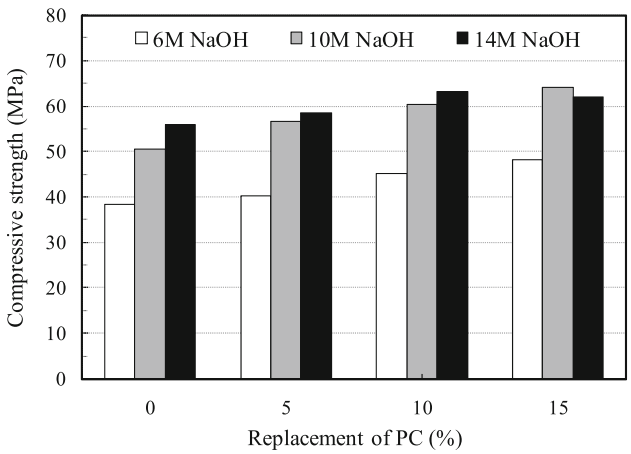

Fig. 2 Compressive strength of geopolymer mortars

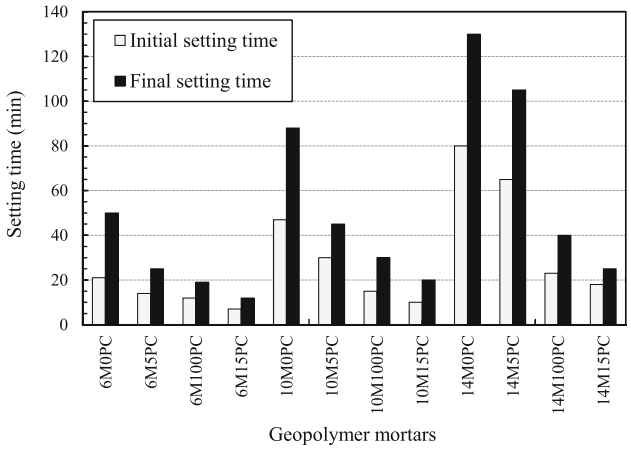

Fig. 3 Setting time of GPM

time of geopolymer mortars. This was due to the increase in dissolution of silica and alumina, whereas the leaching out of calcium from raw materials was hindered [6]. The increase in the leaching out of Si^{4+} and Al^{3+} ions from FA particles at high NaOH concentration also contributed to an increasing of its strength due to subsequent formation of N-A-S-H gel and thus improved the geopolymerization [15].

The SEM of fracture surfaces of high calcium FA geopolymer pastes with various PC replacements cured at ambient temperature for 28 days are given in Fig. 4. The results of compressive strength with various PC replacements agreed well with the SEM analyses.

The SEM of geopolymer pastes without PC replacement showed loose matrices with large number of non-reacted and/or partially reacted FA particles embedded in poor matrices. Normally, the geopolymerization of high calcium FA was slow at ambient temperature and needed temperature curing to accelerate the strength development [16]. With increasing level of PC replacement, the dense structure with continuous matrix and less number of FA particles were observed as illustrated in Fig. 4b, d. Pangdaeng et al. [16] claimed that the increasing calcium content enhanced the degree of reaction from an exothermal reaction with liberated

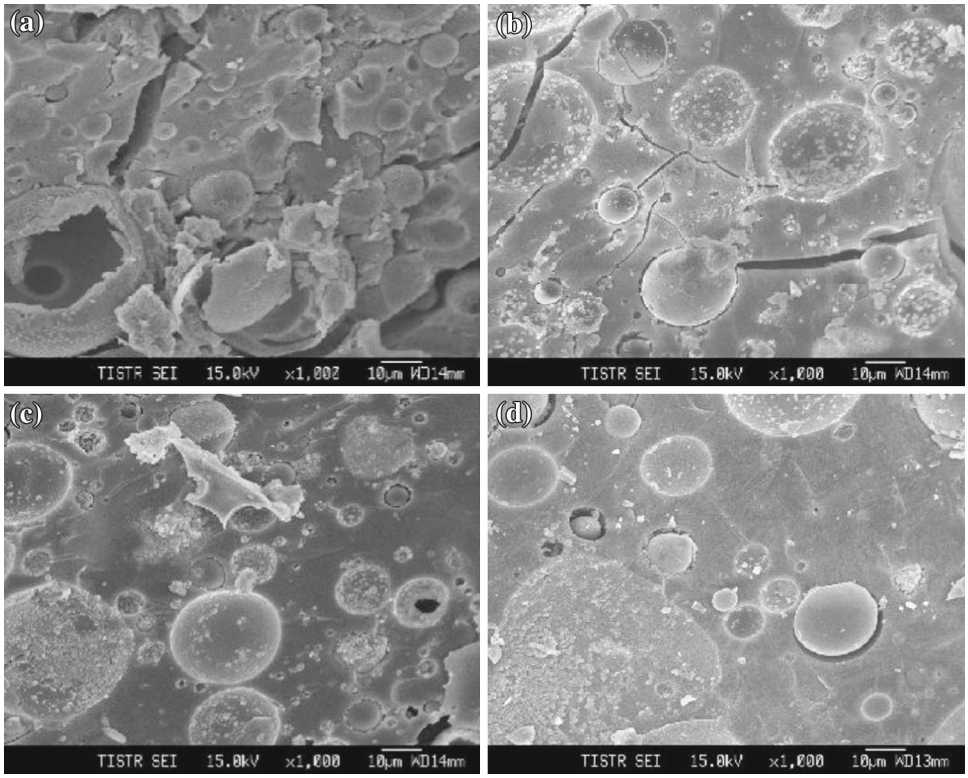

Fig. 4 SEM of geopolymer pastes. **a** 10M0PC, **b** 10M5PC, **c** 10M10PC, **d** 10M15PC

heat which resulted in additional C–S–H and/or C–A–S–H from the reaction of PC and leached calcium from FA co-existing with N–A–S–H gel. Therefore, this resulted in overall to strength development of high calcium FA geopolymer containing PC.

4.2 Modulus of Rupture of Geopolymer Mortars

The MOR of geopolymer mortars as shown in Fig. 5 increased as increasing in both replacement level of PC and NaOH concentration up to the threshold level. The results followed similar trend to that of the compressive strength results. The increase in MOR with the increase in replacement level of PC from 0 to 10 % was due primarily to the formation of C–S–H and C–A–S–H which coexisted with the N-A-S-H gel. However, the incorporation of high amount of PC (15 %) and high NaOH concentration (14 M) resulted in a slight decline in the MOR of mortar. For instance, the MORs of 14M0PC, 14M5PC, 14M10PC and 14M15PC mortars were 7.07, 8.51, 8.96 and 7.49 MPa, respectively. At high NaOH concentration, polycondensation was hindered and the excess OH^- ion concentration caused early aluminosilicate gel precipitation [33]. This affected the beneficial effect of PC incorporation especially at the high replacement level (15 %) and thus lowered the strengths of geopolymer mortars.

The graph between compressive strength and MOR of geopolymer mortars is shown in Fig. 6. MOR increased linearly with increasing square root of compressive strength and

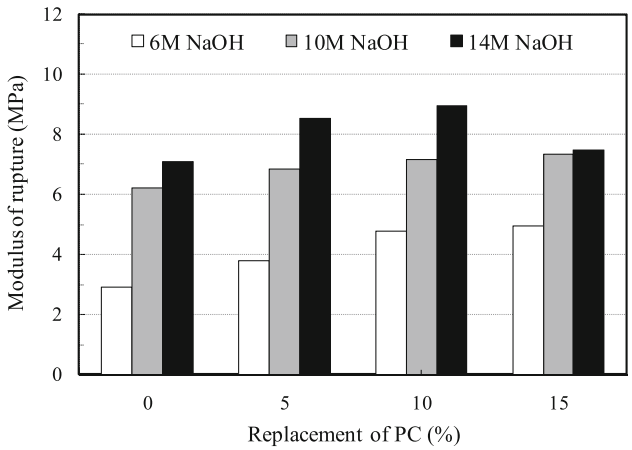

Fig. 5 Modulus of rupture of geopolymer mortars

the finding conformed with those reported by Pacheco-Torgal et al. [31] and Sofi et al. [32]. The equations used for calculations are normally used for concrete. For mortar specimens, the aggregate size is smaller and thus the interpretation and further use of results should be done with care. The relationship between modulus of rupture and compressive strength can be written as

$$MOR = 2.78\sqrt{f'_c} - 13.95 \quad (5)$$

where MOR is the modulus of rupture (MPa) and f'_c is the compressive strength (MPa).

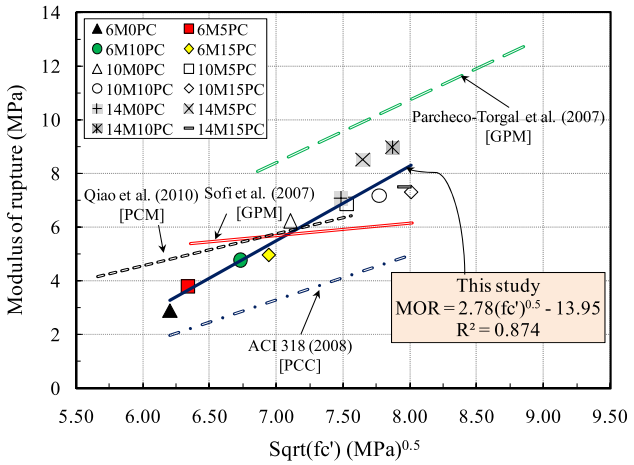

Fig. 6 Relationship between compressive strength and modulus of rupture of geopolymer mortars compared with previously published results of geopolymer mortar and Portland cement mortar

It can be observed from Fig. 6 that the MOR of mortars expressed as a function of compressive strength was higher than those of Portland cement concrete (PCC) predicted by ACI 318 [33]. The MORs of mortars in this study are of the same order as those of geopolymer mortars (GPM) and Portland cement mortars (PCM) given by Sofi et al. [32] and Qiao et al. [34], but were slightly lower than those of geopolymer mortars made from mine waste mud, calcium hydroxide and 24M NaOH reported by Pacheco-Torgal et al. [31] and Pacheco-Torgal et al. [35]. This was due to the differences in the source materials and NaOH concentrations.

4.3 Fracture Energy Of Geopolymer Mortars

The load-defection curves of geopolymer mortar notched beam are shown in Fig. 7. The results of load-defection curve showed that the applied load increased with increase in replacement level of PC and NaOH concentration similar to the behaviors of MOR of mortar. According to Fig. 8, the fracture energy of mortars increased with NaOH concentration which was due to the increase in geopolymer products. However, there was an indication that the rate of fracture energy tended to decrease with very high NaOH concentration. This was similar to the results of strength of geopolymer at high NaOH concentration. The fracture energy values of geopolymer mortar in this study agreed with that of Sarker et al. [24] who reported that the fracture energy increased with compressive strength.

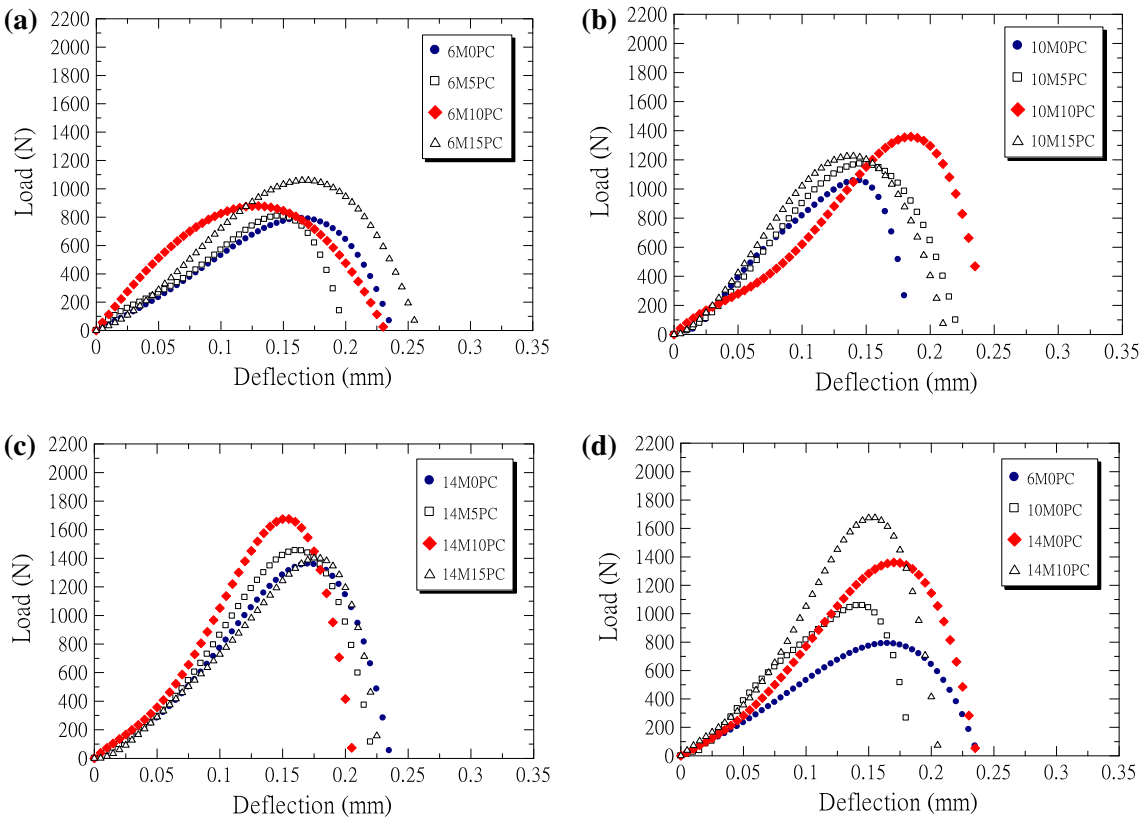

Fig. 7 Load-deflection of geopolymer mortars. **a** 6M NaOH, **b** 10M NaOH, **c** 14M NaOH, **d** Comparison between NaOH concentration

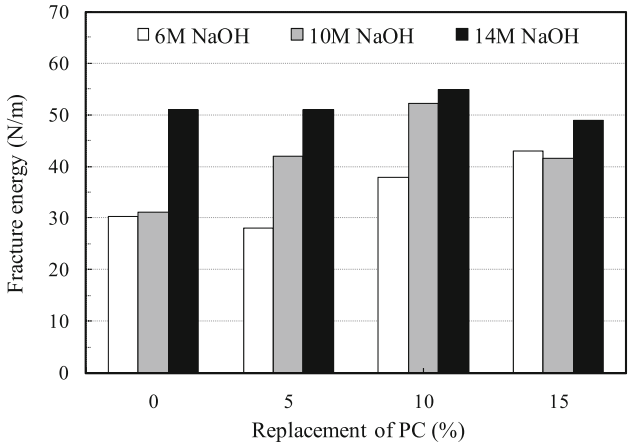

Fig. 8 Fracture energy of geopolymer mortars

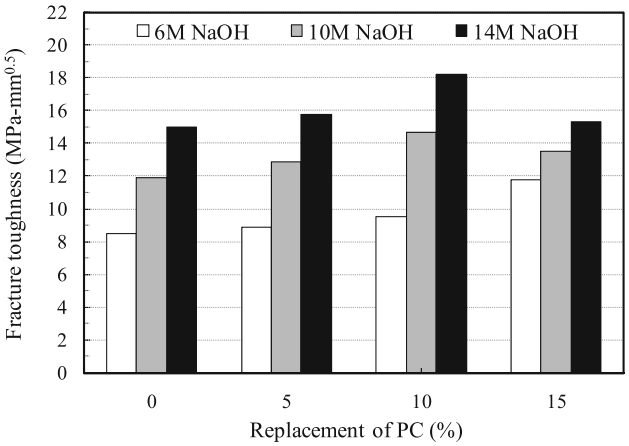

Fig. 9 Fracture toughness of geopolymer mortars

4.4 Fracture Toughness of Geopolymer Mortars

The results of fracture toughness or critical stress intensity factor (K_{IC}) of geopolymer mortars are shown in Fig. 9. The value of fracture toughness indicated the stress concentration in front of the crack tip when the crack starts to propagate. The fracture toughness of mortars slightly increased with increasing in NaOH concentrations and the addition of a proper amount of PC. The results corresponded well with those of compressive strength and MOR behaviors. A slight decrease in fracture toughness was also observed from incorporation of high amount of 15 % PC for mix with high NaOH concentrations similar to the case of MOR. This was because the excess OH^- ion concentration caused early aluminosilicate gel precipitation [30] and polycondensation was hindered at high NaOH concentration [36].

The relationship between fracture toughness and compressive strength of geopolymer mortar is shown in Fig. 10. The fracture toughness linearly increases with the square root of ultimate compressive strength. Again, it should be pointed out here that the equations used for calculations are used for concrete. The relationship between fracture toughness and compressive strength of gepolymer mortar from this work can be written as

$$K_{IC} = 4.30\sqrt{f'_c} - 18.37 \quad (6)$$

where K_{IC} is the fracture toughness (MPa-mm$^{0.5}$) and f'_c is the compressive strength (MPa).

As shown in Fig. 10, the fracture toughness values of mortar in this study followed the same trend with those of Sarker et al. [24] and Bharatkumar et al. [25] which indicated that the fracture toughness tended to increase with the compressive strength. The values of fracture toughness of mortars are similar to that of Portland cement mortar (PCM) given by Mindess and Nadeau [37]. Also given in Fig. 10 for comparison are the values of fracture toughness of geopolymer concrete (GPC) and Portland cement concrete (PCC) which were higher than those of the geopolymer mortar as expected.

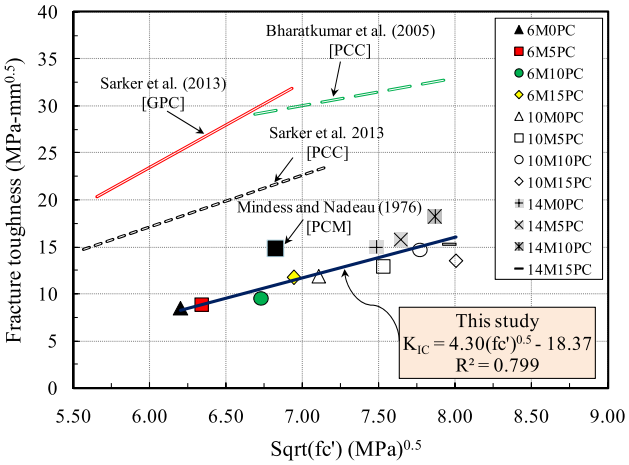

Fig. 10 Relationship between fracture toughness and compressive strength of geopolymer mortars compared with previously published results of geopolymer concrete, Portland cement mortar and Portland cement concrete

5 Conclusions

Based on the results of this study, the following conclusions could be drawn.

(1) The use of high NaOH concentration and the addition of a proper amount of PC enhanced the compressive strength, modulus of rupture and fracture characteristics of the high calcium fly ash geopolymer mortars. These properties increased with increase in NaOH content from 6 to 14 M due to the increase in the leaching out of Si^{4+} and Al^{3+} ions from the FA particles at high

NaOH concentration and the subsequent formation of N–A–S–H gel.

(2) The compressive strength, modulus of rupture, fracture energy and fracture toughness of the mortars also increased with the replacement level of PC from 0 to 10 % due primarily to the increase in the reaction products within geopolymer matrix.

(3) The incorporation of high amount of PC (15 %) with high NaOH concentration (14 M) resulted in a slight decline in these properties of high calcium geopolymer mortars, because the excess of hydroxide ion concentration caused early aluminosilicate gel precipitation which affected the beneficial effect of PC incorporation.

(4) The geopolymer mortar with 14M NaOH and 10 % PC showed best results with 28-day compressive strength, modulus of rupture, fracture energy and fracture toughness of 63.3, 8.96 MPa, 54.81 N/m and 18.21 MPa-mm$^{0.5}$, respectively.

Acknowledgments This work was supported by the Higher Education Research Promotion and National Research University Project of Thailand, Office of the Higher Education Commission, through the Advanced Functional Materials Cluster of Khon Kaen University, and the Thailand Research Fund (TRF) and Khon Kaen University under the TRF Senior Research Scholar, Grant No. RTA5780004.

References

1. Metz, B.; Davidson, O.R.; Bosch, P.R.; Dave, R.; Meyer, L.A.: Climate change 2007. Contribution of working group III to the fourth assessment report of the intergovernmental panel on climate change, 2007. pp. 447–496. Cambridge University Press, Cambridge (2007)
2. Duxson, P.; Provis, J.L.; Lukey, G.C.; van Deventer, J.S.J.: The role of inorganic polymer technology in the development of 'green concrete'. Cement Concrete Res., **37**(12), 1590–1597 (2007)
3. Phoo-ngernkham, T.; Maegawa, A.; Mishima, N.; Hatanaka, S.; Chindaprasirt, P.: Effects of sodium hydroxide and sodium silicate solutions on compressive and shear bond strengths of FA–GBFS geopolymer. Construct. Build. Mater., **91**, 1–8 (2015)
4. Kumar, S.; Kumar, R.; Mehrotra, S.P.: Influence of granulated blast furnace slag on the reaction, structure and properties of fly ash based geopolymer. J. Mater. Sci., **45**(3), 607–615 (2010)
5. Davidovits, J.: Geopolymers–inorganic polymeric new materials. J. Therm. Anal. **37**(8), 1633–1656 (1991)
6. Hanjitsuwan, S.; Hunpratub, S.; Thongbai, P.; Maensiri, S.; Sata, V.; Chindaprasirt, P.: Effects of NaOH concentrations on physical and electrical properties of high calcium fly ash geopolymer paste. Cement Concrete Compos., **45**, 9–14 (2014)
7. Chindaprasirt, P.; Jaturapitakkul, C.; Sinsiri, T.: Effect of fly ash fineness on microstructure of blended cement paste. Construct. Build. Mater., **21**(7), 1534–1541 (2007)
8. Somna, K.; Jaturapitakkul, C.; Kajitvichyanukul, P.; Chindaprasirt, P.: NaOH-activated ground fly ash geopolymer cured at ambient temperature. Fuel, **90**(6), 2118–2124 (2011)
9. Sukmak, P.; Horpibulsuk, S.; Shen, S.L.: Strength development in clay–fly ash geopolymer. Construct. Build. Mater., **40**, 566–574 (2013)
10. Van Jaarsveld, J.G.S.; Van Deventer, J.S.J.: Effect of the alkali metal activator on the properties of fly ash-based geopolymers. Indust. Eng. Chem. Res., **38**(10), 3932–3941 (1999)
11. Bakharev, T.: Thermal behaviour of geopolymers prepared using class F fly ash and elevated temperature curing. Cement Concrete Res., **36**(6), 1134–1147 (2006)
12. Bernal, S.A.; Provis, J.L.; Walkley, B.; San Nicolas, R.; Gehman, J.D.; Brice, D.G.; Kilcullen, A.R.; Duxson, P.; van Deventer, J.S.J.: Gel nanostructure in alkali-activated binders based on slag and fly ash, and effects of accelerated carbonation. Cement Concrete Res., **53**, 127–144 (2013)
13. Bakharev, T.: Heat resistance of geopolymer materials prepared using class F fly ash. J. Australas. Ceramic Soc., **42**(1), 36–44 (2006)
14. Panias, D.; Giannopoulou, I.P.; Perraki, T.: Effect of synthesis parameters on the mechanical properties of fly ash-based geopolymers. Colloids Surf. A Physicochem. Eng. Asp., **301**(1-3), 246–254 (2007)
15. Rattanasak, U.; Chindaprasirt, P.: Influence of NaOH solution on the synthesis of fly ash geopolymer. Miner. Eng., **22**(12), 1073–1078 (2009)
16. Pangdaeng, S.; Phoo-ngernkham, T.; Sata, V.; Chindaprasirt, P.: Influence of curing conditions on properties of high calcium fly ash geopolymer containing Portland cement as additive. Mater. Design, **53**, 269–274 (2014)
17. Guo, X.; Shi, H.; Chen, L.; Dick, W.A.: Alkali-activated complex binders from class C fly ash and Ca-containing admixtures. J. Hazard. Mater., **173**(1-3), 480–486 (2010)
18. Palomo, A.; Fernández-Jiménez, A.; Kovalchuk, G.; Ordoñez, L.M.; Naranjo, M.C.: OPC-fly ash cementitious systems: Study of gel binders produced during alkaline hydration. J. Mater. Sci., **42**(9), 2958–2966 (2007)
19. Temuujin, J.; van Riessen, A.; Williams, R.: Influence of calcium compounds on the mechanical properties of fly ash geopolymer pastes. J. Hazard. Mater., **167**(1-3), 82–88 (2009)
20. Nath, P.; Sarker, P.K.: Use of OPC to improve setting and early strength properties of low calcium fly ash geopolymer concrete cured at room temperature. Cement Concrete Compos., **55**, 205–214 (2015)
21. Phoo-ngernkham, T.; Chindaprasirt, P.; Sata, V.; Pangdaeng, S.; Sinsiri, T.: Properties of high calcium fly ash geopolymer pastes containing Portland cement as additive. Int. J. Miner. Metall. Mater., **20**(2), 214–220 (2013)
22. Suwan, T.; Fan, M.: Influence of OPC replacement and manufacturing procedures on the properties of self-cured geopolymer. Construct. Build. Mater., **73**, 551–561 (2014)
23. Sabir, B.B.; Wild, S.; Asili, M.: On the tortuosity of the fracture surface in concrete. Cement Concrete Res., **27**(5), 785–795 (1997)
24. Sarker, P.K.; Haque, R.; Ramgolam, K.V.: Fracture behaviour of heat cured fly ash based geopolymer concrete. Mater. Design, **44**, 580–586 (2013)
25. Bharatkumar, B.; Raghuprasad, B.; Ramachandramurthy, D.; Narayanan, R.; Gopalakrishnan, S.: Effect of fly ash and slag on the fracture characteristics of high performance concrete. Mater. Struct., **38**(1), 63–72 (2005)
26. ASTM C109: Standard test method of compressive strength of hydraulic cement mortars (using 2-in. or [50 mm] cube specimens). Annual Book of ASTM Standard **Vol.04.01** (2002)
27. ASTM C293-02: Flexural strength of concrete (using simple beam with center-point loading). Annual Book of ASTM Standard **Vol.04.02** (2002)
28. RILEM TC 50–FMC: Determination of the fracture energy of mortar and concrete by means of three-point bend tests on notched beams. Mater. Struct. **18**(4), 287–290 (1985)
29. Peterson, P.E.: Fracture energy of concrete: method of determination. Cement Concrete Res., **10**(1), 79–89 (1980)

30. Lee, W.K.W.; van Deventer, J.S.J.: The effect of ionic contaminants on the early-age properties of alkali-activated fly ash-based cements. Cement Concrete Res., **32**(4), 577–584 (2002)
31. Pacheco-Torgal, F.; Castro-Gomes, J.P.; Jalali, S.: Adhesion characterization of tungsten mine waste geopolymeric binder. Influence of OPC concrete substrate surface treatment. Construct. Build. Mater., **22**(3), 154–161 (2008)
32. Sofi, M.; van Deventer, J.S.J.; Mendis, P.A.; Lukey, G.C.: Engineering properties of inorganic polymer concretes (IPCs). Cement Concrete Res., **37**(2), 251–257 (2007)
33. ACI 318: Building Code Requirement for Structure Concrete Practice (ACI 318-08) and Commentary. American Concrete Institute (2008)
34. Qiao, F.; Chau, C.K.; Li, Z.: Property evaluation of magnesium phosphate cement mortar as patch repair material. Constr. Build. Mater., **24**, 695–700 (2010)
35. Pacheco-Torgal, F.; Castro-Gomes, J.; Jalali, S.: Investigations about the effect of aggregates on strength and microstructure of geopolymeric mine waste mud binders. Cement Concrete Res., **37**(6), 933–941 (2007)
36. Zuhua, Z.; Xiao, Y.; Huajun, Z.; Yue, C.: Role of water in the synthesis of calcined kaolin-based geopolymer. Appl. Clay Sci., **43**(2), 218–223 (2009)
37. Mindess, S.; Nadeau, J.S.: Effect of notch width on K_{IC} for mortar and concrete. Cement Concrete Res., **6**(4), 529–534 (1976)

Journal of Alloys and Compounds 664 (2016) 792–797

Contents lists available at ScienceDirect

Journal of Alloys and Compounds

journal homepage: http://www.elsevier.com/locate/jalcom

Characterization and magnetic properties of cobalt ferrite nanoparticles

Ekaphan Swatsitang [e], Sumalin Phokha [b, *], Sitchai Hunpratub [b], Brian Usher [b], Atipong Bootchanont [c], Santi Maensiri [d], Prinya Chindaprasirt [a]

[a] Sustainable Infrastructure Research and Development Center, Department of Civil Engineering, Faculty of Engineering, Khon Kaen University, Khon Kaen, 40002, Thailand
[b] Department of Physics, Faculty of Science, Udon Thani Rajabhat University, Udon Thani, 41000 Thailand
[c] Division of Physics, Faculty of Science and Technology, Rajamangala University of Technology Thanyaburi (RMUTT), Pathumthani 12110, Thailand
[d] School of Physics, Institute of Science, Suranaree University of Technology, Nakhon Ratchasima, 30000 Thailand
[e] Integrated Nanotechnology Research Center and Department of Physics, Faculty of Science, Khon Kaen University, Khon Kaen, 40002, Thailand

ARTICLE INFO

Article history:
Received 20 November 2015
Accepted 28 December 2015
Available online 30 December 2015

Keywords:
Spinel cobalt ferrite
Polymer pyrolysis method
Ferromagnetism
X-ray absorption near edge structure (XANES)

ABSTRACT

Inverse spinel cobalt ferrite ($CoFe_2O_4$) nanoparticles were synthesized by a polymer pyrolysis method and calcined at various temperatures from 800 to 1000 °C. The structure, morphology, valence states and magnetic properties of the calcined samples were characterized by X-ray diffraction (XRD), transmission electron microscopy (TEM), X-ray absorption near edge structure (XANES) and vibrating sample magnetometer (VSM). All calcined samples had the cubic spinel type structure with average crystallite sizes increasing from 80 ± 2 to 100 ± 3 nm with increasing calcination temperature. The XANES spectra allowed the valence states of the Fe^{3+} and Co^{2+} ions in the samples to be established and simulation of the XANES spectra suggested that the site occupancy of Fe^{3+} and Co^{2+} ions was mixed, with the majority of Co^{2+} ions occupying octahedral sites and the majority of Fe^{3+} ions occupying tetrahedral sites within the spinel structure. All samples exhibited ferromagnetic behavior at room temperature with a maximum saturation magnetization (M_S) of 3.42 μ_B and a coercivity (H_C) of 1100 Oe for crystallite sizes of 100 nm. The origin of the ferromagnetism is discussed in relation to the distribution of Fe^{3+} and Co^{2+} ions within the lattice and the crystallite sizes.

© 2015 Elsevier B.V. All rights reserved.

1. Introduction

Spinel ferrites with a face centered cubic structure have the formula MFe_2O_4 where M represents a divalent metal ion such as zinc, nickel, manganese or cobalt. Among these, $CoFe_2O_4$ is an inverse spinel ferrite with all or most Co^{2+} ions occupying octahedral sites (B sites) and the Fe^{3+} ions on both tetrahedral (A sites) and B sites. Nanocrystalline $CoFe_2O_4$ has attracted considerable attention because of its remarkable catalytic, electronic and magnetic properties which are significantly different from their bulk counterparts [1,2]. It is therefore used in many fields of application such as magnetic recording, magnetic fluids, magnetic drug delivery, sensors and electrical devices as well as showing promise in applications such as optoelectronics, photocatalytic activity and so on [1–5].

Recently, nanocrystalline $CoFe_2O_4$ with high Curie temperatures (T_C), high coercivity, and high saturation magnetization (M_S) have been synthesised by the addition of other elements to the host spinel ferrite structure. The substitution of various transition metals (TM) onto A and/or B sites of a $CoFe_2O_4$ host and the preparation of nanometer-sized pure and/or TM-doped $CoFe_2O_4$ has produced interesting distributions of the Co^{2+}, Fe^{3+} and TM within the structure. For example, large values for M_S and T_C have been measured following TM substitution on B sites in materials such as $Co_{1-x}Mn_x Fe_2O_4$ [6,7], $Zn_{1-x}Co_xFe_2O_4$ [8], $Co_{1-x}Ni_xFe_2O_4$ [9] and $Ni_{1-x}Mg_xFe_2O_4$ [10] as well as TM substitution on A and B sites in materials such as $CoFe_{2-x}Mn_xO_4$ [11] and $CoAl_{0.2}Fe_{1.8}O_4$ [12]. Furthermore, different preparation techniques such as the hydrothermal method [13,14], the sol–gel process [15], co-precipitation [16,17], microwave [8] and thermal decomposition [1] have been employed from which it has become clear that the high magneto–crystalline anisotropy of pure and/or TM-doped $CoFe_2O_4$ depends

* Corresponding author.
E-mail address: sumalinphokha@gmail.com (S. Phokha).

http://dx.doi.org/10.1016/j.jallcom.2015.12.230
0925-8388/© 2015 Elsevier B.V. All rights reserved.

strongly on the synthesizing method and conditions and the type and doping levels of the different TMs used.

In this work, $CoFe_2O_4$ nanoparticles were prepared by the polymer pyrolysis method and their crystallinity and morphology were characterized by XRD and TEM. The valence states of the Fe and Co ions were studied by XANES and the simulation of these spectra gave information about the locations of these ions in the structure. The magnetic properties of the nanoparticles were investigated using a VSM and exhibited a high M_S with significant hysteresis.

2. Experimental

$CoFe_2O_4$ nanoparticles were synthesized by the polymer pyrolysis method using 0.006 mol each of $Co(NO_3)_2.6H_2O$ (Aldrich) and $Fe(NO_3)_3 \cdot 9H_2O$ (Kanto) and 70 ml of acrylic acid ($C_3H_4O_2$) as starting materials. All materials were dissolved in deionized water to promote polymerization after which the precursor solution was heated to 30 °C and stirred until it dried. The final product was then pre-calcined in a furnace at 400 °C for 2 h to form the polyacrylate salt precursor, which was then calcined at temperatures of 800, 900 and 1000 °C for 3 h in air to obtain $CoFe_2O_4$.

The prepared samples were characterized using XRD, TEM, XANES, and VSM. A Bruker D2 Phaser X-ray diffractometer employing Cu Kα radiation ($\lambda = 0.154184$ nm) was used to study the phases of the $CoFe_2O_4$ samples and TEM was performed using a FE-TEM (TECNAI G^2 20) to establish the morphology and crystal sizes. XANES spectra of the Fe and Co K edges were collected in transmission mode on the BL5.2 line at the Synchrotron Light Research Institute in Nakhon Ratchasima, Thailand. The magnetic hysteresis measurements were made using a VSM (Versa Lab VSM, Quantum Design) and were performed at room temperature with applied fields between −10000 and 10000 Oe. The field cooling mode measurements were made using the same equipment, with an applied external field of 500 Oe and sample temperatures between 50 and 390 K.

3. Results and discussion

Fig. 1 shows the XRD patterns obtained from $CoFe_2O_4$ nanoparticles calcined at 800–1000 °C for 3 h in air. All calcined samples exhibited diffraction peaks consistent with the spinel cubic structure of $CoFe_2O_4$ according to the JCPDS 22-1086 standard with no evidence of any impurity phases. The average crystallite sizes were calculated using Scherrer's equation and found to be 80 ± 2, 88 ± 2 and 100 ± 3 nm for the samples calcined at 800, 900 and 1000 °C respectively as listed in Table 1. The effect of increasing calcination temperature is that crystallite sizes increase, corresponding to a narrowing of the diffraction peaks. The values of the lattice parameters listed in Table 1 are in good agreement with the JCPDS 22-1086 figure of 0.8391 nm for cubic $CoFe_2O_4$.

The morphology and structure of the $CoFe_2O_4$ nanoparticles were investigated by TEM by obtaining bright field images and performing selected area electron diffraction (SAED) as shown in Fig. 2. The bright field images show evidence of aggregated particles, particularly at the higher calcining temperatures, and the average particle sizes in the samples were calculated from the histogram insets in Fig. 2 and ranged from 84 ± 24 to 320 ± 38 nm with increasing calcination temperature. The SAED patterns obtained from the samples exhibited the spotty ring patterns typical of polycrystalline materials.

The XRD and TEM estimates of particle sizes were measuring two different properties of the samples. In the case of the XRD analysis the Scherrer [18] formula, which is applicable to crystal sizes less than about 100 or 200 nm, has been used to estimate the

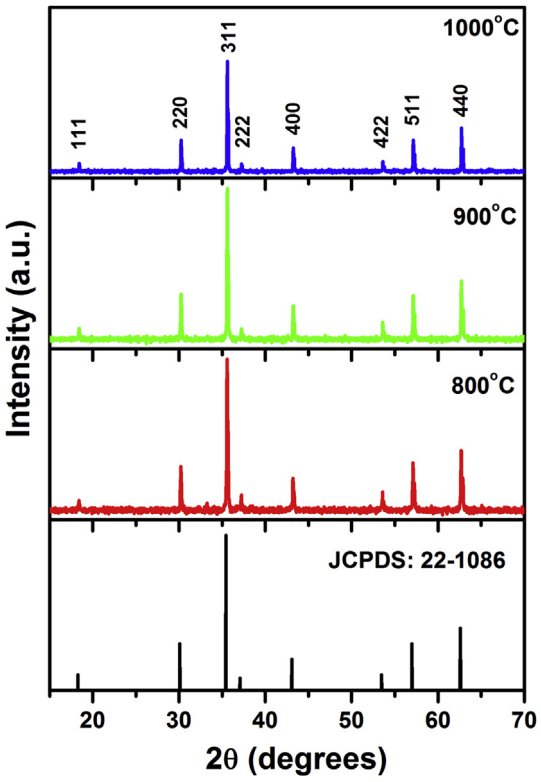

Fig. 1. XRD patterns obtained from $CoFe_2O_4$ samples calcined at 800–1000 °C for 3 h in air.

crystallite sizes assuming that they are each single crystal and that particle size is the main cause of line broadening rather than strain, instrumental or other effects. The TEM bright field images, however, show the actual particle sizes, without regard for whether they are each single crystal or not. In the case of the particles formed by calcination at 800 °C the two estimates are in reasonable agreement and it is therefore likely that the majority of the particles are indeed single crystal and that crystal size is the main cause of line broadening of the XRD peaks. However with increasing calcination temperature there is a divergence between the XRD estimates of crystallite size and the TEM measurements of actual particle size. For samples calcined at a temperature of 1000 °C the estimates are 100 nm and 320 nm by XRD and TEM respectively. Since the particle sizes are larger than 100–200 nm, if they were each single crystals the Scherrer formula would not be reliable and so the TEM images should be taken as the better estimate of particle size. However, it is clear from the bimodal distribution of particle sizes observed in the sample calcined at 1000 °C that there has been significant agglomeration of small particles to create significantly larger particles. It is also very likely that these particles are themselves polycrystals, with the single crystal domains within the particles of the order of 100 nm in diameter as was estimated by the Sherrer formula, which would still be applicable for crystallites of this size. This suggests that at a calcining temperature of 1000 °C significant agglomeration took place without subsequent re-crystallization, which would have resulted in the creation of a single crystal rather than a polycrystal. This is to be expected since the melting temperature of $CoFe_2O_4$ is about 1570 °C and significant reduction of the melting temperature in nanoparticles only occurs for particle sizes less than about 50 nm.

Fig. 3 shows the XANES measurements which were made in transmission mode at room temperature in the vicinity of the Fe K absorption edge. The edge energies of the Fe foil and the FeO (Fe^{2+}),

Table 1
Summary of crystallite sizes as measured by XRD line broadening (D_{XRD}) and TEM direct imaging (D_{TEM}), lattice parameters, saturated magnetization at RT and coercivity of $CoFe_2O_4$ nanoparticles calcined at various temperatures for 3 h in air.

Calcining Temperature (°C)	Average crystallite sizes (nm)		Lattice parameter (nm)	Saturated Magnetization (μ_B)	Coercivity (Oe)
	D_{XRD}	D_{TEM}			
800	80 ± 2	84 ± 45	0.8382 ± 0.0007	3.18	1100
900	88 ± 2	117 ± 11	0.8378 ± 0.0008	3.31	950
1000	100 ± 3	320 ± 38	0.8375 ± 0.0010	3.42	650

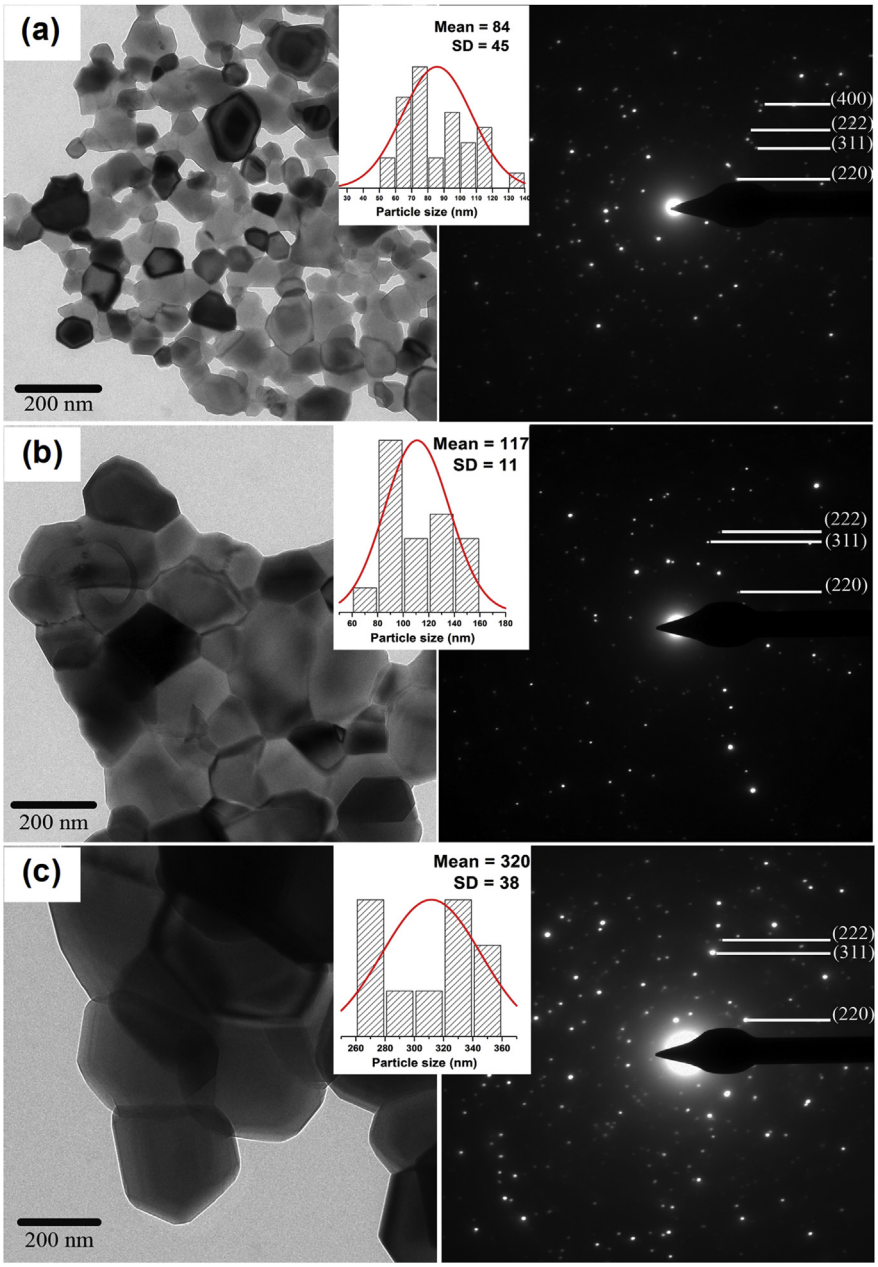

Fig. 2. TEM images with selected-area electron diffraction (SAED) patterns from $CoFe_2O_4$ samples calcined at (a) 800 °C, (b) 900 °C and (c) 1000 °C. The insets in the figure show particle size histograms.

Fe_3O_4 (Fe^{2+}, Fe^{3+}) and Fe_2O_3 (Fe^{3+}) standards are shown in Fig. 3 together with the results obtained from the samples calcined at various temperatures. Similarly, the XANES results in the vicinity of the Co K absorption edge are shown in Fig. 4. It can be seen from the figures that the edge positions of all samples were close to that of the Fe^{3+} and Co^{2+} standards, indicating that these were the valence states of most of the Fe and Co ions.

To determine the locations of the Fe^{3+} and Co^{2+} ions within the spinel structure, XANES spectra were simulated as shown in Figs. 5 and 6 for the respective ions, together with the experimental

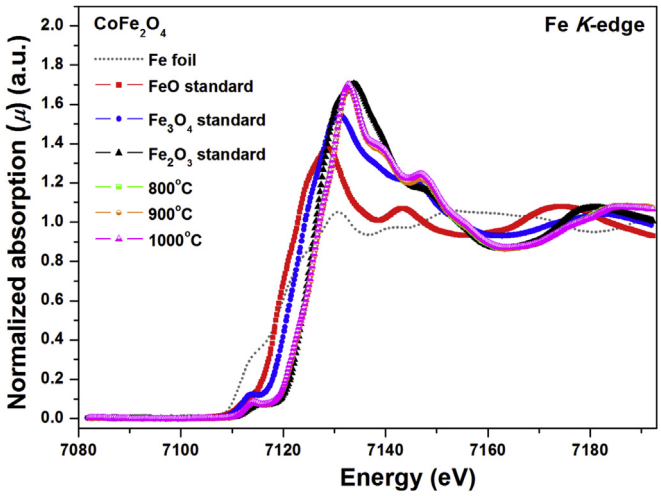

Fig. 3. XANES spectra in the vicinity of the Fe K absorption edge from Fe foil, FeO (Fe^{2+}), Fe_3O_4 (Fe^{2+}, Fe^{3+}) and Fe_2O_3 (Fe^{3+}) standards and from the $CoFe_2O_4$ samples which were calcined at various temperatures for 3 h in air.

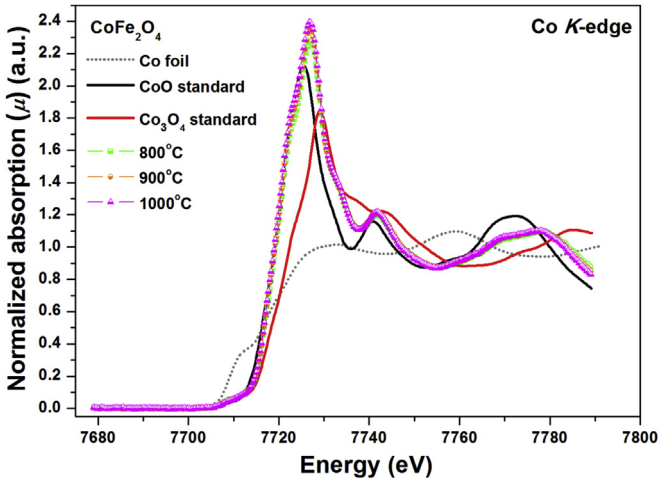

Fig. 4. XANES spectra in the vicinity of the Co K absorption edge from Co foil, CoO (Co^{2+}) and Co_3O_4 (Co^{2+}, Co^{3+}) standards and from the $CoFe_2O_4$ samples which were calcined at various temperatures for 3 h in air.

measurements. From the simulations of Fe^{3+} occupation shown in Fig. 5 it is clear that they don't occupy tetrahedral or octahedral sites exclusively. A clear best fit for relative site occupancies could not be obtained, however an example of a reasonable fit between experiment and theory is shown in Fig. 5 for a 75% occupancy of tetrahedral sites and a 25% occupancy of octahedral sites. The site occupancy of Co^{2+} ions was more clearly established by the XANES simulations, as shown in Fig. 6 there is good agreement between the measurements and a simulation which assumed that 70% of Co^{2+} ions occupied octahedral sites. These observations, that Fe^{3+} and Co^{2+} ions occupy both tetrahedral and octahedral sites within the $CoFe_2O_4$ spinel structure, differ from those made in other studies of the bulk [19] or from several studies of other spinel ferrites. For example, studies of $NiFe_2O_4$ nanofibers and $CoFe_2O_4$ nanoparticles prepared by electrospinning and by the solvothermal route, respectively, have shown that Fe^{3+} ions occupy both types of site but that all the Co^{2+} ions occupy octahedral sites [20,21]. This suggests that the occupancy behavior of these ions can vary depending on the preparation methods or heat treatment temperatures.

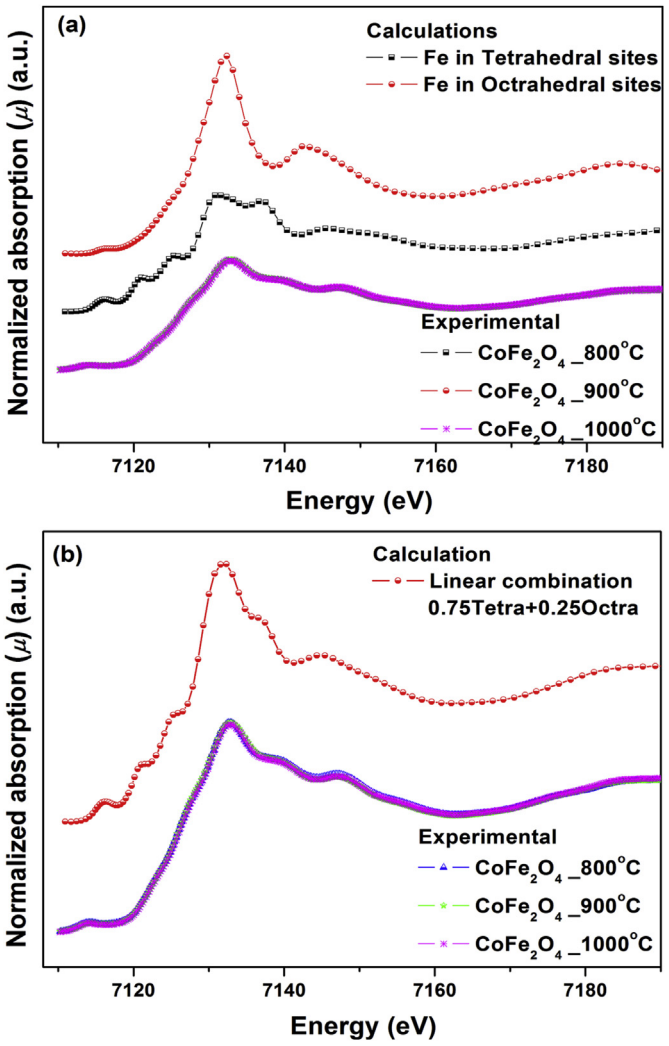

Fig. 5. (a) and (b) show Fe K-edge XANES spectra obtained from $CoFe_2O_4$ samples calcined at various temperatures, together with the simulation results.

Fig. 7 shows the ferromagnetic behavior (FM) of the $CoFe_2O_4$ samples, obtained from VSM measurements with a magnetic field of ±10 kOe at room temperature (RT). The saturation magnetization increased from 3.18 to 3.42 μ_B and the coercivity decreased from 1100 to 650 Oe with increasing calcination temperature as shown in Table 1. This RT-FM behavior can be explained by the relative occupations of Fe^{3+} and Co^{2+} ions in the tetrahedral and octahedral sites and their magnetic interaction. From observations of the bulk form of the $CoFe_2O_4$ inverse spinel, all Co^{2+} ions occupy octahedral sites and half the Fe^{3+} ions occupy tetrahedral and the other half occupy octahedral sites according to the formula: $[Fe^{3+}]^{tet}[Co^{2+}, Fe^{3+}]^{oct}O_4^{2-}$ [22]. The net magnetization is then due to the Co^{2+} ions in the high-spin $3d^7$ state (↑↑↑, $S = 3$) and there is no magnetic moment due to the Fe^{3+} ions in the high-spin $3d$ state (↑↑↑↑↑, $S = 5$) due to the antiparallel spin directions between the two sets of A and B sites. This is the normal source of RT-FM in $CoFe_2O_4$ inverse spinel structures and in such a situation the magnetic moment of $CoFe_2O_4$ is expected to be 3.87 μ_B per formula unit. However, the net magnetic moments measured in our samples are in the range from 3.14 to 3.42 μ_B, which is smaller than expected on the basis of Co^{2+} ions occupying octahedral sites exclusively and Fe^{3+} ions equally divided between octahedral and tetrahedral sites [5,19,23,24]. However, these magnetic moment values are

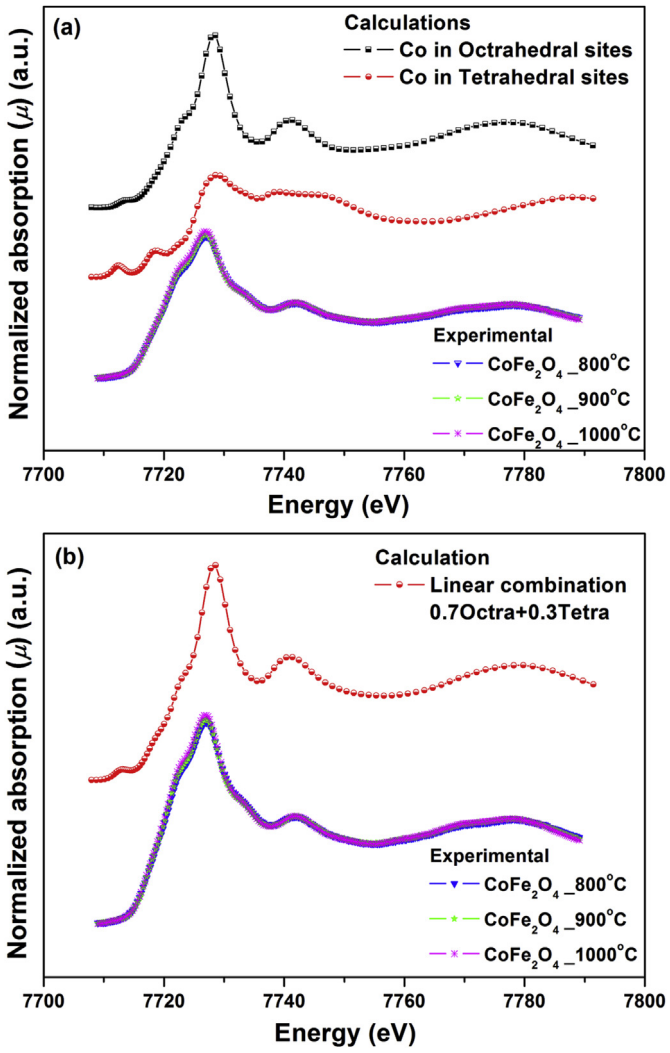

Fig. 6. (a) and (b) show Co K-edge XANES spectra obtained from $CoFe_2O_4$ samples calcined at various temperatures, together with the simulation results.

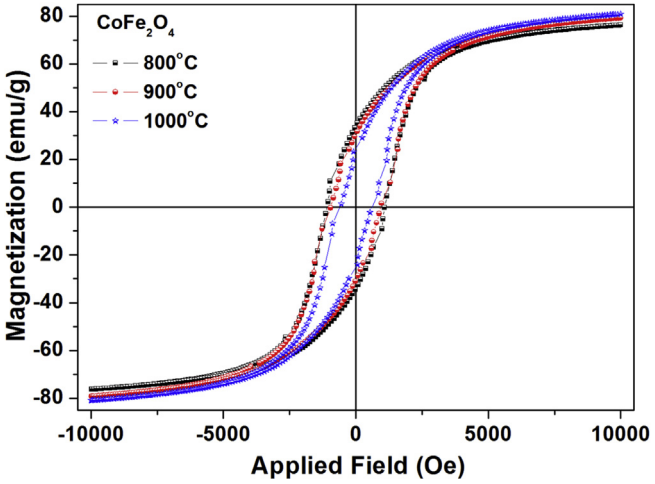

Fig. 7. *M–H* curves measured at room temperature for $CoFe_2O_4$ samples calcined at various temperatures.

consistent with a cation distribution of Fe^{3+} and Co^{2+} at both tetrahedral and octahedral sites. For example, $[Co^{2+}{}_{0.3}, Fe^{3+}{}_{1.5}]^{tet}[Co^{2+}{}_{0.7}, Fe^{3+}{}_{0.5}]^{oct}O_4^{2-}$, with 30% of Co^{2+} ions and 75% of Fe^{3+} ions occupying tetrahedral sites with the balance of both species occupying octahedral sites as was suggested by the XANES measurements, the magnetic moment is expected to be 4.36 μ_B. If the Co^{2+} ion fraction on tetrahedral sites is reduced to 20% and 10% with the Fe^{3+} distribution unchanged, the magnetic moment reduces to 3.58 and 2.81 respectively. It can be seen that a mixed distribution of Fe^{3+} and Co^{2+} ions as suggested by the XANES results is consistent with our magnetic moment measurements.

The measurements of M_S appear to be increasing with increasing particle size and similar size effect results have been obtained in other spinel ferrite systems such as $CoFe_2O_4$ [5,23,24], $NiFe_2O_4$ [20,24,25] and $ZnFe_2O_4$ [26]. For example, $ZnFe_2O_4$ nanoparticles having sizes between 23 and 208 nm exhibited M_S values increasing from 0.84 to 2.35 μ_B [27]. The authors suggested that the RT-FM behavior in such particles is due mainly to the spin ordering of the cations in the particle cores, with spin disorder in a surface shell region contributing less to the magnetization than the core due to spin fluctuations at the surface, thus reducing M_S compared to what it would be if there was no surface effect. With increasing particle size, the surface to volume ratio decreases, resulting in higher values of M_S. It was also observed in the present study that the H_C values measured are decreasing with increasing calcination temperature and therefore particle size. This behavior is not well understood in nanoparticles because demagnetization due to an external field is thought to be a competition between the grain size dependent processes of domain wall displacement and coherent rotation. However these mechanisms are likely to be complicated by near-surface defect structures in grains and further investigation of these issues is beyond the scope of the present study [27–29].

The temperature dependence of the magnetization for the $CoFe_2O_4$ samples, measured with an applied field of 500 Oe between 50 and 400 K in the FC mode, are shown in Fig. 8. The Curie temperature (T_C) can be determined from the derivative of the magnetization $dM_{FC}(T)/dT = 0$ [30] and Fig. 8 shows that the T_C of all samples is above 400 K. A high T_C and thermal stability are necessary for the design of FM devices.

4. Conclusions

Single phase $CoFe_2O_4$ nanoparticles with a cubic spinel structure have been successfully prepared by the polymer pyrolysis method.

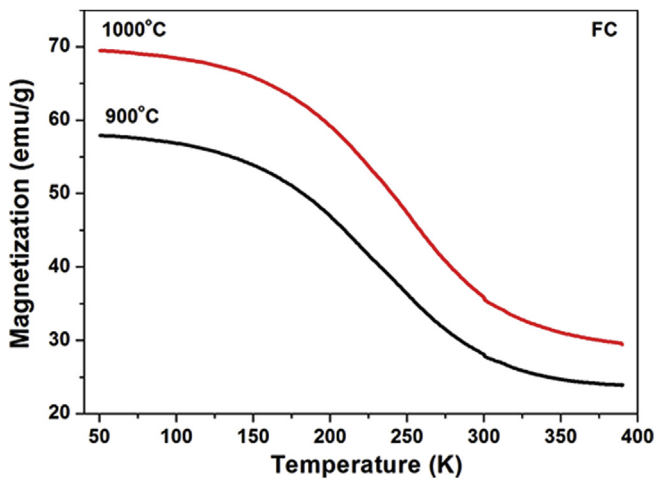

Fig. 8. *M–T* curves at 500 Oe obtained from $CoFe_2O_4$ samples calcined at 900 °C (lower) and 1000 °C (upper).

TEM observations showed that the average particle sizes increased from about 84 to 320 nm as the calcining temperature was increased from 800 °C to 1000 °C. XRD measurements showed that average crystallite sizes only increased from 80 to 100 nm over the same calcination temperature range, suggesting that at higher calcination temperatures significant agglomeration of particles had occurred but that the temperature was not high enough to allow the agglomerated particles to recrystallize to form a single crystal particle. The method of preparation employed resulted in both Fe^{3+} and Co^{2+} ions being distributed across tetrahedral and octahedral sites as indicated by the XANES results. This lead to the M_S obtained with a maximum value of 3.42 μ_B, as well as a large coercivity of 1100 Oe. The size effect was also an important factor influencing our M_S measurements, with the decreasing contribution from the surface shell with increasing particle size improving the magnetization of samples prepared at the highest calcining temperature. Additionally, the $CoFe_2O_4$ nanoparticles exhibited a T_C above 400 K, suggesting that stable room temperature ferromagnetism and a large coercivity in $CoFe_2O_4$ nanoparticles has the potential for its application in future spintronic and transparent nanodevices.

Acknowledgments

The authors would like to thank the Synchrotron Light Research Institute in Nakhon Ratchasima, Thailand for access to their XANES facilities and the Department of Physics, Khon Kaen University, for providing the VSM facilities. This work was financially supported by Khon Kaen University and the Thailand Research Fund (TRF) under a TRF Senior Research Scholar Contract No. RTA5780004.

References

[1] M.G. Naseri, E.B. Saion, H.A. Ahangar, A.H. Shaari, M. Hashim, J. Nanomater (2010), http://dx.doi.org/10.1155/2010/907686.
[2] D.R. Patil, B.K. Chougule, Mater. Chem. Phys. 117 (2009) 35–40.
[3] D.S. Mathew, R.S. Juang, Chem. Eng. J. 129 (2007) 51–65.
[4] H.M. Fan, J.B. Yi, Y. Yang, K.W. Kho, H.R. Tan, Z.X. Shen, J. Ding, X.W. Sun, M.C. Olivo, Y.P. Feng, ACS Nano 3 (2009) 2798–2808.
[5] P. Laokul, S. Arthan, S. Maensiri, E. Swatsitang, J. Supercond. Nov. Magn. 28 (2015) 2483–2489.
[6] Y. Koseoglu, F. Alan, M. Tan, R. Yilgin, M. Ozturk, Ceram. Int. 38 (2012) 3625–3634.
[7] S.D. Bhame, P.A. Joy, J. Appl. Phys. 100 (2006) 113911.
[8] Y. Koseoglu, A. Baykal, F. Gozuak, H. Kavas, Polyhedron 28 (2009) 2887–2892.
[9] N. Kasapoglu, B. Birsoz, A. Baykal, Y. Koseoglu, M.S. Toprak, Cent. Eur. J. Chem. 5 (2) (2007) 570–580.
[10] H. Moradmard, S. Farjami Shayesteh, P. Tohidi, Z. Abbas, M. Khaleghi, J. Alloys Compd. 650 (2015) 116–122.
[11] B. Zhou, Y.W. Zhang, C.S. Liao, C.H. Yan, J. Magn. Magn. Mater 247 (2002) 70–76.
[12] K.P. Chae, J.-G. Lee, H.S. Kweon, Y.B. Lee, J. Magn. Magn. Mater 283 (2004) 103–108.
[13] D.E. Zhang, X.J. Zhang, X.M. Ni, J.M. Song, H.G. Zheng, J. Magn. Magn. Mater 305 (2006) 68–70.
[14] Y. Koseoglu, F. Alan, M. Tan, Y. Yilgin, M. Ozturk, Ceram. Int. 38 (2012) 3625–3634.
[15] I.H. Gul, A. Maqsood, J. Alloys Compd. 465 (2008) 227–231.
[16] M.H. Khedr, A.A. Omar, S.A. Abdel-Moaty, Colloids Surf. A 281 (2006) 8–14.
[17] Z. Zi, Y. Sun, X. Zhu, Y. Yang, J. Dai, W. Song, J. Magn. Magn. Mater 321 (2009) 1251–1255.
[18] P. Scherrer, Bestimmung der Gröss Kolloidteilchen Mittels Nachrichten von der Gesellschaft der Wissenschaften, Göttingen, Mathematisch-Physikalische Kl. 2 (1918) 98–100.
[19] I. Sharifi, H. Shokrollahi, M.M. Doroodmand, R. Safi, J.Magn. Magn. Mater 324 (2012) 1854–1861.
[20] O. Saensuk, S. Phokha, A. Bootchanont, S. Maensiri, E. Swatsitang, Ceram. Int. 41 (2015) 8133–8141.
[21] S. Phumying, S. Phokha, S. Maensiri, J. Supercond. Nov. Magn. 27 (2014) 2573–2579.
[22] C.H. Kim, Y. Myung, Y.J. Cho, H.S. Kim, S.H. Park, J. Park, J. Phys. Chem. C 113 (2009) 7085–7090.
[23] M.P. Gonzalez-Sandoval, A.M. Beesley, M. Miki-Yoshida, L. Fuentes-Cobas, J.A. Matutes-Aquino, J. Alloys Compd. 369 (2004) 190–194.
[24] M. Rajendran, R.C. Pullar, A.K. Bhattacharya, D. Das, S.N. Chintalapudi, C.K. Majumdar, J. Magn. Magn. Mater 232 (2001) 71–83.
[25] A.A. Sattar, H.M. EL-Sayed, I. AlLsuqia, J.Magn. Magn. Mater 395 (2015) 89–96.
[26] J. Feng, Y. Wang, L. Zou, B. Li, X. He, Y. Ren, Y. Lv, Z. Fan, J. Colloid Interf. Sci. 438 (2015) 318–322.
[27] B.D. Cullity, Introduction to Magnetic Materials, Addison-Wesley Publishing Company, Reading, Massachusetts, 1972.
[28] N.G. Gajdhiye, S. Prasad, G. Balaji, IEEE Trans. Mang 35 (1999) 2155–2161.
[29] M.F. de Campos, Mater. Sci. Forum 530–531 (2006) 146–151.
[30] X. Zhou, J. Xue, D. Zhou, Z. Wang, Y. Bai, X. Wu, X. Liu, J. Meng, ACS Appl. Mater. Interfaces 2 (2010) 2689–2693.

Materials and Design 96 (2016) 350–356

Contents lists available at ScienceDirect

Materials and Design

journal homepage: www.elsevier.com/locate/matdes

Characterization of an environment friendly lightweight concrete containing ethyl vinyl acetate waste

Nattakan Dulsang [a], Pornnapa Kasemsiri [a,*], Patcharapol Posi [b], Salim Hiziroglu [c], Prinya Chindaprasirt [d]

[a] Sustainable Infrastructure Research and Development Center and Department of Chemical Engineering, Faculty of Engineering, Khon Kaen University, Khon Kaen, 40002, Thailand
[b] Department of Civil Engineering, Faculty of Engineering, Rajamangala University of Technology Isan Khon Kaen Campus, Khon Kaen 40000, Thailand
[c] Department of Natural Resource Ecology and Management, Oklahoma State University, 303-G Agricultural Hall, Stillwater, OK 74078, USA
[d] Sustainable Infrastructure Research and Development Center and Department of Civil Engineering, Faculty of Engineering, Khon Kaen University, Khon Kaen 40002, Thailand

ARTICLE INFO

Article history:
Received 4 September 2015
Received in revised form 2 January 2016
Accepted 9 February 2016
Available online 11 February 2016

Keywords:
Lightweight aggregate
Lightweight concrete
Ethyl vinyl acetate waste

ABSTRACT

In this paper, the environment friendly lightweight concretes (LWCs) produced from ethyl vinyl acetate (EVA) waste was studied. EVA waste from footwear industry was used as a lightweight aggregate in place of normal aggregate at the contents of 3, 5, 7 and 10% by weight of LWC. The water-cement ratio of 0.45 and EVA waste-sand ratio of 0.50 were used for all mixtures. Test results showed that the unit weight of LWCs containing EVA waste reduced with increasing EVA waste content. The thermal conductivity, chemical resistance and water absorption of LWCs substantially improved and were comparable to those of LWCs containing other polymers. Based on the results, the use of EVA waste as a lightweight aggregate showed a good potential for use in LWCs. This is another good alternative for recycling plastic waste. According to the ASTM standard, this LWC can be used as masonry and partitions.

© 2016 Elsevier Ltd. All rights reserved.

1. Introduction

The increasing use of plastic leads to a drastic increase in plastic waste problem which causes environmental pollution. Recycling of the plastic waste is one of the best approaches considering ecological and economical benefits [1–4]. Recently, many types of plastic wastes such as high-density polyethylene plastic [5], polyethylene and polystyrene [6, 7], polyethylene terephthalate [8–13], polyvinylchloride [14, 15], expanded polystyrene [16–18], rubber tire [19], rubber particle [20] and melamine waste [21] have been reused as aggregates in concretes. Other kinds of artificial aggregates including municipal solid waste, bottom ash [22], municipal solid waste incinerator, fly ash [23] and coal combustion wastes [24] have also been used as aggregates to replace natural aggregates. This approach can sustain natural resources and decrease the secondary pollution and energy consumption during natural aggregates production [24, 25].

Lightweight concrete (LWC) is a concrete with unit weight less than 1840 kg/m^3 [9]. LWCs are classified into three types depending on the method of production viz., LWC with lightweight aggregate, LWC with induced bubble voids and LWC with no fine aggregate [26]. LWCs have been developed for various construction applications such as high rise building, roof deck, long span bridge, floor and wall [26, 27]. This is due to a number of advantages i.e. reduction of building weight, good thermal and acoustic insulation as well as enhanced durability [28].

Recently, utilization of lightweight aggregate from plastic waste especially thermoplastic to produce lightweight concrete has attracted much attention. However, the thermosetting plastic waste cannot be melted and is difficult to recycle [21, 29, 30]. Ethyl vinyl acetate (EVA) copolymer is thermoplastic which is used to produce footwear and EVA waste is thus generated during the manufacturing. The EVA waste in footwear industry accounts for approximately 14%. Therefore, 190,400 tons of EVA waste are generated worldwide every year [31]. EVA waste and construction demolition waste (CDW) were studied for use as recycled aggregates for green LWC production. Dulsang et al. [32] studied the mix proportion parameters of LWC containing EVA waste and showed that EVA waste content and water/cement ratio were the most important parameters affecting density and compressive strength of LWC.

Currently there is very limited information about the effect of usage of EVA waste as aggregate on the physical, mechanical and thermal properties of lightweight concrete for structural and masonry applications. Therefore, the important properties viz., density, water absorption, compressive strength, thermal conductivity as well as chemical resistance of LWCs containing EVA waste were investigated in this research.

2. Materials and methods

2.1. Materials

The cement used was Ordinary Portland cement (OPC) Type I. EVA waste supplied by Pan Asia Footwear Public Company Limited, Thailand

* Corresponding author.
E-mail address: pronkas@kku.ac.th (P. Kasemsiri).

http://dx.doi.org/10.1016/j.matdes.2016.02.037
0264-1275/© 2016 Elsevier Ltd. All rights reserved.

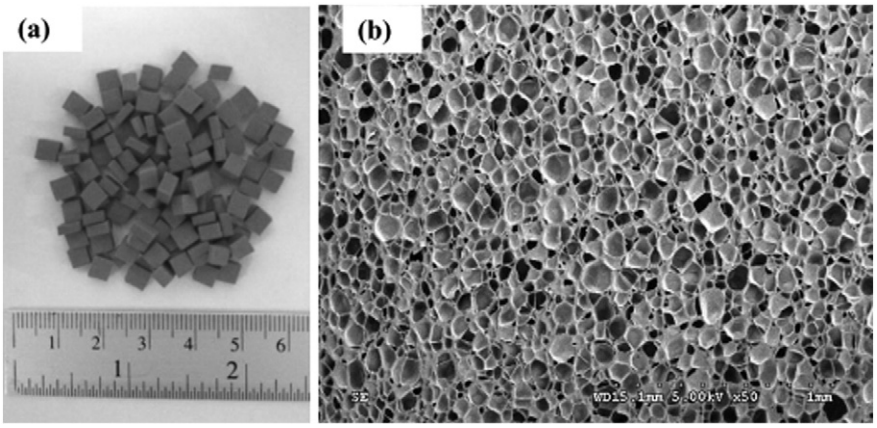

Fig. 1. Shredded ethylene vinyl acetate (EVA) waste (a) and the voids inside of EVA waste (b).

was cut and passed through a 4.75 mm sieve. The average size of EVA waste aggregate was 4.5 mm and its density was 149 kg/m^3 as shown in Fig. 1. The sand was prepared in saturated surface dry (SSD) condition before mixing to prevent the cracking problems due to water absorption of sand. The general properties of materials are summarized in Table 1.

2.2. Mix proportions

The mixes were designed for targeted density between 800 and1840 kg/cm^{3}and compressive strength between 3.4 and 20.0 MPa. All samples were prepared with water-cement (w/c) ratio of 0.45, EVA-sand (EVA/sand) ratio of 0.50 and EVA contents of 3, 5, 7 and 10 wt.% of LWC. The mix proportions are shown in Table 2. For mixing of LWC, cement and sand were first mixed together for 1.5 min. Water was then added and the mixing was done for 1.5 min. In the final step, EVA waste was added and the mixing was done for another 1.5 min. The fresh mixtures were cast into 50 mm cube molds in accordance with ASTM C109 [33], 100 mm cube molds in accordance with ASTM D5334 [34] and 100 × 200 mm cylindrical molds in accordance with ASTM C1585 [35]. They were covered with damped cloth and plastic sheet and left in a controlled 25 °C room. All samples were demoulded at the age of one day, wrapped with cling film and kept in a 25 °C controlled room until testing age.

Table 1
Physical properties of materials.

Properties	Materials	
	EVA waste	Sand
Specific gravity	–	2.61
Median particle size (mm)	4.5	–
Particle size (mm)	–	–
Fineness modulus	–	2.65
Density (kg/m^3)	145	1360
Water absorption (%)	0.005–0.13	1.17

Table 2
The mix proportions by weight (%).

No.	EVA (%)	Cement (%)	Water (%)	Sand (%)
1	3	62.76	28.24	6
2	5	58.62	26.38	10
3	7	54.48	24.52	14
4	10	21.73	48.27	20

2.3. Test procedures

The change in chemical structures of LWCs was analyzed using Attenuated total reflection infrared (FTIR-ATR) spectra, Bruker Tensor 27 spectrometer. The spectra were taken with 64 scans at a resolution of 4 cm^{-1} and a spectral range of 4000–650 cm^{-1}.

The density and compressive strength of specimens were measured at the ages of 7 and 28 days in accordance with ASTM C138 [36] and ASTM C109 [33], respectively. After the density measurement, the specimens were tested for compressive strengths. The averaged values from three samples were reported and the standard deviation error bar was used.

The water absorptions of cube specimens were measured in accordance with ASTM C642 [37]. The specimens were oven-dried at 105 ± 5 °C for 24 h to achieve constant weight before testing. The water absorption values of the samples were calculated using Eq. (1).

$$\text{Water absorption } (\%) = [(B - A)/A] \times 100 \quad (1)$$

where A was the mass of oven-dry sample in air (g); B was the mass of surface-dry sample in air after immersion (g).

The rate of absorption of concrete was tested in accordance with ASTM C1585 [35]. At the age of 28 days, specimens were cut and dried in an oven at 105 °C for 24 h to remove moisture. The water absorption in one dimensional mode was determined by sealing four sides of

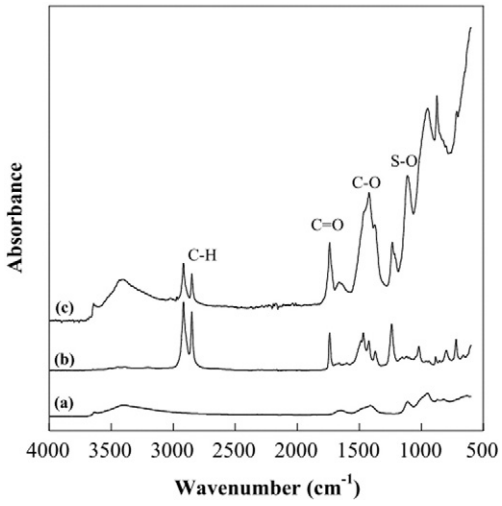

Fig. 2. FTIR results of (a) hydrated cement; (b) EVA waste and (c) hydrated cement mixed with EVA waste.

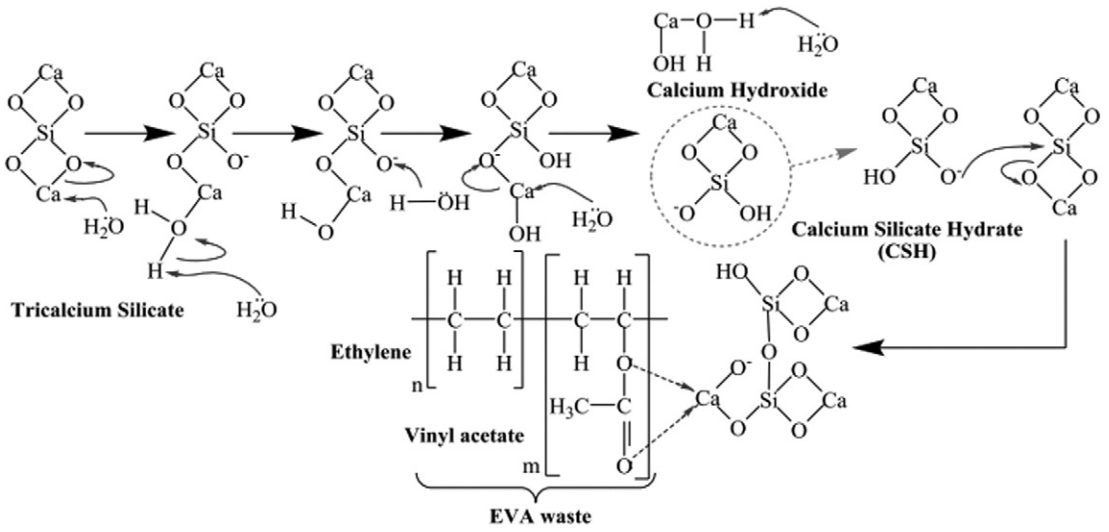

Fig. 3. The interaction between cementitious and EVA waste.

specimen with paraffin film. The prepared specimen was then submerged in water. The relationship between water sorption and time was determined as suggested by Hall [38] as follows:

$$I = A + St^{1/2} \quad (2)$$

where S (m/min$^{0.5}$) was the water sorptivity of concrete and i (mm) was the cumulative absorbed volume per unit area of inflow surface for duration time t. A was the effect of initial water filling at concrete surface.

Sulfuric acid resistances of concrete samples were determined by test method adapted from ASTM C267 [39]. The 1% sulfuric acid solution was used as a simulation of the aggressive environment of sewer [40, 41]. The samples were immersed in 1% sulfuric acid solution for 1, 7, 14, 28 and 56 days. The weight losses of concrete samples after immersion in the acid were monitored. The percentage of mass loss at each time span was calculated according to Eq. (3):

$$\text{Mass loss } (\%) = [M_2 - M_1)/M_1] \times 100 \quad (3)$$

where M_1 and M_2 were the specimen masses before and after immersion, respectively.

The thermal conductivity tests were carried out using cube specimens at the age of 28 days in accordance with ASTM D5334 [34] using a surface probe ISOMET Model 2114, Applied Precision Ltd with the measuring range of 0.3–2.0 W/m.K. The averaged values from three samples were reported and the standard deviation error bar was used.

3. Results and discussion

3.1. Characterization of hydrated cement

Infrared spectra of the EVA waste, hydrated cement and hydrated cement mixed with 7% EVA waste at age of one day are shown in Fig. 2. In Fig. 2(a), the characteristics of infrared adsorption bands of EVA waste were observed at 1737 which corresponded to CO stretching mode of ester. The bands at 1300–1000 cm^{-1} were assigned to the stretching of bound C—O. The characteristic bands at 2848–2916 cm^{-1} were assigned to C—H [42]. From Fig. 2(b), the characteristic adsorption peaks of hydrated cement at 948 cm^{-1} and 1111 cm^{-1} were assigned to Si—O and S—O. The C—O was observed at 1410 cm^{-1} whereas the absorption bands at 1655, 3399 and 3637 cm^{-1} were assigned to O—H [42]. Fig. 2(c) shows the typical peaks of hydrated cement mixed with EVA waste. The C—O stretching vibration at 1410 cm^{-1} shifted towards

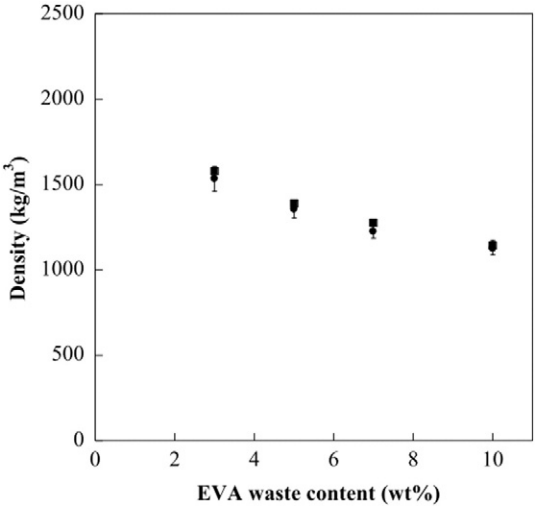

Fig. 4. Density of LWC mixed with EVA waste at (●) 7 days and (■) 28 days.

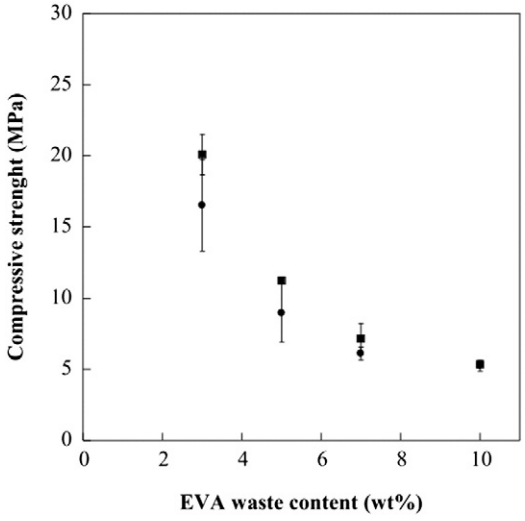

Fig. 5. Compressive strength of LWC mixed with EVA waste at (●) 7 days and (■) 28 days.

Table 3
The classification of LWCs containing EVA waste according to their applications.

EVA content (wt.%)	compressive strengths (MPa)	Density (kg/m^3)	Class of lightweight aggregate concrete
3	20.1	1580	Structure lightweight concrete
5	11.3	1390	Masonry concrete
7	7.2	1280	Masonry concrete
10	5.4	1145	Masonry concrete

the higher frequency of 1422 cm^{-1}. This indicated the coordination between Ca^{2+} of mortar and O of EVA waste as shown in Fig. 3. The interactions developed between cementitious and polymeric phases modified the cement hydration and prolonged the workability duration. The results are in good agreement with those reported in the previous works [43, 44].

3.2. Density and compressive strength of the samples

The densities of LWC mixtures at the ages of 7 and 28 days as shown in Fig. 4 were 1125–1535 kg/m^3 and **11**45–**15**80 kg/m^3, respectively. The density of LWCs tended to decrease with increasing EVA waste content as expected. This was due to the internal voids of EVA aggregates and their low density. The use of EVA waste as lightweight aggregate could thus reduce the density of concrete or the dead load by 48–66% (normal concrete density = 2400 kg/m^3). Reduction in the dead weight of a building or structure helps reduce the risk of earthquake damages [45].

As shown in Fig. 5, the 7-day and 28-day compressive strengths of LWCs containing EVA waste were 5.3–16.5 MPa and 5.4–20.1 MPa, respectively. When the density and compressive strength values were considered together, the LWC with 3 wt.% EVA waste could be classified as a structural lightweight concrete with the densities of 1440–1840 kg/m^3 and the corresponding compressive strengths higher than 17.0 MPa complying with ASTM C330 [46]. Furthermore, the LWCs with 5, 7 and 10 wt.% EVA could be classified as masonry concretes with densities of 800–1440 kg/m^3 and compressive strengths of 3.4–17.0 MPa complying with ASTM C331 [47]. The classification of LWCs according to the applications is summarized in Table 3.

As shown in Figs. 5 and 6, EVA waste content and density of LWCs were important parameters affecting compressive strength. The compressive strength decreased with increasing EVA waste content. This was due to the poor bond between plastic aggregate and cement paste [48, 49]. Moreover, the relationship between density and compressive strength of LWC is shown in Fig. 6. For LWC with 5 wt.% EVA waste, the compressive strength slightly decreased. The relationship between LWC density and compressive strength based on the density in the range of 1145–1580 kg/m^3 can be expressed as.

$$f_c = 0.14e^{(0.003\gamma)} \quad (4)$$

where f_c was the compressive strength (MPa), and γ was the density (kg/m^3) of LWC.

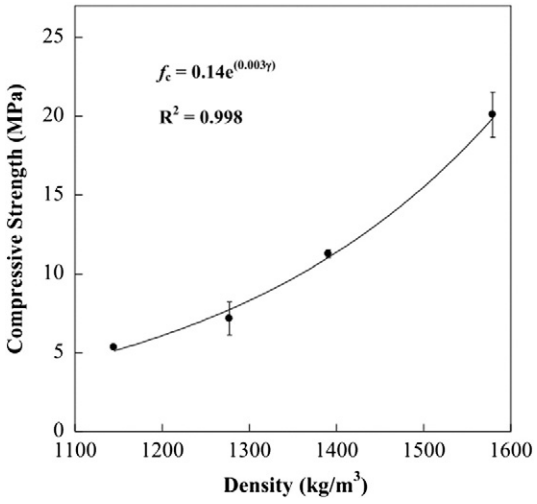

Fig. 6. Relationship between compressive strength and density of LWCs containing EVA waste.

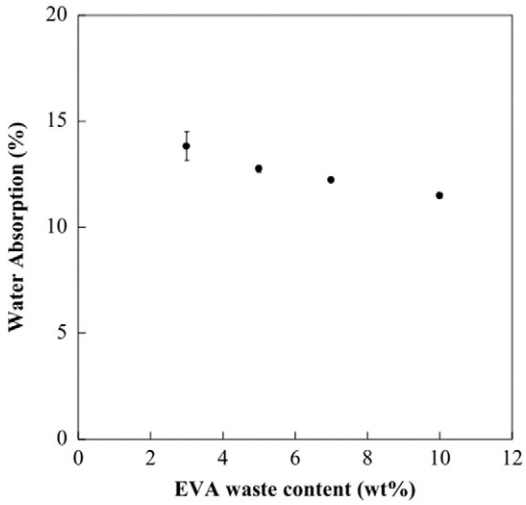

Fig. 7. Water absorption of LWC mixed with EVA waste at 28 days.

3.3. Water absorption and sorptivity of samples

Durability of concrete is one of the important parameters controlling the effective service life. Generally, the durability of concrete depends on the capacity of a fluid such as water penetrating into concrete. The penetrated water and other harmful ions could react and destroy the chemical stability of concrete [50]. The result of water absorption of LWC specimens at 28 days is shown in Fig. 7. The water absorption significantly decreased with increasing EVA waste content from 3 to 10 wt.%. This was due to the low water absorption of EVA waste and the change in pore structure of hydrated cementitious system. Fig. 8 presents good linear relationships between the cumulative absorption of LWCs and the square root of time. The sorptivity coefficients could also be calculated from the slope of plots as summarized in Table 4.

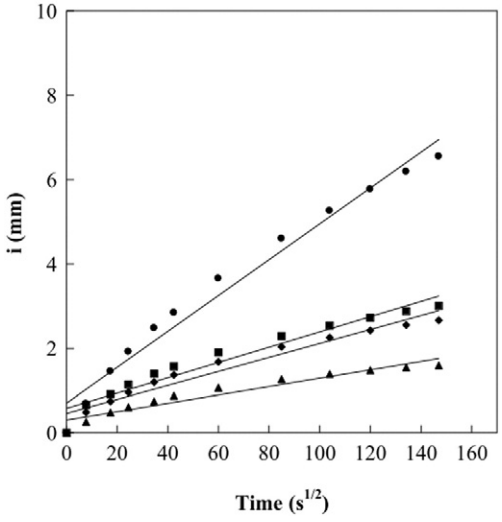

Fig. 8. Sorptivity of LWC containing EVA waste; (●) 3 wt.% EVA waste, (■) 5 wt.% EVA waste, (♦) 7 wt.% EVA waste and (▲) 10 wt.% EVA waste

Table 4
The sorptivity coefficients of LWCs containing EVA waste.

EVA content (wt.%)	Sorptivity coefficient (mm/s$^{/2}$)	R^2
3	0.426	0.98
5	0.018	0.94
7	0.016	0.95
10	0.010	0.93

The obtained sorptivity coefficient values of samples were 0.010–0.426 mm/min$^{0.5}$ which were lower than the typical sorptivity values of 0.094–0.170 mm/min$^{0.5}$ for normal concretes with W/C 0.4–0.6 [51]. The use of EVA waste could thus lower the sorptivity rate of LWCs. This was due to the non-sorptive property of EVA waste which slowed down the progress of hydrous transfer by increasing tortuosity [52]. Similar result was also observed in the system of concrete containing crushed polyethylene terephthalate [45]. As shown in Fig. 7, the incorporation of EVA waste in LWC could reduce the absorption of water and other harmful solutions.

3.4. Resistance to sulfuric acid

The values of weight gain in the sulfuric acid test for the LWCs at various EVA waste loadings are shown in Fig. 9. The percentage of weight gain plotted against time showed a similar behavior. The weight of LWCs increased with increasing immersion time. This was due to three main factors i.e. continued hydration of cement, formation of gypsum and increase of water absorption in specimens [40]. It was clear that the trend of weight gain of LWC depended on EVA waste content. The weight gain of LWC reduced with increasing amount of EVA waste. This indicated that incorporation of EVA waste could resist the absorption of sulfuric solution which was consistent with the water absorption result. The acid resistance of a cement matrix depended on porosity, tortuosity, solubility, and acid neutralization capacity of the matrix components. The increase of tortuosity could reduce the sorptivity and diffusion of solvated species [53]. The resistance to acid attack of EVA waste was better than that of concrete [54]. The addition of EVA waste, thus, increase the resistance to acid attack was due to the reduced cement matrix and increased tortuosity. Interestingly, after 56 days of exposure period, no weight loss was observed for all LWCs containing EVA waste. The mass loss of LWC containing EVA waste after 56 days immersion in 1% sulfuric acid is compared with the previously reported results of normal concretes as shown in Table 5. In fact, the LWC containing EVA waste showed weight gain of 7.8–17.4% after 56 days immersion in contrary to the weight losses of other normal concretes. The mass gain of LWC containing EVA waste of this experiment was 7.8–17.4% as compared to the mass losses of 9% for concrete containing polyvinyl acetate [49], 2% for concrete modified with soluble glass [50], 2% for concrete containing limestone, and 0.5% for concrete containing limestone and slag [36]. Therefore, it could be concluded that EVA waste improved the sulfuric acid resistance of samples and the obtained LWCs could be considered as having a good potential for application in environments under sulfuric acid attack.

Table 5
The acid resistance of various types of concretes after immersion in 1% sulfuric acid for 56 days.

Concrete type	Mass loss after sulfuric resistant test (%)
LWCs containing EVA waste	−7.8 to −17.4
Concrete containing polyvinyl acetate [55]	9
Concrete modified with soluble glass [56]	2
Concrete containing lime stone [43]	2
Concrete containing lime stone and slag [43]	0.5

3.5. Thermal conductivity of the samples

The results of thermal conductivity of LWCs are given in Fig. 10. The thermal conductivity values were 0.407–0.489 W/m·K and tended to decrease with increasing EVA content. The LWC containing 10 wt.% EVA waste had the lowest thermal conductivity which was about one third of that of normal concrete (1.2 W/m·K) [55]. The reduction of thermal conductivity value was due to the low thermal conductivity and density of EVA waste aggregate (0.084 W/m·K and 149 g/m^3). Moreover, the enclosed pores of EVA waste also reduced the thermal conductivity due to low thermal conductivity of air. Similar results were also observed in concrete modified with other types of polymers such as rubber-shoe soles [56], crumb rubber [57] and polyurethane foam [58]. Theoretically, thermal conductivity is inversely proportional to the density of material [57]. The relationship between density and thermal conductivity of concrete modified with polyethylene terephthalate was reported by Akcaozoglu et al. [59]. The thermal conductivity tended to decrease with decreasing density. The relationship between density and thermal conductivity of LWC specimens was linear

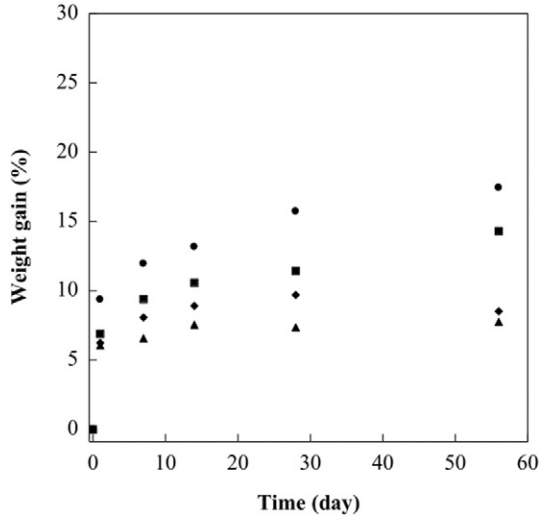

Fig. 9. Curves of weight loss of LWC after immersion in 1% sulfuric acid for 56 days; (●) 3 wt.% EVA waste, (■) 5 wt.% EVA waste, (♦) 7 wt.% EVA waste and (▲) 10 wt.% EVA waste

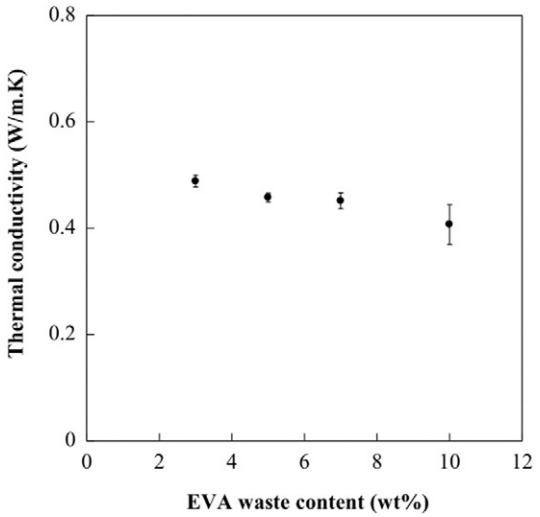

Fig. 10. Thermal conductivity of LWC mixed with EVA waste at 28 days.

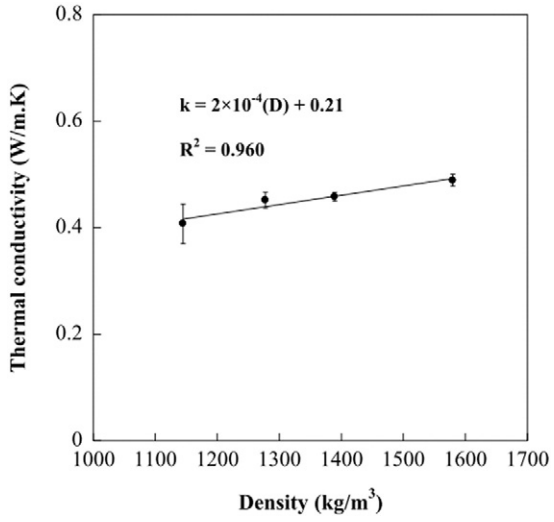

Fig. 11. Relationship between thermal conductivity and density of LWC.

as depicted in Fig. 11. The correlation coefficient of the results was high with R^2 value of 0.96. The equation could be expressed as:

$$k = \left(2 \times 10^{-4}\right)D + 0.21 \quad (5)$$

where k is thermal conductivity (W/m·K) and D is density of lightweight concrete (kg/m^3).

The low thermal conductivity and density combined with good mechanical, water absorption and chemical attack resistant characteristics make the LWCs containing EVA waste suitable for use as a construction material.

4. Conclusions

This paper investigated the properties of lightweight concretes containing 3–10 wt.% EVA waste. Test results indicated that the LWC containing EVA waste provided good thermal insulator. The increase in EVA waste resulted in LWCs with reduced water absorption and sorptivity and increased resistance to sulfuric acid attack. The density and strength values of LWC with 3 wt.% EVA waste and LWC containing 5–10 wt.% EVA waste complied with the requirements of ASTM standards for structure and masonry, respectively. The use of EVA waste for this application helped reduce the environmental pollution from disposal of waste.

Acknowledgment

This work was financially supported by Faculty of Engineering Khon Kaen University. The authors also would like to acknowledge the support of Thailand Research Fund (TRF) under the TRF Senior Research Scholar, Grant No. RTA 5780004 and the Higher Education Research Promotion and National Research University Project of Thailand, Office of the Higher Education Commission, through the Advanced Functional Materials Cluster of Khon Kaen University.

References

[1] F. Iucolano, B. Liguori, D. Caputo, F. Colangelo, R. Cioff, Recycled plastic aggregate in mortars composition: effect on physical and mechanical properties, Mater. Des. 52 (2013) 916–922 (0).
[2] B. Liguori, F. Iucolano, I. Capasso, M. Lavorgna, L. Verdolotti, The effect of recycled plastic aggregate on chemico-physical and functional properties of composite mortars, Mater. Des. 57 (2014) 578–584 (0).
[3] D.E. Ramírez-Arreola, C.S. Rosa, N.B. Haro-Mares, J.A. Ramírez-Morán, A.A. Pérez-Fonseca, L.R. Robledo-Ortíz, Compressive strength study of cement mortars lightened with foamed HDPE nanocomposites, Mater. Des. 74 (2015) 119–124.
[4] N. Petchwattana, S. Covavisaruch, J. Sanetuntikul, Recycling of wood–plastic composites prepared from poly(vinyl chloride) and wood flour, Constr. Build. Mater. 28 (1) (2012) 557–560.
[5] T.R. Naik, S.S. Singh, C.O. Huber, B.S. Brodersen, Use of post-consumer waste plastics in cement-based composites, Cem. Concr. Res. 26 (10) (1996) 1489–1492.
[6] Z.Z. Ismail, E.A. Al-Hashmi, Use of waste plastic in concrete mixture as aggregate replacement, Waste Manag. 28 (11) (2008) 2041–2047.
[7] A. Kan, R. Demirboğa, A novel material for lightweight concrete production, Cem. Concr. Compos. 31 (7) (2009) 489–495.
[8] B.W. Jo, S.K. Park, J.C. Park, Mechanical properties of polymer concrete made with recycled PET and recycled concrete aggregates, Constr. Build. Mater. 22 (12) (2008) 2281–2291.
[9] K.S. Rebeiz, A.P. Craft, Plastic waste management in construction: technological and institutional issues, Resour. Conserv. Recycl. 15 (3–4) (1995) 245–257.
[10] S. Akçaözoğlu, C. Ulu, Recycling of waste PET granules as aggregate in alkali-activated blast furnace slag/metakaolin blends, Constr. Build. Mater. 58 (2014) 31–37 (0).
[11] H. Janfeshan Araghi, I.M. Nikbin, S. Rahimi Reskati, E. Rahmani, An experimental investigation on the erosion resistance of concrete containing various PET particles percentages against sulfuric acid attack, Constr. Build. Mater. 77 (2015) 461–471 (0).
[12] J.M.M. Vidales, L.N. Hernández, J.I.T. López, E.E.M. Flores, L.S. Hernández, Polymer mortars prepared using a polymeric resin and particles obtained from waste pet bottle, Constr. Build. Mater. 65 (2014) 376–383 (0).
[13] V. Corinaldesi, J. Donnini, A. Nardinocchi, Lightweight plasters containing plastic waste for sustainable and energy-efficient building, Constr. Build. Mater. 94 (2015) 337–345.
[14] S.C. Kou, G. Lee, C.S. Poon, W.L. Lai, Properties of lightweight aggregate concrete prepared with PVC granules derived from scraped PVC pipes, Waste Manag. 29 (2) (2009) 621–628.
[15] Y. Senhadjiad, G. Escadeillas, A.S. Benosmancd, M. Moulid, H. Khelafid, Kacie S. Ould, Effect of incorporating PVC waste as aggregate on the physical, mechanical, and chloride ion penetration behavior of concrete, J. Adhes. Sci. Technol. 29 (7) (2015) 625–640.
[16] V. Ferrándiz-Mas, T. Bond, E. García-Alcocel, C.R. Cheeseman, Lightweight mortars containing expanded polystyrene and paper sludge ash, Constr. Build. Mater. 61 (2014) 285–292 (0).
[17] N. Liu, B. Chen, Experimental study of the influence of EPS particle size on the mechanical properties of EPS lightweight concrete, Constr. Build. Mater. 68 (2014) 227–232 (0).
[18] A. Schackow, C. Effting, M.V. Folgueras, S. Güths, G.A. Mendes, Mechanical and thermal properties of lightweight concretes with vermiculite and EPS using air-entraining agent, Constr. Build. Mater. 57 (2014) 190–197 (0).
[19] T. Gupta, S. Chaudhary, R.K. Sharma, Assessment of mechanical and durability properties of concrete containing waste rubber tire as fine aggregate, Constr. Build. Mater. 73 (2014) 562–574 (0).
[20] J. Lv, T. Zhou, Q. Du, H. Wu, Effects of rubber particles on mechanical properties of lightweight aggregate concrete, Constr. Build. Mater. 91 (2015) 145–149.
[21] P. Panyakapo, M. Panyakapo, Reuse of thermosetting plastic waste for lightweight concrete, Waste Manag. 28 (9) (2008) 1581–1588.
[22] R. Cioffi, F. Colangelo, F. Montagnaro, L. Santoro, Manufacture of artificial aggregate using MSWI bottom ash, Waste Manag. 31 (2) (2011) 281–288.
[23] F. Colangelo, F. Messina, R. Cioffi, Recycling of MSWI fly ash by means of cementitious double step coldbonding pelletization: technological assessment for the production of lightweight artificial aggregates, J. Hazard. Mater. 299 (2015) 181–191.
[24] C. Ferone, F. Colangelo, F. Messina, F. Iucolano, B. Liguori, R. Cioffi, Coal combustion wastes reuse in low energy artificial aggregates manufacturing, Materials 6 (11) (2013) 5000–5015.
[25] F. Colangelo, G. De Luca, C. Ferone, A. Mauro, Experimental and numerical analysis of thermal and hygrometric characteristics of building structures employing recycled plastic aggregates and geopolymer concrete, Energies 6 (11) (2013) 6077–6101.
[26] P. Posi, C. Teerachanwit, C. Tanutong, S. Limkamoltip, S. Lertnimoolchai, V. Sata, P. Chindaprasirt, Lightweight geopolymer concrete containing aggregate from recycle lightweight block, Mater. Des. 52 (2013) 580–586 (0).
[27] Q.L. Yu, P. Spiesz, H.J.H. Brouwers, Ultra-lightweight concrete: conceptual design and performance evaluation, Cem. Concr. Compos. 61 (2015) 18–28.
[28] B.S. Mohammed, W.L. Foo, M. Abdullahi, Flexural strength of palm oil clinker concrete beams, Mater. Des. 53 (2014) 325–331.
[29] S. Herrero, P. Mayor, F. Hernández-Olivares, Influence of proportion and particle size gradation of rubber from end-of-life tires on mechanical, thermal and acoustic properties of plaster–rubber mortars, Mater. Des. 47 (2013) 633–642.
[30] J.N. Eiras, F. Segovia, M.V. Borrachero, J. Monzó, M. Bonilla, J. Payá, Physical and mechanical properties of foamed Portland cement composite containing crumb rubber from worn tires, Mater. Des. 59 (2014) 550–557.
[31] S. Rahimifard, T. Staikos, G. Coates, Recycling of Footwear Products for Sustainable Manufacturing and Reuse/recycling Technologies (SMART), Loughborough University, 2007.
[32] N. Dulsang, P. Chindaprasirt, P. Posi, S. Hiziroglu, P. Sutaphakdee, R. Dangsawat, P. Kasemsiri, Optimizing mix proportion of lightweight concrete containing plastic waste by Taguchi method, Adv. Mater. Res. 931-932 (2014) 431–435.
[33] ASTM C109, Standard test method for compressive strength of hydraulic cement mortars (using 2-in. or [50-mm] cube specimens), 04.01, Annual Book of ASTM Standards, 2012.
[34] ASTM D5334, Standard test method for determination of thermal conductivity of soil and soft rock by thermal needle probe procedure, vol 04.08, Annual Book of ASTM Standards, 2013.
[35] ASTM C1585, Standard test method for measurement of rate of absorption of water by hydraulic cement concretes, vol 04.02, Annual Book of ASTM Standards, 2013.

[36] ASTM C138, Standard test method for density (unit weight), yield, and air content (gravimetric) of concrete, vol 04.02, Annual Book of ASTM Standards, 2006.
[37] ASTM C642, Standard test method for density, absorption and voids in hardened concrete, vol 04.02, Annual Book of ASTM Standards, 2006.
[38] C. Hall, Water sorptivity of mortars and concretes: A review, Mag. Concr. Res. 41 (147) (1989) 51–61.
[39] ASTM C267, Standard test methods for chemical resistance of mortars, grouts, and monolithic surfacings and polymer concretes, vol 06.02, Annual Book of ASTM Standards, 2012.
[40] Z.T. Chang, X.J. Song, R. Munn, M. Marosszeky, Using limestone aggregates and different cements for enhancing resistance of concrete to sulphuric acid attack, Cem. Concr. Res. 35 (8) (2005) 1486–1494.
[41] E. Hewayde, M.L. Nehdi, E. Allouche, G. Nakhla, Using concrete admixtures for sulphuric acid resistance, Constr. Mater. 160 (2007) 25–35.
[42] D.L. Pavia, G.M. Lampman, G.S. Kriz, J.R. Vyvyan, Introduction to Spectroscopy, fourth ed. Brooks/Cole Cengage Learning, (USA), 2010.
[43] D.A. Silva, H.R. Roman, P.J.P. Gleize, Evidences of chemical interaction between EVA and hydrating Portland cement, Cem. Concr. Res. 32 (9) (2002) 1383–1390.
[44] Z. Yang, X. Shi, A.T. Creighton, M.M. Peterson, Effect of styrene–butadiene rubber latex on the chloride permeability and microstructure of Portland cement mortar, Constr. Build. Mater. 23 (6) (2009) 2283–2290.
[45] S. Akçaözoğlu, C.D. Atis, K. Akcaozoglu, An investigation on the use of shredded waste PET bottles as aggregate in lightweight concrete, Waste Manag. 30 (2) (2010) 285–290.
[46] ASTM C330, Standard specification for lightweight aggregates for structural concrete, vol. 04.02, Annual Book of ASTM Standards, 2009.
[47] ASTM C331, Standard specification for lightweight aggregates for concrete masonry units, vol. 04.02, Annual Book of ASTM Standards, 2013.
[48] R. Siddique, J. Khatib, I. Kaur, Use of recycled plastic in concrete: a review, Waste Manag. 28 (10) (2008) 1835–1852.
[49] N. Saikia, J.D. Brito, Waste polyethylene terephthalate as an aggregate in concrete, Adv. Mater. 16 (2013) 341–350.
[50] S.P. Zhang, L. Zong, Evaluation of relationship between water absorption and durability of concrete materials, Adv. Mater. Sci. Eng. 1-8 (2014).
[51] A.M. Neville, Properties of Concrete. Sorptivity, fourth ed. Longman Group Limited, 1995 489.
[52] O.Y. Marzouk, R.M. Dheilly, M. Queneudec, Valorization of post-consumer waste plastic in cementitious concrete composites, Waste Manag. 27 (2) (2007) 310–318.
[53] K.M.A. Hossain, M. Lachemi, Lightweight plaster materials with enhanced thermal properties made with polyurethane foam wastes, Constr. Build. Mater. **28** (1) (2012) 653–658.
[54] F. Pacheco-Torgal, S. Jalali, Sulphuric acid resistance of plain, polymer modified, and fly ash cement concretes, Constr. Build. Mater. **23** (12) (2009) 3485–3491.
[55] Kishore VVN. Renewable Energy Engineering and Technology: Principles and Practice. 012; 398.
[56] V. Corinaldesi, A. Mazzoli, G. Moriconi, Mechanical behaviour and thermal conductivity of mortars containing waste rubber particles, Mater. Des. 32 (3) (2011) 1646–1650.
[57] P. Sukontasukkul, Use of crumb rubber to improve thermal and sound properties of pre-cast concrete panel, Constr. Build. Mater. 23 (2) (2009) 1084–1092.
[58] S. Gutiérrez-González, J. Gadea, A. Rodríguez, C. Junco, V. Calderón, Lightweight plaster materials with enhanced thermal properties made with polyurethane foam wastes, Constr. Build. Mater. 28 (1) (2012) 653–658.
[59] S. Akçaözoğlu, K. Akçaözoğlu, C.D. Atiş, Thermal conductivity, compressive strength and ultrasonic wave velocity of cementitious composite containing waste PET lightweight aggregate (WPLA), Compos. Part B 45 (1) (2013) 721–726.

Construction and Building Materials 111 (2016) 15–21

Contents lists available at ScienceDirect

Construction and Building Materials

journal homepage: www.elsevier.com/locate/conbuildmat

Properties of pervious concrete containing recycled concrete block aggregate and recycled concrete aggregate

Yuwadee Zaetang [a], Vanchai Sata [b], Ampol Wongsa [b], Prinya Chindaprasirt [b,*]

[a] Dept. of Civil and Environmental Engineering, Faculty of Science and Engineering, Kasetsart University, Chalermphrakiat Sakonnakhon Province Campus, Sakon Nakhon 47000, Thailand
[b] Sustainable Infrastructure Research and Development Center, Dept. of Civil Engineering, Faculty of Engineering, Khon Kaen University, Khon Kaen 40002, Thailand

HIGHLIGHTS

- We studied pervious concretes containing recycled concrete block aggregate (RBA) and recycled concrete aggregate (RCA).
- Replacement of natural aggregate with RBA and RCA increased compressive strengths.
- For RCA, surface abrasion resistance was improved for all replacement levels.
- For RBA, surface abrasion resistance was improved with up to 20% replacement level.

ARTICLE INFO

Article history:
Received 8 October 2015
Received in revised form 17 December 2015
Accepted 17 February 2016
Available online 21 February 2016

Keywords:
Pervious concrete
Recycled aggregate
Total void
Compressive strength
Surface abrasion

ABSTRACT

The properties of pervious concretes containing two types of recycled aggregates viz., recycled concrete block aggregate (RBA) and recycled concrete aggregate (RCA) were studied. They were incorporated in pervious concretes by replacing natural aggregate at the levels of 0%, 20%, 40%, 60%, 80%, and 100% by weight. Compressive strength, density, total void, water permeability, thermal conductivity and surface abrasion resistance of pervious concrete containing the aggregates were determined. Both RBA and RCA increased the compressive strengths of pervious concretes except at the high replacement level of 100%. The incorporation of RCA at all replacement levels increased the surface abrasion resistance of pervious concrete. For RBA, the improvement in surface abrasion resistance was obtained with only up to 20% replacement level. Although the recycled aggregates were weaker than natural aggregate, the improvements in strength and abrasion resistance were achieved as a result of a better bonding between recycled aggregate and cement paste due to increased surface porosity and roughness of recycled aggregates. The improvements in strength and surface abrasion resistance are important for the utilization of pervious concrete.

© 2016 Elsevier Ltd. All rights reserved.

1. Introduction

Huge quantities of construction and demolition wastes are produced every year [1–3]. In Thailand, these waste materials are usually sent to landfills or dumped illegally. The disposal of these wastes is a severe social and environmental problem. Recycling of construction and demolition wastes for use as aggregates to produce new concrete can reduce the problem of waste storage and preserve natural aggregate resources [4].

A number of studies on recycled aggregate in concrete indicate that the strength of concrete decreases as the amount of recycled aggregate increases. These recycled aggregates are normally low in density and abrasion resistance, and high in absorption and porosity due to the attachment of cement paste and mortar on the aggregate surface [1,5–7]. Due to its low compressive strength and a high degree of variation, recycled aggregate concrete is recommended for non-structural concrete or pavement applications [2,8,9].

Pervious concrete is a special concrete with relatively high void content and high water permeability compared to the conventional concrete. It is an environmentally friendly material and is used for a number of civil engineering and architectural applications such as in park areas, areas with light traffic, pedestrian walkways and tennis courts [10,11]. In addition, the interconnected voids of pervious concrete allow water to pass through and thus it can be used to reduce storm water runoff rate and in other applications such as water purification, acoustic absorption and thermal

* Corresponding author.
E-mail address: prinya@kku.ac.th (P. Chindaprasirt).

http://dx.doi.org/10.1016/j.conbuildmat.2016.02.060
0950-0618/© 2016 Elsevier Ltd. All rights reserved.

insulation [12–14]. Typically, pervious concrete has connected pores ranging in size from 2 to 8 mm and void contents from 18% to 35%. Due to the high void content, its compressive strength is relatively low ranging from 2.8 to 28.0 MPa [15]. The cement paste binder layer of pervious concrete is very thin. Thus, the strength of pervious concrete depends primarily on the strength of thin binder paste [11]. The strength of aggregate is normally much higher than those of cement paste and the interface between cement pastes and aggregate. For this reason, it should be possible to use recycled aggregate as coarse aggregate in pervious concrete and achieve similar properties to those made with natural aggregates.

Therefore, pervious concretes made from natural coarse aggregate replaced with coarse aggregate from recycled concrete block and recycled concrete aggregate at the levels of 0%, 20%, 40%, 60%, 80%, and 100% by weight of aggregate were studied. The effects of replacement level of natural aggregate with recycled aggregates on total void, water permeability coefficient, compressive strength, splitting tensile strength, flexural strength and surface abrasion resistance were evaluated. The obtained data should provide a concrete foundation for the use of recycled aggregates in pervious concrete.

2. Experimental details

2.1. Material

Portland cement Type 1, superplasticizer Type F (SP), natural limestone aggregate (NA), and two types of recycled aggregates viz., recycled concrete block aggregate (RBA) and recycled concrete aggregate (RCA) were the materials used in this experiment. The concrete block was made of low strength dry mortar and the concrete was structural concrete made with limestone aggregate. Their appearances are shown in Fig. 1. They were crushed and sieved to obtain 4.75–9.50 mm particles for use as recycled coarse aggregates. Fig. 2 shows the particle shape and texture of natural and recycled coarse aggregates. Their properties are shown in Table 1. The fineness modulus values of the three aggregates were approximately the same at 5.83–5.97. The dry-rodded densities of NA, RBA, and RCA were 1440, 1240, and 1340 kg/m^3, respectively with corresponding specific gravities of 2.70, 2.49, and 2.53. The water absorptions of RBA and RCA were approximately ten times higher than that of NA. The Los Angeles abrasion losses of NA, RBA, and RCA were 30.2%, 52.0%, and 43.3%, respectively. The low density, high water absorption and high Los Angeles abrasion loss of the recycled aggregate were due to the high porosity of adhered cement mortar on the recycled aggregate as indicated by previous researchers [16,17].

2.2. Mix proportions of pervious concrete

The coarse aggregates were prepared to a saturated surface dry (SSD) condition before mixing. Constant water to cement ratio of 0.24, cement to aggregate ratio of 0.22, and SP dosage of 0.75% by weight of cement were used. The control pervious concrete (NA100) consisted of 316 kg of Portland cement type I, 76 kg of water, 2.4 kg of SP, and 1435 kg of NA for 1 m^3 of concrete. NA was replaced with RBA and RCA at the levels of 0%, 20%, 40%, 60%, 80%, and 100% by weight of coarse aggregate. Table 2 gives the summary of pervious concrete mix proportions. The pervious concretes were denoted by aggregate type and percentage content. For example, RBA60 concrete was pervious concrete with replacement of NA by 60% RBA.

2.3. Mixing and preparation of specimens

Cement paste was mixed in a pan-type mixer for 5 min. The coarse aggregates were added to the mixture and mixed for another 3 min. After mixing, three sizes of concrete specimens were cast. The cylindrical specimen with 100 mm diameter and 200 mm height was used for the measurements of compressive strength, splitting tensile strength, water permeability, and total void. The 200 × 400 × 70 mm prism specimen was used for flexural strength test. The 150 mm cube specimen was used for the measurements of surface abrasion resistance and thermal conductivity. The fresh mixture was placed into the mold in two layers. Each layer was rodded 25 times with 10 mm diameter tamping rod. After rodding, the specimens were placed on a vibrating table and a 1.5 kg loading plate was placed on the top surface of specimen. The compaction vibration was then applied for 10 s using vibrating table at vibrating frequency of 2860 per minute and amplitude of 0.3–0.6 mm. All samples were demolded at the age of 24 h and stored in a moist room until testing age.

2.4. Testing detail

2.4.1. Total void and water permeability

The total void of pervious concrete was determined in accordance with ASTM C1754 [22]. Water permeability of the pervious concrete was measured using the constant head method [15,23]. To protect from the water leakage between sample and test device, the cylindrical specimen was wrapped with a rubber tube and tightened by circular clamps. Water was allowed into the specimen to obtain a steady state flow. The time in seconds (t) required for a certain quantity of water in cubic centimeters (Q) to pass was measured. The coefficient of water permeability (k) in term of centimeters per second (cm/s) was calculated using Darcy's Law as shown in Eq. (1).

$$k = \frac{QL}{HAt} \tag{1}$$

where L is length of specimen (cm), H is water head (cm), and A is cross sectional area of specimen (cm^2).

2.4.2. Compressive, flexural, and splitting tensile strengths

The compressive, splitting tensile, and flexural strengths were determined at the age of 28 days. The compressive and splitting tensile strengths were carried out on cylindrical samples in accordance with ASTM C39 [24] and ASTM C496 [25], respectively. For compressive strength, the samples were capped at both ends with sulfur capping compound to level the loading surface before testing. The flexural strength was investigated in accordance with ASTM C293 [26] using prism specimens. The reported result was the average of three samples.

2.4.3. Surface abrasion resistance

The surface abrasion resistance of pervious concrete surface was tested at 28 days using rotating-cutter method in accordance with ASTM C944 [27]. The specimen was left to air dry for one day before testing (air-dry condition). The normal load of 98 N (22 lbs) was applied through rotating-cutter dressing wheels in contact with the specimen surface for 2 min. Fig. 3 shows the test set-up of surface abrasion resistance. The surface abrasion resistance was determined on two opposite flat sides and presented as average weight loss in grams (g) of three specimens.

(a) RBA (b) RCA

Fig. 1. RBA and RCA before crushing and sieving.

(a) NA

(b) RBA

(c) RCA

Fig. 2. Particle shape and texture of NA, RBA, and RCA.

Table 1
Properties of coarse aggregates.

Properties	NA	RBA	RCA	Standard for testing
Fineness modulus	5.95	5.83	5.97	ASTM C136 [18]
Dry-rodded density (kg/m^3)	1440	1240	1340	ASTM C29 [19]
Specific gravity	2.70	2.49	2.53	ASTM C127 [20]
Absorption (%)	0.46	5.18	4.58	ASTM C127 [20]
Los Angeles abrasion loss (%)	30.2	52.0	43.3	ASTM C131 [21]

2.4.4. Thermal conductivity

The thermal conductivity coefficients of pervious concrete were measured at the age of 28 days using a hand-held measuring instrument (ISOMET2114, Applied Precision Ltd.) for direct measurement of heat transfer properties. The reported results were the average of three samples.

3. Results and discussion

3.1. Density, total void and water permeability

Table 3 shows the test results of density, total void, and water permeability of pervious concrete. As expected, the density of pervious concrete reduced with the increase in recycled aggregate

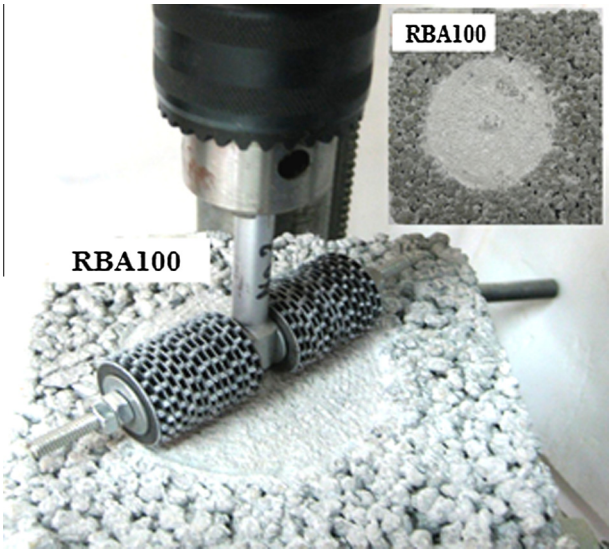

Fig. 3. Testing of surface abrasion resistance.

Table 2
Mix proportions of pervious concretes.

Concretes	Cement (kg/m^3)	Water (kg/m^3)	SP (kg/m^3)	Coarse aggregate (kg/m^3)	
				NA	RBA or RCA
NA100	316	76	2.4	1435	–
RBA20 or RCA20	316	76	2.4	1150	285
RBA40 or RCA40	316	76	2.4	860	575
RBA60 or RCA60	316	76	2.4	575	860
RBA80 or RCA80	316	76	2.4	285	1150
RBA100 or RCA100	316	76	2.4	–	1435

Table 3
Density, total void, and water permeability coefficient of pervious concretes.

Concretes	Density (kg/m^3)	Total void (%)	Water permeability coefficient (cm/s)
NA100	1920	25	1.01
RBA20	1910	23	0.79
RBA40	1980	20	0.80
RBA60	1940	19	0.56
RBA80	1960	17	0.36
RBA100	2000	13	0.22
RCA20	1900	24	0.95
RCA40	1860	24	0.98
RCA60	1820	24	0.89
RCA80	1800	25	0.91
RCA100	1830	23	1.01

content. The reduction was more with the use of RBA as its specific gravity (2.49) was slightly lower than that of RCA (2.53). The specific gravities of both recycled aggregates were substantially lower than that of NA (2.70). For the mixes with RCA, the total voids of all mixes were very similar at 23–25% and not different to the value of 25% of control concrete. It should be noted here that all mixtures had the same mix proportion. This confirmed that the replacement of NA with RCA had no effect on the void of pervious concrete. However, the density of pervious concretes tended to decrease slightly and the water permeability coefficient tended to increase slightly as the RCA replacement level increased. This resulted from the low bulk density of RCA associated with the adhered mortar which was less solid and contained more voids than NA.

For the mixes with RBA, the total void reduced with increasing replacement level of recycled aggregate despite that fact these mixes had the same mix proportion and the aggregate sizes were approximately the same. The RBA was made of dry mortar and thus its strength was low as indicated by the highest Los Angeles abrasion loss value of 52.0%. During mixing, the RBA particles were under abrasion force and a substantial loss from the abrasion of surface and crushing of particles occurred. This led to an increase in the paste content of pervious concrete. With increasing RBA content, the increased amount of paste filled the voids and thus pervious concrete with low void content was obtained.

With the range of void content of pervious concrete containing RBA, a relationship between total void and water permeability coefficient of pervious concretes containing RBA could be established as shown in Fig. 4. The relationship is best described by Eq. (2) with an R^2 value of 0.917. This exponential equation is consistent with the previous published results [28–30].

$$K = 0.0446e^{0.129(V)} \quad (2)$$

where k is the coefficient of water permeability (cm/s) and V is the total void (%).

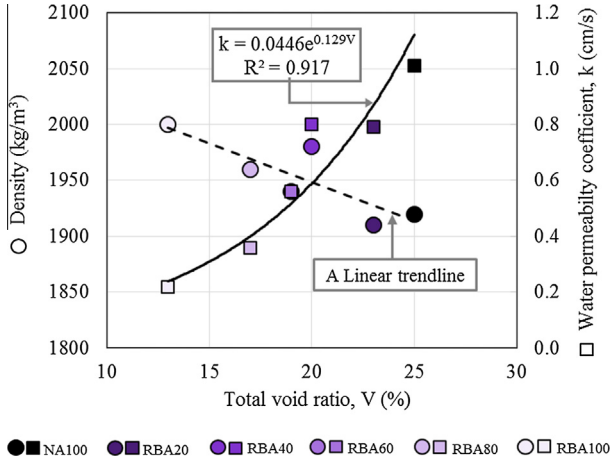

Fig. 4. Density, total void, and water permeability coefficient of pervious concrete replacing NA with RBA.

3.2. Compressive, flexural, and splitting tensile strengths

The results of compressive, flexural, and splitting tensile strengths of pervious concretes at the age of 28 days are shown in Figs. 5 and 6. The strength of pervious concrete is one of the most important parameters of pervious concrete. The use of recycled aggregate should provide pervious concrete with sufficient strength. The compressive strength of control concrete (NA100) was sufficiently high at 13.4 MPa. The incorporation of recycled aggregates resulted in the improvement of pervious concrete strength. This is unexpected as the incorporation of recycled aggregate normally reduced the strength of concrete [31–33]. For RBA, the optimum strength of 17.0 MPa was obtained at 50% recycled aggregate replacement level. For RCA, the optimum strength of 15.0 MPa was obtained at a slightly higher replacement level of 60%. The increases in recycled aggregates content beyond the optimum levels resulted in the decline of pervious concrete compressive strength. The 100% replacement level for both recycled aggregates reduced the compressive strength to the values similar to that of pervious concrete with NA. The increase in compressive strength was due to an increase in bonding between the rough and porous surfaces of recycled aggregates and cement paste compared to normal aggregate [34,35]. As mentioned, the cement paste layer in pervious concrete was quite thin. In addition, the interface between cement paste and aggregate is weaker than the strength of aggregate, thus pervious concrete normally fails at the interface or the binder layer between the aggregate [11,29,36]. The improvement in the bond between aggregate and cement paste thus important to the enhancement of pervious concrete strength.

Increases in compressive strength were significantly higher in pervious concretes containing RBA than those containing RCA. In addition to the good bond between the recycled aggregate and cement paste, the increase in paste content due to the surface abrasion and crushing of RBA particles during mixing reduced the void content of concrete. This made concrete denser and contributed to the increase in compressive strength of pervious concrete [30,37]. A large improvement in compressive strength of pervious concrete with RBA was obtained compared to that with RCA.

For flexural and splitting tensile strengths, test results as shown in Figs. 5 and 6 indicated that the influences of recycled aggregates

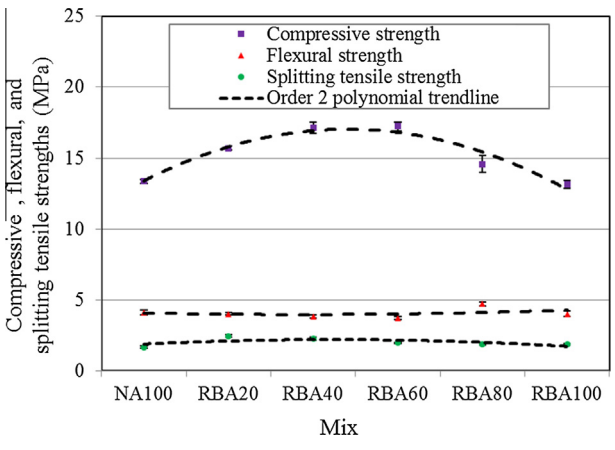

Fig. 5. Strengths at 28 days of pervious concretes containing RBA.

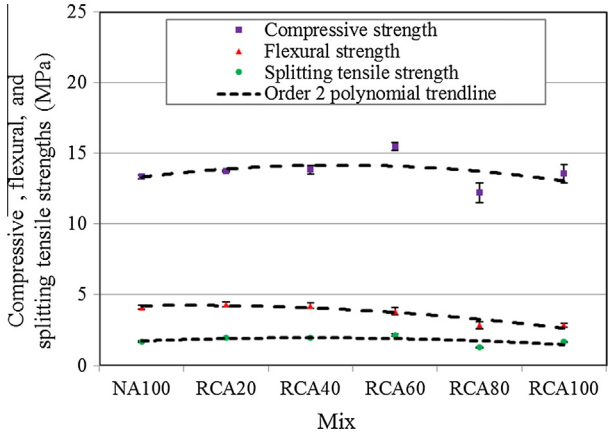

Fig. 6. Strengths at 28 days of pervious concretes containing RCA.

were small. The flexural and splitting tensile strengths of pervious concretes containing RBA were approximately the same. For RCA, there were tendencies for these strengths to reduce slightly with the high replacement levels. For example, the splitting tensile strength of RCA100 was 2.8 MPa compared to 4.1 MPa of the control concrete. Again at the low replacement levels, the increased in the bond between the recycled aggregate and cement paste played an important role and offset the effect of recycled aggregate weakness. At high replacement level, the strengths slightly dropped due to the weakness of recycled aggregate. The ratios of splitting tensile strength to compressive strength ranged between 10.5% and 15.6% with an average of 13.1%. These ratios were slightly higher than 10% for conventional concrete, but were comparable to 9–14% of pervious concrete containing normal aggregate and waste aggregates [38,39].

The increase in compressive strength with the incorporations of both RBA and RCA are very important characteristic. However at high level of replacement with recycled aggregate, the reduction of tensile strength is evident and this should be taken into consideration. The proper amount of recycled aggregate could thus be used to increase the strength of pervious concrete in the real application.

3.3. Surface abrasion resistance

The results of surface abrasion resistance are presented in Fig. 7. The surface abrasion resistance is perhaps the most important factor to have good and long service life of pervious concrete. The weight loss of control pervious concrete (NA100) was 8.2 g. The

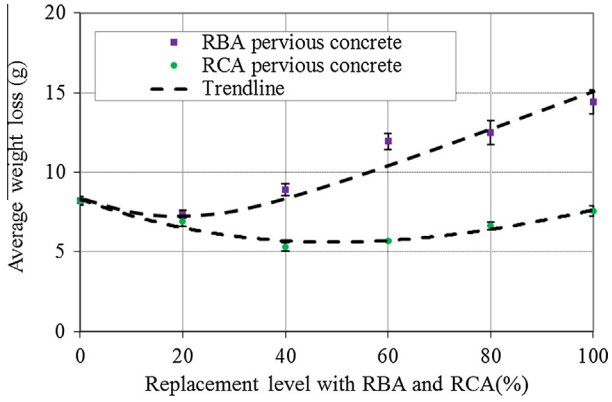

Fig. 7. Average weight loss from surface abrasion testing.

results showed that the surface abrasion resistance of RBA pervious concrete increased with up to 20% replacement level. The improvement was due to the increased strength of pervious concrete resulting from the increased bond between recycled aggregate and cement pate and the increased paste content of pervious concrete. However, when the RBA content was increased beyond 20%, the weakness of RBA became a dominant factor and the surface abrasion resistance reduced with increasing RBA content. The Los Angeles abrasion loss of RBA was 52.0% which was slightly higher than 50% allowed for concrete aggregate according to ASTM C33 [40]. As the RBA was significantly weaker than NA, the increase in RBA content thus had a large adverse effect on the surface abrasion resistance of pervious concrete.

For RCA, the results showed that the surface abrasion resistance of pervious concrete increased with all replacement levels. The optimum replacement level of 40% RCA resulted in the lowest weight loss of 5.3 g which was significantly lower than 8.2 g of control concrete. The weight losses of RCA60, RCA80, and RCA100 concretes were relatively low at 5.7, 6.6 and 7.6 g, respectively. Again, beyond the optimum level of replacement, the weakness of recycled concrete started to play a significant role. In this case, although RCA was weaker than NA, the rate of increase in weight loss was still not large as RCA contained a substantial portion of hard limestone aggregate. However, the weight loss of pervious concrete with 100% RCA was still lower than that with NA. This is an important aspect as the surface abrasion resistance is the major obstacle of the use of pervious concrete. The use of RCA thus gave pervious concrete with better surface abrasion resistance than that with NA and the strengths were also slightly improved.

3.4. Thermal conductivity

Table 4 shows the results of thermal conductivity of pervious concretes. All pervious concretes had low thermal conductivity compared to that of normal strength concrete. The thermal conductivity coefficient of control concrete was 0.78 W/mK while those of RBA and RCA concretes varied in a narrow range between 0.78 and 0.91 W/mK, and between 0.79 and 0.99 W/mK, respectively. The thermal conductivity of normal strength concretes ranged between 0.98 and 1.46 W/mK [41,42]. However, their thermal conductivities were higher than those of concretes containing lightweight aggregates, which ranged from 0.14 to 0.80 W/mK [43–45]. The plot of thermal conductivities of pervious concretes in this study with density values are compared with those of normal and lightweight concretes as shown in Fig. 8. The thermal conductivity of pervious concrete containing recycled aggregate followed the same trend line as those of normal concrete.

From the obtained results, it is clear that recycled aggregates viz., RBA and RCA could be used to advantageous in producing

Table 4
Thermal conductivity coefficient of pervious concretes.

Concretes	Thermal conductivity coefficient (W/m K)
NA100	0.78
RBA20	0.85
RBA40	0.86
RBA60	0.91
RBA80	0.84
RBA100	0.78
RCA20	0.87
RCA40	0.79
RCA60	0.99
RCA80	0.86
RCA100	0.82

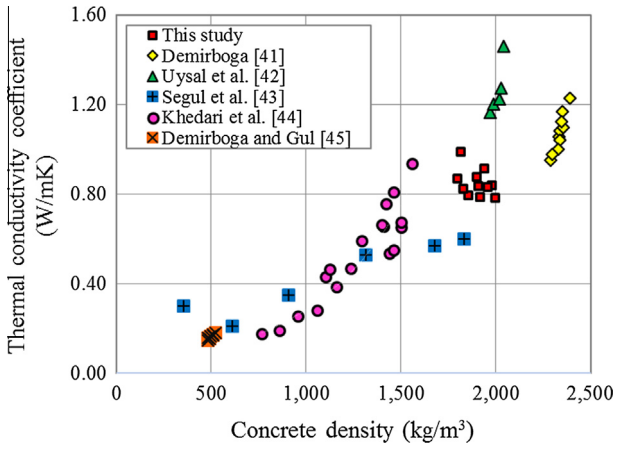

Fig. 8. Comparing thermal conductivity of pervious concrete with normal and lightweight concretes.

pervious concrete. With proper recycled aggregate content, pervious concrete with increased strength and surface abrasion resistance; and comparable thermal conductivity are obtained.

4. Conclusions

The properties of pervious concretes containing natural limestone aggregate replaced with recycled concrete block aggregate (RBA) and recycled concrete aggregate (RCA) were studied. Based on the obtained data, the following conclusions can be drawn.

1. The use of RBA resulted in significant improvement of compressive strength of pervious concrete. The RBA replacement level of 40% was optimum with compressive strength of 17.0 MPa compared to 13.4 MPa of pervious concrete containing NA. The improvement was due to the good bonding between RBA and cement paste, and the increased paste content as a result of abrasion and crushing of RBA particles during mixing. The surface abrasion resistance increased with up to RBA replacement level of 20%. Beyond this replacement level, the surface abrasion resistance dropped significantly due to the increased amount of weak recycled aggregate.
2. The use of RCA also resulted in improvement of compressive strength of pervious concrete but to a lesser extent. The RCA replacement level of 60% was optimum with compressive strength of 15.0 MPa. In this case, the improvement was due to the good bonding between RCA and cement paste. The surface abrasion resistance increased with all RCA replacement levels. The optimum replacement level of 40% RCA resulted in the lowest weight loss of 5.3 g which was significantly lower than 8.2 g of control concrete. For practical purpose, the replacement level could be raised as the 60% RCA concrete still had low weight loss of 5.7 g.
3. The influence of recycled aggregate on the splitting tensile strength and flexural strength of pervious concrete was small. The flexural and splitting tensile strengths of pervious concretes containing RBA remained approximately the same as those with NA. For RCA, there were tendencies for these strengths to drop at high replacement levels. The pervious concrete with recycled aggregate had low thermal conductivity between 0.78 and 0.99 W/mK,
4. Both RBA and RCA could be advantageously used in pervious concrete. For good surface abrasion resistance and strength, the RBA and RCA replacement levels should be 20% and 40–60%, respectively.

Acknowledgments

This work was financially supported by the Higher Education Research Promotion and National Research University Project of Thailand, Office of the Higher Education Commission, through the Advanced Functional Materials Cluster of Khon Kaen University, and Khon Kaen University and the Thailand Research Fund (TRF) under the TRF Senior Research Scholar Contract No. RTA5780004.

References

[1] X. Li, Recycling and reuse of waste concrete in China: Part I. Material behaviour of recycled aggregate concrete, Resour. Conserv. Recycl. 53 (1–2) (2008) 36–44.
[2] J.R. Jiménez, J. Ayuso, F. Agrela, M. López, A.P. Galvín, Utilisation of unbound recycled aggregates from selected CDW in unpaved rural roads, Resour. Conserv. Recycl. 58 (2012) 88–97.
[3] J. Xiao, W. Li, Y. Fan, X. Huang, An overview of study on recycled aggregate concrete in China (1996–2011), Constr. Build. Mater. 31 (2012) 364–383.
[4] V.A. Dakwale, R.V. Ralegaonkar, Development of sustainable construction material using construction and demolition waste, Indian J. Eng. Mater. Sci. 21 (4) (2014) 451–457.
[5] M. Etxeberria, E. Vázquez, A. Marí, M. Barra, Influence of amount of recycled coarse aggregates and production process on properties of recycled aggregate concrete, Cem. Concr. Res. 37 (5) (2007) 735–742.
[6] M. Henry, G. Pardo, T. Nishimura, Y. Kato, Balancing durability and environmental impact in concrete combining low-grade recycled aggregates and mineral admixtures, Resour. Conserv. Recycl. 55 (11) (2011) 1060–1069.
[7] M. Chakradhara Rao, S.K. Bhattacharyya, S.V. Barai, Influence of field recycled coarse aggregate on properties of concrete, Mater. Struct. 44 (1) (2011) 205–220.
[8] L. Courard, F. Michel, P. Delhez, Use of concrete road recycled aggregates for roller compacted concrete, Constr. Build. Mater. 24 (3) (2010) 390–395.
[9] Fd.C. Leite, Rd.S. Motta, K.L. Vasconcelos, L. Bernucci, Laboratory evaluation of recycled construction and demolition waste for pavements, Constr. Build. Mater. 25 (6) (2011) 2972–2979.
[10] M. Scholz, P. Grabowiecki, Review of permeable pavement systems, Build. Environ. 42 (11) (2007) 3830–3836.
[11] J. Yang, G. Jiang, Experimental study on properties of pervious concrete pavement materials, Cem. Concr. Res. 33 (3) (2003) 381–386.
[12] H.K. Kim, H.K. Lee, Influence of cement flow and aggregate type on the mechanical and acoustic characteristics of porous concrete, Appl. Acoust. 71 (7) (2010) 607–615.
[13] J.D. Luck, S.R. Workman, M.S. Coyne, S.F. Higgins, Consequences of manure filtration through pervious concrete during simulated rainfall events, Biosyst. Eng. 102 (4) (2009) 417–423.
[14] S.-B. Park, M. Tia, An experimental study on the water-purification properties of porous concrete, Cem. Concr. Res. 34 (2) (2004) 177–184.
[15] ACI 522R-10, Report on pervious concrete, ACI 522R-102010.
[16] L. Butler, J.S. West, S.L. Tighe, The effect of recycled concrete aggregate properties on the bond strength between RCA concrete and steel reinforcement, Cem. Concr. Res. 41 (10) (2011) 1037–1049.
[17] W. Tangchirapat, R. Buranasing, C. Jaturapitakkul, Use of high fineness of fly ash to improve properties of recycled aggregate concrete, J. Mater. Civ. Eng. 22 (6) (2010) 565–571.
[18] American Society for Testing and Materials. Standard Test Method for Sieve Analysis of Fine and Coarse Aggregates, ASTM C136, Annual Book of ASTM Standard, 2006.
[19] American Society for Testing and Materials. Standard Test Method for Bulk Density ("Unit Weight") and Voids in Aggregate ASTM C29/C29M, Annual Book of ASTM Standard, 2009.
[20] American Society for Testing and Materials. Standard Test Method for Density, Relative Density, Absorption of Coarse Aggregate, ASTM C127, Annual Book of ASTM Standard, 2012.
[21] American Society for Testing and Materials. Standard Test Method for Resistance to Degradation of Small-Size Coarse Aggregate by Abrasion and Impact in the Los Angeles Machine, ASTM C131, Annual Book of ASTM Standard, 2006.
[22] American Society for Testing and Materials. Standard Test Method for Density and Void Content of Hardened Pervious Concrete, ASTM C1754, Annual Book of ASTM Standard, 2012.
[23] N. Neithalath, M.S. Sumanasooriya, O. Deo, Characterizing pore volume, sizes, and connectivity in pervious concretes for permeability prediction, Mater. Charact. 61 (8) (2010) 802–813.
[24] American Society for Testing and Materials. Standard Test Method for Compressive Strength of Cylindrical Concrete Specimens, ASTM C39, Annual Book of ASTM Standard, 2012.
[25] American Society for Testing and Materials. Standard Test Method for Splitting Tensile Strength of Cylindrical Concrete Specimens, ASTM C496/C496M, Annual Book of ASTM Standard, 2011.
[26] American Society for Testing and Materials. Standard Test Method for Flexural Strength of Concrete (Using Simple Beam With Center-Point Loading), ASTM C293, Annual Book of ASTM Standard, 2003.

[27] American Society for Testing and Materials. Standard Test Method for Abrasion Resistance of Concrete or Mortar Surfaces by the Rotating-Cutter Method, ASTM C944/C944M, Annual Book of ASTM Standard, 2012.
[28] T. Tho-in, V. Sata, P. Chindaprasirt, C. Jaturapitakkul, Pervious high-calcium fly ash geopolymer concrete, Constr. Build. Mater. 30 (2012) 366–371.
[29] V. Sata, A. Wongsa, P. Chindaprasirt, Properties of pervious geopolymer concrete using recycled aggregates, Constr. Build. Mater. 42 (2013) 33–39.
[30] Y. Zaetang, A. Wongsa, V. Sata, P. Chindaprasirt, Use of lightweight aggregates in pervious concrete, Constr. Build. Mater. 48 (2013) 585–591.
[31] J.M. Khatib, Properties of concrete incorporating fine recycled aggregate, Cem. Concr. Res. 35 (4) (2005) 763–769.
[32] K. Rahal, Mechanical properties of concrete with recycled coarse aggregate, Build. Environ. 42 (1) (2007) 407–415.
[33] A.K. Padmini, K. Ramamurthy, M.S. Mathews, Influence of parent concrete on the properties of recycled aggregate concrete, Constr. Build. Mater. 23 (2) (2009) 829–836.
[34] G. Moriconi, V. Corinaldesi, R. Antonucci, Environmentally-friendly mortars: a way to improve bond between mortar and brick, Mater. Struct. 36 (10) (2003) 702–708.
[35] Z. Xiao, T.-C. Ling, S.-C. Kou, Q. Wang, C.-S. Poon, Use of wastes derived from earthquakes for the production of concrete masonry partition wall blocks, Waste Manage. 31 (8) (2011) 1859–1866.
[36] Y. Chen, K.-J. Wang, D. Liang, Mechanical properties of pervious cement concrete, J. Central South Univ. 19 (11) (2012) 3329–3334.
[37] P. Chindaprasirt, S. Hatanaka, T. Chareerat, N. Mishima, Y. Yuasa, Cement paste characteristics and porous concrete properties, Constr. Build. Mater. 22 (5) (2008) 894–901.
[38] J.T. Kevern, K. Wang, V.R. Schaefer, Effect of coarse aggregate on the freeze-thaw durability of pervious concrete, J. Mater. Civ. Eng. 22 (5) (2010) 469–475.
[39] W.-T. Kuo, C.-C. Liu, D.-S. Su, Use of washed municipal solid waste incinerator bottom ash in pervious concrete, Cement Concr. Compos. 37 (2013) 328–335.
[40] American Society for Testing and Materials. Standard Specification for Concrete Aggregates, ASTM C33/C33M, Annual Book of ASTM Standard, 2013.
[41] R. Demirboğa, Thermal conductivity and compressive strength of concrete incorporation with mineral admixtures, Build. Environ. 42 (7) (2007) 2467–2471.
[42] H. Uysal, R. Demirboğa, R. Şahin, R. Gül, The effects of different cement dosages, slumps, and pumice aggregate ratios on the thermal conductivity and density of concrete, Cem. Concr. Res. 34 (5) (2004) 845–848.
[43] O. Sengul, S. Azizi, F. Karaosmanoglu, M.A. Tasdemir, Effect of expanded perlite on the mechanical properties and thermal conductivity of lightweight concrete, Energy Build. 43 (2–3) (2011) 671–676.
[44] J. Khedari, B. Suttisonk, N. Pratinthong, J. Hirunlabh, New lightweight composite construction materials with low thermal conductivity, Cement Concr. Compos. 23 (1) (2001) 65–70.
[45] R. Demirboğa, R. Gül, The effects of expanded perlite aggregate, silica fume and fly ash on the thermal conductivity of lightweight concrete, Cem. Concr. Res. 33 (5) (2003) 723–727.

Construction and Building Materials 111 (2016) 637–643

Contents lists available at ScienceDirect

Construction and Building Materials

journal homepage: www.elsevier.com/locate/conbuildmat

Properties of lightweight fly ash geopolymer concrete containing bottom ash as aggregates

Ampol Wongsa [a], Yuwadee Zaetang [b], Vanchai Sata [a,*], Prinya Chindaprasirt [a]

[a] Sustainable Infrastructure Research and Development Center, Department of Civil Engineering, Faculty of Engineering, Khon Kaen University, Khon Kaen 40002, Thailand
[b] Department of Civil and Environmental Engineering, Faculty of Science and Engineering, Kasetsart University, Chalermphrakiat Sakon Nakhon Province Campus, Sakon Nakhon 47000, Thailand

HIGHLIGHTS

- Lightweight geopolymer concrete (LWGC) made from fly ash geopolymer and bottom ash aggregate.
- LWGC with 14.3–18.1 MPa compressive strengths and 1661–1688 kg/m^3 densities were obtained.
- Theirs thermal conductivity coefficients ranged from 0.43 to 0.47 W/m K.
- LWGCs could be used for moderate strength concrete and thermal insulation concrete.

ARTICLE INFO

Article history:
Received 8 September 2015
Received in revised form 25 January 2016
Accepted 22 February 2016
Available online 21 March 2016

Keywords:
Bottom ash
Fly ash
Geopolymer
Lightweight aggregate
Lightweight concrete

ABSTRACT

In order to evaluate the utilization of waste from coal combustion thermal power plant, the properties of lightweight geopolymer concrete (LWGC) containing fly ash as geopolymer binder and bottom ash as aggregates were studied. Sodium silicate solution (NS) and 10 M sodium hydroxide (NH) were used as alkali activators. The NS/NH ratios of 0.5, 1.0, and 1.5 with liquid/ash (L/A) ratios of 0.70, 0.75, and 0.80 were used. The compressive strength, splitting tensile strength, surface abrasion resistance, density, thermal conductivity, and ultrasonic pulse velocity (UPV) of concrete were tested. The results indicated that fly ash and bottom ash could be used to produce LWGCs with compressive strengths of 14.3–18.1 MPa, splitting tensile strengths of 1.2–2.0 MPa, and densities of 1661–1688 kg/m^3. Theirs thermal conductivity coefficients of 0.43–0.47 W/m K were lower than those of the geopolymer concrete containing natural aggregate. LWGCs in this study could thus be used for moderate strength concrete and thermal insulation concrete.

© 2016 Elsevier Ltd. All rights reserved.

1. Introduction

Fly ash and bottom ash are waste materials or by-products from the combustion of coal that need to be disposed of in an environmental friendly way. The annual output of lignite fly ash at Mae Moh thermal power plant in the north of Thailand is around 3.0 million tons [1–3]. It contains high content of silica and alumina which is suitable for using as a pozzolanic material in concrete [4,5] and also as a base material for making geopolymer binder [1,6].

The output of bottom from Mae Moh thermal power plant is around 0.8 million tons per year and is disposed of in landfills [2,3]. This disposal process leads to environmental problems. It is larger in size and very irregular than those of fly ash [1,7]. It contains pores and cavities, and is composed with only a small amount of semi-spherical particles [7] and less glassy phase [8]. However, Kim and Lee [9] indicated that bottom ash was suitable for using as fine and coarse aggregates in high-strength concrete. The slump flow of fresh concrete was slightly decreased when 100% of normal coarse aggregate was replaced with coarse bottom ash, while the fine bottom ash did not affect the slump flow [9]. This was due to the high porosity of coarse bottom ash aggregate. For the fine aggregate, the porosity was much reduced from the grinding of bottom ash and thus the slump flow was less affected. In addition, the densities of hardened concrete linearly decreased as the replacement ratio of bottom ash increased [9].

There are few studies on the use of waste materials or by-products of lignite coal combustion thermal power plant as aggregates for lightweight concrete. Previous study [10] indicated that coal ash from thermal power plant can be used in porous concrete. In this study, lightweight geopolymer concrete (LWGC) containing

* Corresponding author.
E-mail address: vancsa@kku.ac.th (V. Sata).

http://dx.doi.org/10.1016/j.conbuildmat.2016.02.135
0950-0618/© 2016 Elsevier Ltd. All rights reserved.

fly ash (FA) as geopolymer binder and bottom ash (BA) as aggregates were prepared. The compressive strength, splitting tensile strength, surface abrasion resistance, density, thermal conductivity, and ultrasonic pulse velocity (UPV) of concretes were tested. The effects of NS/NH and L/A ratios on LWGC properties were investigated. The results were compared to those containing natural aggregates (sand and crushed limestone). The obtained knowledge would be beneficial for the promotion and utilization of coal fired thermal power plant waste in concrete and thus lead to the reduction of cement consumption and environmental problems.

2. Materials and preparing of sample

2.1. Materials

The raw materials used in this study were lignite coal fly ash (FA) and bottom ash (BA), crushed limestone (CL) and river sand (RS). The FA and BA were obtained from Mae Moh power plant in northern Thailand. The physical properties of these materials and the chemical compositions of FA and BA are summarized in Tables 1 and 2, respectively. The FA with specific gravity of 2.17, a median particle size of 32.58 μm, a Blaine fineness of 2250 cm^2/g, and 44% (by weight) retained on sieve no. 325 (45 μm) was used as the main source material for making geopolymer binder. The sum of SiO_2, Al_2O_3, and Fe_2O_3 of FA was 71.1% and the CaO content was 14.5%. It can be classified as Class C pozzolan as per ASTM C618 [11]. The BA contained 31.8% SiO_2, 12.1% Al_2O_3, 18.0% Fe_2O_3, and 25.3% CaO as the main chemical compositions.

Fig. 1 shows the XRD pattern of FA and BA. The FA had higher glassy phase content as comparing to BA which indicates by the hump at the region of 20–30°2Theta. The as-received BA was crushed and sieved as fine bottom ash (FB) and coarse bottom ash (CB) for making the LWGCs. The LWGC properties were compared to those of control geopolymer concrete (CGC) containing natural aggregates (CL and RS). The grain size distributions of these aggregates are presented in Fig. 2. The particle size of FB and RS ranged from 75 μm to 4.75 mm, and CB and CL ranged from 4.5 mm to 9.50 mm. The particles of CB and FB were porous with rough surface and irregular in shape as shown in Fig. 3. The specific gravity in saturated surface dry (SSD) condition and bulk density of CB and FB were lower than those of CL and RS while the water absorptions were higher as expected. The Los Angeles abrasion losses were 39.4% for CB and 31.0% for CL. The high water absorption and high Los Angeles abrasion loss of BA were due to its high porosity.

Commercial grade sodium silicate solution (NS) with 12.53% Na_2O, 30.24% SiO_2, and 57.23% H_2O by weight and 10 M sodium hydroxide solution (NH) were used as alkali activator to produce geopolymer binder. The 10 M NH was prepared by dissolving 400 g of sodium hydroxide pellets in 1 l of distilled water and left for 24 h before use. NS was used without any modification.

Table 1
Physical properties of CB, FB, CL, and RS.

Properties	BA aggregate		Natural aggregate		Testing standard
	CB	FB	CL	FS	
Bulk density (kg/m^3)	1116	1371	1576	1671	ASTM C29 [12]
Specific gravity (SSD)	2.47	2.54	2.63	2.63	ASTM C127
Water absorption (%)	3.32	3.53	0.54	0.35	[13]
Fineness modulus	6.1	3.2	6.0	3.3	ASTM C136 [14]
Los Angeles abrasion loss (%)	39.4	–	31.0	–	ASTM C131 [15]

Table 2
Chemical composition of FA and BA.

Oxides (%)	FA	BA
SiO_2	39.4	31.8
Al_2O_3	20.8	12.1
Fe_2O_3	11.5	18.0
CaO	14.5	25.3
MgO	2.2	2.4
K_2O	2.4	2.5
TiO_2	0.5	0.5
P_2O_5	0.2	0.3
BaO	0.1	0.2
SO_3	4.2	3.7
Loss on ignition (LOI)	1.5	3.2

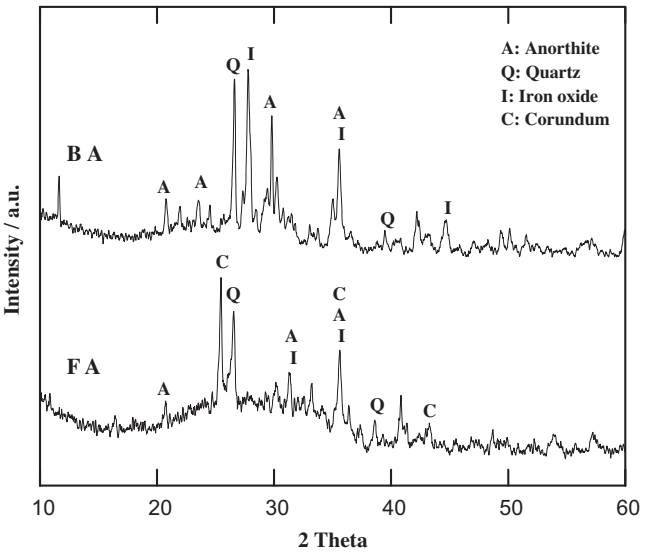

Fig. 1. The XRD pattern of FA and BA (A: Anorthite, Q: Quartz, I: Iron oxide, C: Corundum).

2.2. Mix proportions

In order to study the effect of NS/NH and liquid/ash (L/A) ratio on properties of LWGC containing FB and CB comparing to CGC containing CL and RS, NS/NH ratios of 0.5, 1.0, and 1.5 and L/A ratios of 0.70, 0.75, and 0.80 were used. Twelve mix proportions as shown in Table 3 were prepared. All mix proportions were based on volumetric proportions. The ratio of volume of bulk coarse aggregate to that of fine aggregate and paste volume were kept constant. The name of the mixture was given by the L/A ratio, type of coarse and fine aggregate, and NS/NH ratio. For example, 0.70CLRS0.5 denotes the concrete with L/A ratio of 0.70, CL as coarse aggregate, RS as fine aggregate, and NS/NH ratio of 0.5.

2.3. Mixing, casting, and curing

The mixing of LWGC and CGC was done in a control room at 25 °C. FA and NH were mixed 5 min in a pan-type mixer. Fine and coarse aggregates were then added and mixed for 2 min. Finally, NS was added and mixed for another minute. The total mixing time was 8 min. After mixing, fresh concretes were tested for slump value, then cast in molds and compacted on a vibrating table. The 100 × 200 mm cylindrical samples were prepared for compressive strength, splitting tensile strength, and density tests. The 150 × 150 × 60 mm plate samples were used for surface abrasion resistance test and the 100 × 100 × 100 mm cube samples for thermal conductivity and ultrasonic pulse velocity (UPV) tests. The

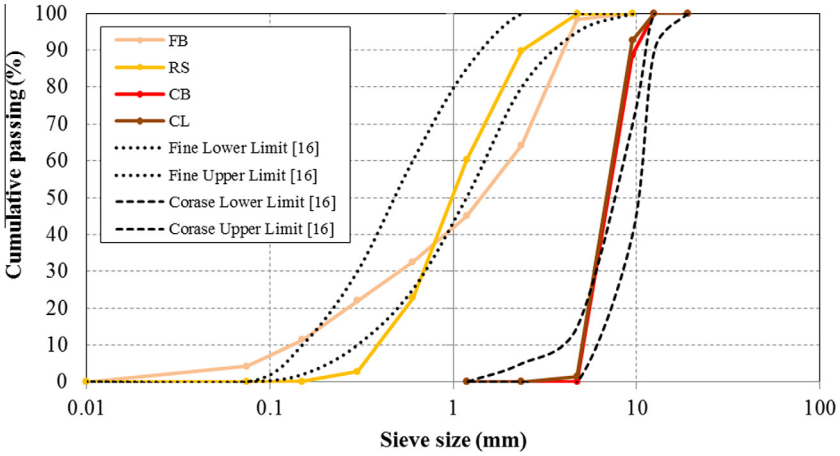

Fig. 2. The grain size distributions of aggregates [16].

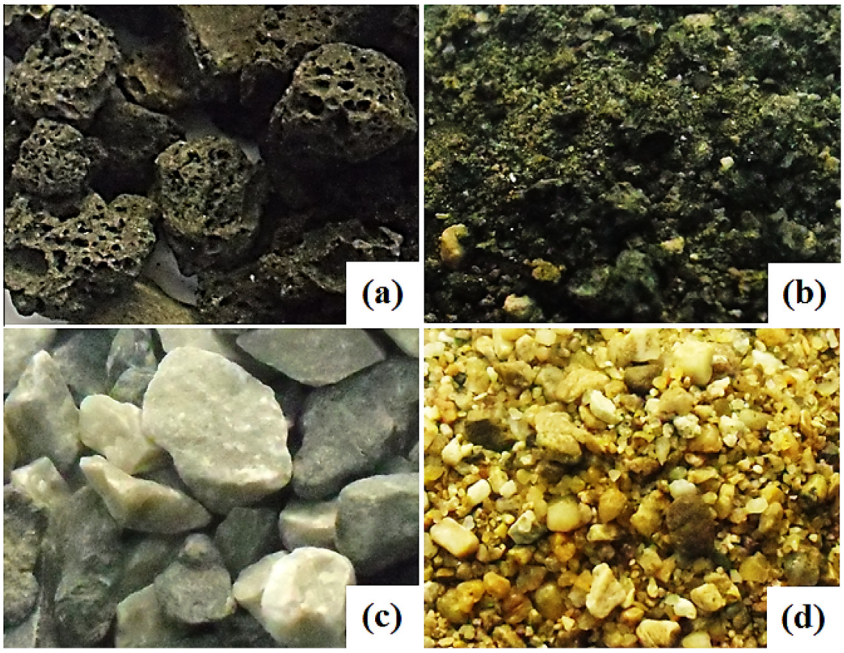

Fig. 3. The particle shape of (a) CB, (b) FB, (c) CL, and (d) RS.

Table 3
Mix proportions per m^3 of LWGCs and CGCs.

Mix	Coarse aggregate		Fine aggregate		Geopolymer binder		
	CB (kg)	CL (kg)	FB (kg)	RS (kg)	FA (kg)	NS (kg)	NH (kg)
0.70CLRS0.5[a]	–	1385	–	383	350	82	163
0.70CLRS1.0[a]	–	1385	–	383	354	124	124
0.70CLRS1.5[a]	–	1385	–	383	357	150	100
0.70CBFB0.5	1005	–	324	–	350	82	163
0.70CBFB1.0	1005	–	324	–	354	124	124
0.70CBFB1.5	1005	–	324	–	357	150	100
0.75CBFB0.5	1005	–	324	–	337	84	169
0.75CBFB1.0	1005	–	324	–	342	128	128
0.75CBFB1.5	1005	–	324	–	345	155	103
0.80CBFB0.5	1005	–	324	–	325	87	174
0.80CBFB1.0	1005	–	324	–	330	132	132
0.80CBFB1.5	1005	–	324	–	333	160	107

[a] Control geopolymer concrete (CGC) containing natural aggregates (CL and RS).

specimens were covered with a thin plastic sheet to protect from moisture loss and allowed to stand for 1 h at 25 °C. After that, the specimens were then cured at 60 °C for 48 h. After the heat curing, the specimens were put in the 25 °C controlled room to cool down and demolded on the next day. The specimens were then wrapped with a thin plastic sheet to minimize moisture loss and stored in the 25 °C controlled room until the testing age.

3. Testing

All mixes were tested for slump using traditional slump cone in accordance with ASTM C143 [17]. The compressive strength, splitting tensile strength, and surface abrasion resistance were tested at the age of 7 days in accordance with ASTM C39 [18], ASTM C496 [19], and ASTM C944 [20], respectively. The reported results were the average of 3 samples. Surface abrasion resistance was tested by the rotating-cutting method. The samples were left to dry for 1 day before the test (air-dry condition) and abraded with 98 N loads on the surface for 120 s after contact between the cutter and the

surface of samples. The abrasion resistances of each sample were done on the two opposite sides of sample. The densities of samples were tested in accordance with ASTM C1754 [21]. The thermal conductivity coefficients were tested using a direct measuring instrument with surface probe (ISOMET2114, Applied Precision Ltd.). The measurement ranges of the device were 0.04–6.0 W/m K. The ultrasonic pulse velocity (UPV) test is a direct and easy tool to judge the quality of concrete [22]. The UPV tests were thus performed on concretes in accordance with ASTM C597 [23]. The transducers used were 50 mm in diameter with a frequency 50 kHz. The UPV was calculated following Eq. (1).

$$V = L/T \times 10^4 \quad (1)$$

where V is the UPV (m/s)
L is the length of sample (cm)
T is the time measured (μs).

4. Results and discussion

4.1. Slump value

The slump values of LWGCs and CGCs as shown in Fig. 4 ranged between 88 and 205 mm. The slump values of LWGCs (88–198 mm) were lower than those of CGCs (190–205 mm). This was due to the high porosity, rough surface texture, and irregular shape of BA compared to those with natural aggregates. The high friction between BA particles decreased the workability of fresh concrete [24,25]. Also, the amount of paste for lubrication between aggregates was reduced due to the high porosity and rough surface of BA particles [9].

In addition, the results clearly showed that the workability characteristics of LWGCs depended on NS/NH and L/A ratio. At the same L/A ratio, the increasing NS/NH ratio decreased the slump value of LWGCs. This was due to the high viscosity of NS which reduced the flow of mixtures [6]. For example, the slump values of 185–198, 169–188, and 88–185 mm were obtained with mixes with NS/NH ratios of 0.5, 1.0, and 1.5, respectively. For the effect of L/A ratio, the slump values increased with the increase in L/A ratio. For example, the slump values of LWGCs with L/A ratios of 0.70, 0.75, and 0.80 were 88–185, 163–195, and 185–198 mm, respectively. Topark-Ngarm et al. [26] reported a similar finding that the slump flow of fresh geopolymer concrete containing limestone and river sand increased with the increase of L/A ratio. The increasing in the amount of liquid alkali activators could improve the workability characteristics of fresh geopolymer concrete. In this study, the 0.70CBFB1.5 sample had the lowest slump value at 88 mm due to the highest NS/NH ratio and the lowest L/A ratio used.

4.2. Compressive strength, splitting tensile strength, and surface abrasion resistance

Figs. 5–7 show the compressive strengths, splitting tensile strengths, and surface abrasion losses of geopolymer concretes. The use of both CB and FB decreased theirs mechanical properties. The compressive strength, splitting tensile strength, and weight loss values of LWGCs were 14.3–18.1 MPa, 1.2–2.0 MPa, and 3.9–5.9 g compared with 34.1–38.2 MPa, 2.2–2.7 MPa, and 1.4–1.7 g of those of CGCs, respectively. This was due to the low density, high Los Angeles abrasion loss, and high porosity of BA particle. The LWGCs also showed higher void and porosity than CGCs as shown in Fig. 8.

The average ratio of splitting tensile to compressive strengths of LWGCs was 9.6% which was higher than 6.6% for CGCs in this study and 6.9% for high-calcium fly ash geopolymer concrete with the same NH concentration and heat curing [27]. The ratios of splitting tensile to compressive strengths of LWGCs were 7.5–14% which were similar to the value of 8–14% for conventional concretes [28,29] as shown in Fig. 9.

The compressive strength, splitting tensile strength, and surface abrasion resistance of LWGCs and CGCs tended to decrease with an increase in the NS/NH ratio as shown in Figs. 5–7. For LWGC with L/A ratio of 0.75, the compressive strength decreased from 18.1 to 15.8 MPa, the splitting tensile strength decreased from 1.5 to 1.2 MPa, and the weight losses from abrasion test increased from 4.2 to 5.3 g with the corresponding increases in NS/NH ratios from 0.5 to 1.5. This consistent with Chindaprasirt et al. work [6] which reported the strength of coarse high calcium fly ash geopolymer mortars with NS/NH ratios of 0.67 and 1.00 were significantly higher than those with NS/NH ratios of 1.5 and 3.0. The different in the NS/NH ratio affects the pH conditions and thus affects the strength development of geopolymer [6]. In this study, the geopolymer paste volume were kept constant, the increase in NS/NH ratio thus decreased the dosage of NH. At high NS/NH ratio, the leaching of alumina and silica was decreased and this resulted in a low level of geopolymerization, and thus the strength decreased. Similar effect was reported by El-Sayed et al. [30] that mortar with a dosage of 6 wt% NH achieved higher gain in compressive strength in comparison with a dosage of 2 wt% NH and this clearly shows the effect of the NH dosage on the early compressive strength gain and on the degree of geopolymerization.

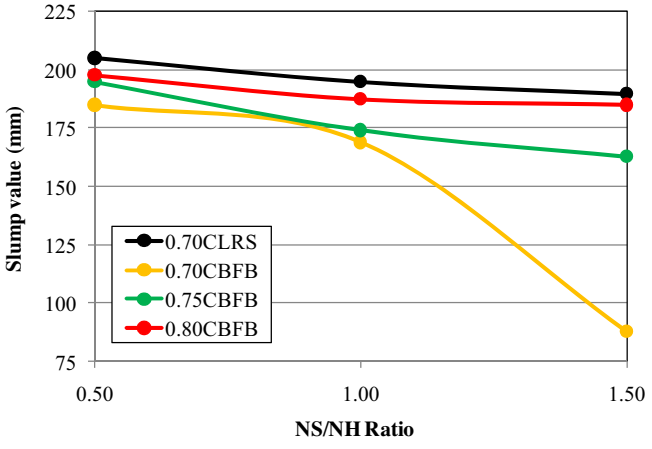

Fig. 4. Slump value and NS/NH ratios at various L/A ratios.

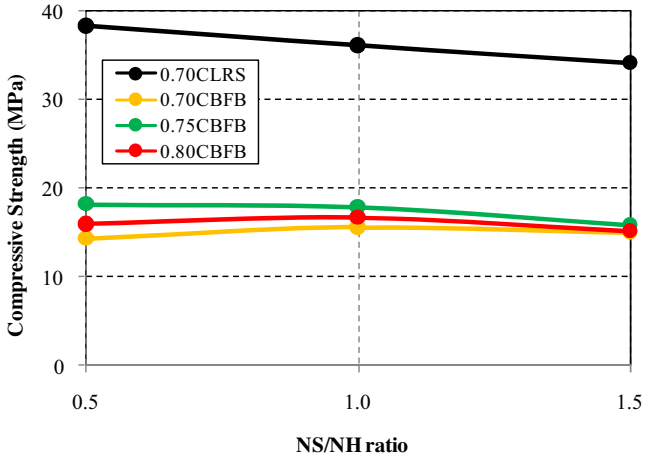

Fig. 5. Compressive strength of geopolymer concretes at various NS/NH and L/A ratios.

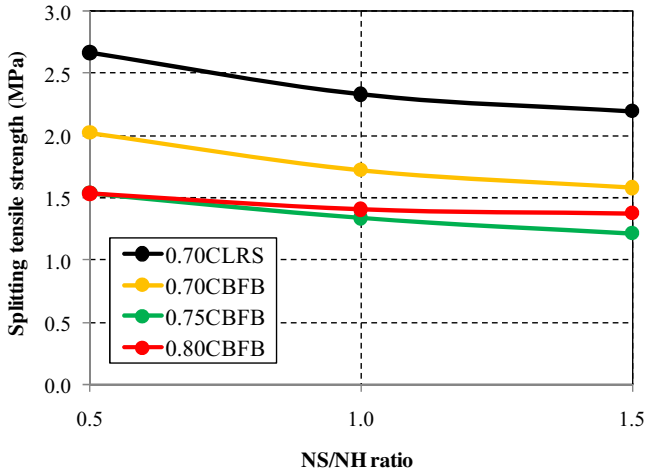

Fig. 6. Splitting tensile strength of geopolymer concretes at various NS/NH and L/A ratios.

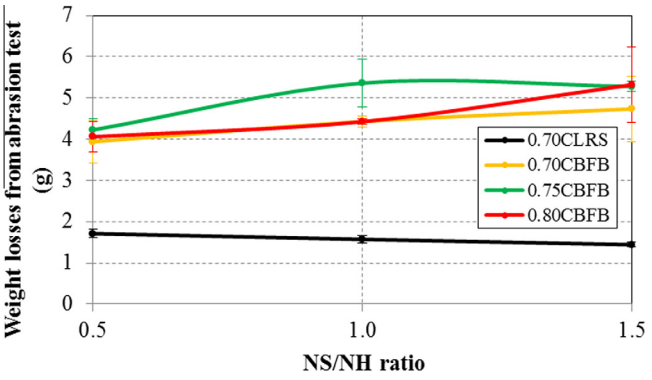

Fig. 7. Weight losses from surface abrasion test of geopolymer concretes at various NS/NH and L/A ratios.

Also, the increasing of NS/NH ratio decreased the workability of LWGCs and resulted in a high void content concrete with lower strength and surface abrasion resistance.

The compressive strength of LWGCs increased with an increase in L/A ratios from 0.70 to 0.75. At low L/A ratio of 0.70, the LWGCs contained low liquid and were difficult to compact which led to high void contents and low compressive strengths [31]. As L/A ratio of lightweight concrete increased to 0.80, the compressive strength started to decline. The optimum L/A to produce a good compressive strength concrete in this study was 0.75. As shown in Fig. 5, the compressive strengths of 14.0–16.3, 15.8–18.6, and 15.5–17.6 MPa were obtained for LWGCs with L/A ratio of 0.70, 0.75, and 0.80, respectively. However, the differences between splitting tensile strengths and surface abrasion resistances of the concretes with three L/A ratios were not significant. For example LWGC with NS/NH ratio of 1.0, the splitting tensile strengths of 1.7, 1.3, and 1.4 MPa and the abrasion weight losses of 4.4, 5.4, and 4.4 g were obtained for LWGCs with L/A ratios of 0.70, 0.75, and 0.80, respectively.

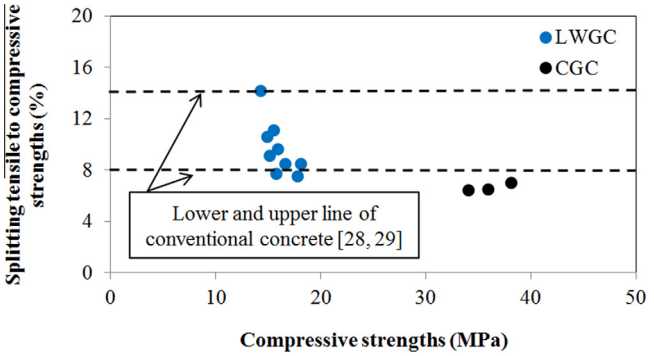

Fig. 9. Splitting tensile to compressive strength ratios and compressive strengths of concretes.

4.3. Density, thermal conductivity, and ultrasonic pulse velocity (UPV)

The results of density, thermal conductivity, and ultrasonic pulse velocity (UPV) are shown in Table 4. The use of CB and FB as aggregates for making LWGCs produced lower density concrete compared to those with natural aggregates (CL and RS). The densities of LWGCs ranged from 1661 to 1688 kg/m^3, which were about 25% lower than those of CGCs (2258–2299 kg/m^3). This was due to the lower density of BA (1116 kg/m^3) compared to CL (1576 kg/m^3). Besides, the densities of LWGCs in this study (1661–1688 kg/m^3) were in the range of 1440–1850 kg/m^3 for structural lightweight concrete in accordance with ACI 213 [32]. However, the compressive strengths of LWGCs (14.3–18.1 MPa) were slightly lower than those reported in ACI 213 [32] (17.24–41.36 MPa). The L/A and NS/NH ratios had slightly effect on the density of LWGCs. For example, the densities of 1673, 1681, and 1664 kg/m^3 were obtained for LWGC with NS/NH ratio of 1.0 and L/A ratios of 0.70, 0.75, and 0.80, respectively, and densities of 1676, 1664, and 1667 kg/m^3 were obtained for LWGC with L/A ratio of 0.80 and NS/NH ratios of 0.5, 1.0, and 1.5, respectively.

In general, the thermal conductivity coefficients and ultrasonic pulse velocity (UPV) depended on the density of concrete [33,34]. In this study, the densities (1661–1688 kg/m^3) and thermal conductivity coefficients (0.43–0.47 W/m K) of LWGCs varied in a narrow range. For the thermal conductivity coefficients, the results indicated that it also depends on the type of aggregate. The thermal

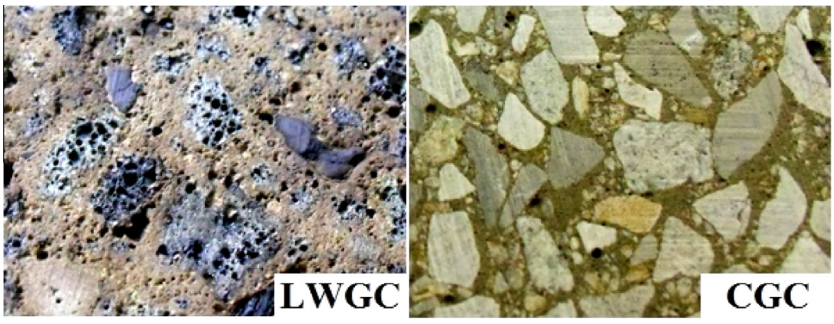

Fig. 8. Cut surface of LWGC and CGC.

Table 4
Density, thermal conductivity coefficient, and ultrasonic pulse velocity of geopolymer concretes.

Mix	Density (kg/m^3)	Thermal conductivity coefficient (W/m K)	Ultrasonic pulse velocity (m/s)
0.70CLRS0.5	2258	1.41	3089
0.70CLRS1.0	2299	1.58	3419
0.70CLRS1.5	2272	1.58	3303
0.70CBFB0.5	1675	0.46	2600
0.70CBFB1.0	1673	0.44	2397
0.70CBFB1.5	1688	0.46	2415
0.75CBFB0.5	1669	0.45	2736
0.75CBFB1.0	1681	0.43	2636
0.75CBFB1.5	1661	0.43	2292
0.80CBFB0.5	1676	0.47	2641
0.80CBFB1.0	1664	0.45	2585
0.80CBFB1.5	1667	0.43	2546

conductivity coefficients of LWGCs containing CB and FB were significantly lower than those of CGCs containing CL and RS. This was due to the high porosity and low density of BA aggregates and low density of LWGCs [35]. This consistent with previous report on the values of thermal conductivity coefficients of lightweight pervious concrete containing lightweight aggregates of 0.16–0.25 W/m K [36]. These values were significantly lower than the values of 0.7–1.4 W/m K of pervious concrete containing natural aggregate [37]. Saygılı and Baykal [38] also reported that the decrease in the thermal conductivity was due to the increase in void ratio of concrete. Ng and Low [39] explained that the air in concrete pores was the poorest in terms of thermal conductivity compared to the solid and liquid, and this thus contributed to a low thermal conductivity of concrete [34]. In this study, the thermal conductivity coefficients of LWGCs were approximately 3 times lower than that of CGCs (1.41–1.58 W/m K) and were also lower than those of metakaolin geopolymer lightweight concretes containing blast furnace slag aggregates (thermal conductivities of 0.47–1.65 W/m K and densities of 600–1800 kg/m^3) [33], oil palm shell foamed geopolymer concrete (thermal conductivities of 0.47–0.58 W/m K and densities of 1290–1795 kg/m^3) [34]. The values were comparable to those of insulating lightweight concrete (0.43 W/m K) given in ASTM C 332 [40].

The UPV of LWGCs (2292–2736 m/s) were lower than those of CGCs (3089–3419 m/s) as shown in Table 4. This was due to the high porosity with low density of BA and low density of LWGCs. The relationship between compression strength and UPV of LWGCs and CGCs in this study was plotted and compared with that of cement concrete [22] as given in Fig. 10. At the same compressive strength, the UPV values of LWGCs in this study were lower than

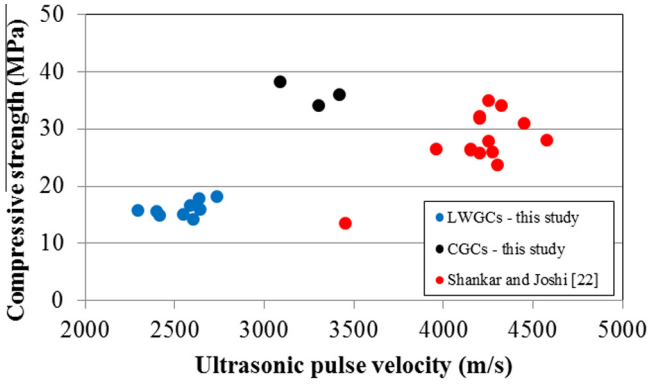

Fig. 10. Compression strength and ultrasonic pulse velocity (UPV).

those of conventional Portland cement concrete due to the low density of BA and LWGCs. In addition, the specific gravity of FA was lower than ordinary Portland cement [3]. The UPVs of CGCs thus showed lower values than the conventional Portland cement concrete. The L/A and NS/NH ratios also had a slight effect on the thermal conductivity coefficients and UPV similar to the effect of density.

These results indicated that BA could be used to produce LWGC with acceptable compressive strengths and splitting tensile strengths. The compressive strength of LWGCs (14.3–18.1 MPa) in this study had slightly lower than those of structural lightweight concrete (17.24–41.36 MPa) while the density (1661–1688 kg/m^3) were in the range of 1440–1850 kg/m^3 and in accordance with ACI 213 [32]. Furthermore, the low thermal conductivity (0.43–0.47 W/m K) and low density indicated better insulating properties of LWGC compared with the other construction materials, viz. fire brick (1.00 W/m K thermal conductivity coefficient and 2000 kg/m^3 density) and mud brick (0.75 W/m K thermal conductivity coefficient and 720–1731 kg/m^3 density) [38]. LWGCs in this study could be used for thermal insulation concrete and moderate strength concrete (6.89–17.24 MPa) in accordance with ACI 213 [32].

5. Conclusions

This study presents the properties of geopolymer concrete containing fly ash as geopolymer binder and bottom ash as aggregates. The results show that bottom ash can be used as fine and coarse aggregates for making lightweight fly ash geopolymer concrete with 14.3–18.1 MPa compressive strengths and 1.2–2.0 MPa splitting tensile strengths. These lightweight geopolymer concretes had the densities and thermal conductivity coefficients of 1661–1688 kg/m^3 and 0.43–0.47 W/m K, respectively, which were lower than geopolymer concrete containing natural aggregates (crushed limestone and river sand). The increase of NS/NH ratio decreased the slump of fresh concrete, compressive strengths, splitting tensile strengths, and surface abrasion resistance, whereas the increase in L/A ratio increased the slump of fresh concrete.

Acknowledgements

The authors would like to acknowledge the financial supports from the Higher Education Research Promotion and National Research University Project of Thailand, Office of the Higher Education Commission, through the Advanced Functional Materials Cluster of Khon Kaen University; the Thailand Research Fund (TRF) and Khon Kaen University under the Royal Golden Jubilee Ph.D. Program (Grant No. PHD 0083/2556), TRF Research Career Development (Grant No. RSA5780013), and TRF Senior Research Scholar (Grant No. RTA5780004).

References

[1] P. Chindaprasirt, C. Jaturapitakkul, W. Chalee, U. Rattanasak, Comparative study on the characteristics of fly ash and bottom ash geopolymers, Waste Manage. 29 (2) (2009) 539–543.
[2] A. Sathonsaowaphak, P. Chindaprasirt, K. Pimraksa, Workability and strength of lignite bottom ash geopolymer mortar, J. Hazard. Mater. 168 (1) (2009) 44–50.
[3] V. Sata, A. Sathonsaowaphak, P. Chindaprasirt, Resistance of lignite bottom ash geopolymer mortar to sulfate and sulfuric acid attack, Cem. Concr. Compos. 34 (5) (2012) 700–708.
[4] S. Aydın, H. Yazıcı, H. Yiğiter, B. Baradan, Sulfuric acid resistance of high-volume fly ash concrete, Build. Environ. 42 (2) (2007) 717–721.
[5] T. Phoo-ngernkham, P. Chindaprasirt, V. Sata, S. Hanjitsuwan, Influence of Portland cement replacement in high calcium fly ash geopolymer paste, KKU Eng. J. 41 (1) (2014) 19–27.

[6] P. Chindaprasirt, T. Chareerat, V. Sirivivatnanon, Workability and strength of coarse high calcium fly ash geopolymer, Cem. Concr. Compos. 29 (3) (2007) 224–229.
[7] I. Demir, R.E. Hughes, P.J. DeMaris, Formation and use of coal combustion residues from three types of power plants burning Illinois coals, Fuel 80 (11) (2001) 1659–1673.
[8] B.R. Hart, M. Powell, W. Fyfe, B. Ratanasthien, Geochemistry and mineralogy of fly-ash from the Mae Moh lignite deposit, Thailand, Energy Sources 17 (1) (1995) 23–40.
[9] H. Kim, H. Lee, Use of power plant bottom ash as fine and coarse aggregates in high-strength concrete, Constr. Build. Mater. 25 (2) (2011) 1115–1122.
[10] Y. Zaetang, A. Wongsa, V. Sata, P. Chindaprasirt, Use of coal ash as geopolymer binder and coarse aggregate in pervious concrete, Constr. Build. Mater. 96 (2015) 289–295.
[11] American Society for Testing and Materials, Standard Specification for Coal Fly Ash and Raw or Calcined Natural Pozzolan for Use in Concrete, ASTM C618-12a: Annual Book of ASTM Standard, 2012.
[12] American Society for Testing and Materials, Standard Test Method for Unit Weight and Voids in Aggregate, ASTM C29/C29M-97a: Annual Book of ASTM Standard, 2001.
[13] American Society for Testing and Materials, Standard Test Method for Density, Relative Density (Specific Gravity), and Absorption of Coarse Aggregate, ASTM C127-07: Annual Book of ASTM Standard, 2007.
[14] American Society for Testing and Materials, Standard Test Method for Sieve Analysis of Fine and Coarse Aggregates, ASTM C136-06: Annual Book of ASTM Standard, 2006.
[15] American Society for Testing and Materials, Standard Test Method for Resistance to Degradation of Small-Size Coarse Aggregate by Abrasion and Impact in the Los Angeles Machine, ASTM C131-96: Annual Book of ASTM Standard, 2001.
[16] American Society for Testing and Materials, Standard Specification for Concrete Aggregates, ASTM C33/C33M-13: Book of Standards, 2013.
[17] American Society for Testing and Materials, Standard Test Method for Slump of Hydraulic-Cement Concrete, ASTM C143/C143M-12: Annual Book of ASTM Standard, 2012.
[18] American Society for Testing and Materials, Standard Test Method for Compressive Strength of Cylindrical Concrete Specimens, ASTM C39-10: Annual Book of ASTM Standard, 2010.
[19] American Society for Testing and Materials, Standard Test Method for Splitting Tensile Strength of Cylindrical Concrete Specimens, ASTM C496-96: Annual Book of ASTM Standard, 2001.
[20] American Society for Testing and Materials, Standard Test Method for Abrasion Resistance of Concrete or Mortar Surfaces by the Rotating-Cutter Method, ASTM C944: Annual Book of ASTM Standard, 2001.
[21] American Society for Testing and Materials, Standard Test Method for Density and Void Content of Hardened Pervious Concrete, ASTM C1754: Annual Book of ASTM Standard, 2012.
[22] S. Shankar, H.R. Joshi, Comparison of concrete properties determined by destructive and non-destructive tests, J. Inst. Eng. 10 (1) (2014) 130–139.
[23] American Society for Testing and Materials, Standard Test Method for Pulse Velocity through Concrete, ASTM C597-09: Annual Book of ASTM Standard, 2002.
[24] M. Singh, R. Siddique, Effect of coal bottom ash as partial replacement of sand on properties of concrete, Resour. Conserv. Recycl. 72 (2013) 20–32.
[25] H.K. Lee, H.K. Kim, E.A. Hwang, Utilization of power plant bottom ash as aggregates in fiber-reinforced cellular concrete, Waste Manage. 30 (2) (2010) 274–284.
[26] P. Topark-Ngarm, V. Sata, P. Chindaprasirt, Workability and strength of high calcium geopolymer concrete cured at room temperature, in: Annual Concrete Conference 7, Rayong, Thailand, 2011.
[27] P. Topark-Ngarm, P. Chindaprasirt, V. Sata, Setting time, strength, and bond of high-calcium fly ash geopolymer concrete, J. Mater. Civ. Eng. 27 (7) (2015) 04014198.
[28] W. Tangchirapat, R. Buranasing, C. Jaturapitakkul, P. Chindaprasirt, Influence of rice husk–bark ash on mechanical properties of concrete containing high amount of recycled aggregates, Constr. Build. Mater. 22 (8) (2008) 1812–1819.
[29] K.K. Sagoe-Crentsil, T. Brown, A.H. Taylor, Performance of concrete made with commercially produced coarse recycled concrete aggregate, Cem. Concr. Res. 31 (5) (2001) 707–712.
[30] H. El-Sayed, E.-E.S. Abo, H. Khater, S. Hasanein, Resistance of alkali activated water-cooled slag geopolymer to sulphate attack, Ceram.-Silik. 55 (2) (2011) 153–160.
[31] T. Tho-in, V. Sata, P. Chindaprasirt, C. Jaturapitakkul, Pervious high-calcium fly ash geopolymer concrete, Constr. Build. Mater. 30 (2012) 366–371.
[32] ACI Committee 213, Guide for Structural Lightweight Aggregate Concrete, American Concrete Institute, Detroit, USA, 2000.
[33] R. Arellano Aguilar, O. Burciaga Díaz, J.I. Escalante García, Lightweight concretes of activated metakaolin-fly ash binders, with blast furnace slag aggregates, Constr. Build. Mater. 24 (7) (2010) 1166–1175.
[34] M.Y.J. Liu, U.J. Alengaram, M.Z. Jumaat, K.H. Mo, Evaluation of thermal conductivity, mechanical and transport properties of lightweight aggregate foamed geopolymer concrete, Energy Build. 72 (2014) 238–245.
[35] P. Chindaprasirt, P. Nuaklong, Y. Zaetang, P. Sujumnongtokul, V. Sata, Mechanical and thermal properties of recycling lightweight pervious concrete, Arab. J. Sci. Eng. (2014) 1–8.
[36] Y. Zaetang, A. Wongsa, V. Sata, P. Chindaprasirt, Use of lightweight aggregates in pervious concrete, Constr. Build. Mater. 48 (2013) 585–591.
[37] J. Wong, F. Glasser, M. Imbabi, Evaluation of thermal conductivity in air permeable concrete for dynamic breathing wall construction, Cem. Concr. Compos. 29 (9) (2007) 647–655.
[38] A. Saygılı, G. Baykal, A new method for improving the thermal insulation properties of fly ash, Energy Build. 43 (11) (2011) 3236–3242.
[39] S.-C. Ng, K.-S. Low, Thermal conductivity of newspaper sandwiched aerated lightweight concrete panel, Energy Build. 42 (12) (2010) 2452–2456.
[40] American Society for Testing and Materials, Standard Specification for Lightweight Aggregates for Insulating Concrete, ASTM C 332: Annual Book of ASTM Standard, 2009.

Construction and Building Materials 112 (2016) 956–961

Contents lists available at ScienceDirect

Construction and Building Materials

journal homepage: www.elsevier.com/locate/conbuildmat

Improvement of durability of cement pipe with high calcium fly ash geopolymer covering

Prinya Chindaprasirt [a], Ubolluk Rattanasak [b,*]

[a] Sustainable Infrastructure Research and Development Center, Department of Civil Engineering, Faculty of Engineering, Khon Kaen University, Khon Kaen 40002, Thailand
[b] Department of Chemistry, Faculty of Science, Burapha University, Chonburi 20131, Thailand

HIGHLIGHTS

- Covering of cement pipe with geopolymeric material.
- 3% H_2SO_4 with pH = 0.3, represents the worst condition in the wastewater system.
- pH and Ca^{2+} content of immersion solutions were measured.
- Covering with geopolymer could protect a cement-based material from aggressive solutions.

ARTICLE INFO

Article history:
Received 17 September 2015
Received in revised form 20 February 2016
Accepted 5 March 2016

Keywords:
Fly ash geopolymer
Calcium leaching
Acid resistance
Covering material

ABSTRACT

Cement pipes have been used to transfer the domestic sewage and industrial wastewater due to its cost effectiveness. However, they faced the acid attack problem owing mainly to the high content of calcium compounds in the composite. Coating of cement pipes is one of the methods to protect the cement pipe surface from acid attack. An alumino-silicate geopolymer provides excellent mechanical properties and resistance to severe environments. Therefore, this research proposed the covering of cement-based materials with geopolymer. The covered specimens were immersed in deionized water (pH = 6.1), 0.005% H_2SO_4 (pH = 3), 5% $MgSO_4$ (pH = 7.7) and 3% H_2SO_4 (pH = 0.3, representing the worst condition in the wastewater system). The pH and Ca^{2+} content of immersion solutions were measured. In addition, mechanical and chemical properties of geopolymeric-covering material were tested after the immersion in solutions for 30 and 90 days.

© 2016 Elsevier Ltd. All rights reserved.

1. Introduction

Cement pipes have been widely used as transportation facilities to transfer the domestic sewage and industrial wastewater due to its cost effectiveness. However, these cement pipes are not resistant to acid since calcium compounds in the cement system can be dissolved in acidic environment resulting in increased porosity and deterioration. Several methods are used to control the concrete degradation in wastewater facilities. Vitrified clay pipe has been proposed due to its resistance to acids, alkalines, septic sewage, scour and erosion [1]. Vitrification process is achieved using very high temperature resulting in the fusing of particle grains and a vitreous surface. The product has low porosity and high hardness, similarly to the glazed ceramic tile. However, this process is suitable for pipes less than 300 mm in diameter, and its production cost is high [2]. Coating or covering is another methods adopted currently to overcome this problem [1]. Bonding strength and chemical resistance of coating material play an important role in performance of coating.

Geopolymer is an alumino-silicate composite and is sometimes called "low-temperature ceramic". The reaction is usually activated with moderate heat at curing temperature up to 90 °C to achieve the required hardening and strength in short period of time. Pulverized coal combustion (PCC) fly ash is a good source material for the synthesis of geopolymer due to its high glassy phase content and pozzolanic property. This composite provides high strength, excellent mechanical properties and good resistance to severe environments. Researches have been done on geopolymer for use as concrete coating materials in marine environment [3] and for thermal application [4,5]. This geopolymer was also found to have excellent anti-corrosion and fire resistant properties.

Due to the good acid resistance of geopolymer [6], covering with geopolymer is, therefore, a good potential to cope with acid attack of cement pipes as well as to extend the methods of

* Corresponding author.
E-mail address: ubolluk@buu.ac.th (U. Rattanasak).

http://dx.doi.org/10.1016/j.conbuildmat.2016.03.023
0950-0618/© 2016 Elsevier Ltd. All rights reserved.

utilization of geopolymer. This research thus proposed the characterization of geopolymeric coating material under acid condition. 3% sulfuric acid solution representing the worst condition in the wastewater system [1] was selected for test in this work. In addition, 0.005% H_2SO_4 (pH = 3) was also used to represent the practical untreated industrial wastewater.

2. Experimental procedure

2.1. Materials

PCC fly ash from Mae Moh power plant in northern Thailand was used as a source material for geopolymer preparation. The pulverized lignite coal was used as a feedstock of combustion unit with temperature of 1200 °C. Chemical compositions of PCC fly ash as determined by X-ray fluorescence (XRF, Philips PW-2404) are shown in Table 1. This fly ash consisted of quartz (SiO_2), aluminium oxide (Al_2O_3), lime (CaO) and hematite (Fe_2O_3) as major oxide components. High CaO content of 16.4% was obtained due to low grade lignite coal. The median particle size (D50) of fly ash as measured by particle size analyzer (Malvern Mastersizer S) was 19 μm. NaOH pellets were dissolved in deionized (DI) water to prepare 10 M NaOH solution. Sodium silicate solution or water glass ($Na_2O{\cdot}SiO_2$, 30 %wt SiO_2 and 9 %wt Na_2O) was also used as alkali activator. Fine river sand (passing through sieve No. 30) with specific gravity of 2.7 and fineness modulus of 1.9 was used to prepare geopolymer mortar for physical test.

2.2. Specimen preparation and test program

2.2.1. Cement mortar preparation

Cement mortar with water-to-cement ratio of 0.55 and sand-to-cement ratio of 2 was used as substrate. The specimen was 15 mm in diameter and 100 mm in height. In addition, 40 × 90 × 20-mm cement mortar prisms were prepared for bond strength test in accordance with ASTM C321. After demolding at the age of 1 day, the specimens were cured in water until the age of 28 days and then air-dried for 24 h before the application of geopolymeric–covering and testing.

2.2.2. Geopolymer mortar preparation

Geopolymer mortar was prepared as covering material as follows. Water glass-to-NaOH solution mass ratio of 2 was used in addition with sand-to-fly ash mass ratio of 2. Mix proportion of geopolymer paste consisted of 60 %wt fly ash, 27 % wt water glass and 13 %wt 10 M NaOH solution. Fly ash was thoroughly mixed with sand to obtain a uniform starting material. Then, alkali activator (NaOH solution and water glass) was added and mixed for 1 min by mixer to obtain geopolymer mortar. The fresh geopolymer mortar was then placed in a cylindrical plastic container. Subsequently, the prepared cement mortar cylinders were dipped in the fresh geopolymer mortar to obtain the geopolymeric covering of specimens. From trial covering, this method gave a uniform geopolymer mortar thickness of 4.0 ± 0.3 mm. The covered specimens were left in a 25 °C and 50% R.H. chamber for 2 h, cured at 65 °C for 24 h. and left to cool down to room temperature. Hardened specimens were immersed in deionized water (*assigned as* DI), 0.005% H_2SO_4 (*assigned as* 0H), 3% H_2SO_4 (*assigned as* 3H) and 5% $MgSO_4$ (*assigned as* 5M) solutions with the corresponding pH values of 6.1, 3.0, 0.3 and 7.7, respectively. The volume of solutions was 125 ml in 300-ml plastic glass and was kept constant. The test set-up is diagrammatically shown in Fig. 1a.

The pH and Ca^{2+} content of solutions were monitored using pH and calcium ion meters at the testing ages of 30 and 90 days. Geopolymeric–covering specimens were tested for hardness using durometer type D (shore D). The coverings were also ground and characterized with X-ray diffraction (XRD, PANalytical/Expert, Cu-Kα radiation) and Fourier transform infrared spectroscopic (FT-IR, Perkin Elmer system 2000, KBr pellet, 1 cm^{-1} resolution) analyses at the age of 90 days.

In addition, bond strength of geopolymer mortar and cement mortar was tested following the method adapted from ASTM C321-00 [7]. Cross-cement mortar with geopolymer material in between for testing of bond is shown in Fig. 1b. The prepared specimens were cured at 65 °C for 24 h and then kept in 25 °C and 50% R. H. chamber. Bond strength test was performed at the ages of 30 and 90 days. The results were reported as an average of five samples.

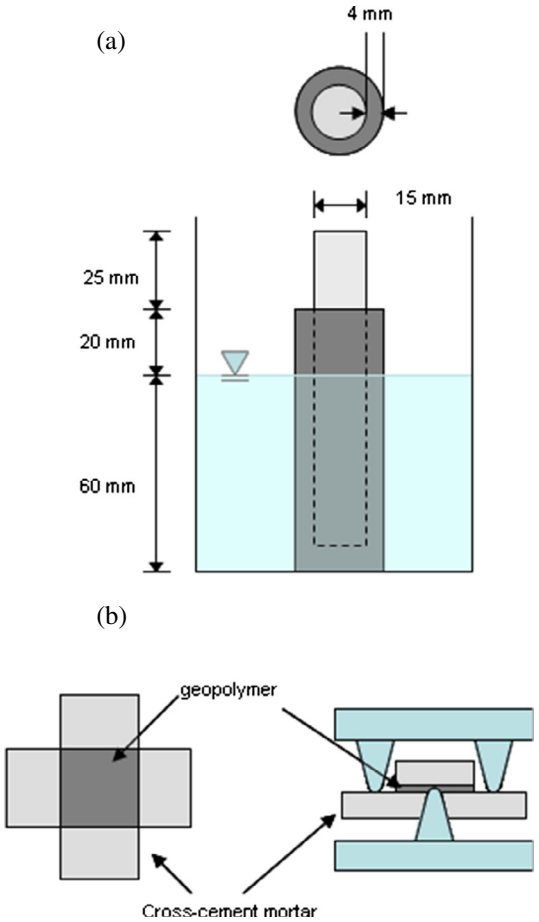

Fig. 1. Test set-up. (a) Geopolymeric–covering specimen in immersion solution. (b) Cross-cement mortar mounted on special fixture.

3. Result and discussion

3.1. pH and Ca^{2+} content of immersion solutions

Acid can easily leach out the calcium ion (Ca^{2+} ion) from cement mortar owing to the high content of free lime and $Ca(OH)_2$. The results of Ca^{2+} ion content of immersion solutions of geopolymeric–covering specimens at 30 and 90 days are shown in Fig. 2. Ca^{2+} ion contents of all fresh solutions were 0 ppm (mg/l). When the geopolymer surface of specimens came into contact with the immersion solutions, calcium ions started to leach out due mainly to the high calcium content of source material. The contents of Ca^{2+} ions in immersion solutions at 30 days were 0, 0, 7 and 8 ppm in DI, 0H, 3H and 5M solutions, respectively. There was no leaching out of Ca^{2+} ions after 30-day immersion in DI water and low acid content solution (0H). However, the high acid (3H) and salt (3 M) solutions provided high Ca^{2+} ion content. In other words, the leaching of calcium ion was very large with the immersion of geopolymeric–covering specimens in 3% H_2SO_4 and 5% $MgSO_4$ solutions. The presence of calcium oxide in the fly ash helped accelerate the setting and hardening of geopolymer [8]. Calcium compound reacted with silica and resulted in the formation of calcium silicate

Table 1
Chemical compositions and LOI of fly ash.

Compositions (%)	SiO_2	Al_2O_3	CaO	Fe_2O_3	SO_3	MgO	K_2O	Na_2O	LOI
Fly ash	36.1	25.0	16.4	12.0	3.3	2.2	2.6	1.6	0.8

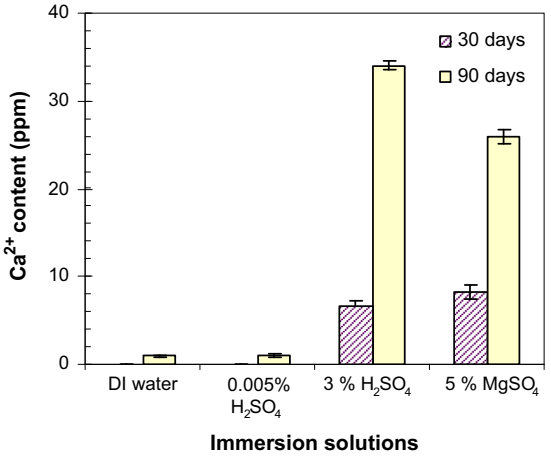

Fig. 2. Ca^{2+} ion content of immersion solutions at 30 and 90 days.

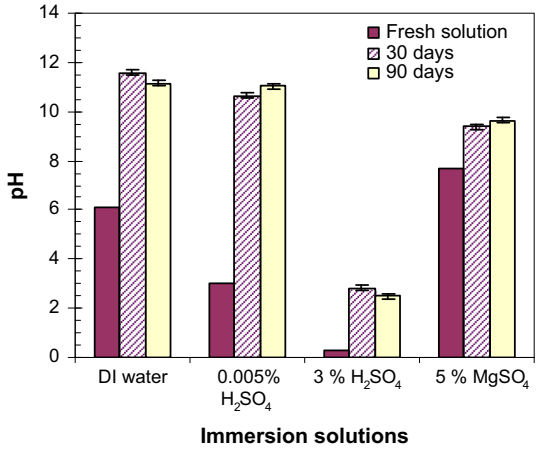

Fig. 3. pH of immersion solutions at 30 and 90 days.

compound which coexisted with the sodium aluminosilicate hydrate (NASH) [9]. Although the calcium silicate compound helps with the strength development of the geopolymer, it is susceptible to the attack by aggressive solutions.

For immersion of 90 days, the Ca^{2+} ion content increased appreciably to 34 and 26 ppm with the immersion in 3H and 3M solution, respectively. For the DI and 0H solution, the Ca^{2+} ion contents slightly increased to 1 ppm. The low leaching in DI and 0H solution were due to the formation of thin water layer on the surface of geopolymer mortar as same as in case of concrete [1]. This indicated that the leaching of Ca^{2+} ion after the immersion of specimens for 30 days was minimal for the no or low acid content solutions. The increase in the amount of Ca^{2+} ions up to immersion of 90 days in 3H solution suggested that the high acidity environment was still conducive for the leaching of the calcium products after immersion for 30 days. In addition to acid environment, sulfate solution also destructively affected the stability of calcium compounds in geopolymer. Mg^{2+} and SO_4^{2-} ions from $MgSO_4$ solution could react with $Ca(OH)_2$ and $CaO{\cdot}SiO_2$ compounds in geopolymer resulting in formation of gypsum and deterioration of covering material [6,10].

For non-covering cement mortar, the Ca^{2+} ion content at 30-day immersion were 7, 13, 265 and 16 ppm for DI, 0H, 3H and 5M solutions, respectively. Increase in Ca^{2+} ion content in 3H solution was detected at 90-day immersion of 470 ppm. Cement mortar specimens were unstable and starting to dissolve at first week of acid immersion. High concentration of acidic solution could attack the calcium compounds i.e. calcium silicate, calcium aluminate, and calcium alumino-ferrite hydrates, which decomposed to amorphous hydrogel [11].

The results of pH values of immersion solutions are presented in Fig. 3. For DI and 5M solution, the initial pH values were 6.1 and 7.7 which were close to the neutral value of 7.0. Since geopolymer is an alkali-activated composite, therefore, its leachate is a base (pH > 7). When geopolymeric–covering specimens were immersed in DI water and 5M solution, hydroxyl group (OH^-) from geopolymer was released resulting in basic solution. The pH of DI water was 11.6 which was higher than 9.4 of 5M solution. This is probably because the released OH^- reacted with Mg^{2+} from $MgSO_4$ solution resulting in solid $Mg(OH)_2$ and consequently low free OH^- ion in solution

For the acidic 0H and 3H solutions, the initial pH values of immersion solutions were 3.0 and 0.3, respectively and after immersion of geopolymeric–covering specimens for 30 days, the pH values of immersion solutions increased to 10.7 and 2.8, respectively. For the low acidic 0H solution, the increase in pH value indicated that the solution was a base with 30-day immersion and thus the leaching out of Ca^{2+} at this stage should be minimal. At pH value lower than 12.6, portlandite is starting dissolution [11]. For the high acidic 3H solution, the pH at 30-day immersion was still low at 2.8. This indicated that the solution was still harmful to the geopolymeric–covering specimens. At low pH value, the H^+ ions from acid could aggressively attack the alumino-silicate network of geopolymer at oxy-alumino bridge and resulted in the breakdown of bond and led to weak material [6,10–13].

After 90 days of immersion, the pH values of solutions were not different from those at 30-day immersion. pH values of cement-based mortar immersed in sodium sulfate solution was also reported by other researcher [14]. Increase in pH was due to the formation of basic compound i.e. $Ca(OH)_2$ during the progress of immersion and Ca^{2+} leaching.

3.2. Characterizations of composites

3.2.1. Hardness

Hardness of geopolymeric–covering material was tested by durameter hardness (Shore D), which is for hard material testing, and the results are shown in Fig. 4. This hardness test is based on depth of indentation by a standard indenter. The shore hardness values of specimens at 30-day immersion were 45, 53, 44 and 55 for DI water, 0H, 3H and 5M solutions indicating all specimens could still be considered as a hard material. Immersion of

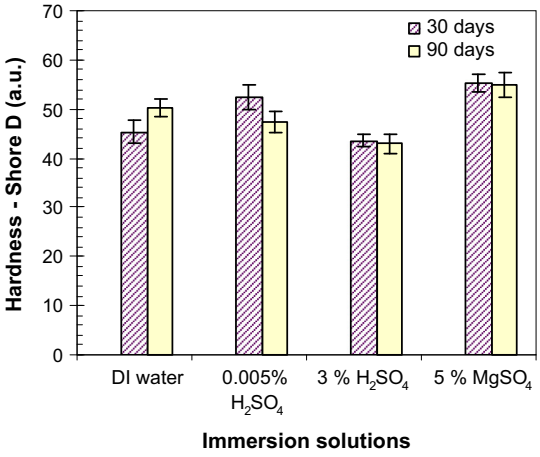

Fig. 4. Hardness of geopolymeric–covering material at 30 and 90 days.

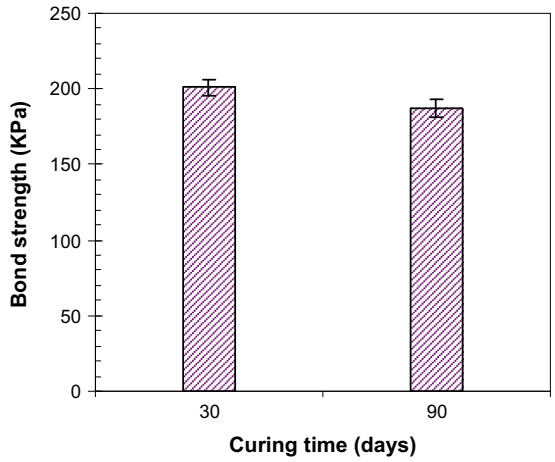

Fig. 5. Bond strength of cross-cement mortar prisms and geopolymer mortar joint at 30 and 90 days.

specimens in $MgSO_4$ solution gave the hardest surface owing to the formation of $Mg(OH)_2$ on geopolymer surface [12]. For immersion in 3% H_2SO_4, the hardness dropped to 44 indicating the increasing attack of sulfuric acid. This hardness number, however, corresponded to the medium hardness material [15].

Increase in immersion time to 90 days, the hardness value of specimens immersed in 3H solution was not significantly changed and could be classified as medium material. The penetration of aggressive solution into geopolymeric–covering material led to the reduction of surface hardness. To overcome this problem, an improvement of water permeability and increase in thickness are recommended.

For cement mortar, hardness could not be measured in case of immersion in 3H solution due to the surface dissolution and unstable specimens. Surface stability was destroyed starting from first week of acid immersion.

3.2.2. Bond strength

The results of bond strength test of cross-cement mortar prisms with joint geopolymer mortar are shown in Fig. 5. The bond strength at curing ages of 30 and 90 days were 201 and 187 kPa, respectively. This result met a minimum bond strength requirement between the masonry bricks and mortar joint of 140 kPa [16]. It has been reported that water content and shrinkage affected the bond strength of composite [17]. The strength of geopolymer mortar could reduce with curing age as a result of shrinkage [18]. Thus the slight drop in bond strength with curing age was probably due to the high water content and subsequent shrinkage. To obtain low shrinkage and good bond strength cement grouts, water-cement ratio less than 0.35 is recommended [17]. This condition, however, caused low workability and not particularly suitable for covering application. Even with a small reduction in bond strength at 90 days curing, the bond strength of geopolymer and cement mortars easily satisfied the minimal requirement.

3.2.3. Fourier transform infrared spectroscopy (FT-IR)

The results of FT-IR spectra recorded between wavenumber 4000–400 cm^{-1} of fly ash and geopolymer mortars immersed in solutions for 90 days are shown in Fig. 6. Bond vibration and peak shift at a specific wavenumber of Si–O and Al–O in geopolymer were compared with that of original fly ash. For fly ash, the significant bands consisted of O–H stretching and O–H bending bands of water molecule at 3450 cm^{-1} and 1600 cm^{-1}, respectively. For geopolymer, Si–O–Al stretching mode was more prominent than that of Si–O–Si bending mode and could be detected at 980–1050 cm^{-1} [6,19].

After immersion for 90 days, geopolymer mortars showed dominant O–H bands at 3450 cm^{-1} and 1600 cm^{-1} owing to the alkali solutions used for preparation of geopolymer. The FTIR spectra of samples in DI, 0H and 5M solutions were similar indicating that the immersion in these solutions did not significantly change the chemical structure of geopolymer. Shift of Si–O stretching band was found to a lower wavenumber of 1000 cm^{-1} as a result of the chemical bond change in materials [6]. In addition, the shift of this stretching mode to lower wavenumber indicated the change in number of tetrahedral aluminium atoms in alumino-silicate material [20].

However, the FT-IR spectrum of geopolymer immersed in 3H solution was different. Dominant peaks of Al–O were found at 600–650 cm^{-1}, peaks of O–H stretching and C=O band were also observed at 3400–3600 cm^{-1} and 1300 cm^{-1}, respectively. Owing to the low pH of 3H solution, this could destroy the chemical bond in geopolymer. H^+ ion from acid could decompose the Si–O–Al network resulting in Si–OH and Al–OH, and hindered the formation of

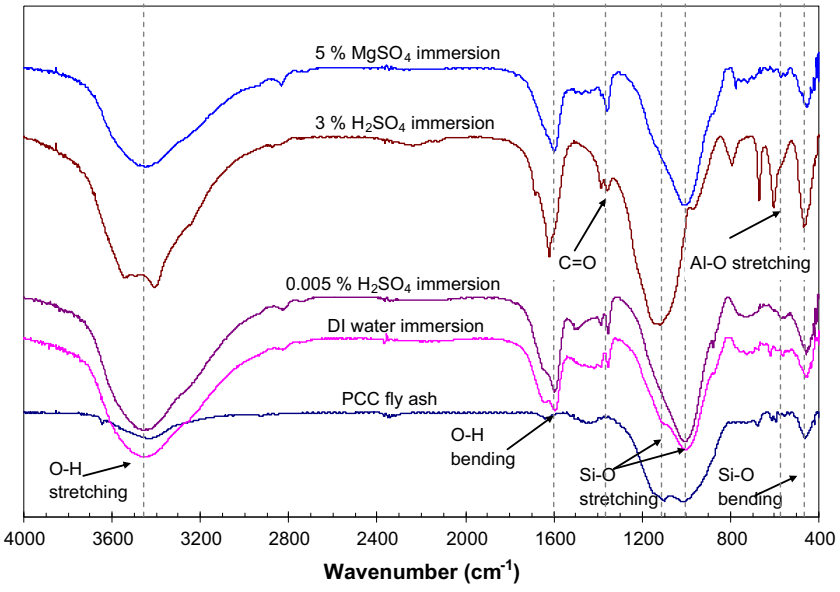

Fig. 6. FT-IR spectra of fly ash and geopolymeric–covering materials immersed in solutions for 90 days.

new geopolymeric Si–O bonding. The polarity of the O–H bond was increased [21] and the peak of O–H stretching was therefore found. Peak of C=O band was due to carbonation of specimen presence in the interlayer of composite [6,22]. In addition, an asymmetry in tetrahedral sites of Al substitution due to acid attack could result in the two peaks of Al–O at 600–650 cm^{-1} [23]. The attack of acid on geopolymer resulted in the change of chemical bonding of geopolymer.

3.2.4. X-ray diffraction (XRD)

In this research, XRD technique was also performed on the fly ash and geopolymeric–covering materials immersed in solutions for 90 days in order to identify and analyze the minerals in materials. The XRD patterns are shown in Fig. 7.

Fly ash contained quartz (SiO_2), Al_2O_3, hematite (Fe_2O_3) and various forms of calcium compounds (calcite, $CaCO_3$; anhydrite, $CaSO_4$; and lime; CaO) conforming to the XRF result. After the synthesis of geopolymer, some minerals remained in the composite and new products were formed. After immersion in solutions, there were changes in the content of the amorphous and crystalline products. For samples immersed in DI and 5M solutions, the XRD results were similar with the presence of amorphous phase as indicated by the broad hump around 25–35° 2θ and crystalline peaks of quartz, hematite, calcite, anhydrite, AlH_3O_3, tobermorite and kyanite. The crystalline quartz, hematite, calcite and anhydrite were the remnant of original crystalline phases in fly ash and the amount was reduced with the geopolymerization. The Al_2O_3 phase transformed to kyanite and some of SiO_2 transformed to tobermorite with CaO phase totally disappeared. For the samples immersed in 0H solution, the crystalline phases were similar to those immersed in DI and 5M solutions. However, the amorphous phase was much reduced as indicated by the very small broad hump compared with those immersed in DI and 5M solutions. The results indicated that immersion of specimen in a very low concentration of acid (0.005% H_2SO_4), the attack on the glassy phase in geopolymers was evident. The results conformed with the reduction in hardness of the specimens immersed in 0H solution comparing with those in DI and 5M solutions.

For the specimen immersed in 3H solution, a number of prominent crystalline peaks of gypsum, AlH_3O_3 and Al_2O_3 with some anhydrite were observed and the amorphous phase disappeared. Gypsum (CaH_4O_6S or $CaSO_4{\cdot}2H_2O$) at 11.63, 20.73, 23.39, 29.12, 31.12 and 33.37° 2θ and anhydrite were formed from the reaction between calcium (from composite) and sulfate ion (from H_2SO_4 acid). H^+ from acid ionization (pH of solution was lower than 2) also attacked the alumino-silicate network and leached out the calcium ion. Consequently, gypsum and anhydrite were formed and deposited on the surface and in voids of geopolymer. The presence of aluminium hydroxide (AlH_3O_3 or $Al(OH)_3$) at 37.25, 40.69 and 47.88° 2θ indicated the destruction of Al–O–Si bridge in alumino-silicate network by acid. This behavior resulted in the lowering of the hardness of geopolymeric–covering materials.

The covering of concrete with geopolymer mortar could reduce the attack of aggressive solutions. With very mild 0.005% H_2SO_4 and quite strong 5% $MgSO_4$ solutions, the covering with 4 mm thick geopolymer mortar provided sufficient protection within the period of 90 days immersion. It is likely that slightly more damage could result for a longer period of immersion, this needs further investigation. For very aggressive solution of 3% H_2SO_4, the geopolymeric–covering material could help to protect the composite for a reasonable time frame, i.e. the results of hardness test still confirmed that the surface of specimen was still hard for the immersion period of 30 days. However, the longer period of immersion of 90 days resulted in a significant attack on the specimen with reduction in the amorphous gel of geopolymeric sample and associated large reduction in surface hardness.

3.2.5. Acid penetration

Geopolymeric–covering specimens were subjected to acid environment (3H solution). The depths of acid penetration were measured with the stereo microscope on the prepared cross-sections of immersed specimens in acid solution. The results of 30 and 90 days of acid immersion are shown in Fig. 8. The depths of acid penetration at 30 and 90 days were 1.7 and 2.9 mm, respectively. This prolonged the time for the acid to get to the cement pipe. Furthermore, the deterioration of geopolymer was relatively small comparing to that of cement mortar, and thus resulted in the stability of material. Low calcium leachate of the material was also detected. In case of cement concrete, rate of acid deterioration was proportional to the square root of time [24]. In addition, the permeability of composite affected the dissolution and stability by acid attack. Geopolymer was a dense alumino-silcate compound

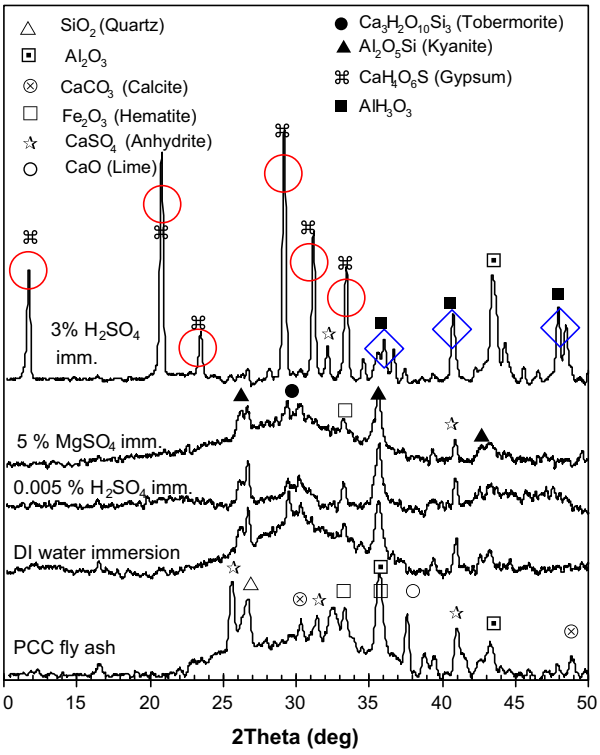

Fig. 7. XRD patterns of fly ash and geopolymeric–covering materials immersed in solutions for 90 days.

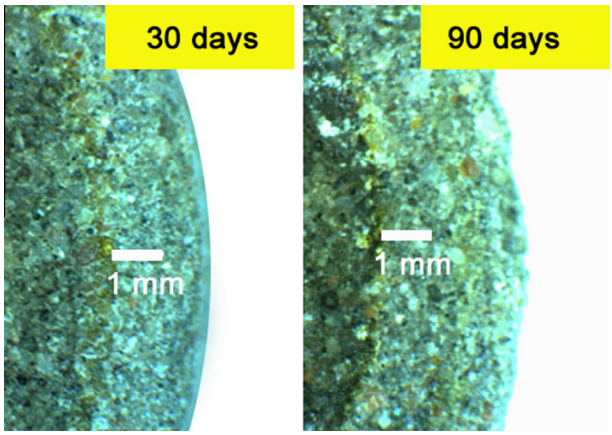

Fig. 8. Depth of acid penetration of cross-sections of specimen after immersion in 3% H_2SO_4 for 30 and 90 days.

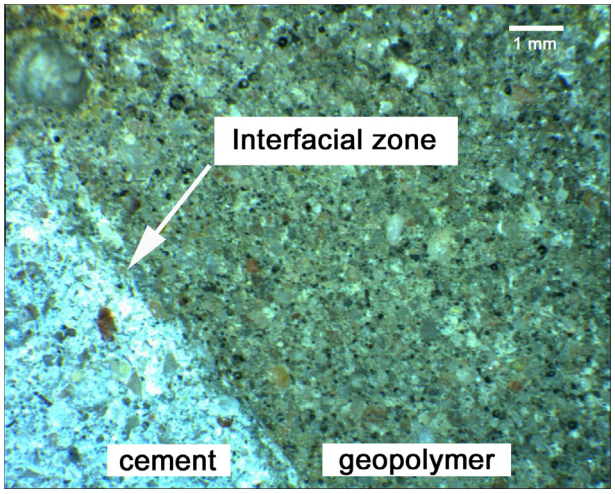

Fig. 9. Interfacial zone of geopolymer-cement mortar.

and thus is a good acid resistant material. Acid attack can be further reduced with the use of low water content in mixture, and low calcium fly ash in order to reduce the silicate hydrates (C–S–H) formation [24]. However, the high calcium fly ash gives a more reasonable setting and strength at ambient temperature comparing to the low calcium fly ash [9]. Fig. 9 shows the interfacial zone of geopolymer-cement mortar. No visible gaps could be observed and the interfacial zone was dense indicating the good bonding between the two materials.

4. Conclusion

Application of geopolymeric–covering material could protect the cement-based materials from aggressive solutions. For immersion in solutions of low acid concentration (0.005% H_2SO_4, pH = 3) and of DI water (pH = 6.1), low amount of Ca^{2+} ions were leached out to the immersion solution. The main products of high calcium fly ash geopolymer consisted of alumino-silicate compounds and calcium silicate hydrates which were resistant to these immersion solutions. However, immersion in high acid concentration (3% H_2SO_4, pH = 0.3), the geopolymeric–covering material was attacked resulting in high Ca^{2+} ion leaching. After immersion for 30 days, the specimen was still intact with hard surface. However, the hardness of geopolymer surface was reduced to low hardness with immersion for 90 days. Gypsum was formed and H^+ from acid ionization attacked the alumino-silicate network resulting in the breaking of Al–O–Si bonds. Thus, for aggressive solution and/or long period of immersions, an improvement in water tightness with low water content and increase in thickness of covering material are recommended.

Acknowledgements

This work was supported by the Thailand Research Fund (TRF) and Khon Kaen University under TRF Senior Research Scholar contract no. RTA5780004; and Burapha University under TRF Research Scholar contract no. RSA5880001.

References

[1] J. Liu, C. Vipulanandan, Evaluating a polymer concrete coating for protecting non-metallic underground facilities from sulfuric acid attack, Tunn. Undergr. Space Technol. 16 (1) (2001) 311–321.
[2] M.R. Lindeburg, Civil Engineering Reference Manual for the PE Exam, 13th ed., Professional Publications, Inc., California, 2012.
[3] Z. Zhang, X. Yao, H. Zhu, Potential application of geopolymers as protection coatings for marine concrete I. Basic properties, Appl. Clay Sci. 49 (1) (2010) 1–6.
[4] J. Temuujin, A. Minjigmaa, W. Rickard, M. Lee, I. Williams, A. van Reissen, Fly ash based geopolymer thin coatings on metal substrates and its thermal evaluation, J. Hazard. Mater. 180 (1–3) (2010) 748–752.
[5] J. Temuujin, W. Rickard, M. Lee, A. van Reissen, Preparation and thermal properties of fire resistant metakaolin-based geopolymer-type coatings, J. Non-Cryst. Solids 357 (5) (2011) 1399–1404.
[6] P. Chindaprasirt, U. Rattanasak, S. Taebuanhuad, Resistance to acid and sulfate solutions of microwave-assisted high calcium fly ash geopolymer, Mater. Struct. 46 (3) (2013) 375–381.
[7] ASTM International, ASTM C 321 – 00: standard test method for bond strength of chemical-resistant mortars, Annual Book of ASTM Standards, vol. 04.05, 2000, p. 4.
[8] P. Chindaprasirt, T. Chareerat, S. Hatanaka, H.T. Cao, High-strength geopolymer using fine high-calcium fly ash, J. Mater. Civ. Eng. 23 (3) (2011) 264–270.
[9] K. Somna, C. Jaturapitakkul, P. Kajitvichyanukul, P. Chindaprasirt, NaOH-activated ground fly ash geopolymer cured at ambient temperature, Fuel 90 (6) (2011) 2118–2124.
[10] A. Allahverdi, F. Skvara, Acidic corrosion of hydrated cement based materials: Part 1. – mechanism of the phenomenon, in: Ceram. Silik. 44 (3) (2000) 114–120.
[11] J. Skalny, J. Marchand, I. Odler, Sulfate Attack on Concrete, Spon Press, London, 2002.
[12] P. Chindaprasirt, S. Jenjirapanya, U. Rattanasak, Characterizations of FBC/PCC fly ash geopolymeric composites, Constr. Build. Mater. 66 (1) (2014) 72–78.
[13] A.D. Wilson, J.W. Nicholson, Acid-Base Cements: Their Biomedical and Industrial Applications (Chemistry of Solid State Materials), Cambridge University Press, New York, 1993.
[14] P. Chindaprasirt, P. Kanchanda, A. Sathonsaowaphak, H.T. Cao, Sulfate resistance of blended cements containing fly ash and rice husk ash, Constr. Build. Mater. 21 (6) (2007) 1356–1361.
[15] ASTM International, ASTM C 2240 – 03 : standard test method for rubber property - durometer hardness, Annual Book of ASTM Standards, vol. 09.01, 2003, p. 12.
[16] J.E. Amrhein, Reinforced Masonry Engineering Handbook: Clay and Concrete Masonry, fifth ed., CRC Press, New York, 1998.
[17] J. Wamer, Practical Handbook of Grouting: Soil, Rock, and Structures, John Wiley & Sons, New Jersey, 2004.
[18] J. Wongpa, K. Kiattikomol, C. Jaturapitakkul, P. Chindaprasirt, Compressive strength, modulus of elasticity, and water permeability of inorganic polymer concrete, Mater. Des. 31 (10) (2010) 4748–4754.
[19] U. Rattanasak, P. Chindaprasirt, Influence of NaOH solution on the synthesis of fly ash geopolymer, Miner. Eng. 22 (12) (2009) 1073–1078.
[20] W.K.W. Lee, J.S.J. Van Deventer, Structural reorganization of class F fly ash in alkaline silicate solutions, Colloids Surf. A 211 (1) (2002) 49–66.
[21] P.J. Krueger, B.F. Hawkin, Infrared absorption band shape studies: fundamental OH stretching vibration of benzyl alcohol conformers in dilute carbon tetrachloride solution, Can. J. Chem. 51 (1973) 3250–3262.
[22] K.J. Theo, F.L. Ray, H. Leisel, FT-Raman and FT-IR spectroscopic study of the local structure of synthetic Mg/Zn/Al-hydrotalcites, J. Raman Spectrosc. 35 (11) (2004) 967–974.
[23] J.L. Bishop, E. Murad, Characterization of minerals and biogeochemicalmarkers on Mars: a Raman and IR spectroscopic study of montmorillonite, J. Raman Spectrosc. 35 (6) (2004) 480–486.
[24] Z. Li, C. Leung, Y. Xi, Structural Renovation in Concrete, Taylor & Francis, Oxon, UK, 2009.

J Mater Sci: Mater Electron (2016) 27:9650–9655
DOI 10.1007/s10854-016-5023-2

Greatly enhanced dielectric permittivity in poly(vinylidene fluoride)-based polymeric composites induced by $Na_{1/3}Ca_{1/3}Bi_{1/3}Cu_3Ti_4O_{12}$ nanoparticles

Pornsawan Kum-onsa[1] · Prasit Thongbai[2] · Santi Maensiri[3] · Prinya Chindaprasirt[4]

Received: 15 March 2016 / Accepted: 18 May 2016 / Published online: 23 May 2016
© Springer Science+Business Media New York 2016

Abstract Greatly enhanced dielectric permittivity (ε′) in poly(vinylidene fluoride) (PVDF) polymeric composites was induced by incorporating $Na_{1/3}Ca_{1/3}Bi_{1/3}Cu_3Ti_4O_{12}$ (NCB) nanoparticles. The NCB/PVDF composites were fabricated by conventional mixed powders and hot pressing. Nanosized (NCB-NPs) and microsized-powders (NCB-MPs) prepared, respectively, by chemical combustion and solid state reaction methods were used as fillers. The dispersion of NCB-NPs was quite **good** in the PVDF matric. A greatly improved ε′ of PVDF-based polymeric composites can be induced by filling with NCB-NPs compared to that of the NCB-MPs/PVDF composite. Interestingly, at 10^3 Hz, the nanocomposite with 50 vol% of NCB-NPs can exhibit good dielectric properties with high ε′ of about 210.8 and low loss tangent ($\tan\delta \approx 0.83$). This enhanced ε′ value is much larger than that of PVDF polymer by a factor of ≈20. The increase in ε′ in the nanocomposites is attributed to large interfacial areas and very short interparticle distance. These can cause a great increase in the interfacial polarization intensity.

✉ Prasit Thongbai
pthongbai@kku.ac.th

[1] Materials Science and Nanotechnology Program, Faculty of Science, Khon Kaen University, Khon Kaen 40002, Thailand

[2] Integrated Nanotechnology Research Center (INRC), Department of Physics, Faculty of Science, Khon Kaen University, Khon Kaen 40002, Thailand

[3] School of Physics, Institute of Science, Suranaree University of Technology, Nakhon Ratchasima 30000, Thailand

[4] Sustainable Infrastructure Research and Development Center, Department of Civil Engineering, Faculty of Engineering, Khon Kaen University, Khon Kaen 40002, Thailand

1 Introduction

Polymer matrix composites with good dielectric performance have been intensively developed in recent years because of their variety potential applications, especially for microelectronics, electrical engineering, and high-energy–density storage devices [1–7]. For practical application in microelectronics, polymeric dielectric materials with high dielectric permittivity (ε′), low dielectric loss tangent (tanδ), mechanical flexibility, low coast, and excellent processing performance as well as compatible with polymers used as support of electronic circuits are highly desired [8–11]. Poly(vinylidene fluoride) (PVDF) is widely used as a polymer matrix due to its high ε′ of about 10 compared to other polymers [1, 11–14].

Usually, the simple and effectively method to obtain enhanced ε′ value of flexible polymer-based composites is the incorporation of high-permittivity ceramic particles into polymer matrix. The common ceramic fillers used are $BaTiO_3$ [5, 13, 15–17], $(Ba_{0.6}Sr_{0.4})TiO_3$ [18–20], $CaCu_3Ti_4O_{12}$ (CCTO) [21–23], $Na_{0.5}Bi_{0.5}Cu_3Ti_4O_{12}$ [24], and $Ba(Fe_{0.5}Nb_{0.5})O_3$ [25]. Although significant efforts have been made for increasing ε′ of these ceramic/polymer composite systems, ε′ values these composites are difficult to significantly enhance by more than 100, in which 50 vol% ceramic particles was filled in. Furthermore, the ferroelectric ceramics usually exhibit piezoelectric effect, which results in a mechanical resonance in the device during charging and discharging. This can cause the reliability limit of the fabricated device. In addition, some ferroelectric ceramics consists of Pb, which might contaminate the environment.

Considering nanosized ceramic fillers, large interfacial areas and very short interparticle distance in the composites containing nanosized fillers promote the exchange coupling

effect through a dipolar interface layer. This results in a significantly enhanced polarization intensity and thus ε' [26], which offers greater possibilities to tailor and optimizes the properties of polymer based composites compared to those of microsized ceramic fillers. Nanosized fillers can decrease the possibility of porosity in polymer matric composite, leading to a better microstructure. For practical applications, moreover, nanoparticles would reduce the dimensions of composites and increase the packing density [25].

Most recently, we found that $Na_{1/3}Ca_{1/3}Bi_{1/3}Cu_3Ti_4O_{12}$ (NCB), a new giant dielectric perovskite ceramic in $ACu_3Ti_4O_{12}$ compounds, has better dielectric properties compared to that of $CaCu_3Ti_4O_{12}$. High $\varepsilon' \approx 2.5 \times 10^4$ and low $\tan\delta \approx 0.038$ at 1 kHz with good temperature stability were notably achieved in the NCB ceramic. Therefore, in this work, nanosized-NCB/PVDF nanocomposites were prepared. The effects of nanosized filler on the microstructure and dielectric properties were investigated. It was found that the largely enhanced ε' of about 528 (210) at 100 Hz (1 kHz) with retaining low $\tan\delta$ in PVDF polymer matrix nanocomposite was successfully obtained by filling with 50 vol% nanosized-NCB.

2 Experimental details

2.1 Preparation of $Na_{1/3}Ca_{1/3}Bi_{1/3}Cu_3Ti_4O_{12}$

Nanosized-$Na_{1/3}Ca_{1/3}Bi_{1/3}Cu_3Ti_4O_{12}$ powder (NCB-NP) was prepared by a chemical combustion (CC) method using urea as fuel. $Ca(NO_3)_2{\cdot}4H_2O$ (99 %, Sigma–Aldrich), $NaNO_3$ (99.99 %, Kanto Chemical), $(CH_3CO_2)_3Bi$ (99.99 %, Sigma–Aldrich), $Cu(NO_3)_2{\cdot}4H_2O$ (99.5 %, Carlo Erba), $C_{16}H_{28}O_6Ti$ (75 wt% in isopropanol, Sigma–Aldrich), acetic acid, deionized water, and urea were used as starting raw materials. Details of the preparation method are given elsewhere [27]. First, stoichiometric amounts of $Ca(NO_3)_2{\cdot}4H_2O$, $NaNO_3$, $(CH_3CO_2)_3Bi$, and $Cu(NO_3)_2{\cdot}4H_2O$ were dissolved in an aqueous solution of acetic acid. Second, a $C_{16}H_{28}O_6Ti$ solution was slowly dropped into the metal ion solution under constant stirring until the formation of a clear and transparent solution was obtained. Then, urea powder was added into the mixed solution with stirring at 150 °C until a viscous gel formed. The gel was dried in air at 350 °C for 30 min. The resulting dried porous precursor was ground and calcined at 750 °C for 4 h. The obtaining NCB-NPs were achieved. Micro-$Na_{1/3}Ca_{1/3}Bi_{1/3}Cu_3Ti_4O_{12}$ powder (NCB-MP) was prepared by a solid state reaction (SSR) method. The mixture of starting powders was mixed by ball milling in ethanol and calcined at 950 °C for 5 h.

2.2 Preparation of NCB/PVDF composites

The NCB-NPs and NCB-MPs were used as filler in PVDF (Sigma-Aldrich Co., France) matrix. The NCB/PVDF composites with different volume fractions of NCB ($f_{NCB} = 0$, 0.1, 0.2, 0.3, 0.4, and 0.5) were prepared by a liquid-phase assisted dispersion method. First, NCB and PVDF particles were mixed by ball-milling in absolute ethanol for 30 min using ZrO_2 balls. Second, the mixture of NCB and PVDF particles was further dried to evaporate absolute ethanol. Finally, the dry mixture powders were molded by hot-pressing at about 200 °C for 30 min under 10 MPa. The final composite samples with a disc-shape are 12 mm in diameter and 1 mm in thickness.

2.3 Characterization techniques

X-ray diffraction (XRD; Bruker, D2 phaser) was used to characterize the phase compositions and crystal structures of the NCB-NPs and NCB-MPs and NCB/PVDF composites. Scanning electron microscopy (SEM) (SEM; LEO 1450VP; Cambridge, UK) and field-emission scanning electron microscopy (FE-SEM) were used to characterize nanosized NCB powders and NCB/PVDF nanocomposites. For the dielectric measurement, surfaces of the nanocomposite samples were painted by silver past. The capacitance (C_p) and dissipation factor ($\tan\delta$) of the polymeric composite samples were measured using an Agilent 4294A Precision Impedance Analyzer over the frequency range of 10^2–10^7 Hz at room temperature with an oscillation voltage of 500 mV.

3 Results and discussion

Figure 1 shows the SEM images of the NCB-NPs and NCB-MPs powders prepared by CC and SSR methods, respectively. Obviously, the particle sizes of the NCB-NPs and NCB-MPs powders are of about 100–200 nm and 1–2 μm, respectively. An agglomeration of both powders is observed. The XRD patterns of the NCB-NPs and NCB-MPs powders are illustrated in Fig. 2. The main phase of NCB is detected in both powders. These XRD patterns are similar to that of CCTO structure (JCPDS 75-2188) with *bcc* structure. However, a small amount of CuO secondary phase is still observed in the XRD pattern of the NCB-NPs powder.

As depicted in the inset of Fig. 3, it is found that the coexistence of α- and γ-phase of PVDF was confirmed [8]. This result is similar to that observed in the $Na_{1/2}Bi_{1/2}Cu_3Ti_4O_{12}$/PVDF composites [24]. Figure 3 demonstrates the XRD patterns of NCB-NPs/PVDF nanocomposites with different loading contents of nanofiller. All XRD peaks of

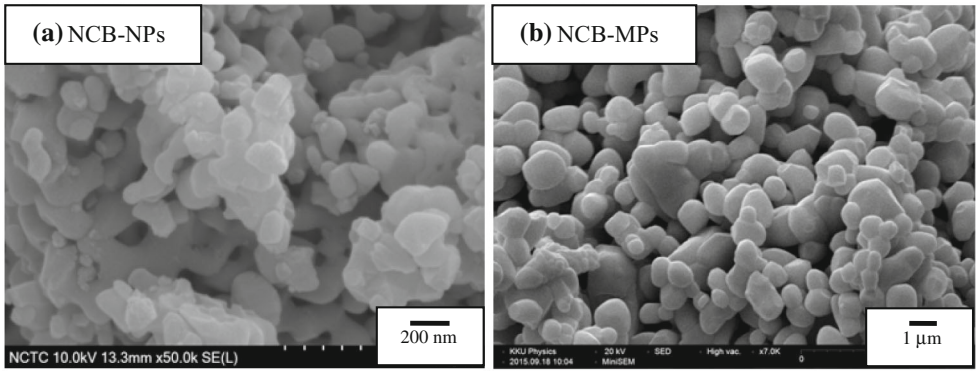

Fig. 1 SEM images of **a** NCB-NPs and **b** NCB-MPs

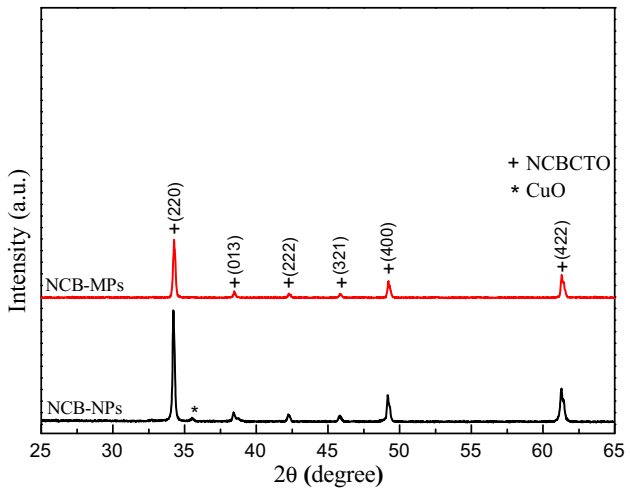

Fig. 2 XRD patterns of NCB-NPs and NCB-MPs

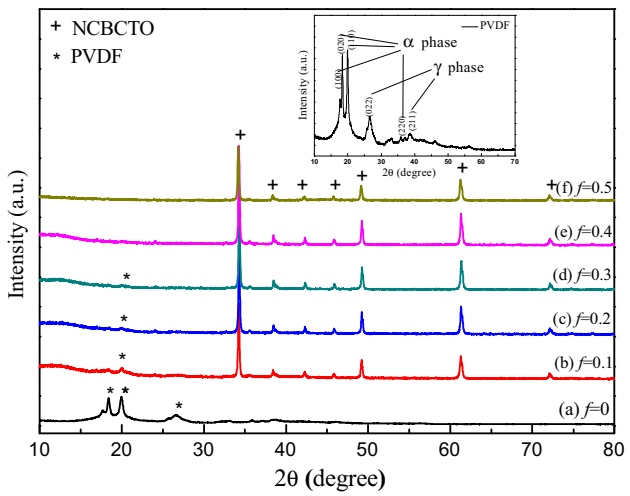

Fig. 3 XRD patterns of NCB-NPs/PVDF nanocomposites with different volume fractions of NCB-NPs ($f = 0$–0.5); *inset* illustrates the XRD pattern of PVDF

the NCB-NPs/PVDF nanocomposites are perfectly indexed as *bcc* structure. XRD peak of PVDF is observed in the composites with low loading content of filler. The XRD patterns of NCB-NPs are unchanged for all compositions. The intensities of PVDF-phase diffraction peaks decrease with increasing NCB-NPs content in the nanocomposites.

The effect of particle sizes of filler on the microstructure of NCB/PVDF polymer composites is shown in Fig. 4. Figures 4a–b reveal the fractured cross section of the NCB-NPs/PVDF nanocomposites. The dispersion of NCB-NPs in the PVDF matrix is quite good. Figures 4c–d show the cross section of the NCB-MPs/PVDF composites. Pores are observed in the NCB-MPs/PVDF composites. It is observed that NCB-NPs and NCB-MPs are randomly surrounded by the polymer matrix, indicating that 0–3 connectivity pattern is formed [1, 25]. For the nanocomposite with 50 vol% (Fig. 4b), NCB-NPs are dispersed homogeneously in the PVDF matrix with small trails of aggregation. In contrast, as the NCB-MPs filler content increases, a large amount of pores can be observed in the NCB-MPs/PVDF composite with 50 vol% NCB-MPs. The porosity resulted from high loading would have a great impact on the dielectric properties of the polymer composites. Usually, the dispersion of fillers would play a significant role on dielectric properties of composites and good dispersion is likely to contribute to excellent dielectric properties [1, 13]. Accordingly, these results indicate the better performance the NCB-NPs on the microstructure of the polymer composites.

The dielectric properties of the NCB-NPs/PVDF nanocomposites are shown in Figs. 5 and 6. ε' of NCB-NPs/PVDF nanocomposites increases with increasing $f_{\text{NCB-NPs}}$. Note that ε' of NCB-MPs/PVDF composites also increased as $f_{\text{NCB-MPs}}$ was increased. As demonstrated in Fig. 5, ε' of the NCB-NPs/PVDF nanocomposites with $f_{\text{NCB-NPs}} \leq 0.2$ is slightly dependent on frequency in the

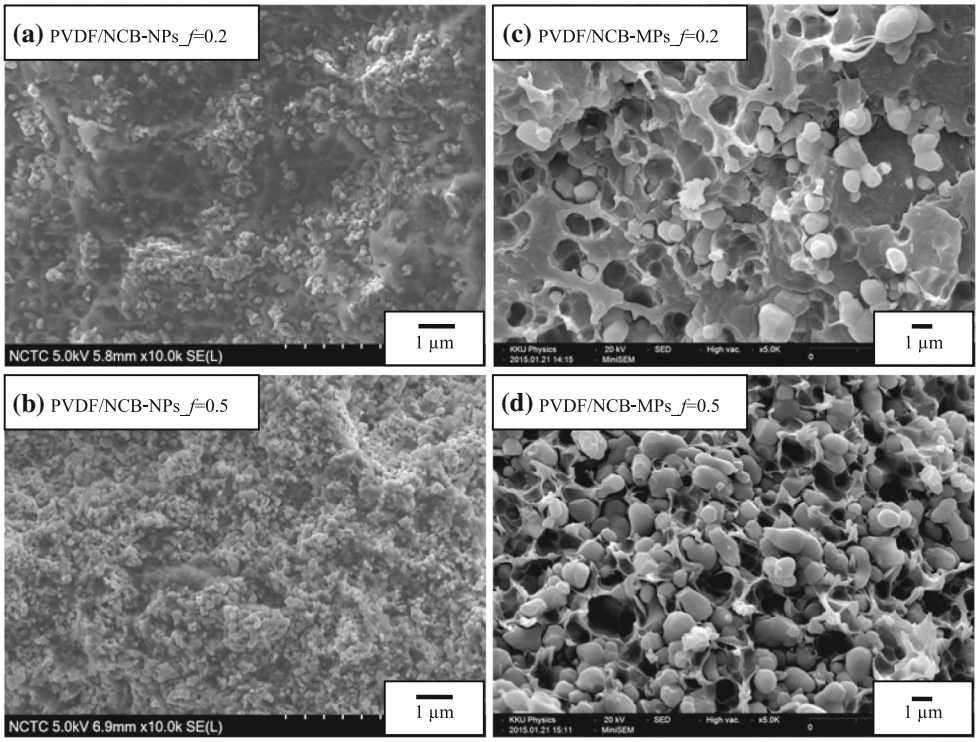

Fig. 4 SEM images of **a–b** NCB-NPs/PVDF and **c–d** NCB-MPs with $f = 0.2$ and 0.5

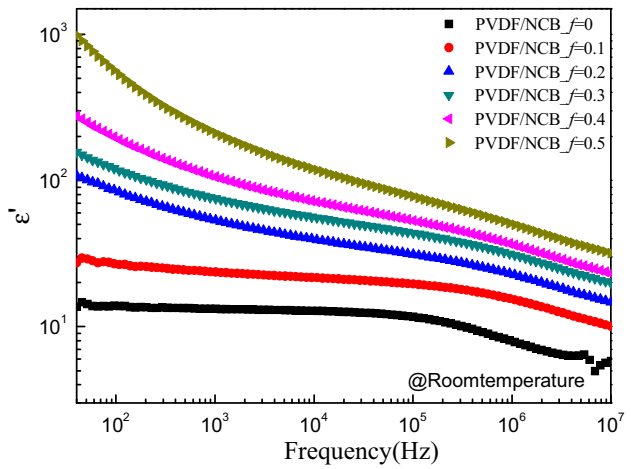

Fig. 5 ε′ as a function of frequency at room temperature of NCB-NPs/PVDF nanocomposites

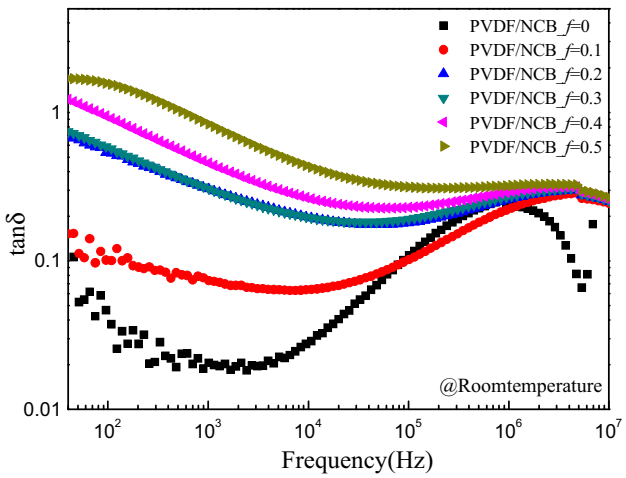

Fig. 6 tanδ as a function of frequency at room temperature of NCB-NPs/PVDF nanocomposites

range of 40–10^7Hz. In the low-frequency range, ε′ of NCB-NPs/PVDF nanocomposites with $f_{NCB\text{-}NPs} \geq 0.2$ is strongly dependent on frequency. This evidently indicates that the dielectric response is primarily caused by the interfacial polarization effect. As the concentration of NCB-NPs fillers was increased to $f_{NCB\text{-}NPs} = 0.1$, 0.2, 0.3, 0.4, and 0.5, the values of ε′ at 10^3 Hz increased to 23.7, 53.4, 75.3, 105.9, and 210.8, respectively. It is worth noting that for the nanocomposite with $f_{NCB\text{-}NPs} = 0.5$, the ε′ at 10^2 and 10^3 Hz is, respectively, 50 and 20 times higher than that of pure PVDF polymer.

The frequency dependence of tanδ at room temperature of the NCB-NPs/PVDF nanocomposites is illustrated in Fig. 6. In the frequency range of 40–10^5 Hz, tanδ of the NCB-NPs/PVDF nanocomposites increases with increasing NCB-NPs loading content. It is observed that tanδ of all nanocomposite samples decreases in the frequency range of 40–10^4 Hz, and then tends to increase over 10^4 Hz. The

dielectric response in a low-frequency range is a typical interface polarization behavior. This was resulted from macroscopical heterogeneous interface of the different diphase structures [1]. On the other hand, the high-frequency dielectric response is a Debye relaxation behavior derived from the C-F dipole orientation polarization of PVDF matrix [25]. Interestingly, at 1 kHz, the nanocomposite with $f_{NCB\text{-}NPs} = 0.5$ can exhibit good dielectric properties with high ε' of about 210.8 and low $\tan\delta \approx 0.83$. This high ε' value is much larger than those of observed in the CCTO/PVDF [21] and $Na_{1/2}Bi_{1/2}Cu_3Ti_4O_{12}$/PVDF composites [27].

Generally, the dispersion of fillers would play a significant role on dielectric properties of composites and good dispersion is likely to contribute to excellent dielectric properties [1]. As revealed in Fig. 4, the NCB-NPs are good dispersed in the PVDF polymer matrix. Furthermore, porosity in the NCB-NPs/PVDF nanocomposites is very low compared to that of the NCB-MPs/PVDF composites. According to the microstructure analysis, ε' of the NCB-NPs/PVDF nanocomposites should therefore be better than that of the NCB-MPs/PVDF composites. As clearly seen in Fig. 7, the ε' value of each NCB-NPs/PVDF composition is larger than that of the NCB-MPs/PVDF composite. Another important reason is that the high ε' of NCB-NPs/PVDF nanocomposites is dominantly caused by enhanced interfacial polarization. This primarily originates in the significant blocking of charge carriers at internal interfaces (i.e., the Maxwell–Wagner–Sillars effect) under an electric field due to the formation of a large number of interfaces between NCB-NPs and PVDF polymer matric. By comparing the NCB-NPs and NCB-MPs ceramic fillers, larger interfacial areas and hence very shorter interparticle distance in the nanocomposites can cause the great exchange coupling effect through a dipolar interface layer. This results in a significantly enhanced ε' as a result of an increased polarization intensity [26].

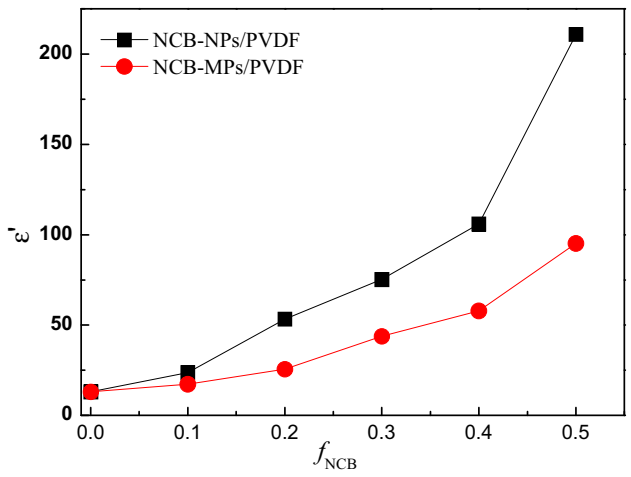

Fig. 7 ε' as a function of volume fraction at room temperature and 1 kHz of NCB-NPs and NCB-MPs

4 Conclusions

In conclusion, ε' of PVDF polymer was greatly enhanced by incorporating with NCB-NPs. It was found that the dispersion of NCB-NPs in PVDF matrix was quite good. The NCB-NPs/PVDF nanocomposite with $f_{NCB\text{-}NPs} = 0.5$ exhibited high ε' of about 210.8 with low $\tan\delta \approx 0.83$. This increased ε' value was much larger than that of PVDF polymer by a factor of ≈ 20. It was also found that the ε' value of the NCB-NPs/PVDF was much larger than that of the NCB-MPs/PVDF microcomposites. Very high ε' of the NCB-NPs/PVDF nanocomposites was originated from the large interfacial areas coupled with very short interparticle distance.

Acknowledgments This work was financially supported by the Thailand Research Fund (TRF) and Khon Kaen University under the TRF Senior Research Scholar Contract No. RTA5780004. P. Kumonsa would like to thank the Science Achievement Scholarship of Thailand (SAST) for her Master of Science Degree scholarship.

References

1. Z.-M. Dang, J.-K. Yuan, J.-W. Zha, T. Zhou, S.-T. Li, G.-H. Hu, Prog. Mater Sci. **57**, 660 (2012)
2. P. Martins, A.C. Lopes, S. Lanceros-Mendez, Prog. Polym. Sci. **39**, 683 (2014)
3. D. Wang, Y. Bao, J.-W. Zha, J. Zhao, Z.-M. Dang, G.-H. Hu, ACS Appl. Mater. Interfaces **4**, 6273 (2012)
4. T. Li, J. Chen, H. Dai, D. Liu, H. Xiang, Z. Chen, J. Mater. Sci. Mater. Electron. **26**, 312 (2014)
5. M.-F. Lin, V.K. Thakur, E.J. Tan, P.S. Lee, RSC Adv. **1**, 576 (2011)
6. P. Thakur, A. Kool, N.A. Hoque, B. Bagchi, S. Roy, N. Sepay, S. Das, P. Nandy, RSC Adv. **6**, 26288 (2016)
7. X. Lin, P. Hu, Z. Jia, S. Gao, J. Mater. Chem. A **4**, 2314 (2016)
8. A. Paleo, C. Martínez-Boubeta, L. Balcells, C. Costa, V. Sencadas, S. Lanceros-Mendez, Nanoscale Res. Lett. **6**, 257 (2011)
9. Q. Xiao, L. Li, B.Q. Zhang, X.M. Chen, Ceram. Int. **39**, S3 (2013)
10. Y. Song, Y. Shen, H. Liu, Y. Lin, M. Li, C.-W. Nan, J. Mater. Chem. **22**, 16491 (2012)
11. N. Levi, R. Czerw, S. Xing, P. Iyer, D.L. Carroll, Nano Lett. **4**, 1267 (2004)
12. J. Bi, Y. Gu, Z. Zhang, S. Wang, M. Li, Z. Zhang, Mater. Des. **89**, 933 (2016)
13. K. Silakaew, W. Saijingwong, K. Meeporn, S. Maensiri, P. Thongbai, Microelectron. Eng. **146**, 1 (2015)
14. K. Yu, H. Wang, Y. Zhou, Y. Bai, Y. Niu, J. Appl. Phys. **113**, 034105 (2013)
15. T. Zhou, J.-W. Zha, R.-Y. Cui, B.-H. Fan, J.-K. Yuan, Z.-M. Dang, ACS Appl. Mater. Interfaces **3**, 2184 (2011)
16. L. Xie, X. Huang, Y. Huang, K. Yang, P. Jiang, ACS Appl. Mater. Interfaces **5**, 1747 (2013)
17. Y.K. Jang, J.C. Won, H.G. Yoon, Appl. Phys. Lett. **95**, 052907 (2009)

18. K. Li, H. Wang, F. Xiang, W. Liu, H. Yang, Appl. Phys. Lett. **95**, 202904 (2009)
19. W. Xia, Z. Xu, F. Wen, Z. Zhang, Ceram. Int. **38**, 1071 (2012)
20. Y. Song, Y. Shen, P. Hu, Y. Lin, M. Li, C.W. Nan, Appl. Phys. Lett. **101**, 152904 (2012)
21. P. Thomas, K.T. Varughese, K. Dwarakanath, K.B.R. Varma, Compos. Sci. Technol. **70**, 539 (2010)
22. Y. Shen, A. Gu, G. Liang, L. Yuan, Compos. A Appl. Sci. Manuf. **41**, 1668 (2010)
23. B.S. Prakash, K.B.R. Varma, Compos. Sci. Technol. **67**, 2363 (2007)
24. Y.-L. Su, C. Sun, W.-Q. Zhang, H. Huang, J. Mater. Sci. **48**, 8147 (2013)
25. Z. Wang, M. Fang, H. Li, Y. Wen, C. Wang, Y. Pu, Compos. Sci. Technol. **117**, 410 (2015)
26. K.S. Deepa, M.T. Sebastian, J. James, Appl. Phys. Lett. **91**, 202904 (2007)
27. W. Tuichai, P. Thongbai, V. Amornkitbamrung, T. Yamwong, S. Maensiri, Microelectron. Eng. **126**, 118 (2014)

Fatigue Assessment of Cement-Treated Base for Roads: An Examination of Beam-Fatigue Tests

Peerapong Jitsangiam, Ph.D.[1]; Korakod Nusit[2]; Suphat Chummuneerat, Ph.D.[3]; Prinya Chindaprasirt, Ph.D.[4]; and Preda Pichayapan, Ph.D.[5]

Downloaded from ascelibrary.org by CURTIN UNIV OF TECHNOLOGY on 04/26/16. Copyright ASCE. For personal use only; all rights reserved.

Abstract: This paper presents an examination of the fatigue characteristics of cement-treated base (CTB), a cement-stabilized material for use in road pavement construction based on CTB beam test specimens prepared and tested under laboratory conditions. The beam fatigue protocol for asphalt concrete, following the Austroads standard test method of AG:PT/T233, were adapted to examine the fatigue characteristics of the CTB test specimens. Standard road base (Granite/Diorite) from the local quarry in Western Australia was employed as the parent material of CTB. The beam-fatigue tests were conducted under the strain-controlled (constant strain) and stress-controlled (constant stress) testing conditions with varying cement contents (3–10%) of CTB test specimens. Two different loading waveforms of sinusoidal and haversine load curves were also investigated. The results show that for the strain-controlled testing condition, the fatigue characteristics of the CTB test specimens were not affected by the difference in both loading waveforms. Furthermore, the fatigue characteristics of the CTB test specimens were significantly influenced by the levels of the applied strains. Under the strain-controlled testing condition, the test results also indicated the existence of fatigue endurance limit, which occurred based on the test condition of the applied strain level of 150 microstrains or less subjected to 5% cement specimens. This fatigue endurance limit increased with respect to higher cement content and initial cyclic flexural stiffness. For the stress-controlled testing condition, this study found that the conclusion cannot be made that a relationship exists between applied stress level and fatigue characteristic of the CTB test specimens. This is because half of the test specimens in this study were damaged in the early stages of loading cycles with small increases in applied stress levels. Considering all the test results, the strain-controlled testing was preferable, based on the test conditions and environment used in this study. This study confirms that the use of the adapted beam-fatigue test protocol of asphalt concrete is suitable to determine the CTB fatigue characteristics, which are difficult to obtain with no standard test protocol. This would lead to more effective use of this material in road pavement design and construction. **DOI: 10.1061/(ASCE)MT.1943-5533.0001601.** © *2016 American Society of Civil Engineers.*

Author keywords: Cyclic flexural stiffness; Fatigue; Base course; Cement-treated base; Pavement.

Introduction

Cement-treated base (CTB) is a product of the soil-cement stabilization technique for creating a superior road base or subbase material in pavement. It could be theoretically categorized as the fully bound (stabilized) material, which generally has much better tensile resistance than a normally used road base material of an unbound granular material (i.e., a zero tensile resistant material). However, CTB inherently exhibits fatigue deterioration under repeated (cyclic) loads. Therefore, for the long-term performance of a CTB pavement, avoidance of a fatigue failure in a CTB layer should be specified as one of the design criteria for road pavement with a CTB layer. Notwithstanding, consideration of a fatigue failure of a CTB layer in a conventional pavement design approach is still unavailable. Based on the current pavement structural design viewpoint, a stabilized base layer (i.e., CTB) is subjected to the wheel load on a pavement surface, causing development of tensile stress at the bottom and compressive stress at the top of the stabilized base layer. Such tensile stress is more critical to the performance of a CTB-layer structure, and generally is considered to be a CTB pavement design criterion (Austroads 2010; NCHRP 2004). The tensile strength of a CTB layer can be determined practically using various test methods (Wen et al. 2014), for example, direct tensile tests (ASTM 2008), indirect tensile tests (ASTM 2011), and flexural tests (Austroads 2010, 2014a). However, all conventional tensile strength tests are under static loading conditions that cannot capture real pavement material behavior under moving vehicles of traffic, particularly the fatigue, and those tensile strength tests would not be suitable to determine a rational design parameter for the mechanistically structural CTB pavement design. Reliable design parameters of a CTB road pavement should be derived from fatigue tests under cyclic loading regime to simulate real fatigue characteristics of a CTB pavement layer under traffic loading conditions. However, a fundamental assessment of fatigue

[1]Senior Lecturer, Dept. of Civil Engineering, School of Civil and Mechanical Engineering, Curtin Univ., Kent St., Bentley, Perth, WA 6102, Australia; Adjunct Professor, Dept. of Civil Engineering, Faculty of Engineering, Chiang Mai Univ., Huai Kaew Rd., Muang, Chiang Mai 50200, Thailand. E-mail: p.jitsangiam@curtin.edu.au

[2]Ph.D. Candidate, Dept. of Civil Engineering, School of Civil and Mechanical Engineering, Curtin Univ., Kent St., Bentley, Perth, WA 6102, Australia (corresponding author). E-mail: korakod.nusit@student.curtin.edu.au

[3]Professional Civil Engineer, Bureau of Location and Design, Dept. of Highways, Bangkok 10400, Thailand. E-mail: sch_cv32@hotmail.com

[4]Professor, Sustainable Infrastructure Research and Development Center, Dept. of Civil Engineering, Faculty of Engineering, Khon Kaen Univ., Khon Kaen 40002, Thailand. E-mail: prinya@kku.ac.th

[5]Lecturer, Excellence Center in Infrastructure Technology and Transportation Engineering, Dept. of Civil Engineering, Chiang Mai Univ., Huai Kaew Rd., Muang, Chiang Mai 50200, Thailand. E-mail: preda@eng.cmu.ac.th

Note. This manuscript was submitted on October 18, 2015; approved on January 21, 2016; published online on April 22, 2016. Discussion period open until September 22, 2016; separate discussions must be submitted for individual papers. This paper is part of the ***Journal of Materials in Civil Engineering***, © ASCE, ISSN 0899-1561.

characteristics of CTB under real loading conditions is almost unobtainable due to requirements of sophisticated laboratory facilities capable of applying cyclic loads with a certain frequency to be compatible with CTB material characteristics.

Fatigue tests under cyclic loading conditions have been employed to assess the fatigue characteristics of asphalt concrete (AC) since the late 1950s (Pell et al. 1961). Currently, four-point bending (4PB) tests using prismatic beams are most popularly used to measure the flexural modulus (stiffness), and evaluate the fatigue characteristics of AC (AASHTO 2007; Austroads 2006a; ASTM 2010; European Committee for Standardization 2004). The 4PB tests are used to simulate a wheel-loading interaction with an AC layer in pavement. Theoretically, the cyclic load (i.e., traffic load) is applied in the midpart of a test beam toward two inner clamps during the test. Based on the loading configuration of the 4PB test, the uniform strain distribution corresponding to the test beam length is believed to take place in this midspan area. Therefore, the maximum tensile stress occurs in the outer beam surface at this midsection of the bottom of the beam (i.e., from the haversine loading waveform) and the bottom and the top (i.e., from the sinusoidal loading waveform) of the test beam. It could be stated that the 4PB test apparatus is acceptable and widely used in advanced pavement laboratories; therefore, it could be a good facility platform for a fatigue examination of CTB. The recent research on characteristics of cement-stabilized materials based on the 4PB test platform can be found from limited sources based on the literature-review perspectives. However, Disfani et al. (2014) and Arulrajah et al. (2015) reported the fatigue behavior of prismatic beam specimens molded from cement-stabilized recycled concrete aggregate blended with recycled crushed brick and fine recycled glass, respectively. Paul and Gnanendran (2015) focused on the static and dynamic stiffness of the granular base materials stabilized by cement-fly ash binder. However, the larger size of prismatic beam specimens ($100 \times 100 \times 400$ mm^3) and only the binder content of 3% were employed in their studies.

This paper seeks to examine the fatigue characteristic of CTB using the 4PB tests adapted from the standard 4PB test protocol of AC (Austroads 2006a). This is to overcome a shortcoming in suitable facilities for fatigue assessment of CTB, and gain a better understanding of fatigue characteristic of CTB under cyclic loading conditions.

Background

The CTB is produced based on a cement stabilization technique in which a prescribed amount of cement is added to an original base course material with an optimum amount of water. The purpose of CTB is to improve the engineering properties of conventional granular materials used in road pavements, such as strength, stiffness, and moisture sensitivity. CTB has been used for pavements in many countries, such as the United States, China, South Africa, and South Korea (Cho et al. 2006). However, limitations of using CTB for roads in some countries, including Australia, remain. For Western Australia in particular, CTB is only permitted for the construction of a road working platform, not for use in main structural layers of road pavements. It must then be overlaid with an unbound granular material. Thickness reduction of the unbound granular layer when using CTB as its foundation is not permitted to prevent a tendency of cracking in pavements. These limitations are specified by the Main Roads authority of Western Australia (MRWA 2010). The short-term and long-term cracking of CTB in pavement cannot be solved well theoretically due to a lack in a fundamental understanding of CTB behavior under traffic loading conditions. Practical experience in road pavement construction since CTB has been introduced has shown that fatigue cracking is one of the major distress modes in CTB pavements; it results from CTB stiffness degradation under repetitive loads from traffic. Cracks from fatigue failure generally originate at the bottom of a CTB layer and propagate to an asphalt pavement surface (George 2002).

Based on the standard 4PB tests of AC, the fatigue failure is generally specified to take place at a number of cyclic loading cycles that reduces the flexural stiffness of a material to 50% of an initial stiffness (Austroads 2006a). The fatigue relationship could be drawn from the correlation between a fatigue life and applied stress or strain conditions. The experimental data for a fatigue life against tensile strains/stresses induced in test samples can be obtained via a number of fatigue tests conducted at different magnitudes of applied strains or stresses. Fatigue tests can be carried out in two modes, *strain-controlled* and *stress-controlled*, depending on testing protocols to simulate real conditions in pavement. In the strain-controlled mode, strain is maintained by reducing the applied load during the test (constant strain test); during the stress-controlled test, the stress is kept constant and strain is increased (constant stress test). The simplest form of the fatigue relationship is shown in Eq. (1) (Chummuneerat et al. 2013)

$$N = \left(\frac{k_1}{\varepsilon}\right)^{k_2} or \left(\frac{k_3}{\sigma}\right)^{k_4} \tag{1}$$

where N = fatigue life or loading cycle to failure; Q = tensile strain at the bottom of the specimen; σ = applied tensile stress; and k_1-k_4 = regression parameters.

The fatigue relationship of CTB is introduced for the structural analysis and design of flexible pavements, as the tensile strain at the bottom of the CTB layer is converted to a number of standard axle load repetitions and compared with the designed number of standard axle repetitions. Eq. (2) is an example of the fatigue relationship for pavement design (Austroads 2014b). If pavement thicknesses are well designed and strains in pavement caused by cyclic loadings are low enough, accordingly, fatigue cracking is not a problem (Soliman et al. 2012)

$$N = RF\left[\frac{(113{,}000/E^{0.804}) + 191}{\mu\varepsilon}\right]^{12} \tag{2}$$

where N = allowable number of standard axle load repetitions; $\mu\varepsilon$ = tensile microstrains at the bottom of the CTB layer; E = cemented material stiffness (MPa); and RF = reliability factor for the fatigue life of cemented materials.

Project Aim

This project aims to report a preliminary fatigue examination of CTB under laboratory controlled conditions, following the 4PB tests adapted from the Austroads standard 4PB test protocol of AC (Austroads 2006a). A reliable fatigue testing protocol and a precise fatigue life prediction model are fundamentally essential to the road pavement design. Therefore, test results will be used for the fatigue testing protocol development of CTB. Nevertheless, the further research on fatigue characteristics of CTB is importantly required for the fatigue prediction model development. The details of the materials, experimental works, and results are explained in the following sections.

Materials and Methods

This study investigated CTB test specimens with varying cement contents of 3, 5, 7.5, and 10%, which are in a normal range of

Downloaded from ascelibrary.org by CURTIN UNIV OF TECHNOLOGY on 04/26/16. Copyright ASCE. For personal use only; all rights reserved.

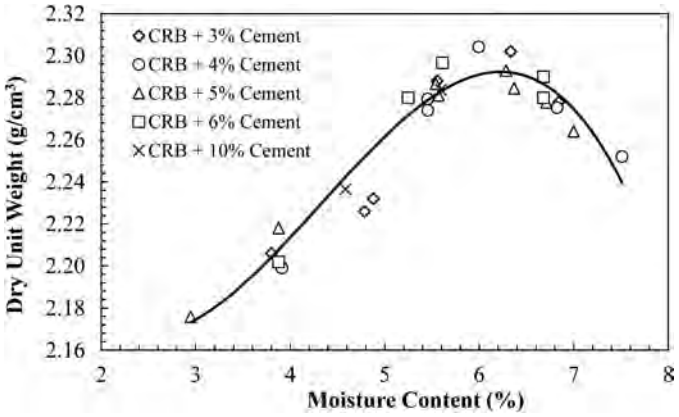

Fig. 1. Moisture-density relationship of CTB

cement application of CTB. The cement content of 3% was selected based on the minimum requirement of cement-stabilized materials (Austroads 2006b); the cement content of 10% was chosen as the upper boundary because it is the highest cement content for economic use in road construction (NAASRA 1970). In addition, the standard 4PB test for AC in accordance with the Austroads standard test method (Austroads 2006a) was adapted to test on CTB specimens with two loading waveforms of sinusoidal and haversine, along with two loading modes of stress-controlled and strain-controlled conditions. The sinusoidal loading waveform was employed in this study because it is recommended by European Committee for Standardization (2004) and AASHTO (2007) for 4PB test of AC; on the other hand, Austroads (2006a) proposed to use the haversine loading waveform for determining the fatigue life of AC from 4PB test. The aforementioned test standards (European Committee for Standardization 2004; AASHTO 2007) and guideline (Austroads 2006a) suggested to measure the fatigue life of AC under strain-controlled and displacement-controlled conditions, respectively.

Materials

In this study the CTB specimens were mixed by blending standard crushed rock base (CRB) with general purpose (GP) portland cement (AS 2010) at the optimum moisture content (OMC) derived from a modified compaction test (ASTM 2012). CRB samples conforming to MRWA specifications (MRWA 2012) were collected from a local quarry in Western Australia (WA). In addition, the employed CRB was geologically classified as granite/diorite (intrusive igneous rock). Fig. 1 presents the moisture-density relationship of CTB (3–10% cement by mass of dry CRB) determined in this study. Based on Fig. 1, cement content has little influence on the maximum dry density (MDD) and OMC of CTB. Accordingly, OMC and MDD equal to 6.20% and 2.29 g/cm^3, respectively, were employed in the specimen preparation for the 4PB tests in this study.

Sample Preparation

CTB slabs, with dimensions of 400×300 mm^2 and thickness of 75 mm, were made from the mixture of CRB, with the specified amount of cement and water at OMC. The mixtures were then compacted to achieve at least 95% of the MDD using a roller compactor [Fig. 2(a)]. The material compaction proceeded according to AG: PT/T220 (Austroads 2005). Each CTB slab was cured for at least seven days to gain sufficient strength before cutting. Three prismatic beams—400 mm in length, 63.5 mm wide, and 50 mm thick—were then cut from each compacted slab, as shown in Figs. 2(b and c). All specimens were cured at 25°C for 28 days (after adding cement and water to CRB) prior to the 4PB tests.

Test Methodology

Fig. 3 illustrates the three stages of the test methodology in this study. In Stage 1, OMC and MDD of CRB and cement mixtures used to produce CTB were determined based on the modified compaction tests in accordance with the standard of ASTM D1557 (ASTM 2012). Therefore, an optimum level of water added and a target density for CTB specimen preparation processes can be established. Moreover, the flexural strength or modulus of rupture (MOR) under static loading conditions was evaluated from prismatic CTB test beams with three replicate specimens in Stage 1. The effects of loading waveforms and applied strain levels were investigated in Stage 2. In addition, a suitable strain level for fatigue life measurements of CTB was introduced according to the test results obtained in Stage 2. In Stage 3, a suitable strain level obtained from Stage 2 was then applied to 4PB tests to investigate the effects of cement contents of CTB. The 4PB tests under the stress-controlled mode were also selected for use in Stage 3.

Flexural Strength Tests of CTB

In this study, the flexural strength test standard for the concrete material, AS 1012.11 (AS 2000), was adapted to measure the static flexural strength of CTB with the different beam size from the standard (AS 2000). The altered test specimens' dimensions of $50 \times 63.5 \times 400$ mm^3, which is the same size as the test specimen of the standard 4PB test for AC (Austroads 2006a), were used instead. Support span width [L in Fig. 4(a)] for the flexural strength measurement is 355.5 mm; therefore, the loading span width is 118.5 mm (L/3). Accordingly, the flexural strength is the

Fig. 2. Manufacturing of beam specimens: (a) roller compactor used for making CTB slabs; (b) cutting machine; (c) prismatic beams cut from compacted slab

Downloaded from ascelibrary.org by CURTIN UNIV OF TECHNOLOGY on 04/26/16. Copyright ASCE. For personal use only; all rights reserved.

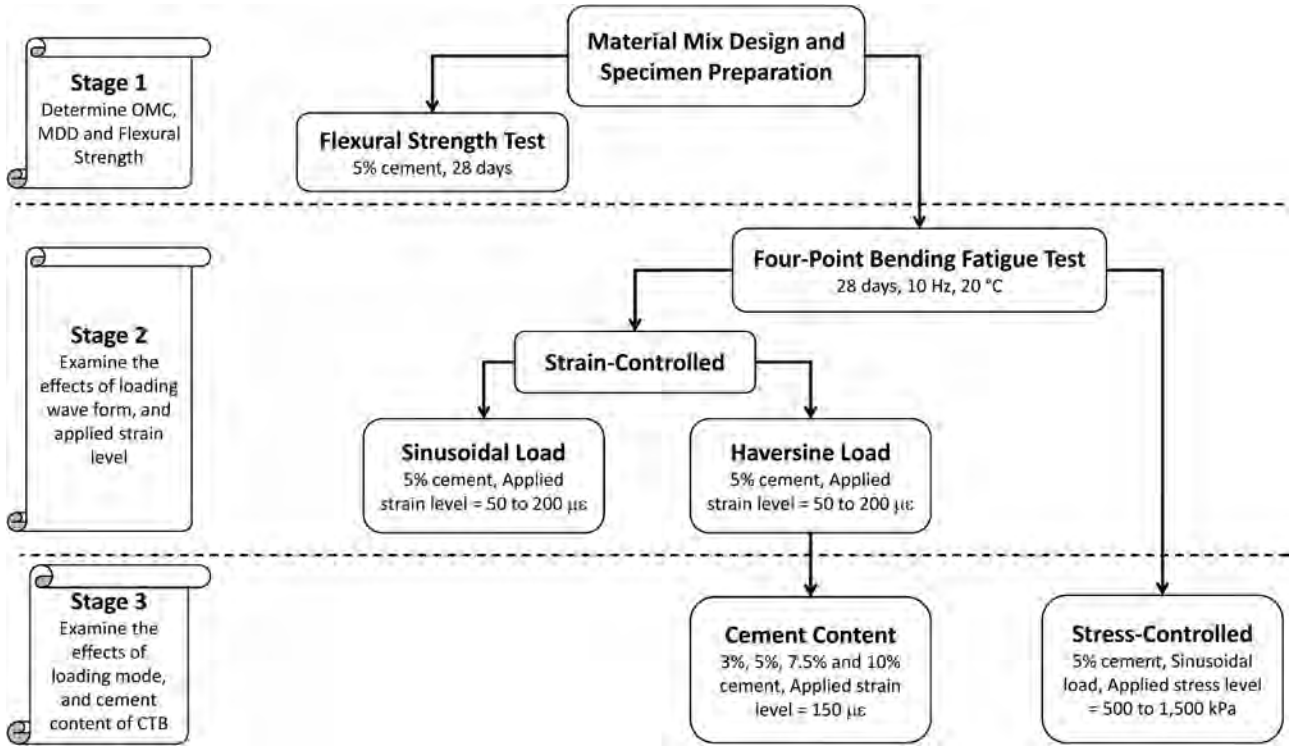

Fig. 3. Test methodology

maximum tensile stress at the bottom fiber of the test specimen, which can be calculated by Eq. (3)

$$f_{cf} = \frac{PL}{bxh^2} \tag{3}$$

where f_{cf} = flexural strength (MPa); P = applied load (kN); L = center-to-center spacing between outside clamp (0.3555 m); b = specimen width (m); and h = specimen height (m). Flexural strengths measured in this study were used for the purpose of comparison with results from the 4PB tests only.

4PB Tests of CTB

The 4PB test standard of AC, according to the Austroads standard test method (Austroads 2006a), was adapted to test CTB specimens in this study. Fig. 4 illustrates the European (EN) standard tester equipped with the 4PB jig manufactured by IPC Global, Victoria, Australia. The tester consists of three major components: the test chamber, the control and data acquisition system (CDAS), and the 4PB jig. The major test control system is a real-time computer control and flexible data acquisition system, called the integrated multi-axis control system (IMACS), which helps to improve data resolution and reduce data noise. Throughout the test process, testing temperature is controlled inside the test chamber [Fig. 4(b)]. The temperature can be assigned to the specimens in the range of 0–60°C with the temperature stability of −0.2°C. Inside the test chamber, the 4PB jig is located at the middle of the loading frame [Fig. 4(a)]. The suitable height and width of the test specimen are either 50×50 mm^2, 50×63.5 mm^2, or 70×70 mm^2. The test specimen is restrained by four clamps, with two outside clamps as beam supports and two points of loading applied via the two central clamps, as shown in Fig. 4(a). The spacing between each clamp is 118.5 mm. During the tests, the cyclic load is continually applied to the prismatic test specimen in the form of the haversine or sinusoidal waveform. The test conditions of the constant applied stress or strain on test specimens are generally used under either the stress-controlled or strain-controlled mode. The load actuator is connected to both central clamps at the bottom of the 4PB jig. The frequency range of the load actuator is 0.01 to 60 Hz. During cyclic loading, beam deflection is measured at the midspan of the top fiber of a test specimen by a linear variable differential transformer (LVDT). The stroke of the LVDT is limited to ±0.50 mm with a resolution of 0.25 μm and an accuracy of 1 μm (Austroads 2006a). Consequently, the maximum tensile stress (σ_t) in the unit of Pascal and the maximum tensile strain (ε_t) at midspan of the top of a test beam can be calculated from Eqs. (4) and (5), respectively

$$\sigma_t = \frac{3xaxP}{bxh^2} \tag{4}$$

$$\varepsilon_t = \frac{12x\delta xh}{(3xL^2) - (4xa^2)} \tag{5}$$

where a = center-to-center spacing between each clamp (0.1185 m), P = applied load (N), b = specimen width (m), h = specimen height (m), δ = maximum beam deflection (m), and L = center-to-center spacing between outside clamp (0.3555 m). Finally, the cyclic flexural stiffness of the prismatic beam can be estimated by dividing the maximum tensile stress with the maximum tensile strain (σ_t/ε_t). The limitations of applied dynamic load and actuator stroke are ±4.4 kN and ±5.0 mm, respectively. Based on Eq. (5), this maximum applied load of 4.4 kN is equivalent to 9,850 kPa of the maximum tensile stress, when 63.5 mm-width and 50.0 mm-height prismatic beam is tested under the haversine waveform. The resolution of the applied dynamic load is ±2.2 N with an accuracy of ±20 N (Austroads 2006a).

The AG:PT/T233 standard (Austroads 2006a) recommends measuring the fatigue life of the AC by applying a haversine cyclic load with a frequency of 10 Hz to the specimens. In this study, the

Downloaded from ascelibrary.org by CURTIN UNIV OF TECHNOLOGY on 04/26/16. Copyright ASCE. For personal use only; all rights reserved.

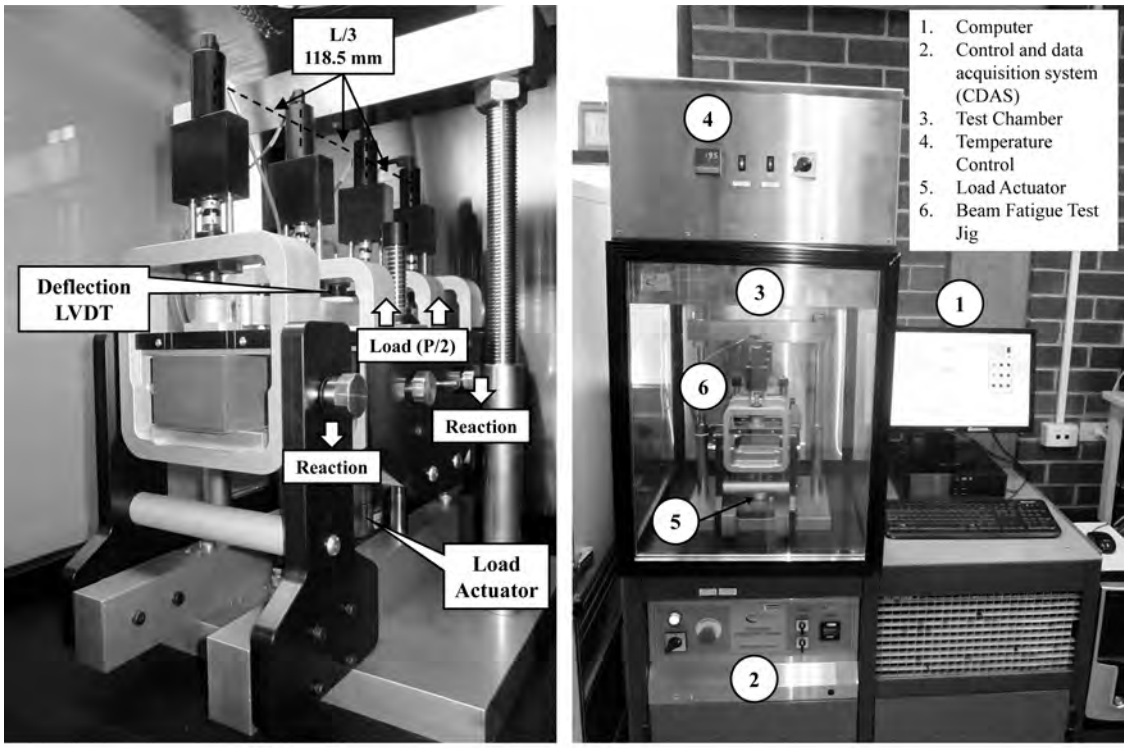

Fig. 4. 4PB test apparatus: (a) the 4PB jig; (b) EN standard tester equipped with 4PB jig

loading frequency of 10 Hz was also applied to the 4PB tests of the CTB material. It should be noticed that in the real situation, applied loading frequencies of an AC layer and a CTB layer may not be the same because the loading time decreases with depth in a pavement. However, with no strong proof of a right frequency magnitude in a CTB layer at this stage, using the applied loading frequency of 10 Hz in this study relies on the hypothesis that CTB layer is conventionally overlaid by an relatively thin AC layer within the same pavement structure; therefore, they would be eventually subjected to almost the same loading frequency in an underneath CTB layer. During the AC tests, the applied tensile strain at the beam top is generally specified to be equal to a constant 400 microstrain under the strain-controlled mode. However, the applied tensile strains in this study were varied to suit the inherent properties of the CTB test specimens. The test temperature in the chamber is kept constant at 20°C throughout the test. The reduction in the cyclic flexural stiffness is monitored and terminated when either the cyclic flexural stiffness is reduced to 50% of the initial value or one million loading cycles is completed (approximately 28 h). According to AG:PT/T233 (Austroads 2006a), initial cyclic flexural stiffness is defined as the flexural stiffness value at the 50th loading cycle of a full series of applied cyclic loading cycles.

Experimental Results and Discussions

Flexural Strength of CTB

Table 1 shows the results of the flexural strength tests performed in this study. According to the test results, the flexural strength of CTB with 5% cement averaged from three replicated specimens is 1.53 MPa. These test results were planned for use as the reference flexural strength of the CTB test specimens in the stress-controlled 4PB test, performed in this study.

Table 1. Flexural Test Result Summary

Specimen identifier	P (kN)	b (mm)	h (mm)	f_{cf} (MPa)
M-1	0.6231	62.10	48.40	1.52
M-2	0.6844	61.30	48.30	1.70
M-3	0.4446	62.10	49.10	1.36
Average	0.5840	—	—	1.53

Effects of Loading Modes and Applied Strain Levels on Fatigue Characteristics of CTB

At this stage, 5% cement specimens were tested under the conditions of the cyclic load and strain-controlled (constant strain) mode. The two main loading waveforms of the repeated sinusoidal and haversine load were applied separately to the CTB test specimens, without the rest period, until the specimens failed by fatigue damage (a reduction in cyclic flexural stiffness to one-half the initial value) or one million cycles of cyclic load was completed. Fig. 5 shows the results of the 4PB tests under the haversine load at different applied strain levels, while Fig. 6 presents the results of the 4PB test under the sinusoidal load at different applied strain levels.

Table 2 provides information on the 4PB test parameters and test results of this study. Note that specimens F-1, F-2, F-3, F-5, F-15, F-16, F-17, and F-18 were prepared and tested prior to the other specimens (first batch).

In Figs. 5 and 6, the normalized cyclic flexural stiffness is defined as the ratio between cyclic flexural stiffness measured at the specified loading cycle and initial cyclic flexural stiffness. According to AG:PT/T233 (Austroads 2006a), the test specimen can be considered as a fail specimen with fatigue damages if the cyclic flexural stiffness is reduced by one-half the initial value; therefore, the maximum and minimum values of normalized cyclic flexural

Downloaded from ascelibrary.org by CURTIN UNIV OF TECHNOLOGY on 04/26/16. Copyright ASCE. For personal use only; all rights reserved.

Downloaded from ascelibrary.org by CURTIN UNIV OF TECHNOLOGY on 04/26/16. Copyright ASCE. For personal use only; all rights reserved.

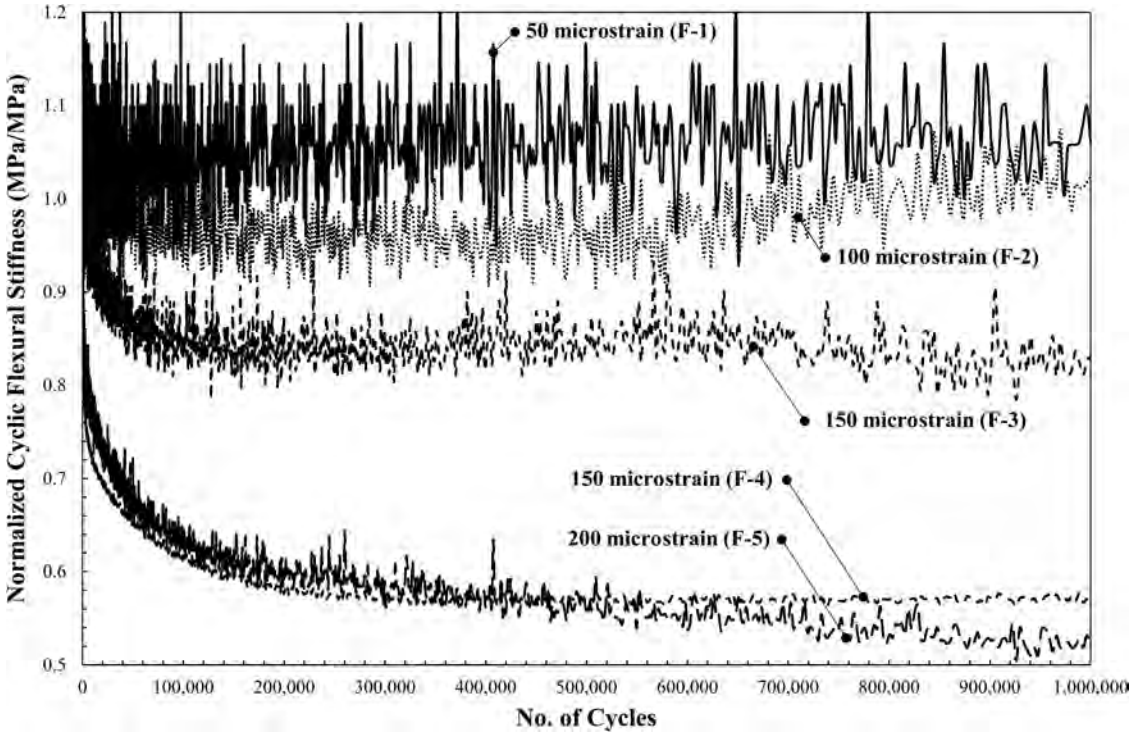

Fig. 5. Strain-controlled 4PB test results of 5% cement specimens under haversine load and different strain levels

stiffness are 1.0 and 0.5, respectively. The test results revealed that the CTB test specimens in this study show fatigue characteristics (i.e., more cyclic flexural stiffness reduction with more loading cycles) when they are subjected to sinusoidal and haversine loads under strain-controlled tests. Furthermore, it can be noticed that the fatigue behavior, represented by the fatigue curves from the tests (Figs. 5 and 6), of the CTB test specimens in this study is significantly influenced by the applied strain levels. Different fatigue curves corresponding to different applied strain levels can be observed. Table 2 also shows that the final cyclic flexural stiffness values of specimens F-1, F-2, F-6, and F-7 are reduced by less than 15% of the initial value. Moreover, the cyclic flexural stiffness values of these specimens were not dropped further after the cyclic load was applied by approximately 150,000 cycles. Therefore, it

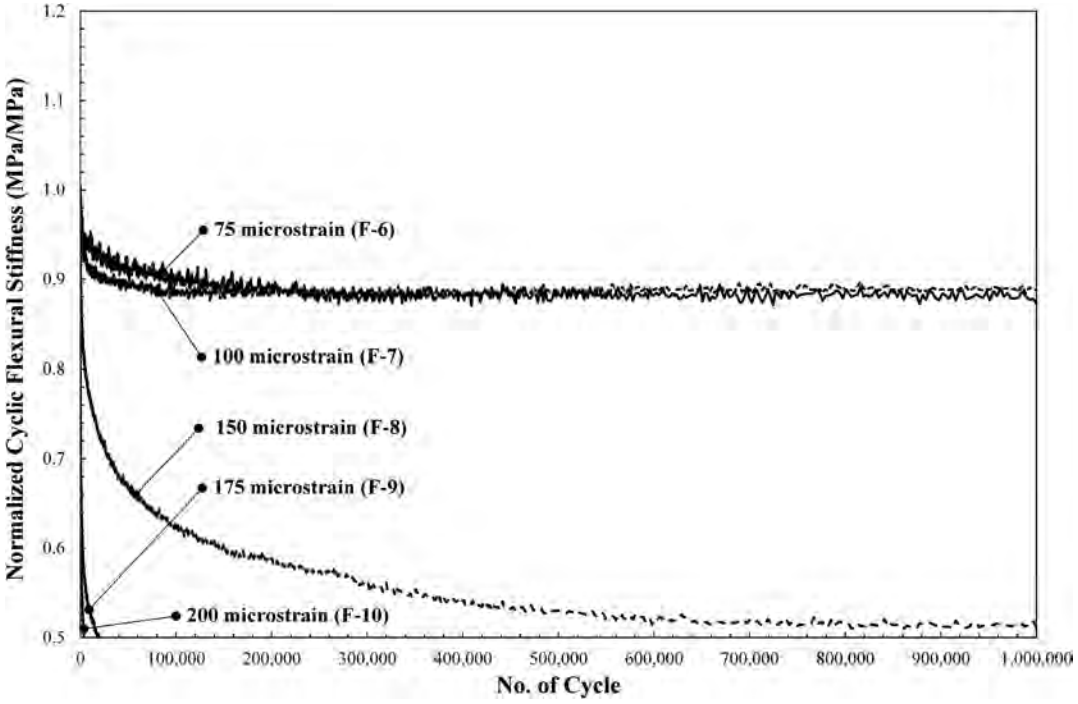

Fig. 6. Strain-controlled 4PB test results of 5% cement specimens under sinusoidal load and different strain levels

Table 2. 4PB Test Parameters and Test Results

Specimen identifier	Cement content (%)	Specimen dimension (mm)		Test controlled mode/applied loading waveform	Applied stress/ strain level	Cyclic flexural stiffness (MPa)		Number of tested cycle (cycles)
		Width	Depth			Initial[a]	Final[b]	
Stage 2: Haversine loading waveform under strain-controlled test								
F-1	5	63.95	49.72	Strain/haversine	50 $\mu\varepsilon$	20,500	21,966	1,000,000
F-2	5	58.30	49.30	Strain/haversine	100 $\mu\varepsilon$	20,407	20,733	1,000,000
F-3	5	62.10	49.00	Strain/haversine	150 $\mu\varepsilon$	14,721	12,155	1,000,000
F-4	5	63.34	49.41	Strain/haversine	150 $\mu\varepsilon$	8,244	4,698	1,000,000
F-5	5	63.40	45.40	Strain/haversine	200 $\mu\varepsilon$	22,510	11,797	1,000,000
Stage 2: Sinusoidal loading waveform under strain-controlled test								
F-6	5	62.52	48.78	Strain/sinusoidal	75 $\mu\varepsilon$	9,982	8,716	1,000,000
F-7	5	62.25	48.47	Strain/sinusoidal	100 $\mu\varepsilon$	12,308	10,934	1,000,000
F-8	5	62.66	49.68	Strain/sinusoidal	150 $\mu\varepsilon$	9,737	4,970	1,000,000
F-9	5	61.67	48.62	Strain/sinusoidal	175 $\mu\varepsilon$	11,097	5,547	18,889
F-10	5	61.21	47.13	Strain/sinusoidal	200 $\mu\varepsilon$	7,818	3,909	3,941
Stage 3: Sinusoidal loading waveform under stress-controlled test								
F-11	5	61.87	49.93	Stress/sinusoidal	800 kPa	9,573	9,724	1,000,000
F-12	5	62.62	49.33	Stress/sinusoidal	1,000 kPa	14,882	14,913	1,000,000
F-13	5	62.62	49.69	Stress/sinusoidal	1,000 kPa	13,916	12,028	1,000,000
F-14	5	62.32	49.02	Stress/sinusoidal	1,500 kPa	13,690	5,574	350
Stages 2 and 3: Haversine loading waveform under strain-controlled test								
F-15	3	63.60	50.10	Strain/haversine	50 $\mu\varepsilon$	12,579	13,504	1,000,000
F-16	3	64.60	48.90	Strain/haversine	100 $\mu\varepsilon$	9,617	8,051	1,000,000
F-17	3	63.20	49.60	Strain/haversine	150 $\mu\varepsilon$	5,687	4,668	1,000,000
F-18	3	62.90	50.20	Strain/haversine	200 $\mu\varepsilon$	1,985	1,740	1,000,000
Stage 3: Haversine loading waveform under strain-controlled test								
F-19	7.5	62.77	50.04	Strain/haversine	150 $\mu\varepsilon$	9,949	4,968	1,000,000[c]
F-20	7.5	62.80	49.36	Strain/haversine	150 $\mu\varepsilon$	7,492	4,927	1,000,000
F-21	7.5	63.33	49.51	Strain/haversine	150 $\mu\varepsilon$	10,339	5,167	1,000,000[d]
F-22	10	62.59	49.84	Strain/haversine	150 $\mu\varepsilon$	15,075	11,434	1,000,000
F-23	10	61.76	49.88	Strain/haversine	150 $\mu\varepsilon$	13,224	7,369	1,000,000
F-24	10	61.94	49.13	Strain/haversine	150 $\mu\varepsilon$	13,349	11,492	1,000,000

[a]Cyclic flexural stiffness at the 50th loading cycle.
[b]Cyclic flexural stiffness measured at the last loading cycle.
[c]Number of cycles to one-half the initial value was 49,660.
[d]Number of cycles to one-half the initial value was 82,856.

should be highlighted that from the results of this particular study, *the CTB specimens subjected to applied strain level less than or equal to 100 microstrain are likely to have minor damages induced by repeated sinusoidal and haversine loads*. In contrast, the cyclic flexural stiffness of specimens F-4, F-5, F-8, F-9, and F-10 were remarkably influenced by cyclic load. For the case of cyclic load with the applied strain level of 150 microstrain (specimens F-4 and F-8), the cyclic flexural stiffness values of the specimens under such a condition were reduced by approximately 50% of their initial values at one millionth cycle. For the strain levels greater than or equal to 175 microstrain, the cyclic flexural stiffness values of the test specimens were dropped by one-half of the initial values within the early cycle of loading. According to the test results in this study, repeated sinusoidal and haversine loads with the strain level greater than 150 microstrain created significant fatigue damages to the CTB specimens. However, this does not conform for specimens F-3 and F-5, from which the results of cyclic load with applied constant strain levels equal to 150 microstrain (F-3) and 200 microstrain (F-5) led to the reduction in the cyclic flexural stiffness by less than 50%. Based on the information illustrated in Table 2, high initial cyclic flexural stiffness of specimens F-3 and F-5 may be the cause of slight reduction in the cyclic flexural stiffness. A similar finding is encountered from the 4PB test of specimens with higher cement content (S-22, S-23, and S-24).

Some levels of stress or strain that are repeatedly applied under cyclic conditions to the pavement materials, for an assigned number of loading cycles, and cause no bottom-up fatigue damages can be defined as the *fatigue endurance limit* (Prowell et al. 2010). The concept of fatigue endurance limit was formally purposed for metal by Wohler in 1870 (Witczak et al. 2013). It was later applied to the perpetual pavement design concept for flexural pavement in the early of 2000s (Portillo 2008). Witczak et al. (2013) defined the concept of the perpetual pavement as a designed and built pavement that could last longer than the designed lifetime of road structure, without the requirements in major rehabilitation and reconstruction. Additional literature and basic knowledge on the perpetual pavement design can be found from Portillo (2008) and Witczak et al. (2013). For concrete pavement, Huang (2004) stated that fatigue damages of concrete pavement can be disregarded if the applied stress levels from vehicles are maintained at 45% of flexural strength of concrete and lower. Note that, the aforementioned concrete pavement is the conventional road structure paved by concrete. Fig. 7 shows the relationship between applied strain levels and fatigue lives (i.e., at the 50% reduction of the cyclic flexural stiffness compared to the original value) of the test CTB specimens in this study. The figure indicates that the test CTB specimens with 5% cement in this particular study did not fail by cyclic loading with the applied strain level of 150 microstrain under

Downloaded from ascelibrary.org by CURTIN UNIV OF TECHNOLOGY on 04/26/16. Copyright ASCE. For personal use only; all rights reserved.

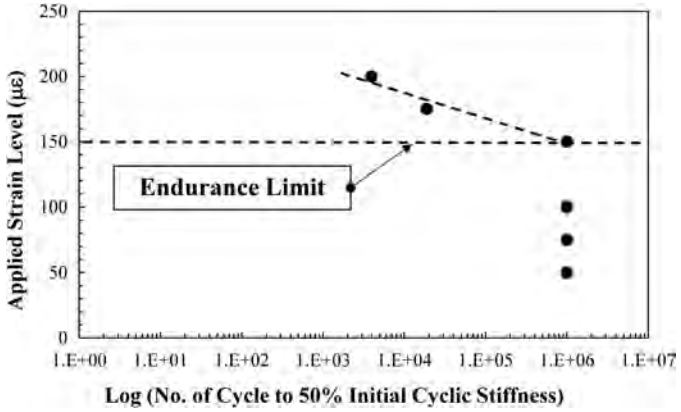

Fig. 7. Proposed fatigue endurance limit of CTB with 5% cement

less than one million cycles. According to Austroads (2014a), the number of load repetitions throughout the design life of road pavement with a CTB layer can be calculated from Eq. (6)

$$N = RF\left[\frac{SFxk}{\mu\varepsilon}\right]^{12} = RF(SF)^{12}\left[\frac{k}{\mu\varepsilon}\right]^{12} \quad (6)$$

where N = design number of load repetition in the field; RF = reliability factor (equal to 1 for project reliability equal to 95%); $\mu\varepsilon$ = load-induced tensile strain at the base of CTB layer (microstrain); SF = laboratory-to-field shift factor; and k = fatigue constant obtained from 4PB test data. Based on this guideline, the presumptive value of 1.8 is recommended for SF. Consequently, the design number of load repetitions in the field can be determined by multiplying the number of load repetitions acquired from the 4PB tests by 1,150 (or 1.8^{12}). This means that one million cycles of the cyclic load from the 4PB tests are equivalent to 1.15×10^9 load repetitions in the field. If traffic estimation assumptions and procedures in Appendix H of Austroads (2010) are applied to this study, therefore, 1.15×10^9 cycles is approximately equal to the number of load repetitions in an 80-year period on the road structure. It should be noted that the number of load repetitions calculated earlier is based on annual averaged daily traffic (AADT) and cumulative growth factor (CGF) equal to 5,350 vehicles per year, and 4% were presumed in the calculation, respectively. Therefore, a CTB layer with 5% cement in the field, under cyclic load-induced tensile strain equal to 150 microstrain and less, may sustain from the fatigue failure up to 80 years based on given conditions. However, this conclusion was established from the certain number of test results. The 4PB tests in this study only revealed the existence of fatigue endurance limit; further verifications are required for endurance limit determination of the CTB material in road pavement design.

The 4PB tests of 3% cement specimens under different applied strain levels were also performed in this study (Table 2). This includes specimen F-15, F-16, F-17, and F-18. However, high variations in the initial cyclic flexural stiffness were observed, which may influence the fatigue life measurement in the 4PB test. Inconsistency in the cyclic initial flexural stiffness of these specimens with the same cement content indicates that the specimen preparation process has relevant effects on 4PB test results, especially specimens with relatively low cement content. Cracks would take place (i.e., more likely for relatively low cement content specimens) during specimen preparation; cutting and handling would be the main reason of considerable fluctuations in the initial cyclic flexural stiffness. Consequently, it should be emphasized that the process of alternative specimen preparation for CTB with low cement content should be developed to manipulate the inconsistency in material properties.

4PB Test under Stress-Controlled Mode

Eight CTB test specimens were examined in this study under the sinusoidal waveform with the stress-controlled mode. However, only these four tests were successful. The other half of the specimens were failed mostly at the very early stage of the test. This could be explained by the fact that CTB is too brittle or fragile to withstand the test condition under the stress-controlled mode. Relatively low excessive stress levels may cause immediate damages to the prismatic beam specimens. Accordingly, only the details of completed tests were given in this section (Table 2 and Fig. 8). Relevant properties of CTB measured from the 4PB test are typically uncertain (Austroads 2014b; Walker and Bloem 1957). Furthermore, determining the appropriate applied stress level for the 4PB test under the stress-controlled mode by means of the trial-and-error approach is difficult and almost impossible. In contrast, an appropriate applied strain level was potentially determined from the test results in the previous section with the strain-controlled mode. In addition, Austroads (2014b) suggests employing the strain-based equation for fatigue life estimation of road pavement with the CTB layer for two main reasons. First, the strain-based equation is fitted with the 4PB test results better than the stress-based equation. Second, fatigue data from full-scale tests by accelerated loading facility (ALF) are more appropriately explained by the strain-based equation. However, the strain-controlled test mode is more suitable in representing the loading regime for relatively thin pavements, while an appropriate loading condition for thick pavements can be found from the stress-controlled tests (Prowell et al. 2010; Rao Tangella et al. 1990; Tayebali et al. 1994). Nevertheless, the strain-controlled test was recommended for fatigue life estimation of all asphalt pavement types (Prowell et al. 2010). Detailed analysis of the loading mode selection for asphalt pavement design can be found from Rao Tangella et al. (1990). Consequently, the 4PB tests under the strain-controlled mode appear to be more suitable than the stress-controlled mode with fatigue life measurements of CTB.

Based on test results shown in Fig. 8, applied sinusoidal load with stress levels equal to 800, 1,000, and 1,500 kPa are equivalent to 52, 65, and 98% of the CTB flexural strength (Table 1). It could be noted that the tensile strains of a test beam at the top and the bottom for applied stress of 800, 1,000, and 1,500 kPa were approximately equal to 75 microstrain, 80 microstrain, and 100 microstrain, respectively. According to the 4PB test guideline of Austroads (2014a), applied force within the range of 60–90% of the ultimate load is recommended for the fatigue life measurement of CTB. This guideline recommended that a loading range that is equivalent to the applied strain levels vary from 50 to 120 microstrain. However, this strain range created only minor damages to the CTB test specimens in this study (Figs. 5 and 6). This is because specimen size, test configurations, and load configurations recommended by Austroads (2014a) are different from those for the 4PB test conducted in this study. In that guideline, larger prismatic beams and cyclic load with rest period are suggested for the 4PB test of a CTB material. In this study, an appropriate stress level for the 4PB test under the stress-controlled mode cannot be correlated with any applied strain levels of the strain-controlled mode tests.

Effects of Cement Content on Fatigue Characteristics of CTB Specimens

In this final stage, the effects of cement content to the fatigue characteristics of the CTB test specimens were examined in this study. Test results from the previous sections indicated that cyclic load with the applied strain level of 150 microstrain reduces the cyclic flexural stiffness of the CTB test specimens by one-half the initial

Downloaded from ascelibrary.org by CURTIN UNIV OF TECHNOLOGY on 04/26/16. Copyright ASCE. For personal use only; all rights reserved.

Downloaded from ascelibrary.org by CURTIN UNIV OF TECHNOLOGY on 04/26/16. Copyright ASCE. For personal use only; all rights reserved.

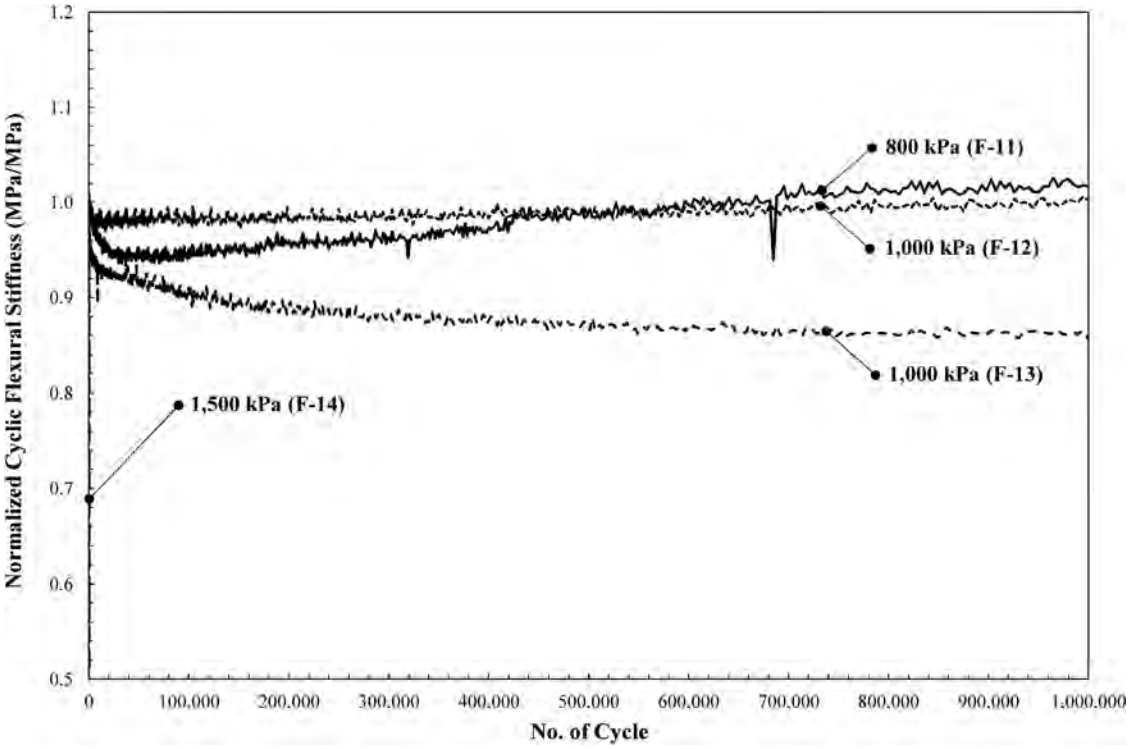

Fig. 8. Stress-controlled 4PB test results of 5% cement specimens under sinusoidal load and different stress levels

value within one million cycles of each applied load condition (Figs. 5 and 6). Therefore, the haversine load with the strain level of 150 microstrain was applied to all tests in this stage. Fig. 9 shows the results of the strain-controlled 4PB test of CTB test specimens with various cement contents. The cyclic flexural stiffness values of CTB test specimens measured in this stage were allowed to reduce to more than one-half the initial value to investigate the completed stiffness-reduction curves. Therefore, the 4PB tests at this stage were terminated at one million cycles without considering the stiffness reduction criteria at the 50% initial cyclic stiffness value. Besides the uncertainty of 4PB test results, it can be seen clearly from Fig. 9 that cement content affects the fatigue characteristics of

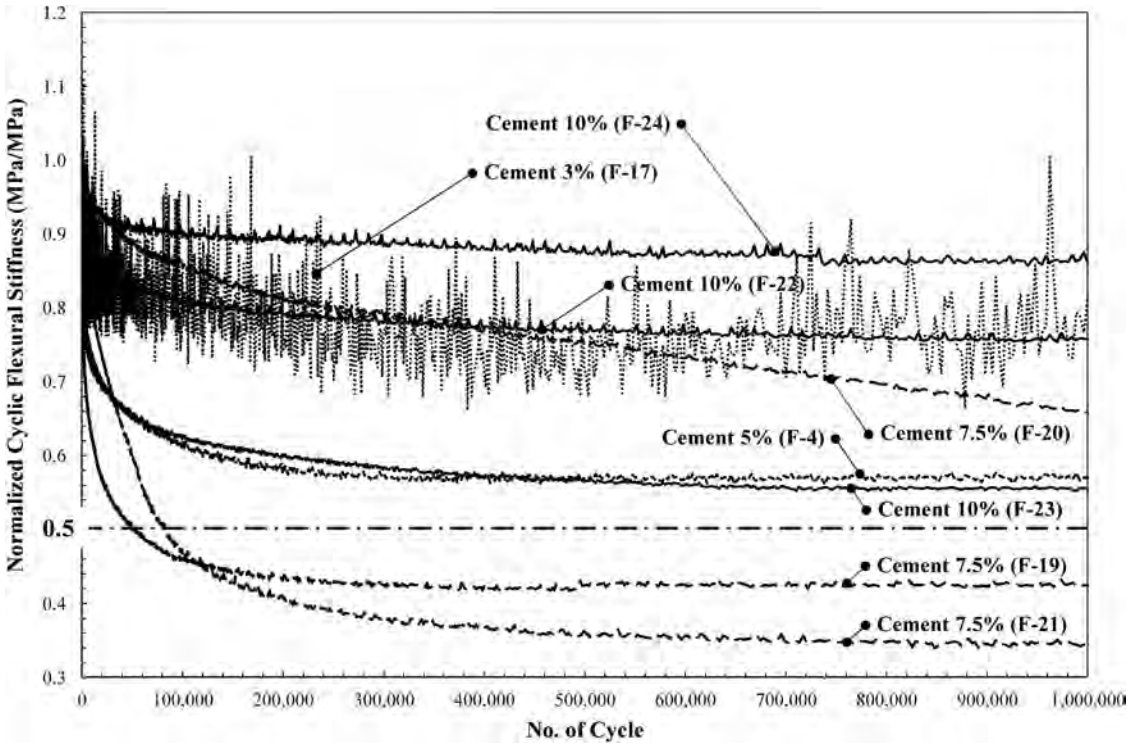

Fig. 9. Strain-controlled 4PB test results of CTB specimens under haversine load with strain level equal to 150 microstrain

the CTB test specimens in this study. The 10% cement specimens showed a lesser tendency to fail by cyclic load compared to the specimens with 5 and 7.5% cement contents. In this study, specimens with different cement contents were tested under the same strain level (150 microstrain), and in the strain-controlled condition. It means that specimens with higher cement content (higher strength) were subjected to lower initial stress ratio (ratio between applied peak stress and flexural strength) compared to the specimen with lower cement content or lower strength. Similar to concrete material, applied lower initial stress ratio to the beam-fatigue test leads to the longer fatigue life of test specimen than the fatigue life of specimen subjected to higher initial stress ratio (Destrebecq 2010). It also indicates that based on the test conditions of this study, a specimen with the higher initial cyclic flexural stiffness has higher fatigue failure resistance than that of specimens with lower initial cyclic flexural stiffness. This finding also supports the hypothesis established in the first stage of this test. Consequently, a suitable applied strain level for the 4PB test should be increased with respect to a level of the initial cyclic flexural stiffness and cement content of the test specimens.

Conclusions

The fatigue characteristics of the CTB material through a set of the CTB test specimens in this study were investigated using the adapted fatigue life measurement method (the 4PB tests) of asphalt concrete in accordance with the test standard of AG:PT/T233 (Austroads 2006a). Prismatic beam test specimens of CTB with 3–10% cement contents were prepared to achieve at least 95% of MDD using a roller compactor. After cutting and trimming, the specimens were cured at 25°C for 28 days. During the 4PB tests, the cyclic load with the constant loading frequency of 10 Hz was applied to test specimens at 20°C in the temperature-controlled chamber throughout the test. Important key findings discovered from this study can be concluded as follows:

- The effects of sinusoidal and haversine loading waveforms to fatigue characteristics of the CTB test specimens were examined in the early stages of testing. For the strain-controlled 4PB tests, the CTB test specimens exhibited fatigue responses under both sinusoidal loads and haversine loads. However, the fatigue characteristics of the CTB test specimens were greatly influenced by applied strain levels. The greater the applied strain level, the shorter the fatigue life of the CTB test specimens.
- The strain-controlled 4PB tests of 5% cement CTB test specimens reveal the existence of the *fatigue endurance limit*. After one million cycles of cyclic loading, the cyclic flexural stiffness values of such specimens under applied strain levels less than 150 microstrain were reduced by only approximately 15% of their initial values. In contrast, applied strain levels greater than 150 microstrain resulted in rapid and significant reductions of the cyclic flexural stiffness to 50% of the initial values within the early cycle of cyclic load. Therefore, the fatigue endurance limit of 5% cement CTB should be the applied strain level located underneath 150 microstrain. In addition, the applied strain level of 150 microstrain could be recommended for the 4PB test of 5% cement CTB based on the particular test conditions of this study. This is because the cyclic flexural stiffness of CTB specimens subjected to the 150 microstrain test condition were reduced by approximately 50% of the initial values at the one millionth cycle, based on the fatigue failure criterion of the 50% cyclic flexural stiffness reduction from the initial value.
- The prismatic beam test specimens for the 4PB tests, prepared based on the particular conditions in this study, were sensitive to the applied stress level in the stress-controlled test conditions. A small increase in an applied stress level may lead to an abrupt failure of test specimens. Accordingly, one-half of the test specimens in this study were failed at the early cycle of loading. The conclusion cannot be made for the suitability of using the stress-controlled test condition to determine the fatigue life of a CTB material based on the particular test conditions of this study.
- The cement content affects the fatigue characteristics of the CTB test specimens in this study. Test results showed that, under the same applied strain level, specimens with higher cement content and initial cyclic flexural stiffness have more fatigue failure resistance compared to that of specimens with lower cement content and initial stiffness. It could be recommended that a suitable applied strain level should be increased to agree with the 4PB test of specimens with higher cement content.

Acknowledgments

Funding for this study was partly provided by the Australian Research Council (ARC) through its support of ARC Linkage Scheme - LP 130100884, and by the project partners of Queensland Department of Transportation and Main Roads, IPC Global, Golders Associates, Hong Kong Road Research Laboratory (HKRRL). The authors would like to thank the ARC and the project partners for their financial support to this project, and their in-kind contributions are also gratefully acknowledged. In addition, the fourth author acknowledges the support of Khon Kaen University and Thailand Research Fund under TRF Senior Research Scholar Contract No. RTA5780004. Moreover, the research team of the Civil Engineering Department, Chiang Mai University, Thailand, is also gratefully endorsed for providing guidance regarding the overview and for its valuable input into this work.

References

AASHTO. (2007). "Standard method of test for determining the fatigue life of compacted hot mix asphalt (HMA) subjected to repeated flexural bending." *AASHTO T321*, Washington, DC.

Arulrajah, A., Disfani, M. M., Haghighi, H., Mohammadinia, A., and Horpibulsuk, S. (2015). "Modulus of rupture evaluation of cement stabilized recycled glass/recycled concrete aggregate blends." *Constr. Build. Mater.*, 84, 146–155.

AS (Standards Australia). (2000). "Methods of testing concrete—Method 11: Determination of the modulus of rupture." *AS 1012.11*, Sydney, Australia.

AS (Standards Australia). (2010). "General purpose and blended cements." *AS 3972*, Sydney, Australia.

ASTM. (2008). "Standard test method for direct tensile strength of intact rock core specimens." *ASTM D2936*, West Conshohocken, PA.

ASTM. (2010). "Standard test method for determining fatigue failure of compacted asphalt concrete subjected to repeated flexural bending." *ASTM D7460*, West Conshohocken, PA.

ASTM. (2011). "Standard test method for splitting tensile strength of cylindrical concrete specimens." *ASTM C496*, West Conshohocken, PA.

ASTM. (2012). "Standard test methods for laboratory compaction characteristics of soil using modified effort (56,000 ft-lbf/ft^3 (2,700 kN-m/m^3))." *ASTM D1557*, West Conshohocken, PA.

Austroads. (2005). "Sample preparation—Compaction of asphalt slabs suitable for characterisation." *AG:PT/T220*, Australia.

Austroads. (2006a). "Fatigue life of compacted bituminous mixes subjected to repeated flexural bending." *AG:PT/T233*, Australia.

Austroads. (2006b). "Guide to pavement technology. Part 4D: Stabilised materials." *AGPT04D-06*, Australia.

Austroads. (2010). "Guide to pavement technology. Part 2: Pavement structural design." *AGPT04 A-08*, Australia.

Downloaded from ascelibrary.org by CURTIN UNIV OF TECHNOLOGY on 04/26/16. Copyright ASCE. For personal use only; all rights reserved.

Austroads. (2014a). "Cemented materials characterisation: Final report." *AP-R462-14*, Australia.
Austroads. (2014b). "Framework for the revision of Austroads design procedures for pavements containing cemented materials." *AP-R463-14*, Australia.
Cho, Y. H., Lee, K. W., and Ryu, S. W. (2006). "Development of cement-treated base material for reducing shrinkage cracks." *J. Transport. Res. Board*, 1952, 134–143.
Chummuneerat, S., Jitsangiam, P., Nikraz, H., and Patel, R. (2013). "Fatigue characteristics of cement treated base for Western Australian roads." *2nd Int. Conf. on Engineering and Applied Sciences*, Emerald Group Publishing Limited, West Yorkshire, U.K.
Destrebecq, J. F. (2010). "Cyclic and dynamic loading fatigue of structural concrete." *Mechanical behavior of concrete*, J. M. Torrenti, G. Pijaudier-Cabot, and J. M. Reynouard, eds., ISTE, London, 185–224.
Disfani, M. M., Arulrajah, A., Haghighi, H., Mohammadinia, A., and Horpibulsuk, S. (2014). "Flexural beam fatigue strength evaluation of crushed brick as a supplementary material in cement stabilized recycled concrete aggregates." *Constr. Build. Mater.*, 68, 667–676.
European Committee for Standardization. (2004). "Bituminous mixtures—Test methods for hot mix asphalt—Part 24: Resistance to fatigue." *EN 12697–24*, Brussels, Belgium.
George, K. P. (2002). "Minimizing cracking in cement-treated materials for improved performance." *Research and Development Bulletin RD123*, Portland Cement Association, Skokie, IL.
Huang, Y. H. (2004). *Pavement analysis and design*, Pearson Education, Upper Saddle River, NJ.
MRWA (Main Roads Western Australia). (2010). "Engineering road note 9." *TRIM 05/5236*, WA, Australia.
MRWA (Main Roads Western Australia). (2012). "Specification 501– Pavements." *04/10110-04*, WA, Australia.
NAASRA (National Association of Australian State Road Authorities). (1970). "Guide to stabilization in roadworks, including metric addendum." Sydney, Australia.
NCHRP (National Cooperative Highway Research Program). (2004). "Guide for mechanistic-empirical design of new and rehabilitated pavement structures." *Final Rep., Project No. 1-37 A*, Washington, DC.
Paul, D. K., and Gnanendran, C. T. (2015). "Characterization of lightly stabilized granular base materials using monotonic and cyclic load flexural testing." *J. Mater. Civ. Eng.*, 10.1061/(ASCE)MT.1943-5533.0001302, 04015074.
Pell, P. S., McCarthy, P. F., and Gardner, R. R. (1961). "Fatigue of bitumen and bituminous mixes." *Int. J. Mech. Sci.*, 3(4), 247–267.
Portillo, M. G. (2008). "Measured and theoretical response of perpetual pavement structures." M.Sc. thesis, Univ. of Texas at Arlington, Arlington, TX.
Prowell, B. D., et al. (2010). "Validating the fatigue endurance limit for hotmix asphalt." *NCHRP Rep. No. 646*, National Cooperative Highway Research Program, Washington, DC.
Rao Tangella, S. C. S., Craus, J., Deacon, J. A., and Monismith, C. L. (1990). "Summary report on fatigue response of asphalt mixtures." *SHRP A-003-A*, Strategic Highway Research Program, National Research Council, Washington, DC.
Soliman, M. I., Zeiada, W. A., Kaloush, K. E., and Mamlouk, M. S. (2012). "Assessment of different flexure fatigue failure analysis methods to estimate the number of cycles to failure of asphalt mixtures." *Four point bending*, J. Pais and J. Harvey, CRC Press, London, 27–34.
Tayebali, A. A., Deacon, J. A., Coplantz, J. S., Harvey, J. T., and Monismith, C. L. (1994). "Fatigue response of asphalt-aggregate mixes. Part I: Test method selection." *SHRP A-404*, Strategic Highway Research Program, National Research Council, Washington, DC.
Walker, S., and Bloem, D. L. (1957). "Studies of flexural strength of concrete—Part 3: Effects of variations in testing procedures." *ASTM Proc.*, ASTM, PA, 1122–1139.
Wen, H., Muhunthan, B., Wang, J., Li, X., Edil, T., and Tinjum, J. M. (2014). "Characterization of cementitiously stabilized layers for use in pavement design and analysis." *NCHRP Rep. No. 789*, National Cooperative Highway Research Program, Washington, DC.
Witczak, M., Mamlouk, M., Souliman, M., and Zeiada, W. (2013). "Validating an endurance limit for HMA pavements: Laboratory experiment and algorithm development." *NCHRP 9-44 A Final Rep.*, National Cooperative Highway Research Program, Washington, DC.

Downloaded from ascelibrary.org by CURTIN UNIV OF TECHNOLOGY on 04/26/16. Copyright ASCE. For personal use only; all rights reserved.

Chiang Mai J. Sci. 2016; 43(5) : 1160-1170
http://epg.science.cmu.ac.th/ejournal/
Contributed Paper

Effect of Nano-silica Addition on the Mechanical Properties and Thermal Conductivity of Cement Composites

Pongsak Jittabut [a], Supree Pinitsoontorn* [b], Prasit Thongbai [b], Vittaya Amornkitbamrung [b] and Prinya Chindaprasirt [c]

[a] Physics and General Science Program, Faculty of Science and Technology, Nakhon Ratchasima Rajabhat University, Nakhon Ratchasima, 30000, Thailand.

[b] Department of Physics, Faculty of Science, Khon Kaen University, Khon Kaen, 40002, Thailand.

[c] Sustainable Infrastructure Research and Development Center, Department of Civil Engineering, Faculty of Engineering, Khon Kaen University, Khon Kaen, 40002, Thailand.

*Author for correspondence; e-mail: psupree@kku.ac.th

Received: 29 July 2014
Accepted: 27 January 2015

ABSTRACT

This research article presents the mechanical properties and thermal conductivity of cement-based composite containing nano-silica. The effects of nano-silica particle size (12 nm, 50 nm and 150 nm) and concentration (1 - 5 wt.%) were systematically investigated. The compressive strength increases with certain amount of nano-silica due to the highly reactive nature of nano-silica which accelerates cement hydration reaction. Excessive nano-silica, on the other hand, leads to the decrease in strength since nano-silica absorb water required for cement hydration. This results in the creation of air void and lowers the bulk density. The maximum strength is obtained for the cement paste with 50 nm nano-silica of 4 wt.%. The compressive strength increases more than 50% in comparison to the control cement paste. For thermal conductivity measurement, adding nano-silica reduces thermal conductivity of the cement paste. The most effective agent for thermal resistivity is the 12 nm nano-silica due to the higher volume percent of air void formation. The thermal conductivity experimental results fit well with the theoretical models: the series model and the Maxwell's model.

Keywords: nanoparticles, cement composite, mechanical property, thermal conductivity, nano-silica, thermal conductivity model

1. INTRODUCTION

Nanoparticles have played an important role in improving properties of cement and concrete in recent years. The most widely used nanoparticle in cement related research is nano-silica [1-10] following the successful use of silica fume in cementitous products in the past [11, 12]. Nano-silica can improve the compressive strength of the cement paste [6, 9], mortar [1, 2] and concrete [3, 8] due to the filler effect of nano-size particles making

the denser products. Also, it can accelerate the cement hydration through the pozzolanic reaction to form C-S-H gel more quickly. Moreover, nano-silica can react with $Ca(OH)_2$ crystals to form C-S-H gel and even further strengthening the composite [1, 2, 4]. Qing et al. compared the effect of nano-silica and silica fume addition, and concluded that nano-silica can improve the mechanical properties much better than the silica fume case due to higher reactivity of nano-silica [6]. Givi et al. studied the size effects of nano-silica on the mechanical properties of binary blended concrete. They showed that the concrete with 15 nm silica particles have higher strength at the early age as compared to the concrete with 80 nm silica particles. This is due to the higher pozzolanic reaction for the smaller size [8]. However, nearly all related research have focused on mechanical properties, durability or workability of nano-silica cement composite but reports on other properties are rare.

Thermal conductivity of construction materials has received a lot of attentions since it is an important parameter related to energy conservation in buildings. Addition of many different materials on the thermal conductivity of cement-based materials has been reported, including cellulose and glass fibre, mineral wool, polystyrene, urethane foam and vermiculite [13-16]. Silica fume has also been introduced into cementitious materials in order to suppress thermal conductivity. It was shown that cement pastes mixed with silica fume exhibits >25% reduction of thermal conductivity in comparison to the plain cement paste [17, 18]. Nevertheless, there has not been any report on thermal conductivity of cement-based materials mixed with nano-silica. Thus, it would be of interest to investigate the effect of nano-silica addition on the thermal conductivity of the cement paste.

In this paper, we present the results on mechanical property and thermal conductivity of cement paste mixed with nano-silica. The concentration as well as the size of nano-silica was systematically investigated. The results were discussed based on cement hydration reaction and air void formation. The experimental results were fitted with thermal conductivity models.

2. MATERIALS AND METHODS

2.1 Sample Preparation

Ordinary Portland cement (OPC) conforming to the ASTM C150 standard was used. The chemical and physical properties of the cement are shown in Table 1. Three different sizes of nano-silica particles (the average diameter of 12, 50 and 150 nm) were used in this study. The properties of the utilized nano-particles are presented in Table 2.

Table 1. The chemical and physical properties of the Portland cement.

SiO_2 (%)	Al_2O_3 (%)	Fe_2O_3 (%)	CaO (%)	MgO (%)	K_2O (%)	Na_2O (%)	SO_3 (%)	Loss of ignition (%)	Specific surface area(m^2/g)
20.80	4.70	3.40	65.30	1.50	0.40	0.10	2.70	0.90	0.38

Table 2. Physical properties of the nano-silica obtained from manufacturers.

Nanoparticle	Purity (%)	Loss of ignition (%)	Specific surface area (m^2/g)
Nano-silica 12 nm	≥ 99.8	0.2	200
Nano-silica 50 nm	≥ 99.8	0.2	50
Nano-silica 150 nm	≥ 99.8	0.2	10

Three series of the nano-silica cement paste composite were prepared in this study. Series SA, SB and SC stand for the cement pastes with different nano-silica sizes of 12, 50 and 150 nm, respectively. In each series, the mixtures were prepared by substituting cement with nano-silica at 1-5 % by weight. The OPC paste was also prepared as a control sample. In order to obtain well dispersed nano-particles, prior to mixing with the cement, a small amount of water was added to the nano-silica powder and stirred at high speed (120 rpm) for 1 min. Subsequently, the wet nano-silica powder was added to the cement powder. The water to binder ratio (W/B) for all mixtures was fixed at 0.5 [1, 7, 10]. The cement - nano-silica pastes were mixed by a cement mixer for 3 min and were cast into 5cm×5cm×5cm moulds. The pastes were then compacted by tamping. After pouring into molds, an external vibrator was used to facilitate compaction and decrease the amount of air bubbles. The samples were demoulded after 24 h and then cured in air at room temperature and a relative humidity of 100% for 7 and 28 days. The mix proportions are presented in Table 3.

The workability of the paste was measured using the penetration test. The method was adapted from the consistency test of the paste using the Vicat needle (ASTMC187-11e1) [19]. The Vicat needle was 300 g in weight with a 10 mm diameter plunger. The penetrations of the plunger into the pastes were measured as an indicator of workability of cement paste.

Table 3. Mixture proportions of the pastes.

Mixture no.	Symbol	Size of nano-silica (nm)	OPC (g)	SA (g)	SB (g)	SC (g)	W/B	Water (g)
1	OPC	-	1,600	-	-	-	0.5	800
2	SA1	12	1,584	25	-	-	0.5	800
3	SA2	12	1,568	50	-	-	0.5	800
4	SA3	12	1,552	75	-	-	0.5	800
5	SA4	12	1,536	100	-	-	0.5	800
6	SA5	12	1,520	125	-	-	0.5	800
7	SB1	50	1,584	-	25	-	0.5	800
8	SB2	50	1,568	-	50	-	0.5	800
9	SB3	50	1,552	-	75	-	0.5	800
10	SB4	50	1,536	-	100	-	0.5	800
11	SB5	50	1,520	-	125	-	0.5	800
12	SC1	150	1,584	-	-	25	0.5	800
13	SC2	150	1,568	-	-	50	0.5	800
14	SC3	150	1,552	-	-	75	0.5	800
15	SC4	150	1,536	-	-	100	0.5	800
16	SC5	150	1,520	-	-	125	0.5	800

2.2 Characterization Techniques

The as-purchased nano-silica particles with the average diameter of 12, 50 and 150 nm were characterized by using an X-ray diffraction (XRD) technique (Bruker D8 Advance) with Cu-Ka radiation. After mixing, each paste was cured for 7 and 28 days and was subjected to the following tests. The morphology of the surface was investigated under the scanning electron microscope (SEM, JEOL-JSM-840A). The density of each sample was measured using an Archimedes method according to the ASTM B962-08 standard [20]. The percentage of air void was determined following the principle described in the ASTM3171-11 standard [21]. The compressive strength was tested in accordance with the ASTM C109 standard [22]. The strength value is an average of three measured data. The thermal conductivity of each paste was measured by a dynamic measurement method using the portable heat transfer analyzer (ISOMET 2114).

2.3 Thermal Conductivity Model

The thermal conductivity data obtain from the experiment was compared with thermal conductivity models. For simplicity, it is assumed that there are three components in the composite: the cement paste, the aggregate (nano-silica) and the air void. The thermal conductivity and density of each component are given in Table 4. Four thermal conductivity models were chosen for the comparison in this work.

Table 4. Thermal conductivity values of the different phases of cement paste.

Component	Thermal conductivity (W/m-K)	Density (kg/m^3)	Reference
Cement paste	1.019	1984	In this work
Nano-silica	1.38	2533	[23]
Air void	0.026	1.18	[24]

2.3.1 Series and parallel model

Mathematical expressions for the average thermal conductivity K for the series and parallel approximations are given in Eqs. (1) and (2). In the series arrangement, the poorest conductor of its component layer dominates the overall heat conduction. However, in the case of a parallel arrangement, the best conductor dominates the overall heat conduction [25].

$$\text{Series: } K = k_v\phi_v + k_c\phi_c + k_a\phi_a \quad (1)$$

$$\text{Parallel: } K = \frac{1}{\frac{\phi_v}{k_v} + \frac{\phi_c}{k_c} + \frac{\phi_a}{k_a}} \quad (2)$$

where K is the thermal conductivity of the composite, k_c is the thermal conductivity of the cement paste, k_a is the thermal conductivity of the aggregates (in this case nano-silica), k_v is the thermal conductivity of air, ϕ_v is the volume fraction of air voids, ϕ_c is the volume fraction of cement paste, and ϕ_a is the volume fraction of the nano-silica.

2.3.2 One-dimensional heat flow model

If the higher W/B ratios are used, the micro/nano pores may develop making the cement a better insulator. Taking this consideration into account, the one-dimensional heat flow model was proposed to predict the thermal conductivity of the cement composites as equation (3) [26]:

$$K = (\phi_a + \phi_c)\left[\frac{k_v k_c}{\phi_c k_v + \phi_v k_c} + (\phi_c k_c + \phi_a k_a)\right](1 - P_t) \quad (3)$$

where P_t is the total cement micro/nano porosity which is defined as

$$P_t = \frac{(W/B) - 0.17H}{0.317 + (W/B)} \quad (4)$$

and H represents the degree of hydration which is assumed to be unity for fully hydrated cement paste.

2.3.3 Maxwell's model

The Maxwell's model was extended by Brailsford and Major [27] for a wide range of dispersions. In this model, the constituent phases are mixed in a definite proportion for a two-phase system. This mixture is then embedded in a random mixture of the same two phase having conductivity equal to the average volume of the conductivity of phase system. Thus, the effective thermal conductivity of such a three-phase system can be determined as:

$$K = \left[\frac{k_c\phi_c + k_a\phi_a\left(\frac{3k_c}{2k_c + k_a}\right) + k_v\phi_v\left(\frac{3k_c}{2k_c + k_a}\right)}{\phi_c + \phi_a\left(\frac{3k_c}{2k_c + k_a}\right) + \phi_v\left(\frac{3k_c}{2k_c + k_a}\right)}\right] \quad (5)$$

3. RESULT AND DISCUSSION

3.1 Phase and Morphology

Figure 1 shows the XRD pattern of the as-purchased nano-silica particles. It can be seen that every pattern is similar. It shows a broad peak around 2θ of 22° which is the characteristic of amorphous silica. In general, the amorphous phase of silica is more reactive than the crystalline counterpart. Also, the higher surface area of the nanoparticles can increase the reaction rate. Thus, it is expected that the addition of nano-silica will influence the hydration reaction and the microstructure of the cement paste. The morphology of the surface of the cement pastes was studied under the SEM as shown in Figure 2. Figure 2 (a) shows the micrographs of the control cement paste cured for 28 days without an addition of nano-silica whereas the images in Figure 2(b) - (d) illustrates the surface of cement pastes with 4% nano-silica for the size of 12, 50 and 150 nm, respectively. From Figure 2(a), it was found that in the plain cement paste in the calcium silicate hydrate (C-S-H) gel existed in the form of the stand-alone clusters, and also lapped and jointed together by many needle-like hydrates. At the same time, deposited $Ca(OH)_2$ crystals were distributed among the cement paste [2]. On the other hand, an addition of nano-silica changed the microstructure of the cement paste shown in Figure 2(b)-(d). The texture of hydrate products was denser and more compact, and the sizes of $Ca(OH)_2$ crystal were also smaller than those of the control paste. This is probably due to the participation of nano-silica in the hydration process to generate C-S-H through the reaction with $Ca(OH)_2$.

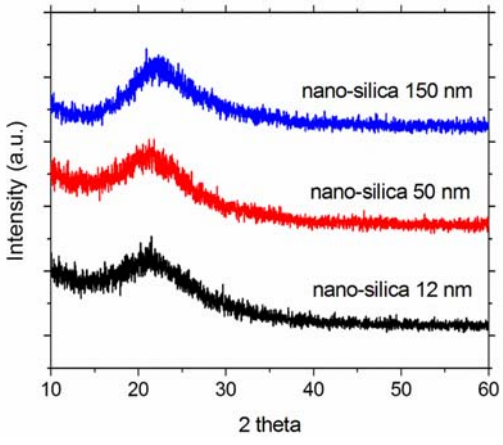

Figure 1. XRD pattern of nano-silica particle sizes of 12, 50 and 150 nm.

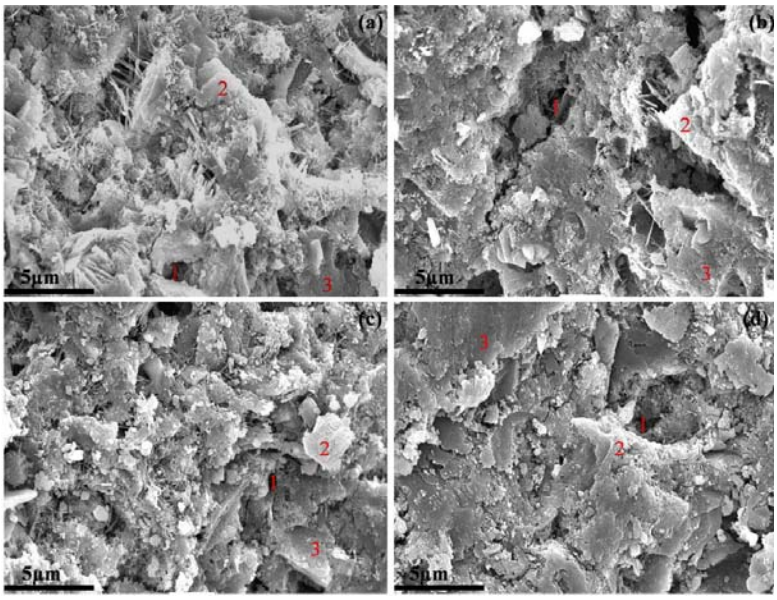

Figure 2. SEM micrographs of 4 wt% nano-silica - cement paste cured for 28 days with different nano-silica particle sizes: (a) without nano-silica, (b) 12 nm, (c) 50 nm, and (d) 150 nm. In the Figure, 1= pore, 2 = C-S-H, and 3= $Ca(OH)_2$.

3.2 Bulk Density of the Pastes

The variation of the paste density when adding nano-silica is shown in Figure 3. It can be clearly seen that for all nano-silica sizes, the addition of nano-silica reduced the sample density in comparison to the control cement paste. For the cement pastes with 12 nm nano-silica (Figure 3a), the density monotonously decreases with increasing amount of nano-silica. On the other hand, the cement pastes with 50 nm and 150 nm nano-silica (Figure 3b and 3c) showed a drop in density for the nano-silica addition of 1-2% and a slightly increase for 3-4% and a drop again at 5%. Overall, it can be concluded that the density has a tendency to decrease with an addition of nano-silica. This observation is different from the previous works [2, 10] where the increase in density was observed when nano-silica was added which was due to the filler effect of nano-silica. However, the earlier studies exploited the addition of superplasticizer in the mixture to control the flow rate. The superplasticizer can reduce the amount of water required in mixing the cement pastes but the amount of superplasticizer in each mixture is different. In the present study, we intend to investigate the effect of nano-silica addition on the mechanical and thermal properties without superplasticizer to control all other parameters under the same condition. As a result, with the same W/B ratios, the cement pastes become thicker for higher nano-silica concentration. This is because nano-silica has high surface area and can absorb water very quickly due to the hydration reaction of nano-silica. This interpretation is supported by the workability test as shown in Figure 3d where the penetration depth decreases for increasing amount of nano-silica. The replacement of cement with nano-silica resulted in the reduction in workability of the fresh pastes. Furthermore, the particle sizes had an effect on the workability of the

paste. The pastes with 12 nm nano-silica exhibited the lowest workability, followed by the pastes with 50 nm nano-silica and the pastes with 150 nm nano-silica. Thus, not all cement particles can react with water. This leads to the creation of small air void in the paste, and the amount of air void is related to the content of nano-silica as shown in Figure 3e. The nano-silica with 12 nm diameter has the highest surface area and therefore results in the more pronounced effect on the density than the 50 nm or 150 nm size.

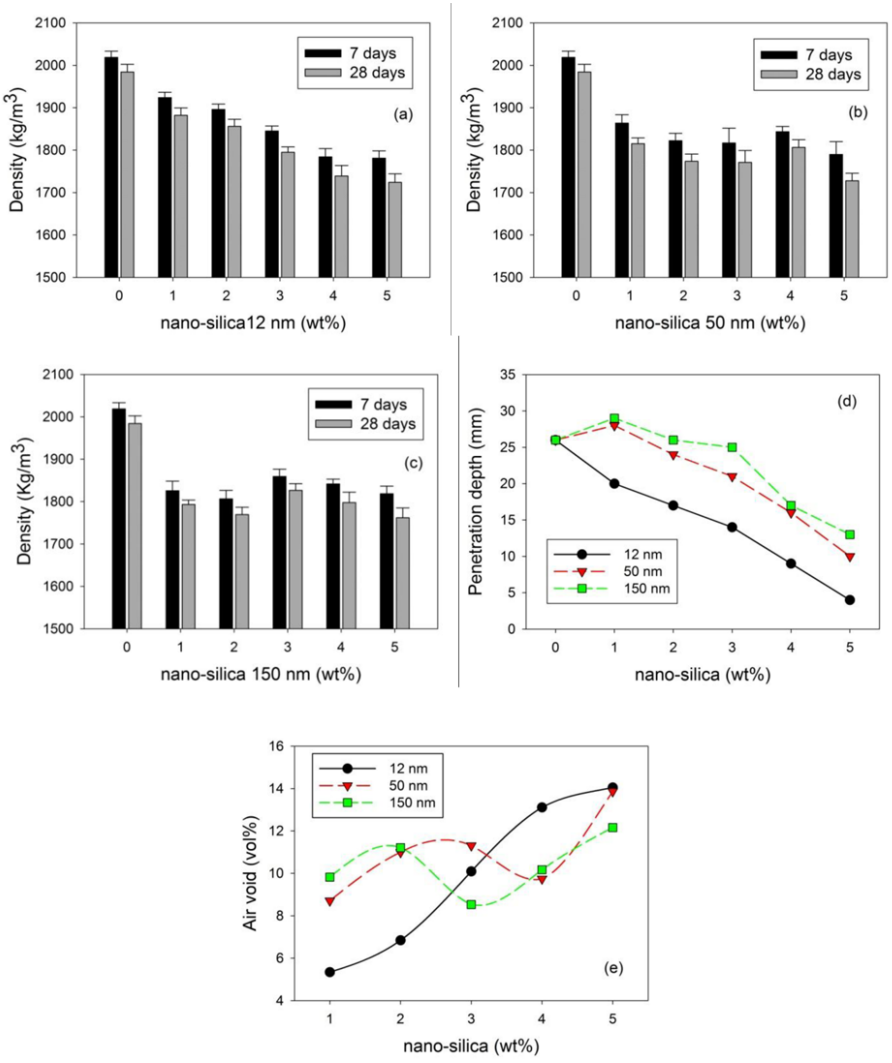

Figure 3. Bulk density of 7- and 28-days cement paste with addition of nano-silica (a) 12 nm, (b) 50 nm, (c) 150 nm. (d) workability of the cement paste by penetration test and (e) the relative volume percent of air void at 28 days.

3.3 Compressive Strength of Pastes

The results of compressive strengths of nano-silica added cement pastes are shown in Figure 4. In order to compare the effect of nano-silica sizes, we plot the strength of cement paste with 12, 50 and 150 nm nano-silica in the same plot and separate the measurement at the age of 7 days and 28 days in Figure 4a and 4b, respectively. There are many interesting points regarding this plot. Firstly, the compressive strength increases to the maximum point with the addition of certain amount of nano-silica and then drops when excessive nano-silica is introduced. For 12 nm nano-silica, the pastes show the maximum strength at 1% addition while for 50 and 150 nm sizes, the strength is maximized at 4% nano-silica. Secondly, the size of nano-silica has a significant effect on the strength. The cement paste with 50 nm nano-silica shows the higher strength than the others, with the maximum strength of >50% higher than the control cement paste. The possible reasons for this experimental result are discussed as follows. When nano-silica was added, it stimulated the hydration reaction of the cement particles and form C-S-H gel resulting in the higher compressive strength. Moreover, nano-silica has pozzolanic reaction with the $Ca(OH)_2$ crystals to form additional C-S-H phase. This prevents the $Ca(OH)_2$ crystals from growing and strengthens the pastes. However, the excessive nano-silica absorbed water required for the cement hydration process, reducing the final C-S-H product. The nano-silica particle may also surround cement particles making them inaccessible to water. Also, when the nano-silica is not well dispersed, as in the case for excessive nano-silica content, the aggregated nano-silica can create weak zone in form of voids and lowered the compressive strength. Since 12 nm nano-silica is the most reactive, it is required only 1% to obtain the maximum strength and more than that amount leads to the adverse effect. On the other hand, for less reactive nano-silica with the particles size of 50 and 150 nm, it requires about 4% for the maximum strength. Furthermore, the strength of cement paste is related to the density. Since the density of pastes with 12 nm nano-silica is lower than those with 50 and 150 nm for high nano-silica%, the strength of paste with 12 nm nano-silica also drops. In addition, for all samples regardless the particle size and concentration, the compressive strength is higher for the samples cured at 28 days due to the advance in hydration.

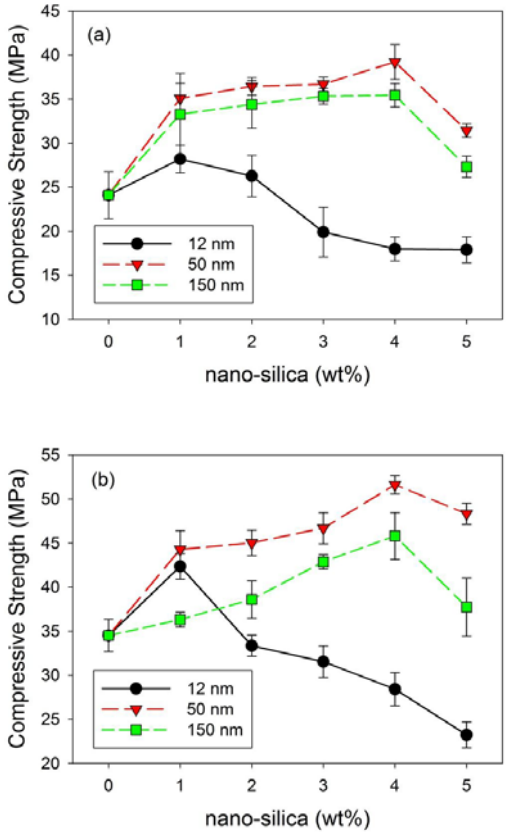

Figure 4. Compressive strength cement paste added nano-silica with different particle size, measured at (a) 7 days and (b) 28 days.

3.4 Thermal Conductivity of Pastes

The nano-silica - cement pastes of the size of 10cm × 10cm × 10cm were cured for 28 days before the thermal conductivity measurement. The results are shown in Figure 5. It can be obviously seen that the addition of nano-silica reduces the thermal conductivity monotonously. The most effective media to suppress thermal conductivity is when using the 12 nm particles. When reaching 5% of nano-silica, the thermal conductivity can be reduced by more than 20%. The main contribution of the reduction in thermal conductivity in the present study is due to the creation of small air void which suppress heat transfer significantly. The cement paste with 12 nm nano-silica contains highest air void and thus the effect is most pronounced. We can use the thermal conductivity model to fit the experimental data using the experimental values of the thermal conductivity and volume fraction of cement paste, nano-silica and air void. The models used are: 1) the series model, 2) the parallel model, 3) the one-dimensional heat flow (1D) model, and 4) Maxwell's model. The results are shown in Figure 6 (a)-(c). It can be clearly seen that the series model and the Maxwell's model fit the experimental values very well whereas the parallel model and the 1D model are significantly different from experiment.

The well fitting of the thermal conductivity values with the theoretical model indicate that the presence of air void is an important mechanism in decreasing thermal conductivity. Figure 7 plots the experimental values of thermal conductivity versus the volume percent of air void for all nano-silica sizes. It can be seen that the relation of the air void and the thermal conductivity is linear. The cement paste with 12 nm nano-silica shows the higher slope. Thus, it can be concluded the most effective media to reduce thermal conductivity is the addition of smallest nano-silica.

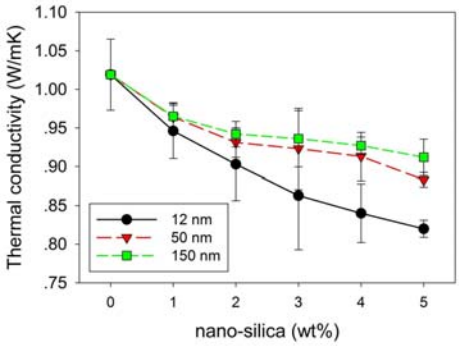

Figure 5. Thermal conductivity of nano-silica added cement paste.

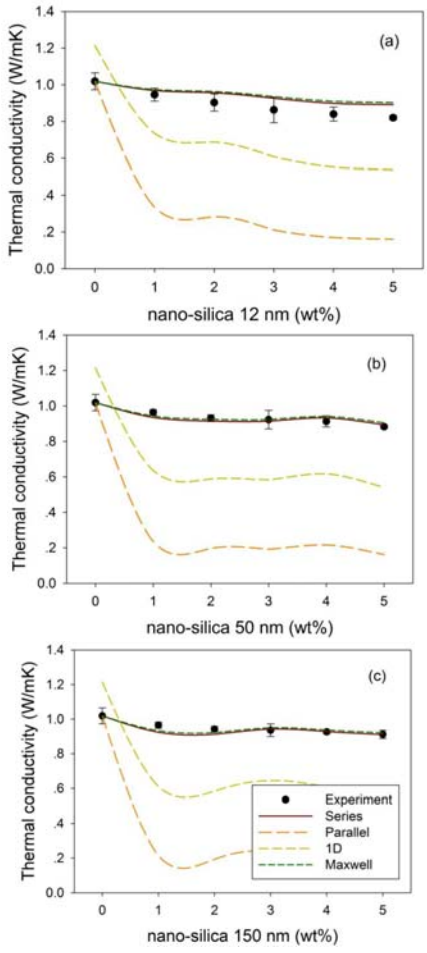

Figure 6. Comparison between experimental values and thermal conductivity models of cement paste with nano-silica (a) 12 nm, (b) 50, (c) 150 nm.

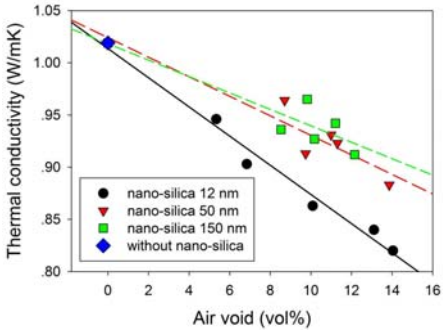

Figure 7. A plot of thermal conductivity of nano-silica added cement paste versus the volume percent of air void.

4. CONCLUSIONS

In this paper, the effects of the addition of nano-silica on both mechanical property and thermal conductivity of cement paste have been investigated. The compressive strength increases to the maximum values with the addition of certain amount of nano-silica due to the highly reactive nature of nano-silica which stimulates the hydration reaction. The 12 nm nano-silica particle with the largest surface area is the most reactive and can enhance the strength even with only 1 % by weight substitution. Higher content of nano-silica decreases the strength due to the lack of water for hydration reaction, the creation of weak zone from nonuniform distribution and the reduction of density. For thermal conductivity, addition of nano-silica can suppress thermal conductivity by means of air void formation. The thermal conductivity is most suppressed for cement paste with 12 nm nano-silica. Both series and Maxwell thermal conductivity models can fit the experimental results satisfactorily. For the use of nano-silica-cement composites for thermal insulation, it requires both strength and low thermal conductivity. Hence, the cement paste with 50 nm nano-silica of 4-5% is the most suitable composition which provides high compressive strength and relatively low thermal conductivity.

ACKNOWLEDGEMENTS

This work was supported by the Higher Education Research Promotion and National Research University Project of Thailand, Office of the Higher Education Commission, through the Advanced Functional Materials Cluster of Khon Kaen University, the Thailand Research Fund (TRF) and Khon Kaen University under the TRF Senior Research Scholar, Grant No. RTA5780004, and the Integrated Nanotechnology Research Center, Khon Kaen University.

REFERENCES

[1] Jo B.W., Kim C.H., Tae G.H. and Park J.B., *Constr. Build. Mater.,* 2007; **21**: 1351-1355. DOI 10.1016/j.conbuildmat. 2005.12. 020.

[2] Li H., Xiao H.G., Yuan J. and Ou J.P., *Compos. Part B-Eng.,* 2004; **35**: 185-189. DOI 10.1016/S1359-8368(03)00052-0.

[3] Nazari A. and Riahi S., *Compos Part B-Eng.,* 2011; **42**: 570-578. DOI 10.1016/j. compositesb.2010.09.025.

[4] Kawashima S., Hou P.K., Corr D.J. and Shah S.P., *Cement Concrete Comp.,* 2013; **36**: 8-15. DOI 10.1016/j.cemconcomp.2012. 06.012.

[5] Hou P.K., Kawashima S., Kong D.Y., Corr D.J., Qian J.S. and Shah S.P., *Compos. Part B-Eng.,* 2013; **45**: 440-448. DOI 10.1016/j.compositesb.2012.05.056.

[6] Qing Y., Zenan Z., Deyu K. and Rongshen C., *Constr. Build. Mater.,* 2007; **21**: 539-545. DOI 10.1016/j. conbuildmat.2005.09. 001.

[7] Senff L., Labrincha J.A., Ferreira V.M., Hotza D. and Repette W.L., *Constr. Build. Mater.,* 2009; **23**: 2487-2491. DOI 10. 1016/j.conbuildmat.2009.02. 005.

[8] Givi A.N., Rashid S.A., Aziz F.N.A. and Salleh M.A.M., *Compos. Part B-Eng.,* 2010; **41**: 673-677. DOI 10.1016/j.compositesb.2010.08.003.

[9] Stefanidou M. and Papayianni I., *Compos. Part B-Eng.,* 2012; **43**: 2706-2710. DOI 10. 1016/j.compositesb.2011.12.015.

[10] Berra M., Carassiti F., Mangialardi T., Paolini A.E. and Sebastiani M., *Constr. Build. Mater.,* 2012; **35**: 666-675. DOI 10.1016/j.conbuildmat.2012.04.132.

[11] Boddy A.M., Hooton R.D. and Thomas M.D.A., *Cem. Concr. Res.,* 2000; **30**: 1139-1150. DOI 10.1016/S0008-8846 (03)00100-5.

[12] Yajun J. and Cahyadi J.H., *Cem. Concr. Res.,* 2003; **33**: 1543-1548. DOI 10.1016/ S0008-8846 (00)00297-0.

[13] Zhou X.Y., Zheng F., Li H.G. and Lu C.L., *Energ Buildings,* 2010; **42**: 1070-1074. DOI 10.1016/j.enbuild.2010.01.020.

[14] Vrana T. and Bjork F., *Constr. Build. Mater.,* 2009; **23**: 1775-1787. DOI 10.1016/j.conbuildmat.2008.10.014.

[15] Mihlayanlar E., Dilmac S. and Guner A., *Mater. Design,* 2008; **29**: 344-352. DOI 10.1016/j.matdes.2007.01.032.

[16] Nicolajsen A., *Build. Environ.,* 2005; **40**: 907-914. DOI 10.1016/j.buildenv.2004.08.025.

[17] Fu X. and Chung D.D.L., *Cem. Concr. Res.,* 1997; **27**: 1799-1804. DOI 10.1023/A:1013889725971.

[18] Chung D.D.L., *J. Mater. Sci.,* 2002; **37**: 673-682. DOI 10.1016/S0008-8846(97)00174-9.

[19] ASTM. C187-98: Standard Test Method for Normal consistency of Hydraulic Cement. West Conshohocken, PA, USA: ASTM International; 2013.

[20] ASTM. B962 - 08: Standard Test Methods for Density of Compacted or Sintered Powder Metallurgy (PM) Products Using Archimedes' Principle. West Conshohocken, PA, USA: ASTM International; 2013.

[21] ASTM. D3171-11: Standard Test Methods for Constituent Content of Composite Materials. West Conshohocken, PA, USA: ASTM International; 2013.

[22] ASTM. C109 / C109M - 12: Standard Test Method for Compressive Strength of Hydraulic Cement Mortars (Using 2-in. or [50-mm] Cube Specimens). West Conshohocken, PA, USA: ASTM International; 2012.

[23] Wright A.F. and Lehmann M.S., *J. Solid State Chem.,* 1981; **36**: 371-380. DOI 10.1016/0022-4596(81)90449-7.

[24] Jirickova M., Pavlik Z., Fiala L. and Cerny R., *Int. J. Thermophys.,* 2006; **27**: 1214-1227. DOI 10.1007/s10765-006-0076-8.

[25] Carson J.K., Lovatt S.J., Tanner D.J. and Cleland A.C., *Int. J. Heat Mass Transfer,* 2005; **48**: 2150-2158. DOI 10.1016/j.ijheatmasstransfer.2004.12.032.

[26] Wong J.M., Glasser F.P. and Imbabi M.S., *Cement Concrete Comp.,* 2007; **29**: 647-655. DOI 10.1016/j.cemconcomp.2007.04.008.

[27] Brailsford A.D., Major K.G., *Br. J. Appl. Phys.,* 1964; **15**: 313-320.

KSCE Journal of Civil Engineering (0000) 00(0):1-9
DOI 10.1007/s12205-016-0327-6
Copyright ⓒ2016 Korean Society of Civil Engineers

Structural Engineering
pISSN 1226-7988, eISSN 1976-3808
www.springer.com/12205

Effect of Sodium Hydroxide and Sodium Silicate Solutions on Strengths of Alkali Activated High Calcium Fly Ash Containing Portland Cement

Tanakorn Phoo-ngernkham*, Sakonwan Hanjitsuwan, Nattapong Damrongwiriyanupap***, and Prinya Chindaprasirt******

Received April 21, 2015/Revised February 27, 2016/Accepted April 27, 2016/Published Online October 25, 2016

Abstract

In this paper, the mechanical performance of fly ash and Portland cement geopolymer activated with sodium hydroxide and sodium silicate solutions was studied. The Geopolymer Mortars (GM) were made from high calcium Fly Ash (FA) and ordinary Portland Cement (PC) with FA:PC weight ratios of 100:0, 95:5, 90:10, 85:15, and 80:20. The GMs were activated with three combinations of sodium Hydroxide Solution (SH) and sodium Silicate Solution (SS) viz., SH, SH+SS (SH:SS=2) and SS. For all mixes, 10 molar SH, alkali activator liquid/solid binder ratio of 0.60 and curing at ambient temperature of 25°C were used. The result indicated that the compressive and shear bond strengths of GM depended on the alkali activators used and the amount of PC. The use of SH and SHSS resulted in the formation of additional Calcium Silicate Hydrate (CSH) which coexisted with sodium aluminosilicate hydrate (NASH) gel. Whereas, the use of SS resulted in NASH gel with only a small amount of CSH. The increasing of PC content enhanced the compressive and shear bond strengths of GMs due to the formation of additional CSH. The 15% PC mixed with SHSS gave the optimum compressive and shear bond strengths.

Keywords: *geopolymer, high calcium fly ash, Portland cement, compressive strength, shear bond strength*

1. Introduction

Ordinary Portland Cement (PC) is widely used as a main building material; however, its manufacturing process results in a high emission of carbon dioxide (CO_2) to the atmosphere (Metz *et al.*, 2007; Sukmak *et al.*, 2013). Currently, geopolymer binder received a lot of attention as an alternative binder due to its low carbon dioxide emission (McLellan *et al*., 2011; Pacheco-Torgal *et al*., 2008), but some investigations demonstrate that low emissions are only possible for geopolymer without sodium silicate (Turner and Collins, 2013). Normally geopolymer is obtained from precursor materials containing silica and alumina such as Fly Ash (FA), calcined kaolin or metakaolin activated with high alkali solutions (Albitar *et al*., 2014; Jun and Oh, 2015; Kumar *et al.*, 2010; Li *et al*., 2010; Ravikumar *et al*., 2010). The main reaction products is sodium aluminosilicate hydrate (NASH) gels. For the system with high calcium content, the main reaction products is CASH gels (Li *et al*., 2010; Palomo *et al.,* 1999). However, both systems are considered as 'alkali activated materials'.

In Thailand, high calcium FA from Mae Moh power plant in the north of Thailand has been shown to be a good precursor materials in providing relatively high strength binder (Chindaprasirt *et al*., 2011; Chindaprasirt *et al*., 2007). This is because of FA with high CaO content which is still contained high SiO_2 and Al_2O_3 contents (Phoo-ngernkham *et al.*, 2014; Phoo-ngernkham *et al.,* 2013; Phoo-ngernkham *et al.*, 2013). The usage of FA as a precursor material provides the greatest opportunity for commercial utilization of this technology due to the plentiful supply of the material worldwide (Sukmak *et al.*, 2013; Sukmak *et al.*, 2013). However, the strength development of FA geopolymer at ambient temperature condition is rather slow and relatively low strength is obtained (Pangdaeng *et al*., 2014; Suwan and Fan, 2014). For normal fly ash gepoolymer system, the setting and hardening are slow at room temperature (Temuujin *et al*., 2009). With the presence of calcium in the system, the reaction at ambient temperature is accelerated (Temuujin *et al.*, 2009) and the products contains both geopolymeric and calcium silicate hydrate (CSH)

*Ph.D., Research Center for Advances in Civil Engineering and Construction Materials, Dept. of Civil Engineering, Faculty of Engineering and Architecture, Rajamangala University of Technology Isan, Nakhon Ratchasima 30000, Thailand (E-mail: tanakorn.ph@rmuti.ac.th)
**Ph.D., Program of Civil Technology, Faculty of Industrial Technology, Lampang Rajabhat University, Lampang 52100, Thailand (Corresponding Author, E-mail: sakonwan@lpru.ac.th)
***Assistant Professor, Civil Engineering Program, School of Engineering, University of Phayao, Phayao 56000, Thailand (E-mail: natpong_chin@hotmail.com)
****Professor, Sustainable Infrastructure Research and Development Center, Department of Civil Engineering, Faculty of Engineering, Khon Kaen University, Khon Kaen 40002, Thailand (E-mail: prinya@kku.ac.th)

Table 1. Chemical Compositions of Fly Ash and Portland Cement (by weight)

Materials	SiO_2	Al_2O_3	Fe_2O_3	CaO	MgO	K_2O	Na_2O	SO_3	LOI
FA	29.3	13.0	15.6	25.8	3.0	2.9	2.8	7.3	0.3
PC	20.8	4.7	3.4	65.3	1.5	0.4	0.1	2.7	0.9

and calcium aluminosilicate hydrate (CASH) (Somna *et al.*, 2011). The temperature curing at 40-70ºC can improve the geopolymerization process and hence the strength development of FA geopolymer (Chindaprasirt *et al*., 2007). In order to put this material into real use, the improvement of strength development at ambient temperature curing is needed (Nath and Sarker, 2015; Palomo *et al.*, 2007; Pangdaeng *et al*., 2014; Phoo-ngernkham *et al*., 2013; Suwan and Fan, 2014; Temuujin *et al.,* 2009; Williams *et al.*, 2002). The usage of calcium-rich materials as an additive to improve the strength development of FA geopolymer such as calcium oxide (CaO), calcium hydroxide ($Ca(OH)_2$) and Portland Cement (PC). In the other words, the increasing of calcium content enhances the mechanical properties of FA geopolymer with additional calcium silicate hydrate (CSH) which coexists with other geopolymer products (Guo *et al.,* 2010; Nazari and Ghafouri Safarnejad, 2013). In addition, the reaction of calcium-rich materials with water generates heat from exothermic process at ambient temperature and thus helps enhance the geopolymerization process (Pangdaeng *et al.*, 2014; Suwan and Fan, 2014).

The alkali activator is one of the most important factors affecting the strength development of geopolymer matrix. Normally, sodium hydroxide and sodium silicate solutions are the most used as liquid activators because they are shown to be the most suitable activators in terms of availability and good mechanical properties (Pimraksa *et al*., 2011). Sodium Hydroxide Solution (SH) is commonly used for dissolution of Si^{4+} and Al^{3+} ions from precursor materials to form aluminosilicate material. While sodium Silicate Solution (SS) contains soluble silicate species and thus is used to promote the condensation process of geopolymer (Panias *et al.*, 2007). A number of researchers (Kumar *et al.,* 2010; Rashad, 2013; Ravikumar and Neithalath, 2012) reported that the best mechanical performance of geopolymer are obtained with combinations of sodium silicate and sodium hydroxide solutions. This paper, therefore, investigates the mechanical properties viz., compressive strength and shear bond strengths, and microstructure of high calcium fly ash geopolymer activated with NaOH and sodium silicate solutions with Portland cement as additive. The outcome of this study would lay a foundation for the future use of high calcium FA as a promoter for manufacturing geopolymer material and the use of Portland cement as additive in this system.

2. Materials and Methods

2.1 Materials and Sample Preparation

The precursors used in this study were Fly Ash (FA) from Mae Moh power plant in northern Thailand and ordinary Portland Cement (PC). The use of PC as calcium-rich material is very attractive due to its availability, low cost and additional formation of aluminosilicate species. PC was, therefore, used as calcium-rich material in this investigation. The FA with median particle size of 8.5 μm, Blaine fineness of 4300 cm^2/g and specific gravity of 2.25; and PC with median particle size of 14.6 μm, Blaine fineness of 3600 cm^2/g and specific gravity of 3.15 were used as precursors. The chemical compositions of FA and PC as shown in Table 1 indicated that FA mainly consisted of SiO_2 and Al_2O_3 and some impurities. The sum of SiO_2, Al_2O_3 and Fe_2O_3 was 57.9%, and the CaO content was high at 25.8%. This FA was Class C fly ash as specified by ASTM C618-15 (2015). 10 molar Sodium Hydroxide (SH) and Sodium Silicate (SS) with 13.89% Na_2O, 32.15% SiO_2, and 46.04% H_2O were used as alkali activators. The SH was obtained from dissolving sodium hydroxide pellets in distilled water and allowed to cool down at room temperature. Local river sand with specific gravity of 2.63 and fineness modulus of 2.2 was used as fine aggregate.

The mix design was based on the previous study on the effect of combined use of sodium hydroxide and sodium silicate (Phoo-ngernkham *et al.*, 2015). The Portland cement dosage was increased to 20% to cover the wider range of addition. The effects of the uses of Sodium Hydroxide (SH) and Sodium Silicate (SS) alone; and the combined use of Sodium Hydroxide Plus Sodium Silicate (SHSS) were studied. The mix proportions of fly ash and Portland cement geopolymer are summarized in Table 2. Mixes 6-9, therefore, had the same mix proportions as those tested by Phoo-ngernkham *et al.* (2015). The abbreviations of 0PC, 5PC, 10PC, 15PC, and 20PC with corresponding FA:PC weight ratios of 100:0, 95:5, 90:10, 85:15, and 80:20, respectively were the mixes used. Constant liquid/solid binder ratio of 0.60, and sand/binder ratio of 1.0 were used in all mixtures. Previous study on high calcium coal ash geopolymer activated with NaOH and sodium silicate solutions (Phoo-ngernkham *et al.*, 2015; Sathonsaowaphak *et al*., 2009) shows that a relatively high strength geopolymer could be obtained with up to liquid/solid binder ratio of 0.60. Three combinations of alkali activators viz., SH, SS and SH+SS (SS/SH=2.0) were used. SH+SS (SHSS) was prepared by mixing SH and SS prior to mixing of geopolymer.

For the mixing of fly ash and Portland cement geopolymer mortar (GM), FA, PC and sand were dry mixed until the mixture was homogenous which took approximately 1 minute. The alkali activator solutions were then added and the mixing was done for another 3 minutes. After mixing, the mortar was then placed into a 50 × 50 × 50 mm^3 cube molds for compressive strength tests as described in ASTM C109 (2002). The samples were wrapped with vinyl sheet to protect moisture loss for 1 day at the 25ºC controlled room and then they were again wrapped with vinyl

Table 2. Mix Proportions of Fly Ash and Portland Cement Geopolymer

Mix No.	Mix symbol	FA (g)	PC (g)	Sand (g)	SH (g)	SS (g)	SiO_2/Al_2O_3 ratios	CaO/SiO_2 ratios
1	SH-0PC	100	-	100	60	-	2.26	0.88
2	SH-5PC	95	5	100	60	-	2.30	0.96
3	SH-10PC	90	10	100	60	-	2.35	1.04
4	SH-15PC	85	15	100	60	-	2.39	1.13
5	SH-20PC	80	20	100	60	-	2.44	1.22
6	SHSS-0PC	100	-	100	20	40	3.25	0.61
7	SHSS-5PC	95	5	100	20	40	3.33	0.66
8	SHSS-10PC	90	10	100	20	40	3.41	0.72
9	SHSS-15PC	85	15	100	20	40	3.49	0.78
10	SHSS-20PC	80	20	100	20	40	3.58	0.83
11	SS-0PC	100	-	100	-	60	3.75	0.53
12	SS-5PC	95	5	100	-	60	3.84	0.58
13	SS-10PC	90	10	100	-	60	3.94	0.62
14	SS-15PC	85	15	100	-	60	4.04	0.67
15	SS-20PC	80	20	100	-	60	4.15	0.72

sheet and kept in the controlled room.

The mixing, molding and demolding of pastes were the same as those of mortar with exception of dry mixing where only FA and PC were dry mixed for 1 minute. The paste samples were used for the SEM and XRD analyses.

2.2 Testing and Analysis

2.2.1 Compressive Strength

The compressive strengths of fly ash and Portland cement geopolymer mortars (GMs) were measured at the age of 28 days. The results were the average value of three samples.

2.2.2 Scanning Electron Microscopy (SEM) and X-ray Diffraction (XRD)

The geopolymer structures were studied using XRD and SEM analyses. The analyses by XRD and SEM experiments are widely used for preliminary observation of the microstructure of geopolymer as shown by several researchers (Chindaprasirt *et al.,* 2012; Lee *et al.,* 2014). For SEM test, the broken sample of 3-6 mm was obtained from the middle portion of geopolymer paste sample and then placed on a brass stub sample holder with double stick carbon tape. The sample was dried using infrared light for 5 minutes and then coated with a layer of gold using a blazer sputtering coater. The micrographs were recorded at 15 kV and 1000x magnification. For XRD test, the samples from the middle portion of geopolymer paste sample was collected and ground to fine powder and the XRD scans were performed for 2theta between 5 and 60°.

2.2.3 Shear Bond Strength between Concrete Substrate and Geopolymer Mortar

The adhesive strength or shear bond strength between Concrete Substrate (CS) and fly ash and Portland cement geopolymer mortar (GM) was evaluated using the slant shear test adapted from ASTM C882 (2005). In this study, the preparation of CS samples and the casting of slant shear samples were based on the previous study (Phoo-ngernkham *et al.*, 2014). The fresh CS samples were cast in a 50 × 50 × 125 mm^3 prism mold. The hardened CSs were cut at the middle section with an interface line of 45° to the vertical axis. The slant angle of 30° to the vertical is officially recommended by ASTM C882 (2005). However, the slant angle of 45° is also officially used for the standard evaluation of bond (FM 3-C882 2015). In the preparation of concrete substrate, the cutting of 45° concrete substrate was better with less chipping and cracking than the 30° concrete substrate. The slant angle of 45° to the vertical was, therefore, used. The compressive strength of CS was 35.0 MPa. For the casting of shear bond strength sample between CS and GM, the GMs were cast into a 50 × 50 × 125 mm^3 prism mold with the other half filled with CS and then they were wrapped with vinyl sheet to protect moisture loss and left for 1 day in the 25°C controlled room. The samples were demoulded and covered with vinyl sheet again and kept in the 25°C controlled room until testing. The samples were tested at the age of 28 days using the constant loading rate of 0.30 MPa/s. The results were the average value of three samples.

3. Results

The 28-day compressive strengths of GMs with difference types of alkali activator are shown in Fig. 1. The compressive strengths of GM were depended on the types of alkali activators. The strengths of GMs with SHSS were highest followed in turn by mixes with SS and SH. The strengths of GMs with SH were low compared with those of the other alkali activators. The strengths of the control mix (without PC) with SH, SHSS, and SS were 5.4, 29.1, and 24.1 MPa, respectively. For all PC replacement levels, the strengths of GMs marginally increased with increasing of PC content and activated with SH and the strengths were between 6.1 and 6.8 MPa. For SHSS and SS solutions, the strengths of GMs obviously increased as the

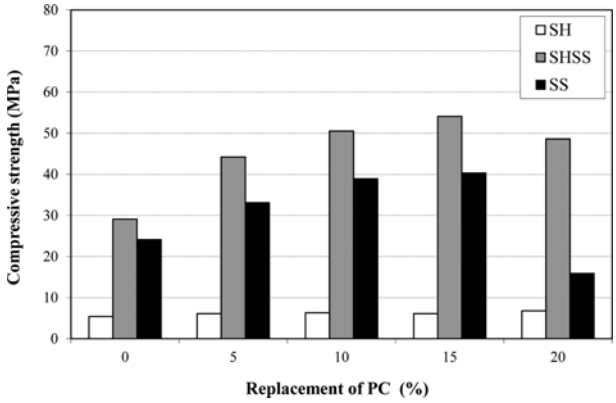

Fig. 1. Compressive Strength of Fly Ash and Portland Cement Geopolymer Mortars

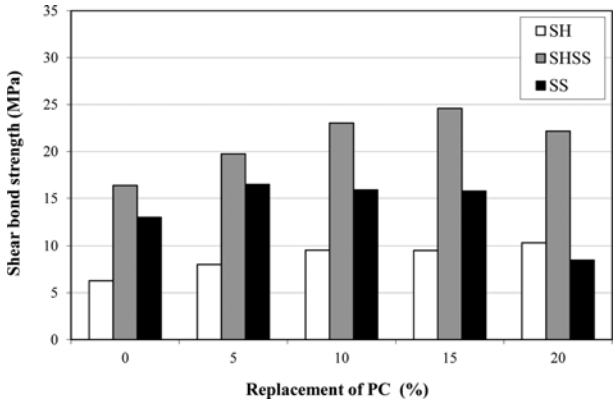

Fig. 2. Shear Bond Strength between Concrete Substrate and Fly Ash and Portland Cement Geopolymer with Interface Line at 45° to the Vertical Axis

replacement of PC increased up to an optimum level and then the strength started to decline. The compressive strength of GMs mixed by SHSS solutions were between 44.2 and 54.1 MPa, whereas the compressive strength of mixes with SS solution were between 15.9 and 40.3 MPa.

The test results of shear bond strength of CS and GMs with different alkali activator types are illustrated in Fig. 2. The 28-day shear bond strengths of CS and GMs of the control mix (without PC) with SH, SHSS, and SS were 6.3, 16.4, and 13.0 MPa, respectively. The increase in shear bond strengths was clearly observed when the mixes contained PC content. The GMs mixed with SH solution was slightly increased from 8.0 to 10.3 MPa as the amount of PC increased. While the strengths of GMs with SS and SHSS solutions tended to increase as the replacement of PC content increased up to a threshold limit. The relatively high shear bond strengths were found with SHSS solutions between 16.4 and 24.6 MPa with the optimum at 15% PC content. The shear bond strength for GMs with SH was between 8.5 and 16.5 MPa with the optimum at 5%PC.

The failure patterns of the samples due to the shear bond tests are important parameters related to the observation of bond strength at contact zone between CS and GMs. Two failure

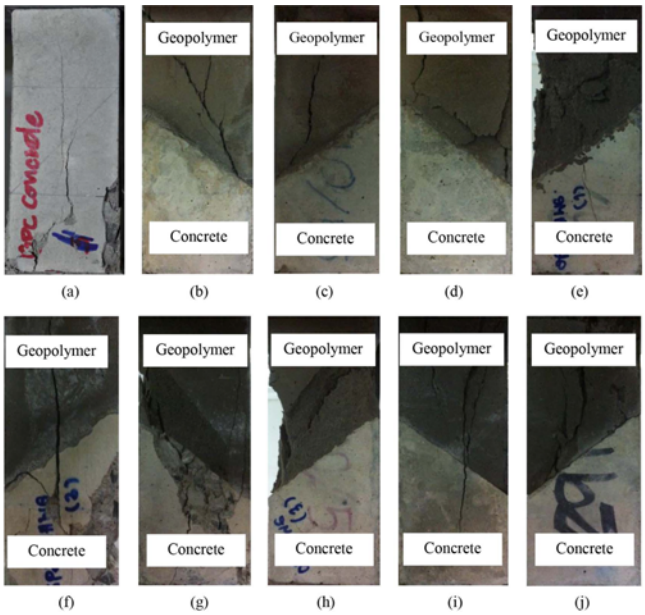

Fig. 3. Specimens Failure Mode: (a) PCC, (b) SH-0PC, (c) SH-15PC, (d) SH-20PC, (e) SHSS-0PC, (f) SHSS-15PC, (g) SHSS-20PC, (h) SS-0PC, (i) SS-5PC, (j) SS-20PC

patterns viz., monolithic failure mode and shear bond failure mode were observed as shown in Fig. 3. The monolithic failure mode is observed in mixes SHSS-15PC (Fig. 3(f)), SHSS-20PC (Fig. 3(g)), and SS-5PC (Fig. 3(i)) which corresponded to relatively high bond strengths. The slant shear test prism acted as a monolithic column and cracks were continuous from CS to GM passing through the slant plane. This monolithic failure mode is similar to that of solid CS prism (Fig. 3(a)). The second mode was the shear bond failure mode whose cracks were found mainly at the interface and some cracks were also found in the weak GM with CS potion remained relatively intact. The low bond strengths were found in mixes SH-0PC (Fig. 3(b)), SH-15PC (Fig. 3(c)), SH-20PC (Fig. 3(c)), SHSS-0PC (Fig. 3(d)), SS-0PC (Fig. 3(h)), and SS-20PC (Fig. 3(j)).

4. Analysis and Discussion

The alkali activator types and PC content are significant parameters controlling the strength development of GM. The increase in PC content can improve the strength of GMs. This is because of free calcium ions in the system which reacts with silica and alumina, resulting in additional CSH and/or CASH gel. The co-existence of geopolymer gels and CSH and/or CASH gel lead to a high compressive strength of the GMs cured at ambient temperature. This is very attractive for the usage of this product in the real construction. It should be noted that the mechanical tests performed at 28 days curing do not allow for a comprehensive understanding of the material performance over time. The long term properties of the fly ash-Portland cement geopolymer activated with sodium hydroxide and sodium silicate solutions cured at ambient condition should be further

investigated.

The enhancement of strength development of GM is possible by the incorporation of PC in the mixture; however, the threshold limit of PC content depends on the types of alkali activator solutions. For the GM activated with SH solution, the strength development of GM is low when cured at ambient temperature for all PC replacement levels. The SH solution is important for dissolving of Si^{4+} and Al^{3+} ions from precursors and hence geopolymerization process. However, the process at ambient temperature condition is very slow and hence low strength is normally obtained (Somna *et al.*, 2011). High strength development of GM is found in the mixes activated with SHSS solutions. The use of SHSS based activators is suitable in terms of strength of gopolymer matrix. The mix has additional silicate species in the system and hence the geopolymerization reaction is enhanced. This is an advantage to the strength development of GMs. For the GM mixes activated with SS solution, its strength development are slightly lower than those of mixes with SHSS solutions, but still higher than those with SH solution. It is thus suggested from this results that the accelerate reaction in FA-PC blends came from a rapid chemical reaction between calcium in PC and alkali activators (Garcia-Lodeiro *et al.*, 2016). Also, the active silica from sodium silicate solution reacts with calcium from precursors to form the reaction products and lead to a high strength geopolymer (Phoo-ngernkham *et al*., 2015). The optimum PC contents for compressive strength of mixes with SHSS and SS are 15%, whilst the use of PC content above 15% leads to a reduction in the strength of GM. The increase in PC content beyond the optimum level resulted in the acceleration of reaction with significant reduction in setting time (Pangdaeng *et al*., 2014; Phoo-ngernkham *et al.*, 2013). This adversely affects the strength development at the later age.

The shear bond strengths of CS and GMs are also related to the alkali activator type and PC content. The shear bond strengths of CS and GMs tends to increase with an increasing of PC content up to an optimum PC content for mixes with SS and SHSS solutions. The increase in shear bond strength is directly related to the increase in compressive strength of GM. The high calcium content from PC can promote the formation of additional CSH and/or CASH gel and hence an enhancement of the bonding strength at the interface transition zone between two materials. The optimum PC contents for shear bond strength of mixes with SHSS and SH are 15 and 5%, respectively. In the case of SHSS mixes, the trend of result is the same of that reported by Phoo-ngernkham *et al.* (2015). For the SS mixes, the optimum PC content was 5%, however the shear bond strengths of the mixes with 10 and 15%PC were only slightly less than that of 5%PC. The strengths were not as high as the SHSS mixes as the leaching of silica and alumina does not occur as for the mix with SHSS. The reaction between PC and sodium silicate is rather fast and this hinders the strength development at the later age. Therefore, the compressive strength and shear bond strengths are slightly lower than the case of SHSS mixes.

The SiO_2/Al_2O_3 and CaO/SiO_2 ratios are the important factors

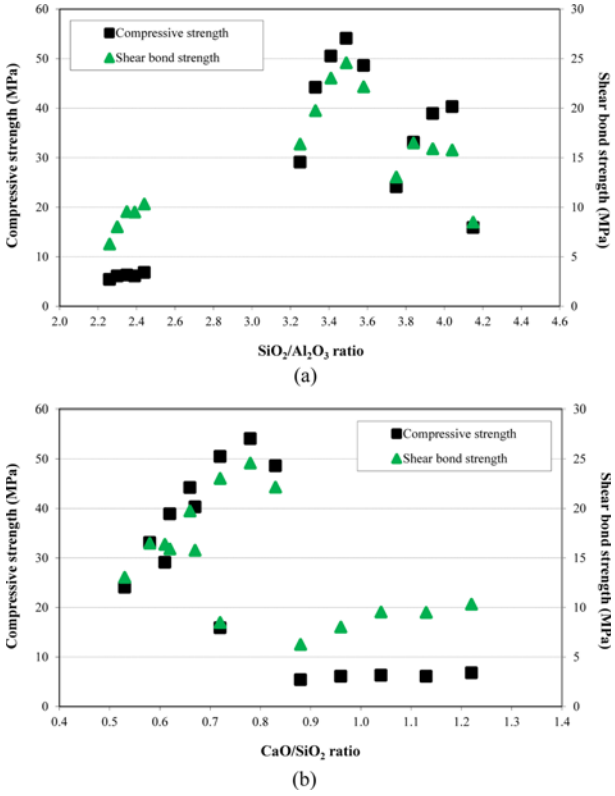

Fig. 4. Compressive Strength and Shear Bond Strength of Fly Ash and Portland Cement Geopolymer with Difference of SiO_2/Al_2O_3 and CaO/SiO_2 Ratios: (a) SiO_2/Al_2O_3 Ratios, (b) CaO/SiO_2 Ratios

controlling the strength development of high calcium geopolymer matrix (Chindaprasirt *et al*., 2012; Phoo-ngernkham *et al*., 2014; Phoo-ngernkham *et al.,* 2013; Puligilla and Mondal, 2013). Fig. 4(a) illustrates the relationship between compressive strength and shear bond strength with various SiO_2/Al_2O_3 ratios. The maximum compressive strength and shear bond strength were at SiO_2/Al_2O_3 ratios of 3.4-3.6. This is in line with the previous research report of high strength geopolymer with SiO_2/Al_2O_3 around 3.50 (Chindaprasirt *et al*., 2012). The relationship between compressive strength and shear bond strength with various CaO/SiO_2 ratios are illustrated in Fig. 4(b). The optimum CaO/SiO_2 ratio for compressive strength and shear bond strength of GMs ranged between 0.72-0.80, which was lower than those of alkali activated slag (0.8-1.1) and Portland cement (1.3-1.8) (Lee *et al*., 2014). The result is in line with the previous study (Puligilla and Mondal 2013) with an optimum CaO/SiO_2 ratio around 0.74.

In this study, the microstructures of fly ash and Portland cement Geopolymer Pastes (GP) were investigated using SEM and the test results are shown in Fig. 5. The microstructure of GPs agrees well with the test results of compressive strength of GMs. The GPs with SH solution (SH-0PC and SH-15PC) have loose matrices with large number of non-reacted and/or partially reacted fly ash particles embedded in poor matrices as shown in Figs. 5(a) and 5(b). While the GP without PC content with SS solution (SS-0PC) as shown in Fig. 5(e), the matrix is denser

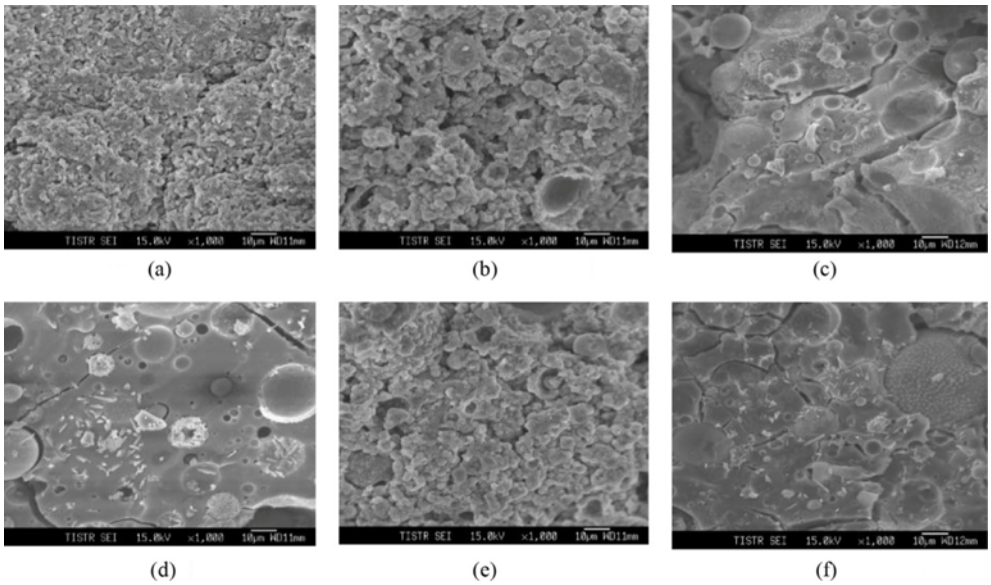

Fig. 5. SEM of Fly Ash and Portland Cement Geopolymer Pastes: (a) SH-0PC, (b) SH-15PC, (c) SHSS-0PC, (d) SHSS-15PC, (e) SS-0PC, (f) SS-15PC

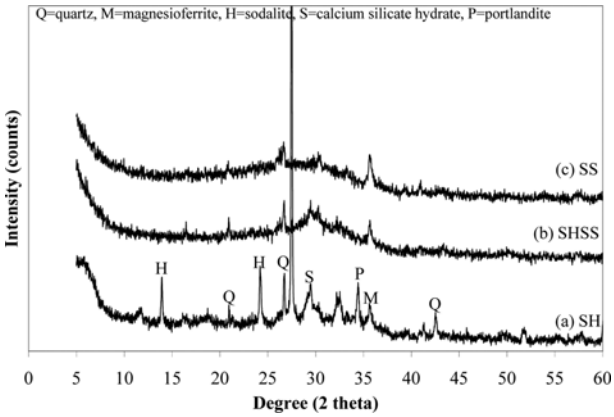

Fig. 6. XRD of Geopolymer Without PC with Difference of Alkali Activators

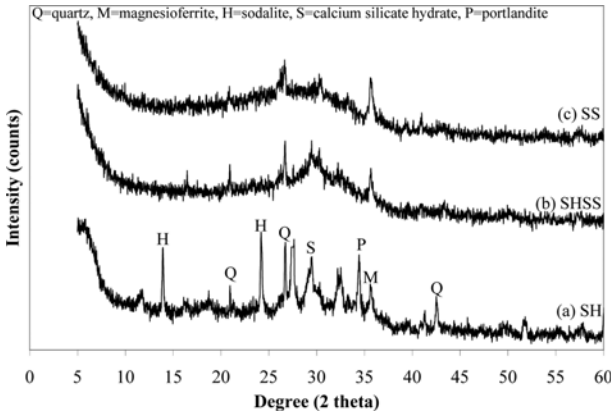

Fig. 7. XRD of Geopolymer Containing 15% PC with Difference of Alkali Activators

than those of SH-0PC and SH-15PC mixes. The dense structure with smooth and continuous matrix is found in the mix with 15%PC (SS-15PC) as illustrated in Fig. 5(f). The increasing of calcium content also enhances the geopolymer reaction from an exothermal reaction with liberated heat and hence additional formation of CSH and/or CASH. Also, the dense surface of SS-15PC mix is due to the reaction between silica from sodium silicate solution and calcium ions from precursors by forming additional CSH gel within geopolymer system (Suwan and Fan 2014). The dense matrices with less number of unreacted fly ash particles of fracture surface of GPs are also clearly noticeable in the mixes activated by SHSS solution (Figs. 5(c) and 5(d)). The activation with SHSS solution can accelerates the geopolymerization process and hence high compressive and shear bond strength of GM are obtained.

The XRD pattern is one of the methods for an observation of the development of geopolymerization products. Fig. 6 shows the XRD patterns for GPs without PC content with different alkali activators viz., SH, SHSS, and SS. It is evident that the GP with SH-0PC (Fig. 6(a)) contains the glassy phase as indicated by a broad hump at 25-35° 2theta and the crystalline phases of quartz (SiO_2), calcium silicate hydrate (CSH), Portlandite ($Ca(OH)_2$), magnesioferrite (Fe_2MgO_4), and hydrosodalite ($Na_4Al_3Si_3O_{12}(OH)$). While the XRD patterns of SH-15PC mix (Fig. 7(a)) show some additional peaks of Portlandite and CSH. In this study, the presence of high content of crystalline phases especially hydrosodalite results in low strength development of fly ash-Portland cement geopolymer with rather loose packing matrix. However, previous work (Oh *et al*., 2012) also demonstrated that the present of hydrosodalite could increase the strength of geopolymer binder. The present of a large amount of crystal was shown to adversely affect the strength of geopolymer (Lee and Lee, 2015). For SHSS-0PC mix (Fig. 6(b)), the XRD pattern shows also the glassy phase as indicated by the hump at 28-35°

2theta and the main crystalline phases of quartz, magnesioferrite and CSH. However, the peaks of these crystalline phases are reduced and no peaks of hydrosodalite are observed. Difference in the XRD pattern of GP is found in the mix containing 15% PC and activated by SHSS solutions as illustrates in Fig. 7(b). The additional CSH and a substantial amount of amorphous phase with reducing amount of quartz are also observed. The presence of amorphous phases are generally corresponded to the overlap between CSH and alumino silicate products (Escalante-García *et al.*, 2003). As mentioned, the formation of additional CSH is responsible for the increase in strength development and hence a high 28-day compressive and shear bond strengths of 54.1 and 24.6 MPa, respectively. For the XRD pattern of SS-0PC mix (Fig. 6(c)), the amorphous gel and a small amount of CSH with some crystalline phases of quartz and magnesioferrite are observed. While the SS-15PC mix (Fig. 7(c)) shows a small increase in the peak of CSH comparable to that of SS-0PC mix. This suggests that the use of suitable alkali activator solutions and amount of PC renders high strength development of fly ash and Portland cement geopolymer. The outcome of this study is thus useful and should lay a ground work for commercial utilization of high calcium FA as a precursor material with Portland cement as additive. This geopolymer cured at ambient curing condition possesses high compressive and shear bond strengths. These conditions are important for the application in the real situation.

5. Conclusions

This paper investigates the effects of combinations of sodium hydroxide and sodium silicate solutions (SH, SHSS, and SS) on the strength development of fly ash and Portland cement based Geopolymer Mortar (GM). It can be concluded that the types of precursors and alkali activator affecting the reaction products and strength development of geopolymer. Additional Calcium Silicate Hydrate (CSH) is found in the GMs activated by SHSS solutions. The CSH gel coexists with the NASH gel, leading to a high strength GM. The active silica from sodium silicate solution reacts with calcium from precursors by forming the reaction products and results in a high strength geopolymer. The increasing of PC content can help the strength development of GM due to the formation of additional CSH and other reaction products within the geopolymer matrix. The use of SH solution gave very low strength development at ambient temperature condition. The shear bond strength between CS and GM increases with the increase in compressive strength of GM. However, for the GM with SS solution, the optimum PC content for the compressive strength is at 5% PC replacement solution. The SiO_2/Al_2O_3 and CaO/SiO_2 ratios also controls the strength development of geopolymer matrix where the maximum compressive and shear bond strengths are found at SiO_2/Al_2O_3 ratio of 3.4-3.6 and CaO/SiO_2 ratio of 0.72-0.80. The GM made from SHSS solution can be used as a sustainable repair binder and its application is very attractive.

Acknowledgements

The authors gratefully acknowledge the financial supported from Lampang Rajabhat University 2014 budget; the Higher Education Research Promotion and National Research University Project of Thailand, Office of the Higher Education Commission, through the Advanced Functional Materials Cluster of Khon Kaen University; Khon Kaen University and the Thailand Research Fund (TRF) under the TRF Senior Research Scholar, Grant No. RTA5780004. The third author is grateful to the Thailand Research Fund (TRF) for the financial support under the TRF New Research Scholar, Grant no. MRG5580222.

The authors also would like to acknowledge the support of the Program of Civil Technology, Faculty of Industrial Technology, Lampang Rajabhat University.

References

Albitar, M., Visintin, P., Mohamed Ali, M. S., and Drechsler, M. (2014). "Assessing behaviour of fresh and hardened geopolymer concrete mixed with Class-F fly ash." *KSCE Journal of Civil Engineering*, pp. 1-11, DOI: 10.1007/s12205-014-1254-z.

ASTM C109 (2002). "Standard test method of compressive strength of hydrualic cement mortars (using 2-in. or [50 mm] cube speciments)." Annual Book of ASTM Standard, Vol.04.01.

ASTM C618 (2008). "Standard specification for coal fly ash and raw or calcined natural pozzolan for use in cement." *Annual Book of ASTM Standard*, Vol.04.01.

ASTM C882 (2005). "Standard test method for bond strength of epoxy-resin systems used with concrete by slant shear." *Annual Book of ASTM Standard*, Vol.04.02.

Chindaprasirt, P., Chareerat, T., and Sirivivatnanon, V. (2007). "Workability and strength of coarse high calcium fly ash geopolymer." *Cement and Concrete Composites*, Vol. 29, No. 3, pp. 224-229, DOI: 10.1016/j.cemconcomp.2006.11.002.

Chindaprasirt, P., Chareerat, T., Hatanaka, S., and Cao, T. (2011). "High strength geopolymer using fine high calcium fly ash." *Journal of Materials in Civil Engineering*, Vol. 23, No.3, pp. 264-270, DOI: 10.1061/(ASCE)MT.1943-5533.0000161.

Chindaprasirt, P., De Silva, P., Sagoe-Crenstil, K., and Hanjitsuwan, S. (2012). "Effect of SiO_2 and Al_2O_3 on the setting and hardening of high calcium y ash-based geopolymer systems." *Journal of Materials Science*, Vol. 47, No. 12, pp. 4876-4883, DOI: 10.1007/s10853-012-6353-y.

Escalante-García, J. I., Fuentes, A. F., Gorokhovsky, A., Fraire-Luna, P. E., and Mendoza-Suarez, G. (2003). "Hydration products and reactivity of blast-furnace slag activated by various alkalis." *Journal of the American Ceramic Society*, Vol. 86, No. 12, pp. 2148-2153, DOI: 10.1111/j.1151-2916.2003.tb03623.x.

FM 3-C 882 (2015). "Florida test method for performance of epoxy-resin systems with concrete by slant shear and compressive strength." *in Florida Department of Transportation Standard Specifications for Road and Bridge Construction*, July.

Garcia-Lodeiro, I., Aparicio-Rebollo, E., Fernández-Jimenez, A., and Palomo, A. (2016). "Effect of calcium on the alkaline activation of aluminosilicate glass." *Ceramics International*, In Press, DOI:10.1016/j.ceramint.2016.01.184.

Guo, X., Shi, H., Chen, L., and Dick, W. A. (2010). "Alkali-activated complex binders from class C fly ash and Ca-containing admixtures."

Journal of Hazardous Materials, Vol. 173, Nos. 1-3, pp. 480-486, DOI: 10.1016/j.jhazmat.2009.08.110.

Jun, Y. and Oh, J. E. (2015). "Microstructural characterization of alkali-activation of six korean class F fly ashes with different geopolymeric reactivity and their zeolitic precursors with various mixture designs." *KSCE Journal of Civil Engineering*, pp. 1-12, DOI: 10.1007/s12205-015-0132-7.

Kumar, S., Kumar, R., and Mehrotra, S. P. (2010). "Influence of granulated blast furnace slag on the reaction, structure and properties of fly ash based geopolymer." *Journal of Materials Science*, Vol. 45, No. 3, pp. 607-615, DOI: 10.1007/s10853-009-3934-5.

Lee, N. K. and Lee, H. K. (2015). "Reactivity and reaction products of alkali-activated, fly ash/slag paste." *Construction and Building Materials*, Vol. 81, pp. 303-312, DOI: 10.1016/j.conbuildmat.2015.02.022.

Lee, N. K., Jang, J. G., and Lee, H. K. (2014). "Shrinkage characteristics of alkali-activated fly ash/slag paste and mortar at early ages." *Cement and Concrete Composites*, Vol. 53, pp. 239-248, DOI: 10.1016/j.cemconcomp.2014.07.007.

Li, C., Sun, H., and Li, L. (2010). "A review: The comparison between alkali-activated slag (Si+Ca) and metakaolin (Si+Al) cements." *Cement and Concrete Research*, Vol. 40, No. 9, pp. 1341-1349, DOI: 10.1016/j.cemconres.2010.03.020.

McLellan, B. C., Williams, R. P., Lay, J., van Riessen, A., and Corder, G. D. (2011). "Costs and carbon emissions for geopolymer pastes in comparison to ordinary portland cement." *Journal of Cleaner Production*, Vol. 19, Nos. 9-10, pp. 1080-1090, DOI: 10.1016/j.jclepro.2011.02.010.

Metz, B., Davidson, O. R., Bosch, P. R., Dave, R., and Meyer, L. A. (2007). "Climate change 2007." *Contribution of Working Group III to the Fourth Assessment Report of the Intergovernmental Panel on Climate Change, 2007*, Cambridge University Press, Cambridge, United Kingdom and New York, NY, USA., pp. 447-496.

Nath, P and Sarker, P. K. (2015). "Use of OPC to improve setting and early strength properties of low calcium fly ash geopolymer concrete cured at room temperature." *Cement and Concrete Composites*, Vol. 55, pp. 205-214, DOI: 10.1016/j.cemconcomp.2014.08.008.

Nazari, A., and Ghafouri Safarnejad, M. (2013). "Prediction early age compressive strength of OPC-based geopolymers with different alkali activators and seashell powder by gene expression programming." *Ceramics International*, Vol. 39, No. 2, pp. 1433-1442, DOI: 10.1016/j.ceramint.2012.07.086.

Oh, J. E., Moon, J., Oh, S. G., Clark, S. M., and Monteiro, P. J. M. (2012). "Microstructural and compositional change of NaOH-activated high calcium fly ash by incorporating Na-aluminate and co-existence of geopolymeric gel and C–S–H(I)." *Cement and Concrete Research*, Vol. 42, No. 5, pp. 673-685, DOI: 10.1016/j.cemconres.2012.02.002.

Pacheco-Torgal, F., Castro-Gomes, J. P., and Jalali, S. (2008). "Adhesion characterization of tungsten mine waste geopolymeric binder. Influence of OPC concrete substrate surface treatment." *Construction and Building Materials*, Vol. 22, No. 3, pp. 154-161, DOI: 10.1016/j.conbuildmat.2006.10.005.

Palomo, A., Fernández-Jiménez, A., Kovalchuk, G., Ordoñez, L. M., and Naranjo, M. C. (2007). "OPC-fly ash cementitious systems: Study of gel binders produced during alkaline hydration." *Journal of Materials Science*, Vol. 42, No. 9, pp. 2958-2966, DOI: 10.1007/s10853-006-0585-7.

Palomo, A., Grutzeck, M. W., and Blanco, M. T. (1999). "Alkali-activated fly ashes: A cement for the future." *Cement and Concrete Research*, Vol. 29, No. 8, pp. 1323-1329, DOI: 10.1016/S0008-8846(98)00243-9.

Pangdaeng, S., Phoo-ngernkham, T., Sata, V., and Chindaprasirt, P. (2014). "Influence of curing conditions on properties of high calcium fly ash geopolymer containing Portland cement as additive." *Materials & Design*, Vol. 53, pp. 269-274, DOI: 10.1016/j.matdes.2013.07.018.

Panias, D., Giannopoulou, I. P., and Perraki, T. (2007). "Effect of synthesis parameters on the mechanical properties of fly ash-based geopolymers." *Colloids and Surfaces A: Physicochemical and Engineering Aspects*, Vol. 301, Nos. 1-3, pp. 246-254, DOI: 10.1016/j.colsurfa.2006.12.064.

Phoo-ngernkham, T., Chindaprasirt, P., Sata, V., Hanjitsuwan, S., and Hatanaka, S. (2014). "The effect of adding nano-SiO_2 and nano-Al_2O_3 on properties of high calcium fly ash geopolymer cured at ambient temperature." *Materials & Design*, Vol. 55, pp. 58-65, DOI: 10.1016/j.matdes.2013.09.049.

Phoo-ngernkham, T., Chindaprasirt, P., Sata, V., Pangdaeng, S., and Sinsiri, T. (2013). "Properteis of high calcium fly ash geopolymer pastes containing Portaland cement as additive." *International Journal of Minerals, metallurgy and Materials*, Vol. 20, No. 2, pp. 214-220, DOI: 10.1007/s12613-013-0715-6.

Phoo-ngernkham, T., Maegawa, A., Mishima, N., Hatanaka, S., and Chindaprasirt, P. (2015). "Effects of sodium hydroxide and sodium silicate solutions on compressive and shear bond strengths of FA–GBFS geopolymer." *Construction and Building Materials*, Vol. 91, pp. 1-8, DOI: 10.1016/j.conbuildmat.2015.05.001.

Phoo-ngernkham, T., Sata, V., Hanjitsuwan, S., Ridtirud, C., Hatanaka, S., and Chindaprasirt, P. (2015). "High calcium fly ash geopolymer mortar containing Portland cement for use as repair material." *Construction and Building Materials*, Vol. 98, pp. 482-488, DOI: doi:10.1016/j.conbuildmat.2015.08.139.

Pimraksa, K., Chindaprasirt, P., Rungchet, A., Sagoe-Crentsil, K., and Sato, T. (2011). "Lightweight geopolymer made of highly porous siliceous materials with various Na_2O/Al_2O_3 and SiO_2/Al_2O_3 ratios." *Materials Science and Engineering A*, Vol. 528, No. 21, pp. 6616-6623, DOI: 10.1016/j.msea.2011.04.044.

Puligilla, S., and Mondal, P. (2013). "Role of slag in microstructural development and hardening of fly ash-slag geopolymer." *Cement and Concrete Research*, Vol. 43, pp. 70-80, DOI: 10.1016/j.cemconres.2012.10.004.

Ravikumar, D. and Neithalath, N. (2012). "Effects of activator characteristics on the reaction product formation in slag binders activated using alkali silicate powder and NaOH." *Cement and Concrete Composites*, Vol. 34, No. 7, pp. 809-818, DOI: 10.1016/j.cemconcomp.2012.03.006.

Ravikumar, D., Peethamparan, S., and Neithalath, N. (2010). "Structure and strength of NaOH activated concretes containing fly ash or GGBFS as the sole binder." *Cement and Concrete Composites*, Vol. 32, No. 6, pp. 399-410, DOI: 10.1016/j.cemconcomp.2010.03.007.

Sathonsaowaphak, A., Chindaprasirt, P., and Pimraksa, K. (2009). "Workability and strength of lignite bottom ash geopolymer mortar." *Journal of Hazardous Materials*, Vol. 168, No. 1, pp. 44-50, DOI: 10.1016/j.jhazmat.2009.01.120.

Somna, K., Jaturapitakkul, C., Kajitvichyanukul, P., and Chindaprasirt, P. (2011). "NaOH-activated ground fly ash geopolymer cured at ambient temperature." *Fuel*, Vol. 90, No. 6, pp. 2118-2124, DOI: 10.1016/j.fuel.2011.01.018.

Sukmak, P., Horpibulsuk, S., and Shen, S. L. (2013). "Strength development in clay–fly ash geopolymer." *Construction and Building Materials*, Vol. 40, pp. 566-574, DOI: 10.1016/j.conbuildmat.2012.11.015.

Sukmak, P., Horpibulsuk, S., Shen, S. L., Chindaprasirt, P., and Suksiripattanapong, C. (2013). "Factors influencing strength development in clay–fly ash geopolymer." *Construction and Building*

Materials, Vol. 47, pp. 1125-1136, DOI: 10.1016/j.conbuildmat.2013.05.104.

Suwan, T. and Fan, M. (2014). "Influence of OPC replacement and manufacturing procedures on the properties of self-cured geopolymer." *Construction and Building Materials*, Vol. 73, pp. 551-561, DOI: 10.1016/j.conbuildmat.2014.09.065.

Temuujin, J., van Riessen, A., and Williams, R. (2009). "Influence of calcium compounds on the mechanical properties of fly ash geopolymer pastes." *Journal of Hazardous Materials*, Vol. 167, Nos. 1-3, pp. 82-88, DOI: 10.1016/j.jhazmat.2008.12.121.

Turner, L. K. and Collins, F. G. (2013). "Carbon dioxide equivalent (CO_2-e) emissions: A comparison between geopolymer and OPC cement concrete." *Construction and Building Materials*, Vol. 43, pp. 125-130, DOI: 10.1016/j.conbuildmat.2013.01.023.

Williams, P. J., Biernacki, J. J., Walker, L. R., Meyer, H. M., Rawn, C. J., and Bai, J. (2002). "Microanalysis of alkali-activated fly ash–CH pastes." *Cement and Concrete Research*, Vol. 32, No. 6, pp. 963-972, DOI: 10.1016/S0008-8846(02)00734-2.

Materials and Structures
DOI 10.1617/s11527-016-0812-x

ORIGINAL ARTICLE

Use of phase change material to improve thermal properties of lightweight geopolymer panel

Piti Sukontasukkul · Nutchayakorn Nontiyutsirikul · Smith Songpiriyakij · Koji Sakai · Prinya Chindaprasirt

Received: 1 September 2015 / Accepted: 25 January 2016
© RILEM 2016

Abstract In this study, the properties of wall panels made of geopolymer containing highly porous aggregate impregnated with phase change material (PCM) were investigated. The coarse aggregate used in this study was a waste lightweight aerated block. The experimental series consisted of 2 parts. Part 1 was the investigation on PCM impregnation technique using heat and pressure. This part investigated the effect of temperature and pressure on PCM impregnation level to determine the optimum temperature and pressure. Part 2 was the study on the properties of geopolymers containing non-PCM and PCM aggregates. The density, compressive strength and thermal storage of geopolymers were tested. Results showed that the density of geopolymer increased with the increasing PCM aggregate content. The increase in density also led to the improvement of compressive strength. The incorporation of PCM aggregate also improved the thermal storage and heat insulation of geopolymer panel. With a high level of impregnation of 65 %, the heat insulation improved significantly as indicated by the delay of time needed to reach the peak temperature. The thermal storage was also improved as reflected by the ability of panel to maintain high temperature after the end of heating. Since geopolymer is considered a green construction material, this material is thus green and sustainable in terms of energy saving.

P. Sukontasukkul (✉)
Department of Civil Engineering, Construction and Building Material Research Center, King Mongkut's University of Technology North Bangkok, Bangkok, Thailand
e-mail: piti_sk@hotmail.com; piti.kmutnb@gmail.com

N. Nontiyutsirikul
Department of Civil Engineering, King Mongkut's University of Technology North Bangkok, Bangkok, Thailand
e-mail: nutchayakorn1831@gmail.com

S. Songpiriyakij
Department of Civil Engineering and Environmental Technology, King Mongkut's University of Technology North Bangkok, Bangkok, Thailand
e-mail: ssy@kmutnb.ac.th

K. Sakai
Japan Sustainability Institute, Sapporo, Japan
e-mail: sakai@jsi-ks.jp

P. Chindaprasirt
Department of Civil Engineering, Sustainable Infrastructure Research and Development Center, Khon Kaen University, Khon Kaen, Thailand
e-mail: prinya@kku.ac.th

Published online: 29 January 2016

Keywords Lightweight geopolymer panel · Phase change material · Impregnation · Thermal properties

1 Introduction

The use of geopolymer in construction and building application in Thailand has been growing substantially due to the availability of raw materials (fly ash from coal base electrical power generation plants) and the increasing amount of research. Geopolymer is a material synthesized from a series of chemical reactions between sodium hydroxide solutions (NaOH), sodium silicate and kaolin. When it was first introduced in 1984 by Davidovits [1, 2], the reactions produced a hard brittle material similar to the hardened cement. Beside from the raw material mentioned, geopolymer can also be synthesized from raw materials with high silica (SiO_2) and alumina (Al_2O_3) contents such as fly ash or slag [3–5].

The mechanical properties of geopolymer are quite similar to those of hardened cement paste making it one of the ideal construction materials [6, 7]. The use of geopolymers also represents the utilization of green construction materials through a few indicators [8]. For example, CO_2 emission is low because it contains no cement and utilizes waste(fly ash)as its main ingredient.

This study focuses on investigating the properties of geopolymer wall panels and the effect of phase change material (PCM) as some concrete components are occasionally required to have high heat storage or high thermal mass (for example, the curing room for aerated concrete block manufacturing which requires to maintain inside temperature of 60–70 °C). To gain such a high thermal mass, the components are usually designed to be thick and massive. However, nowadays, the designing trend is moving toward structures with smaller or thinner components (in order to reduce dead load acting on the foundation), this unfortunately leads to the reduction of heat storage capacity. In order to maintain or increase the heat storage capacity of concrete structures without increasing component thickness or structural mass, the application of PCM is introduced.

PCM are materials capable of changing phase from solid to liquid at melting temperature (or vice versa). During the phase changing process, a certain amount of energy (heat) is captured from or released into the surrounding environment [9, 10]. It is believed that the ability to absorb heat without changing the surrounding temperature can be beneficial in terms of storing heat in the structures and slowing the transmission of heat to the interior or shifting the period of peak temperature.

The applications of PCM were first introduced around the end of World War II [11–13]. In general, there are three main groups of PCM: organic, inorganic and eutectic. For construction materials, the organic group is widely accepted because of the cost effectiveness, temperature range availability, stability and durability (ability to sustain numbers of temperature change cycle without efficiency degradation) [8].

PCM or paraffin can be incorporated into concrete simply by mixing as a part of constituent materials. In this case, paraffin is distributed freely in concrete among void, aggregate and paste. However after a number of temperature change cycles, the leakage of paraffin to the concrete surface is often found. In order to solve this problem, the paraffin is pre-encapsulated or stored into small closed sphere capsules to prevent leakage and then mixed with concrete [14–17]. The encapsulation is in fact quite effective to solve leakage problem; however, it is quite expensive and, in some cases also create weak bonds with the cement paste due to the smooth surface.

The encapsulation can also be divided into macro- and micro-encapsulation [18]. Past studies, however, revealed that macro-encapsulation had limitation due to the solidification of PCM around the edges during the time of heat regaining from liquid phase which prevented effective heat transfer.

For micro-encapsulation, several researchers have investigated this technique and reported the potential applications. Cabeza et al. [19] conducted actual field tests using commercial type micro-encapsulated PCM capsule. Their results showed the improvement in thermal storage of walls with encapsulated PCM in comparison with conventional concrete without PCM due to improved thermal inertia and low inner temperature. Castellón et al. [20] analyzed and compared a concrete cubicle with and without encapsulated PCM. Their results were quite promising with the reduction in daily temperature oscillation up to 4 °C and the shift in peak temperature of PCM cubicle. Successful use of PCM in different components of the

Table 1 Chemical compositions of fly ash and silica fume (% by weight)

Material	SiO_2	Al_2O_3	Fe_2O_3	CaO	SO_3	Loss of ignition (LOI)
Fly ash	36.02	20.58	15.91	18.75	2.24	0.07
Silica fume	88.30	1.17	4.76	0.48	1.05	–

Table 2 Properties of coarse aggregate

Property	Unit	Value
Unit weight	kg/m^3	400
Bulk specific gravity (dry)	–	0.75
Bulk specific gravity (SSD)	–	1.27
App. specific gravity	–	1.58
Absorption	%	71
Size	mm	9.5–19
Fineness modulus		7.54

Fig. 1 Coarse aggregate

Table 3 Properties of paraffin

Property	Unit	Value
Melting point	°C	57.2–59.9
Oil content	% Mass	0.4
Penetration at 25 °C		10.0–17.0
Color		30
UV absorption		1.3

house such as brick wall [21, 22], sandwich panel [23, 24], floor [25] and ceiling free-cooling [26] system have also been reported.

The investigations of PCM encapsulated into porous aggregate were also carried out by a number of researchers. Zhang et al. [27] and Bentz and Turpin [28] used porous lightweight aggregates impregnated with PCM to enhance the heat storage capacity of concrete. The results showed the reduction of PCM leakage due to the enclosure of cement paste around PCM aggregates. Frattini et al. [29] investigated the use of expanded clay aggregate incorporated PCM material (paraffin base) in geopolymer mortar. The results showed that with the paraffin content up to about 30–40 % by weight, the aggregate exhibited good mechanical properties and relatively high fire resistance with no relevant smoke or CO_2 emission being observed.

In the case of geopolymer mixed with PCM, very few studies have been carried out and published. Shadnia et al. [30] studied PCM in the form of micro-encapsulated powder incorporated into geopolymer mixture as a part of constituent material. The result showed the reduction in unit weight and compressive strength and the increase in specific heat with the increasing PCM content. In addition, the temperatures inside the cubical with PCM slabs were found to be lower than those with non-PCM slabs.

In this study, the concept of encapsulating was employed. Instead of using small spheres, the PCM was encapsulated (impregnated) in porous lightweight aggregates by means of heat and pressure using an autoclave chamber. The advantages of this process are cost effectiveness and simplification. By using this technique, the level of impregnation was precisely controlled. Several trial tests with combinations of pressure and heat were carried out until the desired impregnation level was achieved. The PCM aggregates were then used as coarse aggregates in geopolymer concrete mixture. The geopolymer concrete samples were tested for basic mechanical properties and heat insulation to investigate the effect of PCM on the properties of concrete.

Table 4 Mix proportions

Specimen designation	FA:CA	% PCM	Weight (kg/m^3)			
			Solution	Fly ash	Fine agg.	Coarse agg.
40LA/0P	60:40	0	300	375	865	210
40LA/65P		65				
60LA/0P	40:60	0	300	375	695	380
60LA/65P		65				

aLA/bP, where a is the percent of coarse aggregate by volume, b is the percent of paraffin impregnation, LA is the non PCM aggregate, P is the PCM aggregate

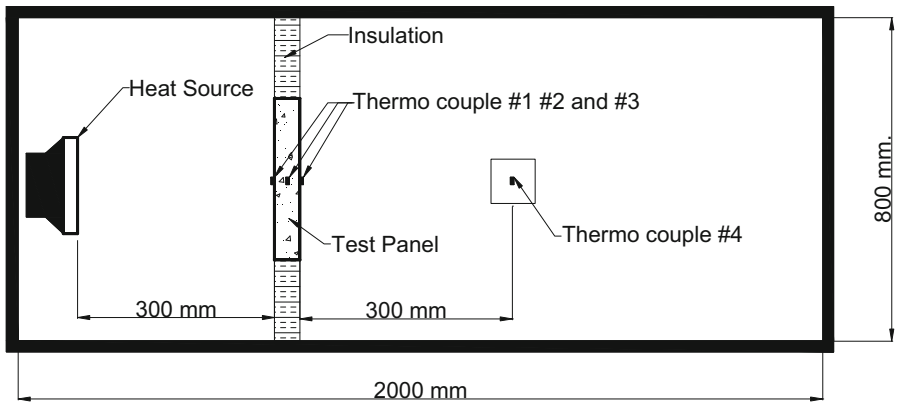

Fig. 2 Heat insulating chamber

2 Experimental procedure

2.1 Materials

Materials used in this study include:

- Fly ash (FA): obtained from Mae Moh electricity power plant, Lampang, Thailand (Table 1).
- Silica fume (SF) (Table 1).
- Sodium hydroxide solution (NaOH) with 14 molar concentration.
- Sodium silicate solution (Na_2OSiO_2) with Na_2O:SiO_2 ratio of 1:2.24.
- Lightweight coarse aggregate—waste aerated concrete block (Table 2; Fig. 1).
- Paraffin type 6035 (Table 3).
- River sand.

2.2 Preparation of PCM aggregates

The paraffin impregnation level for PCM aggregates was set at 65 % by weight. The impregnation process was carried out using heat and heat with pressure. Pressure and temperature were set at 100–120 °C and 5–10 bar, respectively. Graphs between the impregnation levels versus time were plotted in order to determine the optimum time and pressure level to achieve the desired impregnation level.

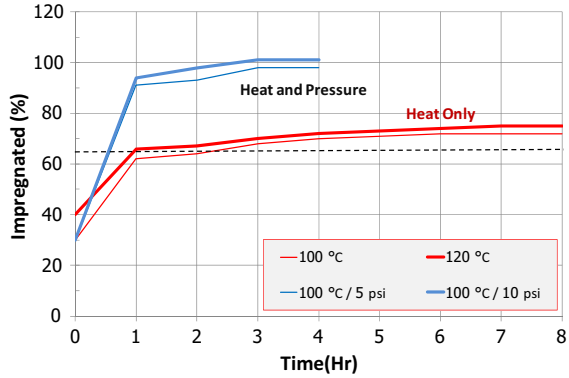

Fig. 3 Impregnation percentage versus time

Table 5 Properties of aggregate

Property	Impregnation level		
	0 %	65 %	100 %
Bulk specific gravity (dry)	0.75	0.965	0.997
Bulk specific gravity (SSD)	1.27	0.966	0.998
Apparent specific gravity	1.58	0.968	0.998
Absorption (%)	71	8.5	5.0

Only aggregate with 65 % paraffin was used to produce geopolymer

2.3 Mix proportions

The mix proportion of geopolymer was as follows: l/b (liquid to fly ash) ratio = 0.80, NaOH concentration = 14 molar and NaOH:Na_2OSiO_2 ratio = 1:1. The samples were cast with non PCM and PCM aggregates with the mix proportions as shown in Table 4. The specimens were cured in water for 28 days until the test age.

2.4 Experimental program

Three experiments viz., density and absorption, compressive strength and thermal storage tests were carried out on geopolymer samples. The density and absorption, and the compressive strength tests were carried out in accordance with ASTM C138 and EN12390, respectively.

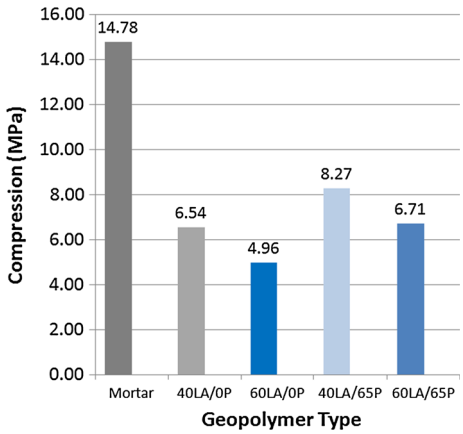

Fig. 4 Compressive strength of geopolymer panels containing non-PCM and PCM aggregates

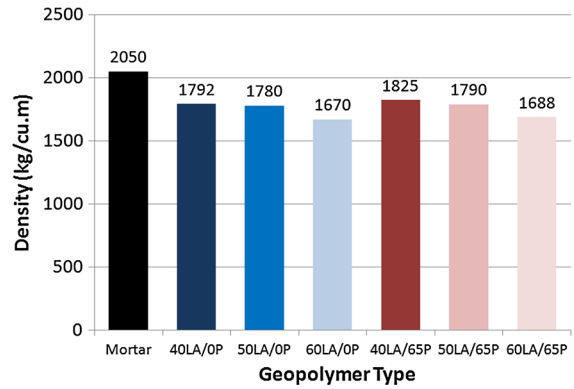

Fig. 5 Density of geopolymer panels containing non-PCM and PCM aggregates

For the thermal storage test, the experiment was carried out using a heat insulating chamber constructed at King Mongkut's University of Technology North Bangkok (KMUTNB) (Fig. 1). The chamber with dimension of 800 × 800 × 2000 mm. equipped with a 1500 Watts spotlight and a supporter was constructed with steel plates and insulating sheets as shown in Fig. 2. The specimens in square shape panel with dimension of 400 × 400 × 50 mm were cast. Four thermocouples were installed, three were embedded at outer surface, mid panel and inner surface of specimen, and the last thermocouple was located inside the chamber (300 mm away) to measure room temperature change. The temperature change was measured and collected automatically every 5 s using a data acquisition system connected to a laptop.

The test configuration was aimed to test the performance and observe the effect of PCM on heat capturing and storage. Therefore, in one cycle of test, the heating was supplied to the panel until the mid-plate temperature reached 65 °C and then ceased. The temperature was recorded every 5 s and continued for 10,000 s to observe the heat storage ability of each panel.

3 Results and discussion

3.1 Impregnation process of PCM aggregate

The aggregates in small lots were dried and weighed prior to the immersion in liquid paraffin and then placed in an oven or autoclave chamber. The weight

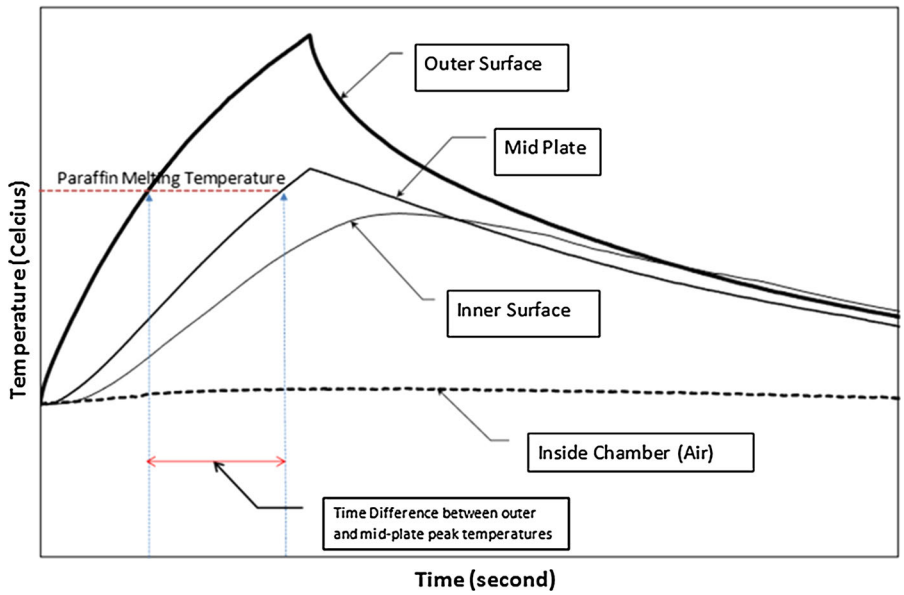

Fig. 6 Typical temperature change record at each location of the panel

change of aggregate with paraffin impregnation was recorded every hour using three samples. Results on the impregnation level versus time are shown in Fig. 2. Due to the high porosity, as soon as the aggregates were submerged into paraffin, the impregnation level increased instantaneously to 30–40 %. Then the impregnation level increased with the increase in submersion duration until reaching the constant condition (steady stage).

For the treatment with heat only, the steady stage was reached at approximately 6 h for both 100 and 120 °C treatments. However, the maximum impregnation levels at the steady stage were different depending on the temperature: 71 and 75 % by weight for 100 and 120 °C treatments, respectively (Fig. 3). The desired impregnation level of 65 % was achieved after approximately 2 h for 100 °C and 1 h for 120 °C. Under heat and pressure, the impregnation level increased at a faster rate, up to 91–94 % impregnation levels were obtained after 1 h. The impregnation reached a steady stage after 3 h with impregnation levels around 98–100 %.

The properties of PCM aggregate with impregnation levels of 65 and 100 % were compared with non-PCM aggregates as shown in Table 5. The specific gravity increased and the absorption decreased with the increasing paraffin impregnation level. For non-PCM aggregate, the absorption was approximately 71 %. After impregnation with PCM, the absorption decreased to approximately 8.5 and 5 % at 65 and 100 % impregnation, respectively. The effect of paraffin filling voids inside the aggregates played an important role on this. Less absorption also caused the specific gravity at different conditions to remain almost unchanged.

3.2 Compressive strength

First let us consider the effect of paraffin content. At the same fine to coarse aggregate ratio (FA/CA), the compressive strength tended to increase with the increasing paraffin content (Fig. 4). This was due to the reduction of voids (filled up by paraffin) which led to the increases in density (Fig. 5) and strength. For the effect of lightweight aggregate content, the compressive strength decreased with the increasing lightweight aggregate content. Regardless of aggregate types, the increasing lightweight aggregate content lowered the compressive strength by approximately 19–24 %. The decrease was more pronounced with the geopolymers containing non-PCM aggregates than those with PCM aggregates. Since lightweight aggregate was much weaker than geopolymer paste, the increase in lightweight aggregate content caused the strength reduction.

3.3 Thermal properties

Typical temperature versus time curve is shown in Fig. 6. The discussion in this section focuses on the

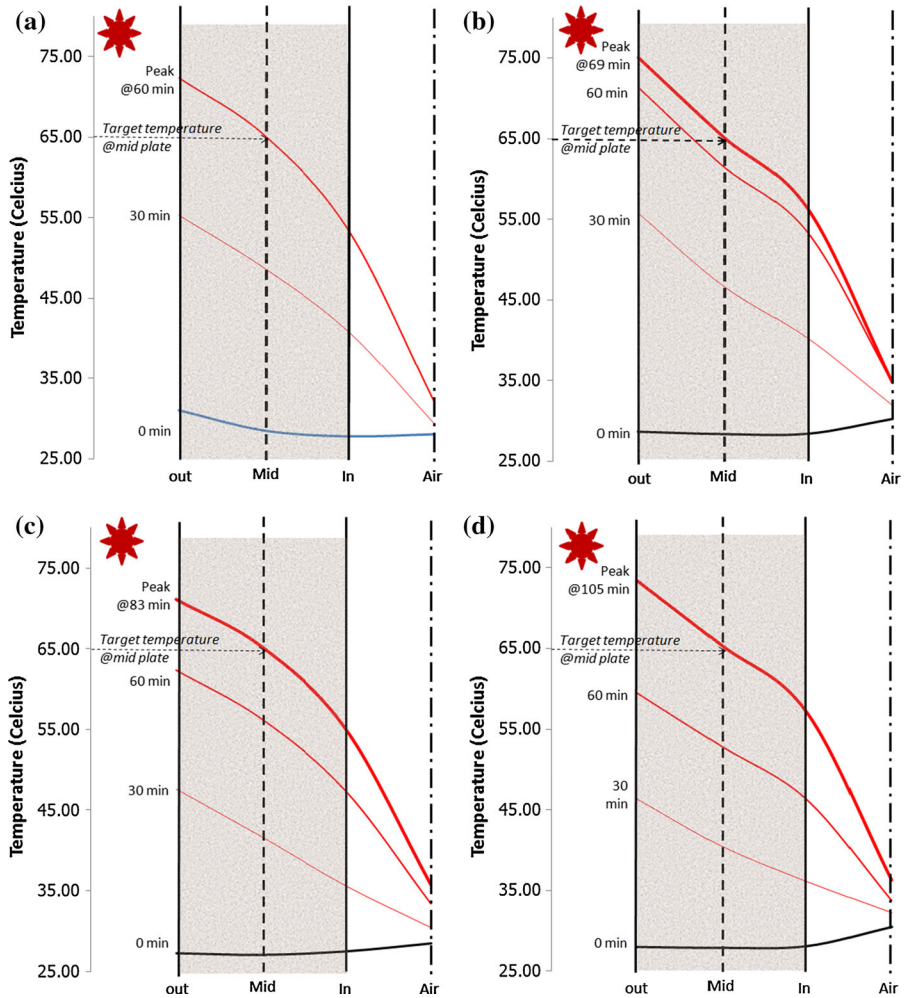

Fig. 7 Temperature patterns at different locations prior to peak temperature. **a** 40LA/0P, **b** 40LA/65P, **c** 60LA/0P, **d** 60LA/65P

behavior or the pattern of temperature change within and outside the wall at different period of time prior to and after the peak temperature.

3.4 Prior to peak temperature

The patterns of temperature change with time at different locations of each geopolymer panel are shown in Fig. 7a–d. As mentioned before, the heat was supplied to the panel until the mid-plate temperature reached 65 °C. This caused the paraffin inside the panel to melt. After the target temperature was reached, the heating was ceased.

Based on the recorded data, the following phenomena were observed. First, the time to reach target temperature increased with the paraffin content and lightweight aggregate content. This showed that paraffin did increase the insulation capacity of panel. Secondly, since the time required to supply heat to panel increased with the PCM and lightweight aggregate contents, the temperature at the outer surface also increased. In other words, more energy (heat) was required to supply to the panels with PCM to reach the target temperature at mid-plate than those without PCM. The reason for this could be that during the phase changing process of paraffin (from solid to liquid), some of the energy or heat was used in the melting process and stored in the liquid paraffin. This caused the temperature to increase at a slower rate and more energy (or heat) was required to reach the target temperature.

3.5 After peak temperature

The temperature patterns after the peak of each panel are given in Fig. 8a–d. The temperatures at different

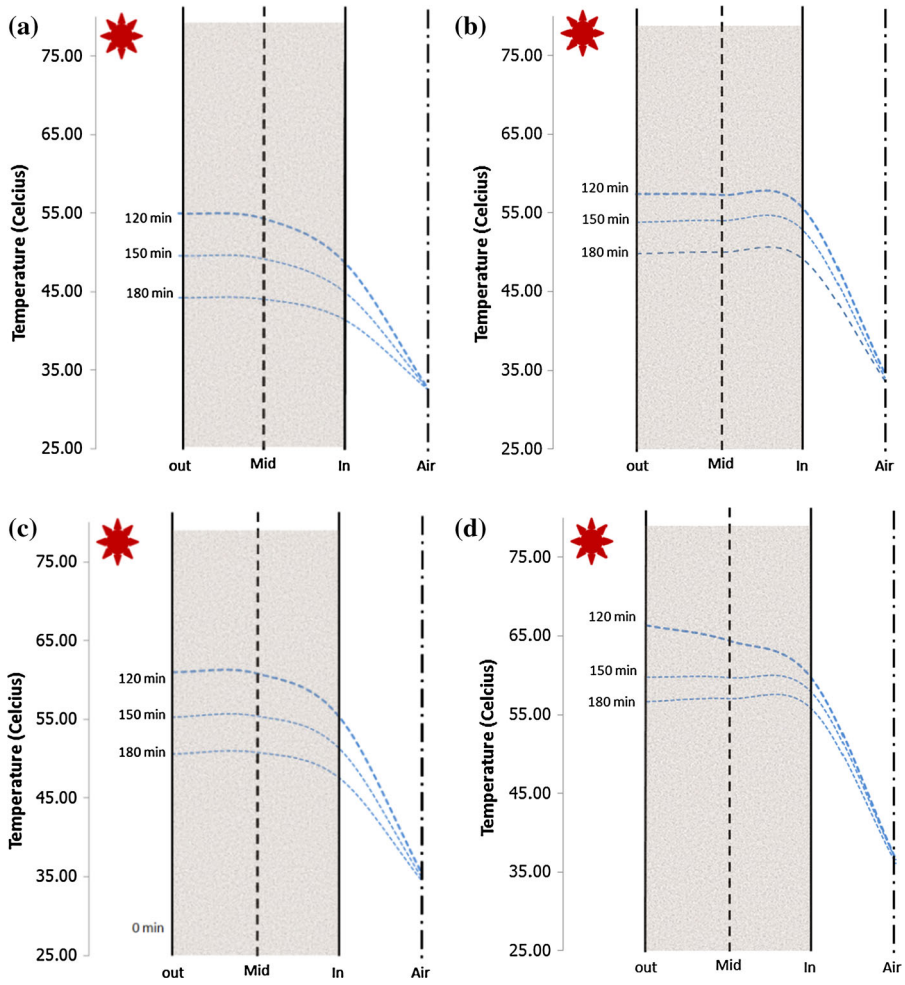

Fig. 8 Temperature patterns at different location after peak temperature. **a** 40LA/0P, **b** 40LA/65P, **c** 60LA/0P, **d** 60LA/65P

time (after the heating stop) in the PCM panels remained higher than those in the non-PCM panels. This indicated that the use of PCM (paraffin) improved the heat storage of the panel. During the phase change process (from liquid back to solid), part of the heat stored in paraffin was released back to the surrounding area and caused the high temperature to remain. It was also observed that the heat storage also increased with the increase in lightweight aggregate content.

4 Conclusion

The use of encapsulated PCM, paraffin type, in waste lightweight aerated concrete block significantly influenced the density, strength and thermal properties of geopolymer concrete. For the aggregate itself, the use of paraffin increased the specific gravity which in turn reduced the absorption. The compressive strength of concrete increased with the increase in paraffin content in aggregate. For the thermal properties, the existence of paraffin in aggregate significantly improved both thermal insulation and storage of geopolymer panels as indicated by the delay of time to reach peak temperature and the ability to maintain high temperatures inside the panel after the end of heating. Since geopolymer is considered a green construction material, the combined use with the PCM lightweight aggregate thus produces a green and sustainable building material.

Acknowledgments The authors would like to acknowledge the support of King Mongkut's University of Technology North Bangkok, Khon Kaen University, Thailand Research Fund (TRF) under the TRF Senior Research Scholar Contract No.

RTA5780004 and Thailand Research Fund (TRF) under the Research and Researcher for Industry (RRI) Contract No. MSD57I0113.

References

1. Davidovits J (1984) Mineral polymers and methods of making them. US Patent no. 4, 472, p 199
2. Davidovits J (1991) Geopolymers—inorganic polymeric new materials. J Therm Anal 37(8):1633–1656
3. Zaetang Y, Wongsa A, Sata V, Chindaprasirt P (2015) Use of coal ash as geopolymer binder and coarse aggregate in pervious concrete. Constr Build Mater 96:289–295
4. Chindaprasirt P, Thaiwitcharoen S, Kaewpirom S, Rattanasak U (2013) Controlling ettringite formation in FBC fly ash geopolymer concrete. Cem Concr Compos 41:24–28
5. Sukmak P, Horpibulsuk S, Shen SL, Chindaprasirt P, Suksiripattanapong C (2013) Factors influencing strength development in clay–fly ash geopolymer. Constr Build Mater 47:1125–1136
6. Guo X, Huisheng S, Warren AD (2010) Compressive strength and microstructural characteristics of class C fly ash geopolymer. Cem Concr Compos 32(2):142–147
7. Wongruk R, Songpiriyakij S, Sukontasukkul P, Chindaprasirt P (2015) Properties of steel fiber reinforced geopolymer. Key Eng Mater 659:143–148
8. McLellan BC, Williams RP, Lay J, Van Riessen A, Corder GD (2011) Costs and carbon emissions for geopolymer pastes in comparison to ordinary Portland cement. J Clean Prod 19(9):1080–1090
9. Hale DV, Hoover MJ, O'Neill MJ (1971) Phase change materials hand book. Marshal Space Flight Center, Alabama
10. Sharma A, Tyagi V, Chen CR, Buddhi D (2009) Review on thermal energy storage with phase change materials and applications. Renew Sustain Energy Rev 12:318–345
11. Abhat A (1983) Low temperature latent heat thermal energy storage, heat storage materials. Solar Energy 30:313–332
12. Lorsch HG, Kauffman KW, Denton JC (1976) Thermal energy storage for heating and air conditioning, future energy production system. Heat Mass Transf Process 1:69–85
13. Abhat A et al (1981) Development of a modular heat exchanger with an integrated latent heat storage. Report no. BMFT FBT 81-050, Germany Ministry of Science and Technology Bonn
14. Tyagi VV, Kaushik SC, Tyagi SK, Akiyama T (2011) Development of phase change materials based microencapsulated technology for buildings: a review. Renew Sustain Energy Rev 15:1373–1391
15. Boh B, Sumiga B (2008) Microencapsulation technology and its applications in building construction materials. RMZ Mater Geoenviron 55(3):329–344
16. Hawlader MNA, Uddin MS, Khin MM (2003) Microencapsulated PCM thermal energy storage system. Appl Energy 74:195–202
17. Ling T-C, Poon C-S (2013) Use of phase change materials for thermal energy storage in concrete: an overview. Constr Build Mater 46:55–62
18. Zhou D, Zhao CY, Tian Y (2012) Review on thermal energy storage with phase change materials (PCMs) in building applications. Appl Energy 92:593–605
19. Cabeza LF, Castellón C, Nogués M, Medrano M, Leppers R, Zubillaga O (2007) Use of microencapsulated PCM in concrete walls for energy savings. Energy Build 39:113–119
20. Castellón C, Castell A, Medrano M, Martorell I, Cabeza LF (2009) Experimental study of PCM inclusion in different building envelopes. J Sol Energy Eng 131:0410061–0410066
21. Alawadhi EM (2008) Thermal analysis of a building brick containing phase changematerial. Energy Build 40:351–357
22. Castell A, Martorell I, Medrano M, Pérez G, Cabeza LF (2010) Experimental studyof using PCM in brick constructive solutions for passive cooling. Energy Build 42:534–540
23. Castellón C, Medrano M, Roca J, Cabeza LF, Navarro ME, Fernández AI, Lázaro A, Zalba B (2010) Effect of microencapsulated phase change material in sandwichpanels. Renew Energy 35:2370–2374
24. Konuklu Y, Paksoy HO (2009) Phase change material sandwich panels for managingsolar gain in buildings. J Sol Energy Eng 131:0410121–0410127
25. Entropa AG, Brouwersb HJH, Reindersc AHME (2011) Experimental research on the use of micro-encapsulated phase change materials to store solar energy in concrete floors and to save energy in Dutch houses. Sol Energy 85(5):1007–1020
26. Butala V, Stritih U (2009) Experimental investigation of PCM cold storage. Energy Build 41:354–359
27. Zhang D, Li Z, Zhou J, Wu K (2004) Development of thermal energy storage concrete. Cem Concr Res 34(2004):927–934
28. Bentz DP, Turpin R (2007) Potential applications of phase change materials in concrete technology. Cem Concr Compos 29:527–532
29. Frattini D, Roviello G, Ferone C, Ricciotti L, Cioffi R (2015) Geopolymer-based composite materials containing PCM for thermal energy storage. Ceramic for Energy, Italy, 2015
30. Shadnia R, Zhang L, Li P (2015) Experimental study of geopolymer mortar with incorporated PCM. Constr Build Mater 84:95–102

Construction and Building Materials 127 (2016) 475–483

Contents lists available at ScienceDirect

Construction and Building Materials

journal homepage: www.elsevier.com/locate/conbuildmat

Optimizing mix proportion and properties of lightweight concrete incorporated phase change material paraffin/recycled concrete block composite

Pattaraporn Suttaphakdee [a], Nattakan Dulsang [a], Narubeth Lorwanishpaisarn [a], Pornnapa Kasemsiri [a,*], Patcharapol Posi [b], Prinya Chindaprasirt [c]

[a] Sustainable Infrastructure Research and Development Center and Department of Chemical Engineering, Faculty of Engineering, Khon Kaen University, Khon Kaen 40002, Thailand
[b] Department of Civil Engineering, Faculty of Engineering, Rajamangala University of Technology, Isan Khon Kaen Campus, Khon Kaen 40000, Thailand
[c] Sustainable Infrastructure Research and Development Center, Department of Civil Engineering, Faculty of Engineering, Khon Kaen University, Khon Kaen 40002, Thailand

HIGHLIGHTS

- Mix proportions of LWC were designed by Taguchi method.
- Multi-linear regression models were developed to predict properties of samples.
- The concrete can be classified as structural LWC for structure.
- Thermal performance of LWC substantially improves by addition of PCMPC.

GRAPHICAL ABSTRACT

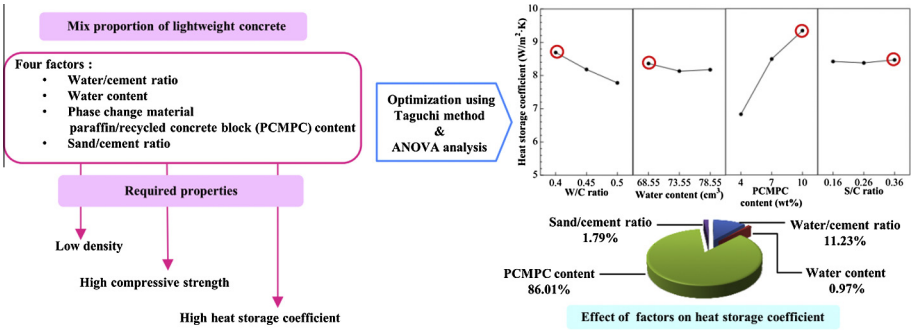

ARTICLE INFO

Article history:
Received 20 June 2016
Received in revised form 20 September 2016
Accepted 6 October 2016

Keywords:
Form stable phase change material
Lightweight concrete
Recycled concrete block
Taguchi method

ABSTRACT

In this study, the phase change material paraffin/recycled concrete block composite (PCMPC) was prepared and used as fine aggregate in manufacturing of lightweight concrete (LWC). The mix proportions of LWC were designed using Taguchi method. L_9 orthogonal array with four factors viz., water/cement (W/C) ratio, water content, PCMPC content and sand/cement (S/C) ratio were selected for the optimization of LWC. The most important factors influencing the properties of LWC were investigated using analysis of variance (ANOVA). Based on the results, the phase transition and latent heat of PCMPC showed good thermally reliable and chemically stability after thermal cycling test. The density and compressive strength of samples containing the PCMPC were in the range of 1711–1812 kg/m^3 and 33–53 MPa, respectively. The density and compressive strength of samples can meet the requirement of lightweight concrete for structure application according to ASTM C330/C330M-14. The results also showed that PCMPC was the most significant factor for heat storage coefficient. The thermal energy absorption and release characteristics of LWC containing PCMPC were significantly better than those of the control sample. The fine PCMPC aggregate is thus another novel building material for use in thermal conditioning of building which can reduce and save electricity consumption.

© 2016 Published by Elsevier Ltd.

1. Introduction

One of the most important renewable energy is solar energy. It has been used for various applications such as of solar-thermal,

* Corresponding author.
E-mail address: pronkas@kku.ac.th (P. Kasemsiri).

http://dx.doi.org/10.1016/j.conbuildmat.2016.10.037
0950-0618/© 2016 Published by Elsevier Ltd.

solar-electrical and solar-chemical conversion [1–5]. Recently, solar thermal applications have attracted much attention due to their high photo-thermal conversion efficiency [6,7]. However, the solar thermal system has some limitations from seasonal and climate variation. To overcome this problem, phase change materials (PCMs) have been developed to store thermal energy collected from solar radiation [8,9]. PCMs are considered as the most effective materials for thermal energy storage, and have been applied for wide application in energy conservation [10,11]. PCMs can absorb and release latent heat during a phase change process i.e. solid to solid or solid to liquid over a narrow temperature range [12–14]. Many researchers have shown that PCM based paraffin has excellent properties i.e. large amount of heat storage, high latent heat storage capacities in the range of 200–250 J/g and good thermal and chemical stability [1,10,15–17]. However, the application of paraffin is limited to certain area due to the leakage of paraffin during phase transition. To overcome this problem, the compounding paraffin with porous materials to obtain form-stable composite PCM is applied [12,18]. Various types of building materials such as diatomite [1,19,20], calcined diatomite [10], cement paste [21], expanded perlite [21], gypsum [22] have been tried as supports for paraffin form-stable composite PCM. The recycling of waste from building structure such a recycled concrete block was also used as support material for paraffin impregnation. The optimum adsorption ratio of paraffin in recycled concrete block was 25 wt% which produced phase transition temperature of 52.85 °C and latent heat of 30.88 J/g. These thermal properties are comparable with other form-stable PCMs. The form stable PCMPC composite is thus a promising PCM for energy storage with ecological utilization of building waste [23].

Form-stable PCM has been widely used for building applications [1,22,24,25]. The incorporate the PCM in building can enhance human comfort by reducing the frequency of internal building temperature swings and keeping the desired temperature for a long period [26–28], improving energy conservation and saving electric energy [29]. Ramakrishnan [25] studied expanded perlite coated with silicone as a support for paraffin impregnation. The modified expanded perlite containing paraffin up to 50 wt% showed a good leakage prevention during phase change process and the thermal energy storage and reliability of panel incorporating paraffin/modified expand perlite was significantly improved. The addition of PCM paraffin/diatomite composite can improve the overall thermal properties such heat capacity and thermal conductivity [24]. The presence of paraffin in cementitious composite can also decrease the thermal conductivity with some effects on the mechanical properties. The maximum reductions in compressive and flexural strengths with incorporation of PCM composite are almost 50% [2].

Generally, the main factors affecting the targeted properties of cementitious composite depend on the mixtures such as W/C ratio, S/C ratio and aggregate content [30–33]. It is a daunting task to investigate all parameters in a particular experiment. Therefore, a suitable design of experiment method (DOE) can take into account some of the factors. Taguchi experiment design is one of the most famous methods for designing the optimum concrete proportions with minimum number of experiments. This approach can determine the effective parameters on the properties of concrete [30,31]. Taguchi's method has been successfully used to develop the modern construction material such as LWC [32,33]. In comparison with ordinary concrete, LWC shows some excellent properties such as low density, high specific strength and great thermal insulation. LWC is used to reduce the unit weight and dead weight of a structure by replacing the conventional aggregate with lightweight aggregate. The application of LWC in construction industry offers many advantages i.e. high strength/weight ratio, saving in dead load for structural design and foundation, superior heat and sound insulation characteristics, low thermal conductivity and good durability [32,34,35].

Currently, there is no information about the optimization of mix proportion of LWC integrated with PCMPC. Therefore, this research aims to use the PCMPC as fine aggregate to produce LWC. The mix proportions of LWC are designed by Taguchi's method. The thermal energy storage and thermal reliability of PCMPC are studied. The heat storage coefficient, thermal conductivity, and physical and mechanical properties of the LWC are also studied.

2. Materials and methods

2.1. Materials

Commercially available Ordinary Portland cement (OPC) and paraffin from Chemipan Co. Ltd., Thailand were the materials used. Recycled concrete block was supplied from Concrete Precision Unique Co. Ltd., Thailand. The concrete block was crushed to fine particles. The fine particle was then passed sieve No. 8 and retained on sieve No. 16 to obtain a single size fine aggregate of 1.19–2.38 mm. The PCMPC used in this work was prepared by impregnation method. The melted paraffin was impregnated into recycled concrete block by continuous mixing with overhead stirrer at 120 rpm for 30 min with a vacuum pressure of 80 kPa [23]. The 25 wt% paraffin impregnation level was optimum and was thus used to prepare fine aggregate for LWC. The physical properties of materials are concluded in Table 1.

2.2. Mix proportions

The four factors viz., W/C ratio, water content, PCMPC content and S/C ratio with three level each were used for the optimization of LWC as summarized in Table 2.

The mix proportions of LWCs were derived from L_9 orthogonal array as shown in Tables 3 and 4. For mixing of LWC, cement and sand were first mixed for 1.5 min to obtain homogenous mixture. Then, water was added and the mixing was done for 1.5 min. In the final step, PCMPC was added and mixed for another 1.5 min. The fresh mixtures were cast in steel molds. The samples were covered with damped cloth and plastic sheet and left in a controlled 25 °C room for 24 h before demoulding. The obtained samples were wrapped with cling film and kept in a controlled 25 °C room. At the age of 28 days, the samples were tested for density, compressive strength, thermal conductivity, heat storage and thermal performance under heating and cooling systems.

2.3. Characterization of thermal and chemical stability of PCMPC

The thermal cycling test consisted of 150 melting and freezing cycles using thermal cycler (Biometra T1 Thermocycler, Whatman Biometra, UK). The sample was placed in plastic tube connected to thermocouple. Water at a constant temperature of 80 °C was circulated for melting process through the tube. After that, the sample was immediately subjected to solidification process by circulating water at a constant temperature of 5 °C. The thermal and chemical stability of sample after thermal cycling were investigated by Differential scanning calorimeter (DSC) and Fourier transform infrared (FTIR). The temperature of melting and freezing and latent heat were analyzed by DSC (Perkin Elmer Diamond) at a heating rate of 5 °C/min under nitrogen atmosphere. The chemical structures of sample were determined using Bruker Tensor 27 spectrometer in the range of 4000–650 cm^{-1}. All spectra were recorded as a function of time with 64 scans at a resolution of 4 cm^{-1}.

Table 1
Physical properties of materials.

Properties	Materials				
	Recycled concrete bock	Paraffin	PCMPC	Sand	OPC
Specific gravity	–	–	–	2.61	3.15
Particle size (mm)	1.19–2.38	–	1.19–2.38	–	
Fineness modulus		–	–	2.65	–
Density (kg/m^3)	635	910	764	1360	–
Water absorption (%)	53.8	–	20.3	1.17	–

Table 2
Factors and levels of mix proportions.

Factors	Levels		
	1	2	3
Water/cement ratio: W/C	0.40	0.45	0.50
Water: W (cm^3)	68.55	73.55	78.55
PCMPC content (wt% of total mass)	4	7	10
Sand/cement ratio: S/C	0.16	0.26	0.36

Table 3
L_9 orthogonal array for mix proportions of LWCs.

Mixture	Factors			
	W/C	W	PCMPC content	S/C
1	1	1	1	1
2	1	2	2	2
3	1	3	3	3
4	2	1	3	3
5	2	2	2	1
6	2	3	1	2
7	3	1	3	2
8	3	2	1	3
9	3	3	2	1

2.4. Characterization of LWCs containing PCMPC

The compressive strength and density of specimens at the age of 28 days were measured on cube specimen (5 cm × 5 cm × 5 cm). Density values of cube specimens were determined following ASTM C 138 [36]. After the density determination, the cube specimens were tested to determine the compressive strength as described in ASTM C 109 [37]. The reported results are the average values from three samples.

The fracture surfaces of samples were examined using a scanning electron microscope (SEM) (Hitachi model S-3000N) at an acceleration voltage of 20 kV. All samples were cut to 3 mm and coated with gold using an ion sputtering device.

Thermal conductivity tests were measured using the cube specimens at the age of 28 days following ASTM D 5334 [38]. The thermal conductivity values were determined using surface probe ISOMET Model 2114, Applied Precision Ltd with the measuring range of 0.3–2.0 W/m·K. The averaged values from three samples were reported.

Heat storage coefficient of LWC was the parameter used to indicate the heat storage/release ability and surface temperature variation resist ability of materials under the heating effect of periodic fluctuation. The high value of heat storage coefficient attributed to the small variation in temperature at surface of material. The heat storage of LWC containing form stable PF/RB composite PCM can be calculated following the literatures [12,39] as shown in Eq (1–3).

$$\Delta H_{LWC-PCMPB} = \Delta H_{Paraffin} \cdot \beta \quad (1)$$

$$C = (\Delta H_{LWC-PCMPB})/(T_E - T_S) \quad (2)$$

$$S = 0.51\sqrt{\lambda C \rho} \quad (3)$$

where $\Delta H_{LWC\text{-}PCMPC}$ is the latent heat of LWC containing PCMPC (kJ/kg), $\Delta H_{Paraffin}$ is the latent heat paraffin (kJ/kg) and β is the mass fraction of PCMPC in LWC. C is the specific heat (kJ/kg·K), ρ is the density (kg/m^3), T_S is the onset temperature and T_E is the end temperature of phase change process (°C), S is the heat storage coefficient (W/m^2·K) for variation of temperature in 24 h, and λ is the thermal conductivity (W/m·K).

The LWC containing PCMPC and control concretes were tested for the thermal performance using the adapted experimental procedure [2]. At the age of 28 days, the prepared 5 mm × 5 mm × 5 mm specimens were tested for the thermal performance using thermal cycle setup as depicted in Fig. 1. In the first step, the specimens were exposed to heat radiation from a 275 W infrared lamp for 150 min. The temperature condition in the thermal performance test was designed to be higher than 50 °C to ensure the phase change performance. The temperature in this test was monitored using temperature data logger and ranged between 30 and 67 °C. After that, they were cooled down at room temperature of 25 °C.

3. Results and discussion

3.1. Thermal and chemical stability of PCMPC

The PCMPC should be stable in terms of thermal and chemical properties over a large number of thermal cycling processes. The

Table 4
Mix proportion of LWCs containing PCMPC.

Mixture	PCMPC content (kg/m^3)	Water (kg/m^3)	Sand (kg/m^3)	Cement (kg/m^3)
1	72.4	443.6	178.1	1113.4
2	123.1	443.6	275.3	1058.7
3	162.1	473.7	331.6	921.0
4	119.6	413.4	339.8	943.8
5	162.8	443.6	161.8	1011.2
6	71.1	473.7	270.1	1039.3
7	154.9	413.4	228.8	880.0
8	68.0	443.6	328.7	931.1
9	109.8	473.7	151.2	944.9

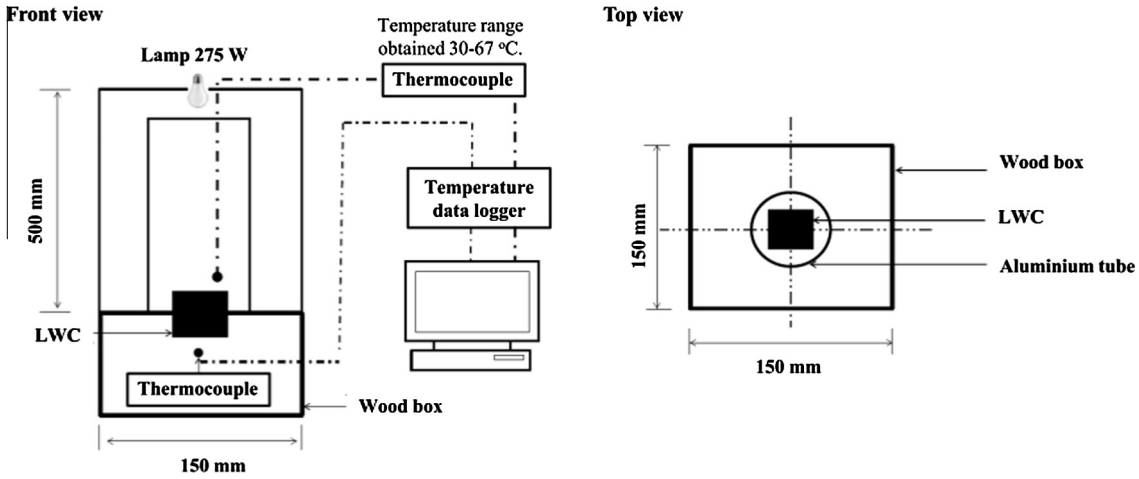

Fig. 1. Schematic diagram of heating/cooling thermal cycle test setup.

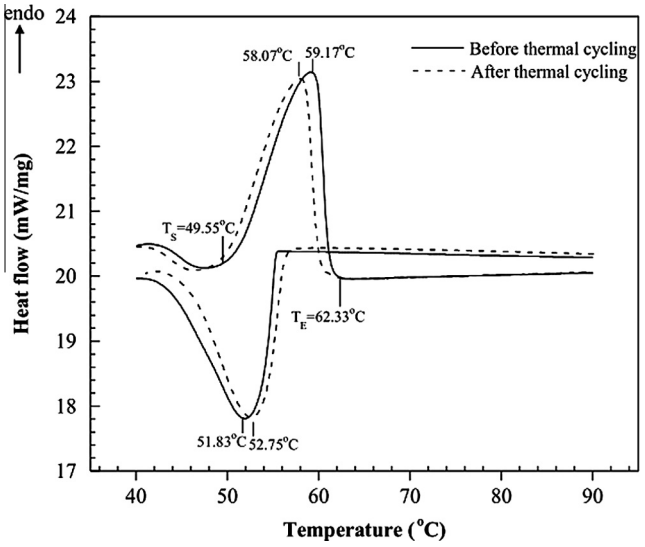

Fig. 2. DSC thermogram of PCMPC before and after thermal cycling.

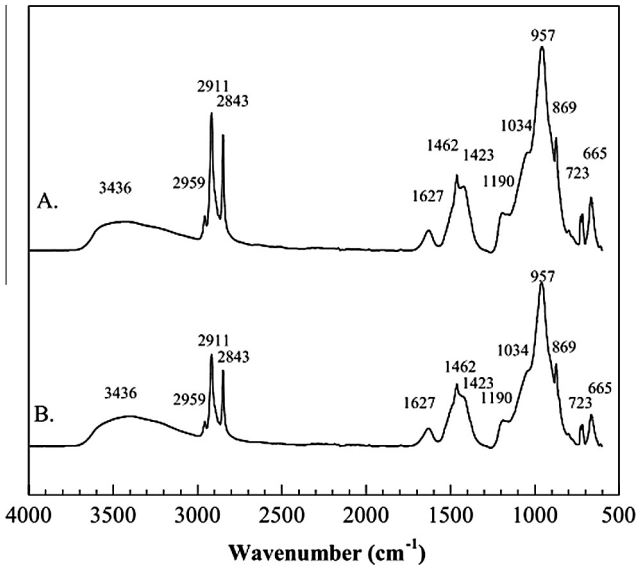

Fig. 3. FT-IR spectrum of PCMPC: before thermal cycling (A) and after thermal cycling (B).

thermal properties of PCMPC after 150 cycles is shown Fig. 2 and summarized in Table 5. According to Fig. 2, when heat flow value was 20 W/g, phase change did not occur. The melting and freezing temperatures were 59.87 °C and 51.83 °C, respectively. The latent heat of melting and freezing were 30.88 kJ/kg and 28.26 kJ/kg. After 150 cycles, the melting temperature reduced by 1.10 °C and the freezing temperature increased by 0.92 °C. The latent heat values of melting and freezing reduced by 2.61 kJ/kg and 1.60 kJ/kg, respectively. These little changes were in line with the previously reported results [12,40]. This indicated that the PCMPC had good thermal reliability with respect to the phase transition.

The chemical stability of PCMPC before and after thermal cycling was investigated using ATR-FTIR analysis. As shown in Fig. 3(A), the FTIR spectra of PCMPC before thermal cycling consisted of the characteristic bands of paraffin and recycled concrete block. The peaks at 2959 and 2843 cm^{-1} of paraffin were attributed to vibration stretching of C–H. The peaks at 1462 and 723 cm^{-1} were assigned to bending vibration and rocking vibration stretching, respectively [10]. The main absorption bands of recycled concrete block were associated with OH (water in concrete) at 3552 cm^{-1} and 1627 cm^{-1}, CO_3^{2-} at 1423 cm^{-1}, S–O at 1190 cm^{-1} and Si–O at 957 cm^{-1} [23]. Fig. 3(B) depicted the FTIR spectra of sample after thermal cycling. The shape and position of peak before and after thermal cycling were in the same range. It can thus be concluded that the PCMPC was chemically stable after 150 thermal cycles.

Table 5
Characterization of PCMPC before and after thermal cycling.

Test	Melting		Freezing	
	Temperature (°C)	Latent heat (kJ/kg)	Temperature (°C)	Latent heat (kJ/kg)
Before thermal cycling	59.17	30.88	51.83	28.26
After thermal cycling (150 cycles)	58.07	28.27	52.75	26.66

3.2. Characterization of hydrated cement containing PCMPC

The FTIR spectra of hydrated cement mix with 7%wt PCMPC are shown in Fig. 4. The characteristic adsorption peaks of hydrated cement at 948 cm^{-1} and 1111 cm^{-1} were assigned to Si-O and S-O. The C-O was observed at 1410 cm^{-1} whereas the absorption bands at 1655, 3399 and 3637 cm^{-1} were assigned to O–H [34,41]. Fig. 4(A) and (B) show the characteristic peaks of hydrated cement mixed with PCMPC at the age of one day and 28 days, respectively. There was no new peak and no shift in the absorption bands of LWC containing PCMPC when compared to the FTIR spectra of hydrated cement. This result indicated that there was no chemical interaction between cement and PCMPC.

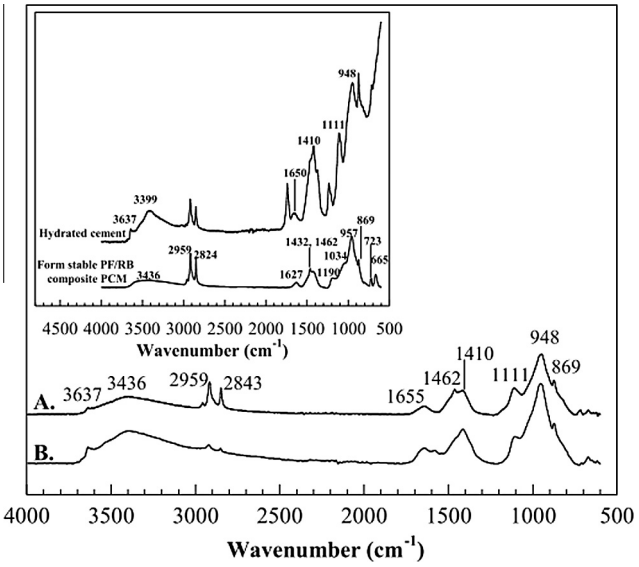

Fig. 4. FT-IR spectrums of LWC containing PCMPC at 1 day (A) and at 28 days (B).

Table 6
Density and compressive strength of LWC containing form stable PF/RB composite PCM.

Mixes	Density (kg/m^3)	Compressive strength (MPa)	Classification of LWC
1	1867	52	Mixes 1–3: Normal concrete
2	1879	53	
3	1906	41	
4	1803	40	Mixes 4–9: Lightweight concrete for structure (ASTM C330/C330M-14)
5	1779	47	
6	1774	45	
7	1717	35	
8	1812	38	
9	1711	33	

3.3. Density and compressive strength of LWC containing PCMPC

Density is one of the important parameters that control the overall physical properties of LWC. Table 6 shows the densities of LWC range of 1711–1906 kg/m^3 which were slightly lighter than those of normal cement mortars of around 1800–2000 kg/m^3. The reduction in dead weight of building or structure helps decrease the cross-section area of steel reinforced column, beam and foundation. It also helps reduce the risk of earthquake damages [34,42]. Fig. 5 shows the optimal mix proportion for minimum density which was at the W/C ratio of 0.50, water content of 73.55 cm^3, 7 wt% PCMPC and S/C ratio of 0.16.

A multi-linear regression model was developed to predict the density of LWCs containing PCMPC as shown in Eq. (4):

$$\text{Density} = 2410.8 - 1373.2X_1 - 0.39X_2 - 523.01X_3 + 305.19X_4 \quad (4)$$

where X_1 is the W/C ratio, X_2 is the water content (cm^3), X_3 is the PCMPC content (wt%) and X_4 is the S/C ratio.

The results of ANOVA analysis are summarized in Table 7. W/C ratio was the main factor affecting the density with the highest percentage contribution of 78.55%. The other factors such as S/C ratio, water content and PCMPC content played less important role. The increasing W/C ratio increased the porosity of concrete. During hydration of cement, excess water acted as free water in the cement structure and form large capillary pores [43]. The increase of porosity resulted in the decreasing of density [44].

The compressive strengths of LWCs containing PCMPC were in the range of 33–53 MPa, as depicted in Fig. 6 and summarized in Table 6. The compressive strength and density values of mixes 4–9 met the requirement of a lightweight concrete structure with density of 1440–1840 kg/m^3 and compressive strength higher than 17.0 MPa according to ASTM C330/C330M-14 [45]. It should be noted here that the standard also requires the minimum splitting tensile strength. Furthermore, the compressive strengths of LWC containing PCMPC were significantly higher than those containing other form stable composite PCM and macro encapsulated

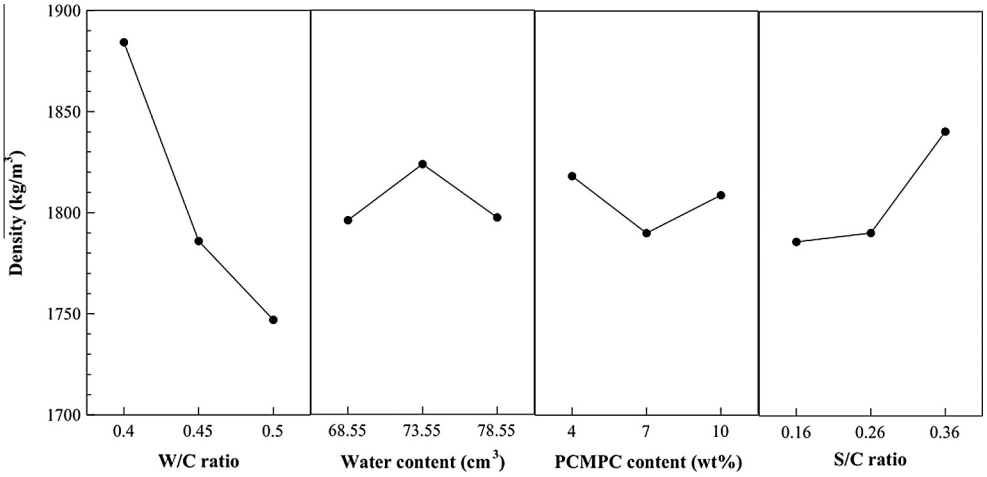

Fig. 5. Effect of factors on density of LWC containing PCMPC.

Table 7
Anova analysis results for properties of LWC containing PCMPC.

Properties		Factors			
		W/C ratio	Water content	PCMPC	S/C ratio
Density	DOF*	2	2	2	2
	SS**	30046.79	1471.73	1232.38	5499.56
	V***	10015.6	490.58	410.79	1833.18
	Contribution (%)	78.55	3.85	3.22	14.83
Compressive strength	DOF*	2	2	2	2
	SS**	258.33	57.79	76.43	44.88
	V***	86.11	19.26	25.48	14.96
	Contribution (%)	59.06	13.21	17.47	10.26
Heat storage coefficient	DOF*	2	2	2	2
	SS**	1.28	0.11	9.83	0.20
	V***	0.43	0.04	3.28	0.07
	Contribution (%)	11.23	0.97	86.01	1.79

DOF*: Degree of freedom.
SS**: Sum of square.
V***: Variance.

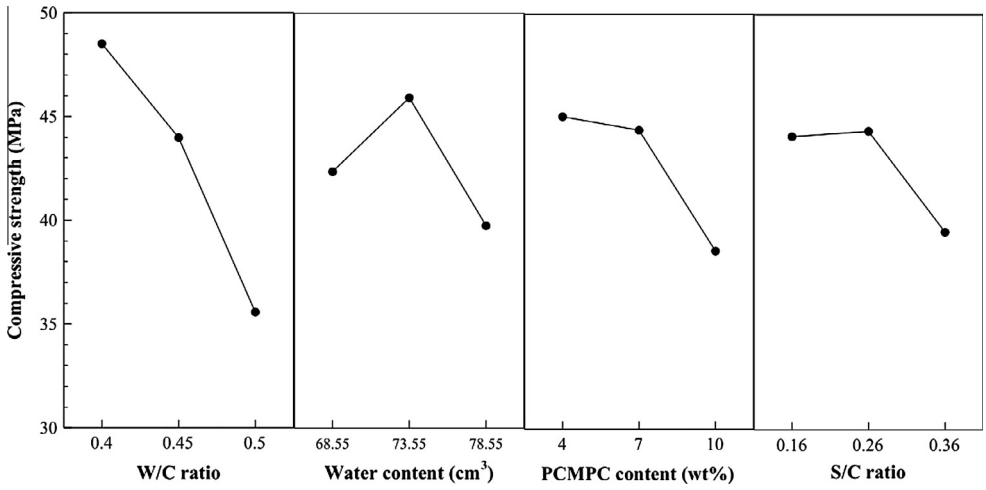

Fig. 6. Effect of factors on compressive strength of LWC containing PCMPC.

PCM/lightweight aggregate e.g. paraffin/diatomite composite PCM (25.7–50.1 MPa) [2], paraffin/lightweight aggregates composite PCM (23.6–30 MPa) [46], paraffin/expanded perlite (11–24 MPa) [7], n-octadecane/expanded graphite (10.5–23.7 MPa) [47], paraffin expanded/vermiculite (18.1–21.9 MPa) [15], macro encapsulated paraffin/lightweight aggregate (16–17 MPa) [48] and macro encapsulated lauryl alcohol–lightweight aggregate (30.0–32.0 MPa) [49], as shown in Table 8 It should also be noted here that the compressive strength of LWC containing PCMPC in this experiment was comparable to the macro encapsulated PCM integrated with normal weight aggregate (33.3–53.1 MPa) [50].

Based on the ANOVA analysis results as shown in Table 7, W/C ratio was the most significant parameter affecting the compressive strength of LWC with 59.06% contribution. The compressive strength decreased with increasing W/C ratio. The hydration reaction between water and cement directly affected the compressive strength of concrete [51]. The high W/C ratio caused voids and pores in concrete structure and resulted in low compressive strength [52]. The results are in good agreement with the density results as shown in Fig. 5. The second most significant parameter was the PCMPC content with 17.47% contribution. The compressive strength of LWC decreased

Table 8
Comparison properties of concrete incorporated PCMPC.

Materials	Content (%)	Properties of concrete	
		Density (kg/m^3)	Compressive Strength (MPa)
Paraffin/diatomite composite PCM [2]	0–30 (wt% cement)	–	25.7–50.1
Paraffin/lightweight aggregates composite PCM [46]	0–100 (wt% composite)	1570–1780	23.6–30.0
Paraffin/expanded perlite [7]	0–30 (wt% cement)	–	11–24
n-octadecane/expanded graphite [47]	0–2.5 (wt% concrete)	–	10.5–23.7
Paraffin expanded/vermiculite [15]	50–100 (wt% sand)	–	18.1–21.9
Macro encapsulated paraffin/lightweight aggregate [48]	50–100 (wt% composite)	–	16–17
Macro encapsulated lauryl alcohol–lightweight aggregate [49]	16 (wt% composite)	–	30–32
Macro encapsulated PCM integrated with normal weight aggregate [50]	17–50 (vol% normal weight aggregate)	–	33.3–53.1
PCMPC (This study)	4–10 (wt% concrete)	1711–1906	33–53

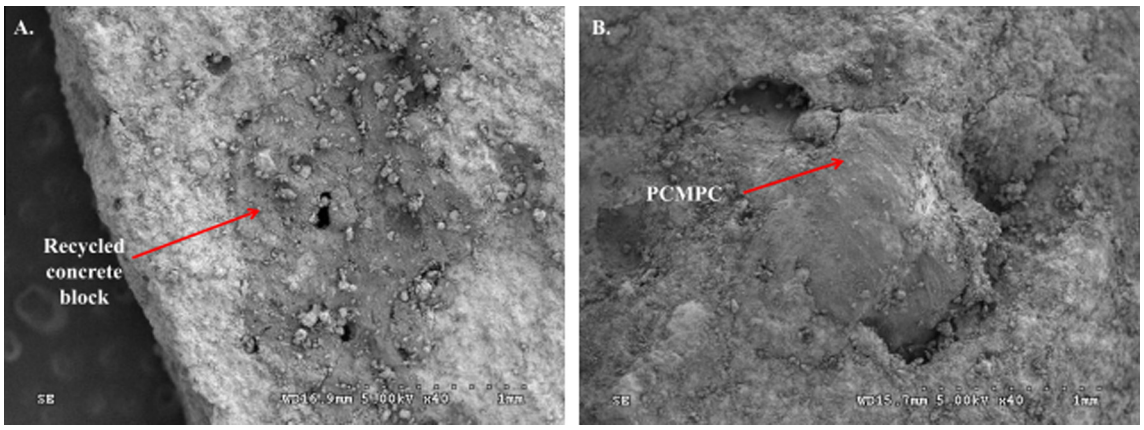

Fig. 7. Micrographs taken from fracture surface of the samples by SEM: (A.) LWC containing recycled concrete block and (B.) LWC containing PCMPC.

with increasing PCMPC content. Similar observation was also reported in cement mortar containing form stable paraffin/expanded perlite [7]. This phenomenon could be explained by the low stiffness of form stable PCM compared to those of sand particle and cement paste. Therefore, the incorporation of low stiffness material adversely affected the mechanical properties of LWC. Moreover, the poor interfacial between PCM and cement paste can result in low compressive strength due to the lower load transfer mechanism [49]. Fig. 7 shows the fracture surfaces of LWC containing PCMPB and control sample without paraffin. The control sample presented the tight interfacial between recycled block concrete and cement paste which indicated a good interfacial bond whereas the interfacial between PCMRB and cement paste showed noticeable gap indicating a decrease in adhesion.

With regards to water content and S/C ratio, these factors had small effect on compressive strength compared to the others. The optimum conditions for maximum compressive strength were obtained with W/C ratio of 0.40, 73.55 cm^3 water content, 4 wt% PCMPC content and S/C ratio of 0.26. The relationship between compressive strength and mix proportion of LWC is shown in Eq. (5).

$$\text{Compressive strength} = 138.33 - 129.3X_1 - 0.36555X_2 - 104.22X_3 - 12.595X_4 \quad (5)$$

where, X_1 is the W/C ratio, X_2 is the water content (cm^3), X_3 is the PCMPC (wt%) and X_4 is the S/C ratio.

3.4. Heat storage of LWC containing PCMPC

The heat storage values of LWCs containing PCMPC were calculated following Eqs. (1–3). The latent heat of LWC containing PCMPC and temperature of phase change process obtained from DSC thermogram are shown in Fig. 2. The parameters for heat storage calculation are summarized in Table 9. The thermal conductivity values of LWCs containing PCMPC were in range of 0.59–0.86 W/m·K. These values were lower than those concretes containing other form stable PCM composites e.g. paraffin/diatomite composite PCM (1.32–5.43 W/m·K) [2] and n-octadecane/expanded graphite (1.84–2.19 W/m·K) [47]. The results also showed that the thermal conductivity of mix 9 was the lowest which was only 50.83% of normal concrete (1.2 W/m·K) [53]. This result indicated that the LWC containing PCMPC provided good thermal insulation. Fig. 8 shows the calculated heat storage coefficient of LWCs. The optimal conditions for maximum heat storage were obtained with W/C ratio of 0.40, 68.55 cm^3 water content, 10 wt% PCMPC content and S/C ratio of 0.36. The relationship between heat storage and mix proportions is shown in Eq. (6).

$$\text{Heat storage coefficient} = 7.87 - 9.15X_1 - 0.03X_2 - 45.76X_3 + 2.79X_4 \quad (6)$$

where, X_1 is the W/C ratio, X_2 is the water content (cm^3), X_3 is the PCMPC content (wt%) and X_4 is the S/C ratio.

As shown in Table 7, the results of ANOVA analysis showed that the PCMPC was the major factor affecting the heat storage with 86.01% contribution. The heat storage value significantly increased with increasing PCMPC content. This result implied that the addition of PCMPC improved the surface temperature variation resistibility of LWC under the heating effect of periodic fluctuation [39].

3.5. Thermal performances of LWC containing PCMPC

The thermal performance was determined by monitoring the temperature variation at the center of a small wood room model. Fig. 9 shows the temperature variation curves of air inside the room with top panel of LWC prepared with mix 9. The control

Table 9
Heat storage of LWC containing PCMPC.

Mixtures	Thermal conductivity (W/m·K)	Thermal properties		
		Latent heat of LWC containing PCMPC (kJ/kg)	Specific heat (kJ/kg·K)	Heat storage coefficient ($W/m^2·K$)
1	0.861	1.64	0.13	7.32
2	0.722	2.61	0.20	8.49
3	0.769	3.54	0.28	10.27
4	0.759	2.63	0.21	8.56
5	0.643	3.76	0.29	9.36
6	0.764	1.59	0.12	6.63
7	0.639	3.78	0.30	9.19
8	0.723	1.60	0.13	6.53
9	0.592	2.81	0.22	7.61

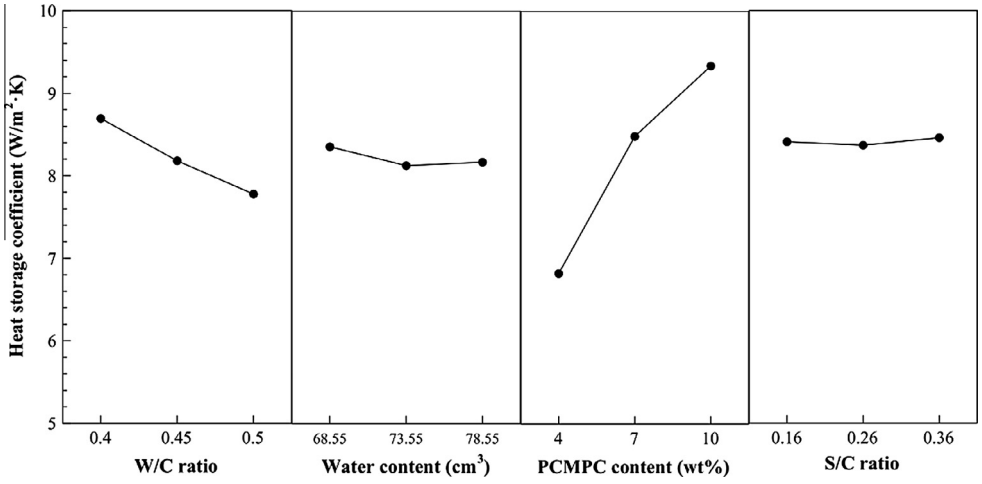

Fig. 8. Effect of factors on heat storage coefficient of LWC containing PCMPC.

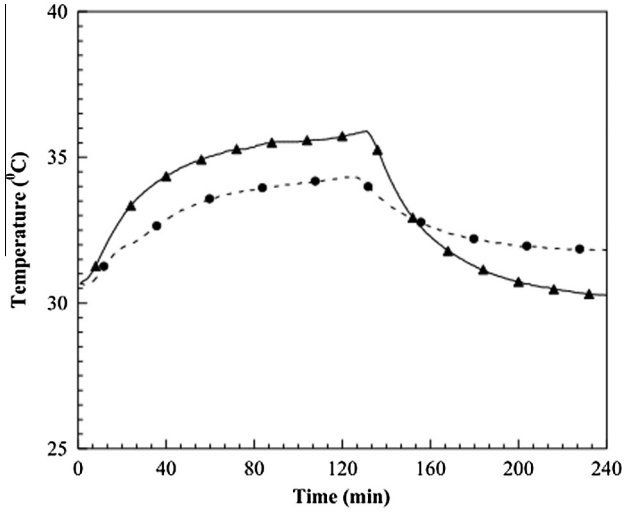

Fig. 9. Thermal Performance Comparison Between LWC Containing PCMPC (--●--) And Control Sample (--▲--).

sample was without paraffin. The maximum temperatures of air were 36 °C for control sample and 34.1 °C for LWC containing PCMPC. The temperature difference was 1.9 °C. This observation indicated that the LWC containing PCMPC could reduce the indoor temperature during the phase change process of paraffin. This process rendered the exchange of heat from environment to LWC. As shown in Fig. 9, the specimens were cooled down after 2 h. The temperatures were reduced by 5.8 °C and 2.3 °C for control sample and LWC containing PCMPC, respectively. The addition of PCMPC could thus decrease the indoor temperature fluctuation and reduce energy consumption by shifting the loads away from peak periods [7,24].

4. Conclusions

The phase change material paraffin/recycled concrete block composites (PCMPC) were prepared and investigated. Test results showed that the PCMPC was thermally and chemically stable after 150 cycles of thermal cycling process. For the application of PCMPC in lightweight concrete (LWC), Taguchi method and ANOVA analysis were employed to determine the effective parameter and best mix proportion considering W/C ratio, water content, PCMPC content and S/C ratio. The experimental results showed that W/C ratio was the most significant factor influencing the density and compressive strength of LWC. For the thermal properties viz., thermal conductivity, latent heat, specific heat and heat storage coefficient of LWC, the PCMPC content was the major factor contributing to the enhancement of heat storage and thermal performance. The incorporation of PCMPC significantly improved the thermal performance of LWC compared to that of the control sample. Furthermore, the mixes with high W/C of 0.45 and 0.50 complied with the requirements of ASTM C330 for high strength lightweight structural concrete. The use of PCMPC could thus reduce the dead load of the structure, decrease the indoor temperature fluctuation and reduce the associated energy consumption.

Acknowledgment

This work was financial supported by the graduate school, Khon Kaen University, Thailand. The authors also would like to acknowledge the support of Thailand Research Fund (TRF) under the TRF Senior Research Scholar, Grant No. RTA 5780004 and the Applied Engineering for Important Crops of the North East Research Group, Khon Kaen University.

References

[1] B. Xu, Z. Li, Paraffin/diatomite/multi-wall carbon nanotubes composite phase change material tailor-made for thermal energy storage cement-based composites, Energy 72 (2014) 371–379.
[2] B. Xu, Z. Li, Paraffin/diatomite composite phase change material incorporated cement-based composite for thermal energy storage, Appl. Energy 105 (2013) 229–237.
[3] M. Li, H. Kao, Z. Wu, J. Tan, Study on preparation and thermal property of binary fatty acid and the binary fatty acids/diatomite composite phase change materials, Appl. Energy 88 (5) (2011) 1606–1612.
[4] A. Jayalath, R.S. Nicolas, M. Sofi, R. Shanks, T. Ngo, L. Aye, P. Mendis, Properties of cementitious mortar and concrete containing micro-encapsulated phase change materials, Constr. Build. Mater. 120 (2016) 408–417.
[5] S.G. Jeong, S.J. Chang, S. Wi, Y. Kang, J.H. Lim, J.D. Chang, S. Kim, Energy efficient concrete with n-octadecane/xGnP SSPCM for energy conservation in infrastructure, Constr. Build. Mater. 106 (2016) 543–549.
[6] Q. Zhang, K. Cui, J. Feng, J. Fan, L. Li, L. Wu, Q. Huang, Investigation on the recovery performance of olefin block copolymer/hexadecane form stable phase change materials with shape memory properties, Solar Energy Mater. Solar Cells 132 (2015) 632–639.
[7] D. Sun, L. Wang, Utilization of paraffin/expanded perlite materials to improve mechanical and thermal properties of cement mortar, Constr. Build. Mater. 101 (2015) 791–796.
[8] J.L. Zeng, S.H. Zheng, S.B. Yu, F.R. Zhu, J. Gan, L. Zhu, Z.L. Xiao, X.Y. Zhu, Z. Zhu, L. X. Sun, Z. Cao, Preparation and thermal properties of palmitic acid/polyaniline/exfoliated graphite nanoplatelets form-stable phase change materials, Appl. Energy 115 (2014) 603–609.

[9] O. Chung, S.G. Jeong, S. Kim, Preparation of energy efficient paraffinic PCMs/expanded vermiculite and perlite composites for energy saving in buildings, Solar Energy Mater. Solar Cells 137 (2015) 107–112.
[10] Z. Sun, Y. Zhang, S. Zheng, Y. Park, R.L. Frost, Preparation and thermal energy storage properties of paraffin/calcined diatomite composites as form-stable phase change materials, Thermochim. Acta 558 (2013) 16–21.
[11] Y. Kang, S.G. Jeong, S. Wi, S. Kim, Energy efficient Bio-based PCM with silica fume composites to apply in concrete for energy saving in buildings, Solar Energy Mater. Solar Cells 143 (2015) 430–434.
[12] A. Sarı, A. Biçer, Preparation and thermal energy storage properties of building material-based composites as novel form-stable PCMs, Energy Build. 51 (2012) 73–83.
[13] R. Shadnia, L. Zhang, P. Li, Experimental study of geopolymer mortar with incorporated PCM, Constr. Build. Mater. 84 (2015) 95–102.
[14] A. Figueiredo, J. Lapa, R. Vicente, C. Cardoso, Mechanical and thermal characterization of concrete with incorporation of microencapsulated PCM for applications in thermally activated slabs, Constr. Build. Mater. 112 (2016) 639–647.
[15] B. Xu, H. Ma, Z. Lu, Z. Li, Paraffin/expanded vermiculite composite phase change material as aggregate for developing lightweight thermal energy storage cement-based composites, Appl. Energy 160 (2015) 358–367.
[16] Z. Sun, W. Kong, S. Zheng, R.L. Frost, Study on preparation and thermal energy storage properties of binary paraffin blends/opal shape-stabilized phase change materials, Solar Energy Mater. Solar Cells 117 (2013) 400–407.
[17] D. Yang, S. Shi, L. Xiong, H. Guo, H. Zhang, X. Chen, C. Wang, X. Chen, Paraffin/Palygorskite composite phase change materials for thermal energy storage, Solar Energy Mater. Solar Cells 144 (2016) 228–234.
[18] A. Karaipekli, A. Sarı, Preparation and characterization of fatty acid ester/building material composites for thermal energy storage in buildings, Energy Build. 43 (2011) 1952–1959.
[19] Q.J. Li, G.Z. Li, C.C. Jiang, Study on paraffin/expanded perlite composite phase change energy-storage materials, Appl. Mech. Mater. 237 (2013) 181–184.
[20] S. Karaman, A. Karaipekli, A. Sarı, A. Biçer, Polyethylene glycol (PEG)/diatomite composite as a novel form-stable phase change material for thermal energy storage, Solar Energy Mater. Solar Cells 95 (2011) 1647–1653.
[21] A. Sarı, A. Karaipekli, Fatty acid esters-based composite phase change materials for thermal energy storage in buildings, Appl. Therm. Eng. 37 (2012) 208–216.
[22] D. Feldman, D. Banu, D.W. Hawes, Development and application of organic phase change mixtures in thermal storage gypsum wallboard, Solar Energy Mater. Solar Cells 36 (1995) 147–157.
[23] P. Suttaphakdee, U. Pongsa, P. Kasemsiri, P. Posi, N. Lorwanishpaisarn, A. Tasai, N. Dulsang, P. Chindaprasirt, Thermal energy storage properties of form-stable paraffin/recycle block concrete composite phase change material, J. Eng. Sci. Technol. (2017).
[24] B. Xu, Z. Li, Performance of novel thermal energy storage engineered cementitious composites incorporating a paraffin/diatomite composite phase change material, Appl. Energy 121 (2014) 114–122.
[25] S. Ramakrishnan, J. Sanjayan, X. Wang, M. Alam, J. Wilson, A novel paraffin/expanded perlite composite phase change material for prevention of PCM leakage in cementitious composites, Appl. Energy 157 (2015) 85–94.
[26] A. Pasupathy, R. Velraj, R.V. Seeniraj, Phase change material-based building architecture for thermal management in residential and commercial establishments, Renewable Sustainable Energy Rev. 12 (2008) 39–64.
[27] A. Karaipekli, A. Sarı, Development and thermal performance of pumice/organic PCM/gypsum composite plasters for thermal energy storage in buildings, Solar Energy Mater. Solar Cells 149 (2016) 19–28.
[28] S.G. Jeong, S.J. Chang, S. We, S. Kim, Energy efficient thermal storage montmorillonite with phase change material containing exfoliated graphite nanoplatelets, Solar Energy Mater. Solar Cells 139 (2015) 65–70.
[29] A. Sarı, A. Biçer, Thermal energy storage properties and thermal reliability of some fatty acid esters/building material composites as novel form-stable PCMs, Solar Energy Mater. Solar Cells 101 (2012) 114–122.
[30] M.J. Khalaj, A. Khoshakhlagh, S. Bahri, M. Khoeini, M. Nazerfakhari, Split tensile strength of slag-based geopolymer composites reinforced with steel fibers: Application of Taguchi method in evaluating the effect of production parameters and their optimum condition, Ceram. Int. 41 (2015) 10697–10701.
[31] A. Nazari, H. Khanmohammadi, M. Amini, H. Hajiallahyari, A. Rahimi, Production geopolymers by Portland cement: Designing the main parameters' effects on compressive strength by Taguchi method, Mater. Des. 41 (2012) 43–49.
[32] N. Dulsang, P. Chindaprasirt, P. Posi, S. Hiziroglu, P. Sutaphakdee, R. Dangsawat, P. Kasemsiri, Optimizing mix proportion of lightweight concrete containing plastic waste by taguchi method, Adv. Mat. Res. 931–932 (2014) 431–435.
[33] Y. Xu, L. Jiang, J. Xu, Y. Li, Mechanical properties of expanded polystyrene lightweight aggregate concrete and brick, Constr. Build. Mater. 27 (2012) 32–38.
[34] N. Dulsang, P. Kasemsiri, P. Posi, S. Hiziroglu, P. Chindaprasirt, Characterization of an environment friendly lightweight concrete containing ethyl vinyl acetate waste, Mater. Des. 96 (2016) 350–356.
[35] Y. Xu, J. Xu, L. Jiang, H. Chu, Y. Li, Prediction of compressive strength and elastic modulus of expanded polystyrene lightweight concrete, Mag. Concrete Res. 67 (2015) 954–962.
[36] ASTM C138. Standard Test Method for Density (Unit Weight), Yield, and Air Content (Gravimetric) of Concrete, vol. 04.02. Annual Book of ASTM Standards, 2006.
[37] ASTM C109. Standard Test Method for Compressive Strength of Hydraulic Cement Mortars (Using 2-in. or [50-mm] Cube Specimens), 04.01. Annual Book of ASTM Standards, 2012.
[38] ASTM D5334. Standard Test Method for Determination of ThermalConductivity of Soil and Soft Rock by Thermal Needle Probe Procedure, vol 04.08. Annual Book of ASTM Standards, 2013.
[39] M. Li, Z. Wu, J. Tan, Heat storage properties of the cement mortar incorporated with composite phase change material, Appl. Energy 103 (2013) 393–399.
[40] S. Xu, L. Zou, X. Ling, Y. Wei, S. Zhang, Preparation and thermal reliability of methyl palmitate/methyl stearate mixture as a novel composite phase change material, Energy Build. 68 (2014) 372–375.
[41] C. Hall, Water sorptivity of mortars and concretes: A review, Mag. Concrete Res. 41 (1989) 51–61.
[42] S. Akçaözoğlu, C.D. Atiş, K. Akçaözoğlu, An investigation on the use of shredded waste PET bottles as aggregate in lightweight concrete, Waste Manage. 30 (2010) 285–290.
[43] X. Chen, S. Wu, Influence of water-to-cement ratio and curing period on pore structure of cement mortar, Constr. Build. Mater. 38 (2013) 804–812.
[44] E.P. Kearsley, P.J. Wainwright, Porosity and permeability of foamed concrete, Cement Concrete Res. 31 (2001) 805–812.
[45] ASTM C330/C330M–14, Standard specification for lightweight aggregates for structural concrete, vol. 04.02, Annual Book of ASTM Standards, 2014.
[46] P. Sukontasukkul, E. Intawong, P. Preemanoch, P. Chindaprasirt, Use of paraffin impregnated lightweight aggregates to improve thermal properties of concrete panels, Mater. Struct. 49 (2015) 1–11.
[47] Z. Zhang, G. Shi, S. Wang, X. Fang, X. Liu, Thermal energy storage cement mortar containing n-octadecane/expanded graphite composite phase change material, Renew. Energy 50 (2013) 670–675.
[48] S.A. Memon, H.Z. Cui, H. Zhang, F. Xing, Utilization of macro encapsulated phase change materials for the development of thermal energy storage and structural lightweight aggregate concrete, Appl. Energy 139 (2015) 43–55.
[49] H. Cui, S.A. Memon, R. Liu, Development, mechanical properties and numerical simulation of macro encapsulated thermal energy storage concrete, Energy Build. 96 (2015) 162–174.
[50] S.A. Memon, H. Cui, T.Y. Lo, Q. Li, Development of structural–functional integrated concrete with macro-encapsulated PCM for thermal energy storage, Appl. Energy 150 (2015) 245–257.
[51] X.H. Vu, Y. Malecot, L. Daudeville, E. Buzaud, Effect of the water/cement ratio on concrete behavior under extreme loading, Int. J. Numer. Anal. Met. 33 (2009) 1867–1888.
[52] N.S. Apebo, A.J. Shiwua, A.P. Agbo, J.C. Ezeokonkwo, P.T. Adeke, Effect of Water-Cement Ratio on the Compressive Strength of gravel-crushed over burnt bricks concrete, Civil Environ. Res. 3 (2013) 74–81.
[53] V.V.N. Kishore, Renewable Energy Engineering and Technology: Principles and Practice, TERI Press, New Delhi, 2010.

Construction and Building Materials 127 (2016) 450–456

Contents lists available at ScienceDirect

Construction and Building Materials

journal homepage: www.elsevier.com/locate/conbuildmat

Pressed lightweight fly ash-OPC geopolymer concrete containing recycled lightweight concrete aggregate

Patcharapol Posi [a], Pearploy Thongjapo [a], Natakorn Thamultree [a], Phongsathon Boontee [a], Pornnapa Kasemsiri [b], Prinya Chindaprasirt [c,*]

[a] Department of Civil Engineering, Faculty of Engineering, Rajamangala University of Technology Isan Khon Kaen Campus, Khon Kaen 40000, Thailand
[b] Sustainable Infrastructure Research and Development Center, Department of Chemical Engineering, Faculty of Engineering, Khon Kaen University, Khon Kaen 40002, Thailand
[c] Sustainable Infrastructure Research and Development Center, Department of Civil Engineering, Faculty of Engineering, Khon Kaen University, Khon Kaen 40002, Thailand

HIGHLIGHTS

- We studied lightweight fly ash-OPC geopolymer concrete containing recycled lightweight concrete block aggregate.
- Incorporation of OPC and temperature curing enhanced strength development.
- The use of OPC enhanced strength development with a slight increase in density.
- Density of 1200–1500 kg/m^3 and compressive strength of 4.5–17.5 MPa were obtained.

ARTICLE INFO

Article history:
Received 13 June 2016
Received in revised form 23 September 2016
Accepted 26 September 2016

Keywords:
Lightweight geopolymer concrete
Recycled lightweight aggregate
Fly ash
Portland cement
Waste lightweight concrete block

ABSTRACT

In this paper, the density and strength of lightweight fly ash-OPC geopolymer concrete containing recycled lightweight concrete aggregate (RLCA) were studied. Waste lightweight concrete was crushed and used as lightweight aggregate. Geopolymer cement was produced from the blend of high calcium fly ash and ordinary Portland cement (OPC), sodium hydroxide and sodium silicate. The fly ash was replaced with OPC at the dosages of 0, 5, 10 and 15% by weight. The results showed that lightweight geopolymer concretes with densities between 1200 and 1500 kg/m^3 and 28-day compressive strengths between 4.5 and 17.5 MPa could be fabricated. The incorporation of RLCA reduced both density and strength of lightweight concrete. The addition of OPC enhanced the strength development of geopolymer concrete but also increased the density. The optimum OPC content for strength development was 10%. The NaOH concentration of 10 M, sodium silicate/NaOH ratio of 1.0, OPC content of 10% by weight of fly ash, liquid/solid binder ratio of 1.4, RLCA/solid binder ratio of 1.8 and curing temperature of 60 °C were recommended for the lightweight fly ash-OPC geopolymer concrete.

© 2016 Elsevier Ltd. All rights reserved.

1. Introduction

Portland cement proofs itself as one of the main construction materials and is being used world-wide. Currently a large amount of concrete is utilized in the construction industry due to the suitable strength, durability, ease of construction and cost. The increase use of concrete is the main concern as the production of Portland cement involves emission of a large amount of greenhouse gas from the calcining of carbonaceous material and consumption of fuel [1]. In addition, the use of natural aggregates and the discarding of construction waste are putting a heavy load on environment [2–4]. The use of recycled aggregate is thus another mean to help the construction industry.

Other binder such as alkali activated cement or geopolymer serves as a good alternative binder [5] to reduce the increasing use of OPC. Fly ash is a good source material for making geopolymer as it is available worldwide. Activated with sodium hydroxide and sodium silicate and cured with moderate temperature, this fly ash geopolymer has good strength and durability [6]. At room temperature, the addition of 5–15% of OPC helps with the setting and strength development of fly ash geopolymer [7,8]. It has also been shown that both low and high calcium fly ash are suitable for use as source materials.

Currently, there is an increasing use of lightweight concrete in both residential and office buildings due to the reduced dead load and other added benefits such as improved heat and sound

* Corresponding author.
E-mail address: prinya@kku.ac.th (P. Chindaprasirt).

http://dx.doi.org/10.1016/j.conbuildmat.2016.09.105
0950-0618/© 2016 Elsevier Ltd. All rights reserved.

absorption properties [9]. Lightweight concrete is used extensively as partition and wall of which the volume is very large. It has been shown that lightweight concrete with sufficient high strength and low density could be made from waste or discarded lightweight concrete aggregate [10].

The use of lightweight concrete block is increasing and its waste is also increasing as the results of damage of blocks from manufacturing, transportation and handling as well as increased demolition of buildings. The use of recycled lightweight block as aggregate was therefore investigated with new binder namely fly ash geopolymer using workable mix and normal casting of sample [11]. The results indicated that the lightweight geopolymer block with recycled lightweight aggregate with strengths of 1.0–16.0 MPa and density of 860–1400 kg/m^3 could be fabricated. The previously published results indicated that slag, fly ash, silica sand and pumice could be used in making lightweight geopolymer concrete [12]. The geopolymer foam concretes have also been tested and found to have good thermal insulation as well [13]. In another investigation, the method of making pressed lightweight concrete with porous diatomite aggregate using a dry mix was found to be satisfactory. Pressed lightweight diatomite concretes with strengths of 7.8–12.9 MPa and density of 1000–1200 kg/m^3 were fabricated [14]. This pressing technique is attractive in terms of continuous pressing and making of blocks without conventional casting and demolding.

This research thus aims to develop lightweight fly ash-OPC geopolymer concrete using recycled lightweight aggregate from crushed waste lightweight concrete. The obtained data should be instrumental for the increasing use of both fly ash geopolymer and recycled lightweight concrete.

2. Experimental program

2.1. Materials

In this study, high calcium fly ash from Mae-Moh power plant in northern Thailand, ordinary Portland cement (OPC), sodium hydroxide (NaOH), sodium silicate and recycled lightweight concrete aggregate (RLCA) were the materials used. The chemical compositions of fly ash and OPC are shown in Table 1. The fly ash consisted of 45.23% SiO_2, 19.94% Al_2O_3, 13.15% Fe_2O_3, and 15.5% CaO with the loss on ignition (LOI) of 0.88%. It was, therefore, a class C fly ash as per ASTM C618 [15]. Three NaOH concentrations of 5, 10, and 15 M (M) and sodium silicate with 15.32% Na_2O, 32.87% SiO_2, and 51.8% water were used as alkali activators. The waste lightweight concrete block was autoclaved aerated concrete (AAC) type. This type of block is a popular commodity in the hot region especially Thailand and neighboring countries. The waste lightweight concrete block was crushed and classified into single size coarse aggregate (CA), medium aggregate (MA) and fine aggregate (FA) with particle sizes of 4.75–12.5, 1.18–4.75 and 0.01–1.18 mm, respectively as shown in Fig. 1. The RLCA was a graded aggregate with the ratios of CA:MA:FA of 30:30:40 by weight [11,16].

The physical properties of materials are shown in Table 2. The values of specific gravity of CA, MA and FA were 1.42, 1.96, and 2.61 respectively. The low S.G. of CA was due to the large amount of internal pore. This also resulted in the low unit weight of CA compared to those of MA and FA. The values of Blaine fineness of fly ash and OPC were 2409 and 3600 cm^2/g with the corresponding median particle sizes of 18.6 and 14.6 μm, respectively. This suggested that this batch of fly ash is relatively fine.

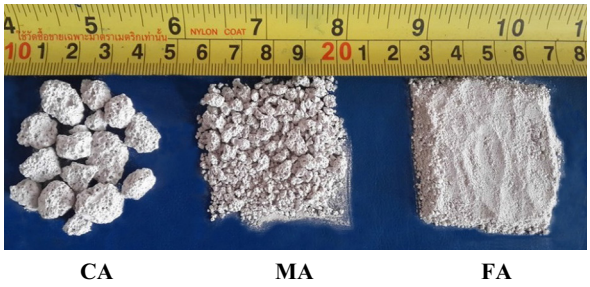

Fig. 1. Recycled lightweight concrete aggregate.

2.2. Mix proportion

The dry mixtures were designed and used for making pressed lightweight concrete block. To study the property of FA-OPC geopolymer, the FA replacement levels with OPC were limited to 0, 5, 10, and 15% by weight as previous researches indicated that the maximum OPC content should be around 10% [7,8]. The pressed lightweight concrete mixture is a dry mix and hence a dry aggregate was used. The density and compressive strength of lightweight geopolymer concretes containing RLCA were determined. In order to obtain adequate data, several series of mixes were tested as shown in Table 3.

Series A/S: To study the effect of aggregate content, the aggregate/solid binder (fly ash + OPC) ratios of 1.6, 1.8, 2.0 and 2.2 was tested.

Series T: To study the effect of temperature of curing, four curing temperatures viz., 25, 40, 60 and 90 °C were tested. The samples were kept at 25 °C for one hour and then temperature cured for 48 h.

Series NHC: Three NaOH concentrations viz., 5, 10 and 15 M were used to study the effect of NaOH concentration.

Series NS/NH: This series was used to study the effect of sodium silicate/NaOH ratios using NS/NH ratios of 0.33, 0.67, 1.0, 1.5 and 3.0.

Series L/S: This series was used to study the effect of liquid alkaline/solid binder ratio (L/S). The L/S of 1.2, 1.4, 1.6 and 1.8 were tested.

2.3. Details of mixing

In the first step, OPC and fly ash were mixed until uniform color was obtained. NaOH solution was then added and mixed for 5 min to obtain homogenous mixture. Sodium silicate solution was then added and the mixing was done for another 5 min. Next, the graded recycled aggregate was added and mixing was done for 1.5 min. The 50 × 50 × 50 mm lightweight geopolymer concrete blocks were fabricated with the aid of a pressing tool using a small pressure of 0.85 MPa [14]. The specimens were placed in a 25 °C controlled room for 1 h [17] and temperature cured for 48 h.

Table 1
Chemical composition of Fly ash and OPC.

Chemical compositions (%)	SiO_2	Al_2O_3	Fe_2O_3	CaO	K_2O	Na_2O	MgO	SO_3	LOI
Fly ash	45.23	19.95	13.15	15.50	2.15	0.52	2.02	0.3	0.88
OPC	20.80	4.70	3.40	65.30	0.40	0.10	1.50	2.7	0.90

Table 2
Physical properties of materials.

Materials	Fly Ash	OPC	CA	MA	FA
Specific gravity	2.22	3.15	1.42	1.96	2.61
Median particle size (μm)	18.5	14.6	–	–	–
Particle size (mm)	–	–	4.75–12.5	1.18–4.75	0.01–1.18
Fineness modulus	–	–	5.75	3.90	1.75
Unit weight (kg/m^3)	1190	1440	360	390	720
Water absorption (%)	–	–	76	68	56

Table 3
Mix proportions of weight ratios of pressed geopolymer lightweight concrete.

Series	Aggregate/Solid binder ratio	NH (M)	NS/NH Ratio	L/S Ratio	Curing Temp. (°C)
A/S	1.6,1.8,2.0,2.2	10	1.00	1.4	60
T	1.8	10	1.00	1.4	25,40,60,90
NHC	1.8	5,10,15	1.00	1.4	60
NS/NH	1.8	10	0.33,0.67,1.0,1.5,3.0	1.4	60
L/S	1.8	10	1.00	1.2,1.4,1.6,1.8	60

Note: OPC replacement levels of 0, 5, 10 and 15% were tested for all series.

Finally, the specimens were wrapped with plastic sheet and stored in a 25 °C controlled room.

2.4. Details of test

The density was determined at the age of 28 days using the compressive strength specimens as described in ASTM C138/C138M-14 [18]. The compressive strength was measured after the density determination in accordance with ASTM C109/C109M-13 [19]. The coarse aggregate (CA) particle size was 4.75–11.8 mm. The maximum size was a little larger than the maximum size of sand i.e. 9.5 mm as per ASTM C33/C33M-16 [20]. For ease of preparing a large number of samples, the 5 × 5 × 5 cm cube recommended for mortar mix in accordance with ASTM C109/C109M-13 was thus used. The reported density and compressive strengths were the average of three samples.

3. Result and discussions

3.1. Aggregate content

The results of density and compressive strength of series A/S are shown in Fig. 2. The density and compressive strength of lightweight geopolymer concrete depended on both aggregate and OPC contents. For low OPC contents of 0 and 5%, the density of sample increased with increasing RLCA content up to a certain A/S and beyond that the density started to reduce. The optimum A/S values for maximum density were at 2.0 and 1.8 for mixes with OPC contents of 0 and 5%, respectively. At low A/S, the mixture contained a large volume of matrix and lightweight concrete with low density were obtained. Beyond the optimum A/S, the mixture contained a low volume of matrix and the pressed blocks with low density were also obtained.

Fig. 3 shows the cut surface of lightweight geopolymer samples at 28 days of series A/S with 10% OPC. Although the specimen of this experiment was small, the cut section indicated that the RCLA distributed quite regularly in the geopolymer matrix as a result of the dry mix design which prevented segregation. There were no obvious visible gaps or voids between aggregate and geopolymer matrix. The increase in the aggregate content reduced the amount of geopolymer matrix. This in turn resulted in the reduction in density and strength of concrete.

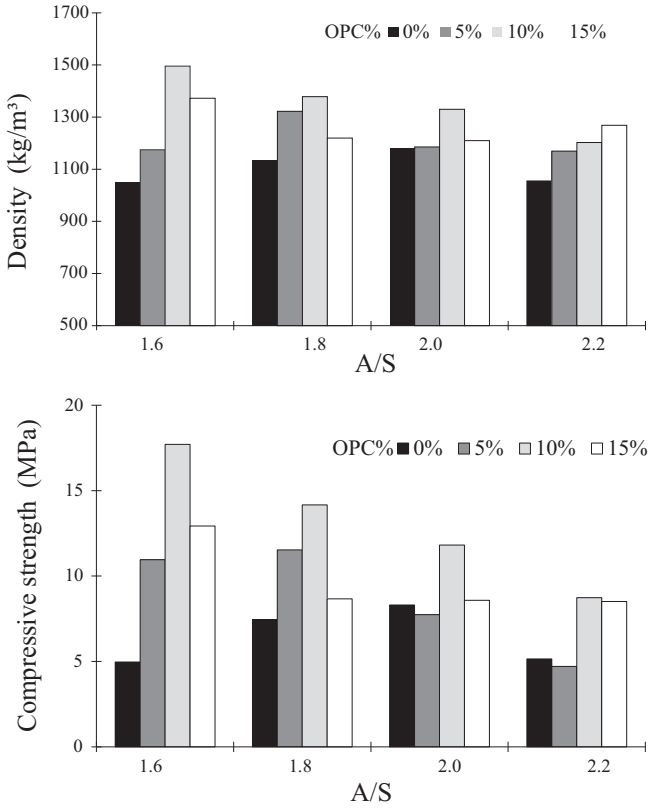

Fig. 2. Density and compressive strength of geopolymer concrete at 28 days, series A/S.

For the high OPC contents of 10 and 15%, the density of sample reduced with increasing RLCA content. For example, the densities of geopolymer concretes with 10% OPC were 1495, 1378, 1330, and 1200 kg/m^3 for samples with A/S of 1.6, 1.8, 2.0, and 2.2, respectively. In this case, the maximum density was at A/S of 1.6 and the increase in aggregate content resulted in the reduced volume of matrix and the density of concrete reduced accordingly.

The compressive strength results followed the same trend as those of density. For low OPC contents of 0 and 5%, the strengths of sample increased with increasing RLCA content up to a certain

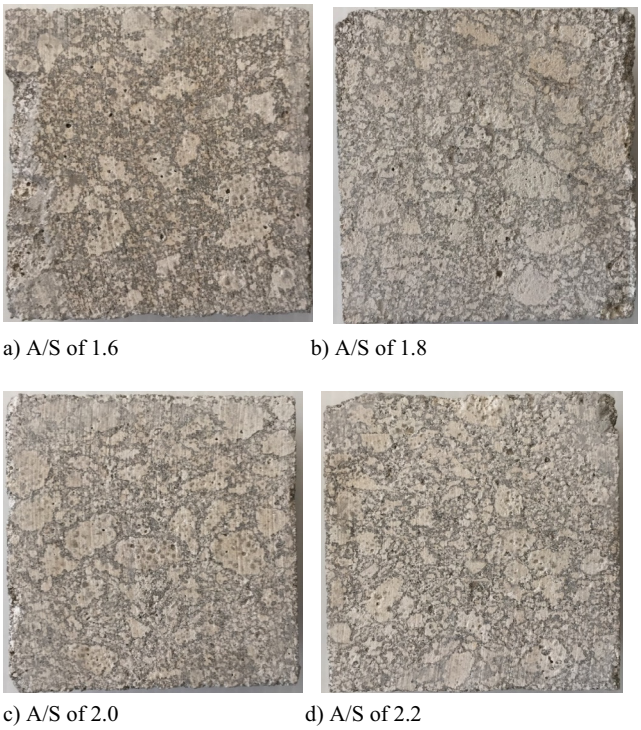

Fig. 3. Cut surface of lightweight geopolymer concretes at 28 days, series A/S, 10% OPC; a) A/S of 1.6, b) A/S of 1.8, c) A/S of 2.0, d) A/S of 2.2.

A/S and beyond that the strength started to reduce. For high OPC contents of 10 and 15%, the strength of sample reduced with increasing RLCA content. For example, the 28-day compressive strengths of mixes with 10% OPC and A/S of 1.6, 1.8, 2.0, and 2.2 were 17.7, 14.1, 11.8, and 8.7 MPa, respectively. The decrease in strength was due to the increase in RLCA which was weaker than the geopolymer matrix. Similar reduction in strength with increasing lightweight aggregate content was reported by other researches [21–23]. The increase in aggregate content also reduced the amount of cementitious matrix and the mix became harsh and the density and strength were reduced.

With regards to the OPC content, the compressive strength increased with increasing OPC content up to 10% by weight of fly ash. For example, the compressive strength at 28 days of mixes with A/S of 1.8 with volume of OPC of 0, 5, 10, and 15% by weight were 7.4, 11.5, 14.1, and 8.6 MPa, respectively. The incorporation of OPC resulted in the increased hydration products with additional calcium reacted and formed additional C-S-H and C-A-S-H products which coexisted with normal geopolymer products [24]. The 10% OPC replacement level was reported to be optimal for strength development of system with temperature curing [7]. For the high OPC replacement level of 15% with 60 °C temperature curing, the compressive strength started to decline. At this curing temperature and OPC content, the negative effects of temperature curing and high OPC content resulted in strength reduction due mainly to the modifications of microstructure of hydration products with temperature curing [6,7].

For density, the trend of result was nearly the same as that of strength i.e. at the same A/S (with the exception of A/S of 2.2), the density of sample increased with the increasing OPC content up to 10% by weight of fly ash. The increase in density was due to the higher S.G. of OPC than that of fly ash. The increase in OPC content to 15% reduced the volume of fly ash and this also reduced the workability of mixture as fly ash particles were spherical and enhanced the workability of mixture. This thus resulted in pressed concrete block with reduced density.

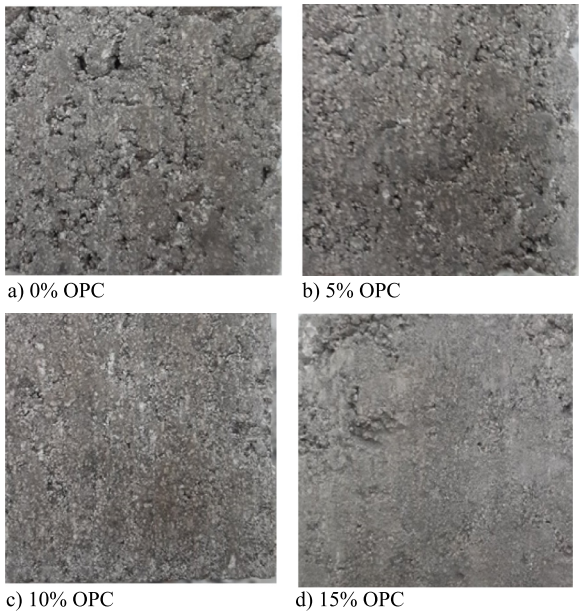

Fig. 4. Cast surface of lightweight geopolymer concretes at 28 days, series A/S, A/S = 1.8; a) 0% OPC, b) 5% OPC, c) 10% OPC, d) 15% OPC.

The as-cast surface condition of concrete block with A/S = 1.8 and 0, 5, 10 and 15% OPC are shown in Fig. 4. With 0% OPC, the density of concrete was low due to numerous voids as shown in Fig. 4a. Addition of 5 and 10% OPC resulted in the reduction of voids and increased in density of the lightweight concrete. The 10% OPC concrete was slightly denser than the 5%OPC concrete. This 10% OPC addition corresponded to the maximum density and strength of concrete. When the OPC content was increased to 15%, uneven surface was noticed as shown in Fig. 4d. The mix became too dry and the casting and pressing of concrete block resulted in the uneven surface of sample. This in turn resulted in the lowering of density and strength.

3.2. Curing temperature

The results of density and compressive strength of geopolymer concrete with various curing temperatures are shown in Fig. 5. The increase in curing temperature from 25 to 90 °C resulted in a slight increase in compressive strength due to the enhanced geopolymerization which resulted in the formation of additional amount of reaction products [25–27]. For example, the 28-day compressive strengths of samples with 5% OPC cured at 25, 40, 60, and 90 °C were 4.5, 8.5, 11.5, and 12.0 MPa, respectively. The increase in temperature of curing resulted in a slightly decrease in density due to the loss of free water and structurally bonded water at high temperature [28].

3.3. Liquid to solid binder ratio

The results of density and compressive strength of lightweight geopolymer concrete with various L/S are shown in Fig. 6. The optimum density was obtained with mixes at L/S of 1.6. For example, the density of 5% OPC lightweight geopolymer concretes with L/S of 1.2, 1.4, 1.6, and 1.8 were 1275, 1320, 1440, and 1340 kg/m^3, respectively. At very low liquid content, the mixtures were dry and the casting and pressing were difficult. At very high liquid content, the mixtures became too wet and the casting and pressing were also difficult. The results thus confirmed that the mixtures

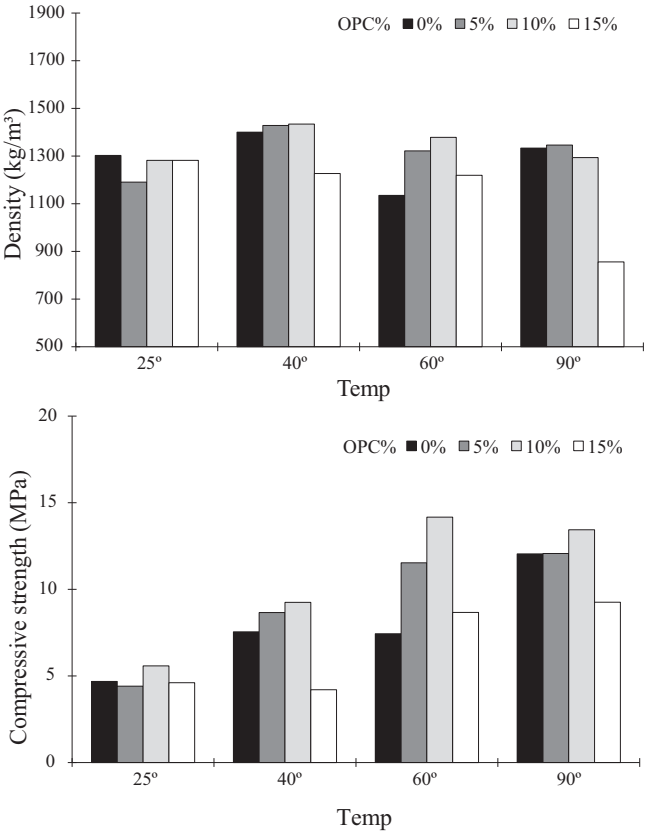

Fig. 5. Density and compressive strength of geopolymer concrete at 28 days, series T.

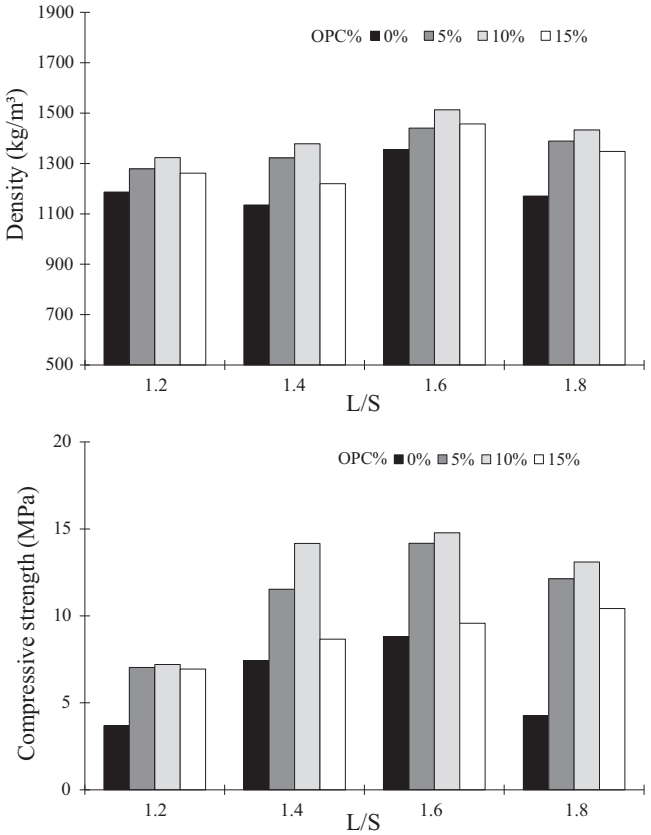

Fig. 6. Density and compressive strength of geopolymer concrete at 28 days, series L/S.

with good casting and pressing characteristics produced relatively high density concretes.

With regards to compressive strength, the optimum strengths were also at L/S of 1.6. For example, the compressive strengths at 28 days of 10% OPC mixes with L/S of 1.2, 1.4, 1.6, and 1.8 were 7.2, 14.1, 14.7, and 13.1 MPa, respectively. At low L/S ratios of 1.2 and 1.4, low compressive strengths were obtained due to the low volume of liquid and low density [23]. In contrast, when L/S was high at 1.8, the compressive strength started to decrease due to the excessive liquid and the mix was also not suitable for pressing into block [6] resulting in low density and strength. The reduction in strength at this L/S was more obvious than the reduction in density.

For the influence of OPC content, the results confirmed that the addition of OPC increased both density and strength. The optimum OPC content of 10% was observed for this series of test for both density and strength.

3.4. Sodium hydroxide concentration

The results of density and compressive strength of lightweight geopolymer concretes with various NaOH concentrations are shown in Fig. 7. The increase in NaOH concentration resulted in the increase in density of geopolymer concrete due to the increase in density of liquid which in turn increased the density of lightweight concrete block. In addition, the setting time of high calcium fly ash geopolymer was rather quick at low NaOH concentration due to the leaching out and precipitation of calcium to form hydration products [29,30]. With short setting time, the mixture became less workable with time and resulted in difficulties in casting and pressing. This also contributed to the low density of low NaOH concentration mix. With high NaOH concentrations of 10 and 15 M, the setting times of mixes were longer [7]. In this case, the casting and pressing were slightly improved and the densities of concretes were also increased.

For compressive strength, the increase in NaOH concentrations from 5 M to 15 M generally resulted in increasing compressive strength. In particular, the compressive strengths of 10 M NaOH mixes with 5 and 10% OPC were significantly higher than others. The compressive strengths at 28 days of 10% OPC mixes with 5, 10, and 15 M NaOH were 2.0, 14.1 and 11.5 MPa, respectively. At low NaOH of 5 M, the leaching out of silica and alumina was low [29,31] and this resulted in low development of geopolymer gel. Coupled with the low density, the obtained compressive strengths were thus low. As shown in Fig. 7, the strength of 10% OPC mix with 5 M NaOH was lowest in the group. This was probably due to the fast setting of this mix and resulted in low density and low strength. Higher strength geopolymer concretes were obtained with high NaOH concentrations of 10 and 15 M. This is in line with the previously published results with high strength geopolymers obtained with NaOH concentrations of 9.5–14.0 M [24]. At very high concentration of NaOH, the excessive hydroxide ions caused aluminosilicate gel precipitation at the very early stages and low compressive strengths were obtained [24,32,33].

The influence of OPC content on density and strength of this series of test was not as clear as the others. However, the general trend of results i.e. the optimal OPC content of 10% for maximum density and strength was clearly indicated in the density graph for 10 M NaOH mixes and the compressive strength graphs for 10 and 15 M NaOH mixes.

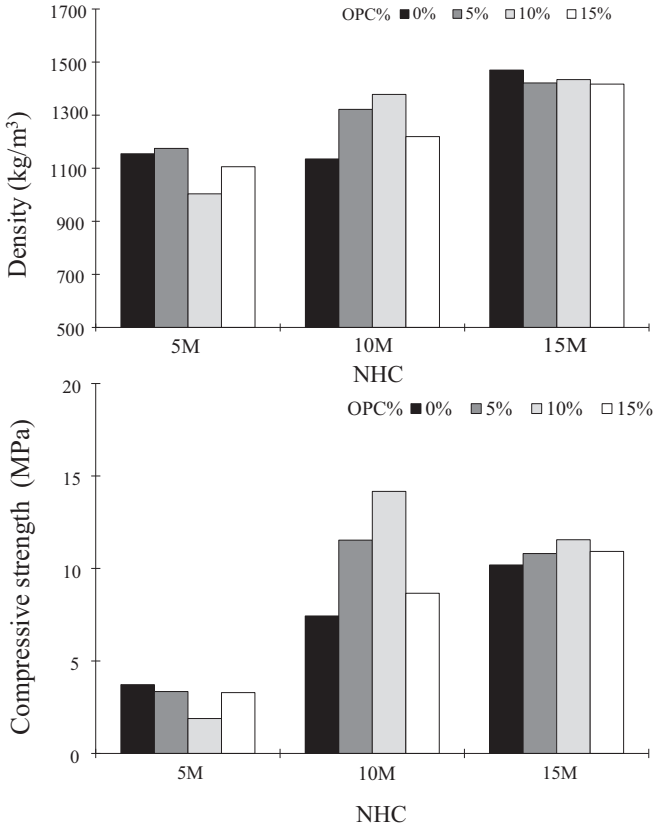

Fig. 7. Density and compressive strength of geopolymer concrete at 28 days, series NHC.

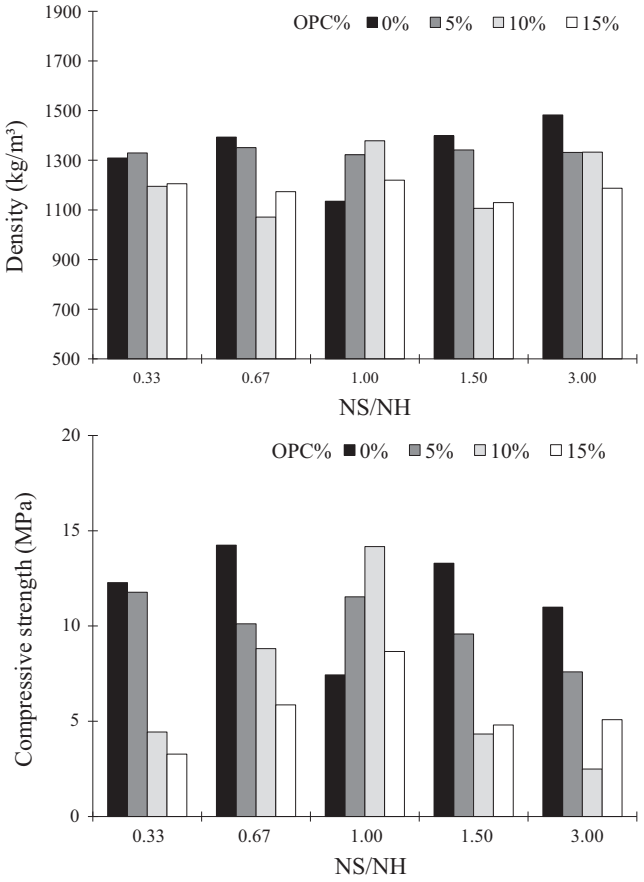

Fig. 8. Density and compressive strength of geopolymer concrete at 28 days, series NS/NH.

3.5. Sodium silicate to sodium hydroxide ratio (NS/NH)

The results of density and compressive strength of geopolymer concrete with different NS/NH ratios are shown in Fig. 8. The density of concretes tended to increase with increasing NS/NH ratio. In general, the density of sodium silicate is higher than those of sodium hydroxide solutions used in this research. The increase in NS/NH ratio thus resulted in the increase in density of liquid and the density of concretes.

With regards to compressive strength, the results indicated that the mixes tended to have high strength at NS/NH ratio of 1.00. For example, the compressive strength at 28 days of mixes with 10% OPC and NS/NH of 0.33, 0.67, 1.00, 1.50, and 3.00 were 4.5, 8.8, 14.1, 4.3, and 2.5 MPa, respectively. Only the mixes without 0% OPC deviated from this general trend. An increase in NS/NH ratio from 0.33 to 1.00 increased the strength of concrete and beyond this, the strength of concrete block started to drop. It has been reported that for high calcium fly ash, the NS/NH ratio of 1.0 produced relatively high strength geopolymer [17]. An increase in sodium silicate normally increases the strength of geopolymer concrete [34] due mainly to the increase of readily available silicate species. However, the increase in sodium silicate content also increased the viscosity of mixture and this resulted in the difficulties in casting and pressing. This is in line with the previously reported result of reduction in workability with increase in sodium silicate content [35].

When considering OPC content; at the same NS/NH ratio, the density of concrete tended to decrease with increasing OPC content except for NS/NH ratio of 1.0. The reduction in fly ash and increase in OPC content reduced the workability of mixture and resulted in difficulties in casting and pressing as well. This resulted in the reduction in density and strength of concrete.

For the application of this material, a number of these blocks could be classified as moderate-strength lightweight concretes according to ACI 213R-03 [36] with suggested density of 800–1350 kg/m^3 and strength of 7.0–14.0 MPa. Admittedly, blocks with high strength is preferred in many instances. In addition, the use of alkali activator and curing temperature should be minimal. For low strength concrete block with ease of fabrication and low cost, curing at ambient temperature of 25 °C is most attractive. This corresponds to concrete with density of 1300 kg/m^3 and compressive strength of 4.5 MPa with mix design of 10 M NaOH, 0% OPC, A/S of 1.8, L/S of 1.4, NS/NH of 1.0 and cured at 25 °C. To obtain block with higher strengths, the use of 10% OPC and 60 °C temperature curing are recommended. Geopolymer concrete with density of 1400 kg/m^3 and strength of 14.5 MPa could be obtained with mix using 10 M NaOH, NS/NH of 1.0, L/S of 1.4, A/S of 1.8. For higher density and strength, the reduction in RCLA is needed. The same mix but with A/S of 1.6 produced lightweight concrete with density of 1500 kg/m^3 and compressive strength of 17.5 MPa.

4. Conclusions

Based on the experimental design using dry mixes and the method of pressing with a small pressure of 0.85 MPa, the following conclusions can be drawn.

1. Lightweight geopolymer concretes with density of 1200–1500 kg/m^3 and 28-day compressive strengths of 4.5–17.5 MPa could be fabricated using RCLA. The incorporation of RCLA reduced the density of concrete block effectively with the suitable A/S ratios in the range of 1.6–1.8.

2. For low strength application, mix with no OPC addition cured at ambient temperature of 25 °C is most attractive. This corresponds to concrete block with density of 1300 kg/m^3 and compressive strength of 4.5 MPa using 10 M NaOH, A/S of 1.8, L/S of 1.4 and NS/NH of 1.0.
3. The incorporation of OPC and temperature curing enhanced the strength development of lightweight geopolymer concrete with a slight increase in the density. The optimum OPC content was 10% OPC replacement level of fly ash and the optimum temperature curing was 60 °C. Concrete with density of 1400 kg/m^3 and strength of 14.5 MPa was obtained using similar mix design with 10% OPC and temperature cured at 60 °C.
4. For higher strength lightweight geopolymer concrete, the reduction in the amount of RCLA is needed. The mix with A/S reduced to 1.6 produced lightweight concrete with density of 1500 kg/m^3 and compressive strength of 17.5 MPa.

Acknowledgements

This work was financially supported by the Higher Education Research Promotion and National Research University Project of Thailand, Office of the Higher Education Commission, through the Advanced Functional Materials Cluster of Khon Kaen University, and Khon Kaen University and the Thailand Research Fund (TRF) under the TRF Senior Research Scholar Contract No. RTA5780004. The support of the Siam Research and Innovation Co. Ltd. is also acknowledged here.

References

[1] Z. Zhang, J.L. Provis, J. Zou, A. Reid, H. Wang, Toward an indexing approach to evaluate fly ashes for geopolymer manufacture, Cem. Concr. Res. 85 (2016) 163–173.
[2] M. Henry, G. Pardo, T. Nishimura, Y. Kato, Balancing durability and environmental impact in concrete combining low-grade recycled aggregates and mineral admixtures, Resour. Conserv. Recycl. 55 (11) (2011) 1060–1069.
[3] A. Rao, K.N. Jha, S. Misra, Use of aggregates from recycled construction and demolition waste in concrete, Resour. Conserv. Recycl. 50 (1) (2007) 71–81.
[4] Dr S. Chandra, Conference report, Cement Concr. Compos. 27 (6) (2005) 738–741.
[5] C. Shi, A.F. Jiménez, A. Palomo, New cements for the 21st century: the pursuit of an alternative to Portland cement, Cem. Concr. Res. 41 (7) (2011) 750–763.
[6] J. Temuujin, A. van Riessen, R. Williams, Influence of calcium compounds on the mechanical properties of fly ash geopolymer pastes, J. Hazard. Mater. 167 (1–3) (2009) 82–88.
[7] S. Pangdaeng, T. Phoo-ngernkham, V. Sata, P. Chindaprasirt, Influence of curing conditions on properties of high calcium fly ash geopolymer containing Portland cement as additive, Mater. Des. 53 (2014) 269–274.
[8] T. Phoo-ngernkham, V. Sata, S. Hanjitsuwan, C. Ridtirud, S. Hatanaka, P. Chindaprasirt, High calcium fly ash geopolymer mortar containing Portland cement for use as repair material, Constr. Build. Mater. 98 (2015) 482–488.
[9] S.B. Park, D.S. Seo, J. Lee, Studies on the sound absorption characteristics of porous concrete based on the content of recycled aggregate and target void ratio, Cem. Concr. Res. 35 (9) (2005) 1846–1854.
[10] R. Ahmmad, M.Z. Jumaat, U.J. Alengaram, S. Bahri, M.A. Rehman, H.B. Hashim, Performance evaluation of palm oil clinker as coarse aggregate in high strength lightweight concrete, J. Clean. Prod. (2016) 112. Part 1:566-74.
[11] P. Posi, C. Teerachanwit, C. Tanutong, S. Limkamoltip, S. Lertnimoolchai, V. Sata, et al., Lightweight geopolymer concrete containing aggregate from recycle lightweight block, Mater. Des. 52 (2013) 580–586.
[12] H. Binici, Engineering properties of geopolymer incorporating slag, fly ash, silica sand and pumice, Adv. Civil Environ. Eng. 3 (2013) 108–123.
[13] Z. Zhang, J.L. Provis, A. Reid, H. Wang, Geopolymer foam concrete: an emerging material for sustainable construction, Constr. Build. Mater. 56 (2014) 113–127.
[14] P. Posi, S. Lertnimoolchai, V. Sata, P. Chindaprasirt, Pressed lightweight concrete containing calcined diatomite aggregate, Constr. Build. Mater. 47 (2013) 896–901.
[15] ASTM C 618, Standard specification for coal fly ash and raw or calcined natural pozzolan for use in concrete, Annual Book of ASTM Standard, Vol. 04.01, 2012.
[16] O. Ünal, T. Uygunoğlu, A. Yildiz, Investigation of properties of low-strength lightweight concrete for thermal insulation, Build. Environ. 42 (2) (2007) 584–590.
[17] P. Chindaprasirt, T. Chareerat, V. Sirivivatnanon, Workability and strength of coarse high calcium fly ash geopolymer, Cement Concr. Compos. 29 (3) (2007) 224–229.
[18] ASTM C138/C138M-14, Standard test of method for unit weight of mortar, Annual Book of ASTM Standard, Vol. 04.01, 2014.
[19] ASTM C109/C109M-13, Standard test method of compressive strength of hydrualic cement mortars (using 2-in. or [50 mm] cube specimens), Annual Book of ASTM Standard, Vol. 04.01, 2013.
[20] ASTM C33/C33M-16, Standard specification for concrete aggregates, Annual Book of ASTM Standard, Vol. 04.02, 2016.
[21] Y. Xu, L. Jiang, J. Xu, Y. Li, Mechanical properties of expanded polystyrene lightweight aggregate concrete and brick, Constr. Build. Mater. 27 (1) (2012) 32–38.
[22] C.-C. Yang, R. Huang, Approximate strength of lightweight aggregate using micromechanics method, Adv. Cem. Based Mater. 7 (3–4) (1998) 133–138.
[23] N.U. Kockal, T. Ozturan, Strength and elastic properties of structural lightweight concretes, Mater. Des. 32 (4) (2011) 2396–2403.
[24] K. Somna, C. Jaturapitakkul, P. Kajitvichyanukul, P. Chindaprasirt, NaOH-activated ground fly ash geopolymer cured at ambient temperature, Fuel 90 (6) (2011) 2118–2124.
[25] A. Noushini, A. Castel, The effect of heat-curing on transport properties of low-calcium fly ash-based geopolymer concrete, Constr. Build. Mater. 112 (2016) 464–477.
[26] P. Rovnaník, Effect of curing temperature on the development of hard structure of metakaolin-based geopolymer, Constr. Build. Mater. 24 (7) (2010) 1176–1183.
[27] M. Soutsos, A.P. Boyle, R. Vinai, A. Hadjierakleous, S.J. Barnett, Factors influencing the compressive strength of fly ash based geopolymers, Constr. Build. Mater. 110 (2016) 355–368.
[28] S.K. Nath, S. Maitra, S. Mukherjee, S. Kumar, Microstructural and morphological evolution of fly ash based geopolymers, Constr. Build. Mater. 111 (2016) 758–765.
[29] U. Rattanasak, P. Chindaprasirt, Influence of NaOH solution on the synthesis of fly ash geopolymer, Miner. Eng. 22 (12) (2009) 1073–1078.
[30] U. Rattanasak, K. Pankhet, P. Chindaprasirt, Effect of chemical admixtures on properties of high-calcium fly ash geopolymer, Int. J. Miner. Metal. Mater. 18 (3) (2011) 364–369.
[31] S. Hanjitsuwan, S. Hunpratub, P. Thongbai, S. Maensiri, V. Sata, P. Chindaprasirt, Effects of NaOH concentrations on physical and electrical properties of high calcium fly ash geopolymer paste, Cement Concr. Compos. 45 (2014) 9–14.
[32] W.K.W. Lee, J.S.J. Van Deventer, The effects of inorganic salt contamination on the strength and durability of geopolymers, Colloids Surf., A 211 (2–3) (2002) 115–126.
[33] K. Pimraksa, P. Chindaprasirt, A. Rungchet, K. Sagoe-Crentsil, T. Sato, Lightweight geopolymer made of highly porous siliceous materials with various Na2O/Al2O3 and SiO2/Al2O3 ratios, Mater. Sci. Eng., A 528 (21) (2011) 6616–6623.
[34] S.E.W.D.M.J.S. Djwantoro Hardjito, B.V. Rangan, On the development of fly ash-based geopolymer concrete, Mater. J. 101 (6) (2004).
[35] A. Sathonsaowaphak, P. Chindaprasirt, K. Pimraksa, Workability and strength of lignite bottom ash geopolymer mortar, J. Hazard. Mater. 168 (1) (2009) 44–50.
[36] ACI 213R-03, Guide for Structural Lightweight Aggregate Concrete, American Concrete Institute, Farmington Hills, 2003.

RESEARCH ARTICLE
doi: 10.2306/scienceasia1513-1874.2016.42.407

ScienceAsia 42 (2016): **407–414**

Bioactivity enhancement of calcined kaolin geopolymer with $CaCl_2$ treatment

Saengsuree Pangdaeng[a], **Vanchai Sata**[b], **J.B. Aguiar**[c], **F. Pacheco-Torgal**[c], **Jarin Chindaprasirt**[d], **Prinya Chindaprasirt**[b,*]

[a] Division of Civil Engineering, Faculty of Engineering, Nakhon Phanom University, Nakhon Phanom 48000 Thailand
[b] Sustainable Infrastructure Research and Development Centre, Department of Civil Engineering, Faculty of Engineering, Khon Kaen University, Khon Kaen 40002 Thailand
[c] C-TAC Research Centre, Department of Civil Engineering, University of Minho, Campus of Azurém, 4800-058, Guimarães, Portugal
[d] Department of Internal Medicine, Faculty of Medicine, Khon Kaen University, Khon Kaen 40002 Thailand

*Corresponding author, e-mail: prinya@kku.ac.th

Received 25 Sep 2015
Accepted 24 Dec 2016

ABSTRACT: This paper reports that surface treatment with $CaCl_2$ enhances the bioactivity of a calcined kaolin geopolymer. Calcined kaolin, NaOH solution, sodium silicate solution, and heat curing were used to form geopolymer pastes. A soaked-treatment method was applied to the geopolymer samples using $CaCl_2$ solution as the ion exchange agent. The bioactivity of the material was determined by the simulated body fluid (SBF) in vitro testing method. Scanning electron microscope images showed a dense apatite formation on the treated geopolymer surface after SBF immersion for only 3 days. The $CaCl_2$ treatment promoted compressive strength and enhanced bioactivity by accelerating apatite precipitation and slowing down the rise in pH.

KEYWORDS: aluminosilicate, metakaolin, apatite, SBF

INTRODUCTION

A geopolymer is an aluminosilicate amorphous structure that results from the polycondensation of inorganic compounds[1]. A geopolymer is defined as an alkali-activated material and is produced through the reaction of aluminosilicate materials with an alkaline activator, which is usually a concentrated alkali hydroxide, silicate, carbonate, or sulphate[2]. Fly ash, ground granulated blast furnace slag, and calcined kaolin are good source materials. Geopolymers can be produced and used as a cementitious material similar to Portland cement as they are strong and durable. Research on the use of geopolymers has been extended to many fields such as fire resistant construction materials[3], and smart materials[4].

Cementitious materials have various applications such as sensing and electrical components[5], self-cleaning material with photo catalysis properties[6], and biocompatible materials[7–9]. Cement and ceramic have been studied in application of biocompatible material and generally used as "in vitro" test method, the outside body test using simulated body fluid (SBF)[10,11]. The use of mechanically compliant interface with living tissue was first observed in 1969 and is now referred as 'bioactivity'[12]. Bioactivity of implant materials is usually identified by precipitation of biolayer on material surface called apatite layers[13]. These biocompounds are connectable bonding between material and living bone and play significant role in nucleation sites for new bone growth[14]. Apatite layers are commonly composed of calcium and phosphate such as $Ca_{10}(PO_4)_6(OH)_2$ hydroxyapatite (HA), $Ca_{10}(PO_4)_6(CO_3)(H_2O)$ carbonate apatite, and $Ca_{10}(PO_4)_6Cl_2$ chlorapatite[15]. Furthermore, the change in pH condition of SBF solution after soaking the material has an important effect on the biocompatibility. High pH changes at the surface of the implant material can harm living cells[16].

Recently, biocompatible metakaolin-aluminosilicate materials have been tested both in vivo[17–19] and in vitro[20–23]. For implant applications[24], geopolymers have been shown to be bioactive with low ion leakage, although the possible leaching of aluminium can result in toxicity[21]. Kaolinite, a good source material for making geopolymers, has been

extensively used as a pharmaceutical excipient. The study of geopolymers for implant material indicates the problem of low bioactivity. The incorporation of $Ca(OH)_2$ in geopolymers can promote the apatite forming ability[21]. The presence of $CaCO_3$ enhances the apatite forming ability by inducing the precipitation of phosphate ions[10]. $CaCl_2$ and white Portland cement produce nontoxic treated cement paste[8], and increase the bioactivity by showing high hydroxyapatite formation after immersion in SBF solution[25]. For geopolymer material, adding of $CaCl_2$ can be applied in a small amount around 1% of binder because of the rapid hardening[26] and is not sufficient to gain high bioactivity. Since geopolymer structure has a weak sodium bond and this can be leached out almost completely[27], thus it can be charge-balanced with other cations by treating with chloride solution of the desired cations[28]. Direct contact of $CaCl_2$ solution provides Ca^{2+} cations to the surface of geopolymer and promotes the precipitation of reactive calcium compound for bioactivity and simultaneously enhances strength and durability of geopolymers[29].

This paper presents the use of $CaCl_2$ to enhance the apatite forming ability of calcined kaolinite geopolymer. The knowledge would be instrumental for future development of calcined kaolinite geopolymer for biomaterial applications.

MATERIALS AND METHODS

Materials

Kaolin from Ra Norng province in southern Thailand was calcined at 600 °C for 6 h to generate high reactivity calcined kaolin (CK)[30] and used as a source material. The CK consisted of 60% SiO_2, 34% Al_2O_3, 0.1% CaO, 0.9% Fe_2O_3, 0.2% MgO, 0.2% Na_2O, 0.1% SO_3, and 1% LOI. NaOH with concentration of 10 molar and sodium silicate with 15% Na_2O, 33% SiO_2, and 52% H_2O were used as alkali activators. $CaCl_2$ solution (CC) with 0.5 molar concentration prepared from $CaCl_2 \cdot 2H_2O$ and deionized water was used for treatment[31]. For the biocompatibility test, a simulated body fluid solution (SBF) with ion concentration similar to human blood plasma[13] was prepared and used.

Sample preparation

Prepared CK was mixed with NaOH for 5 min and then mixed with sodium silicate for another 5 min. The sodium silicate:NaOH ratio of 1 and liquid to binder ratio of 1 were used. Geopolymer paste was cast into $25 \times 25 \times 25$ mm acrylic moulds for compressive strength test and 10 mm diameter and 2 mm thick disks for bioactivity test. The fresh geopolymer pastes were compacted for 10 s with the aid of a vibrating table. The moulds were left in a controlled 23 °C room for 1 h, and then wrapped with plastic film and cured at 60 °C for 24 h. The specimens were left to cool down and demoulded. For the control samples, they were also wrapped with plastic film and kept in the controlled 23 °C room. For $CaCl_2$ treatment, the samples were treated by soaking in CC solution for 24 h at 23 °C[32]. The samples were then dried in a desiccator for 12 h and wrapped with plastic film and stored in the controlled 23 °C room.

In vitro test

At the age of 7 days, the treated and untreated discs were soaked in SBF solution with solution volume to sample surface of 0.1[33]. The immersed duration was left for 28 days with temperature controlled at 37 °C similar to human body[13]. The pH values of SBF solutions were monitored during the soaking.

Other tests

Geopolymers were tested for compressive strength at 7 days in accordance with ASTM C109[34]. The reported results are the average of three samples. Bioactivity characterization of geopolymer surface was made using JEOL JEM-5910LV scanning electron microscopy (SEM). Identification of pH change after sample immersed in SBF was done by ion electrode pH meter. The X-Ray Diffraction (XRD) experiments were performed with step of 0.0229° and step time of 240.5 s at 25 °C using Bruker's TOPAS software to confirm the chemical compound of geopolymer. Fourier transform infrared (FTIR) spectroscopy was also performed on the geopolymer samples.

RESULTS AND DISCUSSION

Compressive strength and surface structure

The 7 days compressive strength of control and treated pastes were 49.9 and 53.7 MPa, respectively. These strength values are comparable to the other reported compressive strengths of calcined kaolinite geopolymers[35,36]. The treatment by $CaCl_2$ had a positive effect on the strength development. The increase of strength was due partly to the additional wet curing of the samples soaked in the $CaCl_2$ solution. The immersion caused sustained water on the surface of geopolymer and affected the geopolymerization[37]. Moisture curing of geopolymer results

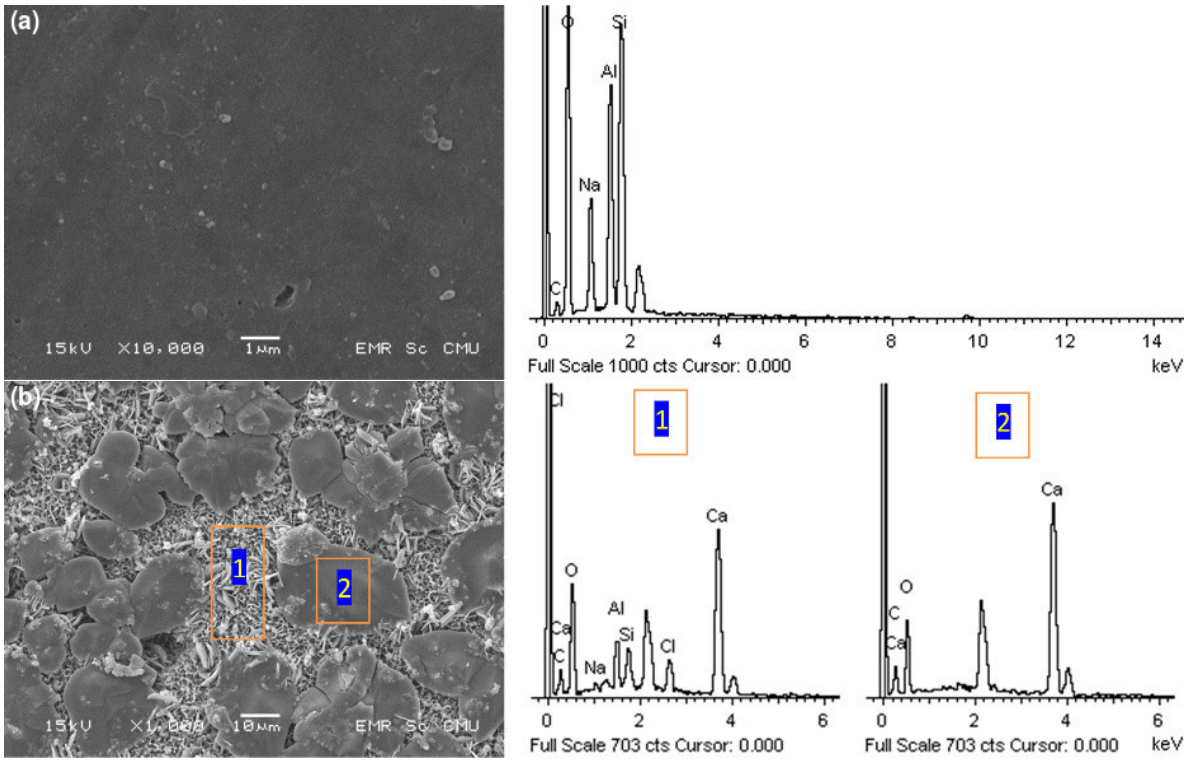

Fig. 1 SEM images of geopolymer surfaces before soaked in SBF solution; (a) control sample, (b) treated sample.

in a slight increase in strength compare to ambient curing condition[38]. Immersion of geopolymer in $CaCl_2$ solution increased the amount of calcium ion absorption and the chemically bonds with geopolymer components similar to the behaviour of cement material[31,32]. The surface hardness of the geopolymer was improved due to the ions charge-balancing between Ca^{2+} and Na^+ cations. The calcium component consequently precipitated and improved surface hardness. This thus favourably affected the strength development of geopolymer paste.

The results of the SEM studies on the geopolymer surfaces are shown in Fig. 1. The surface of control paste was relatively smooth with EDS spectra of Si, Al, O, and Na elements (Fig. 1a). These elements are the composition of kaolinite geopolymer[36,39]. After $CaCl_2$ treatment, the surface structures showed the clear deposits of calcium compounds as shown in Fig. 1b with two different crystallized forms. The first form was the tiny crystals in area 1 which were the plates of calcium and chloride compounds precipitated in the geopolymer structure. Related EDS spectra showed mainly high peaks of Ca and Cl and low content of Na, Si, Al, and C elements. The second form was the large crystal plate in area 2 which was identified as $CaCO_3$ by the EDS spectra of Ca, C, and O elements and by high peak of calcite in XRD patterns in Fig. 2. The results thus show that $CaCl_2$ was absorbed on kaolinite geopolymer surface by solution soaking. The follow-on induced carbonation reaction with CO_2 from the atmosphere resulted in the formation of $CaCO_3$ at the paste surface[26]:

$$CaCl_2 + CO_2 + H_2O \longrightarrow CaCO_3 + 2\,HCl.$$

The weak sodium can be leached out from the geopolymer structure[27] and charged-balance with calcium cations from $CaCl_2$[28]. This phenomenon promotes Ca^{2+} to form at the surface of geopolymer in the form of reactive calcium compounds and enhances the strength development[29]. The use of $CaCl_2$ promotes the strength of geopolymer and the biocompatible layers on geopolymer surface and thus results in a strong interfacial zone between geopolymer and new growth apatite.

Apatite formation after SBF immersion

The surface characteristic of geopolymer after soaking in SBF solution is presented in Fig. 3. For the control mix, the apatite-like layer formed after

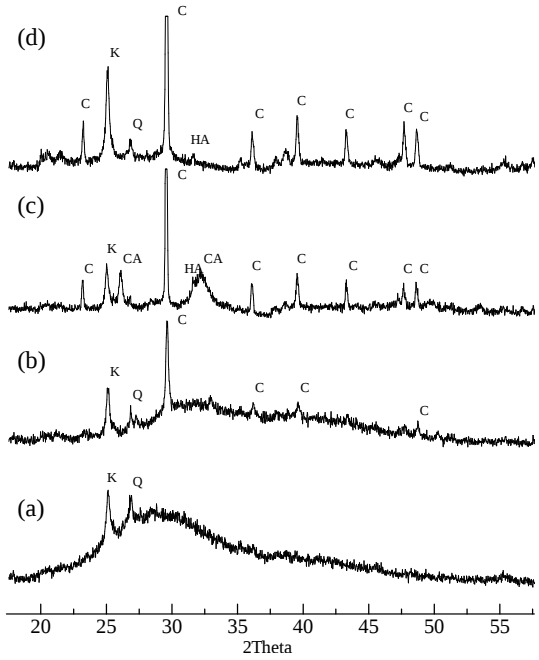

Fig. 2 XRD patterns of geopolymer paste discs; (a) control; (b) treated sample; (c) treated sample after 3 days in SBF; (d) treated sample after 28 days in SBF.

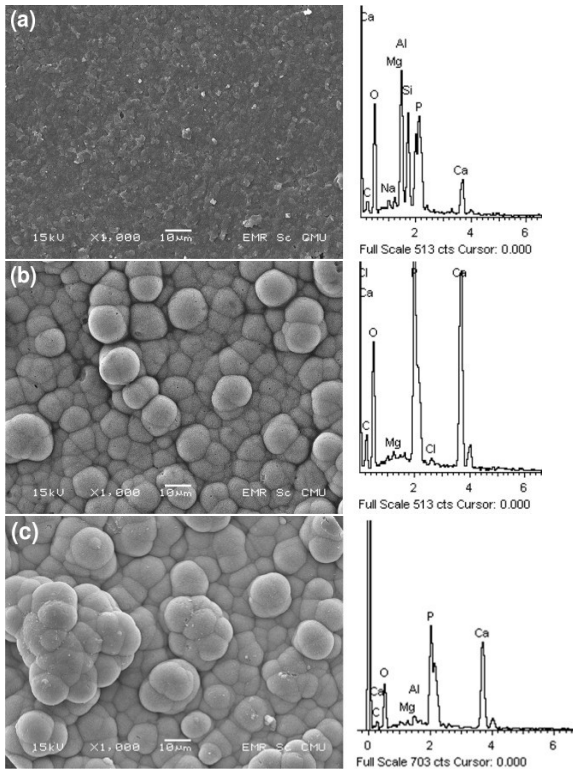

Fig. 3 SEM images of geopolymer surfaces after soaked in SBF solution; (a) control sample after 28 days in SBF solution; (b) treated sample after 3 days in SBF solution; (c) treated sample after 28 days in SBF solution.

28 days of immersion was still not clearly visible (Fig. 3a), but the EDS spectra presented Ca and P as possibly precipitated from SBF solution. Geopolymer without $CaCl_2$ treatment was poor in bioactivity due to the lack of Ca^{2+} ions to act as nucleation sites for apatite precipitation. For the $CaCl_2$ treated geopolymer after 3 and 28 days of soaking in SBF, spherical particles of approximately 10 μm in diameter of apatite phase were clearly observed covering the entire paste surface (Figs. 3b and 3c). The Ca/P molar ratio from EDS analysis was 1.51 and 1.56 represented precipitated HA and/or β-tricalcium phosphate (β-TCP)[40,41]. The morphology of the formed bioapatite layer was similar to the other published results[42,43]. The crystallographic study by XRD technique presented in Fig. 2 indicated the high amount of observed hydroxyapatite and chlorapatite on the $CaCl_2$ treated sample after soaked in SBF. The pattern of observed hydroxyapatite crystal in X-ray patterns was similar to the previous published results[44]. The X-ray pattern also displayed high $CaCO_3$ peak at 29.5° 2θ which correlated well with the FTIR result. The presence of high $CaCO_3$ at the geopolymer surface is very positive in promoting the high apatite precipitation[11]. This showed that calcium compound especially $CaCO_3$ deposited on the geopolymer surface as a result of $CaCl_2$ treatment[10]. Metakaolin geopolymer without calcium treatment exhibited only a small apatite forming after immersion for 21 days[45]. The treatment by $CaCl_2$ improved the forming of apatite as dense apatite was formed after only 3 days of soaking in SBF compared to the 7 days of soaking for calcium rich white cement[46]. The fast forming of hydroxyapatite is considered advantageous for implant materials[47,48].

The EDS spectra as shown in Fig. 3 suggested the forming of dendrite of carbonate substituted hydroxyapatite[49] which was rich in Ca, P, C, Cl, and Mg similar to glass ceramic systems[50]. Side view of apatite growing by SEM image as shown in Fig. 4 showed the interfacial zone of geopolymer and formed apatite. Microstructure of geopolymer matrix on the left showed a dense surface with platy shape of kaolinite as also reported elsewhere[51]. The apatite structure on the right was very dense and covered the thickness around 15 μm. The side view clearly identified the good apatite forming and

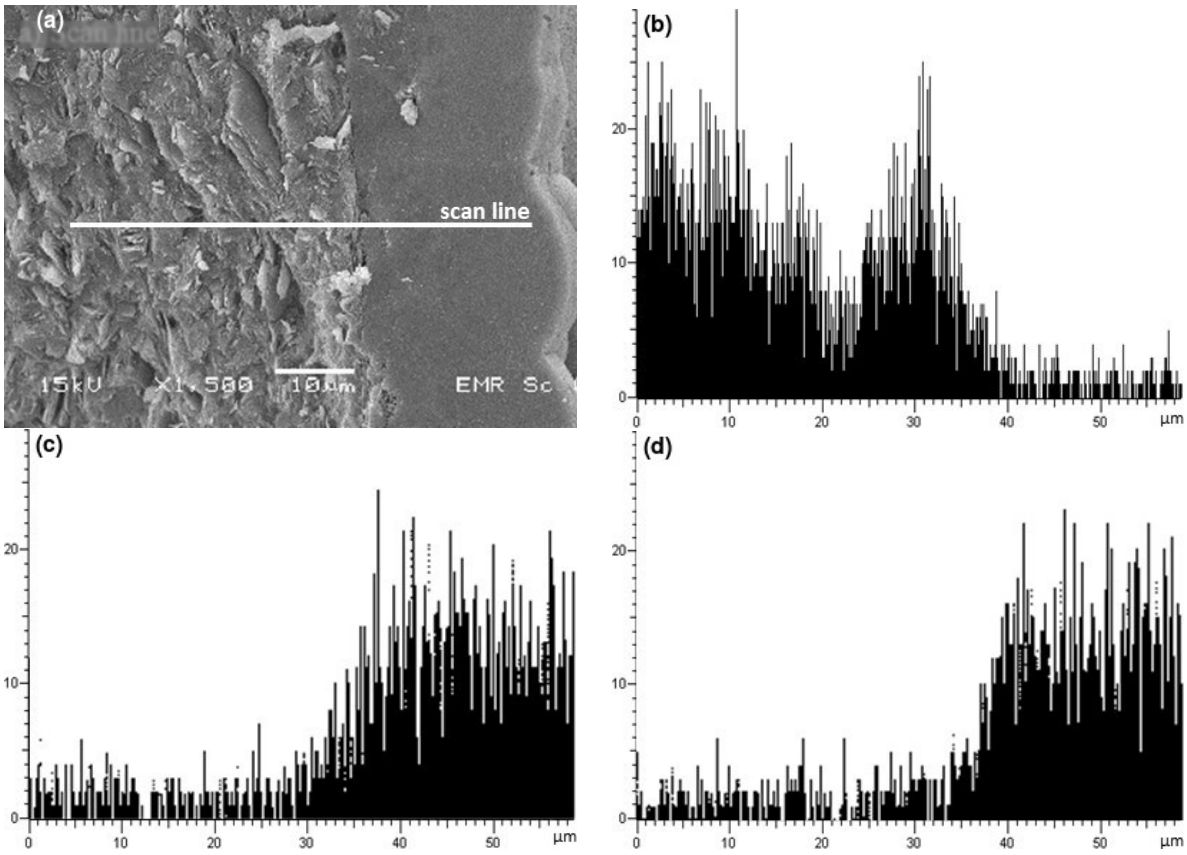

Fig. 4 (a) Side view of apatite forming by SEM and line analysis of (b) Si, (c) Ca, and (d) P.

interface bonding. Additionally, the line analysis showed distributions of important elements, viz., Ca, P, and Si across the transition zone. For Ca and P, spectrum line peak raised at transition zone of geopolymer and apatite layer was clearly evident and the results correlated well with the SEM image. For Si, the spectrum showed migration of Si by illustrating the spectrum dropped towards the transition zone and increased again at the transition zone. When material came into contact with SBF solution, the Si-OH rich layer was formed and supported the migration of Ca^{2+} ions to be incorporated with PO_4^{3-} ions from SBF solution and formed calcium rich film which continuously precipitated as apatite layer[52,53]. It had also been shown that the high reactivity of apatite forming produced a thick silica gel layer between the apatite layer and the glass material[54]. The FTIR spectra of geopolymer after 28 days soaking in SBF solution is shown in Fig. 5. $CaCl_2$ treated sample presented PO_4^{3-} band peak at 1030 cm^{-1} and apatitic PO_4^{3-} at 620 and 578 cm^{-1}. The phosphate absorption bands of PO (cryst) of PO_4^{3-} indicated the formation of apatite[55,56]. The presence of high PO band peak confirmed the enhancement of apatite precipitation on geopolymer surface with $CaCl_2$ treatment. The SBF soaking of 28 days significantly showed higher band peak size of PO at the wavenumber around 1030 cm^{-1} than 3 days of soaking which represented the additional precipitation of apatite layer on sample surface with time. Moreover, treated sample showed the bending vibration peak of CO at 870 cm^{-1} corresponding to CO_3^{2-} functional group of $CaCO_3$. The presence of $CaCO_3$ was an indication of the promotion of apatite forming. For untreated samples, no apatitic or $CaCO_3$ band peaks were significantly observed. Similarly, the SEM results showed no crystalline shape in the untreated sample.

The pH of the SBF solution after soaking for up to 28 days is shown in Fig. 6. Measured pH value of SBF solution increased from 7.40–7.81 for untreated paste. For the paste with $CaCl_2$ treatment, the increase in pH value was smaller at 7.59. This finding was in line with the other published results which reported the lower pH values of SBF solution for the $CaCl_2$ treated samples than those of other

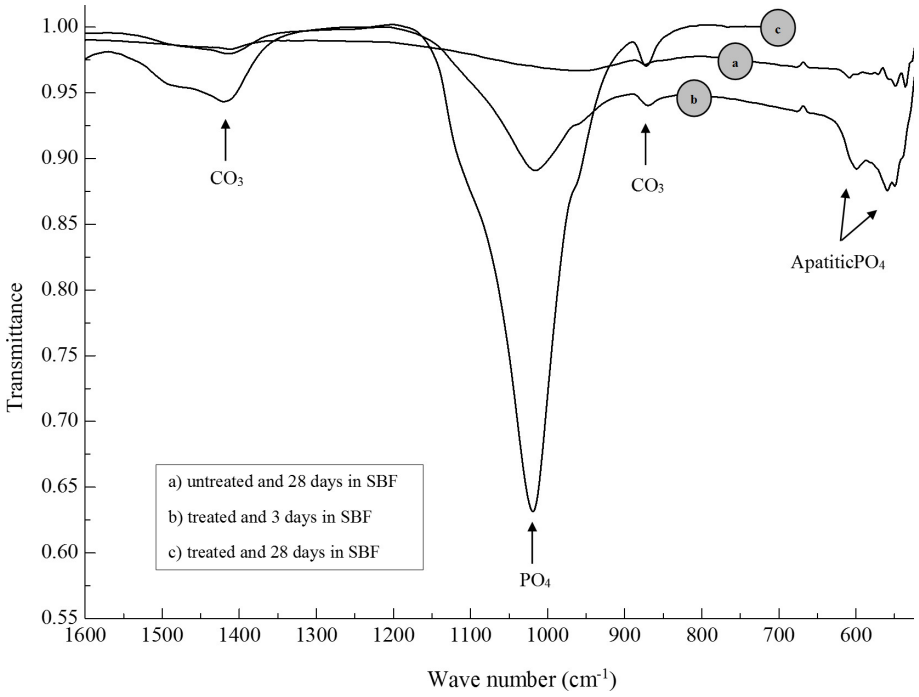

Fig. 5 FTIR spectra of geopolymer surface.

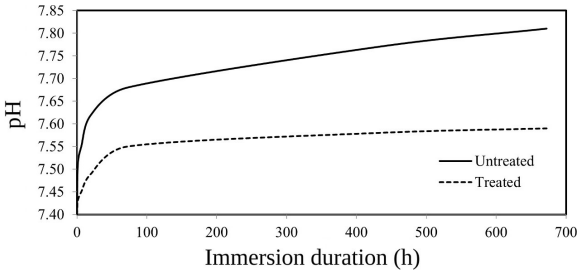

Fig. 6 pH of SBF solution immersed with geopolymer discs.

cementitious materials[10,57]. The pH increase was a typical result of leaching of NaOH from material to SBF solution. The treatment process possibly reduced leaching ability of NaOH due to the forming of calcium compound layer. It can be concluded that $CaCl_2$ treatment of geopolymer samples lowers the pH of the immersed solution and additionally promote the geopolymer surface for the growth of apatite.

CONCLUSIONS

Treatment of calcined kaolin geopolymer surface by soaking in 0.5 molar concentration of $CaCl_2 \cdot 2H_2O$ solution for 24 h can embed calcium, chloride, and carbonate compounds to the material surface. These reactive calcium rich layers promote the apatite precipitation. A good apatite forming on treated calcined kaolin geopolymer surface was obtained after 3 days in SBF immersion. The $CaCl_2$ treatment not only enhances the early compressive strength by the process of moist curing but also renders low pH induction after the contact with SBF solution. This high rate of apatite forming and low alkalinity are preferable for the implant material.

Acknowledgements: This work was financially supported by the Higher Education Research Promotion and National Research University Project of Thailand, Office of the Higher Education Commission, through the Advanced Functional Materials Cluster of Khon Kaen University; and Khon Kaen University and the Thailand Research Fund (TRF) under the TRF-Royal Golden Jubilee Ph.D. program (Grant no. PHD/0143/2554); Post-doctoral training program (Grant no. 58110), Graduate school, Khon Kaen University and TRF Senior Research Scholar Contract No. RTA5780004.

REFERENCES

1. MacKenzie KJD, Welter M (2014) Geopolymer (aluminosilicate) composites: synthesis, properties and applications. In: Low IM (ed) *Advances in Ceramic Matrix Composites*, Woodhead Publishing, pp 445–70.

2. Provis JL (2014) Geopolymers and other alkali activated materials: why, how, and what? *Mater Struct* **47**, 11–25.
3. Provis JL, van Deventer JSJ (2009) *Geopolymers: Structures, Processing, Properties and Industrial Applications*, 1st edn, Woodhead Publishing.
4. Hanjitsuwan S, Hunpratub S, Thongbai P, Maensiri S, Sata V, Chindaprasirt P (2014) Effects of NaOH concentrations on physical and electrical properties of high calcium fly ash geopolymer paste. *Cement Concr Compos* **45**, 9–14.
5. Hanjitsuwan S, Chindaprasirt P, Pimraksa K (2011) Electrical conductivity and dielectric property of fly ash geopolymer pastes. *Int J Miner Metall Mater* **18**, 94–9.
6. Zhang Y, Liu L (2013) Fly ash-based geopolymer as a novel photocatalyst for degradation of dye from wastewater. *Particuology* **11**, 353–8.
7. Forsgren J, Pedersen C, Strømme M, Engqvist H (2011) Synthetic geopolymers for controlled delivery of oxycodone: adjustable and nanostructured porosity enables tunable and sustained drug release. *PLoS ONE* **6**, e17759.
8. Abdullah D, Pitt Ford TR, Papaioannou S, Nicholson J, McDonald F (2002) An evaluation of accelerated Portland cement as a restorative material. *Biomaterials* **23**, 4001–10.
9. Zhang Y, Wang D, Wang F, Jiang S, Shu Y (2015) Modification of dicalcium silicate bone cement biomaterials by using carboxymethyl cellulose. *J Non Cryst Solid* **426**, 164–8.
10. Coleman NJ, Nicholson JW, Awosanya K (2007) A preliminary investigation of the in vitro bioactivity of white Portland cement. *Cement Concr Res* **37**, 1518–23.
11. Hench LL (1991) Bioceramics: From Concept to Clinic. *J Am Ceram Soc* **74**, 1487–510.
12. Hench LL, Andersson Ö (1993) Bioactive glasses. In: Hench LL, Wilson J (eds) *An Introduction to Bioceramics*, World Scientific, Singapore, pp 41–62.
13. Kokubo T, Takadama H (2006) How useful is SBF in predicting in vivo bone bioactivity? *Biomaterials* **27**, 2907–15.
14. Hench LL (1998) Biomaterials: a forecast for the future. *Biomaterials* **19**, 1419–23.
15. Fahami A, Nasiri-Tabrizi B, Ebrahimi-Kahrizsangi R (2013) Mechanosynthesis and characterization of chlorapatite nanopowders. *Mater Lett* **110**, 117–21.
16. Gallego D, Higuita N, Garcia F, Ferrell N, Hansford DJ (2008) Bioactive coatings on Portland cement substrates: surface precipitation of apatite-like crystals. *Mater Sci Eng C* **28**, 347–52.
17. Martin S, Derrien AC, Oudadesse H, Chaucel-Lebret D, Cathelineau G (2005) Implantation of aluminosilicate/calcium phosphate materials: Influence on bone formation in rabbit tibias. *Eur Cell Mater* **9**, Suppl. 1, 71–2.
18. Oudadesse H, Derrien AC, Martin S, Chaair H, Cathelineau G (2008) Surface and interface investigation of aluminosilicate biomaterial by the "in vivo" experiments. *Appl Surf Sci* **255**, 593–6.
19. Leivo J, Meretoja V, Vippola M, Levänen E, Vallittu P, Mäntylä TA (2006) Sol-gel derived aluminosilicate coatings on alumina as substrate for osteoblasts. *Acta Biomater* **2**, 659–68.
20. Todea M, Vanea E, Bran S, Berce P, Simon S (2013) XPS analysis of aluminosilicate microspheres bioactivity tested in vitro. *Appl Surf Sci* **270**, 777–83.
21. MacKenzie KJD, Rahner N, Smith ME, Wong A (2010) Calcium-containing inorganic polymers as potential bioactive materials. *J Mater Sci* **45**, 999–1007.
22. Todea M, Frentiu B, Turcu RFV, Berce P, Simon S (2012) Surface structure changes on aluminosilicate microspheres at the interface with simulated body fluid. *Corrosion Sci* **54**, 299–306.
23. Catauro M, Bollino F, Papale F, Lamanna G (2014) Investigation of the sample preparation and curing treatment effects on mechanical properties and bioactivity of silica rich metakaolin geopolymer. *Mater Sci Eng C* **36**, 20–4.
24. Oudadesse H, Derrien AC, Lefloch M, Davidovits J (2007) MAS-NMR studies of geopolymers heat-treated for applications in biomaterials field. *J Mater Sci* **42**, 3092–8.
25. Torkittikul P, Chaipanich A (2012) Optimization of calcium chloride content on bioactivity and mechanical properties of white Portland cement. *Mater Sci Eng C* **32**, 282–9.
26. Rattanasak U, Pankhet K, Chindaprasirt P (2011) Effect of chemical admixtures on properties of high-calcium fly ash geopolymer. *Int J Miner Metall Mater* **18**, 364–9.
27. Škvára F, Šmilauer V, Hlaváček P, Kopecký L, Cílová Z (2012) A weak alkali bond in (N, K)–A–S–H gels: evidence from leaching and modeling. *Ceram Silikáty* **56**, 374–82.
28. O'Connor SJ, MacKenzie KJD, Smith ME, Hanna JV (2010) Ion exchange in the charge-balancing sites of aluminosilicate inorganic polymers. *J Mater Chem* **20**, 10234–40.
29. Van Deventer JSJ, Provis JL, Duxson P (2012) Technical and commercial progress in the adoption of geopolymer cement. *Miner Eng* **29**, 89–104.
30. Ridtirud C, Chindaprasirt P (2007) Calcined Ranong kaolin geopolymer mortar. *Khon Kaen Univ Eng J* **34**, 231–42. [in Thai]
31. Shiozawa M, Takahashi H, Iwasaki N, Uo M (2013) Effect of calcium chloride solution immersion on surface hardness of restorative glass ionomer cements. *Dent Mater J* **32**, 828–33.
32. Shiozawa M, Takahashi H, Iwasaki N, Wada T, Uo M (2014) Effect of immersion time of restorative glass ionomer cements and immersion duration in calcium

chloride solution on surface hardness. *Dent Mater* **30**, e377–83.
33. Greenspan DC, Zhong JP, LaTorre GP (1994) Effect of surface area to volume ratio on in vitro surface reactions of bioactive glass particulates. In: Andersson ÖH, Yli-Urpo A (eds) *Bioceramics, Proceedings of the 7th International Symposium on Ceramics in Medicine*, Turku, Finland, pp 55–60.
34. ASTM C109 (2002) Standard test method of compressive strength of hydrualic cement mortars (using 2-in. or [50-mm] cube speciments), ASTM International, West Conshohocken, PA 04.01.
35. Liew YM, Kamarudin H, Mustafa Al Bakri AM, Bnhussain M, Luqman M, Khairul Nizar I, Ruzaidi CM, Heah CY (2012) Optimization of solids-to-liquid and alkali activator ratios of calcined kaolin geopolymeric powder. *Construct Build Mater* **37**, 440–51.
36. Yunsheng Z, Wei S, Zongjin L (2010) Composition design and microstructural characterization of calcined kaolin-based geopolymer cement. *Appl Clay Sci* **47**, 271–5.
37. Zuhua Z, Xiao Y, Huajun Z, Yue C (2009) Role of water in the synthesis of calcined kaolin-based geopolymer. *Appl Clay Sci* **43**, 218–23.
38. Pangdaeng S, Phoo-ngernkham T, Sata V, Chindaprasirt P (2014) Influence of curing conditions on properties of high calcium fly ash geopolymer containing Portland cement as additive. *Mater Des* **53**, 269–74.
39. Xu H, Van Deventer JSJ (2000) The geopolymerisation of alumino-silicate minerals. *Int J Miner Process* **59**, 247–66.
40. Dorozhkin SV (2010) Bioceramics of calcium orthophosphates. *Biomaterials* **31**, 1465–85.
41. Raynaud S, Champion E, Bernache-Assollant D, Thomas P (2002) Calcium phosphate apatites with variable Ca/P atomic ratio I. Synthesis, characterisation and thermal stability of powders. *Biomaterials* **23**, 1065–72.
42. Wang XJ, Li YC, Lin JG, Yamada Y, Hodgson PD, Wen CE (2008) In vitro bioactivity evaluation of titanium and niobium metals with different surface morphologies. *Acta Biomater* **4**, 1530–5.
43. Li P, Ohtsuki C, Kokubo T, Nakanishi K, Soga N, Nakamura T (1992) Apatite formation induced on silica gel in a simulated body fluid. *J Am Ceram Soc* **75**, 2094–7.
44. Arsad MSM, Lee PM, Hung LK (2011) Synthesis and characterization of hydroxyapatite nanoparticles and β-TCP particles. In: *2nd International Conference on Biotechnology and Food Science, IPCBEE*, vol 7, IACSIT Press, Singapore, pp 184–8.
45. Catauro M, Bollino F, Kansal I, Kamseu E, Lancellotti I, Leonelli C (2012) Mechanical and biological characterization of geopolymers for potential application as biomaterials. *AZojomo*, doi: 10.2240/azojomo0322.
46. Chaipanich A, Torkittikul P (2011) Microstructure: surface and cross-sectional studies of hydroxyapatite formation on the surface of white Portland cement paste in vitro. *Appl Surf Sci* **257**, 8385–90.
47. Gu YW, Khor KA, Cheang P (2004) Bone-like apatite layer formation on hydroxyapatite prepared by spark plasma sintering (SPS). *Biomaterials* **25**, 4127–34.
48. Zhong JP, Greenspan DC, Feng JW (2002) A microstructural examination of apatite induced by bioglass in vitro. *J Mater Sci Mater Med* **13**, 321–6.
49. Medri V, Papa E, Landi E (2013) Behavior of alkali bonded silicon carbide foams in modified synthetic body fluid. *Mater Lett* **106**, 377–80.
50. Radev L, Hristov V, Michailova I, Samuneva B (2009) Sol-gel bioactive glass-ceramics. Part II: glass-ceramics in the $CaO\text{-}SiO_2\text{-}P_2O_5\text{-}MgO$ system. *Cent Eur J Chem* **7**, 322–7.
51. Cao DG, Su DG (2005) Structure characterization for the geopolymer of sodium silicate and metakaolin. *J Chongqing Univ* **4**, 70–3.
52. Kim HM, Himeno T, Kokubo T, Nakamura T (2005) Process and kinetics of bonelike apatite formation on sintered hydroxyapatite in a simulated body fluid. *Biomaterials* **26**, 4366–73.
53. Branda F, Fresa R, Costantini A, Buri A (1996) Bioactivity of $1.25CaO \cdot SiO_2$ glass: an FTIR and X-ray study on powdered samples. *Biomaterials* **17**, 2247–51.
54. Ohtsuki C, Kamitakahara M, Miyazaki T (2009) Bioactive ceramic-based materials with designed reactivity for bone tissue regeneration. *J Roy Soc Interface* **6**, S349–60.
55. Li HC, Wang DG, Hu JH, Chen CZ (2014) Influence of fluoride additions on biological and mechanical properties of $Na_2O\text{-}CaO\text{-}SiO_2\text{-}P_2O_5$ glass-ceramics. *Mater Sci Eng C* **35**, 171–8.
56. Prokopowicz M, Szewczyk A, Sawicki W (2014) The bioactivity studies of drug-loaded mesoporous silica-polydimethylsiloxane xerogels using FTIR and SEM/XEDS. *J Mol Struct* **1056–7**, 262–6.
57. Torkittikul P, Chaipanich A (2009) Investigation of the mechanical and in vitro biological properties of ordinary and white Portland cements. *Sci Asia* **35**, 358–64.

RSC Advances

PAPER

View Article Online
View Journal | View Issue

Open Access Article. Published on 16 January 2017. Downloaded on 17/02/2017 03:28:00.
This article is licensed under a Creative Commons Attribution-NonCommercial 3.0 Unported Licence.

Cite this: *RSC Adv.*, 2017, **7**, 4092

Improved giant dielectric properties of $CaCu_3Ti_4O_{12}$ *via* simultaneously tuning the electrical properties of grains and grain boundaries by F^- substitution

Jutapol Jumpatam,[a] Bundit Putasaeng,[b] Narong Chanlek,[c] Pinit Kidkhunthod,[c] Prasit Thongbai,*[d] Santi Maensiri[e] and Prinya Chindaprasirt[f]

Received 26th November 2016
Accepted 23rd December 2016

DOI: 10.1039/c6ra27381e

www.rsc.org/advances

A novel concept to simultaneously modify the electric responses of the grain and grain boundaries of $CaCu_3Ti_4O_{12}$ ceramics was proposed, involving doping with F^- anions to improve the giant dielectric properties. The grain growth rate of $CaCu_3Ti_4O_{12}$ ceramics was enhanced by doping with F^- anions, which were found to be homogeneously dispersed in the microstructure. Substitution of F^- anions can cause an increase in the resistance of the insulating grain boundary and a decrease in the grain resistance. The former originated from the ability of the F^- dopant to enhance the Schottky barrier height at the grain boundaries, leading to a great decrease in the dielectric loss tangent by a factor of 5 ($\tan\delta < 0.1$). The latter was primarily attributed to the increase in Ti^{3+} and Cu^+ concentrations due to charge compensation, resulting in a significantly enhanced intensity of space charge polarization at the grain boundaries. This is the primary cause of the increase in dielectric permittivity from $\approx 10^4$ to $\approx 10^5$. The giant dielectric and electrical properties were well described by the Maxwell–Wagner polarization relaxation based on the internal barrier layer capacitor model of Schottky barriers at the grain boundaries.

1. Introduction

Recently, oxide materials with giant dielectric permittivity have found an important role in microelectronic devices and high-density storage applications such as capacitors and memory devices.[1–4] One of the most interesting giant dielectric materials is $CaCu_3Ti_4O_{12}$ (CCTO) ceramics. CCTO exhibited giant dielectric permittivity ($\varepsilon' > 10^4$ at 1 kHz) over a wide temperature range from 100 to 600 K.[5] The ε' value of CCTO ceramics was also weakly dependent on frequency in the radio frequency range. Unfortunately, the loss tangent ($\tan\delta$) of CCTO was still too large for practical applications in ceramic capacitors.[6–19]

Even now, the origin of giant dielectric response is still open to scientific debate. Most research groups believe that the extrinsic origin of the internal barrier layer capacitance (IBLC) mechanism at grain boundaries (GBs) is the primary cause of the giant dielectric response in CCTO ceramics.[12,14,20–23] According to the IBLC mechanism, the giant dielectric response in a polycrystalline ceramic is driven by its electrically heterogeneous microstructure. This special microstructure can be fabricated using a one-step processing method that forms insulating GBs sandwiched between n-type semiconducting grains. The electrical responses of the grain and GB can have a remarkable influence on the dielectric properties of CCTO ceramics.[12,13,15,22] Moreover, due to the existence of this special microstructure, CCTO ceramics can also exhibit the non-ohmic properties (or nonlinear current density–electric field, J–E).[24,25] This special behavior is believed to originate from the existence of an intrinsic potential barrier (*i.e.*, Schottky barrier) at GBs.[20] The presence of an electrostatic barrier at the GBs of CCTO ceramic was clearly confirmed using Kervin probe force microscopy.[24]

To improve the dielectric properties of CCTO ceramics, most investigations have focused on substitution of one of several doping cations into CCTO ceramics to tune the electrical properties of the grains and GBs. It has been widely demonstrated that enhancement of the GB resistance (R_{gb}) can reduce the low-frequency $\tan\delta$ value.[15,23,26] According to the space

[a]*Materials Science and Nanotechnology Program, Faculty of Science, Khon Kaen University, Khon Kaen 40002, Thailand*

[b]*National Metal and Materials Technology Center, National Science and Technology Development Agency, Thailand Science Park, Pathumthani 12120, Thailand*

[c]*Synchrotron Light Research Institute (Public Organization), 111 University Avenue, Muang District, Nakhon Ratchasima 30000, Thailand*

[d]*Integrated Nanotechnology Research Center (INRC), Department of Physics, Faculty of Science, Khon Kaen University, Khon Kaen 40002, Thailand. E-mail: pthongbai@kku.ac.th; Fax: +66 43 202374; Tel: +66 84 4190266*

[e]*Institute of Science, School of Physics, Suranaree University of Technology, Nakhon Ratchasima 30000, Thailand*

[f]*Sustainable Infrastructure Research and Development Center, Department of Civil Engineering, Faculty of Engineering, Khon Kaen University, Khon Kaen 40002, Thailand*

This journal is © The Royal Society of Chemistry 2017

Open Access Article. Published on 16 January 2017. Downloaded on 17/02/2017 03:28:00.
This article is licensed under a Creative Commons Attribution-NonCommercial 3.0 Unported Licence.

charge polarization theory (or interfacial polarization), an increase in mobile charges inside the semiconducting grains can lead to the possibility of accumulating free charges at the interface of insulating layers. This gives rise to a stronger intensity of the polarization at internal insulating interfaces, leading to an increase in ε'. The giant dielectric properties of CCTO ceramics were first reported by Subramanian *et al.*[6] There are further several reports of dopant cations substituted into CCTO ceramic such as Sr^{2+},[23] La^{3+},[7] Ni^{2+},[27] Mg^{2+},[9,28–30] Zn^{2+},[31,32] Ga^{3+},[14] Zr^{4+},[33,34] Sn^{4+},[11] Nb^{5+},[8] Ta^{5+} (ref. 12) and W^{6+}.[13,35] Substitution of many cations into Ca^{2+}, Cu^{2+} and Ti^{4+} sites in CCTO ceramics have significant effects on the values of their ε', tan δ, electrical conductivity of the GBs (σ_{gb}) and activation energies at the GBs (E_{gb}) and inside the grain (E_g). Usually, most of these dopants can be successfully used to improve a particular dielectric property (*e.g.*, to reduce tan δ or enhance ε'), while they simultaneously worsen other important dielectric properties of these materials. For example, substitution of higher cations into Ti^{4+} sites would increase free charges inside the semiconducting grains due to the excess electron of a dopant (*e.g.*, Nb^{5+} or Ta^{5+}). This can cause an increase in ε', which resulted from the enhanced space charges at the insulating interfaces. Unfortunately, it also causes a large decrease in R_{gb}, leading to a significant increase in a low-frequency tan δ.[8,12] Alternatively, doping CCTO with Mg^{2+} into Cu^{2+} sites can decrease tan δ However, the ε' value of Mg-doped CCTO was also decreased due to the decrease in free charges inside the grains, considering by the increase in R_g.[9,36]

It is expected that doping CCTO with an anion can increase free charges inside the grains due to charge compensation. Substitution of F^- into O^{2-} sites is electrically compensated by reduction of valance state of Ti^{4+} to Ti^{3+} and Cu^{2+} to Cu^+. It was clearly demonstrated that filling oxygen vacancies at the GBs can strongly increase the R_{gb} value by annealing in an O_2 atmosphere.[15,20,37] Alternatively, R_{gb} can be reduced by creating the oxygen vacancies at the grain boundaries *via* annealing in a N_2 atmosphere. Thus, it is also expected that substitution of F^- anions may have no effect on the insulating properties of the GBs because oxygen vacancies along the GBs are usually filled during cooling step of the sintering process. This also helps retain the insulating nature of the GBs. To the best our knowledge, there have been few reports of an anion dopant being substituted into CCTO ceramics.[38] The effects of an anion dopant on the microstructure and electrical properties of the grain and GB have never been reported.

In this work, a new strategy to improve the dielectric properties of CCTO ceramics was used by doping with F^- anions to modify the electrical responses of the grains and GBs. The effects of F^- anions on the microstructural evolution and associated dielectric properties were studied and discussed. As expected, doping CCTO ceramics with F^- anions at O^{2-} sites resulted in improved dielectric properties *via* a large enhancement of ε' and significant decrease in tan δ.

2. Experimental procedure

$CaCu_3Ti_4O_{12-x}F_x$ ceramics, where $x = 0$, 0.05, 0.1, and 0.2 (referred to as the CCTO, F05, F10 and F20 samples, respectively), were prepared using a solid state reaction method. The starting materials used were $CaCO_3$ (Aldrich, ≥99.0% purity), CuO (Merck, 99% purity), CuF_2 (Sigma-Aldrich, 99.9% purity) and TiO_2 (Sigma-Aldrich, 99.9% purity). First, a stoichiometric mixture of the starting materials for each composition was mixed by ball milling using zirconia (ZrO_2) media in ethanol for 12 h. Second, the mixed slurries were dried and calcined at 900 °C for 15 h. Then, the calcined powders were ground and pressed into pellets with 9.5 mm in diameter and 1–2 mm in thickness by a uniaxial compression at 200 MPa. Finally, these pellets were sintered in air at 1075 °C for 3 h.

The phase composition and crystal structure were characterized using X-ray diffraction (XRD; PANanalytical EMPYREAN). Rietveld quantitative phase analysis was done using the X'Pert High Score Plus v3.0e software package by PANalytical. The as-sintered ceramics were carefully polished to obtain smooth surfaces. The grain and GB structure of the polished-samples was formed by thermally etching at 1050 °C for 1 h. Surface morphologies of sintered ceramics were revealed using scanning electron microscopy (SEM; SEC, SNE-4500M). Elemental distribution of the F dopant atoms and the major elements (*i.e.*, Ca, Cu, Ti, and O) in the sintered CCTO ceramics was examined using a field-emission scanning electron microscopy (FE-SEM) with energy-dispersive X-ray analysis (EDX) (HITACHI SU8030, Japan). X-ray Absorption Near Edge Structure (XANES) spectra were collected at the SUT-NANOTEC-SLRI XAS beamline (BL5.2) (using an electron energy of 1.2 GeV, a bending magnet, beam current of 80–150 mA, and 1.1 to 1.7 × 10^{11} photons per s) at the Synchrotron Light Research Institute (SLRI), Nakhon Ratchasima, Thailand. Details of this characterization technique have been published.[26] The normalized XANES data were processed and analyzed after background subtraction in the pre-edge and post-edge region using ATHENA software that is included in the IFEFFIT package.[39] The chemical states of Cu and Ti were analyzed using X-ray photoelectron spectroscopy (XPS), PHI5000 VersaProbe II, ULVAC-PHI, Japan) at the SUT-NANOTEC-SLRI Joint Research Facility, Synchrotron Light Research Institute (SLRI), Thailand. The XPS spectra were fitted using PHI MultiPak XPS software with a combination of Gaussian–Lorentzian lines.

Before electrical measurements, both surfaces of the sintered ceramics were polished until smooth, washed, and dried at 150 °C overnight. The polished samples were coated by sputtering Au on their surfaces for 8 min at 25 mA using a Polaron SC500 sputter coating unit. The dielectric properties were measured over the temperature range of −70 to 220 °C using a KEYSIGHT E4990A Impedance Analyzer in the frequency range of 10^2 to 10^7 Hz with an oscillation voltage of 0.5 V. Each measurement temperature was kept constant with a precision of ±0.1 °C. Nonlinear *J–E* properties at room temperature (RT) were determined using a high voltage measurement unit (Keithley Model 247). The breakdown

Open Access Article. Published on 16 January 2017. Downloaded on 17/02/2017 03:28:00.
This article is licensed under a Creative Commons Attribution-NonCommercial 3.0 Unported Licence.

electric field (E_b) was achieved at $J = 1$ mA cm^{-2}. The nonlinear coefficient (α) was calculated using the following formula:

$$\alpha = \frac{\log(J_2/J_1)}{\log(E_2/E_1)} \quad (1)$$

where E_1 and E_2 are the applied electric fields, at $J_1 = 1$ and $J_2 = 10$ mA cm^{-2}, respectively.

3. Results and discussion

The crystal structure and phase composition of all the sintered ceramic samples were studied. Fig. 1 shows the Rietveld refinement profile fits of the XRD patterns for all the samples. The profile fits confirmed the formation of a single CCTO phase (JCPDS 75-2188) in the CCTO and all F$^-$-doped CCTO (CCTOF) ceramics. It was found that all the diffraction peaks were well indexed based on the bcc structure within space group $Im\bar{3}$. Impurities (*e.g.*, TiO_2, CuO, Cu_2O and $CaTiO_3$) were not seen in the profile fits. The lattice parameters (a) of all the samples are summarized in Table 1. The a values of all the samples can be compared to 7.391 Å for un-doped CCTO (JCPDS 75-2188). It is notable that the a values of CCTOF did not change with F$^-$ dopant concentration. This result is similar to that reported in previous work with $CaCu_3Ti_4O_{12-x}F_x$ where x = 0–0.2.[38] The unchanged lattice parameter was likely because the ionic radii of the substituted F$^-$ anion ($r_4 = 1.31$ Å) and the host O^{2-} ion ($r_4 = 1.38$ Å) are not greatly different.[40]

Surface morphologies of the CCTO and CCTOF ceramics sintered at 1075 °C for 3 h are shown in Fig. 2. As can be clearly seen, there was abnormal grain growth in the microstructure of the CCTO ceramic, where the large sized grains (≈30–50 μm) were surrounded by small grains (≈5–10 μm). This is generally reported in literature and was ascribed to the liquid phase sintering mechanism.[14,26,32] It was found that the mean grain size of CCTO ceramics was greatly enlarged by doping with F$^-$ anions. Almost all grains of the F05, F10 and F20 samples were very large (≈40–100 μm).

Usually, the grain growth mechanism of a polycrystalline ceramic is associated with mass transport by diffusion of ions (or atoms) across the GB layer. During sintering, the dopant directly melts and/or reacts with a small part of the major phase to form a eutectic liquid. These can cause a formation of a liquid phase in the microstructure. The liquid was present at the contact areas between the particles in the ceramic microstructure. This can contribute to promotion of the diffusion of ions. For polycrystalline ceramics, a liquid phase generally originates from a eutectic liquid. The eutectic temperature for

Table 1 Lattice parameter (a), dielectric permittivity (ε') and loss tangent (tan δ) at RT and 1 kHz, conduction activation energies of the grain (E_g) and grain boundary (E_{gb}), nonlinear coefficient (α) and nonlinear breakdown electric field (E_b)

Samples	a (Å)	ε'	tan δ	E_g	E_{gb}	α	E_b
CCTO	7.393(2)	23 263	0.145	0.083	0.630	3.77	308.1
F05	7.393(9)	69 732	0.098	0.091	0.696	3.57	345.5
F10	7.392(7)	81 306	0.077	0.091	0.714	3.58	331.5
F20	7.393(8)	98 396	0.087	0.116	0.739	4.18	345.8

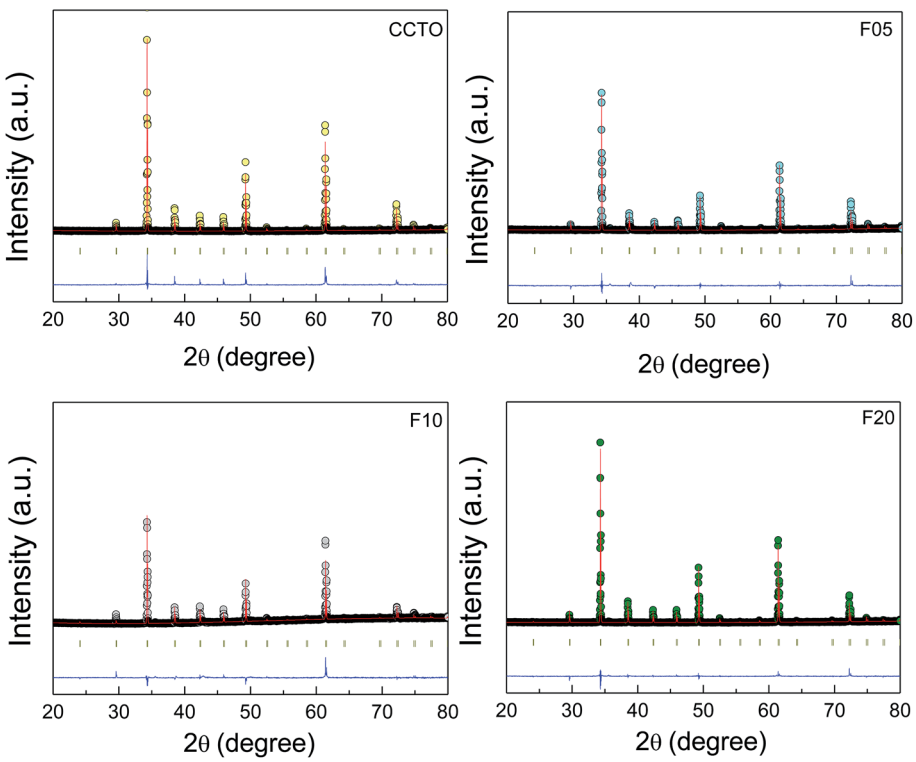

Fig. 1 Profile fits for the Rietveld refinements of the XRD patterns of CCTO, F05, F10 and F20 samples.

This journal is © The Royal Society of Chemistry 2017

Open Access Article. Published on 16 January 2017. Downloaded on 17/02/2017 03:28:00.
This article is licensed under a Creative Commons Attribution-NonCommercial 3.0 Unported Licence.

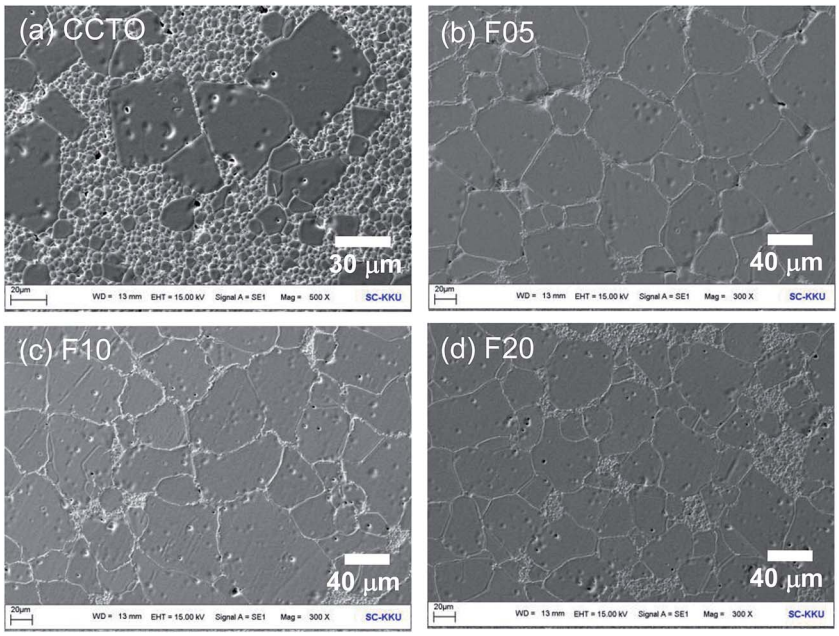

Fig. 2 SEM images of polished surfaces of (a) CCTO, (b) F05, (c) F10 and (d) F20 samples.

$CuO–TiO_2$ is about 950 °C for CCTO ceramics.[35] Although the liquid phase formed by melting of the dopant usually occurs in metallic systems, it is also possible in CCTOF ceramics. This is due to the low melting point of CuF_2 (836 °C). Thus, the formation of a liquid phase is likely caused by these two mechanisms. Enhancement of GB mobility resulted from the presence of the liquid phase(s) and was suggested an important factor for increasing grain growth rate in CCTOF ceramics.

Fig. 3 shows the SEM mapping images of the F05 sample. This result confirms the existence of all major elements (*i.e.*, Ca, Cu, Ti, and O) and confirms the homogeneous dispersion of F^- dopant in both of the grains and GBs. Segregation of the F^- dopant in any specific region was not seen. In contrast, segregation of Cu was observed along the GBs, which is also generally reported in previous studies.[22] This result strongly confirms that the liquid phase is closely associated with a Cu-rich phase, which likely originated from melting of CuF_2 and the eutectic phase of $CuO–TiO_2$.

The frequency dependence of the dielectric properties of all the ceramic samples is shown in Fig. 4 ε' was slightly dependent on frequency in the range of 10^2 to 10^5 Hz. Notably, ε' can be enhanced from $\approx 10^4$ to $\approx 10^5$ by doping with F^- anions. Considering the microstructural change in CCTOF ceramics, the enlarged grain size is one of the most important parameters that increased ε'. However, the linear and continuous increase in ε' of the F^--doped CCTO ceramics was not correlated with their grain sizes. ε' increased with increasing anion dopant concentration, but not for the mean grain sizes. Therefore, variation in ε' cannot be attributed to the change in the microstructure only. As illustrated in the inset of Fig. 4, a low-frequency tan δ of CCTO ceramics was greatly decreased by doping with F^- anions. At 10^2 Hz, the tan δ of the CCTOF

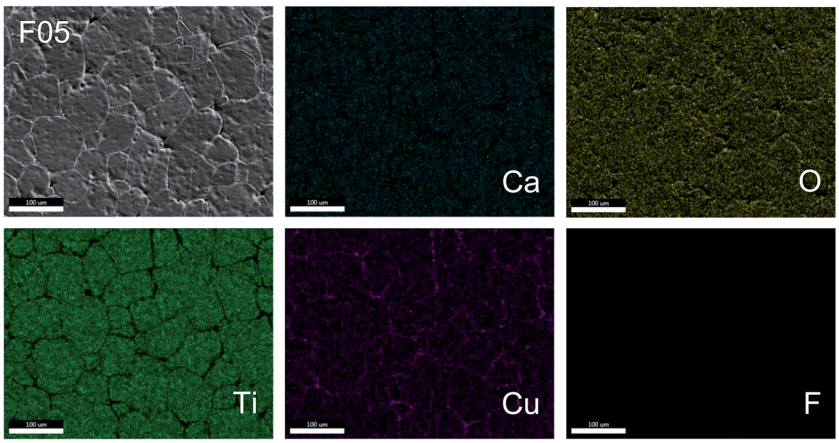

Fig. 3 Element mapping of the F05 sample for Ca, Cu, Ti, O and F.

Open Access Article. Published on 16 January 2017. Downloaded on 17/02/2017 03:28:00.
This article is licensed under a Creative Commons Attribution-NonCommercial 3.0 Unported Licence.

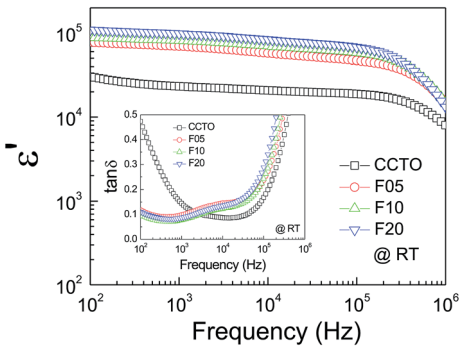

Fig. 4 Frequency dependency of dielectric permittivity (ε') at RT for CCTO, F05, F10 and F20 samples; inset show the loss tangent (tan δ) as a function of frequency at RT.

ceramics was reduced by a factor of 5. At frequencies higher than 10^5 Hz, the frequency dependent behaviors of tan δ for all of the samples were similar, *i.e.*, tan δ increased with increasing frequency. This indicates the dielectric relaxation behavior of primary polarization, which will be discussed below. The ε' and tan δ values at RT and 1 kHz of all the ceramic samples are summarized in Table 1. It is notable that the low-frequency tan δ of the CCTOF ceramics was significantly reduced to <0.1, while ε' greatly increased. Generally, this result is hard to achieve in CCTO ceramics because variations in tan δ and ε' values are usually directly proportional. The ε' and tan δ values of the CCTO and CCTOF ceramics compared to those reported in literature for both of un-doped and metal ions-doped CCTO ceramics prepared by using different method and sintered under various conditions are shown in Table 2.

The dielectric relaxation behavior of CCTO and CCTOF ceramics was studied. As shown in Fig. 5, two dielectric relaxations were observed in distinct frequency ranges. The low-frequency dielectric relaxation likely originated from the sample-electrode effect.[41] The relatively high-frequency dielectric relaxation (*i.e.*, the primary relaxation) has widely been accepted as associated with the IBLC effect, *i.e.*, the Maxwell–Wagner polarization relaxation.[13,21] The step-like decrease in ε' and relaxation peak of ε'' (ε'' is the imaginary part of the complex dielectric permittivity or dielectric loss, $\varepsilon'' = \varepsilon' \times \tan\delta$) shifted to a higher frequency with increasing temperature, indicating a thermally activated relaxation mechanism. The activation energy for dielectric relaxation can be calculated from the critical frequency (f_{max}) at various temperatures at which the relaxation peak appeared as:

$$f_{max} = f_0 \exp\left(\frac{-E_a}{k_B T}\right), \quad (2)$$

where f_0 is the pre-factor, E_a is the activation energy required for relaxation process, T is absolute temperature and k_B is Boltzmann constant. The frequency dependence of f_{max} for all the samples obeyed the Arrhenius law in eqn (2), inset of Fig. 5(d). The E_a values of the CCTO, F05, F10 and F20 samples were about 0.096, 0.096, 0.099 and 0.115 eV, respectively. These values are comparable to the reported values of 0.103 eV,[32] 0.011 eV (ref. 11) and 0.101 eV.[28] Doping CCTO with F^- anions into O^{2-} sites has a small influence on the dielectric-relaxation activation energy of CCTO ceramics.

To elucidate the influences of F^- anion dopant ions on the dielectric properties of CCTO ceramics, the grain and GB responses were studied using an impedance spectroscopy technique. Fig. 6(a) and (b) show Z^* plots for all the samples at RT and 80 °C, respectively. Only the linear part of the semicircular arcs was observed at RT in the frequency range of 10^2 to 10^6 Hz. A nonzero intercept on the Z' axis was observed, inset of Fig. 6(a), indicating an electrical response of the semiconducting grains.[42,43] Thus, the linear part of the semicircular arcs should be due to the electrical response of the GBs. The grain resistance (R_g) values (estimated from the nonzero intercept) of the CCTOF ceramics were smaller than that of the undoped CCTO ceramic by a factor of 2. At RT, R_g of the CCTO sample was ≈100 Ω cm, while R_g values of the CCTOF ceramics were nearly the same in value with $R_g \approx 50$ Ω cm. At RT, it is very difficult (or perhaps impossible) to accurately calculate the value of R_{gb} in the measured frequency range since just few data points on the full arcs appeared in these Z^* plots. The trend of R_{gb} values for the CCTOF ceramics cannot be determined. To obtain this, a Z^* plot at a high temperature should be performed. In Fig. 7(b), the R_{gb} of each sample was estimated and

Table 2 Dielectric permittivity (ε') and loss tangent (tan δ) at RT and 1 kHz of un-doped CCTO and metal ion-doped CCTO ceramics doping with different ions

Doped-CCTO ceramics (preparation method)	Sintering condition	ε'	tan δ
Ni-Doped CCTO (SSR method)[44]	1040 °C/4 h	69 833	0.073
Sn-Doped CCTO (SSR method)[44]	1040 °C/4 h	51 443	0.061
Si-Doped CCTO (SSR method)[44]	1040 °C/4 h	55 240	0.136
Al-Doped CCTO (SSR method)[44]	1040 °C/4 h	30 226	0.100
Un-doped CCTO (SSR method)[44]	1040 °C/4 h	45 972	0.109
Un-doped CCTO (sol–gel method)[16]	1060 °C/48 h	~42 250	~0.15
Un-doped CCTO (SSR method)[17]	1060 °C/48 h	~100 000	~1.0
Un-doped CCTO (molten salt method)[19]	1060 °C/1 h	~10 000	~0.15
	1060 °C/3 h	~10 000	~0.15
Un-doped CCTO (SSR method with quenching in water)[18]	1060 °C/3 h	~17 500	~0.085
Un-doped CCTO (SSR method) [in this work]	1075 °C for 3 h	23 263	0.145
$CaCu_3Ti_4O_{11.9}F_{0.10}$ (SSR method) [in this work]	1075 °C for 3 h	81 306	0.077

This journal is © The Royal Society of Chemistry 2017

Open Access Article. Published on 16 January 2017. Downloaded on 17/02/2017 03:28:00.
This article is licensed under a Creative Commons Attribution-NonCommercial 3.0 Unported Licence.

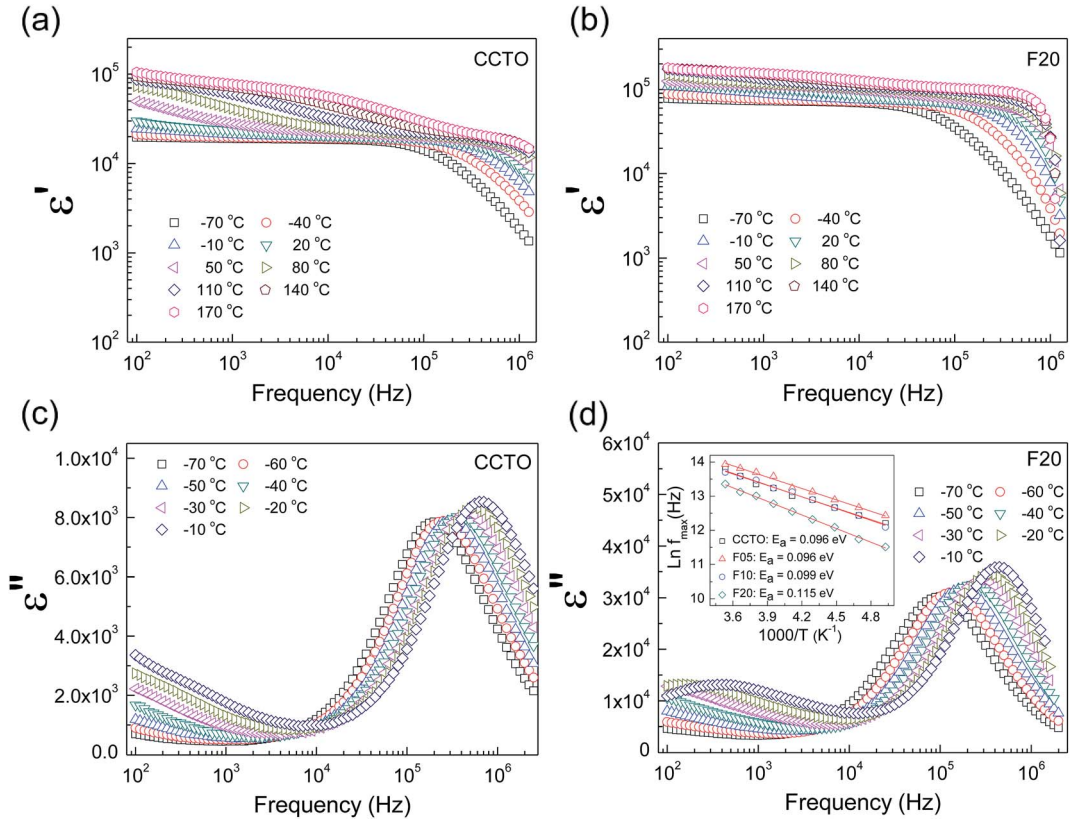

Fig. 5 Frequency dependencies of dielectric permittivity (ε') and dielectric loss (ε'') at various temperatures for (a, c) CCTO and (b, d) F20 samples; inset of (d) shows Arrhenius plots of f_{max} for the dielectric relation.

found to be significantly increased by doping with F^-. R_{gb} of the CCTOF ceramics was enhanced even through the mean grain size increased compared to that of the CCTO sample. This result gives a significant clue, reflecting the largely enhanced resistance of individual GB layers. This is one of the most important factors contributing to reduction in a low-frequency tan δ in CCTOF ceramics [inset of Fig. 4]. Thus, the distribution of dopants near GBs can cause an increase in the GB resistivity, which often make great influence on the low-frequency dielectric properties,[44] as clearly seen in Fig. 5. It is worth noting that all the samples were electrically heterogeneous, consisting of grains with very small R_g values and very high values of R_{gb}. Therefore, it is reasonable to suggest that the giant dielectric response in CCTOF ceramics originated from the IBLC effect.

R_g and R_{gb} values can be calculated in various temperatures. The conductivities of the grain (σ_g) and GB (σ_{gb}) were calculated from R_g and R_{gb}, respectively. As demonstrated in Fig. 6(c) and (d), the temperature dependencies of σ_g and σ_{gb} follow the Arrhenius law:

$$\sigma_{g/gb} = \sigma_0 \exp\left(\frac{-E_{g/gb}}{k_B T}\right), \quad (3)$$

where σ_0 is a constant value and E_g and E_{gb} are the conduction activation energies inside the grains and GBs, respectively. The E_{gb} values of the CCTO, F05, F10 and F20 samples were about 0.630, 0.696, 0.714 and 0.739 eV, respectively. The E_g values for all the samples are summarized in Table 1. E_g slightly increased with increasing F^- dopant concentration. It was observed that the trends of variation in E_g and E_a values were similar. According to the Maxwell–Wagner polarization relaxation model, the temperature dependence at the critical frequency, f_{max}, of a thermally activated relaxation process can be expressed in term of R_g, as the following:[13,21]

$$f_{max} \approx (2\pi R_g C_{gb})^{-1} \approx (2\pi C_{gb})\left(R_g^0\right)^{-1} \exp\left(\frac{-E_g}{k_B T}\right), \quad (4)$$

where C_{gb} is the capacitance of GBs. From eqn (2), the temperature dependence of f_{max} for the dielectric relaxation process in CCTO and CCTOF ceramics follows the temperature dependence of the conduction process of the grains, since C_{gb} is nearly independent of temperature. According to eqn (2)–(4), the activation energies required for electrical conduction in the grain interiors and for dielectric relaxation process should be the very close. Thus, the calculated E_a and E_g values strongly confirm that the giant dielectric response in CCTOF ceramics can be attributed to the Maxwell–Wagner polarization based on the IBLC structural model.

As shown in the inset of Fig. 6(a), R_g of CCTO ceramics was reduced by doping with F^- anions, indicating an increase in the concentration of free charge carriers in the grain interiors. To clarify the effect of F^- doping on the electrical properties of the grains, variation in valence states of Cu^{2+} and Ti^{4+} ions in CCTO

Open Access Article. Published on 16 January 2017. Downloaded on 17/02/2017 03:28:00.
This article is licensed under a Creative Commons Attribution-NonCommercial 3.0 Unported Licence.

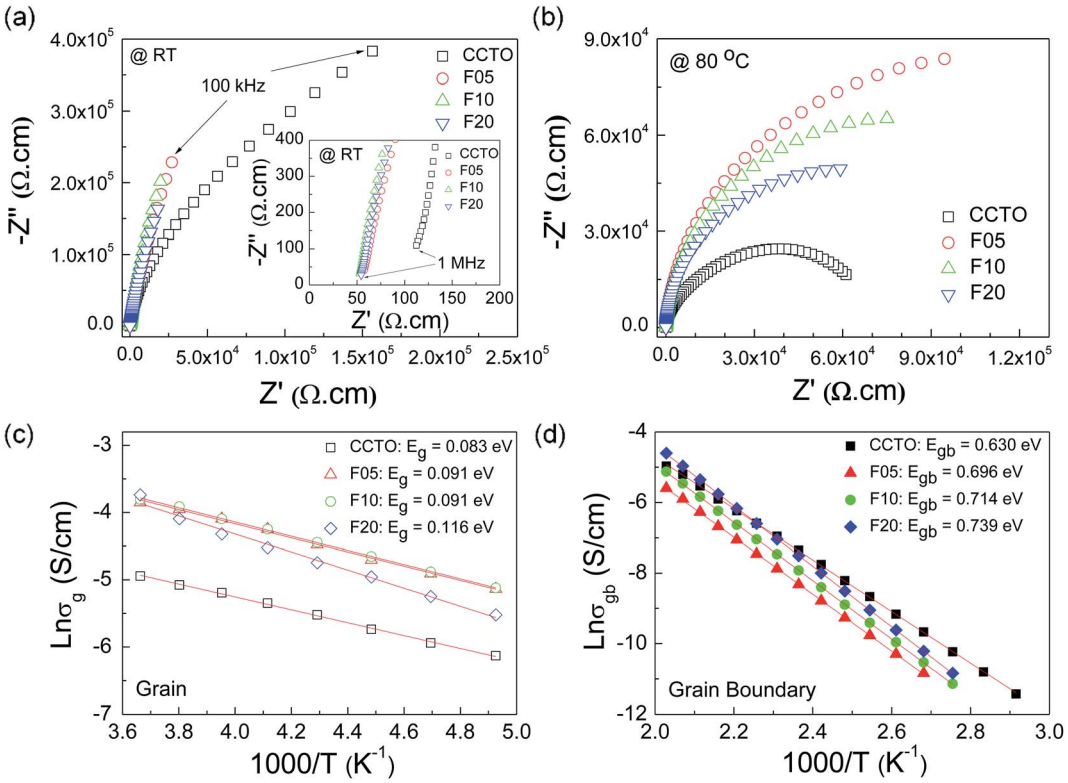

Fig. 6 (a and b) Impedance complex plane (Z^*) plots of CCTO, F05, F10 and F20 samples at room temperature and 80 °C, respectively; inset of (a) shows an expanded view of high frequency Z^* plots at RT, revealing the nonzero intercept on Z' axis. (c and d) Arrhenius plots of σ_g and σ_{gb}, respectively.

and CCTOF samples was investigated using XPS and XANES techniques. As illustrated in Fig. 7(a) and (c), the main XPS peaks at ≈933 eV for the CCTO and F10 samples confirm the existence of large numbers of Cu^{2+} ions.[9,28,32] The Cu $2p_{3/2}$ region can be divided into three peaks using Gaussian–Lorentzian profile fitting. The small XPS peaks at relatively lower and higher binding energies at ≈931 and ≈936 eV indicated the existence of Cu^{+} and Cu^{3+}, respectively.[9,28,32] The Cu^{+}/Cu^{2+} ratios of the CCTO and F10 samples were, respectively, about 4.26% and 5.65%, while their respective Cu^{3+}/Cu^{2+} ratios were 13.62% and 27.22%. Doping CCTO with F^{-} caused an increase in both Cu^{+} and Cu^{3+} concentrations.

In addition to Cu^{+} and Cu^{3+}, the presence of Ti^{3+} ions is usually considered a major cause of the formation of n-type semiconducting grains in CCTO ceramics. As depicted in Fig. 7(b) and (d), the primary XPS peak at ≈458 eV for Ti^{4+} was confirmed in all the samples. Unfortunately, the presence of Ti^{3+} cannot be modeled using Gaussian–Lorentzian profile fitting. This may be due to a small amount of Ti^{3+} in both the samples.[2] Thus, XANES was used to further investigate to the existence of Ti^{3+}. Fig. 8 shows normalized Ti K-edge XANES spectra of the CCTO and F10 samples as well as the standard TiO_2 (Ti^{4+}) and Ti_2O_3 (Ti^{3+}) samples. It was found that the position of the edge energy of both samples was very close to the TiO_2 standard. As expected, a small amount of Ti^{3+} was confirmed to exist. To obtain the ratios of Ti^{3+}/Ti^{4+}, the edge value was calculated from the maximum value of the first derivative in the edge region.[15] The ratio of Ti^{3+}/Ti^{4+} can be calculated from the energy edge value.[39] The ratios of Ti^{3+}/Ti^{4+} in the CCTO and F10 samples were found to be 0.82% and 2.46%, respectively.

Substitution of O^{2-} with F^{-} anions requires charge compensation, which can be achieved by reduction in cation valence ($Cu^{2+} \rightarrow Cu^{+}$ and $Ti^{4+} \rightarrow Ti^{3+}$). This charge compensation behavior is similar to that observed in the case of Y^{3+} doped-CCTO ceramics, which R_g of CCTO was reduced by doping with Y^{3+}.[45,46] It is worth noting that the Cu^{3+}/Cu^{2+} ratio of the F10 sample was significantly increased. As shown in the SEM-mapping image for Cu dispersion, Fig. 3, segregation of Cu-rich phase along the GBs was observed. This indicated the decomposition of CuO from the CCTO lattice, creating cation vacancies. Therefore, it is possible that the increased Cu^{3+}/Cu^{2+} ratio of the F10 sample might be due to the creation of Cu vacancies.[9]

Generally, the conductivity of n-type semiconducting grains is elevated by increasing the number of free electrons. Thus, the reduction in R_g of the CCTOF samples should be correlated with the increase in Cu^{+}/Cu^{2+} and Ti^{3+}/Ti^{4+} ratios over those found in the CCTO sample. For p-type semiconductor CuO ceramics, conduction is primarily caused by hole hopping between $Cu^{3+} \leftrightarrow Cu^{2+}$. The increase in the Cu^{3+}/Cu^{2+} ratio may also be an important cause of the reduced R_g. Form this point of view, hopping of charge carriers between $Cu^{+} \leftrightarrow Cu^{2+}$, $Cu^{3+} \leftrightarrow Cu^{2+}$, and $Ti^{3+} \leftrightarrow Ti^{4+}$ sites in the CCTO structure can result in

 This journal is © The Royal Society of Chemistry 2017

Open Access Article. Published on 16 January 2017. Downloaded on 17/02/2017 03:28:00.
This article is licensed under a Creative Commons Attribution-NonCommercial 3.0 Unported Licence.

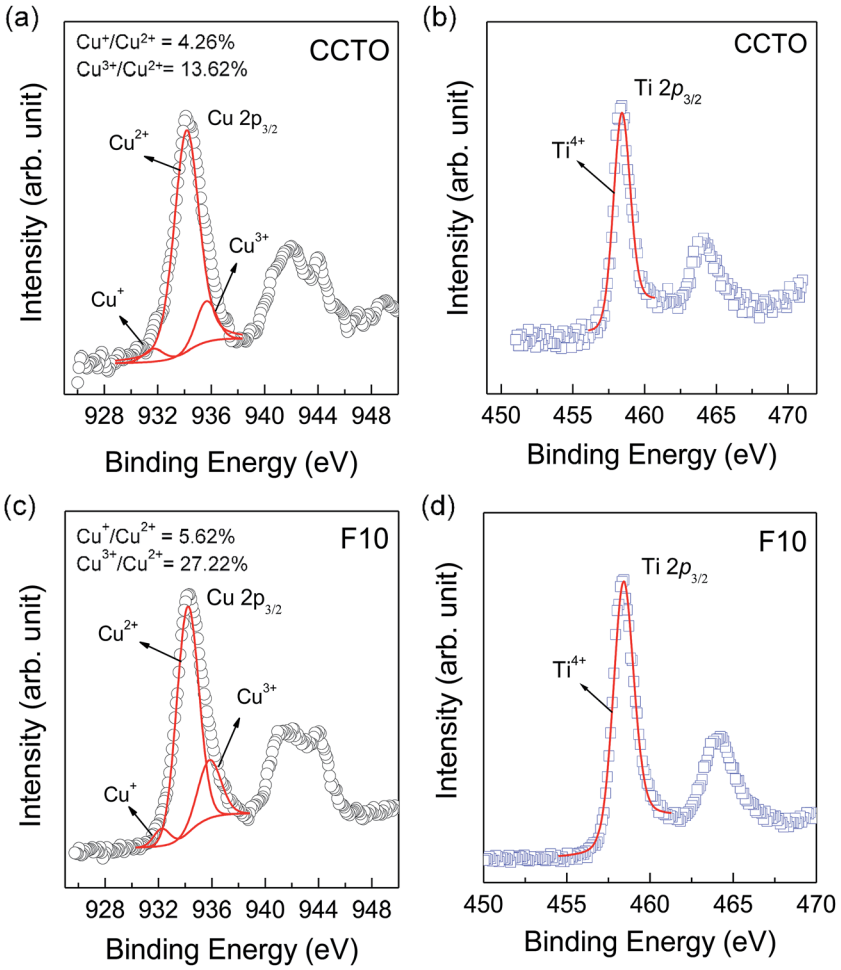

Fig. 7 XPS spectra of CCTO and F10 samples: (a, c) Ti 2p regions and (b, d) Cu 2p regions.

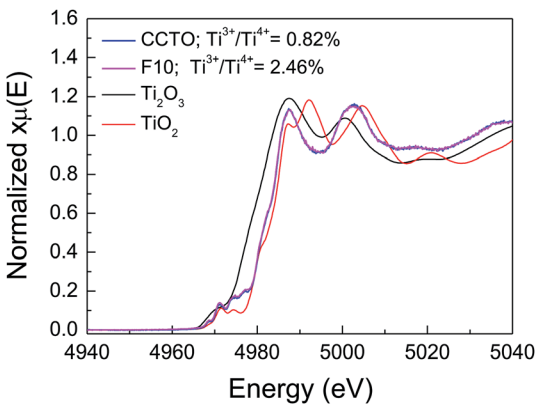

Fig. 8 Normalized X-ray absorption near edge structure (XANES) spectra for Ti K-edge of the CCTO and F10 samples.

electrical conductivity. According to our previous report, we found that the variation in R_g of $Na_{0.5}Y_{0.5}Cu_3Ti_4O_{12}$ ceramics was only consistent with a change in the Ti^{3+}/Ti^{4+} ratio, whereas changes in Cu^+/Cu^{2+} and Cu^{3+}/Cu^{2+} ratios was not correlated to R_g values.[47] The conduction mechanism inside the n-type semiconducting grains might be primarily attributed to electron hopping from a Ti^{3+}–O–Ti^{4+} to a Ti^{4+}–O–Ti^{3+}. Hopping of charge carriers between complex defects, *i.e.*, Cu^+–O–Cu^{2+} ↔ Cu^{2+}–O–Cu^{3+}, was likely difficult owing to much different valance states of Cu^+ and Cu^{3+}.

The effect of F^- anions on the non-ohmic properties of CCTO ceramics is illustrated in Fig. 9. All the samples exhibited nonlinear *J*–*E* characteristics. Accordingly, E_b and α values were calculated and summarized in Table 1. According to the improved dielectric properties and the observed nonlinear electrical properties of CCTOF ceramics, it was suggested that the sample could be applied as capacitor-varistors.[48] α values for all the samples were not significantly different, while E_b values of the CCTOF samples were greater than that of the undoped CCTO sample, even though their grain sizes were larger than those of the CCTO sample. The volume fraction of the GB, which is inversely proportional to its mean grain size, was decreased by doping with F^- anions. The increase in E_b of the CCTOF samples was consistent with their enhanced R_{gb} values over that of the CCTO sample. Although the volume fraction of the GB in the CCTOF samples was lower than that of the CCTO sample, the total resistance of their GBs (R_{gb}) and E_b were larger.

Open Access Article. Published on 16 January 2017. Downloaded on 17/02/2017 03:28:00.
This article is licensed under a Creative Commons Attribution-NonCommercial 3.0 Unported Licence.

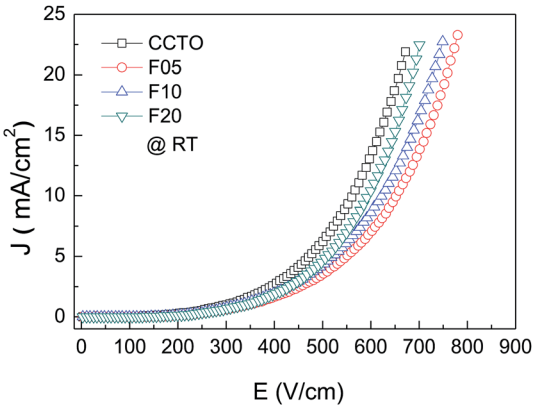

Fig. 9 Nonlinear current density–electric field (J–E) characteristics at RT of CCTO, F05, F10 and F20 samples.

Thus, the resistivity of an individual GB layer of the CCTOF samples should much be larger than that of the CCTO sample. These results indicate that the intrinsic property (*i.e.*, potential barrier height) of the GB of CCTO ceramics was enhanced by F^- doping. It was reasonably proposed that based on the n-type semiconducting grains of CCTO ceramics, the electronic energy band structure across the GB layer was equivalent to n–i–n.[20,49] Double Schottky potential barriers can be created at interfaces between n-type grains caused by trapping at acceptor states. This resulted in the bending of the conduction band across the GB. A potential barrier (Φ_B) was created at the GB sandwiched by n-type semiconducting grains.[20] In the absence of a DC bias, Φ_B can be expressed as:

$$\Phi_B = \frac{qN_s^2}{8\varepsilon_0\varepsilon' N_d}, \quad (5)$$

where N_s is the acceptor (surface charge) concentration, ε' is the relative permittivity of materials, N_d is the charge carrier concentration in the semiconducting grains and q is the electronic charge. It was reported that the activation energy for conduction at the GBs has a close relationship with the potential barrier height at the GBs.[10,20] E_{gb} and Φ_B were nearly the same in value. As shown in Fig. 6(d) and Table 1, the enhanced E_{gb} values indicated an increase in Φ_B. As demonstrated in the inset of Fig. 6(a), R_g (or σ_g) of all the CCTOF samples was smaller than that of the CCTO sample, indicating that the charge carrier concentration in the semiconducting grains (N_d) of the CCTOF samples was higher. This is responsible for the observed increase in the potential barrier height at the GBs in the CCTOF ceramic samples. Generally, it was observed that the mechanism of potential barrier formation in CCTO ceramics was also correlated with oxygen enrichment at the GBs.[25] For this point of view, it was proposed that the GB region may possess a p-type semiconductor nature, resulting from high oxygen content and/or vacancies of metal ions along the GBs compared with the n-type semiconductor nature inside the grains.[50] For CCTOF ceramics, the creation of oxygen vacancies may possibly be inhibited (or decreased) by F^- doping anions due to the lower valence state of the dopant, retaining the p-type semiconductor nature of the GBs and potential barrier height. Thus, substitution of F^- anions not only decreased the possibility of a reduction in Φ_B as a result of creation of oxygen vacancies, but it also enhanced Φ_B resulting from the creation of free charges inside the semiconducting grains.

Substitution of F^- anions into CCTO ceramics can simultaneously improve the electrical properties of the grains and GBs. These can cause increases in both of the free charge carrier concentration inside the semiconducting grains and Schottky barrier height at the GBs, respectively. Under an applied electric field, more charges accumulated at the interface between the semiconducting grain and GB layer due to a high concentration of free charges inside the grain producing a stronger intensity of interfacial polarization (Maxwell–Wagner polarization). This gave rise to a large increase in ε'. Enhanced Φ_B resulting in R_{gb} is the major cause the reduced low-frequency tan δ.

4. Conclusions

Significantly improved giant dielectric properties of CCTO ceramics *via* simultaneously tuning the electric properties of the grains and GBs was successfully done by doping CCTO with F^- anions. The grain size of CCTO ceramics was thus enlarged. The low-frequency tan δ of F^--doped CCTO ceramics was greatly reduced by a factor of 5 compared to that of the undoped CCTO ceramic, which was attributed to a large increase in R_{gb} and potential barrier height at the GBs. These results were confirmed by the slight increase in electric breakdown strength of F^--doped CCTO ceramics, even though the mean grain size was greatly increased. According to the XPS and XANES results, it was shown that the charge carrier concentration inside the semiconducting grains of F^--doped CCTO ceramics was increased corresponding to the observed reduction in R_g. This was responsible for the observed increase in ε' from $\approx 10^4$ to $\approx 10^5$ at 1 kHz due to the increased intensity of interfacial polarization at the GBs. Maxwell–Wagner polarization relaxation based on the internal barrier layer capacitor model of Schottky barriers at the GBs can be used to clearly explain the variations of the giant dielectric behavior and nonlinear electrical properties of F^--doped CCTO ceramics.

Acknowledgements

This work was financially supported by the Thailand Research Fund (TRF) and Khon Kaen University (Contract No. RSA5880012) and under the TRF Senior Research Scholar (Contract No. RTA5780004). The authors would like to thank the Synchrotron Light Research Institute (BL5.2) (Public Organization), Nakhon Ratchasima, Thailand for XANES measurements and the SUT-NANOTEC-SLRI Joint Research Facility for XPS facility. J. Jumpatam thanks the Thailand Research Fund under The Royal Golden Jubilee Ph.D. Program [Grant number PHD/0079/2557] for his Ph.D. scholarship.

References

1 C. C. Homes, T. Vogt, S. M. Shapiro, S. Wakimoto and A. P. Ramirez, *Science*, 2001, **293**, 673–676.

 This journal is © The Royal Society of Chemistry 2017

Open Access Article. Published on 16 January 2017. Downloaded on 17/02/2017 03:28:00.
This article is licensed under a Creative Commons Attribution-NonCommercial 3.0 Unported Licence.

2 W. Hu, Y. Liu, R. L. Withers, T. J. Frankcombe, L. Norén, A. Snashall, M. Kitchin, P. Smith, B. Gong, H. Chen, J. Schiemer, F. Brink and J. Wong-Leung, *Nat. Mater.*, 2013, **12**, 821–826.
3 G. Liu, H. Fan, J. Xu, Z. Liu and Y. Zhao, *RSC Adv.*, 2016, **6**, 48708–48714.
4 W. Tuichai, S. Danwittayakul, S. Maensiri and P. Thongbai, *RSC Adv.*, 2016, **6**, 5582–5589.
5 A. O. Turky, M. M. Rashad, Z. I. Zaki, I. A. Ibrahim and M. Bechelany, *RSC Adv.*, 2015, **5**, 18767–18772.
6 M. A. Subramanian, D. Li, N. Duan, B. A. Reisner and A. W. Sleight, *J. Solid State Chem.*, 2000, **151**, 323–325.
7 B. Shri Prakash and K. B. R. Varma, *J. Mater. Sci.: Mater. Electron.*, 2006, **17**, 899–907.
8 S.-H. Hong, D.-Y. Kim, H.-M. Park and Y.-M. Kim, *J. Am. Ceram. Soc.*, 2007, **90**, 2118–2121.
9 M. Li, G. Cai, D. F. Zhang, W. Y. Wang, W. J. Wang and X. L. Chen, *J. Appl. Phys.*, 2008, **104**, 074107.
10 L. Liu, H. Fan, P. Fang and X. Chen, *Mater. Res. Bull.*, 2008, **43**, 1800–1807.
11 L. Ni, X. M. Chen and X. Q. Liu, *Mater. Chem. Phys.*, 2010, **124**, 982–986.
12 P. Thongbai, J. Jumpatam, T. Yamwong and S. Maensiri, *J. Eur. Ceram. Soc.*, 2012, **32**, 2423–2430.
13 P. Thongbai, J. Jumpatam, B. Putasaeng, T. Yamwong and S. Maensiri, *J. Appl. Phys.*, 2012, **112**, 114115.
14 J. Jumpatam, B. Putasaeng, T. Yamwong, P. Thongbai and S. Maensiri, *Ceram. Int.*, 2013, **39**, 1057–1064.
15 J. Boonlakhorn and P. Thongbai, *J. Electron. Mater.*, 2015, **44**, 3687–3695.
16 L. Liu, H. Fan, P. Fang and L. Jin, *Solid State Commun.*, 2007, **142**, 573–576.
17 L. Liu, H. Fan, X. Chen and P. Fang, *J. Alloys Compd.*, 2009, **469**, 529–534.
18 L. Liu, D. Shi, S. Zheng, Y. Huang, S. Wu, Y. Li, L. Fang and C. Hu, *Mater. Chem. Phys.*, 2013, **139**, 844–850.
19 Y. Huang, L. Liu, D. Shi, S. Wu, S. Zheng, L. Fang, C. Hu and B. Elouadi, *Ceram. Int.*, 2013, **39**, 6063–6068.
20 T. Adams, D. Sinclair and A. West, *Phys. Rev. B: Condens. Matter Mater. Phys.*, 2006, **73**, 094124.
21 J. Liu, C.-G. Duan, W.-G. Yin, W. Mei, R. Smith and J. Hardy, *Phys. Rev. B: Condens. Matter Mater. Phys.*, 2004, **70**, 144106.
22 R. Schmidt, M. C. Stennett, N. C. Hyatt, J. Pokorny, J. Prado-Gonjal, M. Li and D. C. Sinclair, *J. Eur. Ceram. Soc.*, 2012, **32**, 3313–3323.
23 Z. Yang, L. Zhang, X. Chao, L. Xiong and J. Liu, *J. Alloys Compd.*, 2011, **509**, 8716–8719.
24 S.-Y. Chung, I.-D. Kim and S.-J. L. Kang, *Nat. Mater.*, 2004, **3**, 774–778.
25 M. A. Ramírez, P. R. Bueno, J. A. Varela and E. Longo, *Appl. Phys. Lett.*, 2006, **89**, 212102.
26 J. Boonlakhorn, P. Kidkhunthod and P. Thongbai, *J. Eur. Ceram. Soc.*, 2015, **35**, 3521–3528.
27 L. Sun, R. Zhang, Z. Wang, E. Cao, Y. Zhang and L. Ju, *RSC Adv.*, 2016, **6**, 55984–55989.
28 L. Ni and X. M. Chen, *Solid State Commun.*, 2009, **149**, 379–383.
29 A. Nautiyal, C. Autret, C. Honstettre, S. De Almeida-Didry, M. El Amrani, S. Roger, B. Negulescu and A. Ruyter, *J. Eur. Ceram. Soc.*, 2016, **36**, 1391–1398.
30 M. F. Ab Rahman, S. D. Hutagalung, Z. A. Ahmad, M. F. Ain and J. J. Mohamed, *J. Mater. Sci.: Mater. Electron.*, 2015, **26**, 3947–3956.
31 L. Singh, I. W. Kim, B. C. Sin, K. D. Mandal, U. S. Rai, A. Ullah, H. Chung and Y. Lee, *RSC Adv.*, 2014, **4**, 52770–52784.
32 L. Ni and X. M. Chen, *J. Am. Ceram. Soc.*, 2010, **93**, 184–189.
33 W. L. Li, Y. Zhao, Q. G. Chi, Z. G. Zhang and W. D. Fei, *RSC Adv.*, 2012, **2**, 6073.
34 M. Gao, D. Feng, G. Yao, Y. Zhang, C. L. Chen and Y. Lin, *RSC Adv.*, 2015, **5**, 92958–92962.
35 L. Singh, B. C. Sin, I. W. Kim, K. D. Mandal, H. Chung, Y. Lee and J. Varela, *J. Am. Ceram. Soc.*, 2016, **99**, 27–34.
36 J. Boonlakhorn and P. Thongbai, *Jpn. J. Appl. Phys.*, 2015, **54**, 06FJ06.
37 R. Yu, H. Xue, Z. Cao, L. Chen and Z. Xiong, *J. Eur. Ceram. Soc.*, 2012, **32**, 1245–1249.
38 A. E. Smith, T. G. Calvarese, A. W. Sleight and M. A. Subramanian, *J. Solid State Chem.*, 2009, **182**, 409–411.
39 M. Newville, *J. Synchrotron Radiat.*, 2001, **8**, 96–100.
40 R. D. Shannon, *Acta Crystallogr., Sect. A: Cryst. Phys., Diffr., Theor. Gen. Crystallogr.*, 1976, **32**, 751–767.
41 M. Li, Z. Shen, M. Nygren, A. Feteira, D. C. Sinclair and A. R. West, *J. Appl. Phys.*, 2009, **106**, 104106.
42 S. I. R. Costa, M. Li, J. R. Frade and D. C. Sinclair, *RSC Adv.*, 2013, **3**, 7030–7036.
43 R. Schmidt, S. Pandey, P. Fiorenza and D. C. Sinclair, *RSC Adv.*, 2013, **3**, 14580–14589.
44 L. Liu, Y. Huang, Y. Li, D. Shi, S. Zheng, S. Wu, L. Fang and C. Hu, *J. Mater. Sci.*, 2012, **47**, 2294–2299.
45 J. Deng, X. Sun, S. Liu, L. Liu, T. Yan, L. Fang and B. Elouadi, *J. Adv. Dielectr.*, 2016, **06**, 1650009.
46 G. Li, Z. Chen, X. Sun, L. Liu, L. Fang and B. Elouadi, *Mater. Res. Bull.*, 2015, **65**, 260–265.
47 J. Jumpatam, A. Mooltang, B. Putasaeng, P. Kidkhunthod, N. Chanlek, P. Thongbai and S. Maensiri, *Ceram. Int.*, 2016, **42**, 16287–16295.
48 Y. Huang, D. Shi, Y. Li, G. Li, Q. Wang, L. Liu and L. Fang, *J. Mater. Sci.: Mater. Electron.*, 2012, **24**, 1994–1999.
49 L. Liu, L. Fang, Y. Huang, Y. Li, D. Shi, S. Zheng, S. Wu and C. Hu, *J. Appl. Phys.*, 2011, **110**, 094101.
50 M. Li and D. C. Sinclair, *J. Appl. Phys.*, 2013, **114**, 034106.

Received: 30 December 2016 | Accepted: 10 March 2017

DOI: 10.1111/jace.14886

ORIGINAL ARTICLE

Journal of the American Ceramic Society

Microstructural evolution, non-Ohmic properties, and giant dielectric response in $CaCu_3Ti_{4-x}Ge_xO_{12}$ ceramics

Jakkree Boonlakhorn[1] | **Prasit Thongbai**[1,2] | **Bundit Putasaeng**[3] | **Pinit Kidkhunthod**[4] | **Santi Maensiri**[5] | **Prinya Chindaprasirt**[6]

[1]Integrated Nanotechnology Research Center (INRC), Department of Physics, Faculty of Science, Khon Kaen University, Khon Kaen, Thailand

[2]Nanotec-KKU Center of Excellence on Advanced Nanomaterials for Energy Production and Storage, Khon Kaen, Thailand

[3]National Metal and Materials Technology Center, Klong Luang, Pathunthani, Thailand

[4]Synchrotron Light Research Institute (Public Organization), Muang District, Nakhon Ratchasima, Thailand

[5]Institute of Science, School of Physics, Suranaree University of Technology, Nakhon Ratchasima, Thailand

[6]Sustainable Infrastructure Research and Development Center, Department of Civil Engineering, Faculty of Engineering, Khon Kaen University, Khon Kaen, Thailand

Correspondence
Prasit Thongbai, Department of Physics, Faculty of Science, Khon Kaen University, Khon Kaen, Thailand.
Email: pthongbai@kku.ac.th

Funding information
Thailand Research Fund, Grant/Award Number: RSA5880012, RTA5780004; Khon Kaen University; TRF Senior Research Scholar; Nanotechnology Center (NANOTEC); NSTDA; Ministry of Science and Technology.

Abstract

The microstructural evolution, non-Ohmic properties, and giant dielectric properties of $CaCu_3Ti_{4-x}Ge_xO_{12}$ ceramics (x=0-0.10) are systematically investigated. The Rietveld refinement confirms the existence of a pure $CaCu_3Ti_4O_{12}$ phase in all samples. Significantly enlarged grain sizes of $CaCu_3Ti_{4-x}Ge_xO_{12}$ ceramics are associated with the liquid phase sintering mechanism. Enhanced dielectric permittivity from 6.90×10^4 to 1.08×10^5 can be achieved by increasing Ge^{4+} dopant from x=0-0.10, whereas the loss tangent is remarkably reduced by a factor of ≈10. Non-Ohmic properties are enhanced by Ge^{4+} doping ions. Using impedance and admittance spectroscopies, the underlying mechanisms for the dielectric and nonlinear properties are well described. The improved nonlinear properties and reduced loss tangent are attributed to the enhanced resistance and conduction activation energy of the grain boundaries. The largely enhanced permittivity is closely associated with the enlarged grain sizes and the increase in the Cu^+/Cu^{2+} and Ti^{3+}/Ti^{4+} ratios, which are calculated from the X-ray absorption near-edge structure.

KEYWORDS
dielectric materials/properties, dielectric relaxation, grain boundaries, grain growth, impedance spectroscopy

1 | INTRODUCTION

$CaCu_3Ti_4O_{12}$ (CCTO), the perovskite-like ceramic oxide, is a giant dielectric material that has been widely investigated in recent years. CCTO has a high dielectric permittivity (ε') of ~10^3-10^5 in the radio frequency range.[1-6] Furthermore, nonlinear behavior, which is a nonlinear correlation between the current density and electric field, can also be observed in CCTO polycrystalline ceramics.[7] As the giant dielectric properties of CCTO ceramics were first studied,[1] several models have been proposed to explain the giant dielectric behavior. Both intrinsic and extrinsic models have been suggested. The giant

dielectric and nonlinear electrical properties are widely believed to be caused by the internal barrier layer capacitor (IBLC) structure,[8-12] which can be produced by using a one-step processing method with no special sintering steps or dopants. However, special sintering steps or dopants can cause changes in these properties. The *n*-type semiconducting grain and insulating grain boundary (GB) can be controlled using these two methods.[7] The intrinsic effect that originated inside the grains cannot be simply ignored or arbitrarily excluded.[13,14]

The high dielectric loss tangent (tanδ) in CCTO is a significant problem that has been seriously investigated in the past few years.[4,5,15,16] Investigations to reduce tanδ are not only important for practical applications but also may give important data leading to a fundamental understanding of the origin(s) of giant dielectric behavior. Considering the nonlinear electrical properties of CCTO polycrystalline ceramics, important data about the electrical response of the GBs and thus giant dielectric response mechanism may be elucidated even though the nonlinear coefficient is still far from an acceptable value for use in varistor devices.

Many studies have used dopants to improve the dielectric and non-Ohmic properties of CCTO ceramics. This is one of the most widely used methods for increasing dielectric performance.[4,5,16] Many dopants have been substituted into the Cu^{2+} and Ti^{4+} sites of the CCTO structure such as Mg^{2+}, Zn^{2+}, Sn^{4+}, Zr^{4+}, and W^{6+}.[5,13,17-23] Substitution of Ge^{4+} ions into Ti^{4+} sites of CCTO ceramics has rarely been reported.[24] Moreover, the nonlinear electrical behavior of Ge-doped CCTO ceramics has never before been reported. Systematic investigation of the microstructural evolution, deviation of the oxidation states of Cu^{2+} and Ti^{4+}, impedance spectroscopy analysis, giant dielectric properties, and nonlinear electrical property data are lacking.

In this work, $CaCu_3Ti_{4-x}Ge_xO_{12}$ ceramics with x=0-0.10 were prepared using a conventional solid-state reaction method and systematically investigated. Imperfect distribution of Ge^{4+} can be alleviated using a double ball-milling process. Grain sizes of $CaCu_3Ti_{4-x}Ge_xO_{12}$ increased when the Ge^{4+} concentration was raised. Very high $\varepsilon' \approx 1.06\times10^5$ 1.07×10^5 and low tanδ≈0.068-0.064 (at 1 kHz and 25°C) of CCTO ceramics were obtained by doping with Ge^{4+}. Nonlinear electrical properties of $CaCu_3Ti_{4-x}Ge_xO_{12}$ ceramics were investigated and found to be enhanced. All of the experimental results are discussed in detail.

2 | EXPERIMENTAL DETAILS

2.1 | Ceramic preparation

A conventional solid-state reaction method was used to synthesize $CaCu_3Ti_{4-x}Ge_xO_{12}$ (x=0-0.10) ceramics. The raw materials consisted of $CaCO_3$ (Sigma-Aldrich, 99.0% purity, St. Louis, MO), CuO (Merck, 99.99% purity, Darmstadt, Germany), TiO_2 (Sigma-Aldrich, 99.99% purity, Japan), GeO_2 (Aldrich, 99.99% purity, St. Louis, MO), C_2H_5OH (RCI Labscan, 99.5% purity, Bangkok, Thailand), and deionized water. First, stoichiometric amounts of all starting raw materials for each chemical formula were mixed by ball milling in C_2H_5OH for 24 h. Second, the mixed raw materials were dried at 80°C for 24 h. Third, the resulting dried precursors were ground and calcined at 900°C for 12 h. All calcined powders were ground and ball milled again in deionized water for 24 h. Next, they were dried at 100°C for 48 h. After that, the fine powders were ground and annealed at 600°C for 6 h. All the calcined powders were pressed by uniaxial compression at ~200 MPa into pellet shapes of 9.5 mm in diameter and ~1.5 mm in thickness. Finally, all the green bodies were sintered at 1050°C for 6 h. The $CaCu_3Ti_{4-x}Ge_xO_{12}$ ceramics with x=0, 0.05, and 0.10 are referred to as the CCTO, CCTO–Ge05, and CCTO–Ge10 samples, respectively.

2.2 | Characterizations

The phase composition and crystal structure were characterized using an X-ray Diffractometer (PANalytical, EMPYREAN, PANalytical B.V., Eindhoven, the Netherlands). The diffraction spectra were collected over the 2θ range 25°–65° with a scan speed of 0.02°/min. The Rietveld refinement was done using X'Pert HighScore Plus software (PANalytical B.V.) and compared with the crystallographic structure of CCTO. The parameters and coefficients optimized were the zero shift, scale factor, background (with function type: polynomial), profile half-width parameters (v, u, w), lattice parameter (a), atomic site occupancies (Wyckoff), and the preferred orientation parameter. Surface morphologies were characterized using scanning electron microscopy (SEM; LEO 1450VP, Cambridge, UK). The densities of the sintered samples were measured using an Archimedes method. Elemental distribution in the sintered ceramics was examined using field-emission scanning electron microscopy (FE-SEM) with energy-dispersive X-ray analysis (EDX) (HITACHI SU8030, Japan). X-ray absorption near-edge structure (XANES) spectra of all sintered ceramics were collected at the SUT-NANOTEC-SLRI XAS beamline (BL5.2) (electron energy of 1.2 GeV; bending magnet; beam current 80–150 mA; 1.1 to 1.7×10^{11} photon.s^{-1}) at the Synchrotron Light Research Institute (SLRI), Nakhon Ratchasima, Thailand. Details of this characterization technique and analysis are given elsewhere.[25] Normalized XANES data were analyzed after background subtraction in the preedge and postedge regions using ATHENA software included in an *IFEFFIT* package.[26]

2.3 | Dielectric and electrical measurements

Both parallel surfaces of the sintered samples were polished and carefully washed to obtain smooth and clean

surfaces. All the samples were dried at 100°C overnight. Both sides of sample surfaces were coated with Au using a Polaron SC500 sputter coating unit operated at an electric current ~25 mA for 4 min. The dielectric properties were measured using a KEYSIGHT E4990A with an oscillation voltage of 500 mV. This measurement was done in ranges 10^2–10^7 Hz and 60°C to 210°C. Nonlinear current density–electric field (*J*-*E*) characteristics were measured at room temperature (RT) using a high voltage measurement unit (Keithley 247). The rate of increase in the source voltage was 1.33 V/s. The E_b value was defined as the electric field breakdown at which J=1 mA.cm^{-2}. The nonlinear coefficient (α) was calculated in the range 1–10 mA/cm^2.

3 | RESULTS AND DISCUSSION

Figure 1A, the diffraction peaks of the CCTO, CCTO–Ge05, and CCTO–Ge10 ceramics were consistent with standard peaks of CCTO in the 2θ range 25°–65° (JCPDS 75 2188).[1] Only a single phase was detected in all the XRD patterns with no possible impurities from CuO, Cu_2O, TiO_2, $CaTiO_3$, and related-oxide Ge phases. This observation may be due to complete substitution of Ge^{4+} ions into the CCTO structure and/or some small part of a Ge-related phase forming a liquid phase during sintering and flowing along GBs during cooling.

Profile fits of the Rietveld refinement were performed, as illustrated in Figure 1B-D. The quality of the refinement was quantified by the corresponding figures of merit, that is, profile residual (R_p), expected residual (R_{exp}), weighted profile residual (R_{wp}), and the goodness of fit (GOF).[27] The fitted results are summarized in Table 1. R_{exp}, R_{wp}, and R_p values of all samples were less than 10%. The experimental XRD patterns were well fitted, which was confirmed by low GOF values (<4.0 for all the samples).[28] The lattice parameter (*a*) was obtained from the Rietveld refinement and compared to the crystallographic CCTO structure. The calculated *a* values were 7.3942(1), 7.3899 (2), and 7.3880(1) Å for the CCTO, CCTO–Ge05, and CCTO–Ge10 ceramics, respectively. A decrease in *a* value of the $CaCu_3Ti_{4-x}Ge_xO_{12}$ ceramics was likely caused by the smaller ionic radius of Ge^{4+} (r_6=0.53 Å) dopant ion compared to that of the Ti^{4+} (r_6=0.605 Å) host ion.[29] Table 1, significant decreases in bond length between M–O and M–Cu (M=Ti, Ge) were detected. A decrease in *a* confirmed that Ge^{4+} ions could likely enter into the CCTO lattice.

The microstructural evolution of $CaCu_3Ti_{4-x}Ge_xO_{12}$ ceramics is revealed in Figure 2. Dense microstructures of all sintered ceramics were obtained by sintering at 1050°C for 6 h. The relative densities of the CCTO, CCTO–Ge05, and CCTO–Ge10 ceramics compared to the theoretical density of CCTO were 94.39, 95.89, and 95.75%, respectively. Highly dense ceramics were accomplished using a two-step

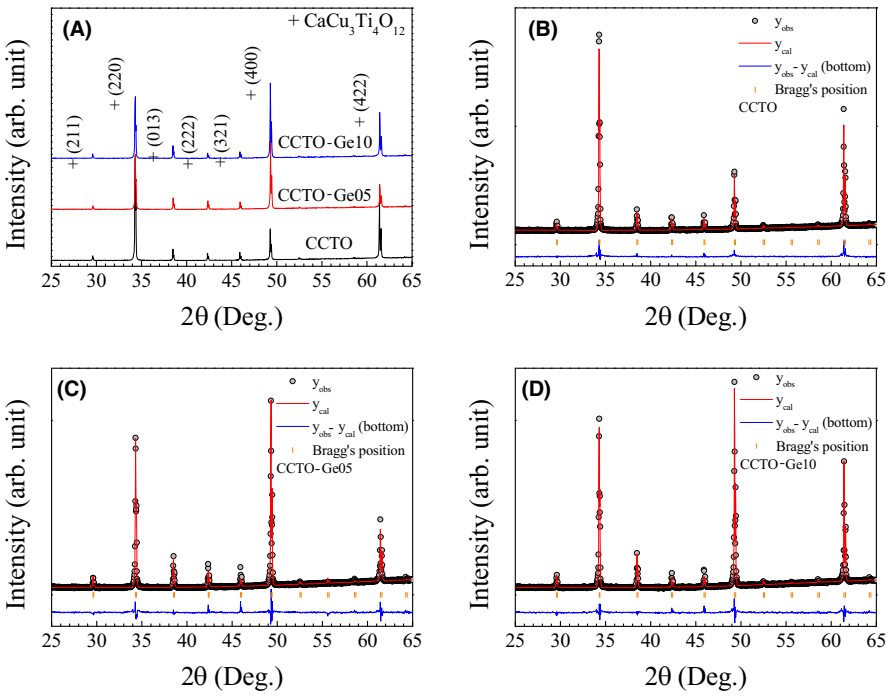

FIGURE 1 (A) XRD patterns of the CCTO, CCTO−Ge05, and CCTO−Ge10 ceramics. (B-D) Profile fits for the Rietveld refinements of the CCTO, CCTO−Ge05, and CCTO−Ge10 ceramics, respectively [Color figure can be viewed at wileyonlinelibrary.com]

TABLE 1 Structural data obtained from the Rietveld refinement for CCTO, CCTO−Ge05, and CCTO−Ge10 ceramics

Sample	CCTO	CCTO−Ge05	CCTO−Ge10
Lattice parameter (Å)	7.3942(1)	7.3899(2)	7.3880(1)
R_{exp}	3.86761	3.90774	3.89240
R_p	4.77845	4.52524	4.43128
R_{wp}	6.50429	6.52736	6.04493
GOF	2.82823	2.79013	2.41184
Bond lengths (Å)		(M=Ti, Ge)	
M–O	1.9590(0)	1.9580(0)	1.9570(0)
M–Cu	3.2020(0)	3.2000(0)	3.1990(0)

ball-milling method. Ge^{4+} doping ions had a great effect on the grain growth of CCTO ceramics. The grain size of $CaCu_3Ti_{4-x}Ge_xO_{12}$ ceramics significantly increased with increasing Ge^{4+} concentration from x=0-0.10. The measured mean grain sizes of the CCTO, CCTO–Ge05, and CCTO–Ge10 ceramics were ≈6.5, ≈81.1, and ≈112.7 μm, respectively. The microstructural evolution in $CaCu_{3-}Ti_{4-x}Ge_xO_{12}$ ceramics was similar to that observed in Te^{4+}-, Mo^{6+}-, and Ga^{3+}-doped CCTO ceramics.[30,31] This result indicates that Ge^{4+}-doping ions played some important role in the grain growth mechanism of CCTO, which is generally associated with the liquid-phase sintering mechanism.[13,20,30,31] Usually, the dopant directly melts and/or reacts with a small part of the major phase to form a eutectic liquid. The liquid phase was present at the contact areas between particles or grains in the microstructure. These can enhance the diffusion of ions across the GB, resulting in enhanced grain growth rate. Thus, the grain growth rate of CCTO ceramics may be activated by a Cu and/or Ge-related liquid phase because the eutectic temperature for $CuO–TiO_2$ is about 950°C.

Figure 3 reveals the SEM mapping of the CCTO−Ge10 ceramic, showing dispersion of all major elements (i.e., Ca, Cu, Ti, and O) and the Ge dopant. Segregation of Cu was observed along the GBs, which is usually reported in the literature.[32] Furthermore, it was found that a small portion of Ge was segregated at the GBs. These results strongly confirm that the liquid phase was closely associated with Cu- and Ge-rich phases. Figure 4 and its inset show the EDS spectrum of the CCTO−Ge10 ceramic and the selected area for EDS measurement, confirming the existence of all elements (i.e., Ca, Cu, Ti, Ge, and O) in the sintered ceramic. The EDS spectra on the grains of six different grains were measured. The averaged percentages of Ca, Cu, Ti, and Ge were found to be ≈7.39, 36.13, 35.48, and 1.35 wt%, respectively.

Although the valance states of the Ge^{4+} dopant and Ti^{4+} host ions are the same, deviation of oxidation states for Cu^{2+} and Ti^{4+} may occur as a result of several factors.

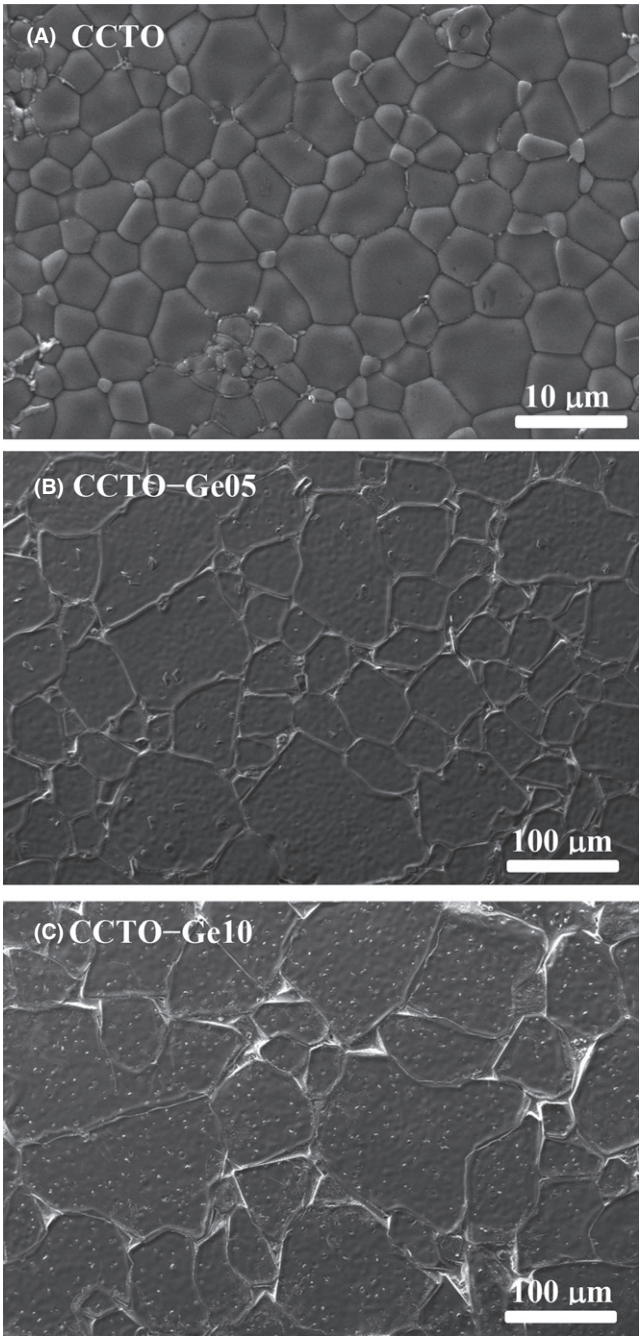

FIGURE 2 SEM images of surface morphologies of (A) CCTO, (B) CCTO−Ge05, and (C) CCTO−Ge10 ceramics

Sintered $CaCu_3Ti_{4-x}Ge_xO_{12}$ ceramics were characterized using a XANES technique. Figures 5A,B demonstrate the XANES spectra, respectively, for Cu and Ti in the CCTO, CCTO–Ge05, and CCTO–Ge10 ceramics. For all the samples, the Cu *K*-edge energy position was between Cu_2O (Cu^+) and $CuCl_2$ (Cu^{2+}) standard samples, whereas the Ti *K*-edge energy position was between Ti_2O_3 (Ti^{3+}) and TiO_2 (Ti^{4+}). These indicate that mixed oxidation states of Cu^+/Cu^{2+} and Ti^{3+}/Ti^{4+} occurred in all sintered ceramics. Quantitative analysis of different valence states

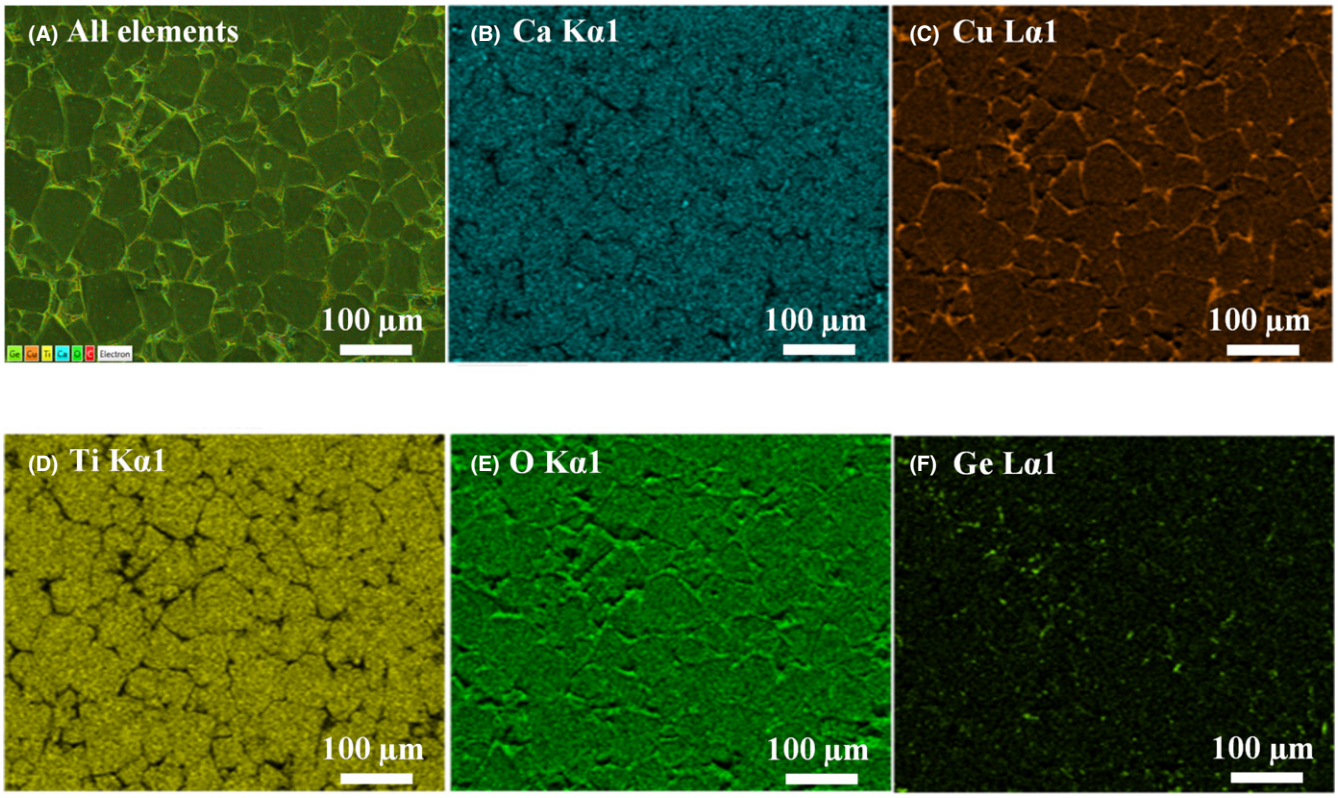

FIGURE 3 SEM mapping images of the CCTO−Ge10 ceramic sintered at 1050°C for 3 h; (A) all elements, (B) Ca, (C) Cu, (D) Ti, (E) O, and (F) Ge [Color figure can be viewed at wileyonlinelibrary.com]

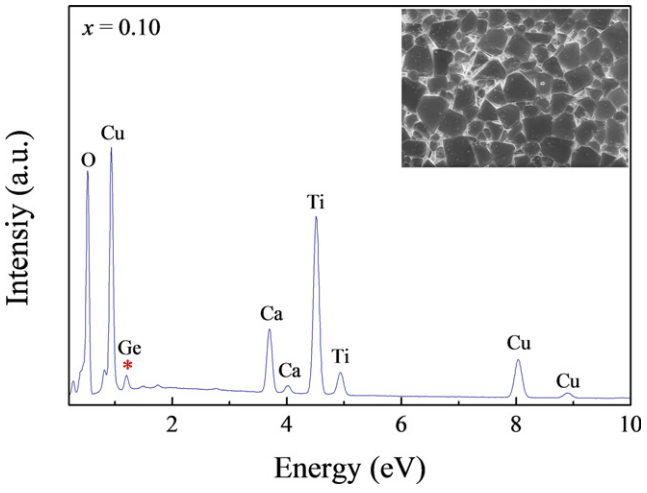

FIGURE 4 EDS spectrum of the CCTO−Ge10 ceramic; inset shows the selected area for measuring the EDS spectrum [Color figure can be viewed at wileyonlinelibrary.com]

was determined using an empirical edge-shift calculation by making comparisons with known standard samples. A slight shift in the values of Cu and Ti *K*-edge was confirmed.[25,33] The maximum value of the first derivative of the edge region was used to calculate the edge value. The amount of Cu^{+} was determined from Equation (1):

$$\%\ \text{of}\ Cu^{+} = \left(1 - \frac{\Delta E\ \text{of sample}}{\Delta E\ \text{of}\ Cu^{+}\ \text{and}\ Cu^{2+}\ \text{standard}}\right) \times 100\% \quad (1)$$

ΔE is the difference in the edge values of samples compared with a Cu^{+} (Cu_2O) standard. The calculated ratios of Cu^{+}/Cu^{2+} for the CCTO, CCTO–Ge05, and CCTO–Ge10 ceramics were 6.03, 6.70, and 7.04%, respectively. The Cu^{+}/Cu^{2+} ratio increased slightly with increasing Ge^{4+} concentration. Similarly, the Ti^{3+}/Ti^{4+} ratios can be also calculated[25,33] and found to be 4.71, 5.83, and 5.50%, respectively. The presence of Cu^{+} and Ti^{3+} is similar to observations reported in the literature for CCTO and related isostructural oxides.[10,12-14,25,34,35] Electron hopping between $Ti^{3+} \leftrightarrow Ti^{4+}$ and $Cu^{+} \leftrightarrow Cu^{2+}$ sites is one of the most possible explanations for conduction in *n*-type semiconducting grains of $CaCu_3Ti_{4-x}Ge_xO_{12}$ ceramics. Interestingly, the Ge^{4+} dopant had effects on the oxidation states of Cu and Ti, even though charge compensation was not required due to their identical oxidation states (Ge^{4+} and Ti^{4+}). It is possible that increases in the Ti^{3+}/Ti^{4+} and Cu^{+}/Cu^{2+} ratios might be caused by an increase in oxygen

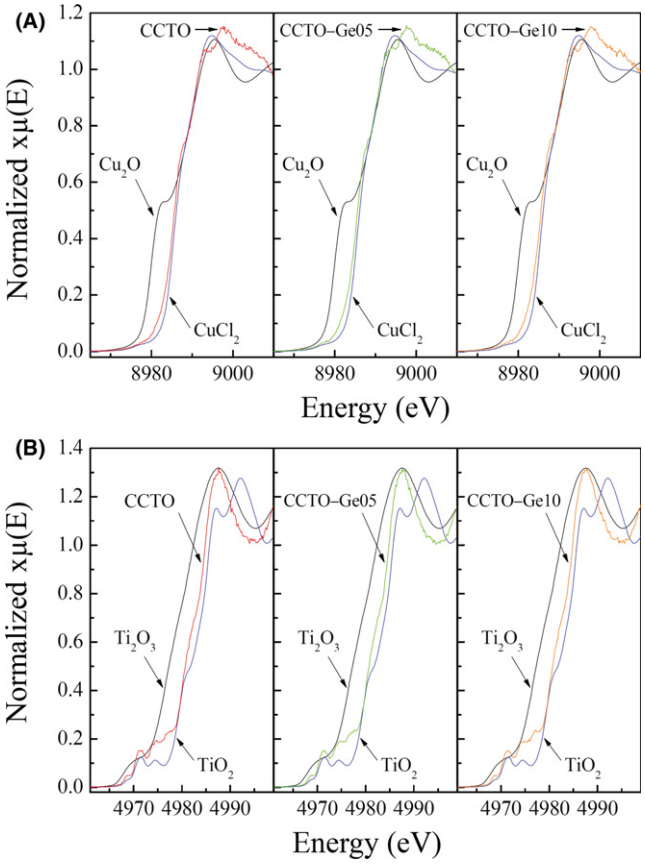

FIGURE 5 (A) Normalized XANES spectra for Cu *K*-edge for the CCTO, CCTO–Ge05, and CCTO–Ge10 ceramics and (B) Normalized XANES spectra for Ti *K*-edge [Color figure can be viewed at wileyonlinelibrary.com]

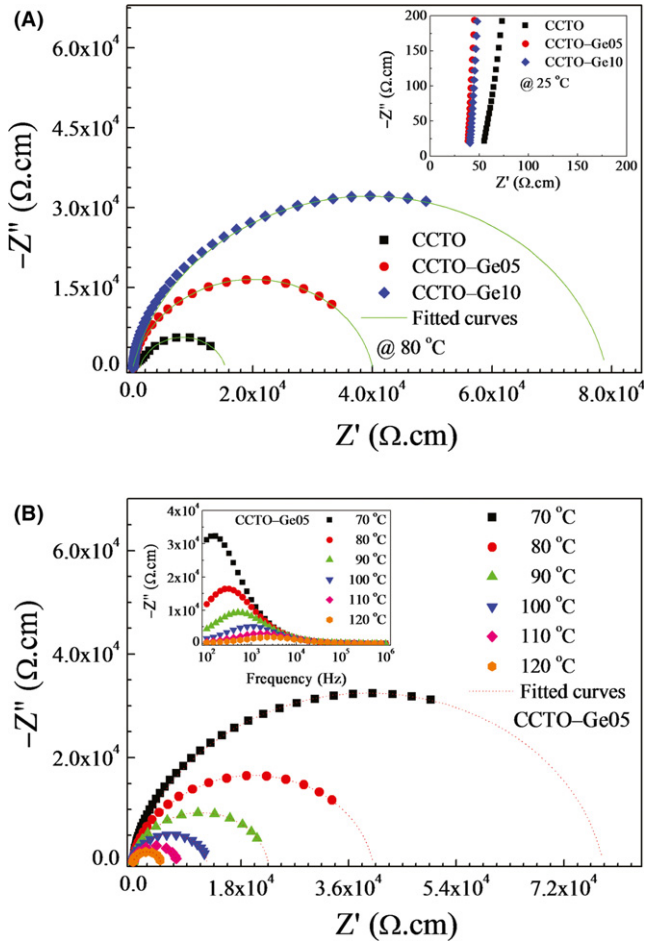

FIGURE 6 (A) Impedance complex plane (Z*) plots at 80°C for the CCTO, CCTO−Ge05, and CCTO−Ge10 ceramics; inset shows an enlarged view of Z* plots at 25°C close to the origin, revealing a nonzero intercept on Z′ axis. (B) Z* plots of the CCTO−Ge05 ceramic in the temperature range 70°C–120°C [Color figure can be viewed at wileyonlinelibrary.com]

vacancies inside the large grains, as the grain growth of CCTO ceramics was shown to be associated with the oxygen vacancies.[32,34]

The effects of Ge^{4+} doping ions electrical properties of the grain and GB of CCTO ceramics were also characterized using impedance spectroscopy. The resistances of the grain and GBs (R_g and R_{gb}, respectively) can usually be estimated from the nonzero intercept on the Z′ axis and the diameter of a large semicircular arc of Z* plots, respectively. The impedance complex (Z*) plots were fitted using a modified equation for a Z* plot for a simple equivalent circuit consisting of parallel $R_{gb}C_{gb}$ elements connected to R_g in series:[30]

$$Z^* = R_g + \frac{R_{gb}}{1 + (j\omega R_{gb}C_{gb})^{\alpha}} \quad (2)$$

where α is a constant parameter ($0<\alpha\leq 1$) and ω is the angular frequency of an applied AC field. Usually, the grain capacitance (C_g) is not accessible and the respective capacitor can simply be removed from the circuit. At around RT, only a linear part of a large semicircle arc was observed. Consequently, Z* plots of all the samples cannot be fitted accurately. Only R_g can be obtained from the nonzero intercept. Therefore, Z* plots of all the samples at 80°C were selected. Notably, Z* plots were well fitted by Equation (2), as illustrated in Figure 6A. R_{gb} values at 80°C for the CCTO, CCTO–Ge05, and CCTO–Ge10 ceramics were 1.15×10^3, 3.30×10^4, and 6.44×10^4 Ω.cm, respectively. The Ge^{4+} dopant has a strong effect on the R_{gb} value, which remarkably increased with increasing Ge^{4+} content. R_{gb} increased even though a number of insulating GB layer decreased (or the mean grain size increased). Theoretically, when doping Ge^{4+} ions into Ti^{4+} sites, charge compensation is not required. Thus, the intrinsic properties (e.g., the potential barrier height) of the GBs should not be altered. A change in R_{gb} may have resulted from geometric parameters of the GB such as thickness. The increase in R_{gb} was likely caused by segregation of Cu- and/or Ge-rich phases along the GBs, as revealed in Figures 2 and 3C,F. As shown in the inset of Figure 6A,

the R_g of CCTO ceramics was slightly reduced by doping with Ge^{4+} ions, corresponding to a small increase in the Cu^{+}/Cu^{2+} and Ti^{3+}/Ti^{4+} ratios. Substitution of Ge^{4+} into CCTO ceramics not only increased R_{gb} but also decreased R_g and the free charge carriers inside the grains.

Figure 6B, Z* plots at higher temperatures of all ceramics were well fitted by Equation (2). R_{gb} values at different temperatures could be obtained. According to our previous work,[35,36] R_g can easily be calculated from the frequency dependence of Y'', the imaginary part of admittance complex (Y*). $R_g \approx 1/2Y''_{max}$, where Y''_{max} is the maximum value at the Y''-peak. R_g values at various temperatures obtained from the impedance and admittance analyses were nearly the same in value. Figure 7A-C, the Y'' peaks at temperatures below 0°C for the CCTO, CCTO–Ge05, and CCTO–Ge10 ceramics were observed in the frequency range 10^5–10^6 Hz. At higher temperatures, the Y'' peaks shifted out of the upper limit of the measured frequency range. The magnitude of the Y'' peak increased with increasing temperature, indicating a decrease in R_g. Variation in R_{gb} and R_g for all the samples followed the Arrhenius law:

$$R_{g,gb} = R_0 \exp\left(E_{g,gb}/k_B T\right) \quad (3)$$

where E_g and E_{gb} are the activation energies for conduction inside the grains and at the GBs, respectively. R_0 is a pre-exponential constant term. k_B and T are the Boltzmann constant and absolute temperature, respectively. Figure 7D and its inset, the temperature dependencies of R_{gb} and R_g were linearly fitted by Equation (3). The activation energies were calculated from the slopes of these linear relationships. E_g of the CCTO, CCTO–Ge05, and CCTO–Ge10 ceramics was found to be 97, 91, and 96 meV, respectively. E_g of $CaCu_3Ti_{4-x}Ge_xO_{12}$ ceramics slightly changed with variation in the Ge^{4+} content. This result was closely associated with a slight decrease in R_g. Alternatively, E_{gb} was enhanced by Ge^{4+} doping. E_{gb} values were 450, 658, and 633 meV, respectively. This result may have been caused by the segregation of Cu- and/or Ge-rich phases along the GBs.

According to the increase in both of R_{gb} and E_{gb} of $CaCu_3Ti_{4-x}Ge_xO_{12}$ ceramics, the influence of Ge^{4+} on the enhanced nonlinear *J-E* properties was expected, even though these two properties were measured at different voltage levels. As shown in the inset (1) of Figure 8, all the samples exhibited nonlinear *J-E* characteristics, confirming a close correlation between the electrically heterogeneous IBLC structure and nonlinear *J-E* behavior. The α values of the CCTO, CCTO–Ge05, and CCTO–Ge10 ceramics were, respectively, found to be 2.60, 4.41, and 4.71, whereas the E_b values were 72.8, 268.8, and 242.7 $V{\cdot}cm^{-1}$, respectively. Usually, an increase in the GB density is the primary factor for enhancement of nonlinear *J-E* properties.[7,16,25] However, the values of E_b and α of $CaCu_3Ti_{4-x}Ge_xO_{12}$ ceramics were enhanced even though the GB density was reduced due to its enlarged grain size. A larger total resistance of a sample with fewer insulating layers indicated that the average resistance of individual

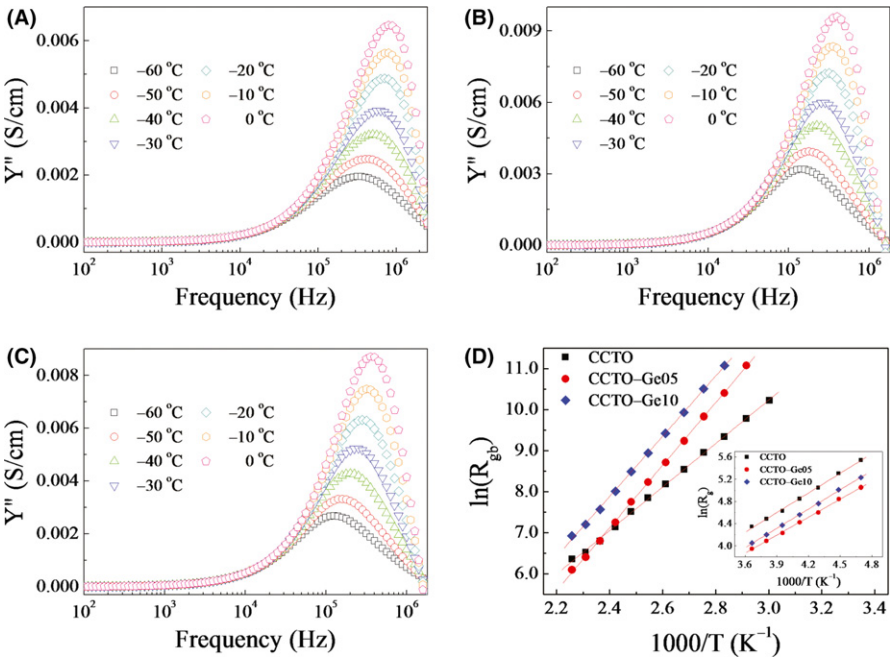

FIGURE 7 (A-C) Frequency dependence of Y'' at different temperatures for the CCTO, CCTO−Ge05, and CCTO−Ge10 ceramics. (D) Arrhenius plots of R_{gb} for all the samples; inset demonstrates the Arrhenius plots of R_g [Color figure can be viewed at wileyonlinelibrary.com]

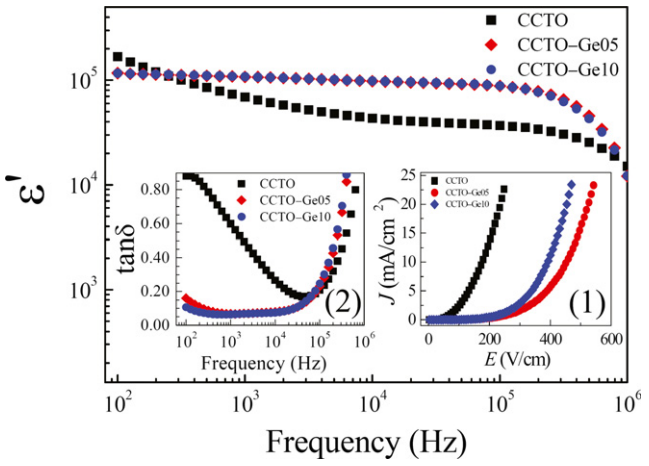

FIGURE 8 Frequency dependence of ε′ at 25°C for the CCTO, CCTO−Ge05, and CCTO−Ge10 ceramics; insets (1) and (2) show tanδ as a function of frequency and *J*-*E* characteristics at RT [Color figure can be viewed at wileyonlinelibrary.com]

insulating layers in the CCTO–Ge05 and CCTO–Ge10 ceramics was much larger in the undoped CCTO ceramics.

According to the impedance spectroscopy analysis and investigation of nonlinear electrical properties, it was clearly shown that $CaCu_3Ti_{4-x}Ge_xO_{12}$ ceramics were electrically heterogeneous, comprised of insulating GBs and semiconducting grains. Thus, the giant dielectric response and tanδ can be controlled by tuning the properties of the grains and GBs. The frequency dependence of ε′ and tanδ of the $CaCu_3Ti_{4-x}Ge_xO_{12}$ ceramics with difference in microstructures is demonstrated in Figure 8 and inset (2). The low-frequency ε′ of the CCTO ceramic was significantly dependent on frequency. Interestingly, substitution of Ge^{4+} ions not only enhanced the ε′ response but also enabled a stable frequency dependence of ε′ in the range 10^2–10^5 Hz. A rapid decrease in ε′ at frequencies higher than 10^5 Hz and the corresponding rapid increase in tanδ were caused by dielectric relaxation.[13,17] The ε′ values at 1 kHz and RT of the $CaCu_3Ti_{4-x}Ge_xO_{12}$ with x=0, 0.05, and 0.10 were, respectively, 69029, 107667, and 108165, whereas tanδ values were 0.600, 0.068, and 0.064, respectively. This significant increase in ε′ is quite consistent with IBLC model as an enhanced ε′ value was related to an increase in the mean grain size. Another important reason for this is the increase free charges inside the grains (in Cu^+/Cu^{2+} and Ti^{3+}/Ti^{4+} ratios). Under an applied electric field, more charge carriers inside the semiconducting grains moved and were eventually trapped at the GBs. This caused an increase in the interfacial polarization intensity, giving rise to an enhanced ε′ value.

Interestingly, tanδ values of the CCTO–Ge05 and CCTO–Ge10 ceramics were decreased by a factor of 10 compared to that of the undoped CCTO ceramic. Generally, both ε′ and tanδ values of undoped CCTO ceramics increased with increasing mean grain size.[37,38] In such a general case, the enhanced low-frequency tanδ can be attributed to a decrease in the number of insulating GB

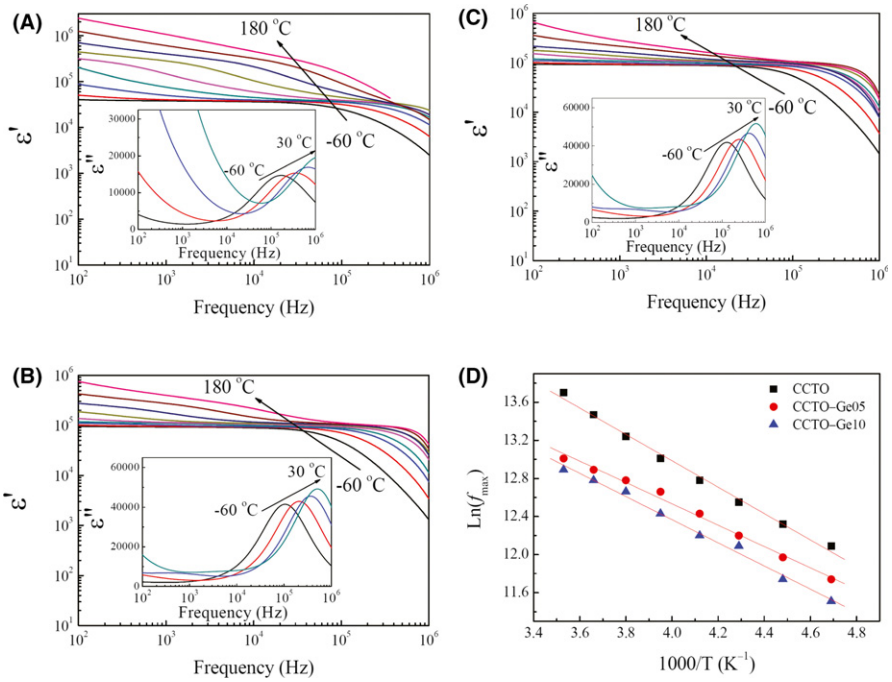

FIGURE 9 Frequency dependence of ε′ at different temperatures (−60°C to 180°C) of (A) CCTO, (B) CCTO−Ge05, and (C) CCTO−Ge10 ceramics; insets show their tanδ values. (D) Arrhenius plot for the relaxation frequency (f_{max}) [Color figure can be viewed at wileyonlinelibrary.com]

layers as the mean grain size increased, giving rise to a decrease in R_{gb}. A significant reduction in tanδ in the CCTO–Ge05 and CCTO–Ge10 ceramics can therefore result in an enhancement of R_{gb}.[16,30,39]

The frequency dependencies of ε′ and ε″ (the imaginary part of the complex dielectric permittivity, $\varepsilon''=\varepsilon'\times\tan\delta$) at different temperatures were studied. Figure 9A-C, a strong dispersion of ε′ as a function of temperature in the range −60°C–180°C was observed in the dielectric spectra of the CCTO ceramic. This was less dominant in the CCTO–Ge05 and CCTO–Ge10 ceramics, indicating a greater temperature stability of ε′. Obviously, two dielectric relaxations were observed in distinct frequency ranges, that is, 10^4–10^5 Hz and 10^5–10^6 Hz. The low-frequency dielectric relaxation is likely attributed to the sample-electrode effect. The rapid decrease in ε′ in a high-frequency range and corresponding ε″ peak (inset figures) shifted to higher frequencies as temperature was increased, indicating a thermally activated dielectric relaxation behavior. The activation energy (E_a) required for the relatively high-frequency dielectric relaxation was calculated from the temperature dependence of the critical frequency (f_{max}) (the frequency at which the relaxation ε″ peak appeared) following:

$$f_{max} = f_0 \exp\left(\frac{-E_a}{k_B T}\right) \quad (4)$$

where f_0 is a constant value. As depicted in Figure 9D, the frequency dependence of f_{max} for all the ceramics followed the Arrhenius law (Equation 4). The E_a values of the CCTO, CCTO–Ge05, and CCTO–Ge10 ceramics were 120, 91, and 96 meV, respectively. The trends of change in the E_g and E_a values were similar. According to the Maxwell-Wagner polarization relaxation model based on the IBLC structure, the temperature dependence of f_{max} can be expressed in terms of R_g.[19] Therefore, the similar values of E_a and E_g indicated that the giant dielectric response in these ceramics was extrinsic in origin and related to their electrically IBLC microstructures. Substitution of Ge^{4+} into Ti^{4+} sites can simultaneously improve the giant dielectric and nonlinear electrical properties of CCTO ceramics. The improved dielectric properties were attributed to a combination causes including an enlarged grain size, increased free charge carriers, and segregation of liquid at the GBs. The last cause can also enhance the nonlinear electrical properties.

4 | CONCLUSIONS

The $CaCu_3Ti_{4-x}Ge_xO_{12}$ ceramics with x=0-0.10 were synthesized using a solid-state reaction method. A pure phase of CCTO was confirmed in all the sintered ceramic samples. All sintered ceramics had a highly dense microstructure. Doping CCTO with Ge^{4+} caused an increase in the mean grain size, which was primarily due to the liquid phase sintering, revealed by SEM mapping elements in the surface morphology. Significantly enhanced R_{gb} coupled with a slightly decreased R_g was achieved. Enhancement of ε′ from 6.90×10^4 to 1.08×10^5 while reducing tanδ by one order of magnitude was achieved. The nonlinear electrical properties of CCTO were enhanced by doping with Ge^{4+} ions. The enhanced giant dielectric properties were ascribed to the enlarged grain size, increased free charge carriers, and segregation of liquid at the GBs.

ACKNOWLEDGMENTS

This work was financially supported by the Thailand Research Fund (TRF) and Khon Kaen University (Contract No. RSA5880012) and under the TRF Senior Research Scholar (Contract No. RTA5780004). This work was partially supported by the Nanotechnology Center (NANOTEC), NSTDA, Ministry of Science and Technology, Thailand, through its program of Center of Excellence Network and the Higher Education Research Promotion and National Research University Project of Thailand, Office of the Higher Education Commission, through the Advanced Functional Materials Cluster of Khon Kaen University. The authors thank the Synchrotron Light Research Institute (BL5.2) (Public Organization), Nakhon Ratchasima, Thailand for XAS measurements. J. Boonlakhorn would like to thank the Graduate School, Khon Kaen University (Grant No. 581T211) for his Ph.D. scholarship.

REFERENCES

1. Subramanian MA, Li D, Duan N, Reisner BA, Sleight AW. High dielectric constant in $ACu_3Ti_4O_{12}$ and $ACu_3Ti_3FeO_{12}$ phases. *J Solid State Chem*. 2000;151:323-325.
2. Liu L, Fan H, Fang P, Chen X. Sol–gel derived $CaCu_3Ti_4O_{12}$ ceramics: synthesis, characterization and electrical properties. *Mater Res Bull*. 2008;43:1800-1807.
3. Liu L, Huang Y, Li Y, et al. Dielectric and non-Ohmic properties of $CaCu_3Ti_4O_{12}$ ceramics modified with NiO, SnO_2, SiO_2, and Al_2O_3 additives. *J Mater Sci*. 2012;47:2294-2299.
4. Sun L, Zhang R, Wang Z, Cao E, Zhang Y, Ju L. Microstructure and enhanced dielectric response in Mg doped $CaCu_3Ti_4O_{12}$ ceramics. *J Alloys Compd*. 2016;663:345-350.
5. Nautiyal A, Autret C, Honstettre C, et al. Local analysis of the grain and grain boundary contributions to the bulk dielectric properties of $Ca(Cu_{3-y}Mg_y)Ti_4O_{12}$ ceramics: importance of the potential barrier at the grain boundary. *J Eur Ceram Soc*. 2016;36:1391-1398.
6. Wang XW, Jia PB, Wang XE, Zhang BH, Sun LY, Liu QB. Calcining temperature dependence on structure and dielectric properties of $CaCu_3Ti_4O_{12}$ ceramics. *J Mater Sci: Mater Electron*. 2016;1–7.
7. Chung S-Y, Kim I-D, Kang S-JL. Strong nonlinear current–voltage behaviour in perovskite-derivative calcium copper titanate. *Nat Mater*. 2004;3:774-778.

8. Schmidt R, Pandey S, Fiorenza P, Sinclair DC. Non-stoichiometry in "$CaCu_3Ti_4O_{12}$" (CCTO) ceramics. *RSC Adv*. 2013;3:14580-14589.
9. Costa SIR, Li M, Frade JR, Sinclair DC. Modulus spectroscopy of $CaCu_3Ti_4O_{12}$ ceramics: clues to the internal barrier layer capacitance mechanism. *RSC Adv*. 2013;3:7030-7036.
10. Hao W, Wu H, Xu P, et al. Influence of Sb-doping on dielectric properties of $NaCu_3Ti_3TaO_{12}$ ceramics and relevant mechanism (s). *Ceram Int*. 2017;43:3631-3638.
11. Liu Y, Wang W, Huang J, Tang F, Zhu C, Cao Y. Dielectric properties of giant permittivity $NaCu_3Ti_3NbO_{12}$ ceramics. *Ceram Int*. 2013;39:9201-9206.
12. Hao W, Zhang J, Tan Y, Zhao M, Wang C. Giant dielectric permittivity properties and relevant mechanism of $NaCu_3Ti_3SbO_{12}$ ceramics. *J Am Ceram Soc*. 2011;94:1067-1072.
13. Ni L, Chen XM. Enhancement of giant dielectric response in $CaCu_3Ti_4O_{12}$ ceramics by Zn substitution. *J Am Ceram Soc*. 2010;93:184-189.
14. Wang Y, Ni L, Chen XM. Effects of Nd-substitution on microstructures and dielectric characteristics of $CaCu_3Ti_4O_{12}$ ceramics. *J Mater Sci: Mater Electron*. 2011;22:345-350.
15. Sun L, Zhang R, Wang Z, Cao E, Zhang Y, Ju L. Microstructure, dielectric properties and impedance spectroscopy of Ni doped $CaCu_3Ti_4O_{12}$ ceramics. *RSC Adv*. 2016;6:55984-55989.
16. Boonlakhorn J, Putasaeng B, Kidkhunthod P, Thongbai P. Improved dielectric properties of (Y + Mg) co-doped $CaCu_3Ti_4O_{12}$ ceramics by controlling geometric and intrinsic properties of grain boundaries. *Mater Des*. 2016;92:494-498.
17. Ni L, Chen XM, Liu XQ. Structure and modified giant dielectric response in $CaCu_3(Ti_{1-x}Sn_x)_4O_{12}$ ceramics. *Mater Chem Phys*. 2010;124:982-986.
18. Sun L, Wang Z, Hao W, Cao E, Zhang Y, Peng H. Influence of zirconium doping on microstructure and dielectric properties of $CaCu_3Ti_4O_{12}$ synthesized by the sol–gel method. *J Alloys Compd*. 2015;651:283-289.
19. ThongbaiP, Jumpatam J, Putasaeng B, Yamwong T, Maensiri S. The origin of giant dielectric relaxation and electrical responses of grains and grain boundaries of W-doped $CaCu_3Ti_4O_{12}$ ceramics. *J Appl Phys*. 2012;112:114115.
20. Singh L, Sin BC, Kim IW, et al. A novel one-step flame synthesis method for tungsten-doped CCTO. *J Am Ceram Soc*. 2016;99:27-34.
21. Li WL, Zhao Y, Chi QG, Zhang ZG, Fei WD. Enhanced performance of core-shell-like structure Zr-doped $CaCu_3Ti_4O_{12}$ ceramics prepared by a flame synthetic approach. *RSC Adv*. 2012;2:6073.
22. Singh L, Kim IW, Sin BC, et al. Dielectric studies of a nanocrystalline $CaCu_{2.90}Zn_{0.10}Ti_4O_{12}$electro-ceramic by one pot glycine assisted synthesis from inexpensive TiO_2 for energy storage capacitors. *RSC Adv*. 2014;4:52770-52784.
23. Ab Rahman MF, Hutagalung SD, Ahmad ZA, Ain MF, Mohamed JJ. The effect of different dopant site (Cu and Ca) by magnesium on$CaCu_3Ti_4O_{12}$ dielectric properties. *J Mater Sci: Mater Electron*. 2015;26:3947-3956.
24. Amaral F, Costa LC, Valente MA, Henry F. Dielectric relaxation and morphologic properties of $CaCu_3Ti_4O_{12}$ doped with GeO_2. *J Non-Cryst Solids*. 2009;355:2160-2164.
25. Boonlakhorn J, Kidkhunthod P, Thongbai P. A novel approach to achieve high dielectric permittivity and low loss tangent in $CaCu_3Ti_4O_{12}$ ceramics by co-doping with Sm^{3+} and Mg^{2+} ions. *J Eur Ceram Soc*. 2015;35:3521-3528.
26. Newville M. EXAFS analysis using FEFF and FEFFIT. *J Synchrotron Radiat*. 2001;8(Pt 2):96-100.
27. Silva Junior E, La Porta FA, Liu MS, Andres J, Varela JA, Longo E. A relationship between structural and electronic order-disorder effects and optical properties in crystalline TiO_2 nanomaterials. *Dalton Trans*. 2015;44:3159-3175.
28. Young RA, Wiles DB. Profile shape functions in Rietveld refinements. *J Appl Crystallogr*. 1982;15:430-438.
29. Shannon RD. Revised effective ionic radii and systematic studies of interatomic distances in halides and chalcogenides. *Acta Crystallogr*. 1976;32:751-767.
30. Thongbai P, Putasaeng B, Yamwong T, Amornkitbamrung V, Maensiri S. Liquid phase sintering behavior and improvement of giant dielectric properties by modifying microstructure and electrical response at grain boundaries of $CaCu_3Ti_{4-x}Mo_xO_{12}$ ceramics. *J Alloys Compd*. 2014;582:747-753.
31. Jumpatam J, Putasaeng B, Yamwong T, Thongbai P, Maensiri S. Enhancement of giant dielectric response in Ga-doped $CaCu_3Ti_4O_{12}$ ceramics. *Ceram Int*. 2013;39:1057-1064.
32. Felix AA, Bezzon VDN, Orlandi MO, et al. Role of oxygen on the phase stability and microstructure evolution of $CaCu_3Ti_4O_{12}$ ceramics. *J Eur Ceram Soc*. 2017;37:129-136.
33. Boonlakhorn J, Kidkhunthod P, Putasaeng B, Thongbai P. Significantly improved non-Ohmic and giant dielectric properties of $CaCu_{3-x}Zn_xTi_4O_{12}$ ceramics by enhancing grain boundary response. *Ceram Int*. 2017;43:2705-2711.
34. Yu R, Xue H, Cao Z, Chen L, Xiong Z. Effect of oxygen sintering atmosphere on the electrical behavior of CCTO ceramics. *J Eur Ceram Soc*. 2012;32:1245-1249.
35. Jumpatam J, Mooltang A, Putasaeng B, et al. Effects of Mg^{2+} doping ions on giant dielectric properties and electrical responses of $Na_{1/2}Y_{1/2}Cu_3Ti_4O_{12}$ ceramics. *Ceram Int*. 2016;42:16287-16295.
36. Jumpatam J, Somphan W, Boonlakhorn J, et al. Non-ohmic properties and electrical responses of grains and grain boundaries of $Na_{1/2}Y_{1/2}Cu_3Ti_4O_{12}$ ceramics. *J Am Ceram Soc*. 2016;100:157-166.
37. De Almeida-Didry S, Autret C, Lucas A, Honstettre C, Pacreau F, Gervais F. Leading role of grain boundaries in colossal permittivity of doped and undoped CCTO. *J Eur Ceram Soc*. 2014;34:3649-3654.
38. Thongbai P, Putasaeng B, Yamwong T, Maensiri S. Current–voltage nonlinear and dielectric properties of $CaCu_3Ti_4O_{12}$ ceramics prepared by a simple thermal decomposition method. *J Mater Sci: Mater Electron*. 2012;23:795-801.
39. Adams TB, Sinclair DC, West AR. Influence of processing conditions on the electrical properties of $CaCu_3Ti_4O_{12}$ ceramics. *J Am Ceram Soc*. 2006;89:3129-3135.

How to cite this article: Boonlakhorn J, Thongbai P, Putasaeng B, Kidkhunthod P, Maensiri S, Chindaprasirt P. Microstructural evolution, non-Ohmic properties, and giant dielectric response in $CaCu_3Ti_{4-x}Ge_xO_{12}$ ceramics. *J Am Ceram Soc*. 2017;100:3478–3487. https://doi.org/10.1111/jace.14886

J Polym Environ
DOI 10.1007/s10924-017-0957-x

ORIGINAL PAPER

Effect of Oregano Essential Oil Content on Properties of Green Biocomposites Based on Cassava Starch and Sugarcane Bagasse for Bioactive Packaging

Surachade Ketkaew[1] · Pornnapa Kasemsiri[1] · Salim Hiziroglu[2] · Wiyada Mongkolthanaruk[3] · Rungnapha Wannasutta[3] · Uraiwan Pongsa[4] · Prinya Chindaprasirt[5]

© Springer Science+Business Media New York 2017

Abstract In this study, 10 wt% sugarcane bagasse fiber-reinforced starch foam composites were prepared with different oregano essential oil (OEO) contents in the range of 2–8 wt% to improve the antimicrobial effectiveness of bioactive packaging. FT-IR analysis confirms that OEO penetrates into starch foam composite. From the result of antimicrobial activity, the incorporation of 8 wt% OEO in starch foam composite achieves the minimum inhibitory concentration against *Escherichia-coli* (*E. coli*) and *Staphylococcus-aureus* (*S. aureus*). OEO is more effective against *S. aureus* (Gram-positive bacteria) than *E. coli* (Gram-negative bacteria). The water absorption capacity and hygroscopicity of foam composite decrease with increasing OEO content. The lowest monolayer value is observed in starch foam composite containing 8 wt% OEO. The soil biodegradation rate and flexural strength of samples slightly decrease with increasing OEO content. As a result, starch foam composite containing OEO can be applied as bioactive packaging to preserve foods.

Keywords Starch foam composite · Essential oil · Moisture absorption · Antimicrobial activity · Soil burial degradation

Introduction

The development of materials from renewable resources has attracted a lot of attention. The use of bio-based material is one alternative to solve a critical environmental problem from petroleum-based products consumption [1, 2]. These products are non-biodegradable and require several years for degradation [3–5]. Various methods such as incineration and recycling have been used to manage the plastic waste. However these methods are insufficient for solving the global environmental pollution [6, 7].

Starch is one of the alternative materials that have been widely used to produce biodegradable packaging due to its abundant and environmentally friendly [8, 9]. The common starch used for producing foam packaging includes cassava [10], corn [11], potato [12], and rice [13]. Novel sugar palm starch has lately been reported to be a good thin film-forming material for food packaging application due to its high amylose content (~37%) as compared to conventional starch polymers [14–16]. Previous research reported that degree of polymerization efficiency was dependent on amylose content of the starch. Starch with different amylose/amylopectin ratio have different phase transition behaviors and rheological properties [17]. However, native starch has some disadvantages i.e. high water absorption and poor mechanical properties [18]. Recently, natural fibers such as

✉ Pornnapa Kasemsiri
pornkas@kku.ac.th

1 Sustainable Infrastructure Research and Development Center and Department of Chemical Engineering, Faculty of Engineering, Khon Kaen University, Khon Kaen 40002, Thailand

2 Department of Natural Resource Ecology and Management, Oklahoma State University, 303-G Agricultural Hall, Stillwater, OK 74078, USA

3 Department of Microbiology, Faculty of Science, Khon Kaen University, Khon Kaen, Thailand

4 Division of Industrial Engineering Technology, Faculty of Industry and Technology, Rajamangala University of Technology Rattanakosin, Wang Klai Kang Won Campus, Hua Hin, Prachuap Khiri Khan 77110, Thailand

5 Sustainable Infrastructure Research and Development Center and Department of Civil Engineering, Faculty of Engineering, Khon Kaen University, Khon Kaen 40002, Thailand

Published online: 06 February 2017

sugarcane bagasse [19], cassava bagasse [20, 21], kraft pulp [22], sugar palm fiber [16] and oil palm fiber [13] have been used as reinforcing phase to improve the mechanical properties. Water absorption of starch foam was also enhanced by the addition of hydrophobic materials such as palm oil [22], essential oil [20, 23–25], beeswax [26] and agar [14]. Essential oils are interesting hydrophobic natural additives with antimicrobial and antioxidant properties [20]. They are classified as generally recognized as safe (GRAS) compound and extensively used in the food industry [27, 28]. Essential oils have been incorporated into various types of bioactive packaging in order to extend the shelf life of food products and inhibit the growth of food-borne bacteria [20, 23–25]. The addition of essential oils into edible films have been reported by many researchers whereas few studies have been focused on the effect of essential oils on the properties of biodegradable foams [29–33]. Debiagi et al. [20] studied foam trays from synthetic biopolymer such a polyvinyl alcohol composite containing clove and oregano essential oils. The addition of essential oils improved the water adsorption and flexibility of specimens. The foam trays incorporated with oregano essential oil was the most effective on antimicrobial activity to inhibit the growth of *Escherichia coli* (*E. coli*) and *Staphylococcus aureus* (*S. aureus*).

Currently, there is no information about the effect of oregano essential oil (OEO) on the overall properties of natural biopolymer foam composite. Therefore, the purpose of this research is to investigate the properties of starch foam composite containing OEO in terms of physical, mechanical and biodegradable characteristics. The antimicrobial properties of the samples against gram-positive bacteria (*S. aureus*) and gram-negative bacteria (*E. coli*) are observed.

Materials and Methods

Materials

Cassava starch was purchased from Bangkok Interfood Ltd., Thailand. Sugarcane fiber with particle size of 180–250 µm was used. The OEO (*Origanum vulgare*) was obtained from Sigma-Aldrich Co. LLC.

Microbial Culture

Gram-positive bacteria (*S. aureus* ATCC25923) and gram-negative bacteria (*E. coli* ATCC25922) were obtained from Department of Microbiology, Faculty of Science, Khon Kaen University, Khon Kaen, Thailand.

Preparation of Starch Foam Composite Containing OEO

The starch foam composite was prepared by adding 30 ml of water to 30 g of cassava starch and mixed for 5 min using kitchen aid mixer (Electrolux EHM 2000). The sugarcane fiber at 10 wt% of starch were added and mixed for another 5 min at 80 °C. The OEO at the dosages of 2, 4, 6 and 8 wt% of starch was added and mixed for 3 min. The obtained compound was pressed in 100 mm × 100 mm × 6.5 mm mold with hydraulic press using a pressure of 4.0 MPa at 230 °C for 5 min. The high temperature in the range of 190–250 °C was recommended to achieve the minimum baking time and maximum venting of water from batter which causes the starch to foam out and take up the shape of the mold [22, 26, 34, 35]. The samples of starch-based foam specimens are demonstrated in Fig. 1.

Characterization of the Starch Foam Composite Containing OEO

Attenuated total reflection infrared (FTIR–ATR) spectra of sample were tested by Bruker Tensor 27 spectrometer. All spectra were taken as a function of time with 64 scans at a resolution of 4 cm^{-1} and a spectral range of 4000–650 cm^{-1}.

The surface of sample was investigated using a scanning electron microscope (SEM) (Hitachi model S-3000N) at an acceleration voltage of 20 kV. All samples were cut to 3 mm and coated with gold using an ion sputtering device.

Water absorption capacity (WAC) was tested in accordance with Cobb test [36]. The dimension of specimen was 50 mm × 25 mm × 6.5 mm. All samples were weighted and submerged in 100 ml of distilled water for 1, 5, 10, 15 and 30 min and then removed, wiped and weighted. WAC was calculated according to the weight difference and expressed as the mass of absorbed water per mass of the original sample. The reported values are the average of five samples.

Water sorption isotherm of starch foam composites containing OEO were determined by GAB (Guggenheim,

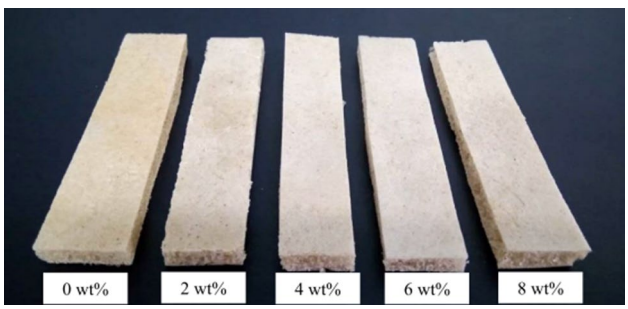

Fig. 1 Samples of starch-based foam specimens

Anderson, de Boer) model. The GAB model was used to calculate the isotherm data and monolayer values of various types of starch foam composites. The GAB isotherm is shown in Eq. (1) [20, 37].

$$M = \frac{m_o CKa_w}{(1 - Ka_w)(1 - Ka_w + CKa_w)} \quad (1)$$

where M is the equilibrium moisture content at a given water activity (a_w), a_w is RH/100, m_o is the monolayer value (g water/g solid) and C and K are the GAB constants.

The 0.5 g samples were weighted and pre-dried for 15 days over anhydrous calcium chloride before the moisture sorption isotherm test. The samples were then placed over saturated salt solution in separate desiccators at specific relative humidity (10, 38, 43, 79 and 84) and held at 25 °C. The equilibrium moisture was calculated from the dry sample mass gain at each relative humidity. At each relative humidity condition, the weight of sample was recorded at the initial and final incubation times (14 days).

Antimicrobial activity of the samples was studied using the agar diffusion method according to a modified version of Hosseini et al. [38]. Two different foodborne pathogens viz., *E. coli* and *S. aureus* were used as representative strains of pathogens. The bacterial were cultured overnight in brain heart fusion broth at 37 °C, then bacterial culture was diluted in medium until turbidity equal to McFarland scale 0.5 (approximately 10^8 CFU/ml). The Muller Hinton Agar plates were seeded with bacterial inoculums by swab plate technique. The sterile samples were cut into 6 mm disk and placed plates. The diameter of inhibition zone (mm) around the disc was measured after 24 h of incubation at 37 °C.

Flexural strength of starch foam composites containing OEO was tested by universal testing machine (Instron, Model 5567) equipped with a 10 kN load cell in accordance with ASTM D 790-10 [39]. The test was performed in a 3-point bending mode with a support span of 100 mm at the crosshead speed of 2.67 mm/min.

Soil burial degradation test was performed using the method suggested by Ibrahim et al. [40]. The dimension of specimen was 40 mm × 6.5 mm × 2 mm. All specimens were buried at 10 cm depth in a mixture of 50% sand and 50% soil with temperature of 30 ± 2 °C and water content of 35 ± 5%. After 30 days, the specimens were collected and washed with distilled water and dried in the oven at 105 °C for 24 h. The weight loss was calculated. The reported results were the average of three samples.

Results and Discussion

Attenuated Total Reflection Infrared Analysis of Starch Foam Composite Containing OEO

The interactions of starch matrix and additives viz., sugarcane bagasse and OEO were analyzed by FTIR spectroscopy. ATR–FTIR spectra of starch, sugarcane bagasse and OEO are shown in Fig. 2. Figure 2a showed the characteristic FTIR graph of starch. The peaks at 3280 and 1645 cm^{-1} were attributed to O–H stretching and bending of water, respectively. The adsorption band at 2918 cm^{-1} was assigned to C–H stretching whereas the peak at 1443 cm^{-1} was related to C–H_2 stretching. The peaks at 986 and 1158 cm^{-1} were attributed to C–O stretching [41, 42]. The characteristic peaks of sugarcane bagasse are shown in Fig. 2b. The main characteristic peaks were attributed to lignin, cellulose and hemicellulose. The broad bands at 3336 and 2926 cm^{-1} were assigned to O–H group and C–H group, respectively. The peaks at 1727 cm^{-1} was related to C=O of hemicellulose. The peaks at 1427 and 1236 cm^{-1} were assigned to C–H_2 and C–O–C of cellulose chain. The band at 1145 cm^{-1} corresponded to the asymmetric deformation of C–O–C of cellulose and hemicellulose [43]. Figure 2c showed the characteristic of adsorption bands of OEO. The broad band in the range of 3300–3600 cm^{-1} was related to O–H group of phenolic compounds. The peak at 1627 cm^{-1} was assigned to C=C vinyl ester stretching from terpenic derivatives such a beta-farnesene in OEO. The peaks at 1581 and 1518 cm^{-1} were attributed to benzene

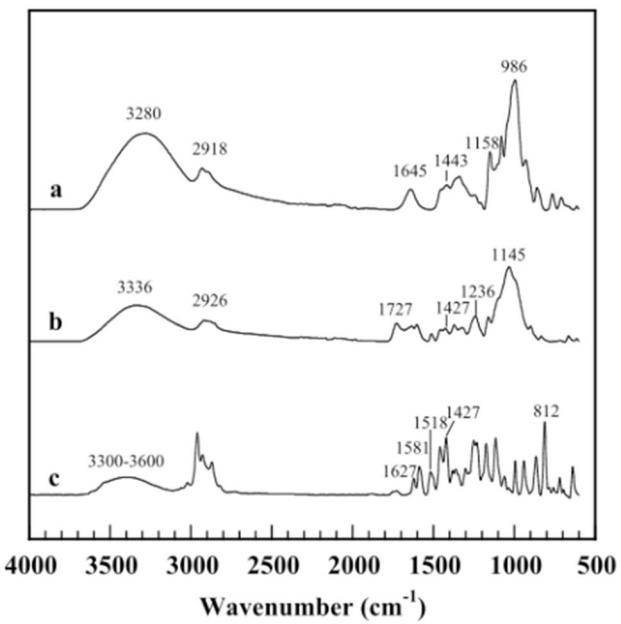

Fig. 2 FTIR spectra of *a* starch, *b* sugarcane bagasse and *c* OEO

ring of the main phenolic compounds i.e. carvacol and thymaol. The peak at 1427 cm^{-1} was also related to O–H bending of the phenolic compounds. The sharp peak at 812 cm^{-1} was assigned to O–H bending out of plane in di- and tri-substituted aromatic compounds such as carvacol, thymol and derivative terpenes [33, 44].

Generally, the shift of characteristic spectra peak indicated the chemical interactions of polymer blend due to hydrogen bond or dipolar interaction [10, 45]. Figure 3 depicted the adsorption bands of starch foam reinforced with sugarcane bagasse (SCB) and blended SCB–OEO. The presence of characteristic peaks of OEO in starch foam composite was observed as shown in Fig. 3b. This result confirmed that the major components of OEO penetrated into the starch foam composite after processing. Furthermore, the shift of spectra at 3200–3400 and 1443 cm^{-1} for SCB and blended SCB–OEO was also observed as illustrated in Fig. 3a, b. This phenomenon indicated the intermolecular hydrogen bond among starch matrix, sugarcane bagasse and OEO.

Antimicrobial Activity

The results of antimicrobial activity of samples containing 2, 4, 6 and 8 wt% OEO against *E. coli* and *S. aureus* are shown in Fig. 4 and summarized in Table 1. The addition of 8 wt% OEO was required for starch foam composite to achieve the minimum inhibitory concentration against *E. coli* and *S. aureus*. The lower concentration of OEO had no observed the growth inhibition. The antimicrobial activity

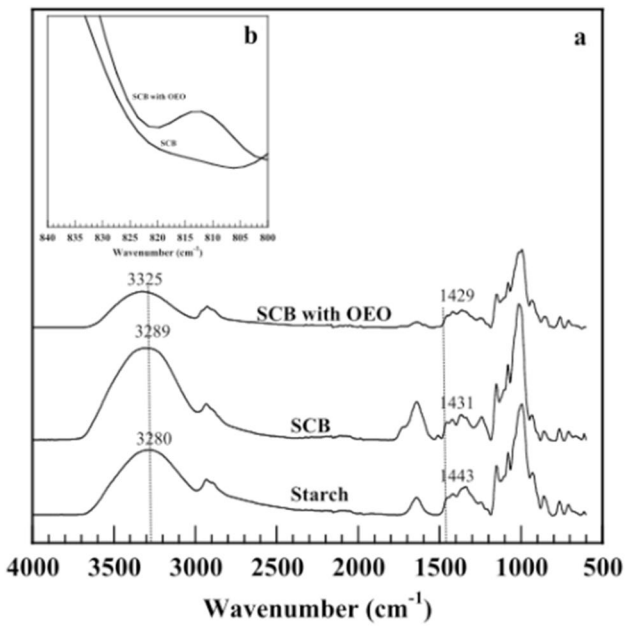

Fig. 3 FTIR spectra of starch foam reinforced with sugarcane bagasse (SCB) and blended SCB–OEO

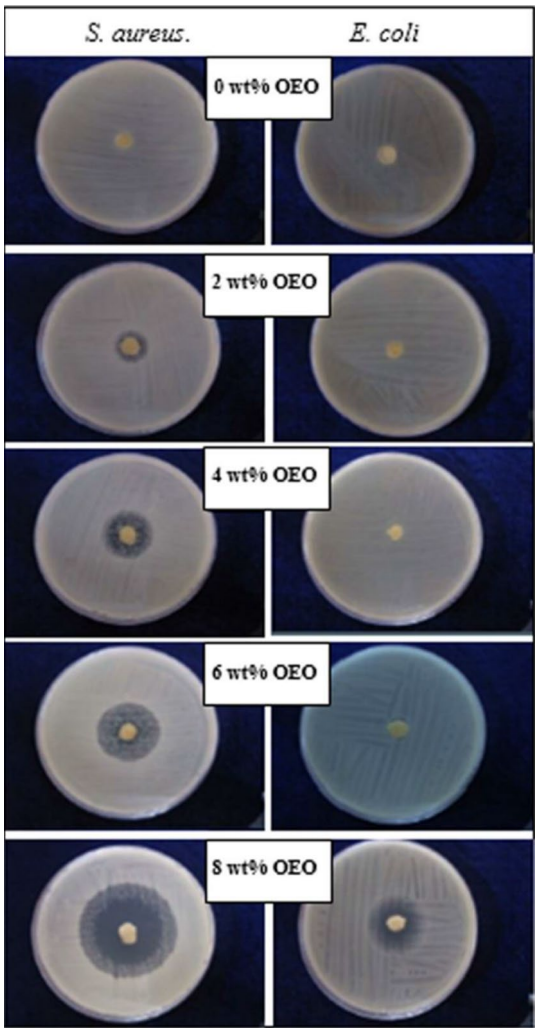

Fig. 4 Antimicrobial activity of starch foam composites containing OEO against *E. coli* and *S. aureus*

of OEO was attributed to oregano's terpenoid fraction consisted of carvacrol, thymol and p-cymene [46, 47]. These components were hydrophobic which enabled them to partition in the lipid of bacterial cell membrane and mitochondria, resulting in the leakage of ions from the cytoplasm and cell death [48]. Moreover, the starch foam incorporated with 8 wt% OEO showed the largest clear zone for *S. aureus*, as clearly depicted in Fig. 4. This observation indicated that OEO was more effective against *S. aureus* (Gram-positive bacteria) than *E. coli* (Gram-negative bacteria). It is hypothesized that the presence of outer membrane surrounding the cell wall in gram negative bacteria restricts the diffusion of hydrophobic compounds via its lipopolysaccharide covering [48, 49]. Similar observations were also observed in biodegradable polymer incorporated with OEO such as cassava bagasse/polyvinyl alcohol [20], fish gelatin/chitosan film [46], biogenic gelatin film [50] and cassava starch/chitosan film [33]. Based on this result,

Table 1 Antimicrobial activity of starch foam composite containing various OEO contents

OEO contents (wt%)	Inhibition zone (mm)	
	S. aureus	*E. Coli*
0	Not detected	Not detected
2	Not detected	Not detected
4	Not detected	Not detected
6	Not detected	Not detected
8	30 ± 3	16 ± 2

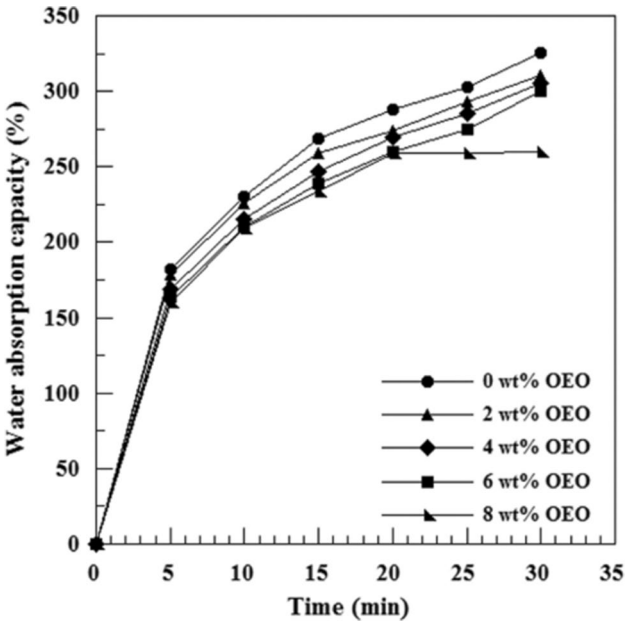

Fig. 5 Water absorption capacity of starch foam composite containing OEO

it can be concluded that the starch foam composite incorporated OEO could be applied as bioactive packaging to preserve foods.

Water Absorption Capacity (WAC)

The WAC of starch foam composite containing 2, 4, 6 and 8 wt% OEO is depicted in Fig. 5. The plot of percentage of WAC against time for all samples showed similar behavior. The sample rapidly absorbed water during first stage (0–5 min). The WAC values of samples decreased with increasing OEO content and ranged between 257 and 324% after 30 min of immersion. The starch foam composite containing 8 wt% OEO was saturated after 20 min of water immersion while the other samples presented the increase of WAC values. This was due to the incorporation of OEO improved the water resistant of samples by increasing the hydrophobicity of composite [41]. This observation is in good agreement with the previous reports. Debiagi et al. [20] showed that the addition of OEO can reduce the WAC of polyvinyl alcohol foam containing cassava bagasse. Kaisangsri et al. [22] reported that the incorporation of palm oil and natural fiber improved both water solubility and water absorption indices of starch foams. The synergistic effect for water resistance of starch foam containing combined additives such as kaolin, beewax and natural fiber were also observed [26].

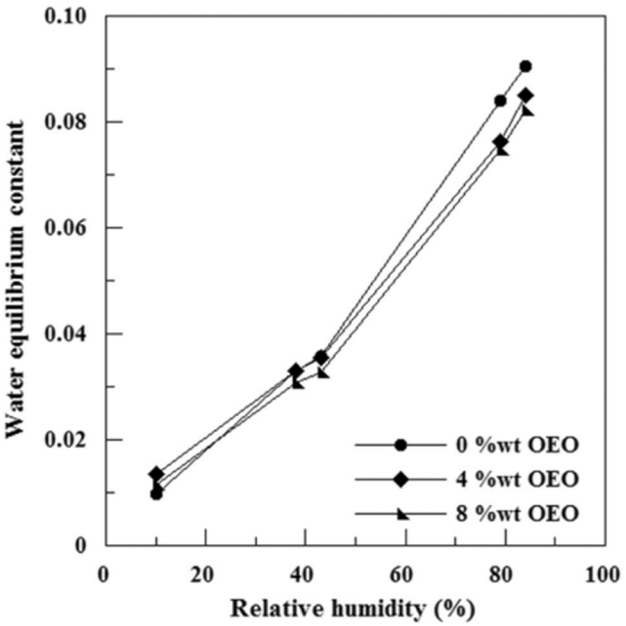

Fig. 6 Water sorption isotherms of the starch foam composites containing various OEO contents

Table 2 GAB model parameters of starch foam composites containing various OEO contents

OEO content (wt%)	m_o (g/g)	C	K	R^2
0	0.0371	3.848	0.769	0.994
4	0.0281	8.685	0.820	0.979
8	0.0271	7.058	0.828	0.960

Water Sorption Isotherms

The water sorption isotherms of the starch foam composites containing 0, 4 and 8 wt% OEO are shown in Fig. 6 and GAB model parameters are summarized in Table 2. All samples showed similar trends of isotherm sorption i.e. the equilibrium moisture content value increased with increasing relative humidity. This observation is in good agreement with the previous works [20, 51].

The monolayer value is a parameter obtained from GAB model. This parameter indicates the maximum amount of absorbed water in a single layer per gram of dry material. It is a measure of number of sorbing sites in the water sample [52]. Table 2 showed that the monolayer value of samples was in range of 0.027–0.037 g/g. The monolayer value tended to decrease with increasing OEO content. The lowest monolayer value was observed with 8 wt% OEO in starch foam composite. This result indicated that the addition of OEO in starch foam composite reduced the hygroscopicity of starch foam.

From Table 2, parameter C corresponded to the difference of water sorption in the upper layers and in monolayer. This parameter was affected by the addition of OEO. Parameter C of composite without OEO was 3.848 and increased to 8.685 and 7.0582 with 4 and 8% additions of OEO, respectively. Parameter K was, however, independent of the composition of starch foam composite. The result is in a good agreement with previous works [53, 54].

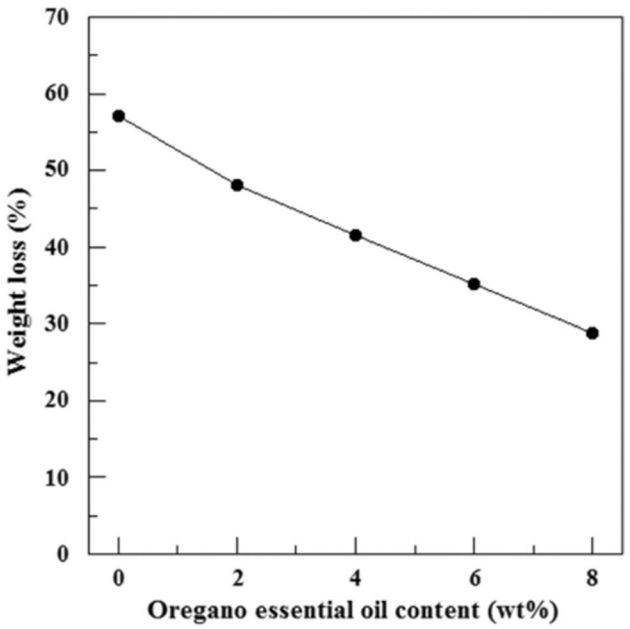

Fig. 7 Weight loss of starch foam composites containing 2, 4, 6 and 8 wt% OEO after 30 days of soil burial

Biodegradation in Soil

The weight loss of sample during soil burial test indicates the biodegradation process by the moisture and microorganism in soil [40, 55]. Figure 7 presents the weight loss of starch foam composites containing 2, 4, 6 and 8 wt% OEO after 30 days of soil burial. The weight loss values were 28.80–57.09%. The weight loss of samples decreased with increasing OEO content. As shown in Fig. 8a–e, the surface morphology of all samples changed after the soil burial test. Some cracks and holes were clearly observed on the surface of starch foam composites due to high biodegradation of starch, especially starch foam composite without OEO as shown in Fig. 8a. For the starch foam composites containing OEO as depicted in Fig. 8b–e, the existence of cracks and holes reduced as the content of OEO increased. This indicated that the OEO hindered the penetration of water and microorganism due to its hydrophobicity. The biodegradation rate decreased when the hydrophobicity of

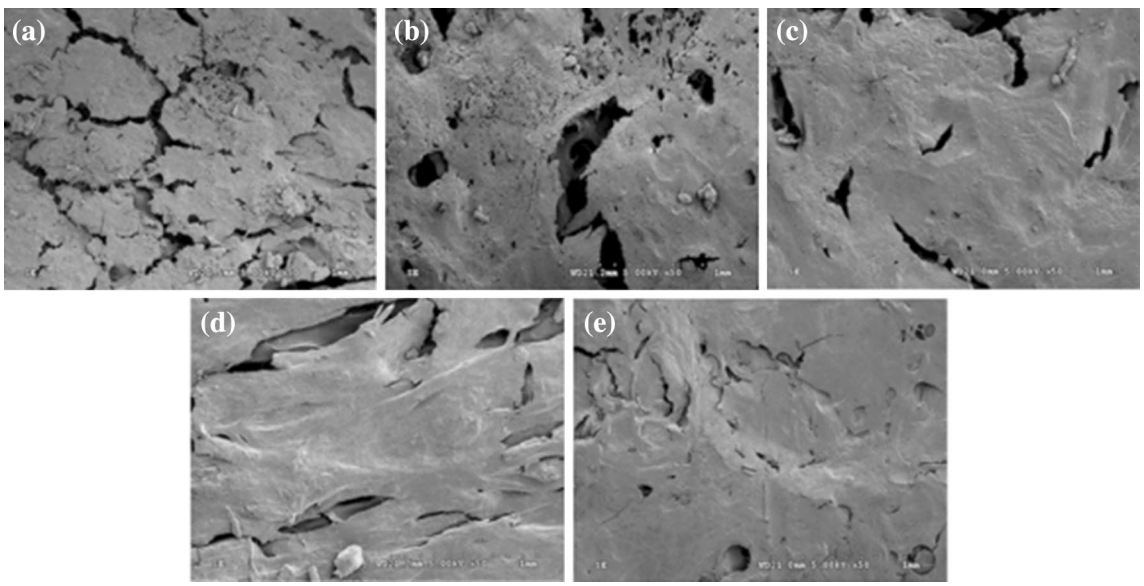

Fig. 8 Surface morphology of starch foam composites containing various OEO contents after soil burial test: **a** 0 wt% OEO, **b** 2 wt% OEO, **c** 4 wt% OEO, **d** 6 wt% OEO and **e** 8 wt% OEO

polymer matrix increased [55]. It should be noted here that the components of essential oil also affected the microorganism in soil. The essential oil can inhibit spore germination and mycelia growth of fungi whereas some microorganism can use the essential oil as substrate of growth [56].

Flexural Strength of Starch Foam Composite Containing OEO

Bending is the most common deformation of starch-based foam packing. The results from the bending mode fracture can indicate the failure of expanded particle of foam and thus reveals the strength of inter-particle-fusion. Therefore, this study focused on the flexural properties of starch foam composites [9, 10]. The flexural properties are necessary starch foam composite. Another type of packaging material such a starch film, it is a thin film and does not have the flexural strength. Figure 9 shows the flexural strength of starch foam composites containing OEO. The flexural strength values ranged from 0.86 to 1.74 iMPa with the addition of 0–8 wt% OEO. The flexural strength of samples slightly decreased with increasing OEO content. The decrease of flexural strength in composite was due to the plasticizing effect of the OEO on starch foam composite. Similar result was also observed in polyvinyl alcohol foam composite modified with essential oil [20]. However, the flexural strength of starch foam composites containing OEO was comparable to those of previous reported composites of starch foam blended with palm oil (0.25–1.10 MPa) [22], soy protein (0.5–0.8 MPa) [22], gluten (0.28–0.34 MPa) [22], oil palm fiber/chitosan/palm oil (1.04–2.21 MPa) [10], latex rubber/calcium carbonate (1.05–3.7 MPa) [57], and polylactic acid (0.4–1.5 MPa) [58]. However, with the high content of 8 wt% OEO, the flexural strength was 0.86 MPa which was comparable with commercial foam packaging based on expanded polystyrene (0.85–0.97 MPa) [20].

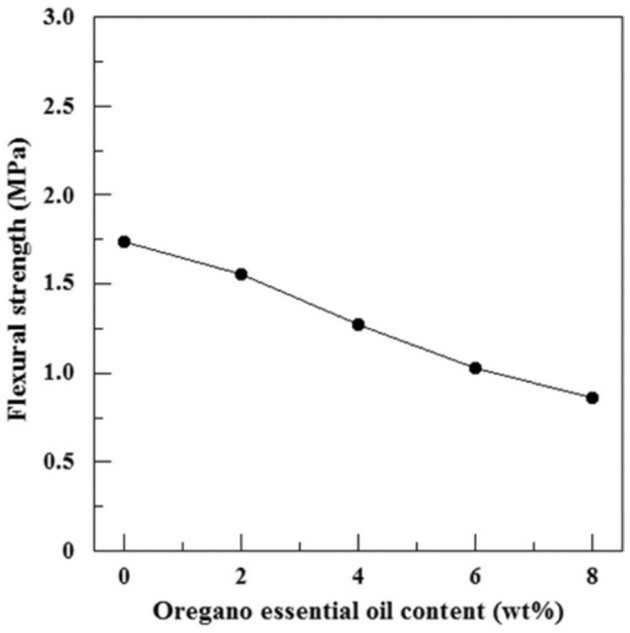

Fig. 9 Flexural strength of starch foam composites containing various OEO contents

Conclusions

The properties of starch foam composites with 10 wt% of sugarcane bagasse and different OEO contents were studied in this research. The antimicrobial effectiveness test revealed that the addition of 8 wt% OEO was required for starch foam composite to achieve the minimum inhibitory concentration against *E. coli* and *S. aureus*. The OEO was more effective against *S. aureus* (Gram-positive bacteria) than *E. coli* (Gram-negative bacteria). The addition of 8 wt% OEO exhibited the largest clear zone for *S. aureus*. The WAC values of samples after 30 min of immersion in water decreased with increasing OEO content. The starch foam composite containing 8 wt% OEO was saturated after 20 min of immersion in water. The water absorption capacity and hygroscopicity of starch foam decreased. The maximum amount of absorbed water in a single layer tended to decrease with increasing OEO content. The presence of 8 wt% OEO in composite provided the lowest monolayer value. The soil biodegradation test indicated that the weight loss of samples decreased with increasing OEO content and the biodegradation rate also decreased. The flexural strength of sample was comparable with that of commercial foam. These results suggested that the starch foam composite containing OEO has potential to be used as a green bioactive composite.

Acknowledgements This work was financial supported by Khon Kaen University (Synchrotron Light Research). The authors also would like to acknowledge the support of Thailand Research Fund (TRF) under the TRF Senior Research Scholar, Grant No. RTA5780004 and the Higher Education Research Promotion and National Research University Project of Thailand, Office of the Higher Education Commission, through the Advanced Functional Materials Cluster of Khon Kaen University. Support from Applied Engineering for Important Crops of the North East Research group, Khon Kaen University, Thailand is also acknowledged.

References

1. Edhirej A, Sapuan SM, Jawaid M, Zahari NI (2016) Polym Compos. doi:10.1002/pc.24121
2. Rodrigues CA, Tofanello A, Nantes IL, Rosa DS (2015) ACS Sustain Chem Eng 3:2756–2766
3. Carmona VB, Corrêa AC, Marconcini JM, Mattoso LHC (2015) J Polym Environ 23:83–89

4. Sun Q, Mekonnen T, Misra M, Mohanty AK (2016) J Polym Environ 24:23–36
5. Trujillo-de Santiago G, Rojas-de Gante C, García-Lara S, Verdolotti L, Maio ED, Iannace S (2015) J Polym Environ 23:72–82
6. Pornsuksomboon K, Holló BB, Szécsényi KM, Kaewtatip K (2016) Carbohydr Polym 136:107–112
7. Guarás MP, Alvarez VA, Ludueña LN (2016) J Appl Polym Sci 133:44163
8. Trujillo-de Santiago G, Rojas-de Gante C, García-Lara S, Verdolotti L, Maio ED, Iannace S (2014) J Polym Environ 22:508–524
9. Aygün A, Uslu MK, Polat S (2016) J Polym Environ. doi:10.1007/s10924-016-0886-0
10. Kasemsiri P, Dulsang N, Pongsa U, Hiziroglu S, Chindaprasirt P (2016) J Polym Environ. doi:10.1007/s10924-016-0818-z
11. Ramesh S, Shanti R, Morris E (2012) Carbohydr Polym 87:701–706
12. Beilvert A, Chaubet F, Chaunier L, Guilois S, Pavon-Djavid G, Letourneur D (2014) Carbohydr Polym 99:242–248
13. Prachayawarakorn J, Limsiriwong N, Kongjindamunee R, Surakit S (2011) J Polym Environ 20:88–95
14. Jumaidin R, Sapuan SM, Jawaid M, Ishak MR, Sahari J (2016) Int J Biol Macromol 89:575–581
15. Sanyang ML, Sapuan SM, Jawaid M, Ishak MR, Sahari J (2016) Carbohydr Polym 146:36–45
16. Sanyang ML, Sapuan SM, Jawaid M, Ishak MR, Sahari J (2016) BioResources 11:4134–4145
17. Zou W, Yu L, Liu X, Chen L, Zhang X, Qiao D et al (2012) Carbohydr Polym 87:1583–1588
18. Ago M, Ferrer A, Rojas OJ (2016) ACS Sustain Chem Eng 4:5546–5552
19. Vercelheze AE, Fakhouri FM, Dall'Antônia LH, Urbano A, Youssef EY, Yamashita F, Mali S (2012) Carbohydr Polym 87:1302–1310
20. Debiagi F, Kobayashi RK, Nakazato G, Panagio LA, Mali S (2014) Ind Crops Prod 52:664–670
21. Debiagi F, Marim BM, Mali S (2015) J Polym Environ 23:269–276
22. Kaisangsri N, Kerdchoechuen O, Laohakunjit N (2014) Carbohydr Polym 110:70–77
23. Petchwattana N, Covavisaruch S, Wibooranawong S, Naknaen P (2016) Measurement 93:442–448
24. Petchwattana N, Naknaen P (2015) Mater Chem Phys 163:369–375
25. Bhullar SK, Kaya B, Jun M-BG (2015) J Polym Environ 23:416–423
26. Polat S, Uslu M-K, Aygün A, Certel M (2013) J Food Eng 116:267–276
27. Rojas-Graü MA, Avena-Bustillos RJ, Friedman M, Henika PR, Martín-Belloso O, McHugh TH (2006) J Agric Food Chem 54:9262–9267
28. Desai MA, Parikh J (2015) ACS Sustain Chem Eng 3:421–431
29. Souza A, Goto G, Mainardi J, Coelho ACV, Tadini CC (2013) LWT Food Sci Technol 54:346–352
30. Jemaa BM, Falleh H, Neves MA, Isoda H, Nakajima M, Ksouri R (2017) Food Chem 217:726–734
31. Bonilla J, Sobral PJA (2016) Food Biosci 16:17–25
32. Klangmuang P, Sothornvit R (2016) Food Hydrocoll 61:609–616
33. Pelissari FM, Grossmann MV, Yamashita F, Pineda EAG (2009) J Agric Food Chem 57:7499–7504
34. Kaisangsri N, Kerdchoechuen O, Laohakunjit N (2012) Ind Crops Prod 37:542–546
35. Soykeabkaew N, Supaphol P, Rujiravanit R (2004) Carbohydr Polym 58:53–63
36. Método de Cobb (1999) NBR NM-ISO 535:1999 Papel E Cartao-Determinacao Da Capacidade De Absorcao De Agua In: ABNT-Associac¸ ão Brasileira de normas Técnicas
37. Bizot H (1984) Using the GAB model to construct sorption isotherms. In: Jowitt R, Escher F, Hallistrom B, Meffert HFT, Spiess WEL, Vos G (eds) Physical properties of foods. Applied Science Publishers, London, pp 27–41
38. Hosseini M, Razavi S, Mousavi M (2009) J Food Process Preserv 33:727–743
39. ASTM D 790-10 (2010) Standard test methods for flexural properties of unreinforced and reinforced plastics and electrical insulating materials, ASTM International, West Conshohocken
40. Ibrahim H, Farag M, Megahed H, Mehanny S (2014) Carbohydr Polym 101:11–19
41. Matsuda DK, Verceheze AE, Carvalho GM, Yamashita F, Mali S (2013) Ind Crops Prod 44:705–711
42. Prachayawarakorn J, Chaiwatyothin S, Mueangta S, Hanchana A (2013) Mater Des 47:309–315
43. Mothé CG, de Miranda IC (2009) J Therm Anal Calorim 97:661–665
44. Salmieri S, Islam F, Khan RA, Hossain FM, Ibrahim HM, Miao C, Hamad WY, Lacroix M (2014) Cellulose 21:4271–4285
45. Prachayawarakorn J, Limsiriwong N, Kongjindamunee R, Surakit S (2012) J Polym Environ 20:88–95
46. Hosseini SF, Rezaei M, Zandi M, Farahmandghavi F (2015) Ind Crops Prod 67:403–413
47. Hosseini SF, Zandi M, Rezaei M, Farahmandghavi F (2013) Carbohydr Polym 95:50–56
48. Burt S (2004) Int J Food Microbiol 94:223–253
49. Kahrilas GA, Haggren W, Read RL, Wally LM, Fredrick SJ, Hiskey M, Prieto AL, Owens JE (2014) ACS Sustain Chem Eng 2:590–598
50. Martucci JF, Gende LB, Neira L, Ruseckaite RA (2015) Ind Crops Prod 71:205–213
51. Mello LR, Mali S (2014) Ind Crops Prod 55:187–193
52. Strauss U, Porcja R, Chen S (1991) Volume effects of starch-water interactions. In: Levine H, Slade L (eds) Water relationships in foods: advances in the 1980s and trends for the 1990s, vol 302. Springer, Boston, pp 351–363
53. Coupland JN, Shaw NB, Monahan FJ, O'Riordan ED, O'Sullivan M (2000) J Food Eng 43:25–30
54. Mali S, Debiagi F, Grossmann MVE, Yamashita F (2010) Ind Crops Prod 32:353–359
55. Riaz U, Ashraf SM, Sharma HO (2011) Polym Degrad Stab 96:33–42
56. Vokou D, Liotiri S (1999) Chemoecology 9:41–45
57. Shey J, Imam SH, Glenn GM, Orts WJ (2006) Ind Crops Prod 24:34–40
58. Preechawong D, Peesan M, Supaphol P, Rujiravanit R (2005) Carbohydr Polym 59:329–337

Construction and Building Materials 135 (2017) 164–176

Contents lists available at ScienceDirect

Construction and Building Materials

journal homepage: www.elsevier.com/locate/conbuildmat

Electrical conductivity and compressive strength of carbon fiber reinforced fly ash geopolymeric composites

Panjasil Payakaniti [a], Supree Pinitsoontorn [b,c,*], Prasit Thongbai [b,c], Vittaya Amornkitbamrung [b,c], Prinya Chindaprasirt [d]

[a] Materials Science and Nanotechnology Program, Department of Physics, Faculty of Science, Khon Kaen University, Khon Kaen 40002, Thailand
[b] Integrated Nanotechnology Research Center, Department of Physics, Faculty of Science, Khon Kaen University, Khon Kaen 40002, Thailand
[c] Nanotec-KKU Center of Excellence on Advanced Nanomaterials for Energy Production and Storage, Khon Kaen University, Khon Kaen 40002, Thailand
[d] Sustainable Infrastructure Research and Development Center, Department of Civil Engineering, Faculty of Engineering, Khon Kaen University, Khon Kaen 40002, Thailand

HIGHLIGHTS

- Effect of carbon fiber in fly ash geopolymer on conductivity and strength.
- I-V curve, CV and EIS techniques for electrical measurement yield similar results.
- Conductivity depends on amount of CF and liquid, curing temperature, and aging time.
- Adding 0.5 wt% CF exhibits the lowest resistance and highest compressive strength.
- The improvement of these properties was due to the composite effects.

ARTICLE INFO

Article history:
Received 16 August 2016
Received in revised form 23 November 2016
Accepted 29 December 2016

Keywords:
Fly ash geopolymer
Carbon fiber reinforcement
Electrical behavior
Mechanical property

ABSTRACT

The effect of carbon fiber (CF) addition on the electrical behavior and mechanical property of fly ash geopolymer was investigated. The electrical resistivity of CF/geopolymer composites was systematically investigated as a function of CF concentration, liquid to ash ratio (L/A), curing temperature, aging time, measurement frequency, and measurement technique. Three different techniques used in this study for measuring electrical properties were I-V curve measurement, cyclic voltammetry, and electrochemical impedance spectroscopy. Each technique yielded similar results. The electrical conductivity was highly dependent on the CF concentration and percolation threshold. Below the threshold, the resistivity varied with curing temperature and time, but above that the resistivity decreased monotonically with respect to CF concentration irrespective of other factors. Changing the L/A shifted the percolation threshold to higher values, but the other electrical characteristics were similar. The composite with 0.5 wt% CF was found to exhibit the lowest resistance and highest compressive strength. Our findings showed that CF addition not only improved the electrical conductivity by several orders of magnitude, but also enhanced its mechanical property. The improvement of these properties was due to the combined effects as confirmed by X-ray diffraction and scanning electron microscopy techniques that the phases of matrix did not change and the fiber distribution was homogeneous and randomly oriented.

© 2016 Elsevier Ltd. All rights reserved.

1. Introduction

The production of ordinary Portland cement (OPC) requires high energy and the process emits large amounts of CO_2 gas to the environment which contributes to the greenhouse effect [1]. As a result, many researchers have sought for new materials for reducing or replacing the use of OPC. Geopolymer is an inorganic aluminosilicate material which can be used as an alternative construction material for OPC. The structure of geopolymer is a three-dimensional network of alumina and silica [2] which provides several advantages such as high thermal stability, corrosion resistance, low shrinkage and environmental friendliness [3,4]. Geopolymer can be produced from by-products or waste materials such as fly ash, rice husk ash and blast furnace slag. Fly ash (FA) is mainly composed of alumina and silica and is a by-product

* Corresponding author at: Integrated Nanotechnology Research Center, Department of Physics, Faculty of Science, Khon Kaen University, Khon Kaen 40002, Thailand.
E-mail address: psupree@kku.ac.th (S. Pinitsoontorn).

http://dx.doi.org/10.1016/j.conbuildmat.2016.12.198
0950-0618/© 2016 Elsevier Ltd. All rights reserved.

obtained from burning coal in a power plant. It has been used as a starting material for preparing geopolymer because of its huge production and a great chemical potential for geopolymerization.

Similar to OPC, plain geopolymer is brittle and its toughness can be improved by incorporating fiber reinforcement. Considering the ease of manufacturing, handling and cost effectiveness, short fibers tend to be selected as reinforcement in civil engineering [5,6]. A number of types of fiber reinforcements have been investigated to enhance the mechanical properties of fiber/geopolymer composites such as carbon nanotube (CNT), polyvinyl alcohol (PVA) fiber, basalt fiber, polypropylene (PP) fiber, steel fiber and carbon fiber (CF) [7,8]. Recently, it was found that adding micro-steel fibers significantly improved both the ultimate flexural capacity and ductility of geopolymer composites, especially at early ages, without a negative effect on its compressive strength [9]. Moreover, incorporating PP fibers at levels up to 3 wt% in a geopolymer matrix was found to reduce its shrinkage and enhance the energy absorption of the composite [10].

Amongst the reinforcing phases for cementious materials, carbon-based materials which can be used as additives to geopolymer-based composites as well as cement based materials have gained significant interest from many research groups. In a recent review, Lu et al. summarized the use of CNT, CF, graphene and graphene oxide for improving properties of cementitious materials [11]. These composites can be exploited in several applications, for instance, in reinforcement, self-sensing, self-heating and deicing, energy harvesting [11]. CNT was also added in geopolymer mortar to reduce its drying shrinkage as well as water absorption [12]. Additionally, the fracture toughness of geopolymer was significantly improved when short carbon fibers were used during the preparation of composite materials [3].

Utilization of carbon-based materials does not only improve the mechanical aspect of the geopolymer composite but also enhances other functionalities. For example, it was reported that electrical conductivity and piezoresistive responses were affected when CNTs were added to geopolymeric composites [4]. In accordance with [4], the electrical conductivity was non-linearly proportional to the concentration of CNT, whereas the piezoresistivity changed directly with the amount of loading. In their study, Vaidya and Allouche [13] mixed carbon fibers with geopolymer concrete and investigated its strain sensing behavior. It was found that the electrical conductivity of the carbon fiber reinforced geopolymer concrete reasonably followed the flexural deflection but for its compressive strain, a more complex behavior was observed. MacKenzie and Bolton [14] compared the effect of CNT and graphite addition on the electrical conductivity of aluminosilicate inorganic polymer composites. CNT was superior in enhancing the electrical conductivity compared to graphite but no linear relationship between the conductivity and CNT concentration was found.

The electrical behavior of geopolymeric materials can be very beneficial for smart sensing applications. In fact, conductive cementitious materials have received great interest for many years due to their useful and outstanding applications. These include electrical grounding and lightning protection for buildings, static charge dissipation for sensitive electronic devices, deicing bridges, highways, pathways and airport runways, cathodic protection for anti-corrosion in concrete and electromagnetic shielding for electronics related to electric power generation and telecommunication [11,15]. A number of reports on electrical conductivity of cements have been published, but very few for geopolymers.

In this work, we investigated the electrical response of CF reinforced fly ash geopolymeric composites. CF was selected over other carbon-based materials due to its lower cost and greater availability. It also possesses a high modulus of elasticity, tensile strength and toughness, but lower specific weight [16]. Moreover, a recent study showed that CF is superior to CNT or graphene nanoplatelets (GNP) in reducing the electrical resistivity of the cementitious composites [17]. Unlike other previous studies that adopted a more practical perspective, the current study aimed to unfold the origin of these behaviors by systematically studying the effect of CF on the electrical and mechanical properties of geopolymers. Several parameters were varied, namely, the liquid to ash ratio, concentration of CF, aging time, measurement frequency and curing temperature. Moreover, several means of measuring the electrical responses were employed, such as use of I-V curves, cyclic voltammetry (CV), and electrochemical impedance spectroscopy (EIS). Additionally, the mechanical property and microstructures of CF/-geopolymer composites were investigated using a universal testing machine (UTM) and scanning electron microscope (SEM), respectively.

2. Materials and methods

2.1. Material

High calcium lignite fly ash (FA) from the Mae Moh power plant in Lampang, Thailand was used. The chemical composition of the as-received FA ash was determined using X-ray fluorescence spectroscopy (XRF) and is presented in Table 1. The microstructure of raw FA was observed under scanning electron microscopy (SEM) and is shown in Fig. 1. FA particles were spherical in shape with smooth surfaces. Also, the particle size distribution of FA size is wide, in the range of sub-micrometers to tens of micrometers. Agglomeration of small particles was also observed.

The X-ray diffraction (XRD) pattern of the as-received FA is shown in Fig. 2. A broad XRD peak was generally observed, which is the common feature of an amorphous phase. Apart from that, several crystalline peaks were found which were attributed to Anhydrite (A), quartz (Q), hematite (F), calcium oxide (C) and mullite (M) [18,19].

Dispersed chopped carbon fiber (CF) was purchased. The properties of the CF are summarized in Table 2. Sodium hydroxide (NaOH) at a 10 M concentration and sodium silicate (Na_2SiO_3) with 12.53 wt% Na_2O, 30.24 wt% SiO_2 and 57.23 wt% H_2O were used as alkaline activating solutions.

2.2. Sample preparation

To prepare the CF/geopolymer composites, the fiber was first dispersed manually in a sodium hydroxide solution for 5 min to avoid agglomeration of CF. After that, FA was added to the solution and thoroughly mixed using a mechanical blender at 1400 rpm for 5 minutes. Then, sodium silicate was added and mixed for another 5 min at the same speed. A ratio of sodium silicate to sodium hydroxide of 1.0 and the liquid to ash ratios (L/A) of 0.4 and 0.5 were selected. CFs with 0.1–0.5 wt% and 0.1–1.0 wt% were added to solutions with L/A = 0.4 and 0.5, respectively. Finally, the

Table 1
Chemical composition of fly ash evaluated by XRF.

Compound	Percentage (wt%)
SiO_2	32.30
CaO	23.20
Al_2O_3	17.20
Fe_2O_3	10.80
SO_3	3.86
K_2O	2.10
MgO	2.10
Na_2O	1.42

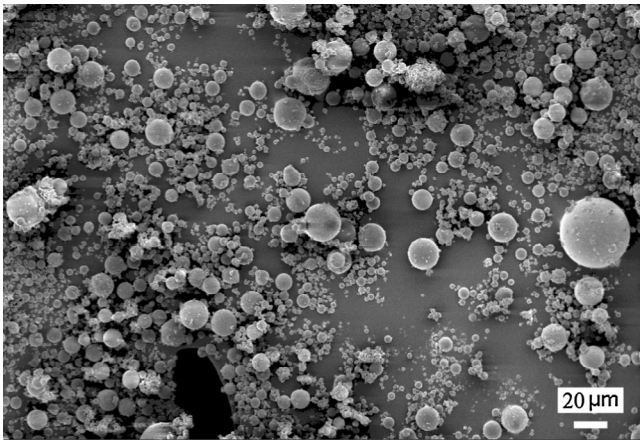

Fig. 1. SEM micrograph of raw fly ash.

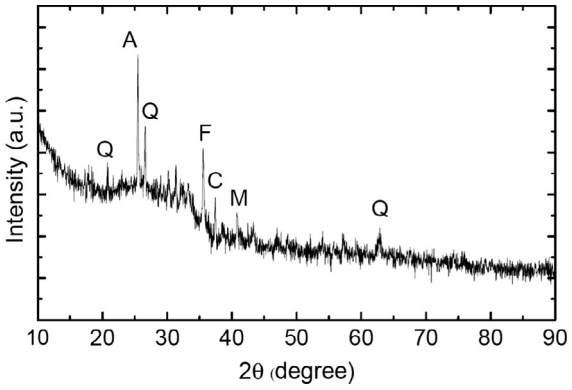

Fig. 2. XRD pattern of the raw FA. The letters identify the detected phases: Q = Quartz, A = Anhydrite, M = Mullite, C = Calcium oxide, F = Hematite.

Table 2
Properties of the as-purchased CF.

Properties	Value
Fiber diameter (μm)	7
Tensile strength (GPa)	3.6–3.8
Tensile modulus (GPa)	220–240
Carbon content (%)	⩾95
Elongation (%)	1.5
Density (g/cm^3)	1.6–1.76
Volume resistivity (Ω cm)	1.5×10^{-3}

geopolymer composite was cast into acrylic molds for mechanical and electrical tests.

For compressive test the specimens were casted into the acrylic molds with the size of $2.5 \times 2.5 \times 2.5$ cm^3. For the electrical response measurement, the set-up was performed according to [20]. The paste was casted in the molds with the size of $2.5 \times 10 \times 2.5$ cm^3 and left at ambient temperature (25 °C). After 5 min, 4 well-polished brass plates, 1 cm wide and 10 cm long, were installed at the center of the specimen, with a 1.2 cm span between each probe (Fig. 3). At 1 h after casting, the specimens for electrical and compressive tests were wrapped with cling film. The specimens were either cured at ambient temperature (25 °C) in a temperature controlled room or at 60 °C for 24 h in an oven. The specimens were demolded after they cooled and tested at the ages of 7, 14, 28 and 290 days.

To ensure that the geopolymer composite paste rheologically suitable, the workability of geopolymer paste was determined

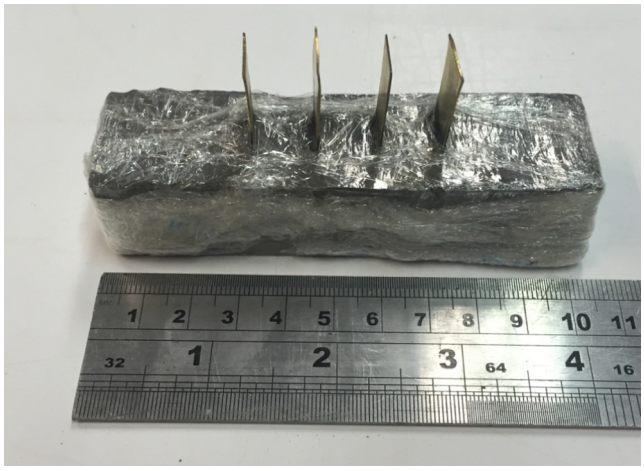

Fig. 3. A specimen with brass plates for electrical measurements.

using a miniature slump (mini-slump) cone test [21,22]. The testing process was done according to ASTM C143. The paste was poured into the lower half of a truncated conical mold and tamped 20 times. Then, the other half was filled and tamped another 20 times. The excess paste on the top of the mold was removed. The mold was carefully lifted in the vertical direction and the paste was left to spread. The diameters of paste were measured in three directions after 30 s, 1, 2, 3, 4 and 5 min. Workability was calculated from the equation:

$$\%W = \left(\frac{d - d_0}{d_0}\right) \times 100$$

where %W is workability, d is the spread-out diameter of fresh geopolymer paste, and d_0 is the diameter of the original conical mold's bottom.

2.3. Characterization techniques

An X-ray diffractometer (XRD) with Cu-Kα radiation was used for determining the phase and composition of the FA and geopolymer pastes. The microstructure of FA was investigated using scanning electron microscopy (SEM).

The electrical resistance of geopolymer composite was determined from I-V curve measurements. Alternating current (AC) was applied to the specimens with a maximum current amplitude of 100 mA and a frequency ranging from 0.3 to 100 Hz. The resistivity of specimens was extracted as the slope of the I-V curves. The cyclic voltammetry (CV) curves and electrochemical impedance spectroscopy (EIS) were performed using a potentiostat electrometer. The CV profiles were obtained at a scan rate between 5 and 100 mV/s with a step size of 10 mV and maximum current of 100 mA. The EIS plots were measured in the frequency range between 0.1 Hz and 300 kHz at an open circuit potential with an AC rms voltage of 10 mV.

The mechanical properties of CF/geopolymer composites were determined using a universal testing machine (UTM) with the maximum load of 50 tons. The sample was compressed at a rate of 50 N/min until the sample fractured. Normally, a 50 mm cube of the specimen material is used for measuring compressive strength of pastes (ASTM C109/C109M – 13). However, a smaller specimen of 25 mm cube has also been successfully used [23–25]. It should be noted that this could lead to higher compressive strength values due to the smaller geometry of specimens. The results however could be compared using the same size of specimens. After the specimens were compressed, the fractured

surfaces were examined under SEM. Alignment and distribution of carbon fibers in the matrix were analyzed using the resulting electron micrographs.

3. Results and discussion

3.1. Workability of CF/geopolymer composite paste

The workability of freshly mixed CF/geopolymer paste is shown in Fig. 4. It can be seen that the mixture without carbon fiber had the highest workability (220% for L/A = 0.4 and 244% for L/A = 0.5). When carbon fiber was introduced into the mixture, the flow of geopolymer paste decreased proportionally to the CF concentration. For the mixture with L/A = 0.4, the maximum concentration of CF was limited to 0.5 wt%. Higher concentrations of CF led to substantial thickening of the paste (workability of 154%) resulting in excessive viscosity of the CF/geopolymer composite prior to molding. Alternatively, for mixes with L/A = 0.5, the CF could be increased to 1.0 wt%. without sacrificing the workability of composite paste (176%). The larger amount of liquid enhanced the flowability of the mixture. A workability between 150 and 250% in the present experiment was suitable for the casting and drying processes.

3.2. Phase formation of CF/geopolymer composite pastes

The phase formation of geopolymer pastes was determined using XRD. The XRD patterns of CF/geopolymer composite, cured at 25 °C and 60 °C, at the age of 7 and 28 days are shown in Fig. 5. Compared with the raw FA XRD pattern, it can be seen that the number of sharp peaks decrease significantly, which is due to the production of a non-crystalline phase from the geopolymerization process after the FA reacted with the alkaline solution. The remaining peaks at 2θ of 26.56° and 35.57° were the crystalline phases of quartz and hematite from the FA. These crystalline phases are highly inert and do not fully react in the geopolymerization process as confirmed by their almost unchanged XRD patterns in Fig. 5(a)–(d). These unreacted phases can be seen clearly in the SEM images (Section 3.5). Fig. 5 also shows that CF did not interact in the geopolymerization process since the XRD patterns of the samples are not different comparing the plain geopolymer paste and the CF/geopolymer composites. The results from the XRD patterns were also confirmed by FTIR analysis.

Fig. 6 shows the FTIR spectra of CF/geopolymer composites cured at 25 °C. According to the literature [24,26–29], the spectrum

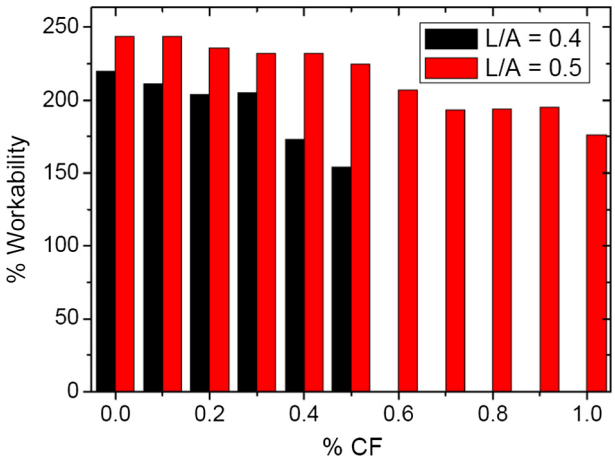

Fig. 4. Workability of CF/geopolymer composite pastes for L/A = 0.4 and 0.5 determined by a mini-slump test.

at 684 cm^{-1} is attributed to the Si-O-Al functional group. The presence of a band at 712 cm^{-1} is confirmation of geopolymer due to the crystalline phase of quartz in the raw fly ash. The strongest band at 948 cm^{-1} represents asymmetric stretching vibrations of Si-O-T where T is tetrahedral Si or Al. The stretching vibration of the O-C-O bond at 1416 cm^{-1} corresponds to the presence of sodium carbonate (Na_2CO_3). The band at 1648 cm^{-1} is due to the bending vibration of H-O-H from water absorption on the geopolymer surface. The peak absorbance at 2649 cm^{-1} is related to asymmetric stretching of methylene groups (CH_2). The broad band at 3356 cm^{-1} correlates to hydroxyl (–OH) functional groups from Si-OH, Al-OH and C-OH. However, it can be seen from Fig. 6 that all of the spectra were very similar. Adding CFs does not have any influential effect on the geopolymerization process. Furthermore, the curing temperature (25 °C and 60 °C) did not alter any characteristic of the spectra. Therefore, the results from XRD and FTIR analyses indicated that the changes in the electrical response or compressive strength in the subsequent section are due to the composite effect, not from a phase change in the geopolymer matrix.

3.3. Electrical behavior of CF/geopolymer composite paste

The results of electrical resistivity of CF/geopolymer composite as illustrated in Fig. 7. Fig. 7(a) and (b) show the resistivity of the pastes cured at 25 °C and 60 °C. One obvious feature that can be observed is the reduction of resistivity when higher amount of CF was added. For example, at 28 days, the pastes without CF showed a resistivity of 1256 Ω cm and 6817 Ω cm for the sample cured at 25 °C and 60 °C, respectively. With only 0.2 wt% CF added, the resistivity values were reduced by nearly two orders of magnitude, to 33 Ω cm and 65 Ω cm for curing temperatures of 25 °C and 60 °C, respectively. Thus, CF is a very effective agent for enhancing electrical conductivity of geopolymers. The resistivity of the composites decreased proportionally with the concentration of CF. This is also an indication that the CF was well dispersed in the matrix since the agglomeration of fiber could lead to limited conductivity [17], which was not in this case.

Another intriguing feature is the variation of resistivity over time. For materials with no CF or a low CF concentration (0.1 wt %), the resistivity continuously increased with time. Even at 290 days, the trend of increasing resistivity did not seem to abate. Unlike the specimens with 0.2 wt% and higher CF, resistivity was relatively constant and independent of aging time. From these observations, it could be inferred that for the paste with 0.1 wt% CF or less, the geopolymer matrix governed the electrical behavior of the samples. Normally, at a curing temperature of 25 °C, the geopolymerization process was not complete, and can continue for a very long time [30]. This is the case for the 0% and 0.1% CF as shown in Fig. 7(a). Due to an incomplete geopolymerization process, the geopolymeric matrix develops gradually, resulting in a continuous increase in resistivity to 290 days. It is quite surprising to find the increase in resistivity for composites cured at 60 °C since the geopolymerization is in a very advanced stage. This finding is an indication that geopolymerization was not complete after curing at 60 °C for 24 h and could continue for several months. For the composites with 0.2% CF or higher, CF reinforcement is the key for controlling electrical transport. Conduction occurs via the pathway of the CF network. Our results suggested that there might be a percolation threshold between 0.1% and 0.2% CF which the conduction changes the behavior (Fig 8a). Below the threshold, the matrix dominates and above that, the CF reinforcing phase is dominant. In fact, for composites with 0.3%, 0.4% and 0.5% CF, the resistivity values of the samples cured at 25 °C and at 60 °C were not different. This means that conductivity is only controlled by the

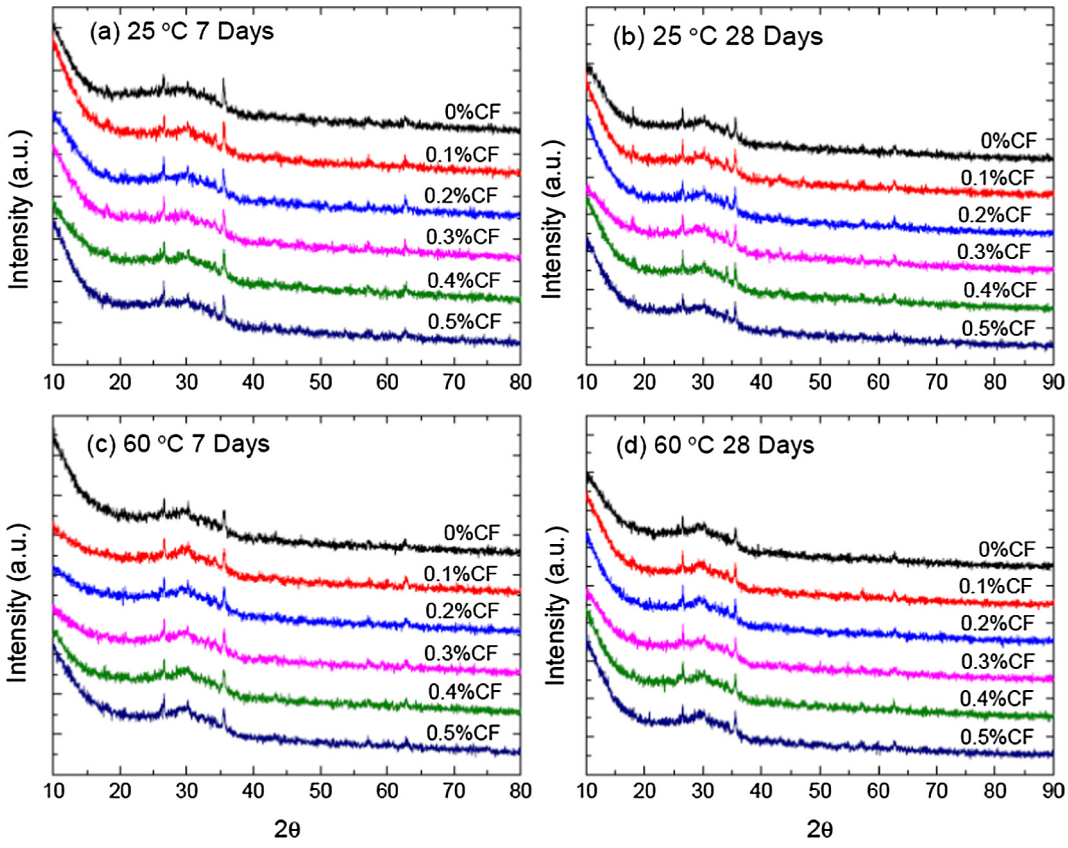

Fig. 5. XRD patterns of CF/geopolymer composites (L/A = 0.4) for (a) 25 °C curing, at 7 days, (b) 25 °C curing, at 28 days, (c) 60 °C curing, at 7 days and (d) 60 °C curing, at 28 days.

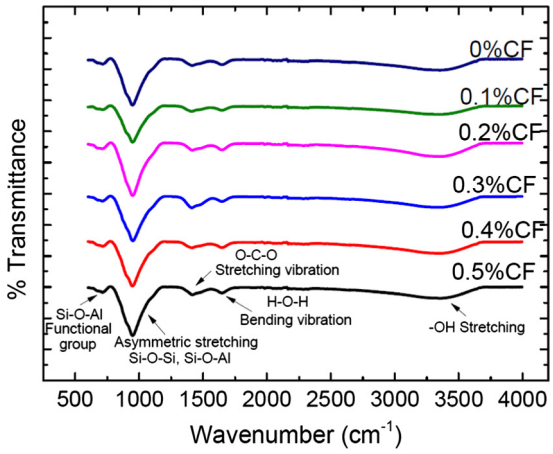

Fig. 6. FTIR spectra of CF/geopolymer composites with L/A = 0.4 cured at 25 °C.

concentration of CF, not by other factors, such as aging time or curing temperature.

The CF concentration is not the only factor that influences the percolation threshold. The L/A ratio can also affect the electrical response. As shown in Fig. 8b, the percolation threshold is located between 0.3% and 0.4% CF when a L/A ratio of 0.5 was used for preparing the CF/geopolymer pastes. This is understandable because at high L/A values, the geopolymerization process is more advanced resulting in electrical conduction dominated by the matrix. Therefore, a higher amount of CF is required for the reinforcing phase to totally govern the electrical behavior of the composites.

The data in Figs. 7 and 8 were measured at a frequency of 0.3 Hz. The frequency dependence of the resistivity is shown in Fig. 9 for the CF/geopolymer composite with L/A = 0.4 cured at 60 °C. It can be seen that the resistivity for all samples was independent of the applied frequency except for a small variation for 0.1% CF paste at a low frequency. The results from the other samples (different aging times, L/A, curing temperature) showed a similar tendency. These results confirm that the resistivity of the CF/geopolymer composites above the percolation threshold is only dependent on the concentration of CF, but not against other factors, i.e., aging time, L/A, curing temperature, and frequency. However, it should be noted that the frequencies used in this experiment were relatively low in comparison to other studies [4,13,17] partly due to instrumental limitations. In fact, the electrical conductivity experiments were purposefully done under this frequency regime. High frequency may be useful in self-monitoring or sensing applications for smart concrete [4,11,13]. The low frequency regime is more suitable for other applications such as electrical grounding, lightning protection, deicing, or electrical energy transport and storage. Especially, our experiment covers the frequency range of 50–60 Hz which is the most common AC power supply for household appliances.

Plain geopolymer paste was reported to be a superionic conductor [31]. The main conduction mechanism in geopolymer was via Na^+ ion hopping between the cation sites. The ionic conductivity of the paste cured at 60 °C was found to be 1.54×10^{-2} S m^{-1} at 100 Hz, equivalent to the resistivity of 6494 Ω cm, with the activation energy of 0.156 eV. The value of the resistivity of the geopolymer paste without CF in this work measured under similar conditions was found to be 6567 Ω cm, very similar to literature [31]. This implies that the conduction mechanism of the plain

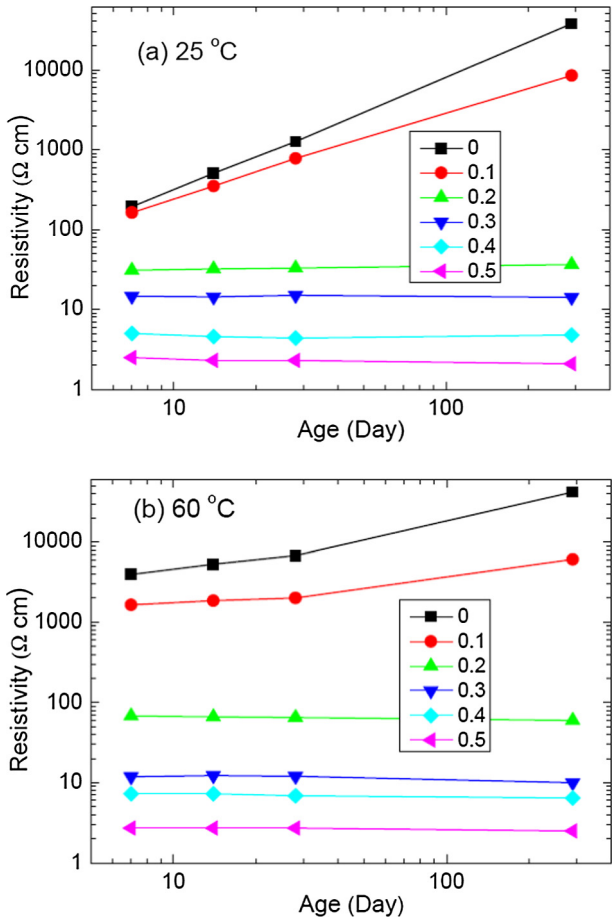

Fig. 7. Electrical resistivity of CF/geopolymer composite (L/A = 0.4) as a function of CF concentration and aging time, (a) cured at 25 °C, (b) cured at 60 °C.

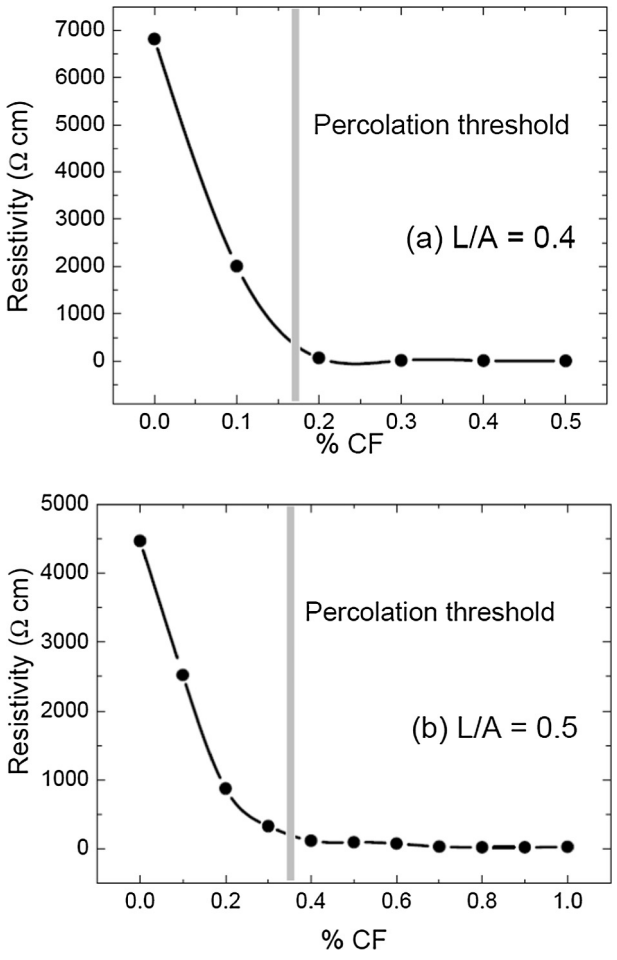

Fig. 8. 28-day resistivity versus wt% CF of CF/geopolymer composites for L/A of (a) 0.4 and (b) 0.5.

geopolymer could be explained using the Na^+ hopping mechanisms. For the CF/geopolymer composites, especially for CF levels above the percolation threshold ($\geqslant$0.2% CF), the conductivity was increased by about 2–3 orders of magnitude. The conduction mechanism in these cases is a combination of both ionic (Na^+ hopping) and electronic (via CF) conductivities. However, the electrical resistivity of CF (1.5×10^{-3} Ω cm) is significantly lower than that of geopolymer, due to its higher mobility of electrons. The presence of CF in the geopolymer matrix, hence, shortens the conduction path in the matrix where the resistivity is much larger. As a result, though the conduction in the matrix is still via ionic hopping, the total conduction distance is small. Therefore, the electrical conductivity of geopolymer composites can be enhanced several orders of magnitude by incorporating CFs.

As discussed in the experimental section, the results in Figs. 7–9 were extracted from the I-V curves. A typical I-V curve from the measurement is shown as a black curve in Fig. 10 for the 0.3% CF sample cured at 60 °C measured at 28 days. The resistivity was calculated from the slope in the middle part of the curve, excluding the flat lines at both ends. It can be seen that the measured voltages from the forward and reverse biases are not perfectly matched resulting in a small loop. This may be a consequence of the electrical charge capacitance due to the accumulative charge in the conducting phases (CFs, trapped liquid or domain boundaries) separated by the non-conducting phases (geopolymer matrix). After a forward bias and then reducing the applied current to neutral, the measured voltage is non-zero. The existing voltage is termed as a remanence voltage, V_r, as shown in Fig. 10. The V_r values depended on the measurement frequency. The red curve in Fig. 10

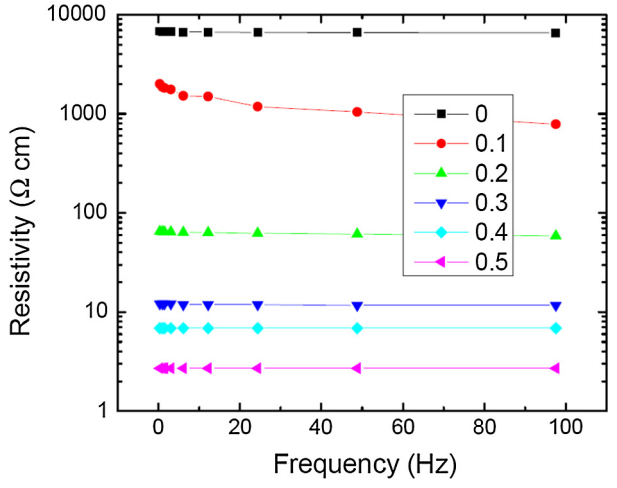

Fig. 9. Resistivity of CF/geopolymer composites as a function of applied frequency.

is from the same specimen but measured at a higher frequency. A larger V_r was obtained, which is a result of the frequency-dependent charge capacity. Fig. 11 shows plots of V_r versus frequency for the CF/geopolymer composites cured at 25 °C and 60 °C. It can be seen from this figure that at low frequency, V_r gradually increased with frequency with a slight fluctuation before becoming relatively constant at a higher frequency. An exception is the plain geopolymer paste. This is understandable since the

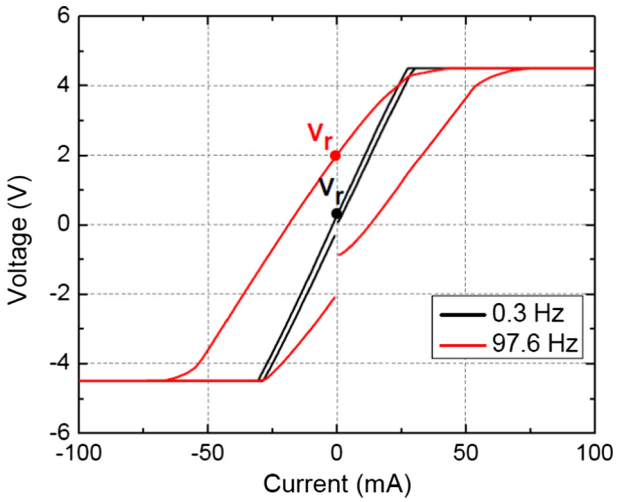

Fig. 10. I-V curves of 0.3% CF paste cured at 60 °C measured at 28 days old.

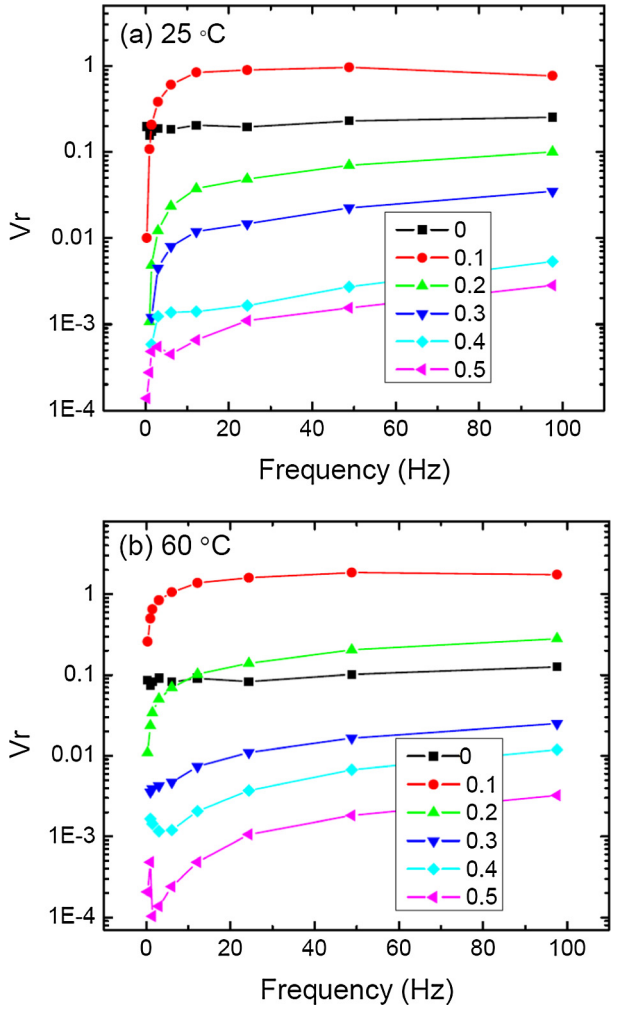

Fig. 11. Remanence voltage (V_r) versus frequency for CF/geopolymer composites cured at (a) 25 °C and (b) 60 °C.

samples do not contain the conductive CF phase which makes their V_r independent of the applied frequency. Another interesting characteristic from Fig. 11 is the trend of V_r with respect to CF concentration. The values of V_r increased with increasing CF content from 0% to 0.1%, but then decrease with increasing CF. The initial increase in V_r can be attributed to the addition of the CF conducting phase which makes the composite more of an ideal capacitive material: the composite consisted of conducting plates separated by an insulator. The decrease in V_r upon further addition of CF could be due to the dominance of the CF conducting phase. Higher amounts of CF creates more short circuit paths and thus an electrical charge cannot be stored when the bias current is removed resulting in a low V_r.

The results of the cyclic voltammetry (CV) measurement are presented in Fig. 12. Generally, CV measurements monitor the *in situ* electrochemical reactions in the system with an applied electrical potential. Fig. 12a shows the CV curves of geopolymer paste cured at 25 °C. It can be seen that the oxidation and reduction peaks were observed in the voltage ranges of 0.2–0.5 V, and −0.2 to −0.7 V, respectively. These peaks were attributed to electrochemical reactivity within the geopolymer structure. It is well known that the geopolymerization process is not fully completed with curing at room temperature [30]. Therefore, when curing at 25 °C, there might be residual water molecules in the material allowing a redox reaction to occur: $2H_2O + 2e^- \leftrightarrows H_2\ (g) + 2OH^-$ [32], resulting in the observed peaks in Fig. 12a. Alternatively, another possibility is a redox reaction of trapped Na^+ ions in the aluminosilicate structure: $Na^+ + e^- \leftrightarrows Na(s)$ [33], which could also result in an electrochemical reaction in geopolymer paste. From Fig. 12a, a few important observations can be made. Firstly, the intensity of the reduction/oxidation peaks of geopolymer paste are dependent on the scan rate. The measured current at the peak position increased with an increasing scan rate. This could be due to increased diffusion layer thickness in the reversible ion transfer reaction. Secondly, the positions of peaks shifted at higher scan rates. This is attributed to quasi-reversible or irreversible ion transfer reactions. The kinetics of the reactions are slow in comparison to the scan rate. As a result, the equilibria are not established leading to the shift in the current maxima.

Fig. 12a and d compare the CV curves of geopolymer pastes cured at 25 °C and 60 °C. It is obvious that the electrochemical reactivity peaks were reduced. This is understandable since the geopolymerization process is more advanced when samples are cured at 60 °C. This could limit the ionic transfer of trapped Na^+ ions making the electrochemical reaction more difficult. When CFs were added to the mixtures, the electrochemical reactivity was reduced for both CF/geopolymer composites cured at 25 °C (Fig. 12b) and 60 °C (Fig. 12e). This is because the conductivity of CFs is better than that of Na^+ ionic motion. The CFs controlled the conductivity of composites and suppressed the response current that arose from the electrochemical reaction in the geopolymer. With further addition of CF (0.2 wt% or more), the electrochemical reaction peaks almost completely vanished (Fig. 12c and f). This confirms that at CF concentrations of 0.2 wt % or larger, the composites surpassed the percolation threshold and behaved as conductors. The electrochemical reactivity in geopolymers has very little influence in the CV curves of composites. The scan rate for composites with >0.2 wt% CF did not show any effect.

The results from the electrochemical impedance spectroscopy (EIS) are shown as the Nyquist plots in Fig. 13. For the composite paste cured at 25 °C (the black dots in Fig. 13a), the pure geopolymer paste produced of at least 2 semicircular arcs representing several electrical conducting elements in the system. The observed feature from the present EIS measurement is similar to the EIS results obtained from cement pastes [34–36]. The incomplete semicircular arcs resulted from an insufficient range in the measurement frequency. The cusp which intersects the x-axis represents the resistance of the sample. It can be seen that when only 0.1% CF was added, the size of this arc was significantly reduced. The cusp was reduced from around 1000 Ω for 0% CF to 350 Ω for 0.1% CF. Larger levels of CF further reduced the size of the arcs.

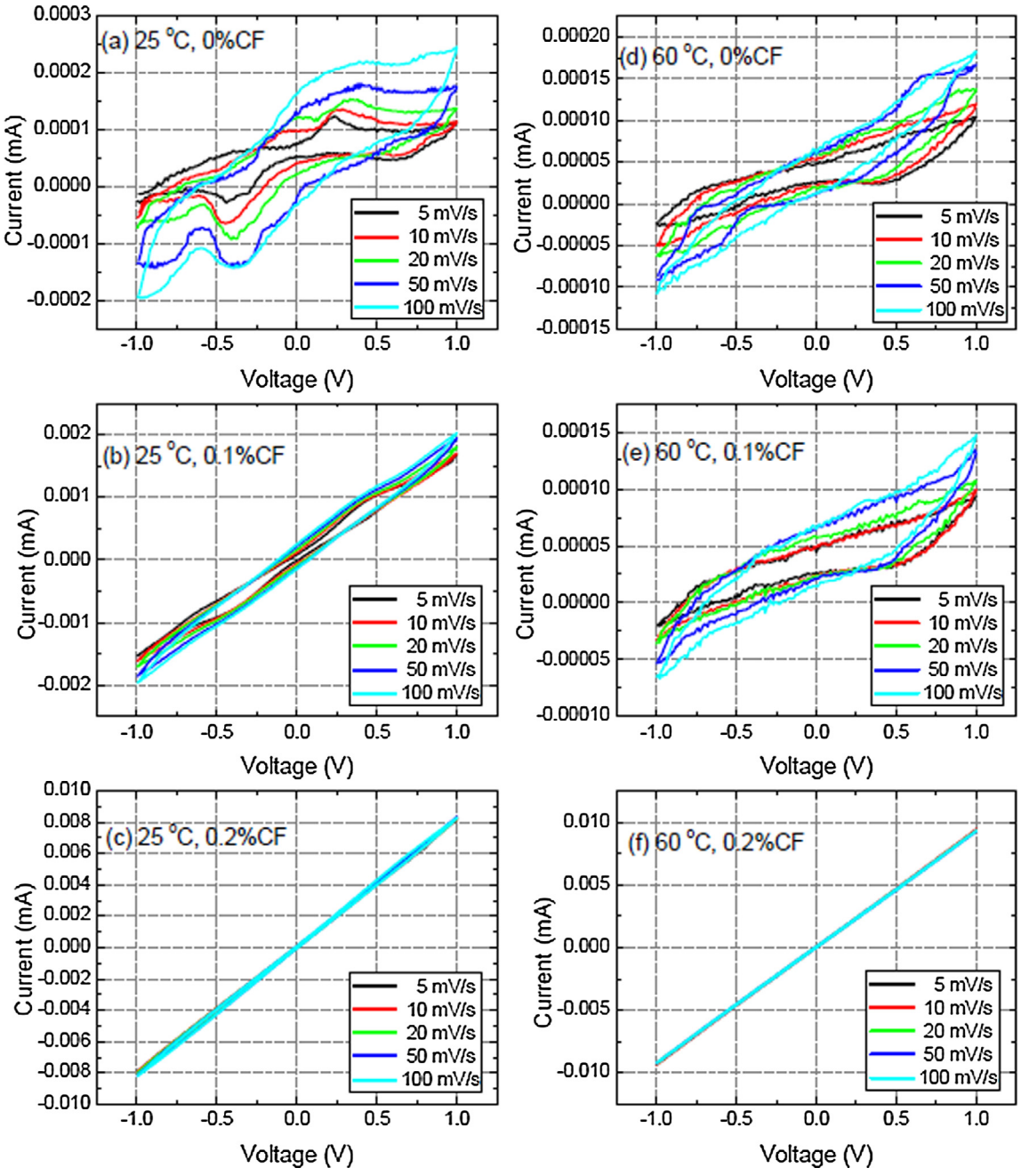

Fig. 12. CV curves of CF/geopolymer pastes cured at (a–c) 25 °C and (d–f) 60 °C. The concentrations of CF are (a and d) 0 wt%, (b and e) 0.1 wt%, (d and f) 0.2 wt%.

Particularly, when the CF concentration was 0.2% and above, very small arcs were observed. The conduction values of the CF/geopolymer composites were above the percolation threshold where the CF reinforcing phase controlled the conduction behavior via the path of CF network. The resistances obtained from the cusps were in the range of 50–150 Ω. The EIS results confirm the observation from I-V and CV measurements not only in a qualitative picture, but the size of the resistances was of the same order of magnitude.

For samples cured at 60 °C, a similar result was seen except that the cusps were higher for pastes with 0% and 0.1% CF. This is justified since a higher content of geopolymer phase was established by curing at this temperature. For CF concentrations of 0.2–0.5%, the resistance obtained from the EIS of composite pastes cured at 25 °C and 60 °C were similar, which is in good agreement with the I-V and CV results.

The results from EIS were further analyzed by fitting the data with the electrochemical models. Based on previous EIS analysis of CNT/cement composites [34], two different models can be used to represent the system. Fig. 14an illustrates the equivalent circuit of the plain geopolymer paste where R_s is the resistance of the electrolyte solution, Q_1 is the double layer capacitance between the geopolymer and electrodes, R_{ct1} is the charge transfer resistance between geopolymer and electrodes, and W_1 is the Warburg resistance caused by charge diffusion. When CFs were incorporated in the system, another equivalent circuit loop is required, as shown in Fig. 14b, where Q_2 represents the double layer capacitance between CFs and geopolymer, R_{ct2} represents for the charge transfer resistance between CFs and geopolymer, and W_2 is the Warburg resistance caused by charge diffusion in the composite system. The results of the fitted data are also shown in Fig. 13 as continuous lines. It is clearly seen that the data fitted the models

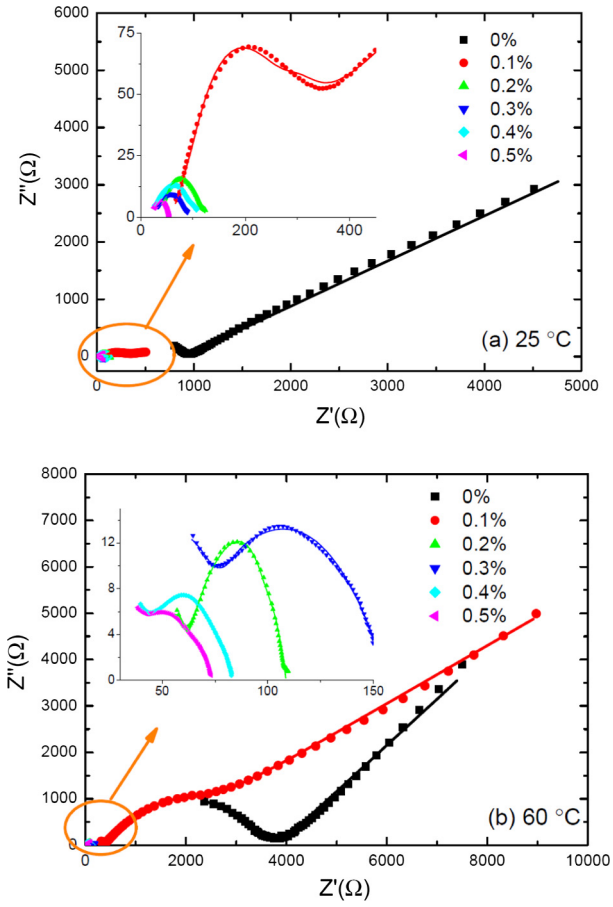

Fig. 13. EIS measurement CF/geopolymer paste cured at (a) 25 °C and (b) 60 °C. The dots represent the measured data whereas the continuous lines represent the fitted curves using the models in Fig. 14.

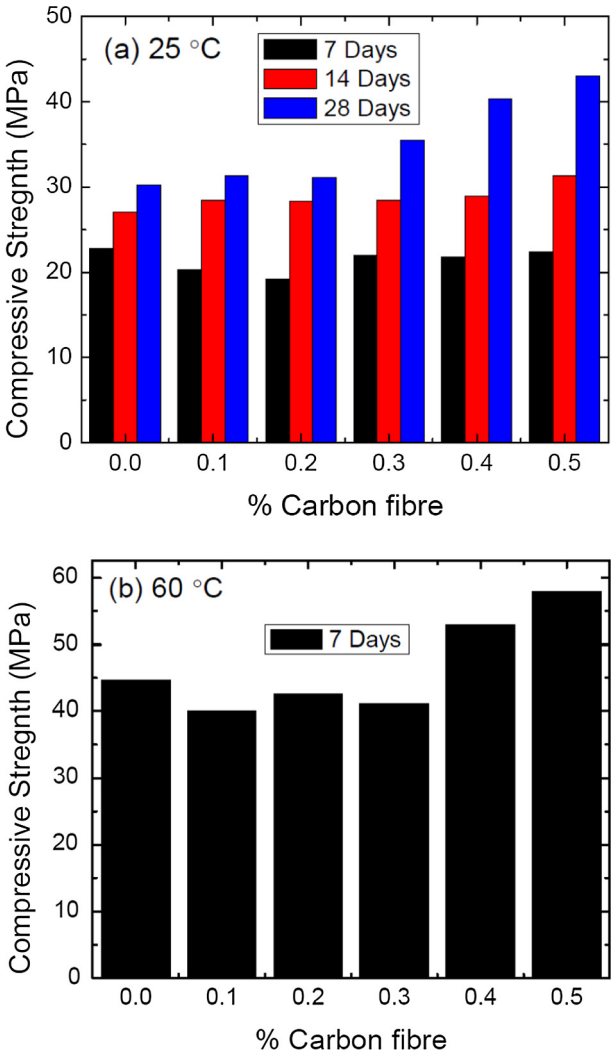

Fig. 15. Compressive strength versus %CF for CF/geopolymer paste cured at (a) 25 °C and (b) 60 °C.

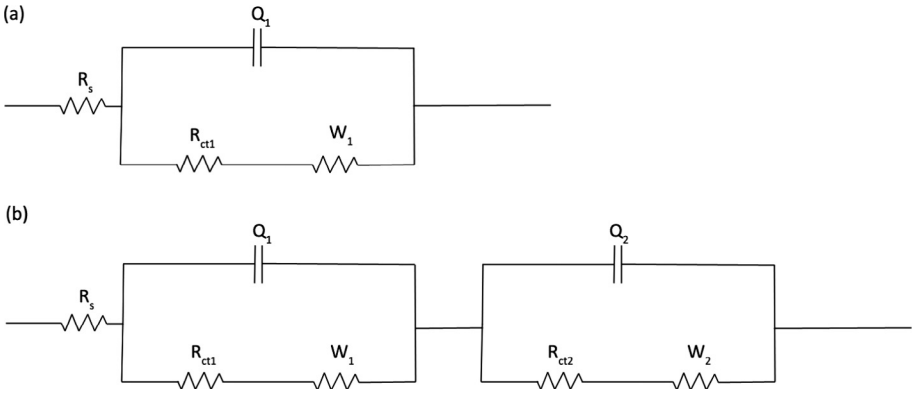

Fig. 14. Equivalent circuits of the electrochemical system for (a) geopolymer paste, (b) CF/geopolymer composites.

Table 3
EIS fitting parameters using the models in Fig. 14 for geopolymer composites with 0 and 0.1 wt% CF.

Sample conditions		Fitting parameters						
Curing temp (°C)	%CF	R_s (Ω)	Q_1 (F)	R_{ct1} (Ω)	W_1 (Ω)	Q_2 (F)	R_{ct2} (Ω)	W_2 (Ω)
25	0	8.86E+01	7.84E+03	1.39E+09	2.53E+10			
	0.1	72.7	6.55E−05	1.66E+02	3.77E+03	2.40E−07	1.80E+00	1.05E+02
60	0	1.14E−02	6.28E−11	3.83E+03	1.19E+04			
	0.1	430	4.41E−06	9.74E+02	2.29E+02	4.44E−04	1.52E+04	1.23E+06

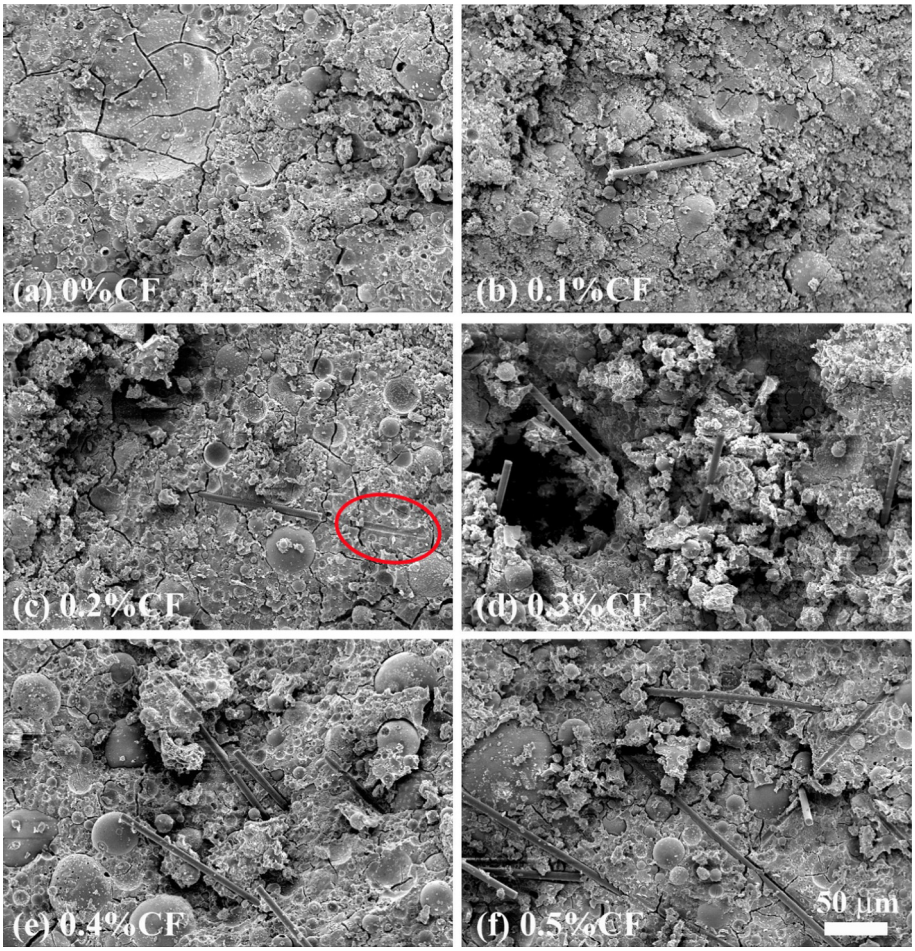

Fig. 16. SEM micrographs of CF/geopolymer composites (L/A = 0.4) cured at 25 °C for the %CF of (a) 0, (b) 0.1, (c) 0.2, (d) 0.3, (e) 0.4, and (f) 0.5.

very well. The parameters from fitting for the plain geopolymer paste and the geopolymer composited with 0.1 wt% CF are shown in Table 3. It can be seen that for the samples cured at 25 °C, incorporating CFs significantly reduced the R_{ct} suggesting that CFs improve the conductive contacts between geopolymer and electrodes. Another important point is the reduction in the Warburg resistance, which implies improvement of Na^+ diffusion in the material. For the samples cured at 60 °C, in which the geopolymerization process is more complete, the double layer capacitance is vastly increased when 0.1 wt% CF was added. This could be a result of the capacitive effect of the geopolymer layer between two adjacent CFs. Alternatively, the Warburg resistance was higher in the 0.1 wt% CF sample indicating that Na^+ diffusion was more difficult. In this case, the electrical conduction of the composite may have taken place to a greater extent via the CF conduction paths, so that the effect of ion diffusion was limited.

At the end of this section, it is useful to compare the values of electrical resistivity from our measurements with reported literature values. Hanjitsuwan et al. reported resistivity (at 100 Hz) of geopolymer pastes in the range of 10^3–10^5 Ω cm depending on the L/A ratios [37] and NaOH concentrations [18]. Vaiday and Allouche measured the resistance of carbon fiber reinforced geopolymer concrete at a frequency of 795 kHz [13]. The resistivity of their beam and cylinder samples was approximately ~2000 Ω cm. Cui et al. studied the electrical conductivity of a chemosynthetic Al_2O_3-$2SiO_2$ geopolymer and found that the lowest resistivity value was 6.7×10^5 Ω cm [38]. Saafi et al. reported resistivities of 60–100 Ω cm for fly ash geopolymer [4]. The resistivity was reduced to 30–40 Ω cm when 1.0 wt% CNT was added. MacKenzie and Bolton reported the resistivity of a potassium aluminosilicate geopolymer of 10^6–10^7 Ω cm at temperatures of 180–340 °C [14]. When CNT and graphite were added to form the composites, the resistivity at around 300 °C was significantly reduced to approximately 2×10^3 Ω cm and 3×10^2 Ω cm, respectively. Al-Dahawi et al. recently studied the electrical properties of cement/FA mortar [17]. They found that the resistivity after curing for 28 days was about 10^4 Ω cm and the resistivity increased with aging time. Adding carbon based materials reduced the resistivity by nearly an order of magnitude.

It can be seen that a very wide range of geopolymer resistivity values have been reported. No consensus on the topic has been reached in the literature. It can be rationalized that the measurement methods and apparatus for each study were different since there is no standard method for evaluation of electrical conductivity in geopolymers. Moreover, as already shown, the electrical conductivity of geopolymer composites is affected by several factors, i.e., raw materials (metakaolin/fly ash), L/A, curing temperature, aging time, concentration of reinforcing materials. Therefore, it is very important to identify and control all these factors for accurate measurements. For example, in our case, the resistivity of the plain FA geopolymer with L/A of 0.4 cured at 60 °C, the 28-day resistivity was recorded as 6×10^3 Ω cm.

3.4. Mechanical property of CF/geopolymer composite paste

Fig. 15 shows compressive strengths of CF/geopolymer pastes with L/A = 0.4, cured at 25 °C for 7, 14 and 28 days (Fig. 15a) and cured at 60 °C for 7 days (Fig. 15b). The specimens cured at 25 °C

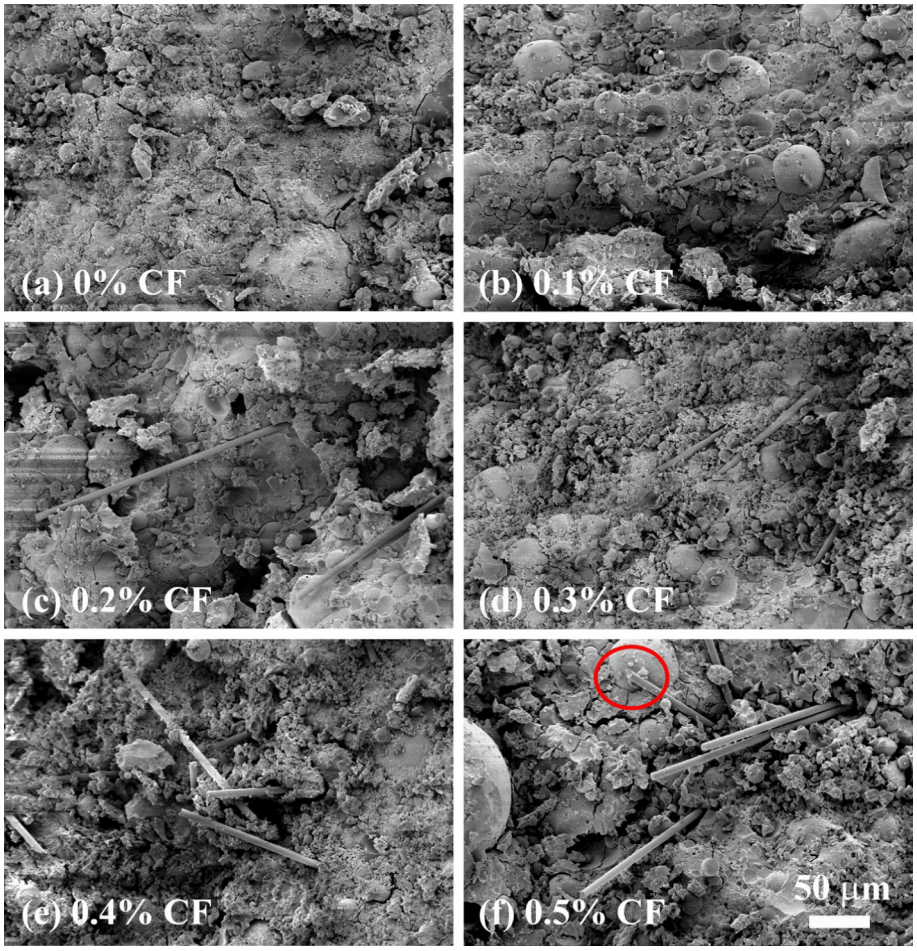

Fig. 17. SEM micrographs of CF/geopolymer composites (L/A = 0.4) cured at 60 °C for the %CF of (a) 0, (b) 0.1, (c) 0.2, (d) 0.3, (e) 0.4, and (f) 0.5.

for 7 days provide relatively similar strength even for different fiber contents. The minimum strength was for the 0.3% CF sample (19.2 MPa) and the highest strength was found in the sample with 0.5% CF (22.4 MPa). After the specimens were cured for 14 days, the strength of all samples was improved. However, the variation of strength amongst samples with different CF contents is not significant. The highest strength was 31.3 MPa for the 0.5% CF/geopolymer composite cured for 14 days. With 28 days of aging, the strength of all samples increased but differences could be observed and the trend was clear. Adding more reinforcing CF led to enhanced compressive strength. The enhancement of compressive strength in composites is attributed to the hydrophilic characteristic of carbon based fiber, which leads to a high fiber/matrix interaction [27]. The highest compressive strength (43.0 MPa) was found in the sample with 0.5% CF which is approximately 40% improvement in comparison to the sample without CF (30.3 MPa).

The 60 °C cured pastes measured at 7 days provided much higher compressive strength compared to the 25 °C cured pastes measured 28 days. This result is justified as the curing temperature is an important factor to stimulate geopolymerization. After curing at 60 °C for 24 h, the geopolymerized reaction is more complete than in the samples cured at room temperature for 28 days. The trend of compressive strength with respect to CF concentration in Fig. 15b may not be as clear as in Fig. 15a. However, the highest strength was found with the sample containing 0.5% CF (58.0 MPa). CF is a reinforcing agent that acts as the bridge to hold the matrix together. Therefore, adding higher amounts of CF causes increased strength. In the present study, the CF/geopolymer composite containing 0.5% CF exhibited the highest values in both strength and electrical conductivity. The only drawback to this sample is its reduced workability.

3.5. Microstructure of CF/geopolymer composite paste

The microstructures of CF/geopolymer pastes were investigated using SEM. Figs. 16 and 17 show the fracture surfaces of the samples cured at 25 °C and 60 °C after mechanical testing. For the pastes without CF, the sample cured at 25 °C contains much more unreacted spherical fly ash (Fig. 16a) than those cured at 60 °C (Fig. 17a). This confirms that the geopolymerisation reaction was more compete with curing at 60 °C. As a consequence, the geopolymer specimens cured at 60 °C showed better mechanical properties compared to the 25 °C cured samples. Additionally, the higher resistivity of 60 °C cured geopolymer could be caused by this more complete reaction.

For the composites with CF 0.1–0.5%, the SEM images in Figs. 16 and 17 show homogeneously and randomly distributed CFs. These results show that the present mixing method adequately dispersed CF in the geopolymer matrix without bundling. Homogeneous distribution of CF can improve both strength and electrical conductivity of composites. Moreover, the randomly oriented CF provides isotropic properties to the samples.

A series of images in Figs. 16 and 17 show the fracture surfaces of the pastes as the CF content was increased. It can be seen that a higher portion of the CFs can be visualized in the SEM images as

the CF concentration was increased. When %CF > 0.3%, the volume density of CF increased so that some fibers were in contact with others (Figs. 16e & f and 17e & f). This resulted in significant reduction of resistivity in the composites since the CF provided short circuit paths for electrical conduction.

The results from the mechanical tests can also be explained from the fracture surface morphology. When the composite paste was compressed, the applied stress was distributed between the matrix and CF. CF helped to support the mechanical loads in the structure. There are two behaviors of fiber that were observed under SEM investigation: the fracturing of fibers (e.g. red circle in Fig. 17f) and fibers pulling out from the matrix (e.g., the circle in Fig. 16c). These two behaviors resulted from different bonding interfaces between fiber and matrix. For the good bonding of fiber and matrix, the fiber tends to fracture. Alternatively, if the bonding interface is weak, the stress leads to delamination and pull-out of fiber before failure of the composite.

4. Conclusions

This work studied the electrical conductivity of CF reinforced fly ash geopolymeric composites as a function of CF concentration, L/A, curing temperature, aging time and measurement frequency. From I-V curve measurements, it was found that for low CF concentrations at a fixed L/A value, the electrical conductivity depends on curing temperature and aging time. For the high CF concentration above the percolation threshold, the conductivity is dependent on CF% but independent of curing temperature, aging time or measurement frequency. For different L/A ratios, the electrical conductivity behavior of composite pastes is very similar except that the CF percolation threshold is higher for larger L/A values. Using different electrical measurement techniques, CV and EIS, yield very similar results. Below the percolation threshold, the matrix has a significant contribution to the electrical conductivity, but above the threshold, CF reinforcing phase is dominant. The XRD and FTIR analyses showed that the change in electrical conductivity is due to a composite effect since the phase of matrix was not altered when CF content was increased. Also, the SEM micrographs showed evidence of homogeneity and random distribution of CFs in the geopolymer matrix. Addition of CF in geopolymer composites does not only improve the electrical behavior but also strongly enhances its mechanical property. The composite with 0.5% CF shows the best performance in terms of the electrical conduction and compressive strength. The only drawback is a reduced workability for higher CF concentration.

The highly conductive geopolymer with improved strength has a potential in many useful applications, e.g. electrical grounding, lightning protection, deicing, or electrical energy transport and storage. Our work has shown that the conductivity of fly ash geopolymer-based materials is tunable and can achieve relatively high value (10^1 S/m). This value could be enhanced further by adding more CFs and sustain the workability by using higher L/A ratio.

Acknowledgements

This work was supported by the Thailand Research Fund (TRF) and Khon Kaen University under the TRF Senior Research Scholar, Grant No. RTA5780004, the Nanotechnology Center (NANOTEC), NSTDA, Ministry of Science and Technology, Thailand, through its program of Center of Excellence Network, and the Higher Education Research Promotion and National Research University Project of Thailand, Office of the Higher Education Commission, through the Advanced Functional Materials Cluster of Khon Kaen University.

References

[1] R.H. Kupaei, U.J. Alengaram, M.Z. Bin Jumaat, H. Nikraz, Mix design for fly ash based oil palm shell geopolymer lightweight concrete, Constr. Build. Mater. 43 (2013) 490–496.
[2] J.L. Provis, J.S.J. Van Deventer, Geopolymers: Structure, Processing, Properties and Industrial Applications, CRC Press, Oxford, 2009.
[3] T. Lin, D. Jia, P. He, M. Wang, D. Liang, Effects of fiber length on mechanical properties and fracture behavior of short carbon fiber reinforced geopolymer matrix composites, Mater. Sci. Eng. A Struct. 497 (1–2) (2008) 181–185.
[4] M. Saafi, K. Andrew, P.L. Tang, D. McGhon, S. Taylor, M. Rahman, S.T. Yang, X.M. Zhou, Multifunctional properties of carbon nanotube/fly ash geopolymeric nanocomposites, Constr. Build. Mater. 49 (2013) 46–55.
[5] G. Masi, W.D.A. Rickard, M.C. Bignozzi, A. van Riessen, The effect of organic and inorganic fibres on the mechanical and thermal properties of aluminate activated geopolymers, Compos. Part B-Eng. 76 (2015) 218–228.
[6] F.L. Matthews, R.D. Rawlings, Composite Materials: Engineering and Science, CRC Press, Cambridge, 1999.
[7] A.R. Sakulich, Reinforced geopolymer composites for enhanced material greenness and durability, Sustain Cities Soc. 1 (4) (2011) 195–210.
[8] F.U.A. Shaikh, Review of mechanical properties of short fibre reinforced geopolymer composites, Constr. Build. Mater. 43 (2013) 37–49.
[9] N. Ranjbar, M. Mehrali, M. Mehrali, U.J. Alengaram, M.Z. Jumaat, High tensile strength fly ash based geopolymer composite using copper coated micro steel fiber, Constr. Build. Mater. 112 (2016) 629–638.
[10] N. Ranjbar, M. Mehrali, A. Behnia, A.J. Pordsari, M. Mehrali, U.J. Alengaram, M.Z. Jumaat, A comprehensive study of the polypropylene fiber reinforced fly ash based geopolymer, PLoS ONE 11 (1) (2016).
[11] S.N. Lu, N. Xie, L.C. Feng, J. Zhong, Applications of nanostructured carbon materials in constructions: the state of the art, J. Nanomater. (2015) 807416.
[12] H.M. Khater, H.A.A. el Gawaad, Characterization of alkali activated geopolymer mortar doped with MWCNT, Constr. Build. Mater. 102 (2016) 329–337.
[13] S. Vaidya, E.N. Allouche, Strain sensing of carbon fiber reinforced geopolymer concrete, Mater. Struct. 44 (8) (2011) 1467–1475.
[14] K.J.D. MacKenzie, M.J. Bolton, Electrical and mechanical properties of aluminosilicate inorganic polymer composites with carbon nanotubes, J. Mater. Sci. 44 (11) (2009) 2851–2857.
[15] D.D.L. Chung, Multifunctional Cement-Based Materials, CRC Press, New York, 2003.
[16] M.F. Ashby, D.R.H. Jones, Engineering Materials 1: An Introduction to Properties, Applications and Design, fourth ed., Butterworth-Heinemann, Oxford, 2012.
[17] A. Al-Dahawi, O. Ozturk, F. Emami, G. Yildlrim, M. Sahmaran, Effect of mixing methods on the electrical properties of cementitious composites incorporating different carbon-based materials, Constr. Build. Mater. 104 (2016) 160–168.
[18] S. Hanjitsuwan, S. Hunpratub, P. Thongbai, S. Maensiri, V. Sata, P. Chindaprasirt, Effects of NaOH concentrations on physical and electrical properties of high calcium fly ash geopolymer paste, Cem. Concr. Compos. 45 (2014) 9–14.
[19] X. Ma, Z.H. Zhang, A.G. Wang, The transition of fly ash-based geopolymer gels into ordered structures and the effect on the compressive strength, Constr. Build. Mater. 104 (2016) 25–33.
[20] H.K. Kim, I.W. Nam, H.K. Lee, Enhanced effect of carbon nanotube on mechanical and electrical properties of cement composites by incorporation of silica fume, Compos. Struct. 107 (2014) 60–69.
[21] A. Mebrouki, N. Belas, K. Bendani, N. Bouhamou, A self-compacting cement paste formulation using mixture design, J. Appl. Sci. 9 (23) (2009) 4127–4136.
[22] D.L. Kantro, Influence of water-reducing admixtures on properties of cement paste – a miniature slump test, Cem. Concr. Aggregates CCAGDP 2 (2) (1980) 95–102.
[23] D.L. Kong, J.G. Sanjayan, K. Sagoe-Crentsil, Comparative performance of geopolymers made with metakaolin and fly ash after exposure to elevated temperatures, Cem. Concr. Res. 37 (12) (2007) 1583–1589.
[24] M.B. Ogundiran, S. Kumar, Synthesis of fly ash-calcined clay geopolymers: reactivity, mechanical strength, structural and microstructural characteristics, Constr. Build. Mater. 125 (2016) 450–457.
[25] M. Sarkar, K. Dana, S. Das, Microstructural and phase evolution in metakaolin geopolymers with different activators and added aluminosilicate fillers, J. Mol. Struct. 1098 (2015) 110–118.
[26] M. Saafi, L. Tang, J. Fung, M. Rahman, J. Liggat, Enhanced properties of graphene/fly ash geopolymeric composite cement, Cem. Concr. Res. 67 (2015) 292–299.
[27] N. Ranjbar, M. Mehrali, M. Mehrali, U.J. Alengaram, M.Z. Jumaat, Graphene nanoplatelet-fly ash based geopolymer composites, Cem. Concr. Res. 76 (2015) 222–231.
[28] M.Y.J. Liu, U.J. Alengaram, M. Santhanam, M.Z. Jumaat, K.H. Mo, Microstructural investigations of palm oil fuel ash and fly ash based binders in lightweight aggregate foamed geopolymer concrete, Constr. Build. Mater. 120 (2016) 112–122.
[29] P. Timakul, W. Rattanaprasit, P. Aungkavattana, Improving compressive strength of fly ash-based geopolymer composites by basalt fibers addition, Ceram. Int. 42 (5) (2016) 6288–6295.
[30] S.K. Nath, S. Maitra, S. Mukherjee, S. Kumar, Microstructural and morphological evolution of fly ash based geopolymers, Constr. Build. Mater. 111 (2016) 758–765.

[31] M. Saafi, G. Piukovics, J. Ye, Hybrid graphene/geopolymeric cement as a superionic conductor for structural health monitoring applications, Smart Mater. Struct. 25 (10) (2016).
[32] W.M. Haynes, D.R. Lide, CRC Handbook of Chemistry and Physics: A Ready-Reference Book of Chemical and Physical Data, 93rd ed., CRC Press, Boca Raton, Fla., 2012.
[33] W.M. Haynes, D.R. Lide, CRC Handbook of Chemistry and Physics: A Ready-Reference Book of Chemical and Physical Data, 92nd ed., CRC Press, Boca Raton; London, 2011.
[34] W.W. Li, W.M. Ji, G.H. Fang, Y.Q. Liu, F. Xing, Y.K. Liu, B.Q. Dong, Electrochemical impedance interpretation for the fracture toughness of carbon nanotube/cement composites, Constr. Build. Mater. 114 (2016) 499–505.
[35] S. Wansom, S. Janjaturaphan, Evaluation of fiber orientation in plant fiber-cement composites using AC-impedance spectroscopy, Cem. Concr. Res. 45 (2013) 37–44.
[36] L.Y. Woo, S. Wansom, N. Ozyurt, B. Mu, S.P. Shah, T.O. Mason, Characterizing fiber dispersion in cement composites using AC-Impedance Spectroscopy, Cem. Concr. Compos. 27 (6) (2005) 627–636.
[37] S. Hanjitsuwan, P. Chindaprasirt, K. Pimraksa, Electrical conductivity and dielectric property of fly ash geopolymer pastes, Int. J. Miner. Metall. Mater. 18 (1) (2011) 94–99.
[38] X.M. Cui, G.J. Zheng, Y.C. Han, F. Su, J. Zhou, A study on electrical conductivity of chemosynthetic Al2O3-2SiO(2) geoploymer materials, J. Power Sources 184 (2) (2008) 652–656.

Journal of Cleaner Production 148 (2017) 49–59

Contents lists available at ScienceDirect

Journal of Cleaner Production

journal homepage: www.elsevier.com/locate/jclepro

Use of municipal solid waste incinerator (MSWI) bottom ash in high calcium fly ash geopolymer matrix

Ampol Wongsa [a, 1], Kornkanok Boonserm [b, 2], Chattichai Waisurasingha [a, 3], Vanchai Sata [a, *], Prinya Chindaprasirt [a, 1]

[a] Sustainable Infrastructure Research and Development Center, Department of Civil Engineering, Faculty of Engineering, Khon Kaen University, Khon Kaen 40002, Thailand
[b] Department of Applied Chemistry, Faculty of Science and Liberal Arts, Rajamangala University of Technology Isan, Nakhon Ratchasima 30000, Thailand

ARTICLE INFO

Article history:
Received 19 October 2016
Received in revised form
26 January 2017
Accepted 26 January 2017
Available online 30 January 2017

Keywords:
Municipal solid waste incinerator (MSWI) bottom ash
Fly ash
Cement
Geopolymer
Alternative cement binder

ABSTRACT

In order to reduce municipal solid waste incinerator (MSWI) ash, the effect of replacement level of high calcium fly ash by MSWI bottom ash on fly ash based geopolymer properties were studied. The results were compared to cement matrix containing MSWI bottom ash. It showed that the 20% MSWI bottom ash replacement level produced the highest compressive strength at 7 d of 52.8 MPa. The MSWI bottom ash could replace fly ash at high dosage level of 40% and the compressive strength was still higher than that of the control geopolymer mortar. The porosity, pore size distribution, and SEM indicated that the use of MSWI bottom ash could increase the denseness and homogeneity of geopolymer and cement matrix. In addition, the increase of MSWI bottom ash level significantly increased the crystalline phases of calcite and quartz as shown in the XRD pattern and C-O stretching in the FTIR images of both matrices.
© 2017 Elsevier Ltd. All rights reserved.

1. Introduction

Geopolymer is an alternative cement binder synthesized by mixing aluminosilicate material and high alkali solutions (Davidovits, 1999). It utilizes by-products such as metakaolin (Pangdaeng et al., 2015), fly ash or bottom ash (Pavithra et al., 2016) as aluminosilicate source to react with high alkali solutions such as sodium hydroxide, potassium hydroxide, sodium silicate or potassium silicate. Fly ash geopolymers were found to have high early and later age strengths (Swanepoel and Strydom, 2002), excellent resistance to sulfate and acid attack (Sata et al., 2012), and well sealant to store CO_2 in the underground (Zhuang et al., 2016). Chindaprasirt et al. (2007) showed that high calcium fly ash could react with sodium hydroxide solution and sodium silicate solution to produce high strength geopolymers. A number of researchers indicated that supplementary materials such as metakaolin, ground granulated blast-furnace slag (GGBFS), iron ore tailing (IOT), ordinary Portland cement (OPC), and silica fume could be used to improve properties of fly ash geopolymer. Duan et al. (2016a) indicated that partial replacement of fly ash at levels ranging from 0 to 20% by metakaolin improves the mechanical properties, optimizes the microstructure and reduces the level of damage from sulfate attack. A denser microstructure with higher surface Vickers-hardness of metakaolin containing geopolymer paste than those of geopolymer paste without metakaolin can be obtained. Deb et al. (2014) reported that the compressive strength of fly ash geopolymer concrete increased with the increase of GGBFS content. Strength development of those blended geopolymer concrete cured at ambient temperature was similar to that of water-cured OPC concrete. The optimum amount of GGBFS in fly ash geopolymer also reflected a dense microstructure and reduced porosity for fly ash-slag geopolymer composites (Khan et al., 2016). Okoye et al. (2016) reported that addition of silica fume improved the compressive, tensile and flexural strengths of the fly ash geopolymer concretes and those strength also increased as the silica fume content increased. In another study (Duan et al., 2016b), replacing of fly ash with 20% iron ore tailing (IOT) leads to a reduction of the porosity and microcrackings which results in much

* Corresponding author. Tel.: +6643 202846 127; fax: +6643 202846 102.
E-mail address: vancsa@kku.ac.th (V. Sata).
[1] Tel.: +6643 202846 209; fax: +6643 202846 102.
[2] Tel.: +6644 233000 4000; fax: +6644 233072.
[3] Tel.: +6643 202846 140, fax: +6643 202846 102.

http://dx.doi.org/10.1016/j.jclepro.2017.01.147
0959-6526/© 2017 Elsevier Ltd. All rights reserved.

denser microstructure of fly ash geopolymer paste blended. Aliabdo et al. (2016) showed that the adding of OPC improved compressive strength, splitting tensile strength, and modulus of elasticity of fly ash based geopolymer concrete except workability. Moreover, many researchers also indicated that industrial materials or residual wastes have extensively been studied as raw materials for geopolymer synthesis. Amin et al. (2016) found that sugar industry waste and locally available china clay can be utilized as raw material for synthesis of geopolymers. Antunes Boca Santa et al. (2013) studied the use of bottom ash from coal and calcined paper sludge from paper sludge as raw materials for geopolymer synthesis and showed that the best results were obtained with a solution of 15 M NaOH and sodium silicate and a mixture of 2:1 bottom ash and calcined paper sludge. Topçu et al. (2014) showed that durable geopolymer concrete without cement can be produced by using waste bottom coal ash. Haq et al. (2014) reported that bottom coal ash geopolymer showed higher thermal conductivity and lower compressive strength than that fly coal ash geopolymer.

Municipal solid waste incinerator (MSWI) ash is a residual waste from the disposal waste management by the combustion of municipal solid waste in combustor facilities (Hassan, 2005). The quantity of residual waste or MSWI ash was also increased with the increase of the disposal waste management by the combustion. These residual waste has 2 components such as MSWI fly ash and MSWI bottom ash (Hassan, 2005). Ninety percent of the total amount is bottom ash and ten percent is fly ash (Lin and Lin, 2006). The utilization of these ashes in cement and concrete industry reduces the environmental problems (Sikalidis et al., 2002), waste-management cost (Zhang et al., 2010), the amount of solid waste (Kurama et al., 2009), greenhouse gas emissions associated with Portland clinker production (Aydın et al., 2007), conserves existing natural resources and decreasing waste volume stored in landfills (Müller and Rübner, 2006). Previous study indicated that the MSWI fly and bottom ashes could be used as a blended cement material up to 10–30% by weight of binder. Goh et al. (2003) conducted a series of studies on the use of MSWI fly ash as a blended cement material. The compressive strength of blended cement mortar containing 10% of MSWI fly ash indicates that in higher than the control cement mortar. The 7 d strength activity index of 123.6% achieved by the MSWI fly ash, which is higher than the requirement of 75%, suggests its contribution toward the strength development of the blended cements. Lin et al. (2004) further studied paste specimens in which 10–40% of OPC was replaced by the MSWI fly ash. The compressive strength at a later stage of blended cement paste samples containing 10% and 20% of MSWI fly ash, varied from 95 to 110%. Moreover, the wet ground MSWI bottom ashes can be advantageously used as a partial replacement in the production of cement concrete with improved properties of strength, elastic modulus, and water penetration (Bertolini et al., 2004). These reports indicate that MSWI ash can be used as supplementary cementing material. For geopolymer system, Jin et al. (2016) studied the effect of the geopolymerization of MSWI fly ash and the stability of the metakaolin-MSWI fly ash based geopolymer as a desirable candidate for structural materials in the environment and reported that the metakaolin-MSWI fly ash based geopolymer presented excellent stability in the acid and alkaline environments, and also exhibited highly similar characteristics in the metakaolin-based geopolymers microstructures. However, there is still a lack of study on the use of these ashes in high calcium fly ash geopolymer system.

This work aimed to study the possibility of MSWI bottom ash used as a replacement material for fly ash geopolymer matrix. The MSWI bottom was used in combination with high calcium fly ash to produce geopolymer matrix. The effect of the replacement levels of fly ash by MSWI bottom ash on compressive strength, porosity, pore size distribution, scanning electron micrographs (SEM), x-ray diffraction (XRD), and fourier transform infrared spectroscopy (FTIR) of geopolymer matrix were presented and compared to Portland cement mortar containing MSWI bottom. This study would lay a groundwork for the future utilization of MSWI bottom ash in the geopolymer concrete product and lead to reduce cement consumption and waste materials.

2. Materials and preparation of sample

2.1. Materials

Main materials used in this study consisted of MSWI bottom ash (WA), ordinary Portland cement (OPC), and fly ash (FA). WA obtained from the combustion of municipal solid waste such as dry branches, paper, and dry leaves in Khon Kaen University, northeastern Thailand. In order to improve reactive of WA, they were ground by ball mill until 5% retained on a sieve No. 325 (45 μm). The OPC, tab water, and type F superplasticizer (SP) were used for making cement matrix, while the FA from Mae Moh Electricity power station in the north of Thailand was used as the main source material for making geopolymer matrix. Sodium hydroxide solution (NaOH, NH) at 10 Molar concentration and commercial grade sodium silicate solution (Na_2SiO_3, NS) with 12.53% Na_2O, 30.24% SiO_2, and 57.23% H_2O by weight were used as alkali activators. Local river sand with specific gravity of 2.63 and fineness modulus (F.M.) of 2.55 in saturated surface dry condition was used for making cement and geopolymer mortars.

2.2. Mix proportions

In order to study the effect of the replacement levels of OPC and FA by WA on cement and geopolymer mortar properties, three cement mortars and four geopolymer mortars were prepared. The mix proportions are shown in Table 1.

The OPC was replaced by WA at 0%, 20%, and 40% by weight of binder for preparing cement mortar in accordance with the procedure given in ASTM C618 (2015). The water to binder ratio of 0.484 and the sand to binder ratio of 2.75 were used. Flow of mortar was controlled at 110 ± 5% by superplasticizer (SP) in accordance with the procedure given in ASTM C1437-15 (2015).

For geopolymer mortar, the replacement levels of 0%, 20%, and 40% of FA by WA were also studied. However, in order to study the possibility of MSWI bottom ash used as raw material for geopolymer matrix, the replacement of 100% WA was used to produce geopolymer mortar. The liquid alkaline to binder ratio of 0.65, the sodium silicate to sodium hydroxide ratio of 1.00, and the sand to binder ratio of 2.75 were kept constant. The mortar samples were prepared for the compressive strength and porosity tests, while the paste samples were prepared for pore size distribution, SEM, XRD, and FTIR analyses. The name of the mixture was given by the type of cementitious binder and replacement levels of WA. For example, C-40WA denotes the cement binder with OPC replaced by WA at 40% by weight of binder and G-20WA denotes the geopolymer binder with FA replaced by WA at 20% by weight of binder.

2.3. Mixing, casting, and curing

For cement mortar, binder, water and superplasticizer (SP) were mixed in a pan-type mixer. Sand with the saturated surface dry condition was then added and mixed. After being mixed, they were placed in 50 × 50 × 50 mm^3 cubic molds and compacted in accordance with the procedure given in ASTM C109/C109M-16a (2016). The specimens were covered with a thin plastic sheet for moist curing. They were demolded at 1 d and stored in saturated

Table 1
Mix proportions of cement and geopolymer samples.

Mix	OPC (g)	FA (g)	WA (g)	SP (g)	Water (g)	NS (g)	NH (g)	Sand[a] (g)
C-0WA	100	–	–	0.8	48.0	–	–	275
C-20WA	80	–	20	2.0	47.4	–	–	275
C-40WA	60	–	40	3.8	46.5	–	–	275
G-0WA	–	100	–	–	–	32.5	32.5	275
G-20WA	–	80	20	–	–	32.5	32.5	275
G-40WA	–	60	40	–	–	32.5	32.5	275
G-100WA	–	–	100	–	–	32.5	32.5	275

[a] Sand was not used in paste sample.

limewater until the testing age. For geopolymer mortar, binder and NH were mixed in a pan-type mixer for 5 min. Sand with the saturated surface dry condition was then added and mixed for 5 min. Finally, NS was added and mixed for 5 min. After mixing, the geopolymer mortars were cast in 50 × 50 × 50 mm^3 cubic molds and compacted in accordance with ASTM C109/C109M-16a (2016). The specimens were wrapped with a thin plastic sheet to minimize moisture loss and allowed to stand for 1 h at 25 °C. It was then cured at 60 °C for 48 h and stored in the controlled room at 25 °C and 50% RH until testing age.

3. Testing

3.1. Compressive strength and porosity

Cement and geopolymer mortars were tested for compressive strength at 7 and 28 d in accordance with ASTM C109/C109M-16a (2016). The compressive strength test was carried out using a universal testing machine (UTM). The specimens were placed so that the load is applied at a constant loading rate of 0.9–1.8 kN/s. The failure load for the specimen was recorded. Compressive strength of each specimen was calculated in MPa (N/mm^2) as

$$\sigma = \frac{F}{A} \quad (1)$$

Where σ is the compressive strength (MPa), F is the maximum load indicated by the universal testing machine (N) and A is the average gross area of the upper and lower bearing surface of the specimen (mm). The reported compressive strengths were the average of three samples.

Porosity of mortars were tested at the age of 28 d in accordance with ASTM C642-13 (2013) and calculated using the following equation:

$$p = \frac{Wssd - Wd}{Wssd - Ww} \times 100 \quad (2)$$

Where p is porosity (%), $Wssd$ is specimen weight in air of saturated sample (g), Wd is specimen dry weight after 24 h in oven at 100 ± 5 °C (g) and Ww is specimen weight in water (g). The method for measuring porosity was used successfully in the Chen et al. (2013) report.

3.2. Pore size distribution, SEM, XRD, and FTIR analysis

The cement and geopolymer pastes were used for the study of microstructures at the age of 7 and 28 d. Three types of pore size viz., gel pore (0.007–0.01 μm), capillary pore (0.01–10 μm), and air void (10–180 μm) tested using a mercury intrusion porosimeter (MIP) with a pressure range from 0 to 228 MPa and capable of measuring pore size diameter down to 0.0057 μm (Diamond, 2000). The fractured surface of sample were dried and then coated with a layer of gold using a blazer sputtering coater and scanned using JEOL scanning electron microscope (SEM). The ground paste samples with particle size less than 75 μm (passed sieve No. 200) were prepared for XRD analysis by using PANalytical X-ray diffractometer with CuKα radiation. The XRD scans were performed at 10–60° 2theta. The fourier transform infrared spectroscopy (FTIR) at the wavenumber of 4000-500 cm^{-1} was used to determine the original material and paste composition.

4. Results and discussion

4.1. Characterization of raw materials

The chemical composition as determined by X-ray fluorescence (XRF) and physical characteristics of the WA, OPC, and FA are shown in Table 2 and Table 3. The specific gravity and median particle size of WA was 2.45 and 5.15 μm. The main chemical compositions of WA were CaO and SiO_2 and the loss on Ignition (LOI) was high at 23.0% which were similar to the other MSWI bottom ash (Chimenos et al., 1999) or MSWI fly ash (Pan et al., 2008). Fig. 1 shows the scanning electron microscope (SEM) of the WA, OPC, and FA. The particle shape of WA and OPC were irregular, angular, and crushed shaped particles whereas the particle shape of FA was mainly spherical. The XRD pattern of WA, OPC, and FA are shown in Fig. 2. The WA consisted of crystalline phases of calcite (C, $CaCO_3$) and

Table 2
Chemical composition of WA, OPC, and FA.

Oxides	WA	OPC	FA
CaO	38.1	61.1	14.5
SiO_2	15.8	18.1	39.4
Al_2O_3	0.9	4.2	20.8
Fe_2O_3	4.2	3.0	11.5
K_2O	7.3	0.6	2.4
MgO	3.5	1.1	2.2
MnO	0.1	–	–
Na_2O	0.2	0.2	1.4
P_2O_5	1.7	0.1	0.2
TiO_2	0.3	0.2	0.5
ZnO	–	0.1	–
BaO	0.1	–	0.1
Cl	0.5	–	–
SrO	0.1	–	–
SO_3	1.5	3.9	4.2
Loss on Ignition (LOI)	23.0	5.9	1.5

Table 3
Physical characteristics of WA, OPC, and FA.

Materials	WA	OPC	FA
Mean particle size (μm)	5.15	14.1	32.58
Retained on a sieve No. 325 (%)	5	5	44
Specific gravity	2.45	3.15	2.17

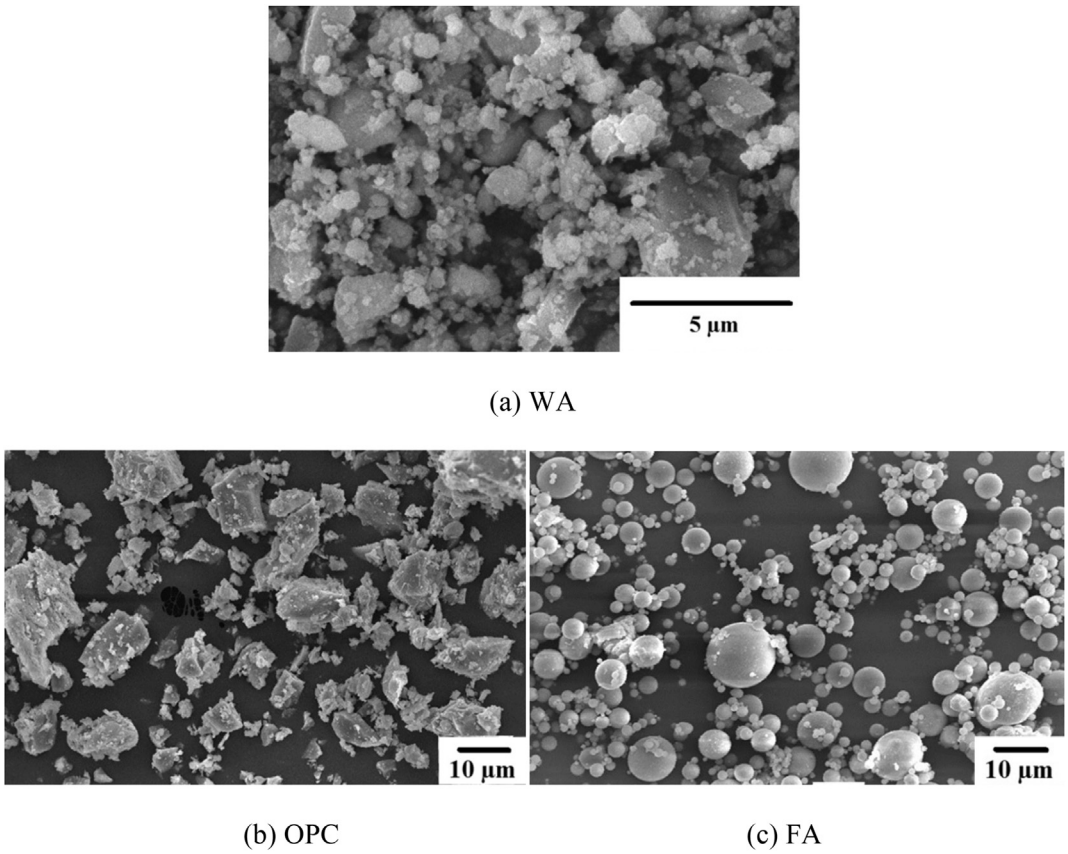

Fig. 1. SEM of WA, OPC, and FA particles.

quartz (Q, SiO_2). It had low glassy phase content as comparing to FA indicated by a small broad hump at the region of 25–37° 2Theta. The XRD pattern of FA shows some peaks of crystals of anhydrite (A, $Ca(SO_4)$), quartz (Q, SiO_2), lime (O, CaO) and magnesioferrite (M, $MgFe_2O_4$) whereas the OPC shows calcium silicate (CS, Ca_3SiO_5, Ca_2SiO_4). The total of SiO_2, Al_2O_3, and Fe_2O_3 oxide of FA was 71.1%, which was higher than the minimum requirement (70%) whereas the CaO content was 14.5%. For CaO content more than 10%, FA can be classified as Class C pozzolan (High calcium FA) as specified by ASTM C618 (2015). The specific gravity, a median particle size and percentage retain on a sieve No. 325 of FA were 2.17, 32.58 μm, and 44% by weight, while the specific gravity, a median particle size and Blaine fineness of OPC were 3.15, 14.10 μm, and 3120 cm^2/g.

4.2. Compressive strength

Table 4 summarizes the compressive strength and percentage of compressive strength of cement and geopolymer mortars. The compressive strength at 7 and 28 d of control cement mortar (C-0WA) were 45.5 MPa and 46.9 MPa. The compressive strength at 7 d of cement mortars decreased with the increase of WA replacement levels. For example, the compressive strength of C-0WA, C-20WA and C-40WA at 7 d were 45.5 MPa, 40.8 MPa, and 29.3 MPa. The decreasing in compressive strength was due to the decrease of hydration degree from cement reduction and the low pozzolanic reaction of WA at early age (Lin et al., 2004). However, the C-20WA had the compressive strength at 28 d of 47.7 MPa (102% of C-0WA compressive strength). The compressive strength of C-20WA was slightly higher than C-0WA at 28 d due to the filler effect of high fineness and pozzolanic reactions of WA (Goh et al., 2003), leading to the improvement of compressive strength. This was consistent with Lin et al. (2004) work which indicated that the active amorphous ions (Si, Al) of MSWI bottom ash slag reacted with the hydration products, $Ca(OH)_2$ to form C-S-H in 10% and 20% MSWI bottom ash blended cement pastes.

The compressive strength of fly ash geopolymer mortars replaced by WA at 0%, 20%, 40%, and 100% by weight of binder are also presented in Table 4. The compressive strength development of geopolymer mortars (G-0WA, G-20WA, G-40WA and G-100WA) in this study increased at a lower rate compared to those of cement mortars (C-0WA, C-20WA, and C-40WA). This was due to the fact that the curing at temperature of 60 °C for 48 h increased the early age compressive strengths of geopolymer mortars and the later age strength was less affected (Sata et al., 2012). The control geopolymer mortar (G-0WA) had compressive strengths at 7 and 28 d of 37.7 MPa and 42.0 MPa. High calcium FA contained a substantial amount of silica and alumina and is suitable to use as a source material for geopolymerization (Chindaprasirt et al., 2009). These components reacted with alkali silicate solutions to from geopolymerization products (CSH, CASH, and NASH) which contributed to the strength development (Hanjitsuwan et al., 2014). The compressive strength of G-20WA and G-40WA were higher than that of G-0WA. This may due to the increase of WA replacement levels increased the available free calcium ion (Ca^{2+}) which could react with silicate to form calcium silicate hydrate (CSH) gel (Rattanasak et al., 2011). In addition, the high fineness WA supported the filler effect property and also improved the strength of geopolymer mortars. The G-20WA mix had highest compressive strengths at 7 and 28 d of 52.8 MPa and 53.0 MPa and G-40WA mix had slightly lower compressive strength at 7 and 28 d of 44.6 MPa and 45.6 MPa. However, the high replacement level of WA seemed to give low compressive strength, such as the compressive

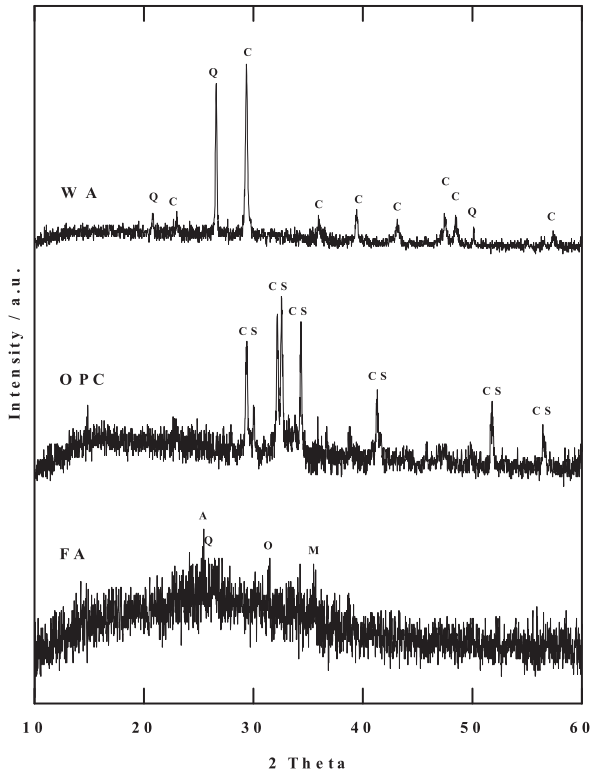

Calcite (C, $CaCO_3$), quartz (Q, SiO_2), calcium silicate (CS, Ca_3SiO_5, Ca_2SiO_4), anhydrite (A, $Ca(SO_4)$), lime (O, CaO) and magnesioferrite (M, $MgFe_2O_4$)

Fig. 2. XRD pattern of WA, OPC, and FA.

Table 4
Compressive strength and percentage of compressive strength of cement and geopolymer mortars.

Mix	7 d		28 d	
	MPa	%	MPa	%
C-0WA	45.5	100	46.9	100
C-20WA	40.8	90	47.7	102
C-40WA	29.3	64	35.7	76
G-0WA	37.7	100	42.0	100
G-20WA	52.8	140	53.0	126
G-40WA	44.6	118	45.6	109
G-100WA	9.2	24	10.6	25

strengths at 7 and 28 d of G-100WA were 9.2 MPa and 10.6 MPa. The low alumina oxide of WA (0.9% in Table 2.) resulted in the low geopolymerization and compressive strength.

The compressive strength results indicated that the WA could be used to replace OPC and FA to making cement and geopolymer mortar. In this range of study of 0–40% WA, the optimum replacement level of WA was 20% for geopolymer and cement mortars due to it produced the highest compressive strength at 28 d. In addition, WA could be used to replace FA at higher volume of up to 40% WA and the compressive strength was still higher than that of the control geopolymer mortar. At the same replacement level of WA, the compressive strength at early age of C-20WA and C-40WA was lower than that of C-0WA whereas G-20WA and G-40WA showed higher compressive strength than that of G-0WA. This was due to the increase in WA replacement levels for geopolymer matrix increased the available free Ca^{2+} which could react with silicate to form CSH gel. While the increase in WA replacement levels for cement matrix decreased the hydration resulted from the reduction of cement and the low pozzolanic reaction of WA at the early age. It should be noted here that the WA had been shown to be a good starting material for geopolymer matrix, while for cement matrix, it acted as supplementary material.

4.3. Porosity and pore size distribution

Table 5 shows the porosity of cement and geopolymer mortars. The porosity at 28 d of C-0WA, C-20WA, and C-40WA were 17.7%, 16.3% and 18.9%. The porosity of C-20WA was slightly lower than that of C-0WA due to the filler effect of high fineness of WA and this resulted in a less permeable mortar and an increase in compressive

Table 5
Porosity of cement and geopolymer mortars.

Mix	Porosity (%)
C-0WA	17.7
C-20WA	16.3
C-40WA	18.9
G-0WA	25.1
G-20WA	20.4
G-40WA	22.8
G-100WA	23.9

strength. At high replacement level of WA, the porosity of C-40WA increased in comparison to those of C-0WA and C-20WA. The increase in porosity of C-40WA resulted from the reduced amount of cement content and also led to the lower compressive strength compared to those of C-0WA and C-20WA. This was consistent with Chindaprasirt and Rukzon (2008) work which reported that the porosity of cement mortar containing fly ash and rice husk ash reduced with the low replacement level of up to 20% of binder, but increases with the high 40% replacement level.

For geopolymer mortar, the replacement of WA also showed a similar trend of results as that of cement mortar. The control geopolymer mortar (G-0WA) at 28 d contained the porosity of 25.1%. The replacement of WA significantly reduced the porosity of geopolymer mortar. The porosity values of G-20WA, G-40WA and G-100WA decreased to 20.4%, 22.8%, and 23.9%. This was due to the filler effect property of WA which contributed to an increase in the compressive strengths of G-20WA and G-40WA. However, the porosity of geopolymer mortars containing WA tended to increase with the increase of WA replacement levels from 20 to 100% WA and this resulted in a decrease in the compressive strength.

The porosity of cement and geopolymer mortar significantly reduced with the replacement level of 20% WA and tended to increase with the WA replacement level higher than 20%. In addition, although the porosity of geopolymer mortars was nearly the same as that of cement mortars, the compressive strengths of geopolymer mortars were higher than that of cement mortars.

The results of pore volume of cement and geopolymer paste at 28 d are shown in Fig. 3. The pore size distribution of cement and geopolymer pastes were significantly consistent with the porosity of cement and geopolymer mortars. For the control mixer, C-0WA contained the air void, capillary pore, and gel pore of 1.03%, 96.19%, and 2.78%. The air void, capillary pore, and gel pore of C-20WA were 0.47%, 95.11%, and 4.42%, and those of C-40WA were 7.07%, 89.53%, and 3.40%. The amount of air void and capillary pores decreased while the gel pore increased in 20% WA (C-20WA) due to the filling effect and this resulted in an increase in the compressive strength. This was consistent with Goh et al. (2003) work which reported the mercury porosimetry performed on hardened cement pastes indicated a reduction in the average pore diameter with an increasing percentage of cement replacement, indicating a pore refining capability of MSWI fly ash particles. However, the C-40WA sample showed the largest amount of air void owing to the low cement content from the high replacement of WA and led to the lower compressive strength compare to those of C-0WA and C-20WA.

The trends of pore volumes of G-0WA, G-20WA, and G-40WA as show in Fig. 3 were also similar to those of cement pastes. The air void, capillary pore, and gel pore of G-0WA were 1.91%, 87.78%, and 10.31%. While G-20WA contained the air void, capillary pore, and gel pore of 1.27%, 82.45%, and 16.28%. The replacement level of 20% WA significantly decreased the amount of capillary pores and air void, while the gel pores seemed to increase, which led to the dense matrix and highest compressive strength. For G-40WA, the air void, capillary pore, and gel pore were 7.12%, 80.59%, and 16.28%. The air void started to increase at the replacement level of 40% WA, which caused the reduction in the compressive strength but were still higher than that of G-0WA. The G-100WA contained the air void, capillary pore, and gel pore of 18.80%, 80.25%, and 0.95%. This set of results showed the largest amount of air void and the minimum amount of gel pore. The compressive strength was related to the porosity of samples. At the same replacement level of WA, the amount of gel pores of geopolymer paste were higher than that of cement paste. It should be noted that the compressive strength of gepolymer mortar was also higher.

4.4. Scanning electron micrographs (SEM)

Fig. 4 shows the SEM-photomicrographs of C-0WA, C-20WA, and C-40WA pastes at 28 d. The matrix of 100% OPC content appeared a continuous mass of hydration product matrix. The replacement level of 20% WA (C-20WA) appeared denser and more homogeneous than that of the control cement matrix as shown in Fig. 5b. Since, the high fineness of WA allowed denser packing of the matrix (Goh et al., 2003) and the filling of pores by calcium silicate hydrate from the pozzolanic reactions (Lin and Lin, 2006), which caused the improvement of denseness and homogeneity of matrix. For C-40WA (Fig. 5c), the matrix appeared less dense and less homogenous than that of C-20WA indicating that the amount of WA replacement at this level of 40% was excessive for the cement sample. The dense and homogeneity matrix led to the sample with high compressive strength (Boonserm et al., 2012a).

For geopolymer matrix, G-0WA appeared dense and contained a larger number of non-reacted and/or partially reacted fly ash particles as shown in Fig. 5a. The replacement levels of 20% and 40% WA (Fig. 5b and c) appeared to improve the denseness and the homogeneity of matrices due to the filler effect property of WA which was similar to those of cement mortar containing WA. The G-40WA appeared to be less dense and less homogenous than the G-20WA. The high WA content led to a decrease of the amorphous phase and alumino-silicate source materials. The G-100WA was significantly less dense and homogeneous (Fig. 5d). This was due to the low glassy phase content (Fig. 2) and low reactivity of WA compared to that of FA, which caused the reduced geopolymerization and reduced the strength of the geopolymer product.

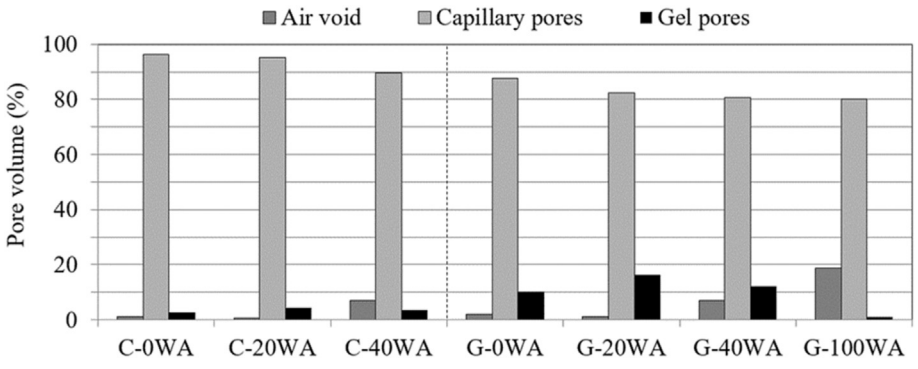

Fig. 3. Pore distribution of cement and geopolymer pastes at 28 d.

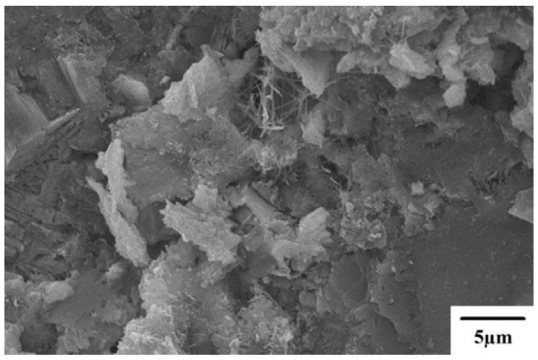

(a) C-0WA

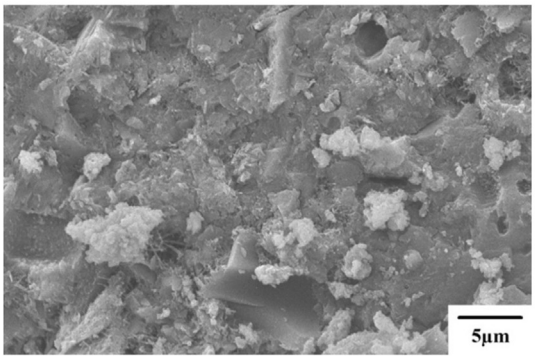

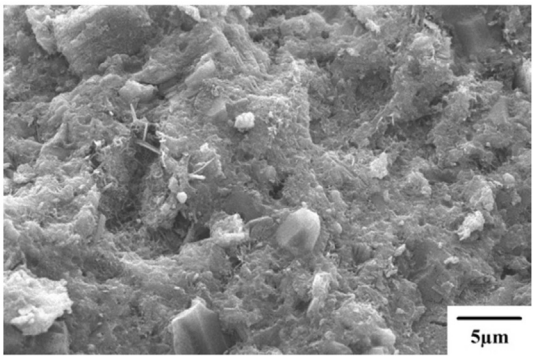

(b) C-20WA (c) C-40WA

Fig. 4. SEM micrographs of cement pastes at 28 d.

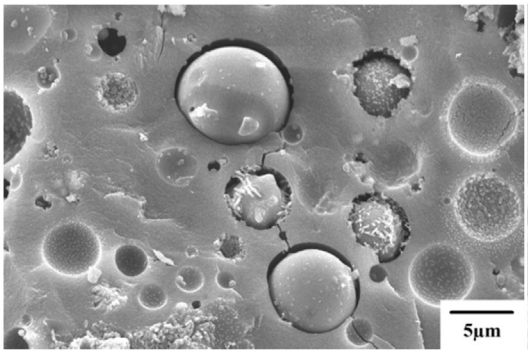

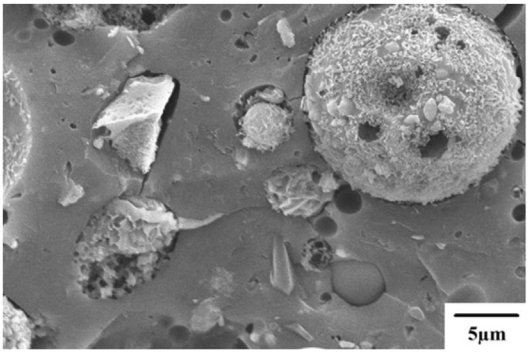

(a) G-0WA (b) G-20WA

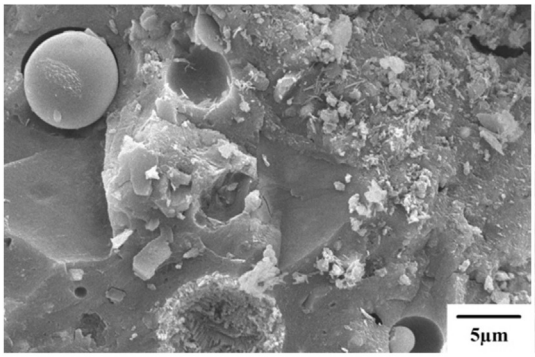

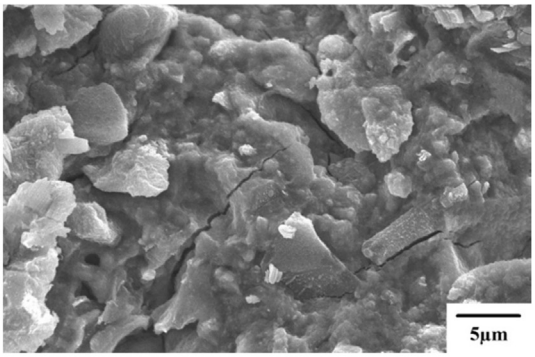

(c) G-40WA (d) G-100WA

Fig. 5. SEM micrographs of geopolymer pastes at 28 d.

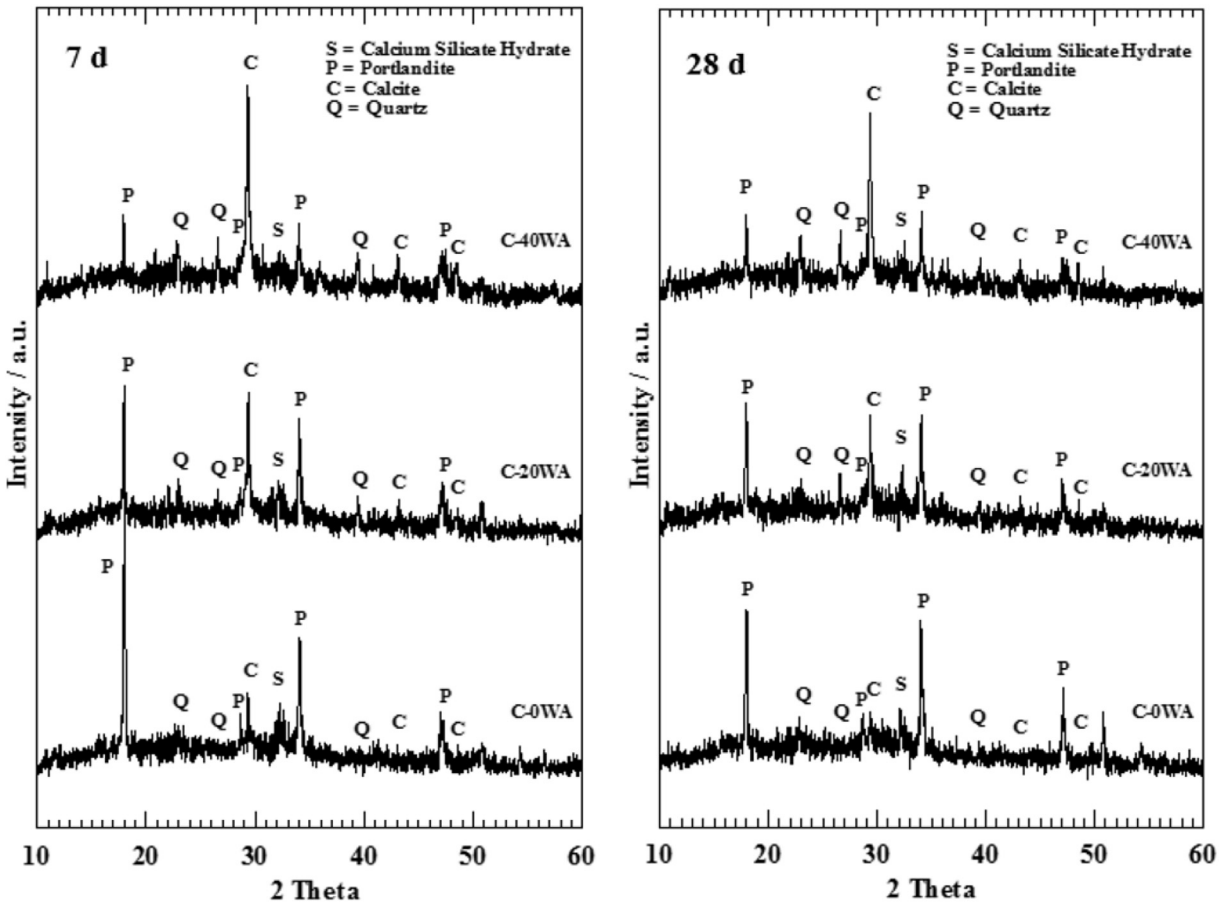

Fig. 6. The XRD patterns of cement pastes at 7 and 28 d.

4.5. X-ray diffraction (XRD)

The XRD patterns of cement pastes containing WA (C-0WA, C-20WA, and C-40WA) at 7 and 28 d are shown in Fig. 6. In general, the major phase of ordinary Portland cement paste are portlandite ($Ca(OH)_2$), calcium silicate hydrate (CSH), quartz (SiO_2), and calcite ($CaCO_3$) (Qiao et al., 2008) which were similar to C-0WA in this study. The cement paste containing WA, C-20WA and C-40WA paste showed similar phases to those of C-0WA paste. At the early age, the portlandite and calcium silicate hydrate phases decreased with the increase in the replacement level of WA. This may due to the replacement of WA led to a significant decrease of degree of hydration and hydration products in the mixture (Lin et al., 2004), caused reduction in compressive strength. In addition, the intensity of calcite and quartz seemed to increase with the replacement level of WA (Saikia et al., 2008) due to the major oxides compositions of CaO and SiO_2 in the MSWI (Rémond et al., 2002). The XRD patterns of cement pastes at 28 d showed similar phases to those of 7 d. However, the cement paste containing 20% WA (C-20WA) showed higher calcium silicate hydrate phase than that of 100% cement paste (C-0WA). This was due to the pozzolanic reaction between the $Ca(OH)_2$ and SiO_2 in WA to from calcium silicate hydrate (Lin and Lin, 2006), which improved its compressive strength.

The XRD patterns of geopolymer pastes containing WA at 7 and 28 d are shown in Fig. 7. The geopolymer paste with 100% FA (G-0WA) at 7 d consisted of a glassy matrix as confirmed by the broad hump in the region of 23–37 °2Theta (Phoo-ngernkham et al., 2014) and crystalline phases of calcite ($CaCO_3$), and quartz (SiO_2). For the WA paste, the amorphous phases reduced while calcite and quartz increased with the increase of replacement level of WA similar to those of cement pastes. This was due to the high CaO and SiO_2 oxide compositions in WA. The G-100WA paste showed the lowest amorphous phases. In addition, the geopolymer paste containing 20% and 40% WA (G-20WA and G-40WA) had calcium silicate hydrate phase higher than that of G-0WA as confirmed by the presence of peaks at 32.05 °2theta (Lecomte et al., 2006).

Generally, the main geopolymerization products are different from Portland cement hydration reaction products (Lecomte et al., 2006). The XRD patterns of geopolymer pastes and cement paste are also different. However, this study showed that the crystalline phases of calcite and quartz of cement and geopolymer paste significant increased with the increase of replacement revel of WA.

4.6. Fourier transform infrared spectroscopy (FTIR)

The results of the IR spectra of materials (OPC, FA and WA) and pastes are shown in Fig. 8. The O-H stretching and H-O-H bending at the wavenumber of 3700–2200 cm^{-1} and 1700–1600 cm^{-1} were the spectrum of stretching and deformation vibration from the weakly bound water molecules which were easily adsorbed on the surface or trapped in large cavities between the rings of cement and geopolymer matrix (Boonserm et al., 2012b). For cement matrix (Fig. 8a), the IR spectra of OPC showed the band at 919 cm^{-1} due to Si-O asymmetric stretching vibration of C_3S and/or C_2S. The strong asymmetric stretching Si-O band was shifted to high frequencies centered at 970 cm^{-1} with hydration indicated that the formation of CSH in cement paste (Yousuf et al., 1995). The asymmetric stretching S-O bands of OPC appeared at 1100–1160 cm^{-1}

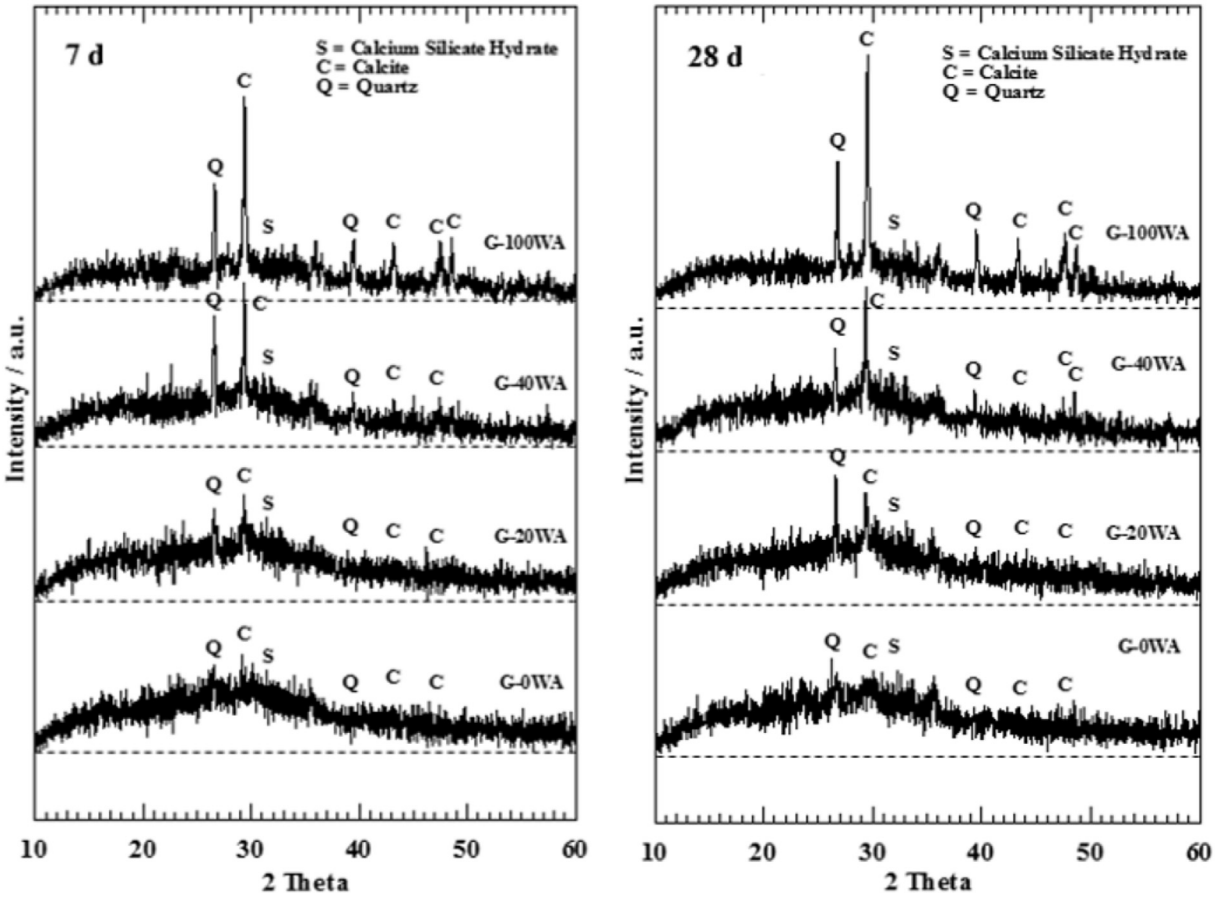

Fig. 7. The XRD patterns of geopolymer pastes at 7 and 28 d.

were the formation of SO_4^{2-} (Govindarajan and Gopalakrishnan, 2011). The IR spectra of cement pastes showed a sharp band at 3643 (3641–3644) cm^{-1} (Ylmén et al., 2009) related to O-H stretching vibrations of $Ca(OH)_2$ (Djouani et al., 2008) which reduced with the increasing of replacement level of WA. The increasing of replacement level of WA also resulted in the increase of C-O stretching of the carbonates peak at the wavenumber of 1425 (1400–1500) cm^{-1} and 875 cm^{-1} due to the high calcite ($CaCO_3$) in WA.

The IR spectra of geopolymer matrix (Fig. 8b) showed that the geopolymer bonding (Si-O-Si and Al-O-Si stretching vibrations) were detected at the wavenumber of 1200-950 cm^{-1}. These stretching of geopolymer matrix were more prominent than that of cement matrix. For geopolymer paste, the degree of geopolymerization were related with the Si-O-Si and Al-O-Si stretching (Boonserm et al., 2012a). The increase in the Si-O-Si and Al-O-Si stretching band indicated the increase in the geopolymerization (Chindaprasirt et al., 2011). The replacement level of 20%, 40%, and 100% FA by WA resulted in the increase of C-O stretching at the wavenumber of 1430 cm^{-1} and 875 cm^{-1}, which was indicated the $CaCO_3$ (Reig et al., 2002) similar to those of cement pastes.

The IR spectra of cement paste and geopolymer paste in this study were different due to the difference of IR spectra of OPC and FA. The O-H stretching and H-O-H bending reduced with the increasing replacement level of WA in cement system while the Si-O-Si and Al-O-Si stretching vibrations increased in the geopolymer matrix. However, this study also found that the increase of replacement revel of WA significant increased C-O stretching of cement and geopolymer paste.

5. Conclusions

This work aimed to study the possibility of use of MSWI bottom ash (WA) as a replacement material for high calcium fly ash (FA) geopolymer matrix. The effect of the replacement levels of FA by WA on compressive strength, porosity and microstructure of geopolymer mortar were presented. Based on the results, the following conclusions can be drawn.

1. The WA could replace FA at 0%, 20%, and 40% by weight for making geopolymer mortar with compressive strength of 37.7–53.0 MPa which were higher than those of cement mortars (29.3–47.7 MPa). The replacement level of 20% WA produced the highest compressive strength at 7 and 28 d of 52.8 MPa and 53.0 MPa. In addition, WA could replace FA at high dosage of up to 40% WA, while the compressive strength was still higher than that of control geopolymer mortar.
2. The results of porosity, pore size distribution, and SEM were consistent with compressive strength results which indicated that the replacement level of 20% WA could increase the denseness and the homogeneity of geopolymer and cement matrix.
3. The XRD pattern showed that the geopolymer and cement pastes containing 20% WA had higher calcium silicate hydrate phase than that of control paste without WA. The IR spectra of geopolymer and cement paste were difference due to the different in chemical and phase composition of raw materials. However, this study also found that the increase of WA replacement level significant increased the crystalline phases of

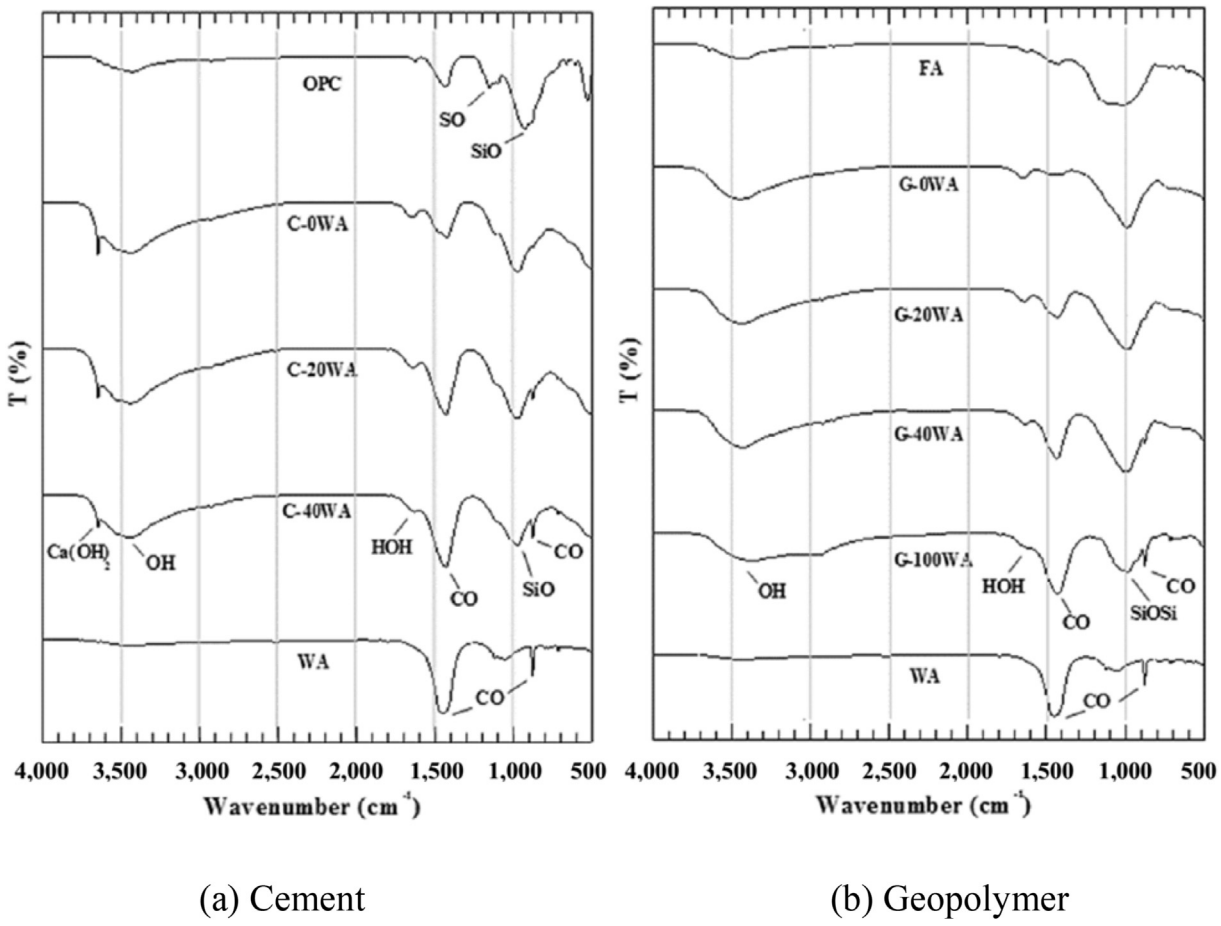

Fig. 8. FTIR of source materials (OPC, FA, and WA) and pastes containing WA.

calcite and quartz in the XRD pattern and C-O stretching in the FTIR images of both matrices.

Acknowledgements

The authors would like to acknowledge the financial supports from the Higher Education Research Promotion and National Research University Project of Thailand, Office of the Higher Education Commission, through the Advanced Functional Materials Cluster of Khon Kaen University; the Thailand Research Fund (TRF) and Khon Kaen University under the Royal Golden Jubilee Ph.D. Program (Grant No. PHD 0083/2556), TRF Research Career Development (Grant No. RSA5780013), and TRF Senior Research Scholar (Grant No. RTA5780004).

References

Aliabdo, A.A., Abd Elmoaty, A.E.M., Salem, H.A., 2016. Effect of cement addition, solution resting time and curing characteristics on fly ash based geopolymer concrete performance. Constr. Build. Mater. 123, 581–593.

American Society for Testing and Materials, 2013. Standard Test Method for Density, Absorption, and Voids in Hardened Concrete, ASTM C642–13. Developed by Subcommittee C09.24, Book of Standards Volume: 04.02. West Conshohocken, USA.

American Society for Testing and Materials, 2015a. Standard Specification for Coal Fly Ash and Raw or Calcined Natural Pozzolan for Use in Concrete, ASTM C618–15. Developed by Subcommittee C09.24, Book of Standards Volume: 04.02. West Conshohocken, USA.

American Society for Testing and Materials, 2015b. Standard Test Method for Flow of Hydraulic Cement Mortar, ASTM C1437–15. Developed by Subcommittee C01.22, Book of Standards Volume: 04.01. West Conshohocken, USA.

American Society for Testing and Materials, 2016. Standard Test Method for Compressive Strength of Hydraulic Cement Mortars (Using 2-in. or [50-mm] Cube Specimens), ASTM C109/C109M-16a. Developed by Subcommittee C01.27, Book of Standards Volume: 04.01. West Conshohocken, USA.

Amin, N., Faisal, M., Muhammad, K., Gul, S., 2016. Synthesis and characterization of geopolymer from bagasse bottom ash, waste of sugar industries and naturally available China clay. J. Clean. Prod. 129, 491–495.

Antunes Boca Santa, R.A., Bernardin, A.M., Riella, H.G., Kuhnen, N.C., 2013. Geopolymer synthetized from bottom coal ash and calcined paper sludge. J. Clean. Prod. 57, 302–307.

Aydın, S., Yazıcı, H., Yigiter, H., Baradan, B., 2007. Sulfuric acid resistance of high-volume fly ash concrete. Build. Environ. 42, 717–721.

Bertolini, L., Carsana, M., Cassago, D., Quadrio Curzio, A., Collepardi, M., 2004. MSWI ashes as mineral additions in concrete. Cem. Concr. Res. 34, 1899–1906.

Boonserm, K., Sata, V., Pimraksa, K., Chindaprasirt, P., 2012a. Improved geopolymerization of bottom ash by incorporating fly ash and using waste gypsum as additive. Cem. Concr. Compos. 34, 819–824.

Boonserm, K., Sata, V., Pimraksa, K., Chindaprasirt, P., 2012b. Microstructure and strength of blended FBC-PCC fly ash geopolymer containing gypsum as an additive. Sci. Asia 38, 175–181.

Chen, X., Wu, S., Zhou, J., 2013. Influence of porosity on compressive and tensile strength of cement mortar. Constr. Build. Mater. 40, 869–874.

Chimenos, J.M., Segarra, M., Fernández, M.A., Espiell, F., 1999. Characterization of the bottom ash in municipal solid waste incinerator. J. Hazard. Mater. 64, 211–222.

Chindaprasirt, P., Chareerat, T., Sirivivatnanon, V., 2007. Workability and strength of coarse high calcium fly ash geopolymer. Cem. Concr. Compos. 29, 224–229.

Chindaprasirt, P., Jaturapitakkul, C., Chalee, W., Rattanasak, U., 2009. Comparative study on the characteristics of fly ash and bottom ash geopolymers. Waste Manag. 29, 539–543.

Chindaprasirt, P., Rattanasak, U., Jaturapitakkul, C., 2011. Utilization of fly ash blends from pulverized coal and fluidized bed combustions in geopolymeric materials. Cem. Concr. Compos. 33, 55–60.

Chindaprasirt, P., Rukzon, S., 2008. Strength, porosity and corrosion resistance of ternary blend Portland cement, rice husk ash and fly ash mortar. Constr. Build. Mater. 22, 1601–1606.

Davidovits, J., 1999. Geopolymer: inorganic polymeric new materials. J. Therm. Anal. 37, 1633–1656.

Deb, P.S., Nath, P., Sarker, P.K., 2014. The effects of ground granulated blast-furnace slag blending with fly ash and activator content on the workability and strength properties of geopolymer concrete cured at ambient temperature. Mater. Des. (1980–2015) 62, 32–39.
Diamond, S., 2000. Mercury porosimetry: an inappropriate method for the measurement of pore size distributions in cement-based materials. Cem. Concr. Res. 30, 1517–1525.
Djouani, F., Connan, C., Chehimi, M.M., Benzarti, K., 2008. Interfacial chemistry of epoxy adhesives on hydrated cement paste. Surf. Interface Anal. 40, 146–150.
Duan, P., Yan, C., Zhou, W., 2016a. Influence of partial replacement of fly ash by metakaolin on mechanical properties and microstructure of fly ash geopolymer paste exposed to sulfate attack. Ceram. Int. 42, 3504–3517.
Duan, P., Yan, C., Zhou, W., Ren, D., 2016b. Fresh properties, compressive strength and microstructure of fly ash geopolymer paste blended with iron ore tailing under thermal cycle. Constr. Build. Mater. 118, 76–88.
Goh, C., Show, K., Cheong, H., 2003. Municipal solid waste fly ash as a blended cement material. J. Mater. Civ. Eng. 15, 513–523.
Govindarajan, D., Gopalakrishnan, R., 2011. Spectroscopic studies on Indian Portland cement hydrated with distilled water and sea water. Front. Sci. 1, 21–27.
Haq, E., Kunjalukkal Padmanabhan, S., Licciulli, A., 2014. Synthesis and characteristics of fly ash and bottom ash based geopolymers–A comparative study. Ceram. Int. 40, 2965–2971.
Hanjitsuwan, S., Hunpratub, S., Thongbai, P., Maensiri, S., Sata, V., Chindaprasirt, P., 2014. Effects of NaOH concentrations on physical and electrical properties of high calcium fly ash geopolymer paste. Cem. Concr. Compos. 45, 9–14.
Hassan, H.F., 2005. Recycling of municipal solid waste incinerator ash in hot-mix asphalt concrete. Constr. Build. Mater. 19, 91–98.
Jin, M., Zheng, Z., Sun, Y., Chen, L., Jin, Z., 2016. Resistance of metakaolin-MSWI fly ash based geopolymer to acid and alkaline environments. J. Non-Crystal. Solids 450, 116–122.
Khan, M.Z.N., Shaikh, F.u.A., Hao, Y., Hao, H., 2016. Synthesis of high strength ambient cured geopolymer composite by using low calcium fly ash. Constr. Build. Mater. 125, 809–820.
Kurama, H., Topçu, İ.B., Karakurt, C., 2009. Properties of the autoclaved aerated concrete produced from coal bottom ash. J. Mater. Process. Technol. 209, 767–773.
Lecomte, I., Henrist, C., Liégeois, M., Maseri, F., Rulmont, A., Cloots, R., 2006. (Micro)-structural comparison between geopolymers, alkali-activated slag cement and Portland cement. J. Eur. Ceram. Soc. 26, 3789–3797.
Lin, K.L., Lin, D.F., 2006. Hydration characteristics of municipal solid waste incinerator bottom ash slag as a pozzolanic material for use in cement. Cem. Concr. Compos. 28, 817–823.
Lin, K.L., Wang, K.S., Lin, C.Y., Lin, C.H., 2004. The hydration properties of pastes containing municipal solid waste incinerator fly ash slag. J. Hazard. Mater. 109, 173–181.
Müller, U., Rübner, K., 2006. The microstructure of concrete made with municipal waste incinerator bottom ash as an aggregate component. Cem. Concr. Res. 36, 1434–1443.
Okoye, F.N., Durgaprasad, J., Singh, N.B., 2016. Effect of silica fume on the mechanical properties of fly ash based-geopolymer concrete. Ceram. Int. 42, 3000–3006.
Pan, J.R., Huang, C., Kuo, J.-J., Lin, S.-H., 2008. Recycling MSWI bottom and fly ash as raw materials for Portland cement. Waste Manag. 28, 1113–1118.
Pangdaeng, S., Sata, V., Aguiar, J.B., Pacheco-Torgal, F., Chindaprasirt, P., 2015. Apatite formation on calcined kaolin-white Portland cement geopolymer. Mater. Sci. Eng. C 51, 1–6.
Pavithra, P., Srinivasula Reddy, M., Dinakar, P., Hanumantha Rao, B., Satpathy, B.K., Mohanty, A.N., 2016. A mix design procedure for geopolymer concrete with fly ash. J. Clean. Prod. 133, 117–125.
Phoo-ngernkham, T., Chindaprasirt, P., Sata, V., Hanjitsuwan, S., Hatanaka, S., 2014. The effect of adding nano-SiO_2 and nano-Al_2O_3 on properties of high calcium fly ash geopolymer cured at ambient temperature. Mater. Des. 55, 58–65.
Qiao, X.C., Ng, B.R., Tyrer, M., Poon, C.S., Cheeseman, C.R., 2008. Production of lightweight concrete using incinerator bottom ash. Constr. Build. Mater. 22, 473–480.
Rattanasak, U., Pankhet, K., Chindaprasirt, P., 2011. Effect of chemical admixtures on properties of high-calcium fly ash geopolymer. Int. J. Min. Metall. Mater 18, 364–369.
Reig, F.B., Adelantado, J.V.G., Moya Moreno, M.C.M., 2002. FTIR quantitative analysis of calcium carbonate (calcite) and silica (quartz) mixtures using the constant ratio method. Application to geological samples. Talanta 58, 811–821.
Rémond, S., Pimienta, P., Bentz, D.P., 2002. Effects of the incorporation of Municipal Solid Waste Incineration fly ash in cement pastes and mortars: I. Experimental study. Cem. Concr. Res. 32, 303–311.
Saikia, N., Cornelis, G., Mertens, G., Elsen, J., Van Balen, K., Van Gerven, T., Vandecasteele, C., 2008. Assessment of Pb-slag, MSWI bottom ash and boiler and fly ash for using as a fine aggregate in cement mortar. J. Hazard. Mater. 154, 766–777.
Sata, V., Sathonsaowaphak, A., Chindaprasirt, P., 2012. Resistance of lignite bottom ash geopolymer mortar to sulfate and sulfuric acid attack. Cem. Concr. Compos. 34, 700–708.
Sikalidis, C.A., Zabaniotou, A.A., Famellos, S.P., 2002. Utilisation of municipal solid wastes for mortar production. Resour. Conserv. Recycl. 36, 155–167.
Swanepoel, J.C., Strydom, C.A., 2002. Utilisation of fly ash in a geopolymeric material. Appl. Geochem. 17, 1143–1148.
Topçu, İ.B., Toprak, M.U., Uygunoğlu, T., 2014. Durability and microstructure characteristics of alkali activated coal bottom ash geopolymer cement. J. Clean. Prod. 81, 211–217.
Ylmén, R., Jäglid, U., Steenari, B.-M., Panas, I., 2009. Early hydration and setting of Portland cement monitored by IR, SEM and Vicat techniques. Cem. Concr. Res. 39, 433–439.
Yousuf, M., Mollah, A., Palta, P., Hess, T.R., Vempati, R.K., Cocke, D.L., 1995. Chemical and physical effects of sodium lignosulfonate superplasticizer on the hydration of Portland cement and solidification/stabilization consequences. Cem. Concr. Res. 25, 671–682.
Zhang, D.Q., Tan, S.K., Gersberg, R.M., 2010. Municipal solid waste management in China: status, problems and challenges. J. Environ. Manag. 91, 1623–1633.
Zhuang, X.Y., Chen, L., Komarneni, S., Zhou, C.H., Tong, D.S., Yang, H.M., Yu, W.H., Wang, H., 2016. Fly ash-based geopolymer: clean production, properties and applications. J. Clean. Prod. 125, 253–267.

Downloaded from ascelibrary.org by King Mongkut's University of Technology, Thonburi on 04/20/17. Copyright ASCE. For personal use only; all rights reserved.

Influence of Activation Methods on Strength and Chloride Resistance of Concrete Using Calcium Carbide Residue–Fly Ash Mixture as a New Binder

Saofee Dueramae[1]; Weerachart Tangchirapat[2]; Prinya Chindaprasirt[3]; and Chai Jaturapitakkul, A.M.ASCE[4]

Abstract: This research aimed to investigate the compressive strength and chloride resistance of concrete made with 30% of calcium carbide residue (CCR) and 70% fly ash (FA) as a binder without portland cement. There were three activation methods to promote strength development of a new cementing material: (1) adding 1% of NaOH by weight of binder; (2) curing concrete at elevated temperature of 60°C; and (3) increasing the fineness of binder by grinding. All concretes were tested to determine the compressive strengths at 1, 3, 7, 28, and 90 days. The chloride resistance of the concrete was also investigated at 28 and 90 days. The results revealed that three activation methods used in this study could improve the compressive strength of concrete made from CCR and FA mixture, with more significant effects occurring at the early age than at the later age. Increasing the fineness of a new cementing material was found be the most effective method compared with the other methods. The compressive strength of concrete activated by increasing the fineness of a new cementing material could be as high as 55.0 MPa at 28 days and increased to 65.1 MPa at 90 days. Moreover, the chloride resistance of concrete in terms of the chloride ion penetration and corrosion resistance of reinforcing steel in concrete could be considerably improved by three activation methods used in this study. **DOI: 10.1061/(ASCE)MT.1943-5533.0001808.** *© 2016 American Society of Civil Engineers.*

Author keywords: Fly ash; Calcium carbide residue; Compressive strength; Chloride resistance; Activation.

Introduction

Portland cement is a primary material used in many construction projects. The manufacturing of portland cement requires a lot of energy to burn raw materials, leading to environmental problems. The production of approximately 1 ton of cement causes the release of up to 0.9 t of CO_2 gas into the atmosphere (Mehta 2009). Although many construction projects can now use fly ash as one of the constituent in ready mixed concrete for the construction, it is used at low levels of replacement in concrete, generally below 30% cement replacement by weight because the high levels of fly ash replacement had a longer setting time and low early age compressive strength (Thomas 2007; Choi et al. 2012). Thus, portland cement remains the main binder of concrete.

To reduce portland cement consumption, many studies have proposed new cementitious materials to use as a binder of concrete, one of which involves a waste of calcium carbide residue mixed with pozzolanic materialsm namely fly ash (Makaratat et al. 2010; Amnadnua et al. 2013), rice husk ash (Jaturapitakkul and Roongreung 2003), or bagasse ash (Rattanashotinunt et al. 2013). In addition, from the previous researches studies, it is clear that the mixture of calcium carbide residue (CCR) and fly ash (FA) has a good potential to be develop as a binder in concrete. However, the compressive strength of concrete made with CCR and FA mixture is low compared to portland cement concrete, particularly at an early age. Moreover, studies of CCR and FA mixture for use as a concrete binder have been rarely conducted.

CCR is a by-product of the process of manufacturing acetylene gas. The main composition of CCR is calcium hydroxide [$Ca(OH)_2$]. In Thailand, the volume of CCR from one acetylene gas industrial factory is approximately 21,500 t/year and the volume has a tendency to increase every year (Amnadnua et al. 2013). Moreover, most of the CCR is disposed of in landfills and causes many environmental problems due to its high pH value.

FA is one of the pozzolanic materials that has been widely used in concrete work. The main chemical compositions of FA are Si_2O, Al_2O_3, and, Fe_2O_3. FA can react with calcium hydroxide to from calcium silicate hydrate (C-S-H) with moisture and enhance the strength of concrete. In addition, many studies found that FA can react with $Ca(OH)_2$ from CCR in a manner similar to the reaction with $Ca(OH)_2$ from a product of hydration. Krammart et al. (1996) reported that the optimal ratio of CCR to FA was 30:70 by weight, and produced the highest compressive strength of mortar. The results also showed that the mixture made from CCR and FA could be used as a new binder. However, the compressive strength of binder from CCR and FA was low, especially at an early age (Makaratat et al. 2010; Amnadnua et al. 2013; Krammart et al. 1996) because the compressive strength of binder produced from CCR and FA was solely obtained from a pozzolanic reaction, which is usually slow in the early stages. In addition, the CCR received directly from an acetylene gas industry has large particle sizes; thus, the reactivity between CCR and FA is slow. Srisen (2013) observed

[1]Ph.D. Candidate, Dept. of Civil Engineering, Faculty of Engineering, King Mongkut's Univ. of Technology Thonburi, Bangmod, Tungkru, Bangkok 10140, Thailand.

[2]Assistance Professor, Dept. of Civil Engineering, Faculty of Engineering, King Mongkut's Univ. of Technology Thonburi, Bangmod, Tungkru, Bangkok 10140, Thailand (corresponding author). E-mail: weerachart.tan@kmutt.ac.th

[3]Professor, Dept. of Civil Engineering, Sustainable Infrastructure Research and Development Center, Faculty of Engineering, Khon Kaen Univ., Khon Kaen 40002, Thailand.

[4]Professor, Dept. of Civil Engineering, Faculty of Engineering, King Mongkut's Univ. of Technology Thonburi, Bangmod, Tungkru, Bangkok 10140, Thailand.

Note. This manuscript was submitted on April 12, 2016; approved on September 1, 2016; published online on November 9, 2016. Discussion period open until April 9, 2017; separate discussions must be submitted for individual papers. This paper is part of the ***Journal of Materials in Civil Engineering***, © ASCE, ISSN 0899-1561.

that the mixture of CCR and FA had a high potential to be used as a concrete binder. However, the compressive strength of concrete made from the CCR–fly ash mixture is very low. Thus, it is necessary to improve the reaction between calcium carbide residue and fly ash, especially in the early stages. The results of Srisen (2013) also showed that use of 10% of ordinary portland cement (OPC) to replace the binder of CCR and FA could improve the compressive strength of concrete from 43 to 47% compared to concrete made from OPC at 7 days.

This study aimed to develop the compressive strength of concrete made from CCR and FA as a new cementing material without portland cement. CCR was mixed with FA at a constant ratio of 30:70 by weight. All concrete mixtures had a water to binder ratio of 0.25. Three activation methods were used to promote the reactivity between CCR and FA: (1) adding 1% of NaOH by weight of binder; (2) curing at elevated temperature of 60°C; and (3) increasing the fineness of the CCR and FA by intergrinding using a ball mill. The compressive strength, chloride resistance in terms of chloride ion penetration, and corrosion of reinforcing steel in concrete made from CCR and FA with and without activation methods were examined and compared with the OPC concrete.

Experimental Investigation

Materials

The materials used in this study were CCR, FA, OPC, crushed limestone, local river sand, and superplasticizer Type F. Table 1 shows the chemical compositions materials tested by X-ray fluorescence analysis and the physical properties of the materials are given in Table 2.

CCR used in this research was obtained from a disposal area of an acetylene gas industry in Samutsakorn Province, Thailand. The main chemical of CCR was 56.5% of CaO. CCR had a high degree of loss on ignition (LOI), which was 36.1% of LOI. It was found that the value of LOI of CCR was very high because CCR was rich in $Ca(OH)_2$; the value of LOI in CCR was tested over the temperature range of 750°C. Generally, $Ca(OH)_2$ was decomposed into CaO and H_2O (gas) at a temperature of approximately 550°C (Jaturapitakkul and Roongreung 2003).

FA was collected from the Mae Moh power plant in Lumpang Province, Thailand. The total oxide content of SiO_2, Fe_2O_3, and Al_2O_3 was 76.1%; thus, it can be categorized as class F fly ash as specified by ASTM C618 (ASTM 2015).

In this study, CCR was mixed with FA at a constant ratio of 30:70 by weight (original CCR-FA was assigned as OFC) and used as a binder for casting concrete, as suggested by the previous results of Krammart et al. (1996). As seen from Table 2, the specific gravity of OFC was 2.43, while that of OPC was 3.15. The median particle size (d_{50}) of OFC was 12.92 μm, and the particles retained on a sieve of No. 325 were 22.9% by weight. OPC had a median particle size of 14.60 μm and the particles retained on the sieve No. 325 was 20.0% by weight. After grinding to increase the fineness of CCR and FA (assigned as FFC), the particles retained on a sieve No. 325 of FFC was reduced to 1.1% by weight. The median particle size of the binder was reduced from 12.92 (OFC) to 2.93 (FFC) μm, while the specific gravity increased from 2.43 (OFC) to 2.73 (FFC).

Table 1. Chemical Compositions of the Materials

Chemical composition (%)	Cement (OPC)	FA	CCR	FFC
Silicon dioxide (SiO_2)	20.9	41.9	4.3	29.0
Aluminum oxide (Al_2O_3)	4.8	21.5	0.4	13.6
Iron oxide (Fe_2O_3)	3.4	12.7	0.9	7.6
Calcium oxide (CaO)	65.4	13.9	56.5	32.6
Sulfur trioxide (SO_3)	2.7	0.6	0.1	0.5
Magnesium oxide (MgO)	1.3	2.6	1.7	1.9
Sodium oxide (Na_2O)	0.3	2.7	—	2.1
Potassium oxide (K_2O)	0.4	2.5	—	1.7
Loss on ignition (LOI)	0.9	0.7	36.1	10.1

Table 2. Physical Properties of the Materials

Material	Specific gravity	Retained on a sieve no. 325 (%)	Median particle size d_{50} (μm)
Cement (OPC)	3.15	20.0	14.60
Original CCR-FA (OFC)	2.43	22.9	12.92
Ground CCR-FA (FFC)	2.73	1.1	2.93

Mix Proportions of Concrete

The mix proportions of concretes are summarized in Table 3. The CCR–FA concrete mixture had a binder content of 550 kg/m^3, while OPC control concrete used 500 kg/m^3 of portland cement type I. All concrete mixtures had a water-to-binder ratio of 0.25, and the superplasticizer was employed to control slump of fresh concrete between 150 and 200 mm. There were three activation methods to promote the strength development of a new cementing material. These activation methods are the following:

1. Chemical activation: adding 1% of sodium hydroxide solution (NaOH) by weight of binder to enhance the pozzolanic activity of FA and CCR (assigned as OFC-C concrete).
2. Physical activation: increasing the fineness of both CCR and FA by grinding until the particles retained on a sieve No. 325 were less than 1.1% by weight (assigned as FFC concrete).
3. Thermal activation: curing concrete at temperature of 60°C for 24 h after removal from the molds (assigned as OFC-H concrete).

Testing of Specimens

Test of the Compressive Strength of Concrete

Concrete cylindrical specimens of 100 mm in diameter and 200 mm in height were cast and were allowed to set for 24 h. OPC, OFC, OFC-C, and FFC concretes were cured in water until the date of testing to determine the compressive strength at 1, 3, 7, 28, and 90 days.

For the thermal activation, OFC-H concrete was wrapped by a plastic sheet to protect the evaporation of free water after the specimens were removed from the molds. The specimens were cured at temperature of 60°C for 24 h, and the plastic sheet was later removed, and the specimens continued to cure in water. The compressive strengths of OFC-H concretes were determined at 3, 7, 28, and 90 days. The average of three concrete samples was used as a substitute for the compressive strength of concrete at each age.

Test of the Chloride Ion Penetration Resistance

The chloride ion penetration resistance of concrete was tested at 28 and 90 days. The specimens were prepared by sawing a 50-mm-thick slice from the middle of the 100 × 200 mm concrete cylinder. The side surface of the sliced concrete was coated with silicone rubber. Next, the specimen was installed in a cell block; one of the testing cells was filled with 0.3 M NaOH solution

Downloaded from ascelibrary.org by King Mongkut's University of Technology, Thonburi on 04/20/17. Copyright ASCE. For personal use only; all rights reserved.

Table 3. Mix Proportions of the Concretes

Mix	Mix proportion (kg/m^3)									
	CR	FA	Cement	Fine aggregate	Coarse aggregate	Water	SP[a]	NaOH	W/B	Slump (cm)
OPC	—	—	500	820	1,040	126	4.0	—	0.25	20.0
OFC	165	385	—	720	915	135	5.5	—	0.25	20.0
OFC-C	165	385	—	720	915	135	5.5	5.5	0.25	18.5
OFC-H	165	385	—	720	915	135	5.5	—	0.25	18.5
FFC	165	385	—	755	960	135	5.5	—	0.25	19.0

[a]The water in the superplasticizer is 50%.

(positive pole) and the other cell with 3% NaCl solution (negative pole). During the test, a voltage of 60 V direct current (DC) was applied between the two cells and the current was measured at every 30 min over 6 h. The total charge passed in coulombs was calculated using Eq. (1) according to ASTM C1202 (ASTM 2012)

$$Q = 900(I_0 + 2I_{30} + 2I_{60} + \cdots + 2I_{300} + 2I_{330} + I_{360}) \quad (1)$$

where Q = charge passed (coulombs); I_0 = current (amperes) immediately after the voltage is applied; and I_t = current (amperes) at t min after the voltage is applied.

Test of the Corrosion of Reinforcing Steel in Concrete

The corrosion of reinforcing steel in concrete was investigated in accordance with the modified NT BUILD 356 (NT Build 1989). The cylindrical concrete specimens of 100 mm in diameter and 200 mm in height with a steel round bar of 12 mm in diameter and 150 mm in length at the center of cross section of the concrete were cast. At ages of 28 and 90 days after casting, the concretes were tested to determine the corrosion of reinforcing steel and the current flows of the concretes. The impressed voltage test setup is shown in Fig. 1. Specimens were placed in a tank and then partly immersed in a 5% NaCl solution. A constant direct current (DC) potential of 12 V was applied across the specimens, with the steel round bar being the positive electrode and a stainless steel sheet being the negative electrode. The current was measured via the voltage drop over a 10-ohm resistance, and the value was calculated in amperes using the equation for the electric circuit. The current flow was recorded every 6 h until 168 h (7 days); afterwards, the concrete specimens were split to investigate the weight loss due to corrosion of reinforcing steel in accordance with ASTM G1 (ASTM 2011). To determine the weight loss due to corrosion, the reinforcing steel was immersed in acid solution at 20–25°C for a period of 10 min. The surface of reinforcing steel was washed with acid solution. The acid solution used was 500 mL of hydrochloric acid with 3.5 g of hexamethylenetetramine added with reagent water to make the solution 1,000 mL in volume.

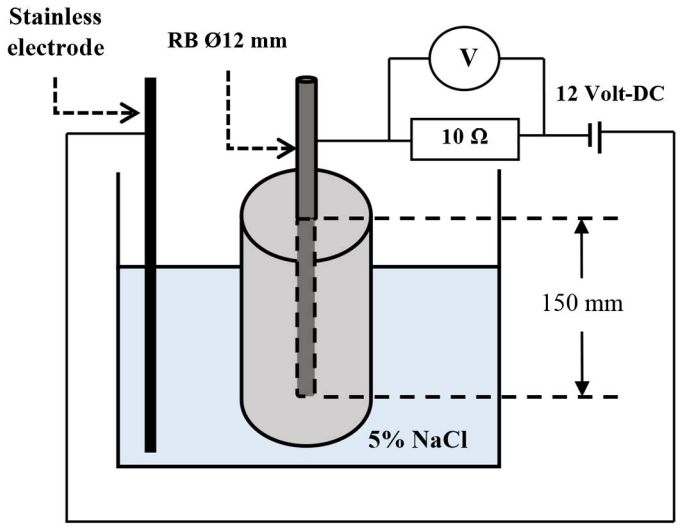

Fig. 1. Corrosion of reinforcing steel in concrete by impressed voltage test

Results and Discussion

Compressive Strength of Concrete

The compressive strengths of concrete were reported in Table 4. The results showed that the compressive strength of concrete using CCR and FA mixture as a binder increased with curing age similar to that of portland cement concrete. OFC concrete had compressive strengths of 2.6, 4.2, 7.7, 19.7, and 30.6 MPa at 1, 3, 7, 28, and 90 days, respectively. The compressive strength of OFC concrete is lower than the concrete using OPC at all test ages. This property is due to the compressive strength of OFC concrete based only on the pozzolanic reaction between CCR and FA. Similar results were obtained by Makaratat et al. (2010), who found that the compressive strength of concrete using FA and CCR without portland cement was lower than that of OPC concrete, especially at an early age. Fig. 2 shows the relationship between the compressive strength and the curing age of concrete. The results also showed that the compressive strength of concretes using CCR and FA as a binder could be improved by all of the activation methods. The compressive strengths of concretes with all activation methods were higher than the concrete without activation method at both early and later ages. The compressive strengths of concretes using CCR and FA mixture with various activation methods ranged from 21.0 to 37.4, 34.0 to 55.0, and 37.9 to 65.1 MPa at 7, 28, and 90 days, respectively.

The addition of 1% NaOH into a new binder could improve the reactivity between CCR and FA. The addition of NaOH in the binder increased in leaching of silica and alumina from the FA particles (Rattanasak and Chindaprasirt 2009), thereby increasing the reaction with $Ca(OH)_2$ from CCR. This result also revealed that NaOH was effective in promoting the reaction between CCR and FA. Thus, NaOH could be used to improve the compressive strength of concrete, but the compressive strength of OFC-C concrete was still lower than that of the OPC concrete. However, OFC-C concrete had higher compressive strength than OFC concrete at both the early and later ages because the products of C-S-H and C-A-H increased with the addition of NaOH, thereby increasing the strength of the paste (Hanjitsuwan et al. 2014). The OFC-C concrete, from which 1% of NaOH was used as an activated

Downloaded from ascelibrary.org by King Mongkut's University of Technology, Thonburi on 04/20/17. Copyright ASCE. For personal use only; all rights reserved.

Table 4. Compressive Strength and Normalized Compressive Strength of the Concretes

Mix	Compressive strength (MPa) [normalized compressive strength (%)]				
	1 day	3 days	7 days	28 days	90 days
OPC	28.0 (100)	38.9 (100)	43.5 (100)	51.3 (100)	58.3 (100)
OFC	2.6 (9)	4.2 (11)	7.7 (18)	19.7 (38)	30.6 (52)
OFC-C	5.5 (20)	13.4 (34)	21.0 (48)	34.0 (66)	37.9 (65)
OFC-H	2.6 (9)	27.3 (70)	27.9 (64)	37.2 (72)	44.2 (76)
FFC	10.6 (38)	23.4 (60)	37.4 (86)	55.0 (107)	65.1 (112)

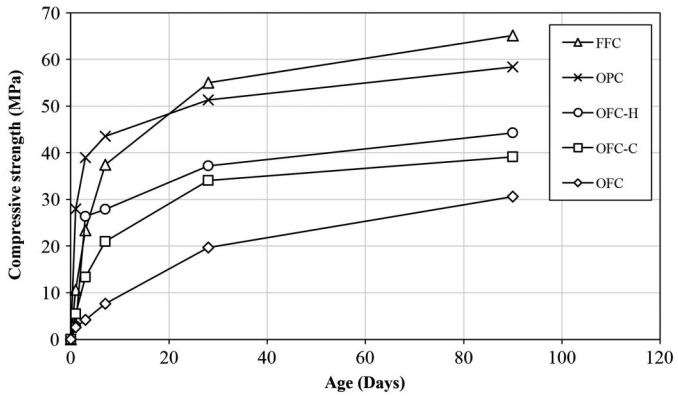

Fig. 2. Relationship between the compressive strength and the curing age of concrete

strength, had a compressive strength that increased from 48% of the OPC concrete at 7 days to 66% of the OPC concrete at 28 days, while the OFC concrete without NaOH had a compressive strength at 7 and 28 days of 18 and 38% of OPC concrete, respectively. Thus, adding 1% of NaOH in concrete can be used to improve the compressive strength of concrete from which CCR and FA was used as a binder.

The elevated curing temperature of 60°C for the binder from CCR and FA also improves the compressive strengths of concrete. The compressive strengths of OFC-H concrete at 3 and 7 days were 27.3 and 27.9 MPa, respectively, and increased to 37.2 and 44.2 MPa at 28 and 90 days, respectively. In other words, the pozzolanic reaction was increased with the elevated curing temperature. Moreover, the compressive strength development rate was faster at the early ages but was not significantly improved at the later ages, because during the initial period of the elevated curing period, the formation of pozzolanic reaction products had a physical structure less compacted and higher unfilled pore structure and led to a lower development of strength at the later ages when compared to the one cured at lower temperature (Benammar et al. 2013). This behavior is in agreement with the findings of Kim et al. (2002). The current results showed that the increased curing temperature caused faster strength development rates at the early ages and then increased gradually at the later ages.

The best method to improve the compressive strength of concrete was to increase the activated strength by increasing the fineness of both CCR and FA via grinding; it was the most effective method to increase the compressive strength of concrete. Although FFC concrete produced lower compressive strength than OPC concrete at the early ages between 1 and 7 days, its compressive strength was approximately 86% of OPC concrete at 7 days. Thereafter, the compressive strength of FFC concrete was greater than that of OPC concrete. For example, the compressive strength of FFC was 55.0 MPa at 28 days and increased to 65.1 MPa at 90 days and could be classified as a high-strength concrete, whereas the strength of OPC concrete was 51.3 and 58.3 MPa at 28 and 90 days, respectively. This finding is observed because the small particles sizes of both CCR and FA had high surface area and also improved the pozzolanic reaction. Moreover, the small particles of FFC could fill the voids between the cement and the aggregate, thus increasing the compressive strength of FFC concrete (Jaturapitakkul et al. 2011).

The results showed that these three activation methods had affected the strength development of concrete made from CCR and FA mixture. The compressive strength of OFC-C, OFC-H, and FFC concretes were 20–86% of OPC concrete at the early and increased to 65–112% of OPC concrete at the later age. Srisen (2013) found that using 10% of OPC to replace in CCR and FA binder produced the compressive strength at 19–47% and 73–76% of OPC concrete at the early age and later age, respectively. It can be concluded that the development of compressive strength of concrete made from CCR and FA with 10% OPC replacement had lower effect as compared to the three activation methods used in this study. These findings indicated that the mixture of CCR and FA with various activation methods could be used as a new cementitious material to produce concrete without using portland cement. These three activation methods, i.e., adding 1% of NaOH, increasing fineness of binder, and curing at temperature of 60°C for 24 h, could improve the compressive strength of concrete to be higher than OFC concrete. Moreover, increasing the fineness of the binder produced the highest compressive strength of the concrete. In addition, FFC concrete could produce the compressive strength of more than 55 MPa at 28 days.

Chloride Resistance of Concrete

The total charge passed through the concrete samples in terms of coulombs (C), according to ASTM C1202 (ASTM 2012), is shown in Fig. 3. The OFC concrete had an amount of total charge passed more than that of OPC concrete at the age of 28 days because: the total charge passed of OFC concrete was 1,283 C, whereas that of OPC concrete was 1,094 C. The higher charge passed of the OFC concrete may be to the low compressive strength of OFC concrete. Moreover, the total charge passed of concrete decreased with the increase of compressive strength of concrete as well as the increase in the curing age of concrete. Note that the total charge passed at 90 days of OFC concrete was 355 C, or approximately 40% of OPC concrete (OPC concrete had total charge passed of 883 C). This may be attributed that OFC concrete contained a high amount of fly ash, which could help refine the porosity and pore size of concrete and resulted in a highly impermeable and denser concrete (Chindaprasirt et al. 2005). Moreover, the C-S-H product from the pozzolanic reaction could reduce the chloride ion penetration because C-S-H could absorb chloride ions on the surface (Hoppe Filho et al. 2013). However, the reaction between CCR and FA was a pozzolanic reaction, and the reaction was very slow and took longer than the hydration reaction of cement. Thus, the total charge

Downloaded from ascelibrary.org by King Mongkut's University of Technology, Thonburi on 04/20/17. Copyright ASCE. For personal use only; all rights reserved.

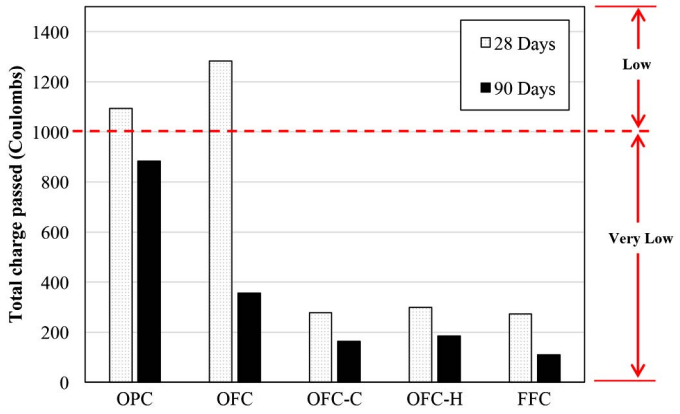

Fig. 3. Total charge passed of the concretes

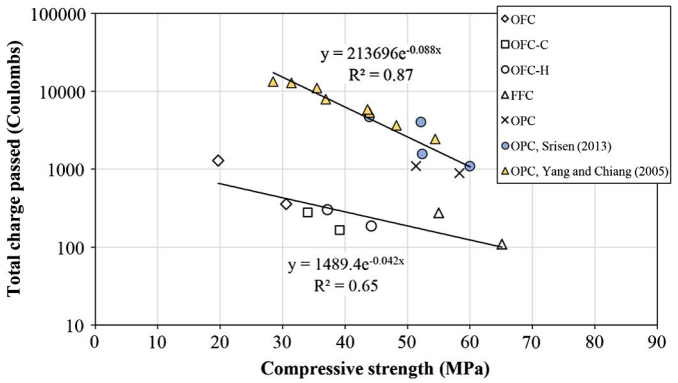

Fig. 4. Relationship between the total charge passed and the compressive strength of concrete

passed of OFC concrete decreased to be lower than OPC concrete at the later age of 90 days.

These data clearly show that all activated concretes had lower chloride ion penetration than OPC concrete at both 28 and 90 days. The results also showed that the chemical activated strength by adding 1% of NaOH had significantly affected the increase of the chloride resistance of concrete. The total charge passed of OFC-C concrete was lower than OPC concrete at 28 and 90 days and was only 277 and 163 C or approximately 25 and 18% of the OPC concrete, respectively. This result may be due to the effect of adding of 1% of NaOH in the binder had affected on leaching of silica and alumina from the FA particles, enabling reaction with $Ca(OH)_2$ from CCR and increasing the amounts of the pozzolanic products (C-S-H and C-A-H), thereby resulting in the increase of the chloride ion penetration resistance of the concrete.

In the case of concrete with thermal activated strength, it had lower chloride ion penetration resistance compared with the increased fineness of binder and the chemical activation methods. The total charge passed of OFC-H concrete at 28 days was 27% of the OPC concrete. At the later age, the total charge passed slightly reduced and was 21% of the OPC concrete at 90 days due to elevated curing temperature produces a nonuniform distribution of C-S-H product. This result confirms the findings of Benammar et al. (2013), who found that the porosity of concrete was increased with the increased of curing temperature and the CSH products were less homogeneous in the cement paste matrix, allowing for the development of a larger pore network.

It was observed that FFC concrete had the lowest total charge passed because FFC concrete had small particle sizes of the binder, which improved concrete strength as well as reducing the water permeability. Moreover, FFC concrete had a cumulative charge passed classified as a low to very low values when compared with ASTM C1202 (ASTM 2012). At 90 days, the total charge passed of FFC concrete was only 109 C.

Fig. 4 shows the relationship between the total charge passed and the compressive strength of concrete. The concrete had higher chloride resistance when the compressive strength increased. Srisen (2013) and Yang and Chiang (2005) also found similar results in OPC concrete. At 90 days, all concretes from a binder of CCR and FA had total charge passed lower than OPC concrete, although OFC, OFC-C, and OFC-H concretes had lower compressive strength than OPC concrete. Nevertheless, OFC concrete without strength activated had total charge passed of 1,283 C, which was higher than OPC concrete at 28 days. Thus, it can be classified as low chloride ion penetrability according to ASTM C1202 (ASTM 2012). Note that all of CCR and FA concretes had much lower chloride ion penetration at the later ages than at the early ages. This phenomenon may be the result of the proportion of fly ash in the binder improving the chloride binding capacity of hardened concrete. Many studies (Leng et al. 2000; Talero et al. 2011) reported that fly ash could reduce chloride ion penetration due to both the chemical and physical properties. Moreover, the chloride ion could react with the reactive alumina oxide from the partly chemical component of fly ash and the calcium hydroxide from the CCR contributing to the formulation of Friedel's salt.

Furthermore, chloride ion penetration could be reduced due to physical binding, in which chloride ions were absorbed on the surface of C-S-H, thereby reducing the chloride ion ingress by the electrostatic attraction from the surface of hydrated product (Hoppe Filho et al. 2013). Thomas et al. (2012) investigated the chloride binding in hardened cement paste of concrete containing OPC with various pozzolanic materials. They found that the increase in the level of replacement of fly ash and slag could increase the chloride binding capacity. In this research, the binder is from CCR and FA, with 70% by weight of the binder being fly ash. This finding also explains why concrete using CCR and FA as a binder had higher chloride penetration resistance than the OPC binder. In addition, the use of NaOH activation was very effective to reduce the chloride ion penetration because Na^+ ions could adsorb Cl^- ions due to electrostatic attraction and bind the chloride ions onto the surface of paste, i.e., Na^+ ions have a positive charge that enables it to absorb the Cl^- ions (Lloyd et al. 2010; Hossain et al. 2015).

Current Flow of Concrete

The relationships between the current passed of concrete and the immersed time of concrete at 28 and 90 days are reported in Figs. 5

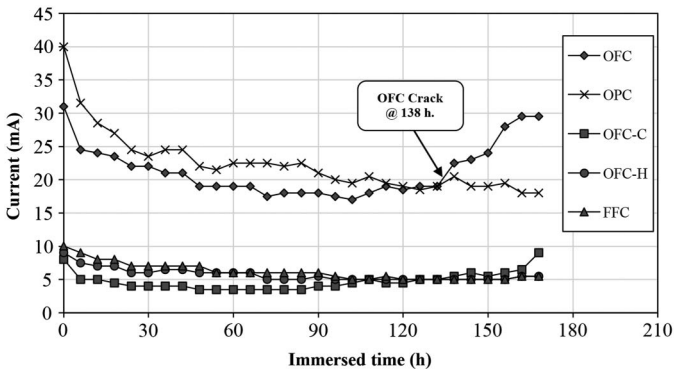

Fig. 5. Current flow of concrete at a curing age of 28 days

Downloaded from ascelibrary.org by King Mongkut's University of Technology, Thonburi on 04/20/17. Copyright ASCE. For personal use only; all rights reserved.

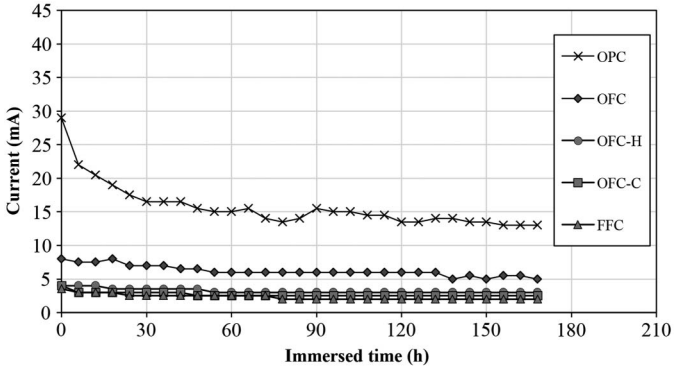

Fig. 6. Current flow of concrete at a curing age of 90 days

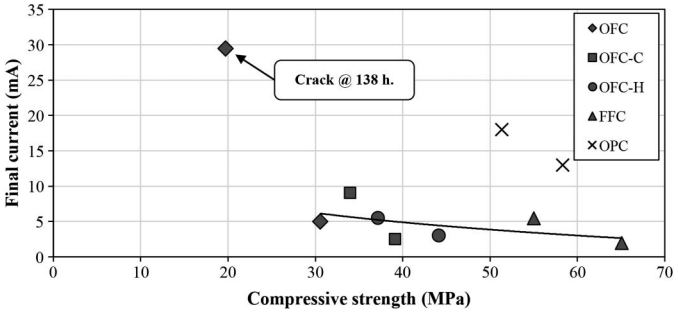

Fig. 8. Relationship between the final current and the compressive strength of concrete

and 6, respectively. The current flow was attributed to the electrical resistance and chloride permeability resistance of the concrete. The current was increased by the chloride permeability, and corrosion occurred when the chloride ions reached the reinforcing steel in concrete. At 168 h after the impressed current, the concrete specimens were broken to determine the corrosion of reinforcing steel. The final current was used to indicate corrosion current rate of the reinforcing steel in the concrete. The final current values at 28 days of OFC, OFC-C, OFC-H, and FFC concretes were 30, 9, 6, and 6 mA, respectively, while that of the OPC concrete was 18 mA, with a similar trend in chloride permeability. As seen from Fig. 5, at the curing age of 28 days, OFC concrete had a lower final current than OPC concrete and had higher final current flow than OPC concrete after the OFC concrete had been cracked. The time of the first crack of OFC concrete was 138 h. Similar results were also obtained by Sangoju et al. (2011), who stated that the charge passed and chloride ion penetration were increased when the crack width of concrete was increased. Note that the current flow values of concretes from a binder of CCR and FA mixture were lower than that of OPC concrete for all activation methods as well as for increased of curing age and compressive strength. At 90 days, the final current values of OFC, OFC-C, OFC-H, and FFC concretes were reduced to 5, 3, 3, and 2 mA, respectively, while OPC had a final current value of 13 mA.

The result of the impressed voltage test according to NT Build 356 (NT Build 1989) had a similar trend as that of the total charge passed in according with ASTM C1202 (ASTM 2012). As seen from Fig. 7, a very strong correlation was found for the relationship between final current and total charge passed of concrete ($R^2 = 0.89$). The results also indicated that the final current value tended to reduce when compressive strength increased, as shown in Fig. 8. However, the relationship between final current and the compressive strength of concrete had a low correlation. This is because the final current of concrete did not relate to only the compressive strength of the concrete; it also affected by other factors such as effect of the prevention of the ingress of chloride due to type of binder of concrete and chloride binding capacity of concrete (Cheewaket et al. 2010). Thus, this can clarify the reason why the concrete using CCR and FA as a binder had lower total charge passed and final current than OPC concrete although it had lower compressive strength, as confirmed by the test results from Fig. 4.

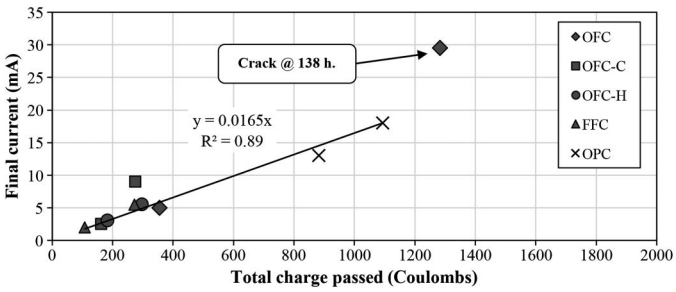

Fig. 7. Relationship between the final current and the total charge passed of concrete

Corrosion Damage and Weight Loss of the Reinforcing Steel

After the impressed voltage test, the corrosion of reinforcing steel in concrete specimens was examined. The damage due to steel corrosion and percentage weight loss of reinforcing steel in concrete at 28 and 90 days are shown in Figs. 9(a and b), respectively. The results showed that the OFC had higher weight loss of reinforcing steel than that of OPC concrete at 28 days. This result may be related to the low compressive strength of OFC concrete. OFC concrete had a weight loss of reinforcing steel of 2.31%, and its compressive strengths was 19.7 MPa at 28 days, while OPC concrete had weight loss of reinforcing steel of 1.80% and had a compressive strength of 51.3 MPa at 28 days. Moreover, OFC concrete cracked at 138 h after testing. Because the volume of rusted steel was 2–2.5 times higher than the volume of original reinforcing steel, the rusted steel caused an internal tensile force that was higher than the tensile strength of concrete; as a result, cracks and splits off the concrete occurred (Arya and Xu 1995). In addition, after the OFC concrete was cracked, the corrosion increased very rapidly due to easy access of oxygen, moisture, and further aggressive agents through the cracks. However, OFC concrete could reduce the weight loss of reinforcing steel at 90 days, similar to the reduction of the final current flow and the total charge passed of concrete.

OFC concrete could reduce the charge passed, but it did not significantly reduce the corrosion of reinforcing steel in the concrete. However, adding 1% NaOH, curing at a temperature of 60°C, and increasing fineness of the binder could decrease corrosion in terms of the weight loss of the reinforcing steel. The use of NaOH to activate strength of concrete could also reduce corrosion of reinforcing steel in concrete. This reduced corrosion may be due to the ability of NaOH solution in OFC-C concrete to reduce the free chloride content. Similar results were also found by Chindaprasirt and Chalee (2014), who studied the effect of NaOH on steel corrosion of fly-ash-based geopolymer concrete. They reported that the use of high NaOH concentration in geopolymer concrete could decrease the corrosion of reinforcing steel in concrete when compared with concrete with lower NaOH concentration because the use of high NaOH concentration increased the chloride binding capacity of concrete and led to reduction of the

Downloaded from ascelibrary.org by King Mongkut's University of Technology, Thonburi on 04/20/17. Copyright ASCE. For personal use only; all rights reserved.

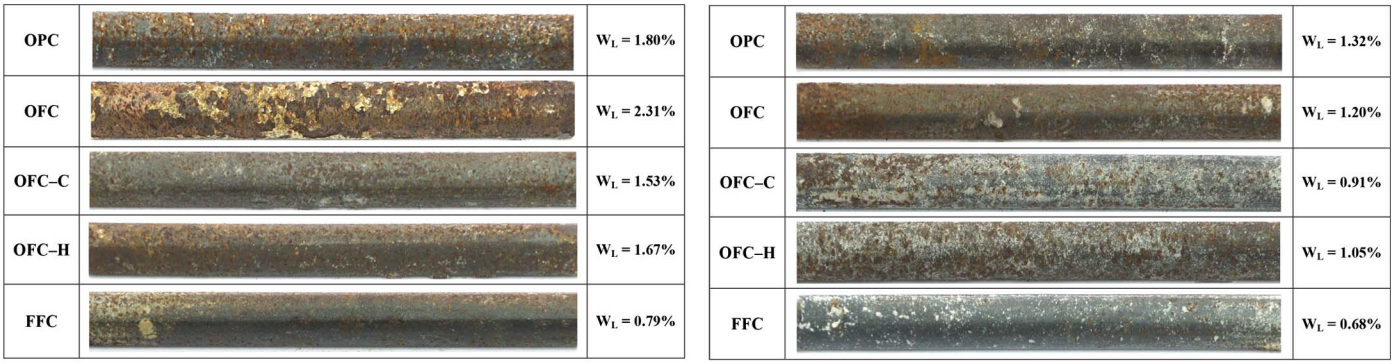

Fig. 9. Corrosion of reinforcing steel in concrete: (a) concrete at 28 days; (b) concrete at 90 days

free chloride content. Moreover, Saraswathy et al. (2003) studied the effect of various activation techniques of concrete blended fly ash and found that the use of chemical activation with sodium hydroxide solution was highly effective in reducing the corrosion rate and free chloride of concrete.

OFC-H concrete had a percentage weight loss due to corrosion of reinforcing steel in concrete less than those of the OFC and OPC concretes, but it had higher weight loss than the OFC-C concrete; this result was consistent with the rapid chloride penetration test (as mentioned in the section "Chloride Resistance of Concrete"). In addition, increasing the fineness of the binder appeared to be the most effective activation method when compared with chemical and thermal activation methods. FFC concrete had the lowest corrosion of reinforcing steel in concrete (as seen in Fig. 9) at both the early and later ages. This behavior is observed because the small particle sizes of both CCR and FA increase the pozzolanic reaction and reduced the pore structure by reducing the pore size (Sinsiri et al. 2010). This reduced pore size inhibits the penetration of water and oxygen into concrete.

The experiment results from this study demonstrated that the mixture of CCR and FA had high potential to be used as a new cementing material for concrete. Moreover, the three activation methods used in this study had a positive effect on the compressive strength development (at the early and later ages) and the chloride resistance of concrete made from CCR and FA mixture. The result also suggested that CCR and FA mixture activated by increasing the fineness of binder can be used to produce a high compressive strength of 55 MPa at 28 days.

Conclusions

Based on these results, the following conclusions can be drawn:

1. Three activation methods used in this study could be used to enhance the strength of concrete made from CCR and FA mixture, with the increase in fineness of a new cementing material being the most effective method. The compressive strength of concrete activated by this method could be as high as 55.0 MPa at 28 days and increased to 65.1 MPa at 90 days.
2. The chloride resistance of concrete in terms of chloride ion penetration and corrosion of reinforcing steel in concrete could be considerably improved by three activation methods used in this study. All of the concrete mixtures using CCR and FA as a binder with and without activated strength significantly improved the resistance of chloride ion penetration of concrete, with the total change passed of the concretes being lower than 400 C.
3. Among the activated strength methods, physical and chemical activation (OFC-C and FFC) could reduce the corrosion of reinforcing steel in concrete, with the weight loss of the reinforcing steel being lower than that of OPC concrete.
4. The use of CCR mixed with FA as a new cementing material to cast concrete could mitigate environmental problems by lowering the amount of waste in landfills and reducing the production of cement.

Acknowledgments

The authors gratefully acknowledge the financial support from the Petchra Pra Jom Klao Ph.D. Scholarship, King Mongkut's University of Technology Thonburi and the Thailand Research Fund (TRF) under TRF Grant for New Researcher Scholar Grant No. TRG 5780073. Thanks are also extended to Khon Kaen University and the Thailand Research Fund (TRF) under the TRF Senior Research Scholar Grant No. RTA5780004.

References

Amnadnua, K., Tangchirapat, W., and Jaturapitakkul, C. (2013). "Strength, water permeability, and heat evolution of high strength concrete made from the mixture of calcium carbide residue and fly ash." *Mater. Des.*, 51, 894–901.

Arya, C., and Xu, Y. (1995). "Effect of cement type on chloride binding and corrosion of steel in concrete." *Cem. Concr. Res.*, 25(4), 893–902.

ASTM. (2011). "Standard practice for preparing, cleaning, and evaluating corrosion test specimens." *ASTM G1-03*, West Conshohocken, PA.

ASTM. (2012). "Standard test method for electrical indication of concrete's ability to resist chloride ion penetration." *ASTM C1202*, West Conshohocken, PA.

ASTM. (2015). "Standard specification for coal fly ash and raw or calcined natural pozzolan for use in concrete." *ASTM C618*, West Conshohocken, PA.

Benammar, B., Mezghiche, B., and Guettala, S. (2013). "Influence of atmospheric steam curing by solar energy on the compressive and flexural strength of concretes." *Constr. Build. Mater.*, 49, 511–518.

Cheewaket, T., Jaturapitakkul, C., and Chalee, W. (2010). "Long term performance of chloride binding capacity in fly ash concrete in a marine environment." *Constr. Build. Mater.*, 24(8), 1352–1357.

Chindaprasirt, P., and Chalee, W. (2014). "Effect of sodium hydroxide concentration on chloride penetration and steel corrosion of fly ash-based geopolymer concrete under marine site." *Constr. Build. Mater.*, 63, 303–310.

Chindaprasirt, P., Jaturapitakkul, C., and Sinsiri, T. (2005). "Effect of fly ash fineness on compressive strength and pore size of blended cement paste." *Cem. Concr. Compos.*, 27(4), 425–428.

Downloaded from ascelibrary.org by King Mongkut's University of Technology, Thonburi on 04/20/17. Copyright ASCE. For personal use only; all rights reserved.

Choi, S. J., Lee, S. S., and Monteiro, P. J. M. (2012). "Effect of fly ash fineness on temperature rise, setting, and strength development of mortar." *J. Mater. Civ. Eng.*, 10.1061/(ASCE)MT.1943-5533.0000411, 499–505.

Hanjitsuwan, S., Hunpratub, S., Thongbai, P., Maensiri, S., Sata, V., and Chindaprasirt, P. (2014). "Effects of NaOH concentrations on physical and electrical properties of high calcium fly ash geopolymer paste." *Cem. Concr. Compos.*, 45, 9–14.

Hoppe Filho, J., Medeiros, M. H. F., Pereira, E., Helene, P., and Isaia, G. C. (2013). "High-volume fly ash concrete with and without hydrated lime: Chloride diffusion coefficient from accelerated test." *J. Mater. Civ. Eng.*, 10.1061/(ASCE)MT.1943-5533.0000596, 411–418.

Hossain, M. M., Karim, M. R., Hossain, M. K., Islam, M. N., and Zain, M. F. M. (2015). "Durability of mortar and concrete containing alkali-activated binder with pozzolans: A review." *Constr. Build. Mater.*, 93, 95–109.

Jaturapitakkul, C., and Roongreung, B. (2003). "Cementing material from calcium carbide residue-rice husk ash." *J. Mater. Civ. Eng.*, 10.1061/(ASCE)0899-1561(2003)15:5(470), 470–475.

Jaturapitakkul, C., Tangpagasit, J., Songmue, S., and Kiattikomol, K. (2011). "Filler effect of fine particle sand on the compressive strength of mortar." *Inter. J. Min. Met. Mater.*, 18(2), 240–246.

Kim, J. K., Han, S. H., and Song, Y. C. (2002). "Effect of temperature and aging on the mechanical properties of concrete: Part I. Experimental results." *Cem. Concr. Res.*, 32(7), 1087–1094.

Krammart, P., Martputhorn, S., Jaturapitakkul, C., and Ngaopisadarn, V. (1996). "A study of compressive strength of mortar made from calcium carbide residue and fly ash." *Res. Dev. J.*, 7(2), 65–75 (in Thai).

Leng, F., Feng, N., and Lu, X. (2000). "An experimental study on the properties of resistance to diffusion of chloride ions of chloride ions of fly ash and blast furnace slag concrete." *Cem. Concr. Res.*, 30(6), 989–992.

Lloyd, R. R., Provis, J. L., and Van Deventer, J. S. (2010). "Pore solution composition and alkali diffusion in inorganic polymer cement." *Cem. Concr. Res.*, 40(9), 1386–1392.

Makaratat, N., Jaturapitakkul, C., and Laosamathikul, T. (2010). "Effects of calcium carbide residue-fly ash binder on mechanical properties of concrete." *J. Mater. Civ. Eng.*, 10.1061/(ASCE)MT.1943-5533.0000127, 1164–1170.

Mehta, P. K. (2009). "Global concrete industry sustainability." *Concr. Int.*, 31(2), 45–48.

NT Build. (1989). "Concrete, repairing materials and protective coating: embedded steel method, chloride permeability." *NT Build 356*, Espoo, Finland.

Rattanasak, U., and Chindaprasirt, P. (2009). "Influence of NaOH solution on the synthesis of fly ash geopolymer." *Miner. Eng.*, 22(12), 1073–1078.

Rattanashotinunt, C., Thairit, P., Tangchirapat, W., and Jaturapitakkul, C. (2013). "Use of calcium carbide residue and bagasse ash mixtures as a new cementitious material in concrete." *Mater. Des.*, 46, 106–111.

Sangoju, B., Gettu, R., Bharatkumar, B. H., and Neelamegam, M. (2011). "Chloride-induced corrosion of steel in cracked OPC and PPC concretes: Experimental study." *J. Mater. Civ. Eng.*, 10.1061/(ASCE)MT.1943-5533.0000260, 1057–1066.

Saraswathy, V., Muralidharan, S., Thangavel, K., and Srinivasan, S. (2003). "Influence of activated fly ash on corrosion-resistance and strength of concrete." *Cem. Concr. Compos.*, 25(7), 673–680.

Sinsiri, T., Chindaprasirt, P., and Jaturapitakkul, C. (2010). "Influence of fly ash fineness and shape on the porosity and permeability of blended cement pastes." *Inter. J. Min. Met. Mater.*, 17(6), 683–690.

Srisen, A. (2013). "Strength and durability of normal strength and high strength concretes using fly ash and calcium carbide residue as binder." Master of Engineering thesis, King Mongkut's Univ. of Technology, Thonburi, Thailand, 93 (in Thai).

Talero, R., et al. (2011). "Comparative and semi-quantitative XRD analysis of Friedel's salt originating from pozzolan and portland cement." *Constr. Build. Mater.*, 25(5), 2370–2380.

Thomas, M. D. A. (2007). *Optimizing the use of fly ash in concrete*, Portland Cement Association, Skokie, IL, 5420.

Thomas, M. D. A., Hooton, R. D., Scott, A., and Zibara, H. (2012). "The effect of supplementary cementitious materials on chloride binding in hardened cement paste." *Cem. Concr. Res.*, 42(1), 1–7.

Yang, C. C., and Chiang, C. T. (2005). "On the relationship between pore structure and charge passed from RCPT in mineral-free cement-based materials." *Mater. Chem. Phys.*, 93(1), 202–207.

Downloaded from ascelibrary.org by King Mongkut's University of Technology, Thonburi on 04/20/17. Copyright ASCE. For personal use only; all rights reserved.

J Mater Sci: Mater Electron (2017) 28:11762–11768
DOI 10.1007/s10854-017-6981-8

Improved dielectric properties of PVDF composites by employing Mg-doped $La_{1.9}Sr_{0.1}NiO_4$ particles as a filler

Keerati Meeporn[1] · Prasit Thongbai[2,3] · Santi Maensiri[4] · Prinya Chindaprasirt[5]

Received: 5 March 2017 / Accepted: 17 April 2017 / Published online: 22 April 2017
© Springer Science+Business Media New York 2017

Abstract The dielectric properties of $La_{1.9}Sr_{0.1}Ni_{0.6}Mg_{0.4}O_4$/poly(vinylidene fluoride) (LSNMO/PVDF) composites were investigated. A giant-permittivity LSNMO ceramic was used as a filler to enhance the dielectric permittivity (ε′) of a PVDF polymer. LSNMO particles were well dispersed in the PVDF matrix. ε′ and the loss tangent (tanδ) of the composites increased with increasing LSNMO volume fraction. Interestingly, a greatly enhanced $\varepsilon' \approx 10^3$ was obtained in the LSNMO/PVDF composite with 50 vol% LSNMO, which was ≈100 times higher than that of pure PVDF. The percolation theory, effective medium theory, and effective medium percolation theory (EMPT) models were employed to describe the dielectric behavior of the LSNMO/PVDF composites. The calculated values obtained by the EMPT model were in close agreement with the experimental values. The large increases in ε′ was described as a combination of strong interfacial polarization due to a short inter-particle distance between LSNMO particles and a high ε′ of LSNMO ceramic filler.

✉ Prasit Thongbai
pthongbai@kku.ac.th

1 Materials Science and Nanotechnology Program, Faculty of Science, Khon Kaen University, Khon Kaen 40002, Thailand

2 Integrated Nanotechnology Research Center (INRC), Department of Physics, Faculty of Science, Khon Kaen University, Khon Kaen 40002, Thailand

3 Nanotec−KKU Center of Excellence on Advanced Nanomaterials for Energy Production and Storage, Khon Kaen 40002, Thailand

4 School of Physics, Institute of Science, Suranaree University of Technology, Nakhon Ratchasima 30000, Thailand

5 Sustainable Infrastructure Research and Development Center, Department of Civil Engineering, Faculty of Engineering, Khon Kaen University, Khon Kaen 40002, Thailand

1 Introduction

High-permittivity dielectric materials have attracted increasing attention because of their important applications in the electrical and electronic industries, especially for high energy storage devices [1–6]. Ferroelectric oxides such as $BaTiO_3$, $Ba_xSr_{1-x}TiO_3$ and $Pb(Zr, Ti)O_3$, as well as perovskite-like $CaCu_3Ti_4O_{12}$ ceramics can exhibit high dielectric permittivity ($\varepsilon' \approx 10^3$–$10^5$), but they are brittle, require high processing temperatures and have a low dielectric strength [1, 2, 7–10]. The uses of these ceramics may be limited in some electronics applications. Alternatively, polymers are flexible, easy to process and have a high dielectric strength as well as low dielectric loss tangent (tanδ) [8, 9, 11–13]. The only disadvantage of a dielectric polymer is its low ε′ compared to those of ceramic oxides. Therefore, investigations on the enhancement of ε′ values of polymers have been widely conducted in recently years [8, 9, 11–23]. A conventional method is to incorporate high-permittivity ceramics into polymers to enhance ε′ values, following conventional mixture rules. This method is an effective and promising way to overcome the disadvantage of dielectric polymers. It is expected that ceramic–polymer composites will be a better alternative and offer excellent material characteristics, including flexibility, low-temperature manufacture and good dielectric properties.

Generally, poly(vinylidene fluoride) (PVDF) is used as a polymer matrix because of its high ε′ value of ≈10–12 at room temperature. Furthermore, PVDF has high electric breakdown field, low tanδ, low cost and high reliability [3, 13, 24, 25]. High-permittivity dielectric ceramics, including

$BaTiO_3$, $Ba_xSr_{1-x}TiO_3$, Pb(Zr, Ti)O_3, $CaCu_3Ti_4O_{12}$ and (Li, Ti) co-doped NiO (LNTO), have often been used as a filler material in the polymer matrix to enhance the ε′ of polymer matrix [1, 3, 5, 8, 9, 13, 24]. Although many excellent studies have been done, there still exists some limitations, especially with regard to attaining low ε′ values and/or high tanδ (>1.0 at 1 kHz) of these composite systems. ε′ values of some composite systems were quite high and can be as high as ≈100 at 10^3 Hz even when the loading of a filler was ≥50 vol%. The polymer composite loses its flexibility at high ceramic contents. Therefore, it is crucial to choose suitable high-permittivity dielectric ceramic fillers.

Recently, extremely high ε′ values of ≈10^5–10^6 at room temperature were observed in $Ln_{2-x}Sr_xNiO_4$ ceramics (Ln = La^{3+}, Sm^{3+}, and Nd^{3+}) in the radio frequency range. The ε′ values were still too large (≈10^4) even when the frequency was increased into the GHz region [26]. However, tanδ values of these $Ln_{2-x}Sr_xNiO_4$ ceramics were too large (>10) [26–29], which is one of the most serious obstacles to their use in practical applications. In considering these $Ln_{2-x}Sr_xNiO_4$ ceramics for use as filler materials in polymeric composites, the very high tanδ of these ceramics may cause an extreme increase in the tanδ of $Ln_{2-x}Sr_xNiO_4$/polymer composites. Thus, improved dielectric properties of $Ln_{2-x}Sr_xNiO_4$ ceramics should be obtained before attempting to use these ceramics in polymer composites.

In the current study, reduction of tanδ with retaining the high ε′ value of $La_{2-x}Sr_xNiO_4$ (LSNO) ceramics was first done by doping with Mg^{2+} ions. This Mg-doped LSNO ceramic was expected to be suitable for use as a filler material in a PVDF matrix to obtain enhanced ε′ value, while retaining appropriate tanδ values of the polymer composites.

2 Experimental details

2.1 Preparation of Mg-doped $La_{2-x}Sr_xNiO_4$ particles

In this work, $La_{1.9}Sr_{0.1}Ni_{0.6}Mg_{0.4}O_4$ (LSNMO) powder was prepared by a combustion method using urea as a fuel for reaction initiation. The starting raw materials consisted of $La(NO_3)_3{\cdot}6H_2O$ (99.99%, Sigma-Aldrich), $Sr(NO_3)_2$ (99.0%, Sigma-Aldrich), $Ni(NO_3)_2{\cdot}6H_2O$ (99.0%, Kanto Chemical), $Mg(NO_3)_2{\cdot}6H_2O$ (99%, Sigma-Aldrich), deionized water, citric acid ($C_6H_8O_7{\cdot}H_2O$, 99.7%) and urea (CH_4N_2O, 99.0%). First, stoichiometric amounts of $Ni(NO_3)_2{\cdot}6H_2O$, $La(NO_3)_3{\cdot}6H_2O$, $Sr(NO_3)_2$ and $Mg(NO_3)_2{\cdot}6H_2O$ were dissolved in an aqueous solution of citric acid with constant stirring at room temperature until a transparent clear solution was obtained. Second, 0.7 g of urea powder was added into the mixed solution with stirring at 200 °C until a viscous gel formed. Then, the gel was dried at 300 °C for 0.5 h yielding a dried porous precursor. Finally, the resulting dried porous precursor was ground and calcined at 1000 °C for 6 h to form a pure LSNMO phase. A portion (0.35 g) of the calcined LSNMO powder was pressed into pellets having dimensions of 9.5 mm in diameter and ≈1.2 mm in thickness by uniaxial compression at 200 MPa. This green body was sintered in air at 1375 °C for 6 h and used for studying the dielectric properties of its bulk ceramic.

2.2 Preparation of LSNMO/PVDF composites

LSNMO/PVDF composites were prepared using a liquid-phase assisted dispersion method [30]. First, the prepared LSNMO particles and commercially obtained PVDF (Sigma-Aldrich Co., France) were mixed by ball-milling in absolute ethanol for 5 h using ZrO_2 balls. Second, the mixture was further dried to evaporate the ethanol. Finally, the dry mixture of LSNMO and PVDF powders was molded by hot-pressing at 200 °C for 30 min. The resulting composite samples had a disc-shape that was 12 mm in diameter and ≈1 mm in thickness.

2.3 Characterization techniques and electrical measurements

X-ray diffraction (XRD) (PANalytical, EMPYREAN) and scanning electron microscopy (SEM) (SEC, SNE4500M) were used to characterize the phase composition and microstructure of pure PVDF, LSNMO-NPs and LSNMO/PVDF composites. The dielectric properties were measured using a KEYSIGHT E4990A Impedance Analyzer over the frequency range of 10^2 to 10^6 Hz at room temperature with an oscillation voltage of 500 mV. Silver paint was used as an electrode material.

3 Results and discussion

Figure 1 shows the XRD patterns of the LSNMO powder, pure PVDF and LSNMO/PVDF composites with different volume fractions of LSNMO (*f*). A single phase of LSNO with a tetragonal structure was found in the LSNMO powder, which was used as a ceramic filler in the PVDF polymer matrix. All diffraction peaks of the LSNMO powder were indexed to the tetragonal crystal structure (JCPDS 32-1241). No impurity phase was detected in the XRD patterns of the LSNMO powder. Even the Mg-related oxide phase was absent. This may indicate that Mg^{2+} dopant was completely substituted into the Ni sites in the LSNO structure. The XRD pattern is similar to those reported in the literature for LSNO ceramics [31, 32]. As shown in

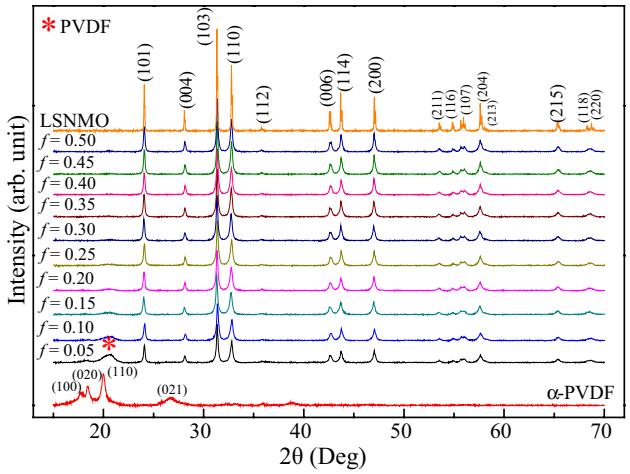

Fig. 1 XRD patterns of LSNMO particles, pure PVDF and LSNMO/PVDF composites with different volume fractions of LSNMO

Fig. 2a, particle sizes of the LSNMO powder were of about 1–3 μm.

The XRD pattern of PVDF indicates the presence of a semi-crystalline structure. The shape peaks were observed at $2\theta \approx 17.69°$, 18.36°, 19.93° and 26.61°. These were respectively attributed to diffraction at the (100), (020), (110) and (021) planes of the α-phase of PVDF [33]. The XRD peaks of PVDF were only observed in the LSNMO/PVDF composites with low loadings of LSNMO filler (at $f < 0.2$). For the composites with high volume fractions of LSNMO, no diffraction peaks of PVDF were seen. This was due to the shielding effect of relatively high intensity of the diffraction peaks of the LSNMO ceramic.

Figure 2b–d show SEM images of the cross-section of the LSNMO/PVDF composites films with $f = 0.20$, 0.40 and 0.50, respectively, revealing good dispersion of LSNMO particles in the PVDF polymer matrix. The 0–3 connectivity pattern of the composites was observed. This is because LSNMO particles were randomly surrounded by a PVDF matrix. Interestingly, only a small number of pores were observed in the composites, even though the volume fraction of filler was as high as 50 vol% ($f = 0.5$). The thickness of LSNMO/PVDF composites was in the range of 0.83–0.89 mm (insets of Fig. 2b–d). Generally, the dispersion of filler particles in the polymer matrix has a great effect on the dielectric properties of polymeric composites. Thus, good dispersion of LSNMO particles

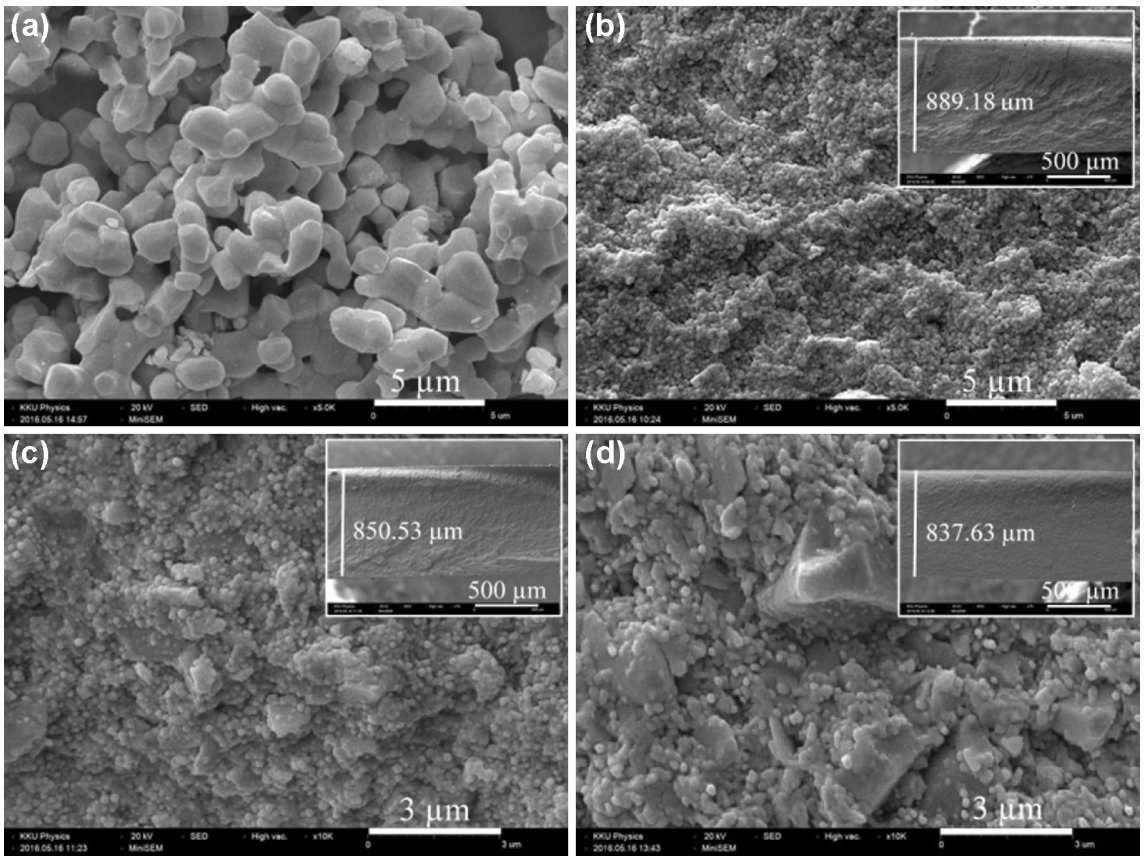

Fig. 2 **a** SEM image of LSNMO particles. **b–d** SEM images of cross sections of LSNMO/PVDF composites with $f = 0.20$, 0.40 and 0.50, respectively; *insets* are their SEM images with low magnification to determine the thickness of the polymer composites

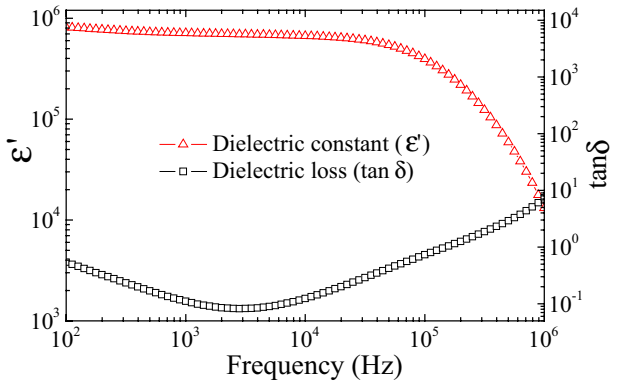

Fig. 3 Frequency dependence of ε′ and tanδ (measured at room temperature) for the LSNMO ceramic sintered at 1375 °C for 6 h

is expected to contribute to the improved dielectric properties of PVDF polymer composites.

The dielectric properties of the sintered LSNMO ceramics are shown in Fig. 3. As clearly seen, ε′ showed a weak frequency dependence in the range of 10^2–10^5 Hz, while tanδ was lower than 1.0 under this condition. Usually, tanδ values of un-doped LSNO ceramics are larger than 10 over a wide frequency range [31, 32]. Thus, the LSNMO ceramic particles may be suitable for use as filler due to their low tanδ and very high ε′.

The frequency dependencies of ε′ and tanδ measured at room temperature for LSNMO/PVDF composites with various loadings of LSNMO filler are shown in Fig. 4. As expected, ε′ and tanδ increased with increasing LSNMO content in PVDF. ε′ of pure PVDF and the composites with $f \leq 0.30$ showed a relatively stable frequency dependence in the range of 10^2–10^6 Hz. Over this frequency range, ε′ of the LSNMO/PVDF composites increased with increasing LSNMO content. However, an obvious frequency dependence of ε′ was observed with further increases in the volume fraction of LSNMO in the range of $f = 0.35$–0.5, especially for the composite with $f = 0.5$. This observed frequency dependence of ε′ in a low-frequency range may be associated with the strong interfacial polarization and/or long range motion of charges. The ε′ values of all the LSNMO/PVDF composites were higher than that of pure PVDF, but much lower than that of the sintered LSNMO ceramic. As demonstrated in Fig. 1, only the α-phase of PVDF was detected, which is a non-polar phase [33]. The constrained polymer chain inhibited the electrical polarization in the composite system [12]. Therefore, the ε′ value of the LSNMO/PVDF composites was much lower than that of the LSNMO ceramic [12]. Interestingly, strongly enhanced $\varepsilon' \approx 10^3$ at 10^2 Hz was obtained for the LSNMO/PVDF composite with $f = 0.5$, which was ≈100 times higher than that of pure PVDF.

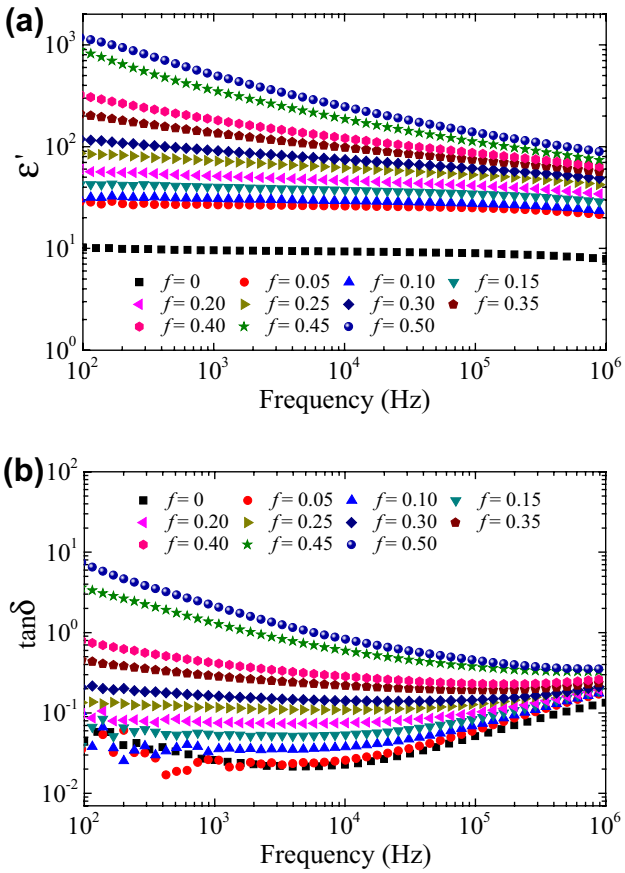

Fig. 4 Frequency dependence of **a** ε′ and **b** tanδ at room temperature for LSNMO/PVDF composites with various volume fractions of LSNMO (*f*)

As shown in Fig. 4b, tanδ of PVDF and the composites with $f = 0.05$–0.30 increased with increasing frequency from 10^4 to 10^6 Hz. This signifies the appearance of a relaxation peak of tanδ, which is indicative of dielectric relaxation behavior. This dielectric relaxation can be referred to α_a relaxation and it is due to dipole polarization of PVDF [16]. For high volume fractions of LSNMO ($f \geq 0.35$), a low-frequency tanδ of LSNMO/PVDF composites increased with increasing LSNMO loading. This low-frequency dielectric response of the LSNMO/PVDF composites can be caused by the DC conduction behavior inside the composites and/or the low-frequency relaxation process [1]. To confirm this, the AC conductivity of the composites was studied. As shown in Fig. 5, the low-frequency conductivity of the composite gradually increased as the LSNMO volume fraction increased from in the range of $f < 0.4$. When $f > 0.4$, the low-frequency conductivity of the LSNMO/PVDF composite was greatly enhanced and it was nearly independent of frequency in the range of 10^2–10^3 Hz. These results clearly indicate the dominate effect of DC conduction in the composites.

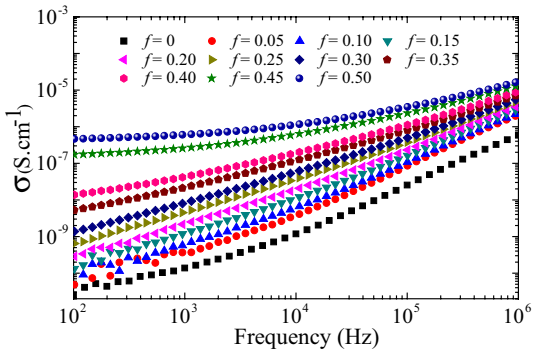

Fig. 5 AC conductivity (σ) at room temperature of LSNMO/PVDF composites (f=0–0.5)

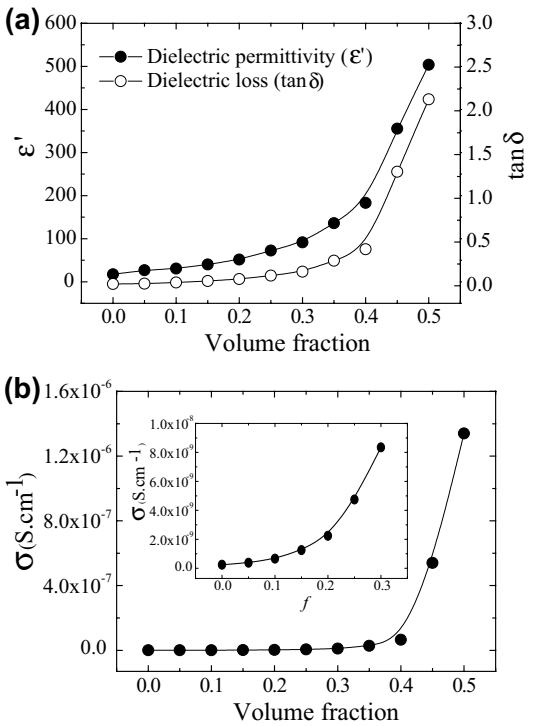

Fig. 6 **a** Dependence of ε′ and tanδ values (at 1 kHz and room temperature) on the volume fraction of LSNMO filler. **b** AC conductivity (σ) of LSNMO/PVDF composites as a function of LSNMO volume fraction (f) measured at 1 kHz and room temperature; *inset* shows the enlarged scale in the range of f=0–0.3

To clearly understand the possible mechanisms of the dielectric response in the composites over the range of LSNMO loadings, the volume-fraction dependency of the dielectric properties (ε′ and tanδ) and conductivity (σ) of the LSNMO/PVDF composites at room temperature (at 1 kHz) was studied. As shown in Fig. 6, variations in ε′, tanδ and σ as a function of LSNMO loading show a similar trend. The ε′, tanδ and σ (inset of Fig. 6b) values gradually increased with increasing volume fraction of LSNMO for f<0.4. Interestingly, with further increases in the LSNMO volume fraction above f=0.4, the ε′, tanδ and σ values dramatically increased. When the LSNMO volume fraction was 0.40, good dielectric properties were achieved. At 1 kHz, ε′ was ≈183, which is ≈18 times larger than that of pure PVDF (≈10), while its tanδ was lower than 0.5. At f=0.5, ε′ was as high as 503.73, which is ≈50 times higher than that of PVDF.

As discussed above, the overall dielectric and electrical properties likely obeyed the percolation theory, which is usually found in conductive-polymer composite systems. However, another important observation with a relatively low volume fraction of filler (f<0.4) should be carefully considered. The ε′ and tanδ values of the LSNMO/PVDF composites continuously increased with increasing filler concentration (Fig. 6a and the inset of Fig. 6b). These behaviors are totally different from that observed in the conductive-polymer composites, where ε′ and σ rise very slowly at low concentrations of filler (or at a filler concentration lower than the percolation threshold). At f<0.4, it was observed that the variation in ε′ and σ was similar to that observed in other ceramic–polymer composites such as $CaCu_3Ti_4O_{12}$/PVDF [12] and $BaTiO_3$/PVDF composites [16]. Thus, the overall dielectric and electrical properties of the LSNMO/PVDF composites cannot be fully described by the percolation theory or any conventional mixed model. In contrast, the combination of these two models may be suitable for describing the dielectric behavior of LSNMO/PVDF composites.

To better understand the dielectric behavior of the LSNMO/PVDF composites, the effective medium percolation theory model (EMPT) was developed [5, 14]. This model is the combination of the effective medium theory (EMT) model and the percolation model [14]. The effective dielectric permittivity (ε_r) of the EMPT model is expressed as follows:

$$\varepsilon_r = \varepsilon_1 \left[1 + \frac{f_{cer}(\varepsilon_2 - \varepsilon_1)}{\varepsilon_1 + n(1 - f_{cer})(\varepsilon_2 - \varepsilon_1)} \right] |(f_c - f_{cer})/f_{cer}|^{-q} \quad (1)$$

where f_c is the percolation threshold of the conductive or semi-conductive filler. ε_1 and ε_2 are dielectric permittivity values of polymer matrix and filler (ε_1=10 and $\varepsilon_2 = 7.13 \times 10^5$). f_{cer} is the volume fraction of the ceramic semi-conductive filler. n and q are the ceramic morphology fitting factor and the critical exponent, respectively. As illustrated in Fig. 7, according to the fitted result using the EMPT model and compared to the EMT or percolation theory model, the fitted result of EMPT closely matches the experimental data over a filler loading content (f=0–0.5). The EMT model cannot fit the data in the range of f>0.4, while the fitting results are in good accordance with the

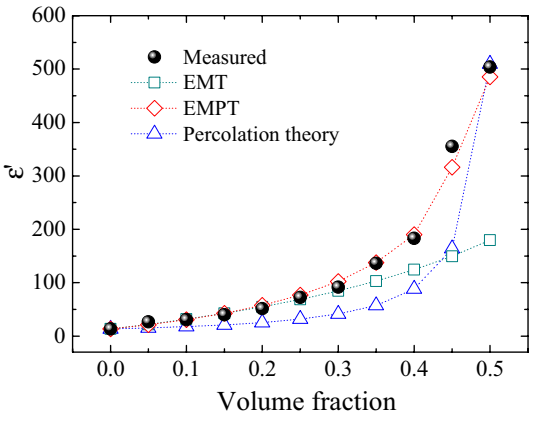

Fig. 7 Experimental data and theoretical ε′ values from different models of LSNMO/PVDF composites with different volume fractions of LSNMO at 1 kHz and room temperature

experimental data in the range of $f<0.4$. Alternatively, percolation theory cannot fit the data when $f<0.4$ where the fitted data deviate from the experimental data. At $f>0.4$, the experimental data can be well fitted by percolation theory.

Therefore, at least two mechanisms are responsible for the observed overall dielectric behavior in the LSNMO/PVDF composites. The best fitting parameters for the EMPT model are $f_c=0.54$, $n=0.10$ and $q=0.50$. The filler morphology fitting factor n and the critical exponent q are similar to that reported by Fang et al. [5]. It is notable that f_c of the LSNMO/PVDF composites was much higher than the theoretical percolation threshold of a conductive-polymer composite, which is about $f_c=0.16$ for conductive-filler with a spherical shape [34]. It was clearly shown that f_c increased with increasing conductivity of the fillers [4, 17, 35]. Therefore, the obtained high f_c value is attributed to the semiconductor properties of the LSNMO ceramic filler. At $f=0.05$–0.035, LSNMO particles are separated from another and surrounded by an insulating PVDF matrix. Thus, the continuously enhanced dielectric response in the LSNMO/PVDF composites arose from the giant ε′ values of the LSNMO particles and the strong interfacial polarization between the insulating PVDF matrix and semiconducting LSNMO particles. At $f=0.35$–0.5, a rapid increase in ε′ was observed. This is typically caused by the formation of a percolation network [34]. This is evidenced by the observed increase in both the conductivity and tanδ.

4 Conclusions

The LSNMO/PVDF polymeric composites with volume fractions of LSNMO filler from $f=0$–0.5 were fabricated to enhance the dielectric response in PVDF polymer. LSNMO particles were homogeneously dispersed in the PVDF matrix, confirming the formation of a 0–3 composite. ε′ and tanδ of the composites increased with increasing filler loading. For the composite with $f=0.5$, interestingly, largely increased $\varepsilon' \approx 10^3$ and ≈500 at 10^2 and 10^3 Hz, respectively, were achieved. The variation in dielectric properties as a function of filler volume fraction for the LSNMO/PVDF composites was well fitted and obeyed the combined model of the percolation theory and EMT model, which was referred to the effective medium percolation theory (EMPT) model. At a low filler loading, a continuous increase in ε′ was caused by strong interfacial polarization and a very high ε′ value of LSNMO particles. At a relatively high volume fraction, the dramatic increase in ε′ was due to the formation of a percolation network throughout the PVDF polymer matrix, increasing both of ε′ and the conductivity of the composites.

Acknowledgements This work was financially supported by the Thailand Research Fund (TRF) and Khon Kaen University (Contract No. RSA5880012) and under the TRF Senior Research Scholar (Contract No. RTA5780004). This work was partially supported by the Nanotechnology Center (NANOTEC), NSTDA, Ministry of Science and Technology, Thailand, through its program of Center of Excellence Network and the Higher Education Research Promotion and National Research University Project of Thailand, Office of the Higher Education Commission, through the Advanced Functional Materials Cluster of Khon Kaen University. K.M. would like to thank the Thailand Research Fund through the Royal Golden Jubilee Ph.D. Program (Grant No. PHD/0191/2556) for his Ph.D. scholarship.

References

1. M. Arbatti, X. Shan, Z.Y. Cheng, Adv. Mater. **19**, 1369–1372 (2007)
2. L. Xie, X. Huang, K. Yang, S. Li, P. Jiang, J. Mater. Chem. A **2**, 5244–5251 (2014)
3. Z. Wang, M. Fang, H. Li, Y. Wen, C. Wang, Y. Pu, Compos. Sci. Technol. **117**, 410–416 (2015)
4. Z.M. Dang, J.B. Wu, L.Z. Fan, C.W. Nan, Chem. Phys. Lett. **376**, 389–394 (2003)
5. F. Fang, W. Yang, S. Yu, S. Luo, R. Sun, Appl. Phys. Lett. **104**, 132909 (2014)
6. D. Wang, T. Zhou, J.-W. Zha, J. Zhao, C.-Y. Shi, Z.-M. Dang, J. Mater. Chem. A **1**, 6162–6168 (2013)
7. Z.-M. Dang, J.-K. Yuan, J.-W. Zha, T. Zhou, S.-T. Li, G.-H. Hu, Prog. Mater. Sci. **57**, 660–723 (2012)
8. E.-Q. Huang, J. Zhao, J.-W. Zha, L. Zhang, R.-J. Liao, Z.-M. Dang, J. Appl. Phys. **115**, 194102 (2014)
9. J. Fu, Y. Hou, M. Zheng, Q. Wei, M. Zhu, H. Yan, ACS Appl. Mater. Interfaces **7**, 24480–24491 (2015)

10. K. Yu, H. Wang, Y. Zhou, Y. Bai, Y. Niu, J. Appl. Phys. **113**, 034105 (2013)
11. X.-J. Zhang, G.-S. Wang, Y.-Z. Wei, L. Guo, M.-S. Cao. J. Mater. Chem. A **1**, 12115–12122 (2013)
12. P. Thomas, K.T. Varughese, K. Dwarakanath, K.B.R. Varma, Compos. Sci. Technol. **70**, 539–545 (2010)
13. S. Liu, S. Xue, W. Zhang, J. Zhai, G. Chen, J. Mater. Chem. A **2**, 18040–18046 (2014)
14. Prateek, V.K. Thakur, R.K. Gupta, Chem. Rev. **116**, 4260–4317 (2016)
15. Y.-L. Su, C. Sun, W.-Q. Zhang, H. Huang, J. Mater. Sci. **48**, 8147–8152 (2013)
16. S. Luo, S. Yu, R. Sun, C.-P. Wong, ACS Appl. Mater. Interfaces **6**, 176–182 (2014)
17. Z.-M. Dang, T. Zhou, S.-H. Yao, J.-K. Yuan, J.-W. Zha, H.-T. Song, J.-Y. Li, Q. Chen, W.-T. Yang, J. Bai, Adv. Mater. **21**, 2077–2082 (2009)
18. Z.-M. Dang, B. Peng, D. Xie, S.-H. Yao, M.-J. Jiang, J. Bai, Appl. Phys. Lett. **92**, 112910 (2008)
19. Z.-M. Dang, C.-W. Nan, Ceram. Int. **31**, 349–351 (2005)
20. M. Yao, S. You, Y. Peng, Ceram. Int. **43**, 3127–3132 (2017)
21. M. Fang, Z. Wang, H. Li, Y. Wen, Ceram. Int. **41**, (Supplement 1), S387–S392 (2015)
22. P. Kum-onsa, P. Thongbai, S. Maensiri, P. Chindaprasirt, J. Mater. Sci. Mater. Electron. **27**, 9650–9655 (2016)
23. K. Meeporn, S. Maensiri, P. Thongbai, Appl. Surf. Sci. **380**, 67–72 (2016)
24. M.-F. Lin, P.S. Lee, J. Mater. Chem. A **1**, 14455–14459 (2013)
25. H. Tang, H.A. Sodano, Nano Lett. **13**, 1373–1379 (2013)
26. S. Krohns, P. Lunkenheimer, C. Kant, A.V. Pronin, H.B. Brom, A.A. Nugroho, M. Diantoro, A. Loidl, Appl. Phys. Lett. **94**, 122903 (2009)
27. T. Park, Z. Nussinov, K. Hazzard, V. Sidorov, A. Balatsky, J. Sarrao, S.W. Cheong, M. Hundley, J.-S. Lee, Q. Jia, J. Thompson, Phys. Rev. Lett. **94**, 017002 (2005)
28. X.Q. Liu, B.W. Jia, W.Z. Yang, J.P. Cheng, X.M. Chen, J. Phys. D **43**, 495402 (2010)
29. B.W. Jia, W.Z. Yang, X.Q. Liu, X.M. Chen, J. Appl. Phys. **112**, 024104 (2012)
30. K. Silakaew, W. Saijingwong, K. Meeporn, S. Maensiri, P. Thongbai, Microelectron. Eng. **146**, 1–5 (2015)
31. K. Meeporn, N. Chanlek, P. Thongbai, RSC Adv. **6**, 91377–91385 (2016)
32. K. Meeporn, T. Yamwong, P. Thongbai, Jpn. J. Appl. Phys. **53**, 06JF01 (2014)
33. P. Martins, A.C. Lopes, S. Lanceros-Mendez, Prog. Polym. Sci. **39**, 683–706 (2014)
34. C.W. Nan, Y. Shen, J. Ma, Annu. Rev. Mater. Res. **40**, 131–151 (2010)
35. J. Fu, Y. Hou, Q. Wei, M. Zheng, M. Zhu, H. Yan, J. Appl. Phys. **118**, 235502 (2015)

Powder Technology 313 (2017) 417–426

Contents lists available at ScienceDirect

Powder Technology

journal homepage: www.elsevier.com/locate/powtec

TiO_2-zeolite photocatalysts made of metakaolin and rice husk ash for removal of methylene blue dye

Naruemon Setthaya [a], Prinya Chindaprasirt [b], Shu Yin [c], Kedsarin Pimraksa [a,*]

[a] Department of Industrial Chemistry, Faculty of Science, Chiang Mai University, Chiang Mai 50200, Thailand
[b] Sustainable Infrastructure Research and Development Center, Faculty of Engineering, Khon Kaen University, Khon Kaen 40002, Thailand
[c] Institute of Multidisciplinary Research for Advanced Materials, Tohoku University, Sendai 980-8577, Japan

ARTICLE INFO

Article history:
Received 27 September 2016
Received in revised form 7 December 2016
Accepted 5 January 2017
Available online 6 January 2017

Keywords:
TiO_2
Zeolites
Photocatalyst
Metakaolin
Rice husk ash

ABSTRACT

In this study, synthesized zeolites were performed by solvothermal method using metakaolin and rice husk ash as starting materials. The TiO_2-zeolites photocatalysts obtained from the solvothermal method was compared with that obtained from impregnation method. The synthesized products were characterized using X-ray Fluorescence spectrometer (XRF), X-ray diffraction (XRD), scanning electron microscopy (SEM), the Fourier transform infrared (FTIR), ultraviolet -visible spectroscopy (UV–vis), particle size analyzer and surface area measurement. The results showed that the incorporation of TiO_2 in a form of transparent titanium solution into zeolites obtained from solvothermal method was very similar to that obtained from impregnation method confirmed by their mineralogical compositions, microstructures and specific surface areas. The adsorption and degradation efficiency of the TiO_2-zeolites photocatalysts obtained from solvothermal method of 97.32% was slightly lower than 99.43% of impregnation method. In addition, the synthesized TiO_2-zeolites photocatalysts showed a greater adsorption and degradation of methylene blue than pure zeolites and pure TiO_2 anatase.

© 2017 Elsevier B.V. All rights reserved.

1. Introduction

Textile dyeing industry produces a massive quantity of contaminated effluent which exerts serious harmful effect on photochemical phenomena. The increasing demand for dye by the textile manufactures resulted in a risk of highly contaminated environment. Textile wastewaters normally need high chemical oxygen demand due to the high toxicity and high total suspended solids [1–3]. Consequently, various technologies for the degradation of dyes from wastewater were constantly improved to obtain the best methodology for wastewater treatment.

Recently, a photocatalytic process has shown a high potential to reduce organic pollution since it provides the absolute decrement of toxic substances [4,5]. Titanium dioxide (TiO_2) is considered as the prominent photocatalyst due to its superior photocatalytic oxidation, thermal stability, nonphotocorrosion and nontoxicity properties. Its reasonable price also makes its utilization in an industrial scale possible. Due to its low adsorption ability as well as the low concentration of pollutants in ambient water and air, the efficiency of TiO_2 photocatalyst is often limited [6–12]. One of the promising ways to lever this issue is to combine the better adsorber to the TiO_2 photocatalyst to improve adsorptive ability. Many researchers have thus dedicated in search for appropriate support materials to improve the regeneration efficiency of TiO_2. Among various support materials, porous aluminosilicate material called "zeolite" has been shown to be the most desirable supporting material for TiO_2 as a result of their unique properties [13–15]. Zeolites act as electron donors and acceptors of moderate strength to the guest species based on the adsorption site. They show excellent absorption ability, high specific surface area including uniform pores and channels with unique structures [16,17]. Zeolites generally possess cages and channels of 4–14°A that can confine substrate molecules to improve the photocatalytic reactivity [18]. Therefore, zeolite is selected as supporting material for TiO_2 in this research.

From our previous works, nanoscale faujasite and zeolite P1 could be obtained from the solvothermal treatment using rice husk ash (RHA) and metakaolin (MK) as sources of silica and alumina with SiO_2/Al_2O_3 molar ratio of 4. The solvothermal treatments using alcohol as a media affected the nucleation rate and crystal growth of zeolite [19]. The aim of this study is therefore to propose the way to synthesize nanoactive adsorber with TiO_2-containing zeolite materials using MK and RHA as the starting materials in order to improve the catalytic efficiency. The TiO_2-zeolite photocatalyst obtained from the solvothermal method was compared with that obtained from impregnation method. The solvothermal method is selected in this research as it points to the synthesis above boiling point of water in nonaqueous solution at relatively high temperatures under closed system. These techniques have been accepted to obtain resulting materials with metastable structure,

* Corresponding author.
E-mail address: kedsarin.p@cmu.ac.th (K. Pimraksa).

http://dx.doi.org/10.1016/j.powtec.2017.01.014
0032-5910/© 2017 Elsevier B.V. All rights reserved.

condensed and aggregation statuses, controllable morphology and particle size, and dopant ions directly in synthetic reaction [20,21]. As a result, solvothermal process is referred to incorporating of Ti species during solvothermal treatment of zeolite production. For impregnation method, Ti species are introduced later after zeolite production has been done.

Kaolin, a hydrated aluminium silicate mineral with the chemical composition of $Al_2O_3 \cdot 2SiO_2 \cdot 2H_2O$, when calcined, undergoes dehydroxylation resulting in a collapse of kaolin structure, called "metakaolin ($Al_2O_3 \cdot 2SiO_2$)" [22,23]. Metakaolin is readily dissolved in alkaline solution and is thus a good precursor for zeolite synthesis [24–26]. RHA, a combustion by-product rich in silica is very reactive to alkaline solution and forms sodium silicate gel which is used in the synthesis of zeolite [27–30].

The main objectives of the present work were to synthesis zeolites (faujasite and zeolite P1), to prepare the TiO_2-containing zeolite composites using solvothermal method compared with impregnation method and to determine the photocatalytic activities of the samples. The comparison of photocatalytic activities was also carried out for the synthesized zeolites and pure anatase TiO_2. A series of complementary techniques: X-ray diffraction (XRD), Field emission scanning electron microscopy (SEM), Fourier transform infrared spectroscopy (FTIR), UV–visible diffuse reflectance spectroscopy (UV–vis DRS) were used to characterize the synthesized TiO_2 containing zeolite composites. The photocatalytic activities of samples were evaluated by the degradation of methylene blue dye (MB) in water as a representative dye in water. The findings from this work would help in the finding of environmental cleaning up materials.

2. Experimental

2.1. Materials

Kaolin clay was supplied from Sibelco Mineral (Thailand) Co., Ltd. Rice husk was collected from paddy fields in Chiang Mai, a province in Northern Thailand. China clay and rice husk were subjected to calcination at temperatures of 750 °C and 700 °C, respectively for 3 h with the heating rate of 5 °C/min in an oxidizing atmosphere resulting in MK and RHA, respectively. After that, they were ground and passed through a sieve No.325 [19,31]. The chemical compositions, average particle sizes and specific surface area of MK and RHA were characterized using X-ray fluorescence (XRF), Zetasizer nanoparticle analyzer and Brunauer–Emmett–Teller (BET) analysis, respectively and show in Table 1. The mineralogical compositions and morphology were detected by X-ray diffractometer (XRD) and field-emission scanning electron microscope (FE-SEM), and show in Figs. 1 and 2. Anatase TiO_2 was a reagent grade supplied from Sigma Aldrich with 99.7% of purity and less than 25 nm of particle size. Titanium (IV) butoxide was a reagent grade supplied from Sigma Aldrich with 97% of purity.

Table 1
Characteristics of starting materials and synthesized products.

Characteristics	MK	RHA	Zeolite	ZI	ZS
1. Chemical composition (wt%)					
SiO_2	58.03	94.52	46.23	45.71	46.58
Al_2O_3	32.69	1.34	24.49	23.15	20.67
CaO	0.28	0.46	0.78	0.90	0.56
K_2O	2.84	1.83	1.42	1.29	1.29
Na_2O	0.06	0.05	11.28	11.20	12.44
Fe_2O_3	1.65	0.28	1.19	1.08	0.84
MgO	0.55	0.03	0.51	0.59	0.35
TiO_2	0.07	0.02	0.06	6.43	6.79
LOI	3.39	0.56	0.13	0.11	0.11
2. Average particle size (μm)	1.31	2.81	0.621	0.704	0.663
3. Specific surface area by BET (m^2/g)	15.10	23.34	487.10	437.60	442.10

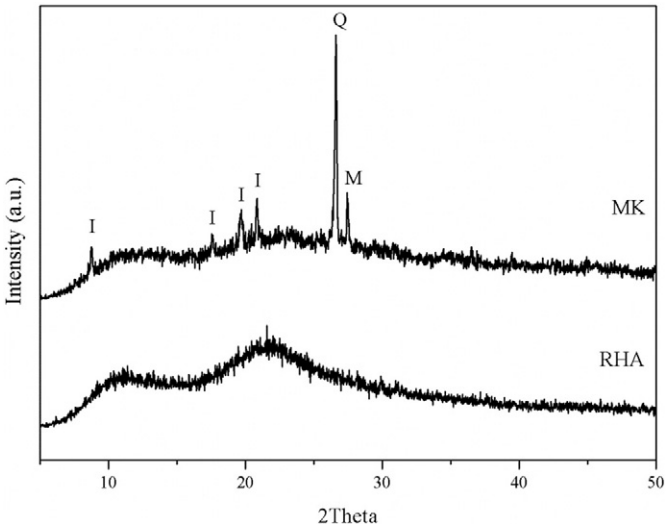

Fig. 1. XRD patterns of starting materials. I; Illite, Q; Quartz, M; Microcline.

2.2. Preparation of zeolite and TiO_2-containing zeolite catalysts

The TiO_2-zeolite photocatalysts were prepared using titanium (IV) butoxide ($Ti(OC_4H_9)_4$) as the titanium source. The transparent titanium solution was prepared using the method modified from the method reported by Li et al. [13] and Son et al. [32]. The 10 ml $Ti(OC_4H_9)_4$ and 40 ml absolute ethanol was gradually instilled and then slowly dripped into an aqueous solution containing 40 ml ethanol, 4 ml acetic acid and 3 ml distilled water under vital stirring to obtain the transparent titanium solution.

Zeolites (Z) and TiO_2 containing zeolite composites (ZS) were prepared by a solvothermal method. An alkaline solution used in this method was prepared using 10% ethanol in aqueous NaOH solution. The SiO_2/Al_2O_3 molar ratio of 4 was used for preparing a precursor gel. In the first step, MK or RHA was mixed with the alkaline solution at solid to liquid ratio of 1:8 with continuous stirring at 220 rpm for 48 h at room temperature to obtain precursor gel. To prepare zeolites, the precursor gel was then treated using solvothermal reactor at 120 °C for 6 h in the second step. For the preparation of ZS, the transparent titanium solution was added to the precursor gel at the precursor gel solid to transparent titanium solution ratio of 1:3 to obtain 5% TiO_2. The prepared mixture was then treated with solvothermal reactor under the same condition. After that, the precipitates were separated by filtration and thorough washing with distilled water until the solution pH reached 10 before being dried at 60 °C to obtain dried zeolite powders. The dried ZS powders were then calcined at 480 °C for 3 h to get rid of residual chemicals. TiO_2 containing zeolite composites prepared from impregnation method (ZI) were prepared by mixing 1 g of the synthesized zeolite (Z) in 3 and 12 ml of transparent titanium solutions to obtain 5% and 20% TiO_2, respectively. The resulting colloidal suspension was stirred for 2 h and aged for 48 h to form gel. The gel was dehydrated in an oven at 80 °C for 48 h and calcined at 480 °C for 3 h to obtain the ZI powders.

2.3. Characterization

The crystalline phases of synthesized products were detected by X-ray diffractometer (XRD, Bruker AXS D2 Phaser) using graphite-monochromized CuKα radiation. The chemical compositions were identified by X-ray fluorescence (XRF) using a Philips Magix Pro. The morphology observation and elemental analysis were detected using a field-emission scanning electron microscope (FE-SEM, SU-6600, Hitachi) and an energy dispersive X-ray spectrometer (EDS, Inca x-act, Oxford Instruments), respectively. The specific surface area was

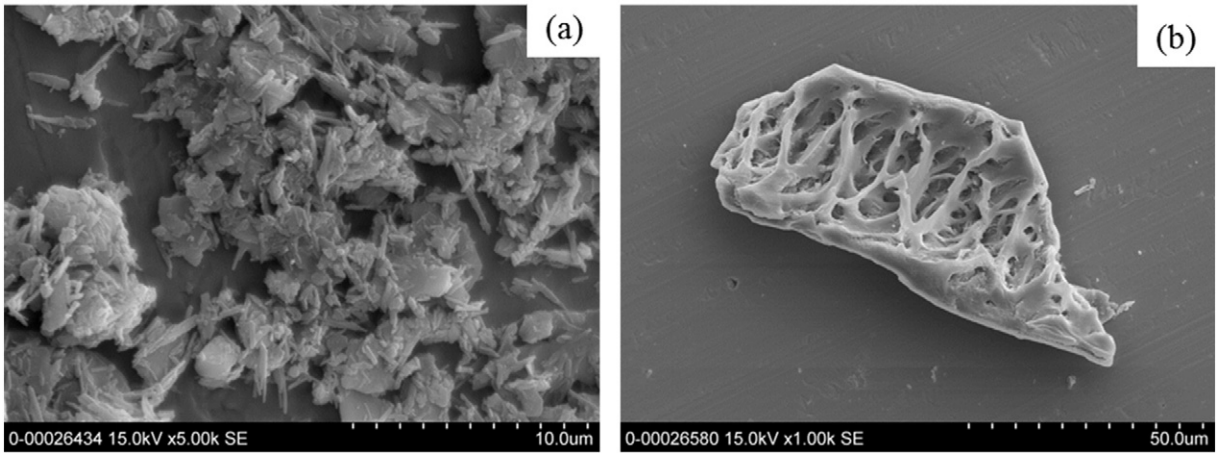

Fig. 2. FE-SEM photomicrographs of starting materials (a) MK and (b) RHA.

obtained from the Brunauer–Emmett–Teller (BET) method using a Quantachrome Autosorp-1. Average particle size was performed using a Malvern Zetasizer nano ZS. Fourier transform infrared spectra (FTIR) were analyzed using a Perkin Elmer Spotlight 400. The UV–vis diffuse reflectance spectra (DRS) were measured using a JASCO's V-670, UV–VIS-NIR spectrophotometer.

2.4. Methylene blue removal efficiency and photocatalytic activity test

The removal efficiency and photocatalytic degradation of methylene blue (MB) solution were studied using 0.1 g of TiO_2-zeolite catalyst suspended in 100 ml of 20 ppm MB solution. In addition, the MB degradation using 0.1 g of anatase TiO_2 was also studied to compare the quality of the products. Specific surface area of anatase TiO_2 was 55 m^2/g. The initial MB concentration was analyzed by measuring its maximum absorbance ($\lambda_{max} = 664$ nm) using a JASCO's V-670, UV–VIS-NIR spectrophotometer. The suspension was stirred at 500 rpm in a dark chamber for 30 min to reach the adsorption equilibrium. Then the obtained suspension was illuminated under a 300 W HAL-302 xenon light source with UV lamp (250–385 nm) at room temperature. UV lamp (300–365 nm; Osram Ultra Vitalux 300 W) was also used to compare degradation performances of ZI and ZS samples in different UV wavelengths. The illuminated suspension was then collected and centrifuged at 5000 rpm to obtain the clear solution. The remaining concentration of MB was also analyzed using a UV-VIS-NIR spectrophotometer at a wavelength of 664 nm. The MB degradation efficiency (X) was calculated by the following equation:

$$X = [(C_0 - C_t)/C_0] \times 100$$

where C_0 and C_t represent the initial concentration of MB solution and the concentration of MB analyzed at t time of illumination, respectively.

3. Results and discussion

3.1. Characterization of starting materials

The chemical compositions of MK and RHA are shown in Table 1. MK composed of 58.03% SiO_2 and 32.69% Al_2O_3 contents, corresponding to a SiO_2/Al_2O_3 molar ratio of 3.02. The main components of RHA was

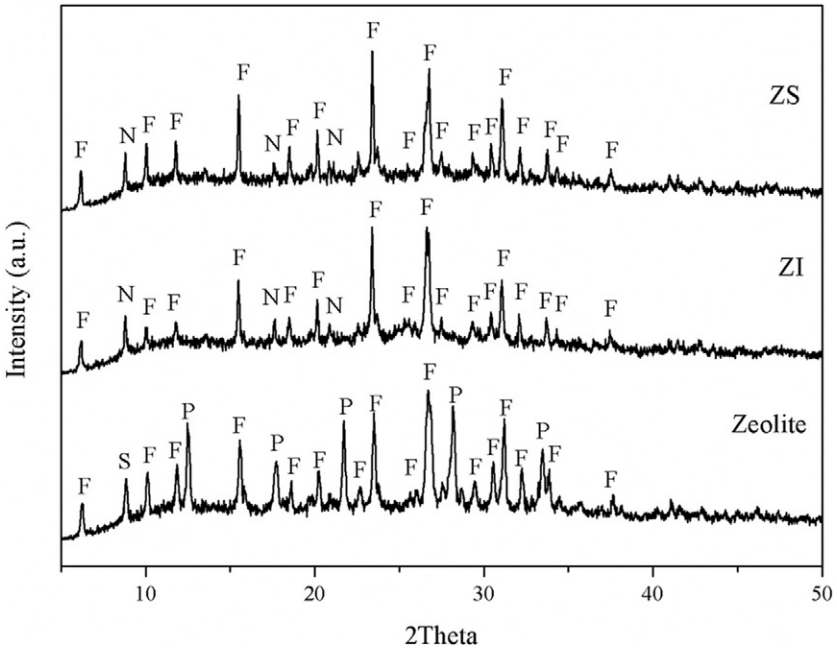

Fig. 3. XRD patterns of synthesized products prepared by different method. F: Faujasite, N: Zeolite Nu-5, P: Zeolite P1, S: Zeolite SSZ16.

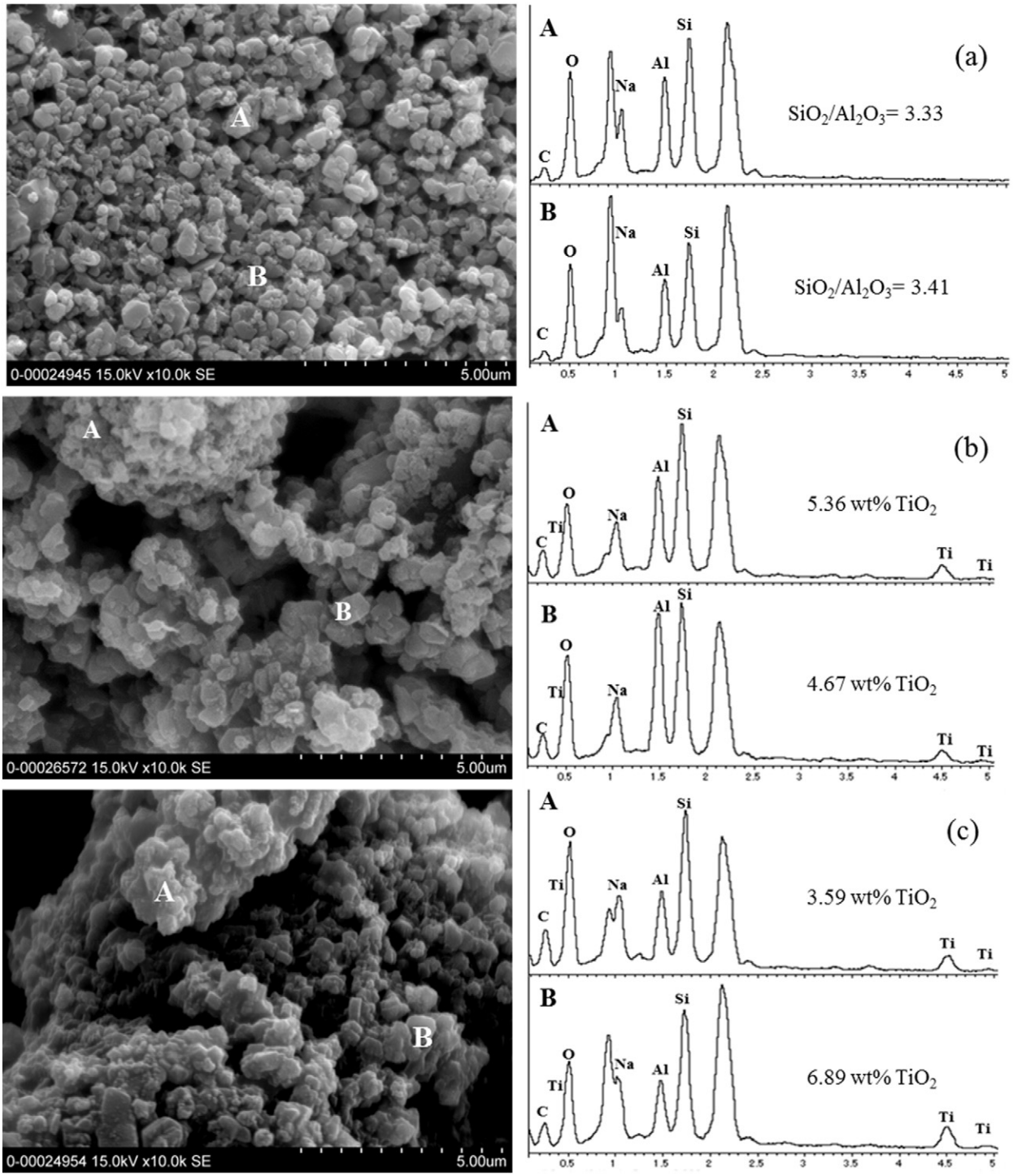

Fig. 4. FE-SEM photomicrographs and EDS of synthesized products prepared by different method (a) zeolites, (b) ZI and (c) ZS.

94.52 wt% of SiO_2. The mineralogical compositions of MK and RHA are shown in Fig. 1. MK consisted mainly of amorphous aluminosilicate, resulting from dehydroxylation that driven off water from kaolinite. Some quartz, illite and muscovite were also found together with MK due to their inert phases showing no disruptive structures on calcination. RHA consisted of amorphous silica as indicated by the strong broad peaks of pure silica in the range of $2\theta \approx 22–23°$. The average particle size of ground MK and ground RHA were 1.31 and 2.81 μm, respectively and the specific surface areas of MK and RHA were 15.10 and 23.34 m^2/g, respectively. The FE-SEM image of MK and RHA as shown in Fig. 2 indicated that the MK particles composed of stacks of platelets with hexagonal shape and the RHA particles were very irregular particles with the remains of porous cellular fabric of rice husk, thus leading to a high surface area of RHA in comparison with that of MK.

3.2. Characterization of zeolite and TiO_2-containing zeolite catalysts

X-ray powder diffraction was used to discover the existences of TiO_2 and zeolite as shown in Fig. 3. Diffraction peaks of the synthesized zeolites corresponded to zeolite faujasite; $Na_2Al_2Si_{3.3}O_{10.6}(H_2O)_7$ (major phase), zeolite P1; $Na_6Al_6Si_{10}O_{32}(H_2O)_{12}$ and zeolite SSZ16; $Na_{3.06}H_{4.14}(Si_{40.80}Al_{7.20}O_{96})$. It was obvious that the XRD patterns of ZS and

Table 2
Weight/atomic percent of Si, Al and Ti elements from EDS in synthesized products prepared by different methods.

Position	Element	Zeolite (a)		ZI (b)		ZS (c)	
		Wt%	At%	Wt%	At%	Wt%	At%
A	Si	12.45	7.98	11.86	10.02	3.05	8.50
	Al	7.20	3.54	6.28	5.53	0.88	2.55
	Ti	–	–	3.21	1.59	2.15	3.51
B	Al	4.95	3.92	12.52	9.33	13.13	7.98
	Si	8.75	9.66	9.88	7.66	5.60	3.54
	Ti	–	–	2.80	1.22	4.13	1.47

ZI mainly contained faujasite phase incorporating with zeolite Nu-5 as minority. With the presence of TiO_2, zeolite P1 and zeolite SSZ16 obtained from the TiO_2-absenced system were transformed into faujasite and zeolite Nu-5; $Na_{0.14}Al_2Si_{70}O_{143.07}(H_2O)_{0.97}$. It should be noted here that ZS and ZI were subjected to calcinations at high temperature while the pure zeolite was only dried in electric oven. Diffraction peaks of TiO_2 phase was not detected in ZS and ZI samples. Similar results were also reported by Li et al. [13] and Faghihian and Bahranifard [33] showing no TiO_2 peak, although using different zeolite types. Li et al. used commercially natural clinoptilolite and Faghihian and Bahranifard used zeolite X synthesized using metakaolin and sodium silicate as starting materials. However, synthesized temperature and time of this present work were different from Faghihian and Bahranifard in that 120 °C and 6 h for this work and 90 °C and 24 h for Faghihian and Bahranifard. The framework structure of zeolite was not destroyed with the loading of TiO_2. It was also probable that after the calcination step, the clusters of TiO_2 formed were too small to give clear diffraction patterns for ZS and ZI samples [34]. As detected by using XRF, the chemical compositions of ZS and ZI contained 6.79 and 6.43 wt% of TiO_2, respectively as shown in Table 1. Synthesized zeolites with TiO_2-absenced system, on the other hand, consisted mainly of SiO_2 and Al_2O_3 with 46.23 and 24.49 wt%, respectively and extremely low TiO_2 contents of only 0.06 wt%. The existence of TiO_2 in the TiO_2-absenced zeolite was from MK and RHA.

The average particle size of the synthesized zeolite, ZS and ZI were 0.621, 0.663 and 0.743 μm, respectively with corresponding specific surface areas of 487.1, 452.1 and 437.6 m^2/g as shown in Table 1. The average particle size was in good agreement with specific surface area being that material with smaller particles had higher specific surface area. The decreases in specific surface areas of ZS and ZI was due to the deposition of TiO_2 particles on the zeolite surfaces that filled up the pore, and the TiO_2 agglomeration/growth phenomena during the calcination treatments [17].

Fig. 4a–c shows the FE-SEM photomicrographs and EDS spectrum of synthesized products (a) synthesized zeolites, (b) ZI and (c) ZS with the data of weight and atomic percent of Si, Al and Ti elements from EDS analysis as shown in Table 2. It can be seen that the morphology of zeolite faujasite composed of various sizes of agglomerated particles with octahedral shapes [19,35] with a SiO_2/Al_2O_3 molar ratio of 3.33 as shown in Fig. 4a. This was slightly lowered than deviated from the used starting SiO_2/Al_2O_3 molar ratio of 4.0. The other particles with prismatic shape corresponded to the zeolite *P*1 [19,36] with a SiO_2/Al_2O_3 molar ratio of 3.41. The obtained SiO_2/Al_2O_3 molar ratios was similar the values of 3.21 and 3.33 detected by XRF and XRD, respectively. From the EDS in Fig. 4b, the octahedral shape of faujasite phase of ZI sample encompassed TiO_2 in the range of 4.67–5.36 wt%. While, the EDS in Fig. 4c showed TiO_2 content of ZS sample, in the range of 3.59–6.89 wt%. This result was also similar to results obtained from the XRF analysis. In addition, it can be observed that the surface morphology of ZI and ZS sample showed nanoparticles of spherical TiO_2 in the range 100–200 nm and its clusters attached onto the surfaces of zeolites as also reported by Gomez et al. [17].

The results of FTIR Spectroscopy as shown in Fig. 5 were used to examine the chemical structures of the synthesized products. The stretching and bending vibration bands of hydroxyl groups in zeolites were s observed at 3470 cm^{-1} and 1650 cm^{-1}, respectively. The broad band around 991 cm^{-1} was assigned to the internal asymmetric stretching vibration of Si—O—T (T = Si or Al) in zeolite [29,37] The presences of adsorption modes at 747 and 564 cm^{-1} were due to the external symmetric stretching of Si—O—T, while the absorption bands at 683 and 463 cm^{-1} corresponded to the Si—O—Al symmetric stretching and symmetric bending, respectively [37,38]. For the FTIR spectra of TiO_2-zeolite photocatalysts, no band of Si-O-Ti antisymmetric

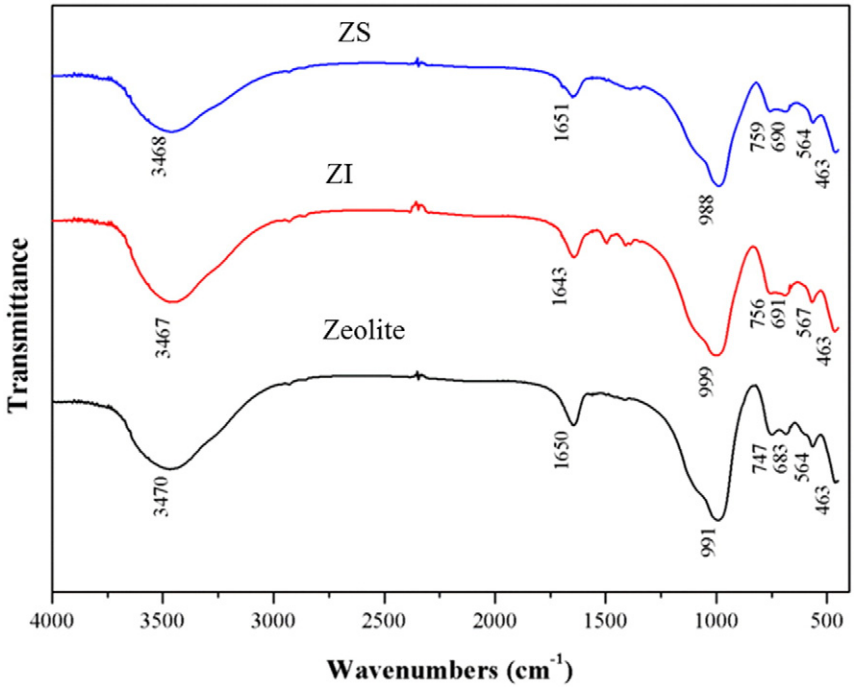

Fig. 5. FTIR spectra of synthesized products prepared by different method.

stretching vibration in the region near 960 cm^{-1} was detected. Accordingly, the replacement of the tetrahedral Si sites with Ti did not take place for both ZS and ZI samples. It was demonstrated that titanium compound was deposited on the surfaces of zeolites in a form of TiO_2 rather than the Ti incorporated into the SiO_4 framework [1,17].

The results of UV–vis diffuse reflectance spectra (UV–vis DRS) of the synthesized products and anatase TiO_2 are shown in Fig. 6a. It could be clearly seen that zeolite with no TiO_2 had the lowest intensity absorption band compared with TiO_2-zeolite photocatalysts and anatase TiO_2. The broad absorption band of ZI was found at 268.4 nm which was slightly lower than the 263.6 nm of ZS. While using pure anatase TiO_2 provided the highest intensity absorption band at 335.2 nm. The diffuse reflectance spectra presented that TiO_2-zeolite photocatalysts have a significant shift to longer wavelengths and an extension of the absorption in the visible range in comparison with that of anatase TiO_2. This result was in agreement with previous finding of Wang et al. [39]. The band gap energies of the catalysts were obtained from the Kubelka Munk theory which could be evaluated by a plot of $[F(R)h\nu]^2$ as a function of $h\nu$ [40] as shown in Fig. 6b. The calculated band-gap energies of pure anatase TiO_2, ZI and ZS were 3.24, 3.20 and 3.45 eV, respectively. These results implied that TiO_2-zeolite photocatalysts had the photocatalytic performance of TiO_2.

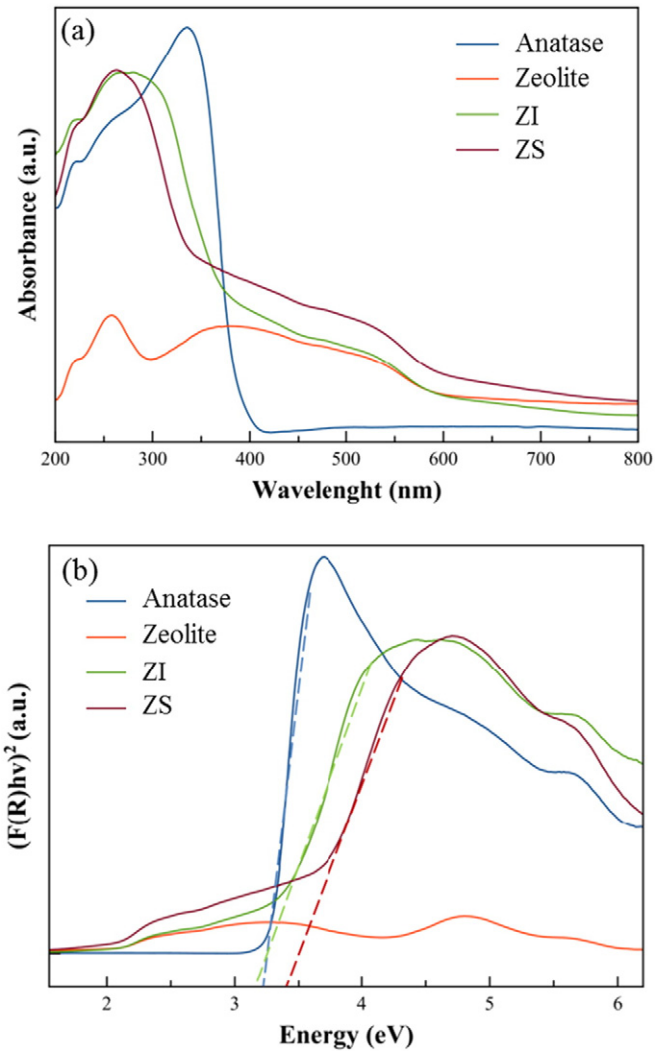

Fig. 6. Graphical representation of (a) absorbance versus wavelength and (b) Kubelka-Munk $(F(R)h\nu)^2$ versus energy of synthesized products and anatase.

3.3. Methylene blue removal efficiency and photocatalytic activity test

The degradation of MB dye was measured in the solution system to assess the photocatalytic activity of the synthesized catalysts. The activation of TiO_2 by UV light generated electron (e^-) - hole (h^+) pairs on the surfaces of material that reacted with bound O_2 or H_2O in order to generate reactive oxygen species like hydroxide radicals (OH^-), superoxide radicals (O^{2-}) and hydrogen peroxide (H_2O_2) in various chain reactions. These active species worked for disruption of organic molecule structures. In the degradation of MB ($C_{16}H_{18}N_3SCl$), the OH^- obtained from the oxidation of adsorbed water or adsorbed OH^- played a great role on the elimination of MB. For an absolute reaction, the final products of the reaction are CO_2 and H_2O [41,42] as shown in the following equation.

$$MB + \cdot OH \rightarrow \text{products}\left(CO_2 + H_2O + NH^{4+} + NO_3{}^- + SO_4{}^{2-} + Cl^-\right)$$

Fig. 7a–d shows the UV–vis absorption spectra of 20 ppm MB solution under the illumination with UV light at 250–385 nm for different durations of time with 4 catalysts viz., (a) anatase TiO_2, (b) zeolite, (c) ZI and (d) ZS. The characteristic absorption spectrum of MB at 663.8 nm was examined as a function of the UV light revelation time. The results revealed that the major peak of MB gradually was reduced over time accompanied by a significant shift of the peak in the case of using anatase TiO_2 as a photocatalyst similar to Nagarjuna et al.'s work [43] and Zuo et al.'s work [44]. While using zeolite powder with no TiO_2, the absorption peak of MB decreased by a half from initial concentration of MB indicating the adsorption capacity of zeolite alone could not hand on the photocatalytic performance. However, adsorption of the MB on the photocatalyst surface was one of the significant reaction steps in degradation [33]. In using ZI and ZS as the photocatalysts, the intensity of an absorption peak of MB from initial concentration (2.78) was obviously reduced after adsorption in the dark or 0 min of UV illumination time demonstrating not only the adsorption capacity of zeolite but also TiO_2 in comparison with anatase TiO_2. In addition, the photocatalytic activity could be enhanced by TiO_2-containing zeolite at low concentration (calculated as 7.6 mg and 7.1 mg of TiO_2 for ZS and ZI, respectively) while the amount of anatase TiO_2 was 0.1 g in this test. The intensity of an absorption peak of MB gradually decreased with time as shown in Fig. 7c and d. It was worth noting here that the ZI sample showed slightly better MB degradation performance than ZS sample. This was due to the incorporation of TiO_2 chiefly on the external surface of zeolite in the impregnation method which was slightly better than the solvothermal synthesis method. To prove photodegradation performance, MB decolorization experiments of ZI and ZS under illumination of longer wavelength UV lamp (300–365 nm; Osram Ultra Vitalux 300 W) were carried out at room temperature. The results proved that under illumination with longer wavelength (300–365 nm), the main peak of MB was higher than that illuminated under shorter wavelength (250–385 nm) in every illumination time as shown in Fig. 8. This result indicated the photodegradation effect of ZI and ZS. Shorter UV wavelength carried more energy thus affecting the MB degradation. The photodegradation of ZI and ZS using different sources of illumination reflected the influence of wavelengths and light intensity on the reaction rates of degradation [45]. Moreover, to reveal a TiO_2-doping limitation of the photocatalysts, effect of TiO_2 doped contents in ZI composite on photodegradation performance were studied, as shown in Fig. 9. Absorption peak of MB of 20wt% TiO_2 doped ZI was compared with that of 5wt% TiO_2 doped ZI under 300–365 nm illumination. It is obvious that without illumination, the absorption peaks of MB of both samples were similar that resulted from only adsorption phenomena. For 3 h of illumination time with wavelength of 300–365 nm, absorption peak of MB of 20 wt% TiO_2 doped ZI sample slightly lowered than 5wt% TiO_2 doped ZI sample indicating the doping limitation of photocatalysts. Therefore, effect of TiO_2 content on photocatalytic rate of MB dye was

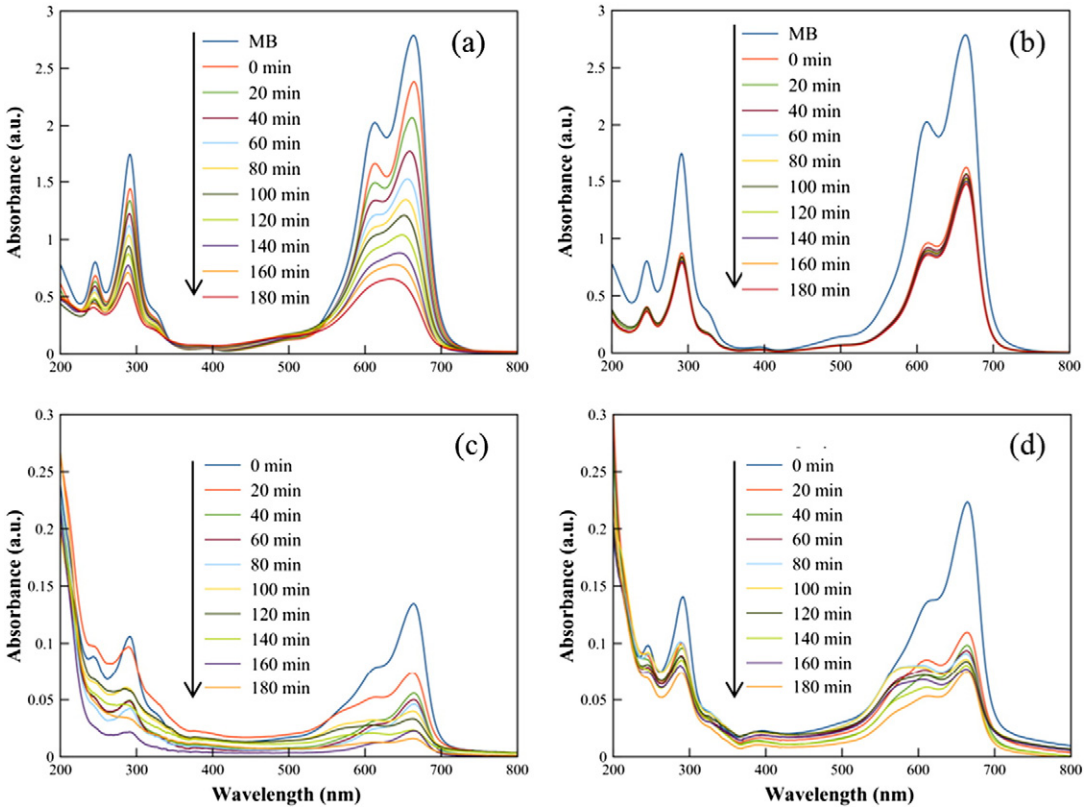

Fig. 7. UV–vis absorbance spectra of MB as a function of illumination times with (a) anatase, (b) zeolite, (c) ZI and (d) ZS.

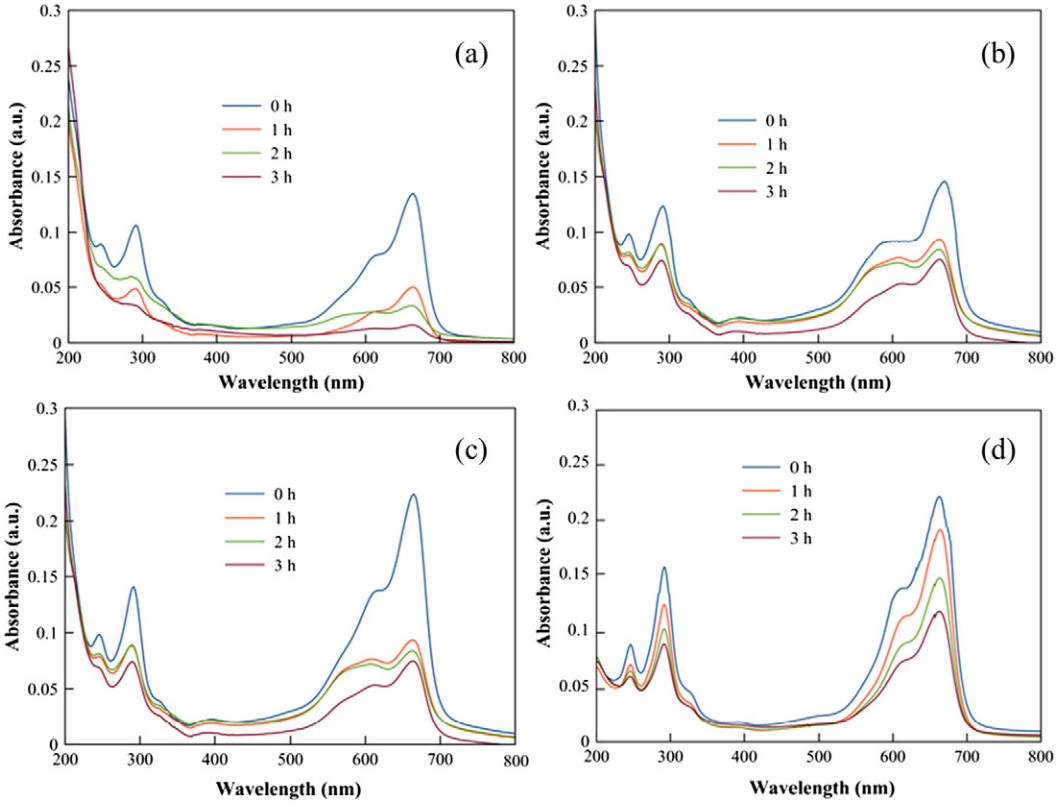

Fig. 8. UV–vis absorbance spectra of MB as a function of illumination times with difference of UV wavelengths (a) ZI; 250–385 nm, (b) ZI; 300–365 nm, (c) ZS; 250–385 nm and (d) ZS; 300–365 nm.

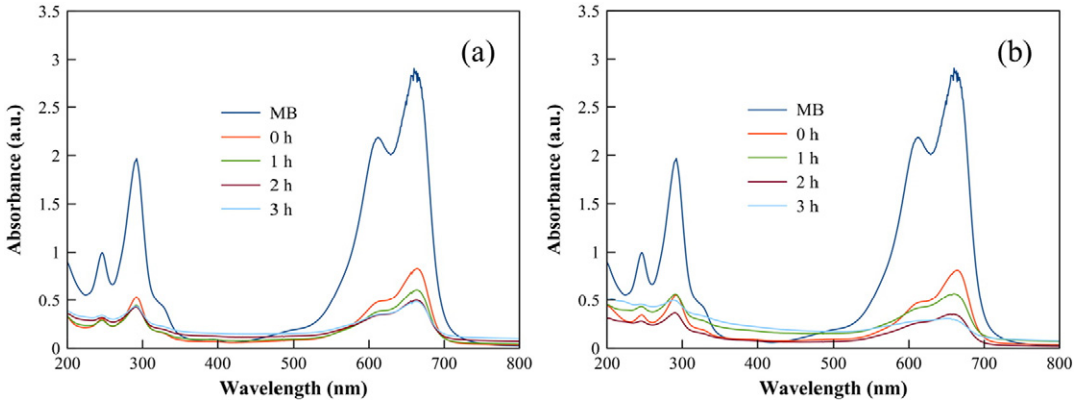

Fig. 9. UV–vis absorbance spectra of MB as a function of illumination times with difference of TiO_2 doping contents in ZI (a) 5 wt% and (b) 20 wt% under illumination with 300–365 nm of UV wavelength.

insignificant when added greater than 5 wt%. However, TiO_2 doping limitation reported in Wang et al.'s work [1] was at 20 wt% TiO_2. It was worth noting here that zeolite types used were different in that faujasite and Na-Y zeolites were used in this work and Wang's work, respectively. The limitation was due to a reduction in specific surface area of TiO_2 doped zeolites.

Fig. 10 shows the adsorption and photocatalytic degradation of MB with time with various synthesized catalysts. MB removal efficiency was calculated by the remaining concentration of MB in the solution after illumination at 1, 2 and 3 h. The decolorization rates after 30 min of the adsorption equilibrium in dark conditions of MB solution for both of ZI and ZS were faster than that with zeolite and anatase TiO_2. It was worth noting here that the MB degradation with zeolite without TiO_2 took place only via adsorption phenomena not via photocatalytic process. In the adsorption process before UV illumination, the adsorption capacity of MB by anatase TiO_2 was relatively low and was significantly improved by zeolite adsorption. More than 90% of MB was removed by TiO_2-containing zeolites within 30 min as shown in Fig. 11, ascribing to its high surface area and high adsorbability of zeolitic characteristics. In the process of photodegradation, anatase TiO_2 was a high potential photocatalysts achieving 82% of MB photodegradation in 3 h. Nevertheless, the degradation by pure anatase TiO_2 was lower than that of TiO_2-zeolite photocatalyst. The high decolorization rate was caused by the high porosity and proper pore sizes of zeolites. MB dye had an effective molecular diameter of approximately 0.77 nm which was smaller than that of synthesized zeolite with the average pore size of approximately 1.36 nm [19]. MB could be stored in the large internal surfaces and on the external surfaces of both zeolite and TiO_2. The MB removal efficiency was 99.43% and 97.32% at 3 h illumination while the adsorption efficiency (without illumination) was 95.2% and 92.0% at 20 ppm MB concentration using ZI and ZS samples, respectively. When compared with Faghihian and Bahranifard's finding [33], MB removal efficiency using zeolite X was 90% as a concern of similar zeolite to MB solution ratio. For using natural clinoptilolite of Li et al.'s work, the removal efficiency test was performed using methyl orange as a tester and the result was 85–95% removal efficiency. In addition to the adsorption, the adherence of MB on zeolite could be from cation exchange capacity of zeolite [2]. This proposed that the total rate of the adsorption procedure was controlled by chemisorption which complicated valency forces through exchange or sharing of electrons between the sorbent (zeolite) and sorbate (MB solution) [46]. It was quite obvious that MB removal of ZI and ZS samples

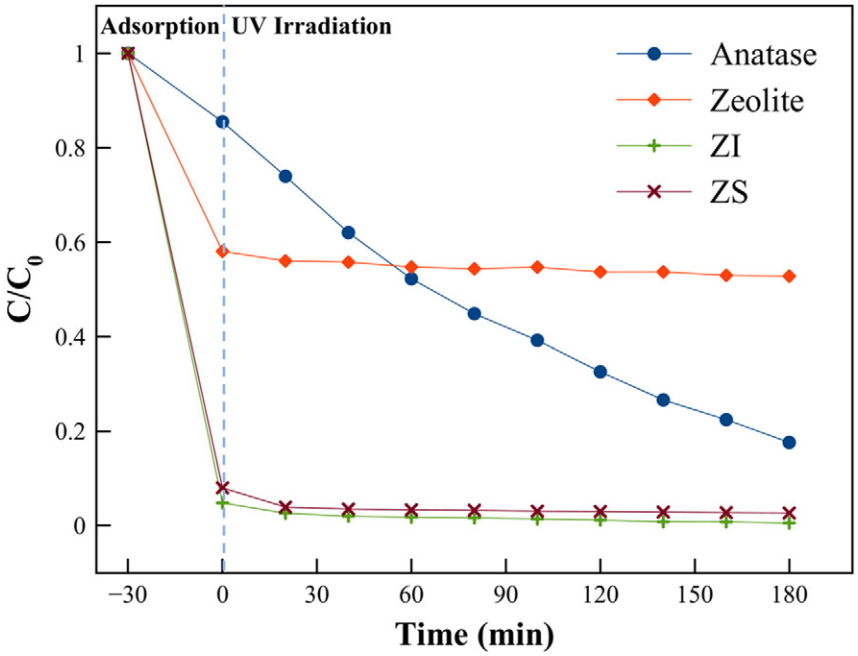

Fig. 10. Adsorption and photocatalytic degradation of MB from initial concentrations of 20 mg/l with time with different photocatalysts.

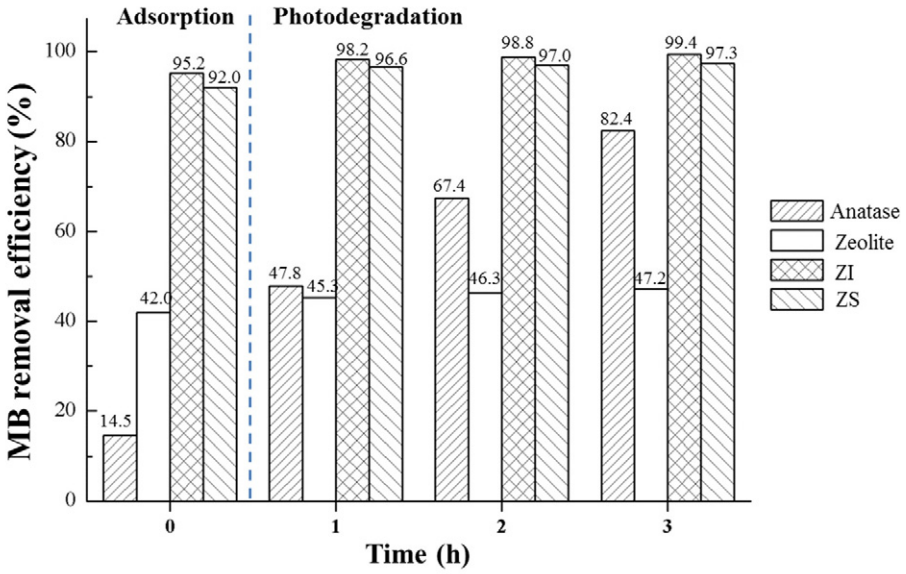

Fig. 11. The percent of adsorption and photodegradation of MB from initial concentrations of 20 mg/l with different photocatalysts.

was mainly from adsorption process and was slightly increased by photodegradation. However, the total photocatalytic activity of ZI and ZS samples was not yet measured in term of quantity which would be figured out in the next phase. It was worth noting here that the used TiO_2 contents in ZI and ZS samples were 16 times lower than pure TiO_2 anatase.

4. Conclusion

Synthesized TiO_2-zeolite photocatalyst using solvothermal method was successfully prepared with metakaolin and rice husk ash as starting materials and transparent titanium solution as TiO_2 source. The synthesized TiO_2-zeolite photocatalyst using impregnation method (ZI) was also performed for the comparison. The photodegradation efficiency of synthesized TiO_2-zeolite photocatalyst was found to be better TiO_2-absenced zeolites. The band gap energy of ZI was lower than ZS (3.20 eV for ZI and 3.45 eV for ZS). The MB removal efficiency was 99.43% and 97.32% at 20 ppm MB concentration using ZI and ZS samples, respectively. While these were 82.37% and 47.21% at 20 ppm MB concentration using pure TiO_2 anatase and pure synthesized zeolites, respectively. It was demonstrated that association of the adsorption and photocatalytic degradation enhanced the removal efficiency. The synthesis of zeolite nanocrystals using natural raw materials viz., rice husk and kaolin clays is economical advantageous and thus offers valuable option for cleaning up the contaminated environment.

Acknowledgements

This work was financially supported by the Thailand Research Fund (TRF) through the Royal Golden Jubilee Ph.D. program, (Grant No. PHD/0011/2557), the Graduate School, Chiang Mai University, and the Khon Kaen University and TRF under TRF Senior Research Scholar Contract No. RTA5780004.

References

[1] C.C. Wang, C.K. Lee, M.D. Lyu, L.C. Juang, Photocatalytic degradation of C.I. Basic violet 10 using TiO_2 catalysts supported by Y zeolite: an investigation of the effects of operational parameters, Dyes Pigments 76 (2008) 817–824.
[2] A.K. Hammed, N. Dewayanto, D. Du, M.H.A. Rahim, M.R. Nordin, Novel modified ZSM-5 as an efficient adsorbent for methylene blue removal, J. Environ. Chem. Eng. 4 (2016) 2607–2616.
[3] W. Yuan, P. Yuan, D. Liu, W. Yu, M. Laipan, L. Deng, F. Chen, In situ hydrothermal synthesis of a novel hierarchically porous TS-1/modified-diatomite composite for methylene blue (MB) removal by the synergistic effect of adsorption and photocatalysis, J. Colloid Interface Sci. 462 (2016) 191–199.
[4] P.A. Deveau, F. Arsac, P.X. Thivel, C. Ferronato, F. Delpech, J.M. Chovelon, P. Kaluzny, C. Monnet, Different methods in TiO_2 photodegradation mechanism studies: gaseous and TiO_2-adsorbed phases, J. Hazard. Mater. 144 (2007) 692–697.
[5] P. Klankaw, C. Chawengkijwanich, N. Grisdanurak, S. Chiarakorn, The hybrid photocatalyst of TiO_2-SiO_2 thin film prepared from rice husk silica, Superlattice. Microst. 51 (2012) 343–352.
[6] S. Ko, J. Pekarovic, P.D. Fleming, P.A. Gur, High performance nano-titania photocatalytic paper composite. Part I: experimental design study for TiO_2 composite sheet using a natural zeolite microparticle system and its photocatalytic property, Mater. Sci. Eng. B 166 (2010) 127–131.
[7] G. Jiang, X. Zheng, Y. Wang, T. Li, X. Sun, Photo-degradation of methylene blue by multi-walled carbon nanotubes/TiO_2 composites, Powder Technol. 207 (2011) 465–469.
[8] S. Chin, E. Park, M. Kim, J. Jeong, G.B. Bae, J. Jurng, Preparation of TiO_2 ultrafine nanopowder with large surface area and its photocatalytic activity for gaseous nitrogen oxides, Powder Technol. 206 (2011) 306–311.
[9] Y. Kuwahara, J. Aoyama, K. Miyakubo, T. Eguchi, T. Kamegawa, K. Mori, H. Yamashita, TiO_2 photocatalyst for degradation of organic compounds in water and air supported on highly hydrophobic FAU zeolite: structural, sorptive, and photocatalytic studies, J. Catal. 285 (2012) 223–234.
[10] T. Kamegawa, R. Kido, D. Yamahana, H. Yamashita, Design of TiO_2-zeolite composites with enhanced photocatalytic performances under irradiation of UV and visible light, Microporous Mesoporous Mater. 165 (2013) 142–147.
[11] B. Wang, G. Zhang, Z. Sun, S. Zheng, Synthesis of natural porous minerals supported TiO_2 nanoparticles and their photocatalytic performance towards rhodamine B degradation, Powder Technol. 262 (2014) 1–8.
[12] S. Liu, M. Lim, R. Amal, TiO_2-coated natural zeolite: rapid humic acid adsorption and effective photocatalytic regeneration, Chem. Eng. Sci. 105 (2014) 46–52.
[13] F. Li, Y. Jiang, L. Yu, Z. Yang, T. Hou, S. Sun, Surface effect of natural zeolite (clinoptilolite) on the photocatalytic activity of TiO_2, Appl. Surf. Sci. 252 (2005) 1410–1416.
[14] W. Zhang, F. Bi, Y. Yu, H. He, Phosphoric acid treating of ZSM-5 zeolite for the enhanced photocatalytic activity of TiO_2/HZSM-5, J. Mol. Catal. A Chem. 372 (2013) 6–12.
[15] F.F.B. Nóbrega, A.N.B. Polo, A.M. Benedetti, M.M.D. Leão, V.S. Santana, N.R.C.F. Machado, Evaluation of photocatalytic activities of supported catalysts on NaX zeolite or activated charcoal, J. Hazard. Mater. 263 (2013) 61–66.
[16] M. Takeuchi, T. Kimura, M. Hidaka, D. Rakhmawaty, M. Anpo, Photocatalytic oxidation of acetaldehyde with oxygen on TiO_2/ZSM-5 photocatalysts: effect of hydrophobicity of zeolites, J. Catal. 246 (2007) 235–240.
[17] S. Gomez, C.L. Marchena, L. Pizzio, L. Pierella, Preparation and characterization of TiO_2/HZSM-11 zeolite for photodegradation of dichlorvos in aqueous solution, J. Hazard. Mater. 258-259 (2007) 19–26.
[18] C. Yang, C. Ke, Y. Liu, Y. Inoue, Molecular Encapsulation: Organic Reactions in Constrained Systems: Reaction Control by Molecular Recognition-a Survey from the Photochemical Perspective, John Willey & Sons, United Kingdom, 2010.
[19] N. Setthaya, P. Chindaprasirt, K. Pimraksa, Preparation of zeolite nanocrystals via hydrothermal and solvothermal synthesis using of rice husk ash and metakaolin, Mater. Sci. Forum 872 (2016) 242–247.
[20] K. Byrappa, M. Yoshimura, Handbook of Hydrothermal Technology: A Technology for Crystal Growth and Materials Processing, William Andrew, New York, 2001.

[21] M. Inoue, Chemical Processing of Ceramics: Solvothermal Synthesis, second ed. Taylor & Francis, New York, 2005.
[22] L.H. Kallai, I. Lapides, Reactions of kaolinites and metakaolinites with NaOH-comparison of different samples (part 1), Appl. Clay Sci. 35 (2007) 99–107.
[23] S. Chandrasekhar, P.N. Pramada, Microwave assisted synthesis of zeolite A from metakaolin, Microporous Mesoporous Mater. 108 (2008) 152–161.
[24] A.Y. Atta, B.Y. Jibril, B.O. Aderemi, S.S. Adefila, Preparation of analcime from local kaolin and rice husk ash, Appl. Clay Sci. 61 (2012) 8–13.
[25] M. Kazemimoghadam, T. Mohammadi, Preparation of nano pore hydroxysodalite zeolite membranes using of kaolin clay and chemical sources, Desalination 278 (2011) 438–442.
[26] Z. Zhou, G. Jin, H. Liu, J. Wu, J. Mei, Crystallization mechanism of zeolite A from coal kaolin using a two-step method, Appl. Clay Sci. 97-98 (2014) 110–114.
[27] K. Pimraksa, P. Chindaprasirt, N. Setthaya, Synthesis of zeolite phases from combustion by-products, Waste Manag. 28 (2010) 1122–1132.
[28] I.O. Ali, A.M. Hassan, S.M. Shaaban, K.S. Soliman, Synthesis and characterization of ZSM-5 zeolite from rice husk ash and their adsorption of Pb^{2+} onto unmodified and surfactant-modified zeolite, Sep. Purif. Technol. 83 (2011) 38–44.
[29] A. Tadjarodi, M. Haghverdi, V. Mohammadi, Preparation and characterization of nano-porous silica aerogel from rice husk ash by drying at atmospheric pressure, Mater. Res. Bull. 47 (2012) 2584–2589.
[30] K.P. Dey, S. Ghosh, M.K. Naskar, Organic template-free synthesis of ZSM-5 zeolite particles using rice husk ash as silica source, Ceram. Int. 39 (2013) 2153–2157.
[31] N. Setthaya, C. Pindi, P. Chindaprasirt, K. Pimraksa, Synthesis of faujasite and analcime using of rice husk ash and metakaolin, Adv. Mater. Res. 770 (2013) 209–212.
[32] S. Sun, J. Ding, J. Bao, C. Gao, Z. Qi, X. Yang, B. He, C. Li, Photocatalytic degradation of gaseous toluene on Fe-TiO_2 under visible light irradiation: a study on the structure, activity and deactivation mechanism, Appl. Surf. Sci. 258 (2012) 5031–5037.
[33] H. Faghihian, A. Bahranifard, Application of TiO_2–zeolite as photocatalyst for photodegradation of some organic pollutants, Iran, J. Catal. 1 (2011) 45–50.
[34] A.H. Alwash, A.Z. Abdullah, N. Ismail, TiO_2-zeolite Y catalyst prepared using impregnation and ion-exchange method for sonocatalytic degradation of amaranth dye in aqueous solution, World Acad. Sci. Eng. Technol. 7 (2013) 375–383.
[35] T.F. Chaves, H.O. Pastore, D. Cardoso, A simple synthesis procedure to prepare nanosized faujasite crystals, Microporous Mesoporous Mater. 161 (2012) 67–75.
[36] R.M. Mohamed, I.A. Mkhalid, M.A. Barakat, Rice husk ash as a renewable source for the production of zeolite NaY and its characterization, Arab. J. Chem. 8 (2015) 48–53.
[37] P. Thuadaij, K. Pimraksa, A. Nuntiya, Synthesis of high cation exchange capacity faujasite from high calcium fly ash, Aust. J. Basic Appl. Sci. 6 (2012) 194–208.
[38] L.P. Wu, X.J. Li, Z.H. Yuan, Y. Chen, The fabrication of TiO_2-supported zeolite with core/shell heterostructure for ethanol dehydration to ethylene, Catal. Commun. 11 (2009) 67–70.
[39] C. Wang, H. Shia, Y. Li, Synthesis and characterization of natural zeolite supported Cr-doped TiO_2 photocatalysts, Appl. Surf. Sci. 258 (2012) 4328–4333.
[40] H. Yahiro, T. Miyamoto, N. Watanabe, H. Yamaura, Photocatalytic partial oxidation of α-methylstyrene over TiO_2 supported on zeolites, Catal. Today 120 (2007) 158–162.
[41] N. Soltani, E. Saion, M.Z. Hussein, M. Erfani, A. Abedini, G. Bahmanrokh, M. Navasery, P. Vaziri, Visible light-induced degradation of methylene blue in the presence of photocatalytic ZnS and CdS nanoparticles, Int. J. Mol. Sci. 13 (2012) 12242–12258.
[42] J. Mo, Y. Zhang, Q. Xu, J.J. Lamson, R. Zhao, Photocatalytic purification of volatile organic compounds in indoor air: a literature review, Atmos. Environ. 43 (2009) 2229–2246.
[43] R. Nagarjuna, S. Roy, R. Ganesan, Polymerizable sol-gel precursor mediated synthesis of TiO_2 supported zeolite-4A and its photodegradation of methylene blue, Microporous Mesoporous Mater. 211 (2015) 1–8.
[44] R. Zuo, G. Du, W. Zhang, L. Liu, Y. Liu, L. Mei, Z. Li, Photocatalytic degradation of methylene blue using TiO_2 impregnated diatomite, Adv. Mater. Sci. Eng. 170148 (2014).
[45] I. Ahmad, Q. Fasihullah, F.H.M. Vaid, Effect of light intensity and wavelengths on photodegradation reactions of riboflavin in aqueous solution, J. Photochem. Photobiol. B 82 (2006) 21–27.
[46] I.A.W. Tan, A.L. Ahmad, B.H. Hameed, Adsorption of basic dye on high-surface-area activated carbon prepared from coconut husk: equilibrium, kinetic and thermodynamic studies, J. Hazard. Mater. 154 (2008) 337–346.

J Polym Environ
DOI 10.1007/s10924-016-0818-z

ORIGINAL PAPER

Optimization of Biodegradable Foam Composites from Cassava Starch, Oil Palm Fiber, Chitosan and Palm Oil Using Taguchi Method and Grey Relational Analysis

Pornnapa Kasemsiri[1] · Nattakan Dulsang[1] · Uraiwan Pongsa[2] · Salim Hiziroglu[3] · Prinya Chindaprasirt[4]

© Springer Science+Business Media New York 2016

Abstract The objective of this work was to investigate properties of biodegradable foam manufactured from cassava starch containing the combination of additives. The mix proportions of starch foam composites were designed using Taguchi method. L16 orthogonal array with three factors i.e. oil palm fiber content, chitosan content and palm oil content at four-levels each was chosen for optimization. Based on the signal-to-noise (S/N) ratio results, oil palm fiber and palm oil enhanced the flexural strength and water resistance of starch foam composites. Addition of chitosan reduced the density and increased the flexibility of samples. The analysis of variance of results indicated that chitosan was the major parameter influencing density, flexural strength and water absorption index. The oil palm fiber and palm oil were main parameters affecting water solubility index. The multi-linear regression models were developed to predict the properties of starch foam composites. The best mix proportion of starch foam composite was obtained from Grey relational analysis. The starch foam composite could be used as an alternative packaging for dry material.

Keywords Biodegradable · Foam composite · Taguchi method · Grey relational analysis

✉ Prinya Chindaprasirt
prinya@kku.ac.th

[1] Sustainable Infrastructure Research and Development Center and Department of Chemical Engineering, Faculty of Engineering, Khon Kaen University, Khon Kaen 40002, Thailand

[2] Division of Industrial Engineering Technology, Faculty of Industry and Technology, Rajamangala University of Technology Rattanakosin Wang Klai Kang Won Campus, Prachuap Khiri Khan 77110, Thailand

[3] Department of Natural Resource Ecology and Management, Oklahoma State University, 303-G Agricultural Hall, Stillwater, OK 74078, USA

[4] Sustainable Infrastructure Research and Development Center and Department of Civil Engineering, Faculty of Engineering, Khon Kaen University, Khon Kaen 40002, Thailand

Introduction

Petroleum-based polymers have been extensively used for various applications such as packaging, thermal insulator and transportation due to their low density, good mechanical properties and low cost [1–3]. However, the increasing of petroleum-based products consumption has created a critical environmental problem. These products require several years to degrade and in many instances generate toxic decomposition products [4–8]. Natural polymers produced from renewable source such as native starch, chitosan and natural fiber are good alternative to replace petroleum-based polymers [9–11]. Nowadays, the biodegradable polymer materials are used in various areas such as agriculture, medicine, automotive, packaging and drug release [12].

Starch has been widely used to produce biodegradable foam because of its low cost, low density, low toxicity and biodegrability [13, 14]. Furthermore, the production of starch foam is a simple technique using water as the blowing agent and baking of foam [1, 13]. However, starch foam still has some limitations due to its poor mechanical properties and high water absorption [15]. Recently, a number of researchers have tried to tackle these drawbacks in order to improve the overall properties of starch foam. The starch reinforced with lignocellulosic fiber such as

Published online: 19 August 2016

cassava bagasse [16], kraft pulp and soft wood can enhance the physical and mechanical properties of products [11]. Oil palm fiber is obtained from the oil palm empty fruit bunch (OPEFB) which is the waste of crude palm oil manufacturing. OPEFB consists of 44.4 % cellulose, 30.9 % hemicellulose and 14.2 % lignin [17, 18]. Therefore, the oil palm fiber has attracted a large attention for use as reinforcement in various types of polymer composites such as natural rubber, epoxy, urethane foam and starch. Ibrahim et al. [19] investigated the starch based biodegradable composite containing oil palm fiber and flax fiber. The hybrid composites with oil palm fiber and flax at 50 wt% provided the highest tensile strength.

Chitosan is a biopolymer material manufactured from deacetylation of chitin in exoskeleton of crustaceans [20]. It has been used for various applications such as medical, cosmetic and biodegradable materials, due to its non-toxic, excellent strength and elongation. Chitosan in combination with lignocellulosic fiber substantially improved the mechanical properties of polymer composites [21]. Kaisangsri et al. [16] reported that the biodegradable foam containing 30 % kraft pulp and 4 % chitosan had the density and mechanical properties similar to that of commercial polystyrene foam. Furthermore, the addition of kraft pulp and chitosan also reduced the water absorption and water solubility indices. Generally, the water resistance of biodegradable foam can be enhanced by two main strategies. The first strategy involves chemically modified functional group of starch [22]. The second method is by addition of hydrophobic materials such as latex [23], beewax [24] and palm oil [10]. Palm oil is an edible vegetable oil extracted from the ripe fruits of oil palm. The oil palm trees are mainly planted in the Southeat Asia i.e. Thailand, Malaysia and Indonesia [25]. The output of palm oil is very high compared with that of other edible vegetable oils in the world [26]. Therefore, palm oil is an inexpensive and abundant additive for water resistance of materials [27]. Khaisaengsri et al. [10] also observed that the addition of 15 wt% palm oil remarkably enhanced the water solubility and water absorption of starch foam. However, the flexural and compressive strength of starch foam decreased with increasing palm oil content. Polat et al. [24] also investigated the effect of hydrophobic material such a beewax on the properties of corn starch foam containing corn husk fiber and kaolin. The water resistance increased with increasing beewax content. However, the addition of beewax adversely affected the mechanical properties due to the prevention of homogenous foam formation from beewax's hydrophobic characteristic [28, 29]. Taguchi's method is an experimental design commonly used to evaluate the influence of parameters on a selected response [30]. Furthermore, Taguchi's method can also reduce the number of process parameters on product response. The major factors affecting the response are separately considered. The traditional Taguchi method has been applied to optimize a single response. In the case of multi response optimization problem, it can be analyzed by Taguchi method coupled with Grey relational analysis. This approach can optimize the multi response which is converted to a single relational grade. Recently, many literatures have reported about the relationship between optimal mixing proportion of material, processing condition and properties [31–33]. From the literatures, the optimize mix proportions of the potential additives such as oil palm fiber, chitosan and palm oil is one alternative to improve the density, mechanical properties and water resistance of the biodegradable foam based starch.

Currently, there is no information about optimizing mixing parameters of biodegradable based starch foam. Therefore, this research aims to study the effect of additions of chitosan, oil palm fiber and palm oil on the properties of starch foam using Taguchi's method. The chemical compatibility, physical and mechanical properties as well as water resistance of the obtained biodegradable foam composites are also observed. Furthermore, ANOVA interaction is performed to investigate the significance of relative interdependence of biodegradable foam mix proportions. The multi response optimization of overall properties of starch foam composite is determined by Grey relational analysis.

Materials and Methods

Materials

Cassava starch was from Bangkok Interfood Ltd., Thailand. Oil palm fiber with average particle size of 180 μm was used. Palm oil was obtained from Lam Soon PCL, Thailand. Chitosan was from Union science, Co., Ltd. with average particle size of 150 μm and degree of deacetylation of 92.18 %.

Taguchi Experimental Design

In this study, the three factors i.e. chitosan content, oil palm fiber content, palm oil content with four levels are used to optimize the properties of biodegradable foam composite. The compositions of three factors were calculated on the dry mass of starch. The parameters and their variation levels are shown in Table 1. A total sixteen experiments derived from the L_{16} (4^3) orthogonal as depicted in Table 2 was used.

To investigate the optimum design of factors and levels, the signal to noise (S/N) ratio is used. The signal is the

Table 1 Factors and factor levels

Levels	Factors		
	Oil palm fiber (%wt): A	Chitosan (%wt): B	Palm oil (%wt): C
1	9	0	0
2	11	2	5
3	13	4	10
4	15	6	15

Table 2 L_{16} (4^3) orthogonal array

Mix No.	Oil palm fiber (%wt)	Chitosan (%wt)	Palm oil (%wt)
1	9	0	0
2	9	2	5
3	9	4	10
4	9	6	15
5	11	0	5
6	11	2	0
7	11	4	15
8	11	6	10
9	13	0	10
10	13	2	15
11	13	4	0
12	13	6	5
13	15	0	15
14	15	2	10
15	15	4	5
16	15	6	0

desirable of output characteristics. The noise represents the undesirable output characteristics. There are three categories of S/N ratio i.e. (1) nominal is better, (2) smaller is better and (3) larger is better [30]. In this study, the larger-better type quality characteristic provides the better performance in the flexural strength of biodegradable composites. Therefore, the "larger is better" was selected for the optimization of parameters, as described in Eq. (1) [34, 35]

$$(\text{S/N}) = -10\log\left[1/R\sum_{f=1}^{R}1/y_i^2\right] \quad (1)$$

In the case of density and water resistance of the obtained foams, the lower values give better performance. Hence, the "smaller is better" was selected as described in Eq. (2) [34, 35]

$$(\text{S/N}) = -10\log\left[1/R\sum_{f=1}^{R}y_i^2\right] \quad (2)$$

where, R is the number of all data points and y_i is the value of the i^{th} data point.

Grey Relational Analysis

Grey relational analysis is a suitable approach for solving the problems with complicated inter relationships between multiple factor and variables. The multiple response optimization problems can be converted to a single response optimization [36]. The results of grey relational analysis are calculated using the obtained data from Taguchi method. The highest overall grey relational represents the optimal parametric combination [37]. Grey relational analysis depends on the characteristics of original sequence data. The original reference sequence and sequence for comparison are $x_o(k)$ and $x_i(k)$, i = 1, 2,…, m; k = 1, 2,…, n, respectively, where m is the total number of experiment to be considered, and n is the total number of observation data. Data preprocessing converts the original sequence to a comparable sequence.

In this work, the multi responses such a density, flexural strength and water resistance are optimized. The lower-the-better quality characteristic is used to minimize the density and water resistance, as expressed in Eq. (3). The flexural strength of the starch foam composites follows the larger-the-better criterion as shown in Eq. (4) [38]

$$x_i(k) = \frac{\max y_i(k) - y_i(k)}{\max y_i(k) - \min y_i(k)} \quad (3)$$

$$x_i(k) = \frac{y_i(k) - \min y_i(k)}{\max y_i(k) - \min y_i(k)} \quad (4)$$

where $x_i(k)$ is the value after the Grey relational generation, min $y_i(k)$ is the smallest value of $y_i(k)$ for the kth response, and max $y_i(k)$ is the largest value of $y_i(k)$ for the k^{th} response.

Grey Relational Coefficients and Grey Relational Grades

The Grey relational coefficient is calculated from the pre-processed sequences as follows [32, 38].

$$\gamma(x_o^*(k), x_i^*(k)) = \frac{\Delta_{\min} + \zeta\Delta_{\max}}{\Delta_{0i}(k) + \zeta\Delta_{\max}} \quad (5)$$

$0 < \gamma(x_o^*(k),\ x_i^*(k) \leq 1$

where $\Delta_{0i}(k)$ is the deviation sequence of reference sequence $x_0^*(k)$ comparability sequence $x_i^*(k)$, namely $\Delta_{0i}(k) = \left|x_0^*(k) - x_i^*(k)\right|$, $\Delta_{\max} = \overset{\max.}{\forall j \in i}\ \overset{\max.}{\forall k}\left|x_0^*(k) - x_j^*(k)\right|$, $\Delta_{\min} = \overset{\min.}{\forall j \in i}\ \overset{\min.}{\forall k}\left|x_0^*(k) - x_j^*(k)\right|$, ζ is the distinguishing coefficient, $\zeta \in [0, 1]$. If all the process parameters have equal weighting, ζ is set to be 0.5.

A Grey relational grade is a weighted sum of the Grey relational coefficients and is obtained as follows.

$$\gamma(x_o^*, x_i^*) = \sum_{k=1}^{n} \beta_k \gamma(x_o^*(k), x_i^*(k))$$

$$\sum_{k=1}^{n} \beta_k = 1 \quad (6)$$

Grey relational grade $\gamma(x_o^*, x_i^*)$ means the level of correlation between the reference and comparability sequence.

Biodegradable Foam Composite Preparation

The biodegradable foam matrix was prepared by adding 30 ml of water to 30 g cassava starch and mixed for 5 min using kitchen aid mixer (Electrolux EHM 2000). The additives viz., oil palm fiber, palm oil and chitosan solution in 1 % acetic acid were added into starch matrix and mixed for another 5 min at 80 °C to prepare compounds. The proportions of all additives are described in Table 2. The obtained compound was poured in 100 mm × 100 mm × 6.5 mm mold and then compressed with hydraulic press using a pressure of 4.0 MPa at 230 °C for 5 min. Schematic of sample preparation is shown in Fig. 1.

Biodegradable Foam Composite Characterization

Fourier Transform Infrared Spectroscopy (FTIR)

Attenuated total reflection infrared (FTIR-ATR) spectra of all samples were performed using Bruker Tensor 27 spectrometer in the range of 4000–650 cm^{-1}. All spectra were recorded as a function of time with 64 scans at a resolution of 4 cm^{-1}.

Density

The density of biodegradable foam composite was calculated from the relationship between mass (g) and volume (cm^3) [28, 39]. The specimens with dimensions of 100 mm × 20 mm × 6.3 mm were weighted to the accuracy of 0.001 g. The volume of specimen was evaluated by multiplying the length, width and thickness. The averaged density values were determined from ten specimens.

Morphology of Biodegradable Foam Composite

The cross-section of biodegradable foam composite was examined using a scanning electron microscope (SEM) (Hitachi model S-3000 N) at an acceleration voltage of 20 kV. All samples were cut to 3 mm and coated with gold using an ion sputtering device.

Mechanical Properties

A universal testing machine (Instron, Model 5567) equipped with a 10 kN load cell was used to investigate the flexural strength of biodegradable foam composites in accordance with ASTM D 790-10. The test was performed in a 3-point bending mode with a support span of 100 mm at the crosshead speed of 2.67 mm/min.

Water Resistance

Water absorption index (WAI) and water solubility (WSI) of biodegradable foam composites were evaluated following AACC method 56–20 (1983). The sample weighing 10–20 mg was dispersed in 40 ml distilled water in pre-weight centrifuge tubes and then placed in a shaking water bath at 30 °C for 30 min. The sample was centrifuged for 30 min. The supernatants were decanted into pre-weight aluminum dishes and dried at 105 °C for 24 h, and weighed. The remaining sediment with tube was then weighted. WAI and WSI were calculated following Eqs. (7) and (8).

$$\text{WAI} = \frac{\text{Weight of tube with sediment} - \text{Weight of tube}}{\text{Weight of sample}} \quad (7)$$

$$\text{WSI} = \frac{\text{Weight of dish with solid} - \text{Weight of dish}}{\text{Weight of sample}} \times 100\,\% \quad (8)$$

Results and Discussion

Characterization of chemical interaction between starch and additives

FTIR spectroscopy was used to study the interactions between starch and additives. The FTIR spectra of starch, oil palm fiber, palm oil and chitosan are shown in Fig. 2.

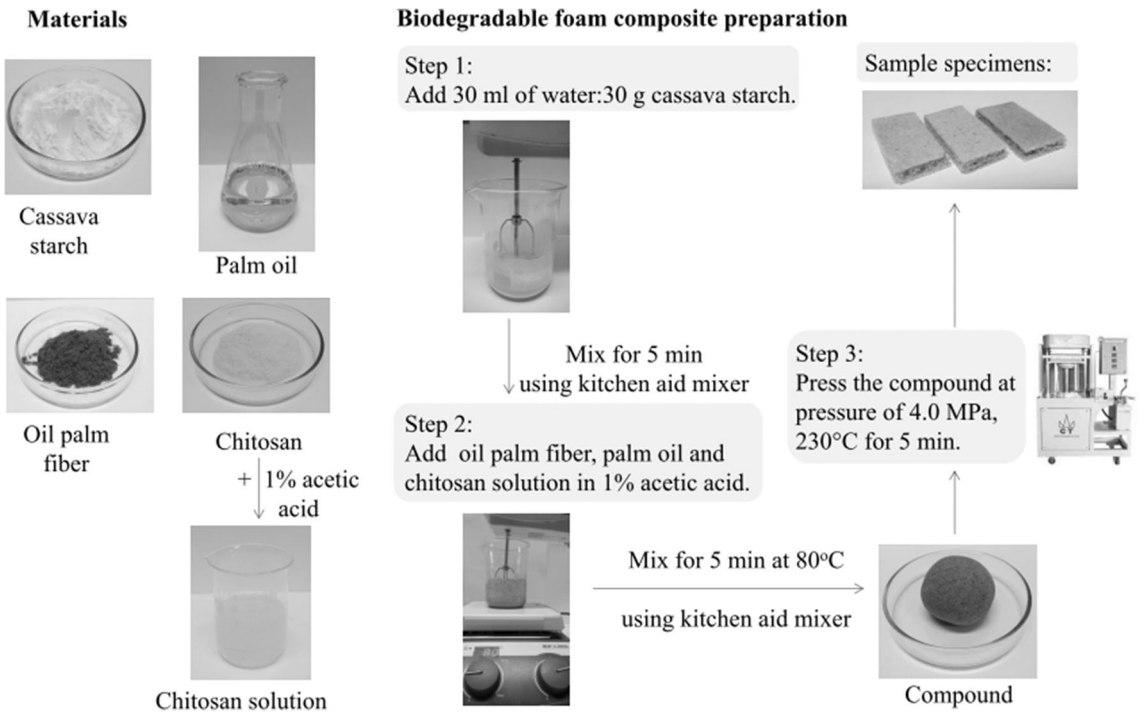

Fig. 1 Preparation of starch foam composite

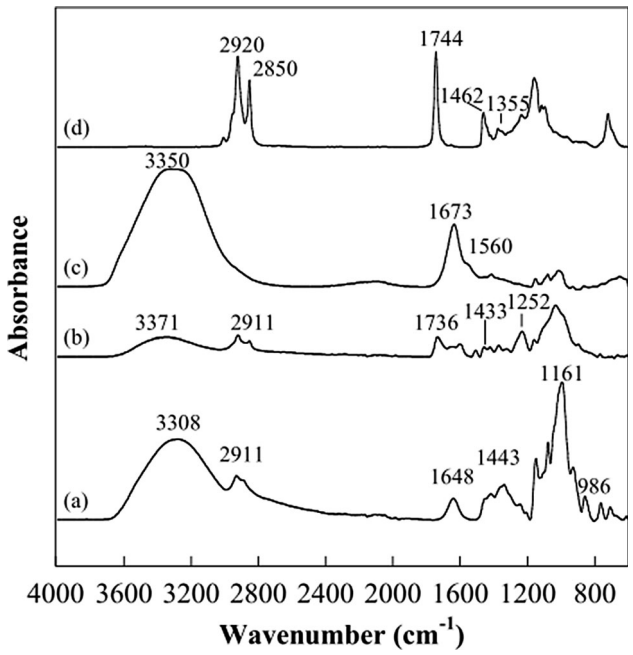

Fig. 2 FTIR results of **a** starch, **b** oil palm fiber, **c** chitosan and **d** palm oil

From Fig. 2a, the characteristic bands of starch at 3308 and 2911 cm^{-1} were related to OH stretching and CH stretching, respectively [24, 40]. The adsorption band at 1648 was assigned to the bending of water, while the peak at 1443 cm^{-1} was assigned to the CH_2 stretching. Both peaks at 986 and 1161 cm^{-1} corresponded to C-O bond stretching [41]. Figure 2b showed the FTIR spectra of oil palm fiber. The broad band in the range of 3371 cm^{-1} corresponded to OH vibration of cellulose structure. The peaks at 2911 and 1736 cm^{-1} were attributed to CH stretching of cellulose and hemicellulose and CO stretching of carbonyl group in hemicellulose, respectively [42]. The peaks at 1433 and 1252 cm^{-1} indicated the lignin and hemicellulose structure [43]. The chitosan spectrum was depicted in Fig. 2c. The broad band at 3350 cm^{-1} was assigned to OH stretching. The small peak at 1673 cm^{-1} was assigned to C=O stretching (amide I) and the peak at 1560 cm^{-1} was attributed to NH stretching (amide II) [44, 45]. Figure 2d presented palm oil characteristic. The sharp peaks at 2920 and 2850 cm^{-1} were related to CH_2 stretching of methylene group. The peak at 1744 cm^{-1} was assigned to ester carbonyl group of tryglycerides. The bands in range of 1462 and 1355 cm^{-1} were attributed to the bending of CH_2 and CH_3 aliphatic group [46].

Generally, the chemical interactions of polymer blended with additives were investigated by the change in characteristic spectra peak due to hydrogen bond or dipolar interaction [47]. The absorption bands of starch blended with additives are shown in Fig. 3a–c. The incorporation of additives shifted the broad band of all spectra at 3200–3400 cm^{-1} and the band at 1443 cm^{-1}. The phenomenon indicated the intermolecular hydrogen bond between starch and oil palm fiber, chitosan and palm oil. Furthermore, the interaction between the hydroxyl group of starch and amino group of chitosan was also observed. As

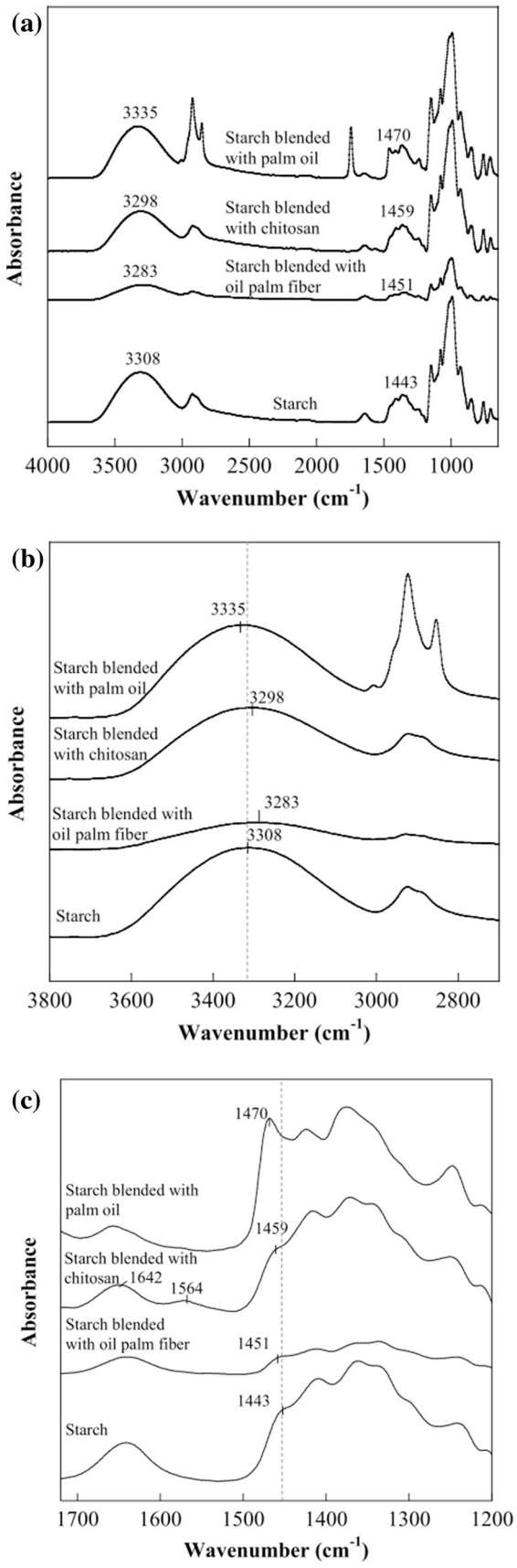

◀**Fig. 3** FTIR results of biodegradable foam composites: starch, starch blended with 9 wt% oil palm fiber, starch blended with 2 wt% chitosan and starch blended with 5 wt% palm oil

shown in Figs. 2 and 3c, the amino group peaks of chitosan and starch blended with chitosan shifted from 1560 to 1564 cm^{-1} and 1673 to 1642 cm^{-1}.

Density

The low density is an important physical property of foam. The density and S/N ratio of starch foam composites were plotted for each factor and their levels as shown in Fig. 4. The density values of starch foam composites were in the range of 0.11–0.34 g/cm^3. Optimal factors and levels for minimum density was observed at 9 wt% oil palm fiber, 2 wt% chitosan and 0 wt% palm oil. The density values obtained from experiment were developed to predict the density of starch foam composite using multi-linear regression model as expressed in Eq. (9). The lowest density value in this study was slightly higher than that of polystyrene foam (0.05–0.09 g/cm^3) [23, 48]. However, the obtained density value was in the same range with cassava starch reinforced with chitosan and kraft fiber (0.11–0.15 g/cm^3) [11] and was lower than other biodegradable foams based starch i.e. cassava starch foam containing cellulose fiber and sunflower protein isolate (0.46–0.59 g/cm^3) [49] and cassava starch blended with palm oil (0.58–0.78 g/cm^3) [10].

$$\text{Density} = 0.118 - 0.003X_1 + 0.012X_2 + 0.003X_3 \quad (9)$$

where X_1 is dosage of oil palm fiber content (%wt), X_2 is dosage of palm oil content (%wt) and X_3 is dosage of chitosan content (%wt).

From Fig. 4, the higher S/N ratio response value at each level implied that the effect of contributing factor was more significate to decrease the density of starch foam composites. It was clearly seen that chitosan was a major contributing factor which affected to reduction of the density. This result corresponded to the obtained data from ANOVA analysis as summarized in Table 3. The addition of chitosan in starch foam composites shows the highest percentage contribution at 82.41 %. The added chitosan resulted in a good distribution of pores in the starch foam composite in both the outer skin and the interior of sample as illustrated in Fig. 5c. The cross-section micrograph of starch foam containing chitosan showed the expansion of cells at the outer skin and the large cells with thin walls at the interior. Glenn and Orts [48] observed that the microstructure of foam based starch depended on the moisture content of materials. The sample made from materials with low moisture content had a dense structure

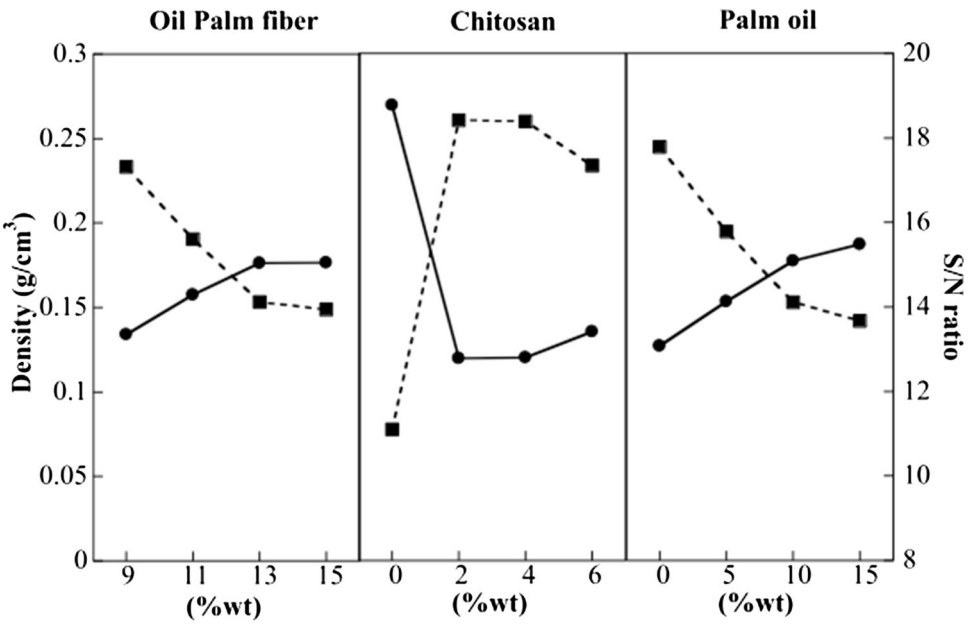

Fig. 4 Effect of factors on density: (*bullet*) density value and (*square*) S/N ratio

with closed cell and thick cell wall. Therefore, the incorporated chitosan dissolved in acetic solution increased the moisture content of sample and created large cell with thin wall during foam preparation.

For the addition of oil palm fiber and palm oil, the density of starch foam composites increased with increasing additives as shown in Fig. 4. The incorporation of oil palm fiber increased the viscosity of mixture whereas the addition of palm oil caused a less expandable foam with formation of thicker cell wall and smaller cell [10, 39]. These results are in good agreement with the obtained SEM results depicted in Fig. 5b, d. The cross section of neat starch and starch blended with additives foam had the sandwich type structure with dense outer skin containing small cells as depicted in Fig. 5a–d.

Mechanical Properties

Bending is the most common deformation of packing foam. The results from the bending mode fracture can indicate the failure of expanded particle of foam and thus reveals the strength of inter-particle-fusion [50]. Therefore, this study focused on the flexural properties of starch foam composites. Other mechanical properties such as tensile properties, compression properties and impact properties are also important parameters and should thus be further investigated to compare and consolidate the findings. The results of flexural strength and strain of starch foam composites are illustrated in Figs. 6 and 7. The flexural strength values were in range of 1.04–2.21 MPa. The optimal conditions for maximum flexural strength were obtained with 13 wt% oil palm fiber, 0 wt% chitosan and 10 wt% palm oil. The

Table 3 ANOVA analysis result

Properties	Factors		
	Oil palm fiber	Chitosan	Palm oil
Density			
Degree of freedom	3	3	3
SS*	0.005	0.063	0.009
V**	0.002	0.021	0.003
Contribution (%)	6.33	82.40	11.26
Flexural strength			
Degree of freedom	3	3	3
SS*	0.043	1.572	0.124
V**	0.014	0.524	0.041
Contribution (%)	2.49	90.36	7.15
Flexural strain			
Degree of freedom	3	3	3
SS*	1.088	0.791	0.611
V**	0.363	0.264	0.204
Contribution (%)	43.69	31.77	24.55
WAI			
Degree of freedom	3	3	3
SS*	7.189	28.373	0.444
V**	2.396	9.458	0.148
Contribution (%)	19.97	78.80	1.23
WSI			
Degree of freedom	3	3	3
SS*	71.998	11.379	71.994
V**	23.999	3.793	23.991
Contribution (%)	46.33	7.32	46.33

*SS** Sum of square

*V*** Variance

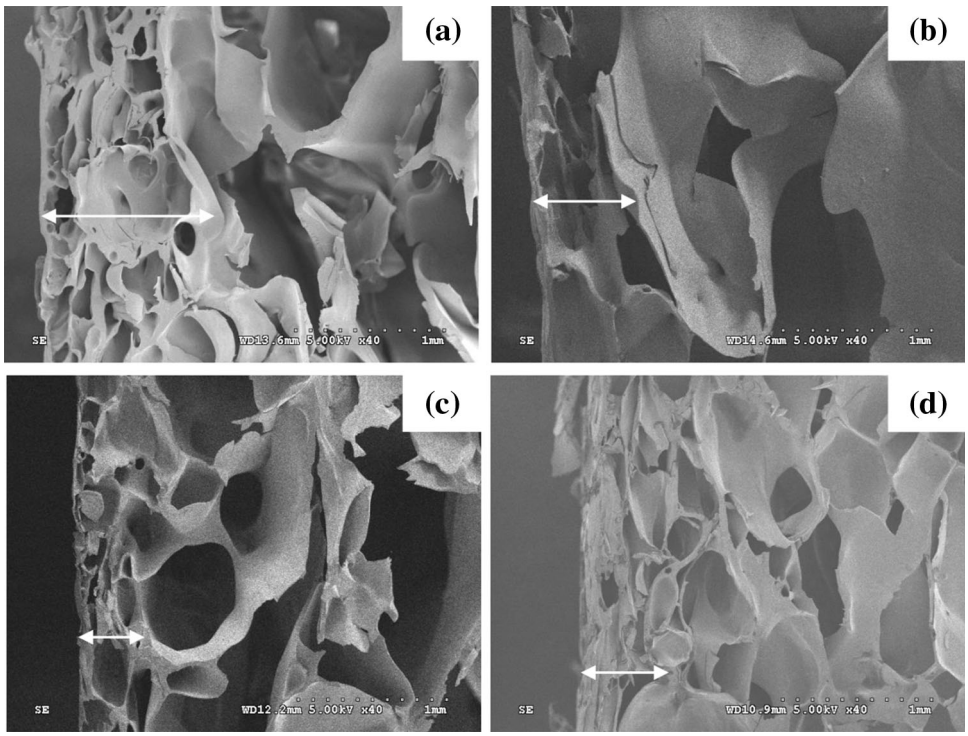

Fig. 5 Scanning electron micrograph of cross-sections: **a** starch, **b** starch blended with 9 wt % oil palm fiber, **c** starch blended with 2 wt % chitosan and **d** starch blended with 5 wt % palm oil

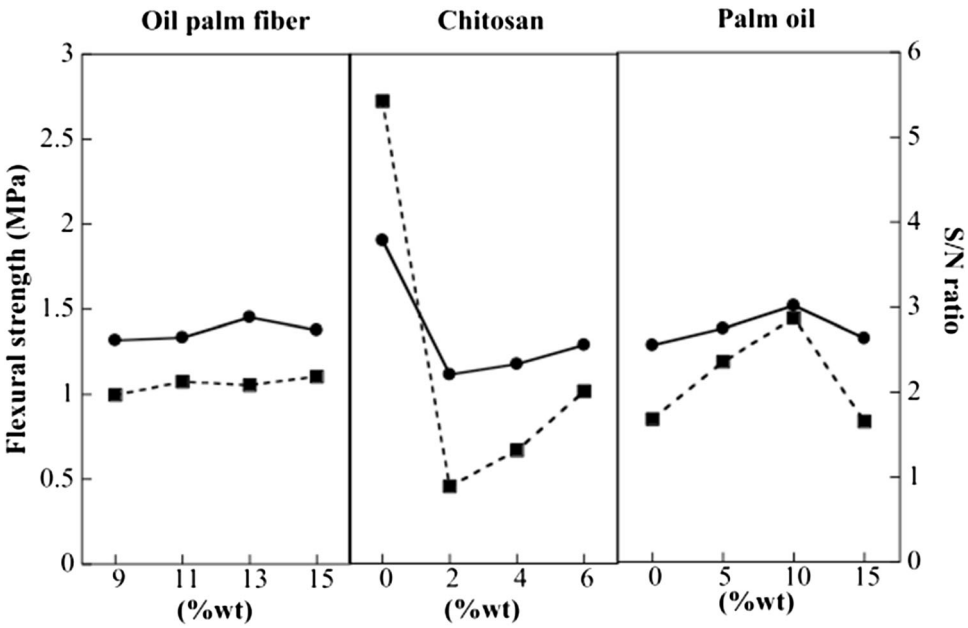

Fig. 6 Effect of factors on flexural strength: (*bullet*) flexural strength value and (*square*) S/N ratio

flexural strength of starch foam composites was significantly higher than that of commercial expanded polystyrene (0.85–0.97 MPa) [10] and comparable with those of reported starch based biodegradable foam i.e. cassava starch foam blended with palm oil (0.3–1.0 MPa) [10], potato starch reinforced with linter cotton fiber (2.47 MPa) [51] and potato starch reinforced with cellulose (2.0–2.3 MPa) [52]. The flexural strain values ranged from 0.54 to 2.33 % and the optimal mix proportion was obtained with 9 wt% oil palm fiber, 6 wt% chitosan and 0 wt% palm oil. The relationship between flexural strength and dosages of oil palm fiber, palm oil and chitosan is shown in Eq. (10) and the relationship between flexural strain and dosages of oil palm fiber, palm oil and chitosan is shown in Eq. (11).

$$\text{Flexural strength} = 1.06 - 0.003X_1 + 0.083X_2 + 0.013X_3 \quad (10)$$

$$\text{Strain} = 2.675 - 0.114X_1 + 0.089X_2 - 0.022X_3 \quad (11)$$

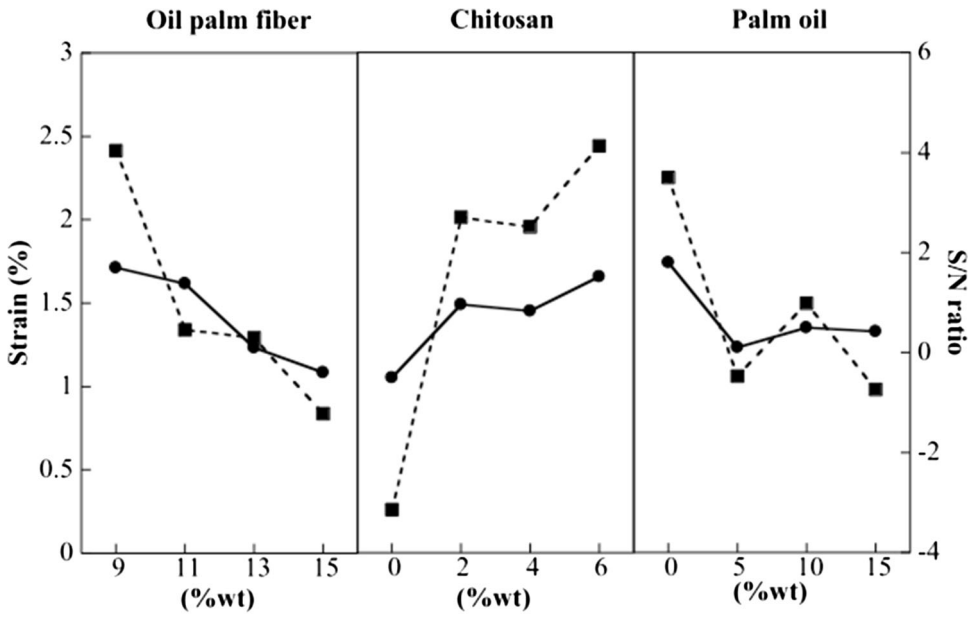

Fig. 7 Effect of factors on flexibility: (*bullet*) maximum strain value and (*square*) S/N ratio

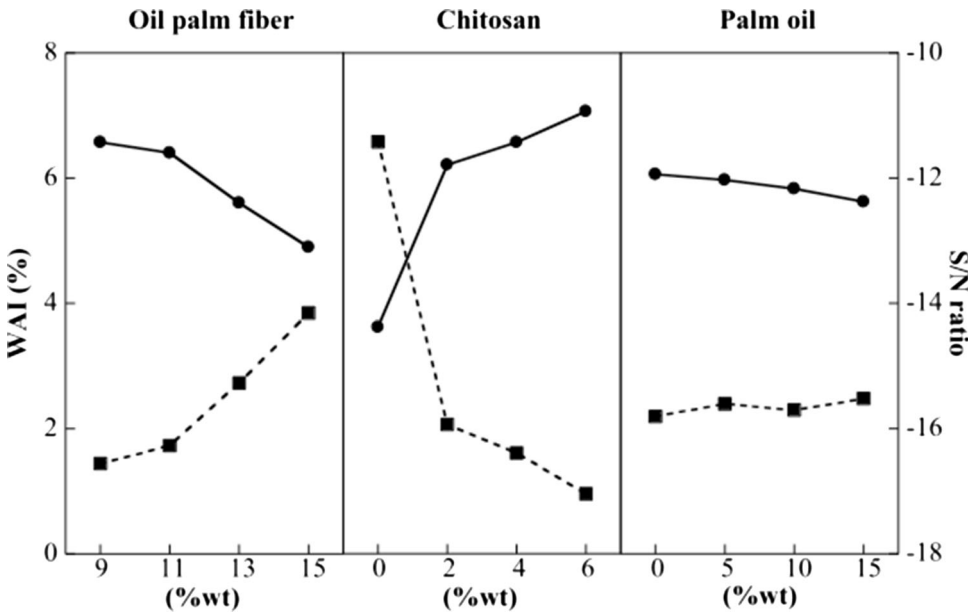

Fig. 8 Effect of factors on water absorption index: (*bullet*) WAI value and (*square*) S/N ratio

where X_1 is dosage of oil palm fiber (%wt), X_2 is dosage of palm oil (%wt) and X_3 is dosage of chitosan (%wt).

The plots of S/N ratio versus flexural strength and flexural strain are shown in Figs. 6 and 7, respectively. The highest S/N ratio implied a high flexural strength and strain values. As depicted in Fig. 6, the S/N ratio tended to increase with increasing oil palm fiber content from 9 to 13 wt %. This is due to the good interfacial interaction of oil palm fiber and starch matrix. During deformation, the stress could transfer from starch matrix to fiber effectively and this resulted in greater strength [51]. The enhancement of flexural strength was also obtained by addition of 0–10 wt % palm oil content. This is due to the fact that the dense and thick cell walls of foam can resist the deformation and provide the high mechanical strength [53]. Polat et al. [24] also observed that the starch foam with beewax and other additives such natural fiber and/or kaolin can significantly improve the flexural strength.

For the starch foam composites with chitosan, the obtained flexural strength was decreased. The amino groups

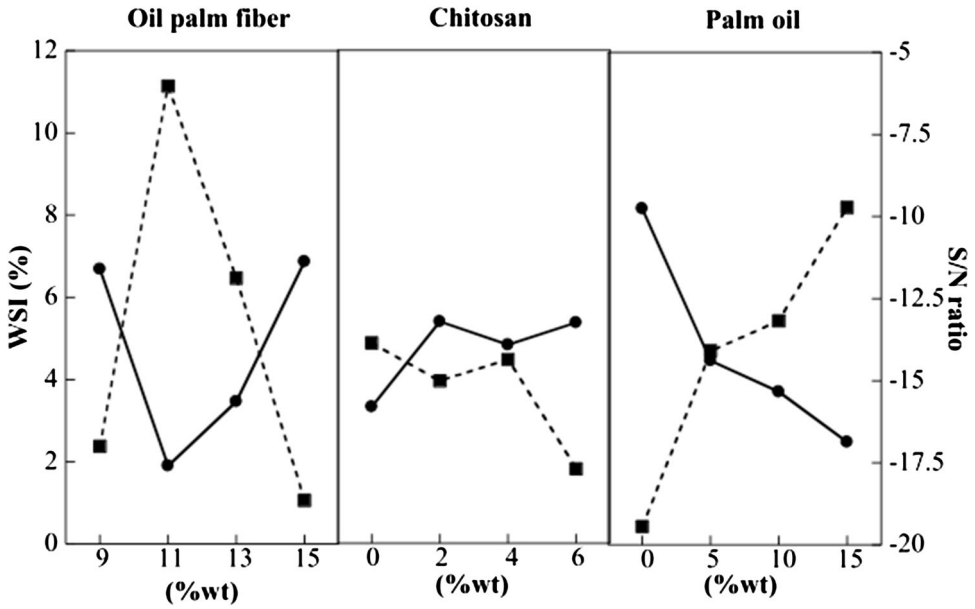

Fig. 9 Effect of factors on water solubility index: (*bullet*) WSI value and (*square*) S/N ratio

Table 4 The relational analysis for each parameter

Experimental run	Density	Flexural strength	WAI	WSI
1	0.753	0.583	0.677	0.368
2	1.000	0.063	0.251	0.511
3	0.962	0.234	0.131	0.580
4	0.845	0.057	0.000	0.824
5	0.415	0.580	0.621	0.885
6	0.978	0.063	0.150	0.839
7	0.902	0.103	0.323	0.944
8	0.863	0.251	0.090	0.948
9	0.066	1.000	0.879	0.967
10	0.903	0.000	0.421	0.681
11	0.992	0.014	0.218	0.656
12	0.872	0.386	0.237	0.877
13	0.000	0.780	1.000	1.000
14	0.928	0.114	0.4948	0.611
15	0.944	0.106	0.3871	0.621
16	0.959	0.140	0.3813	0.000

Table 5 The calculated Grey relational coefficient and Grey relational grade for sixteen comparability sequences

Experimental run	Grey relational coefficient				Grey relational grade
	Density	Flexural strength	WAI	WSI	
1	0.669	0.545	0.608	0.442	0.566
2	1.000	0.348	0.400	0.506	0.564
3	0.930	0.395	0.365	0.543	0.558
4	0.763	0.346	0.333	0.740	0.546
5	0.461	0.544	0.569	0.813	0.596
6	0.958	0.348	0.370	0.756	0.608
7	0.837	0.358	0.425	0.898	0.629
8	0.785	0.401	0.355	0.906	0.611
9	0.349	1.000	0.806	0.938	0.773
10	0.83	0.333	0.464	0.610	0.561
11	0.985	0.336	0.390	0.593	0.576
12	0.796	0.449	0.396	0.802	0.611
13	0.333	0.694	1.000	1.000	0.757
14	0.874	0.361	0.497	0.562	0.574
15	0.898	0.359	0.449	0.568	0.569
16	0.920	0.368	0.447	0.333	0.518

(NH_2) of chitosan were protonated to NH_3^+ in the acetic acid solvent during foam preparation process while the gelatinization of starch destroyed the crystalline structure of starch molecule and generated the OH groups. The inter-molecular hydrogen bonds between OH group and NH_3^+ provided a good interfacial bond between chitosan and starch matrix [45]. The FTIR result supported this observation. The interaction between starch and all additives occurred via inter-molecular hydrogen bonds. The decreasing of mechanical strength was observed when the influence of starch intra-molecular hydrogen bond is higher than that of inter-molecular hydrogen bond [54]. However, the flexural strain increased with increasing chitosan content, as depicted in Fig. 5. This phenomenon indicated that chitosan improved the flexibility of starch foam composites. The result ANOVA analysis as shown in Table 3 showed that chitosan was the major factor affecting the flexural strength of starch foam composites. Furthermore, chitosan was one of the two main factors affecting flexural strain.

Table 6 The response table for Grey relational

Levels	A	B	C
1	0.558	0.673	0.567
2	0.611	0.577	0.585
3	0.630	0.583	0.629
4	0.604	0.571	0.623

Table 7 Results of confirmation experiment

	Predicted $A_3B_1C_3$	Experiment $A_3B_1C_3$
Grey relation grade	0.730	0.773

Water Absorption Index and Water Solubility Index

Water resistance is an important parameter determining its applications. Starch foams are susceptible to the attack of moisture when they contact water. Water molecules attack the hydrogen bonds of starch and decreased the functional properties of foam [10, 28]. The swelling and degree of molecular damage of starch were measured in term of WAI and WSI, respectively. Figure 8 depicted the WAI values of starch foam composites in range of 2.47–8.05 %. The lowest WAI was obtained with 15 wt % oil palm fiber, 0 wt % chitosan and 15 wt % palm oil. The WSI values ranged from 0.52 to 14.88 % and the optimal mix proportion was obtained with 11 wt % oil palm fiber, 0 wt % chitosan and 15 wt % palm oil, as shown in Fig. 9. The relationship between WAI values and additive contents is shown in Eq. (12) and the relationship between WSI values and additive contents is shown in Eq. (13).

$$\mathrm{WAI} = 7.987 - 0.292X_1 + 0.534X_2 - 0.029X_3 \quad (12)$$

$$\mathrm{WSI} = 5.306 + 0.105X_1 + 0.279X_2 - 0.357X_3 \quad (13)$$

where X_1 is dosage of oil palm fiber content (%wt), X_2 is dosage of palm oil content (%wt) and X_3 is dosage of chitosan content (%wt).

The S/N ratio value of WAI and WSI are shown in Figs. 8 and 9, respectively. The high S/N ratio implied the low WAI and WSI and the good stability of composites in terms of water resistance. The addition of 9–15 wt % of oil palm fiber and 0–15 wt % of palm oil increased the S/N ratio of WAI. The reason for reduction of WAI was possibly due to the increase in crystalline phase of natural fiber in starch matrix. The linkage between fiber and starch could prevent the absorption of water molecule [23, 55]. The incorporation of 0–15 wt % of palm oil improved the water resistance of composite. The fatty acid in palm oil increased the hydrophobicity of composites [10, 24]. On the contrary, the decrease of S/N ratio was observed for the composites incorporated with chitosan [11]. This is due to the amino group presence in chitosan enhanced the absorption of water in composite. The ANOVA analysis results as shown in Table 3 indicated that chitosan was the main factor affecting the WAI.

From Fig. 9, the S/N ratio tended to increase with increasing oil palm fiber in range of 9–11 wt % and palm oil in range of 0–15 wt %. Both oil palm fiber and palm oil were the major factors affecting WSI as shown in Table 3. From Fig. 5, it is clear that the starch foam composites containing oil palm fiber and palm oil had dense outer skin which resisted the water molecule. Similar observations were reported in the previous works. Kaisangsri et al. [10] observed that the addition of karft fiber and palm oil can improve both WAI and WSI of starch foams. Polat et al. [24] also reported that the starch foam containing combined additives such as kaolin, beewax and natural fiber showed synergistic effect for water resistance.

Parametric Optimization of Starch Foam Composite Mix Proportion

Optimal Condition of Mix Proportion

The normalized data following Grey relational analysis for each parameter is calculated from Eqs. (3) and (4) as summarized in Table 4. Grey relational coefficient can be calculated from Eq. (5) and Grey relational grade is determined following Taguchi method as shown in Table 5. In fact, Grey relational grades represent the level of correlation between the reference and the comparability sequences. The larger Grey relational grade implies the comparability sequence exhibiting a stronger correlation with the reference sequence [56]. From Table 6, the highest Grey relational grade values were obtained with A_3, B_1 and C_3. Therefore, the 13 wt % oil palm fiber, 0 wt % chitosan and 10 wt % palm oil was the optimal mix proportion for starch foam composites.

Confirmatory Test

The predicted optimal value of starch foam composite can be calculated by means of additive law as follows:

$$\hat{\gamma} = \gamma_m + \sum_{i=1}^{q} (\gamma_i - \gamma_m) \quad (14)$$

where γ_m is total mean of Grey relational grade, γ_i is mean of Grey relational grade at optimal level and q is number of machining parameters that significantly affect multiple performance characteristics. Table 7 shows the comparison of the predicted values with the actual values using the optimum mix proportion. A good agreement between predicted and actual results was observed. The properties

Table 8 Properties of various types of starch foams

Types of starch based biodegradable foams	Additives content	Density (g/cm^3)	Flexural strength (MPa)	WAI	WSI
Starch foam-$A_3B_1C_3$ [Present work]	13 wt% oil palm fiber and 10 wt% palm oil	0.32	2.21	3.14	1.00
Cassava starch foam [10]	5–10 wt % palm oil	0.56–0.71	0.25–1.10	9.5–11.0	2.0–2.2
Cassava starch foam [10]	5–15 wt% karft	0.22–0.36	2.5–5.3	5.8–9.0	6.91–7.47
Cassava starch foam [10]	5–15 wt % zein	0.22–0.45	1.9–4.15	3.00–5.80	2.5–3.5
Cassava starch foam [10]	5–15 wt % soy	0.28–0.30	0.5–0.8	4.8–5.9	5.5–20.0
Cassava starch foam [10]	5–15 wt % gluten	0.28–0.34	1.4–3.9	5.2–5.5	2.0–3.5
Cassava starch foam [11]	10–20 wt % chitosan	0.12–0.15	–	8.07–12.55	6.05–8.55
Starch acetate foam [57]	–	–	–	3.8–6.2	2.2–9.8
Wheat starch [58]	8–32 wt % wood pulp	0.13–0.41	1.3–12.0	–	–
Starch poly-glutamic acid foam [59]	–	–	–	2.65–23.05	41.3–89.9
Tapioca starch-polylactic acid foam [60]	3 wt % organoclay	0.023–0.061	–	1.96–7.14	46.3–76.3

of the optimal mix proportion for starch foam composite (starch foam-$A_3B_1C_3$) obtained from mix number 9 was summarized in Table 8. The density and flexural strength values of the starch foam-$A_3B_1C_3$ were comparable with those of previously reported starch based foam composites [10, 58]. Interestingly, the starch foam-$A_3B_1C_3$ showed a high water resistance in term of WAI and WSI. The WAI value of starch foam-$A_3B_1C_3$ was significantly lower than those of the reported starch foam composites [10, 11] and starch acetate foam [57]. The WAI value was comparable with those of the starch foam copolymer such as starch poly-glutamic acid foam [59] and tapioca starch-polylactic acid nanocomposite foam [60]. As shown in Table 8, the WSI of starch foam-$A_3B_1C_3$ was the lowest compared to those of starch foam composites [10, 11], starch acetate [57] and starch foam copolymers [59, 60].

Conclusions

In this study, the Taguchi method coupled with Grey relational analysis were applied for optimizing mix proportion of starch foam composite. The results indicated that the addition of chitosan was the main factor in decreasing the density of composite. The density of starch foam composite was slightly higher than that of commercial polystyrene foam. The flexural strength and water resistance of the samples was improved by the addition of oil palm fiber and palm oil. The ANOVA results showed the most effective parameters on the properties of starch foam composite. Chitosan was the main parameter influencing density, flexural strength and WAI whereas oil palm fiber and palm oil were the main parameters affecting WSI. Based on Grey relational analysis result, the sample with 13 % oil palm fiber, 0 wt % chitosan and 10 wt % palm oil showed the best overall properties. The developed biodegradable starch foam composite could be used as an alternative packaging for dry material.

Acknowledgments This work was financial supported by National Science and Technology Development Agency, Thailand. The authors also would like to acknowledge the support of Thailand Research Fund (TRF) under the TRF Senior Research Scholar, Grant No. RTA 5780004 and the Higher Education Research Promotion and National Research University Project of Thailand, Office of the Higher Education Commission, through the Advanced Functional Materials Cluster of Khon Kaen University. Support from Applied Engineering for Important Crops of the North East Research group, Khon Kaen University, Thailand is also acknowledged.

References

1. Pornsuksomboon K, Holló BB, Szécsényi KM, Kaewtatip K (2016) Carbohyd Polym 136:107–112
2. Debiagi F, Kobayashi RKT, Nakazato G, Panagio LA, Mali S (2014) Ind Crop Prod 52:664–670
3. Puglia D, Dominici F, Kenny JM, Santulli C, Governatori C, Tosti G, Benincasa P (2015) J Polym Environ 24:37–47
4. Mello LRPF, Mali S (2014) Ind Crop Prod 55:187–193
5. Vercelheze AES, Fakhouri FM, Dall'Antônia LH, Urbano A, Youssef EY, Yamashita F, Mali S (2012) Carbohyd Polym 87:1302–1310
6. Sun Q, Mekonnen T, Misra M, Mohanty AH (2015) J Polym Environ 24:23–36
7. Carmona VB, Correa AC, Marconcini JM, Mattoso LHC (2015) J Polym Environ 23(1):83–89
8. Santiago GT, Gante CR, Garcıa-Lara S, Verdolotti L, Maio ED, Iannace S (2015) J Polym Environ 23:72–82
9. Yang W, Kenny JM, Puglia D (2015) Ind Crop Prod 74:348–356
10. Kaisangsri N, Kerdchoechuen O, Laohakunjit N (2014) Carbohyd Polym 110:70–77

11. Kaisangsri N, Kerdchoechuen O, Laohakunjit N (2012) Ind Crop Prod 37:542–546
12. Edhirej A, Sapuan SM, Jawaid M, Zahari NI (2015) Polym Compos
13. Lopez-Gil A, Silva-Bellucci F, Velasco D, Ardanuy M, Rodriguez-Perez MA (2015) Ind Crop Prod 66:194–205
14. Teodoro AP, Mali S, Romero N, de Carvalho GM (2015) Carbohyd Polym 126:9–16
15. Rafieian F, Shahedi M, Keramat J, Simonsen J (2014) Ind Crop Prod 53:282–288
16. Debiagi F, Marim BM, Mali S (2015) J Polym Environ 23:269–276
17. Shinoj S, Visvanathan R, Panigrahi S, Kochubabu M (2011) Ind Crop Prod 33(1):7–22
18. Kakou CA, Arrakhiz FZ, Trokourey A, Bouhfid R, Qaiss A (2014) Mater Design 63:641–649
19. Ibrahim H, Farag M, Megahed H, Mehanny S (2014) Carbohyd Polym 101:11–19
20. Dayarian S, Zamani A, Moheb A, Masoomi M (2014) J Polym Environ 22(3):409–416
21. Suyatma NE, Copinet A, Tighzert L, Coma V (2004) J Polym Environ 12(1):1–6
22. Yeh JT, Hou YJ, Cheng L, Wang YZ, Yang L, Wang CK (2015) Carbohyd Polym 127:135–144
23. Shey J, Imam SH, Glenn GM, Orts WJ (2006) Ind Crop Prod 24:34–40
24. Polat S, Uslu MK, Aygün A, Certel M (2013) J Food Eng 116:267–276
25. Edem DO (2002) Plant Food Hum Nutr 57(3):319–341
26. Mba OI, Dumont MJ, Ngadi M (2015) Food Biosc 10:26–41
27. Xiao J, Wang W, Wang K, Liu Y, Liu A, Zhang S, Zhao Y (2016) Food Hydrocolloid 60:243–251
28. Mali S, Debiagi F, Grossmann MVE, Yamashita F (2010) Ind Crop Prod 32:353–359
29. Biswas S, Satapathy A (2009) Mater Design 30:2841–2853
30. Roy R (1990) A primer on the Taguchi method. Nostrand Reinhold, New York
31. Datta S, Bandyopadhyay A, Pal P (2008) Int J Adv Manuf Technol 39:1136–1143
32. Subbaya KM, Suresha B, Rajendra N, Varadarajan YS (2012) Mater Design 41:124–130
33. KC B, Faruk O, Agnelli JAM, Leao AL, Tjong J, Sain M (2015) Comp Part A-Appl S
34. Taguchi G (1993) Taguchi on robust technology development. ASME Press, New York
35. Taguchi G, Chowdhury S, Taguchi S (2000) Robust engineering. McGraw-Hill, New York
36. Morán J, Granada E, Míguez JL, Porteiro J (2006) Fuel Process Technol 87:123–127
37. Deng J (1989) J Grey Syst 1:1–24
38. Datta S, Bandyopadhyay A, Pal PK (2008) Int J Advan Manuf Technol 39(11):1136–1143
39. Shogren RL, Lawton JW, Tiefenbacher KF, Chen L (1998) J Poly Sci 68:2129–2140
40. Matsuda DKM, Verceheze AES, Carvalho GM, Yamashita F, Mali S (2013) Ind Crop Prod 44:705–711
41. Prachayawarakorn J, Chaiwatyothin S, Mueangta S, Hanchana A (2013) Mater Design 47:309–315
42. Rahman MM, Mallik AK, Khan MA (2007) J Appl Polym Sci 105:3077–3086
43. Fahma F, Iwamoto S, Hori N, Iwata T, Takemura A (2010) Cellulose 17(5):977–985
44. Mathew S, Brahmakumar M, Abraham TE (2006) Biopolymers 82:176–187
45. Bourtoom T, Chinnan MS (2008) T Technol 41:1633–1641
46. Rohman A, Man YBC (2010) Food Res Int 43:886–892
47. Prachayawarakorn J, Limsiriwong N, Kongjindamunee R, Surakit S (2012) J Polym Environ 20:88–95
48. Glenn GM, Orts WJ (2001) Ind Crop Prod 13:135–143
49. Salgado PR, Schmidt VC, Molina Ortiz SE, Mauri AN, Laurindo JB (2008) J Food Eng 85:435–443
50. Pilla S (2011) Handbook of bioplastics and biocomposites engineering applications. Wiley, New YorK
51. Bénézet JC, Stanojlovic-Davidovic A, Bergeret A, Ferry L, Crespy A (2012) Ind Crop Prod 37:435–440
52. Bergeret A, Benezet JC (2011) Int J Polym Sci 2011:14
53. Zhou J, Song J, Parker R (2006) Carbohyd Polym 63:466–475
54. Xu YX, Kim KM, Hanna MA, Nag D (2005) Ind Crop Prod 21:185–192
55. Soykeabkaew N, Supaphol P, Rujiravanit R (2004) Carbohyd Polym 58:53–63
56. Goel P, Khan Z, Siddiquee A, Kamaruddin S, Gupta R (2012) Int J Adv Manuf Technol 61:859–871
57. Xu Y, Hanna MA (2005) Carbohyd Polym 59(4):521–529
58. Glenn GM, Orts WJ, Nobes GAR (2001) Ind Crop Prod 14(3):201–212
59. Xu J, Krietemeyer EF, Finkenstadt VL, Solaiman D, Ashby RD, Garcia RA (2016) Carbohyd Polym 140:233–237
60. Lee SY, Chen H, Hanna MA (2008) Ind Crop Prod 28(1):95–106

J Therm Anal Calorim
DOI 10.1007/s10973-016-6024-3

Characterization of paraffin/ultrasonic-treated diatomite for use as phase change material in thermal energy storage of buildings

Narubeth Lorwanishpaisarn[1] · Pornnapa Kasemsiri[1] · Patcharapol Posi[2] · Prinya Chindaprasirt[3]

Received: 23 June 2016 / Accepted: 27 November 2016
© Akadémiai Kiadó, Budapest, Hungary 2016

Abstract In this study, paraffin-/ultrasonic-treated diatomite was characterized for use as phase change material (PCM) for thermal energy storage in buildings. The diatomite was treated with ultrasound at various periods of time. The diatomite treated with ultrasound for 60 min (DA-60) was the optimum condition providing the highest surface area without structural degradation. The melting point and latent heat of the paraffin/DA-60 composite PCM were 59 °C and 45.90 J g^{-1}, respectively. The obtained form-stable PCM had good thermal reliability after 500 cycles of thermal cycling test. The thermal performance of PCM was tested by incorporating the paraffin/DA-60 composite PCM into gypsum board. The results showed that the gypsum board containing the paraffin/DA-60 composite PCM had better thermal energy absorption and release characteristics than those of the control sample. The incorporation of paraffin/DA-60 composite PCM into suitable building materials could thus considerably reduce the energy consumption of cooling system in buildings.

Keywords Diatomite · Form-stable phase change material · Thermal energy storage · Ultrasonic treatment

✉ Pornnapa Kasemsiri
pronkas@kku.ac.th

[1] Sustainable Infrastructure Research and Development Center, Department of Chemical Engineering, Faculty of Engineering, Khon Kaen University, Khon Kaen 40002, Thailand

[2] Department of Civil Engineering, Faculty of Engineering, Rajamangala University of Technology Isan, Khon Kaen Campus, Khon Kaen 40000, Thailand

[3] Sustainable Infrastructure Research and Development Center, Department of Civil Engineering, Faculty of Engineering, Khon Kaen University, Khon Kaen 40002, Thailand

Introduction

Nowadays, energy consumption in buildings is the major energy consumer with a total of 30–40% share of overall energy consumption. The demand energy for buildings has increased rapidly due to the growth of population and increase in comfort standards [1–4]. The thermal energy storage (TES) technique is widely used for saving thermal energy and increasing of the comfort level in buildings by decreasing of the frequency of internal air temperature swings and maintains the desired indoor temperature for a long period time [5–8]. PCM is one of the TES methods used for thermal energy storage applications such as in wall, ceiling, and floor [9–12]. During phase transition of PCM, it can store and release large amounts of thermal energy [13, 14]. It has been reported that the PCM has many advantages such as high heat capacity, good chemical stability, no corrosion, and inexpensive [15]. Xu et al. [16] fabricated a new paraffin/expanded vermiculite composite PCM for use as an aggregate in thermal energy storage cement-based composites. The prepared cement-based composites significantly enhanced the thermal performance and energy saving. Karaipekli and Sarı [17] studied and developed thermal plaster composites consisting of composite PCM from pumice and organic PCMs. The results showed that the plasters with composite PCM could maintain the room temperature at a comfortable range for a long time, and the energy consumption was significantly reduced.

Paraffin is an organic PCM consisting of normal alkane (CH_3–$(CH_2)_n$–CH_3). From previous works, paraffin is able to store and release a large amount of thermal energy during phase change. Since paraffin is chemically inert, non-corrosive, odorless, commercial available, and non-toxic, it has been widely applied for PCM applications

Published online: 28 December 2016

[18–20]. However, the use of PCM still has limitation due to the leakage of PCM from supporting material during a phase transition from solid to liquid. One way to solve this problem is the use of a form-stable composite PCM to avoid the leakage of PCM during phase change temperature [21]. As the heat storage capacity of PCM depends on its amount, the selection of supporting material is important [22, 23]. Good supporting materials must have high surface area to carry a large amount of PCM. According to previous researches, the most common material used is diatomite (diatomaceous earth) which is a naturally occurring, soft, siliceous sedimentary rock with low density and high porosity. The typical chemical composition of oven-dried diatomite is silica [24]. Generally, diatomite has been used for several industrial applications such as filter in beverage industry and adsorbent for contaminants in water [20, 25, 26]. With these characteristics, diatomite is thus suitable for use as a supporting material to produce a form-stable composite PCM.

Recently, it has been shown that the surface area and pore of diatomite can be improved by several techniques. Sun et al. [27] enhanced the surface area of diatomite by calcinations at 600–1200 °C to obtain form-stable composite PCMs with high latent heat storage capacity. Surface area, porosity and purity of diatomite can also be improved with acid treatment [28]. Nevertheless, the process required high energy consumption and generated the waste of acid solvent. The mechanical process is a simple and environmentally friendly technique to improve the surface area of diatomite. The ultrasonication has also been used to enhance the physical properties of diatomite. The vibration from ultrasonication can remove impurities from raw diatomite [29]. Zhang et al. [29] improved the microstructure of diatomite using sonication. The diatomite sonicated for 8 min showed increased porosity leading to the decreased density and increased surface area.

Currently, there is no study on the modified diatomite by ultrasonication for use as PCM support materials. In this study, the characterizations of modified diatomite were determined using scanning electron microscopy (SEM–EDX), X-ray fluorescence spectrometry (XRF), Fourier transformation infrared (FTIR) analysis, and specific BET surface area analyzer. The properties of paraffin/diatomite composite PCM were also investigated by differential scanning calorimetry (DSC) analysis and thermogravimetric analysis (TG). The thermal performance for building application was observed by incorporated the paraffin/diatomite composite PCM into gypsum board.

Experimental

Materials

The raw diatomite used in this study was supplied from Lampang province in the north of Thailand. The chemical composition of raw diatomite is shown in Table 1. Paraffin was obtained from Chemipan Co. Ltd, Thailand. Gypsum was supplied from Thai Gypsum Products Pcl., Thailand.

Sonication of raw diatomite

The raw diatomite was crushed into powder and passed through a 180-mm sieve. The diatomite was dispersed in distilled water with diatomite/water ratio of 1:8 (g mL^{-1}). The obtained mixture was treated using a DT 255 H Bandelin ultrasonicator at an output power of 160 W for 15, 30, 45, 60, 90, and 120 min. The modified diatomite was separated from the mixture using a centrifuge and then dried in an oven at 105 °C for 24 h. The diatomite samples were denoted with DA-0, DA-15, DA-30, DA-45, DA-60, and DA-120 where the numbers indicated the ultrasonic time.

Preparation of the form-stable composite PCM

Paraffin/diatomite composite PCM was prepared using vacuum impregnation method. The composite PCMs were fabricated with various paraffin mass percentages viz., 30, 45, 60, and 75% of diatomite. The modified diatomite and paraffin were placed inside a flask equipped with vacuum pump and overhead stirrer. The evacuation process at vacuum pressure of 80 kPa was performed for 30 min to evacuate air from the porous material. The flask was then heated at 70 °C with vacuum pressure of 80 kPa for another 30 min to melt the paraffin. The melted paraffin was impregnated into the modified diatomite by continuous mixing with overhead stirrer at 200 rpm for 30 min. After that, the vacuum system was turned off, and air was

Table 1 Chemical compositions of raw diatomite and modified diatomites

Samples	SiO_2	Al_2O_3	Fe_2O_3	K_2O	MgO	TiO_2	CaO	Na_2O	Other
DA-0	70.20	13.90	4.25	1.62	0.608	0.404	0.403	0.145	8.470
DA-30	74.00	11.00	4.75	1.32	0.447	0.358	0.333	0.127	7.665
DA-60	79.10	9.49	4.90	1.36	0.367	0.372	0.265	0.137	4.009
DA-120	74.40	13.00	4.28	1.57	0.546	0.404	0.367	0.121	5.312

allowed to enter the flask again to force paraffin to penetrate into the pore space of modified diatomite. The obtained form-stable composite PCMs were cooled down to room temperature for further characterization.

Preparation of gypsum board containing form-stable paraffin/modified diatomite PCM composite

The gypsum board containing the composite PCM was prepared for the thermal performance test. Gypsum and water were mixed at water to gypsum ratio of 0.8. The mixture was mixed with 20 mass% of paraffin/modified diatomite PCM composite for 5 min and then poured into 100 mm × 140 mm × 20 mm molds.

Characterization of modified diatomite and form-stable composite PCM

The chemical compositions of samples were obtained using Bruker model S8 Tiger X-ray fluorescence spectrometer (XRF). The microstructures and morphologies of samples were observed using LEO 1450 scanning electron microscopy coupled with EDX spectrometer (SEM/EDX). The specific surface areas were determined using a specific area analyzer (ASAP 2010 model) with the Brunauer–Emmett–Teller method.

The chemical compatibility between paraffin and diatomite was analyzed using Bruker Tensor 27 Fourier transform infrared spectrophotometer (FTIR). The infrared spectra were obtained at wavenumber range of 4000–650 cm^{-1}.

The thermal properties of composite PCMs were measured using a PerkinElmer DSC 6000 differential scanning calorimeter (DSC) at a heating rate of 4 °C min^{-1} under nitrogen atmosphere. The thermal behavior and kinetic parameters of samples were also determined by DSC at the heating rate of 5, 10, 15, and 20 °C min^{-1}. The thermal stabilities of the form-stable paraffin/diatomite composite PCMs were determined using Shimadzu TGA-50 thermogravimetric analyzer (TG). The analysis was operated at temperature range of 25–700 °C at heating rate of 10 °C min^{-1} under nitrogen at atmosphere with a flow rate of 10 mL min^{-1}. Thermal reliability of the composite PCM was evaluated by thermal cycling test by using Biometra T1 Thermocycler, Whatman Biometra, UK. The thermal and chemical stability of sample after thermal cycling were observed by DSC and FTIR, respectively.

The thermal performance test of the gypsum board containing form-stable paraffin/diatomite composite PCM and control gypsum board was investigated following the experimental procedure in the literature [16, 30]. The prepared samples with dimensions of 100 mm × 140 mm × 20 mm were used for measuring thermal performance using the experimental setup shown in Fig. 1. The samples were

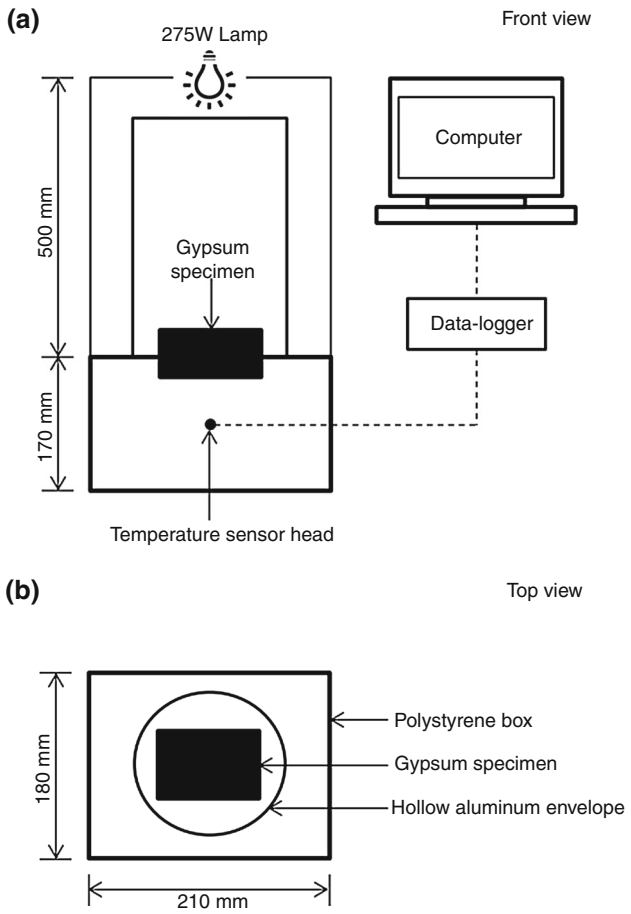

Fig. 1 **a** Front and **b** top views of the heating setup

exposed to heat radiation from a 275 W infrared lamp for 120 min and then naturally cooled down for 120 min. The temperature data of air inside the room were recorded by data logger-temperature system.

Results and discussion

Effects of sonication on raw diatomite

Surface area

The latent heat of form-stable composite PCM depended on its PCM adsorption capacity. Therefore, the higher specific surface area of support materials provided the better adsorption capacity of the PCM [29, 31]. Figure 2 shows the effect of ultrasonic treatment with different times on BET surface area of diatomite. It can be seen that BET surface area substantially increased with increasing treatment time up to 60 s. The DA-60 had the highest surface area of approximately twelve times of that of raw diatomite. This was due to the vibratory bubble generated from ultrasound wave induced the negative pressure area and shrank in the positive

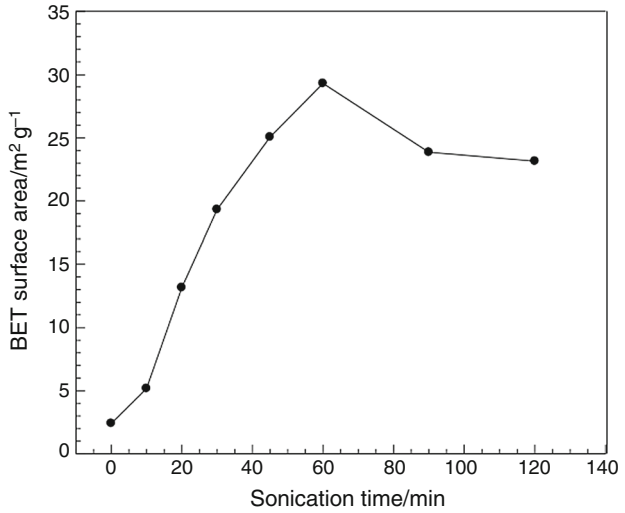

Fig. 2 BET surface area of the modification of diatomite with different times

pressure area of longitudinal ultrasonic transmission. The shrunken air bubble produced atmospheric pressure to attack the diatomite surface which was helpful to eliminate the clogged pores without damaging the diatomite [29].

Microstructural analysis

Microanalysis was applied to investigate the success of modification of porous structure of diatomite. The SEM image and EDX analysis of samples are shown in Fig. 3a–d. Figure 3a shows the characteristic cylindrical-shaped structure of diatomite. Some of the pores at the surface of raw diatomite were blocked with impurities. The modified diatomites at different treatment times are depicted in Fig. 3b–d. At 30 min of treatment, a number of pores at the surface were still clogged with the impurity as shown in Fig. 3b. Almost all opened pores were observed at 60 min of treatment as depicted in Fig. 3c. From the EDX analysis, it was clear that the SiO_2 content significantly increased with increasing treatment time up to 60 min whereas the other compositions decreased.

Chemical analysis

The effect of different treatment times on chemical composition of modified diatomite was examined using XRF. Generally, the major chemical composition of diatomite was amorphous $SiO_2 \cdot H_2O$. The high content of SiO_2 indicated the high purity of diatomite [31]. The chemical composition of modified diatomite is shown in Fig. 4 and summarized in Table 1. The silica content of modified diatomite increased with increasing time of treatment. The highest SiO_2 content was obtained when the treatment time was 60 min.

Thermal properties of paraffin and form-stable composite PCM

DSC analysis is an effective method to determine phase change temperature and latent heat of PCM. The DSC curves of paraffin and DA-60 impregnated with paraffin at 0–75 mass% are shown in Fig. 5. The endothermic peaks of all DSC curves indicated the phase change temperatures of DA-60 composite PCMs which were in the range of 56.25–58.93 °C. The phase change temperatures of all DA-60 composite PCMs were lower than that of paraffin. This was due to the interactions between paraffin and the inner surface of diatomite and the confinement of paraffin in the fine pores [13]. Moreover, the latent heats of composite PCMs determined from the area under the curve were in the range of 14.77–50.64 J g^{-1}. The latent heat of DA-60 composite PCM increased with increasing paraffin content.

The optimum ratio of form-stable composite PCM

Although it is advantageous to have high paraffin content inside the modified diatomite to produce high latent heat of composite PCM, the paraffin content could be excessive and caused the leakage problem leading to the change of material properties. The optimum or maximum amount of paraffin impregnated into diatomite was determined following Eq. (1) [21].

$$\Delta H = n \cdot \Delta H_{\mathrm{PCM}} \tag{1}$$

where ΔH represents the calculated enthalpy of composite PCM, n is the mass percentage of paraffin impregnated into the composite PCM, and ΔH_{PCM} represents the enthalpy of paraffin measured using DSC.

From Fig. 6, the theoretical latent heat increased with increasing paraffin content. Based on the experimental results, the composite PCM containing 13.0–37.5 mass% (15–60 mass% of paraffin impregnated in DA-60) showed a linear relationship between the latent heat value and the paraffin content. It could thus be concluded that the paraffin content of 37.5 mass% was optimal for preparing the form-stable composite PCM. The latent heat of DA-60 impregnated with 37.5 mass% of paraffin was 49.17 J g^{-1}.

Thermal kinetic analysis

The thermal behavior and kinetic parameters of paraffin and DA-60 composite PCM were investigated using non-isothermal method from the DSC experiment. Figure 7 demonstrates the DSC curves of paraffin/DA-60 composite at different heating rates. The endothermic peak shifted toward higher temperature when the heating rate was increased. This was due to the fact that the high heating rate enhanced the heat transfer during each investigation

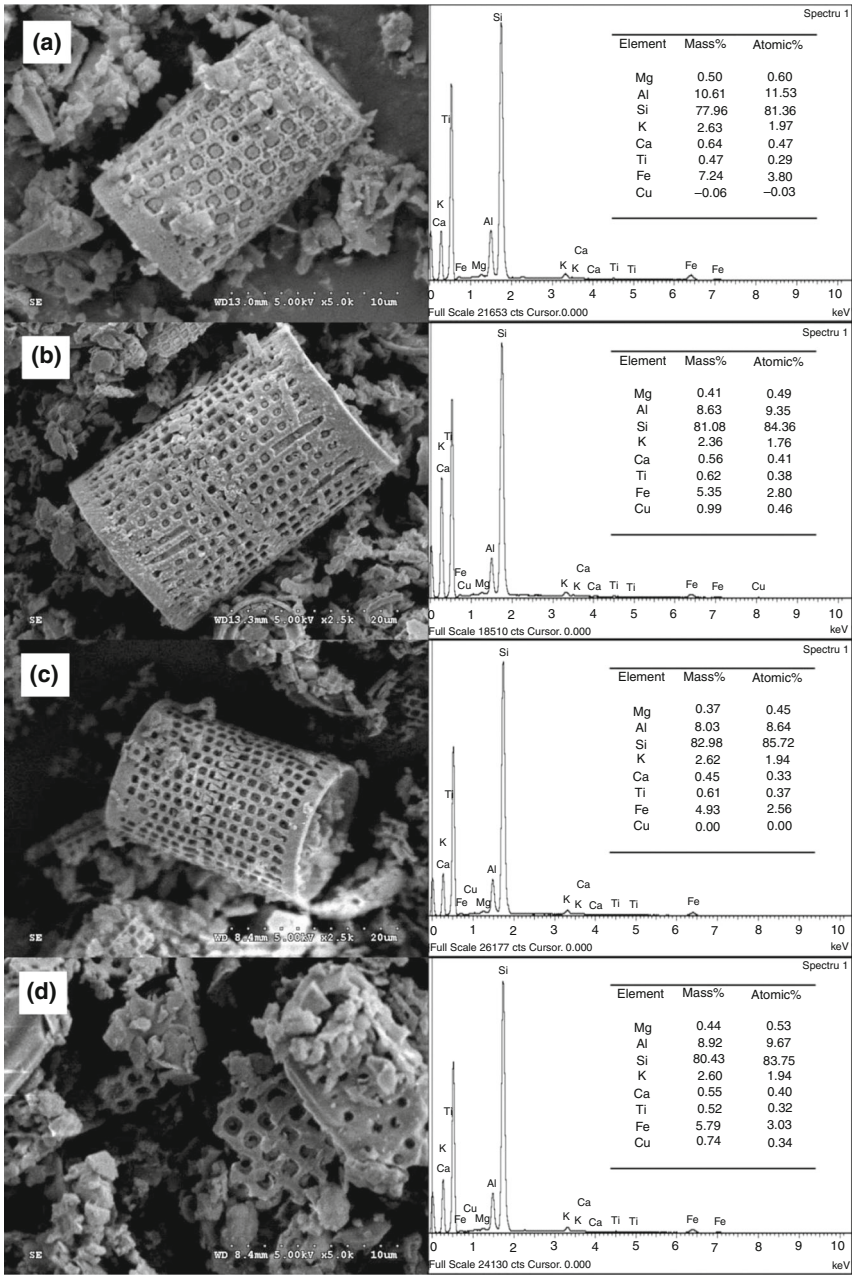

Fig. 3 SEM images and EDX analysis of the modification of diatomite at different times: **a** 0 min, **b** 30 min, **c** 60 min, and **d** 120 min

process [32]. Kissinger method was used successfully to estimate the activation energy in physical or chemical process [33, 34]. The activation energy of phase change can be obtained from a linear relationship between $\ln\left(\beta/T_p^2\right)$ versus the inverse of temperature of endothermic melting process ($1/T_p$) as follows:

$$\ln\left(\frac{\beta}{T_p^2}\right) = -\frac{E_a}{R}\left(\frac{1}{T_p}\right) + C \quad (2)$$

where β is the rate of heating (5, 10, 15, and 20 °C min^{-1}), T_p is the temperature of the maximum melting endothermic peak (K), E_a is the activation energy (kJ mol^{-1}), R is a gas constant, and C is a y intercept.

The plot of $\ln\left(\beta/T_p^2\right)$ versus $1/T_p$ showed a good linear correlation as depicted in Fig. 8. The activation energy can be calculated from the slope of the graph. The activation energy of paraffin of 189.6 kJ mol^{-1} was lower than the

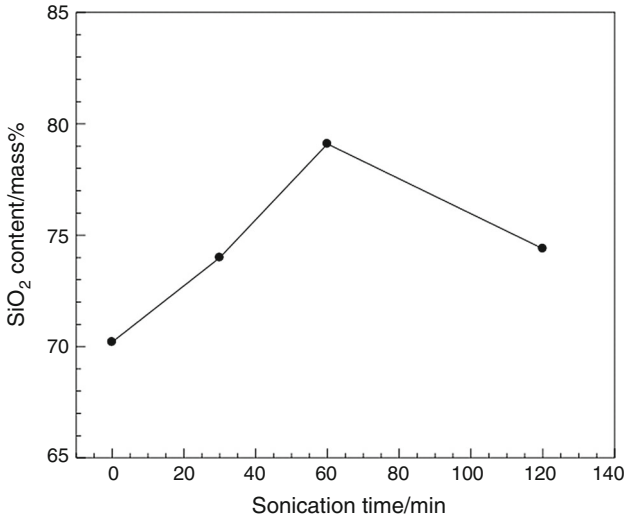

Fig. 4 SiO_2 content of the modification of diatomite with different times

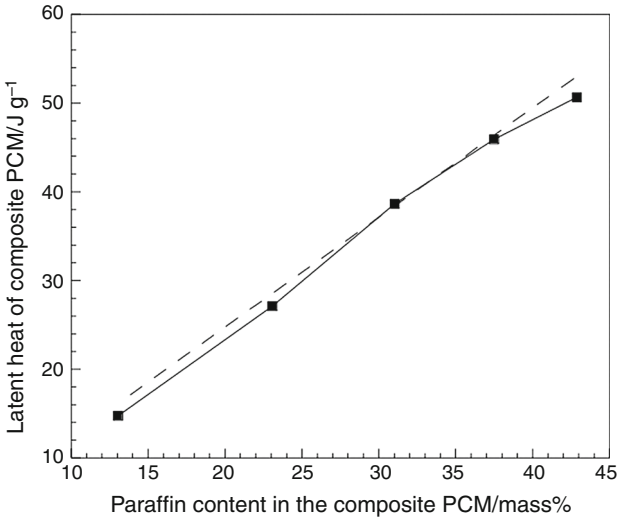

Fig. 6 Latent heat of paraffin/DA-60 composite PCM (*open square*) actual latent heat and (*filled circle*) theory latent heat

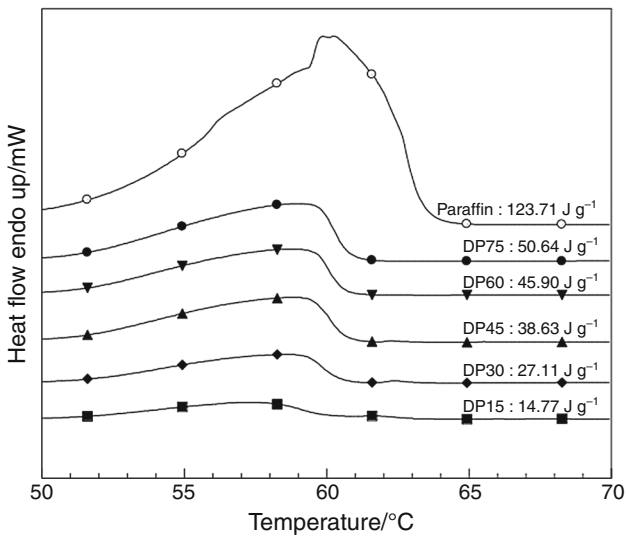

Fig. 5 DSC curves of paraffin/DA-60 composite PCM at various paraffin compositions: (*open circle*) paraffin/DA-60 100/0 (*filled square*) paraffin/DA-60 15/85, (*filled diamond*) paraffin/DA-60 30/70, (*filled triangle*) paraffin/DA-60 45/55, (*filled inverted triangle*) paraffin/DA-60 60/40, and (*filled circle*) paraffin/DA-60 75/25

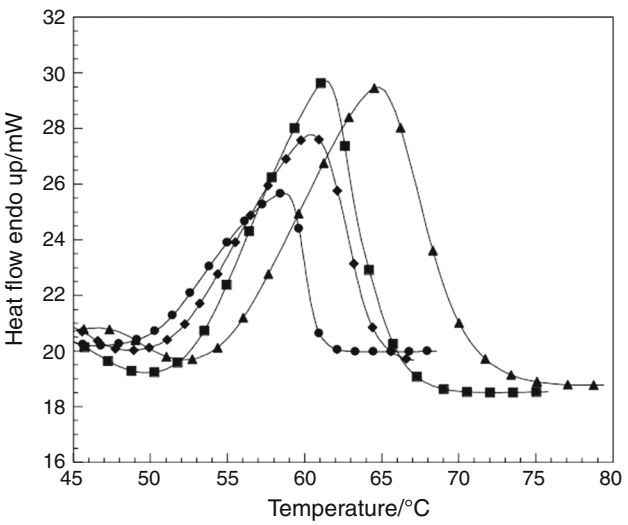

Fig. 7 DSC diagrams of the paraffin/DA-60 composite at (*filled circle*) 5, (*filled diamond*) 10, (*filled square*) 15, and (*filled triangle*) 20 °C min^{-1}

value of 192.2 kJ mol^{-1} for paraffin/DA-60 composite PCM. This is due to the porous support affected to the increasing of phase change resistance [33]. Similar observations were reported by Feng et al. [33, 35] in the study of activation energy of polyethylene glycol/active carbon composite PCM.

FTIR analysis of form-stable composite PCM

The results of chemical compatibility paraffin/DA-60 composite PCM investigated by ATR-FTIR. FTIR spectra of the paraffin, DA-60 and paraffin/DA-60 composite PCM are depicted in Fig. 9a–c. Figure 9a shows the characteristic of DA-60 at 3430 and 1630 cm^{-1} which were assigned to absorbed water and H–O–H vibration of water, respectively. Two characteristic peaks associated with Si–O–Si asymmetric stretching mode and Si–O–Si symmetric stretching vibration were observed at 1100 and 800 cm^{-1}, respectively. The peaks at 912 and 914 cm^{-1} were assigned to Al–O–H. The characteristic peaks of paraffin at 723, 1457, 2843 and 2911 cm^{-1} were assigned to CH_2 and CH_3 groups [8] as illustrated in Fig. 9b. The characteristic peaks of both paraffin and DA-60 were observed in paraffin/DA-60 composite PCM spectra as depicted in Fig. 9c. No new peak was observed indicating no chemical interaction between

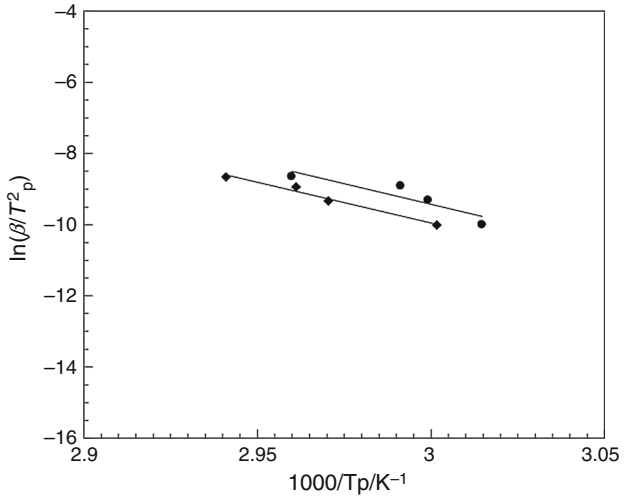

Fig. 8 Kissinger plots for averaged activation energy determination of (*filled diamond*) paraffin and (*filled circle*) paraffin/DA-60 composite PCM

paraffin and DA-60. As shown in Fig. 8, some small shifts of characteristic peaks of paraffin/DA-60 were observed when compared the FTIR results of paraffin and DA-60 as summarized in Table 2. This observation indicated that the physical interactions such as capillary and surface tension forces between the components of composite PCM prevented the leakage of paraffin during heating process. Similar results were reported for form-stable PCMs for building materials [1], montmorillonite-based composite PCMs [23], and granular PCM composites [24].

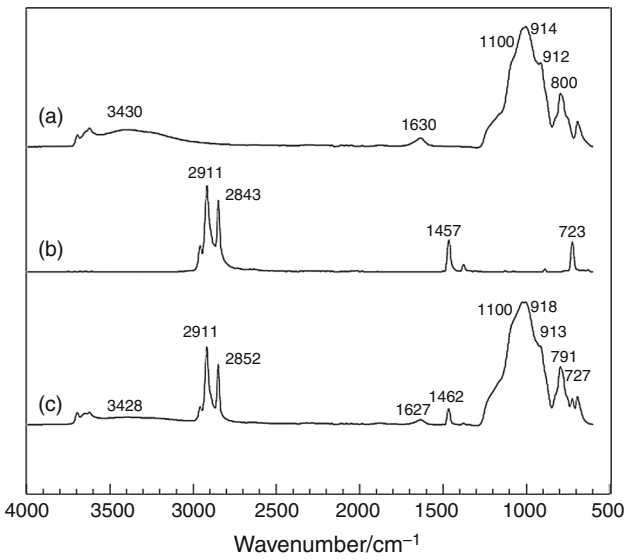

Fig. 9 FTIR spectra of (*a*) DA-60, (*b*) paraffin, and (*c*) paraffin/DA-60 composite PCM

Thermal stability of form-stable composite PCM

Thermal stability of DA-60 impregnated with paraffin was investigated by TG. The TG curves of paraffin, DA-60, and paraffin/DA-60 composite PCM are illustrated in Figs. 10 and 11. Figure 10 shows the rate of mass loss and maximum mass loss temperature in single step for all samples. The rate of mass loss indicated that paraffin/DA-60 reduced the degradation rate from 1.6 to 0.9% min^{-1}. This was due to the heat resistance of diatomite retarding the evaporation of paraffin [16]. Furthermore, the temperature for maximum mass loss of paraffin and paraffin/DA-60 composite PCM was observed at 274 and 237 °C, respectively. The earlier occurrence of thermal degradation of paraffin/DA-60 composite PCM was due to the difference in physical behavior between free paraffin and pore confined paraffin [36]. Figure 11 shows the excellent stable thermal performance of paraffin/DA-60 composite PCM. The results clearly showed that the paraffin was completely evaporated at 500 °C. Therefore, the actual paraffin content could be obtained as 34.5 mass%, which was slightly lower than the designed value of 37.5 mass%. The small discrepancy was in the same range with the previously reported result [2]. This also confirmed that paraffin was uniformly impregnated into DA-60, and the amount was close to the designed value of 37.5 mass%.

Thermal reliability of form-stable composite PCM

One important aspect of composite PCM properties is the thermal and chemical stability over a large number of melting and freezing cycles. Its thermal property and chemical structure should not change significantly after long-term usability period. In this study, thermal cycling tests were performed to determine the changes in thermal properties and chemical structure of the composite PCM after repeated 500 melting-freezing cycles. Figure 12 shows DSC curves of the paraffin/DA-60 composite PCMs before and after thermal cycling test. From Table 3, the phase change temperatures of both samples were 59 °C for melting temperature and 51 °C for freezing temperature. The latent heats of samples before and after thermal cycling test were 45.90 and 45.68 J g^{-1} for melting process and 45.98 and 45.94 J g^{-1} for freezing process, respectively, corresponding to the slight decreases of 0.43 and 0.09%, respectively. The change of latent heat values was at an acceptable level for a form-stable composite PCM [21, 37]. This indicates that there was no change in the thermal properties of composite PCM after thermal cycling test.

The TG curves of composite PCM before and after thermal cycling tests are depicted in Fig. 13. Slight difference between the mass losses of paraffin/DA-60 composite PCMs before and after thermal cycling test was

Table 2 Comparison of the wavenumbers (cm^{-1}) of the characteristic peaks of the composite PCM with those of paraffin and DA-60

Vibration	Paraffin	DA-60	PF/DA-60
Absorbed water	–	3430	3428
H–O–H	–	1630	1627
Si–O–Si asymmetric stretch	–	1100	1100
Si–O–Si symmetric stretch	–	800	791
Al–O–H	912, 914	–	913, 918
Stretching vibration of functional group CH_2	2911, 2843	–	2911, 2852
Stretching vibration of functional group CH_3	1457, 723	–	1462, 727

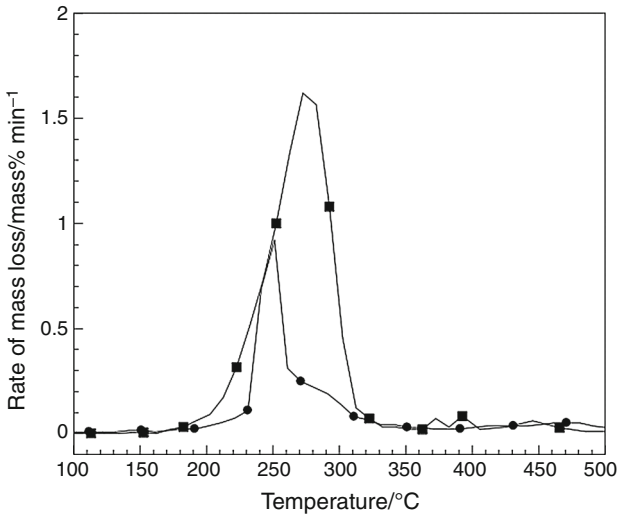

Fig. 10 Rates of mass loss of (*filled square*) paraffin and (*filled circle*) paraffin/DA-60 composite PCM

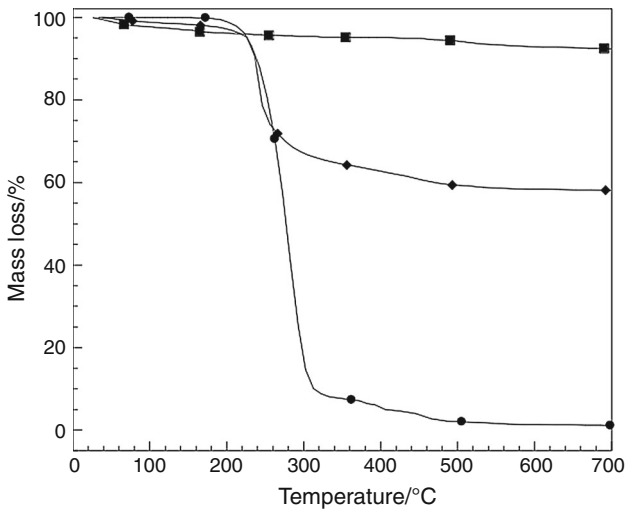

Fig. 11 TG curves of (*filled circle*) paraffin, (*filled square*) DA-60, and (*filled diamond*) paraffin/DA-60 composite PCM

observed. This confirmed that there was no leakage of paraffin from the composite PCM throughout the thermal cycling process. Figure 14 demonstrates FTIR spectra of

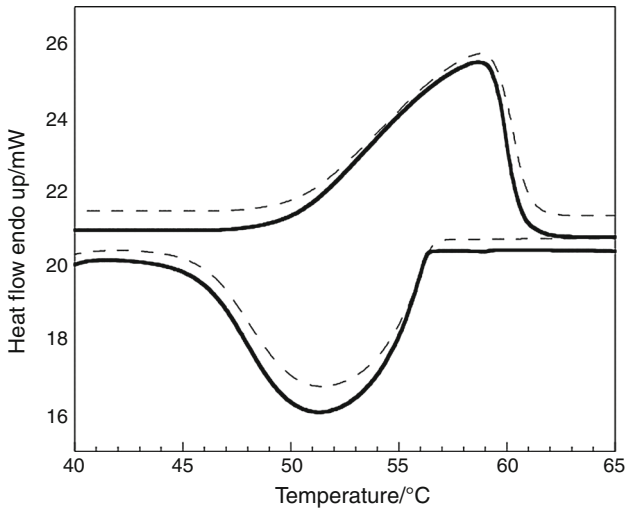

Fig. 12 DSC curves of paraffin/DA-60 composite PCM (*solid line*) before and (*dashed line*) after thermal cycling test

the prepared composite PCM before and after thermal cycling test. The two spectra were similar which indicated that there was no chemical interaction after thermal cycling test. The results thus confirmed the good thermal reliability of paraffin/DA-60 composite PCM after 500 thermal cycling.

Thermal performance of form-stable composite PCM

The thermal performance of form-stable composite PCM was evaluated by monitoring the temperature variation of the gypsum board containing form-stable composite exposed to heat radiation. Figure 15 shows the temperature variation curves of air inside the polystyrene box model with top panel of gypsum panel containing paraffin/DA-60 composite PCM. The presence of paraffin/DA-60 composite PCM in gypsum board significantly reduced the maximum temperatures of air from 53 to 49 °C. This result implied that the gypsum panel containing paraffin/DA-60 composite PCM could reduce the indoor temperature during phase change process of paraffin. During the cool down

Table 3 DSC data of the composite PCM before and after thermal cycling test

Samples	Melting point/°C	Freezing point/°C	Latent heat/J g^{-1}	
			Melting	Freezing
PF/DA-60	58.70	51.38	45.90	45.11
PF/DA-60 after 500 cycles	58.82	51.37	45.68	44.78

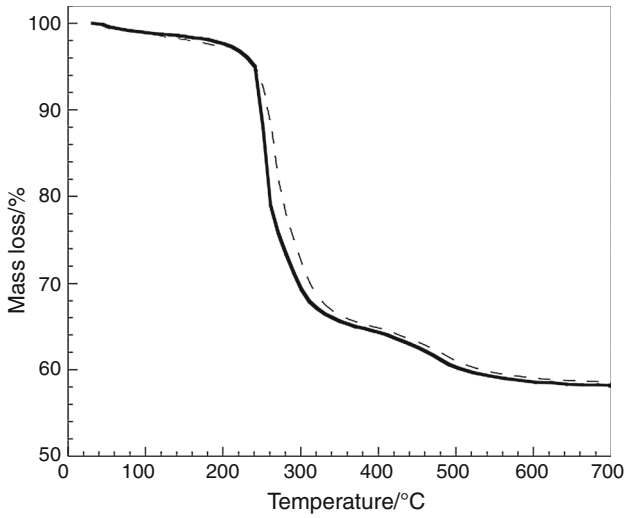

Fig. 13 TG curves of paraffin/DA-60 composite PCM (*solid line*) before and (*dashed line*) after thermal cycling test

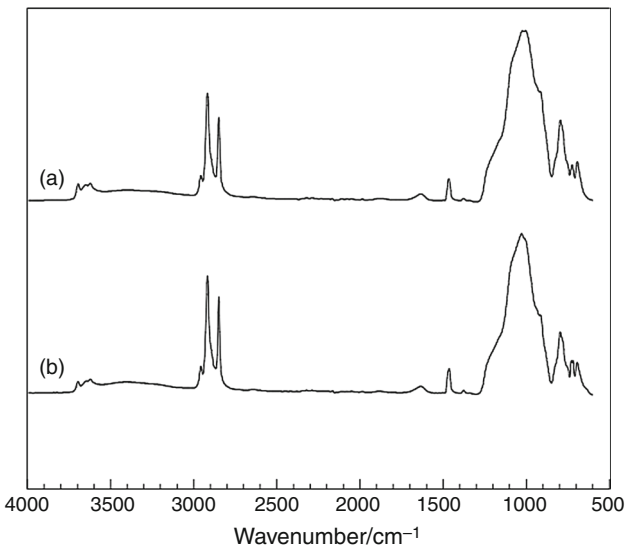

Fig. 14 FTIR spectra of paraffin/DA-60 composite PCM (*a*) before and (*b*) after thermal cycling test

process, the temperatures reduced by 23 °C for control panel (panel without composite PCM) and 16 °C for gypsum panel containing paraffin/DA-60 composite. The incorporation of paraffin/DA-60 composite PCM in building is thus another good alternative to reduce the indoor

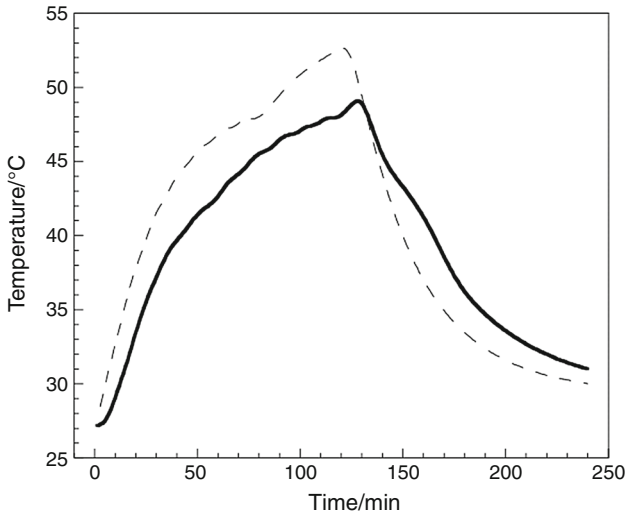

Fig. 15 Indoor temperature variation curves of the heating setup with the top boards: (*dashed line*) normal gypsum and (*solid line*) gypsum containing paraffin/DA-60 composite PCM

temperature fluctuation and decrease energy consumption by shifting the loads away from peak periods [38]. The gypsum board containing paraffin/DA-60 composite PCM showed promising characteristic for a good thermal insulator. The important parameter such a thermal conductivity should be further studied to consolidate the material characteristics.

Conclusions

The form-stable composite PCM was prepared with paraffin and modified diatomite treated with ultrasound. The surface area and the removal of impurities of diatomite were enhanced with increasing treatment time up to 60 min. Consequently, the DA-60 was chosen as a supporting material for composite PCM. The optimum ratio of paraffin in DA-60 was 60%. The melting temperature and latent heat of this composite PCM were 59 °C and 49.17 J g^{-1}, respectively. The thermal and chemical stabilities after thermal cycling test were reinforced with the studies using DSC, FTIR, and TG. Based on the thermal performance results, the gypsum board containing paraffin/DA-60 composite PCM could decrease the indoor

temperature fluctuation for a reasonable period of time and also reduced energy consumption.

Acknowledgements This work was financial supported Research Fund for Supporting Lecturer to Admit High Potential Student to Study and Research on His Expert Program Year 2015, Graduate School, Khon Kaen University. The authors also would like to acknowledge the support of Thailand Research Fund [TRF] under the TRF Senior Research Scholar, Grant No. RTA 5780004.

References

1. Chen Z, Qin M, Yang J. Synthesis and characteristics of hygroscopic phase change material: composite microencapsulated phase change material (MPCM) and diatomite. Energy Build. 2015;106:175–82.
2. Akeiber H, Nejat P, Majid MZA, Wahid MA, Jomehzadeh F, Zeynali Famileh I, et al. A review on phase change material (PCM) for sustainable passive cooling in building envelopes. Renew Sustain Energy Rev. 2016;60:1470–97.
3. Raven J. Cooling the public realm: climate-resilient urban design. In: Otto-Zimmermann K, editor. Resilient cities: cities and adaptation to climate change—proceedings of the global forum 2010. Dordrecht: Springer; 2011. p. 451–63.
4. Jeon J, Lee J-H, Seo J, Jeong S-G, Kim S. Application of PCM thermal energy storage system to reduce building energy consumption. J Therm Anal Calorim. 2013;111(1):279–88.
5. Gude VG. Energy storage for desalination processes powered by renewable energy and waste heat sources. Appl Energy. 2015;137:877–98.
6. Sánchez P, Sánchez-Fernandez MV, Romero A, Rodríguez JF, Sánchez-Silva L. Development of thermo-regulating textiles using paraffin wax microcapsules. Thermochim Acta. 2010;498(1–2):16–21.
7. Fuensanta M, Paiphansiri U, Romero-Sánchez MD, Guillem C, López-Buendía ÁM, Landfester K. Thermal properties of a novel nanoencapsulated phase change material for thermal energy storage. Thermochim Acta. 2013;565:95–101.
8. Sarier N, Onder E. The manufacture of microencapsulated phase change materials suitable for the design of thermally enhanced fabrics. Thermochim Acta. 2007;452(2):149–60.
9. Tyagi VV, Buddhi D. PCM thermal storage in buildings: a state of art. Renew Sustain Energy Rev. 2007;11(6):1146–66.
10. Shilei L, Guohui F, Neng Z, Li D. Experimental study and evaluation of latent heat storage in phase change materials wallboards. Energy Build. 2007;39(10):1088–91.
11. Yahay N, Ahmad H. Numerical investigation of indoor air temperature with the application of PCM gypsum board as ceiling panels in buildings. Proc Eng. 2011;20:238–48.
12. Castellón C, Medrano M, Roca J, Cabeza LF, Navarro ME, Fernández AI, et al. Effect of microencapsulated phase change material in sandwich panels. Renew Energy. 2010;35(10):2370–4.
13. Memon SA. Phase change materials integrated in building walls: a state of the art review. Renew Sustain Energy Rev. 2014;31:870–906.
14. Fu X, Liu Z, Wu B, Wang J, Lei J. Preparation and thermal properties of stearic acid/diatomite composites as form-stable phase change materials for thermal energy storage via direct impregnation method. J Therm Anal Calorim. 2016;123(2):1173–81.
15. Yuan Y, Li T, Zhang N, Cao X, Yang X. Investigation on thermal properties of capric–palmitic–stearic acid/activated carbon composite phase change materials for high-temperature cooling application. J Therm Anal Calorim. 2016;124(2):881–8.
16. Xu B, Ma H, Lu Z, Li Z. Paraffin/expanded vermiculite composite phase change material as aggregate for developing lightweight thermal energy storage cement-based composites. Appl Energy. 2015;160:358–67.
17. Karaipekli A, Sarı A. Development and thermal performance of pumice/organic PCM/gypsum composite plasters for thermal energy storage in buildings. Sol Energy Mater Sol C. 2016;149:19–28.
18. Sarier N, Onder E. Organic phase change materials and their textile applications: an overview. Thermochim Acta. 2012;540:7–60.
19. Anghel EM, Georgiev A, Petrescu S, Popov R, Constantinescu M. Thermo-physical characterization of some paraffins used as phase change materials for thermal energy storage. J Therm Anal Calorim. 2014;117(2):557–66.
20. Jeong S-G, Jeon J, Chung O, Kim S, Kim S. Evaluation of PCM/diatomite composites using exfoliated graphite nanoplatelets (xGnP) to improve thermal properties. J Therm Anal Calorim. 2013;114(2):689–98.
21. Karaipekli A, Sarı A. Preparation and characterization of fatty acid ester/building material composites for thermal energy storage in buildings. Energy Build. 2011;43(8):1952–9.
22. Li M, Wu Z, Kao H. Study on preparation and thermal properties of binary fatty acid/diatomite shape-stabilized phase change materials. Sol Energy Mater Sol C. 2011;95(8):2412–6.
23. Sarier N, Onder E. Thermal characteristics of polyurethane foams incorporated with phase change materials. Thermochim Acta. 2007;454(2):90–8.
24. Korunic Z. ReviewDiatomaceous earths, a group of natural insecticides. J Stored Prod Res. 1998;34(2–3):87–97.
25. Wang H, Zhu M, Li Y, Zhang Q, Wang H. Mechanical properties of dental resin composites by co-filling diatomite and nanosized silica particles. Mater Sci Eng C. 2011;31(3):600–5.
26. Hadjar H, Hamdi B, Kessasia Z. Adsorption of heavy metal ions on composite materials prepared by modification of natural silica. Desalination. 2004;167:165–74.
27. Sun Z, Zhang Y, Zheng S, Park Y, Frost RL. Preparation and thermal energy storage properties of paraffin/calcined diatomite composites as form-stable phase change materials. Thermochim Acta. 2013;558:16–21.
28. Şan O, Gören R, Özgür C. Purification of diatomite powder by acid leaching for use in fabrication of porous ceramics. Int J Miner Process. 2009;93(1):6–10.
29. Zhang G, Cai D, Wang M, Zhang C, Zhang J, Wu Z. Microstructural modification of diatomite by acid treatment, high-speed shear, and ultrasound. Micropor Mesopor Mater. 2013;165:106–12.
30. Ali Memon S, Yiu Lo T, Shi X, Barbhuiya S, Cui H. Preparation, characterization and thermal properties of Lauryl alcohol/Kaolin as novel form-stable composite phase change material for thermal energy storage in buildings. Appl Therm Eng. 2013;59(1–2):336–47.
31. Sun Z, Yang X, Zhang G, Zheng S, Frost RL. A novel method for purification of low grade diatomite powders in centrifugal fields. Int J Miner Process. 2013;125:18–26.
32. Castelein O, Soulestin B, Bonnet JP, Blanchart P. The influence of heating rate on the thermal behaviour and mullite formation from a kaolin raw material. Ceram Int. 2001;27(5):517–22.
33. Feng L, Zheng J, Yang H, Guo Y, Li W, Li X. Preparation and characterization of polyethylene glycol/active carbon composites as shape-stabilized phase change materials. Sol Energy Mater Sol C. 2011;95(2):644–50.

34. Blaine RL, Kissinger HE. Homer Kissinger and the Kissinger equation. Thermochim Acta. 2012;540:1–6.
35. Kissinger HE. Reaction kinetics in differential thermal analysis. Anal Chem. 1957;29(11):1702–6.
36. Xu B, Li Z. Paraffin/diatomite composite phase change material incorporated cement-based composite for thermal energy storage. Appl Energy. 2013;105:229–37.
37. Deng Y, Li J, Qian T, Guan W, Wang X. Preparation and characterization of KNO_3/diatomite shape-stabilized composite phase change material for high temperature thermal energy storage. J Mater Sci Technol. 2016. doi:10.1016/j.jmst.2016.02.011.
38. Sun D, Wang L. Utilization of paraffin/expanded perlite materials to improve mechanical and thermal properties of cement mortar. Constr Build Mater. 2015;101(part 1):791–6.

Journal of Alloys and Compounds 708 (2017) 605–611

Contents lists available at ScienceDirect

Journal of Alloys and Compounds

journal homepage: http://www.elsevier.com/locate/jalcom

Effect of synthesis temperature on the magneto-electrochemical properties of $LaFe_{0.9}Co_{0.1}O_3$ nanoparticles

Sumalin Phokha [a, *], Sitchai Hunpratub [a], Brian Usher [a], Narong Chenlek [b], Atipong Bootchanont [c], Santi Maensiri [d], Prinya Chindaprasirt [e]

[a] Department of Physics, Faculty of Science, Udon Thani Rajabhat University, Udon Thani, 41000, Thailand
[b] Synchrotron Light Research Institute (Public Organization), 111 University Avenue, Muang District, Nakhon Ratchasima, 30000, Thailand
[c] Division of Physics, Faculty of Science and Technology, Rajamangala University of Technology Thanyaburi (RMUTT), Pathumthani, 12110, Thailand
[d] School of Physics, Institute of Science, Suranaree University of Technology, Nakhon Ratchasima, 30000, Thailand
[e] Sustainable Infrastructure Research and Development Center, Department of Civil Engineering, Faculty of Engineering, Khon Kaen University, Khon Kaen, 40002, Thailand

ARTICLE INFO

Article history:
Received 21 October 2016
Received in revised form
14 January 2017
Accepted 4 March 2017
Available online 7 March 2017

Keywords:
$LaFe_{0.9}Co_{0.1}O_3$
Ferromagnetic properties
Electrochemical properties
X-ray absorption near edge spectroscopy (XANES)
X-ray photoelectron spectroscopy (XPS)

ABSTRACT

Orthoferrites $LaFe_{0.9}Co_{0.1}O_3$ nanoparticles were synthesized by a polymer pyrolysis method and calcined at 700, 800, 900 and 1000 °C for 3 h in air. The structure, morphology, valence states, magnetic and charge-discharge properties of the nanoparticles were characterized using X-ray diffraction (XRD), transmission electron microscopy (TEM), X-ray absorption near edge structure (XANES), X-ray photoelectron spectroscopy (XPS), vibrating sample magnetometer (VSM) and a potentiostat/galvanostat electrochemical cell system, respectively. Rietveld analysis confirmed the presence of a single phase and that the perovskite lattice exhibited an orthorhombic distortion. The average crystallite sizes increased from 32 ± 6 to 78 ± 6 nm with increasing calcination temperature. From the XANES and XPS results, the valence states of Fe and Co ions in samples were Fe^{3+}, Co^{3+} and Co^{2+} and the ratio of the number of Co^{3+} and Co^{2+} states varied between samples. All samples exhibited ferromagnetic behavior at room temperature with a maximum magnetization value of 1.0 emu/g for the sample calcined at 900 °C. The relationship between the Co^{3+}/Co^{2+} ratio and the origin of the ferromagnetism is discussed. The highest discharge capacity of electrodes made from $LaFe_{0.9}Co_{0.1}O_3$ nanoparticles was 1150 mAh/g, suggesting the high surface area to volume ratios of the nanoparticles.

© 2017 Elsevier B.V. All rights reserved.

1. Introduction

Orthoferrites have the formula $XFeO_3$ where X represents an alkali or rare earth ion such as Bi, La, Pr, Nd, Sm, Eu and Gd etc [1–9] which sits on an A site (tetrahedral) within the oxygen fcc sublattice and the B sites (octahedral) are occupied by Fe ions. The nanocrystal forms of these materials have attracted much attention because their physical and chemical properties are significantly different from their bulk counterparts due to their high surface area to volume ratios. Some of these properties are important in various applications such as solid oxide fuel cells, photocatalysts, chemical sensors, batteries and super-capacitors [1,6]. These materials also show promise in application such as magnetic field sensors, magneto-optical and spintronic devices [2,3,6–8] due to their room temperature (RT) ferromagnetic (FM) properties.

The substitution of various transition metals (TM) onto $LaFeO_3$ A and/or B sites and the preparation of nanometer-sized particles has produced improvements in its structural, magnetic and electrochemical properties. For example, RT-FM behavior has been reported following TM substitution on A sites in materials such as $La_{1-x}Zn_xFeO_3$ [10], $La_{1-x}Ga_xFeO_3$ [11] and $La_{0.5}Al_{0.5}FeO_3$ [12] as well as TM substitution on B sites in materials such as $LaFe_{1-x}Ti_xO_3$ [13], $LaFe_{1-x}Cr_xO_3$ [14], $LaFe_{0.9}Mn_{0.1}O_3$ [15] and $LaFe_{0.75}Mn_{0.25}O_3$ [16] or both A and B sites, for example in $La_{0.8}Sr_{0.2}Fe_{1-x}Cu_xO_{3-w}$ [17]. A structural transition from orthorhombic to rhombohedral can change a materials magnetic behavior, for example higher Mn concentrations in $LaFe_{1-x}Mn_xO_3$ ($x > 0.5$) results in a rhombohedral structure which exhibits antiferromagnetic behavior [16]. In another example Lim et al. [18] have reported that polycrystalline $LaFeO_3$ has a charge-discharge current density of approximately

* Corresponding author.
E-mail address: sumalinphokha@gmail.com (S. Phokha).

http://dx.doi.org/10.1016/j.jallcom.2017.03.041
0925-8388/© 2017 Elsevier B.V. All rights reserved.

50 mAh/g at RT, whereas $La_{1-x}Sr_xFeO_3$ showed more than 500 mAh/g at 60 °C [19]. To date there have been no studies of the magnetic and electrochemical properties following Co ion substitution on B sites within a $LaFeO_3$ host. It is therefore of interest to study these properties in $LaFe_{1-x}Co_xO_3$ nanoparticles to further our scientific understanding of this class of materials and also for their potential applications.

In this work, Co-doped $LaFeO_3$ ($LaFe_{0.9}Co_{0.1}O_3$) nanoparticles were prepared by the polymer pyrolysis method and their crystallinity and morphology were characterized by XRD and TEM. The valence states of Fe and Co ions were studied by XANES and XPS from which the ratio of the number of Co^{3+} and Co^{2+} ions in the samples could be determined. The magnetic properties of the nanoparticles were investigated using a VSM. The charge-discharge capacity of electrodes made from $LaFe_{0.9}Co_{0.1}O_3$ were measured using a potentionstat/galvanostat electrochemical cell system.

2. Experimental

Nanoparticle of $LaFe_{0.9}Co_{0.1}O_3$ was synthesized by the polymer pyrolysis method according to procedures established in previous work [2,20–24]. Briefly, 0.006 mol of $La(NO_3)_3.6H_2O$ (Aldrich), $Fe(NO_3)_3.9H_2O$ (Kanto), $Co(NO_3)_2.6H_2O$ (Aldrich) and 70 ml of acrylic acid ($C_3H_4O_2$) were dissolved in deionized water to promote polymerization after which the precursor solution was heated to 30 °C and stirred until it dried. The dried precursor was then pre-calcined in a furnace at 400 °C for 2 h to form a polyacrylate salt which was then calcined at temperatures of 700, 800, 900 and 1000 °C for 3 h in air to obtain $LaFe_{0.9}Co_{0.1}O_3$ nano-crystals.

The prepared samples were characterized using XRD, TEM, XANES, XPS and VSM.

An XRD system (Bruker D2 Phaser) equipped with a Cu anode source (λ = 0.154184 nm) and TEM (Ziess, EM902) were used to study the phases, crystal sizes and morphology of the $LaFe_{0.9}Co_{0.1}O_3$ samples. XANES and XPS experiments to allow determination of the Fe and Co valence states were performed in transmission mode on the BL5.2 and BL5.1 beam lines at the Synchrotron Light Research Institute in Nakhon Ratchasima, Thailand, respectively. Magnetic hysteresis measurements were performed at room temperature using a VSM (Versa Lab, Quantum Design) with applied fields between −10000 and 10000 Oe. Field cooling mode measurements were made using the same equipment, with an applied external field of 500 Oe and sample temperatures between 50 and 390 K. Charge–discharge measurements were made at RT using a potentionstat/galvanostat electrochemical cell system (Austin, TX).

3. Results and discussion

Fig. 1 shows the XRD patterns obtained from the $LaFe_{0.9}Co_{0.1}O_3$ samples calcined at various temperatures. The peaks match with those of the orthorhombic structure of $LaFeO_3$ according to the JCPDS standard 88-0641 (space group *Pnma*) for all samples. There are no diffraction peaks associated with impurity phases, indicating the formation of a pure phase with Co doping. The goodness of fit (GOF, χ^2) was found to be in the range of 1.1–1.5 as shown in Table 1. It can also be seen from Table 1 that the crystallite sizes (D_{XRD}) calculated using Scherrer's equation increase from 32 ± 6 to 78 ± 6 nm, for calcination temperatures from 700 to 1000 °C. One of the effects of increasing the calcination temperature was to create significantly larger crystals as a result of agglomeration. Because increasing calcination temperature was also associated with a narrowing of the XRD peaks it suggests there may have been some recrystallization following agglomeration [20]. However, there was no significant difference in the D_{XRD} for Co-doped samples compared to those of 34.8 ± 1.5–74.0 ± 2.8 nm for undoped

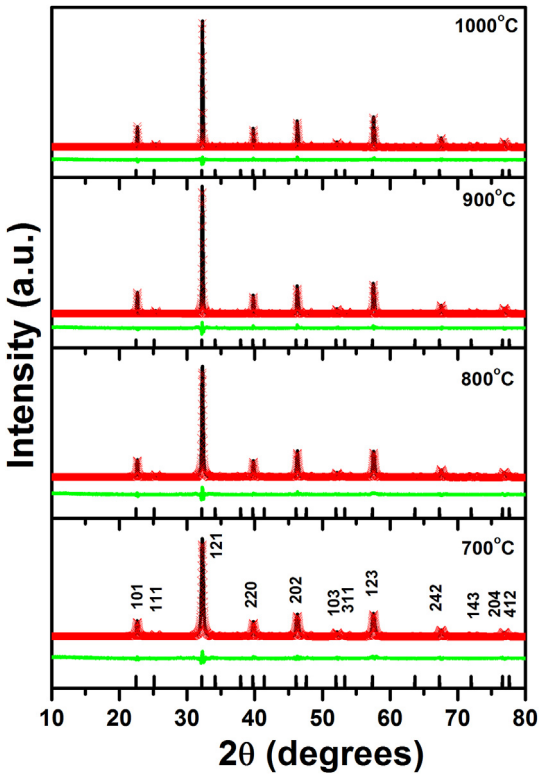

Fig. 1. XRD patterns obtained from $LaFe_{0.9}Co_{0.1}O_3$ samples calcined at various temperatures for 3 h in air. The measured data are indicated by the dots and the calculated data by solid lines overlaying the data. The lower curve in each window shows the difference between the observed and calculated data and the vertical bars are the peak positions obtained from the JCPDS standard 88-0641 for $LaFeO_3$.

samples at the same calcination temperatures [2]. This is possibly due to the substitution of the Fe^{3+} sites by the small amount Co ions (10 at %), leading to a small change in the lattice parameter and the crystallite sizes which is in good agreement with earlier reports [23]. This increase of calcination temperatures is observed that

Table 1
Summary of crystallite sizes as measured by XRD line broadening (D_{XRD}) and TEM direct imaging (D_{TEM}), parameters as calculated by Rietveld analysis, Gaussian fits of XPS spectra, saturated magnetization (M_S) at RT, remanence magnetization (M_R) and coercivity (H_C) of $LaFe_{0.9}Co_{0.1}O_3$ nanoparticles calcined at various temperatures for 3 h in air.

Parameter	Calcined temperatures			
	700 °C	800 °C	900 °C	1000 °C
D_{XRD} (nm)	32 ± 6	46 ± 4	65 ± 4	78 ± 6
D_{TEM} (nm)	51 ± 5	81 ± 7	172 ± 20	258 ± 20
a (Å)	5.551(1)	5.543(7)	5.543(4)	5.541(2)
b (Å)	7.829(9)	7.832(9)	7.832(4)	7.829(2)
c (Å)	5.546(1)	5.545(8)	5.545(4)	5.545(3)
Volume (Å^3)	241.03	240.72	240.70	240.56
GOF (χ^2)	1.1	1.3	1.5	1.4
Rp (%)	8.7	9.3	9.4	9.6
Rwp (%)	11.6	12.6	13.4	13.8
Peak Position (eV)				
Co^{3+}	780.5/795.2	780.2/794.7	780.2/794.8	–
Co^{2+}	782.4/796.4	782.4/796.5	782.1/797.0	–
Peak Area (eV)				
Co^{3+}	695.4/168.2	875.5/217.6	589.3/321.5	–
Co^{2+}	585.3/62.1	755/150.4	457.9/76.0	–
Percentage of Co^{3+} (%)	57.2	54.7	63.1	–
Percentage of Co^{2+} (%)	42.8	45.3	36.9	–
M_S (emu/g)	0.67	0.55	1.00	0.98
M_R (emu/g)	0.21	0.19	0.48	0.41
H_C (Oe)	1016	1003	850	620

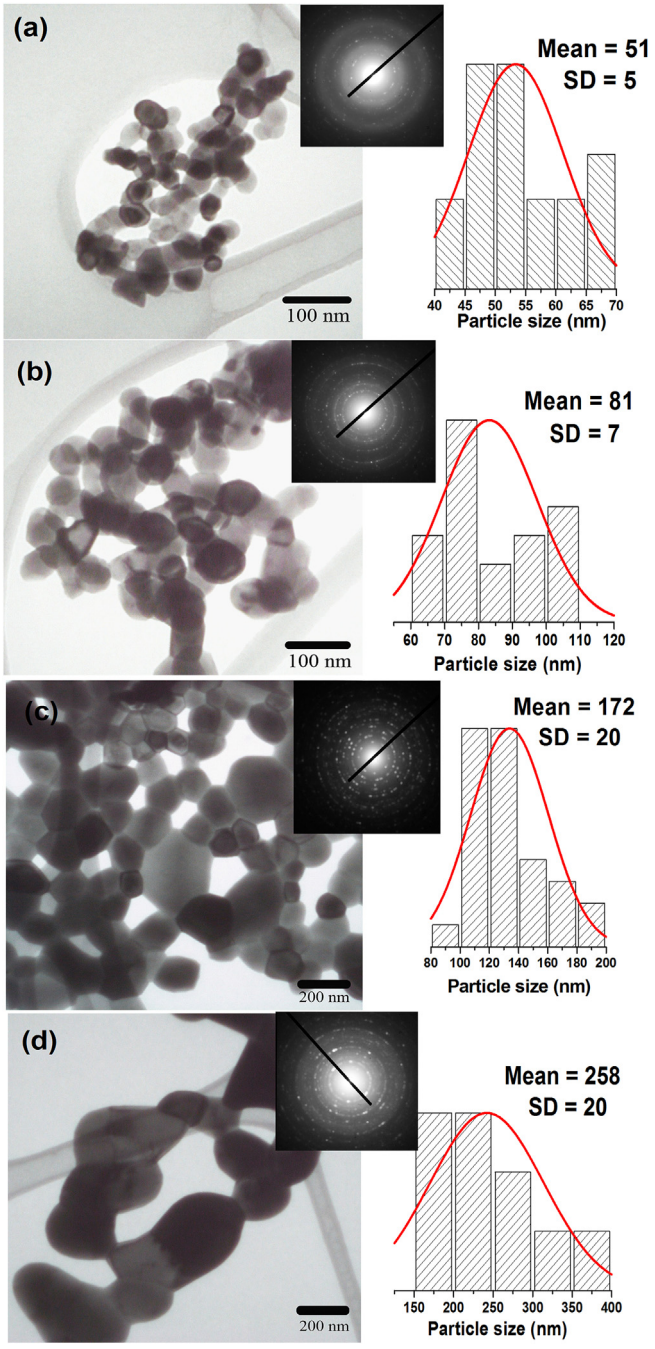

Fig. 2. TEM images with histograms of the $LaFe_{0.9}Co_{0.1}O_3$ samples calcined at (a) 700 °C, (b) 800 °C, (c) 900 °C and (d) 1000 °C. Inset shows the selected area electron diffraction (SAED) patterns.

lattice parameters (*a*, *b*, *c*) decrease as well as the lattice volume in $LaFe_{0.9}Co_{0.1}O_3$ samples from 241.03 to 240.56 $Å^3$ with increasing calcination temperatures from 700 to 1000 °C as listed in Table 1. This behavior is made possible on the decrease of the lattice volume with the increase in the D_{XRD}, being ascribed to the truncation of the attractive Madelung potential responsible for the stability of the crystal structure [25]. The substitution of Co ions on Fe sites was observed that the lattice volume was small changed similar to that of undoped samples which were decreased from 242.83 to 242.66 $Å^3$ [2] with increasing calcination temperature. This small change of lattice volume is due to small amount of 10 at % Co substitution at Fe^{3+} sites and smaller ionic radii of Co^{3+} (0.55 Å) and

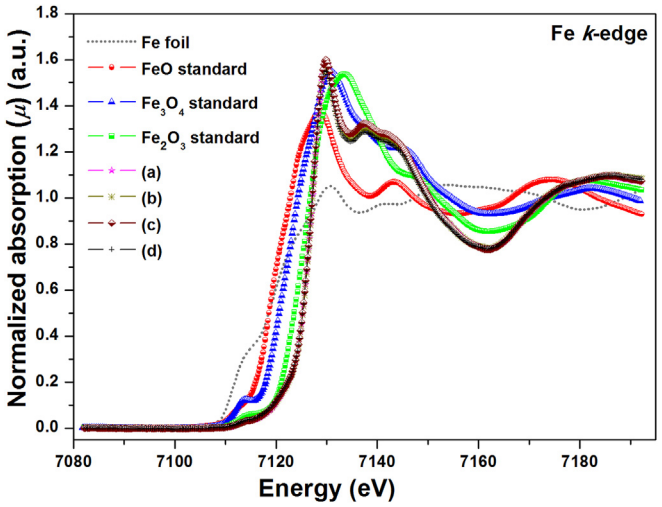

Fig. 3. XANES spectra at the Fe K absorption edge from Fe foil, Fe_3O_4 (Fe^{2+}, Fe^{3+}) and Fe_2O_3 (Fe^{3+}) standards. The data from the $LaFe_{0.9}Co_{0.1}O_3$ samples calcined at (a) 700 °C, (b) 800 °C, (c) 900 °C and (d) 1000 °C are indistinguishable from each other on the scale of this plot and are the right-most curves at the absorption edge transition.

Co^{2+} (0.65 Å) compared to that of Fe^{3+} (0.67 Å). This causes a change in the bond length (lattice distortion) and the overall lattice volume which is in good agreement with other reports such as Cu^{2+} (0.73 Å) [26] and Cr^{3+} (0.64 Å) [14] substitute at Fe sites or when Al^{3+} (0.53 Å) [27], Ca^{2+} (0.134 Å) [28], Sr^{2+} (1.26 Å) [29] and Ga^{3+} (0.62 Å) [11] substitute at La sites or Co^{2+} substitute at Ni^{2+} (0.74 Å) sites [30] or co-substitute of Cu^{2+} and Zn^{2+} (0.74 Å) at Mg^{2+} (0.89 Å) sites of ferrite materials [31].

Bright field TEM images and selected area electron diffraction (SAED) allowed the morphology and structure of the $LaFe_{0.9}Co_{0.1}O_3$ materials to be investigated, as shown in Fig. 2. Bright field TEM images showed aggregated particles with a bi-modal size distribution at low calcining temperatures which becomes a single, broader peak at high calcining temperatures. The average particle sizes in the samples were calculated from the histogram to increase from 51 ± 5 to 258 ± 20 nm with increasing calcination temperatures from 700 to 1000 °C, as agreement with the XRD results. It is clear observed that both doped and undoped $LaFeO_3$ samples [2]

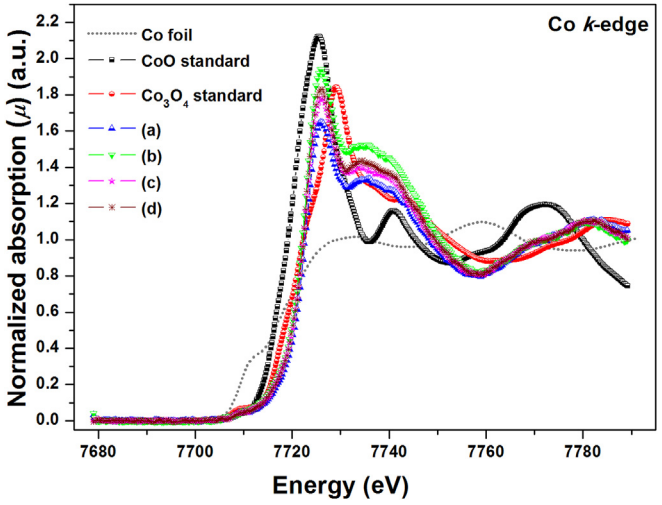

Fig. 4. XANES spectra at the Co K absorption edge from Co foil, CoO (Co^{2+}) and Co_3O_4 (Co^{2+}, Co^{3+}) standards and the $LaFe_{0.9}Co_{0.1}O_3$ samples calcined at (a) 700 °C, (b) 800 °C, (c) 900 °C and (d) 1000 °C.

have been similar agglomeration of small particles to create significantly larger particles with increasing calcination temperatures. The SAED patterns showed the spotty ring pattern typical of polycrystalline materials.

Figs. 3 and 4 show normalized XANES spectra obtained from $LaFe_{0.9}Co_{0.1}O_3$ samples in the vicinity of the Fe and Co K-edges measured in transmission mode at room temperature. The edge energies of the Fe foil, FeO (Fe^{2+}), Fe_3O_4 (Fe^{2+}, Fe^{3+}) and Fe_2O_3 (Fe^{3+}) standards and the $LaFe_{0.9}Co_{0.1}O_3$ samples calcined at various temperatures can be compared in Fig. 3 and the Co edge results are shown in Fig. 4. In both figures the experimental data for all four samples are so similar that they are indistinguishable, but are sufficiently different to the standards against which the edge energies are to be compared that the valence states can be determined. It can be seen from Fig. 3 that the edge position of all samples is close to that of the Fe_2O_3 standard, indicating that most, if not all, of the Fe ions were in the Fe^{3+} valence state. From Fig. 4 it can be seen that the absorption edge position for all samples was close to the Co_3O_4 standard which, by an electron counting argument, contains both Co^{2+} and Co^{3+} ions in the ratio of 1:2 since all oxygen ions are in the O^{-2} state.

To confirm the valence states of the various ions in the $LaFe_{0.9}Co_{0.1}O_3$ samples calcined at 700 to 900 °C, XPS spectra were measured as shown in Fig. 5. The Co $2p_{3/2}$ (780.2–780.5 eV for Co^{3+} $2p_{3/2}$ and 782.1–782.4 eV for Co^{2+} $2p_{3/2}$) and Co $2p_{1/2}$ (794.7–795.2 eV for Co^{3+} $2p_{1/2}$ and 796.4–797.0 eV for Co^{2+} $2p_{1/2}$) peaks were present in all samples as shown in Fig. 5(a)–(c) indicating that both Co^{3+} and Co^{2+} ions were present in the samples [32,33]. The Co $2p_{3/2}$ and Co $2p_{1/2}$ peaks obtained from our samples exhibited spits of between ~14.5 and 14.7 eV which is not the same as the 15.5 eV observed for Co_3O_4 [34] suggesting different ratios in the Co^{3+} and Co^{2+} ion populations. Unlike in Co^{3+} and Co^{2+} ions, the shake-up satellites peak at 787.3–788.0 eV was observed in the samples. The relative amounts of Co^{3+} to Co^{2+} present in all samples was determined by fitting Gaussians to each of the peaks present in the XPS spectra shown in Fig. 5(a)–(c). The relative concentrations of Co^{3+} and Co^{2+} were obtained by summing the areas beneath both peaks associated with each of the Co^{3+} and Co^{2+} states and calculating their relative fractions and the results of this process are given in Table 1. It was observed that the percentage of Co^{3+} in the sample calcined at 900 °C was higher than for the other samples. These results showed that the Co^{3+}: Co^{2+} ratio was 1.34:1, 1.20:1 and 1.71:1 for samples calcined at 700, 800 and 900 °C, respectively.

Fig. 5(d)–(f) show that the Fe $2p_{3/2}$ peaks were at approximately 710.2–710.5 eV and 712.2–712.5 eV and the Fe $2p_{1/2}$ peaks were at

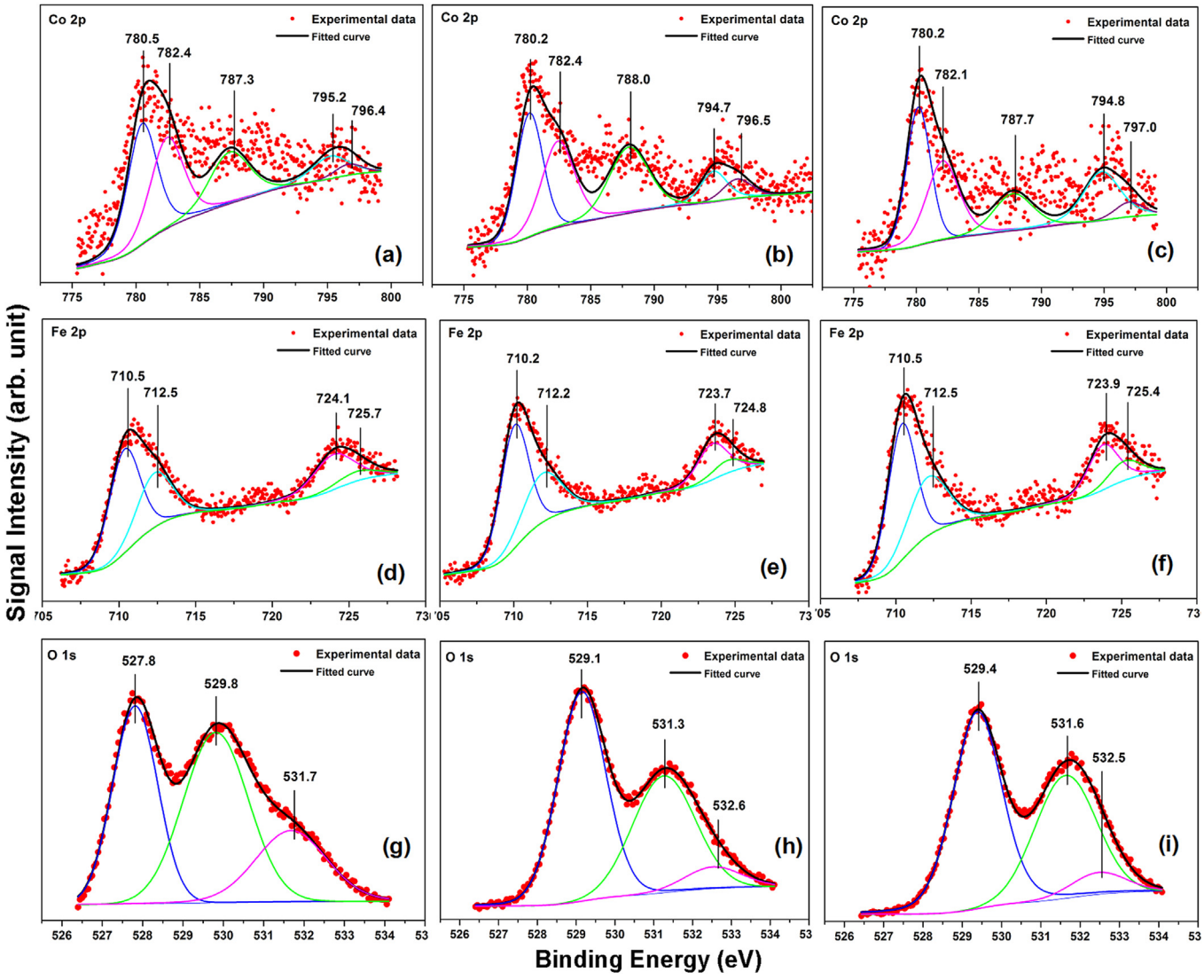

Fig. 5. XPS spectra in the vicinity of the Co 2p, Fe 2p and O 1s peaks obtained from $LaFe_{0.9}Co_{0.1}O_3$ samples calcined at 700 °C for (a, d, g), 800 °C for (b, e, h) and 900 °C for (c, f, i).

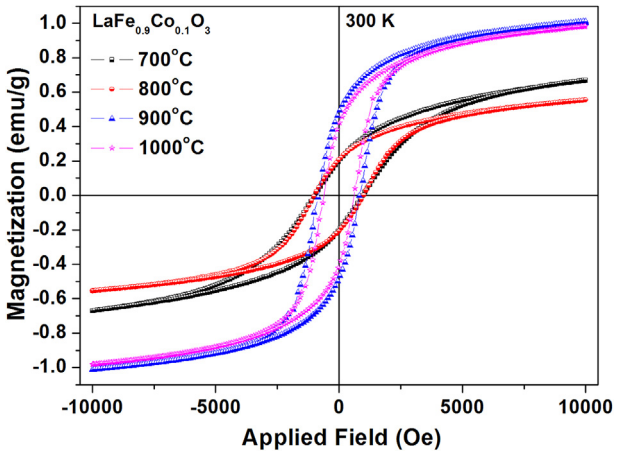

Fig. 6. M-H curves at ±10 kOe measured at room temperature from $LaFe_{0.9}Co_{0.1}O_3$ samples calcined at various temperatures.

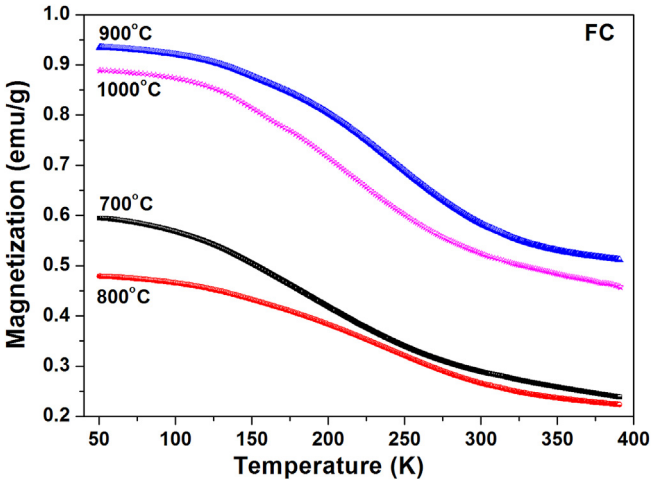

Fig. 7. *M-T* curves at 500 Oe of $LaFe_{0.9}Co_{0.1}O_3$ samples calcined at various temperatures.

approximately 723.7–724.1 eV and 724.8–725.7 eV for all samples and could therefore be assigned to the Fe^{3+} ion [3,4,11,35]. The O 1s in Fig. 5(g)–(i) for all samples had similar peak positions to those previously reported [4–7] corresponding to oxygen in crystal lattice (O_L) of metal–O at approximately 527.8–529.4 eV and hydroxyl oxygen (O_H) of chemisorbed water at approximately 529.8–532.6 eV. This result indicates that the determination of the valence states of Co and Fe ions by XPS is in good agreement with the XANES results. From XANES and XPS results, it is observed that the Fe^{3+} state is stable valence with increasing calcination temperatures, indicating no change in $LaFeO_3$ structure. This is similar to those obtained when Co-doped or Cu-doped [26] or undoped $LaFeO_3$ samples [2].

The magnetic field dependence of the specific magnetization (*M-H* curve) obtained from room temperature VSM measurements on the $LaFe_{0.9}Co_{0.1}O_3$ samples using magnetic fields (*H*) in the range of ±10 kOe are shown in Fig. 6. All the samples exhibit weak ferromagnetic (FM) behavior at RT with saturated magnetizations (M_S) at 10 kOe of 0.55–1.00 emu/g and coercivities (H_C) of 600–1000 Oe. As a result, the sample calcined at 900 °C, having crystallite sizes of 65 ± 4 nm, showed the highest M_S value of 1.0 emu/g. The values of M_S, H_C and remanence magnetization (M_R) of the $LaFe_{0.9}Co_{0.1}O_3$ samples are summarized in Table 1. It has been found that the M_S measured in our Co-doped $LaFeO_3$ samples does not depend on the calcination temperatures or size effect. In contrast, RT-FM observed in undoped $LaFeO_3$ samples showed increase of M_S with decreasing crystallite size. This behavior was due to increasing surface area to volume ratio, resulting in higher disordering of the Fe^{3+} spins at the surface and giving rise to higher Fe^{3+} spins interaction [2]. However, with Co-doped $LaFeO_3$, its behavior has been found that the M_S results corresponded with the concentration of Co^{3+} ions as found from the XPS results. Obviously, it showed the highest M_S value with the highest concentration of Co^{3+} ions as summarized in Table 1. The substitution of Co ions onto Fe^{3+} sites within a $LaFeO_3$ host has produced interesting distributions of the Co^{3+} and Co^{2+} ions within the structure. The net magnetization is then due to the Co^{3+} ions in the high-spin $3d^6$ state (↑↑↑↑, S = 4) and the Co^{2+} ions in the high-spin $3d^7$ state (↑↑↑, S = 3) providing more coupling pairs compared to the situation when there is only coupling within the high-spin $3d^5$ state of Fe^{3+} (↑↑↑↑↑, S = 5). Therefore, increasing the number of Co^{3+} coupling pair causes increased M_S values, indicating that optimal Co^{3+} distribution of the $LaFe_{0.9}Co_{0.1}O_3$ samples is with the vicinity of calcination temperature at 900 °C. Moreover, the highest M_S value of 1.0 emu/g and a large H_C of 1000 Oe measured in 10 at % Co replacement at Fe^{3+} sites is much higher than has been measured in undoped $LaFeO_3$ [2,7,14] for the same calcination temperatures and other doped $LaFeO_3$ materials such as for TM doped Fe^{3+} sites or RE doped La^{3+} sites. For example a value of 0.2 emu/g was obtained for 20 at % Ti^{4+}-doped $LaFeO_3$ ($LaFe_{0.9}Ti_{0.1}O_3$) nanoparticles prepared by the polymer pyrolysis method [22] or 0.8 emu/g in 10 at% Ce^{4+}-doped $LaFeO_3$ ($La_{0.9}Ce_{0.1}FeO_3$) nanoparticles prepared by solution combustion [36]. Thus it can be concluded that the RT-FM of perovskite-type $LaFeO_3$ can be improved by Co substitution at Fe^{3+} sites with small amount.

Fig. 7 displays the temperature dependence of the magnetization (*M-T*) curve for all the $LaFe_{0.9}Co_{0.1}O_3$ samples measured under an applied field of 500 Oe between 50 and 390 K in the FC mode. The *M-T* curves obtained in FC mode were similar for all samples but the magnetization values were different as shown by the *M-H* curves in Fig. 6. In addition, the magnetization curve in FC mode show no evidence of secondary phases down to 50 K. However, the Curie temperatures (T_C) of α-Fe_2O_3 (T_C ~ 240 K) and Neel temperatures (T_N) of FeO (T_N ~ 200 K), Co_3O_4 (T_N ~ 40 K) and CoO

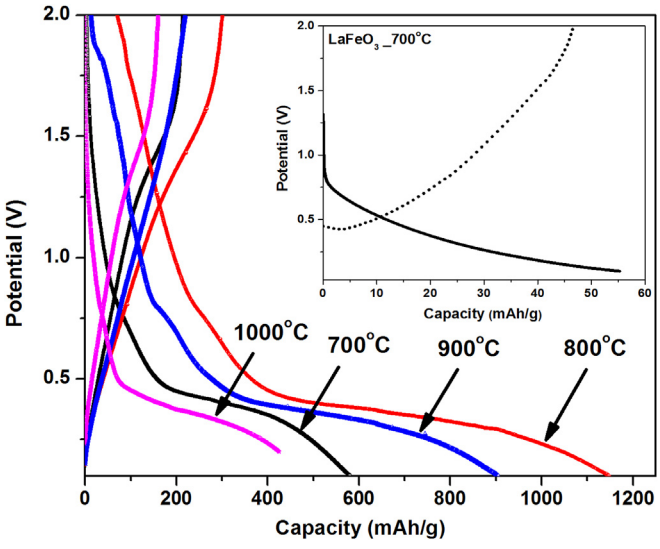

Fig. 8. First cycle charge–discharge curves obtained using $LaFe_{0.9}Co_{0.1}O_3$ electrodes at room temperature. Inset of Fig. shows plot of first cycle charge–discharge curves obtained using $LaFeO_3$ electrode.

(T_N ~ 292 K) cannot be detected. It is therefore clear that the observed FM behavior is not due to secondary phases in our $LaFe_{0.9}Co_{0.1}O_3$ samples. From the FC curves, the Curie temperature (T_C) can be determined from the derivative of the magnetization $dM_{FC}(T)/dT = 0$ [37] however the magnetization curves show that T_C is above 390 K for all calcination temperatures in both undoped and Co-doped $LaFeO_3$ samples. This is confirmed that all calcination temperatures of 700–1000 °C are suitable heat treatment for small randomization of polarization direction and then magnetic coupling is still remained with increasing temperature.

The first cycle charge–discharge, capacity-voltage profiles obtained from all $LaFe_{0.9}Co_{0.1}O_3$ samples measured at RT exhibited cutoff voltages between 0.1 and 2 V at a current density of 37.5 mA/g as shown in Fig. 8. The discharge capacities obtained were 580, 1150, 905 and 425 mAh/g for $LaFe_{0.9}Co_{0.1}O_3$ samples calcined at 700, 800, 900 and 1000 °C, respectively. The discharge capacity of the $LaFe_{0.9}Co_{0.1}O_3$ samples increased as the calcination temperature increased from 700 to 800 °C and then decreased at higher calcination temperatures (≥900 °C). This observation is normally related to surface area and porosity, which is indicated that the effect of different calcination temperatures results on various surface area and porosity. For sample calcined at 800 °C, this might be due to their high surface area and porosity and then leads to higher discharge capacities. However, the difference in surface area and porosity depends on the preparation conditions or preparation method of the materials. In addition, it can be seen from Fig. 8 that the discharge capacities in our Co-doped $LaFeO_3$ samples were higher than those in undoped $LaFeO_3$ for the same calcined at 700 °C which were measured at RT to be 55 mAh/g (inset in Fig. 8) and 50 mAh/g for a sample calcined at 1000 °C [18]. Thus the $LaFe_{0.9}Co_{0.1}O_3$ samples showed an increase of approximately 10 times the discharge capacity over those that were achieved for $LaFeO_3$. This is thought to be due to the existence of both Co^{3+} and Co^{2+} ions in Co-doped $LaFeO_3$ samples. Similar behavior has been observed in Co_3O_4 materials prepared in various ways which exhibit properties that are strongly affected by the surface area and by the presence of Co^{3+} and Co^{2+} ions [38–40]. Moreover, their discharge capacity in Co-doped $LaFeO_3$ is higher than that to other doping. For example, measured $La_{1-x}Sr_xFeO_3$ (x = 0.2, 0.4) powders showed decreasing discharge capacities from 324.4 to 147.0 mAh/g with increasing Sr content with a current density of 31.25 mA/g measured at RT [19].

4. Conclusions

Single phase $LaFe_{0.9}Co_{0.1}O_3$ nanoparticles with an orthorhombic structure have been successfully prepared by the polymer pyrolysis method. The average crystallite size of samples increased from 32 ± 6 to 78 ± 6 nm with increasing calcination temperature from 700 to 1000 °C. The Co^{3+}/Co^{2+} ratio as measured by XPS showed the highest value for the sample calcined at 900 °C and this sample exhibited the highest M_S value of 1.0 emu/g. Additionally, all the $LaFe_{0.9}Co_{0.1}O_3$ samples exhibited a T_C above 390 K, suggesting that the stable room temperature ferromagnetism of $LaFe_{0.9}Co_{0.1}O_3$ nanoparticles makes them a candidate for future spintronic devices. The substitution of Co ions at Fe^{3+} sites within a $LaFeO_3$ host exhibited novel super-capacitor behavior with a high discharge capacity, making them also a candidate for the design of high capacity energy storage devices.

Acknowledgments

The authors would like to thank the Synchrotron Light Research Institute (Public Organization), Nakhon Ratchasima, Thailand for access to their XANES and XPS facilities, the Department of Physics, Khon Kaen University for providing VSM facilities and the Advanced Functional Materials (AFM) Laboratory for TEM facilities. This work was financially supported by Khon Kaen University and the Thailand Research Fund (TRF) under the TRF Senior Research Scholar Contract No. RTA5780004.

References

[1] S.N. Tijare, M.V. Joshi, P.S. Padole, P.A. Mangrulkar, S. Rayalu, N.K. Labhsetwar, Photocatalytic hydrogen generation through water splitting on nano-crystalline $LaFeO_3$ perovskite, Int. J. Hydrogen Energy 37 (2012) 10451–10456.
[2] S. Phokha, S. Pinitsoontorn, S. Rujirawat, S. Maensiri, Polymer pyrolysis synthesis and magnetic properties of $LaFeO_3$ nanoparticles, Phys. B 476 (2015) 55–60.
[3] W.-Y. Lee, H.J. Yun, J.-W. Yoon, Characterization and magnetic properties of $LaFeO_3$ nanofibers synthesized by electrospinning, J. Alloy. Compd. 583 (2014) 320–324.
[4] F. Soderlind, L. Selegard, P. Nordblad, K. Uvdal, P.-O. Kall, Sol–gel synthesis and characterization of polycrystalline $GdFeO_3$ and $Gd_3Fe_5O_{12}$ thin films, J. Sol Gel Sci. Technol. 49 (2009) 253–259.
[5] S. Thirumalairajan, K. Girija, V. Ganesh, D. Mangalaraj, C. Viswanathan, N. Ponpandian, Novel synthesis of $LaFeO_3$ nanosructure dendrites: a systematic investigation of growth mechanism, properties, and biosensing for highly selective determination of neurotransmitter compounds, Cryst. Growth Des. 13 (2013) 291–302.
[6] Z.X. Wei, Y. Wang, J.P. Liu, C.M. Xiao, W.W. Zeng, S.B. Ye, Synthesis, magnetization, and photocatalytic activity of $LaFeO_3$ and $LaFe_{0.9}Mn_{0.1}O_{3-d}$, J. Mater. Sci. 48 (2013) 1117–1126.
[7] S. Phokha, S. Pinitsoontorn, S. Maensiri, S. Rujirawat, Structure, optical and magnetic properties of $LaFeO_3$ nanoparticles prepared by polymerized complex method, J. Sol Gel Sci. Technol. 71 (2014) 333–341.
[8] S. Yuvaraj, S. Layek, S.M. Vidyavathy, S. Yuvaraj, D. Meyrick, R.K. Selvan, Electrical and magnetic properties of spherical $SmFeO_3$ synthesized by aspartic acid assisted combustion method, Mater. Res. Bull. 72 (2015) 77–82.
[9] M.A. Ahmed, S.F. Mansour, S.I. El-Dek, M. Abu-Abdeen, Conduction and magnetization improvement of $BiFeO_3$ multiferroic nanoparticles by Ag^+ doping, Mater. Res. Bull. 49 (2014) 352–359.
[10] K. Mukhopadhyay, A.S. Mahapatra, P.K. Chakrabarti, Multiferroic behavior, enhanced magnetization and exchange bias effect of Zn substituted nano-crystalline $LaFeO_3$ ($La_{(1-x)}Zn_xFeO_3$, x = 0.10 and 0.30), J. Magn. Magn. Mater. 329 (2013) 133–141.
[11] S. Hunpratub, A. Karaphun, S. Phokha, E. Swatsitang, Optical and magnetic properties of $La_{1-x}Ga_xFeO_3$ nanoparticles synthesized by polymerization complex method, Appl. Surf. Sci. 380 (2016) 52–59.
[12] S. Acharya, P.K. Chakrabarti, Some interesting observations on the magnetic and electric peoperties of Al^{3+} doped lanthanum orthoferrite ($La_{0.5}Al_{0.5}FeO_3$), Solid State Commun. 150 (2010) 1234–1237.
[13] S. Phokha, S. Hunpratup, S. Pinitsoontorn, B. Putasaeng, S. Rujirawat, S. Maensiri, Structure, magnetic, and dielectric properties of Ti-doped $LaFeO_3$ ceramics synthesized by polymer pyrolysis method, Mater. Res. Bull. 67 (2015) 118–125.
[14] A. Paul Blessington Selvadurai, V. Pazhanivelu, C. Jagadeeshwaran, R. Murugaraj, I. Panneer muthuselvam, F.C. Chou, Influence of Cr substitution on structural, magnetic and electrical conductivity spectra of $LaFeO_3$, J. Alloy. Compd. 646 (2015) 924–931.
[15] Z.X. Wei, Y. Wang, J.P. Liu, C.M. Xiao, W.W. Zeng, S.B. Ye, Synthesis, magnetization, and photocatalytic activity of $LaFeO_3$ and $LaFe_{0.9}Mn_{0.1}O_{3-\delta}$, J. Mater. Sci. 48 (2013) 1117–1126.
[16] S. Vansutre, P. Das, H. Muthurajan, S. Radha, N. Basaviah, Magnetic and dielectric measurements of Mn substituted $LaFeO_3$ compounds, Int. J. Chem. Phys. Sci. 3 (2014) 83–90.
[17] I. Natali Sora, T. Caronna, F. Fontana, C. deJulian Fernandez, A. Caneschi, M. Green, Crystal structures and magnetic properties of strontium and copper doped lanthanum ferrites, J. Solid State Chem. 191 (2012) 33–39.
[18] D.K. Lim, H.N. Im, J. Kim, S.J. Song, Electrochemical properties of $LaMO_3$ (M=Co or Fe) as the negative electrode in a hydrogen battery, J. Phys. Chem. Solids 74 (2013) 115–120.
[19] G. Deng, Y. Chen, M. Tao, C. Wu, X. Shen, H. Yang, Electrochemical properties of $La_{1-x}Sr_xFeO_3$ (x = 0.2, 0.4) as negative electrode of Ni–MH batteries, Electrochim. Acta 54 (2009) 3910–3914.
[20] E. Swatsitang, S. Phokha, S. Hunpratub, B. Usher, A. Bootchanont, S. Maensiri, Prinya Chindaprasirt, Characterization and magnetic properties of cobalt ferrite nanoparticles, J. Alloy. Compd. 664 (2016) 792–797.
[21] E. Swatsitang, S. Phokha, S. Hunpratub, S. Maensiri, Characterization of Sm-doped CeO_2 nanoparticles and their magnetic properties, Phys. B 485 (2016) 14–20.
[22] S. Phokha, S. Hunpratup, S. Pinitsoontorn, B. Putasaeng, S. Rujirawat, S. Maensiri, Structure, magnetic, and dielectric properties of Ti-doped $LaFeO_3$ ceramics Synthesized by polymer pyrolysis method, Mater. Res. Bull. 67 (2015) 118–125.
[23] S. Phokha, J. Klinkaewnarong, S. Hunpratub, K. Boonserm, E. Swatsitang, S. Maensiri, Ferromagnetism in Fe-doped MgO nanoparticles, J. Mater. Sci.

Mater. El 27 (2016) 33–39.
[24] E. Swatsitang, S. Phokha, S. Hunpratub, S. Maensiri, Modification of Ce valence states by Sm/Sr co-doping of CeO_2 nanoparticles for improved magneto-electrochemical properties, Mater. Des. 108 (2016) 27–33.
[25] V. Perebeinos, S.-W. Chan, F. Zhang, Madelung model prediction for dependence of lattice parameter on nanoparticle size, Solid State Commun. 123 (2002) 295–297.
[26] T. Caronna, F. Fontana, I.N. Sora, R. Pelosato, Chemical synthesis and structural characterization of the substitution compound $LaFe_{1-x}Cu_xO_3$ (x = 0–0.40), Mater. Chem. Phys. 116 (2009) 645–648.
[27] S. Acharya, A.K. Deb, D. Das, P.K. Chakrabarti, Enhanced magnetic behavior of Al Substituted $LaFeO_3$ ($La_{(1-x)}Al_xFeO_3$, x=0.10 and 0.30), Mater. Lett. 65 (2011) 1280–1282.
[28] F.-T. Li, Y. Liu, R.-H. Liu, Z.-M. Sun, D.-S. Zhao, C.-G. Kou, Preparation of Ca-doped $LaFeO_3$ nanopowders in a reverse microemulsion and their visible light photocatalytic activity, Mater. Lett. 64 (2010) 223–225.
[29] M.V. Patrakeev, J.A. Bahteeva, E.B. Mitberg, I.A. Leonidov, V.L. Kozhevnikov, K.R. Poeppelmeier, Electron/hole and ion transport in $La_{1-x}Sr_xFeO_{3-d}$, J. Solid State Chem. 172 (2003) 219–231.
[30] R.C. Kambale, P.A. Shaikh, S.S. Kamble, Y.D. Kolekar, Effect of cobalt substitution on structural, magnetic and electric properties of nickel ferrite, J. Alloys Compd. 478 (2009) 599–603.
[31] S.S. Kamble, Vrushali S. Jagtap, P.C. Pingale, Synthesis of $Mg_{0.48}Cu_{0.12}Zn_{0.40}Fe_2O_4$ ferrite and its aptness for multilayer chip component application, Ceram. Int. 39 (2013) 3597–3601.
[32] T. Warang, N. Patel, R. Fernandes, N. Bazzanella, A. Miotello, Co_3O_4 nanoparticles assembled coatings synthesized by different techniques for photodegradation of methylene blue dye, Appl. Catal. B Environ. 132–133 (2013) 204–211.
[33] Y. Zhang, J. Huang, Y. Ding, Porous Co_3O_4/CuO hollow polyhedral nanocages derived from metal-organic frameworks with heterojunctions as efficient photocatalytic water oxidation catalysts, Appl. Catal. B Environ. 198 (2016) 447–456.
[34] G. Chena, X. Sia, J. Yub, H. Baic, X. Zhang, Doping nano-Co_3O_4 surface with bigger nanosized Ag and itsphotocatalytic properties for visible light photodegradationof organic dyes, Appl. Surf. Sci. 330 (2015) 191–199.
[35] B.-R. Koo, I.-K. Park, H.-J. Ahn, Fe-doped In_2O_3/a-Fe_2O_3 core/shell nanofibers fabricated by using a co-electrospinning method and its magnetic properties, J. Alloy. Compd. 603 (2014) 52–56.
[36] P. Shikha, T.S. Kang, B.S. Randhawa, Effect of different synthetic routes on the structural, morphological and magnetic properties of Ce doped $LaFeO_3$ nanoparticles, J. Alloy. Compd. 625 (2015) 336–345.
[37] X. Zhou, J. Xue, D. Zhou, Z. Wang, Y. Bai, X. Wu, X. Liu, J. Meng, Mn valence, magnetic, and electrical properties of $LaMnO_{3+\delta}$ nanofibers by electrospinning, ACS Appl. Mater. Interfaces 2 (2010) 2689–2693. Peter C.J. Graat-Peter C.J. GraatSimultaneous determination of composition and thickness of thin iron-oxide films from XPS Fe 2p spectraOpens overlay Peter C.J. Graat, Opens overlay Marcel A.J. SomersOpens overlay Peter C.J. Graat, Opens overlay Marcel A.J. Somers.
[38] Y. Ding, P. Zhang, Z. Long, Y. Jiang, J. Huang, W. Yan, G. Liu, Synthesis and electrochemical properties of Co_3O_4 nanofibers as anode materials for lithium-ion batteries, Mater. Lett. 62 (2008) 3410–3412.
[39] L. Shi, C. Fan, X. Fu, S. Yu, G. Qian, Z. Wang, Carbonate-assisted hydrothermal synthesis of porous hierarchical Co_3O_4/CuO composites as high capacity anodes for lithium-ion batteries, Electrochim. Acta 197 (2016) 23–31.
[40] C. Feng, J. Zhang, Y. Deng, C. Zhong, L. Liu, W. Hu, One-pot fabrication of Co_3O_4 microspheres via hydrothermal method at low temperature for high capacity supercapacitor, Mater. Sci. Eng. B 199 (2015) 15–21.

Advanced Powder Technology 28 (2017) 2317–2324

Contents lists available at ScienceDirect

Advanced Powder Technology

journal homepage: www.elsevier.com/locate/apt

Original Research Paper

Characterization of the high-calcium fly ash geopolymer mortar with hot-weather curing systems for sustainable application

Prinya Chindaprasirt [a], Ubolluk Rattanasak [b,*]

[a] Sustainable Infrastructure Research and Development Center, Department of Civil Engineering, Faculty of Engineering, Khon Kaen University, Khon Kaen 40002, Thailand
[b] Department of Chemistry, Faculty of Science, Burapha University, Chonburi 20131, Thailand

ARTICLE INFO

Article history:
Received 1 March 2017
Received in revised form 22 April 2017
Accepted 16 June 2017
Available online 11 July 2017

Keywords:
High-calcium fly ash
Geopolymer
Calcium silicate hydrate
Heat curing
Ambient temperature curing

ABSTRACT

Fly ash geopolymers are an alumino-silicate material and thus enable the utilization of waste containing alumino-silicate effectively. Geopolymeric reaction occurs as a result of the activation of fly ash with alkali solutions. In Thailand, a large amount of high-calcium fly ash is available due to the use of low-grade lignite coal feedstock for pulverized coal combustion process and the calcium content becomes very high. In this study, heat curing at 35 °C as a representative of a high ambient temperature (hot weather) and low cost was investigated. Curing at temperature of 65 °C and room temperature of 25 °C were also conducted to compare the results. Geopolymeric products were tested for compressive strength and characterized by XRD, IR, SEM and TGA techniques. The results showed that heat curing enhanced the geopolymerization resulting in the formation of Si—O—Al network product. Heat curings at 35 °C and 65 °C led to the formation of calcium silicate hydrate (C-S-H) and alumino-silicate (geopolymer bonding). Without heat curing, the product was predominantly C-S-H compound and the matrix was as strong as the heat-cured product. The immersion of samples in 3% sulfuric acid solution revealed that the performance of the heat-cured samples were better than those cured at room temperature. In addition, application of research results was to produce the geopolymer brick with outdoor heat exposure of 35 °C. Pedestrian pathway was demonstrated.

© 2017 The Society of Powder Technology Japan. Published by Elsevier B.V. and The Society of Powder Technology Japan. All rights reserved.

1. Introduction

Fly ash-based geopolymer is a green binder as the source materials are often from waste containing alumino-silicate. The carbon footprint of this material is, therefore, 9 times smaller than that of ordinary Portland cement [1]. Geopolymeric reaction occurs when alumino-silicate source materials (e.g. fly ash) react with base and sodium silicate solutions [2]. Sodium silicate solution provides the external dissolved SiO_2 to the system. NaOH solution is a common base and usually used to leach out the glassy phases of alumino-silicate source materials resulting in the gel formation [3,4]. A moderate temperature of 60–100 °C is applied to enhance the geopolymerization reaction [1,5,6]. Amorphous to semi-crystalline geopolymer products are formed by co-polymerisation of individual alumino-silicate species [7]. With heat curing, this material has desirable mechanical properties due to the amorphous alumino-silicate product with some semi-crystalline phases. Fast high strength gain can be achieved. In addition, geopolymer is more durable than OPC mortar under the acid and sulfate environment e.g. less loss of mass and decline in mechanical strength [6]. Owning to its good resistance to acid attack, it makes geopolymer very favorable to the sustainable development [8]. Generally, a temperature between 40 and 80 °C is used for the curing of fly ash geopolymer to obtain a strength gain up to 65 MPa within a short period [8]. However, application of heat curing requires additional effort and equipment in the construction site and thus hinders the extensively use of geopolymer as commercial building materials. Several attempts have been made successfully to produce the fly ash geopolymers with the reasonable strength (20–23 MPa at 28 days) at low curing temperature of 25 °C [9–11].

In Thailand, fly ash used in construction is mainly obtained from a pulverized coal-fired power plant in the North where lignite coal is the feed stock. The calcium content is rather high and increases with the increasing depth of coal mining. The high-calcium fly ash geopolymer consists of alumino-silicate product and C-S-H. C-S-H results from the reaction between calcium in fly ash and alkali solution in mixture leading to the strength development with curing age. High calcium content of fly ash in cement-based or geopolymeric composites, generally, results in unsoundness and

* Corresponding author.
E-mail address: ubolluk@buu.ac.th (U. Rattanasak).

http://dx.doi.org/10.1016/j.apt.2017.06.013
0921-8831/© 2017 The Society of Powder Technology Japan. Published by Elsevier B.V. and The Society of Powder Technology Japan. All rights reserved.

can lead to crack formation [12,13]. In addition, rapid setting and low strength under acid environment of materials can be obtained [13]. Heat curing up to 80 °C helps to accelerate the geopolymerization reaction in order to gain high strength, particularly when high-calcium fly ash geopolymer has been used in acid environment as waste water pipe [14]. However, the production cost is higher for heat curing process that limits the manufacturing of heat-cured fly ash geopolymer products. Therefore, high-calcium fly ash is an interesting source material for geopolymer preparation at room temperature with a reasonable strength development owing to C-S-H formation [9,10]. Durability in acid environment should be focused and improved for products with this type of curing.

Many researchers have investigated the use of high-calcium fly ash in geopolymer [4,9,10,15–17]. It was reported that high-calcium fly ash has a potential as a source material for geopolymer synthesis. For the utilization of geopolymer in oil well cementing operations, the high early strength of high- calcium fly ash geopolymer was achieved with high pressure and high temperature of curing [16]. For normal heat curing of 65 °C, high-calcium fly ash geopolymer presented the high strength gain up to 70 MPa after curing in presence of alumino-silicate bond formation [4]. Due to the high calcium content of fly ash, this geopolymer could also set and harden at room temperature and strength was developed with time [9,10,15]. C-S-H was also formed in the composite owing to the reaction between calcium, amorphous silica in fly ash, and silica from water glass in the presence of base [15].

Thailand locates near the equator with hot weather all year round. Normal temperature during daytime is approximately 30 °C with high temperature up to 40 °C in the summer time. Researchers have reported that the use of 40 °C-temperature curing gives fly ash geopolymer with sufficient compressive strength for use as structural masonry units [18,19]. In order to utilize the hot climate to increase the alumino-silicate bond formation, this research, therefore, proposed the synthesis of high-calcium fly ash geopolymer with heat curing at 35 °C. Heat curing at 35 °C (representing a hot weather curing), normal curing temperature of 65 °C and room temperature curing of 25 °C were also tested for comparison.

2. Experimental program

2.1. Materials

In this research, lignite coal fly ash with high-calcium content was used as alumino-silicate source material for geopolymer preparation. With low grade of lignite coal, high calcium content was detected by X-ray fluorescence (XRF, PANalytical PW-2404) as shown in Table 1. The XRD pattern of this fly ash is presented in Fig. 1. High calcium content of 30.0 %wt was detected in the fly ash. In addition to calcium, quartz (SiO_2), aluminium oxide (Al_2O_3) and magnetite (Fe_3O_4) were the main compositions. It was classified as class C fly ash according to ASTM C618. The median particle size (D50) of fly ash as measured by particle size analyzer (Malvern Mastersizer S) was 9 μm. For alkali activators, sodium silicate solution (water glass, $Na_2O{\cdot}SiO_2$, 27 %wt SiO_2 and 8 %wt Na_2O) was used as external dissolved silica, and 8 M NaOH solution was used as a leaching solution. From preliminary study, it was found that high concentration of NaOH (more than 8 M) resulted in low workability. Therefore, 8 M NaOH was used without extra water added to the mixture. Graded-fine river sand (passing sieve No. 30, 0.6 mm opening) with fineness modulus of 1.9 was used to prepare the geopolymer mortar for strength test.

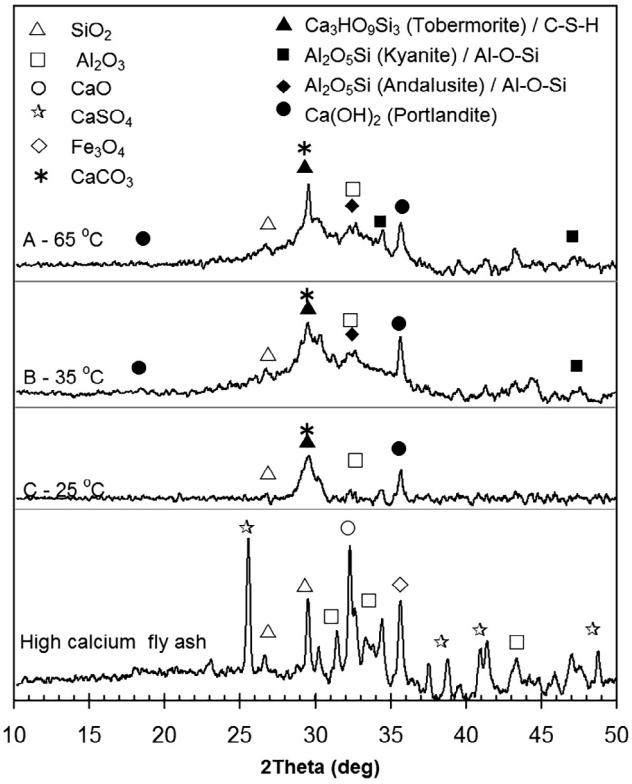

Fig. 1. XRD patterns of fly ash and composites.

2.2. Geopolymer preparation and test program

Geopolymer paste and mortar were prepared and tested. Paste composition was 55 %wt fly ash, 15 %wt 8 M NaOH and 30 %wt water glass. Mix proportions are showed in Table 2.

Molar ratios of paste mixture are following; SiO_2/Al_2O_3 = 5.3, Na_2O/SiO_2 = 0.4 and H_2O/Na_2O = 11.9 which is in the ranges recommended by Davidovit [2]. The high-calcium fly ash was thoroughly mixed with alkali activator (NaOH solution and water glass) for 1 min before molding in small plastic mold. Initial setting time was 8 min. Samples were covered with cling film to avoid the rapid water evaporation at the surface during the heat curing. Three curing conditions viz., 65 °C for 24 h (A: normal temperature curing), 35 °C for 72 h (B: representing a hot weather curing), and room temperature for 7 days (C: 25 °C controlled temperature) as shown in Table 3. Hot air oven was used in heating process of 65 °C and 35 °C. For 35 °C curing, 72-h or 3-day curing time was selected based on the calculation of equivalent heat transfer by conduction formula. Owing to the use of high-calcium fly ash, specimens hardened within 1 h after mixing. However, all samples were demolded after the temperature curing and the specimens were then kept in water (25 ± 2 °C) until the age of testing. The use of high-calcium fly ash resulted in the final products with the coexistence of

Table 1
Chemical compositions and LOI of high calcium fly ash.

Compositions (%)	SiO_2	Al_2O_3	CaO	Fe_3O_4	SO_3	MgO	K_2O	Na_2O	Others	LOI
Fly ash	25.0	13.2	30.0	15.0	7.1	2.1	1.8	1.4	1.1	3.4

Table 2
Mix proportion of mixture.

Materials	Paste (g)	Mortar (g)
Fly ash	55	55
8 M NaOH	15	15
Water glass	30	30
Sand	–	110

Table 3
Curing conditions of specimens.

Condition	Symbol	Curing condition	Note
A	A-65 °C	65 °C for 24 hr	Normal curing
B	B-35 °C	35 °C for 72 hr	Hot weather curing
C	C-25 °C	Room temperature	25 °C

sodium aluminosilicate hydrate (N-A-S-H) and some calcium silicate hydrate (C-S-H) and calcium alumino-silicate hydrate (C-A-S-H) [17]. XRD (PANalytical/Expert, Cu Kα radiation, step-size = 0.001), SEM (Leo 1455VP, gold coating), FT-IR (Perkin-Elmer System 2000, KBr technique) and TGA-DTG (Mettler, N_2 gas, 10 °C/min) techniques were performed at the age of 1 month.

For mortar, sand was added to fresh paste with sand-to-fly ash mass ratio of 2, and then mixed for 1 min. Fresh mortar was molded in 5-cm cube mold and also cured in the 3 conditions. After temperature curing, the samples were demolded. One series of the sample was kept in water (25 °C) and the other series were immersed in a 3% H_2SO_4 and 5% $MgSO_4$ solutions. 3% H_2SO_4 represented the severely acid environment and 5% $MgSO_4$ represented the sulfate-bearing environment. Calcium content of immersion solutions (water, 3% H_2SO_4 and 5% $MgSO_4$) was also monitored. In addition, the mortar samples were tested for compressive strength at the ages of 1 and 3 months. The results were reported as an average of five samples.

2.3. Geopolymer brick preparation

Geopolymer bricks were produced using the outdoor heat exposure (OHE). Geopolymer mortar mixture was cast in the molds and left to harden for 2 h before demolding. Size of specimen was $6.5 \times 14 \times 4$ cm^3. Specimens were then covered with the black plastic boxes and exposed to sunlight for 3 days. Boxes helped to keep the uniform temperature, and to avoid the airflow over the surface. Average daytime temperature of inside boxes was 38 °C, and 30 °C at night. The geopolymer bricks were used for the construction of a pedestrian pathway in according to ASTM C902 [20].

The construction procedure of the demonstrated pedestrian pathway was briefly discussed as follows. Wood frames were measured and installed. Sand was laid and compacted to obtain sand bedding. Geopolymer blocks were then laid in the agreed random ratio pattern. Finally, sand was put into the pave joint and compacted until the joints were filled.

3. Result and discussion

3.1. Characterization of geopolymer pastes

3.1.1. XRD pattern

The XRD patterns of hardened geopolymer pastes with different curing conditions at the age of 1 month are shown in Fig. 1. The XRD pattern of high- calcium fly ash contained a number of sharp peaks which disappeared after the geopolymer synthesis. Some crystalline structures in fly ash converted to amorphous inorganic compounds during the geopolymerization of fly ash in the presence of alkaline solution. Particularly, the Si—O—Al network was detected as indicated by the peak at 33° 2θ in composites with heat curing (Conditions A and B). For all curing conditions, calcium silicate hydrate (C-S-H) compound was found as indicated by the peak at approximately 29° 2θ. However, for curing at 25 °C (Condition C), the Si—O—Al network was not detected. At room temperature of 25 °C, the product was predominantly C-S-H from the reaction between the high calcium content in fly ash and the alkaline solutions which contributed to the strength development of materials [21].

The geopolymerization requires heat to activate the reaction and to break the chemical bonds of reactants (e.g. Si—O bond of SiO_2 and Al—O bond of Al_2O_3 in fly ash) resulting in new Si—O—Al products [22]. Geopolymer has a different reaction pathway from pozzolanic reaction. Pozzolanic reaction generally depends on the presence of calcium and silica resulting in C-S-H. Geopolymer strength is thus not based on the C-S-H formation and strength. It is the product of polymerization of silica and alumina precursors with high alkali solutions to attain the structural strength [7]. Therefore, the reaction between high-calcium fly ash and alkaline solutions (Condition C, 25 °C) was predominantly pozzolanic reaction with C-S-H formation as suggested by the XRD pattern. In addition, portlandite ($Ca(OH)_2$), which located at the same 2θ position as magnetite (Fe_3O_4) was detected in all samples.

It was reported that for Class F fly ash activated with NaOH and sodium silicate cured at ambient temperature, the geopolymer product (alumino-silicate compound) co-existed with C-S-H [7]. When the calcium content was high, in this case 30%, C-S-H was also formed in the final product.

3.1.2. FT-IR spectra

Fig. 2 shows the FT-IR spectra of hardened geopolymers at the age of 1 month. The characteristic of fly ash —OH stretching vibration peak was observed at 3450 cm^{-1}. Si—O and Al—O bonds played an important role in the composite, therefore, these bonds were focused. Si—O stretching and bending vibrations were detected in the raw materials. Si—O stretching peak in fly ash was at 1150–950 cm^{-1} and bending peak was at 500 cm^{-1}. In addition, C=O bonds from the carbonation reaction and calcium carbonate in fly ash was found at 1450 cm^{-1}.

When high calcium fly ash came into contact with alkaline solutions, this resulted in the phase transformation into new material. Location of —OH stretching band and Si—O bending bands were gradually shifted indicating the structural disorder of composites [23]. In addition, the Si—O stretching peak at 780 cm^{-1} was dominant while the Si—O stretching peak at 1150 cm^{-1} disappeared. It implied that the Si—O bond in raw material was transformed to the new Si—O bond in product. The absorption band of Si—O at 1000–800 cm^{-1} was the stretching Si—O bond of silicon tetrahedron, and that of Si—O at lower frequencies of 500–400 cm^{-1} was due to the symmetric and anti-symmetric bending of O—Si—O bonds [24]. Moreover, Al—O stretching band at 755 cm^{-1} with Al in the octahedral co-ordinate was detected in the materials. The change in co-ordination number of Al from 6 to 4 caused the appearance of Al—O peak [25,26].

With high calcium fly ash in geopolymer, the —OH bending band at 1600 cm^{-1} and Al-O stretching vibration at 755 cm^{-1} were less evident compared with those of normal high calcium fly ash geopolymer [4]. This indicated that alumino-silicate products in the high-calcium fly ash geopolymer were less than those in the Class F calcium fly ash geopolymer.

3.1.3. SEM microstructure

SEM images of fly ash and hardened geopolymers with different curing conditions at the age of 1 month are shown in Fig. 3. Original fly ash had a smooth surface. During coal combustion, the min-

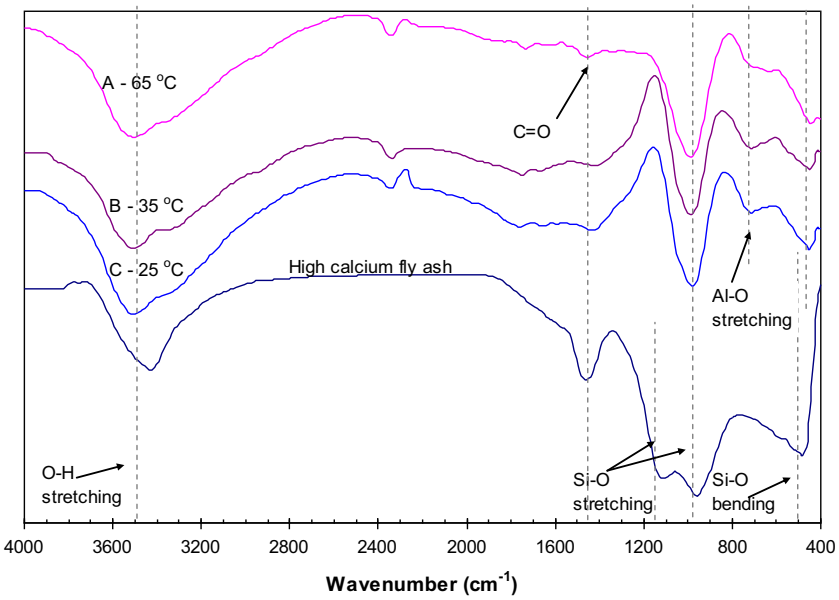

Fig. 2. FT-IR spectra of fly ash and composites.

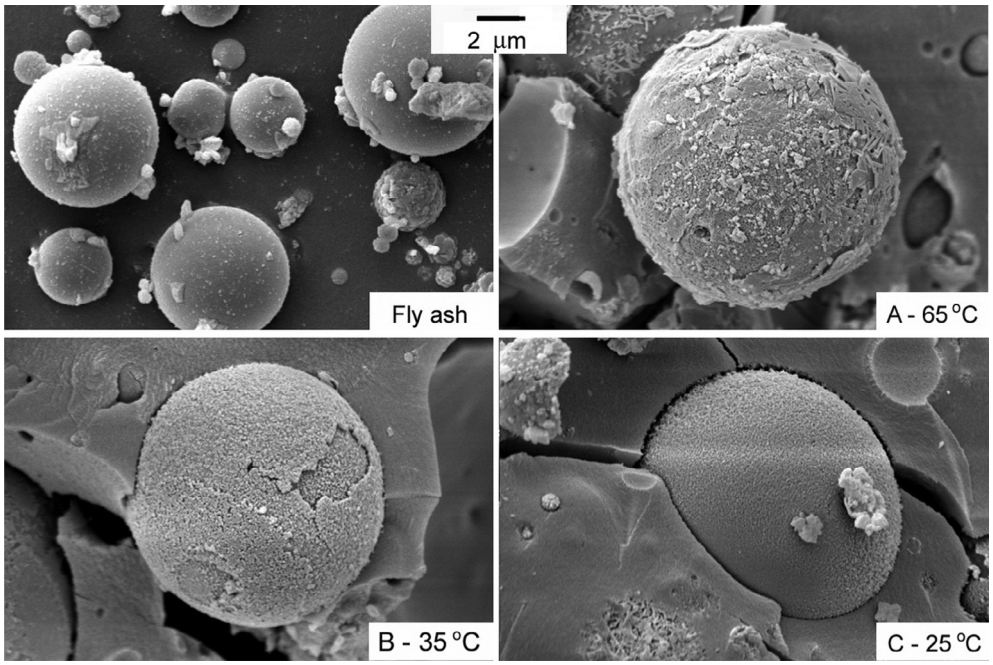

Fig. 3. Microstructure of fly ash and composites.

eral melted forming fly ash particles which crystalline phase was in the core, and a glassy phase of silica and alumina was at the surface layer [27]. This glassy phase played an important role in the system due to the high solubility in alkaline solution. When fly ash particles came into contact with alkaline solutions in the presence of heat, the surface of fly ash was attacked and the reaction products were formed around the fly ash particles as shown in Samples A (65 °C heat curing) and B (35 °C heat curing). According to the XRD patterns, these products were C-S-H and alumino-silicate (geopolymer) compounds. With 65 °C heat curing, the leaching of fly ash surface by alkaline solutions was enhanced. The geopolymer gel precipitated and dense matrix was formed [28]. However, fewer cracks were found in sample cured at room temperature compared to the heat-cured samples owing to the high moisture loss.

For room temperature curing (25 °C), the reaction was mild, and some deposits were formed at the surface of fly ash, which some smooth fly ash surface could still be seen. Main composition of the geopolymer matrix was C-S-H according to the XRD pattern identification. In this case, C-S-H was responsible for the strength development of materials. However the strength development was slow, and a longer curing period was required to obtain reasonable strength [10]. The reaction of this system was mainly the reaction between calcium compound and glassy silica in the presence of alkaline solutions at room temperature. This reaction was slow and generated less heat to surroundings than that of hydra-

tion reaction of cement. For low-calcium fly ash (less than 5% of CaO content), previous work reveals that the setting and hardening at ambient temperature is extremely slow [29].

3.1.4. Thermogravimetric analysis (TGA) and differential thermogravimetry (DTG)

Fig. 4 shows the TGA/DTG results of fly ash and composites with different curing conditions at the age of 1 month. The TGA plot shows the mass percentage as a function of heating temperature under a nitrogen purge with a heating rate of 10 °C/min. The DTG presented the decomposition temperature of specific volatile compound in materials. The high calcium fly ash showed the weight changes at 100, 450 and 700 °C corresponding to water evaporation, and decompositions of $Ca(OH)_2$, and $CaCO_3$ into CaO and CO_2, respectively [30]. The total weight loss was 3.4% after heating to 800 °C.

For the geopolymeric composites, the DTG peak was found at 100 °C corresponding to water evaporation. Water was from NaOH, sodium silicate solutions and pore solution in composite. High weight loss was observed in the temperature range of 100–400 °C. Apart from water evaporation, this was due to the decomposition of $Ca(OH)_2$. This indicated that $Ca(OH)_2$ was the main compound formed in composites. Heat curing at 65 °C (Sample A) converted calcium in fly ash to more thermally stable calcium compounds in the presence of alkali solutions as lower weight loss of approximately 12% was detected. The resulted calcium compound was calcium silicate hydrate as shown in the XRD pattern. In addition, the thermal binding alumino-silicate compound was formed in this matrix resulting in a strong composite. The weight loss of samples cured at 35 °C (Sample B) and 25 °C (Sample C) were approximately the same, and were higher than that of Sample A. This was due to the increased formation of $Ca(OH)_2$ in composites at low temperature.

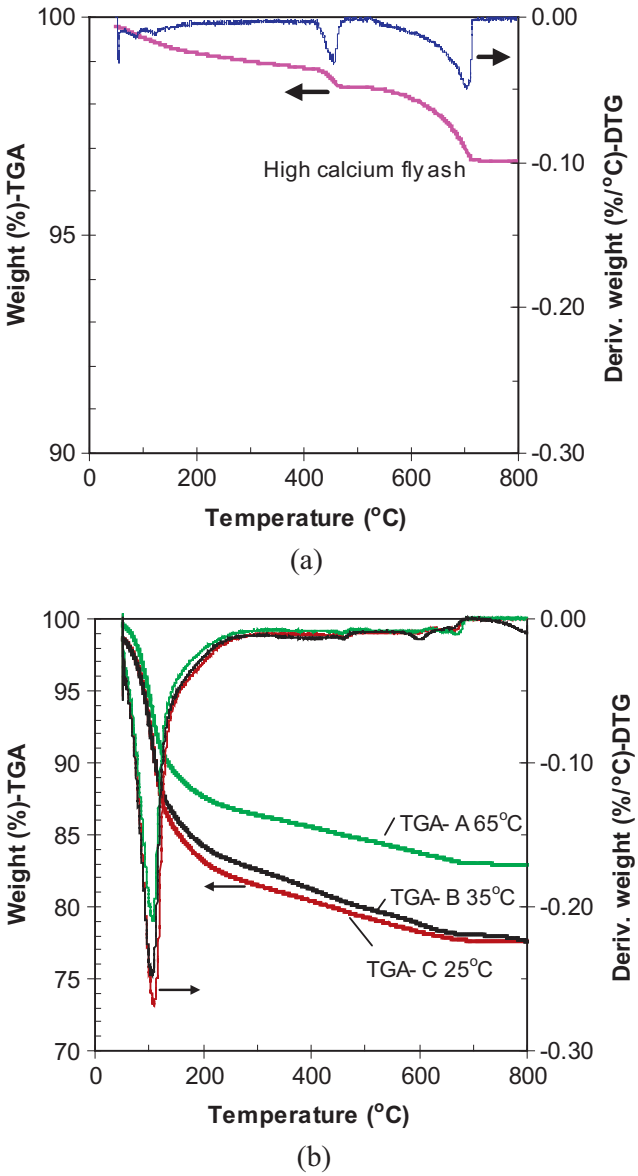

Fig. 4. TGA/DTG curves of (a) fly ash and (b) composites.

3.2. Calcium leachate

As the fly ash contained a high amount of calcium, the calcium compound in composite were leached out during immersion in both H_2SO_4 and $MgSO_4$ solutions. Therefore, calcium leaching (Ca^{2+} ion) in the immersion solutions were monitored at the age of 1 and 3 months and the results are shown in Table 4. The Ca^{2+} ion contents at all ages were very low for water and 5% $MgSO_4$ solution. Ca^{2+} ion contents of water and 5% $MgSO_4$ solution were 3–5 ppm (mg/l) and 10–25 ppm, respectively. The leaching of Ca^{2+} ion from the composites was obstructed with the formation of a thin water layer on the composite surface [14].

A rather high Ca^{2+} ion leaching was detected in the case of 3% H_2SO_4 solution. Ca^{2+} ion contents at 1-month immersion of 241, 513 and 650 ppm were obtained for samples A, B, C, respectively and increased to 265, 849 and 971 ppm at 3-month immersion. For sample A (65 °C heat curing), the increase in Ca^{2+} ion in 3% H_2SO_4 was lower than those of samples A and B. With 65 °C heat curing, the strength and the acid resistance of sample were enhanced owing to the formation of strong alumino-silicate network in composite. For 35 °C heat curing and room temperature curing (25 °C), Ca^{2+} ion contents in 3% H_2SO_4 solutions very high. At low temperature curing, the enhancements of strength and acid resistance were not high. This resulted from the moderate alumino-silicate network and C-S-H formation in composites. Even though, these compounds helped the strength development of composites, acid could leach out the calcium compound from the sample. Normally, the penetration of acid into geopolymer is low compared to that of the cement-based system [14]. For properly cured sample, the alumino-silicate system is dense and relatively stable in acid solution.

3.3. Compressive strength of the geopolymer mortars

3.3.1. Resistance to acid solution

The compressive strength tests were performed on the samples after immersed in the water, 3% H_2SO_4 and 5% $MgSO_4$ solutions for 1 month and 3 months. Fig. 5a shows the results of the compressive strength of geopolymer mortar at 1-month immersion. The compressive strengths of high-calcium fly ash geopolymer mortars increased with time owing to the formation of C-S-H and alumino-silicate in composites. Under water immersion, the compressive strength of sample A (65 °C heat curing) was 32.1 MPa which slightly higher than other curing temperatures. The compressive strength of sample B (35 °C heat curing) was 29.8 MPa and that of sample C (25 °C) was 31.8 MPa. At longer curing time of 3 months (Fig. 5b), sample C (25 °C), however, had the highest strength of 35.7 MPa. Curing at temperature of 35 °C for 72 hr also resulted in composite with reasonable early strength and good later age strength (3 months). The later age enhancement of strength was due to the increased hydration with time resulting in increased C-S-H and formation of alumino-silicate compound.

Table 4
Calcium content in immersion solutions.

Solutions	Ca^{2+} at 1 month (ppm)			Ca^{2+} at 3 months (ppm)		
	A – 65 °C	B – 35 °C	C – 25 °C	A – 65 °C	B – 35 °C	C – 25 °C
Water	3	3	5	3	3	6
3% H_2SO_4	241	513	650	265	849	971
5% $MgSO_4$	9	10	12	10	15	25

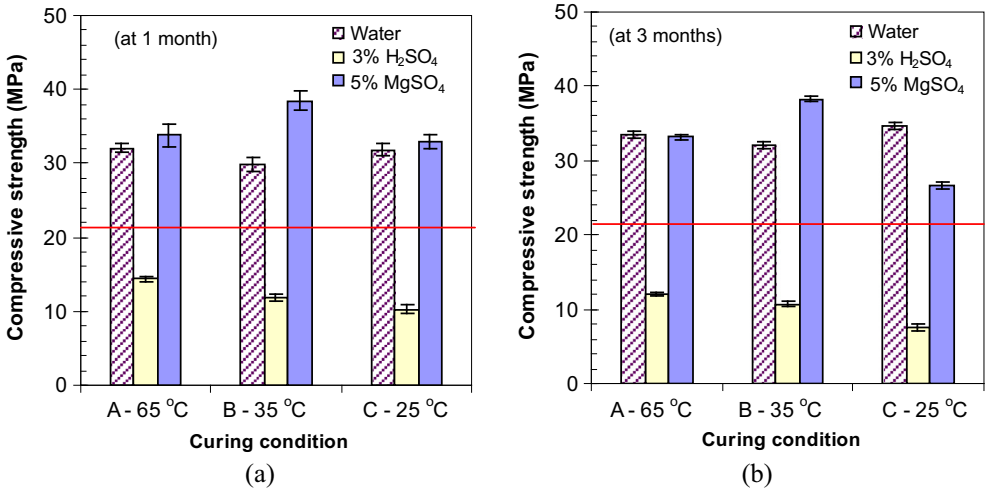

Fig. 5. Compressive strengths of geopolymer mortars with different curing conditions and exposed to water and 3% H_2SO_4 for (a) at 1 month and (b) at 3 months.

For the immersion in acid solution, all samples showed significant reduction in strength. The sample with 65 °C (for 24 h) heat curing performed better than the other curing conditions. The high heat curing activated the geopolymerization reaction at the early age resulting in the formation of alumino-silicate compound with high resistance in acid solution [31]. However, the alumino-silicate network in geopolymer could also be destroyed by H^+ (from H_2SO_4 ionization) leading to the breaking of oxy-aluminium bridge and the deterioration of geopolymer [32]. For the room temperature curing (Condition C), the main product was C-S-H and the resistance to acid of this product was low compared to that of alumino-silicate compound obtained from the temperature curing. The high strength losses of this geopolymer in 3% H_2SO_4 immersion were thus detected. This caused an adverse effect on the leaching of calcium and resulted in the physical and chemical damages. C-S-H could react with H_2SO_4 and formed $CaSO_4$ and amorphous silica gel [33]. At heat curing of 35 °C, Al—O—Si network was not as durable compared to the sample with high heat curing of 65 °C. In addition, the C-S-H product from this geopolymeric system was more sustainable than that from cement-based materials. This is in line with the previous work which indicates that the cement-based materials started to dissolve at first week of 3% H_2SO_4 immersion [14]. The geopolymer matrix is generally more durable than the cement-based matrix.

3.3.2. Resistance to salt solution

In this test, the attack of 5% $MgSO_4$ (Fig. 5) on sample was minimal. In fact, the compressive strength of mortar immersed in $MgSO_4$ was on the average a little higher than that immersed in water. In high-calcium fly ash geopolymer, 5% $MgSO_4$ increased the strength of composite. The good resistance to $MgSO_4$ was due to the reaction between $MgSO_4$ and $Ca(OH)_2$ from composite, resulting in $Mg(OH)_2$ which deposited mainly in the pores of composite. Filling the pores with this product resulted in a strong and stable composite, particularly for samples with heat curing of 65 °C and 35 °C. C-S-H phase and aluminol site (Al—OH) in the heat curing composites were strong and resistant to $MgSO_4$ attack resulting in low void ratio and high compressive strength [14].

In the case of exposure to harmful solution or environment, it is thus advisable to use an adequately high temperature curing. For normal case, the use of moderate temperate of 35 °C, as can be captured from the hot climate for 72 h, or room temperature curing are sufficient. This reduces the cost and increases the performances of the high-calcium fly ash geopolymers.

High-calcium fly ash geopolymer met the minimum compressive strength requirement of 20.7 MPa (red line reference) for paving brick according to ASTM C902 [20]. The application of this material for pedestrian pathways was discussed in the next section.

3.4. Application of the product as pedestrian pathways

Geopolymer bricks were produced using the outdoor heat exposure (OHE). Size of specimen was $6.5 \times 14 \times 4\ cm^3$. Specimens were then covered with the black plastic boxes providing average daytime temperature of inside boxes was 38 °C, and 30 °C at night. Specimens were paved the path for the pedestrian pathways as shown in Fig. 6. According to ASTM C902 (Standard Specification for Pedestrian and Light Traffic Paving Brick) [20], these geopolymer bricks were classified as Type III-Brick subjected to low abrasion which would be used in such places as floors or patios in single-family homes. Minimum requirement of compressive strength (average of 5 bricks) is 20.7 MPa. Geopolymer bricks are durable, versatile and strong. Compressive strength of brick was up to 30 MPa, however, high acid cleaner is not recommended to treat any stains on brickwork. With an environment heat exposure, geopolymer bricks can be alternative choice to replace the fireclay bricks, which consume high heat treatment for firing.

Fig. 6. Demonstrated pedestrian pathways from geopolymer bricks.

4. Conclusion

Curing of high-calcium fly ash geopolymer can be achieved with moderate temperature of 35 °C for 3 days. This temperature is achievable in the hot climate. Test results also indicated that the reactions of high calcium fly ash geopolymer involved the activation and forming of a new Si—O—Al network of product, and the reaction between calcium and silica in alkaline condition resulting in C-S-H. Heat curings at 65 °C (for 24 h) and 35 °C (for 72 h) resulted in both alumino-silicate compounds (geopolymer) and C-S-H. The high temperature 65 °C curing for 24 h enhanced the early strength of geopolymer. The moderate temperature 35 °C curing for 72 h produced geopolymer with high later age strength and reasonable early age strength. For normal usage, the heat curing of 65 °C could thus be replaced with the low temperature heat curing (35 °C). For room temperature curing at 25 °C, the products were mainly C-S-H compound and high-strength geopolymer was also obtained.

For immersion in severe acid environment of 3% H_2SO_4, the strengths of all samples were reduced. The samples cured at room temperature were most affected. The predominant C-S-H product was very susceptible to acid attack. For heat-cured samples, the strengths were also reduced but to a lesser extent as the matrix also contained alumino-silicate compounds which were more resistant to acid attack than the ambient cured samples. This is be revealed that hot-weather could be sustainable energy applying to the geopolymer curing.

Acknowledgements

This work was supported by the Thailand Research Fund (TRF) and Khon Kaen University under TRF Senior Research Scholar contract no. RTA5780004; and Burapha University under TRF Research Scholar contract no. RSA5880001.

References

[1] J. Davidovits, Geopolymer: Chemistry and Applications, Lulu Enterprises Inc, Morrisville, 2008.
[2] J. Davidovits, Geopolymer: inorganic polymeric new materials, J. Therm. Anal. 31 (1991) 1633–1656.
[3] M. Hussain, R.J. Varley, Y.B. Cheng, Z. Mathys, G.P. Simon, Synthesis and thermal behavior of inorganic-organic hybrid geopolymer composites, J. Appl. Polym. Sci. 96 (2005) 112–121.
[4] U. Rattanasak, P. Chindaprasirt, Influence of NaOH solution on the synthesis of fly ash geopolymer, Miner. Eng. 22 (2009) 1073–1078.
[5] J.C. Swanepoel, C.A. Strydom, Utilisation of fly ash in a geopolymeric material, Appl. Geochem. 17 (2002) 1143–1148.
[6] A. Fernández-Jiménez, I. García-Lodeiro, A. Palomo, Durability of alkali-activated fly ash cementitious materials, J. Mater. Sci. 42 (2007) 3055–3065.
[7] J.G.S. van Jaarsveld, J.S.J. van Deventer, G.C. Lukey, The effect of composition and temperature on the properties of fly ash- and metakaolinite-based geopolymers, Chem. Eng. J. 89 (2002) 63–73.
[8] J. Temuujin, W. Rickard, A. van Riessen, Characterization of various fly ashes for preparation of geopolymers with advanced applications, Adv. Powder Technol. 24 (2013) 495–498.
[9] J. Wongpa, K. Kiattikomol, C. Jaturapitakkul, P. Chindaprasirt, Compressive strength, modulus of elasticity, and water permeability of inorganic polymer concrete, Mater. Des. 31 (2010) 4748–4754.
[10] K. Somna, C. Jaturapitakkul, P. Kajitvichyanukul, P. Chindaprasirt, NaOH-activated ground fly ash geopolymer cured at ambient temperature, Fuel 90 (2011) 2118–2124.
[11] P. Chindaprasirt, T. Chareerat, S. Hatanaka, H.T. Cao, High-strength geopolymer using fine high-calcium fly ash, J. Mater. Civ. Eng. 23 (2011) 264–270.
[12] V.M. Malhotra, P.K. Mehta, Pozzolanic and Cementitious Materials, Gordon and Breach Publishers, Amsterdam, 1996.
[13] S. Mindess, J.F. Young, D. Darwin, Concrete, second ed., Prentice Hall, New Jersey, 2002.
[14] P. Chindaprasirt, U. Rattanasak, Improvement of durability of cement pipe with high calcium fly ash geopolymer covering, Constr. Build. Mater. 112 (2016) 956–961.
[15] P. Chindaprasirt, W. Chalee, Effect of sodium hydroxide concentration on chloride penetration and steel corrosion of fly ash-based geopolymer concrete under marine site, Constr. Build. Mater. 63 (2014) (2014) 303–310.

[16] M. Khalifeh, A. Saasen, T. Vralstad, H. Hodne, Potential utilization of class C fly ash-based geopolymer in oil well cementing operations, Cem. Concr. Res. 53 (2014) 10–17.
[17] T. Phoo-ngernkham, V. Sata, S. Hanjitsuwan, C. Ridtrirud, S. Hatanaka, P. Chindaprasirt, High calcium fly ash geopolymer mortar containing Portland cement for use as repair material, Constr. Build. Mater. 98 (2015) 482–488.
[18] A. Arulrajah, E. Kua, S. Horpibulsuk, C. Phetchuay, C. Suksiripattanapong, Y. Du, Strength and microstructure evaluation of recycled glass-fly ash geopolymer as low carbon masonry units, Constr. Build. Mater. 114 (2016) 400–406.
[19] A. Arulrajah, A. Mohammadinia, S. Horpibulsuk, W. Simingthong, Influence of class F fly ash and curing temperature on strength development of fly ash-recycle concrete aggregate blends, Constr. Build. Mater. 127 (2016) 743–750.
[20] ASTM Standard C902, Standard Specification for Pedestrian and Light Traffic Paving Brick, ASTM International, West Conshohocken, PA, 2003.
[21] S. Alonso, A. Palomo, Calorimetric study of alkaline activation of calcium hydroxide-metakaolin solid mixtures, Cem. Concr. Res. 31 (2001) 25–30.
[22] A. Fernández-Jiménez, A. Palomo, M. Criado, Microstructure development of alkali-activated fly ash cement: a descriptive model, Cem. Concr. Res. 35 (2005) 1204–1209.
[23] W.K.W. Lee, J.S.J. van Deventer, Structural reorganization of class F fly ash in alkaline silicate solutions, Colloids Surf. A 211 (2002) 49–66.
[24] L.F. Carrasco, D.T. Martin, L.M. Morales, S.M. Ramirez, Infrared spectroscopy in the analysis of building and construction materials, in: T. Theophile (Ed.), Infrared Spectroscopy – Materials Science, Engineering and Technology, Rijeka, InTech Europe, 2012, pp. 369–382.
[25] V. Stubican, R. Roy, Isomorphous substitution and infrared spectra of lattice layer silicates, Am. Miner. 46 (1961) 32–51.
[26] L. Weng, K. Sagoe-Crentsil, T. Brown, S. Song, Effects of aluminates on the formation of geopolymer, Mater. Sci. Eng. B 117 (2005) 163–168.
[27] M. Inada, H. Tsujimoto, Y. Eguchi, N. Enomoto, J. Hojo, Microwave-assisted zeolite synthesis from coal fly ash in hydrothermal process, Fuel 84 (2005) 1482–1486.
[28] H. Xu, J.S.J van Deventer, The geopolymerisation of alumino-silicate minerals, Int. J. Miner. Process. 59 (2000) 247–266.
[29] V.F.F. Barbosa, K.J.D. MacKenzie, C. Thaumaturgo, Synthesis and characterization of materials based on inorganic polymers of alumina and silica: sodium polysialate polymers, Int. J. Inorg. Mater. 2 (2000) 309–317.
[30] P. Chindaprasirt, U. Rattanasak, S. Taebuanhuad, Resistance to acid and sulfate solutions of microwave-assisted high calcium fly ash geopolymer, Mater. Struct. 46 (2013) 375–381.
[31] T. Bakharev, Thermal behaviour of geopolymers prepared using class F fly ash and elevated temperature curing, Cem. Concr. Res. 36 (2006) 1134–1147.
[32] A.D. Wilson, J.W. Nicholson, Acid-Base Cements: Their Biomedical and Industrial Applications (Chemistry of Solid State Materials), Cambridge University Press, New York, 1993.
[33] J. Skalny, J. Marchand, I. Odler, Sulfate Attack on Concrete, Spon Press, London, 2002.

Cement and Concrete Composites 83 (2017) 10–19

Contents lists available at ScienceDirect

Cement and Concrete Composites

journal homepage: www.elsevier.com/locate/cemconcomp

Synthesis of low-temperature calcium sulfoaluminate-belite cements from industrial wastes and their hydration: Comparative studies between lignite fly ash and bottom ash

A. Rungchet [a], C.S. Poon [b], P. Chindaprasirt [c], K. Pimraksa [d, e, *]

[a] Department of Physics and Materials Science, Faculty of Science, Chiang Mai University, 50200, Thailand
[b] Department of Civil and Environmental Engineering, The Hong Kong Polytechnic University, 999077, Hong Kong
[c] Sustainable Infrastructure Research and Development Center, Department of Civil Engineering, Faculty of Engineer, Khon Kaen University, 40002, Thailand
[d] Materials Science Research Center, Faculty of Science, Chiang Mai University, 50200, Thailand
[e] *Department of Industrial Chemistry, Faculty of Science, Chiang Mai University, 50200, Thailand

ARTICLE INFO

Article history:
Received 28 March 2016
Received in revised form
2 May 2017
Accepted 22 June 2017
Available online 8 July 2017

Keywords:
Calcium-sulfoaluminate-belite cement
Hydrothermal-calcination method
Lignite fly ash
Bottom ash
Hydration

ABSTRACT

The aim of this research was to study the production of calcium sulfoaluminate-belite (CŜAB) cement from industrial waste materials via hydrothermal-calcination process. Lignite fly ash and bottom ash were used as starting materials for comparison. Other waste materials viz., Al-rich sludge and flue gas desulfurization gypsum were also key players in raw mixes for the synthesis of CŜAB cement. For lignite fly ash as a starting material, mixed phases between ye'elimite and larnite were obtained, whereas for lignite bottom ash as starting material, only ye'elimite was obtained The hydration reaction was studied in terms of heat evolution, setting time, compressive strength and hydration product formation with various gypsum contents. The results showed a rapid formation of ettringite as a main hydration product mixed with calcium silicate hydrate, monosulfate and strätlingite phases as minority, with a fast final setting time of 24–26 min and high early compressive strength of 16.0 and 18.0 MPa in 1 day for CŜAB cements made of fly ash and bottom ash, respectively.

© 2017 Elsevier Ltd. All rights reserved.

1. Introduction

Nowadays, the reductions of greenhouse gas emissions and energy preservation have become a focus for the environmental protection of the world [1–3]. Calcium sulfoaluminate-belite (CŜAB) cements have been promoted as an alternative binder to Portland cement because of much less CO_2 emission. Compared to the alite (C_3S) phase release of 578 kg CO_2 per ton of clinker made from limestone and silica, the calcium sulfoaluminate ($C_4A_3\hat{S}$) phase made from limestone, alumina and anhydrite releases only 216 kg CO_2 per ton of clinker [4]. The low calcination temperatures (1250 °C) and the improved grindability of CŜAB cement also reduce the energy consumption during cement production [5]. Furthermore, this kind of cement can be synthesized from industrial wastes such as fly ash, red mud and FGD-gypsum instead of the natural quarried clay, bauxite and natural gypsum [6,7]. The basic components of CŜAB cement are calcium sulfoaluminate ($4CaO \cdot 3Al_2O_3 \cdot SO_3$; $C_4A_3\hat{S}$), dicalcium silicate ($2CaO \cdot SiO_2$; C_2S), tetra calcium aluminoferrite ($4CaO \cdot Al_2O_3 \cdot Fe_2O_3$; C_4AF), calcium sulfate ($CaO \cdot SO_3$; $C\hat{S}$) and some minor aluminate phases depending on the raw materials [8,9].

A review of previous publication indicates that the production and hydration behavior of belite cement having high hydraulic reactivity can be achieved using hydrothermal process. To achieve the highly reactive phases, the hydrothermal method is used with the focus on fly ash (FA) as a starting material owing to its aluminosilicate compositions, fine particle size, significant amount of glassy phase content and availability across the world [10–12]. Bottom ash (BA) is, however, another industrial waste need to be utilized instead of the disposal at the landfill site. It has similar chemical compositions to fly ash as it is from the same coal origin. The main difference is the lower reactivity of bottom ash due to its larger particle size and irregular in shape with pore and cavities [13]. Although containing the similar chemical compositions, the important difference between FA and BA is the mineralogy [14]. In

* Corresponding author. Department of Industrial Chemistry, Faculty of Science, Chiang Mai University, Chiang Mai, 50200, Thailand.
E-mail address: kedsarin.p@cmu.ac.th (K. Pimraksa).

http://dx.doi.org/10.1016/j.cemconcomp.2017.06.013
0958-9465/© 2017 Elsevier Ltd. All rights reserved.

producing belite cement, a higher calcination temperature is needed for BA because of the higher content of stable minerals than that of fly ash. With the same temperature of solid state reaction, FA and BA provided totally different products [14]. BA is not attractive for the cement production as it requires intensive grinding. In Thailand, the annual output of FA, BA and FGD-gypsum (Flue gas desulfurization-gypsum) are approximately 2.3, 1.5 and 2.5 million tons, respectively. Only FA has been used in concrete production. So far, BA is left unused and only 10% of FGD-gypsum is consumed in cement production and agricultural purpose. The leftover wastes can cause severe issue for landfill limitation. Therefore, the potential utilization of BA and FGD-gypsum for the production of valuable products like calcium sulfoaluminate-belite ($C\hat{S}AB$) cement becomes a challenge.

As $C\hat{S}AB$ cement composes of a number of cement phases, its hydration becomes an important factor which has to be considered in more detail in order to improve its mechanical properties as well as durability. The hydration products of $C\hat{S}AB$ cement depend on the presence of calcium sulfate compound which has significant impact on setting time, strength development and volume stability [5,15,16]. The hydration reaction of $C_4A_3\hat{S}$ with calcium sulfate is very fast, leading to the formation of ettringite ($C_3A.3C\hat{S}.32H$; $C_6A\hat{S}_3H_{32}$) and aluminum hydroxide ($Al(OH)_3$); AH_3) [15,17,18]. This is responsible for the quick setting and contributes to the early-age strength. In the absence of calcium sulfate, $C_4A_3\hat{S}$ reacts with water and forms monosulfate ($C_3A.C\hat{S}.12H$; $C_4A\hat{S}H_{12}$) [18]. Calcium sulfates can either be in a form of anhydrite ($CaSO_4$; $C\hat{S}$) in the synthesized cement or gypsum ($CaSO_4\cdot 2H_2O$; $C\hat{S}H_2$) interground with clinker after calcination or the combination of the two.

For the hydration of C_2S [19], the reaction is much slower than that of $C_4A_3\hat{S}$. The hydration products are calcium silicate hydrate (C–S–H) and calcium hydroxide ($Ca(OH)_2$; CH) which contribute to long-term strength of $C\hat{S}AB$ cement. In addition, strätlingite ($Ca_2Al_2SiO_2(OH)_{10}\cdot 3H_2O$; C_2ASH_8) could also be formed as a result of the chemical reaction between the leftover C_2S and gibbsite ($Al(OH)_3$) produced from the reaction of $C_4A_3\hat{S}$ [18,20,21]. It has been shown that the amount of gypsum affects the properties of hardened cement pastes [22]. The incorporation of insufficient amount of gypsum adversely affects the mechanical property of $C\hat{S}AB$ cement as a substantial amount of $C_4A_3\hat{S}$ remains unreacted. The use of too much gypsum may, however, adversely affects the dimensional stability.

Only a few research works was carried out using pathway of hydrothermal-calcination method for $C\hat{S}AB$ synthesis. Previous works using hydrothermal method focused only on belite synthesis [10,11]. In this research, two $C\hat{S}AB$ cements with similar phase composition were synthesized using FA and BA as the main starting materials for comparison. In addition, Al-rich sludge and FGD-gypsum as a source material for Al_2O_3 and $CaSO_4$, respectively were also used. Commercial grade hydrated lime ($Ca(OH)_2$) is also used as corrective material to obtain the stoichiometry of $C_4A_3\hat{S}$, C_2S, C_4AF, $C\hat{S}$ and free CaO according to Bogue's equation [21].

This paper shows the physical and mineralogical characteristics of the $C\hat{S}AB$ cements obtained from hydrothermal-calcination method. The hydraulic reactivity was investigated using a number of methods viz., isothermal calorimetry, X-ray diffraction (XRD), thermogravimetric analysis (TGA), setting times and mechanical test. The optimum gypsum content to produce ettrigite was also investigated.

The knowledge on the use of hydrothermal-calcination method to produce $C\hat{S}AB$ cement, therefore, would be beneficial to the understanding and for the improvement of $C\hat{S}AB$ cement properties for construction industry. Furthermore, this should help with the environmental issues viz., CO_2 emission and the mitigation of waste landfill.

2. Experimental procedure

2.1. Raw materials

The industrial waste materials used for the synthesis of $C\hat{S}AB$ cement were Class F fly ash (FA), bottom ash (BA) and FGD-gypsum (FGDG) from Mae Moh power plant in the north of Thailand, and Al-rich sludge (AS) from aluminum anodizing or powder coating industrial process of Zodiac Aircatering Equipment (Thailand) Ltd. All wastes were dried in an oven at 60 °C for 24 h and then ground to obtain particles pass sieve No.100. The particle sizes ($d_{4,3}$) of FA, BA, FGDG and AS were 15, 65, 46 and 25 μm, respectively. The chemical compositions of these materials were identified by X-ray fluorescence (XRF) and the results are shown in Table 1. Both FA and BA were good source materials for SiO_2, Al_2O_3 and CaO.

Mineralogical compositions of FA, BA, FGDG and AS determined by X-ray diffraction are shown in Fig. 1. The FA and BA composed mainly of quartz (SiO_2), calcite ($CaCO_3$) and hematite (Fe_2O_3), with other minerals such as anhydrite ($CaSO_4$; $C\hat{S}$) (mainly in FA) and gypsum ($CaSO_4\cdot 2H_2O$; $C\hat{S}H_2$) (mainly in BA). The dihydrate calcium sulfate was from the chemical reaction between anhydrite and water at the exit zone of BA where water was sprayed for cooling. Another important phase was glassy phases as indicated by the broad hump between 20 and 40° 2θ. It was worth to note here that FA contained approximately 41 wt% of the glassy phase which was higher than 33 wt% of that of BA as detected by the dissolving of FA and BA powders in 1% HF solution [23]. The FGDG consisted mainly of gypsum. The XRD pattern of AS showed gibbsite and amorphous aluminate material as the main phases. Such amorphous phase was indicated from a weak degree of crystallinity with the major peak at 49.2° 2θ. The commercial-grade hydrated lime was used as CaO source as corrective material. The hydrated lime (CH) mainly composed of portlandite ($Ca(OH)_2$) and some calcite ($CaCO_3$) as minor phase.

2.2. Materials proportioning

Theoretical phase compositions were predicted from each batch using modified Bogue's equation for $C\hat{S}AB$ cement [8,9,24]. The phase expected to synthesis were C_4AF, $C_4A_3\hat{S}$, C_2S, $C\hat{S}$ and free CaO (C) as shown in Eqs. (1)–(5).

$$\%C_4AF = 3.043(\%Fe_2O_3) \quad (1)$$

$$\%C_4A_3\hat{S} = 1.995(\%Al_2O_3) - 1.273(\%Fe_2O_3) \quad (2)$$

$$\%C_2S = 2.867\ (\%SiO_2) \quad (3)$$

$$\%C\hat{S} = 1.700(\%SO_3) - 0.445(\%Al_2O_3) + 0.284(\%Fe_2O_3) \quad (4)$$

$$\%C = 1.000(\%CaO) - 1.867(\%SiO_2) - 1.054(\%Fe_2O_3) - 0.550(\%Al_2O_3) - 0.700(\%SO_3) \quad (5)$$

For comparison, two $C\hat{S}AB$ cements were synthesized from 2 starting materials (FA and BA) together with other waste materials (AS and FGDG) and commercial-grade hydrated lime. The proportions of the raw mixes are shown in Table 2. The $C\hat{S}AB$ cement from FA was named as FAS cement and the one from BA was named as BAS cement. Mineralogical compositions of both cements obtained from Bogue's calculation and actual measurement using XRD-Rietveld method are given in Table 3.

Table 1
Chemical composition of raw materials.

Raw materials	Chemical composition (wt.%)										
	SiO_2	Al_2O_3	Fe_2O_3	CaO	Na_2O	K_2O	MgO	MnO	TiO_2	SO_3	LOI
FA	42.05	22.95	12.52	15.57	1.24	2.54	2.47	0.09	0.34	–	0.23
BA	40.70	21.47	12.16	16.52	0.89	0.97	2.11	0.09	0.24	–	4.85
FGDG	1.26	0.12	0.39	47.81	–	–	–	–	–	50.42	–
AS	1.00	70.72	0.32	0.77	–	–	–	0.20	–	21.99	5.00
CH	0.67	0.79	0.29	73.25	0.15	0.02	1.10	0.01	0.02	–	23.70

LOI: loss on ignition at 950 °C.

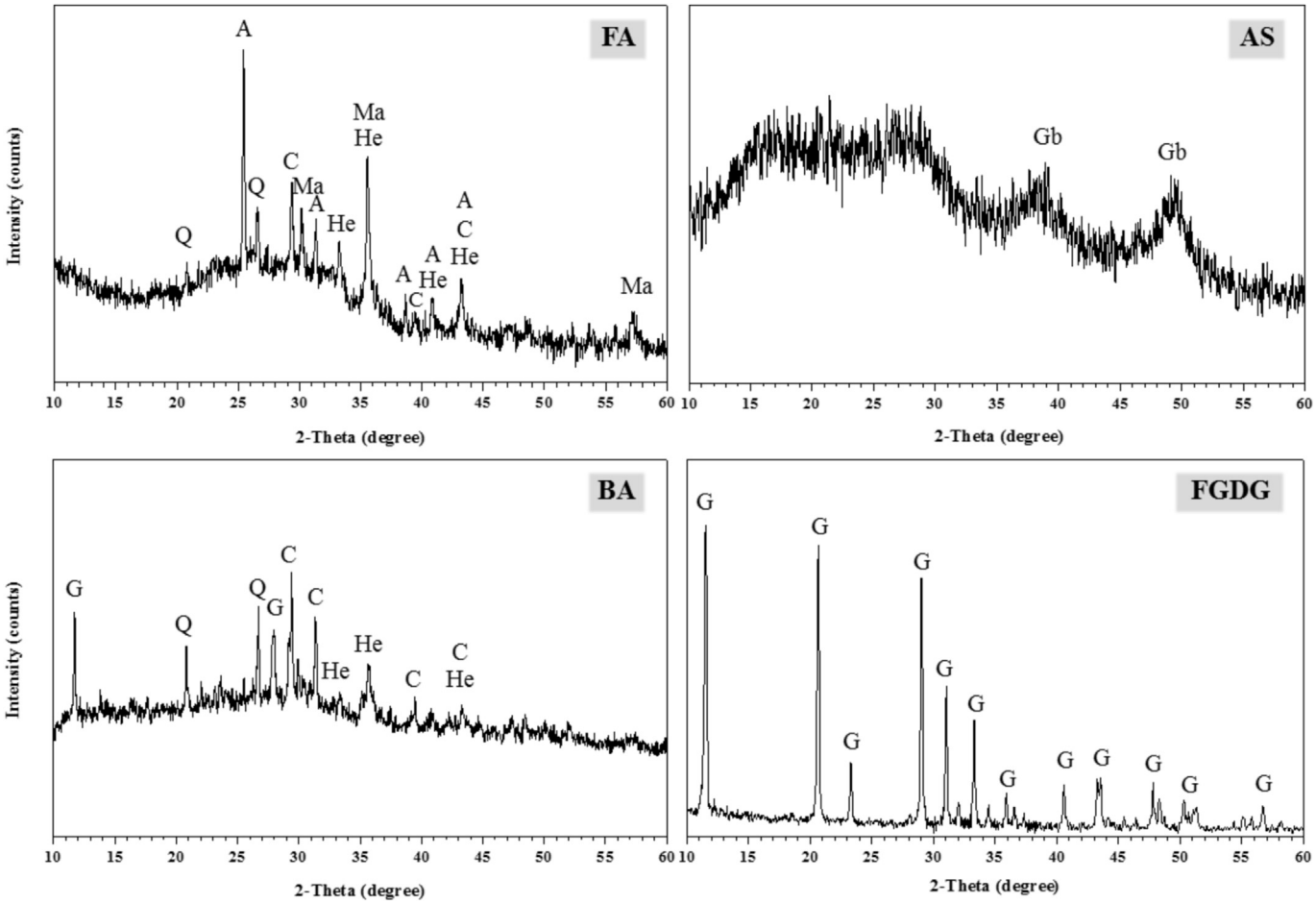

Fig. 1. XRD patterns of industrial waste materials.
A: Anhydrite ($C\hat{S}$) G: Gypsum ($C\hat{S}H_2$) Q: Quartz (SiO_2) C: Calcite ($CaCO_3$)
Ma: Magnesioferrite ($MgFe_2O_3$) He: Hematite (Fe_2O_3) Gb: Gibbsite ($Al(OH)_3$).

Table 2
Proportion of raw ingredients for the FAS and BAS cements.

Raw materials	Proportion of raw materials (wt.%)	
	FAS	BAS
FA	20	0
BA	0	20
AS	25	25
FGDG	10	10
CH	45	45

2.3. Synthesis procedure

The optimum synthesis condition obtained from the previous study of the authors [21] was chosen. The raw mixes were

Table 3
Phase compositions of FAS and BAS cements obtained from modified Bogue calculation and Rietveld method measurement.

Phase	Phase composition (wt.%)			
	FAS		BAS	
	Calculation	Rietveld	Calculation	Rietveld
$C_4A_3\hat{S}$	48.4	76.2	48.1	75.1
C_2S	30.3	9.7	29.5	6.1
$C_{12}A_7$	0.00	6.9	0.00	5.5
C_4AF	9.7	2.6	9.5	4.1
$C\hat{S}$	10.0	3.6	10.2	6.8
C	1.6	0.8	2.7	1.4
MgO	0.00	0.2	0.00	1.0

dispersed in deionized water with a liquid to solid ratio of 7 by stirring at 250 rpm for 1 h to obtain a homogeneous mixture and pre-dissolving of starting materials. The liquid mixture was subjected to hydrothermal condition for reacting times of 3 h under atmospheric pressure (1.45 bar) at 130 °C. After hydrothermal treatment, the suspension was filtered and dried at 60 °C for 24 h. The hydrothermal product was calcined in an electric furnace at 1050 °C, with a heating rate of 5°C/min and soaking at the maximum temperature for 1 h. This was followed by air quenching. Finally, the calcination product or synthesized cement was ground into fine powders using a mortar grinder.

2.4. Sample characterization and testing

2.4.1. Particle size distribution and specific surface area

The ground calcination products were observed for particle size distribution by laser diffractometer (Malvern Mastersizer 2000) and specific surface area by BET method. Both the specific surface area and particle size distribution results were compared to those of Portland cement Type I (PC).

2.4.2. X-ray diffraction

X-ray diffraction (Rigaku Miniflex II) was used to determine mineralogical compositions of hydrothermal and calcination products, and hydrated cements with additions of different FGDG contents. For the hydrated cement, pastes with water to cement ratio (w/c) of 0.8 by mass were cast in 25 ml polyethylene cup. The hydration of sample was measured at 1 day. The hydration of sample was stopped by immersing in ethanol solution and dried at 40 °C for 24 h. The instrument was operated under 40 keV and 30 mA with the step size 0.02°/6 s. Data were collected from 5 to 60° 2θ for the hydrothermal products and hydrated cements, and 10-60° 2θ for the calcination products. Quantitative information for each cement phase was obtained using Rietveld method with X'Pert Highscore Plus software from PANalytical B·V., version 2.2d.

2.4.3. Scanning electron microscopy

Scanning electron microscopy and energy dispersive spectroscopy (SEM&EDS; JEOL JSM-5910 LV) were used to study the morphology of calcination products.

2.4.4. Isothermal calorimetry

The calcined CŜAB cement powders were studied in term of heat released on hydration by adding different contents of FGDG (0–35 wt%). The resulting cements were tested for heat flow using isothermal calorimeter (I-CAL 4000) to determine suitable gypsum content based on early hydration behavior. Hydration was evaluated using samples with a water to cement (w/c) ratio of 0.8 cured for 3 days at 20 °C and 95% R.H.

2.4.5. Setting time and compressive strength test

Cement pastes were prepared with constant water to cement ratio (w/c) of 0.8. The fresh and paste were cast into 25 mm acrylic cube moulds. The high water to cement ratio was used because of the very high surface area of the hydrothermally synthesized products. The setting time tests were performed on the cement pastes using procedure described in ASTM C191-13.

For compressive strength testing, the specimens were demoulded at the age of 1 h and cured in moist chamber (20 °C ± 5 and 95% R.H.) until the testing age. The compressive strength tests were carried out at the ages of 1, 6, 12, 24, 72, 168, 672 h were carried out in accordance with ASTM C109/C109M-16a. The report results were the average of three specimens. The results were compared to the requirements of compressive strength for Portland cement Type I and Type III.

2.4.6. Thermogravimetric analysis

Thermogravimetric analysis (Rigaku TG 8120) was used to charactertize the hydration products. The chosen samples were from cement pastes containing suitable gypsum content with different curing times. 15–25 mg of finely ground sample was loaded into platinum crucible for analysis. The instrument was operated from ambient temperature of 25 °C to 1000 °C at a heating rate of 10°C/min in atmospheric air.

3. Results and discussion

3.1. Synthesis of CŜAB cements (FAS and BAS)

3.1.1. Quality and quantity of CŜAB cement phases

The CŜAB cements were prepared by hydrothermal treatment at 130 °C and 1.45 bar for 3 h. The mineralogical compositions of hydrothermal products (HT-FAS and HT-BAS) are shown in Fig. 2 (a). After hydrothermal treatment, ettringite was formed due to the reaction between FGDG and aluminum species from AS and FA. From previous works, ettringite was unstable at high temperature during 100–120 °C under hydrothermal treatment [25,26]. The finding from this research was discovered differently in that ettringite could be formed at 130 °C when starting materials were entirely immersed in water to avoid dehydration. In addition, the starting mixture was prepared to form calcium sulfoaluminate cement in which Al_2O_3/SO_3 molar ratios were 1.68 and 1.66 for FA and BA as starting material, respectively, while starting mixture with Al_2O_3/SO_3 of 0.69 to form ettringite was used in previous works. Anhydrite in FA was completely dissolved and formed additional ettringite. Monosulfate was also found indicating the surplus of aluminate phase over sulfate phase. For the use of BA as starting material, ettringite was also formed after the reaction between FGDG, gypsum and aluminum species containing in BA and Al species. There was a disappearance or reduction of inert materials such as quartz. Other crystallized minerals were also found after hydrothermal treatment:

- For the HT-FAS system, calcium aluminum silicate hydroxide, identified as cebolite ($Ca_5Al_2Si_3O_{12}(OH)_4$; $C_5AS_3H_2$) and crystalline C–S–H ($Ca_{1.5}SiO_{3.5}$. xH_2O; $C_{1.5}SH_x$) were found. The sources of silicon and aluminum for both cebolite and C–S–H formations came from the dissolution of amorphous phases of FA and AS.
- For the HT-BAS system, the new hydrothermal phases called calcium aluminum oxide carbonate hydrate ($Ca_8Al_4O_{14}$-$CO_2 \cdot 24H_2O$; $C_8A_2\hat{C}H_{24}$) was formed due to the presence of calcite in BA. The reflection of calcite formation indicated that the dissolution of BA under steam pressure were limited. The formation of crystalline C–S–H could also be observed.

The XRD patterns of CŜAB cements qualitatively obtained from both mixtures are shown in Fig. 2(b). Their quantitative phase compositions determined by Boque equation and Rietveld method are shown in Table 3. After calcinations at 1050 °C, FAS cement was obtained with formation of both $C_4A_3\hat{S}$ and β-C_2S phases, while $C_4A_3\hat{S}$ was the main phase in BAS cement. The small amount of β-C_2S in BAS cement was due to the relative high calcium aluminum sulfate hydrate or ettringite content in the hydrothermal reaction products, since this compound favored the formation of $C_4A_3\hat{S}$ and inhibited the crystallization of β-C_2S phase.

In other words, C–S–H phase in HT-BAS was unable to form β-C_2S. It should be noted here that the use of FA promoted the formation of both $C_4A_3\hat{S}$ and β-C_2S while using BA promoted the formation of $C_4A_3\hat{S}$. Both synthesized cements contain $C_{12}A_7$ or mayenite which has been known to be highly reactive phase and

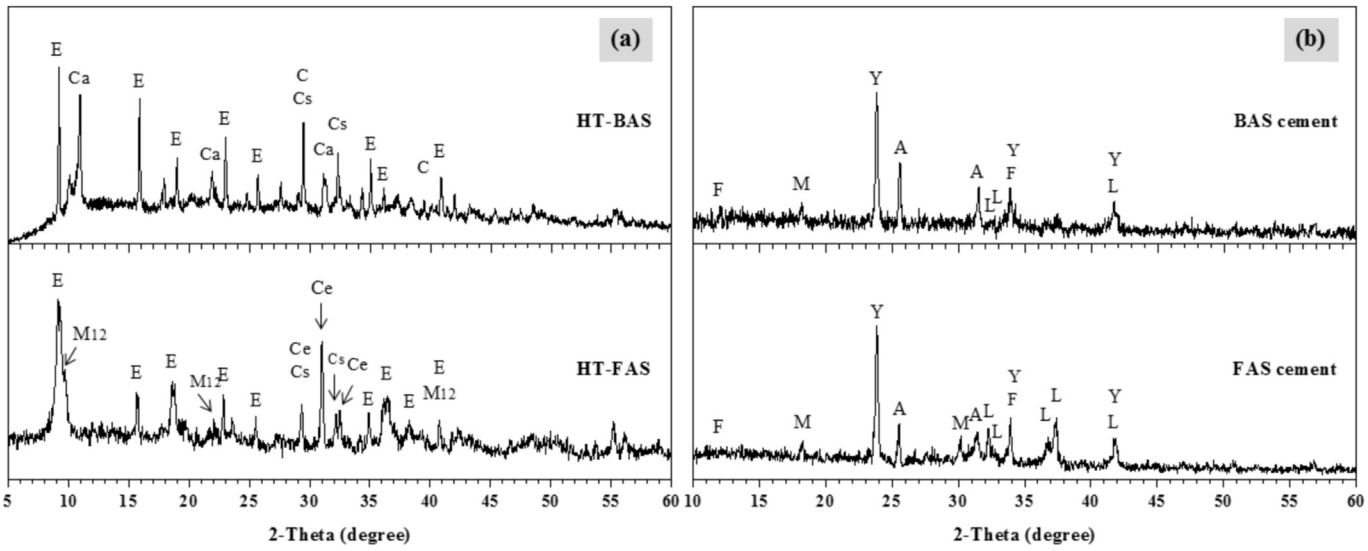

Fig. 2. XRD pattern of (a) hydrothermal products and (b) calcination products in different mixtures.
E: Ettringite ($C_6A\hat{S}_3H_{32}$) Ce: Cebolite ($C_5AS_3H_2$) Cs: Calcium silicate hydrate ($C_{1.5}SH_x$)
M_{12}: Monosulfate ($C_4A\hat{S}H_{12}$) Ca: calcium aluminum oxide carbonate hydrate ($C_8A_2CH_{24}$) C: Calcite ($CaCO_3$) Y: Ye'elimite ($C_4A_3\hat{S}$) L: Larnite (β-C_2S) A: Anhydrite ($C\hat{S}$)
M: Mayenite ($C_{12}A_7$) Th: Thenardite ($N\hat{S}$) F: Brownmillerite (C_4AF).

can give mechanical strengths at the early-age of hydration [11,20]. The quantitative results obtained by Bogue's calculation and Rietveld method were significantly different for the two cements. $C_4A_3\hat{S}$ contents of both cements were overestimated using Bogue calculation. However, $C_4A_3\hat{S}$ content of FAS was slightly higher than BAS. The difference between the calculation and the measurement was attributed to the fact that Bogue method was based on an ideal stoichiometry for solid state reaction without taking into consideration of solid solutions and other pathways such as conversion of hydrate phases into final products such in this research [21]. Moreover, BAS cement contained more C_4AF and sulfate compound than FAS cement. In fact, variations in chemical compositions of FA and BA can be occasionally found dependent on coal quality. Therefore, the calculation of starting materials for CSAB synthesis can be varied according to stoichiometry of CaO, Al_2O_3 and SO_3 to obtain hydrothermal products as required to be transformed into $C_4A_3\hat{S}$ phase.

3.1.2. Particle size distribution and specific surface area

The particle size distributions of OPC and both synthesized C$\hat{S}$AB cements are given in Fig. 3. The OPC and C$\hat{S}$AB cements had similar particle size distributions and OPC, FAS and BAS median diameters were 15.68, 17.37 and 19.91 μm, respectively. It should be emphasized here that the FAS cement contained finer particles than BAS cement.

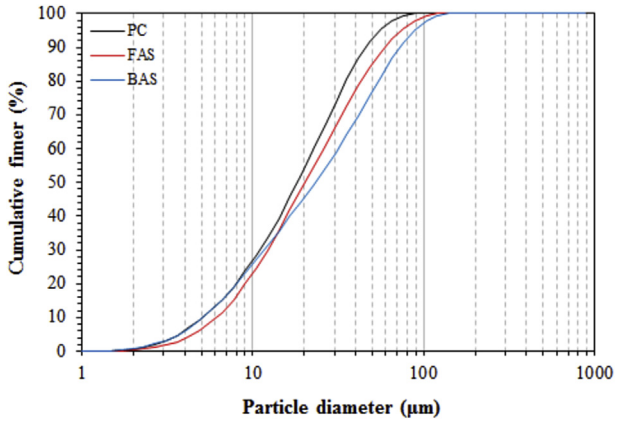

Fig. 3. Particle size distributions of OPC, FAS and BAS cements.

As shown in Table 4, the specific surface areas obtained from BET method for FAS and BAS cements were 1275 and 1240 m^2/kg, respectively. These values were approximately three times of the fineness of the rapid hardening Portland cement synthesized using clinkerization method (400–450 m^2/kg by Blaine method) [12,27]. It should be noted here that the dissolution-precipitation of hydrothermal synthesis produced very large surface area of the final products.

3.1.3. Morphology of C$\hat{S}$AB cement

The morphology, texture and crystal size of both C$\hat{S}$AB cements were studied by SEM as shown in Fig. 4. The synthesized cement particles obtained from hydrothermal-calcination synthesis were irregular in shape and highly porous. Their grindability was favorable due to a small amount of liquid phase formed in the calcination process. The EDS analysis of synthesized cements indicated elementary compositions consisting of Ca, Al, Si and S.

3.2. Hydration behavior

In this part, the calcination products were blended with 0–35 wt% FGDG in order to determine suitable gypsum content for hydration of C$\hat{S}$AB cements using heat evolution for the analysis. The heat flows of FAS and BAS cements with different gypsum contents are shown in Fig. 5. The optimum gypsum content for the C$\hat{S}$AB cements was defined by Chen and Juenger [22]. There were two cycles of heat release for suitably sulfated C$\hat{S}$AB cements and the shape of the curve did not change with increasing gypsum content. The C$\hat{S}$AB cements mixed with water initially displayed the first heat release caused mainly by the rapid dissolution of cement phases, while the second heat cycle caused by the hydration reaction of $C_4A_3\hat{S}$ with calcium sulfate to form ettringite and AH_3 according to Eq. (6). Calcium sulfates in these cement were a combination of anhydrite (C$\hat{S}$) formed in the synthesized cement (3.6 wt% and 6.8 wt% for FAS and BAS cements, respectively) and

Table 4
Weight loss ralated to the presence of different compounds in hydration products of cement pastes.

Sample	Curing time (h)	Weight loss (%)						
		C_2AH_8	Ettringite + C–S–H	Gypsum	Strätlingite	Monosulfate	AH_3	CH
FAS	1	7.11	19.45	2.88	2.04	1.43	2.79	0
	6	6.82	19.72	2.54	2.24	2.06	2.84	0
	12	3.56	20.96	1.96	2.73	2.24	2.99	0
	24	2.21	22.80	1.41	3.42	2.44	3.17	0
	72	1.79	21.22	0.68	3.11	2.53	3.25	1.67
	168	1.21	18.48	0.42	2.90	2.59	3.41	2.01
	672	0.83	16.76	0.11	2.02	2.66	3.78	3.38
BAS	1	2.20	19.00	2.91	1.87	1.42	3.02	0
	6	2.07	19.54	2.65	2.07	2.13	3.13	0
	12	1.80	20.87	2.12	2.42	2.29	3.40	0
	24	1.55	21.34	1.55	2.80	2.56	3.67	0
	72	1.32	20.54	0.73	2.95	2.60	3.99	0
	168	1.08	17.42	0.44	3.17	2.71	4.12	0.41
	672	0.74	15.60	0.19	1.04	2.49	4.67	3.18

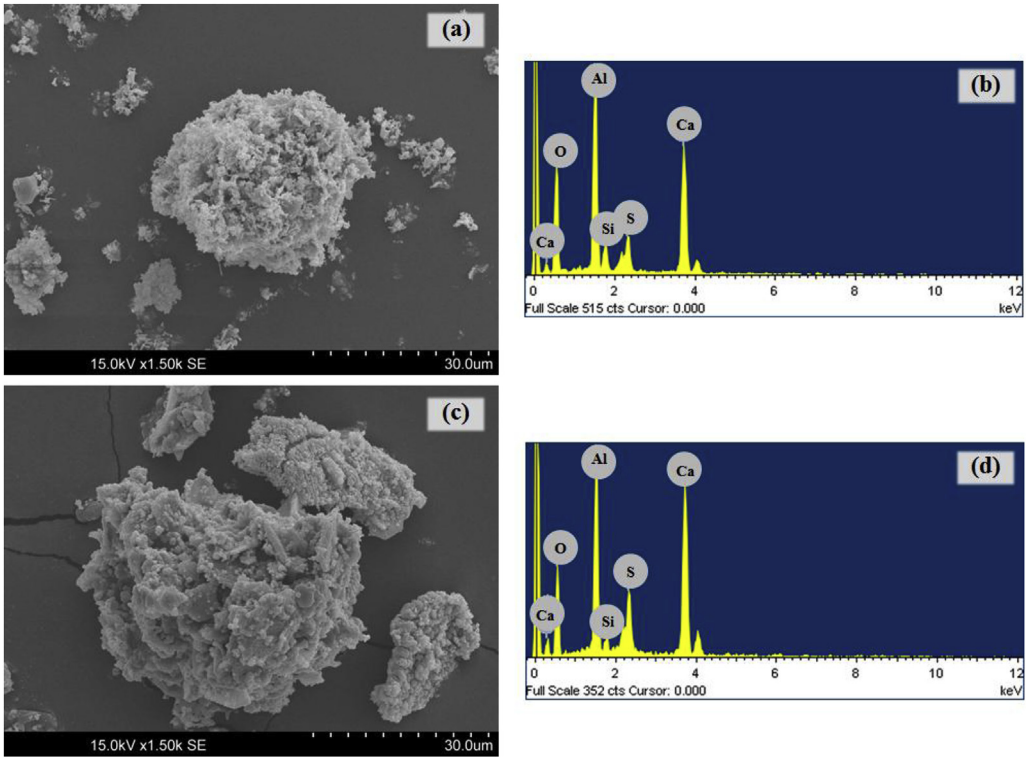

Fig. 4. SEM-EDS images of (a and b) FAS and (c and d) BAS cements.

FGD mixed after calcination. However, a clear second peak was not present for either FAS or BAS cements. For the insufficient sulfate systems, the third heat release peak occurred due to further rapid dissolution of $C_4A_3\hat{S}$ after sulfates in the solution had been depleted due to the initial reaction resulting in the formation of monosulfate together with ettringite and aluminum hydroxide [18] as shown in Eq. (7). The gypsum depletion peak was clearly observed in both FAS and BAS cements for all blended gypsum, but was much weaker and shifted to earlier times caused by the reduction of relative mineral content of cement with higher gypsum content. Beyond 25% gypsum content, the shape of the heat flow cycle did not change in both FAS and BAS cements, indicating the optimum reaction throughout this region. The heat flow results for the FAS and BAS cements showed that the FAS cement reacted extremely quickly and had much higher maximum heat flow than that of BAS cement, even though they had quite similar clinker phase compositions. It was worth noting here that FAS cement contained slightly higher cementitious materials such $C_4A_3\hat{S}$ and $C_{12}A_7$.

$$C_4A_3\hat{S} + 2C\hat{S}H_2 + 34H \Leftrightarrow C_6A\hat{S}_3H_{32} + 2AH_3 \quad (6)$$

$$2C_4A_3\hat{S} + 2C\hat{S}H_2 + 47H \Leftrightarrow C_6A\hat{S}_3H_{32} + 3AH_3 + C_4A\hat{S}H_{12} \quad (7)$$

$$C_4A_3\hat{S} + 18H \Leftrightarrow C_4A\hat{S}H_{12} + 2AH_3 \quad (8)$$

The change of phase compositions with different amounts of gypsum at 1-day hydration time was determined by XRD as shown in Fig. 6. With no gypsum addition, only FAS cement showed a slight AFt formation corresponding to the finding of Berger et al. [28] while BAS cement showed only monosulfate according to eq. (8). In the gypsum deficient system, calcium aluminate hydrate ($Ca_2Al_2(OH)_{10}\cdot 3H_2O$; C_2AH_8) and monosulfate were also observed

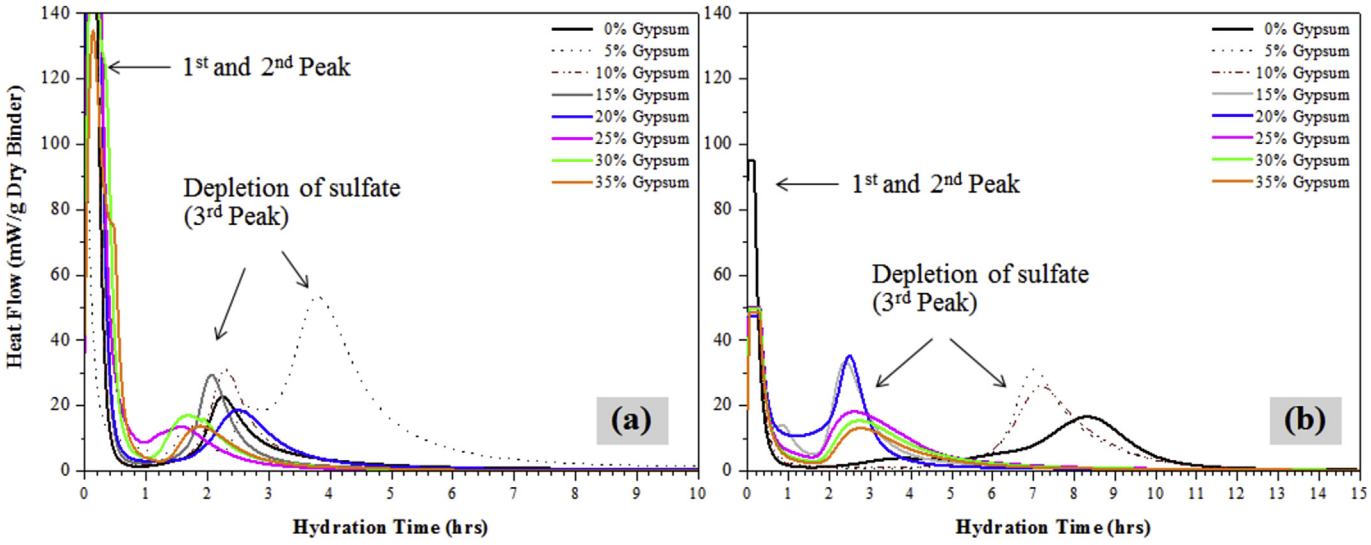

Fig. 5. Heat flow behaviors for (a) FAS and (b) BAS cements with varying amounts of gypsum blended.

implying the imbalance between calcium sulfate compound, and $C_{12}A_7$ and $C_4A_3\hat{S}$. $C_{12}A_7$ (6.9 wt% for FAS and and 5.5 wt% for BAS) underwent hydration very quickly to form C_2AH_8 as shown in Eq. (9). It was worth noting here that only 1 day of hydration, all $C_4A_3\hat{S}$ phase could be dissolved. This was quite different from $C_4A_3\hat{S}$ obtained from clinkerization as reported in the previous works [References]. This was due to very fine grain sizes of FAS and BAS cements.

$$C_{12}A_7 + 51H \rightarrow 6C_2AH_8 + AH_3 \quad (9)$$

With 5–20% blended FGDG, gypsum and anhydrite were consumed and ettringite was obtained as a new crystalline phase with trace of monosulfate and C_2AH_8 still present in the paste during the time of testing. It has been reported that C_2AH_8 was metastable phase which would transform to hydrogarnet phase (C_3AH_6) under long term curing [29]. The balance between calcium sulfate compound and $C_4A_3\hat{S}$ phase to form ettringite was about 20–25 wt% of blended FGDG for both FAS and BAS cements and conformed with isothermal calorimetry results above. As a result, the FGDG content of 20–25 wt% was a boundary for complete consumption. With excess calcium sulfate compound (25–30 wt%), gypsum was leftover as detected by the XRD analysis.

3.3. Thermal analysis for cement pastes

The formation of hydration products in $C\hat{S}AB$ cement pastes was studied by thermogravimetric analysis (TGA). Fig. 7 shows the TG and DTG curves of FAS and BAS cement pastes at different curing times. Thermal behavior of hydration products in cement pastes, and the reactions occurred at elevated temperatures were described as follows:

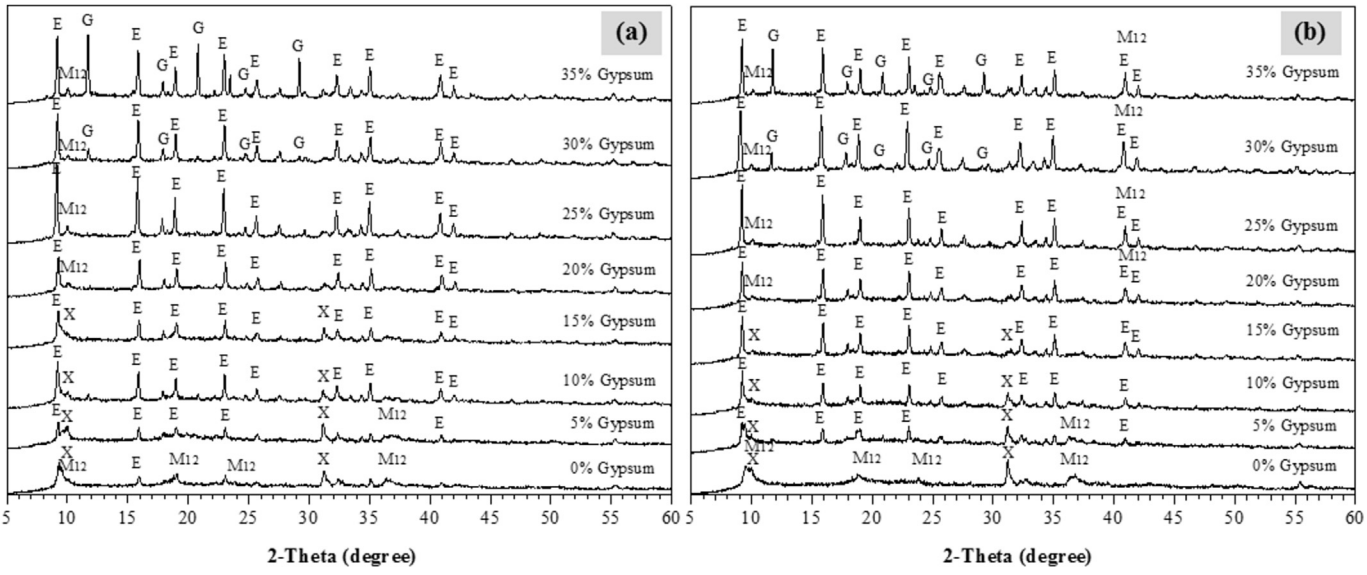

Fig. 6. XRD patterns of (a) FAS and (b) BAS cement pastes after 1 day of curing with various amounts of gypsum blended.
X: Calcium aluminate hydrate (C_2AH_8) M_{12}: Monosulfate ($C_4A\hat{S}H_{12}$)
E: Ettringite ($C_6A\hat{S}_3H_{32}$) G: Gypsum ($C\hat{S}H_2$).

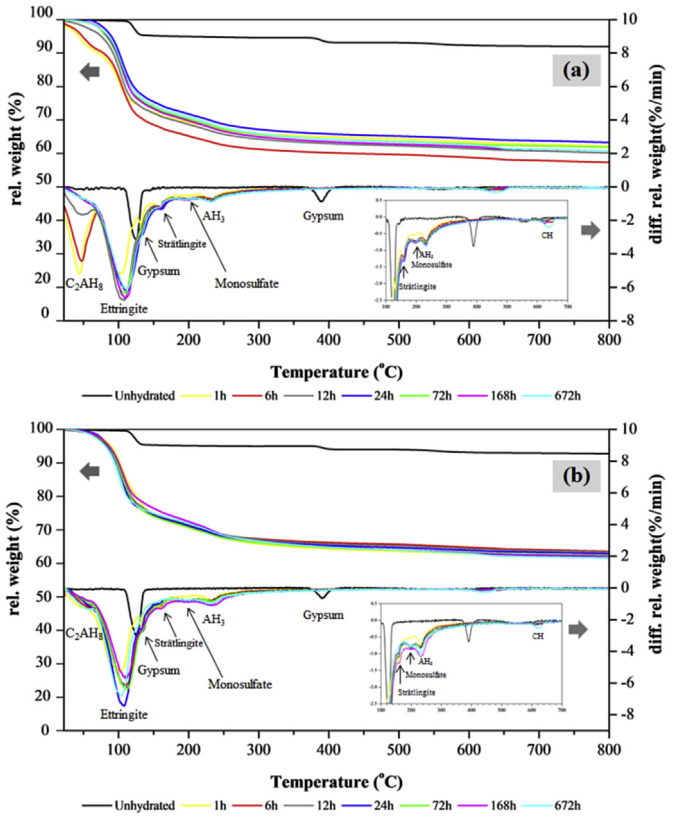

Fig. 7. TG-DTG of hydrated (a) FAS and (b) BAS cement pastes after 1, 6, 12, 24, 72, 168 and 672 h of hydration.

(I) First peak at around 50 °C corresponded to dehydration of C_2AH_8.
(II) Weight loss between 70 and 120 °C corresponded to dehydrations of ettringite [30,31] and C–S–H (weight loss at 110–120 °C) [32].
(III) Dehydration of gypsum was observed at around 130 and 400 °C related to the transformation of dihydrate to hemihydrate ($CaSO_4$. ½ H_2O) and anhydrite ($CaSO_4$).
(IV) Loss of mass at 160 °C involved the decomposition of strätlingite ($Ca_2Al_2SiO_2(OH)_{10}\cdot 3H_2O$; C_2ASH_8) [18].
(V) Weight loss at around 190 °C was mainly from the dehydration of monosulfate [30].
(VI) Weight loss at 250 °C corresponded to dehydroxylation of AH_3 [18].
(VII) Dehydroxylation of $Ca(OH)_2$ was observed at 440–650 °C.

The higher numbers of weight loss represented the larger amount of each phase in hydration products. Table 4 lists the weight losses related to the above compound in the CŜAB cement pastes. Even after 1 h of hydration, ettringite was formed together with some AH_3. The amount of ettringite in the pastes increased with increasing curing times, while gypsum was depleted. The ettringite formation was fully formed after 24 h of hydration for both FAS and BAS cement pastes. The hydration kinetics of BAS cement was slightly slower than that of FAS cement. As listed in Table 4, C_2AH_8 decreased over time representing its instability in long-term curing as mentioned above. Ettringite content also decreased slightly in long-term curing with transformation to monosulfate phase with gypsum consumption. $Ca(OH)_2$, a byproduct of belite phase hydration, was found up to 72 h of curing time. Strätlingite started to form rapidly after 1 h as a result of the chemical reaction between the β-C_2S and leftover $C_4A_3\hat{S}$ and/or AH_3 [18,20,33] according to Eqs. (10) and (11). Here, stratlingite could be detected using thermal analysis but it was not detected using XRD.

$$C_4A_3\hat{S} + 2C_2S + 23H \rightarrow C_4A\hat{S}H_{12} + C_2ASH_8 + AH_3 \quad (10)$$

$$C_2S + AH_3 + 5H \rightarrow C_2ASH_8 \quad (11)$$

In addition, the amount of strätlingite decreased with increasing CH fraction. Evident from a finding with the hypothesis about strätlingite was stable only in the absence of CH [18,34]. Furthermore, the increases of these hydration products viz., ettringite, C–S–H and strätlingite also support the results for compressive strength development of CŜAB cements. These results suggest that the CŜAB cement produced from coal combustion ash has great potential for engineering application where rapid setting and high early strength development are desirable such as in building repair and in cold weather concreting.

3.4. Setting time and compressive strength development

Table 5 presents the initial and final setting time results of both CŜAB cements with 25 wt% blended FGDG. The initial set of FAS cement was only 11 min while that of BAS cement was slightly longer at 13 min. The setting times were relatively short due to the large surface areas of both cements and the presence of highly reactive phases such as $C_4A_3\hat{S}$ and $C_{12}A_7$. To be practical for real use, retarder is recommended to adjust workability of both CŜAB cements.

The compressive strength results for the FAS and BAS cements are shown in Fig. 8. The early strength of both CŜAB cement pastes developed rapidly and the 1-day compressive strengths were 16.0

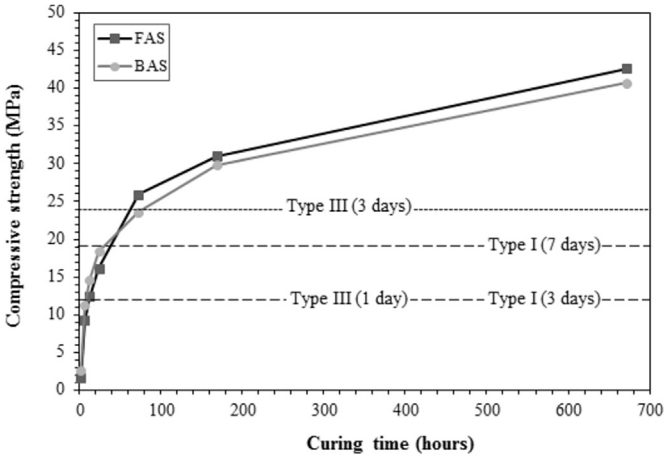

Fig. 8. Compressive strength of the FAS and BAS cement pastes with different curing times.

Table 5
Characteristics and properties of CŜAB cements.

Sample	Main phases	d_{50} (μm)	Fineness (m^2/kg)	Initial setting time (min)	Final setting time (min)
FAS cement	Ye'elimite, Belite	17.37	1275	11	24
BAS cement	Ye'elimite	19.91	1240	13	26

and 18.0 MPa for FAS and BAS cements, respectively. The 1-day strength of BAS cement paste was slightly higher than that of FAS cement, even though $C_4A_3\hat{S}$ and $C_{12}A_7$ contents in BAS was less than those in FAS as shown in Table 3. However, the later age strength of the FAS cement paste increased steadily between 72 and 672 h and exceeded that of BAS cement at 168 h. This was due to the high β-C_2S in hydrated FAS cement which contributed to the long-term compressive strength development.

Fig. 8 also shows standards of compressive strength for Portland cement Types I and III, based on ASTM C150/C150M-16e1 Standard Specification for Portland cement [35]. FAS cement satisfied the specification for Portland cement Types I and III and BAS cement failed to meet the standard of Portland cement Type III.

4. Conclusions

Based on the study, the following conclusions could be drawn.

- The $C\hat{S}AB$ cements can be synthesized from industrial wastes viz., lignite fly ash or bottom ash, Al-rich sludge and FGD-gypsum together with hydrated lime via hydrothermal-calcination method with calcination temperature of only 1050 °C. The optimum FGD-gypsum contents were 25% for the cements made from both fly ash (FAS) and bottom ash (BAS).
- The use of fly ash as the main silica source in the synthesis of $C\hat{S}AB$ cement promoted the formation of ye'elimite ($4CaO\cdot3Al_2O_3\cdot SO_3$) and larnite ($2CaO\cdot SiO_2$) with a small amount of mayenite ($12CaO\cdot7Al_2O_3$) and anhydrite ($CaSO_4$). With the presence of 25 wt% FGD-gypsum, the hydration products were ettringite ($C_3A.3C\hat{S}.32H$) and calcium silicate hydrate ($C_{1.5}SH_x$) as major phases with monosulfate ($C_3A.C\hat{S}.12H$), gibbsite ($Al(OH)_3$) and strätlingite ($4CaO\cdot Al_2O_3\cdot SiO_2\cdot 8H_2O$) phases as minor phases.
- The use of bottom ash as the main silica source promoted the formation of ye'elimite ($4CaO\cdot3Al_2O_3\cdot SO_3$) with a small amount of larnite ($2CaO\cdot SiO_2$), mayenite ($12CaO\cdot7Al_2O_3$) and anhydrite ($CaSO_4$). With 25 wt% FGD-gypsum, the hydration products were mainly ettringite ($C_3A.3C\hat{S}.32H$) and some calcium silicate hydrate ($C_{1.5}SH_x$) and monosulfate ($C_3A.C\hat{S}.12H$).
- The final setting times of synthesized cement were very fast (11 min for FAS, 13 min for BAS). The cement paste also developed a high 1-day compressive strength (16.0 MPa for FAS, 18.0 MPa for BAS).

The synthesized cements could be developed and used in the applications where rapid setting and high early strength development are needed. The recycles of high alumina and silica containing waste materials such as Al-rich sludge, fly ash and bottom ash could reduce the use of expensive alumina-silica bearing materials such as bauxite and clay mineral, thereby reducing cost and the environmental impact of cement manufacturing.

Acknowledgements

The authors gratefully acknowledge the financial supports from the Royal Golden Jubilee (RGJ) Ph.D. program and Grant No. PHD/0070/2556; Khon Kaen University and the Thailand Research Fund (TRF) under the TRF Senior Research Scholar, Grant No. RTA 5780004. In addition, SEM analysis was supported by Prof. Tsugio Sato's laboratory under Institute of Multidisciplinary Research for Advanced Materials, Tohoku University, Japan.

References

[1] R.I. Iacobescu, D. Koumpouri, Y. Pontikes, R. Saban, G.N. Angelopoulos, Valorisation of electric arc furnace steel slag as raw material for low energy belite cements, J. Hazard. Mater 196 (2011) 287–294.
[2] E. Benhelal, G. Zahedi, E. Shamsaei, A. Bahadori, Global strategies and potentials to curb CO_2 emissions in cement industry, J. Clean. Prod. 51 (2013) 142–161.
[3] S.A. Ishak, H. Hashim, Low carbon measures for cement plant – a review, J. Clean. Prod. 103 (2015) 260–274.
[4] E.M. Gartner, D.E. Macphee, A physico-chemical basis for novel cementitious binders, Cem. Concr. Res. 41 (2011) 736–749.
[5] F.P. Glasser, L. Zhang, High-performance cement matrices based on calcium sulfoaluminate–belite compositions, Cem. Concr. Res. 31 (2001) 1881–1886.
[6] P. Arjunan, M.R. Silsbee, D.M. Roy, Sulfoaluminate-belite cement from low-calcium fly ash and sulfur-rich and other industrial by-products, Cem. Concr. Res. 29 (1999) 1305–1311.
[7] M. Singh, S.N. Upadhayay, P.M. Prasad, Preparation of special cements from red mud, Waste Manag. 16 (1996) 665–670.
[8] J.H. Sharp, C.D. Lawrence, R. Yang, Calcium sulfoaluminate cements—low-energy cements, special cements or what? Adv. Cem. Res. 11 (1999) 3–13.
[9] J. Majling, S. Sahu, M. Vlna, D.M. Roy, Relationship between raw mixture and mineralogical composition of sulphoaluminate belite clinkers in the system $CaO-SiO_2-Al_2O_3-Fe_2O_3-SO_3$, Cem. Concr. Res. 23 (1993) 1351–1356.
[10] L. Kacimi, M. Cyr, P. Clastres, Synthesis of α′L-C2S cement from fly-ash using the hydrothermal method at low temperature and atmospheric pressure, J. Hazard. Mater 181 (2010) 593–601.
[11] W. Mazouzi, L. Kacimi, M. Cyr, P. Clastres, Properties of low temperature belite cements made from aluminosilicate wastes by hydrothermal method, Cem. Concr. Compos 53 (2014) 170–177.
[12] K. Pimraksa, S. Hanjitsuwan, P. Chindaprasirt, Synthesis of belite cement from lignite fly ash, Ceram. Int. 35 (2009) 2415–2425.
[13] T. Xie, T. Ozbakkaloglu, Behavior of low-calcium fly and bottom ash-based geopolymer concrete cured at ambient temperature, Ceram. Int. 41 (2015) 5945–5958.
[14] B. Na Lampang, Synthesis of Belite and Ye'elimite Cements from Combustion Byproduct for Construction Applications and Heavy Metal Encapsulation, Ms Thesis, Chiang Mai University, 2012 ([in Thai]).
[15] F. Winnefeld, S. Barlag, Calorimetric and thermogravimetric study on the influence of calcium sulfate on the hydration of ye'elimite, J. Therm. Anal. Calorim. 101 (2009) 949–957.
[16] M. García-Maté, A.G. De la Torre, L. León-Reina, E.R. Losilla, M.A.G. Aranda, I. Santacruz, Effect of calcium sulfate source on the hydration of calcium sulfoaluminate eco-cement, Cem. Concr. Compos 55 (2015) 53–61.
[17] F. Hanic, I. Kaprálik, A. Gabrisová, Mechanism of hydration reactions in the system C_4A_3S-CS-CaO-H_2O referred to hydration of sulphoaluminate cements, Cem. Concr. Res. 19 (1989) 671–682.
[18] F. Winnefeld, B. Lothenbach, Hydration of calcium sulfoaluminate cements — experimental findings and thermodynamic modelling, Cem. Concr. Res. 40 (2010) 1239–1247.
[19] H.J.H. Brouwers, Chemical reactions in hydrated ordinary Portland cement based on the work by powers and brownyard, in: H.B. Fisher (Ed.), Proc. 15th Ibausil Int. Conf. Build. Mater. Int. Baustofftagung, F.A, Finger-Institut fur Baustoffkunde, Weimar, Germany, 2003, pp. 1–0553.
[20] M.C. Martín-Sedeño, A.J.M. Cuberos, Á.G. De la Torre, G. Álvarez-Pinazo, L.M. Ordónez, M. Gateshki, et al., Aluminum-rich belite sulfoaluminate cements: clinkering and early age hydration, Cem. Concr. Res. 40 (2010) 359–369.
[21] A. Rungchet, P. Chindaprasirt, S. Wansom, K. Pimraksa, Hydrothermal synthesis of calcium sulfoaluminate–belite cement from industrial waste materials, J. Clean. Prod. 115 (2016) 273–283.
[22] I.A. Chen, M.C.G. Juenger, Synthesis and hydration of calcium sulfoaluminate-belite cements with varied phase compositions, J. Mater. Sci. 46 (2010) 2568–2577.
[23] A. Fernández-Jimenez, A.G. de la Torre, A. Palomo, G. López-Olmo, M.M. Alonso, M.A.G. Aranda, Quantitative determination of phases in the alkali activation of fly ash. Part I. Potential ash reactivity, Fuel 85 (2006) 625–634.
[24] P. Mehta, Investigations on energy-saving cements, World Cem. Technol. 11 (1980) 166–177.
[25] A.N. Christensen, T.R. Jensen, J.C. Hanson, Formation of ettringite, $Ca_6Al_2(SO_4)_3(OH)_{12}.26H_2O$, AFt, and monosulfate, $Ca_4Al_2O_6(SO_4).14H_2O$, AFm-14, in hydrothermal hydration of Portland cement and of calcium aluminum oxide-calcium sulfate dihydrate mixtures studied by in situ synchrotron X-ray powder diffraction, J. Solid State Chem. 177 (2004) 1944–1951.
[26] Q. Zhou, F.P. Glasser, Thermal stability and decomposition mechanisms of ettringite at < 120°C, Cem. Concr. Res. 31 (2001) 1333–1339.
[27] P. Barnes, J. Bensted, Structure and Performance of Cements, second ed., CRC Press, 2002.
[28] S. Berger, C.C.D. Coumes, P. Bescop, D. Damidot, Influence of a thermal cycle at early age on the hydration of calcium sulfoaluminate cements with variable gypsum content, Cem. Concr. Res. 41 (2011) 149–160.
[29] I. Odler, Special Inorganic Cements, CRC Press, 2003.
[30] C.W. Hargis, A. Telesca, P.J.M. Monteiro, Calcium sulfoaluminate (Ye'elimite) hydration in the presence of gypsum, calcite, and vaterite, Cem. Concr. Res. 65 (2014) 15–20.
[31] F. Song, Z. Yu, F. Yang, Y. Lu, Y. Liu, Microstructure of amorphous aluminum hydroxide in belite-calcium sulfoaluminate cement, Cem. Concr. Res. 71

(2015) 1–6.
[32] B. Ma, X. Li, X. Shen, Y. Mao, H. Huang, Enhancing the addition of fly ash from thermal power plants in activated high belite sulfoaluminate cement, Constr. Build. Mater 52 (2014) 261–266.
[33] L. Yang, Y. Yan, Z. Hu, X. Xie, Utilization of phosphate fertilizer industry waste for belite–ferroaluminate cement production, Constr. Build. Mater 38 (2013) 8–13.
[34] D. Damidot, F.P. Glasser, Investigation of the $CaO-Al_2O_3-SiO_2-H_2O$ system at 25°C by thermodynamic calculations, Cem. Concr. Res. 25 (1995) 22–28.
[35] ASTM, C150/C150M-16e1, Standard Specification for Portland Cement, 2016.

Clean Techn Environ Policy (2017) 19:1985–1992
DOI 10.1007/s10098-017-1380-7

ORIGINAL PAPER

Synthesis of polypropylene fiber/high-calcium fly ash geopolymer with outdoor heat exposure

Prinya Chindaprasirt[1] · **Ubolluk Rattanasak**[2]

Received: 29 December 2016 / Accepted: 17 June 2017 / Published online: 22 June 2017
© Springer-Verlag GmbH Germany 2017

Abstract Solar energy is an important source of renewable and sustainable energy. Thailand is near the equator and thus experiences hot weather throughout the year. The average maximum temperature is 35 °C and can reach 40 °C in the summer time. This outdoor heat exposure (OHE) was, therefore, used for the curing of a polypropylene (PP) fiber fiber-reinforced high-calcium fly ash geopolymer composite, in order to reduce energy consumption. Fly ash is an abundant solid waste generated from the coal-power generation process. In this research, a high-calcium fly ash was used as a source material for the geopolymer synthesis. PP fiber was also incorporated in the composites to improve tensile characteristics and control crack development. The results show that the incorporation of PP fiber in composites led to improved tensile strength, crack control, and resistance to acid solution. OHE could thus be used as an energy source for the heat curing of high-calcium fly ash PP-fiber geopolymers, resulting in a strong matrix.

Keywords Outdoor heat exposure · Polypropylene fiber · Fly ash · Geopolymeric composite

✉ Ubolluk Rattanasak
ubolluk@buu.ac.th

[1] Sustainable Infrastructure Research and Development Center, Department of Civil Engineering, Faculty of Engineering, Khon Kaen University, Khon Kaen 40002, Thailand

[2] Department of Chemistry, Faculty of Science, Burapha University, Chonburi 20131, Thailand

Introduction

Geopolymers are an alternative green binder made from source materials containing silica and alumina (Davidovits 1991). Fly ash from the coal-combustion process is the most common pozzolan, which consists mainly of silica and alumina, and is suitable for geopolymer production. A geopolymeric reaction is achieved when alumino-silicate source materials react with base and sodium silicate solutions (Davidovits 1991; Van Jaarsveld et al. 2002; Hussain et al. 2005; Rattanasak and Chindaprasirt 2009). Sodium silicate solution provides additional dissolved SiO_2 to the system. A NaOH solution is commonly used as a base solution for the leaching of silica and alumina from fly ash particles. This leads to initial gel formation around the fly ash particles (Rattanasak and Chindaprasirt 2009) and leads to the setting and hardening of materials. The mechanism of the geopolymeric reaction involves the dissolution of alumino-silicate source materials in the presence of alkali solutions. A series of ionic species are formed and polymerization takes place resulting in the formation of tetrahedra of Si and Al distributed along the polymeric chains (Fernández-Jiménez et al. 2005; Tchadjié et al. 2016). This material has desirable mechanical performance, owing to the formation of alumino-silicate products with a semicrystalline phase from fly ash (Van Jaarsveld et al. 2002; Hussain et al. 2005).

In Thailand, lignite coal fly ash is the solid waste generated by the pulverized coal-fired (PCC) power plant in the northern region. This fly ash is mainly used as a pozzolan in concrete mixtures. Owing to the limited use of fly ash, abundant amounts of fly ash are still disposed of in landfill sites. Presently, the calcium content is increasing in this fly ash owing to the use of low-grade lignite obtained from coal deposits at a greater depth. The high calcium

content can lead to geopolymers with a fast setting time and low strength (Mindess et al. 2002). However, the utilization of high-calcium fly ash in geopolymer is beneficial as the material can set at room temperature and requires no heat curing, thus resulting in energy saving. Excess calcium content in fly ash can react with the base solutions leading to a hardened composite without heat curing (Somna et al. 2011). Strength is obtained in a similar manner to Portland cement since additional calcium silicate hydrate is formed in the composites (Mindess et al. 2002). However, cracks can form when high-calcium fly ash is used.

Fibers have been used to control the cracking in concrete and to modify the cracked behavior of material (Mindess et al. 2002). Polypropylene (PP) fiber is widely used in cementitious composites as its price is relatively low, and it is able to control cracking due to shrinkage and temperature change. Even though polyvinyl alcohol (PVA) fiber is superior in performance, its high cost and an availability problem in Thailand limits the use of PVA fibers. In addition, the application of PP fiber in building materials can improve their tensile characteristics and resistance to crack formation and growth (Lopez-Buendia et al. 2003; Banthia and Gupta 2006; Ostertag and Yi 2007). However, the elastic modulus of PP fiber is much lower than that of the cementitious material, and it can thus reduce the compressive strength of the high strength concrete (Richardson 2006). PP fiber is, therefore, mainly used to control cracking in concrete. PP fiber has hydrophobic characteristics and a smooth surface (Ranjbar et al. 2016a). Its surface can also be treated with alkaline, in order to eliminate the protection layer and to modify the interfacial bonding strength with a matrix, which makes it very suitable for a geopolymer matrix (Lopez-Buendia et al. 2003; Wang et al. 2006; Zhang et al. 2009; Shaikh 2013). It has been reported that the PP-fiber content affects the workability and setting time of fly ash geopolymer mixtures. Furthermore, the toughness of materials is improved due to the toughness-enhanced mechanism of PP fiber (Ranjbar et al. 2016a, b).

In order to utilize the high-calcium fly ash in geopolymers with crack control, this research proposed the use of PP fiber in the composite. Conventional curing at 40–60 °C requires some additional energy and equipment, and thus was replaced by outdoor heat exposure (OHE), in order to obtain Al–O–Si bond in the composite with good resistance to an acid environment. In addition, it has been reported that the use of 40 °C-temperature curing provides the fly ash geopolymers with sufficient compressive strength for use as structural masonry units (Arulrajah et al. 2016). Thailand is located near the equator and experiences hot weather throughout the year. The daytime temperature is around 30–35 °C, and the nighttime temperature is around 26–31 °C. The Thai Meteorological Department (TMD) reported that, in the summer time, the temperature can be as high as 40–43 °C (Thai Meteorological Department 2015). An OHE-curing system can provide a temperature of approximately 35 °C, thus curing and conserving energy.

In this research, morphological and physical studies were performed on composites. Since using PP fiber in high-calcium geopolymers has rarely been reported, the results pave the way to use the hot weather curing for high-calcium fly ash geopolymers, and also provide knowledge about PP-fiber reinforcement in high-calcium fly ash geopolymers.

Experimental program

Materials

High-calcium fly ash from lignite coal PCC power plant was used as an alumino-silicate source material for geopolymer preparation. The chemical composition was monitored using X-ray fluorescence (XRF). The oxide compounds are listed in Table 1. This fly ash had a high calcium content of 30.0 wt% with 25.0 wt% SiO_2, 13.2 wt% Al_2O_3 and 15.0 wt% Fe_2O_3. The fly ash was brownish in color as a result of a high iron content.

The particle size distribution of fly ash was performed using a particle size analyzer (Malvern Mastersizer S). The median particle size (D50) of fly ash was 9 μm. Monofilament PP fiber (construction grade) with a smooth surface and dimensions of 3 mm in length, and 15 μm in diameter was used for reinforcement. The modulus of elasticity and the tensile strength of PP fiber were 4.16 GPa and 557 MPa, respectively. For alkali activators, sodium silicate solution (water glass, $Na_2O{\cdot}SiO_2$, 27 wt% SiO_2 and 8 wt% Na_2O) and 8 M NaOH solution were used. For the preparation of the geopolymer mortar, saturated-surface-dry (SSD) graded river sand passed through sieve No. 30 (0.6 mm opening) with a fineness modulus of 1.9 was used.

Composite preparation and test program

A paste mixture was composed of 60 wt% fly ash, 13 wt% 8 M NaOH and 27 wt% water glass solution. The high-calcium fly ash was mixed with an alkali activator (NaOH solution and water glass) for 1 min to achieve uniformity, before casting in 25-mm × 25-mm cylindrical plastic molds. Samples were cured at room temperature (RT) with an average temperature of 28 °C for 7 days and with outdoor heat exposure (OHE) for 3 days. The average outdoor daytime temperature was 35 °C, with 30 °C at night. For OHE condition, samples were put in a black plastic box in

Table 1 Chemical compositions and loss on ignition (LOI) of high-calcium fly ash

Compositions (%)	SiO_2	Al_2O_3	CaO	Fe_2O_3	SO_3	MgO	K_2O	Na_2O	Others	LOI
Fly ash	25.0	13.2	30.0	15.0	7.1	2.1	1.8	1.4	1.1	3.4

order to maintain the uniform temperature of the samples and to avoid the rapid water evaporation at the surface of composites. The temperature in the black plastic box was around 3–5 °C higher than the ambient temperature.

When the PP fiber was applied, the fiber was blended homogeneously with fly ash before adding the alkali activator. The fiber content of 0.5% by weight of fly ash was applied to the mixtures according to the manufacturer recommendation and previous reports (Banthia and Gupta 2006; Ranjbar et al. 2016a). Specimens were demolded after curing (7 days for RT-curing and 3 days for OHE-curing), and then immersed in water and 3% H_2SO_4 solution for 1 month to investigate the acid resistance of composites. X-ray powder diffraction (XRD) and scanning electron microscopy (SEM) were performed on samples. An optical microscope was also used to investigate cracks that developed in samples. In addition, a single-fiber pull-out test for geopolymers was performed according to ASTM D7913/D7913M-14 (2014). PP fiber was embedded in the geopolymer paste with an embedded length of 5 mm. The specimen was fixed to the clamps, and the fiber was glued to the upper mounting plate of the testing machine. The test was performed at a loading rate of 0.05 mm/s, with the monitoring of a 10 N load cell. The interfacial shear strength was calculated (Teuber et al. 2013).

For the mechanical test, geopolymer mortar was prepared. The river sand was incorporated into the fresh geopolymer paste using a sand-to-fly ash mass ratio of 2. The mixing was continued for 1 min. The fresh mortar was then cast into a 50-mm cube mold for the strength test, and into a briquette mold for the tensile strength test (with a cross-section of the briquette of 25.4 × 25.4 mm^2). Vibration was applied for 10 s to remove air bubbles from the samples. Curing conditions were similar to that of the paste. Specimens were immersed in water and in 3% H_2SO_4 solution for an acid resistance test. The results were reported as the average of five samples.

Result and discussion

XRD pattern of composites

XRD patterns of high-calcium fly ash and geopolymer cured with RT and OHE are presented in Fig. 1. Fly ash contained both crystalline phases (with sharp peaks, e.g., SiO_2, Al_2O_3, $CaSO_4$) and amorphous phases (with a broad peak at 30°–35° 2θ). When fly ash reacted with sodium silicate and sodium hydroxide, semicrystalline phases were detected in the composites. The OHE-curing showed a high amorphous phase with a distinct broad peak at 25°–35° 2θ. The products of the reaction included tobermorite, kyanite, and portlandite. OHE-curing promoted the occurrence of an alumino-silicate compound, i.e., kyanite (Al–O–Si bond), which contributed to the strength development and acid resistance of composite (Temuujin et al. 2013; Chindaprasirt et al. 2014). In addition, the formation of calcium silicate hydrate (C–S–H) and tobermorite were detected, owing to the high calcium content of the fly ash (Chindaprasirt et al. 2014). However, portlandite ($Ca(OH)_2$) was also detected as a result of the high calcium content of fly ash. This compound can have an adverse effect on the durability of the composite (Mindess et al. 2002).

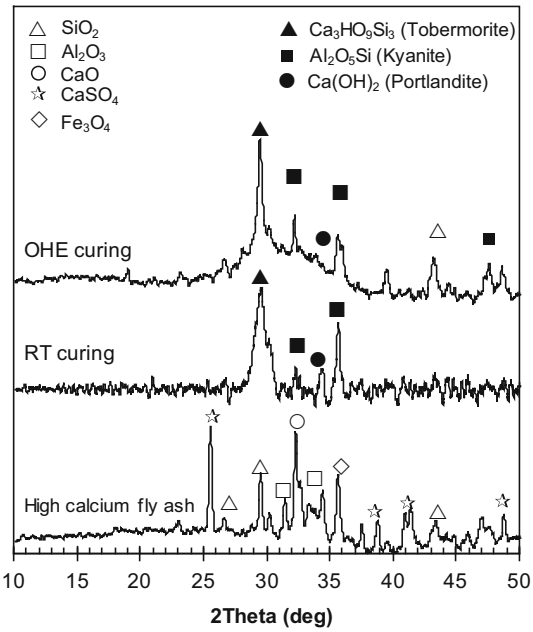

Fig. 1 XRD pattern of high-calcium fly ash and composites at 1 month

RT-curing generally resulted in C–S–H formation similar to that found in Portland cement composites (Somna et al. 2011). This compound contributed to the strength development of the material. For fly ash geopolymers, heat is normally required to activate a similar reaction to the synthesis of crystalline zeolite (Tanaka and Fujii 2009; Chindaprasirt et al. 2013). However, less heat is needed as

the product of geopolymer mainly contains the semicrystalline phase (Chindaprasirt et al. 2013).

Microstructural study of composites

The microstructure of the paste composites was studied using a scanning electron microscope (SEM) as shown in Fig. 2. The surface of the PP fiber was roughened by the alkaline solution, and this improved the bonding of the fiber and the geopolymer (Lopez-Buendia et al. 2003). The roughness of the fiber surface modified the fiber/composite interaction and increased the bonding with the geopolymer matrix (Lopez-Buendia et al. 2003). More microcracks were also found in the composite when the heat was applied, owing to the geopolymerization reaction and water evaporation (water from alkali solutions). However, a denser matrix and better anchoring between fibers and composite were achieved with heat curing. Fly ash particles were also seen with the dissolution of the surface and gel formation (Chindaprasirt et al. 2013). In this aspect, the number of unreacted fly ash particle was less seen with the OHE-cured composite compared to that with the normal RT-cured composite. Since the amorphous or glassy phase of fly ash was on the surface of fly ash and the more crystalline phase was present at the core, the glassy phase was leached out by the alkaline solution forming the geopolymer gel, with regard to the XRD results. This gel bound the fly ash geopolymer matrix and fiber together (Rattanasak and Chindaprasirt 2009).

The rough surface of the PP fiber and the typical products of the reaction in the paste composite with OHE-curing are shown in Fig. 3. The products consisted of portlandite, C–S–H, and the dense matrix of alumino-silicate geopolymer. With OHE-curing, greater roughness of the PP-fiber surface was clearly observed compared to RT-curing, because NaOH solution treated the fiber surface, resulting in good bridging properties (Lopez-Buendia et al. 2003; Wang et al. 2006). Since the high-calcium fly ash was used as a source material for geopolymer synthesis, elongated crystals of portlandite were seen in the composite, as shown in Fig. 3b. Generally, portlandite has a distinct hexagonal shape; however, the dimensions depend on the concentration of the $Ca(OH)_2$ solution and the age of the crystal (Mindess et al. 2002). The morphology of portlandite may vary in the forms of small equidimensional crystals, large flat, platy crystals, thin and elongated crystals, and all variations in between (Mindess et al. 2002). In addition, the flaky and needle-like C–S–H crystals were formed in the composite. Their morphology depends on the curing condition.

Strengths of composites

Compressive strength

Figure 4 presents the 1-month compressive strength of composites with RT and OHE curings. The compressive strength of the PP fiber/fly ash geopolymer composites was slightly lower than that of plain geopolymers, for both curing regimes. For RT-curing, the 1-month compressive strengths of the PP fiber/fly ash geopolymer and plain geopolymer composites were 31.8 and 30.2 MPa, respectively, and for OHE-curing, they were 33.8 and 32.1 MPa, respectively. Immersion of the composite in water promotes the formation of C–S–H and strength development (Mindess et al. 2002). The aim of water immersion is to ensure the continued hydration of the composite, since water could be lost from the mortar by evaporation, or by other means such as absorption of aggregates. The addition of the PP fiber results in a slight reduction in the compressive strength of the composites.

When the composites were exposed to 3% H_2SO_4 solution, the strength was significantly affected. The compressive strengths of the plain geopolymer and PP-fiber geopolymer with RT-curing (Fig. 4a) were reduced to 10.3 and 15.4 MPa, respectively. This was due to the occurrence of C–S–H and portlandite products, with RT-curing leading

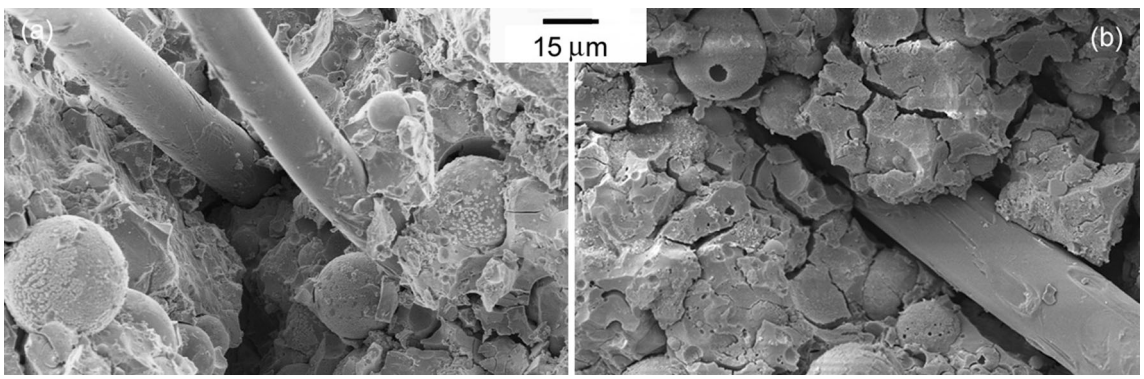

Fig. 2 Microstructure of paste: **a** RT-curing, **b** OHE-curing

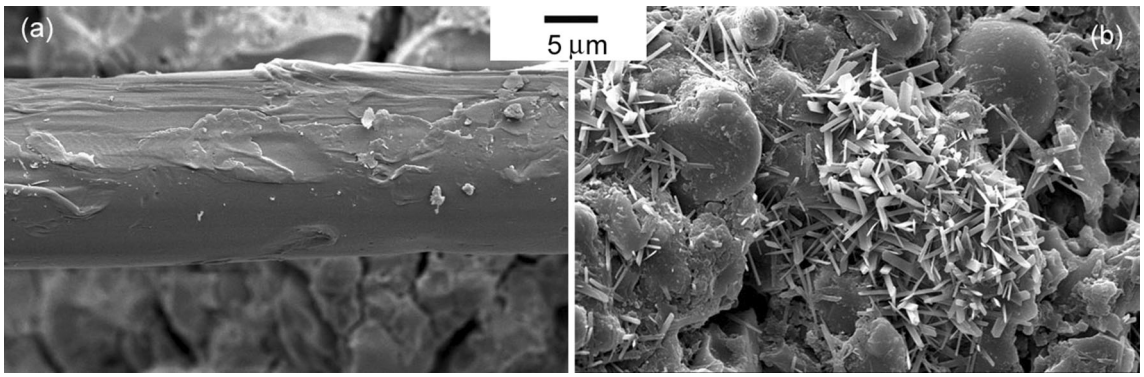

Fig. 3 Microstructure of composite: **a** roughness of PP-fiber surface, and **b** product of high-calcium fly ash geopolymer

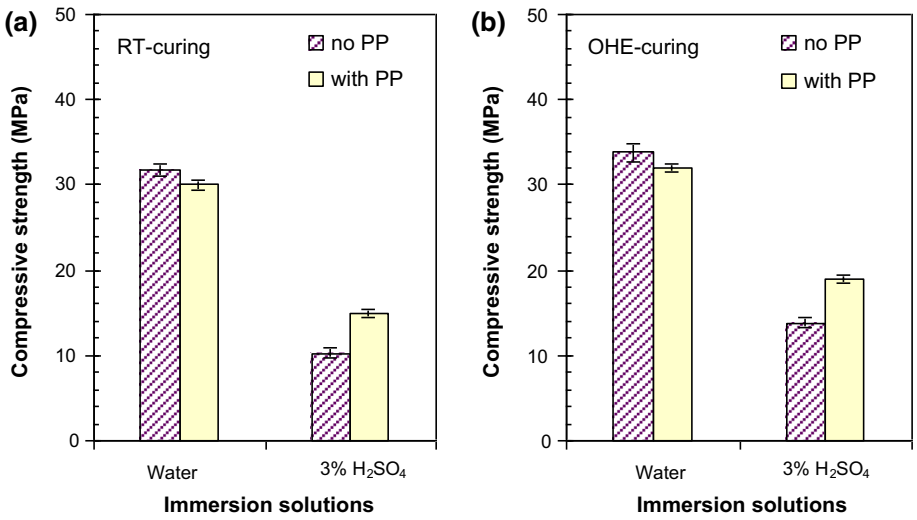

Fig. 4 Compressive strength of composites: **a** RT-curing, **b** OHE-curing

to a susceptible matrix in the acid environment (Chindaprasirt and Rattanasak 2017). These calcium compounds can easily be attacked by acid solution and leach out from the composites, resulting in pores and cavities (Mindess et al. 2002). It has been reported that the decalcifications of portlandite [$Ca(OH)_2$] and C–S–H lead to the loss of cementing properties, i.e., paste cohesion, binding, strength, and durability (Skalny et al. 2002). The presence of the PP fiber in the composite enhanced the resistance to acid due to the reinforcement of fiber.

Comparing the two curing systems, the results showed that the composites with OHE-curing were more resistant to the acid solution than the composites with RT-curing. The compressive strengths of the plain and fiber-reinforced geopolymers, subjected to OHE-curing immersed in acid solution, were 15.4 and 19.0 MPa, respectively, which were significantly higher than those of the RT-cured composites (Fig. 4b). The OHE-curing with higher temperature promoted the Al–O–Si bond formation of the alumino-silicate compound and dense matrix, leading to higher acid resistance. Since the geopolymer system is highly alkaline (pH ≈ 12–14), these composites are therefore resistant to acid environments (Chindaprasirt et al. 2013). Free sulfuric acid can be found in ground water and can be formed by the oxidation of a sulfide (particularly of pyrite) presence in soil, or in industrial waste water (Skalny et al. 2002). The inclusion of the PP fiber helps to bind the matrix together (Natali et al. 2011; Bernal et al. 2012) and thus increases the resistance to acid attack. Hence, a low strength loss is obtained in a PP fiber/fly ash geopolymer composite. It should be pointed out here that although the test was done with five replicates, the difference in compressive strength was small and thus care should be taken when interpreting the results.

The XRD pattern of OHE-geopolymer paste under the acid condition for 1 month is shown in Fig. 5. Gypsum (CaH_4O_6S or $CaSO_4{\cdot}2H_2O$), SiO_2, and geopolymer products were detected in the composite. Gypsum is the product from the reaction between calcium (from fly ash) and sulfate ions (from H_2SO_4 acid). This compound is formed on the surface and in the void of the geopolymer matrix. Dissolution of calcium compounds in the geopolymer

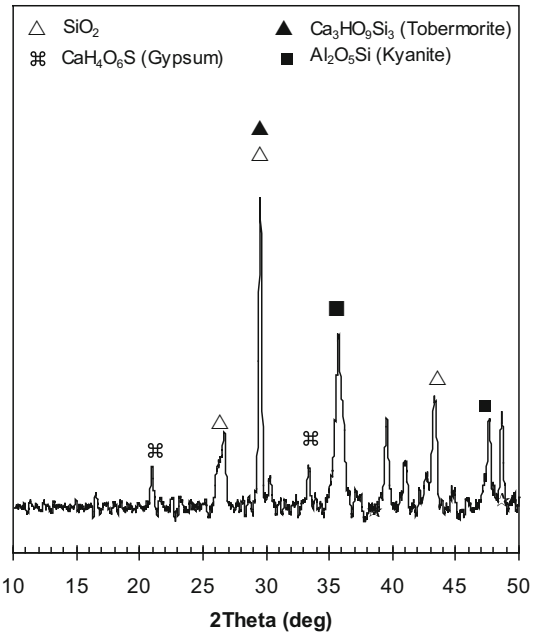

Fig. 5 XRD pattern of OHE-geopolymer under 3% H_2SO_4 solution

results in the lowering of the strength and hardness of the geopolymer (Chindaprasirt and Rattanasak 2016).

Tensile strength

The results of tensile strengths of geopolymer briquettes at the age of 1 month are shown in Fig. 6. The tensile strengths of PP fiber/fly ash geopolymer composites were slightly higher than those of plain geopolymers, for both curing regimes. This result trend was opposite to that of compressive strength. For RT-curing, the 1-month tensile strengths of PP fiber/fly ash geopolymer and plain geopolymer composites were 1.56 and 1.43 MPa, respectively, and for OHE-curing, they were 1.73 and 1.56 MPa, respectively. OHE-curing produced the geopolymer with higher tensile strength due to the geopolymerization reaction as a result of higher temperature curing.

For the immersion in the acid solution, the samples with PP fibers showed a significant increase in resistance to acid attack, compared to the plain geopolymer mortar without PP fiber. For RT-curing, the tensile strengths were 1.17 MPa for the plain composite, and 1.45 MPa for the PP fiber/fly ash geopolymer composites. For OHE-curing, the strengths increased to 1.44 and 1.71 MPa for plain and PP fiber/fly ash geopolymers, respectively. It has been reported that well-made fiber-reinforced materials are slightly less permeable than plain materials (Mindess et al. 2002). The PP fiber marginally enhances the tensile characteristic of the composites and thus helps to reduce microcracks, resulting in a less permeable composite. In addition, improvement of the tensile strength and cracking control in composites are achieved due to the bridging of fibers between cracks. With OHE-curing and the incorporation of the PP fiber, a relatively dense cementitious material with improved tensile strength was obtained, and this composite also had good resistance to the acid solution. The PP fiber/fly ash geopolymer composite was stable in the acid solution, particularly with OHE-curing, and was protected by the alkaline environment of the geopolymer system.

Interfacial shear strength (IFSS)

A typical single-fiber pullout result of PP fiber embedded in the geopolymer (embedded length of 5 mm) is shown in

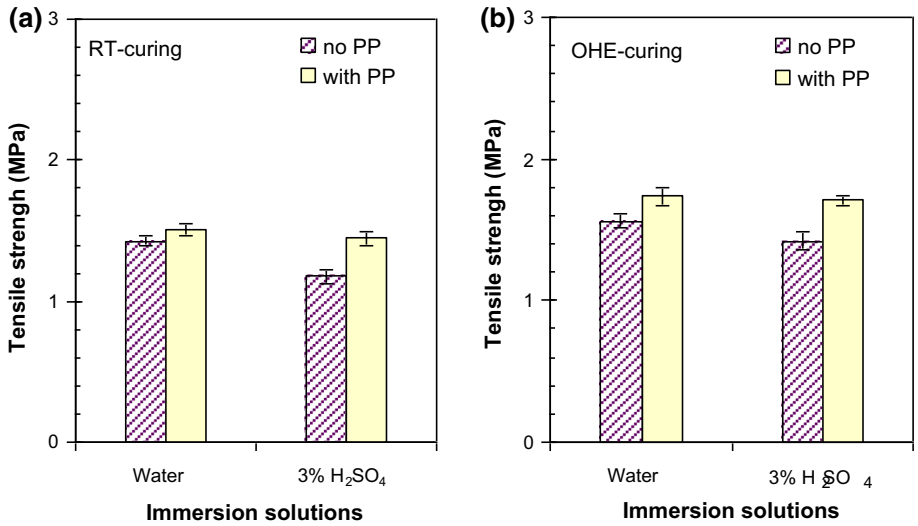

Fig. 6 Tensile strength of composites: **a** RT-curing, **b** OHE-curing

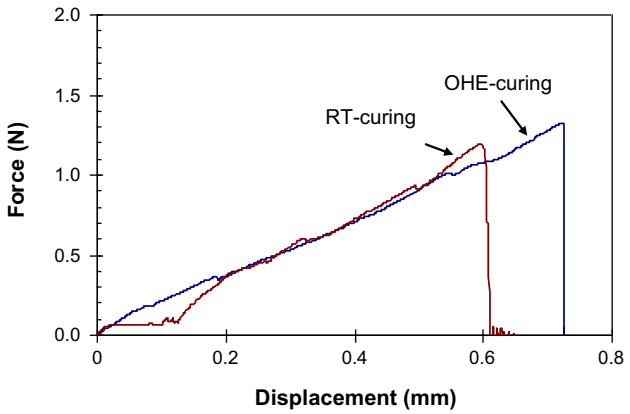

Fig. 7 Single-fiber pullout test of PP fiber embedded in geopolymer

Fig. 7. Interfacial shear strengths (IFSS) of composites were 5.1 and 6.4 N/mm^2 for the RT-cured and OHE-cured systems, respectively. OHE-curing resulted in slightly higher shear strength than that of RT-curing. The OHE-curing enhances the geopolymerization reaction of composite resulting in a dense and strong matrix (Davidovits 1991; Van Jaarsveld et al. 2002; Hussain et al. 2005) compared to that of RT-curing. Furthermore, the IFSS of PP fiber embedded in the geopolymer was higher than the value reported for the PP fiber embedded in cement mortar. It has been reported that the IFSS of PP fiber embedded in cement mortar was 0.9 N/mm^2 for untreated PP fiber, and 5.1 N/mm^2 for treated PP fiber (Lopez-Buendia et al. 2003). This implies that the adhesion property of PP fiber embedded in OHE-curing geopolymer is stronger than that of PP fiber embedded in the cement composite.

It has been reported that the incorporation of fiber in a cementitious matrix results in a noticeable crack reduction, since the principal role of fibers is to control the cracking of composites, and to modify the behavior of material once the matrix has cracked (Mindess et al. 2002). When crack starts to grow, the fibers at the crack surface of the matrix act as a crack-arrester, and crack propagation is inhibited, as shown in Fig. 8a. As load continues, the PP fibers in the geopolymer matrix bridging across a crack are formed, as shown in Fig. 8b.

Energy conservation

Generally, the conventional curing of geopolymer is 60–90 °C for up to 24 h in order to achieve a strong alumino-silicate compound (Davidovits 1991; Van Jaarsveld et al. 2002; Hussain et al. 2005). Energy for the heat curing is primarily supplied by electrical oven, which can present high energy costs for the geopolymer product. Fortunately, fly ash from low-grade lignite combustion in Thailand contains a high calcium content leading to the fast setting time of the geopolymer without heat curing. However, the low strength and poor durability of the product are obtained. This is due to calcium compound formation of calcium silicate hydrate and calcium hydroxide. Heat is needed to promote the formation of Al–O–Si linkage at the alumino-silicate site of the geopolymer, particularly when the composite has been applied in an acidic environment, e.g., domestic sewage and industrial wastewater pipes (Chindaprasirt and Rattanasak 2016). To utilize the energy from hot weather, outdoor heat exposure (OHE) with an average temperature of 35 °C is an alternative source energy for geopolymer synthesis, with no cost. From the results, 35 °C-OHE provides Al–O–Si linkage in the composite as indicated by the XRD peak of kyanite (Al_2O_6Si). In addition, using PP fiber enhances the durability of the specimens, particularly for application in an acidic environment. Therefore, solar energy can be a sustainable energy for the production of high-calcium fly ash geopolymers and can also reduce the production cost. This high-calcium fly ash geopolymers can be a cleaner product, which effectively utilize the fly ash and solar energy. Geopolymer brick is produced, which applies a solar energy for a low temperature curing (Chindaprasirt and Rattanasak 2017). This material can be a new commercialized building material product in Thailand in the near future.

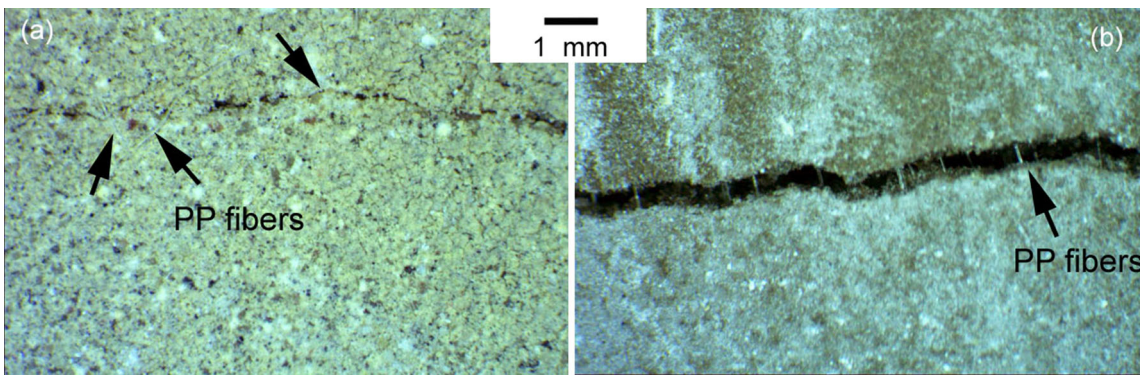

Fig. 8 Optical microscope of PP fibers bridging across a crack: **a** hairline crack with PP fibers, **b** PP fiber bridging

Conclusion

High-calcium fly ash can be used as a source material for geopolymer synthesis without heat curing. However, the composites are not resistant to an acid environment, owing to the high calcium content of the fly ash. The incorporation of PP fiber in composites resulted in improved tensile characteristics, crack control, and increased resistance to the acid solution, particularly with outdoor heat exposure (OHE) cured composites. Solar energy is a renewable and sustainable energy resource for OHE-curing of composites leading to strong bridging properties between the PP fiber and the matrix, and dense and strong composites. PP fiber helps to improve the tensile strength and the crack-growth resistance in composites, due to the bridging of fibers between crack surfaces. In an acid environment, the PP fiber/fly ash geopolymer with OHE-curing thus performs much better than the plain geopolymer with room temperature curing.

Acknowledgements This research was supported by the Thailand Research Fund (TRF) and Khon Kaen University under TRF Senior Research Scholar Contract No. RTA5780004; and Faculty of Science, Burapha University under TRF Research Scholar Contract No. RSA5880001.

References

Arulrajah A, Kua E, Horpibulsuk S, Phetchuay C, Suksiripattanapong C, Du Y (2016) Strength and microstructure evaluation of recycled glass-fly ash geopolymer as low carbon masonry units. Constr Build Mater 114:400–406

ASTM D7913, D7913M-14 (2014) Standard test method for bond strength of fiber-reinforced polymer matrix composite bars to concrete by pullout testing. ASTM International, West Conshohocken

Banthia N, Gupta R (2006) Influence of polypropylene fiber geometry on plastic shrinkage and cracking in concrete. Cem Concr Res 36:1263–1267

Bernal S, Bejarano J, Garzon C, de Gutierrez RM, Delvasto S (2012) Performance of refractory alumino-silicate particle/fibre-reinforced geopolymer composites. Compos Part B 43:1919–1928

Chindaprasirt P, Rattanasak U (2016) Improvement of durability of cement pipe with high-calcium fly ash geopolymer covering. Constr Build Mater 112:956–961

Chindaprasirt P, Rattanasak U (2017) Characterization of the high-calcium fly ash geopolymer mortar with hot-weather curing systems for sustainable application. Adv Powder Technol. doi:10.1016/j.apt.2017.06.01x

Chindaprasirt P, Rattanasak U, Taebuanhuad S (2013) Role of microwave radiation in curing the fly ash geopolymer. Adv Powder Technol 24:703–707

Chindaprasirt P, Paisitsrisawat P, Rattanasak U (2014) Strength and resistance to sulfate and sulfuric acid of ground fluidized bed combustion fly ash–silica fume alkali-activated composite. Adv Powder Technol 25:1087–1093

Davidovits J (1991) Geopolymer: inorganic polymeric new materials. J Therm Anal 37:1633–1656

Fernández-Jiménez A, Palomo A, Criado M (2005) Microstructure development of alkali-activated fly ash cement: a descriptive model. Cem Concr Res 35:1204–1209

Hussain M, Varley RJ, Cheng YB, Mathys Z, Simon GP (2005) Synthesis and thermal behavior of inorganic–organic hybrid geopolymer composites. J Appl Polym Sci 96:112–121

Lopez-Buendia AM, Romero-Sanchez MD, Climent V, Cuillem C (2003) Surface treated polypropylene (PP) fibres for reinforced concrete. Cem Concr Res 54:29–35

Mindess S, Young JF, Darwin D (2002) Concrete, 2nd edn. Prentice Hall, Englewood Cliffs

Natali A, Manzi S, Bignozzi MC (2011) Novel fiber-reinforced composite materials based on sustainable geopolymer matrix. Procedia Eng 21:1124–1131

Ostertag CP, Yi CK (2007) Crack/fiber interaction and crack growth resistance behavior in microfiber reinforced mortar specimens. Mater Struct 40:679–691

Ranjbar N, Telebian S, Mehrali M, Kuenzel C, Metselaar HSC, Jumaat M (2016a) Mechanisms of interfacial bond in steel and polypropylene fiber reinforced geopolymer composites. Compos Sci Techol 122:73–81

Ranjbar N, Mehrali M, Behnia A, Pordsari AJ, Mehrali M, Alengaram UJ, Jumaat MZ (2016b) A comprehensive study of the polypropylene fiber reinforced fly ash based geopolymer. PLoS ONE 11(1):e0147546. doi:10.1371/journal.pone.0147546

Rattanasak U, Chindaprasirt P (2009) Influence of NaOH solution on the synthesis of fly ash geopolymer. Miner Eng 22:1073–1078

Richardson A (2006) Compressive strength of concrete with polypropylene fibre additions. Struct Surv 24(2):138–153

Shaikh FUA (2013) Deflection hardening behaviour of short fibre reinforced fly ash based geopolymer composites. Mater Des 50:674–682

Skalny J, Marchand J, Odler I (2002) Sulfate attack on concrete. Spon Press, London

Somna K, Jaturapitakkul C, Kajitvichyanukul P, Chindaprasirt P (2011) NaOH-activated ground fly ash geopolymer cured at ambient temperature. Fuel 90:2118–2124

Tanaka H, Fujii A (2009) Effect of stirring on the dissolution of coal fly ash and synthesis of pure-form Na-A and -X zeolites by two-step process. Adv Powder Technol 20:473–479

Tchadjié LN, Djobo JNY, Ranjbar N, Tchakouté HK, Kenne BBD, Elimbi A, Njopwouo D (2016) Potential of using granite waste as raw material for geopolymer synthesis. Ceram Int 42:3046–3055

Temuujin J, Rickard W, Van Riessen A (2013) Characterization of various fly ashes for preparation of geopolymers with advanced applications. Adv Powder Technol 24:495–498

Teuber L, Fischer H, Graupner N (2013) Single fibre pull-out test versus short beam shear test: comparing different methods to assess the interfacial shear strength. J Mater Sci 48:3248–3253

Thai Meteorological Department (TMD) (2015) Thailand annual weather summary. http://www.tmd.go.th/en/climate.php?FileID=5. Accessed 14 Sept 2016

Van Jaarsveld JGS, Van Deventer JSJ, Lukey GC (2002) The effect of composition and temperature on the properties of fly ash- and metakaolinite-based geopolymers. Chem Eng J 89:63–73

Wang W, Wang L, Shi Q, Yu H, Chen T, Wang C, Sun T (2006) Progress of the surface modification of PP fiber used in concrete. Polym Plast Technol Eng 45:29–34

Zhang Z, Yao X, Zhu H, Hua S (2009) Preparation and mechanical properties of polypropylene fibre reinforced calcined kaolin-fly ash based geopolymer. J Cent South Univ Technol 16:42–52

KSCE Journal of Civil Engineering (0000) 00(0):1-8
DOI 10.1007/s12205-017-0144-6
Copyright ⓒ2017 Korean Society of Civil Engineers

Structural Engineering
pISSN 1226-7988, eISSN 1976-3808
www.springer.com/12205

Mechanical Properties, Thermal Conductivity, and Sound Absorption of Pervious Concrete Containing Recycled Concrete and Bottom Ash Aggregates

Chanchai Ngohpok*, Vanchai Sata, Thaned Satiennam***, Pongrid Klungboonkrong****, and Prinya Chindaprasirt*****

Received January 31, 2017/Accepted May 16, 2017/Published Online August 1, 2017

Abstract

This paper presents the effect of replacement level of natural aggregate (crushed limestone aggregate, LS) with Recycled Concrete (RC) and coal Bottom Ash aggregates (BA) on pervious concrete properties. Mechanical properties, thermal conductivity, and sound absorption of pervious concrete were tested. Results showed that the compressive strength of BA pervious concrete was excellent and comparable to that of LS pervious concrete. While the compressive strength of RC pervious concrete was slightly reduced to between 85 and 99% of that of LS pervious concrete. The thermal conductivity and sound absorption of pervious concretes containing RC and BA were significantly improved compared to those of pervious concretes containing conventional LS.

Keywords: *porous concrete, recycled concrete aggregate, coal bottom ash solid waste; acoustic absorption*

1. Introduction

Pervious concrete is a special type of concrete with high porosity and continuous void consisting of Portland cement, coarse aggregate, little or no fine aggregate, admixture, and water (ACI 522, 2010). As a result, pervious concrete has been used in road paving, sidewalk and pathways, parking lots and drainage of retaining walls to efficiently solve the problem of storm water runoff drainage. Furthermore, it can be used as a water treatment filter to reduce pollutants (Golroo and Tighe, 2011; Haselbach *et al*., 2006; Lee *et al.*, 2014). In addition, the pores inside the material exhibit good thermal properties and they have the ability to absorb sound energy through internal friction. It is, therefore, used for highway noise barriers and thermal insulating material in buildings (Arenas *et al*., 2013). Generally, the compressive strengths of pervious concrete are not high and average between 2.8 and 28.0 MPa depending on the void ratio content (ACI 522, 2010; Chindaprasirt *et al.,* 2008).

One of the main factors affecting the quality and carbon footprint of concrete products is the type of aggregate. The recycling of solid material as aggregate in concrete can reduce the problem of waste and conserve natural aggregate resources. A number of researchers (Cristián *et al*., 2014; Hwang *et al*., 2013; Limbachiya *et al*., 2012) found that recycled concrete can be used as aggregate in new concrete. The application of recycled concrete aggregate provides pervious concrete strength in the range of 13-19 MPa upon void content (Park *et al*., 2005), which is similar to those of natural aggregate pervious concrete of 15-20 MPa (Sata *et al.*, 2016). Bottom ash is waste material from the combustion of coal in thermal power plant that needs to be disposed of in an environmental friendly way. The utilization of coal bottom ash as a substitute for coarse aggregate in concrete production is also a good option in terms of environmental and economic considerations (Park *et al*., 2009; Kim and Lee, 2015; Wongsa *et al*., 2016).

The purpose of this research is to study the effect of replacement level crushed limestone with solid wastes (recycled concrete and coal bottom ash aggregates) on the mechanical properties, thermal conductivity and sound absorption of pervious concrete. This is aimed at producing get pervious concrete displaying

*Ph.D. Student, Sustainable Infrastructure Research and Development Center, Dept. of Civil Engineering, Faculty of Engineering, Khon Kaen University, Khon Kaen 40002, Thailand (E-mail: chanchai.ng@gmail.com)
**Associate Professor, Sustainable Infrastructure Research and Development Center, Dept. of Civil Engineering, Faculty of Engineering, Khon Kaen University, Khon Kaen 40002, Thailand (Corresponding Author, E-mail: vancsa@kku.ac.th)
***Associate Professor, Sustainable Infrastructure Research and Development Center, Dept. of Civil Engineering, Faculty of Engineering, Khon Kaen University, Khon Kaen 40002, Thailand (E-mail: sthaned@kku.ac.th)
****Associate Professor, Sustainable Infrastructure Research and Development Center, Dept. of Civil Engineering, Faculty of Engineering, Khon Kaen University, Khon Kaen 40002, Thailand (E-mail: ponklung@gmail.com)
*****Professor, Sustainable Infrastructure Research and Development Center, Dept. of Civil Engineering, Faculty of Engineering, Khon Kaen University, Khon Kaen 40002, Thailand (E-mail: prinya@kku.ac.th)

acceptable mechanical property with ample thermal as well as sound absorption properties.

2. Materials and Methods

2.1 Materials

Ordinary Portland Cement (OPC) with specific gravity of 3.14 and Blaine fineness of 3,300 cm^2/g, tap water and standard type F superplasticizer (SP) were used in this study. Three coarse aggregate types, viz crushed limestone aggregate (LS), recycled concrete aggregate (RC) and coal bottom ash aggregate (BA) displaying 4.75-9.0 mm size as shown in Fig. 1 were employed. The RC was obtained from crushed concrete cylinders with compressive strengths of 30-40 MPa. The BA was a high calcium bottom ash obtained from Mae Moh coal power station located in the north of Thailand. The physical properties of aggregates are presented in Table 1. The specific gravities of LS, RC, and BA were 2.79, 2.62, and 2.19 respectively. The dry-rodded densities of LS, RC, and BA were 1440, 1365, and 1068 kg/m^3. Meanwhile, void contents were 46.1, 45.3, and 51.1% respectively. The dry-rodded density of BA gave the lowest reading due to its low specific gravity and high void content. The water absorptions for LS, RC, and BA were 0.2, 6.5, and 2.8% respectively. The high water absorption of RC was due to the high porosity of attached mortar.

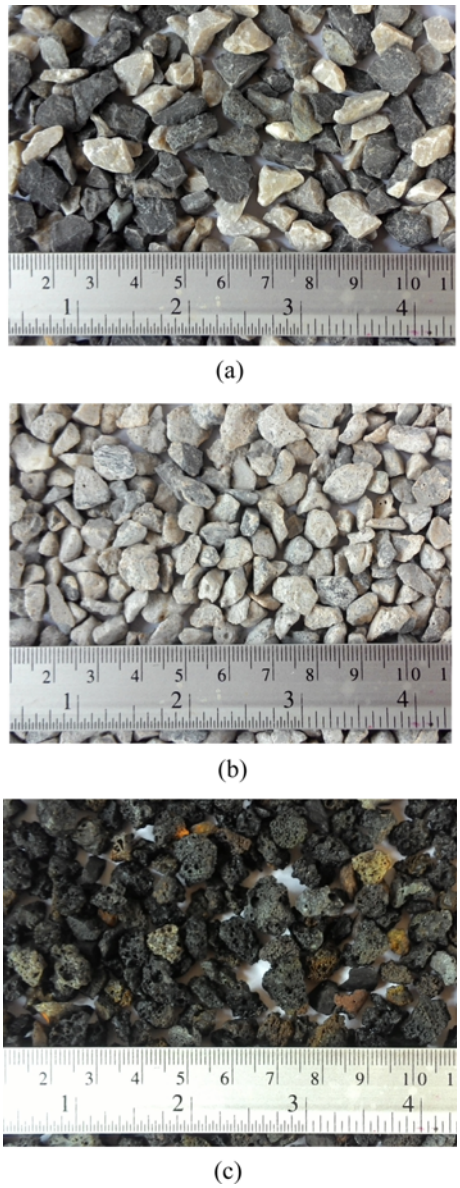

Fig. 1. Coarse Aggregates Used in This Study: (a) Limestone Aggregate (LS), (b) Recycled Concrete Aggregate (RC), (c) Coal Bottom Ash Aggregate (BA)

2.2 Mix Proportions and Preparation of Samples

In this study, pervious concretes with paste volumes of 15, 20, and 25%, water to cement ratio (W/C) of 0.30 and paste flow values of 190-230 mm were selected. The mix proportions of pervious concretes are given in Table 2. Additionally, the symbols of mix are given by AATTPP, where AA is the percentage of aggregate replacement level by volume, TT is the type of aggregate and PP is the paste volume (%). For example, 40RC20 stands for mix with 40% recycled concrete aggregate and paste volume of 20%. The cement paste was mixed at 50 rpm for 240 s in a mixer subsequent to the addition of OPC, water, and SP. After that, the coarse aggregate was added and mixed for another 120s. Then, the fresh concrete was placed into 100 × 150 and 100 × 200 mm cylindrical molds, 150 × 150 × 500 mm prism mold and 150 × 150 × 50 mm slab mold in two layers with 10s of vibration for each layer.

2.3 Testing of Concrete

The void content of pervious concrete was measured using the test method for pervious concrete in accordance with ASTM C1754 (2016) as shown in Eq. (1)

Table 1. Physical Properties of Coarse Aggregates

Physical properties	LS	RC	BA
Specific gravity	2.79	2.62	2.19
Dry-rodded density (kg/m^3)	1440	1365	1068
Void content (%)	46.1	45.3	51.1
Water absorption (%)	0.5	6.5	2.8
Los Angeles abrasion loss (%)	31.5	36.8	46.5

Table 2. Mix Proportion of Pervious Concrete (kg/m^3)

Mixes	OPC	LS	RC	BA	Water	SP
100LS15	243	1487	-	-	73	1.67
100LS20	323	1487	-	-	97	2.00
100LS25	404	1487	-	-	121	1.94
40RC20	323	892	581	-	97	2.00
60RC20	323	595	872	-	97	2.00
100RC20	323	-	1454	-	97	2.00
40BA20	323	892	-	439	97	2.00
60BA20	323	595	-	658	97	2.00
100BA20	323	-	-	1097	97	2.00

$$V = \left(1 - \frac{W_2 - W_1}{\rho_W V_S}\right) \times 100 \quad (1)$$

where V = Is the void content of pervious concrete (%),
W_1 = Is the weight of the specimen in water (g),
W_2 = Is the weight of the air dried specimen subsequent to being placed in room temperature for 24 hrs. (g),
ρw = Is the density of water at water bath temperature (g/cm^3), and
V_S = is the volume of specimen (cm^3).

Water permeability was determined by applying constant head permeability test apparatus. The coefficient of permeability (k) was calculated in accordance with Darcy's Law using Eq. (2).

$$k = \frac{H}{h} \times \left(\frac{Q}{A(T_2 - T_1)}\right) \quad (2)$$

where A = Is the cross sectional area of test piece (mm^2)
h = Is the difference in water level (mm),
H = Is the length of sample (mm),
k = Is the water permeability coefficient (mm/s),
$T_2 - T_1$ = Is the measurement of time (s)
Q = Is the flow quantity during T_1 to T_2 (mm^3),

The compressive, flexural, and splitting tensile strengths of pervious concrete samples were tested in accordance with ASTM C39 (2016), ASTM C78 (2016), and ASTM C496 (2016) respectively. The thermal conductivity coefficients were tested by employing a direct measuring instrument with surface probe (ISOMET Model 2114, Applied Precision Ltd.) with measurement ranges of 0.04–6.0 W/m.K.

The sound absorption coefficient of pervious concrete was determined by impedance tube method according to ISO 10534-2 (1998). Absorption coefficient (α) is the ratio of absorbed energy to total incident energy. Sound Absorption Average (SAA) was obtained by calculating the arithmetic mean of absorption coefficients of 200 Hz to 2500 Hz (Mirjalili and Mohammad-Shah, 2012). The reported value was the average of three samples.

3. Experimental Results and Discussion

3.1 Void Content, Water Permeability, and Bulk Density

The results of void contents and water permeability with three different aggregates (LS, RC, and BA) and four different aggregate replacement levels of 0, 40, 60, and 100% by volume of pervious concrete are shown in Fig. 2. The results revealed that the void content of pervious concrete with 100% LS decreased as paste content increased. At paste contents of 15, 20, and 25%, void contents were 35.1, 29.6, and 25.9% respectively. High paste content (100LS25) resulted in the filling of voids with extra paste and reduced air void content. Based on the experimental outcomes, medium paste content of 20% was selected for the study in the variation of aggregate types. For the case of aggregates replacement, the results indicated, increase in RC and BA

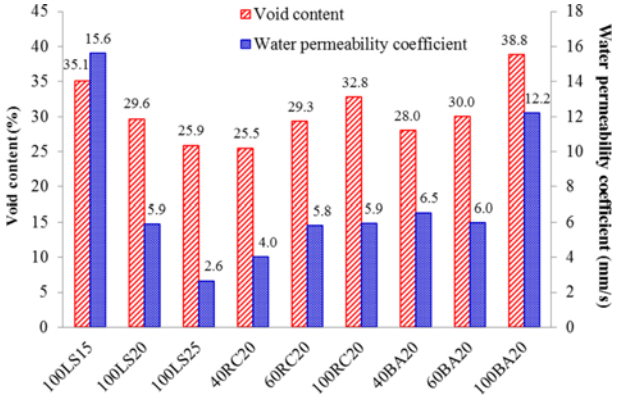

Fig. 2. Void Content and Water Permeability Coefficient of Pervious Concrete with Various Paste Volume and Type of Aggregate

replacement levels proliferated the void content of concretes. The pervious concretes with 20% paste volume and 40, 60, and 100% RC aggregate exhibited void contents of 25.5, 29.3, and 32.8% respectively. The pervious concrete with higher void contents of 28.0, 30.0, and 38.8% were found in 40BA20, 60BA20, and 100BA20 concretes respectively. From Fig. 2, void content decreased with the increase of paste content as expected. In addition, it was discovered that, as the percentages of RC and BA increased, void contents tended to increase. This was due to the large amount of void in BA aggregate (Park *et al*., 2009) and the high porosity of attached mortar amid RC aggregate (Limbachiya *et al*., 2012). For the results of water permeability, void content was the most significant factor. The water permeability coefficient of 100LS15, 100LS20, and 100LS25 concretes were 15.6, 5.9, and 2.6 mm/s respectively. What's more, aggregate replacement level and type, also affected water permeability. As the BA replacement increased, the water permeability coefficient had the tendency to increase similar to the effect on void content. The water permeability coefficients of 40RC20, 60RC20, and 100RC20 concretes were 25.5, 29.3, and 32.8 mm/s respectively. In addition, they were 28.0, 30.0, and 38.8 mm/s for 40BA20, 60BA20, and 100BA20 concretes respectively. The relationship between water permeability coefficient and void content could be fitted with an exponential curve as shown in Fig. 3 using Eq. (3) as follows:

$$k = 0.2517 e^{0.1054V} \quad (3)$$

where k = Is the water permeability coefficient of pervious concrete (mm/s) and
V = Is the void content of pervious concrete (%).

From Fig. 3, the water permeability coefficients of pervious concretes were 2-16 mm/s with corresponding void contents of 25.5-38.8%. The results also indicated that the water permeability coefficient of pervious concrete increased exponentially with void content as also reported in previous studies (Neithalath *et al*., 2010; Sata *et al*., 2016). The bulk densities of pervious

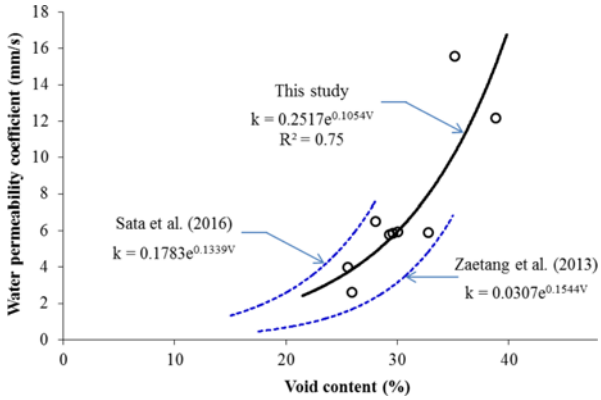

Fig. 3. Relationship between Void Content and Water Permeability Coefficient of Pervious Concrete

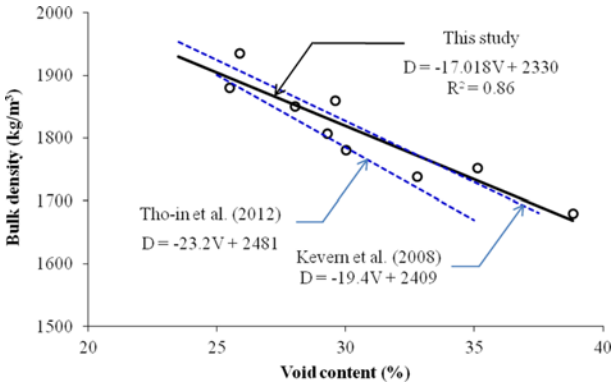

Fig. 5. Relationship between Void Content and Bulk Density of Pervious Concrete

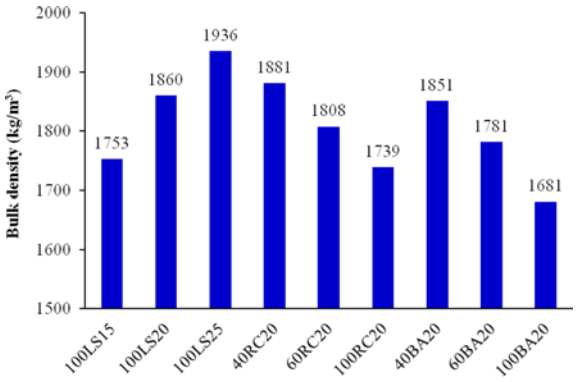

Fig. 4. Bulk Density of Pervious Concrete with Various Paste Volumes and Types of Aggregate

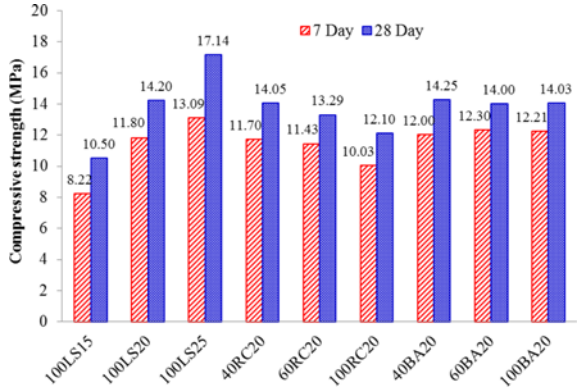

Fig. 6. Compressive Strength of Pervious Concrete with Various Paste Volume and Type of Aggregate at 7 and 28 days

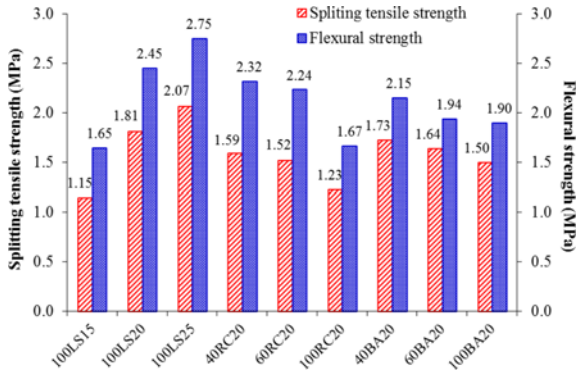

Fig. 7. Splitting Tensile and Flexural Strength of Pervious Concrete with Various Paste Volume and Type of Aggregate at 28 days

concrete at 28 days are shown in Fig. 4. The increase in paste contents resulted in the increase in bulk density owing to the reduction of air void content in the mixes. The bulk densities of 100% LS pervious concrete with paste contents of 15, 20, and 25% were 1753, 1860, and 1936 kg/m^3 respectively. The increase in RC levels to 40, 60, and 100% by volume bought about the reduction in bulk density due to the high porosity of the RC attached mortar. The bulk densities of 40RC20, 60RC20, and 100RC20 concretes were 1881, 1808, and 1739 kg/m^3 respectively. The augmentation in BA replacement level to 40, 60, and 100% by volume, produced concrete bulk densities of 1851, 1781, and 1681 kg/m^3 respectively. Both RC and BA reduced the bulk density of pervious concretes. The reduction with BA replacement was larger than that of RC due to the high contents of micro and macro pores in BA, as also indicated by the low specific gravity of BA. The relationship between void content and bulk density of pervious concrete could be fitted with linear relationship as presented in Fig. 5 and Eq. (4). Accordingly, the trend line is comparable to those of Tho-in *et al.* (2012) and Kevern *et al.* (2008).

$$D = -17.018V + 2330 \quad (4)$$

where D = Is the bulk density of pervious concrete (kg/m^3) and
V = Is the void content of pervious concrete (%).

3.2 Compressive, Splitting Tensile, and Flexural Strengths

The compressive, splitting tensile, and flexural strengths of pervious concrete at the age of 28 days are shown in Figs. 6 and 7. The results indicated that the increasing of paste contents enhanced the mechanical properties of concretes at 28 days aimed 100LS15, 100LS20, and 100LS25 concretes. The high paste content (100LS25) increased the thickness of the paste and enhanced mechanical properties accordingly. Meanwhile, low paste content (100LS15) resulted in a thin layer of paste, and

increased air void content which contributed to the lowering of mechanical properties.

The partial replacement of LS with RC at 40, 60, and 100% by volume gave rise to decreasing strengths with the increase in RC content. This was caused mainly by the low strength of attached mortar on the RC surface. Furthermore, subsequent to mixing the paste could not be filled directly into the pores of the attached mortar in RC and thusly provided weak bonding between paste and RC (Cristián *et al*., 2014; Nuaklong *et al*., 2016). In addition, an increase in the partial replacement of LS with BA at 40, 60, and 100% by volume also decreased the pervious concrete strength due to the large amount of void in BA aggregate (Park *et al*., 2009).

The splitting tensile and flexural strengths followed the same trend as that of compressive strength. The splitting tensile strengths of pervious concrete were 1.65-2.75 MPa. From this outcome, the compressive strength values were virtually the same as that of mix100LS20. This was mainly due to the increasing of contact points per unit area in macro pores between paste and BA, hence resulting in enhanced mechanical properties. Moreover, this amorphous aluminosilicate was known to exhibit some pozzolanic reaction in cement paste. This reactivity was potentially beneficial in improving the bond between cement paste and aggregate (Hemmings *et al.*, 2009). From observation of the fractured surface, it was discovered that for the specimen of 100LS20 mix, the cracks could be found in the aggregate itself, cement paste, as well as at the interface between aggregate and cement paste. Nonetheless, as the BA content increased, a large portion of cracks were observed in the BA itself. This may be down to the high porosity of BA, consequently, more cracks were observed in the BA.

3.3 Thermal Conductivity

The thermal conductivity of conventional concrete generally depends on the types of aggregate, moisture content, and temperature of specimen (Kodur and Sultan, 2003). Thermal conductivity coefficient results of pervious concrete in this study are presented in Fig. 8. It showed that the thermal conductivity of 100LS15, 100LS20, and 100LS25 concretes were 0.85, 1.00, and 1.02 W/m.K respectively. The trend of thermal conductivity of pervious concrete increased with the filling paste ratio due to the porosity of bulk material decreasing as the amount of cement paste increased (Scanlon, 1994). For 20% cement paste value, the results indicated that thermal conductivities decreased with increasing RC replacements. For example, thermal conductivities were 0.88, 0.84, and 0.82 W/m.K for 40RC20, 60RC20, and 100RC20 mixes. This increase resulted in the high absorption of latent heats in RC (Scanlon, 1994). The results also revealed that the use of BA in pervious concrete significantly decreased the thermal conductivity. The thermal conductivity of the 20% cement paste pervious concretes with 40 and 60% BA (40BA20 and 60BA20) were 0.58 and 0.46 W/m.K. Meanwhile, the thermal conductivity of 20% cement paste and 100% BA (100BA20) was the lowest at 0.29 W/m.K. This was due to the aluminosilicate aggregate as BA presenting low thermal conductivity value (2.98 W/m.K) and containing a very high total porosity with predominantly open pore structure (Hemmings *et al.*, 2009). Even though, the calcium carbonates aggregate (LS) also had lower thermal conductivity of 2.93 W/m.K, it contained a low total pore volume (Kodur and Sultan, 2003). All results of thermal conductivity of pervious concrete were 0.29-1.02 W/m.K and lower than that of conventional concretes of 0.62 to 3.30 W/m.K (Kodur and Sultan, 2003). Besides that, they were lower than that of lightweight concrete of 0.40 and 1.89 W/m.K (Steiger and Hurd, 1978). These reports gave similar thermal conductivity values of pervious concretes (Zaetang *et al.*, 2013; Chindaprasirt *et al*., 2014). However, thermal conductivity values aimed this study were higher than those of lightweight concretes with polystyrene beads with thermal conductivity of 0.07-0.33 W/m.K (Schackow *et al.*, 2014).

The relationship between bulk density and thermal conductivity coefficient of pervious concrete in this study was plotted and compared with the equation of ACI 213 (2010) as shown in Fig. 9. The thermal conductivity trend lines of pervious concrete with LS, RC, and BA were similar to ACI 213 (2010). Moreover, all pervious concretes provided R^2 values above 0.90. It can thus be employed to predict the thermal conductivity of pervious concrete as presented in Eq. (5)-(7).

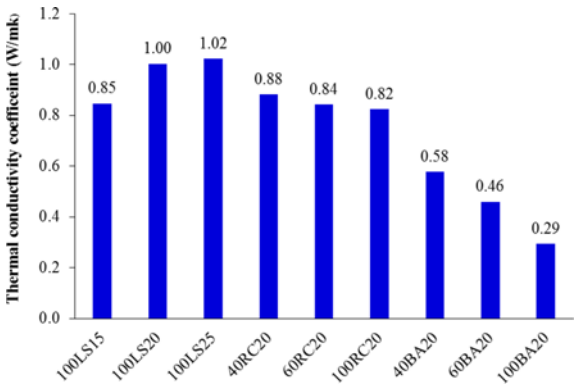

Fig. 8. Thermal Conductivity Coefficient of Pervious Concrete with Various Paste Volume and Type of Aggregate

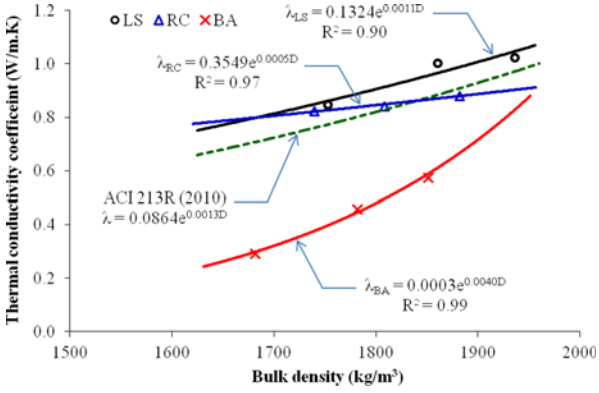

Fig. 9. Relationship between Bulk Density and Thermal Conductivity Coefficient of Pervious Concrete

$$\lambda_{LS} = 0.1324e^{0.0011D} \quad (5)$$

$$\lambda_{RC} = 0.3549e^{0.0005D} \quad (6)$$

$$\lambda_{BA} = 0.0003e^{0.0040D} \quad (7)$$

where λ_{LS}, λ_{RC}, and λ_{BA} are thermal conductivity coefficient of pervious concrete with LS, RC, and BA respectively (W/m.K) and

D = Is the bulk density of pervious concrete (kg/m^3).

The bulk density of pervious concrete was the most important factor affecting thermal conductivity. The subsiding of bulk density gave decreasing trends of thermal conductivity. Additionally, types of aggregate also had great impact on thermal conductivity aimed pervious concrete. From the results, BA aggregate contained some air bubbles thus generated entrapped air in the cement matrix more than LS and RC and hence provided lighter bulk density and thermal conductivity coefficient. Moreover, the amorphous aluminosilicate materials in BA displayed low thermal conductivity. Indeed, these results are compatible the previous studies (Demirboğa and Gül, 2003; Sengula *et al*., 2011).

3.4 Sound Absorption

The sound absorption of pervious concrete can be measured by using the sound absorption coefficient (α). In this study, the sound absorption of pervious concrete was measured under frequency ranges of 100-2500 Hz. The results of pervious concrete sound absorption coefficients are shown in Figs. 10-12. All pervious concrete samples presented first and second loop peaks in the range of 450-500 and 1270-1600 Hz. This is in accordance with the literature (Kim and Lee, 2010) in relation to normal pervious concrete of 10 cm thickness. From Fig. 10, the high absorption coefficient (α more than 0.70) of 100LS15, 100LS20, and 100LS25 concretes aimed the first loop exhibited frequency ranges of 425-590, 420-570, and 400-510 Hz. with the first peak absorption coefficients of 0.99, 0.96, and 0.82 at frequencies of 505, 490, and 450 Hz respectively. What's more, absorption coefficient values of the second loop peak were lower than those of the first loop peak. They were 0.84, 0.67, and 0.65 at frequency approximately 1600, 1440, and 1270 Hz respectively. This signifies that the sound absorption coefficients of pervious concrete reduced with an increase in cement paste content since the sound absorption became lower as the specific surface area of voids decreased (Park *et al*., 2005; Arenas *et al*., 2011). The use of RC replacement of LS resulted in absorption coefficients of 100LS20, 40RC20, 60RC20, and 100RC20 concretes for the first loop peak of 0.96, 0.92, 0.97, and 0.98 at frequencies of 490, 445, 460, and 490 Hz respectively. Second loop peaks were 0.67, 0.77, 0.85, and 0.91 at frequencies of 1440, 1405, 1485, and 1580 Hz respectively as shown in Fig. 11. The results indicated that the sound absorption of pervious concrete with RC increased with an increase in the amount of RC. This was due to the upsurge in the void content of pervious concrete as a result of the increased RC content (Park *et al.*, 2005). From Fig. 12, the absorption coefficient of pervious concrete with BA increased along with a proliferation in the BA content. This was due to many pores inside BA pervious concrete which could absorb sound energy through internal friction (Arenas *et al.*, 2011). In addition, it indicates that the pervious concrete with BA had higher absorption coefficient than the pervious concrete with RC and LS. The finding conformed to the result of void content.

Sound Absorption Average (SAA) is a single-number rating of

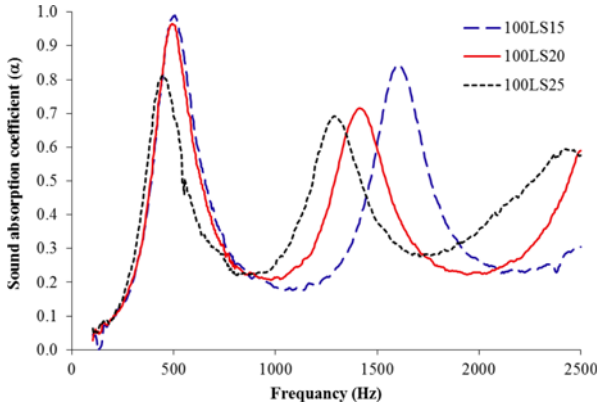

Fig. 10. Relationship between Frequency and Sound Absorption Coefficient of Pervious Concrete Various Paste Volume

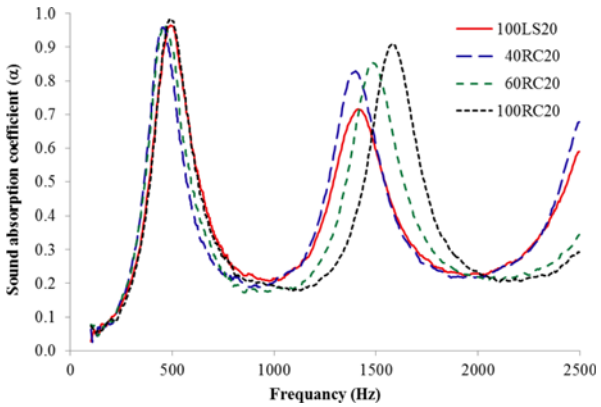

Fig. 11. Relationship between Frequency and Sound Absorption Coefficient of Pervious Concrete Various RC Replacements

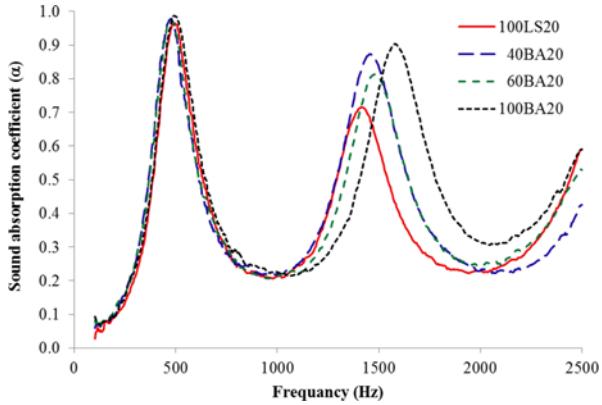

Fig. 12. Relationship between Frequency and Sound Absorption Coefficient of Pervious Concrete Various BA Replacements

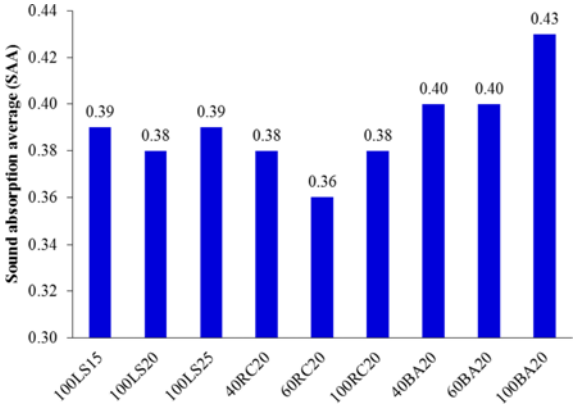

Fig. 13. Sound Absorption Average of Pervious Concrete with Various Paste Volume and Type of Aggregate

sound absorption properties aimed a material. The employed sound absorption values are taken from 200 to 2500 Hz (Mirjalili and Mohammad-Shah, 2012). The SAA measurement results are presented in Fig. 13. The results showed that the SAA of 100% LS at cement paste volumes of 15, 20, and 25% (100LS15, 100LS20, and 100LS25) were 0.39, 0.38, and 0.39 respectively. While, the SSA of 40RC20, 60RC20, and 100RC20 concretes were 0.38, 0.36, and 0.38 respectively. SSA for 40BA20, 60BA20, and 100BA20 concretes were 0.40, 0.40, and 0.43 respectively. In general, the sound absorption coefficient depended on the total surface area, diameter of pores, shape of aggregate, and micro pores (Arenas *et al*., 2011). The pervious concretes with various amounts of cement pastes had similar SAA values. This was down to the high level of paste content in the mix (100LS25) which reduced the air void size. Although, the sound absorption peak of 100LS25 was lower than that of 100LS15, the wave loop number was similar. Besides that, the pervious concrete using the RC presented SAA values virtually the same as that of 100LS20. Furthermore, the SAA of pervious concrete employing the BA increased with the BA content. This was due to the sound energy loss via friction on the surface of BA, and absorption into numerous pores inside (Arenas *et al.*, 2011).

4. Conclusions

This paper presents the properties of pervious concrete using recycled concrete and coal bottom ash as coarse aggregate replacement. The main conclusions are summarized as follows:

1. The increasing of cement paste volume increased the bulk density of pervious concrete as a result of the reducing of void content in the mixes. For the uses of recycled concrete aggregate (RC) and coal bottom ash aggregate (BA), the void content of pervious concretes significantly increased as the RC and BA replacement levels increased. While, the bulk density of pervious concrete decreased with increasing replacement of RC and BA. The water permeability of pervious concrete also increased with increasing void content.
2. The compressive strengths at 28 days of pervious concretes in this study were higher than 10.5 MPa. The increasing of cement paste volume caused to improve the strength of pervious concrete. In addition, the use of BA brought about pervious concrete with similar compressive strength to that of containing limestone aggregate (LS). Besides that, the compressive strengths of RC pervious concrete were 85-99% of LS pervious concrete.
3. The thermal conductivity of pervious concrete substantially reduced by replacing LS with the RC or BA. Moreover, thermal conductivity lessened as bulk density of pervious concrete declined. Furthermore, the declining of volume of cement paste reduced both the bulk density and thermal conductivity of pervious concretes.
4. The sound absorption coefficients depended on the void content of pervious concrete. The application of RC and BA in pervious concrete gave pervious concretes with higher sound absorption than those containing LS. The optimum sound absorption and low thermal conductivity was obtained with pervious concrete containing BA.

Acknowledgements

The authors sincerely acknowledge the financial support of Rajamangala University of Technology Isan (RMUTI); the Higher Education Research Promotion and National Research University Project of Thailand, Office of the Higher Education Commission, through the Advanced Functional Materials Cluster of Khon Kaen University; the Thailand Research Fund (TRF) and Khon Kaen University under TRF Senior Research Scholar Contract No. RTA5780004.

References

ACI committee 213 (2010). *Guide for structural lightweight-aggregate concrete*. American Concrete Institute, Detroit, USA.

ACI committee 522R-10 (2010). *Pervious concrete.* American Concrete Institute, Detroit, USA.

ASTM C39/C39M–16b (2016). *Standard test method for compressive strength of cylindrical concrete specimens.* Annual Book of ASTM Standard.

ASTM C78/C78M-16 (2016). *Standard test method for flexural strength of concrete (using simple beam with third-point loading),* Annual Book of ASTM Standard.

ASTM C496/C496M-11 (2016). *Standard test method for splitting tensile strength of cylindrical concrete specimens,* Annual Book of ASTM Standard.

ASTM C1754/C1754M-12 (2016). *Standard test method for density and void content of hardened pervious concrete*, Annual Book of ASTM Standard.

Arenas, C., Leiva, C., Vilches, L. F., and Cifuentes, H. (2013). "Use of co-combustion bottom ash to design an acoustic absorbing material for highway noise barriers." *Waste Management,* Vol. 33, Issue 11, pp. 2316-2321, DOI: 10.1016/j.wasman.2013.07.008.

Arenas, C., Vilches, L. F., Cifuentes, H., Leiva, C., Vale, J., and Fernández-Pereira, C. (2011). "Development of acoustic barriers mainly composed of co-combustion bottom ash." *Proceedings of World of Coal Ash*

(WOCA), May 9-12, Denver, Colorado, USA.

Chindaprasirt, P., Hatanaka, S., Chareerat, T., Mishima, M., and Yuasa, Y. (2008). "Cement paste characteristics and porous concrete properties." *Construction and Building Materials,* Vol. 22, Issue 5, pp. 894-901, DOI: 10.1016/j.conbuildmat.2006.12.007.

Chindaprasirt, P., Nuaklong, P., Zaetang, Y., Sujumnongtokul, P., and Sata, V. (2014). "Mechanical and thermal properties of recycling lightweight pervious concrete." *Arabian Journal pf Science and Engineering,* Vol. 39, pp. 3579-3590, DOI: 10.1007/s13369-014-1563-z.

Cristián, G., Armando, M., and Farel, M. (2014). "A method for comparing cores and cast cylinders in virgin and recycled aggregate pervious concrete." *Construction and Building Materials,* Vol. 52, pp. 494-503, DOI: 10.1016/j.conbuildmat.2013.11.043.

Demirboğa, R. and Gül, R. (2003). "The effect of expanded perlite aggregate, silica fume and fly ash on the thermal conductivity of lightweight concrete." *Cement and Concrete Research,* Vol. 33, Issue 5, pp. 723-727, DOI: 10.1016/S0008-8846(02)01032-3.

Golroo, A. and Tighe, S. L. (2011). "Alternative modeling framework for pervious concrete pavement condition analysis." *Cement and Concrete Research,* Vol. 25, Issue 10, pp. 4043-4051, DOI: 10.1016/j.conbuildmat. 2011.04.040.

Haselbach, L. M., Valavala, S., and Montes, F. (2006). "Permeability predictions for sand-clogged Portland cement pervious concrete pavement systems." *Journal of Environmental Management,* Vol. 81, Issue 1, pp. 42-49, DOI: 10.1016/j.jenvman.2005.09.019.

Hemmings, R. T., Cornelius, B. J., Yuran, P., and Wu, M. (2009). "Comparative study of lightweight aggregates." *World of Coal Ash (WOCA),* May 4-7, Lexington, Kentucky, USA.

Hwang, J. P., Shim, H. B., Lim, S., and Ann, K. Y. (2013). "Enhancing the durability properties of concrete containing recycled aggregate by the use of pozzolanic materials." *KSCE Journal of Civil Engineering,* Vol. 18, No. 1, pp. 155-163, DOI: 10.1007/s12205-013-1245-5.

ISO 10534-2 (1998). *Acoustics determination of sound absorption coefficient and impedance or admittance by the impedance tube, Part 2: Transfer function method,* International Organization for Standardization.

Kevern, J. T., Wang, K., and Schaefer, V. R. (2008). "A novel approach to characterize entrained air content in pervious concrete." *Journal of ASTM International*, Vol. 5, No. 2, pp. 1-10, DOI: 10.1520/JAI101434.

Kim, H. K. and Lee, H. K. (2010). "Acoustic absorption modeling of porous concrete considering the gradation and shape of aggregates and void ratio." *Journal of Sound and Vibration,* Vol. 329, pp. 866-879, DOI: 10.1016/j.jsv.2009.10.013.

Kim, H. K. and Lee, H. K. (2015). "Coal bottom ash in field of civil engineering: A review of advanced applications and environmental considerations." *KSCE Journal of Civil Engineering,* Vol. 19, No. 6, pp. 1802-1818, DOI: 10.1007/s12205-015-0282-7.

Kodur, V. K. R. and Sultan, M. A. (2003). "Effect of temperature on thermal properties of high- strength concrete." *Journal of Materials in Civil Engineering,* Vol. 15, No. 2, DOI: 10.1061/(ASCE)0899-1561(2003)15:2(101).

Lee, M. G., Tia, M., Chuang, S. H., and Chiang, C. L. (2014). "Pollution and purification study of the pervious concrete pavement material." *Journal of Materials in Civil Engineering,* Vol. 26, No. 8, DOI: 10.1061/(ASCE)MT.1943-5533.0000916.

Limbachiya, M., Meddah, M. S., and Ouchagour, Y. (2012). "Use of recycled concrete aggregate in fly-ash concrete." *Construction and Building Materials,* Vol. 27, pp. 439-449, DOI: 10.1016/j.conbuildmat. 2011.07.023.

Mirjalili, S. A. and Mohammad-Shah, M. (2012). "Investigation on the acoustic characteristics of multi-layer nonwoven structures Part 1-Multi-layer nonwoven structures with the simple configuration." *Fibres & Textile in Eastern Europe,* Vol. 20, pp. 73-77.

Neithalath, N., Sumanasooriya, M. S., and Deo, O. (2010). "Characterizing pore volume, sizes, and connectivity in pervious concretes for permeability prediction." *Materials Characterization,* Vol. 61, pp. 802-813, DOI: 10.1016/j.matchar.2010.05.004.

Nuaklong, P., Sata, V., and Chindaprasirt, P. (2016). "Influence of recycled aggregate on fly ash geopolymer concrete properties." *Journal of Cleaner Production*, Vol. 112, pp. 2300-2307, DOI: 10.1016/j.jclepro. 2015.10.109.

Park, S. B., Jang, Y. I., Lee, J., and Lee, B. J. (2009). "An experimental study on the hazard assessment and mechanical properties of porous concrete utilizing coal bottom ash coarse aggregate in Korea." *Journal of Hazardous Materials,* Vol. 166, No. 1, pp. 348-355, DOI: 10.1016/j.jhazmat.2008.11.054.

Park, S. B., Seo, D. S., and Lee, J. (2005). "Studies on the sound absorption characteristics of porous concrete based on the content of recycled aggregate and target void ratio." *Cement and Concrete Research,* Vol. 35, Issue 19, pp. 1846-1854, DOI: 10.1016/j.cemconres.2004. 12.009.

Sata, V., Ngohpok, C., and Chindaprasirt, P. (2016). "Properties of pervious concrete containing high-calcium fly ash." *Computer and Concretes*, Vol. 17, Issue 3, pp. 337-351, DOI: 10.12989/cac.2016.17.3.337.

Scanlon, J. M. (1994). "Factors influencing concrete workability." in: P. Klieger, J.F. Lamond (Eds.), Significance of tests properties of concrete and concrete-making, STP 169C, ASTM, Philadelphia, PA.

Schackow, A., Effting, C., Folgueras, M. V., Guths, S., and Mendes, G. A. (2014). "Mechanical and thermal properties of lightweight concretes with vermiculite and EPS using air-entraining agent." *Construction and Building Materials,* Vol. 57, pp. 190-197, DOI: 10.1016/j.conbuildmat.2014.02.009.

Sengula, O., Azizi, S., Karaosmanoglu, F., and Tasdemir, M. A. (2011). "Effect of expanded perlite on the mechanical properties and thermal conductivity of lightweight concrete." *Energy and Buildings,* Vol. 43, pp. 671-676, DOI: 10.1016/j.enbuild.2010.11.008.

Steiger, R. W. and Hurd, M. K. (1978). "Lightweight insulating concrete for floors and roof decks." *Concrete Construction,* Vol. 23, pp. 411-422.

Tho-in, T., Sata, V., Chindaprasirt, P., and Jaturapitakkul, C. (2012). "Pervious high-calcium fly ash geopolymer concrete." *Construction and Building Materials,* Vol. 30, pp. 366-371, DOI: 10.1016/j.conbuildmat.2011.12.028.

Wongsa, A., Zaetang, Y., Sata, V., and Chindaprasirt, P. (2016). "Properties of fly ash geopolymer concrete containing bottom ash as aggregates." *Construction and Building Materials,* Vol. 111, pp. 637-643, DOI: 10.1016/j.conbuildmat.2016.02.135.

Zaetang, Y., Wongsa, A., Sata, V., and Chindaprasirt, P. (2013). "Use of lightweight aggregates in pervious concrete." *Construction and Building Materials,* Vol. 48, pp. 585-591, DOI: 10.1016/j.conbuildmat. 2013.07.077.

ijems@niscair.res.in Aug 9 (13 days ago)

to me

Dear Dr Chindaprasirt,

I am pleased to inform you that your paper IJEMS-6502 has been accepted for publication in Indian Journal of Engineering & Materials Sciences. It would be included in the forthcoming of the journal.

With regards,

Dr R S Beniwal

Editor, IJEMS

CSIR-NISCAIR

New Delhi 110012, INDIA

(12) INTERNATIONAL APPLICATION PUBLISHED UNDER THE PATENT COOPERATION TREATY (PCT)

(19) World Intellectual Property Organization
International Bureau

(43) International Publication Date
3 November 2016 (03.11.2016)

WIPO | PCT

(10) International Publication Number
WO 2016/175714 A1

(51) International Patent Classification:
H01G 9/20 (2006.01)

(21) International Application Number:
PCT/TH2016/000042

(22) International Filing Date:
27 April 2016 (27.04.2016)

(25) Filing Language: English

(26) Publication Language: English

(30) Priority Data:
1501002551 28 April 2015 (28.04.2015) TH

(71) Applicants: **KHON KAEN UNIVERSITY** [TH/TH]; 123 Moo 16 Mittapap Rd., Nai-Muang, Muang District, Khon Kaen 40002 (TH). **THE THAILAND RESEARCH FUND** [TH/TH]; 14th Floor, SM Tower, 979/17-21, Phaholyothin Road, Samsennai, Phayathai, Bangkok 10400 (TH).

(72) Inventors: **CHINDAPRASIRT, Prinya**; The Sustainable Infrastructure Research and Development Center, Dept. of Civil Engineering, Khon Kaen University, Khon Kaen 40002 (TH). **JERERNBOON, Wirat**; The Integrated Nanotechnology Research Center, Department of Physics, Faculty of Science, Khon Kaen University, Khon Kaen 40002 (TH). **AMORNKITBAMRUNG, Vittaya**; The Integrated Nanotechnology Research Center, Department of Physics, Faculty of Science, Khon Kaen University, Khon Kaen 40002 (TH). **RATCHAPOLTHAVISIN, Nattawat**; The Integrated Nanotechnology Research Center, Department of Physics, Faculty of Science, Khon Kaen University, Khon Kaen 40002 (TH).

(74) Agents: **THAVARANUNT, Napawan** et al.; Axis Associates International Co., Ltd., 211/6, 3rd Floor, Ratchadapisek Road, Din Daeng, Din Daeng, Bangkok 10400 (TH).

(81) Designated States *(unless otherwise indicated, for every kind of national protection available)*: AE, AG, AL, AM, AO, AT, AU, AZ, BA, BB, BG, BH, BN, BR, BW, BY, BZ, CA, CH, CL, CN, CO, CR, CU, CZ, DE, DK, DM, DO, DZ, EC, EE, EG, ES, FI, GB, GD, GE, GH, GM, GT, HN, HR, HU, ID, IL, IN, IR, IS, JP, KE, KG, KN, KP, KR, KZ, LA, LC, LK, LR, LS, LU, LY, MA, MD, ME, MG, MK, MN, MW, MX, MY, MZ, NA, NG, NI, NO, NZ, OM, PA, PE, PG, PH, PL, PT, QA, RO, RS, RU, RW, SA, SC, SD, SE, SG, SK, SL, SM, ST, SV, SY, TH, TJ, TM, TN, TR, TT, TZ, UA, UG, US, UZ, VC, VN, ZA, ZM, ZW.

(84) Designated States *(unless otherwise indicated, for every kind of regional protection available)*: ARIPO (BW, GH, GM, KE, LR, LS, MW, MZ, NA, RW, SD, SL, ST, SZ, TZ, UG, ZM, ZW), Eurasian (AM, AZ, BY, KG, KZ, RU, TJ, TM), European (AL, AT, BE, BG, CH, CY, CZ, DE, DK, EE, ES, FI, FR, GB, GR, HR, HU, IE, IS, IT, LT, LU, LV, MC, MK, MT, NL, NO, PL, PT, RO, RS, SE, SI, SK, SM, TR), OAPI (BF, BJ, CF, CG, CI, CM, GA, GN, GQ, GW, KM, ML, MR, NE, SN, TD, TG).

[Continued on next page]

(54) Title: CARBON NANOTUBE - CEMENT COMPOSITE COMPOSITION FOR CATALYSIS ON COUNTER ELECTRODES OF DYE SENSITIZED SOLAR CELLS

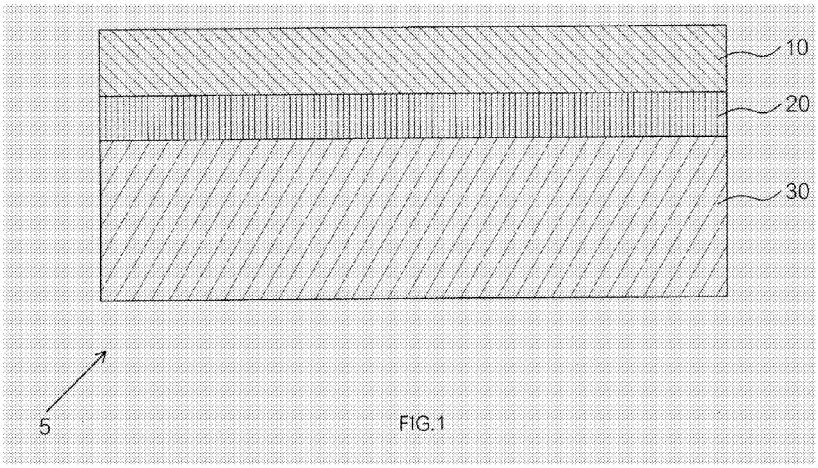

FIG.1

(57) Abstract: In accordance with embodiments of the present disclosure, a catalyst layer for electrolyte based tri-iodide/iodine redox couples of a dye- sensitized solar cell (DSSC) includes carbon nanotubes and cement, such as a conventional type of cement suitable for use as an infrastructure construction or building material. Representative example catalyst layers were prepared by mixing carbon nanotube powders with cement powder as a binder, and such catalyst layers were coated on a transparent conducting oxide (TCO) glass substrate using a painting technique without heating. By mixing carbon nanotubes and cement at different carbon nanotube to cement weight percentage ratios, i.e., 17:83, 29:71, 38:62, 44:56 and 50:50, to establish an appropriate cement fraction, catalyst layers with low electrical resistivity, high electro-catalytic activity, and excellent photoelectric conversion efficiency have been fabricated, where the photoelectric conversion efficiency has been measured as 85.56% of that of a DSSC having a conventional platinum catalyst based counter electrode.

WO 2016/175714 A1

Declarations under Rule 4.17:

— *as to the applicant's entitlement to claim the priority of the earlier application (Rule 4.17(iii))*

Published:

— *with international search report (Art. 21(3))*

CARBON NANOTUBE – CEMENT COMPOSITE COMPOSITION FOR CATALYSIS ON COUNTER ELECTRODES OF DYE SENSITIZED SOLAR CELLS

TECHNICAL FIELD

Aspects of the present disclosure are directed to a carbon - cement based catalyst layer that acts as a photoelectric conversion material or element in a dye-sensitized solar cell (DSSC).

BACKGROUND

Dye-sensitized solar cells (DSSCs) have existed since 1991, as described by B. O'Regan and M. *Grätzel (B.O'Regan and M. Grätzel. A Low-cost, high-efficiency solar cell based on dye-sensitized colloidal TiO_2 films. Nature. 1991: 353; 737-740).* The efficiency of DSSCs has reached at least 7%. The typical configuration of a DSSC consists of a working electrode, also called a photo-electrode; an electrolyte solution; and a counter electrode. The working electrode acts as an anode, and is typically formed from a transparent conductive oxide (TCO) glass substrate coated with mesoporous titanium dioxide nanoparticles, and anchored with sensitizer molecules capable of harvesting energy in the visible region of the electromagnetic spectrum (400-700 nm).

The liquid electrolyte, which is in the middle between both electrodes, contains tri-iodide/iodide as a redox couple.

The counter electrode acts as a cathode, and consists of a catalyst layer such as platinum, carbon, conducting polymer, metal oxide, metal sulfide and metal carbide coated on transparent conductive oxide glass. The catalyst is used for reducing tri-iodide ions (I_3^-) to iodide ions (I^-) in an electrolyte. In other words, the catalyst material(s) transfer electrons from an external load to an electrolyte solution.

When the cell is under sunlight illumination, the dye molecules in the ground state will absorb photons in the visible spectral region, and then jump to an excited state; while titanium dioxide will absorb higher energy photons outside of the visible spectral region,

i.e., the ultra-violet region. The excited dye injects an electron into the conduction band (CB) of the titanium dioxide which is coated on the TCO, and consequently becomes oxidized dye. An electron is transferred to an external circuit via the working electrode, and goes back to the cell via the counter electrode. A tri-iodide molecule is reduced by receiving an electron from the counter electrode, and correspondingly becomes iodide. Meanwhile, the oxidized dye will receive an electron from the iodide molecule via a redox reaction, returning back to its original state. At this stage, the mechanism is closed and still working as long as the cell remains in the aforementioned light illumination condition.

At present, the three main DSSC components, i.e., working electrode, electrolyte solution, and counter electrode, have been intensively developed to improve DSSC performance. The counter electrode consisting of catalyst material(s) coated on the substrate is one important component. Improving the performance of the counter electrode is an effective approach to enhance DSSC performance and reduce the DSSC fabrication cost. A DSSC requires a counter electrode having platinum, which is an expensive rare-earth element, as a catalyst because of its high electrochemical activity and low resistivity. Many efforts have been proposed for solving the issue of requiring this expensive element by replacing it with other efficient yet less expensive materials. Carbon is a suitable candidate because of various special properties, such as high surface area, low cost, high electrical conductivity, and easy synthesis. Several forms of carbon materials can be utilized, such as carbon nanotubes, nanoparticles, and graphene sheets.

Lee and his research group *(W.J. Lee et al. Efficient Dye-sensitized Solar Cells with Catalytic Multiwall Carbon Nanotube Counter Electrodes. Applied Materials & Interfaces 2009: 1(6): 1145-1149)* fabricated DSSCs with multi-walled carbon nanotubes (MWCNTs) as the catalyst. The MWCNTs were mixed with a binder, and then coated on a transparent conductive oxide glass substrate using a screen printing technique. The substrates coated with MWCNT were sintered at 50 °C for 10 hours. The samples were then applied as counter electrodes of DSSCs. It was found from performance testing that a DSSC with the MWCNT catalyst gave an efficiency of 7.67% which is comparable to that of the Pt catalyst (7.85%).

Zhang and his research group *(Zhang D et al. Performance of Dye-Sensitized Solar Cells with Various Carbon Nanotube Counter Electrodes. Microchimica Acta 2011: 174; 73-79)* studied the efficiency of DSSCs having various forms of carbon, i.e., multi-walled carbon nanotubes (MWCNTs), double-walled carbon nanotubes (DWCNTs), and single-walled carbon nanotubes (SWCNTs) as catalysts. The efficiency of DSSCs with the DWCNT as catalyst was 8.03% while cells with SWCNT and MWCNT showed efficiency of 7.61% and 7.06%, respectively, which can comparable to what this group measured for the Pt catalyst (8.49%).

As mentioned above, carbon nanotubes can be used as an efficient catalyst for DSSCs, and the performance of DSSCs that utilize carbon nanotubes as the catalyst can be comparable to that for platinum catalysts. However, a binder is needed for carbon catalyst layer preparation in order to improve adhesion between carbon nanotubes-carbon nanotubes and carbon nanotubes-TCO glass substrate. The most common binder is a conductive polymer, which unfortunately is not stable at high temperatures, and which is undesirably expensive.

SUMMARY

In accordance with aspects of the present disclosure, at least one type of cementitious material, cement based material, cement material, or cement (hereafter cement for purpose of brevity and simplicity) having good mechanical properties and high porosity, and which can typically include calcined limestone and clay material, and/or which can be formed or provided as a powder that includes various compounds such as alumina, lime, iron oxide, and magnesium oxide that have been burned together in a kiln and subsequently pulverized, is utilized as a binder material or binder for carbon based counter electrodes of DSSCs. The cement can include or be conventional cement that is suitable for use as a physical infrastructure construction material (e.g., a building construction material), such as a conventional type of Portland cement. Various embodiments in accordance with the present disclosure utilize cement as the DSSC counter electrode binder instead of using a conventional conductive polymer binder. More particularly, various embodiments in accordance with the present disclosure provide a carbon based material – cement counter electrode structure or counter electrode for DSSC applications, which is referred to hereafter as a carbon – cement counter electrode structure or carbon – cement counter

electrode. DSSCs using a carbon – cement counter electrode, which includes a carbon based catalyst combined or mixed with cement as the counter electrode binder, and which can omit or exclude a conductive polymer binder. A carbon – cement counter electrode in accordance with embodiments of the present disclosure can be inexpensively fabricated and can achieve high power conversion efficiency, as further detailed below.

In general, a carbon – cement counter electrode in accordance with various embodiments of the present disclosure includes three layers, namely: (i) a carbon based or carbon material mixed with cement as a catalyst layer; (ii) a TCO layer; and (iii) a transparent substrate (e.g., a glass substrate). The carbon material, which can include or be in the form of carbon nanomaterials, nanostructures, or nanoparticles such as carbon nanotubes, exhibits high catalytic activity as well as low resistivity, similar to a conventional platinum catalyst; while the cement is used to improve adhesion between the carbon nanotubes and the TCO layer carried by the substrate, and can further aid adhesion between carbon nanotubes and the substrate itself.

An objective of particular embodiments in accordance with the present disclosure is the use of carbon nanotubes as a DSSC counter electrode catalyst material, and cement as the counter electrode binder. A DSSC having a carbon material mixed with cement as its catalyst layer can achieve high power conversion efficiency generally comparable or comparable to that for conventional DSSCs that utilize a platinum catalyst. Furthermore, the use of cement as binder provides a suitable, simple, reliable, easily manufacturable, and inexpensive replacement for conventional conductive polymer binders.

In accordance with an aspect of the present disclosure, a counter electrode structure for a dye-sensitized solar cell (DSSC) includes: (i) a carbon – cement catalyst layer that includes cement comprising calcined limestone and a clay material, and carbon nanotubes mixed with the cement; (ii) a transparent conductive oxide (TCO) layer in contact with the catalyst layer; and (iii) a substrate that carries the TCO layer and the catalyst layer, wherein the cement serves as a binder material that facilitates adhesion of the carbon nanotubes to the TCO layer. Such a DSSC counter electrode structure need not include, and can exclude, electrically conductive polymer. The carbon – cement catalyst layer acts as a catalyst for electrolyte based tri-iodide and iodide redox couples, and the TCO layer

acts as an electron carrier from a load to the carbon – cement catalyst layer. The carbon – cement catalyst layer typically has a thickness of 10.0 – 100.0 microns.

The cement typically includes silicon dioxide, aluminum oxide, calcium oxide, sulfur trioxide, magnesium oxide, and iron oxide. For instance, the cement can include carbon, silicon, oxygen, aluminum, iron, sulfur, calcium, and magnesium at respective volumetric concentrations of 10.0-20.0%, 2.0-10.0%, 30.0-60.0%, 1.0-5.0%, 0.2-5.0%, 0.5-5.0%, 10.0-40.0%, and 0.1-1.0% in relative amounts that sum to 100%. The carbon – cement catalyst layer includes carbon, oxygen, silicon, aluminum, iron, sulfur, magnesium, and calcium. The carbon nanotubes typically include at last one of single-walled carbon nanotubes (SWCNTs), double-walled carbon nanotubes (DWCNTs), and multi-walled carbon nanotubes (MWCNTs).

In various embodiments, the relative weight percentage ratio of carbon nanotubes to cement is selected to fall within a range of 27:73 to 37:63. The weight percentage ratio of carbon nanotubes to cement can be selected to provide a particular, target, or minimum power conversion efficiency, such as a power conversion efficiency greater than or equal to approximately 9.3%. In some embodiments, the weight percentage ratio of carbon nanotubes to cement is 29.0:71.0.

The TCO layer can include one of fluorine doped tin oxide, indium doped tin dioxide, aluminum doped zinc oxide, gallium doped zinc oxide, germanium doped indium oxide, titanium metal, and stainless steel metal.

In accordance with an aspect of the present disclosure, a process for fabricating a carbon – cement counter electrode structure for a dye-sensitized solar cell (DSSC) includes: (i) grinding carbon nanotubes together with a cement powder to obtain a homogeneous carbon nanotube – cement powder mixture; (ii) adding deionized (DI) water to the homogenous carbon nanotube – cement powder mixture to form a paste; (iii) grinding the paste to form a homogeneous paste; (iv) providing a substrate that carries a transparent conductive oxide (TCO) layer thereon; (v) coating the homogeneous paste onto the substrate; and (vi) drying the paste coated on the substrate.

Adding DI water can include adding 8 parts by volume of DI water to one part by volume of the homogeneous carbon nanotube – cement powder mixture. Drying the paste typically